Conference Proceedings of the Society for Experimental Mechanics Series

Gaetan Kerschen *Editor*

Nonlinear Dynamics, Volume 1

Proceedings of the 34th IMAC, A Conference and Exposition on Structural Dynamics 2016

Springer

Conference Proceedings of the Society for Experimental Mechanics Series

Series Editor
Kristin B. Zimmerman, Ph.D.
Society for Experimental Mechanics, Inc.,
Bethel, CT, USA

More information about this series at http://www.springer.com/series/8922

Gaetan Kerschen
Editor

Nonlinear Dynamics, Volume 1

Proceedings of the 34th IMAC, A Conference and Exposition on Structural Dynamics 2016

Springer

Editor
Gaetan Kerschen
University of Liege in Belgium
Liege, Belgium

ISSN 2191-5644 ISSN 2191-5652 (electronic)
Conference Proceedings of the Society for Experimental Mechanics Series
ISBN 978-3-319-29738-5 ISBN 978-3-319-29739-2 (eBook)
DOI 10.1007/978-3-319-29739-2

Library of Congress Control Number: 2016937010

Printed on acid-free paper

This Springer imprint is published by Springer Nature
The registered company is Springer International Publishing AG Switzerland

Preface

Nonlinear Dynamics represents one of ten volumes of technical papers presented at the 34th IMAC, A Conference and Exposition on Structural Dynamics, organized by the Society for Experimental Mechanics and held in Orlando, Florida, on January 25–28, 2016. The full proceedings also include volumes on *Dynamics of Civil Structures*; *Model Validation and Uncertainty Quantification*; *Dynamics of Coupled Structures*; *Sensors and Instrumentation*; *Special Topics in Structural Dynamics*; *Structural Health Monitoring, Damage Detection & Mechatronics*; *Rotating Machinery, Hybrid Test Methods, Vibro-Acoustics and Laser Vibrometry*; *Shock & Vibration, Aircraft/Aerospace, Energy Harvesting, Acoustics & Optics*; and *Topics in Modal Analysis &Testing*.

Each collection presents early findings from experimental and computational investigations on an important area within structural dynamics. Nonlinearity is one of these areas.

The vast majority of real engineering structures behave nonlinearly. Therefore, it is necessary to include nonlinear effects in all the steps of the engineering design: in the experimental analysis tools (so that the nonlinear parameters can be correctly identified) and in the mathematical and numerical models of the structure (in order to run accurate simulations). In so doing, it will be possible to create a model representative of the reality which, once validated, can be used for better predictions.

Several nonlinear papers address theoretical and numerical aspects of nonlinear dynamics (covering rigorous theoretical formulations and robust computational algorithms) as well as experimental techniques and analysis methods. There are also papers dedicated to nonlinearity in practice where real-life examples of nonlinear structures will be discussed.

The organizers would like to thank the authors, presenters, session organizers, and session chairs for their participation in this track.

Liege, Belgium — Gaetan Kerschen

Contents

Chapter 1
Nonlinear Vibrations of a Beam with a Breathing Edge Crack Using Multiple Trial Functions

Ali C. Batihan and Ender Cigeroglu

Abstract In this paper, a beam like structure with a single edge crack is modeled and analyzed in order to study the nonlinear effects of breathing crack on transverse vibrations of a beam. In literature, edge cracks are generally modeled as open cracks, in which the beam is separated into two pieces at the crack location and these pieces are connected to each other with a rotational spring to represent the effect of crack. The open edge crack model is a widely used assumption; however, it does not consider the nonlinear behavior due to opening and closing of the crack region. In this paper, partial differential equation of motion obtained by Euler-Bernoulli beam theory is converted into nonlinear ordinary differential equations by using Galerkin's method with multiple trial functions. The nonlinear behavior of the crack region is represented as a bilinear stiffness matrix. The nonlinear ordinary differential equations are converted into a set of nonlinear algebraic equations by using harmonic balance method (HBM) with multi harmonics. Under the action of a harmonic forcing, the effect of crack parameters on the vibrational behavior of the cracked beam is studied.

Keywords Breathing crack • Euler-Bernoulli beam • Galerkin's method • Harmonic balance method • Nonlinear vibrations

1.1 Introduction

Identification of cracks and determination of their location is an important consideration, since crack propagation may cause unexpected failure. Therefore, beams with edge cracks has been an interesting area of research. Dimarogonas [1] provides a review paper in which studies on open breathing crack, continuous crack beam theories and vibration of cracked plates are covered. Aydin [2], carried out a study considering arbitrary number of cracks and axial loads applied on a beam. Khiem and Lien [3], used a transfer matrix method in order to calculate natural frequencies of a beam with an arbitrary number of cracks. In order to see the effect of crack clearly, beam models with mass attachments are used by Mermertaş and Erol [4] and Zhong and Oyadiji [5]. Mazanoğlu et al. [6] applied Rayleigh-Ritz and finite element methods in order to study vibrations of non-uniform cracked beams. In a study of Chondros et al. [7], flexibility due to crack region is distributed along the whole beam by developing a continuous theory of cracked beams. In another study of Chondros et al. [8], breathing edge crack was studied by combining vibration characteristics of open and closed period as a bi-linear model. Cheng et al. [9] represented the breathing crack with time dependent stiffness. Finite element method was used by Chati et al. [10] in order to study modal analysis of a beam with a breathing edge crack. Giannini et al. [11] also used finite element method to identify sub and super harmonics of a beam with a breathing edge crack. Baeza and Ouyang [12], developed an analytical approach by using beam modes to calculate a scale factor matrix which indicates crack location.

In most of the studies available in literature, the beam is modeled by Euler-Bernoulli beam theory and the crack region is represented by a rotational spring whose stiffness is obtained by fracture mechanics methods. A significant number of studies are investigated the effect of crack parameters on natural frequencies. In addition, application of finite element methods for beams with breathing edge cracks is a common modeling approach.

In this paper, based on the previous study of authors [13], beam is modeled using Euler-Bernoulli beam theory and breathing edge crack is modeled as a piecewise linear stiffness. In the analytical model, the state of the crack is determined by checking the slope difference at the crack location. The governing equations are obtained by Galerkin's method utilizing multiple trial functions and the resulting set of nonlinear equations are solved by application of harmonic balance method with multi harmonics.

A.C. Batihan • E. Cigeroglu (✉)
Department of Mechanical Engineering, Middle East Technical University, Ankara 06800, Turkey
e-mail: ender@metu.edu.tr

G. Kerschen (ed.), *Nonlinear Dynamics, Volume 1*, Conference Proceedings of the Society for Experimental Mechanics Series,
DOI 10.1007/978-3-319-29739-2_1

1.2 Formulation of the Breathing Edge Crack Problem

Equation of motion of a uniform beam vibrating in transverse direction under the action of an external point force $f(t)$ located at L_f can expressed by utilizing Euler-Bernoulli beam theory as follows

$$EI\frac{\partial^4 w(x,t)}{\partial x^4} + c\frac{\partial w(x,t)}{\partial t} + m\frac{\partial^2 w(x,t)}{\partial t^2} = f(t)\delta\left(x - L_f\right), \tag{1.1}$$

where $w(x,t)$ is transverse displacement, EI is flexural rigidity, c is viscous damping coefficient and m is mass per unit length of the beam. Using expansion theorem, transverse displacement can be expressed as follows

$$w(x,t) = \sum_j a_j(t)\phi_j(x), \tag{1.2}$$

where $\phi_j(x)$ is the j^{th} mass normalized eigenfunction of a beam with an open edge crack and $a_j(t)$ is the corresponding modal coefficient. Substituting Eq. (1.2) into Eq. (1.1), the following expression is obtained

$$\sum_j \left(EIa_j(t)\frac{d^4\phi_j(x)}{dx^4}\right) + \sum_j \left(c\dot{a}_j(t)\phi_j(x)\right) + \sum_j \left(m\ddot{a}_j(t)\phi_j(x)\right) = f(t)\delta\left(x - L_f\right). \tag{1.3}$$

Multiplying Eq. (1.3) by $\phi_i(x)$ and integrating over the spatial domain of the beam result in the following equation

$$\sum_j \left(k_{ij}\right) a_j(t) + \sum_j \left(c_{ij}\right)\dot{a}_j(t) + \sum_j \left(m_{ij}\right)\ddot{a}_j(t) = F_i(t), \tag{1.4}$$

where

$$k_{ij} = \int_0^L EI\phi_i(x)\frac{d^4\phi_j(x)}{dx^4}dx, \tag{1.5}$$

$$c_{ij} = \int_0^L c\phi_i(x)\phi_j(x)dx, \tag{1.6}$$

$$m_{ij} = \int_0^L m\phi_i(x)\phi_j(x)dx, \tag{1.7}$$

$$F_i(t) = \phi_i\left(L_f\right)f(t). \tag{1.8}$$

Equation (1.4) can be rearranged as a matrix equation as follows

$$[M]\{\ddot{a}\} + [C]\{\dot{a}\} + [K]\{a\} = \{F\}, \tag{1.9}$$

where $[M]$, $[C]$ and $[K]$ are the corresponding mass, damping and stiffness matrices of a beam with an open edge crack.

Figure 1.1 shows the deformed shape of a cantilever crack beam at two different time instants. During vibration, due to breathing effect of the edge crack, the beam behaves as if it is an undamaged beam for some period of cycle; whereas, in the rest of the cycle it behaves as a beam with an open edge crack. Therefore, beam with a breathing edge crack can be represented as a combination of two linear systems as shown in Fig. 1.1.

In order to consider the breathing effect, two different sets of mass normalized eigenfunctions are utilized as trial functions. For the time instant when the crack is closed, mass, damping and stiffness matrices are calculated by utilizing first few mass normalized eigenfunctions of the undamaged beam; whereas mass normalized eigenfunctions of a beam with an open crack are used in case the crack is in open state. The details and derivation of these eigenfunctions can be found in [14]. As the

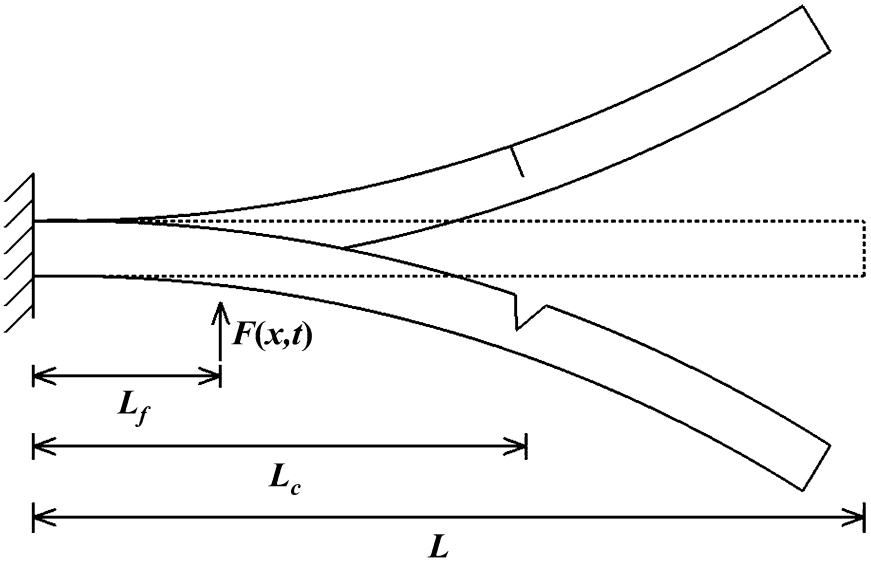

Fig. 1.1 Cantilever beam with a breathing edge crack

crack switches from open state to closed state, mass and damping matrices remain unchanged; however, the stiffness matrix increases when the crack closes. The increase in the stiffness matrix is given by the following relation

$$[B] = [K_c] - [K]\,, \tag{1.10}$$

where $[K_c]$ is the stiffness matrix of the beam when the crack is at the closed state.

In this study, in order to identify whether the crack is open or not, the slope difference at the crack location is checked. Negative slope difference states that the crack is open and the nonlinear forcing term is zero; whereas positive slope difference indicates that the crack is closed and the nonlinear forcing term is nonzero. The periodic change in the stiffness of the beam which results from the breathing effect of the crack, leads to the following nonlinear forcing term

$$\{R(\{a\})\} = \begin{cases} [B]\{a\} & if \ \left.\frac{\partial w(x,t)}{\partial x}\right|_{x=L_c} \geq 0 \\ \{0\} & if \ \left.\frac{\partial w(x,t)}{\partial x}\right|_{x=L_c} < 0 \end{cases}. \tag{1.11}$$

Adding the nonlinear forcing term $\{R(\{a\})\}$, into Eq. (1.9) leads to the following equation in which the breathing effect of the crack is taken into consideration

$$[M]\{\ddot{a}\} + [C]\left\{\dot{a}\right\} + [K]\{a\} + \{R(\{a\})\} = \{F\}\,. \tag{1.12}$$

1.3 Harmonic Balance Method

In order to utilize harmonic balance method with multi harmonics, modal coefficient of each trial function is expressed as follows

$$a_j(t) = a_{j0} + \sum_p a_{jcp}\cos(p\omega t) + \sum_p a_{jsp}\sin(p\omega t), \tag{1.13}$$

where a_{j0} is the bias term of the j^{th} modal coefficient, a_{jcp} and a_{jsp} are the coefficients of cosine and sine components of the p^{th} harmonic of the j^{th} modal coefficient. Letting $\theta = \omega t$ and rearranging Eq. (1.13), the modal coefficients can be written in vector form as

$$\{a\} = \{a_0\} + [a_c]\{h_c(\theta)\} + [a_s]\{h_c(\theta)\}, \tag{1.14}$$

where

$$[a_c] = \left[\{a_{c1}\} \cdots \{a_{cp}\}\right], \tag{1.15}$$

$$[a_s] = \left[\{a_{s1}\} \cdots \{a_{sp}\}\right], \tag{1.16}$$

and $\{h_c(\theta)\}$ & $\{h_s(\theta)\}$ are the following vectors whose lengths are equal to the number harmonics (p) used

$$\{h_c(\theta)\} = \begin{Bmatrix} \cos(\theta) \\ \vdots \\ \cos(p\theta) \end{Bmatrix}, \tag{1.17}$$

$$\{h_s(\theta)\} = \begin{Bmatrix} \sin(\theta) \\ \vdots \\ \sin(p\theta) \end{Bmatrix}. \tag{1.18}$$

The periodic nonlinear forcing term $\{R(\{a\})\}$ can be expressed by Fourier series as

$$\{R\} = \frac{1}{2}\{R_0\} + [R_c]\{h_c(\theta)\} + [R_s]\{h_s(\theta)\}. \tag{1.19}$$

where

$$[R_c] = \left[\{R_{c1}\} \cdots \{R_{cp}\}\right], \tag{1.20}$$

$$[R_s] = \left[\{R_{s1}\} \cdots \{R_{sp}\}\right], \tag{1.21}$$

and

$$R_{j0} = \frac{1}{\pi}\int_0^{2\pi} R_j(\theta)\, d\theta, \tag{1.22}$$

$$R_{jcp} = \frac{1}{\pi}\int_0^{2\pi} R_j(\theta)\cos(p\theta)\, d\theta, \tag{1.23}$$

$$R_{jsp} = \frac{1}{2\pi}\int_0^{2\pi} R_j(\theta)\sin(p\theta)\, d\theta. \tag{1.24}$$

Similarly external forcing, $f(t)$ can be represented by Fourier series as follows

$$f(t) = \{f_{cp}\}'\{h_c(\theta)\} + \{f_{sp}\}'\{h_s(\theta)\}. \tag{1.25}$$

Substituting Eqs. (1.14), (1.19) and (1.25) into Eq. (1.12) and collecting sine and cosine terms leads to the following set of nonlinear equations

$$\left(\begin{bmatrix}[K] & & 0\\ & \ddots & \\ 0 & & [K]\end{bmatrix} - \omega^2 \begin{bmatrix}[M] & & 0\\ & \ddots & \\ 0 & & [M]\end{bmatrix}\begin{bmatrix}[I] & & \\ & \ddots & \\ & & p^2\,[I]\end{bmatrix}\right)\begin{Bmatrix}\{a_{c1}\}\\ \vdots \\ \{a_{cp}\}\end{Bmatrix} + \begin{Bmatrix}\{R_{c1}\}\\ \vdots \\ \{R_{cp}\}\end{Bmatrix}$$
$$+\omega\begin{bmatrix}[C] & & 0\\ & \ddots & \\ 0 & & [C]\end{bmatrix}\begin{bmatrix}[I] & & \\ & \ddots & \\ & & p\,[I]\end{bmatrix}\begin{Bmatrix}\{a_{s1}\}\\ \vdots \\ \{a_{sp}\}\end{Bmatrix} - \begin{bmatrix}[\phi_{L_f}] & & 0\\ & \ddots & \\ 0 & & [\phi_{L_f}]\end{bmatrix}\begin{Bmatrix}f_{c1}\,\{I\}\\ \vdots \\ f_{cp}\,\{I\}\end{Bmatrix} = \begin{Bmatrix}\{0\}\\ \vdots \\ \{0\}\end{Bmatrix}, \tag{1.26}$$

$$\left(\begin{bmatrix}[K] & & 0\\ & \ddots & \\ 0 & & [K]\end{bmatrix} - \omega^2 \begin{bmatrix}[M] & & 0\\ & \ddots & \\ 0 & & [M]\end{bmatrix}\begin{bmatrix}[I] & & \\ & \ddots & \\ & & p^2\,[I]\end{bmatrix}\right)\begin{Bmatrix}\{a_{s1}\}\\ \vdots \\ \{a_{sp}\}\end{Bmatrix} + \begin{Bmatrix}\{R_{s1}\}\\ \vdots \\ \{R_{sp}\}\end{Bmatrix}$$
$$+\omega\begin{bmatrix}[C] & & 0\\ & \ddots & \\ 0 & & [C]\end{bmatrix}\begin{bmatrix}[I] & & \\ & \ddots & \\ & & p\,[I]\end{bmatrix}\begin{Bmatrix}\{a_{c1}\}\\ \vdots \\ \{a_{cp}\}\end{Bmatrix} - \begin{bmatrix}[\phi_{L_f}] & & 0\\ & \ddots & \\ 0 & & [\phi_{L_f}]\end{bmatrix}\begin{Bmatrix}f_{s1}\,\{I\}\\ \vdots \\ f_{sp}\,\{I\}\end{Bmatrix} = \begin{Bmatrix}\{0\}\\ \vdots \\ \{0\}\end{Bmatrix}, \tag{1.27}$$

$$[K]\{a_0\} + \frac{1}{2}\{R_0\} = \{0\}, \tag{1.28}$$

where $[I]$ is the identity matrix, $\{I\}$ is a vector elements of which are all 1, and

$$\left[\phi_{L_f}\right] = \begin{bmatrix}\phi_1\left(L_f\right) & & 0\\ & \ddots & \\ 0 & & \phi_j\left(L_f\right)\end{bmatrix}. \tag{1.29}$$

1.4 Case Study and Discussion

Effect of breathing edge crack for different crack parameters is studied by using a cantilever beam model with the following properties: $L = 1$ m, $I = 2.667 \cdot 10^{-8}$ m^4, $\rho = 7850$ kg/m^3, $A = 8 \cdot 10^{-4}$ m^2, $E = 206$ GPa, $\zeta = 0.07$, $L_f = 0.1$ m and $f(t) = 100\cos(\omega t)$ N. Galerkin's method is applied by utilizing first three modes of the beam and the resulting set of nonlinear ordinary differential equations are converted into a set of nonlinear algebraic equations by using harmonic balance method with multi harmonics. According to [13], as crack ratio increases fundamental frequency decreases. Similarly, crack location also affects the fundamental frequency depending on the boundary conditions of the beam. The effect of different crack ratio and crack location on natural frequencies is given in Fig. 1.2. It is observed from the results that the effect of crack parameters on natural frequencies are not significant. Therefore, alternative features should be considered in crack detection problems.

In Fig. 1.3, absolute value of bias term of each modal coefficient as function of frequency is given. It is observed that bias term of each modal coefficient is influenced by both crack location and crack ratio. In Fig. 1.3a, bias term of each modal coefficient is plotted for different crack locations and it is observed that depending on the crack location bias term of different modal coefficient becomes dominant. Bias terms are also affected by the crack ratio, however the effect of crack ratio is not similar to the effect of crack location. For instance, from Fig. 1.3b it is observed that, an increase in crack depth shifts all the plots upward and the order of dominancy is conserved.

The amplitude of p^{th} harmonic of j^{th} modal coefficient is expressed by the following equation

$$a_{jp} = \sqrt{{a_{jcp}}^2 + {a_{sjp}}^2}. \tag{1.30}$$

In Fig. 1.4, amplitudes of the first harmonic of modal coefficients with respect to frequency are given for different crack location and ratio. From the plots, it is observed that first harmonics are slightly influenced by crack parameters. However, the first harmonic is the most dominant harmonic on the total response among the higher harmonics. This fact also explains why crack parameters have negligible effect on the total response.

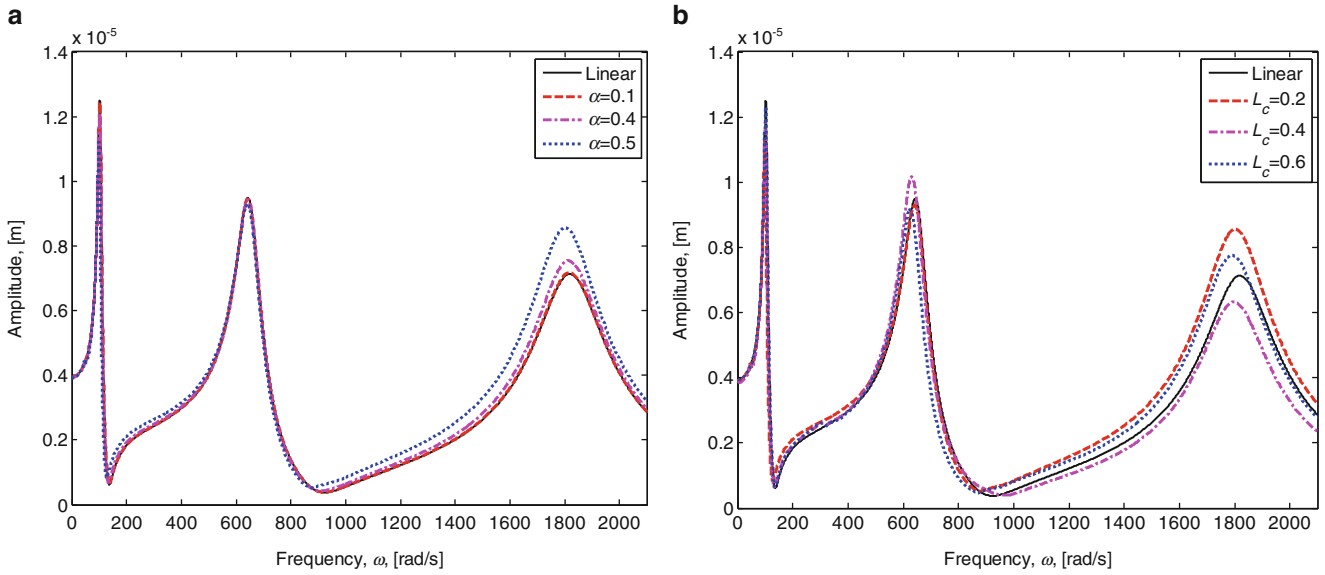

Fig. 1.2 Transverse displacement of a point at location $L_p = 0.1$ m vs. frequency. (**a**) For $L_c = 0.2$ m and different crack ratio. (**b**) For $\alpha = 0.5$ and different crack location

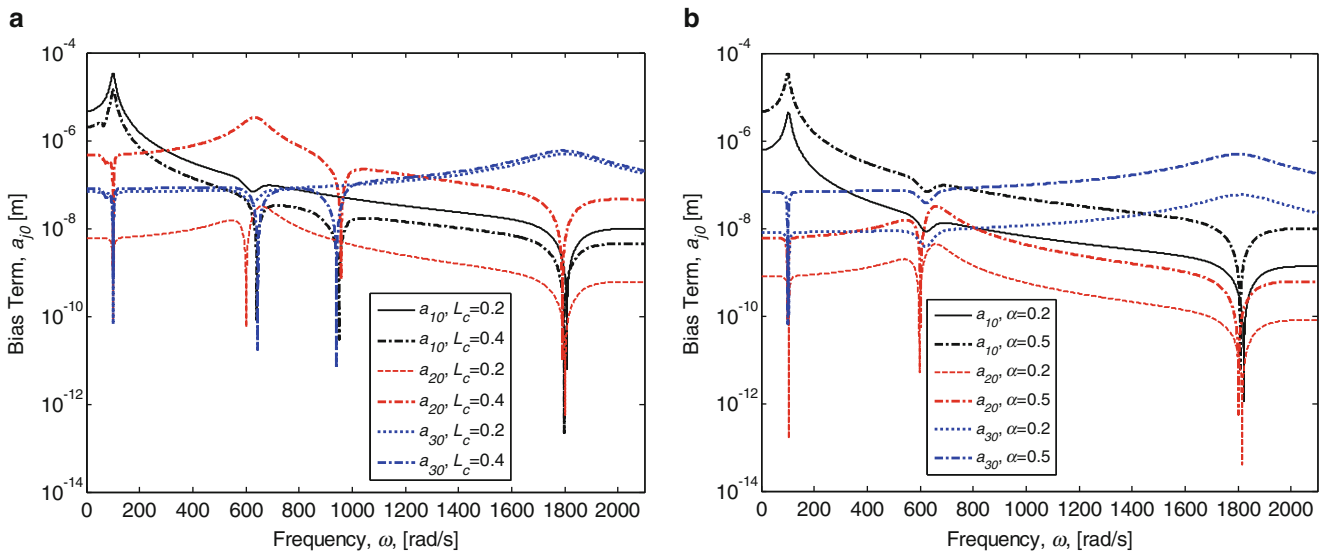

Fig. 1.3 Bias term of each modal coefficient vs. frequency. (**a**) For $\alpha = 0.5$ and different crack location. (**b**) For $L_c = 0.2$ m and different crack ratio

Higher harmonics of different trial functions for different crack parameters are shown in Figs. 1.5, 1.6, 1.7, and 1.8. Studying these figures, it is observed that higher harmonics can be grouped as even and odd harmonics depending on the similarities of the plots. Observing Figs. 1.5 and 1.6, it is seen that effect of crack parameters on even harmonics is similar to the effect of crack parameters on bias terms. As crack location changes, even harmonic of a different trial function becomes more dominant; whereas increase in crack depth causes an increase in the overall amplitude of the even harmonics.

Effect of crack parameters can also be observed in the odd harmonics. As depicted in Figs. 1.7 and 1.8, effect of crack location on odd harmonics is similar to the effect of crack location on bias terms and even harmonics. Studying the same figures, it is also observed that, odd harmonics of the first modal coefficient are significantly affected by crack depth. However, getting information from the odd harmonics of the second and the third modal coefficient is a more challenging due to scattered pattern. Therefore, analyzing the even harmonics can be used as means for crack detection problems. In Table 1.1,

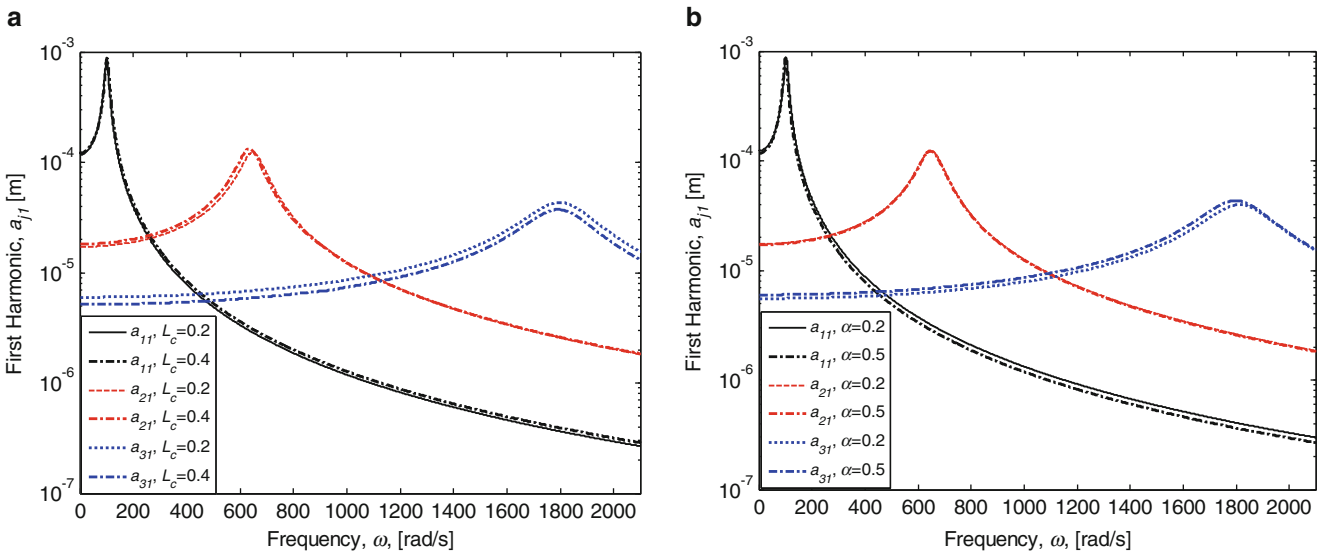

Fig. 1.4 First harmonic of each modal coefficient vs. frequency. (**a**) For $\alpha = 0.5$ and different crack location. (**b**) For $L_c = 0.2$ m and different crack ratio

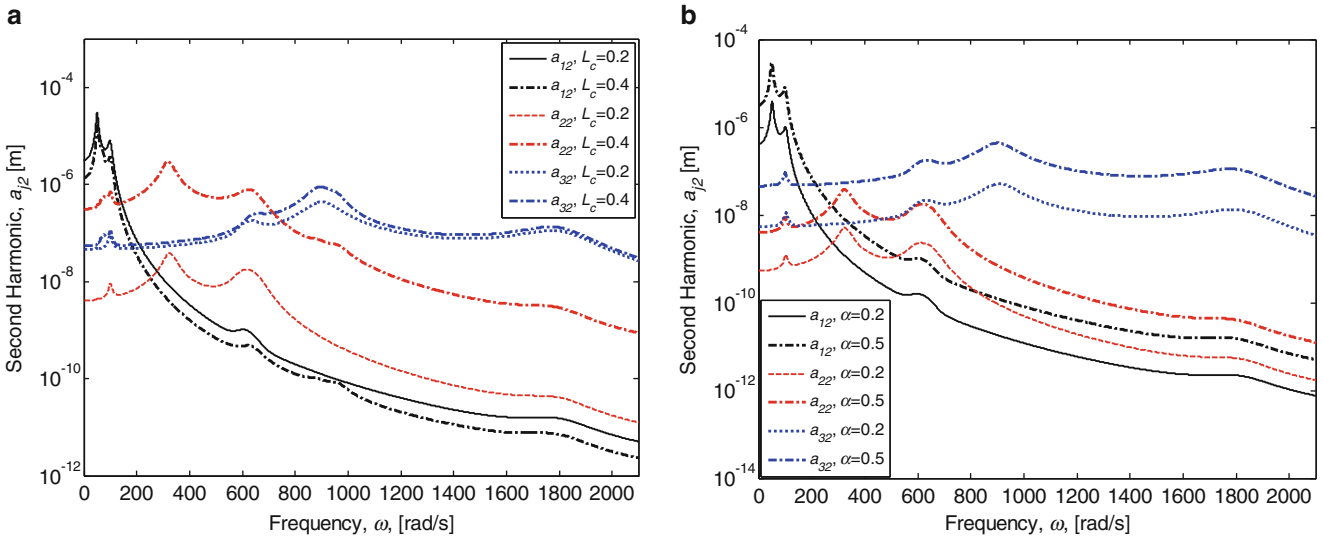

Fig. 1.5 Second harmonic of each modal coefficient vs. frequency. (**a**) For $\alpha = 0.5$ and different crack location. (**b**) For $L_c = 0.2$ m and different crack ratio

ratio of maximum amplitudes of the even harmonics are provided. The ratio is obtained by dividing maximum amplitude of p^{th} harmonic of each modal coefficient to the maximum amplitude of p^{th} harmonic of the first modal coefficient. Studying Table 1.1, significant effect of crack location on other trial functions can be observed.

In order to study the effect of crack depth on harmonics of different modal coefficients Table 1.2 is prepared in a similar way. In Figs. 1.5b and 1.6b it is observed that the increase in crack depth also increases all the plots with a similar magnitude. As a result of this fact, order of magnitude of the harmonics do not change. Therefore, in Table 1.2, it is observed that the maximum amplitude ratio is not influenced by the crack ratio.

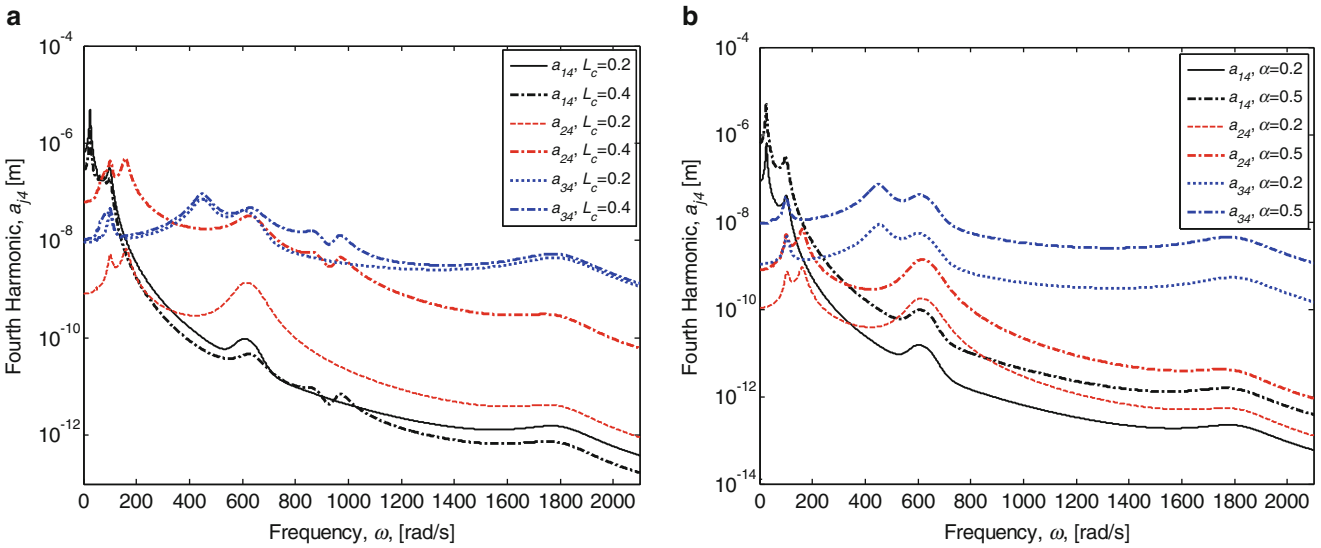

Fig. 1.6 Fourth harmonic of each modal coefficient vs. frequency. (**a**) For $\alpha = 0.5$ and different crack location. (**b**) For $L_c = 0.2$ m and different crack ratio

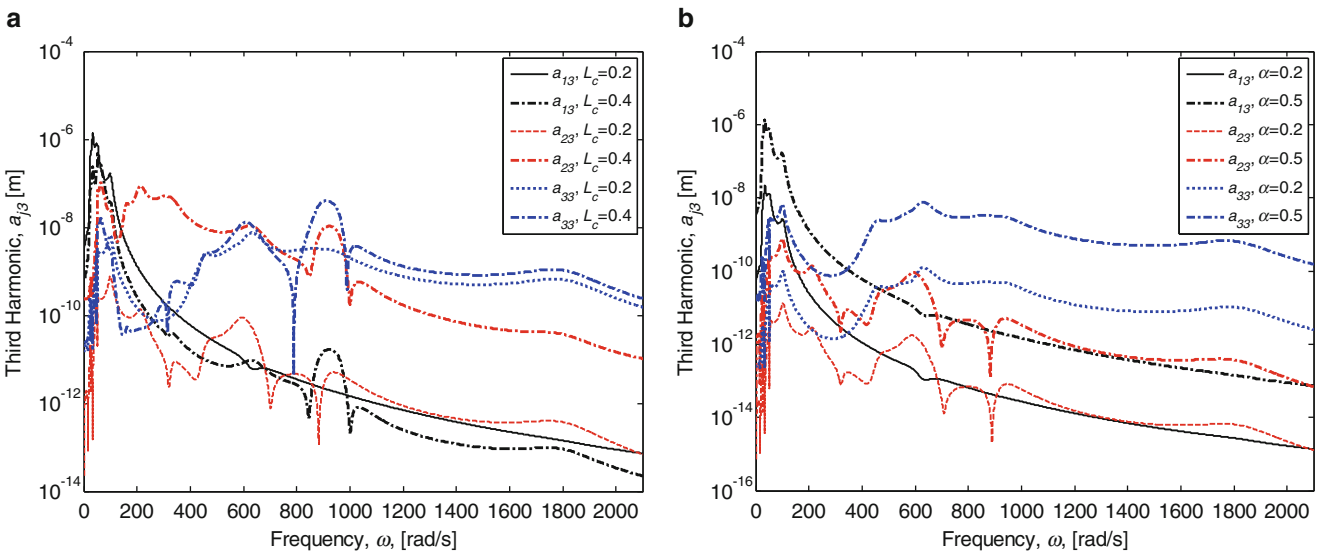

Fig. 1.7 Third harmonic of each modal coefficient vs. frequency. (**a**) For $\alpha = 0.5$ and different crack location. (**b**) For $L_c = 0.2$ m and different crack ratio

1.5 Conclusion

In this study, beam with breathing edge crack is modelled by using Euler-Bernoulli beam theory and nonlinear piecewise linear stiffness. Multiple trial functions are used to represent the response in Galerkin's method where a piecewise linear stiffness matrix based on the slope difference at the crack location is introduced. Harmonic Balance Method with multiple harmonics is used to convert nonlinear ordinary differential equation into a set of nonlinear algebraic equations. It is observed from the results that effect of crack parameters on the natural (resonance) frequency of the cracked beam is insignificant. However, it is observed that harmonics of the response are affected from the crack parameters significantly; hence, this information can be used for the crack detection. Both crack depth and crack location affects the amplitudes of the harmonics of each modal coefficient. As crack ratio increases the amplitudes of the harmonics also increase, however the order of magnitudes of the harmonics are not affected by the crack ratio. The crack location affects amplitudes of the harmonics as well as the order of magnitudes of the harmonics. Depending on the crack location, a harmonic of a different modal coefficient becomes dominant. This fact explains the necessity of using multiple trial functions.

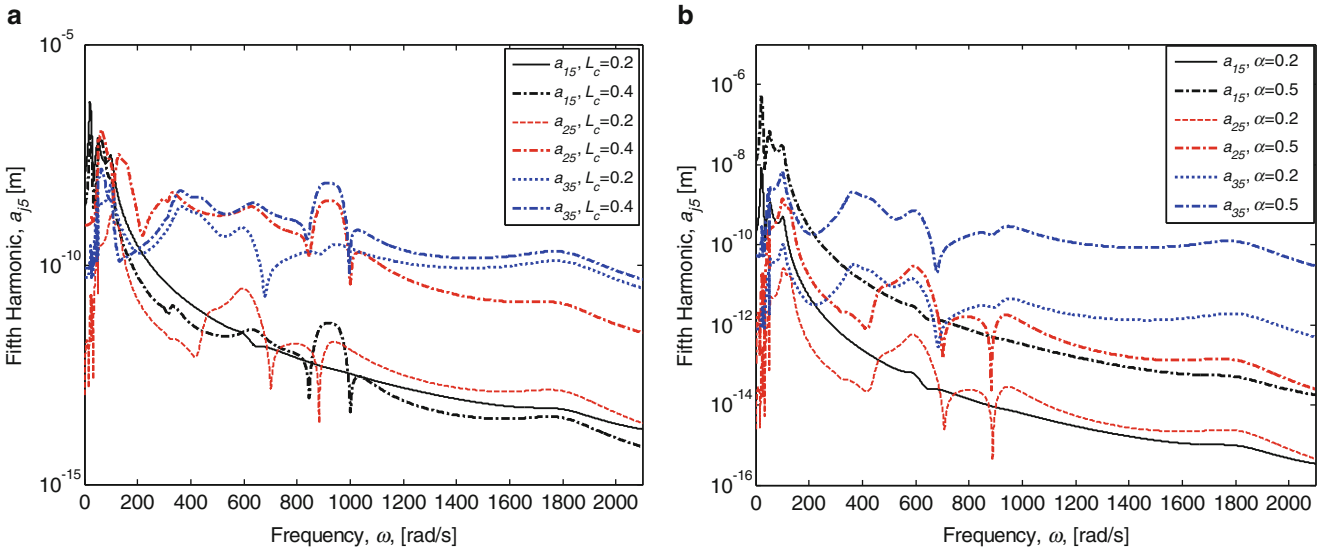

Fig. 1.8 Fifth harmonic of each modal coefficient vs. frequency. (**a**) For $\alpha = 0.5$ and different crack location. (**b**) For $L_c = 0.2$ m and different crack ratio

Table 1.1 Ratio of maximum amplitudes of even harmonics of each modal coefficient for different crack location

	$\alpha = 0.5$					
L_c	a_{12}/a_{12}	a_{22}/a_{12}	a_{32}/a_{12}	a_{14}/a_{14}	a_{24}/a_{14}	a_{34}/a_{14}
0.2	1	0.00128	0.01438	1	0.00141	0.0151
0.4	1	0.18786	0.05545	1	0.22663	0.04163

Table 1.2 Ratio of maximum amplitudes of even harmonics of each modal coefficient for different crack depth

	$L_c = 0.2$					
α	a_{12}/a_{12}	a_{22}/a_{12}	a_{32}/a_{12}	a_{14}/a_{14}	a_{24}/a_{14}	a_{34}/a_{14}
0.2	1	0.00132	0.01327	1	0.00147	0.01385
0.5	1	0.00128	0.01437	1	0.00141	0.01507

References

1. Dimarogonas, A.D.: Vibration of cracked structures: a state of the art review. Eng. Fract. Mech. **55**(5), 831–857 (1996)
2. Aydın, K.: Vibratory characteristics of Euler-Bernoulli beams with arbitrary number of cracks subjected to axial load. J. Vib. Control. **14**(4), 485–510 (2008)
3. Khiem, N.T., Lien, T.V.: A simplified method for natural frequency analysis of multiple cracked beam. J. Sound Vib. **254**(4), 737–751 (2001)
4. Mermertaş, V., Erol, H.: Effect of mass attachment on the free vibration of cracked beam. In: The 8th International Congress on Sound and Vibration (2001)
5. Zhong, S., Oyadiji, S.O.: Analytical predictions of natural frequencies of cracked simply supported beam with stationary roving mass. J. Sound Vib. **311**, 328–352 (2008)
6. Mazanoğlu, K., Yeşilyurt, I., Sabuncu, M.: Vibration analysis of multiple cracked non-uniform beams. J. Sound Vib. **320**, 977–989 (2009)
7. Chondros, T.G., Dimarogonas, A.D., Yao, J.: A continuous cracked beam vibration theory. J. Sound Vib. **215**(1), 17–34 (1998)
8. Chondros, T.G., Dimarogonas, A.D., Yao, J.: Vibration of a beam with a breathing crack. J. Sound Vib. **239**(1), 57–67 (2001)
9. Cheng, S.M., Wu, X.J., Wallace, W.: Vibrational response of a beam with a breathing crack. J. Sound Vib. **225**(1), 201–208 (1999)
10. Chati, M., Rand, R., Mukherjee, S.: Modal analysis of a cracked beam. J. Sound Vib. **207**(2), 249–270 (1997)
11. Giannini, O., Casini, P., Vestroni, F.: Nonlinear harmonic identification of breathing cracks in beams. Comput. Struct. **129**, 166–177 (2013)
12. Baeza, L., Ouyang, H.: Modal approach for forced vibration of beams with a breathing crack. Key Eng. Mater. **413–414**, 39–46 (2009)
13. Batihan, A.C., Cigeroglu, E.: Nonlinear vibrations of a beam with a breathing edge crack. In: IMAC XXXIII (2015)
14. Batihan, A.C.: Vibration analysis of cracked beams on elastic foundation using Timoshenko beam theory. Master Thesis, Middle East Technical University (2011)

Chapter 2
Enforcing Linear Dynamics Through the Addition of Nonlinearity

G. Habib, C. Grappasonni, and G. Kerschen

Abstract The current trend of developing more slender structures is increasing the importance of nonlinearities in engineering design, which, in turn, gives rise to complicated dynamical phenomena. In this study, we evidence the somewhat paradoxical result that adding purposefully nonlinearity to an already nonlinear structure renders the behavior more linear.

Isochronicity, i.e., the invariance of natural frequencies with respect to oscillation amplitude, and the force-displacement proportionality are two key properties of linear systems that are lost for nonlinear systems. The objective of this research is to investigate how these properties can be enforced in a nonlinear system through the addition of nonlinearity. To this end, we exploit the nonlinear normal modes theory to derive simple rules, yet applicable to real structures, for the compensation of nonlinear effects. The developments are illustrated using numerical experiments on a cantilever beam possessing a geometrically nonlinear boundary condition.

Keywords Nonlinear normal modes • Linearization • Compensation of nonlinearity • Isochronicity • Perturbation

2.1 Introduction

Many engineering applications, as for instance tuned vibration absorbers [1], ultrasensitive mass and force sensing devices [2], time keeping devices [3], nanoscale imaging systems [4] and many others, rely on linear properties of mechanical systems, such as force-displacement proportionality and invariance of the resonant frequency. However, if high excitation amplitudes are considered, nonlinearities are activated, invalidating linear properties. This situation is particularly relevant for nano- and micro-electromechanical systems, where nonlinearities are activated already at moderate forcing amplitudes [5]. Furthermore, the current trend of developing more slender structures increases the importance of nonlinearities also in macro systems.

The loss of force-displacement proportionality, the dependence of the resonant frequency on the amplitude, the appearance of quasiperiodic or chaotic solutions, variations in stability properties, coexistence of different solutions, boundedness of basins of attraction, appearance of bifurcations are some of the effects typically generated by nonlinearities [6] that have no linear counterpart. Most of these phenomena have been studied in depth during the last decades, and it is now possible to predict the consequences of many different types of nonlinearities, although unexpected behaviors are always possible. Nevertheless, there are few studies that attempt to eliminate these usually unwanted phenomena. Most existing studies deal with the implementation of active controllers [7, 8], which is referred to as feedback linearization.

The objective of this paper is to enforce linear properties in a nonlinear system through the addition of passive nonlinear elements. The two target properties are the force-displacement proportionality and the invariance of the resonant frequency with respect to the amplitude, which are generally lost even at low level of excitation.

The developed procedure exploits the nonlinear normal modes (NNMs) [9] of undamped, unforced systems, because they give a good approximation of the system's backbone curves. Thanks to the energy balance criterion, the undamped, unforced dynamics can be related to the forced damped dynamics, thus giving complete (but approximate) information about the location of the resonant peaks in the force-frequency space. The resulting equations are solved through reduction to a single harmonics and a standard perturbation technique, which allows to derive equations that can be solved explicitly.

G. Habib (✉) • C. Grappasonni • G. Kerschen
Department of Aerospace and Mechanical Engineering, Space Structures and Systems Laboratory (S3L),
Structural Dynamics Research Group, University of Liège, Liège, Belgium
e-mail: giuseppe.habib@ulg.ac.be

G. Kerschen (ed.), *Nonlinear Dynamics, Volume 1*, Conference Proceedings of the Society for Experimental Mechanics Series,
DOI 10.1007/978-3-319-29739-2_2

This procedure prepares the ground for the definition of linear equations, whose solution is directly related to the target linear property. The analytical developments are validated using a two-degree-of-freedom (DoF) reduced-order model of a cantilever beam possessing a geometrically nonlinear boundary condition and a nonlinear attachment.

2.2 Model

We consider a general n-DoF mechanical system with concentrated polynomial nonlinearities of odd orders, subject to harmonic excitation. The system has the form

$$\mathbf{M}\ddot{\mathbf{x}} + \mathbf{D}\dot{\mathbf{x}} + \mathbf{K}\mathbf{x} + \tilde{\mathbf{b}}(\mathbf{x}) = \sqrt{\varepsilon}\tilde{\mathbf{v}} f \cos(\omega t) \tag{2.1}$$

where $\mathbf{M}$, $\mathbf{D}$ and $\mathbf{K}$ are the mass, damping and stiffness matrices, $\mathbf{x}$ is the position vector, $\tilde{\mathbf{b}}$ contains the nonlinear terms, $\tilde{\mathbf{v}}$ indicates which DoFs are excited, f is the forcing amplitude, ω is the excitation frequency and ε is a small parameter, while t is time. $\mathbf{M}$, $\mathbf{D}$ and $\mathbf{K}$ are assumed to be symmetric, real and positive-definite, while $\tilde{\mathbf{b}}$ has the generic form

$$\tilde{\mathbf{b}} = \begin{bmatrix} \vdots \\ \sum_{m=3,5,\dots} \sum_{h_1+\dots+h_n=m} \tilde{b}_{jh_1\dots h_n} \prod_{i=1}^{n} x_i^{h_i} \\ \vdots \end{bmatrix}, \tag{2.2}$$

where $j = \overline{1,n}$, such that, for example, for a 2-DoF system the cubic terms of the first raw of $\tilde{\mathbf{b}}$ are $\tilde{b}_{130}x_1^3 + \tilde{b}_{121}x_1^2x_2 + \tilde{b}_{112}x_1x_2^2 + \tilde{b}_{103}x_2^3$.

In order to decouple the linear part of the system, we apply classical modal analysis, i.e., denoting $\mathbf{U}$ the matrix containing the eigenvectors of $\mathbf{M}^{-1}\mathbf{K}$, we apply the transformation $\mathbf{x} = \mathbf{U}\mathbf{y}$ to Eq. (2.1) and we pre-multiply it by $\mathbf{U}^{\mathrm{T}}$. The resulting system has the form

$$\mathbf{U}^{\mathrm{T}}\mathbf{M}\mathbf{U}\ddot{\mathbf{y}} + \mathbf{U}^{\mathrm{T}}\mathbf{D}\mathbf{U}\dot{\mathbf{y}} + \mathbf{U}^{\mathrm{T}}\mathbf{K}\mathbf{U}\mathbf{y} + \mathbf{U}^{\mathrm{T}}\tilde{\mathbf{b}} = \sqrt{\varepsilon}\mathbf{U}^{\mathrm{T}}\tilde{\mathbf{v}} f \cos(\omega t)\,, \tag{2.3}$$

where $\mathbf{U}^{\mathrm{T}}\mathbf{M}\mathbf{U}$ and $\mathbf{U}^{\mathrm{T}}\mathbf{K}\mathbf{U}$ are diagonal. Pre-multiplying then the system by the inverse of $\mathbf{U}^{\mathrm{T}}\mathbf{M}\mathbf{U}$ and applying the transformation $\mathbf{y} = \sqrt{\varepsilon} f \mathbf{q}$, we have

$$\ddot{\mathbf{q}} + \mathbf{C}\dot{\mathbf{q}} + \boldsymbol{\Omega}\mathbf{q} + \mathbf{b} = \mathbf{v}\cos(\omega t)\,, \tag{2.4}$$

where $\mathbf{C}$ is not symmetric (differently from $\mathbf{D}$), and $\boldsymbol{\Omega}$ is diagonal and contains the squares of the natural frequencies of the different modes of vibration. $\boldsymbol{\Omega}$, $\mathbf{C}$ and $\mathbf{b}$ have the general form

$$\boldsymbol{\Omega} = \begin{bmatrix} \ddots & & 0 \\ & \Omega_j^2 & \\ 0 & & \ddots \end{bmatrix}, \quad \mathbf{C} = \begin{bmatrix} c_{11} & \dots & c_{1n} \\ \vdots & & \vdots \\ c_{n1} & \dots & c_{nn} \end{bmatrix},$$

$$\mathbf{b} = \begin{bmatrix} \vdots \\ \sum_{m=3,5,\dots} \varepsilon^{\frac{m-1}{2}} f^{m-1} \sum_{h_1+\dots+h_n=m} b_{jh_1\dots h_n} \prod_{i=1}^{n} q_i^{h_i} \\ \vdots \end{bmatrix}. \tag{2.5}$$

The forcing amplitude f is contained uniquely in $\mathbf{b}$, i.e. the system depends on the forcing amplitude only through the coefficients of the nonlinear terms. This clearly illustrates that considering small nonlinearities or small forcing amplitudes is equivalent, in many cases. Furthermore, terms of order m are proportional to $\varepsilon^{\frac{m-1}{2}}$ (see $\mathbf{b}$), which prepares the ground for the perturbation procedure implemented in the following sections.

For the sake of simplicity, we consider only cubic nonlinearities in this analytical development. Neglecting terms higher than the third order allows us to develop the equations up to order ε^1. Nevertheless, the procedure can be extended to higher-order nonlinear terms.

2.3 Calculation of Unforced, Undamped Response Using Nonlinear Normal Modes

NNMs give a good approximation of the system backbone curves. In order to calculate them, we consider the undamped unforced equations of motion

$$\ddot{\mathbf{q}} + \mathbf{\Omega}\mathbf{q} + \mathbf{b} = \mathbf{0}. \tag{2.6}$$

Adopting a standard perturbation procedure, the solution of Eq. (2.6) can be approximated to a single harmonic by

$$\mathbf{q} = \left(\mathbf{q}_0 + \varepsilon\mathbf{q}_1 + O\left(\varepsilon^2\right)\right)\sin\left(\omega t\right), \tag{2.7}$$

where

$$\mathbf{q}_0 = \begin{bmatrix} \vdots \\ q_{j0} \\ \vdots \end{bmatrix}, \quad \mathbf{q}_1 = \begin{bmatrix} \vdots \\ q_{j1} \\ \vdots \end{bmatrix} \text{ and } \omega = \omega_0 + \varepsilon\omega_1 + O\left(\varepsilon^2\right), \tag{2.8}$$

which is valid for small values of ε.

Substituting Eq. (2.7) into Eq. (2.6) and adopting the standard single harmonic approximation $\sin^3\left(\omega t\right) \approx 3/4\sin\left(\omega t\right)$, we obtain n equations of the form

$$\begin{aligned} -\left(\omega_0^2 + 2\varepsilon\omega_1\omega_0\right)\left(q_{j0} + \varepsilon q_{j1}\right) + \Omega_j^2\left(q_{j0} + \varepsilon q_{j1}\right) + \frac{3}{4}\varepsilon\left(\sum_{h_1+\ldots+h_n=3} b_{jh_1\ldots h_n}\prod_{i=1}^{n} q_i^{h_i}\right) \\ + O\left(\varepsilon^2\right) = 0. \end{aligned} \tag{2.9}$$

Considering the terms of order ε^0, related to the underlying linear system, we have

$$-\omega_0^2 q_{j0} + \Omega_j^2 q_{j0} = 0. \tag{2.10}$$

In order to obtain the NNM associated with the lth mode of vibration, we impose that the linear part of all other modes have zero amplitude, i.e.

$$\text{for} j \neq l \Rightarrow q_{j0} = 0, \tag{2.11}$$

while $q_{l0} \neq 0$, such that the we refer to the lth mode of vibration and $\omega_0 = \Omega_l$.

Considering now the terms of order ε^1 of Eq. (2.9), we obtain

$$j \neq l \qquad -\Omega_l^2 q_{j1} + \Omega_j^2 q_{j1} + \frac{3}{4} b_{j0\ldots3\ldots0} q_{l0}^3 = 0 \tag{2.12}$$

$$j = l \qquad -\Omega_l^2 q_{l1} - 2\omega_1\Omega_l q_{l0} + \Omega_l^2 q_{l1} + \frac{3}{4} b_{l0\ldots3\ldots0} q_{l0}^3 = 0. \tag{2.13}$$

($b_{j0\ldots3\ldots0}$, for example in a 4-DoF system where $l = 2$, would be b_{j0300}). Thus, from Eq. (2.12) we have

$$q_{j1} = \frac{3}{4}\frac{b_{j0\ldots3\ldots0} q_{l0}^3}{\Omega_l^2 - \Omega_j^2}, \quad j \neq l, \tag{2.14}$$

that indicates how the modes not directly excited by the force ($j \neq l$) are excited by the nonlinear coupling. While from Eq. (2.13) we have

$$\omega_1 = \frac{3}{4}\frac{b_{l0\ldots3\ldots0}q_{l0}^2}{2\Omega_l}, \tag{2.15}$$

where ω_1 represents the variation of the lth natural frequency with respect to the amplitude of oscillations, in first approximation.

2.4 Calculation of Forced, Damped Response Using Energy Balance

The energy balance criterion can be used to relate the undamped, unforced dynamics of the NNMs to the forced damped dynamics [10, 11], thus obtaining complete information of the resonant peaks. Given a general linearly-damped mechanical system, the balance between the dissipated and input energies is expressed by the equation

$$\int_0^T \dot{\mathbf{x}}(t)^{\mathrm{T}}\mathbf{D}\dot{\mathbf{x}}(t)\mathrm{d}t = \int_0^T \dot{\mathbf{x}}(t)^{\mathrm{T}}\mathbf{f}(t)\mathrm{d}t, \tag{2.16}$$

where T is the period of vibration and f is the external force. In the case of harmonic excitation $\mathbf{f} = \tilde{\mathbf{v}}f\cos(\omega t)$, approximating the solution to a single harmonics $\mathbf{x}(t) \approx \mathbf{x}_0 \sin(\omega t)$ in resonant conditions, Eq. (2.16) has the form

$$\omega^2\mathbf{x}_0^{\mathrm{T}}\mathbf{D}\mathbf{x}_0\int_0^T \cos(\omega t)^2\,\mathrm{d}t \approx \omega\mathbf{x}_0^{\mathrm{T}}\tilde{\mathbf{v}}f\int_0^T \cos(\omega t)^2\,\mathrm{d}t \quad \Rightarrow \quad \omega\mathbf{x}_0^{\mathrm{T}}\mathbf{D}\mathbf{x}_0 \approx \mathbf{x}_0^{\mathrm{T}}\tilde{\mathbf{v}}f. \tag{2.17}$$

Inserting in Eq. (2.17) the solution of the undamped unforced system, it is possible to estimate the ratio between the forcing amplitude and the amplitude of oscillation.

Applying the aforementioned procedure, considering the system in Eq. (2.4) and the tentative solution (2.7), we obtain the energy balance equation

$$\begin{aligned}(\Omega_l + \varepsilon\omega_1)&\left(\begin{bmatrix}0\\ \vdots\\ q_{l0}\\ \vdots\\ 0\end{bmatrix}^{\mathrm{T}} + \varepsilon\begin{bmatrix}q_{11}\\ \vdots\\ q_{n1}\end{bmatrix}^{\mathrm{T}}\right)\mathbf{C}\left(\begin{bmatrix}0\\ \vdots\\ q_{l0}\\ \vdots\\ 0\end{bmatrix} + \varepsilon\begin{bmatrix}q_{11}\\ \vdots\\ q_{n1}\end{bmatrix}\right)\\ &= \left(\begin{bmatrix}0\\ \vdots\\ q_{l0}\\ \vdots\\ 0\end{bmatrix}^{\mathrm{T}} + \varepsilon\begin{bmatrix}q_{11}\\ \vdots\\ q_{n1}\end{bmatrix}^{\mathrm{T}}\right)\begin{bmatrix}v_1\\ \vdots\\ v_n\end{bmatrix} + O\left(\varepsilon^2\right).\end{aligned} \tag{2.18}$$

Collecting terms of order ε^0 we obtain

$$\Omega_l q_{l0}^2 c_{ll} = q_{l0}v_l \quad \Rightarrow \quad q_{l0} = \frac{v_l}{\Omega_l c_{ll}}, \tag{2.19}$$

which yields the relation in the linear range between the forcing amplitude (here normalized) and the oscillation amplitude at resonance as a function of the modal damping.

Collecting terms of order ε^1 of Eq. (2.18) we have

$$\Omega_l q_{l0}\left(\sum_{\substack{j=1\\ j\neq l}}^{n} c_{lj}q_{j1}+\sum_{\substack{j=1\\ j\neq l}}^{n} c_{jl}q_{j1}\right)+2\Omega_l q_{l0}c_{ll}q_{l1}+\omega_1 q_{l0}^2 c_{ll}=\sum_{\substack{j=1\\ j\neq l}}^{n} q_{j1}v_j+q_{1l}v_l, \tag{2.20}$$

thus

$$q_{l1}=\frac{\Omega_l q_{l0}\left(\sum_{\substack{j=1\\ j\neq l}}^{n} c_{lj}q_{j1}+\sum_{\substack{j=1\\ j\neq l}}^{n} c_{jl}q_{j1}\right)+\omega_1 q_{l0}^2 c_{ll}-\sum_{\substack{j=1\\ j\neq l}}^{n} q_{j1}v_j}{v_l-2\Omega_l q_{l0}c_{ll}}, \tag{2.21}$$

which indicates the variation of the modal amplitude of oscillation due to nonlinearity.

2.5 Enforcement of Linear Properties

The set of Eqs. (2.11), (2.14), (2.15), (2.19) and (2.21) characterize the NNMs and forced resonant response of the lth structural mode. Equations (2.11) and (2.19) refer to the underlying linear system; Eq. (2.11) is due to the imposed resonant condition, while Eq. (2.19) gives the relationship between the forcing amplitude and the amplitude of oscillation in the linear case. Equations (2.14), (2.15) and (2.21) refer to the nonlinear properties of the system. q_{j1} ($j=\overline{1n}, j\neq l$) are directly proportional to $b_{j0\ldots3\ldots0}$, ω_1 is directly proportional to $b_{l0\ldots3\ldots0}$, while q_{l1} depends linearly on all the coefficients $b_{j0\ldots3\ldots0}$ ($j=\overline{1,n}$), which are the coefficients of the solely nonlinear terms relevant at order ε^1, when the lth resonance is excited. If the system includes higher-order nonlinear terms, other coefficients come into play.

The objective of this section is to show that, through an appropriate tuning of the coefficients $b_{j0\ldots3\ldots0}$, the dynamics of the nonlinear system can resemble that of a linear system.

2.5.1 *Enforcing Force-Displacement Proportionality*

We consider the general case for which the objective is to keep the force-displacement proportionality typical of linear systems for the kth DoF (x_k in the physical coordinate system), while the system vibrates at the lth resonant frequency. Recalling that $\mathbf{x}=\sqrt{\varepsilon}f\mathbf{U}\mathbf{q}$ and considering the lth resonance, it follows that

$$x_k=\sqrt{\varepsilon}f\left(u_{kl}q_{l0}+\varepsilon\left(\sum_{j=1}^{n}u_{kj}q_{j1}\right)+O\left(\varepsilon^2\right)\right). \tag{2.22}$$

where u_{ij} is an element of matrix $\mathbf{U}$. If we impose that

$$\sum_{j=1}^{n}u_{kj}q_{j1}=0 \tag{2.23}$$

x_k obeys, in first approximation, a force-displacement proportionality. Equation (2.23) depends on the n coefficients $b_{j0\ldots3\ldots0}$ ($j=\overline{1n}$), which, in turn, depend on the parameters characterizing the physical nonlinearities of the system.

2.5.2 *Enforcing Straight Line Frequency Backbone*

Another property, typical of linear systems and generally not satisfied in nonlinear systems, is the invariance of the resonance frequencies with respect to forcing amplitude, giving rise to straight backbone curves. Hardening (softening) nonlinearities

shift resonance frequencies toward greater (lower) values for increasing amplitudes of oscillation. To enforce a straight backbone curve for the lth resonance, ω_1 should be set to 0, and, hence, $b_{l0\ldots3\ldots0} = 0$. An important feature of the proposed approach is that the final equations are fully explicit. Thus, in spite of their complexity, they can be rapidly implemented.

2.6 Beam Example

To validate the previous theoretical developments, a nonlinear cantilever beam with a nonlinear attachment, similar to that studied in [12, 13], is considered. The two nonlinearities of the attachment, k_{nl2} and k_{nl3}, are designed so as to enforce linear properties in the coupled system. A 2-DoF reduced-order model of this system is

$$\begin{bmatrix} 0.46 & 0 \\ 0 & 0.069 \end{bmatrix}\begin{bmatrix} \ddot{x}_1 \\ \ddot{x}_2 \end{bmatrix} + \begin{bmatrix} 0.52 & -0.15 \\ -0.15 & 0.25 \end{bmatrix}\begin{bmatrix} \dot{x}_1 \\ \dot{x}_2 \end{bmatrix} + \begin{bmatrix} 14065 & -1709 \\ -1709 & 1709 \end{bmatrix}\begin{bmatrix} x_1 \\ x_2 \end{bmatrix}$$
$$+ \begin{bmatrix} k_{nl1}x_1^3 + k_{nl2}\left(x_1 - x_2\right)^3 \\ k_{nl2}\left(x_2 - x_1\right)^3 + k_{nl3}x_2^3 \end{bmatrix} = f\begin{bmatrix} 1 \\ 0 \end{bmatrix}. \tag{2.24}$$

The cantilever beam has a single concentrated nonlinearity, $k_{nl1} = 3.3 \times 10^9\,\mathrm{N/m^3}$.

Figure 2.1a illustrates the normalized frequency response of the first degree of freedom of the system without the additional nonlinearities, i.e., $k_{nl2} = k_{nl3} = 0$, for three forcing amplitudes. A substantial hardening effect is observed, while the amplitude of the first (second) resonance decreases (increases) when the forcing amplitude increases.

The displacement x_1 around the first resonance obeys force-displacement proportionality if

$$-0.0128 + 1.39 \times 10^{-10}k_{nl2} + 2.17 \times 10^{-10}k_{nl3} = 0. \tag{2.25}$$

which is verified if $k_{nl2} = 9.2 \times 10^7\,\mathrm{N/m^3}$ and $k_{nl3} = 0$. Figure 2.1b that depicts the corresponding normalized frequency response confirms that the amplitude of the first resonance is almost identical for the three forcing amplitudes. The linearization of the force-displacement relation can be further improved if a fifth-order spring is added between the two lumped masses. This is evidenced in Fig. 2.1c, which compares the envelopes of the resonant peaks in the different considered cases.

Aiming now to enforce isochronicity of the first resonance, i.e., $\omega_1 = 0$, we obtain

$$62.6 + 7.39 \times 10^{-7}k_{nl2} + 2.84 \times 10^{-6}k_{nl3} = 0. \tag{2.26}$$

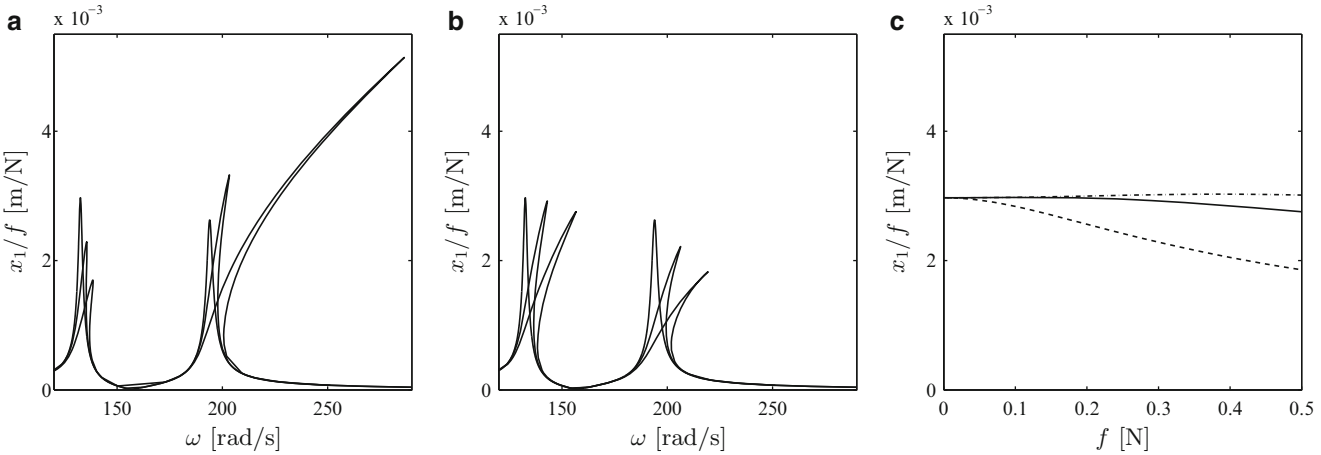

Fig. 2.1 (**a**), (**b**) frequency response of the system in Eq. (2.24) for forcing amplitudes $f \to 0$, $f = 0.3$ and $f = 0.5\,\mathrm{N}$, for $k_{nl2} = k_{nl3} = 0$ (**a**) and for $k_{nl2} = 9.2 \times 10^7\,\mathrm{N/m^3}$ and $k_{nl3} = 0$ (**b**); (**c**) envelope of the first resonant peak with respect to the forcing amplitude. *Dashed line*: $k_{nl2} = k_{nl3} = 0$; *solid line*: $k_{nl2} = 9.2 \times 10^7\,\mathrm{N/m^3}$ and $k_{nl3} = 0$; *dash-dotted line*: $k_{nl2} = 9.2 \times 10^7\,\mathrm{N/m^3}$, $k_{nl3} = 0$ and additional quintic spring $k_{nl4} = 3.9 \times 10^{12}\,\mathrm{N/m^5}$

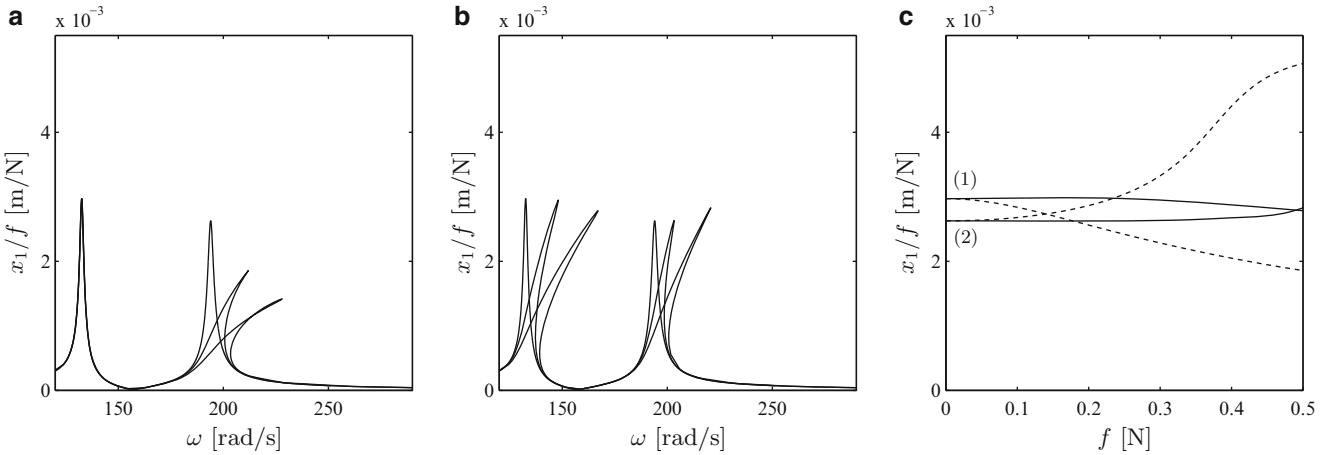

Fig. 2.2 Frequency response of the system in Eq. (2.24) for forcing amplitudes $f \to 0$, $f = 0.3$ and $f = 0.5$ N, for $k_{nl2} = 2.11 \times 10^7$ and $k_{nl3} = -7.7 \times 10^7$ (**a**) and for $k_{nl2} = 2.75 \times 10^7$ and $k_{nl3} = 4.14 \times 10^7$ (**b**); envelope of the two resonant peaks with respect to the forcing amplitude. *Dashed lines*: $k_{nl2} = k_{nl3} = 0$; *solid lines*: $k_{nl2} = 2.11 \times 10^8$ and $k_{nl3} = -7.7 \times 10^7$; the numbers in brackets indicate the first *(1)* and the second *(2)* resonant peak

Equations (2.25) and (2.26) can be simultaneously satisfied if and only if $k_{nl2} = 2.11 \times 10^8$ and $k_{nl3} = -7.7 \times 10^7$. Doing so, the first resonance peak can be made practically unchanged with respect to the linear resonance, as plotted in Fig. 2.2a.

The developed framework can go beyond operating on a single resonance. For instance, force-displacement proportionality of the second peak (with respect to x_1) can be imposed through

$$0.00654 - 1.53 \times 10^{-10} k_{nl2} - 5.63 \times 10^{-11} k_{nl3} = 0. \tag{2.27}$$

For $k_{nl2} = 2.75 \times 10^7$ and $k_{nl3} = 4.14 \times 10^7$, Eqs. (2.25) and (2.27) are simultaneously verified, which means that both resonances obey approximately force-displacement proportionality. The corresponding normalized frequency response is illustrated in Fig. 2.2b. Figure 2.2c depicts the envelopes of the two peaks with respect to the forcing amplitude. The dashed lines, referring to the original system ($k_{nl2} = k_{nl3} = 0$), either decrease (first peak) or increase (second peak) whereas the solid lines are almost horizontal for a large range of forcing amplitudes.

2.7 Conclusions

This paper has demonstrated how it is possible to design nonlinearities of a mechanical system so that its dynamics resemble that of a linear system, which include force-displacement proportionality and isochronocity. The developments exploited a standard perturbation technique, combined with NNM theory and energy balance of periodic solutions at resonance, and were validated using a 2-DoF reduced-order model of a nonlinear cantilever beam.

Acknowledgements The authors G. Habib, C. Grappasonni and G. Kerschen would like to acknowledge the financial support of the European Union (ERC Starting Grant NoVib 307265).

References

1. Hartog, J.D.: Mechanical Vibrations. Courier Corporation, Chelmsford (1985)
2. Ono, T., Li, X., Miyashita, H., Esashi, M.: Mass sensing of adsorbed molecules in sub-picogram sample with ultrathin silicon resonator. Rev. Sci. Instrum. **74**(3), 1240–1243 (2003)
3. Piazza, G., Stephanou, P.J., Pisano, A.P.: Piezoelectric aluminum nitride vibrating contour-mode MEMS resonators. J. Microelectromech. Syst. **15**(6), 1406–1418 (2006)
4. Rega, G., Settimi, V.: Bifurcation, response scenarios and dynamic integrity in a single-mode model of noncontact atomic force microscopy. Nonlinear Dyn. **73**(1–2), 101–123 (2013)

5. Kacem, N., Hentz, S.: Bifurcation topology tuning of a mixed behavior in nonlinear micromechanical resonators. Appl. Phys. Lett. **95**(18), 183104 (2009)
6. Guckenheimer, J., Holmes, P.: Nonlinear Oscillations, Dynamical Systems, and Bifurcations of Vector Fields, vol. 42. Springer Science & Business Media, New York (1983)
7. Mittal, S., Menq, C.-H.: Precision motion control of a magnetic suspension actuator using a robust nonlinear compensation scheme. IEEE/ASME Trans. Mechatron. **2**(4), 268–280 (1997)
8. Charlet, B., Lévine, J., Marino, R.: On dynamic feedback linearization. Syst. Control Lett. **13**(2), 143–151 (1989)
9. Vakakis, A.F., Gendelman, O., Bergman, L.A., McFarland, D.M., Kerschen, G., Lee, Y.S.: Nonlinear Targeted Energy Transfer in Mechanical and Structural Systems, vol. 156. Springer, Berlin (2008)
10. Hill, T., Cammarano, A., Neild, S., Wagg, D.: An analytical method for the optimisation of weakly nonlinear systems. In: Proceedings of Eurodyn 2014, pp. 1981–1988 (2014)
11. Kuether, R., Renson, L., Detroux, T., Grappasonni, C., Kerschen, G., Allen, M.: Nonlinear normal modes, modal interactions and isolated resonance curves. J. Sound Vib. **351**, 299–310 (2015)
12. Grappasonni, C., Habib, G., Detroux, T., Kerschen, G.: Experimental demonstration of a 3d-printed nonlinear tuned vibration absorber. In: XXXIII IMAC Conference & Exposition On Structural Dynamics (2015)
13. Grappasonni, C., Habib, G., Detroux, T., Wang, F., Kerschen, G., Jensen, J.S.: Practical design of a nonlinear tuned vibration absorber. In: Proceedings of International Conference on Noise and Vibration Engineering (ISMA) (2014)

Chapter 3
Experimental Analysis of a Softening-Hardening Nonlinear Oscillator Using Control-Based Continuation

L. Renson, D.A.W. Barton, and S.A. Neild

Abstract Control-based continuation is a recently-developed approach for testing nonlinear dynamic systems in a controlled manner and exploring their dynamic features as system parameters are varied. In this paper, control-based continuation is used to track directly in the experiment the steady-state periodic solutions of a single-degree-of-freedom oscillator presenting a softening-hardening restoring force. The oscillator forced response is investigated and fully characterized in forcing amplitude and frequency. The oscillator's backbone curve is then extracted directly in the experiment by following a phase quadrature condition between the oscillator response and the base excitation.

Keywords Experimental nonlinear dynamics • Forced response • Backbone curves • Softening-hardening • Control-based continuation

3.1 Introduction

Modern aerospace structures are prone to nonlinearity as, for instance, weight reduction has brought an increase of flexibility. In this context, the development of nonlinear models is gaining interest in the structural dynamics community. However, developing such models and addressing the associated dynamics is often very challenging because nonlinear systems generally exhibit a wide range of complicated dynamic phenomena that cannot be understood and predicted using standard linear methods. Experimental validation has therefore, more than ever, an important role to play.

The theory of nonlinear normal modes (NNMs) has proved useful for uncovering some essential features of nonlinear systems such as modal interactions [1], mode bifurcations [2], isolated solutions [3] or frequency-energy dependence [4, 5]. The latter can be characterized by the so-called backbone curve which represents the evolution of the resonance frequency for increasing oscillation amplitudes. In addition to its practical engineering relevance, this nonlinear dynamic feature is attractive because it can be extracted from the physical system using appropriate testing; thus allowing the subsequent model validation and updating process to be performed. The experimental identification of backbone curves was first proposed in [6, 7]. Following the principle of linear phase separation techniques, the method isolates a single NNM using an excitation in phase quadrature with the system response. The applied force is then stopped and the relation between amplitude and frequency of oscillation is extracted from the free, damped, response of the system using time-frequency analysis tools such as the Hilbert or Wavelet transforms. As such, the method is often termed *resonant decay* or *free decay*. It was successfully applied to several academic systems of moderate complexity as, for instance, a single-degree-of-freedom oscillator [8], a nonlinear beam [7] and a steel frame structure [9]. More recently, a phase separation method where multiple NNMs are identified simultaneously from broad-band data was introduced and demonstrated on noisy synthetic data in [10].

In [11], a novel approach which traces out the backbone curve directly in the experiment instead of post-processing it from recorded experimental data was presented. Using the concept of control-based continuation (CBC), the method combines a stabilizing feedback controller and path following techniques to follow in the experiment the steady-state periodic responses describing the backbone curve of the system. If the method relies on the same phase quadrature criterion as the resonant decay method, it nevertheless presents a number of advantages over the latter. For instance, the method is naturally robust to bifurcation and stability issues because of the presence of the stabilizing control system. Furthermore, the discretization of the backbone curve is no longer governed by the damping characteristics of the system and the quality of the results can be verified and controlled (within experimental limits) using user-defined parameters. In [11], this novel method was demonstrated on a single-degree-of-freedom nonlinear oscillator (SDOF) presenting a hardening characteristic.

L. Renson (✉) • D.A.W. Barton • S.A. Neild
Faculty of Engineering, University of Bristol, Bristol, UK
e-mail: l.renson@bristol.ac.uk

G. Kerschen (ed.), *Nonlinear Dynamics, Volume 1*, Conference Proceedings of the Society for Experimental Mechanics Series,
DOI 10.1007/978-3-319-29739-2_3

In this paper, the CBC identification of backbone curves is demonstrated on a SDOF oscillator featuring a more complicated restoring force with softening and hardening characteristics. The CBC approach developed in [11] is briefly presented in Sect. 3.2. The experimental set-up considered as demonstrator is presented in Sect. 3.3, and experimental results are discussed in Sect. 3.4. Conclusions are drawn in Sect. 3.5.

3.2 Backbone Curve Identification Using CBC

CBC is a testing method inspired from numerical continuation techniques [12–14] that aims to follow, experimentally, the evolution of the steady-state response of a system (e.g., equilibrium, periodic solution) as parameters are varied. Contrary to numerical simulations, the states of a physical system cannot be set arbitrarily and CBC relies therefore on a controller and its control target $x^\star$ as a proxy for the states. The dynamical system of interest is however the uncontrolled system, so the added control system should be non-invasive, i.e. the control input $u(t)$ should vanish for all time. In that case, the steady-state solution x_{asy} observed for the controlled system is also a steady-state solution of the uncontrolled system. In practice, $u(t)$ is only approximately zero. Though the controller does not change the steady-state solution itself, it does change its linearisation thus making unstable orbits stable if implemented correctly.

The presence of the controller is advantageous because CBC is thus robust to stability changes and bifurcations. However, investigating the stability of the underlying uncontrolled response, and hence detecting bifurcations, is more complicated. In [15], a number of measures are suggested to overcome this problem but all require turning off the control for a period of time; in many situations this is not desirable as damage could be caused to the experiment or even the experimenter. In [16], Barton identifies a multi-input multi-output (MIMO) auto-regressive model with exogenous inputs (ARX) from the experiment response perturbed around a steady-state periodic orbit. The model is then exploited to determine the so-called Floquet multipliers and conclude the periodic orbit stability.

In the context of finding steady-state behaviour, choosing $x^\star$ such that $u(t) \equiv 0$ plays the role of the equations of motion of a model. In [15, 17–19], the problem is iteratively solved (to experimental accuracy) using a Newton-like algorithm where derivatives are evaluated experimentally using finite differences. Starting from a given steady-state, the search for the next solution is then performed using a pseudo-arclength continuation algorithm (see, for instance, [20]). In this paper, a simplification of this procedure is used because the studied parameter, the total forcing amplitude, and the control signal have the same action on the system. This simplified method is approximately 15 times faster than the approach reported in [17] because no derivative is required. The general aspects of this CBC approach are briefly introduced in Sect. 3.2.1, and the reader is referred to [21] for a more detailed description. The use of CBC for backbone curve tracking is then discussed in Sect. 3.2.2.

3.2.1 Steady-State Periodic Solutions of the Forced System

This section shows how CBC can extract a steady-state periodic solution of the uncontrolled system in response to an excitation $f(t)$. In our experiment, we consider a single-point, single-harmonic forcing of arbitrary phase of the form $f(t) = a\cos(\omega t) + b\sin(\omega t)$. The forcing amplitude $r = \sqrt{a^2 + b^2}$ is considered as a parameter.

Consider what happens if we pick a specific harmonic forcing $f^\star(t)$ defined by the pair of coefficients $(a^\star, b^\star)$ and an arbitrary periodic control target signal $x^\star(t)$ expanded to m (finite) Fourier modes as

$$x^\star(t) = \frac{A_0^\star}{2} + \sum_{j=1}^{m} A_j^\star \cos(j\omega t) + B_j^\star \sin(j\omega t). \tag{3.1}$$

A feedback control signal is added to the excitation signal. For simplicity, the particular case of a proportional-plus-derivative (PD) controller as later used in our experimental investigations is considered. The method works however for more general control strategies. The total input to the system is given by

$$f_{\text{tot}}(t) = f(t) + u(t) = f^\star(t) + k_p(x^\star(t) - x(t)) + k_d(\dot{x}^\star(t) - \dot{x}(t)), \tag{3.2}$$

where $x(t)$ is the response of the system. Assuming that the chosen controller is stabilizing, the experiment settles into a periodic steady-state output defined as

$$x_{\text{asy}}(t) := \lim_{t\to+\infty} x(t) = \frac{A_0}{2} + \sum_{j=1}^{m} A_j \cos(j\omega t) + B_j \sin(j\omega t). \tag{3.3}$$

We assume that the experiment has periodic input after the transients have settled. The signal $u(t)$ is generally not equal to zero and the control system is thus invasive. The general solution to this problem is to use a root-finding algorithm to modify the control target coefficients $(A_0^\star, A_j^\star, B_j^\star)_{(j=1)}^m$ such that $u(t) \equiv 0$. However, realizing that $f(t)$ and $u(t)$ have the same action on the experiment, the applied force and control signals can be lumped together such that $f(t) = f_{\text{tot}}$ and $u(t) \equiv 0$ in the first mode. The steady-state response (3.3) is unchanged as the total input to the system $f(t) + u(t)$ remains unchanged, but (3.3) is now a steady-state solution of the underlying uncontrolled system of interest. The amplitude of this new forcing at fundamental frequency ω equals $r = \sqrt{a^2 + b^2}$, where

$$a = a^\star + k_p(A_1^\star - A_1) + \omega k_d(B_1^\star - B_1), \tag{3.4}$$

$$b = b^\star + k_p(B_1^\star - B_1) + \omega k_d(A_1 - A_1^\star). \tag{3.5}$$

Equations (3.4) and (3.5) are not sufficient because the total input force generally does not have the required single-harmonic form due to the presence of nonlinearities. Even if the reference signal $x^\star(t)$ is harmonic, the output x_{asy} contains higher-harmonics introduced by the nonlinearities of the experimental system. The control signal $u(t)$ has therefore higher-harmonic Fourier coefficients given by

$$A_0^u = k_p(A_0^\star - A_0), \tag{3.6}$$

$$A_j^u = k_p(A_j^\star - A_j) + j\omega k_d(B_j^\star - B_j) \qquad (j > 1), \tag{3.7}$$

$$B_j^u = k_p(B_j^\star - B_j) + j\omega k_d(A_j - A_j^\star) \qquad (j > 1). \tag{3.8}$$

If these coefficients are zero then the forcing $f(t)+u(t)$ is harmonic with amplitude $r = \sqrt{a^2 + b^2}$ such that the point (r, x_{asy}) is a periodic orbit of the uncontrolled system.

The requirement for the coefficients $(A_0^u, A_j^u, B_j^u)_{(j=2)}^m$ to be zero is a nonlinear system of $2m-1$ equations in the Fourier coefficients $X^\star = [A_0^\star, (A_j^\star, B_j^\star)_{j=2}^m]$ of the reference signal $x^\star$. This problem is very similar to the original one, with the notable difference that the first mode (j=1) is no longer included in the problem. This first mode usually contains all the instability present in the periodic solution. Removing this coefficient from the problem allows therefore to use a more effective fixed-point iteration method where derivatives do not need to be evaluated. The kth iteration of the method reads:

$$X_{k+1}^\star = X(X_k^\star) \tag{3.9}$$

where $X = [A_0, (A_j, B_j)_{j=2}^m]$. In other words, the new control target coefficients $X_{k+1}^\star$ are simply set equal to the Fourier coefficients X of the asymptotic steady-state response x_{asy} reached under the control input defined with coefficients $X_k^\star$.

In summary, the overall CBC methodology to trace out the steady-state periodic response of a system in function of the forcing amplitude r is:

1. Set $X^\star := X_n + h[X_n - X_{n-1}]$ where (X_n, X_{n-1}) are the Fourier coefficients of the previous two points along the branch of periodic solutions.
2. Run the experiment with input (3.2) and $x^\star$ defined using the Fourier coefficients $X^\star$.
3. Measure the Fourier coefficients X of the output $x(t)$ after the transients have died out. Although not necessary, the control can be tuned appropriately such that the transients die out quickly.
4. Check if the root-mean-square error

$$e[u] = \sqrt{(A_0^\star - A_0)^2 + \sum_{j=2}^{m}(A_j^\star - A_j)^2 + (B_j^\star - B_j)^2} \tag{3.10}$$

is smaller than the desired tolerance. If not, proceed to the fixed-point iteration. Set $X^\star = X$ for all Fourier modes except the first ($A_1^\star$ and $B_1^\star$ are left unchanged) and go to step (3).

5. After the fixed-point iterations, the higher-harmonic coefficients of $u(t)$ are below the user-specified tolerance and the total input to the system can be considered as harmonic. The next point X_{n+1} on the branch is $X_{n+1} = X$ and the forcing is given by Eqs. (3.4)–(3.5).

This method can be regarded as an amplitude sweep carried out at constant forcing frequency.

Note that the methodology described above can be further simplified by omitting $f(t)$. The total input to the system boils down to the sole control signal $u(t)$, which now also plays the role of the excitation. The next point X_{n+1} on the branch is then given by $X_{n+1} = X$ and $(a_{n+1}, b_{n+1}) = (A_1^u, B_1^u)$.

3.2.2 Tracking the Backbone Curve

To track the backbone curve, the oscillation frequency must be updated to maintain the phase quadrature between the excitation and the response signals. This problem can be formalized as solving the scalar equation

$$q(\omega) = (\phi_{\text{out}}(\omega) - \phi_{\text{in}}(\omega)) + \frac{\pi}{2}, \tag{3.11}$$

where $\phi_{\text{out}}(\omega)$ and $\phi_{\text{in}}(\omega)$ are the phase of the fundamental Fourier modes of the response, $x(t)$, and total input, $f(t) + u(t)$, respectively. The evaluation of $q(\omega)$ is performed after the fixed-point iterations and replaces step 5 in the methodology of Sect. 3.2.1. If $q(\omega)$ is below a used-defined tolerance, the point X is recorded as the next point on the backbone curve (with $X_{n+1} = X$ and forcing given by Eqs. (3.4)–(3.5)). If $q(\omega)$ is above the prescribed tolerance, the frequency is updated and we go to step 3. Equation (3.11) can be solved using a Newton-Raphson procedure but, in practice, a simple bisection method suffice.

Equation (3.11) only accounts for the fundamental harmonic component because the excitation signal considered in the present study is harmonic. If a richer, multi-harmonic, excitation signal was to be considered, the higher-harmonic coefficients would have to be updated to satisfy the quadrature criterion. These extra unknowns could be balanced by extending the quadrature condition (3.11) to include the phase between the higher harmonics. As these higher-harmonic coefficients would now be considered as part of the excitation, they would not be included in the error (3.10) and would no longer be updated in the fixed point iteration procedure.

3.2.3 Multi-Harmonic Force Feedthrough

The presence of a feedback controller and the nonlinear nature of the tested system introduce harmonics in the applied excitation. These harmonics are addressed by the method described in Sect. 3.2.1. Despite the success of this process, the total forcing applied to the system can still possess a multi-harmonic content if, for instance, the amplifier-shaker system is nonlinear and introduces harmonics into the excitation signal. These harmonics cannot be addressed by solving Eq. (3.9) and need to be compensated for directly through the excitation signal $f(t)$. The problem of finding the appropriate forcing signal leading to a total forcing that is harmonic can be formalized as:

$$A_j^{\bar{f}}(A_j^f, B_j^f) = 0, \tag{3.12}$$

$$B_j^{\bar{f}}(A_j^f, B_j^f) = 0, \tag{3.13}$$

where $\left(A_j^f, B_j^f\right)_{(j=2)}^m$ are the Fourier coefficients of the force theoretically applied to the system and $\left(A_j^{\bar{f}}, B_j^{\bar{f}}\right)_{(j=2)}^m$ the Fourier coefficients of the force actually applied to the system $\bar{f}(t)$ (and measured in the experiment). Equations (3.12)–(3.13) can be solved using a Newton-Raphson procedure for which the Jacobian matrix $\mathbf{J}$ representing the sensitivity of the Fourier coefficients of the actual force with respect to the Fourier coefficients of the force theoretically applied can be determined experimentally using finite differences.

Remarks:

- Every modification of the applied excitation changes the system response and requires to solve Eq. (3.9) again.
- All the harmonics in Eqs. (3.12)–(3.13) do not need to be considered and the size of the Jacobian **J** can often be tailored to the first few most important harmonics.
- The perturbation used to compute **J** using finite differences might need to be adapted for each harmonic depending on the amplification or attenuation introduced by the excitation system transfer function.
- Depending on the characteristics of the excitation system, the Jacobian **J** might not need to be updated at each periodic solution.

3.3 Description of the Experimental Set-Up

The methods presented in Sect. 3.2 are demonstrated on the system shown in Fig. 3.1a. This system is made of a thin steel plate clamped at one end on an aluminum armature. At the other end of the plate, two sets of neodymium magnets are attached. The system acts as a SDOF oscillator and is fixed vertically to avoid gravity-induced deformations transverse to the plate thickness. Under base excitation, the moving magnets interact with a laminated iron stator and a coil. The magnetic interactions introduce a complex nonlinear restoring force with hardening, softening-hardening, or bi-stable characteristics depending on the distance between the magnets and the iron stator. In this study, the distance is such that the system presents a softening-hardening restoring force. The frequency range of interest is 20.5–21.35 Hz and corresponds to oscillation amplitudes of maximum 2.5 mm. The damping in the system can be adjusted with the load connected to the coil. Here, the circuit is left open producing the smallest possible damping.

Base and plate tip absolute displacements are measured using two Omron lasers, ZX2-LD50 and ZX2-LD100, respectively. Their sampling period is set to 60 µs. A strain gauge also measures the plate deformation at the clamping (see Fig. 3.1b).

The nonlinear oscillator is excited at the base by a long-stroke electrodynamic shaker, model APS 113, equipped with linear bearings and operated in current control mode using a Maxon ADS-50/10-4QDC motor controller. Typical base displacements are sinusoidal with a frequency ranging from 20.5 to 21.35 Hz and an amplitude ranging from 0 to 0.3 mm. A PID feedback control system is used to center the position of the shaker's arm. Proportional, derivative and integral gains are 0.09, 0.0085, and 0.008, respectively. The fine tuning of the control gains was not necessary for CBC to work. A second-order IIR Butterworth filter with a cutoff frequency at 500 Hz was applied to the error signal. The real-time control of the oscillator is achieved through a PD control system implemented in parallel with the PID base displacement controller. Proportional and derivative gains are 0.05 and 0.003, respectively. The error signal is based on the strain gauge signal. The latter presents a very low noise level such that filtering the error signal was not required.

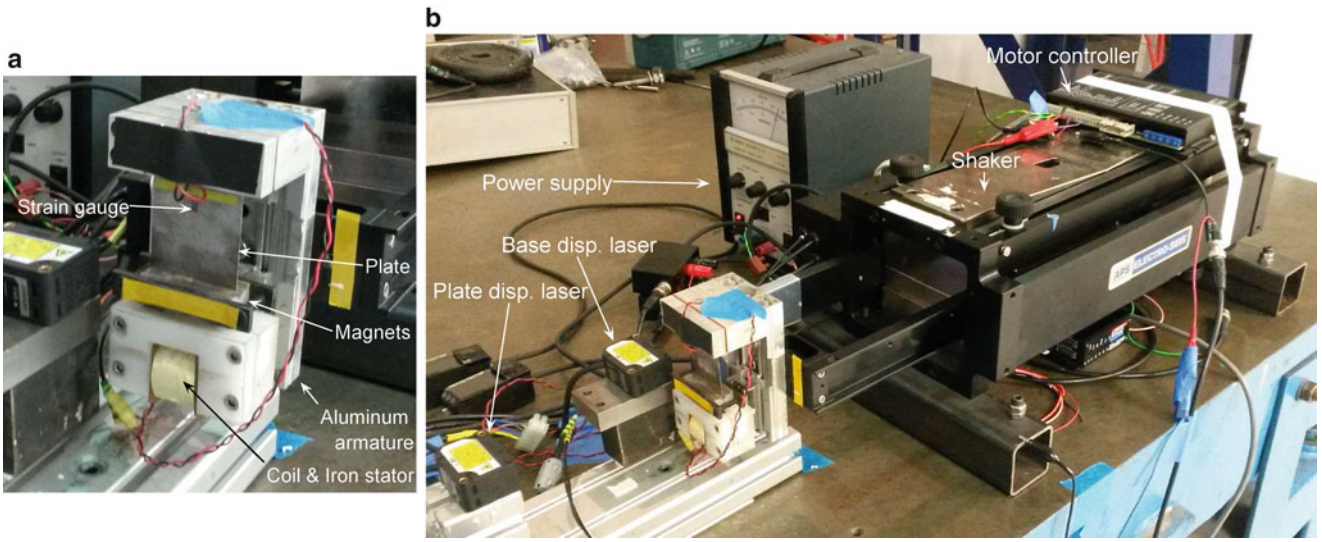

Fig. 3.1 (**a**) Picture of the nonlinear oscillator. (**b**) Picture of the experimental set-up

The controllers are implemented on a BeagleBone Black fitted with a custom data acquisition board (hardware schematics and associated software are open source and freely available [22]). All measurements are made at 5 kHz with no filtering. Estimations of the Fourier coefficients of the response, base displacement, and control action are calculated in real time on the control board. However, this was for convenience rather than a necessity.

3.4 Experimental Results

3.4.1 Preliminary Tests

The forced response of the nonlinear oscillator is studied using the CBC algorithm detailed in Sect. 3.2.1. Recorded Fourier coefficients were averaged over ten samples, and each modification of the target coefficients $X^\star$ was followed by maximum 10 waiting periods of 0.4 s each to let the transients die out. Fourier coefficients were assumed stationary if their absolute and relative variance was lower than 5×10^{-4} and 1×10^{-7}, respectively. Starting from rest, the target coefficient $A_1^\star$ was initially increased by 0.05 mm to overcome the shaker stiction. The following amplitude increments were 0.02 mm. The tolerance on Eq.(3.9) was set to 5×10^{-4} for each Fourier coefficient and a maximum of 25 iterations was allowed to reach convergence.

Figure 3.2a (solid line) shows the response amplitude of the oscillator in function of the base displacement for an excitation frequency of 20.9 Hz. Despite the good convergence of the fixed-point iteration at all measured points, Fig. 3.2b clearly shows that the base excitation contains a higher-harmonic content that can represent more than 20 % of the fundamental component amplitude. The regions with the largest higher-harmonic content were found to coincide with the fold regions where the base displacement is minimum. The presence of these higher harmonics is therefore attributed to friction forces in the shaker, which was also found to introduce small-amplitude higher harmonics when it was tested independently.

The harmonic forcing procedure described in Sect. 3.2.3 was used to retrieve the harmonic base excitation of interest. Equations (3.12)–(3.13) are solved such that the total amplitude of the higher harmonics is limited to 1.5 % of the fundamental component. The excitation was corrected for the second, third and fourth harmonics only. For the Jacobian matrix calculation, the Fourier coefficient perturbation was 1.5×10^{-2} mm, and only two or three Jacobian matrix calculations per forcing frequency were sufficient to ensure the proper resolution of Eqs. (3.12)–(3.13). The maximum number of iterations was limited to 3. The oscillator response is significantly modified by applying this procedure as illustrated by the dashed line in Fig. 3.2a. The major source of error remains now limited to the first few points with very small base displacements.

For the rest of our experimental investigations, the harmonic forcing procedure presented in Sect. 3.2.3 is always applied between the steps 4 and 5 of the methodology of Sect. 3.2.1. For the backbone identification, the procedure is also applied after the convergence of the phase quadrature condition. However, its effect on the objective function value was found to be minor such that it never required any further modification of the forcing frequency.

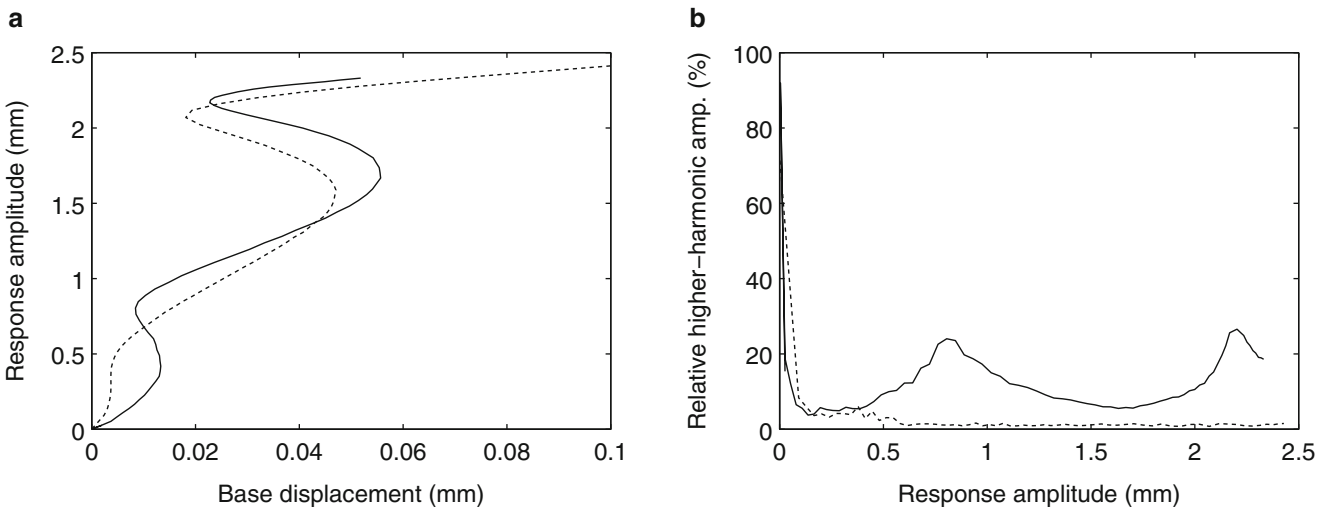

Fig. 3.2 Amplitude sweep performed on the nonlinear oscillator at 20.9 Hz. (**a**) Oscillation amplitude in function of the base displacement amplitude. (**b**) Evolution of the higher-harmonic content normalized by the amplitude of the fundamental component. *Solid* (*dashed*) *line* shows the test performed without (with) the harmonic forcing procedure presented in Sect. 3.2.3

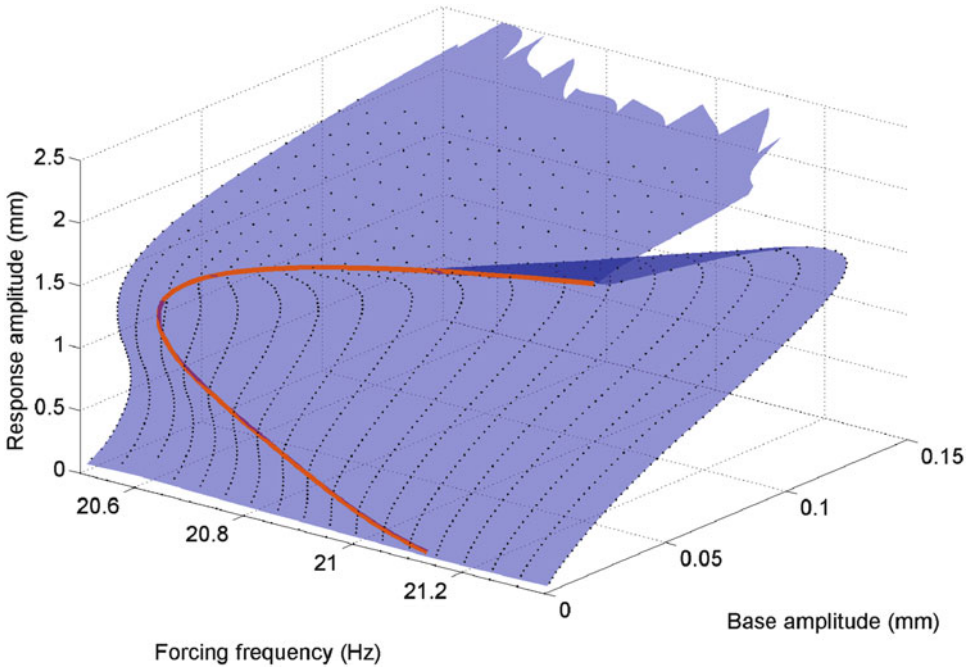

Fig. 3.3 Forced response of the SDOF shown in Fig. 3.1. (*Filled circle*) Amplitude of steady-state periodic responses measured during a series of amplitude sweeps. (*Blue surface*) The complete forced-response surface obtained using Gaussian process regression. (*Red solid line*) Backbone curve measured using CBC

3.4.2 Forced Response and Backbone Curve

Repeated amplitude sweeps for fixed values of the forcing frequency were carried out between 20.5 and 21.35 Hz in steps of 0.05 Hz. CBC parameters are identical to those used in Sect. 3.4.1. At each data point, full time series measurements were made. These are shown as black dots in Fig. 3.3 where the forcing frequency and forcing amplitude (in mm) are plotted against the response amplitude. To aid visualisation, a continuous surface constructed from the individual data points is plotted in blue. This surface was created using Gaussian Process regression on the collected data points where the hyper-parameters for the Gaussian process are calculated by maximizing the marginal likelihood of the hyper-parameters [23]. Due to the softening-hardening character of the system, the surface presents four fold regions between 20.55 and 21.15 Hz.

The CBC algorithm was also used to extract the backbone curve of the nonlinear oscillator. The objective function (3.11) was defined using the phase difference between the base displacement and the strain gauge measurement. The tolerance on (3.11) was 5×10^{-3} rad, and the minimum frequency step was 10^{-4} Hz. The backbone curve was then discretized using a constant amplitude step $h = 0.02$ mm. The frequency was adapted as described in Sect. 3.2.2.

The backbone curve measured using CBC and the phase quadrature condition introduced in Sect. 3.2.2 is superimposed (in red) to the nonlinear oscillator forced response in Fig. 3.3. The total experimental time required to generate the curve was 71 min for a total of 68 points. The measured backbone curve is also presented in a forcing frequency—response amplitude plot in Fig. 3.4. The system presents a softening characteristic up to 1.3 mm where the oscillation frequency has dropped by 3 %. At 1.3 mm the backbone curve presents a turning point, above which the system presents a hardening characteristic with a resonance frequency increasing from 20.6 to 21.3 Hz in the [1.3–2.5] mm displacement range. At high-amplitude, the fundamental Fourier coefficients still contribute the most to the response. The second and third harmonics are the largest higher harmonics in the oscillator response. However, their relative importance compared to the fundamental component does not exceed 5 and 2 %, respectively, such that, in the present case, a single-harmonic excitation was sufficient to accurately reach quadrature and isolate the NNM motion.

The variability of our experimental results is also investigated in Fig. 3.4. The results obtained for two different (consecutive) CBC runs are superimposed to the first one. Overall, the result repeatability is excellent.

The CBC method offers means to verify and validate the quality of the experimental results. Besides the convergence of the objective function (3.11), the assumption of single-harmonic base excitation and the invasive character of the (PD) controller can be assessed. This verification is performed in Fig. 3.5 where the root-mean-square (RMS) values of three different time series are shown in function of the base displacement amplitude. RMS values were normalized by the RMS

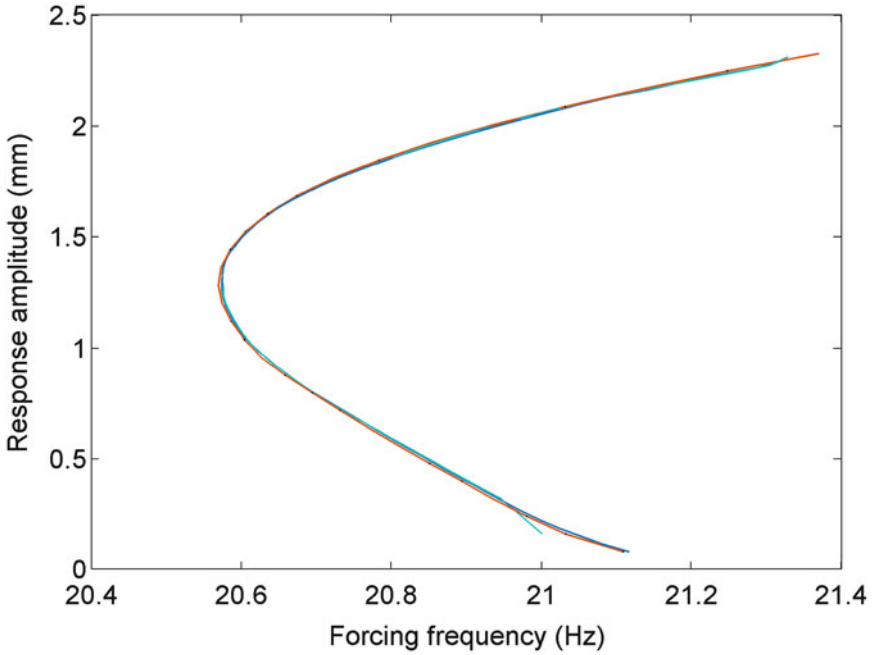

Fig. 3.4 Backbone curve tracing out the amplitude dependence of the resonance frequency of the experimental set-up shown in Fig. 3.1. Three different, consecutive, runs are shown to illustrate the low variability of the experimental results

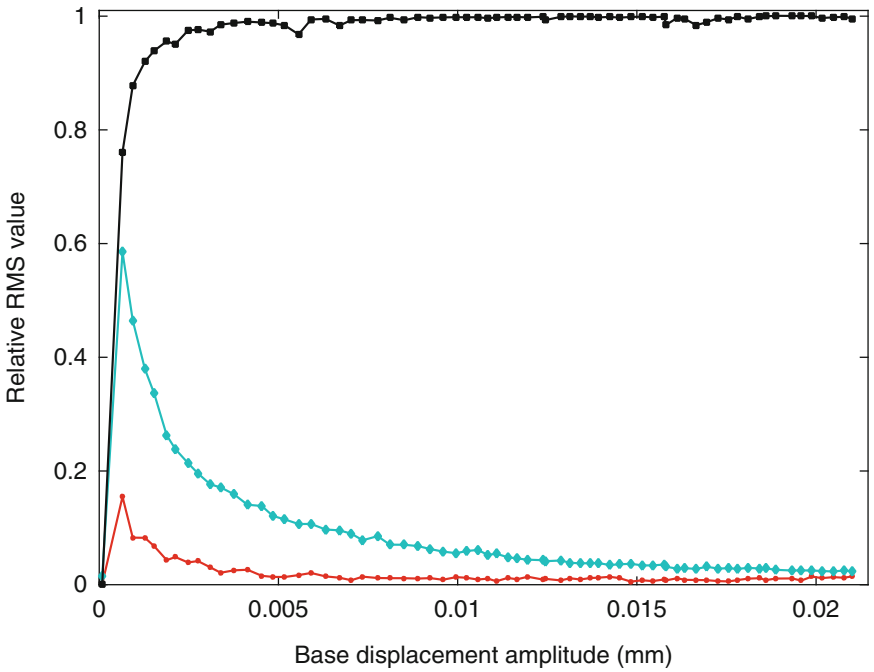

Fig. 3.5 Analysis of the base excitation in function of the base displacement amplitude. (*Solid line with filled square*) RMS value of the fundamental component; (*blue solid line with diamond*) RMS value of the non-harmonic component of the signal; (*red solid line with filled circle*) RMS value of the higher-order harmonic components

value of the total base excitation signal. The first time series (-■-) represent the first (fundamental) harmonic component of the base displacement. The second time series (-●-) is made of the sum of the higher-order harmonics, and the third one (-◇-) accounts for the non-harmonic content present in the unfiltered data and that is not decomposed in the seven first Fourier modes. From Fig. 3.5, we can see that the RMS value of the fundamental component is overall comparable to the RMS value of the entire time series. For low base displacement, the error introduced by the non-harmonic content appears to be important. However, this is essentially attributed to noise which represents therefore a non-resonant contribution to

the excitation and has a small effect on the results. The higher-harmonic content, which can significantly affect the results (as shown in Fig. 3.2), reaches approximately 10 % for the first few points but decreases below 1.5 % after about the 10 first points.

3.5 Conclusions

In this paper, the dynamics of a nonlinear oscillator with a softening-hardening restoring force was investigated experimentally. CBC was used to characterize the steady-state periodic responses of the oscillator for different forcing amplitudes and frequencies. Strong harmonics were observed in the base excitation and successfully cancelled out by changing the harmonic content of the applied force. Finally, the method developed in [11] for the identification of backbone curves using CBC was successfully demonstrated on this new system. The softening-hardening characteristic of the oscillator was captured accurately and matched the forced response.

Acknowledgements L.R. is a Marie-Curie COFUND Postdoctoral Fellow of the University of Liége, co-funded by the European Union, S.A.N. is funded by EPSRC fellowship EP/K005375/1, D.A.W.B. by EPSRC grant EP/K032738/1, which are gratefully acknowledged.

References

1. Renson, L., Noël, J.P., Kerschen, G.: Complex dynamics of a nonlinear aerospace structure: numerical continuation and normal modes. Nonlinear Dyn. **79**(2), 1293–1309 (2015)
2. Cammarano, A., Hill, T.L., Neild, S.A., Wagg, D.J.: Bifurcations of backbone curves for systems of coupled nonlinear two mass oscillator. Nonlinear Dyn. **77**(1–2), 311–320 (2014)
3. Kuether, R.J., Renson, L., Detroux, T., Grappasonni, C., Kerschen, G., Allen, M.S.: Nonlinear normal modes, modal interactions and isolated resonance curves. J. Sound Vib. **351**, 299–310 (2015)
4. Kerschen, G., Peeters, M., Golinval, J.C., Vakakis, A.F.: Nonlinear normal modes, part I: a useful framework for the structural dynamicist. Mech. Syst. Signal Process. **23**(1), 170–194 (2009)
5. Peeters, M., Viguié, R., Sérandour, G., Kerschen, G., Golinval, J.C.: Nonlinear normal modes, part II: toward a practical computation using numerical continuation techniques. Mech. Syst. Signal Process. **23**(1), 195–216 (2009)
6. Peeters, M., Kerschen, G., Golinval, J.C.: Dynamic testing of nonlinear vibrating structures using nonlinear normal modes. J. Sound Vib. **330**(3), 486–509 (2011)
7. Peeters, M., Kerschen, G., Golinval, J.C.: Modal testing of nonlinear vibrating structures based on nonlinear normal modes: experimental demonstration. Mech. Syst. Signal Process. **25**(4), 1227–1247 (2011)
8. Londono, J.M., Neild, S.A., Cooper, J.E.: Identification of backbone curves of nonlinear systems from resonance decay responses. J. Sound Vib. **348**, 224–238 (2015)
9. Zapico-Valle, J.L., Garcia-Diéguez, M., Alonso-Camblor, R.: Nonlinear modal identification of a steel frame. Eng. Struct. **56**, 246–259 (2013)
10. Noël, J.P., Renson, L., Grappasonni, C., Kerschen, G.: Identification of nonlinear normal modes of engineering structures under broadband forcing. Mech. Syst. Signal Process. (in press). http://dx.doi.org/10.1016/j.ymssp.2015.04.016
11. Renson, L., Gonzalez-Buelga, A., Barton, D.A.W., Neild, S.A.: Robust identification of backbone curves using control-based continuation. J. Sound Vib. **367**, 145–158 (2016)
12. Doedel, E.J., Paffenroth, R.C., Champneys, A.R., Fairgrieve, T.F., Kuznetsov, Y.A., Oldeman, B.E., Sandstede, B., Wang, X.J.: Auto2000: continuation and bifurcation software for ordinary differential equations, Technical Report, California Institute of Technology (2000). Available via http://cmvl.cs.concordia.ca/
13. Dhooge, A., Govaerts, W., Kuznetsov, Y.A.: Matcont: a matlab package for numerical bifurcation analysis of odes. ACM Trans. Math. Softw. **29**(2), 141–164 (2003)
14. Dankowicz, H., Schilder, F.F.: Recipes for Continuation. Computational Science and Engineering, vol. 11. SIAM, Philadelphia (2013)
15. Bureau, E., Schilder, F., Ferreira Santos, I., Thomsen, J.J., Starke, J.: Experimental bifurcation analysis of an impact oscillator - tuning a non-invasive control scheme. J. Sound Vib. **332**(22), 5883–5897 (2013)
16. Barton, D.A.W.: Control-based continuation: bifurcation and stability analysis for physical experiments. Mech. Syst. Signal Process. (in press). http://dx.doi.org/10.1016/j.ymssp.2015.12.039
17. Sieber, J., Krauskopf, B.: Control based bifurcation analysis for experiments. Nonlinear Dyn. **51**(3), 365–377 (2008)
18. Barton, D.A.W., Mann, B.P., Burrow, S.G.: Control-based continuation for investigating nonlinear experiments. J. Vib. Control **18**(4), 509–520 (2012)
19. Barton, D.A.W., Burrow, S.G.: Numerical continuation in a physical experiment: investigation of a nonlinear energy harvester. J. Comput. Nonlinear Dyn. **6**(1), 011010-1:6 (2010)
20. Seydel, R.: Practical Bifurcation and Stability Analysis. Interdisciplinary Applied Mathematics, vol. 5. Springer, New York (2010)
21. Barton, D.A.W., Sieber, J.: Systematic experimental exploration of bifurcations with noninvasive control. Phys. Rev. E **87**(5), 052916 (2013)
22. Barton, D.A.W.: Real-time control hardware/software based on the BeagleBone Black, (2015) http://github.com/~db9052/rtc
23. Rasmussen, C.E., Williams, C.: Gaussian Processes for Machine Learning. MIT, Cambridge (2006)

Chapter 4
Experimental Nonlinear Dynamics of Laminated Quasi-Isotropic Thin Composite Plates

H.G. Kim and R. Wiebe

Abstract Composite panels and plates are increasingly used and continuously developed in diverse industrial domains such as aerospace, automobile, civil and naval structures. However, nonlinear dynamic behavior and failure mechanisms of these structures are still obscure in many respects. A representative example of this issue is nonlinear dynamic behavior of damaged curved composite plates, which is not well represented in the literature although the phenomena could have a detrimental effect on the safety of the aforementioned structures. In this work, free vibrations of (a) an isotropic flat plate (ASTM A36 steel) under fully clamped (CCCC) and cantilever (CFFF) boundary conditions, (b) a symmetrically laminated quasi-isotropic flat composite plate (unidirectional carbon/epoxy) under the same boundary conditions (CCCC and CFFF), and (c) a post-buckled symmetrically laminated quasi-isotropic flat composite plate (carbon fibers woven fabrics) under a clamped and free (CCFF) boundary condition are investigated. A single-point laser is used to capture the dynamic responses of the plates. The von Kármán strain-displacement relations and Rayleigh-Ritz method are employed based on the classical laminated plate theory (CLPT) to establish a theoretical model. This research will ultimately be extended to the nonlinear modeling of vibrations and damage of curved laminated composite plates subjected to large deformations.

Keywords Nonlinear dynamics • Free vibration • Experimental mechanics • Quasi-isotropic composite plate • Post-buckled plate

4.1 Introduction

The industrial application of composite materials has been significantly growing during the last half century due to its well-known properties, high strength and low density [1]. The Boeing 787 which is the first commercial airliner with a composite fuselage and wings is a compelling example of the structural application of composite materials. Fifty percent of its primary structures, including the fuselage and wings, is made up of carbon fiber/epoxy composite materials, or carbon fiber-reinforced plastics (CFRP) [2]. This design has led to 20 % of weight savings and 30 % lower airframe maintenance cost [3]. Despite the increasing demand and application of the composite structures, its failure mechanism is still obscure. Considerable efforts to develop accurate failure theories of composites and to prove their validity have been made as shown in the so-called World Wide Failure Exercise (WWFE-I: 1996–2004, WWFE-II: 2007–2013, and WWFE-III: 2013–Present); however, no composite material failure criteria are making precise predictions on damage and failure of composite materials and a global consensus about the validity of the leading theories has yet to be reached [2, 4].

Quasi-isotropic laminates have been very popular due to their isotropic behavior under in-plane extension (but not locally), and this fact has motivated engineers to substitute metals with quasi-isotropic laminates simply using the previous designs for the metals [5]. Similarly, black quasi-isotropic carbon/epoxy laminates are called as *black aluminum* because their in-plane effective elastic properties can be remarkably close to those of aluminum alloys [5]. However, this approach overlooks the crucial properties of quasi-isotropic laminates such as anisotropic out-of-plane behavior, delamination, and inter-laminar failure [5]. Moreover, although quasi-isotropic laminates exhibit isotropic behavior under in-plane extension at the laminate level, each ply experiences different magnitude of stresses depending on its material properties and geometry, which determines the failure of the plies. In this paper, to address these challenges, linear and nonlinear out-of-plane dynamic responses of both flat and post-buckled laminated quasi-isotropic composite plates are presented.

A robust review and analysis of theories on linear dynamic behaviors of isotropic plates was presented by Leissa in [6] and [7]. Chia exhaustively discussed nonlinear static and dynamic behaviors of isotropic and anisotropic plates in [8]. Many

H.G. Kim (✉) • R. Wiebe
Civil and Environmental Engineering, University of Washington, Seattle, WA 98195, USA
e-mail: hgyukim@uw.edu

G. Kerschen (ed.), *Nonlinear Dynamics, Volume 1*, Conference Proceedings of the Society for Experimental Mechanics Series,
DOI 10.1007/978-3-319-29739-2_4

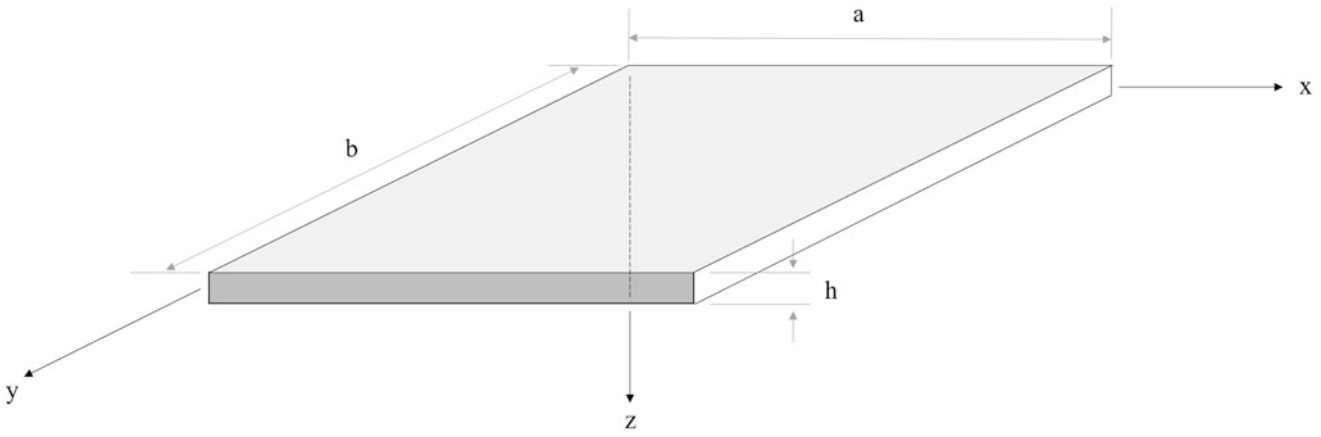

Fig. 4.1 Geometry and coordinate system for a rectangular plate

different types of laminated composite plate theories have been proposed or discussed in the literature such as Classical laminated plate theory (CLPT), First-order shear deformation theories (FSDT), Higher-order shear deformation theories (HOSDTs), and Layerwise theory (LT) [1]. Despite the challenges from other theories, CLPT is still preferred to model behaviors of thin composite plates and shows relatively accurate predictions on balanced symmetric laminates under pure bending or tension [1]. In this paper, CLPT is used to establish the theoretical model of free vibration of quasi-isotropic plates. The experiment results on free vibration of isotropic plates under fully clamped (CCCC) and cantilever (CFFF) boundary conditions are used to prove the validity of the model. In addition, the nonlinear dynamic behaviors of initially flat, and post-buckled quasi-isotropic plates are analyzed.

4.2 Theoretical Model for Linear Free Vibrations

The derivation of the equation of motion for linear free vibrations of anisotropic plates are well explained many books such as [9] and [10]. In this section, the derivation of the theoretical model will be presented based on the Reddy's work in [9].

Based on Hamilton's principle, the dynamic version of the principle of virtual work is

$$0 = \int_0^T (\delta U + \delta V - \delta K) dt \tag{4.1}$$

where the virtual strain energy δU, virtual work done by applied force δV, and the virtual kinetic energy δK are given by

$$\delta U = \int_{\Omega_0} \int_{-\frac{h}{2}}^{\frac{h}{2}} (\sigma_{xx}\delta\epsilon_{xx} + \sigma_{yy}\delta\epsilon_{yy} + 2\sigma_{xy}\delta\epsilon_{xy}) dz dx dy \tag{4.2}$$

$$\begin{aligned} \delta V = &- \int_{\Omega_0} \left[q_b(x,y)\delta w\left(x,y,\frac{h}{2}\right) + q_t(x,y)\delta w\left(x,y,-\frac{h}{2}\right) \right] dx dy \\ &- \int_{\Gamma_\sigma} \int_{-\frac{h}{2}}^{\frac{h}{2}} [\hat{\sigma}_{nn}\delta u_n + \hat{\sigma}_{ns}\delta u_s + \hat{\sigma}_{nz}\delta w] dz ds \end{aligned} \tag{4.3}$$

$$\begin{aligned} \delta K = \int_{\Omega_0} \int_{-\frac{h}{2}}^{\frac{h}{2}} \rho_0 \Big[&\left(\dot{u}_0 - z\frac{\partial \dot{w}_0}{\partial x}\right)\left(\delta\dot{u}_0 - z\frac{\partial \delta\dot{w}_0}{\partial x}\right) \\ &+ \left(\dot{v}_0 - z\frac{\partial \dot{w}_0}{\partial y}\right)\left(\delta\dot{v}_0 - z\frac{\partial \delta\dot{w}_0}{\partial y}\right) + \dot{w}_0\delta\dot{w}_0 \Big] dz dx dy \end{aligned} \tag{4.4}$$

where q_b and q_t are the distributed forces at the bottom and at the top, respectively, and $\hat{\sigma}_{nn}$, $\hat{\sigma}_{ns}$, and $\hat{\sigma}_{nz}$ are the specified stress components on the portion Γ_σ of the boundary Γ.

Applying the von Kármán strain-displacement relations, the Euler-Lagrange equations of motion in terms of δw_0 obtained from Eq. (4.1) is

$$\begin{aligned}\frac{\partial^2 M_{xx}}{\partial x^2}+2\frac{\partial^2 M_{xy}}{\partial y\partial x}+\frac{\partial^2 M_{yy}}{\partial^2 y}+\frac{\partial}{\partial x}(N_{xx}\frac{\partial w_0}{\partial x}+N_{xy}\frac{\partial w_0}{\partial y})+\frac{\partial}{\partial y}(N_{xy}\frac{\partial w_0}{\partial x}+N_{yy}\frac{\partial w_0}{\partial y})+q\\ =\rho h\frac{\partial^2 w_0}{\partial t^2}\end{aligned} \tag{4.5}$$

where N_{xx}, N_{yy}, and N_{xy} are in-plane force resultants, and M_{xx}, M_{yy}, and M_{xy} are moment resultants.

Taking the weak form of Eq. (4.5) and setting N_{xx}=N_{yy}=N_{xy}=0 and q=0 for natural vibration,

$$\begin{aligned}0=\int_o^b\int_0^a\Big\{&D_{11}\frac{\partial^2 w_0}{\partial x^2}\frac{\partial^2\delta w_0}{\partial x^2}+D_{12}\Big(\frac{\partial^2 w_0}{\partial y^2}\frac{\partial^2\delta w_0}{\partial x^2}+\frac{\partial^2 w_0}{\partial x^2}\frac{\partial^2\delta w_0}{\partial y^2}\Big)\\&+D_{22}\frac{\partial^2 w_0}{\partial y^2}\frac{\partial^2\delta w_0}{\partial y^2}+4D_{66}\frac{\partial^2 w_0}{\partial x\partial y}\frac{\partial^2\delta w_0}{\partial x\partial y}+2D_{16}\Big(\frac{\partial^2 w_0}{\partial x\partial y}\frac{\partial^2\delta w_0}{\partial x^2}+\frac{\partial^2 w_0}{\partial x^2}\frac{\partial^2\delta w_0}{\partial x\partial y}\Big)\\&+2D_{26}\Big(\frac{\partial^2 w_0}{\partial x\partial y}\frac{\partial^2\delta w_0}{\partial y^2}+\frac{\partial^2 w_0}{\partial y^2}\frac{\partial^2\delta w_0}{\partial x\partial y}\Big)-\omega^2\rho h w_0\delta w_0\Big\}dxdy\end{aligned} \tag{4.6}$$

where ω and D_{ij} denote the frequency of free vibrations and bending stiffness, respectively. Applying Rayleigh-Ritz approximation to (4.6),

$$\begin{aligned}0=\sum_i^M\sum_j^N\Big\{\int_0^b\int_0^a\Big[&\Big(D_{11}\frac{d^2X_i}{dx^2}\frac{d^2X_k}{dx^2}Y_jY_l+4D_{66}\frac{\mathrm{d}X_i}{\mathrm{d}x}\frac{\mathrm{d}X_k}{\mathrm{d}x}\frac{\mathrm{d}Y_j}{\mathrm{d}y}\frac{\mathrm{d}Y_l}{\mathrm{d}y}\\&+D_{12}\Big(X_i\frac{d^2X_k}{dx^2}\frac{d^2Y_j}{dy^2}Y_l+\frac{d^2X_i}{dx^2}X_kY_j\frac{d^2Y_l}{dy^2}\Big)+D_{22}X_iX_k\frac{\mathrm{d}^2Y_j}{\mathrm{d}y^2}\frac{\mathrm{d}^2Y_l}{\mathrm{d}y^2}\\&+2D_{16}\Big(\frac{dX_i}{dx}\frac{d^2X_k}{dx^2}\frac{dY_j}{dy}Y_l+\frac{d^2X_i}{dx^2}\frac{dX_k}{dx}Y_j\frac{dY_l}{dy}\Big)\\&+2D_{26}\Big(\frac{dX_i}{dx}X_k\frac{dY_j}{dy}\frac{d^2Y_l}{dy^2}+X_i\frac{dX_k}{dx}\frac{d^2Y_j}{dy^2}\frac{dY_l}{dy}\Big)\Big]dxdy\Big\}c_{ij}\\-\sum_i^M\sum_j^N\Big\{\int_0^b\int_0^a&\omega^2\rho hX_iX_kY_jY_l dxdy\Big\}c_{ij}\quad fork=1,\ldots,M,l=1,\ldots,N\end{aligned} \tag{4.7}$$

where

$$\begin{aligned}w_0(x,y)\simeq W_{MN}(x,y)=\sum_{i=1}^M\sum_{j=1}^N c_{ij}\varphi_{ij}(x,y),\quad \varphi_{ij}(x,y)=X_i(x)Y_j(y)\\ \delta w_0(x,y)\simeq \delta W_{MN}(x,y)=\sum_{k=1}^M\sum_{l=1}^N \delta c_{kl}\varphi_{kl}(x,y),\quad \varphi_{kl}(x,y)=X_k(x)Y_l(y)\end{aligned} \tag{4.8}$$

where X_i and Y_j denote any admissible approximation functions for geometric boundary conditions.

In the matrix form,

$$\big(\,[R]-\omega^2[B]\,\big)\,\{\,c\,\}=0 \tag{4.9}$$

where

$$
\begin{aligned}
R_{(ij)(kl)} =& D_{11}\int_0^a \frac{d^2X_i}{dx^2}\frac{d^2X_k}{dx^2}dx\int_0^b Y_jY_ldy + 4D_{66}\int_0^a \frac{\mathrm{d}X_i}{\mathrm{d}x}\frac{\mathrm{d}X_k}{\mathrm{d}x}dx\int_0^b \frac{\mathrm{d}Y_j}{\mathrm{d}y}\frac{\mathrm{d}Y_l}{\mathrm{d}y}dy \\
&+ D_{12}\Big(\int_0^a X_i\frac{d^2X_k}{dx^2}dx\int_0^b \frac{d^2Y_j}{dy^2}Y_ldy + \int_0^a \frac{d^2X_i}{dx^2}X_kdx\int_0^b Y_j\frac{d^2Y_l}{dy^2}dy\Big) \\
&+ D_{22}\int_0^a X_iX_kdx\int_0^b \frac{\mathrm{d}^2Y_j}{\mathrm{d}y^2}\frac{\mathrm{d}^2Y_l}{\mathrm{d}y^2}dy \\
&+ 2D_{16}\Big(\int_0^a \frac{dX_i}{dx}\frac{d^2X_k}{dx^2}dx\int_0^b \frac{dY_j}{dy}Y_ldy + \int_0^a \frac{d^2X_i}{dx^2}\frac{dX_k}{dx}dx\int_0^b Y_j\frac{dY_l}{dy}dy\Big) \\
&+ 2D_{26}\Big(\int_0^a \frac{dX_i}{dx}X_kdx\int_0^b \frac{dY_j}{dy}\frac{d^2Y_l}{dy^2}dy + \int_0^a X_i\frac{dX_k}{dx}dx\int_0^b \frac{d^2Y_j}{dy^2}\frac{dY_l}{dy}dy\Big)
\end{aligned}
\tag{4.10}
$$

and

$$
B_{(ij)(kl)} = \rho h\int_0^a X_iX_kdx\int_0^b Y_jY_ldy \tag{4.11}
$$

Simple beam functions are used for X_i and Y_j. For a rectangular plate clamped on all sides (CCCC), $X_i(x) = (\frac{x}{a})^{i+1}(1-\frac{x}{a})^2$ and $Y_j(y) = (\frac{y}{b})^{j+1}(1-\frac{y}{b})^2$ are used while for a cantilever rectangular plate (CFFF), $X_i(x) = (\frac{x}{a})^{i+1} - \frac{2i}{i+2}(\frac{x}{a})^{i+2} + \frac{i(i+1)}{(i+2)(i+3)}(\frac{x}{a})^{i+3}$ and $Y_j(y) = (\frac{y}{b})^{j-1}$ are used.

The eigenvalue problem in Eqs. (4.9)–(4.11) was solved using MatLab.

4.3 Experiment

In this experiment, three types of plates are analyzed: (a) a square isotropic plate (ASTM A36 Steel, named *Plate 1*), (b) a symmetrically laminated square quasi-isotropic composite plate (unidirectional carbon/epoxy, named *Plate 2*), and (c) a symmetrically laminated rectangular quasi-isotropic composite plate (carbon fibers woven fabrics, named *Plate 3*). Their geometrical and material properties are defined in Table 4.1. The values of *Plate 2* is based on the manufacturer's report. The technical report of *Plate 3* is unavailable and thus could not be included in this table. The dimension of *Plate 3* is a=254 mm (10 in.) and b=127 mm (5 in.).

Table 4.1 Geometrical and material properties

	Plate 1	Plate 2 (Manufacturer's specs)
Material	ASTM A36 Steel	Pyrofil TR50S 12K, Newport 301
Number of layers	N/A	8 ([0/45/90/135]s)
a mm (in.)	254 (10)	254 (10)
b mm (in.)	254 (10)	254 (10)
h mm (in.)	1.524 (0.06)	2.54 (0.1)
E_{11} GPa (Msi)	200 (29)	131 (19)
E_{22} GPa (Msi)	200 (29)	8.963 (1.3)
G_{12} GPa (Msi)	79.3	6.895 (1.0)
ν_{12}	0.26	0.3
ρ kg/m^3 (lb/in.^{3})	7750 (0.28)	1533 (0.0556)
D_{ij} GPa-mm^3 (ksi-in.^{3})	63.2 (0.56)	D_{11}=124 (1.097), D_{12}=15.2 (0.1345), D_{16}=D_{26}=11.8 (0.1044), D_{22}=45.4 (0.4014), D_{66}=20.9 (0.1852)

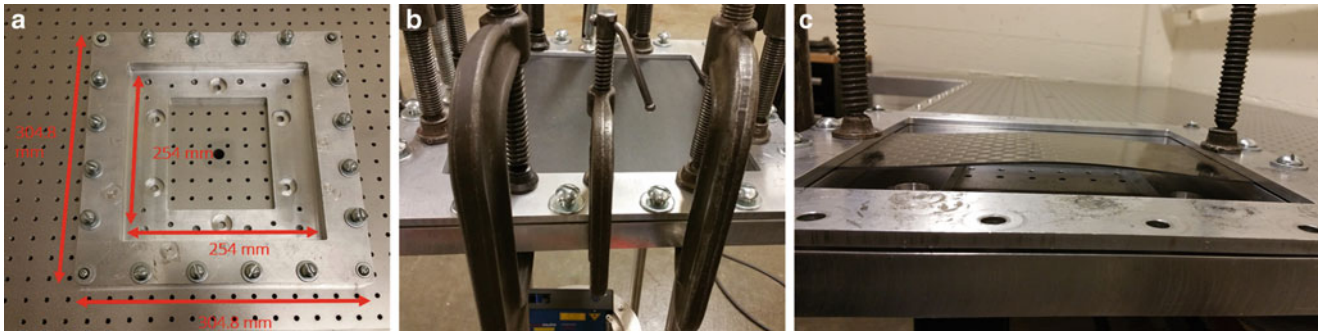

Fig. 4.2 Experimental setup: (**a**) an aluminum square clamp, (**b**) the plates are embedded into the square clamp and fastened with several C-clamps and bolts of the clamp, which tightened the clamp to prevent any rotation, (**c**) post-buckled rectangular plate a=254 mm (10 in.), b=127 mm (5 in.) under CCFF

A single-point laser, Micro-epsilon optoNCDT 1700-500 is used to capture dynamic responses of the plate. For the fully clamped condition, an aluminum square clamp is used (Fig. 4.2a) and the plates are embedded 25.4 mm (1 in.) into the clamp and several C-clamps are placed to ensure fixed boundary conditions at the edges. The C-clamps augmented the bolts used to tighten the frame, and were needed because the plate stiffness was higher than anticipated (Fig. 4.2b).

The steel plate, *Plate 1*, was tested to verify the validity of the theoretical model. The cantilever test of the quasi-isotropic plate, *Plate 2*, was done in two different directions: 0° and 90°. In 0°, 0° fiber direction is in the direction of x axis, while in 90°, 0° fiber direction is in the direction on y axis. For both cases, the plate is clamped at x=0. For the free vibrations of the post-buckled plate, *Plate 3* is placed and buckled by the strong-bow effect on the same square clamp with the boundary conditions: clamped at x=0 and x=a, and free at y=0 and y=b. The free vibration of *Plate 3* was investigated first to compare with the post-buckled behavior.

The plates were subjected to impact loading and the fast Fourier transform (FFT) of the responses was adopted to obtain the natural frequencies of the plates. Although they are not steady state responses but time varying responses, the FFT provides a good approximation.

4.3.1 Results

The experiment result of the fully clamped CCCC *Plate 1* showed a very good agreement with the theoretical value (0.74 % error) as shown in Fig. 4.3 and Table 4.2. However, the test results of the cantilever (CFFF) *Plate 1* showed a bigger error (6.37 %) than the did the clamped plate. Compared to the CCCC condition case, the free edges of the cantilever, especially at x=a, are difficult to control and to make the mode shape we want with impact loading. The free edge at x=a can make various unpredictable mode shapes when it is excited. Thus, the error could be caused by the difference between the beam function $Y_j(y)$ used in the theoretical model and the mode shape the tested plate made.

The fully clamped (CCCC) test of *Plate 2* shows a considerable error (17.0 %) from the theoretical value (Fig. 4.4). This error consistently happened to the cantilever (CFFF) test of *Plate 2*. As shown on Fig. 4.5, it shows 18.52 and 16.90 % errors from the theoretical model. Although considering the error of the CFFF test can be, to some extent, attributed to what has led to the error of the CFFF *Plate 1*, the remaining portion of the error is a relatively large value and that does not explain the error of the CCCC *Plate 2*. Moreover, the steel plate tests confirm the method is working well; thus, material uncertainty remains the only plausible source of the error as composites are notoriously variable. A quality control issue during manufacturing the plate can cause the uncertainty, which makes the actual stiffness of *Plate 2* smaller than the manufacturer suggests. As shown on Table 4.3, with the 30 % reduction of E11 and E22 of *Plate 2*, the theoretical model shows a fair agreement with the experiment result, which substantiate the argument for the source of the error.

While the flat *Plate 3* showed 115 Hz as the first natural frequency, due to the nonlinearity, the post-buckled *Plate 3* shows the increase in natural frequency, 140 Hz (21.74 % increase) in the buckled up and 125 Hz (8.70 % increase) in the buckled down configuration (Fig. 4.6a). This indicates that it was well past buckling, as near buckling, the frequency drops to zero (for an imperfection free plate). Figure 4.6b presents an interesting phenomenon. With a bigger excitation, the post-buckled plate showed several snap-through events during the free vibration. This is a representative example of the topic we are extending from this research, the nonlinear modeling of vibrations and damage of curved laminated composite plates subjected to large deformations.

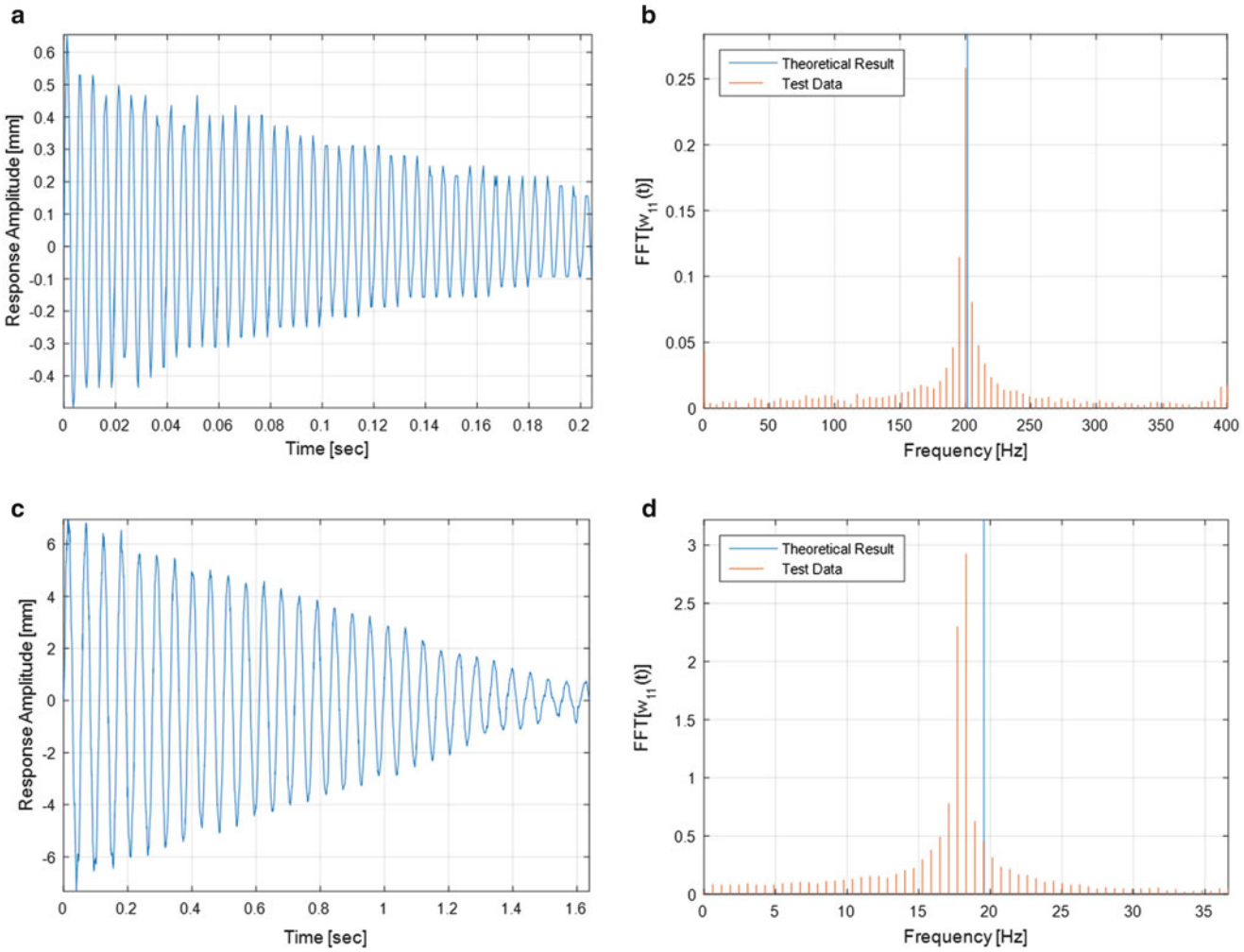

Fig. 4.3 Free vibration of the isotropic plate (ASTM A36 Steel, *Plate 1*): (**a**) fully clamped (CCCC) response amplitude vs. time, (**b**) the FFT of (**a**) shows 200.195 Hz against the theoretical result 201.691 Hz, (**c**) cantilever (CFFF) response amplitude vs. time, (**d**) the FFT of (**c**) shows 18.311 Hz against the theoretical result 19.556 Hz

Table 4.2 Theoretical and experimental natural frequency of the first mode of *Plate 1*

Boundary condition	Theory (Hz)	Experiment (Hz)	Error (%)
CCCC	201.691	200.195	0.74
CFFF	19.556	18.311	6.37

4.4 Conclusions and Future Work

The free vibrations of the flat isotropic and quasi-isotropic composite plates are investigated. While the experiment results of the isotropic steel plate showed a good agreement with the theoretical model based on CLPT, the results of the quasi-isotropic composite plate showed a considerable difference from the same model. The adjusted material properties of the tested plates helped the model well match with the test results, which suggests that the material properties inconsistent from indicated by the manufacturer has made a significant contribution to the error. This highlights that the well-known uncertainty of material properties of composite plates can produce a detrimental effect on the process of validating the plausibility of theoretical models. Thus, for future works, composite plates fabricated in-house under proper quality control will be used for experiments.

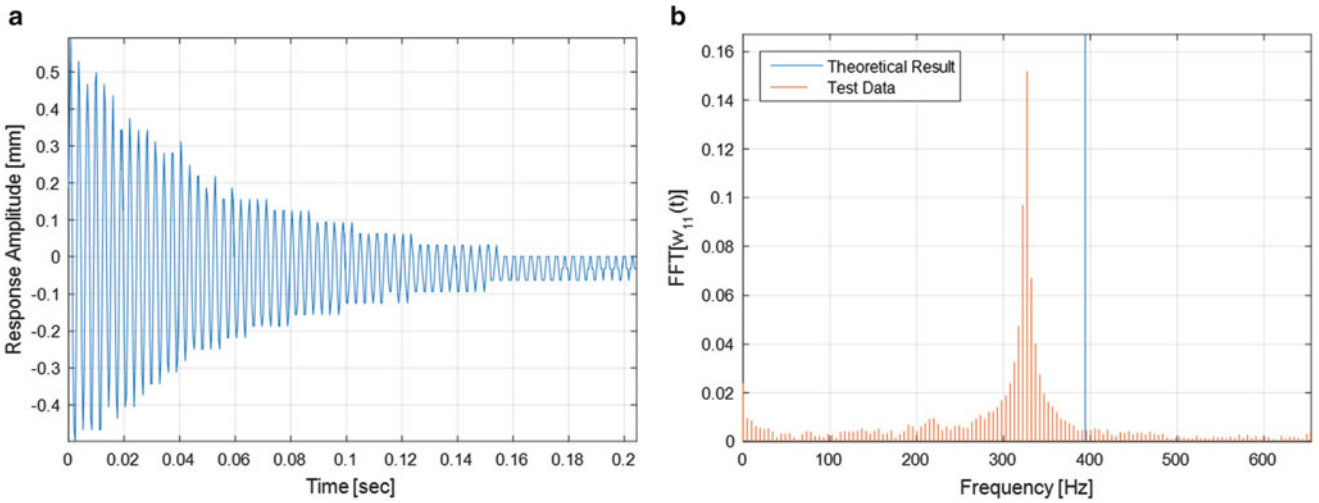

Fig. 4.4 Free vibration of the fully clamped (CCCC) quasi-isotropic plate ([0/45/90/135]s carbon fiber-epoxy, *Plate 2*): (**a**) response amplitude vs. time, (**b**) the FFT of (**a**) shows 327.148 Hz against the theoretical result 394.157 Hz

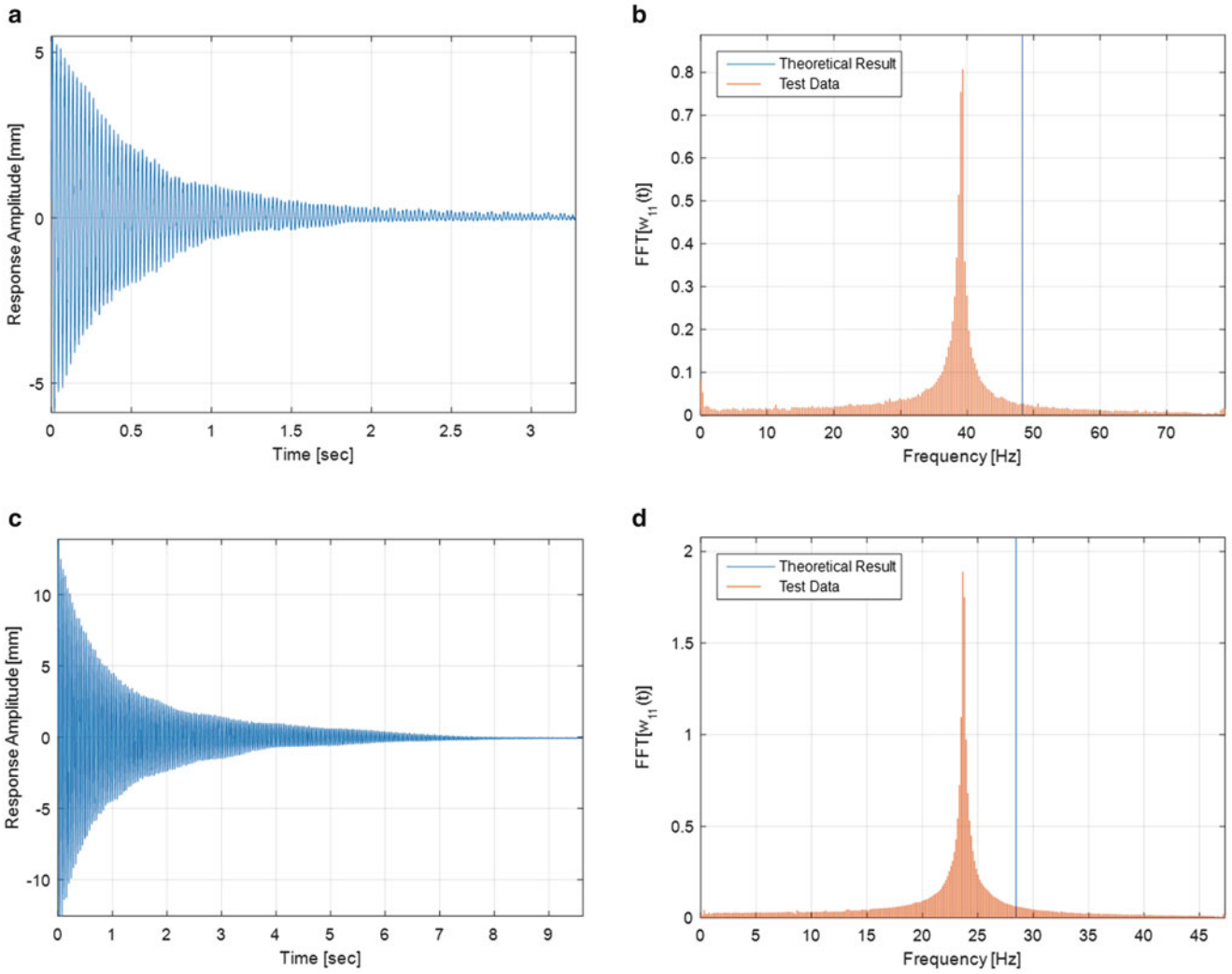

Fig. 4.5 Free vibration of the cantilever (CFFF) quasi-isotropic plate ([0/45/90/135]s carbon fiber-epoxy, *Plate 2*): (**a**) 0° response amplitude vs. time, (**b**) the FFT of (**a**) shows 39.368 Hz against the theoretical result 48.314 Hz, (**c**) 90° response amplitude vs. time, (**d**) the FFT of (**c**) shows 23.651 Hz against the theoretical result 28.462 Hz

Table 4.3 Theoretical and experimental natural frequency of the first mode of *Plate 2*

Boundary condition	Experiment (Hz)	Theory (Hz)	Error (%)	30 % reduction of E11 and E22 (Hz)	Error (%)
CCCC	327.148	394.157	17.00	334.008	2.05
CFFF (0°)	39.368	48.314	18.52	40.68	3.23
CFFF (90°)	23.651	28.462	16.90	24.27	4.61

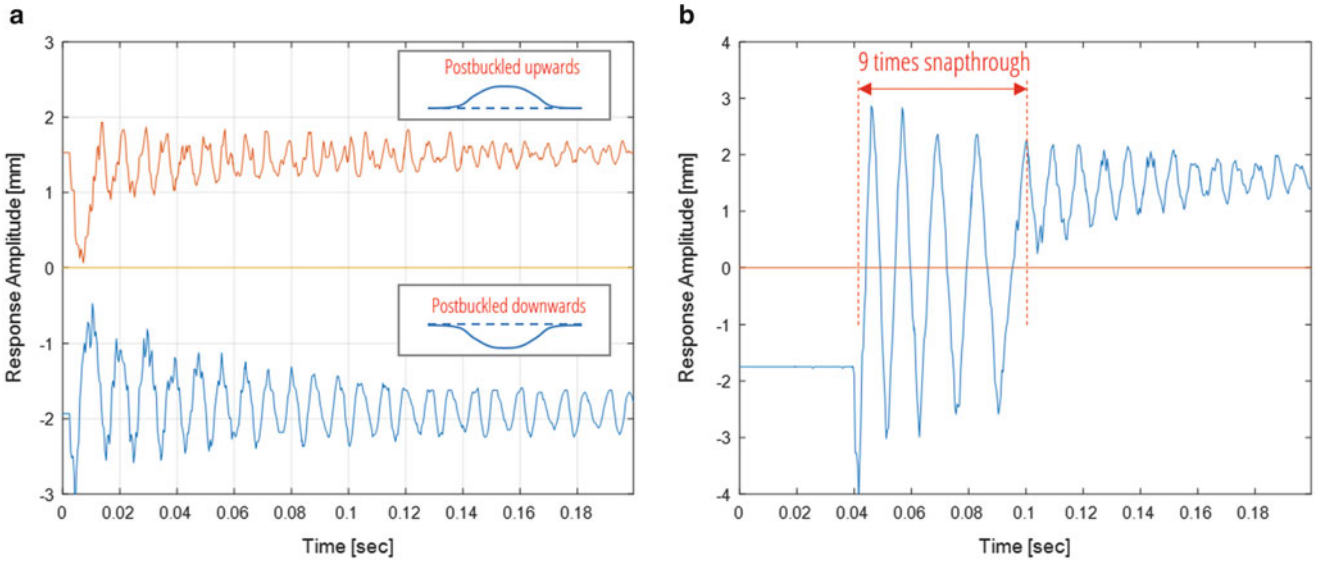

Fig. 4.6 Free vibration of the clamped and free (CCFF) post-buckled quasi-isotropic plate ([0/45/90/135]s carbon woven fabrics, *Plate 3*): (**a**) free vibration of *Plate 3* post-buckled upwards and downwards shows 140 and 125 Hz as the natural frequency, respectively, (**b**) free vibration shows nine times snap-through responses

The post-buckled plate experiment demonstrated an interesting nonlinearity. With a certain level of excitation, the plate showed several dynamic snap-through with a single excitation. This phenomenon is a fascinating topic and will be further investigated to model the nonlinear behavior of particular interest in delamination and axial load induced by snap-through.

In future work, the model will be extended to capture the snap-through loading. Of interest will be the in plane loading induced by snap-through and its potential for causing delaminations.

Acknowledgements The authors wish to thank Michelle Hickner and Bill Kuykendall for their assistance in the laboratory.

References

1. Khandan, R., Noroozi, S., Sewell, P., Vinney, J.: The development of laminated composite plate theories: a review. J. Mater. Sci. **47**, 5901–5910 (2012)
2. Gibson, R.F.: Principles of Composite Material Mechanics. CRC, Boca Raton (2012)
3. Hale, J.: Boeing 787 from the ground up. AERO Mag. **Q406**, 16–23 (2006)
4. Kaddour, A.S., Hinton, M.J., Smith, P.A., Li, S.: The background to the third world-wide failure exercise. J. Compos. Mater. **47**(20–21), 2417–2418 (2013)
5. Aboudi, J., Arnold, S.M., Bednarcyk, B.A.: Micromechanics of Composite Materials: A Generalized Multiscale Analysis Approach. Butterworth-Heinemann, Oxford (2012)
6. Leissa, A.W.: Vibrations of Plates. National Aeronautics and Space Administration, Washington, D.C. (1969)
7. Leissa, A.W.: The free vibration of rectangular plates. J. Sound Vib. **31**(3), 257–293 (1973)
8. Chia, C.-Y.: Nonlinear Analysis of Plates. McGraw-Hill, New York (1980)
9. Reddy, J.N.: Mechanics of Laminated Composite Plates and Shells. CRC, Boca Raton (2004)
10. Reddy, J.N.: Theory and Analysis of Elastic Plates and Shells. CRC, Boca Raton (2007)

Chapter 5
Experimental Identification of a Structure with Internal Resonance

Alexander D. Shaw, Tom L. Hill, Simon A. Neild, and Michael I. Friswell

Abstract Engineered structures are becoming increasingly lightweight and flexible, and as such more likely to achieve large amplitude and nonlinear vibratory responses. This leads to a demand for new methods and experimental test structures to see how in practice nonlinearity can be handled. In previous work, the authors studied a continuous modal structure with a local nonlinearity. The structure has been designed to have transparent underlying physics, and easily adjustable natural frequencies, and this leads to the ability to investigate an approximately 3:1 internal resonance between the 1st and 2nd modal frequencies. Therefore the structure exhibits complex responses to harmonic excitation, including isolated regions of the frequency response and quasiperiodic behaviour. In the present work we discuss a rapid means of identifying the structure with the minimum requirements of test data and time. A particular aim is to characterise the underlying linear system using data that is strongly influenced by nonlinearity. A harmonic balance procedure is used to identify a nonlinear discrete spring-mass system, that is modally equivalent to the structure under test. It is found that the inclusion of harmonic components in the test data and the presence of internal resonance leads to surprising amounts of information about modes that are not directly excited by the fundamental stepped-sine excitation.

Keywords Internal resonance • Nonlinear vibration • Identification • Harmonic balance • Nonlinear modes

5.1 Introduction

There is significant research interest in the vibrations of structures that exhibit nonlinear responses. This is due to the ubiquity of such structures; for example numerous fundamental structural forms such as plates, shells and beams will exhibit nonlinear phenomena when vibrating at sufficient amplitude. Furthermore, flexible materials exhibit nonlinear stress/strain when at large strains, and mechanisms can introduce nonlinear phenomena due to geometrical effects, as well as non-smooth nonlinearities due to friction, freeplay, impact and backlash [1–3]. In addition to the academic interest in such systems, there is strong interest within industry. This is driven by the increasing demand for lightweight and flexible structures such as large wind turbine blades, or long span bridges [1]. Furthermore, new technologies such as Micro Electromechanical Systems (MEMS) utilise structures that operate on scales where effects such as static electromagnetic forces generate significant nonlinear forces [4]. Nonlinearity is also being exploited in applications such as vibration isolation [5] and energy harvesting [6].

Of particular interest is the requirement to use dynamic testing methods to characterise the vibratory response of structures in order to make performance predictions, so called system identification. While this practice has the well established methodology of modal testing in the case of linear systems [7], the presence of nonlinearity greatly complicates this task, due to the wide range of phenomena that nonlinear systems may exhibit [8, 9].

The interest in nonlinear system identification has led to a demand for experimental demonstrators featuring continuous structures with nonlinearity; however experimental works on these types of systems are heavily outnumbered by analytical

A.D. Shaw (✉) • M.I. Friswell
Swansea University, Bay Campus, Fabian Way, Swansea SA1 8EP, UK
e-mail: a.d.shaw@swansea.ac.uk

T.L. Hill • S.A. Neild
University of Bristol, Queen's Building, University Walk, Clifton BS8 1TR, UK

G. Kerschen (ed.), *Nonlinear Dynamics, Volume 1*, Conference Proceedings of the Society for Experimental Mechanics Series,
DOI 10.1007/978-3-319-29739-2_5

and numerical studies. A well known example is the configuration first presented by Thouverez [10], widely known as the 'Liege beam', for examples see [11, 12]. This consists of a well understood linear structure—a cantilever beam—with a local nonlinearity at the tip; this is caused by a smaller beam that achieves geometrically nonlinear amplitudes. Recent numerical work on this type of structure has shown that it has rich dynamics, exhibiting internal resonance effects including isolated response regions and torus bifurcations [13, 14].

This paper extends recent experimental work by the authors, which draw on the approach of the Liege beam, but replaces the nonlinearity at the tip with a spring mechanism [15]. Stepped sine tests on this structure revealed some fascinating responses, including an experimental demonstration of an isolated region (or isola) of periodic responses, and also quasiperiodic response regions.

Despite the adjustability of the experimental structure, the results presented in [15] consider just one configuration. A natural extension of the work is to tune the modal frequencies to explore the effect on the 3:1 internal resonance that the structure possessed; however the time taken to experimentally characterise such a range of configurations could be excessive if the data gathering and identification process is not optimized. There are two particular issues that slow the progress of the experimental study:

1. Characterising the underlying linear system required additional tests at low amplitude—however response at such low amplitude that the cubic nonlinearity had no effect could be affected by issues such as friction and low sensor readings, making these readings slow to acquire and potentially unreliable.
2. The internal resonance meant that significant additional harmonic content could appear in the forcing signal due to shaker interactions. Therefore a numerical algorithm was deployed to condition the input force to a pure sinusoid; it was shown that failure to address this issue had a significant effect on response. The algorithm could require multiple iterations, each of which required settling time to achieve a steady state response—the product of which led to long stepped sine sweep times.

It is believed that these issues will be common to many attempts to experimentally characterise nonlinear structures. This work discusses means of reducing these two issues.

The approach to issue 1 is to adopt an identification procedure that identifies linear system properties simultaneously to nonlinear properties, using the same data. This saves the need for additional tests that can be difficult and unreliable. It means that while underlying linear modes have a crucial effect on the response, they are never observed directly; instead they are inferred through their effect on nonlinear system response. It also means that underlying linear modal properties can be assigned even when it is impossible to observe a truly linear response. This is a plausible situation that may occur when there is no region of response amplitude where large displacement nonlinearities can be avoided at the same time as low level nonlinearities such as dry friction.

The proposed identification procedure accepts and makes use of harmonics in the response. However it can be readily extended to allow additional harmonic components in the forcing signal, meaning that there is no need to eliminate these using experimental control techniques. This relieves issue number 2, and in addition could be exploited by deliberately adding harmonic components to the forcing to allow a wider set of forcing conditions to be included in the test data.

The present work proceeds as follows; firstly the experimental structure is described and some of the findings of Shaw et al. [15] are summarised. Secondly, the identification method is described. The following section then presents the results of identification, comparing the use of different options and data in the procedure. Finally, conclusions are drawn.

5.2 Experimental Structure

The experimental structure is shown in Fig. 5.1. It consists of a steel beam, with an arrangement of springs that achieves nonlinear force-displacement through the angle change of the springs when the beam oscillates. The structure is excited by a small shaker connected at position x_1 in Fig. 5.1a, and the force that this exerts is measured by a piezoelectric force transducer. The motion of the beam is measured through accelerometers located at x_1, x_2 and x_3.

The arrangement of springs shown in Fig. 5.1b gives rise to geometric nonlinearity at large amplitudes. The force displacement curve for this arrangement can be shown to be given by:

$$P(z) = 2kz(1 - \frac{\ell_0}{\sqrt{a^2 + z^2}}) \tag{5.1}$$

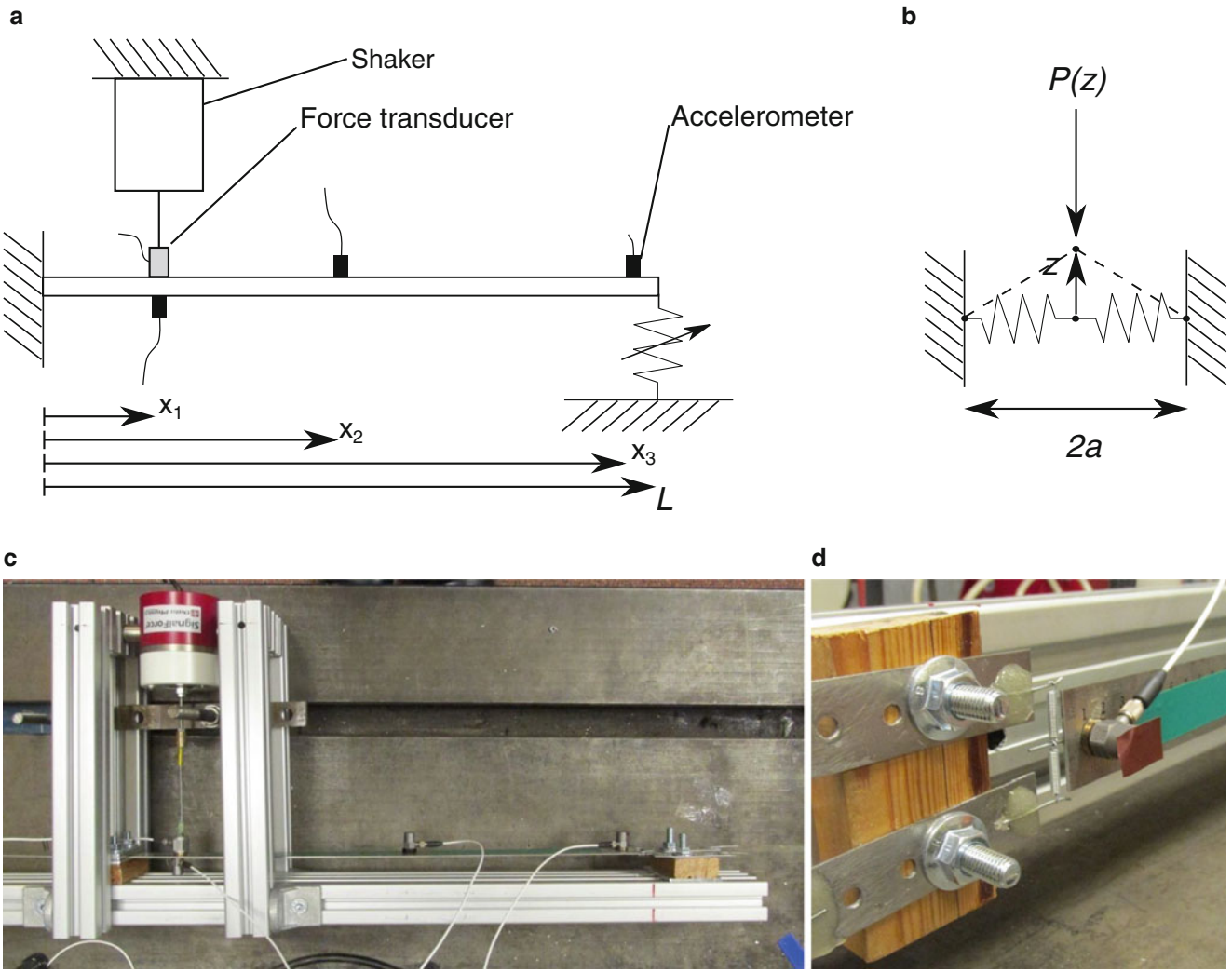

Fig. 5.1 (**a**) Schematic of the experiment. (**b**) Detail of nonlinear spring mechanism. (**c**) Photograph of experimental setup. (**d**) Closer perspective on the nonlinear spring mechanism

where k is the rate of each spring, ℓ_0 is the original length of each spring and a is the half span of the mechanism. This may be approximated in the form:

$$P(z) \approx k_1 z + k_3 z^3 \tag{5.2}$$

through Maclaurin expansion, and it may be shown that this approximation is highly accurate up to displacements of approximately $a/3$. The apparatus allows the static force displacement at the tip to be measured directly, and this confirms the analytical predictions.

The experiment was designed to have linear modal frequencies of approximately 9 and 31 Hz for the first and second modes respectively. This gave an approximate 3:1 internal resonance between the second and third modes, and allowed the examination of the response as the first mode stiffened at higher amplitudes, so that it passed through an exact 3:1 relationship with the second mode.

A controller was implemented using National Instruments Labview software running on an NI cRIO-9024 [16] chassis that interfaced with the sensors. The controller numerically corrected the drive voltage so that the forcing signal was a true sinusoid of the desired amplitude, with no harmonics. It was possible to choose the degree of control that was applied, from simply controlling the fundamental amplitude, up to controlling the first five harmonics.

5.3 Identification Method

5.3.1 Overview

The identification method follows three stages:

1. A limited degree-of-freedom system equivalent to the modal system we are seeking is identified using physical insights into the possible dynamics of the system.
2. Use a least squares method to establish system parameters that resolve harmonic balance equations.
3. Use identified mass and stiffness properties to establish underlying linear modes.

These are described in the following subsections.

5.3.2 Equivalent System

The degrees of freedom of the equivalent discrete system are taken to be displacement at each sensor location x_i as enumerated in Fig. 5.1a, denoted y_i. The system is forced at x_1, and a cubic nonlinearity is located at x_3. Hence the equations of motions may be taken as:

$$[M]\{\ddot{y}\} + [C]\{\dot{y}\} + [K]\{y\} + \{N_y\} = \{f\} \tag{5.3}$$

where

$$\{N_y\} = [0, 0, k_3 y_3^3]^T \tag{5.4}$$

and

$$\{f\} = [p(t), 0, 0]^T \tag{5.5}$$

and the matrices have their usual meanings. The forcing function has form

$$p(t) = P_{c1} \cos \Omega t + P_{s1} \sin \Omega t + P_{c3} \cos 3\Omega t + P_{s3} \sin 3\Omega t \tag{5.6}$$

although initially we consider purely cosine forcing, i.e. only the first amplitude is nonzero. Furthermore, $[M]$ is assumed to be diagonal, and $[C]$ and $[K]$ are fully populated and symmetric. Hence there are 16 terms to identify—three masses m_i, six stiffness k_{ij} and six damping coefficients c_{ij} plus the cubic term k_3.

5.3.3 Parameter Identification

The identification method now follows a procedure first described by Yasuda et al. [17], which uses the harmonic balance method to form a least squares problem in terms of the required parameters. All responses are taken as truncated Fourier series coefficients, where the included coefficients are the sin and cos terms at the fundamental frequency and the third harmonic. This is based on our insight that the only relevant harmonic is the third, due to the 3:1 internal resonance and the assumed cubic nonlinearity. The equations are formed from 18 values read at each data point—the four Fourier coefficients read for each of the three displacement sensors, plus four Fourier components taken from the time signal of y_3^3, the forcing amplitude and the forcing frequency. Note that three further values are introduced if the full form of (5.6) is used. There are a total of 12 equations to be balanced, four for each DOF:

$$\begin{aligned} -m_1 \Omega^2 Y_{c1,1} + \Omega \left(c_{11} Y_{s1,1} + c_{12} Y_{s1,2} + c_{13} Y_{s1,3}\right) + k_{11} Y_{c1,1} + k_{12} Y_{c1,2} \\ + k_{13} Y_{c1,3} = P_{c1} \end{aligned} \tag{5.7}$$

$$-m_1\Omega^2 Y_{s1,1} - \Omega\left(c_{11}Y_{c1,1} + c_{12}Y_{c1,2} + c_{13}Y_{c1,3}\right) + k_{11}Y_{s1,1} + k_{12}Y_{s1,2} + k_{13}Y_{s1,3} = P_{s1} \tag{5.8}$$

$$-9m_1\Omega^2 Y_{c3,1} + 3\Omega\left(c_{11}Y_{s3,1} + c_{12}Y_{s3,2} + c_{13}Y_{s3,3}\right) + k_{11}Y_{c3,1} + k_{12}Y_{c3,2} + k_{13}Y_{c3,3} = P_{c3} \tag{5.9}$$

$$-9m_1\Omega^2 Y_{s3,1} - 3\Omega\left(c_{11}Y_{c3,1} + c_{12}Y_{c3,2} + c_{13}Y_{c3,3}\right) + k_{11}Y_{s3,1} + k_{12}Y_{s3,2} + k_{13}Y_{s3,3} = P_{s3} \tag{5.10}$$

$$-m_2\Omega^2 Y_{c1,2} + \Omega\left(c_{12}Y_{s1,1} + c_{22}Y_{s1,2} + c_{23}Y_{s1,3}\right) + k_{12}Y_{c1,2} + k_{22}Y_{c1,2} + k_{23}Y_{c1,3} = 0 \tag{5.11}$$

$$-m_2\Omega^2 Y_{s1,2} - \Omega\left(c_{12}Y_{c1,1} + c_{22}Y_{c1,2} + c_{23}Y_{c1,3}\right) + k_{12}Y_{s1,1} + k_{22}Y_{s1,2} + k_{23}Y_{s1,3} = 0 \tag{5.12}$$

$$-9m_2\Omega^2 Y_{c3,2} + 3\Omega\left(c_{12}Y_{s3,1} + c_{22}Y_{s3,2} + c_{23}Y_{s3,3}\right) + k_{12}Y_{c3,1} + k_{22}Y_{c3,2} + k_{23}Y_{c3,3} = 0 \tag{5.13}$$

$$-9m_2\Omega^2 Y_{s3,2} - 3\Omega\left(c_{12}Y_{c3,1} + c_{22}Y_{c3,2} + c_{23}Y_{c3,3}\right) + k_{12}Y_{s3,1} + k_{22}Y_{s3,2} + k_{23}Y_{s3,3} = 0 \tag{5.14}$$

$$-m_3\Omega^2 Y_{c1,3} + \Omega\left(c_{13}Y_{s1,1} + c_{23}Y_{s1,2} + c_{33}Y_{s1,3}\right) + k_{13}Y_{c1,2} + k_{23}Y_{c1,2} + k_{33}Y_{c1,3} + 3k_3\hat{Y}^3_{c1,3}/4 = 0 \tag{5.15}$$

$$-m_3\Omega^2 Y_{s1,3} - \Omega\left(c_{13}Y_{c1,1} + c_{23}Y_{c1,2} + c_{33}Y_{c1,3}\right) + k_{13}Y_{s1,1} + k_{23}Y_{s1,2} + k_{33}Y_{s1,3} + 3k_3\hat{Y}^3_{s1,3}/4 = 0 \tag{5.16}$$

$$-9m_3\Omega^2 Y_{c3,3} + 3\Omega\left(c_{13}Y_{s3,1} + c_{23}Y_{s3,2} + c_{33}Y_{s3,3}\right) + k_{13}Y_{c3,1} + k_{23}Y_{c3,2} + k_{33}Y_{c3,3} + k_3\hat{Y}^3_{c3,3}/4 = 0 \tag{5.17}$$

$$-9m_3\Omega^2 Y_{s3,3} - 3\Omega\left(c_{13}Y_{c3,1} + c_{23}Y_{c3,2} + c_{33}Y_{c3,3}\right) + k_{13}Y_{s3,1} + k_{23}Y_{s3,2} + k_{33}Y_{s3,3} - k_3\hat{Y}^3_{s3,3}/4 = 0 \tag{5.18}$$

where $Y_{ci,j}$ and $Y_{si,j}$ are the cosine and sine coefficients respectively of the ith harmonic of the jth DOF. $\hat{Y}^3_{ci,3}$ and $\hat{Y}^3_{si,3}$ are the cosine and sine coefficients respectively of the ith harmonic of the time series of y_3^3—note that this is not the same as $(Y_{ci,j})^3$. The terms $\hat{Y}^3_{ci,3}$ and $\hat{Y}^3_{si,3}$ are sensitive to truncation error, so ideally should be calculated from the test data in the most exact way possible, by taking Fourier coefficients from the true time series of y_3^3. However, in the cases that follow they are inferred from the 5-harmonic Fourier series terms that are returned by the data acquisition system.

Equations (5.7)–(5.18) are solved for all required parameters using a least squares method. The resulting $[M]$ and $[K]$ may then be used to resolve the mode shapes of the underlying conservative linear system.

5.4 Results of Identification

In this section, some initial identifications are performed in the manner described above. The results of the identifications are compared to natural frequencies that were obtained through very low amplitude stepped sine tests, which were simply voltage controlled, and also experienced some of the difficulties discussed in the introduction. Hence it is possible that these values contain some error, and therefore estimates of the identification error should be treated with some caution. Furthermore, with only one test structure considered, this must be treated as a preliminary study only. A comparison is also made for the nonlinear parameter k_3, which was identified with a quasistatic measurement on the tip of the beam.

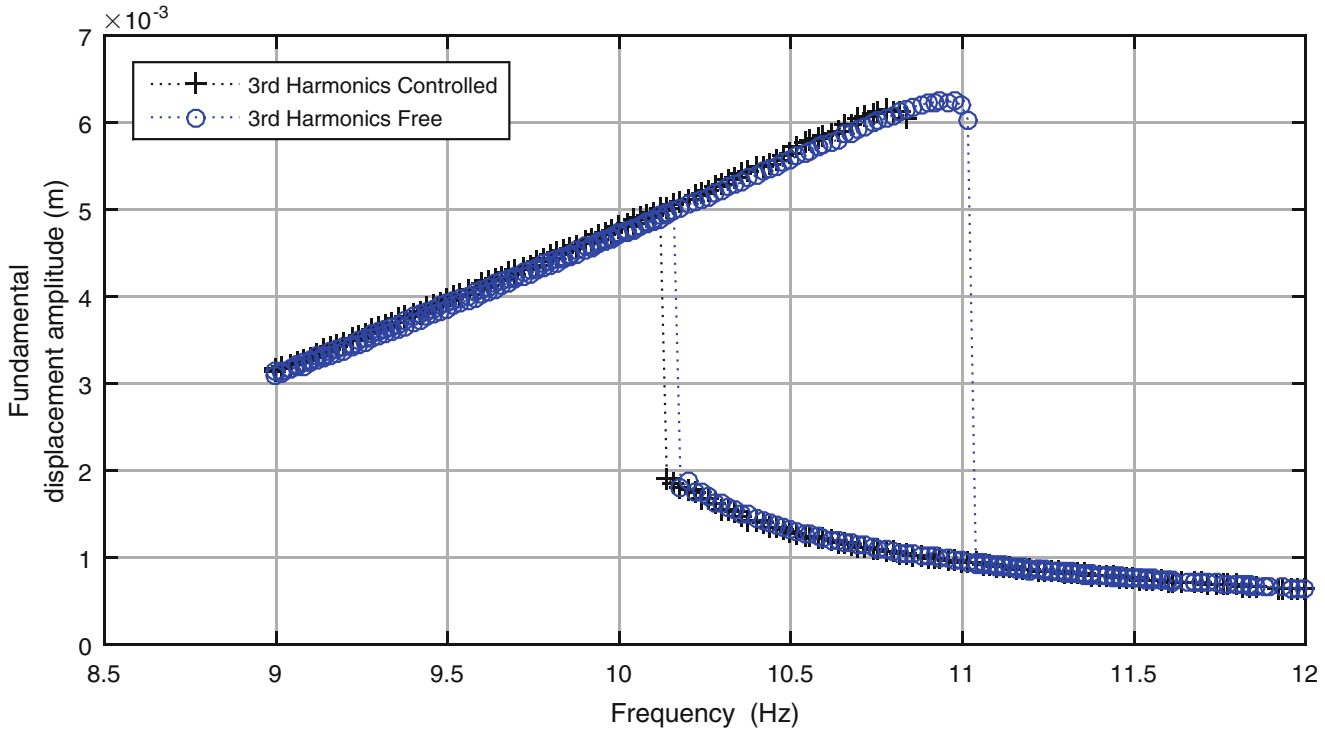

Fig. 5.2 Data used for identification. *Cross markers* denote data where the control algorithm has suppressed 3rd harmonic content from the forcing signal. *Circle markers* denote data where only the fundamental amplitude is controlled, and therefore the force signal contains 3rd harmonics due to interaction between the nonlinear vibration and the shaker

Table 5.1 Comparison of different ID methods with experimental values

	ω_{n1} (rad/s)	ω_{n2} (rad/s)	ω_{n3} (rad/s)	$k3$ (N/m^3)
Experiment	55.92	199.18	552.14	2.516×10^6
ID1	53.62 (−4.1 %)	199.84 (+0.3 %)	498.52 (−9.7 %)	2.342×10^6 (−6.9 %)
ID2	55.20 (−1.3 %)	203.02 (+1.9 %)	615.45 (+11.5 %)	1.785×10^6 (−29.1 %)
ID3	54.14 (−3.2 %)	201.54 (+1.2 %)	796.54 (+44.3 %)	2.354×10^6 (−6.4 %)
ID4	54.29 (−2.9 %)	195.57 (−1.8 %)	557.57 (+1.0 %)	2.417×10^6 (−3.9 %)
ID5	57.46 (+2.8 %)	230.26 (+15.6 %)	608.80 (+10.3 %)	4.536×10^5 (−82.0 %)

Each of the following subheadings describe an identification using the above method, but with variations in terms of the subset of experimental data used and the method. The identification method uses two variations. The first variation assumes that all terms except P_{c1} in Eq. (5.6) are zero, and that therefore the forcing is a pure cosine signal. This is a reasonable assumption if harmonics were controlled during testing. The second variation relaxes this assumption and includes all terms from (5.6) in the test data.

All cases make use of one of the datasets in Fig. 5.2, while cases 2 and 5 introduce some additional data as discussed. Both sets of data in Fig. 5.2 consist of an up sweep and a down sweep near the first mode. However, in the case denoted '3rd harmonics controlled', the vibration controller has forced the third harmonic content in the force signal to zero. By contrast, in the case denoted '3rd harmonics free', the harmonics have been allowed to take the value they naturally form due to the interaction of the nonlinear vibrations with the shaker. It may be seen that the two datasets have significantly different drop frequencies. Each sweep has between 90 and 151 datapoints.

The results of all identifications are compared in Table 5.1.

5.4.1 ID1: Controlled Data, Sweep Near First Mode

This identification uses the '3rd harmonics controlled' data from Fig. 5.2, and assumes that the forcing was a pure cosine. Interestingly, the identification obtains an accurate value for ω_{n2}, despite there being no test data around this mode. This suggests that the internal resonance effect is transferring significant information about mode 2 into the response. The accuracy for ω_{n3} is poor; again no test data from this frequency region is included, however in this case there is no coupling to our test data via the 3:1 internal resonance.

5.4.2 ID2: Additional Low Level Data for Third Mode

This identification uses the same data and assumption as ID1, with the addition of the low amplitude data used to identify the linear ω_{n3} experimentally. However, it is seen that in this case, this extra data does not improve the accuracy of the ω_{n3} prediction.

5.4.3 ID3: Uncontrolled Harmonics, Only Fundamental Force Considered

This ID uses the '3rd harmonic free' data from Fig. 5.2. However, only the fundamental amplitude of the forcing signal is used, despite the fact that higher amplitude cases will experience significant distortion to the input force. As the results in Table 5.1 show, there is little evidence that this problem has significantly reduced the accuracy for the first two modes, although there is a particularly spurious value for ω_{n3}.

5.4.4 ID4: Uncontrolled Harmonics, Harmonics in Force Considered

This ID uses the '3rd harmonic free' data from Fig. 5.2, but this time the harmonics in the forcing signal are used in the identification. This identification gave the best accuracy for k_3, and surprisingly seems to have accurately located ω_{n3}, although chance cannot be ruled out at this stage.

5.4.5 ID5: Isola Data

This ID uses the same method and data as ID4, only this time additional data from the isola region is included. The isola is a region of stable high amplitude responses that is separate from the initial peak near mode 1, and consists of a combination of mode 1 and mode 2 responses. This data is shown in Fig. 5.3. Whilst in principle this data should be ok to use in identification, it can be seen from Table 5.1 that it is detrimental to accuracy, particularly for k_3. It is believed that this is due to the isola region occurring outside the nonlinear spring's cubic range, and that higher order polynomial approximations are needed to identify with this data.

5.5 Conclusions

This paper has discussed an identification method for a highly nonlinear structure with internal resonance. The method identifies both linear and nonlinear properties simultaneously, and therefore this approach has the potential to greatly reduce the effort required to characterise nonlinear systems. It also naturally handles some harmonic distortion in the input signal, reducing the requirements for accurate control whilst collecting data.

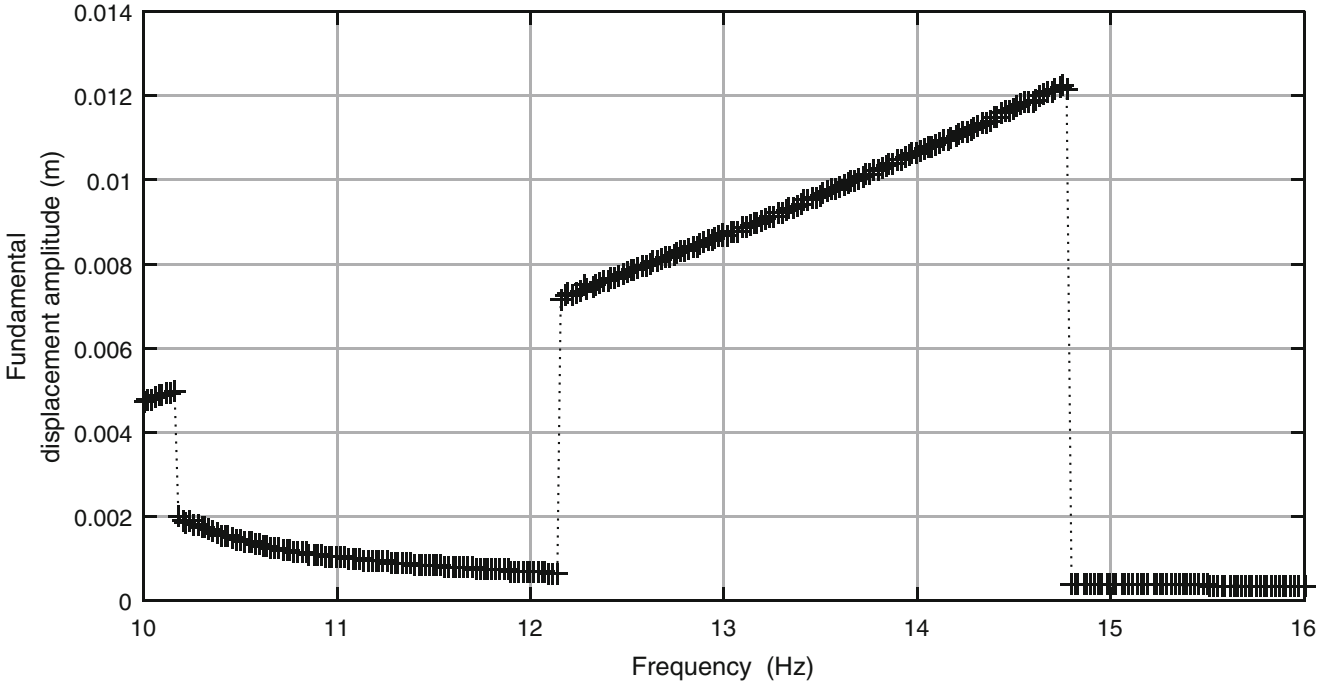

Fig. 5.3 Test data from isolated branch

While it is too early to draw firm conclusions about the robustness and general applicability of the approach used, it captured numerous properties of the system under test with reasonable accuracy. There also appears to be some ability of the method to gather information beyond the immediate frequency range under test when internal resonance exists. In particular the second modal frequency was captured with high accuracy in nearly all tests, despite no test data from the vicinity if this frequency being included.

Some different variations of the method were deployed, and although it is too early to form firm conclusions, it appears that an ID method that allows harmonic distortion in the force input has the potential to give the highest accuracy whilst reducing the experimental effort.

Acknowledgements The research leading to these results has received funding from EPSRC programme grant Engineering Nonlinearity (EP/G036772/1). In addition, Simon Neild and Tom Hill are supported by an EPSRC Fellowship (EP/K005375/1).

References

1. Wagg, D.J., Neild, S.A.: Nonlinear Vibration with Control. Springer, New York (2009)
2. Amabili, M.: Nonlinear Vibrations and Stability of Shells and Plates. Cambridge University Press, Cambridge (2008)
3. Ogden, R.W.: Non-linear Elastic Deformations. Courier Corporation, Dover Publications, New York (1997)
4. Rebeiz, G.M.: RF MEMS: Theory, Design, and Technology. Wiley, New York (2004)
5. Carrella, A.: Passive Vibration Isolators with High-Static-Low-Dynamic-Stiffness. VDM Verlag Dr. Muller, Saarbrücken, Germany (2010)
6. Daqaq, M.F., Masana, R., Erturk, A., Quinn, D.D.: On the role of nonlinearities in vibratory energy harvesting: a critical review and discussion. Appl. Mech. Rev. **66**(4), 040801 (2014)
7. Ewins, D.: Modal Testing: Theory, Practice, and Application. Mechanical Engineering Research Studies: Engineering Dynamics Series. Research Studies Press, Baldock, Herfordshire, England (2000)
8. Worden, K., Tomlinson, G.R.: Nonlinearity in Structural Dynamics. Institute of Physics, Bristol (2001)
9. Kerschen, G., Worden, K., Vakakis, A.F., Golinval, J.-C.: Past, present and future of nonlinear system identification in structural dynamics. Mech. Syst. Signal Process **20**(3), 505–592 (2006)
10. Thouverez, F.: Presentation of the ECL benchmark. Mech. Syst. Signal Process. **17**(1), 195–202 (2003)
11. Demarie, G.V., Ceravolo, R., Sabia, D., Argoul, P.: Experimental identification of beams with localized nonlinearities. J. Vib. Control **17**(11), 1721–1732 (2011)
12. Peeters, M., Kerschen, G., Golinval, J.: Modal testing of nonlinear vibrating structures based on nonlinear normal modes: experimental demonstration. Mech. Syst. Signal Process. **25**(4), 1227–1247 (2011)

13. Kuether, R.J., Renson, L., Detroux, T., Grappasonni, C., Kerschen, G., Allen, M.S.: Nonlinear normal modes, modal interactions and isolated resonance curves. J. Sound Vib. **351**, 299–310 (2015)
14. Detroux, T., Noël, J.P., Masset, L., Kerschen, G., Virgin, L.N.: Numerical study of the intrinsic features of isolas in 2-DOF nonlinear system. In: Proceedings of International Conferences on Structural Engineering Dynamics (ICEDyn) (2015)
15. Shaw, A.D., Hill, T.L., Neild, S.A., Friswell, M.I.: Periodic responses of a structure with 3:1 internal resonance (manuscript submitted for publication)
16. LabVIEW System Design Software, http://www.ni.com/labview/. October 2015
17. Yasuda, K., Kawamura, S., Watanabe, K.: Identification of nonlinear multi-degree-of-freedom systems. Presentation of an identification technique. JSME Int. J. Ser. III, Vib. Control Eng. Eng. Ind. **31**(1), 8–14 (1988)

Chapter 6
Shock Response of an Antenna Structure Considering Geometric Nonlinearity

Yunus Emre Ozcelik, Ender Cigeroglu, and Mehmet Caliskan

Abstract Antenna structures used in electronic warfare, radar, naval, satellite, spacecraft systems encounter mechanical shock from various sources such as near miss under water explosion, pyrotechnic and ballistic shocks. Since most of the antenna structure has larger dimension in longitudinal direction and experience high frequency, high amplitude shock energy, geometric nonlinearity become crucial to predict dynamic behavior in real life. In this study, the antenna structure is modeled by Euler-Bernoulli beam theory including geometrical nonlinearity. The resulting partial differential equations of motion are converted into a set of nonlinear ordinary differential equations by using Galerkin's Method, which are solved by Newmark. The results for the linear system obtained from time integration and approximate methods such as Absolute Method, Naval Research Method, and Shock Response Spectrum Method (SRS) are compared to the nonlinear ones. Moreover, these results are compared with the ones obtained from commercial Finite Element software.

Keywords Antenna structure • Mechanical shock • Nonlinear dynamic analysis • Finite element method

6.1 Introduction

In all around the world, approximately 40 % of the total world population uses internet [1], and cell phones are used by around 97 people out of every 100 people [2], which can provide a valid evidence for the idea that wireless communication is used worldwide. These infrastructures communicate with each other via antennas. In other words, the Internet and cell phones services are not functional without antennas. Thus, it can be said that the antenna structure is an irreplaceable and vital component of such electronic systems. IEEE defines what antenna does as "transmitting or receiving electromagnetic waves". In other words, the antenna structure converts electrical signal into electromagnetic or electrical signal. For military applications, antenna structures are used in electronic warfare (EW), radar, naval, satellite and spacecraft systems so that devices and vehicles associated with these systems can communicate with each other. Common antenna types used in civil and military systems are dipole antennas, monopoles antennas (see Fig. 6.1), loops antennas, helix antennas, etc. As can be seen from Fig. 6.1, most of these antenna structures have inherently cantilever beam type configuration since one end is connected to the antenna hub, while the other end is free to receive or transmit electromagnetic wave, known as radio frequency (RF). Moreover, these antenna structures are generally made up of high conductive materials since the performance of an antenna structure is proportional to conductivity of the material [4]. Table 6.1 summarizes the most widely used materials in antenna structures. Copper and aluminum are the most widely used materials because of cost and weight concerns.

However, antenna structures used in military and civil systems can encounter many mechanical shocks from various sources such as near miss underwater explosion, ballistic shock due explosion of mine, pyrotechnic shock, dropping of an antenna structure and so forth. Mechanical shock can be described as "a sudden and violent change in the state of motion of the component parts or particles of a body or medium resulting from sudden application of a relatively large external force, such as a blow or impact" according to first Shock and Vibration Symposium in 1947 [5]. Generally mechanical shocks contain high amplitude and rich spectral energy since the duration of mechanical shock is measured in milliseconds and the amplitude may be as high as 1000 G (see Fig. 6.2). Therefore, even if only one of the antennas in the electronic warfare and

Y.E. Ozcelik • E. Cigeroglu (✉) • M. Caliskan
Department of Mechanical Engineering, Middle East Technical University, Ankara 06800, Turkey
e-mail: ender@metu.edu.tr

G. Kerschen (ed.), *Nonlinear Dynamics, Volume 1*, Conference Proceedings of the Society for Experimental Mechanics Series,
DOI 10.1007/978-3-319-29739-2_6

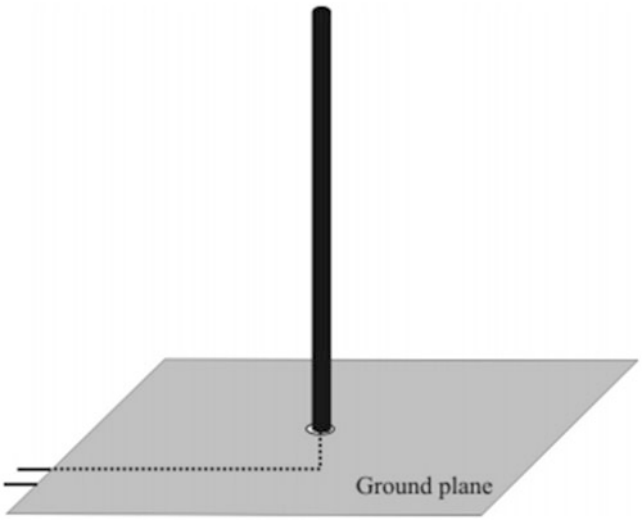

Fig. 6.1 Monopole antenna structure [3]

Table 6.1 Conductivity of the some common materials [4]

Material	Conductivity (S/m)	Material	Conductivity (S/m)
Silver	6.30E+07	Zinc	1.70E+07
Copper	5.80E+07	Brass	1.00E+07
Gold	4.10E+07	Phosphor Bronze	1.00E+07
Aluminum	3.50E+07	Tin	9.00E+06
Tungsten	1.80E+07	Lead	5.00E+06

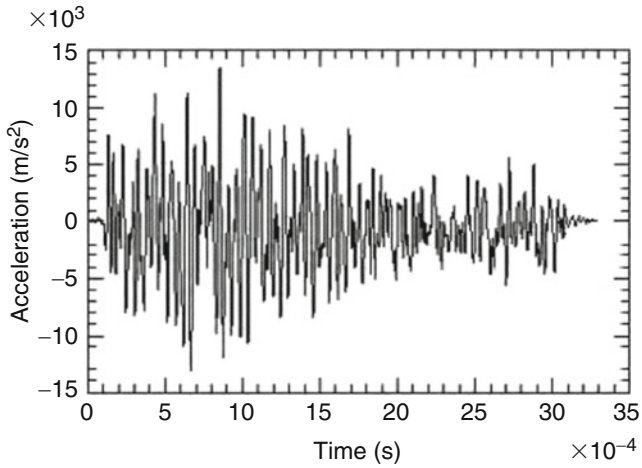

Fig. 6.2 Time history of mechanical shock [6]

communication systems is broken down due to a mechanical shock, the whole system will be unable to function properly. For example, a printed circuit board (PCB), printed on the antenna structure, may be damaged due to exposure of a high level of mechanical shock, and as a result of this, the system becomes dysfunctional. Therefore, antenna structures must be designed to withstand mechanical shock types, which are explained briefly below, to ensure their reliability.

Transportation and handling shock is received by electronic and mechanical systems used in military and civil applications as a result of transportation and human errors in handling of materials. For instance, while a military armored vehicle is running over a bump at unwary speed, all systems including antennas are exposed to mechanical shocks. Furthermore, ballistic shock is another type of mechanical shock containing high amplitude and high frequency content which is mainly caused by the impact of non-perforating mine blast, projectiles or ordnances on armored vehicle [7]. In addition to that

pyroshock which is the response of a system to high-frequency stress waves one example of mechanical shock. Generally, pyroshock is generated as a result of explosive charges in order to separate two stages of a rocket [8]. Moreover, gunfire shock is a repetitive wave originated from artillery shooting of military vehicle. Consequently, the antenna structure should withstand these mechanical shocks originating from various environmental effects.

In literature, studies on the nonlinear dynamic characteristics of antenna structures exposed to mechanical shocks are limited since most researchers have investigated modal and random vibrations analyses of the antenna structure. Concerning the linear dynamic analyses of antenna structure, the simulations were performed by commercial finite element programs such as ABAQUS® and NASTRAN®. Static and dynamic analyses of dipoloop antenna radome were simulated by a linear finite element analysis by Reddy and Hussain [9]. Mechanical shock analysis was conducted on ABAQUS®. In this study, only stresses were evaluated on the dipoloop antenna radome. Lopatin and Morozov [10] studied the free vibration of thin-walled composite spoke of an umbrella-type deployable space antenna. The composite spoke of the deployable space antenna was modeled as a cantilever beam via including effects of transverse shear. On the other hand, the nonlinear dynamic response of the antenna structure under dynamic loads is characterized by limited number of researchers. Random and modal analyses of a gimbaled antenna including gap nonlinearity resulting from small clearances in the joints are studied by Su [11] where the nonlinearity is linearized and then the resulting linear systems is solved commercial finite element software. Moreover, Sreekantamurthy et al. [12] investigated static and dynamic loads such as inflation pressure, gravity and pretension loads on a parabolic reflector antenna by using commercial finite element software. In their work, geometric nonlinearity was included into the model, since the deformation of parabolic reflector antenna was large.

Inherently, antenna structures have a larger dimension in longitudinal direction. When they receive high mechanical shock such as ballistic and pyrotechnical shocks, nonlinear effects play an important role on shock response of antenna structures.

Although the nonlinear dynamic characteristics, under mechanical shock are different from the linear ones, there appears almost no study on this specific topic. However, especially in micro and nanoscale areas, many researchers investigated the dynamics response of micro electro mechanical systems, micro beams, micro switches and so forth which are under mechanical shock even by considering the nonlinear effects. As an initial attempt, some authors used single degree of freedom assumption to get a rough estimation of the dynamic response of micro systems. For example, Younis et al. [13] studied the performance of capacitive switches modeled as a single degree of freedom (SDOF) system under mechanical shock through including the effects of squeeze-film damping and electrostatic forces. Moreover, Li and Shemansky [14] treated the micro-machined structure as a single degree of freedom system as well as a distributed parameter model. For more accurate analysis, many authors used continuous beam models to simulate the response of micro systems to a mechanical shock. As an example, Younis et al. [15] investigated the simultaneous effects of mechanical shock and electrostatic forces on microstructures simulated as cantilever and clamped-clamped beams. In this particular study, reduced order model results based on Galerkin's Method were compared with the ones obtained from commercial finite element software. Due to the large deformation of micro systems resulting from the applied mechanical shock, some researchers included nonlinearity to the models to predict the dynamic behavior in real life. For instance, Younis and Arafat included both geometric and inertia nonlinearities into their studies while analyzing the response of the cantilever microbeam activated by mechanical shock and electrostatic forces [16]. In their work, they analyzed the effects of cubic geometric and inertia nonlinearities on the cantilever microbeam by using reduced order model which is based upon Galerkin's Method. In another study of Younis et al. [17], the response of the clamped-clamped microbeam was investigated through using four modes in the Galerkin based reduced order model including geometric nonlinearity. Moreover, Younis et al. [17] studied the effects of shape of shock pulse and package on the response of microbeam and validated the results via commercial finite element software. Furthermore, some researchers employed approximate solutions to the response of systems under mechanical shock through frequency domain approaches rather than time domain approach which is computationally expensive. As an example, Liang et al. [18] estimated shock response of the mast in ships using frequency domain method such as square root of the sum of squares (SRSS), complete quadratic combination method (CQC), naval research laboratory method (NRL) and absolute summation method (ABS). Alexander [19] mentioned the frequency domain methods which are applied to the nonlinear systems as well. Younis and Pitarresi [20] emphasized synthetic methods utilizing the static response and shock spectrum based on maximum responses of many single degree of freedom systems. In this study [20], linear and nonlinear response of microbeam found in synthetic method and Galerkin-based reduced order method employing six modes were compared in terms of different values of shock amplitude.

Mechanical shock excitation is inherently applied to the base of structures. In literature, mechanical shock was simulated for continuous systems by base excitation which is either applied to the fixed boundary condition [21, 22] or distributed force applied through the structure [15–17, 20].

Antenna structures, which are used for military and civil applications, are vital component of the many the electronic systems. These antenna structures are subjected to mechanical shock from various environments such as transportation, ballistic, pyrotechnic shocks. Therefore, correct modeling of dynamic characteristic of the antenna structure under mechanical shock is needed because of the need to accurately predict the performance of the antenna structure. Inherently, most of the antenna structures have slender shape and larger dimension in longitudinal direction. Moreover, they are subjected to high frequency, high amplitude mechanical shocks. Thus, mathematical modeling of the antenna structure through linear theory can yield incorrect results, since antenna structures experience large deformation, where nonlinear effects become dominant. In other words, nonlinearities due to large deformation must be included in order to predict dynamic behavior accurately.

6.2 Mathematical Modeling

In this section, antenna structure is modeled by equivalent lumped mass model, Euler-Bernoulli Beam Theory, finite element method and approximate methods.

6.2.1 Equivalent Lumped Mass Model

In this section, the antenna structure is treated as a single degree of freedom system utilizing an equivalent lumped mass model. Basically, most of the antenna structures such as monopole antennas (see Fig. 6.3) have a cantilever beam structure since one end is fixed to the antenna hub while the other end is free to transmit or receive electromagnetic waves.

Equivalent mass and stiffness of the antenna structure described in Fig. 6.3 is given as [23].

$$m_{eq} = 0.2427mL, \tag{6.1}$$

$$k_{eq} = \frac{3EI}{L^3}, \tag{6.2}$$

where m is the mass per unit length of the antenna structure, l is the length of the antenna structure and E is Young's modulus of the antenna's material. Therefore, the antenna structure shown in Fig. 6.3 is reduced to a single degree of freedom system as shown in Fig. 6.4.

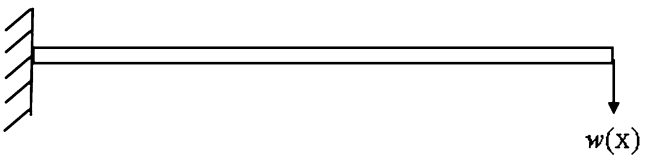

Fig. 6.3 Cantilever beam type the antenna structure

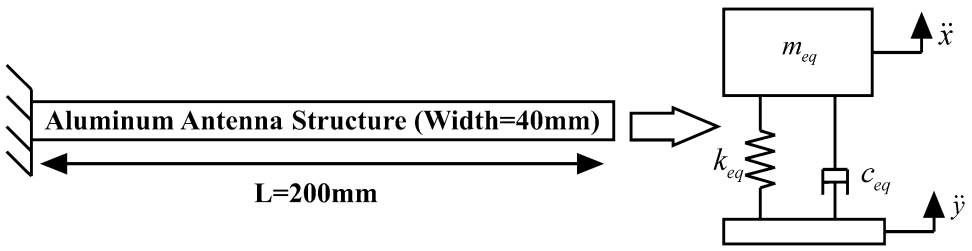

Fig. 6.4 Equivalent lumped mass model of the antenna structure

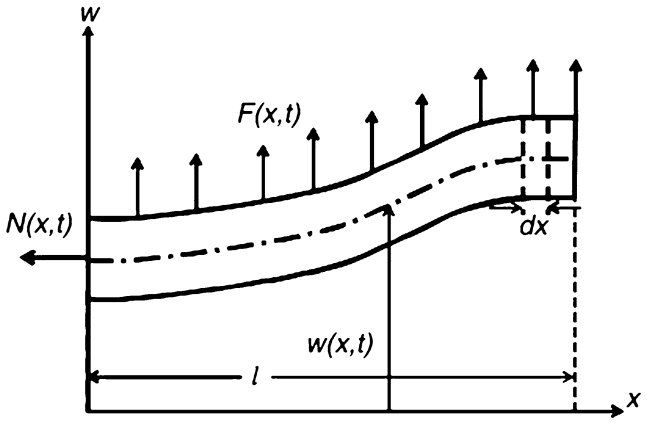

Fig. 6.5 Nomenclatures of the antenna structure in bending direction [25]

6.2.2 Linear Continuous Model

In this part, the antenna structure is modeled by Euler-Bernoulli beam theory, which is widely used in literature, in order to predict dynamic characteristic of slender beam like structure [13, 15–17, 20, 21]. However, due to inherent assumptions of the theory, accuracy of the results is poor when the thickness to length ratio is larger than 10 %. In such cases Timoshenko beam model is applied to get accurate results [24]. In this paper, Euler-Bernoulli beam theory is used to model the antenna structure, since most of the antenna structures naturally have thickness to length ratio much less than 10 %.

Consider the antenna structure, whose length, density, cross sectional area and flexural rigidity are represented as l, ρ, A and EI, respectively. As can be seen in Fig. 6.5, the transverse deflection of the antenna structure is defined as $w(x,t)$, where x is the axial position, t represents time and $F(x,t)$ is the distributed force that is applied through the length of the antenna structure. Equation of motion of the antenna structure is given as [25]

$$\frac{\partial^2}{\partial x^2}\left(EI\frac{\partial^2 w\left(x,t\right)}{\partial x^2}\right)+c\frac{\partial w\left(x,t\right)}{\partial t}+\rho A\frac{\partial^2 w\left(x,t\right)}{\partial t^2}=F\left(x,t\right). \tag{6.3}$$

In this paper, mechanical shock is applied as distributed force through the length of the antenna structure (see Fig. 6.5). Hence, equation of motion of the antenna structure subjected to mechanical shock can be given as

$$\frac{\partial^2}{\partial x^2}\left(EI\frac{\partial^2 w\left(x,t\right)}{\partial x^2}\right)+c\frac{\partial w\left(x,t\right)}{\partial t}+\rho A\frac{\partial^2 w\left(x,t\right)}{\partial t^2}=-\left(\rho A a_{\max}\right)a_{pulse}(t), \tag{6.4}$$

where, $a_{\max}$ is the maximum value of mechanical shock and a_{pulse} is a unit mechanical shock profile such as half sine, terminal peak sawtooth and so forth. The equation of motion given by Eq. (6.4) can be nondimensionalized by using following non dimensional parameters

$$\widehat{x}=\frac{x}{l},\ \widehat{\mathrm{w}}=\frac{w}{l},\ \widehat{\mathrm{t}}=\frac{t}{T}, \tag{6.5}$$

where T is the time scale parameter. Substituting Eq. (6.5) into Eq. (6.4), the outcome is

$$\frac{\partial^4 w\left(x,t\right)}{\partial t^4}+c_{non}\frac{\partial w\left(x,t\right)}{\partial t}+\frac{\partial^2 w\left(x,t\right)}{\partial t^2}=F_{non}a_{pulse}(t), \tag{6.6}$$

where, nondimensional damping and forcing terms are as follows

$$c_{non}=\frac{cl^4}{EIT},\ \mathrm{F}_{non}=\frac{-\rho A a_{\max}l^3}{EI}. \tag{6.7}$$

The nondimensional force given in Eq. (6.7) implies that effects of the mechanical shock increases sharply with increasing length and decreasing thickness of the antenna structure. This is in agreement with the experimental findings available in the literature [26].

The resulting partial differential equation of motion can be converted into a set of ordinary differential equations by using Galerkin's method. In this method, the following form of solution is assumed

$$w(x,t) = \sum_{i=1}^{n} a_i(t)\phi_i(x), \tag{6.8}$$

where, $\phi_i(x)$ is a comparison function which satisfies both geometric and natural boundary conditions as well as differentiable at least to the order of the partial differential equation. $a_i(t)$ is generalized coordinate to be determined, and n is the number of modes used in the analysis [27]. After substituting Eq. (6.8) into Eq. (6.6), multiplying the resulting equation with ϕ_j and integrating from 0 to 1, the following result is obtained

$$\sum_{i=1}^{n} u_i(t)\left(\int_0^1 \phi_j(x)\phi_i{}''''(x)dx\right) + c_{non}\sum_{i=1}^{n} \dot{u}_i(t)\left(\int_0^1 \phi_j(x)\phi_i(x)dx\right) + \sum_{i=1}^{n} \ddot{u}_i(t)\left(\int_0^1 \phi_j(x)\phi_i(x)dx\right) = \int_0^1 \phi_j(x)F_{non}a_{pulse}(t)dx. \tag{6.9}$$

If orthogonal comparison functions are used, Eq. (6.9) is reduced to an uncoupled form as follows

$$\ddot{u}_j(t) + 2\zeta_j\omega_{non,j}\dot{u}_j(t) + \omega_{non,j}{}^2u(t) = \int_0^1 \phi_j(x)F_{non}a_{pulse}(t)dx, \tag{6.10}$$

where, ζ_j is the modal damping ratio of the j^{th} mode and it is given by

$$\zeta_j = \frac{c_{non}}{2\omega_{non,j}}. \tag{6.11}$$

6.2.3 Nonlinear Continuous Model

In this section, shock response of an antenna structure considering geometric and inertia nonlinearities is analyzed. In real life, response of almost all systems to any forcing is nonlinear, where superposition property of linear systems does not hold. For simplicity, many engineering systems are treated as linear which is a valid assumption in most cases. For instance, in order to obtain linear equation of motion of an antenna structure under mechanical shock, small deformation is assumed. This assumption gives accurate results if the deformation in the real case is small with respect to the thickness of the antenna structure. However, if the deformation is large, small deformation assumption results in highly inaccurate results. Therefore, linear modeling may result in a design which is not optimum and hence, increases weight and cost. In addition to this, estimated acceleration of a PCB on the antenna structure is not accurate. Since mechanical shocks result in large deformations, antenna structure needs to be modeled by including nonlinearities.

Nonlinearities common in structures are geometric nonlinearity, damping nonlinearity, inertia nonlinearity, curvature nonlinearity, material nonlinearity and boundary condition nonlinearity. Since, the antenna structure experiences large deformation due to its long and slender structure, curvature and inertia nonlinearities are included into the model.

In the light of above mentioned information, equation of motion of the antenna structure, which has uniform density and constant cross section, under mechanical shock including geometric curvature and inertia nonlinearities is given as [25]

$$EI\frac{\partial^4 w}{\partial x^4} + c\frac{\partial w}{\partial t} + \rho A\frac{\partial^2 w}{\partial t^2} = -EI\frac{\partial}{\partial x}\left(\frac{\partial w}{\partial x}\frac{\partial}{\partial x}\left(\frac{\partial w}{\partial x}\frac{\partial^2 w}{\partial x^2}\right)\right) - \frac{1}{2}\rho A\frac{\partial}{\partial x}\left(\frac{\partial w}{\partial x}\int_L^x\left(\frac{\partial^2}{\partial t^2}\int_0^x\left(\frac{\partial w}{\partial x}\right)^2 dx\right)dx\right) - (\rho A a_{\max})\, a_{pulse}(t). \tag{6.12}$$

Equation (6.12) is converted into a set of nonlinear ordinary differential equations by using Galerkin's method. Similar to the previous case, substituting Eq. (6.8) into Eq. (6.12) multiplying the result by ϕ_j and integrating from 0 to 1 the following result is obtained

$$\begin{aligned}
&\sum_{i=1}^{n} u_i(t)\int_0^1 \phi_j(x)\phi_i''''(x)dx + c_{non}\sum_{i=1}^{n}\dot{u}_i(t)\int_0^1 \phi_j(x)\phi_i(x)dx + \sum_{i=1}^{n}\ddot{u}_i(t)\int_0^1 \phi_j(x)\phi_i(x)dx = \\
&-\int_0^1 \phi_j\left(\left(\sum_{i=1}^{n} u_i\phi_i''\right)^2 + 4\left(\sum_{i=1}^{n} u_i\phi_i'\right)\left(\sum_{i=1}^{n} u_i\phi_i''\right)\left(\sum_{i=1}^{n} u_i\phi_i'''\right) + \left(\sum_{i=1}^{n} u_i\phi_i'\right)^2\left(\sum_{i=1}^{n} u_i\phi_i''''\right)\right)dx \\
&-\alpha_{in}\int_0^1 \phi_j\left(\frac{\partial}{\partial x^2}\left(\left(\sum_{i=1}^{n} u_i\phi_i'\right)\int_1^x\left(\frac{\partial^2}{\partial t^2}\int_0^x\left(\sum_{i=1}^{n} u_i\phi_i'\right)^2 dx\right)dx\right)\right)dx + \int_0^1 \phi_j(x)F_{non}a_{pulse},
\end{aligned} \tag{6.13}$$

where nondimensional damping, inertia and forcing parameters are given as

$$c_{non} = \frac{cl^4}{EIT},\ \alpha_{in} = \frac{l^4\rho A}{2T^2EI},\ \mathrm{F}_{non} = \frac{-\rho A a_{\max} l^3}{EI}. \tag{6.14}$$

Equation (6.13) can be represented in matrix form, where in this study MUPAD® available in MATLAB® is used for the symbolic calculations.

6.2.4 *Finite Element Simulation by ANSYS*

In this section, shock response of an antenna structure is obtained by using ANSYS, which is commonly used commercial finite element software. In this paper, the antenna structure is modeled by 3-D 2 Node beam elements known as BEAM188 (see Fig. 6.6). This element type is used to analyze slender beam like structures. Moreover, this element has six degrees of freedom which are three translational degrees of freedom in X, Y and Z directions and three rotational degrees of freedom about X, Y and Z axes. In addition to that, the element is suitable for the consideration of stress stiffening and large deformation effects. The theory behind this element is Timoshenko beam theory, which includes shear deformation [28].

ANSYS Workbench does not have a tool for mechanical shock simulation, since mechanical shocks are applied to a structure from its base. In literature, Application Customization Toolkit exists for transient base excitation analysis. However, this toolkit is applicable for only linear transient analysis. As a result of that, ANSYS Parametric Design Language (APDL) is used to simulate mechanical shock. The APDL code which is embedded into "Transient Structural" module is written by "ACCEL" command. This command gives acceleration to the selected nodes. Furthermore, Rayleigh damping is used to model damping which is defined as

$$[C] = \alpha_m[M] + \beta_m[K], \tag{6.15}$$

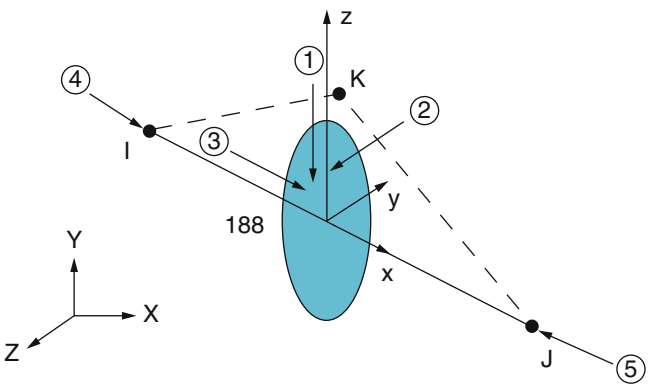

Fig. 6.6 Geometry of BEAM188 [28]

where, α and β are mass and stiffness constants, respectively. In this example, the first two modes are used in order to find these damping coefficient, which is implemented into ANSYS Transient Structural.

6.2.5 *Approximate Methods*

In this part, approximate methods based on modal combination are introduced. In these methods, the maximum response of the antenna structure is estimated by combination of mass normalized eigenfunction coefficient, modal participation factor and dynamic constant obtained from shock response spectrum. Moreover, mass normalized eigenfunction coefficient is obtained by using a mode shape function of the antenna structure at a desired location. Furthermore, the modal participation factor shows effectiveness of a particular mode on the response [29]. Thus, the modal participation factor, Γ_n, of the antenna structure is given as [30]

$$\Gamma_n = \rho A \int_0^L \phi_n(x) dx, \tag{6.16}$$

where, ρ and A are uniform density and cross sectional area of an antenna structure, respectively and $\phi_n(x)$ is the mode shape of the n^{th} mode.

Absolute sum (ABS), square root of sum of squares (SRSS), naval research (NRL) and complete quadratic combination methods are examples of approximate methods. These methods are used to get maximum shock response of an antenna structure. The main advantage of these methods is their computational efficiency compared to transient analysis. Moreover, these methods are conservative compared to transient analysis, since modal maximum responses are assumed to act simultaneously and have the same sign.

6.3 Case Studies

In this section, several case studies are conducted in order to analyze shock response of the antenna structure in detail. Moreover, linear and nonlinear ordinary differential equations are solved by Newmark method, which is also used in finite element software ANSYS.

Firstly, finite element method is compared with the linear continuous model. Consider the antenna structure given in Fig. 6.3 with constant cross section and uniform density. The antenna structure has 350 mm length, 40 mm width and 2 mm thickness. Moreover, the antenna structure is made up of aluminum, the density and Young's modulus of which are 2700 kg/m^3 and 70 GPa, respectively. In addition to that, the antenna structure is subjected to 50 G 11 ms half sine mechanical shock which is the transportation shock for wheeled vehicle and aircraft according to International Standard IEC-60068-2-27 [31]. Acceleration responses of the antenna structure to the given input mechanical shock using reduced order model and finite element simulation are given in Fig. 6.7. It is observed that the result of ROM is in agreement with the result of the finite element method.

In nonlinear finite element analysis, there are some drawbacks which affect shock response of an antenna structure. One of them is Rayleigh damping, which depends on mass and stiffness matrices as seen from Eq. (6.15). Using constant β_m leads to undesirable results in the nonlinear analysis, since ANSYS updates stiffness matrix for each iteration. Therefore, β_m constant cannot be used in nonlinear analysis. In this case study, damping is assumed to be zero and artificial damping is introduced as 0.5.In Newmark method, the amount of numerical dissipation is controlled by artificial damping. Furthermore, this damping leads to reduction of numerical errors. Linear and nonlinear shock responses of the antenna structure are compared in Fig. 6.8. According to the results obtained, nonlinearity reduces the shock response of the antenna structure significantly.

Nonlinear mathematical model used in this study is validated by Ref. [16]. Younis et al. [16] studied nonlinear analysis of the cantilever MEMS under mechanical shock. The maximum nondimensional deflection versus shock amplitude graph given in [16] is used to validate the nonlinear mathematical model used in this study. Consider the cantilever MEMS, whose length,

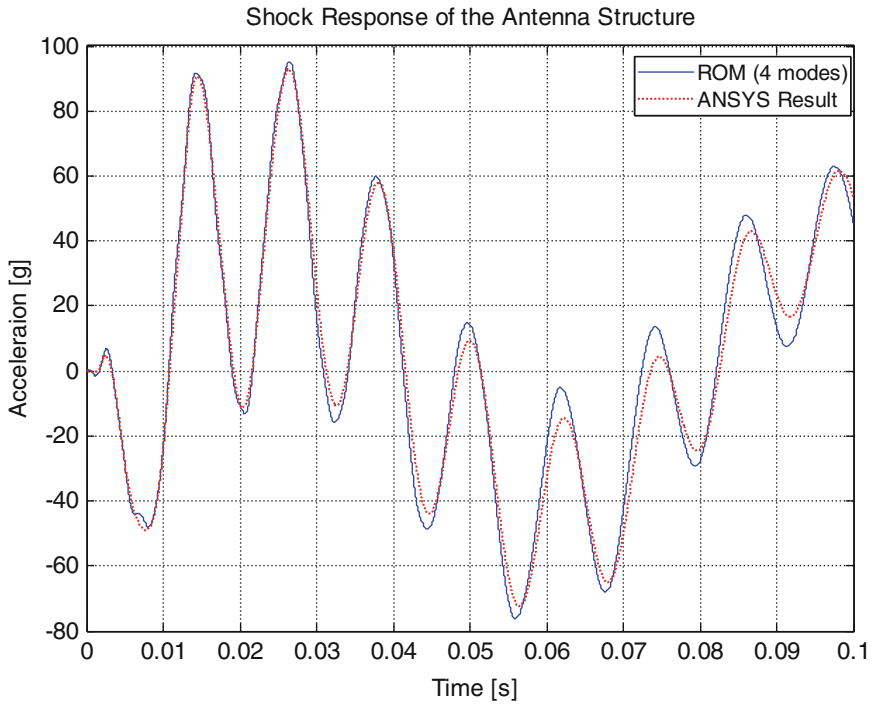

Fig. 6.7 Shock response of the antenna structure

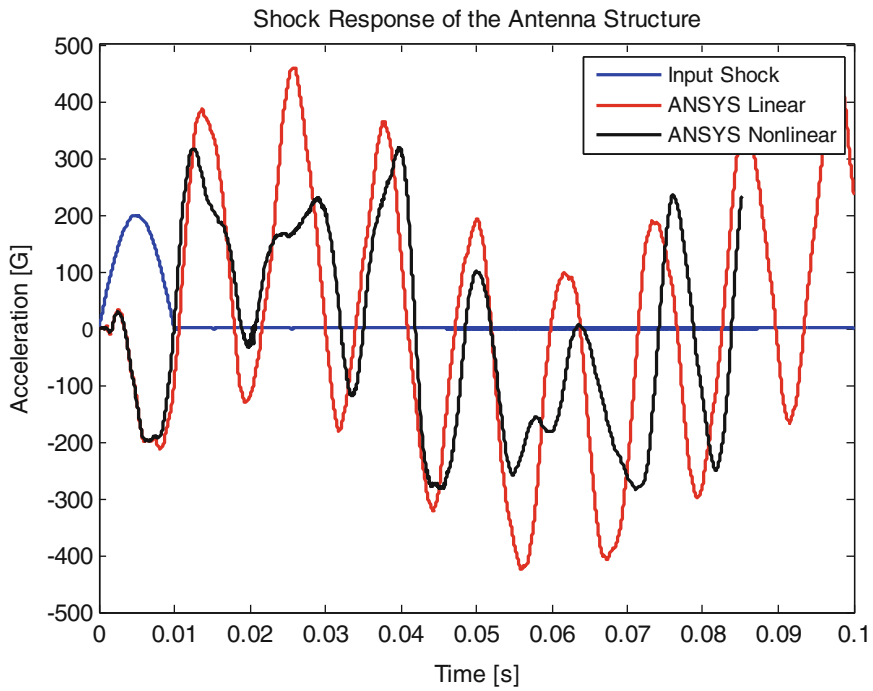

Fig. 6.8 Linear and nonlinear shock response of the antenna structure

thickness and width are $L = 100\ \mu\text{m}$, $h = 0.1\ \mu\text{m}$ and $b = 10\ \mu\text{m}$, respectively. The cantilever MEMS is made up of silicon, whose density and Young's modulus are $2332\ \text{kg/m}^3$ and 169 GPa, respectively. The results obtained are compared with the ones given in [16] in Figs. 6.9 and 6.10b. The results obtained are in well agreement with the ones given in [16]; hence, the nonlinear model and the solution method used are validated.

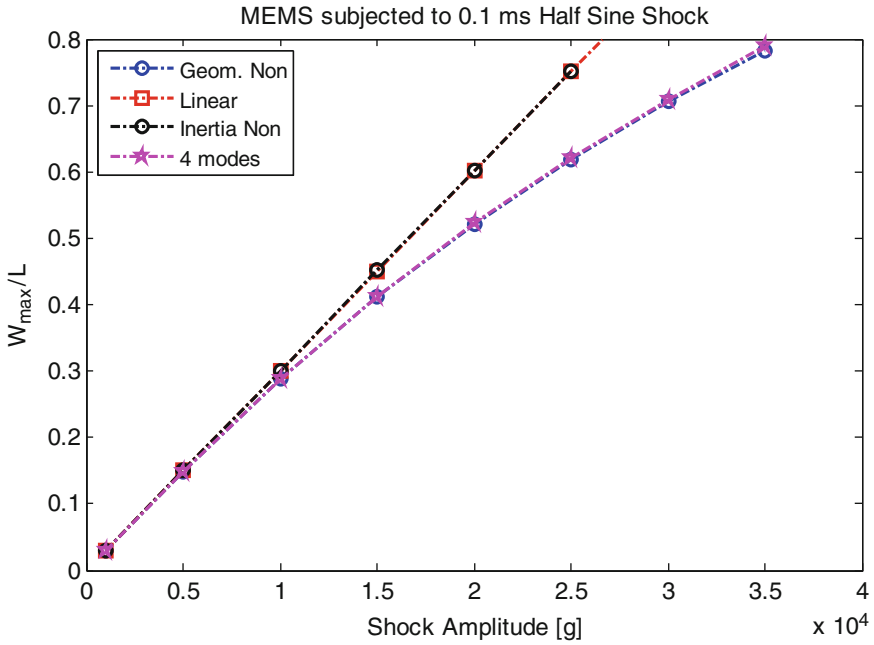

Fig. 6.9 Calculated shock response of the cantilever MEMS

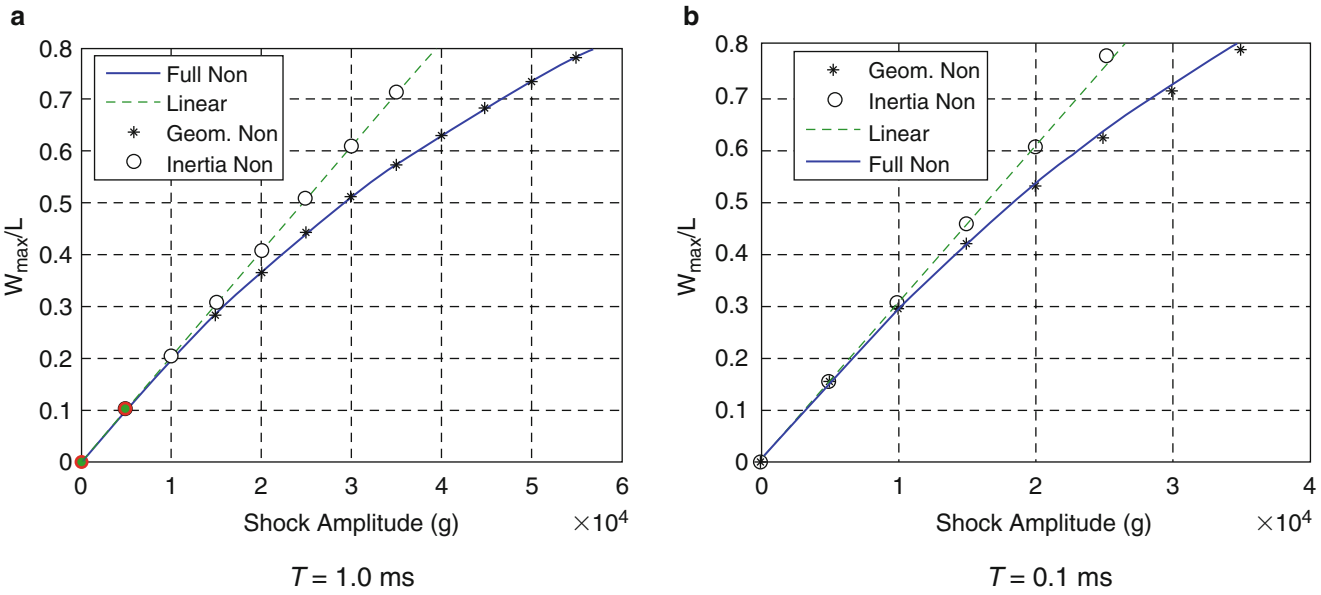

Fig. 6.10 The paper shock response of the cantilever [16]

The maximum relative displacement and acceleration tip response of an antenna structure is critical for design, since PCB, which is placed on the tip of an antenna structure, is sensitivity to the amplitude of the mechanical shock. Therefore, plot of the maximum response of the antenna structure vs. shock amplitude gives a better idea in terms of durability of the antenna structure. It can be observed from Figs. 6.11 and 6.12, both acceleration and relative displacement responses of the antenna structure is reduced when geometric nonlinearity is considered. Moreover, approximate methods can be used as a starting point of shock analysis of an antenna structure. Although approximate methods give conservative results compared to linear transient counterparts, computation time is significantly reduced. Furthermore, equivalent lumped mass model leads to enormous error in this case study, since the second, the third and the fourth modes also contribute to the shock response of the antenna structure in addition to the first mode. In other words, acceleration response of the antenna structure is composed of the first, the second, the third and the fourth modes of the structure which can be deduced from Fig. 6.13.

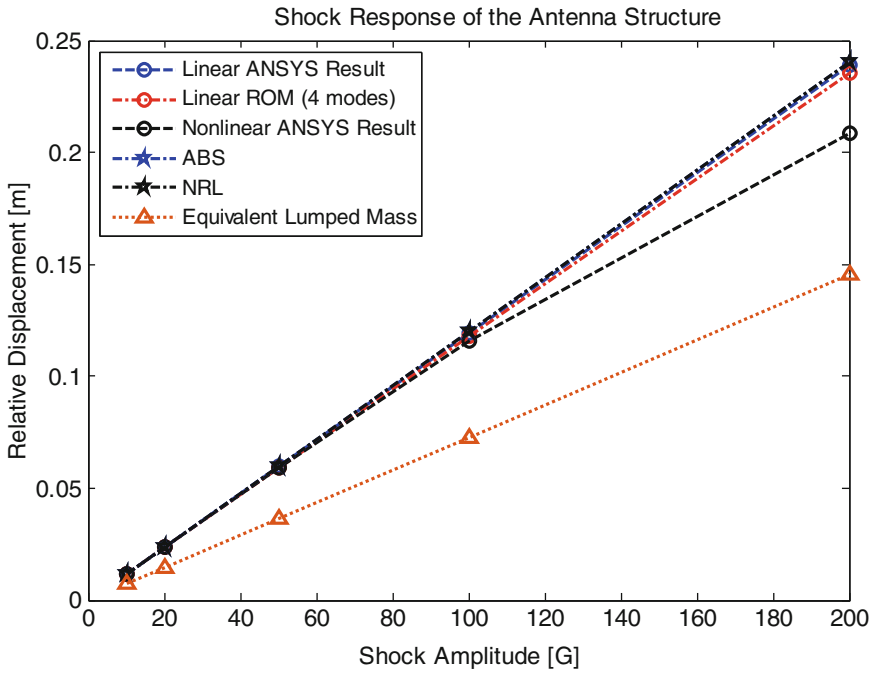

Fig. 6.11 Maximum acceleration response of the antenna structure

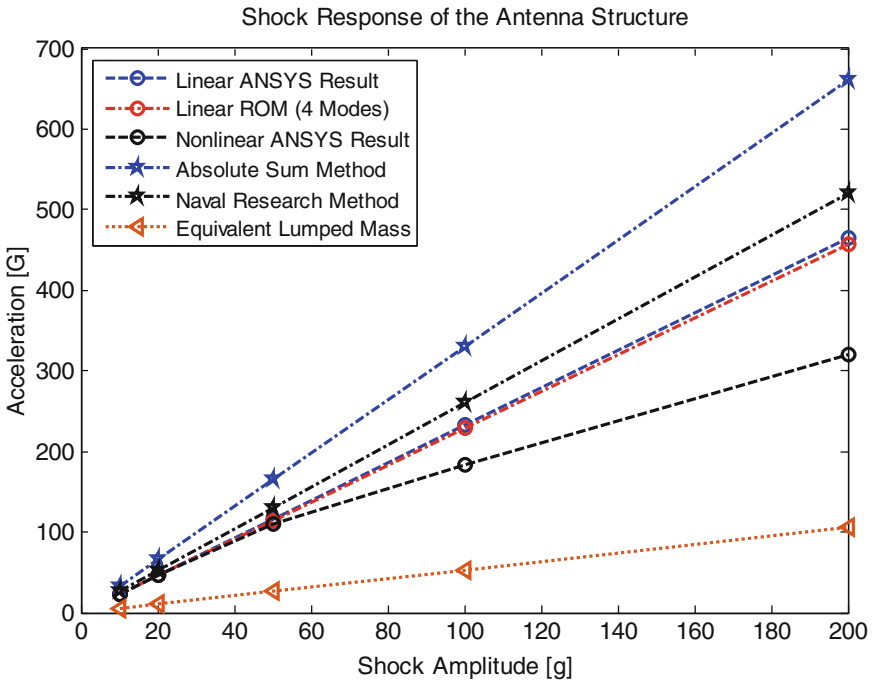

Fig. 6.12 Maximum relative displacement of the antenna structure

6.4 Conclusion

In this study, shock response of an antenna structure including geometric nonlinearity is investigated. Firstly, lumped mass model of an antenna structure is studied. Although lumped mass model is a fundamental and computationally efficient model, this is not applicable for case studies where contribution of the modes higher than the first mode cannot be neglected. Therefore, modeled continuous beam model by using Euler-Bernoulli beam theory results in highly accurate results due to

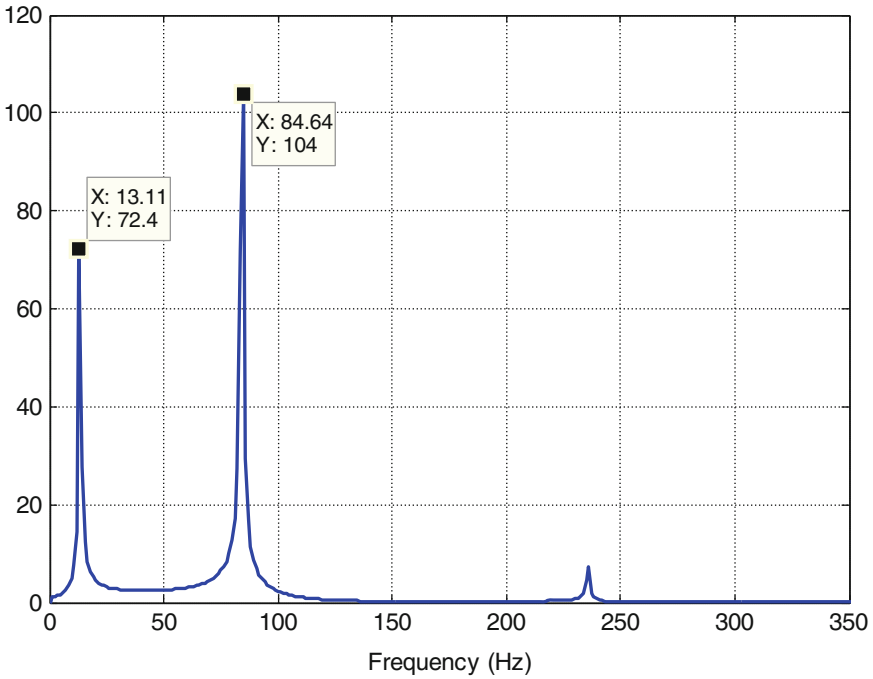

Fig. 6.13 Frequency content of acceleration response of the antenna structure

the fact that the effects of higher modes can as well be retained in the solution. Although both linear reduced order model (ROM) and finite element model are in agreement with each other, ROM is computationally very efficient, since a fine mesh is required in order to capture the propagation of shock wave properly. However, this leads to increased solution times. Furthermore, geometric nonlinearity plays an important role on shock response of an antenna structure, since many antenna structures have larger dimension in longitudinal direction. It is interesting to note that geometric nonlinearity reduces both relative displacement and acceleration response, especially in the case of high shock acceleration. It is similar to the case where as if shock isolator is used. In other words, when the antenna structure is modeled properly including geometric nonlinearity, response is similar to the case where an antenna structure is modeled by linear theory including shock isolator. Therefore, nonlinear modeling can eliminate the usage of shock isolator. It can be concluded that approximate methods are inherently conservative methods and may be used as a starting point of shock analysis due to their little computation time.

References

1. Internet Live Stats: Number of Internet Users (2014) - Internet Live Stats, 2014. [Online]. Available: http://www.internetlivestats.com/internet-users/. Accessed 01 Jun 2015
2. Wikipedia, F.: List of countries by number of mobile phones in use. Notes, 2011. [Online]. Available: https://en.wikipedia.org/wiki/List_of_countries_by_number_of_mobile_phones_in_use. Accessed 01 Jun 2015
3. Poisel, R.A.: Antenna Systems and Electronic Warfare Applications. Artech House, Norwood (2012)
4. Huang Y., Boyle, K.: Antennas: From Theory to Practice, First Edit. John Willey and Sons Ltd (2008)
5. Alexander, J.E.: Shock response spectrum – a primer. Sound Vib. (June), 6–14 (2009)
6. Lalanne, C.: Mechanical Shock: Mechanical Vibration and Shock Analysis, vol. 2. John Willey and Sons Ltd (2009)
7. Department of Defense Test Method Standard Environmental Engineering Considerations and Laboratory Tests, 2008
8. Eriksson, J., Kropp, W.: Measuring and Analysis of Pyrotechnic Shock. Chalmers University of Technology (1999)
9. Reddy, M.C.S., Hussain, J.: Structural analysis of dipoloop antenna radome for airborne applications. Int. J. Eng. Res. Technol. **4**(03), 724–735 (2015)
10. Lopatin, A.V., Morozov, E.V.: Modal analysis of the thin-walled composite spoke of an umbrella-type deployable space antenna. Compos. Struct. **88**(1), 46–55 (2009)
11. Su, H.: Structural Analysis of Ka-Band gimbaled antennas. COM DEV Ltd, Ontario, p. 15
12. Sreekantamurthy, T., Mann, T., Behun, V., Pearson, J.C., Scarborough, S., Engineer, A., Aerospace, S.: Nonlinear structural analysis methodology and dynamics scaling of inflatable parabolic reflector antenna concepts. Am. Inst. Aeronaut. Astronaut. (April), 1–15 (2007)

13. Younis, M.I., Alsaleem, F.M., Miles, R., Su, Q.: Characterization of the performance of capacitive switches activated by mechanical shock. J. Micromech. Microeng. **17**(7), 1360–1370 (2007)
14. Li, G.X., Shemansky, F.a.: Drop test and analysis on micro-machined structures. Sens. Actuators, A Phys. **85**(1), 280–286 (2000)
15. Younis, M.I., Miles, R., Jordy, D.: Investigation of the response of microstructures under the combined effect of mechanical shock and electrostatic forces. J. Micromech. Microeng. **16**(11), 2463–2474 (2006)
16. Younis, M.I., Arafat, H.N.: Investigation of the effect of nonlinearities on the response of cantilever microbeams under mechanical shock and electrostatic loading. Soc. Exp. Mech., 5–10 (2008)
17. Younis, M.I., Alsaleem, F., Jordy, D.: The response of clamped-clamped microbeams under mechanical shock. Int. J. Non-Linear Mech. **42**(4), 643–657 (2007)
18. Liang, C., Yang, M., Tai, Y.: Prediction of shock response for a quadrupod-mast using response spectrum analysis method. Ocean Eng. **29**(8), 887–914 (2002)
19. Alexander, J.E.: Nonlinear system mode superposition given a prescribed shock response spectrum input. In: Proc. Int. Modal Anal. Conf. - IMAC, no. 3, pp. 346–355 (2002)
20. Younis, M.I., Jordy, D., Pitarresi, J.M.: Computationally efficient approaches to simulate the dynamics of microbeams under mechanical shock. In: IMECE 2006 2006 ASME Int. Mech. Eng. Conf. Expo., vol. 16, no. 3, pp. 628–638 (2006)
21. Erturk, A., Inman, D.J.: On mechanical modeling of cantilevered piezoelectric vibration energy harvesters. J. Intell. Mater. Syst. Struct. **19**(11), 1311–1325 (2008)
22. Thomson, W.T., Dahleh, M.D.: Theory of Vibration and Applications, Fifth Edit. Pearson Education (1998)
23. Irvine, T.: Bending frequencies of beams, rods, and pipes. Available on the web on site: http://www.vibrationdata.com, pp. 1–61 (2012)
24. Majkut, L.: Free and forced vibrations of Timoshenko beams described by single difference equation. J. Theor. Appl. Mech. **47**(1), 193–210 (2009)
25. Younis, M.I.: MEMS Linear and Nonlinear Statics and Dynamics. Springer (2011)
26. Yee, J.K., Yang, H.H., Judy, J.W.: Shock resistance of ferromagnetic micromechanical magnetometers. Sens. Actuators, A Phys. **103**(1–2), 242–252 (2003)
27. Gatti, P.L., Ferrari, V.: Applied Structural and Mechanical Vibrations, First Edit. Taylor & Francis Group (1999)
28. ANSYS 15 Help Viewer, 2014
29. Abed, E.H., Lindsay, D., Hashlamoun, W.a.: Technical report on participation factors for linear systems. Automatica **36**(10), 1489–1496 (1999)
30. Irvine, T.: Effective modal mass and modal participation factors. Vibrationdata (1), 1–36 (2013)
31. International Standard-IEC 60068-2-27. Basic Safety Publication, p. 80 (2008)

Chapter 7
Investigation on Friction-Excited Vibration of Flexibly Supported Shafting System

Wenyuan Qin, Zhenguo Zhang, Suining Hu, and Zhiyi Zhang

Abstract Self-excited vibration of a flexibly supported shafting system in a gravity water tunnel was investigated by experiment and numerical simulation. Vibration of the flexibly supported shafting system, such as the acceleration responses of the shaft and the dynamic reaction forces at the propeller support, were measured at different shaft speeds. Experimental results demonstrated that the self-excited vibration, characterized by a single-mode vibration modulated by the shaft speed, emerges as the shaft speed decreases in a speed range. To reveal the mechanism of the self-excited vibration, a fluid-structure coupling model was established. Simulation results show that the instable modes are associated with the rotational vibration modes of the flexible support, which can be easily excited by the circumferential friction, and the coupling between the vibration of the flexible support and the friction of the water-lubricated rubber bearing is the main factor leading to the vibration instability in the flexibly supported shafting system.

Keywords Flexible support • Coupled vibration • Self-excited vibration • Friction of rubber bearings

7.1 Introduction

Water-lubricated rubber bearings are widely used as the supports in propeller shaft system [1–3] and the unexpected vibration even squeal induced by the friction in rubber bearings is often encountered [4–6]. Due to the suspension of the propeller, it is inconceivable for the bearing-shaft contacting surfaces to be fully separated by water especially during the start-up, shut-down, low-speed and high-load operational conditions. In those cases, bearings may be located in the mixed and boundary lubrication regimes and even contact directly with the shaft, which may result in the friction-induced vibration and squeal leading to excessive wear of bearing components and badly work performances in vessels [4–9].

Researches on the mechanism of the friction-induced vibration can be tracked back to about 40 years ago and four instability mechanisms gradually form [10–16], including the negative slope of the friction-velocity, the kinematic sprag-slip instability, follower force nature of the friction forces, the mode coupling instability. In the past, most studies [4–6, 10, 11, 17–20] on the friction-induced vibration in shaft systems often were limited to the theoretical and experimental analysis of the friction pair characteristics of water-lubricated rubber bearings. However, special investigations on the friction-induced dynamics in the propeller-shaft systems gradually prevail. Krauter [10] emulated the dynamic behavior of a bearing-shaft interaction system with an analytical model containing three degrees of freedom. The negative slope of the friction-velocity curve was determined to play a primary role in the instability conditions of the system, while the pattern of manifestation is the instability of the vibration mode. Simpson and Ibrahim [11] investigated the detailed dynamical behavior of a two-degree-of-freedom model that emulates the dynamics of water-lubricated bearings. The friction-velocity relationship is also found to be responsible for the occurrence of squeal and other nonlinear phenomena, while additional system parameters such as damping ratios and the initial conditions have less influence on the friction-induced vibration. Mihajlović et al. [13] theoretically and experimentally analyzed the interaction between the friction-induced vibration and the self-sustained lateral vibration caused by a mass unbalance. Zhang et al. [7, 8, 15, 16] analytically modelled the coupled dynamics of the bearing-shaft system and analyzed the system vibration responses under the excitation of the water-lubricated bearing friction. Research [9] experimentally analyzed the influences of rotor speeds, bearing loads, cooling water temperatures and installation states of bearing on friction-induced noise in shaft system supported by water-lubricated rubber bearings.

W. Qin (✉) • Z. Zhang • S. Hu • Z. Zhang
Institute of Vibration, Shock & Noise, Shanghai Jiao Tong University, Dongchuan Road 800, 200240 Shanghai, China

State Key Laboratory of Mechanical System and Vibration, Shanghai Jiao Tong University, Dongchuan Road 800, 200240 Shanghai, China
e-mail: qinwenyuan@sjtu.edu.cn

G. Kerschen (ed.), *Nonlinear Dynamics, Volume 1*, Conference Proceedings of the Society for Experimental Mechanics Series,
DOI 10.1007/978-3-319-29739-2_7

Accordingly, the present study will concentrate on the above-mentioned issues and especially focus on the coupling effect between bearing friction and dynamic characteristics of the system to obtain an improved understanding of the excitation mechanism leading to self-excited vibration.

7.2 Experiment

7.2.1 Experimental Set Up

The flexibly supported shafting system in a gravity water tunnel is shown as in Fig. 7.1a, mainly consisted of stern support, middle support, water-lubricated rubber bearings, propeller, flexible coupling and servo motor. The interface of the stern support is shown as in Fig. 7.1b. One end of a sword in the support is hinged with the bearing sleeve and the other end, longitudinally pre-tightened by force F_P to improve support stiffness of the sword, is fixed on the mounting base which is isolated from ground with rubber isolators.

7.2.2 Experimental Results

The vibration characteristics of the flexibly supported shafting system in the gravity water tunnel is measured to obtain the natural vibration and the dynamic response of the system.

The hammer method is adopted for measuring the statically natural vibration frequency. The modal test under the static state is carried out without water, driving at single point and picking at multi points shown as in Fig. 7.2, and the result is shown as in Table 7.1.

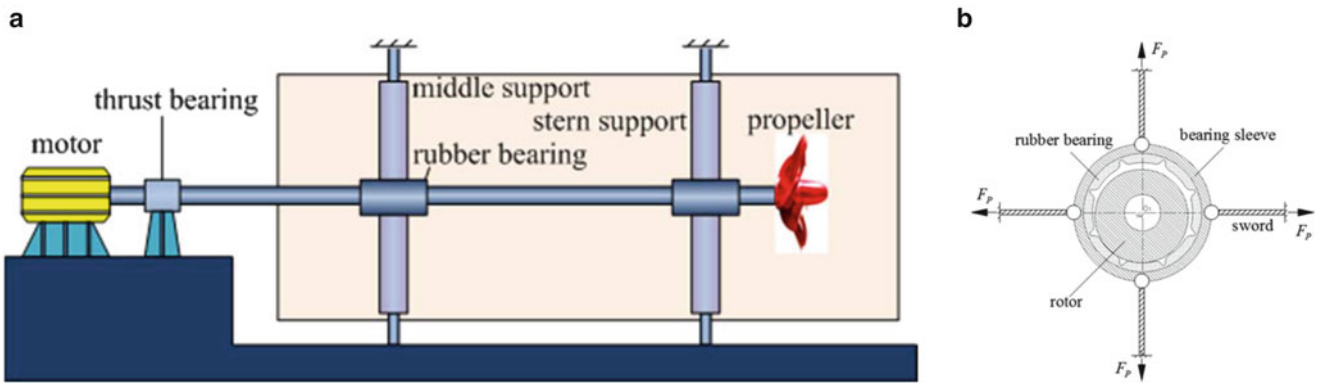

Fig. 7.1 (**a**) Schematic of flexibly supported shafting system in a gravity water tunnel, (**b**) the interface of the stern support

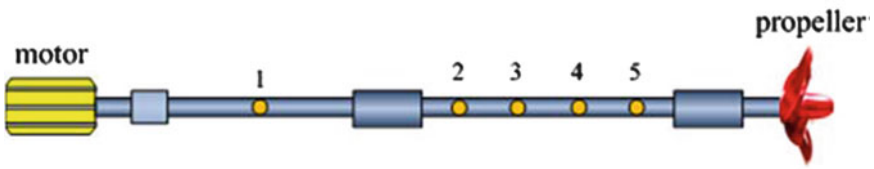

Fig. 7.2 The arrangement of measurement points under static state

Table 7.1 The measured frequencies of the system

Order	Static (without water)	Description
1	21.1 Hz	Bending vibration of shaft
2	29.5 Hz	Bending vibration of shaft
3	49.4 Hz	Bending vibration of shaft
4	72.6 Hz	Bending vibration of shaft

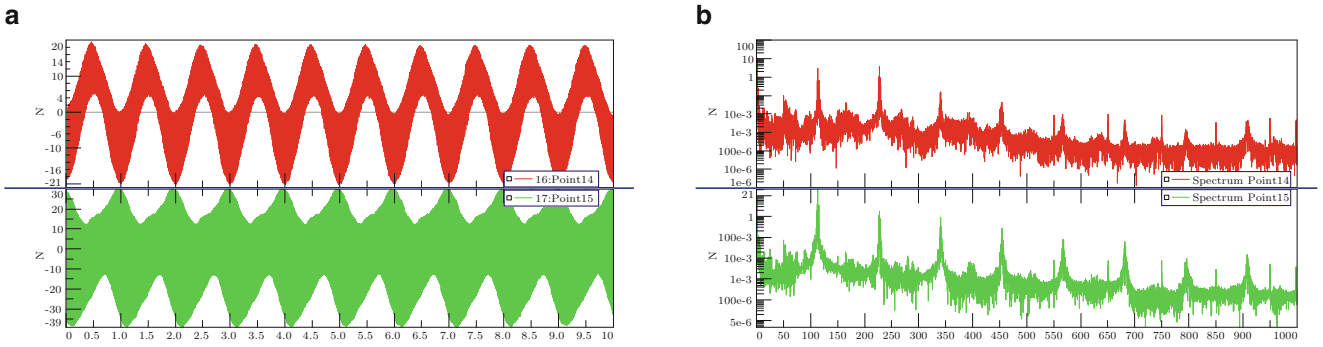

Fig. 7.3 The dynamic response when the shaft speed is 60 rpm: (**a**) the dynamic reaction force of the horizontal swords in time, (**b**) the dynamic reaction in frequency

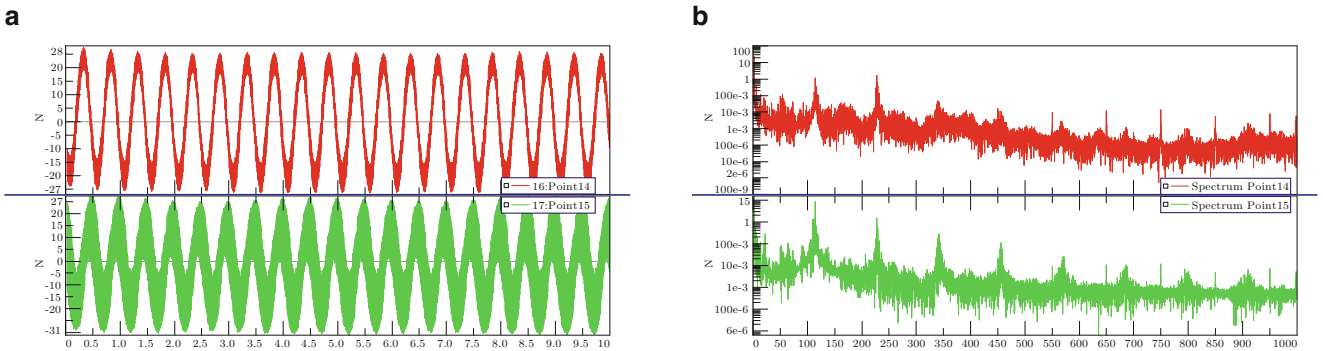

Fig. 7.4 The dynamic response when the shaft speed is 120 rpm: (**a**) the dynamic reaction force of the horizontal swords in time, (**b**) the dynamic reaction in frequency

The system in the gravity water tunnel is measured after the tunnel is filled with water, to obtain the dynamically reaction force of the horizontal swords in the stern support, when it is located at the steady state under every associated shaft speed which continuously decreases from 600 rpm to 30 rpm and each gap is 30 rpm. Experiment results show that the system come to instability when the shaft speed come to the 210 rpm, and the self-excited vibration become stronger when the speed is 180 rpm, then the self-excited vibration grow much stronger as the shaft speed decreases and become very strong when the shaft speed is located in the range from 180 rpm to 60 rpm, but it comes to the end when the shaft speed comes to 30 rpm. The dynamically reaction forces of the horizontal swords in the stern support are respectively shown in Figs. 7.3 and 7.4, characterized with a single mode instability, when the shaft speed are 60 rpm and 120 rpm. Figures 7.3a and 7.4a demonstrate that the self-excited spectrum is characterized with shaft frequencies superposed with instability frequency which is about 114 Hz. Figure 7.5 clearly demonstrates the process of the instability decreases to end. The maintenance of self-excited vibration need energy from servo motor. If the shaft work at a relatively low speed, relatively worse friction torque from water-lubricated rubber bearings will disturbed the drive torque from the servo motor to a large extent. In this case, the shaft can't keep state and the self-excited vibration will disappear.

7.3 Numerical Simulation

To analyze the mechanism of self-excited vibration in the flexibly supported shafting system and find the associated instability mode, the finite element model of flexibly supported shafting system, shown as in Fig. 7.6, is set up and analyzed its natural vibration features.

The parameters of the shaft: length is 6.16 m, radius is 0.03 m, the distance between propeller and the stern is 0.18 m and the distance between the stern support and the middle support is 2.6 m. The parameters of a sword in the support: length is 0.33 m, width is 0.07 m, thickness is 2.36 mm. The radius of the bearing sleeve is 42.7 mm. The density of material is 8034 kg/m^3, the modulus is 2.03e11 Pa and the Poisson's Ration is 0.28.

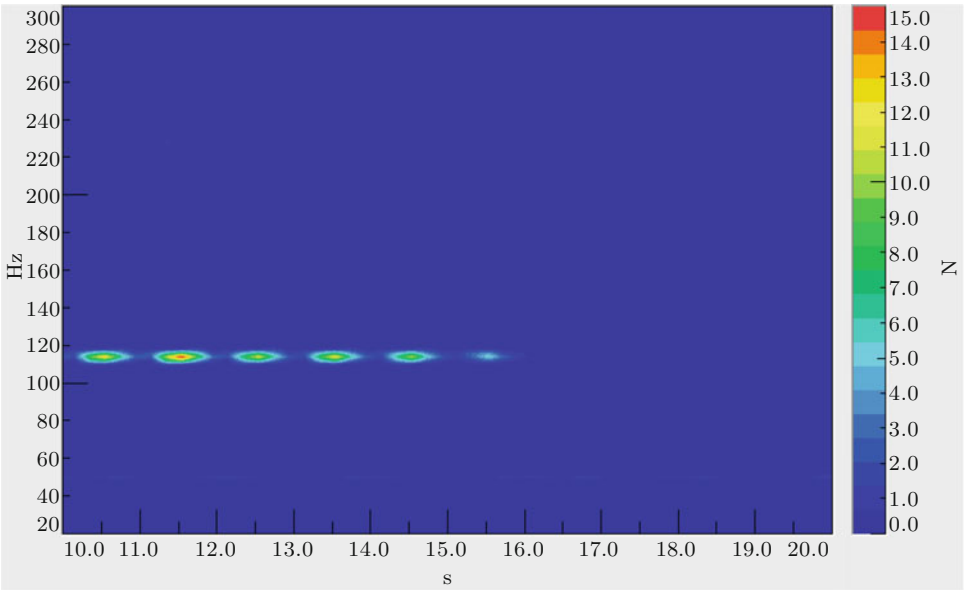

Fig. 7.5 The dynamic reaction force of the horizontal swords when the shaft speed is 30 rpm

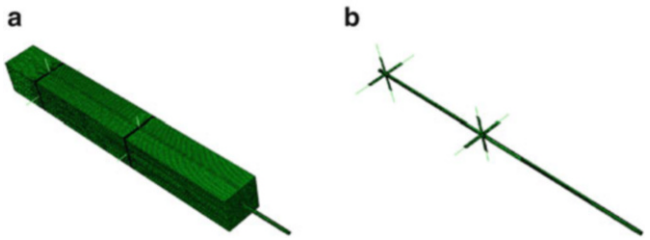

Fig. 7.6 The finite element model of the flexibly supported shafting system, (**a**) structure-fluid coupled model, (**b**) the structure model

Table 7.2 The numerically simulation frequencies of the system

Order	Without water	Description
1	20.1 Hz	Bending vibration of shaft
2	29.5 Hz	Bending vibration of shaft
3	49.7 Hz	Bending vibration of shaft
4	69.8 Hz	Bending vibration of shaft

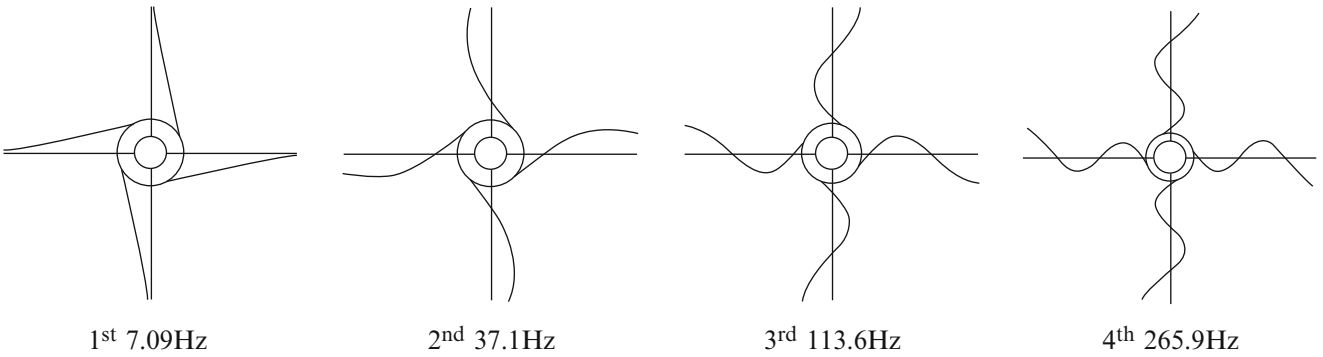

Fig. 7.7 The first four rotational modes of the support

Some numerically simulation frequencies of the system, can reach a good agreement with the measured frequencies shown in Table 7.1, are shown as in Table 7.2 and the first four rotational modes of the stern support, considering the water coupling effect, is shown as in Fig. 7.7. The third mode of the stern support in the system is associated with the instable mode.

7.4 Conclusions

The self-excited vibration easily induced by the friction from water-lubricated rubber bearings when the shaft work at a specific range, and the associated vibration at the instability frequency is magnified several times and destroy the performance of the system. Abased on the above analysis, the frequency feature of self-excited is characterized by the support instability modulated by the shaft speed. The coupling effect of rotational vibration of support and friction in the shaft-support interface is decisive for instability, and the associated mode shape of support is determinant for self-excited vibration. Especially, the bearing normal load, friction coefficient and shaft speed are essential factors of the shaft-support interface friction which can induce shaft and support vibration. The above results presented in this work can provide references for ascertaining abnormal vibration and squeal in the shafting system.

Acknowledgement This research is sponsored by the National Natural Science Foundation of China (NSFC), Grant no. 11172166.

References

1. Orndorff Jr., R.L.: Water-lubricated rubber bearings, history and new development. Naval Eng. J. **97**(7), 39–52 (1985)
2. Chen, Z.Y.: Vibration of Ship Propulsion Shafting System. Shanghai Jiao Tong University Press (1987)
3. Carlton, J.: Marine Propellers and Propulsion. Butterworth-Heinemann (2012)
4. Hirani, H., Verma, M.: Tribological study of elastomeric bearings for marine propeller shaft system. Tribol. Int. **42**(2), 378–390 (2009)
5. Yang, L.Y.: Study on lubrication an rub impact characteristics of stern shaft-bearing in ships. Master Thesis, Wuhan University of Technology (2010)
6. Zhang, L.: Mechanism analysis and experimental research on vibration noise phenomenon of water-lubricated composite rubber bearing. Master Thesis, Wuhan University of Technology (2013)
7. Zhang, Z.G., Zhang, Z.Y., Wang, J., et al.: Friction induced self-excited vibration in a propeller shaft system. J. Vib. Shock **32**(19), 153–158 (2013)
8. Zhang, Z.G., Chen, F., Zhang, Z.Y., et al.: Analysis of friction-induced vibration in a propeller-shaft system with consideration of bearing-shaft friction. Proc. Inst. Mech. Eng., C: J. Mech. Eng. Sci. **228**(8), 1131–1328 (2014)
9. Wang, L., Yu, Q., Liu, Y.J.: Characteristic analysis and experimental study on friction-induced noise in water-lubricated rubber bearings. J. Wuhan Univ. Technol. (Transp. Sci. Eng.) 2015(2), (2015)
10. Krauter, A.I.: Generation of squeal/chatter in water-lubricated elastomeric bearings. ASME J. Lubr. Technol. **103**, 406–412 (1981)
11. Simpson, T.A., Ibrahim, R.A.: Nonlinear friction-induced vibration in water-lubricated bearings. J. Vib. Control **2**(1), 87–113 (1996)
12. Eriksson, M., Jacobson, S.: Friction behavior and squeal generation of disc brakes at low speeds. Proc. Inst. Mech. Eng., D: J. Automob. Eng. **215**(12), 1245–1256 (2001)
13. Mihajlović, N., Van de Wouw, N., Rosielle, P., et al.: Interaction between torsional and lateral vibrations in flexible rotor systems with discontinuous friction. Nonlinear Dyn. **50**(3), 679–699 (2007)
14. Li, F., Shuai, C.G., He, L.: Dynamic analysis of rotor system coupled by rubber bearings. Noise Vib. Control **31**(3), 37–41 (2011)
15. Zhang, Z.G., Zhang, Z.Y., Chen, F., et al.: Research on the coupling between torsional and lateral vibrations in propeller-shaft system with friction. J. Mech. Eng. **49**(6), 74–80 (2013)
16. Zhang, Z., Zhang, Z., Huang, X., et al.: Stability and transient dynamics of a propeller-shaft system as induced by nonlinear friction acting on bearing-shaft contact interfaces. J. Sound Vib. **333**(12), 2608–2630 (2014)
17. Zhou, C., Wang, J.X., Yu, J.B.: Effect of thickness and hardness of rubber underlayer on frictional coefficient of water-lubricated integer bearings. Lubr. Eng. **2006**(2), 40–41 (2006)
18. Yao, S.W., Hu, Z.C., Ma, B., et al.: The new development of rubber bearing and its application in warships. J. Ship Sci. Technol. **2008**(Z1), 27–30 (2008)
19. Wang, H.: Experimental research on the type of water-lubricated stern tube rubber bearings. Master Thesis, Wuhan University of Technology (2012)
20. Duan, H.T., Wu, Y.M., Wang, X.M., et al.: Study on the tribological properties of new water-lubricated bearing materials. J. Wuhan Univ. Technol. **34**(2006), 17–21 (2012)

Chapter 8
Resonant Analysis of Systems Equipped with Nonlinear Displacement-Dependent (NDD) Dampers

Javad Jahanpour, Shahab Ilbeigi, and Mojtaba Porghoveh

Abstract Resonant analysis of a vibration system equipped with a nonlinear displacement-dependent (NDD) damper is investigated. The frequency of the external forcing is chosen to be close to the natural frequency of the system. The system is modeled and the approximate analytical solution of the governing equation is developed using the multiple scales method (MSM). Several case studies with various amounts of external force's frequencies are performed to investigate the resonant excitation analysis. The proposed analytical solution is also verified by the fourth order Runge-Kutta method. Moreover, the performance of the used NDD damper is analyzed and compared with the ordinary linear damper through the same periodic resonant excitation. It is found that the NDD damper has a superior performance in reducing the vibration amplitude, compared to the traditional linear damper when resonance occurs. In addition, utilizing the NDD damper in the resonant-excited system provides a smaller force transmitted to the base than the system with the ordinary linear damper.

Keywords Resonant analysis • Nonlinear displacement-dependent (NDD) damper • Periodic excitation • Multiple scales method (MSM) • Vibration amplitude reduction

8.1 Introduction

In general, to perform the vibration analysis on a system, its response under free and forced vibration is to be investigated. In free vibration analysis, the system oscillates without being subjected to forcing from the surrounding environment. While, under the forced vibrations, the system is excited by the continuously applied, time-dependent external forces which act on the system [1]. Most often these are periodic forces.

In many applications, vibration may cause discomfort, disturbance, and damage. In particular, with the forced vibration, when the external excitation frequency tends the natural frequency of the system, destruction of the system or the structure may occur [2, 3]. This phenomenon is named as resonance, which is a well-known concept in forced vibration problems. In an ideal resonance, when the frequency of an exciting force matches the natural frequency of the system; the amplitude of vibration is considerably increased. The study of resonance is an important issue in many applications such as: vehicle design [4], steam-turbine rotor-bearing systems [5], wind turbines [6, 7], bridge design [8], controllers and isolators design [9], beams [10–17], CNC tool-path planning [18] and tuned liquid damper (TLD) as an absorber [19, 20]. Also, understanding resonances is essential to ensure an appropriate running condition and a desired behavior of systems. Most studies of resonance assume that the system is linear. However, most of dynamical systems have nonlinear components, which cannot be described by a linear model. For example, vibration components with clearances [21, 22], motion limiting stops [23, 24], vibration analysis of the milling process [25], vibration modes with internal resonance [26], or a nonlinear displacement-dependent (NDD) damper [27], which cause changes in damping coefficients, represent a significant proportion of these systems.

In order to avoid the undesired effects of the resonance in both linear and nonlinear systems, different kinds of viscous dampers are added to the vibratory system. Dampers absorb the energy and do not allow the vibration amplitude to reach the infinity in resonance phase, while in conservative systems without any damper; the amplitude reaches infinity when resonance happens. Most of viscous dampers have a constant damping coefficient, however, variable dampers have already found their way to industrial/commercial applications [28, 29]. The variable dampers can be classified as active, semiactive

J. Jahanpour • M. Porghoveh
Department of Mechanical Engineering, Mashhad Branch, Islamic Azad University, Mashhad, Iran

S. Ilbeigi (✉)
Department of Mechanical, Industrial, and Systems Engineering, University of Rhode Island, Kingston, RI 02881, USA
e-mail: ilbeigi@uri.edu

G. Kerschen (ed.), *Nonlinear Dynamics, Volume 1*, Conference Proceedings of the Society for Experimental Mechanics Series,
DOI 10.1007/978-3-319-29739-2_8

and passive [30–34]. Active dampers are activated by an external source of power which usually is provided by hydraulic actuators [35–37]. In most cases, the active dampers have high energy consumption, heavy weight, large size and high cost. Semiactive dampers inherit properties of controllable electromagnetic valves or magneto rheological (MR) fluid to control the damping characteristics of the system and they are a compromise between the active and passive dampers [29–38]. Passive dampers have generally fixed properties which are determined and preset according to the design goals and intended application [38]. Even though the active and semiactive dampers have higher performance, passive dampers are still the most commonly used ones [29].

While there are many types of passive dampers, the passive variable dampers have been recently developed. Among the passive variable dampers, those with stroke and displacement/position dependent sensitivity have been studied in several works [39–50]. Fukushima et al. [43] suggested that dampers should have a stroke dependent characteristic; such that for a given velocity, a longer stroke would give a greater force. However, the force in the stroke sensitivity cannot be identified directly with the actual position of the piston in the cylinder [28]. The displacement sensitive dampers have been used on aircraft landing gear, motorcycles, and vehicle suspension applications. The displacement sensitive schemes for landing gears employ positive recoil control or two and three level position dependent damping [32]. In a motorcycle front fork, a short and blunt rubber as a needle causes the damper orifice to get closed which allows weaker springing with improved ride quality pressure [28]. Etman et al. [45] designed a stroke dependent damper for the front axle suspension of a truck. The displacement sensitive damper suggested for vehicle suspension applications follows the idea of using a long tapered needle entering an orifice in the piston [16, 34]. This type of damper is merely limited to utilizing a tapered needle and is not mathematically modeled. Lee and Moon [47, 48] reported on tests of a displacement sensitive damper with a longitudinally grooved pressure cylinder to relax the damping around the central position.

Some researchers have also investigated thoroughly the nonlinear dampers [27, 34, 49]. For instances, Haque et al. [50] proposed an integral formulation to obtain the damping force of a displacement sensitive nonlinear damper. This method was based on the transformation of the displacement sensitivity characteristic of the damper into a velocity sensitivity characteristic. Farjoud et al. [51] presented a nonlinear model of monotube hydraulic dampers with an emphasis on the effects of shim stack on damper performance. Guo et al. [52] studied the force and displacement transmissibility of nonlinear viscous damper based vibration isolation. Peng et al. [53] investigated resonant phenomena for a class of nonlinear systems using the Nonlinear Output Frequency Response Functions (NOFRFs).

Free and forced vibration analyses of systems equipped with nonlinear damper have also been studied in several researches [27, 54–57]. For instances, Bugra et al. [55] implemented several experiments to determine the dynamic characterization of nonlinear oil-free wire mesh dampers. To this end, the free and forced vibrations were investigated using the Hilbert transform procedure and controlled amplitude single frequency excitation tests, respectively. Main and Jones [56] demonstrated the free vibration of a taut cable with a nonlinear amplitude dependent damper. Diotallevi et al. [57] proposed a simplified design method to analyze the forced vibration of single- and Multi-degrees of freedom (SDF and MDF) systems equipped with nonlinear viscous damper under harmonic external forces. In their work, the responses of the SDF and MDF systems were also calculated numerically.

Recently, Ilbeigi et al. [27, 58] introduced a novel scheme for NDD dampers, in which the damping coefficient and damping force were both continuous and smooth functions of displacement. In contrast with a linear damper, where the damping force only depends on the velocity, the damping force produced by the proposed NDD damper depends on the position of the system as well as the velocity. In their work, the vibratory mass-spring system equipped with a NDD damper was also mathematically modeled and free vibration analysis of the system was analyzed. The results presented in [27] indicate that the advised passive NDD damper scheme is capable to reduce the free vibration amplitude rather than the existing traditional linear damper.

In this paper, resonant analysis of a mass-spring system utilizing the NDD damper is presented. The nonlinear differential equation of the system under an external force with the frequency close to the natural frequency of the system is derived. To study the resonance vibration analysis of the system, the external excitation's frequency is described using a detuning parameter presenting the closeness of the external force's frequency to the natural frequency of the system. The stationary response of the system is elaborated using the multiple scales method (MSM). The rest of the paper is organized as follows. Section 8.2 is a review on the NDD damper mechanism. In Sect. 8.3, the mathematical model of the nonlinear mass-spring system equipped with the NDD damper under an external resonant-force excitation is formulated and the governing differential equation is derived. The forced-resonant vibration analysis of the system is illustrated in the Sect. 8.4. Several numerical examples are presented in Sect. 8.5. The results are analyzed and discussed in Sect. 8.6. Finally, Sect. 8.7 concludes the paper.

8.2 Review on the NDD Damper Mechanism

An ordinary simple viscous damper consists of a piston having one or more orifices moving inside a cylinder filled with a viscous fluid (Fig. 8.1). The damping force produced by a damper is linearly related as follows:

$$F = -c\frac{du}{dt} \tag{8.1}$$

In which c is the damping coefficient.

By taking advantages of Hagen–Poiseuille equation for laminar flows, c can be obtained by the following equation for the case of piston with one orifice:

$$c_{linear} = \hbar\left[\left(\frac{D}{d}\right)^2 - 1\right]^2 \tag{8.2}$$

where, D and d are the cylinder diameter and the opening fluid gap diameter, respectively. Also, $\hbar = 8\pi\mu L$, in which, μ denotes for dynamic viscosity of the fluid and L is the piston width.

For a set of chosen parameters D, d and L, the damping coefficient has a constant value. The mechanism can be designed to make the linear damper into nonlinear and displacement-dependent one. To this end, [15] proposed a solid cone shaped generated by rotating the interior region of the following function in Cartesian r-u coordinates around the $u-$ axis:

$$u = nr^s \text{ or } r = \left(\frac{u}{n}\right)^{\frac{1}{s}} \tag{8.3}$$

where, $\beta = \frac{2}{d.n^{\left(\frac{1}{s}\right)}}$ and $\gamma = \frac{D}{d}$.

The fixed cone shaped part is assembled to the linear damper, so that the origin of coordinates is located on the center of the piston, the fluid travels through its outer surface and the inner surface of the orifice (Fig. 8.2), while, the opening fluid gap is changed and the damping coefficient is consequently varied. Therefore, the ordinary linear damper with a constant damping coefficient is converted to the nonlinear damper with a variable displacement-dependent damping coefficient

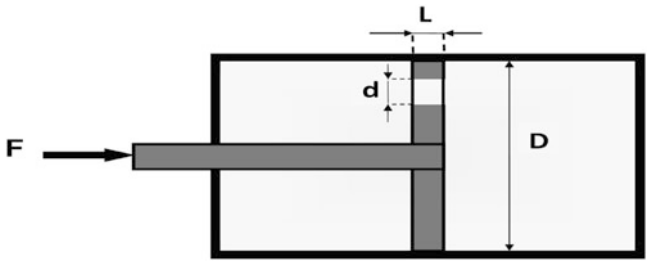

Fig. 8.1 Schematic of a simple viscous damper

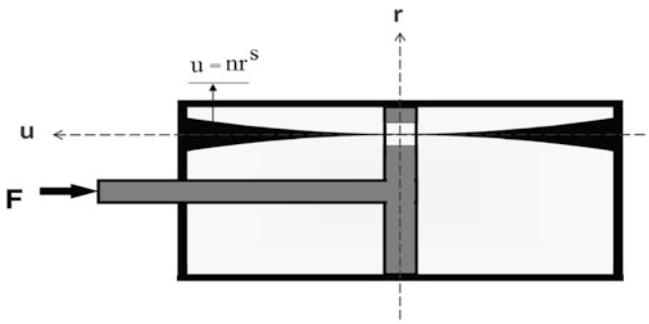

Fig. 8.2 Schematic of the nonlinear displacement-dependent (NDD) damper [27]

For the designed displacement-dependent damping mechanism shown in Fig. 8.2, the opening fluid gap diameter is equal to $d-2r$. Substituting r from Eq. (8.3), and $d-2r$ for d into Eq. (8.2) leads to

$$c=\hbar\left[\gamma^2\left(\frac{1}{1-\beta u^{\left(\frac{1}{s}\right)}}\right)^2-1\right]^2 \tag{8.4}$$

where, $\beta=\frac{2}{d_n{}^{\left(\frac{1}{s}\right)}}$ and $\gamma=\frac{D}{d}$.

Using the 2nd-order Taylor series expansion, Eq. (8.4) can be expressed as follows [27].

$$c=\alpha_1+\alpha_2|u|^{\left(\frac{1}{s}\right)}+\alpha_3|u|^{\left(\frac{2}{s}\right)}+\alpha_4|u|^{\left(\frac{3}{s}\right)}+\alpha_5|u|^{\left(\frac{4}{s}\right)} \tag{8.5}$$

For the case of $n=1$ and $s=\frac{1}{2}$, Eq. (8.5) will be rewritten as follows:

$$c=\alpha_1+\alpha_2u^2+\alpha_3u^4+\alpha_4u^6+\alpha_5u^8 \tag{8.6}$$

The parameters α_i in Eq. (8.6) are given in Appendix.

It is noticed that the damping coefficient of the traditional damper is constant value, whereas the damping coefficient of a NDD damper changes as the system moves. More details on mathematical formulation of the NDD damper can be found in [15].

8.3 Mathematical Formulation of the Forced-Resonant Mass-Spring-NDD Damper System

The governing differential equation of a simple mass-spring-damper system with an external periodic force follows:

$$\ddot{u}+\frac{c}{m}\dot{u}+{\omega_n}^2u=\frac{F\cos(\Omega t)}{m} \tag{8.7}$$

where, $\omega_n=\sqrt{\frac{k_s}{m}}$ is the natural frequency of the system, Ω is the external force's frequency and F is the excitation amplitude.

For a linear damper with constant damping coefficient, the forced-resonant response of the system is as follows:

$$\begin{aligned}u_l(t)=A_1e^{-\zeta\omega_nt}\sin\left(\sqrt{1-\zeta^2}\omega_nt+\psi\right)\\+A_2\cos(\Omega t-\varphi)\end{aligned} \tag{8.8}$$

where, $\zeta=\frac{c}{2\sqrt{mk_s}}$. Also, A_1 and ψ are evaluated using initial conditions. Moreover, A_2 and φ related to the particular solution of Eq. (8.7), are given in Appendix.

The damping force and the total force transmitted to the base can be calculated by the following equations:

$$F_{\text{Damping}}=c\frac{du(t)}{dt}. \tag{8.9}$$

$$F_{\text{Transmitted}}=c\,\dot{u}+k_s\,u. \tag{8.10}$$

In order to achieve the governing differential equation of a basic mass-spring system equipped with NDD damper with an external force, c from Eq. (8.6) must be replaced into Eq. (8.7) as follows:

$$\begin{aligned}\frac{d^2u}{d\widehat{t}^2}+u=-\varepsilon\left(1+\beta_1u^2+\beta_2u^4+\beta_3u^6+\beta_4u^8\right)\frac{du}{d\widehat{t}}\\+K\cos\left(\lambda\widehat{t}\right)\end{aligned} \tag{8.11}$$

In which, $\widehat{t}=\omega_n\,t$, $\varepsilon=\frac{\hbar\left(\gamma^4-2\gamma^2+1\right)}{m\omega_n}$, $\beta_i=\frac{\alpha_{i+1}}{\alpha_1}$, $K=\frac{F}{m{\omega_n}^2}$ and $\lambda=\frac{\Omega}{\omega_n}$.

By adding a small term to the mathematical description (ε in this paper), a perturbation method can be used to find an approximate solution to the governing differential Eq. (8.11). The parameter ε is directly proportional to $\hbar$ and, accordingly, to the fluid viscosity. It is also dependent to γ. Hence, increasing the viscosity or increasing γ, causes increasing ε, and strength of nonlinearity in Eq. (8.11), successively.

The shape parameters, i.e. n and s, effect on β as $\beta = \frac{2}{d.n^{\frac{1}{s}}}$ and successively on the damping coefficient c as given by Eq. (8.4). Accordingly, the dimensionless form of the governing equation of the vibration system utilizing the NDD damper with an external periodic excitation is affected by these shape parameters (see Eq. (8.11)). It should be noted that the values of the shape parameters n and s do not have any effect on ε the one parameter which describes the strength of nonlinearity of the governing equation. Since the main focus of this paper is to analyze forced-resonant vibration of a system equipped with NDD damper, the shape parameters have been selected as a fixed set for a general application. However, the couple of the values of these parameters can be optimized according to the desire goal and intended particular application.

For the forced-resonant analysis of the mass-spring-NDD damper system, the excitation frequency is considered as:

$$\Omega = \omega_n + \delta\varepsilon \tag{8.12}$$

where, δ is the detuning parameter to present the deviation of the external force's frequency from the natural frequency of the system. Also, the external force amplitude coefficient, i.e. K, can be expressed as $K = \varepsilon k$ without any loss of the generality of the mathematical model. Therefore, the term related to the periodic-resonant external force in Eq. (8.11) can be expressed as following equation:

$$K\cos\left(\lambda\widehat{t}\right) = \varepsilon k\cos\left[\widehat{t} + \frac{\varepsilon\delta}{\omega_n}\widehat{t}\right] \tag{8.13}$$

Substituting Eq. (8.13) in Eq. (8.11) leads to:

$$\begin{aligned}\frac{d^2u}{d\widehat{t}^2} + u = -\varepsilon\left(1 + \beta_1u^2 + \beta_2u^4 + \beta_3u^6 + \beta_4u^8\right)\frac{du}{d\widehat{t}} + \\ \varepsilon k\cos\left[\widehat{t}\left(1 + \frac{\varepsilon\delta}{\omega_n}\right)\right]\end{aligned} \tag{8.14}$$

where, $\beta_i = \frac{\alpha_{i+1}}{\alpha_1}$ are given in Appendix.

In the following section, the procedure of employing MSM as a perturbation technique is illustrated to solve Eq. (8.14).

8.4 Forced-Resonant Vibration Analysis of the Mass-Spring-NDD Damper Using MSM

This method is based on the idea of representing multiple independent variables, which are all functions of the time variable, and express all other time dependent functions including the response, as functions of the represented variables [54, 59–61]. For this aim, the independent variables are introduced as:

$$T_n = \varepsilon^n\widehat{t} \quad \text{for} \quad n = 0, 1, 2, 3 \tag{8.15}$$

Thus, the term related to the periodic-resonant external force in Eq. (8.14) can be determined using the terms T_0 and T_1 as follows

$$\varepsilon k\cos\left[\widehat{t}\left(1 + \frac{\varepsilon\delta}{\omega_n}\right)\right] = \varepsilon k\cos\left(T_0 + \frac{\delta}{\omega_n}T_1\right) \tag{8.16}$$

Assuming $n = 0$ and 1, the solution of Eq. (8.14) can be expressed as

$$u = u_0\left(T_0, T_1\right) + \varepsilon u_1\left(T_0, T_1\right) + O\left(\varepsilon^2\right) \tag{8.17}$$

With regard to the chain rule of derivation, the first and second derivatives with respect to $\widehat{t}$ can be represented as the following forms:

$$\begin{aligned}\frac{d}{d\widehat{t}} &= D_0 + \varepsilon D_1 \\ \frac{d^2}{d\widehat{t}^2} &= D_0^2 + 2\varepsilon D_0 D_1 + \varepsilon^2 D_1^2\end{aligned} \tag{8.18}$$

where $D_n = \frac{\partial}{\partial T_n}$.

Substituting Eqs. (8.16), (8.17), and (8.18) into Eq. (8.14) and equating coefficient of each power of ε in the two sides of equation together, leads to

$$D_0^2 u_0 + u_0 = 0 \tag{8.19}$$

$$\begin{aligned}D_0^2 u_1 + u_1 = -2D_0 D_1 u_0 - \Big(1 + \beta_1 u_0^2 + \\ \beta_2 u_0^4 + \beta_3 u_0^6 + \beta_4 u_0^8\Big) D_0 u_0 + k\cos\left(T_0 + \tfrac{\delta}{\omega_n} T_1\right).\end{aligned} \tag{8.20}$$

Assuming $\eta = \frac{\delta}{\omega_n}$, then, the term $k\cos\left(T_0 + \frac{\delta}{\omega_n} T_1\right)$ in Eq. (8.20) can be rewritten as:

$$\begin{aligned}k\cos\left(T_0 + \eta T_1\right) &= \tfrac{k}{2}\left[e^{i(T_0+\eta T_1)} + e^{-i(T_0+\eta T_1)}\right] \\ &= \tfrac{k}{2} e^{i\eta T_1}.e^{iT_0} + \tfrac{k}{2} e^{-i\eta T_1}.e^{-iT_0}\end{aligned} \tag{8.21}$$

The general solution of Eq. (8.19) can be expressed as

$$u_0 = A\left(T_1\right)\ e^{iT_0} + \overline{A}\left(T_1\right)\ e^{-iT_0} \tag{8.22}$$

Substituting for u_0 from Eq. (8.22) and the term related to the external force from Eq. (8.21) into Eq. (8.20) gives

$$\begin{aligned}{D_0}^2 u_1 + u_1 = -i\Big[\Delta_s e^{iT_0} + \Delta_3 e^{3iT_0} + \Delta_5 e^{5iT_0} \\ + \Delta_7 e^{7iT_0} + \Delta_9 e^{9iT_0} + \mathrm{CC}\Big].\end{aligned} \tag{8.23}$$

In which,

$$\begin{aligned}\Delta_s = 2D_1 A + A + \beta_1 A^2\overline{A} + 2\beta_2 A^3\overline{A}^2 + \\ 5\beta_3 A^4\overline{A}^3 + 14\beta_4 A^5\overline{A}^4 - \tfrac{1}{2} ike^{i\eta T_1}\end{aligned} \tag{8.24}$$

Also, Δ_i ' s are given in Appendix and CC stands for complex conjugate.

Omitting the terms that produce secular terms leads to solvability for the first-order approximation, therefore, the coefficients of $e^{\pm iT_0}$ must be vanished; that is

$$\Delta_s = 0 \tag{8.25}$$

Thus

$$\begin{aligned}-2D_1 A = A + \beta_1 A^2\overline{A} + 2\beta_2 A^3\overline{A}^2 + \\ 5\beta_3 A^4\overline{A}^3 + 14\beta_4 A^5\overline{A}^4 - \tfrac{1}{2} ike^{i\eta T_1}\end{aligned} \tag{8.26}$$

In order to solve Eq. (8.26) and for omitting the secular terms one let

$$A = \frac{1}{2}a\left(T_1\right)\ e^{i\phi(T_1)} \tag{8.27}$$

Substituting Eq. (8.27) and its conjugate and derivatives into Eq. (8.26) and separating the imaginary and real parts leads to

$$\begin{aligned}&\tfrac{da}{dT_1} = -a - \tfrac{1}{4}\beta_1 a^3 - \tfrac{1}{8}\beta_2 a^5 - \tfrac{5}{64}\beta_3 a^7 - \\ &\tfrac{7}{128}\beta_4 a^9 + k\sin\left(-\phi + \eta T_1\right)\end{aligned} \tag{8.28a}$$

$$\frac{d\phi}{dT_1} = -\frac{k\cos\left(-\phi + \eta T_1\right)}{a} \tag{8.28b}$$

To eliminate the explicit time dependence of the right-hand sides of (8.28a) and (8.28b) one let

$$\psi = \eta T_1 - \phi \tag{8.29a}$$

Or

$$\frac{d\psi}{dT_1} = \eta - \frac{d\phi}{dT_1} \tag{8.29b}$$

Hence (8.28a) and (8.28b) can be rewritten as follows

$$\begin{aligned}&\tfrac{da}{dT_1} = -a - \tfrac{1}{4}\beta_1 a^3 - \tfrac{1}{8}\beta_2 a^5 - \tfrac{5}{64}\beta_3 a^7 - \\ &\tfrac{7}{128}\beta_4 a^9 + k\sin\left(\psi\right)\end{aligned} \tag{8.30}$$

$$\frac{d\psi}{dT_1} = \eta + \frac{k\cos\left(\psi\right)}{a} \tag{8.31}$$

Periodic solution of the externally excited system correspond to the stationary solutions of Eqs. (8.30) and (8.31), where both a and ψ become constant, that is

$$\frac{da}{dT_1} = 0 \tag{8.32}$$

$$\frac{d\psi}{dT_1} = 0 \tag{8.33}$$

Suppose $\tilde{a}$ and $\tilde{\psi}$ refer to the stationary solution of a and ψ, thus Substituting (8.30) and (8.31), respectively in (8.32) and (8.33), results in

$$\begin{aligned}&\tilde{a} + \tfrac{1}{4}\beta_1\tilde{a}^3 + \tfrac{1}{8}\beta_2\tilde{a}^5 + \tfrac{5}{64}\beta_3\tilde{a}^7 + \tfrac{7}{128}\beta_4\tilde{a}^9 \\ &- k\sin\left(\tilde{\psi}\right) = 0\end{aligned} \tag{8.34a}$$

$$\eta + \frac{k\cos\left(\tilde{\psi}\right)}{\tilde{a}} = 0 \tag{8.34b}$$

Elimination $\tilde{\psi}$ from (8.34a) and (8.34b) leads to the following algebraic equation, which describes the stationary amplitude response of the resonant excited system.

$$\tilde{a}^2 \frac{\delta}{\omega_n^2}^2 + \left(\tilde{a} + 0.25\beta_1\tilde{a}^3 + \frac{1}{8}\beta_2\tilde{a}^5 + \frac{5}{64}\beta_3\tilde{a}^7 + \frac{7}{128}\beta_4\tilde{a}^9\right)^2 = k^2 \tag{8.35}$$

For a given set of excitation amplitude and frequency, the stationary amplitude response of the resonant excited system, i.e. $\tilde{a}$ is computed via Eq. (8.35).

Substituting A from Eq. (8.27) into Eq. (8.22), the following first approximation to the response of the excited system is obtained as

$$u = a\cos\left(\widehat{t} + \phi\left(\widehat{\varepsilon t}\right)\right) + O(\varepsilon) \tag{8.36}$$

The frequency of the above periodic-resonant response of the system is determined as follows.

$$\begin{aligned}\omega = \frac{d}{dt}\left(\widehat{t} + \phi\left(\widehat{\varepsilon t}\right)\right) &= \frac{d}{dt}\left(\omega_n t + \phi\left(\widehat{\varepsilon t}\right)\right) \\ &= \omega_n + \frac{d\phi\left(\widehat{\varepsilon t}\right)}{dt}\end{aligned} \tag{8.37}$$

According to Eqs. (8.29b) and (8.33), $\frac{d\phi}{dT_1}$ is obtained as

$$\frac{d\phi}{dT_1} = \eta = \frac{\delta}{\omega_n} \tag{8.38}$$

where $T_1 = \widehat{\varepsilon t} = \varepsilon\omega_n t$. Thus:

$$\frac{d\phi}{dt} = \varepsilon\delta \tag{8.39}$$

Substituting Eq. (8.39) into Eq. (8.37) leads to the frequency of the resonant response of the system, that is

$$\omega = \omega_n + \varepsilon\delta = \omega_n\lambda = \Omega \tag{8.40}$$

According to Eq. (8.40), the frequency of the response matches the external force's frequency for the periodic resonant excitation.

8.5 Numerical Examples

The system characteristics such as mass, spring stiffness, viscosity, orifice diameter, etc. affect the values of the parameters $\omega_n, \gamma, \varepsilon, \beta_1, \beta_2, \beta_3, \beta_4$ and consequently the approximate analytical response of the resonant excited system via Eq. (8.36) and its stationary amplitude via Eq. (8.35), as well. Table 8.1 exhibits the selected values for several numerical case studies of resonant-excitation with different values of deviation factor δ. According to Table 8.1, the external force's frequency has been selected to be close to the natural frequency of the system for the cases of (1)–(4). While, the deviation of the external force's frequency from the natural frequency of the system is chosen as a large value for the fifth case.

For all cases, $k_s = 1000\frac{N}{m}$, m = 20 Kg, $d = 4$ cm, D = 20 cm, $n = 1$, $s = \frac{1}{2}$, and L = 1 cm have been selected. Using these values, the parameters $\omega_n, \gamma, \beta_1, \beta_2, \beta_3$ and β_4 can be calculated for all cases given in Table 8.1. Those are:

$$\begin{aligned}&\omega_n = 7.071 \text{ rad/s}^{-1}, \gamma = 5, \beta_1 = 208.3, \\ &\beta_2 = 16059, \beta_3 = 542000, \beta_4 = 6782 \times 10^3\end{aligned}$$

For instance, for the fourth case of Table 8.1 with the initial conditions as: $u(0) = 0.002$ m, $\dot{u}(0) = 1.23$ ms^{-1}, $F = 50$N and $\mu = 0.0493$ Pa.s (i.e. $\hbar = 0.0123$ and $\varepsilon = 0.05$) along with $\delta = 2$, the amount of the stationary response amplitude

Table 8.1 The selected values and the affected parameters for the resonant-excitation analysis

		Selected values					Affected parameters				
Case	F (N)	μ (Pa.s)	u_0 (m)	$\dot{u}_0$ (ms^{-1})	δ	ε	$\hbar$	ζ	c_{linear} (Nsm^{-1})	Ω (rad/s^{-1})	$\tilde{a}$ (m)
1	50	0.0493	0.002	1.23	0	0.05	0.0123	0.025	7.08	7.071	0.173
2	50	0.0493	0.002	1.23	1	0.05	0.0123	0.025	7.08	7.121	0.172
3	50	0.49	0.002	0.54	1	0.5	0.59	0.25	71	7.571	0.074
4	50	0.0493	0.002	1.23	2	0.05	0.0123	0.025	7.08	7.170	0.172
5	50	0.0493	0.002	1.35	20	0.05	0.0123	0.025	7.08	8.071	0.168

for the resonant-excited system is computed as $\tilde{a} = 172.88$ mm by solving the algebraic Eq. (8.35). Also, the excitation frequency is computed as $\Omega = \omega_n + \varepsilon\delta = 7.171$ rad/s, and the response of the excited system is obtained by Eq. (8.36) as:

$$u = 172.88\cos(7.171t + 1.56) \text{ mm}$$

The response of the mass-spring system equipped with the traditional linear damper having the same external force and initial conditions is calculated as follows:

$$x = -422\cos(7.171t) + 745\sin(7.171t) + 711e^{-0.177t}\sin(7.07t + 2.50)\,\text{mm}$$

8.6 Results and Discussion

The simulation results for the resonant excitation analysis are shown in Figs. 8.3, 8.4, 8.5, and 8.6. In order to verify the accuracy of the approximate analytical response of the system equipped with the NDD damper, given by Eq. (8.36), the numerical integration technique is also applied to solve Eq. (8.14) using the fourth order Runge Kutta method.

The displacements of the excited system using the NDD damper, for the first four cases presented in Table 8.1 are shown in Fig. 8.3. These results for the system with the linear damper are also depicted in Fig. 8.3. Figure 8.3a shows the comparison between the approximate analytical solution and the numerical result obtained by the Runge Kutta method for the ideal resonant case, i.e. the first case given in Table 8.1 with $F = 50\text{N}, \delta = 0$, (i.e. $\Omega = \omega_n = 7.071$ rad/s) and $\varepsilon = 0.05$. This comparison is carried out for the cases (2)–(4) in Fig. 8.3b–d, respectively. As can be seen the proposed analytical solution is extremely close to the numerical solution for these cases as well as the ideal resonant case, i.e. case (1). As shown in Fig. 8.3a–d, the response of the system using the linear damper considerably grows in each cycle up to an extremely large stationary amplitude at a long time for the cases of (1)–(4). But, in the system with the NDD damper, the amplitude of the vibration tends to its stationary value immediately. Therefore, there is no need to evaluate the second order approximation of u for the governing equation of the system via Eq. (8.14). Besides, as it is observed in Fig. 8.3a–d, for the system employing the NDD damper, the amount of the stationary response amplitude is significantly smaller than its value for the system with linear damper. Hence, utilizing the NDD damper in the excited system under periodic-resonant force has substantial advantage over the linear damper in terms of decreasing the amplitude response of the system.

In order to investigate the effect of increasing the perturbation parameter ε, the results related to the case (2) with $\varepsilon = 0.05$ and case (3) with $\varepsilon = 0.5$ can be evaluated. According to Fig. 8.3b, c, increasing the value of ε causes increasing the error between the approximate analytical solution and the exact numerical solution. This is due to the properties of the multiple scales method, whereas the value of ε must be small. Moreover, in Fig. 8.3c, where the amount of displacement is not considerable as the other cases, the displacements of the systems with the NDD and linear damper are close to each other, because the small amplitude vibration weakens the nonlinearity of Eq. (8.16).

Figure 8.4 exhibits the damping force of the both nonlinear and linear dampers versus displacement for the first four cases of Table 8.1. That is the work done by the damper, i.e. the amount of energy absorbed by the damper. For instance, as can be seen in Fig. 8.4b, for the case (2) with $\delta = 1$, the damping force of the linear damper has the maximum value of 42.3N, whereas, the nonlinear damper provides the larger damping force amount of 114.6N. This explains how the NDD damper outclasses the traditional linear damper in the terms of amplitude reduction.

Figure 8.5 demonstrates the transmitted force to the base versus time for the cases presented in Table 8.1. According to Fig. 8.5, in the system with the linear damper, a larger amount of force is being transmitted to the base compared to

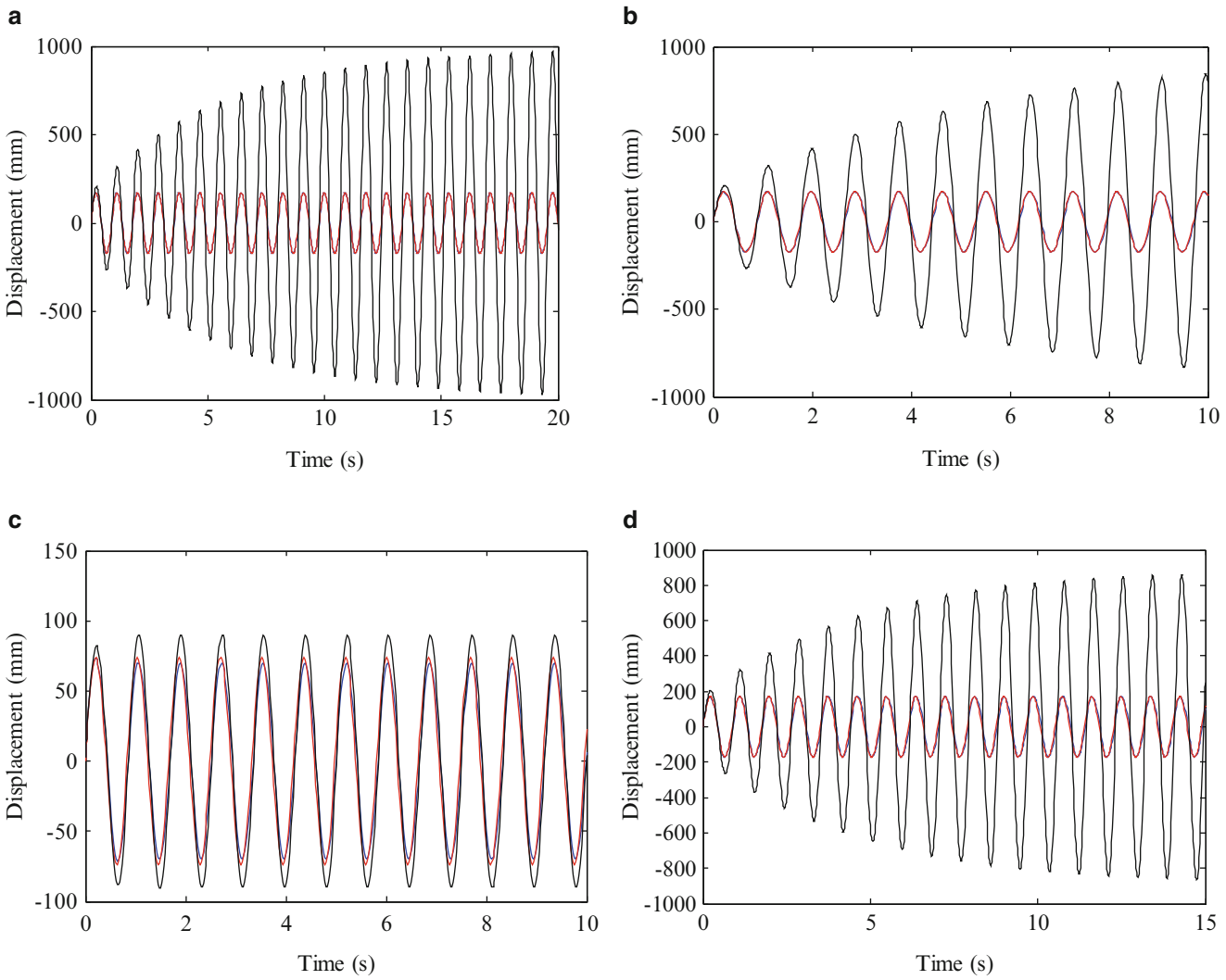

Fig. 8.3 Response of the resonant-excited system with $F = 50N$ for (**a**) $\varepsilon = 0.05$ and $\delta = 0$ (**b**) $\varepsilon = 0.05$ and $\delta = 1$ (**c**) $\varepsilon = 0.5$ and $\delta = 1$ (**d**) $\varepsilon = 0.05$ and $\delta = 2$: (*red line*) approximate analytical solution of the system with the NDD damper; (*blue line*) numerical solution of the system with the NDD damper; (*dark line*) analytical solution of the system with the linear damper

the system using the NDD damper. In the system with the linear damper; not only an undesired significant higher force is transmitted to the base but also the traditional damper is unable to provide the system with the effective amplitude reduction compared to the NDD damper.

In Fig. 8.6 the damping force versus time is shown for the first four cases given in Table 8.1. It is observed that the NDD damper provides a higher damping force and keeps the amplitude far more limited than the traditional damper while the system is excited with a resonant force. In addition, it is worthwhile to note that in Fig. 8.6c, in which the vibration amplitude is small compared to the other cases, the damping force of the NDD damper gets close to the linear damper. This is due to the fact that small amplitudes weaken of the higher powers of u in Eq. (8.6). Therefore, the damping coefficient of the NDD damper gets closer to the linear damper for the small displacements.

To study the effect of increasing the deviation factor δ, the displacement of the excited system for the case (5) where $\delta = 20$ is presented in Fig. 8.7. Figure 8.7 confirms that as the value of δ rises, the error between the approximate analytical solution given by Eq. (8.36) and the exact numerical solution increases. This is due to the fact that the scheme is elaborated for the resonant analysis, in which the value of δ is small.

As expected, when the external force's frequency gets close to the natural frequency of the system, i.e. $\delta \to 0$, the resonant excitation is more severe and consequently results in vibration with higher amplitude. On the contrary, increasing the difference between the external force's frequency and the natural frequency of the system causes decreasing the stationary

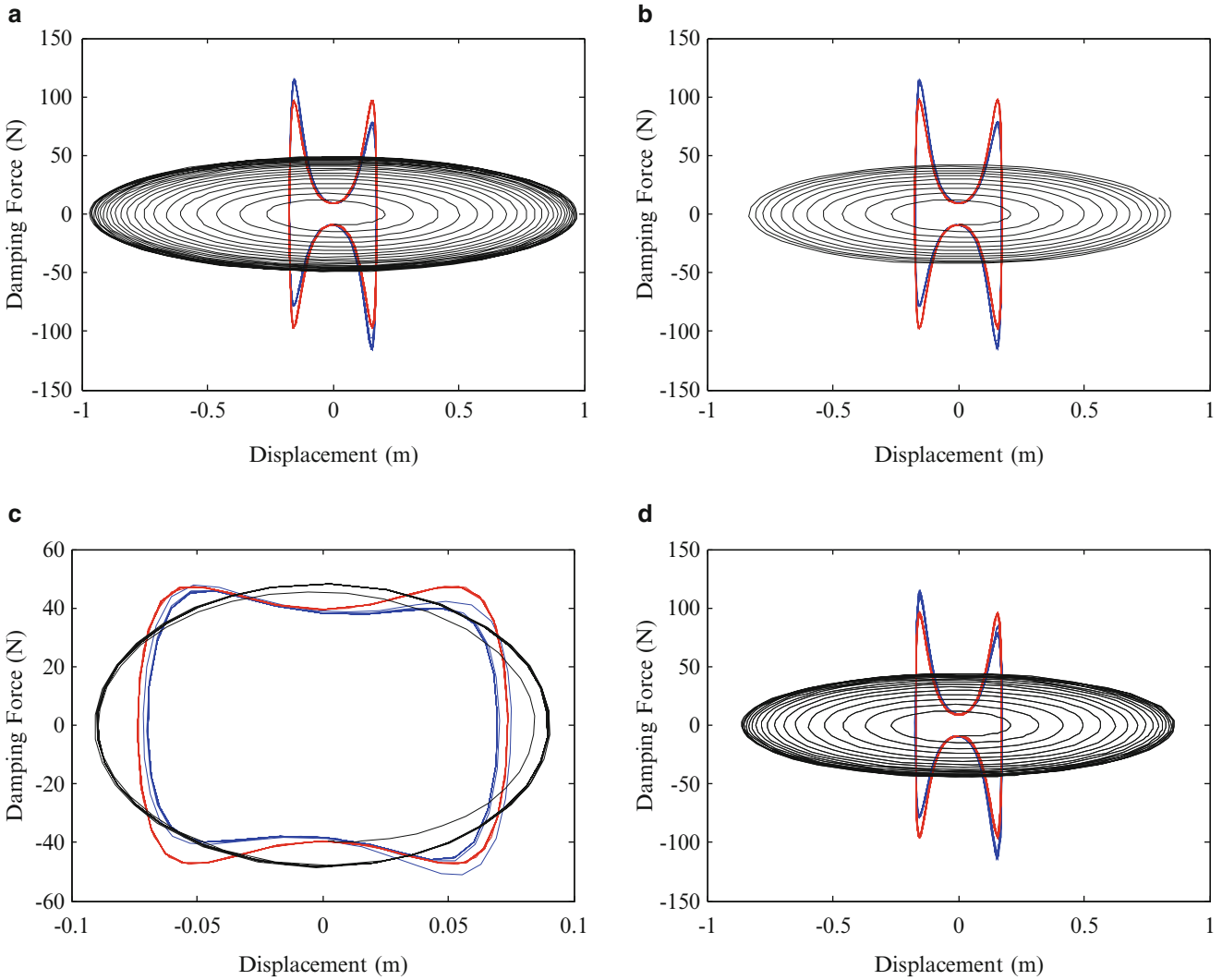

Fig. 8.4 Damping force versus displacement of the resonant-excited system with $F = 50N$ for (**a**) $\varepsilon = 0.05$ and $\delta = 0$ (**b**) $\varepsilon = 0.05$ and $\delta = 1$ (**c**) $\varepsilon = 0.5$ and $\delta = 1$ (**d**) $\varepsilon = 0.05$ and $\delta = 2$: (*red line*) damping force of the NDD damper obtained by the MSM; (*blue line*) damping force of the NDD damper obtained by the Runge–Kutta method; (*dark line*) damping force of the linear damper

amplitude response of the excited system. For the case (5) with $\delta = 20$, the response of the system with the NDD damper reaches its stationary amplitude of 168 mm, which is smaller than the stationary amplitude of the case (1) with $\delta = 0$ and case (2) with $\delta = 1$.

8.7 Conclusion

The resonant vibration analysis of a mass-spring system equipped with the nonlinear displacement-dependent (NDD) damper was studied in this paper. The governing equation of the excited system was derived for the external force with a frequency closed to the natural frequency of the system. To obtain the forced-resonant response of the system, the approximate analytical solution algorithm was developed by the multiple scales method (MSM). The advised solution algorithm was performed for several case studies with various amounts of external force's frequencies and also verified by the numerical fourth-order Runge–Kutta method. It is found that the proposed analytical solution algorithm is able to achieve the satisfactory performance for the resonant excitation analysis. In contrast to the system with the linear damper, in which the response considerably grows in each cycle up to extremely large stationary amplitude at a long time; in the system employing the NDD damper, the amplitude of the vibration tends to its stationary value immediately. Moreover, the results

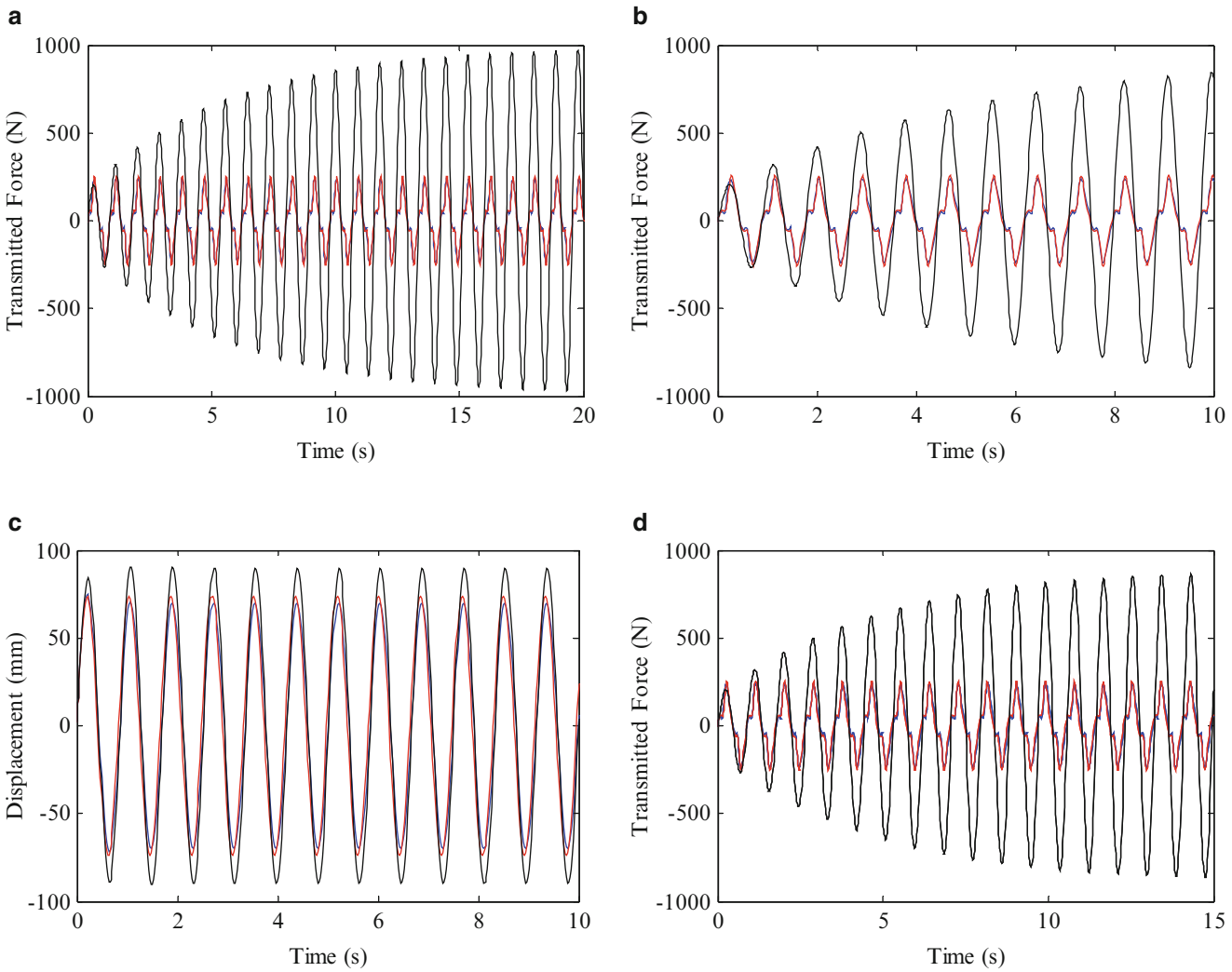

Fig. 8.5 Comparison between the transmitted force by the system in a linear system and nonlinear system with NDD damper with resonant external force as $F = 50N$ for (**a**) $\varepsilon = 0.05$ and $\delta = 0$ (**b**) $\varepsilon = 0.05$ and $\delta = 1$ (**c**) $\varepsilon = 0.5$ and $\delta = 1$ (**d**) $\varepsilon = 0.05$ and $\delta = 2$: (*red line*) approximate analytical solution of the system with the NDD damper; (*blue line*) numerical solution of the system with the NDD damper; (*dark line*) analytical solution of the system with the linear damper

confirm that utilizing the NDD damper in the resonant-excited system not only causes more vibration amplitude reduction rather than the traditional linear damper but also provides the lower force transmitted to the base compared to the linear damper, where an undesired significant higher transmitted force is produced.

A.1 Appendix

$$\begin{aligned}
\alpha_1 &= \left(\gamma^4 - 2\gamma^2 + 1\right)\lambda \\
\alpha_2 &= \left(4\gamma^4 - 4\gamma^2\right)\lambda\beta \\
\alpha_3 &= \left(6\gamma^4 - 2\gamma^2\right)\lambda\beta^2 \\
\alpha_4 &= \left(4\gamma^4\right)\lambda\beta^3 \\
\alpha_5 &= \left(\gamma^4\right)\lambda\beta^4
\end{aligned} \tag{8.41}$$

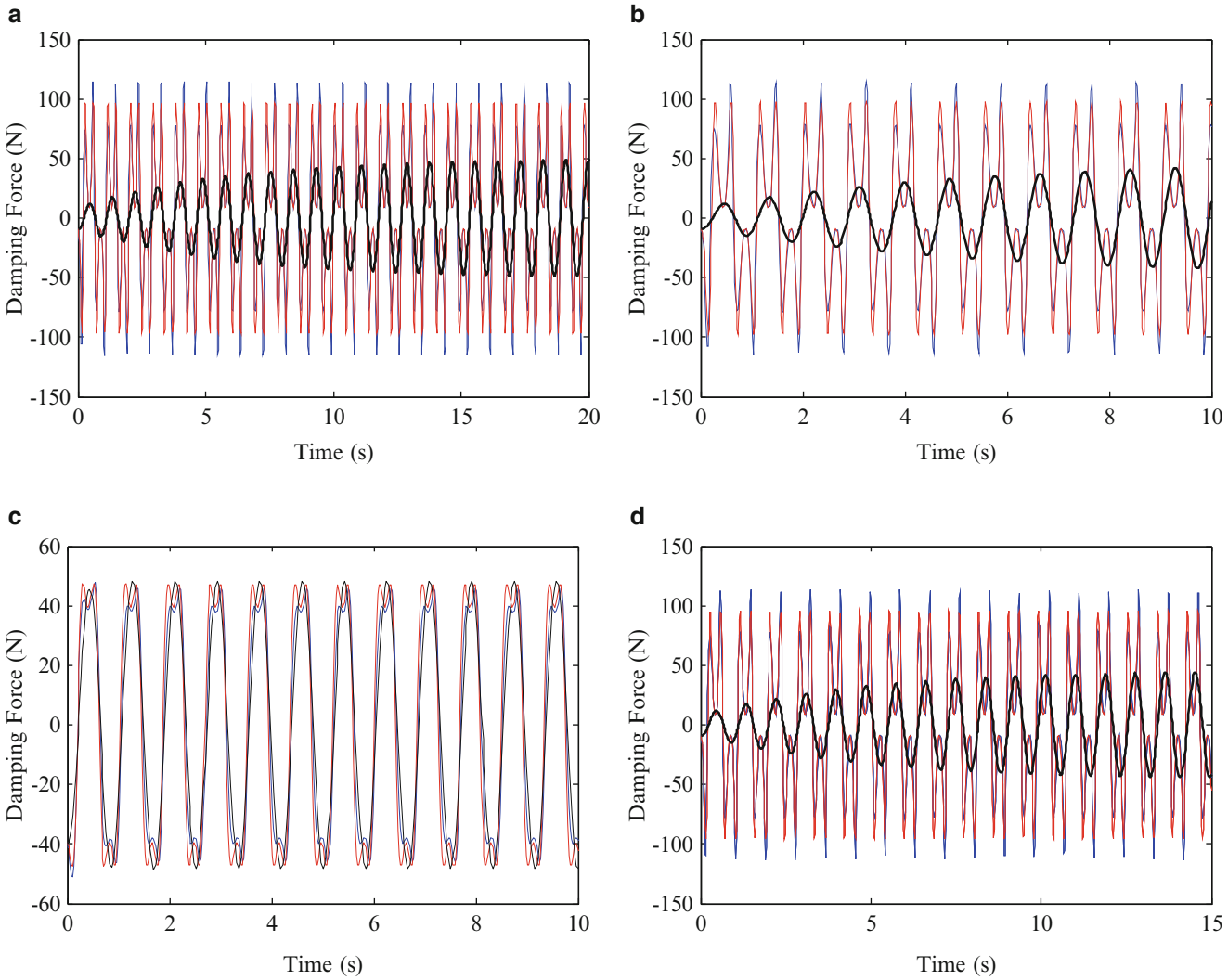

Fig. 8.6 Damping force of the resonant-excited system versus time with $F = 50N$ for (**a**) $\varepsilon = 0.05$ and $\delta = 0$ (**b**) $\varepsilon = 0.05$ and $\delta = 1$ (**c**) $\varepsilon = 0.5$ and $\delta = 1$ (**d**) $\varepsilon = 0.05$ and $\delta = 2$: (*red line*) damping force of the NDD damper obtained by the MSM; (*blue line*) damping force of the NDD damper obtained by the Runge–Kutta method; (*dark line*) damping force of the linear damper

$$\begin{aligned} A_2 &= \frac{\frac{F}{k_s}}{\sqrt{\left(1-\left(\frac{\Omega}{\omega_n}\right)^2\right)^2+\left(2\zeta\frac{\Omega}{\omega_n}\right)^2}} \\ \varphi &= \tan^{-1}\left(\frac{2\zeta\frac{\Omega}{\omega_n}}{1-\left(\frac{\Omega}{\omega_n}\right)^2}\right) \end{aligned} \tag{8.42}$$

$$\begin{aligned} \beta_1 &= \frac{(4\gamma^4-4\gamma^2)\beta}{(\gamma^4-2\gamma^2+1)} \\ \beta_2 &= \frac{(6\gamma^4-2\gamma^2)\beta^2}{(\gamma^4-2\gamma^2+1)} \\ \beta_3 &= \frac{4\gamma^4\beta^3}{(\gamma^4-2\gamma^2+1)} \\ \beta_4 &= \frac{\gamma^4\beta^4}{(\gamma^4-2\gamma^2+1)} \end{aligned} \tag{8.43}$$

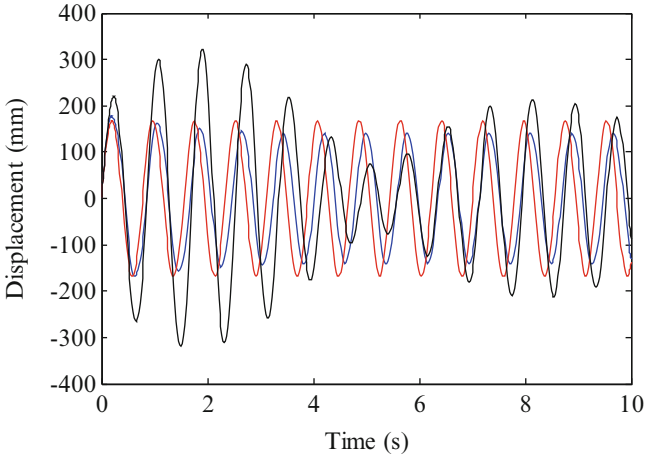

Fig. 8.7 Response of the system to the non-resonant excitation with $F = 50$ N for $\varepsilon = 0.05$ and $\delta = 20$: (*red line*) approximate analytical solution of the system with the NDD damper; (*blue line*) numerical solution of the system with the NDD damper; (*dark line*) analytical solution of the system with the linear damper

$$\begin{aligned}
\Delta_3 &= \beta_1 A^3 + 3\beta_2 A^4 \overline{A} + 28\beta_4 A^6 \overline{A}^3 + 9\beta_3 A^5 \overline{A}^2 \\
\Delta_5 &= \beta_2 A^5 + 5\beta_3 A^6 \overline{A} + 20\beta_4 A^7 \overline{A}^2 \\
\Delta_7 &= \beta_3 A^7 + 7\beta_4 A^8 \overline{A} \\
\Delta_9 &= \beta_4 A^9
\end{aligned} \tag{8.44}$$

References

1. De Silva, C.W.: Vibration: Fundamentals and Practice, 2nd edn. CRC Press, Boca Raton (2006)
2. Rao, S.S.: Mechanical Vibrations, 4th edn. Prentice-Hall, Englewood Cliffs (2004)
3. Tomson, W.T., Diloon, D.M.: Theory of Vibration with Applications, 5th edn. Nelson Thornes Ltd, Cheltenham (1998)
4. Jang, H.K.: Design guideline for the improvement of dynamic comfort of a vehicle seat and its application. Int. J. Automot. Technol. **6**, 383–390 (2005)
5. Yang, B.S., Choi, S.P., Kim, Y.C.: Vibration reduction optimum design of a steam-turbine rotor-bearing system using a hybrid genetic algorithm. Struct. Multidiscip. Optim. **30**, 43–53 (2005)
6. Asl, M.E., et al.: Predicting the vibration response in subcomponent testing of wind turbine blades. In: Allemang, R. (ed) Special Topics in Structural Dynamics, vol. 6, pp. 115–123. Springer International Publishing (2015)
7. Gibanica, M., et al.: Spread in modal data obtained from wind turbine blade testing. In: Mayes, R., Rixen, D., Allen, M. (eds.) Topics in Experimental Dynamic Substructuring, vol. 2, pp. 207–215. Springer, New York (2014)
8. Museros, P., Alarcon, E.: Influence of the second bending mode on the response of high-speed bridges at resonance. J. Struct. Eng. **131**, 405–415 (2005)
9. Jalili, N., Knowles, D.W.: Structural vibration control using an active resonator absorber: modeling and control implementation. Smart Mater. Struct. **13**, 998–1005 (2004)
10. Ilbeigi, S., Chelidze, D.: Model order reduction of nonlinear Euler-Bernoulli beam. In: Nonlinear Dynamics, vol. 1, pp. 377–385. Springer International Publishing (2016)
11. Nasiri, N., Ilbeigi, S., Nazari, F., Asmar, B., Karimi, M., Baghalian, S.: Comparison of radial basis function and back-error propagation neural networks for crack detection in variable cross-section beams (2012)
12. Kazemi, M.A., et al.: Detection of multiple cracks in beams using particle swarm optimization and artificial neural network. In: 4th International Conference on Modeling, Simulation and Applied Optimization (ICMSAO). IEEE (2011)
13. Abolbashari, M.H., Nazari, F.: A multi-crack effects analysis and crack identification in functionally graded beams using particle swarm optimization algorithm and artificial neural network. Struct. Eng. Mech. **51**, 299 (2014)
14. Aminpour, H., Nazari, F., Baghalian, S.: Applying artificial neural network and wavelet analysis for multiple cracks identification in beams. Int. J. Veh. Noise Vib. **8**(1), 51–59 (2012)
15. Nazari, F., Abolbashari, M.H., Hosseini, S.M.: Three dimensional natural frequency analysis of sandwich plates with functionally graded core using hybrid meshless local Petrov-Galerkin method and artificial neural network. Comput. Model. Eng. Sci. **105**(4), 271–299 (2015)
16. Nazari, F., Abolbashari, M.H.: Double cracks identification in functionally graded beams using artificial neural network. J. Solid Mech. **5**(1), 14–21 (2013)

17. Shobeiri, V.: Topology optimization using bi-directional evolutionary structural optimization based on the element-free Galerkin method. Eng. Optim. **48**(3), 380–396 (2016)
18. Karimi, M., Jahanpour, J., Ilbeigi, S.: A novel scheme for flexible NURBS-based C2 PH Spline Curve contour following task using Neural Network. Int. J. Precis. Eng. Manuf. **15**(12), 2659–2672 (2014)
19. Love, J.S., Tait, M.J.: Non-linear multimodal model for tuned liquid dampers of arbitrary tank geometry. Int. J. Non-Linear Mech. **46**, 1065–1075 (2011)
20. Afsharfard, A., Farshidianfar, A.: Design of nonlinear impact dampers based on acoustic and damping behavior. Int. J. Mech. Sci. **65**(1), 125–133 (2012)
21. Butcher, E.A.: Clearance effects on bilinear normal mode frequencies. J. Sound Vib. **224**, 305–328 (1999)
22. Metallidis, P., Natsiavas, S.: Vibration of a continuous system with clearance and motion constraints. Int. J. Non-Linear Mech. **35**, 675–690 (2000)
23. Pun, D., Lau, S.L., Liu, Y.B.: Internal resonance of an L-shaped beam with a limit stop I, free vibration. J. Sound Vib. **193**, 1023–1035 (1996)
24. Pun, D., Lau, S.L., Liu, Y.B.: Internal resonance of an L-shaped beam with a limit stop II, forced vibration. J. Sound Vib. **193**, 1037–1047 (1996)
25. Moradi, H., Vossoughi, G., Movahhedy, M.R., Ahmadian, M.T.: Forced vibration analysis of the milling process with structural nonlinearity, internal resonance, tool wear and process damping effects. Int. J. Non-Linear Mech. **54**, 22–34 (2013)
26. Perepelkin, N.V., Mikhlin, Y.V., Pierre, C.: Non-linear normal forced vibration modes in systems with internal resonance. Int. J. Non-Linear Mech. **57**, 102–115 (2013)
27. Ilbeigi, S., Jahanpour, J., Farshidianfar, A.: A novel scheme for nonlinear displacement-dependent dampers. Nonlinear Dyn. **70**, 421–434 (2012)
28. Dixon, J.C.: The Shock Absorber Handbook, 2nd edn. Wiley, Chichester (2007)
29. Eslaminasab, N.: Development of a semi-active intelligent suspension system for heavy vehicles. Ph.D. Thesis, University of Waterloo, Canada (2008)
30. Zhou, N., Liu, K.: A tunable high-static-low-dynamic stiffness vibration isolator. J. Sound Vib. **329**, 1254–1273 (2010)
31. Wang, W.L., Xu, G.X.: Fluid formulae for damping changeability conceptual design of railway semi-active hydraulic dampers. Int. J. Non-Linear Mech. **44**, 809–819 (2009)
32. Dong, X.-M., Yu, M., Liao, C.-R., Chen, W.-M.: Comparative research on semi-active control strategies for magnet-rheological suspension. Nonlinear Dyn. **59**(433–453) (2010)
33. Song, X., Ahmadian, M.: characterization of semi-active control system dynamics with magneto-rheological suspensions. J. Vib. Control **16**(10), 1439–1463 (2010)
34. Go, C.-G., Sui, H., Shih, M.-h, Sung, W-P.: A linearization model for the displacement dependent semi-active hydraulic damper. J.Vib. Control **16**(14), 219–2214 (2010)
35. Preumont, A.: Vibration Control of Active Structures. Kluwer Academic Publishers, Dordrecht. EBook ISBN: 0-306-48422-6 (2002)
36. Crosby, M.J., Karnopp, D.C.: The active damper—a new concept for shock and vibration control. Shock Vib. Bull. **43**(4), 119–133 (1973)
37. Ahmadian, M.: On the isolation properties of semiactive dampers. J. Vib. Control **5**(2), 217–232 (1999)
38. Simon, D.E.: Experimental evaluation of semiactive magneto-rheological primary suspensions for heavy truck applications. Ph.D. Thesis, Virginia Tech (2000)
39. Venkatesan, C., Krishnan, R.: Harmonic response of a shock mount employing dual-phase damping. J. Sound Vib. **40**(3), 409–413 (1975)
40. Jackson, G.W.: Fundamentals of the Direct Acting Shock Absorber. SAE paper 37R, National Passenger Car Body and Materials Meeting, Detroit, (1959)
41. Puydak, R.C., Auda, R.S.: Designing to achieve optimum dynamic properties in elastomeric cab and body mounts. SAE 660439 (and SAE Transactions V75), (1966)
42. Lewitske, C., Lee, P.: Application of elastomeric components for noise and vibration isolation in the automotive industry. SAE Paper 2001-01-1447 (2001)
43. Fukushima, N., Hidaka, K., Iwata, K.: Optimum characteristics of automotive shock absorbers under various driving conditions and road surfaces. JSAE Rev. 62–69 (1983)
44. Young, D.W.: Aircraft Landing Gears. Proc. I. Mech. E. **200**(D2), 75–92 (1986)
45. Etman, L.F.P., Vermeulen, R.C.N., Van Heck, J.G.A.M., Schoofs, A.J.G., Van Campen, D.H.: Design of a stroke dependent damper for the front axle suspension of a truck using multibody system dynamics and numerical optimization. Veh. Syst. Dyn. **38**, 85–101 (2002)
46. Komamura, S., Mizumukai, K.: History of shock absorbers. Automob. Technol. **41**(1), 126–131 (1987) (in Chinese)
47. Lee, C.-T., Moon, B.-Y.: Study on the damping performance characteristics analysis of shock absorber of vehicle by considering fluid force. J. Mech. Sci. Technol. **19**(2), 520–528 (2005)
48. Lee, C.-T., Moon, B.-Y.: Simulation and experimental validation of vehicle dynamic characteristics for displacement-sensitive shock absorber using fluid-flow modeling. Mech. Syst. Sig. Process. **20**, 373–388 (2006)
49. Hundal, M.S.: Impact absorber with two-stage variable area orifice hydraulic damper. J. Sound Vib. **50**(2), 195–202 (1977)
50. Haque, M.M., Ahmed, A.K.W., Sankar, S.: Simulation of displacement sensitive non-linear dampers via integral formulation of damping force characterization. J. Sound Vib. **187**, 95–109 (1995)
51. Farjoud, A., Ahmiadian, M., Craft, M., Burke, W.: Nonlinear modeling and experimental characterization of hydraulic dampers: effects of shim stack and orifice parameters on damper performance. Nonlinear Dyn. **67**(2), 1437–1456 (2012)
52. Guo, P.F., Lang, Z.Q., Peng, Z.K.: Analysis and design of the force and displacement transmissibility of nonlinear viscous damper based vibration isolation systems. Nonlinear Dyn. **67**(4), 2671–2687 (2012)
53. Peng, Z.K., Lang, Z.Q., Billings, S.A.: Resonance and resonant frequencies for a class of nonlinear systems. J. Sound Vib. **300**, 993–1014 (2007)
54. Asfar, K.R., Masoud, K.K.: Damping of parametrically excited single-degree-of-freedom systems. Int. J. Non-Linear Mech. **29**, 421–428 (1994)

55. Bugra, H., Ertas, B.H., Luo, H.: Nonlinear dynamic characterization of oil-free Wire mesh dampers. Gas Turbines Power **130**(3), 032503 (2008)
56. Main, J.A., Jones, N.P.: Analysis and design of linear and nonlinear dampers for stay cables. In: Proceedings Fourth International Symposium on Cable Dynamics, Montreal, Canada, AIM, 2001
57. Diotallevi, P.P., Landi, L., Dellavalle, A.: Simplified design methodology for systems equipped with non-linear viscous dampers. In: The 14th World Conference on Earthquake Engineering, Beijing, China, 2008
58. Ilbeigi, S., Jahanpour, J., Farshidianfar, A.: Forced vibration analysis of a system equipped with the nonlinear displacement-dependent (NDD) damper. Article in press in Scientia Iranica, Int. J. Sci. Technol.
59. Nayfeh, A.H., Mook, D.T.: Nonlinear Oscillations. Wiley, New York (1979)
60. Nayfeh, A.H.: Perturbation Methods. Wiley, New York (1973)
61. Alijania, F., Amabilib, M., Bakhtiari-Nejada, F.: On the accuracy of the multiple scales method for non-linear vibrations of doubly curved shallow shells. Int. J. Non-Linear Mech. **46**, 170–179 (2011)

Chapter 9
Performance Comparison Between a Nonlinear Energy Sink and a Linear Tuned Vibration Absorber for Broadband Control

Etienne Gourc, Lamberto Dell Elce, Gaetan Kerschen, Guilhem Michon, Gwenaelle Aridon, and Aurelien Hot

Abstract The performance of a linear tuned vibration absorber (LTVA) and a nonlinear energy sink (NES) for the vibration mitigation of an uncertain linear primary system is investigated. An analytic tuning rule for the LTVA when the primary system contains uncertainty is derived. The behavior of the linear system coupled to the NES is analyzed theoretically. A tuning methodology for the NES in the deterministic as well as for the uncertain case is presented.

Keywords NES • LTVA • Broadband • Uncertainties • Equal-peaks

9.1 Introduction

Mitigation of resonant vibrations of a linear system is a widely encountered problem in engineering [8]. In the early 1900, Frahm proposed the use of linear resonator to reduce the amplitude of the oscillations around the resonance of a primary system [3]. This problem was later formalized by Den Hartog [2] who developed a tuning procedure based on invariant points to find appropriate stiffness and damping of the absorber.

A recent trend in the literature is to exploit and take advantage of nonlinear phenomena for vibration mitigation and energy harvesting [7, 11, 12, 19]. Among them, the nonlinear energy sink (NES), which consists of an absorber with essential nonlinearity, received particular attention. It was shown that a NES can lead to targeted energy transfer, which is an irreversible channelling of vibrational energy from the host structure to the absorber [5, 17]. Such an appealing feature makes the NES a suitable candidate for vibration isolation. However, due to the nonlinearity, it can also exhibit classic nonlinear behavior such as jumps or sensitivity to motion amplitude and therefore, it must be carefully designed.

Passive control of resonance using a NES was analyzed both theoretically [15, 16] and experimentally [6]. In addition to periodic response, systems with NES were shown to exhibit relaxation oscillations. The performance comparison between a linear absorber and a NES for the vibration mitigation of a linear system was addressed in [14]. However, in this study, both absorbers are constrained to have the same damping and the presence of detached resonance curve was not taken into account. In [13], a linear flexible beam with an embedded NES/linear absorber was investigated, but no proper design procedure was proposed, which makes difficult the comparison of both solutions.

The present work aims at giving an objective comparison between a NES and a linear absorber for passively controlling the resonance of a linear primary system. Two case studies are considered: first, the primary system is assumed to be deterministic; second, the stiffness of the primary system is assumed to be a random variable. In other words, the first case corresponds to the nominal case whereas in the second case, the stiffness of the primary system can vary to take into account model uncertainties or ageing effects.

E. Gourc (✉) • L.D. Elce
Space Structure and Systems Laboratory (S3L), University of Liège, Liège, Belgium
e-mail: etienne.gourc@ulg.ac.be

G. Kerschen
University of Liege in Belgium Liege, Belgium

G. Michon
Institut Clément Ader (ICA), ISAE, University of Toulouse, Toulouse, France

G. Aridon
Airbus Defence and Space, Toulouse Cedex 4, France

A. Hot
Centre National d'Etudes Spaciales, Paris Cedex 01, France

G. Kerschen (ed.), *Nonlinear Dynamics, Volume 1*, Conference Proceedings of the Society for Experimental Mechanics Series,
DOI 10.1007/978-3-319-29739-2_9

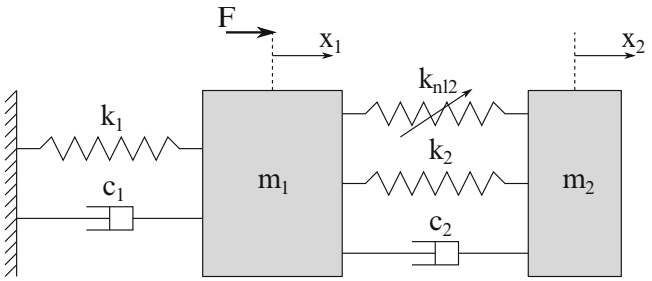

Fig. 9.1 Linear oscillator coupled to a nonlinear vibration absorber

The paper is organized as follows. In Sect. 9.2, a general model encompassing both linear and nonlinear absorber is presented. In Sect. 9.3, a tuning procedure for the linear absorber in the case of an uncertain primary system is presented. In Sect. 9.4, the theoretical treatment of the system coupled with the NES is presented. In Sect. 9.5, a tuning procedure for the NES in both the deterministic and uncertain case is discussed. In Sect. 9.6, the performance of the linear absorber and the NES for vibration mitigation are compared. Finally, conclusions are drawn.

9.2 Description of the Model

A schematic of the studied system is depicted in Fig. 9.1. m_j, k_j, c_j and x_j ($j = 1, 2$) are the mass, stiffness, damping and absolute displacement of the primary system and the absorber, respectively. F denotes the forcing amplitude and k_{nl2} the nonlinear stiffness of the absorber. The equations of motion of the corresponding system are

$$\begin{aligned} m_1\ddot{x}_1 + c_1\dot{x}_1 + k_1x_1 + c_2(\dot{x}_1 - \dot{x}_2) + k_2(x_1 - x_2) + k_{nl2}(x_1 - x_2)^3 &= F\cos\Omega t \\ m_2\ddot{x}_2 + c_2(\dot{x}_2 - \dot{x}_1) + k_2(x_2 - x_1) + k_{nl2}(x_2 - x_1)^3 &= 0 \end{aligned} \tag{9.1}$$

where the dots represent the differentiation with respect to the time t and Ω is the pulsation of harmonic excitation. In order to take into account an uncertainty of the primary system, the linear stiffness is expressed as $k_1 = k_{10} + k_{11}$, where k_{10} is the nominal stiffness and k_{11} ($|k_{11}| < k_{10}$) a random variable.

The configuration of the primary system coupled either to the LTVA or the NES is obtained by setting k_{nl2} or k_2 to zero in Eq. (9.1), respectively. Introducing non-dimensional time $\tilde{t} = \omega_1 t$, the equations of motion are recast into

$$\begin{aligned} x_1'' + 2\xi_1x_1' + (1+\delta)x_1 + \epsilon\lambda(x_1' - x_2') + \epsilon\rho^2(x_1 - x_2) + \epsilon K(x_1 - x_2)^3 &= G\cos\tilde{\Omega}\tilde{t} \\ x_2'' + \lambda(x_1' - x_2') + \rho^2(x_1 - x_2) + K(x_1 - x_2)^3 &= 0 \end{aligned} \tag{9.2}$$

here, primes denote differentiation with respect to the non-dimensional time $\tilde{t}$ and

$$\epsilon = \frac{m_2}{m_1}, \quad \omega_{1i} = \sqrt{\frac{k_{1i}}{m_1}}, \quad \xi_1 = \frac{c_1}{2m_1\omega_{10}}, \quad \tilde{\Omega} = \frac{\Omega}{\omega_{10}}, \quad \lambda = \frac{c_2}{m_2\omega_{10}},$$
$$\rho = \sqrt{\frac{k_2}{m_2\omega_{10}^2}}, \quad K = \frac{k_{nl2}}{m_2\omega_{10}^2}, \quad G = \frac{F}{m_1\omega_{10}^2}, \quad \delta = \frac{k_{11}}{k_{10}}$$

9.3 Linear Tuned Vibration Absorber

In this section the linear primary system coupled to a linear tuned vibration absorber (LTVA) is analyzed. The equation of motion of the primary system coupled to a LTVA is simply obtained by letting $K = 0$ in Eq. (9.2).

9.3.1 Deterministic Primary System

First, we deal with the case of deterministic primary system, thus imposing $\delta = 0$ in Eq. (9.2). Den Hartog showed that the FRF of the primary mass has two invariant fixed points which are independent of the absorber damping λ [2]. He proposed to adjust the stiffness of the absorber so that these two invariant points have equal heights in the FRF. The damping of the absorber is then determined so that the FRF presents an horizontal tangent through one of the fixed points. An approximate value of the optimal damping is obtained by taking an average value that leads to the horizontal tangent to both fixed points. This method is the so-called equal-peak method. Quite surprisingly, it is only recently that an exact closed-form formula for this classical problem has been found by Asami and Nishihara [1]

$$\begin{aligned} \rho_{opt} &= \frac{2}{1+\epsilon}\sqrt{\frac{2\left[16+23\epsilon+9\epsilon^2+2\left(2+\epsilon\right)\sqrt{4+3\epsilon}\right]}{3\left(64+80\epsilon+27\epsilon^2\right)}} \\ \lambda_{opt} &= \frac{\rho_{opt}}{2}\sqrt{\frac{8+9\epsilon-4\sqrt{4+3\epsilon}}{1+\epsilon}} \end{aligned} \tag{9.3}$$

9.3.2 Uncertain Primary System

In this section, the tuning of the LTVA for the case of an uncertain primary system is addressed. The problem is formulated as follows

$$[\rho_{opt}, \lambda_{opt}] = \arg\left[\min_{\rho,\lambda}\left(\max_{\delta\in I_\delta}|H|_\infty(\rho,\lambda,\delta,\epsilon,\xi_1)\right)\right] \tag{9.4}$$

By solving numerically problem (9.4), we observed that the solution is such that

$$|H|_\infty(\rho_{opt}, \lambda_{opt}, \delta_{min}) = |H|_\infty(\rho_{opt}, \lambda_{opt}, \delta_{max}) \tag{9.5}$$

Therefore, in the uncertain case, the optimal tuning of the absorber is obtained when the FRF of the system at the uncertainty bounds has equal peaks. Based on this observation, we express an analytic tuning rule for the LTVA in the uncertain case. Neglecting the damping of the primary system to simplify the calculation (i.e. $\xi_1 = 0$), the normalized steady state amplitude of the primary mass is given by

$$H^2 = \left|\frac{X1}{G}\right|^2 = \frac{\Omega^2\lambda^2 + \left(\Omega^2-\rho^2\right)^2}{\Omega^2\lambda^2\left(\Omega^2\left(1+\epsilon\right)-\delta-1\right)^2 + \left(\Omega^4-\Omega^2\left(\rho^2\left(1+\epsilon\right)+\delta+1\right)+\rho^2\left(\delta+1\right)\right)^2} \tag{9.6}$$

Using the optimal values for the tuning of the LTVA in the nominal case given in Eq. (9.3), Fig. 9.2 shows the FRF of the primary system for different values of λ. Black and gray lines correspond to $\delta = \mp 0.15$, respectively. Solid lines correspond to $\lambda = \lambda_{opt}$ from Eq. (9.3) and dash-dotted and dashed lines correspond to $\lambda = \lambda_{opt} \pm 50\%$. P_j, Q_j $(j = 1, 2)$ indicates the invariant fixed points. Using the classical equal-peaks methodology, the FRF of the primary system (9.6) is rewritten as follows

$$H^2 = \frac{A\lambda^2 + B}{C\lambda^2 + D} \tag{9.7}$$

where A, B, C, D are simply identified from Eq. (9.6). The above expression is independent of damping if $A/C = B/D$. Substituting the expressions of A, B, C, D into this relation and solving for Ω gives

$$\Omega_{Pj,Qj} = \sqrt{\frac{\rho^2\left(1+\epsilon\right)+\delta_j+1 \mp \sqrt{\rho^4\left(1+\epsilon\right)^2 - 2\rho^2\left(1+\delta_j\right)+\left(1+\delta_j\right)^2}}{\epsilon+2}}, \quad j = 1, 2 \tag{9.8}$$

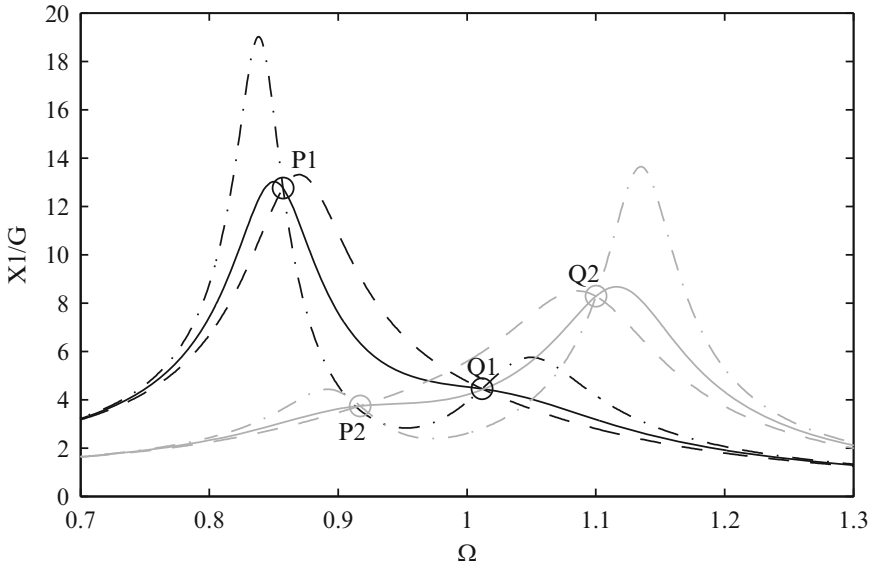

Fig. 9.2 FRF of the primary system coupled to the LTVA for different value of λ

where the subscript $j = 1, 2$ refer to the lower and upper bound of δ, respectively. Equation (9.8) defines the abscissa of the invariant fixed points.

The ordinates of points P_j and Q_j can be found by letting $\lambda \to \infty$ in Eq. (9.7)

$$H(\Omega_{Pj,Qj}) = \frac{1}{\Omega^2_{Pj,Qj}(1+\epsilon) - 1 - \delta_j} \tag{9.9}$$

The optimum value of ρ is obtained by requiring $H(\Omega_{P1}) = H(\Omega_{Q2})$. Substituting Eq. (9.8) into Eq. (9.9) and solving for ρ yields a complicated expression. This expression can be greatly simplified when considering symmetric bound, i.e. $|\delta_1| = |\delta_2|$. In this case, the optimal value of ρ is expressed by

$$\rho_{opt} = \frac{\sqrt{1 - |\delta_1|\sqrt{|\delta_1|^2(1+\epsilon)^2 + \epsilon(\epsilon+2)}}}{(1+\epsilon)\sqrt{1+|\delta_1|^2}} \tag{9.10}$$

Following Den Hartog approach, we impose an horizontal tangent successively at points $P1$ and $Q2$. Differentiating Eq. (9.7) with respect to Ω gives

$$\frac{dH^2}{d\Omega} = \alpha_1\lambda^4 + \alpha_2\lambda^2 + \alpha_3 = 0 \tag{9.11}$$

where

$$\begin{aligned}
\alpha_1 &= -2\Omega^4(\epsilon+1)\left(\Omega^2(\epsilon+1) - \delta - 1\right)\\
\alpha_2 &= -4\Omega^2\rho^4(\epsilon+1)\left(\Omega^2(\epsilon+1) - \delta - 1\right)\\
&\quad +2\Omega^4\rho^2\left(2\Omega^2\left(\epsilon^2+3\epsilon+2\right) - (3\epsilon+4)(1+\delta)\right)\\
&\quad -\Omega^6\left(\Omega^2\left(\epsilon^2+2\epsilon+4\right) - 4(1+\delta)\right)\\
\alpha_3 &= -2\left(\Omega^2-\rho^2\right)\left(\Omega^4+\rho^4(\epsilon+1) - 2\Omega^2\rho^2\right)\left(\Omega^4 - \Omega^2\left(\rho^2(\epsilon+1)+\delta+1\right)\right.\\
&\quad \left.+\rho^2(1+\delta)\right)
\end{aligned}$$

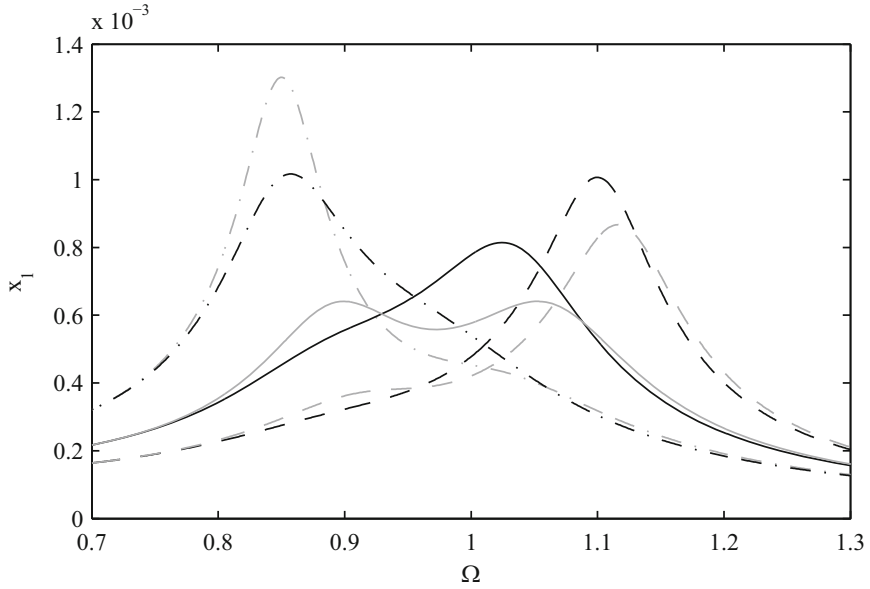

Fig. 9.3 Comparison of the FRF of the LTVA for the nominal tuning and robust tuning for $\epsilon = 0.05$, $\delta = \pm 0.15$

Substituting $\Omega = \Omega_{P1}$ from Eqs. (9.8) and (9.10) into (9.11) and solving for λ^2 a first value λ_1 is obtained. Repeating the same operation for $\Omega = \Omega_{Q2}$, the value λ_2 is obtained. The optimum value of damping parameter is taken as the average value $(\lambda_1 + \lambda_2)/2$. The comparison between the FRF of the uncertain primary system in the case of deterministic tuning and uncertain tuning is depicted in Fig. 9.3. Black and gray lines are referred to robust and nominal tuning, respectively. Continuous lines correspond to $\delta = 0$ whereas dash-dotted and dashed lines correspond to $\delta = \mp 0.15$. The parameters of the linear absorber are $\lambda = 0.25$, $\rho = 0.95$ in the case of nominal tuning and $\lambda = 0.31$, $\rho = 0.92$ in the case of robust tuning. Therefore, to increase the bandwidth of the LTVA, the stiffness of the absorber is reduced and the damping is increased compared to the nominal case.

9.4 Theoretical Analysis of the Nonlinear Energy Sink

In this section, the behavior of the primary system coupled to the NES (i.e. $\rho = 0$ in Eq. (9.2)) is analyzed using the mixed multiple scale/harmonic balance method [10]. First a new coordinate $r = x_1 - x_2$ representing the relative displacement of the NES is introduced in Eq. (9.2).

$$\begin{aligned} &x_1'' + 2\xi_1 x_1' + (1+\delta)x_1 + \epsilon\lambda r' + \epsilon K r^3 = G\cos\tilde{\Omega}\tilde{t} \\ &r'' - x_1'' + \lambda r' + K r^3 = 0 \end{aligned} \tag{9.12}$$

Considering small mass ratio $\epsilon \ll 1$, according to the multiple scale method, independent time scales $t_0 = \tilde{t}$, $t_1 = \epsilon\tilde{t}$ are introduced and the variables are expanded in series

$$\begin{aligned} x_1(\tilde{t};\epsilon) &= x_{10}(t_0,t_1) + \epsilon x_{11}(t_0,t_1) + \ldots \\ r(\tilde{t};\epsilon) &= r_0(t_0,t_1) + \epsilon r_1(t_0,t_1) + \ldots \end{aligned} \tag{9.13}$$

The variable are rescaled so that $\xi_1 = \epsilon\xi_1$, $G = \epsilon G$. Substituting the previous scaling, Eq. (9.13) into Eq. (9.12) and equating coefficients of like power of ϵ to zero yields to the following set of equations

$$\begin{aligned} O(\epsilon^0) : d_0^2 x_{10} + x_{10}(1+\delta) = 0 \\ d_0^2 r - d_0^2 x_{10} + \lambda d_0 r_0 + K r_0^3 \end{aligned} \tag{9.14}$$

$$O(\epsilon^1) : d_0^2 x_{11} + x_{11}(1+\delta) = -2d_0 d_1 x_{10} - 2\xi_1 d_0 x_{10} - \lambda d_0 r_0 - K r_0^3 + G\cos\tilde{\Omega} t_0 \tag{9.15}$$

where $d_j^i = \partial^i / \partial t_j^i$. Note that only the first equation at $O(\epsilon^1)$ is given since it is the only one to be used.

9.4.1 Order ϵ^0

The solution of the first equation of (9.14) is given by

$$x_{10} = A(t_1)\mathrm{e}^{i\omega t_0} + [c.c], \quad \omega = \sqrt{1+\delta} \tag{9.16}$$

where $[c.c]$ denotes the complex conjugate of the preceding terms. The second equation of (9.14) is now investigated. As mentioned in [10], this equation does admit solution neither in terms of standard trigonometric function nor in term of Jacobi function. Therefore, we seek a solution using the method of harmonic balance. Since 1:1 resonance between the primary system and the NES is expected, it reads

$$r_0 = B(t_1)\mathrm{e}^{i\omega t_0} + [c.c] \tag{9.17}$$

here, only a single harmonic expansion is used. The effect of higher harmonics has been discussed in [9]. Substituting Eqs. (9.16) and (9.17) into the second equation of (9.14) and balancing terms of the fundamental harmonic gives

$$A = B\left(1 - \frac{i\lambda}{\omega} - \frac{3K|B|^2}{\omega^2}\right) \tag{9.18}$$

Equation (9.18) defines the slow invariant manifold (SIM) of the problem [4]. Substituting polar form $A = a\mathrm{e}^{i\alpha}$, $B = b\mathrm{e}^{i\beta}$, a real valued expression is obtained as

$$a^2 = \frac{b^2}{\omega^2}\left[\lambda^2 + \frac{\left(3Kb^2 - \omega^2\right)^2}{\omega^2}\right] \tag{9.19}$$

It can be shown that the slow invariant manifold can admit extrema. Vanishing the derivative of the right hand side of Eq. (9.19) with respect to b and solving for b gives

$$Z_j = \frac{\omega}{9K}\left(2\omega \mp \sqrt{\omega^2 - 3\lambda^2}\right), \quad j = 1, 2, \quad Z_j = b_j^2 \tag{9.20}$$

The corresponding amplitude of the primary system is obtained when substituting Eq. (9.20) into Eq. (9.19) and is given by

$$a_i^2 = \frac{2}{81K\omega}\left[\omega\left(9\lambda^2 + \omega^2\right) \pm \left(\omega^2 - 3\lambda^2\right)^{\frac{3}{2}}\right] \tag{9.21}$$

Therefore, if $\lambda < \lambda_c = \omega/\sqrt{3}$, the SIM admit extrema and is composed of two stable and one unstable branches. It is well known that systems with NES can perform relaxation cycles. In the framework of NES, such a response is often denoted strongly modulated response (SMR). When the system exhibits SMR, the maximum amplitude of the relaxation cycle, when $\epsilon \to 0$ is given by Eq. (9.21).

9.4.2 Order ϵ^1

In order to analyze SMR regimes, Eq. (9.15) is considered. The proximity of the forcing frequency and the natural frequency of the primary system is emphasized by defining $\tilde{\Omega} = \omega + \epsilon\sigma$. Substituting Eqs. (9.16) and (9.17) into Eq. (9.15) and eliminating secular terms yields

$$2id_1A\omega + 2i\xi_1A\omega + i\lambda B\omega - 3KB|B|^2 + \frac{G}{2}e^{i\sigma t_1} = 0 \tag{9.22}$$

We are interested in the behavior of the system on the stable branches of the SIM. Substituting Eq. (9.18) into (9.22) gives

$$-2id_1\left(\omega B - i\lambda B - \frac{3K}{\omega}B|B|^2\right) - (2i\xi_1\omega - i\lambda\,(1-\omega))\,B + \left(1 - \frac{2i\xi_1}{\omega}\right)3KB|B|^2 = 0 \tag{9.23}$$

Expressing B in polar form and splitting into real and imaginary parts yields

$$d_1 b = \frac{f_1(b,\psi)}{g(b)}, \quad d_1\psi = \frac{f_2(b,\psi)}{g(b)} \tag{9.24}$$

where $\psi = t_1\sigma - \beta$ and

$$\begin{aligned}
f_1(b,\psi) &= 36K^2\xi_1 b^5 - 24K\omega^2\xi_1 b^3 + 3GK\omega b\sin\psi + 2\omega^2\left(2\lambda^2\xi_1 + \lambda\omega^2 + 2\omega^2\xi_1\right)b \\
&\qquad - G\omega^2\left(\omega\sin\psi + \lambda\cos\psi\right) \\
f_2(b,\psi) &= \frac{1}{b}\left[-54K^2\left(\omega + 2\sigma\right)b^5 + 6K\omega\left(4\lambda\xi_1 + \omega + 8\sigma\right)b^3 + 9GK\omega b^2\cos\psi\right. \\
&\qquad \left. -2\omega^2\left(\lambda^2\omega + 2\lambda^2\sigma + 2\omega^2\sigma\right)b + G\omega^2\left(\lambda\sin\psi - \omega\cos\psi\right)\right] \\
g(b) &= -4\left(27K^2b^4 - 12Kb^2\omega^2 + \lambda^2\omega^2 + \omega^4\right)
\end{aligned} \tag{9.25}$$

According to [16], Eq. (9.24) admits two types of fixed points. The first type is referred as ordinary fixed points and is computed by solving for $f_1 = f_2 = 0$ and $g \neq 0$. The types of fixed points are referred as folded singularities and are found for $f_1 = f_2 = g = 0$.

The ordinary fixed points are obtained by solving $f_1 = f_2 = 0$ for $\cos\psi$, $\sin\psi$ and using trigonometric identity. A third order polynomial in $Z = b^2$ is then obtained. The folded singularities are generated by setting $f_1 = g = 0$ or equivalently $f_2 = g = 0$, giving

$$\begin{aligned}
\psi_{ij} &= -\arctan\left(\frac{3Kb_i^2 - \omega^2}{\lambda\omega}\right) \\
&\quad \pm \arccos\left[\frac{2b_i\left(2K\xi_1 b_i^2\left(9Kb_i^2 - 6\omega^2\right) + 2\lambda^2\omega^2\xi_1 + \lambda\omega^4 + 2\omega^4\xi_1\right)}{G\omega\sqrt{3Kb_i^2(3Kb_i^2 - 2\omega^2) + \lambda^2\omega^2 + \omega^4}}\right]
\end{aligned} \tag{9.26}$$

From Eq. (9.26), a condition on the forcing amplitude is obtained as follows

$$G_{ifs} \geq \frac{2b_i\left(2K\xi_1 b_i^2\left(9Kb_i^2 - 6\omega^2\right) + 2\lambda^2\omega^2\xi_1 + \lambda\omega^4 + 2\omega^4\xi_1\right)}{\omega\sqrt{3Kb_i^2(3Kb_i^2 - 2\omega^2) + \lambda^2\omega^2 + \omega^4}} \tag{9.27}$$

here, the subscript *fs* stands for folded singularities.

9.4.3 Detached Resonance Curve

An important feature that can affect the performance of the NES is the possible presence of detached resonance curves (DRC). This can be analyzed by locating the boundary of the saddle-node bifurcation in Eq. (9.24). Introducing perturbations around the fixed points and linearizing with respect to the perturbation, the so-called variational equation is obtained. By imposing the roots of the characteristic polynomial to be zero, an equation for Z is obtained as

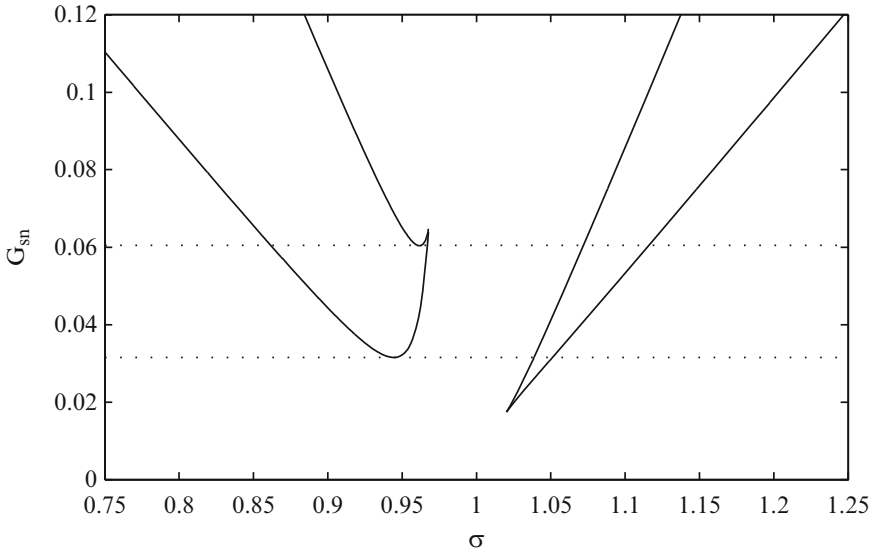

Fig. 9.4 Boundary of saddle-node bifurcation

$$27K^2\left(\omega^2+4\omega\sigma+4\sigma^2+4\xi_1^2\right)Z^2-24K\omega^2\left(\omega\sigma+2\sigma^2+2\xi_1^2\right)Z$$
$$+\omega^2\left(\lambda^2\omega^2+4\lambda^2\omega\sigma+4\lambda^2\sigma^2+4\lambda^2\xi_1^2+4\lambda\omega^2\xi_1+4\omega^2\sigma^2+4\omega^2\xi_1^2\right)=0 \tag{9.28}$$

Solving for Z and substituting into the fixed points equation, an expression for G_{sn} is obtained. An example of boundary of saddle node bifurcation in the space of parameters (σ, G) is displayed in Fig. 9.4. Continuous lines correspond to the boundary of the saddle-node bifurcations. The creation or merging of detached resonance curves is computed for $\partial G_{sn}/\partial\sigma = 0$ and it is represented by the dotted lines. The lower one corresponds to the appearance of a DRC, while the upper one corresponds to the merging of the DRC with the principal resonance curve.

9.5 Tuning of the NES

In this section, the theoretical developments are used to define a tuning rule for the NES. Both the deterministic and the uncertain case are addressed.

9.5.1 Deterministic Primary System

First, the case $\delta = 0$ is analyzed. The theoretical analysis allows us to determine critical forcing amplitudes G that will determine different response characteristics. Since in our case, the forcing amplitude is considered fixed, the tuning procedure consists in finding appropriate value of (λ, K) for the NES. Critical forcing amplitude can be converted into critical nonlinear stiffness by using the forcing-nonlinearity equivalence principle [18] which states that if the ratio $G^2/K = \text{cst}$, the behavior of the system, compared to the supplied energy, remains unchanged. By doing so, the sizing chart depicted in Fig. 9.5 is obtained.

Continuous and dash-dotted lines represent the boundary of folded-singularities and DRC, respectively. Vertical dashed line represents the maximum value of damping for which the SIM admits extrema (i.e. the maximum value of the damping for which the system may perform relaxation cycles). In order to highlight the influence of the different boundaries on the response of the primary system, the frequency response curve corresponding to each zones is presented in Fig. 9.6.

In zone I, the couple (λ, K) is below the boundary of folded singularities and DRC. In this case, the system behaves quasi-linearly, so that this zone is not interesting from a vibration mitigation point of view. In zone II, the system can exhibit SMR without detached resonance curve. The amplitude of the oscillations is halved compared to the case in zone I and

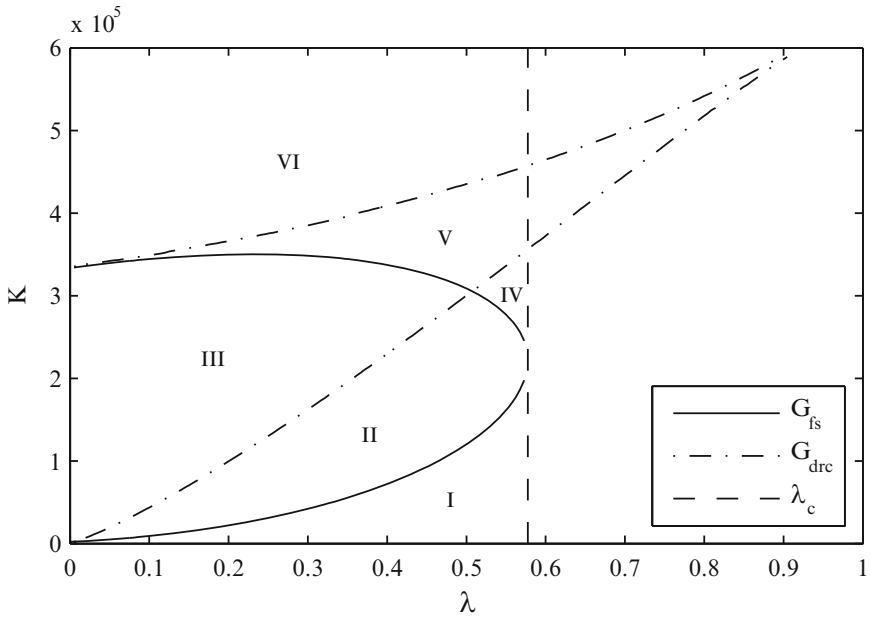

Fig. 9.5 Sizing zones for the primary system coupled to the NES

SMR takes place on the unstable part of the frequency response curve denoted by dotted lines. In zone III, high amplitude DRC is present, so that this zone must be avoided. In zone IV, the parameters of the NES are above the boundary of folded singularities but under the boundary of DRC so that fixed points on the right stable branch of the SIM exist. This can be seen on Fig. 9.6 where stable fixed points exist on the upper part of the frequency response curve. The zone V is located inside the boundary of DRC and above the boundary of folded singularities. Therefore the frequency response curve presents both a DRC and fixed points on the right stable branch of the SIM. Finally, in zone VI, the parameters of the NES are higher than the second boundary of DRC, yielding to the merging of the DRC with the main branch of the frequency response curve.

From the above observation, the parameters of the NES have to be chosen in zone II or IV. This choice can be further restricted to zone II by making the following observations. In zone IV, we do not have any a priori information about the amplitude of the fixed points lying on the right stable branch of the SIM. In addition, in zone II, in the absence DRC and fixed points on the right stable branch of the SIM, the maximum amplitude of the oscillation (when $\epsilon \to 0$) is determined by the maximum of the SIM in Eq. (9.21). As a conclusion, although potentially conservative, zone II is regarded as the optimal tuning region.

Optimal values of the parameters of the NES have now to be chosen inside zone II. As mentioned in the previous paragraph, the maximum amplitude of the primary system is determined by looking at the maximum of the SIM. The superposition of the amplitude of the extremums on zone II is depicted in Fig. 9.7. It is observed that the optimal value of the parameters of the NES is located at the intersection of the upper boundary of folded singularities and the boundary of creation of DRC.

9.5.2 Uncertain Primary System

The case where the stiffness of the primary system is uncertain is now analyzed. This uncertainty is represented by parameter δ in Eq. (9.2). The sizing curves in the space of parameters (λ, K) for $\delta \in [-0.15, +0.15]$ are depicted in Fig. 9.8. Continuous lines correspond to the nominal case ($\delta = 0$), dash-dotted and dashed lines correspond to $\delta = -0.15$ and $\delta = +0.15$, respectively.

We note that the upper part of zone II for $\delta = -0.15$ is included in the zone II for $\delta = 0.15$. Therefore, passive control through SMR exists for the whole range of detuning. So that the system can perform SMR as long as the zone II for $\delta = \delta_{min}$ is contained in the zone II corresponding to $\delta = \delta max$, which occurs for $|\delta| \approx 0.3$. The tuning rule may be summarized as follows. The optimum parameters of the NES (λ_{opt}, K_{opt}) are found at the intersection of the folded singularities and DRC. If the natural frequency of the primary system is uncertain, the tuning of the NES is determined by the lower bound of the uncertainty, i.e. $\delta = \delta_{min}$.

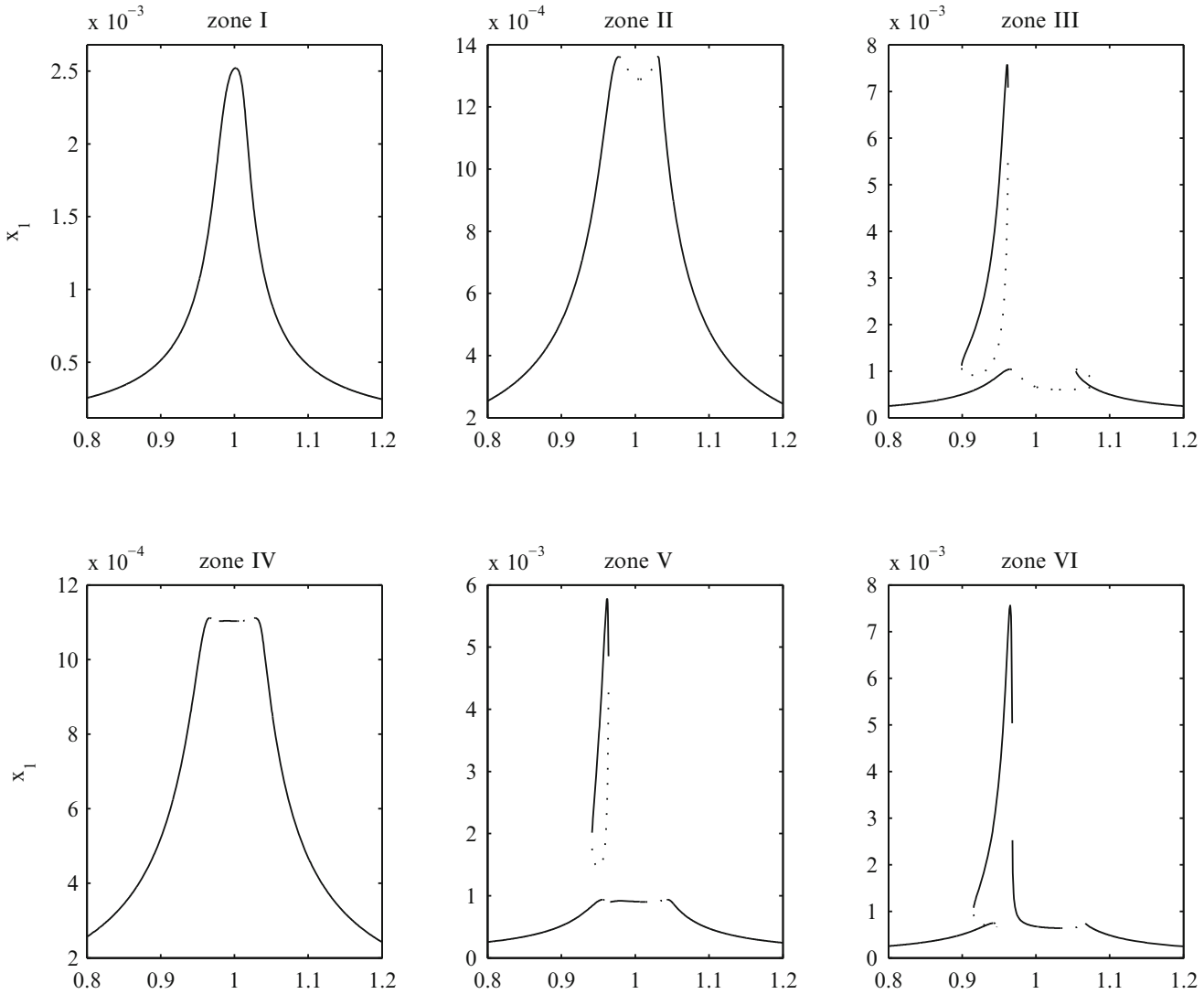

Fig. 9.6 FRF of the primary system coupled to the NES for the different sizing zones

9.6 Performance Comparison of the NES and LTVA

In this section, the performance of the NES and LTVA from a vibration mitigation point of view are compared. The deterministic case is first addressed, then the case of uncertain primary system is considered. For both cases, a damping factor $\xi_1 = 0.5\,\%$ is considered. Also, a single forcing amplitude $G = 10^{-4}$ is considered whereas the frequency detuning parameter is assumed to vary in the range $\delta = \mp 0.15$.

9.6.1 Deterministic Primary System

As shown in Fig. 9.5, given a forcing amplitude, the optimum stiffness and damping of the NES are found at the intersection between the boundary of creation of DRC and the folded singularities. For $\epsilon = 5\,\%$, this gives $\lambda \approx 0.51$, $K \approx 3.03 \times 10^5$. For the LTVA, the optimum parameters are given in Eq. (9.3). Note that these equations are valid in the case of an undamped

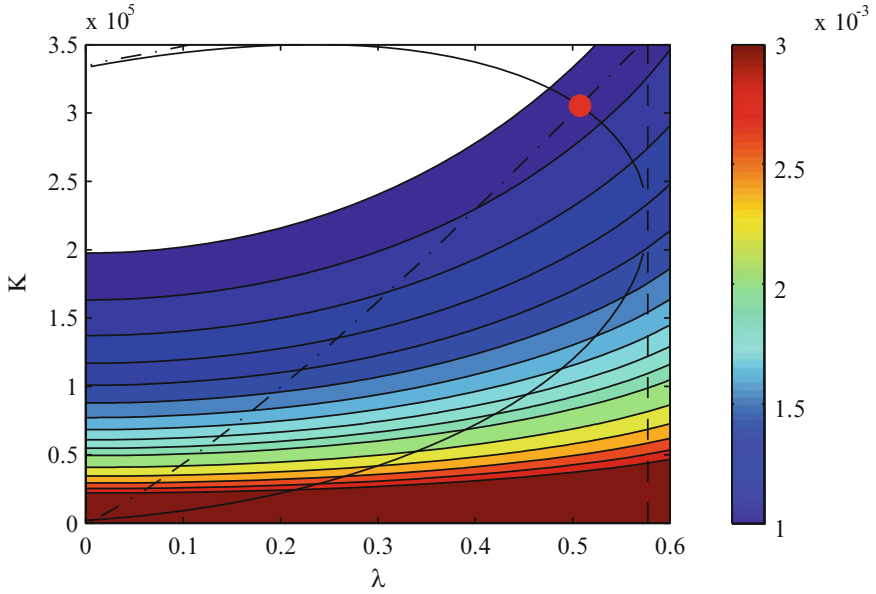

Fig. 9.7 Maximum amplitude of the linear oscillator inside zone II

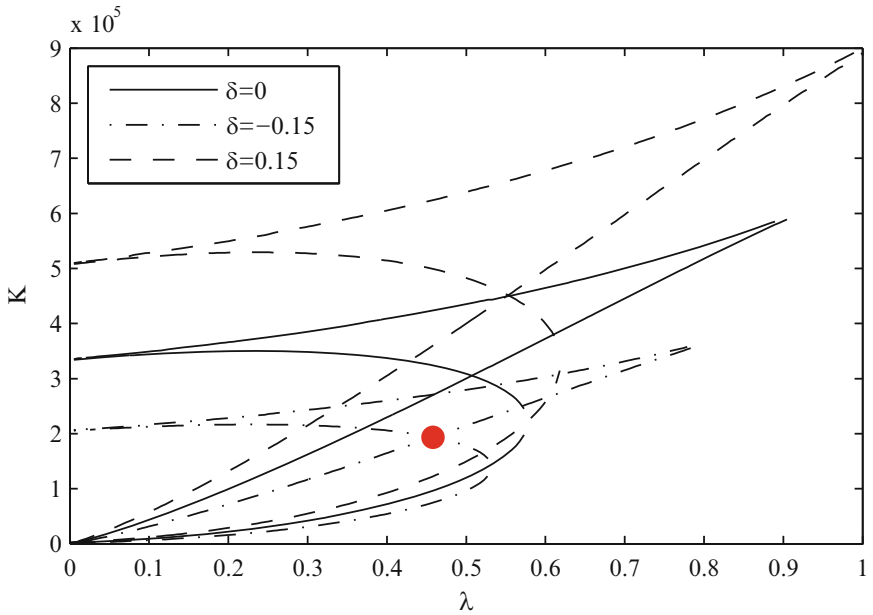

Fig. 9.8 Sizing zones of the NES for different uncertainties

primary system. However, for lightly damped primary system, the performance of the LTVA is not really affected since almost equal peaks is observed, as depicted in Fig. 9.9. Both the displacements of the primary system and the absorber are illustrated. Gray correspond to the system coupled to the LTVA. Black solid and dotted lines correspond to stable and unstable periodic solution of the system coupled to the NES. Black dots correspond to the results of time step integration of the equation of motion (9.2).

It is clear from Fig. 9.9 that in the case of deterministic, linear primary system, the LTVA is far more efficient than the NES for vibration mitigation.

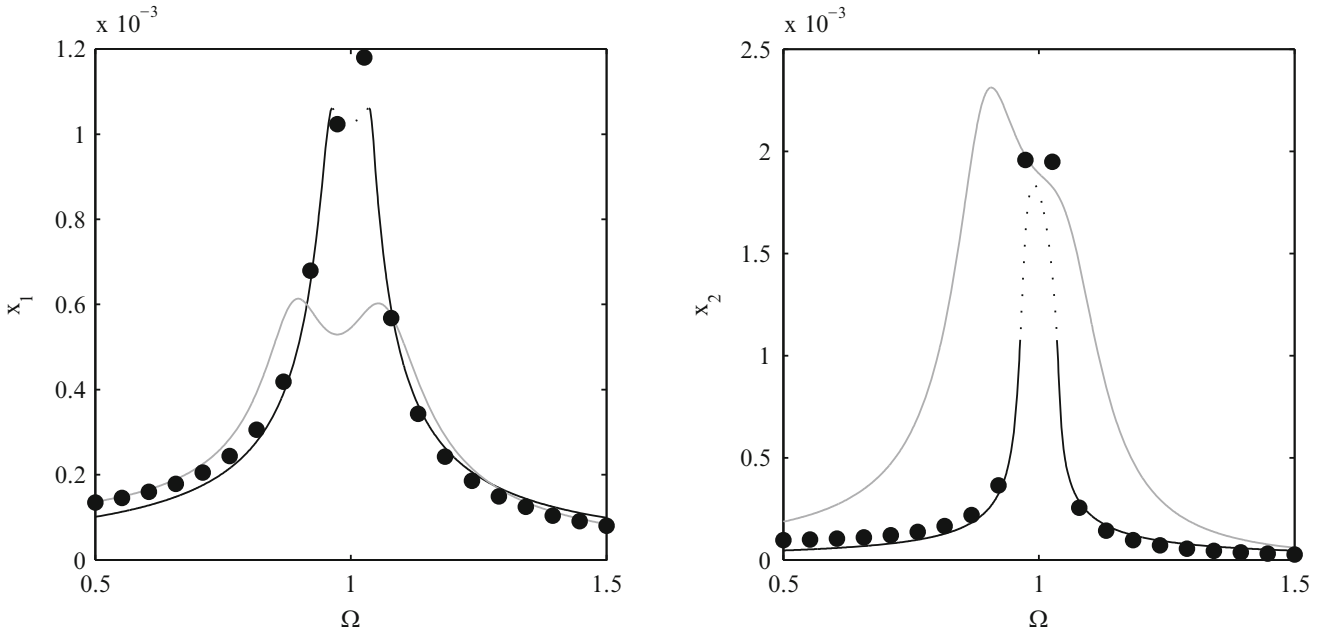

Fig. 9.9 Comparison of the frequency response curve of the LTVA and the NES for a deterministic primary system with $\epsilon = 0.05$. *Left*: amplitude of the linear oscillator and *right*: amplitude of the absorber

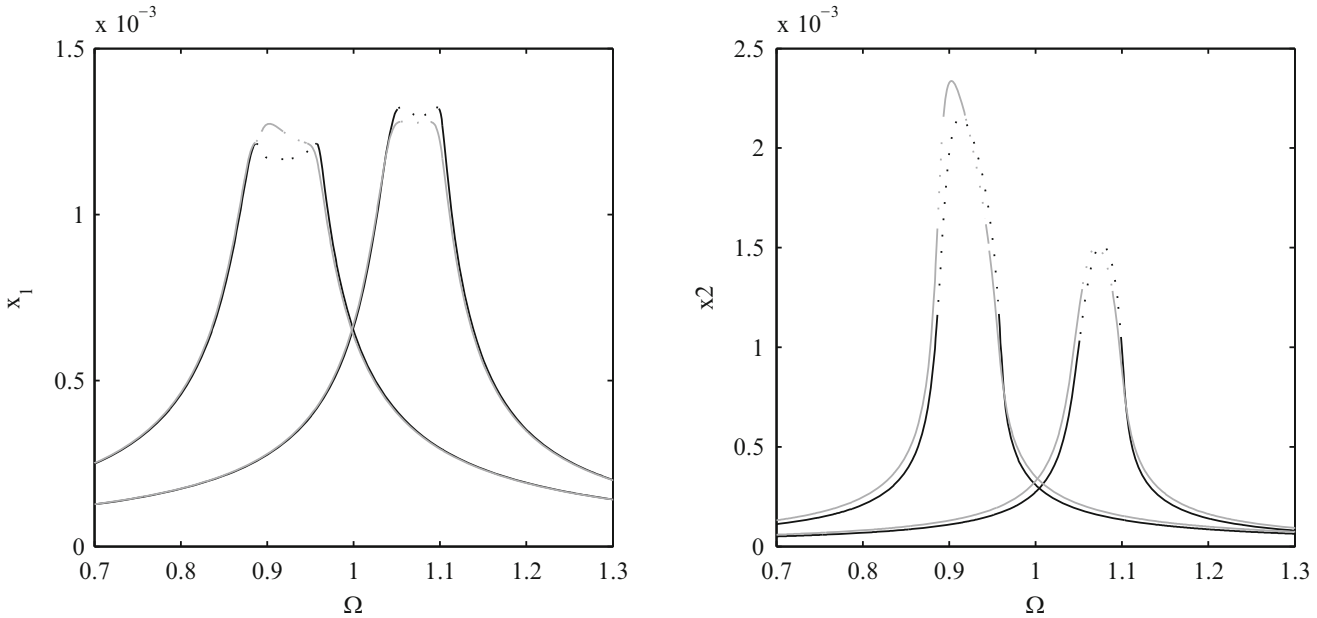

Fig. 9.10 Comparison of the frequency response curve of the robust NES vs robust LTVA

9.6.2 Uncertain Primary System

The frequency response curves of the uncertain primary system coupled to the optimal NES or LTVA are depicted in Fig. 9.10. Black and gray lines refer to the primary system coupled to the NES and LTVA, respectively. Even if SMR is expected over the range of detuning $\delta = \mp 15\,\%$, the LTVA performs better than the NES since the maximum is reduced of about 20 % compared to the NES.

The results for $\epsilon = 5\,\%$ and $\epsilon = 1\,\%$ are summarized in Table 9.1. It is observed that for a smaller mass ratio (i.e. $\epsilon = 1\,\%$) the difference between the LTVA and the NES is even larger.

Table 9.1 $|H|_\infty$ of the primary system coupled to the LTVA/NES for $\epsilon = 5\,\%$ and $\epsilon = 1\,\%$ in the deterministic and uncertain case

	Deterministic		Uncertain	
ϵ	NES	LTVA	NES	LTVA
5 %	1.06×10^{-3}	0.61×10^{-3}	1.32×10^{-3}	0.94×10^{-3}
1 %	3.37×10^{-3}	1.23×10^{-3}	4.42×10^{-3}	2.72×10^{-3}

9.7 Conclusion

The paper proposed an objective comparison between a NES with cubic stiffness nonlinearity and a linear absorber for vibration mitigation of a linear host system. A design procedure for the NES, which minimizes the maximum amplitude of the linear oscillator while preventing the presence of detached resonance curves has been presented. Surprisingly, the proposed design procedure yields highly damped NES which is contrary to conventional wisdom. A novel tuning procedure for the LTVA, when the natural frequency of the primary system contains uncertainty has also been presented.

For both deterministic and uncertain primary system, the LTVA outperforms the NES. The only way to achieve a better performance of the NES is to allow the presence of DRC, however, this is a risky solution since the system may be attracted to high amplitude solution under some perturbations.

References

1. Asami, T., Nishihara, O.: Closed-form exact solution to h∞ optimization of dynamic vibration absorbers (application to different transfer functions and damping systems). J. Vib. Acoust. **125**(3), 398–405 (2003)
2. Den Hartog, J.P.: Mechanical Vibrations. Dover Civil and Mechanical Engineering (1956)
3. Frahm, H.: Device for damping vibrations of bodies. US Patent 989,958, 18 April 1911
4. Gendelman, O.V.: Bifurcations of nonlinear normal modes of linear oscillator with strongly nonlinear damped attachment. Nonlinear Dyn. **37**(2), 115–128 (2004)
5. Gendelman, O.V., Manevitch, L.I., Vakakis, A.F., Mcloskey, R.: Energy pumping in nonlinear mechanical oscillators: part I—dynamics of the underlying Hamiltonian systems. J. Appl. Mech. **68**(1), 34–41 (2001)
6. Gourc, E., Michon, G., Seguy, S., Berlioz, A.: Experimental investigation and design optimization of targeted energy transfer under periodic forcing. J. Vib. Acoust. **136**(2), 021021 (2014)
7. Habib, G., Kerschen, G.: Suppression of limit cycle oscillations using the nonlinear tuned vibration absorber. Proc. R. Soc. B **471**, 20140976 (The Royal Society) (2015)
8. Ibrahim, R.A.: Recent advances in nonlinear passive vibration isolators. J. Sound Vib. **314**(3), 371–452 (2008)
9. Luongo, A., Zulli, D.: Dynamic analysis of externally excited NES-controlled systems via a mixed multiple scale/harmonic balance algorithm. Nonlinear Dyn. **70**(3), 2049–2061 (2012)
10. Luongo, A., Zulli, D.: Aeroelastic instability analysis of NES-controlled systems via a mixed multiple scale/harmonic balance method. J. Vib. Control (2013). doi:1077546313480542
11. Mann, B.P., Sims, N.D.: Energy harvesting from the nonlinear oscillations of magnetic levitation. J. Sound Vib. **319**(1), 515–530 (2009)
12. Náprstek, J., Fischer, C.: Auto-parametric semi-trivial and post-critical response of a spherical pendulum damper. Comput. Struct. **87**(19), 1204–1215 (2009)
13. Parseh, M., Dardel, M., Ghasemi, M.H.: Performance comparison of nonlinear energy sink and linear tuned mass damper in steady-state dynamics of a linear beam. Nonlinear Dyn. **81**, 1–22 (2015)
14. Starosvetsky, Y., Gendelman, O.V.: Attractors of harmonically forced linear oscillator with attached nonlinear energy sink. II: optimization of a nonlinear vibration absorber. Nonlinear Dyn. **51**(1–2), 47–57 (2008)
15. Starosvetsky, Y., Gendelman, O.V.: Dynamics of a strongly nonlinear vibration absorber coupled to a harmonically excited two-degree-of-freedom system. J. Sound Vib. **312**(1), 234–256 (2008)
16. Starosvetsky, Y., Gendelman, O.V.: Strongly modulated response in forced 2D of oscillatory system with essential mass and potential asymmetry. Physica D **237**(13), 1719–1733 (2008)
17. Vakakis, A.F., Gendelman, O.: Energy pumping in nonlinear mechanical oscillators: part II—resonance capture. J. Appl. Mech. **68**(1), 42–48 (2001)
18. Vaurigaud, B., Savadkoohi, A.T., Lamarque, C.-H.: Targeted energy transfer with parallel nonlinear energy sinks. Part I: design theory and numerical results. Nonlinear Dyn. **66**(4), 763–780 (2011)
19. Warminski, J., Kecik, K.: Instabilities in the main parametric resonance area of a mechanical system with a pendulum. J. Sound Vib. **322**(3), 612–628 (2009)

Chapter 10
Experimental and Numerical Investigation of the Nonlinear Bending-Torsion Coupling of a Clamped-Clamped Beam with Centre Masses

David A. Ehrhardt, Simon A. Neild, and Jonathan E. Cooper

Abstract The vibration characteristics of beams have been extensively studied due to their wide application across multiple fields (i.e. spacecraft antennae, aircraft wings, turbine blades, skyscrapers). Of particular interest, specific geometries of beams have been shown to induce coupling between the fundamental bending and torsion modes. This coupled motion can be observed in a beam's linear normal modes can be avoided with the correct selection of geometric properties. This work investigates the coupled bending-torsion behaviour of a clamped-clamped beam that is coupled perpendicularly, mid-span to mid-span, to a second beam with tip masses within the nonlinear response regime. The first torsion mode of the beam system is tuned by modifying the mass distribution such that closely spaced bending and torsion linear normal modes can be realized. The nonlinear behaviour is presented using nonlinear normal mode backbone curves and forced responses in the vicinity of the modes of interest.

Keywords Nonlinear normal modes • Close nodes • Mode veering

10.1 Introduction

An important feature of continuous structures is the potential occurrence of close natural frequencies. In some cases, close natural frequencies are a result of a dense number of modes of vibration (natural frequencies and mode shapes) of the structure. The 'closeness' of these natural frequencies is not due to a specific property of the structure, but instead an accident of the mass and stiffness distribution of the structure. In other cases, the 'closeness' of natural frequencies is an inherent and inevitable property connected to spatial symmetries of the structure resulting in pseudo-repeated roots to the Eigen decomposition of the underlying equations of motion. A structure that is perfectly symmetric about an axis will contain certain natural frequencies (eigenvalues) that are repeated, where the mode shapes (eigenvectors) are qualitatively similar, but rotated around the axis of symmetry. The dynamic motion of structures containing closely spaced modes of this nature include coupled modal deformations requiring special attention.

It has been shown that in linear systems containing symmetries, the eigenvectors associated with closely spaced eigenvalues can be highly sensitive to small perturbations of the symmetry of the physical structure as described in [1]. Over large distortions of the symmetry of the physical structure the phenomena of mode veering can be observed [2]; however, care must be taken to assure that the observed veering is not a result of discretization of the system [3]. Veering can be described as follows: as a structure's symmetric parameters change enough for closely spaced eigenvalues to cross, the eigenvalues will reach a limit of 'closeness' and the eigenvectors will undergo a rapid change until the modes of vibration have changed relative location (i.e. eigenvector 2 becomes eigenvector 1). The change in the eigenvectors throughout this region of veering can be thought of as a rotation in a subspace spanned by the two eigenvectors as they come out of the Eigen decomposition [4]. Examples of mode veering in linear structures have been shown in a pressure vessel [5], cable dynamics [6, 7], a pre-stressed frame [8], and imperfect beams [9]. If the geometry of the physical structure is perturbed, but the symmetry of the physical structure is preserved, the closely spaced modes will cross instead of veer.

It is well known that for nonlinear systems, internal coupling forces lead to an exchange of energy between the linear modes of vibration termed internal resonances, or auto parametric resonances. For closely spaced natural frequencies, 1-1 internal resonances have been observed in the dynamics of symmetric systems such as stretched strings, beams, plates,

D.A. Ehrhardt (✉) • S.A. Neild • J.E. Cooper
Department of Mechanical Engineering, University of Bristol, Bristol, UK
e-mail: david.ehrhardt@bristol.ac.uk

G. Kerschen (ed.), *Nonlinear Dynamics, Volume 1*, Conference Proceedings of the Society for Experimental Mechanics Series,
DOI 10.1007/978-3-319-29739-2_10

and rotating disks as discussed by Nayfeh in [10]. Additionally, it has been shown that as physical parameters of stretched cables and symmetric shallow arches are changed, but symmetry is preserved, a crossing occurs between uncoupled natural frequencies (i.e. symmetric and antisymmetric modes). At the point of crossing, a 1-1 internal resonance can be realized if the system of interest contains the proper orthogonality conditions as discussed in [11–13]. Again, if the symmetry is broken, the natural frequencies will veer instead of cross. Lacarbonara et al. [9] investigated the nonlinear dynamics of an imperfect beam at veering, finding similar 1-1 internal resonances; however, only coupled motions of the modes of vibration are physically realized in the vicinity of veering, contrary to the perfect beams investigated in [13] where uncoupled dynamic motions are also observed.

This investigation seeks to create a structure that contains closely spaced fundamental torsion and bending modes, while being easily tuneable to permit the perturbation of the 'closeness' of these modes. Due to the potential coupled nature of close natural frequencies, veering is expected in the linear system when spatial asymmetries are introduced. It is of particular interest to investigate the effects of nonlinear coupling of the modes on different sides of veering. Abaqus® is used to numerically determine the linear eigenvalues and eigenvectors of the physical structure at different levels coupling. The natural frequencies and modes shapes are experimentally determined using multi-input multi-output testing and the algorithm of mode isolation [14]. Since the modes are lightly damped, the level of complexity in the response is expected to be minimal. For ease of computational burden as the structure is forced in the nonlinear response regimes, nonlinear reduced order models (NLROMs) are determined using the geometric nonlinearity capabilities of Abaqus® as described in [15]. The structure's first two nonlinear normal modes (NNMs) and pertinent forced responses are computed with the resulting NLROMs. Finally, the resulting NNMs are compared with numerically calculated NNMs using the full order model build confidence in the NLROM [16].

10.2 Structure and Model Description

The structure under consideration was created to exhibit 'closeness' between the first bending and first torsion mode of vibration. The structure consists of two beams joined in the middle with one beam clamped at both ends and one beam mounted to concentrated masses at both ends. A schematic of this structure is shown in Fig. 10.1. One of the benefits of a structure of this type is the ability to change the torsional inertia with limited effect to the bending inertia. For instance, a change in the distance of each mass from the centre of the structure, i.e. L_1 and L_2 shown in Fig. 10.1, changes the effective torsional inertia with minimal effects on bending inertia.

A finite element model was created in Abaqus to establish a high quality linear and nonlinear model as shown in Fig. 10.2a. A total of 289 B31 beam elements were used to discretise the main sections of each beam where the main beam's cross section has dimensions $l \times w \times h$ of 1000 mm × 12 mm × 6 mm and the cross beam's cross section has dimensions $l \times d$ of 410 mm × 12 mm. B31 beam elements were also used to model the concentrated masses on the ends with dimensions of $d \times h$ of 38 mm × 24 mm. The cross sections were chosen to constrain the three dimensional motion to planar motions and to provide the desired nonlinear effect within the elastic region of steel. The final experimental setup is shown in Fig. 10.2b.

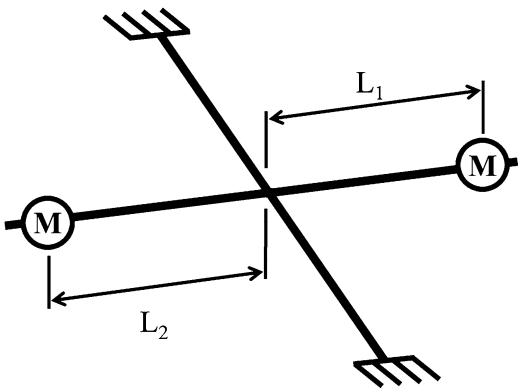

Fig. 10.1 Schematic of clamped-clamped cross beam

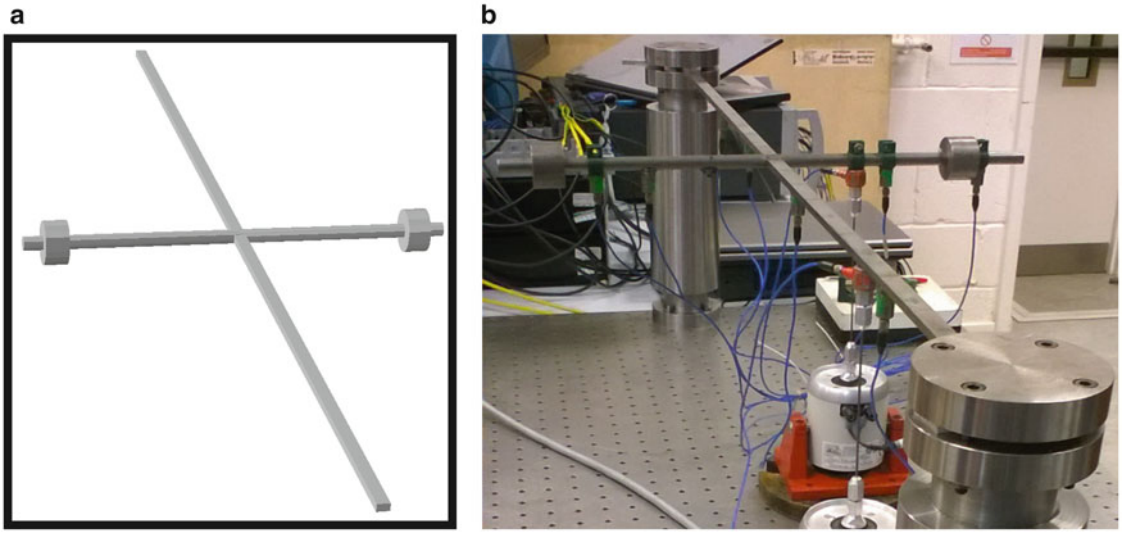

Fig. 10.2 Clamped-clamped cross beam, (**a**) Abaqus model, (**b**) actual structure

10.3 Linear Results

The perturbation of physical geometries of a structure with closely spaced natural frequencies will cause the natural frequencies to either veer or cross depending on the coupling observed between the modes [3]. The numerical eigenvectors and eigenvalues presented in this section were found in Abaqus using a Lanczos eigensolver. The experimental residues and poles presented in this section were found using the multi-input multi-output extensions to the algorithm for mode isolation [14].

In the case where $L_1 = L_2$, the model predicts the crossing point to be at $L_1 = 182.4$ mm, where the modes remain uncoupled torsion and bending modes to with a spacing of 0.006 Hz. As illustrated in Fig. 10.3, an increase in L_1 of +10 mm results in a torsion mode at 15.66 Hz and a bending mode at 16.19 Hz. Alternatively, a decrease in L_1 of −10 mm results in a bending mode at 16.22 Hz and a torsion mode at 16.85 Hz. For a better illustration of this instance of eigenvalue crossing, a plot of the natural frequency versus change in length is shown in Fig. 10.4 in blue. As the change in length is increased from −10 mm to 0 mm, the mode 1 (bending mode) approached mode 2 (torsion mode). At the point of crossing, mode 1 becomes the torsion mode and mode 2 becomes the bending mode with no coupling observed between the eigenvectors of these modes as the change in length is increased to 10 mm.

For cases where $L_1 \neq L_2$, the torsion and bending mode become coupled and deviate from a purely bending or torsion motion and demonstrate veering as the spacing of the eigenvalues is changed as shown in Fig. 10.3. For the cases $L_2 = 0.95{*}L_1$ and $L_2 = 0.90{*}L_1$, veering is predicted when the $L_1 = 187.0$ mm and $L_1 = 191.0$ mm, respectively. At these two cases of veering, the eigenvectors shown in Fig. 10.3 appear as rotated versions of the uncoupled bending and uncoupled torsion modes (i.e. bending and torsion are equally represented in the deformation of the beam). As L_1 is increased +10 mm, the eigenvectors become almost completely uncoupled for both cases where the torsion dominate mode is mode 1 and the bending dominated mode is mode 2. Alternatively, as L_1 is decreased −10 mm, the eigenvectors become almost completely uncoupled, but the bending dominated mode is mode 1 and the torsion dominated mode is mode 2. For a better illustration of these instances of eigenvalue veering, a plot of the natural frequency versus change in length is shown in Fig. 10.4 in green and red. As the change in length is increased from −10 mm to 0 mm, both instances demonstrate a limit of closeness in the eigenvalues as the eigenvectors rotate and couple. As the change in length is increased from 0 to 10 mm, the opposite behaviour is demonstrated with the dominate mode shape switched.

Similarly, the experimental results reveal the veering phenomena observed in the numerical model, with minor differences due to limitations and variations of the experimental setup. For instance, the case when $L_1 = L_2$ exhibits veering in the experimental results as opposed to the crossing observed in the numerical results giving an indication of asymmetries in the experimental setup. The point of veering for this case is at $L_1 = 200$ mm where coupled mode shapes are observed in Fig. 10.3. As L_1 is increased by 5 mm (the limit in the experimental setup), the torsion mode begins to dominate mode 1 and the bending mode begins to dominate mode 2. As L_1 is decreased by −5 mm, the opposite is observed and the bending mode begins to dominate mode 1 and the torsion mode begins to dominate mode 2. The limit for the closeness of the identified

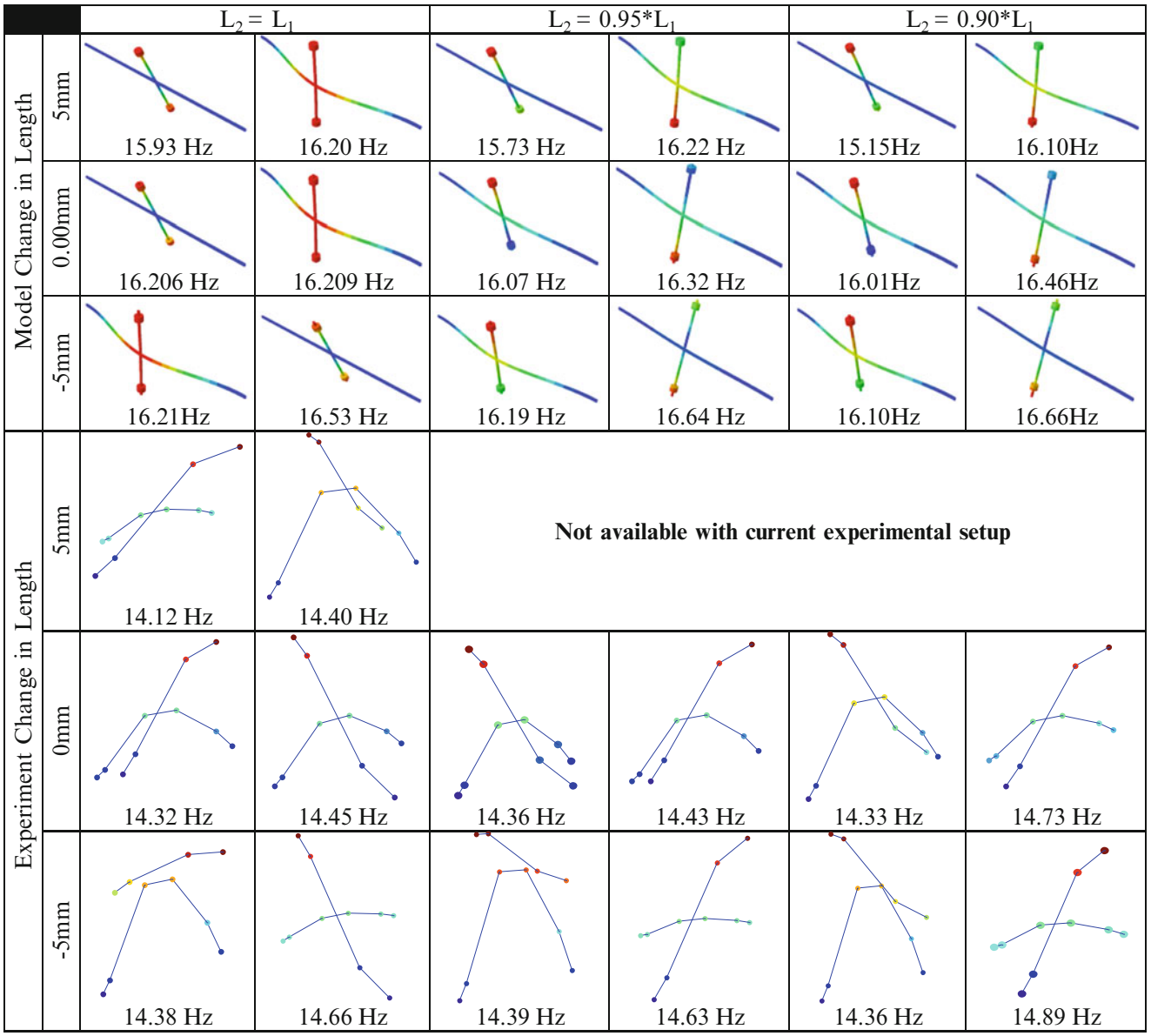

Fig. 10.3 Experimental and numerical mode veering results. Rows 2–4 are the eigenvectors and associated eigenvalues of the numerical model of the coupled beam system. Rows 5–7 are the eigenvectors and associated eigenvalues of the experimental setup of the coupled beam system

natural frequencies for this case is 0.13 Hz. For the experimental case where $L_2 = 0.95*L_1$, the point of veering is observed at $L_1 = 205$ mm (the limit in the experimental setup). Here the limit for the closeness of the identified natural frequencies for this case is 0.07 Hz. Again, as L_1 is decrease by −5 mm, the bending mode begins to dominate mode 1 and the torsion mode begins to dominate mode 2 following a similar trend as previously observed. Finally, where $L_2 = 0.90*L_1$, the exact point of veering is not identified; however, coupled natural frequencies are identified in Fig. 10.3, showing the approach to the veering location. As L_1 is decreased by −5 mm, the bending mode again dominates mode 1 and the torsion mode begins to dominate mode 2. Although the entire region of veering cannot be identified experimentally due to limitations in the experimental setup, by plotting the available identified natural frequencies and mode shapes, a trend of veering is shown (Fig. 10.4b) that is qualitatively similar to that identified in the numerical model shown in Fig. 10.4a. If the exact region of veering and crossing is of interest, additional tests could be used with heavier masses to further identify the veering/crossing regions.

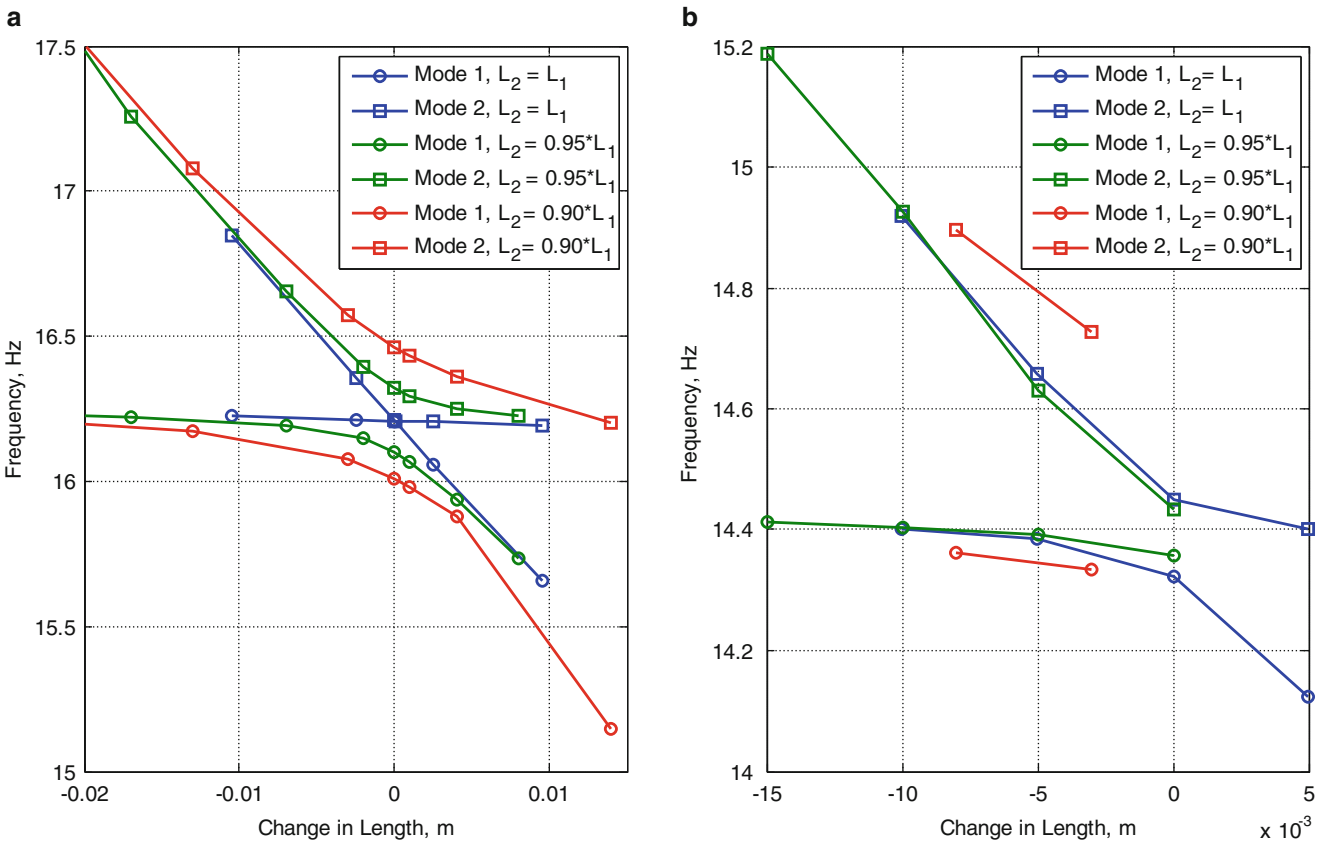

Fig. 10.4 Summary of mode veering/crossing results. (**a**) Numerical results, (**b**) Experimental results

10.4 Nonlinear Results

Although mode veering in the linear system provides interesting coupled dynamics between the two modes of interest, the goal of this work is to identify potential areas of nonlinear coupling between the modes of interest. Using the linear system described in the previous section, nonlinear reduced order models (NLROMs) are created using nonlinear static deformations and the built in geometric nonlinearity formulation used in Abaqus as discussed in [17]. Using the two modes of interest as a modal basis, two degree-of-freedom models can be created. A NLROM of this nature permits the exploration of several variations of the underlying structure so nonlinear coupling can be explored in a reasonable time frame.

Beginning with the symmetric case when $L_1 = L_2$, the nonlinear normal modes (NNMs) and selected forced responses are computed and shown in Fig. 10.5. NNMs contain the periodic solutions to the unforced nonlinear equations of motion and provide insight into the behaviour of the first two modes of this system as shown in blue in Fig. 10.5. A good summary of the dynamics of the total system can be observed in the frequency-energy domain (Fig. 10.5a, d, and g). In these plots, as the input force level is increased, the NNM shows a spring hardening effect for both the torsion and bending mode in all three cases. This is independent of the order of modes (i.e. bending before torsion or torsion before bending). The uncoupled nature of these two modes is investigated by projecting the NNMs in the frequency-energy domain into the modal domain Fig. 10.5b, c, e, f, h, and i. For the three cases of the symmetric system presented, the bending and torsion mode act as independent oscillations with only linear shifts in the natural frequency due to changes in the physical setup. As the response is pushed into nonlinear regions, the two modes of interest act as nonlinear continuations of their linear counterparts. It is interesting to note that for the case near crossing (Fig. 10.5c), the NNMs remain independent throughout increasing energies. Although not further explored here, it should be noted that as the modes cross as shown in Fig. 10.5g, the response can exhibit 1-1 internal resonances as previously investigated in [11–13]. The forced response of the system to sinusoidal inputs at two input locations, one near the clamping root and one on the cross bar near the centre of the beam, are also shown in Fig. 10.5 at 0.01 N, 0.1 N, 1 N and 10 N. The peak force was limited to 10 N as greater forces approach the elastic limit of the steel used as the material for this system. As expected, the forced response of the system follows the NNMs at low and high energies since the forcing locations will excite both modes. Of particular interest, the case where the bending mode

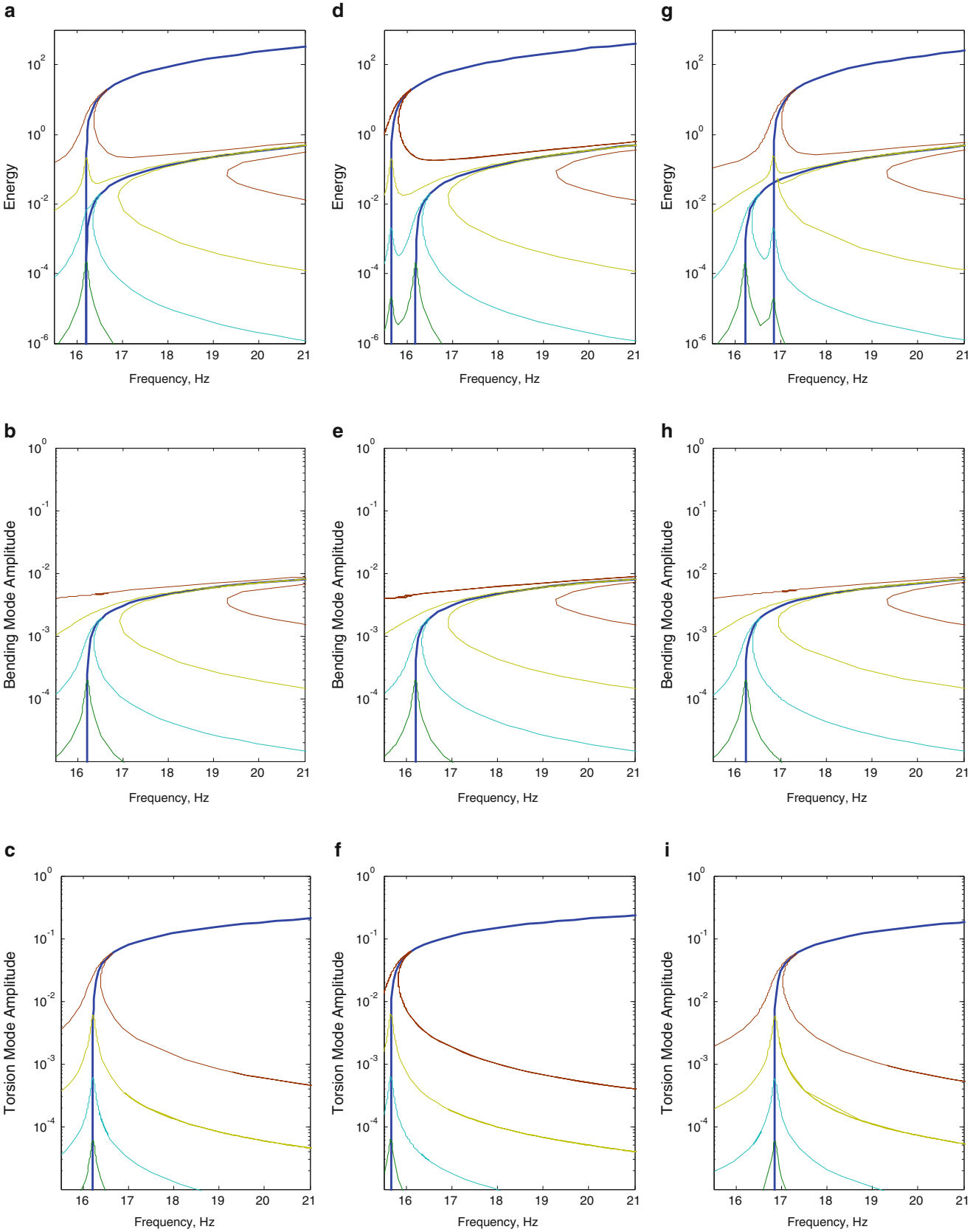

Fig. 10.5 Nonlinear normal modes (*blue line*) and forced responses (*green line* 0.01 N, *aqua line* 0.1 N, *light green line* 1 N, and *brown line* 10 N) of the symmetric system when $L_2 = L_1$ at (**a**–**c**) Change in Length = 0 mm. (**d**–**f**) Change in length = 10 mm, (**g**–**i**) Change in length = −10 mm

is before the torsion mode (Fig. 10.5c), shows the NNMs cross over and retain their initial eigenvectors as the deformation of the NNM branch. This behaviour is similar to that observed in the linear crossing case for this structure, and provides a further insight to the uncoupled nature of these NNMs.

The next case of interest is when $L_2 = 0.95*L_1$. As shown in the linear results section, the modes of interest in this case become coupled and exhibit veering due to the asymmetry introduced by the differences in location of the tip masses. Due to the coupled nature of the linear modes, the nonlinear response will also be coupled. Again, a good summary of the overall dynamics of the system can be observed in the frequency energy domain as shown in (Fig. 10.6a, d, and g). In the coupled system, instead of the bending and torsion mode crossing, as observed in Fig. 10.5g, the NNMs appear to 'veer' as they approach the crossing point as shown in Fig. 10.6g. Similar to linear veering, the deformation of the first NNM experiences a rapid transformation in this region of 'veering' where the bending dominated mode becomes a torsion dominated mode at higher energies. The reverse is observed for the second NNM. A deeper understanding of this region is obtained by examining the modal deformations in Fig. 10.6h and i. Again due to the coupled nature of the linear modes, both modes participate in the both NNMs as opposed to the uncoupled system described in Fig. 10.5. The transition of mode 1 from dominating the first NNM to dominating the second can be observed in the forced responses in Fig. 10.6h. The lowest two forcing levels (0.01 N and 0.1 N) shown here primarily follow the first NNM, while the second two forcing levels (1 N and 10 N) begin to follow the second NNM. The opposite is observed in Fig. 10.6i, where mode 2 transitions from the second NNM to the first. Similar observations can be made for the case where the modes are exactly at veering in the linear system (Fig. 10.6a–c). Although not as dramatic a transition as the case in Fig. 10.6g–i, the first and second NNMs experience a small transition between the mode 1 and mode 2 dominated responses. In the final case (Fig. 10.6d–f), the torsion mode is before the bending mode in the linear region. As the system is forced to the nonlinear region, there is no transition observed between the modes and the NNMs. The torsion mode remains dominant in the first NNM and the bending mode remains dominant in the second NNM.

It is important to remember that the behaviour observed and discussed previously is from a low order representation of a continuous structure. In this context, the validity of the use of a 2 mode NLROM comes into question. Due to the cumbersome nature of the full order model, only one of the cases is selected and compared with results obtained with its subsequent NLROM. To further ease the computational burden, comparisons are made between the NNMs calculated with the full order model [16] and the reduced order model. Recent work suggests that if the NLROM accurately predicts the NNMs of the full order model, then the NLROM will be able to predict the nonlinear response of the structure in the regions of the NNMs [4]. The case where $L_2 = 0.95*L_1$, where the bending mode has a lower frequency than the torsion mode, is used for comparison here and shown in Fig. 10.7. In the energy domain, Fig. 10.7a, the NLROM predicts the second NNM within 1 % error for the frequency range shown. However, as the first NNM reaches higher energies, the NLROM begins to diverge from the predicted solution. This divergence is also observed in the modal deformations of the first and second NNM shown in Fig. 10.7b and c, respectively. The observed divergence begins near the elastic limit of the structure and after the first NNM transitions from a bending dominant response to a torsion dominant response. Therefore, it is concluded that the NLROM produces an accurate representation of the system in the dynamic range of interest. Of course further comparison is needed between the experimental structure and the predicted results.

10.5 Conclusion

The linear and nonlinear results of a clamped-clamped beam attached to a cross beam with tip masses is presented. This system is unique as it demonstrates eigenvalue crossover and veering when the tip masses are moved. The case of veering is observed numerically and experimentally, providing confidence in the observed behaviour. Using nonlinear reduced order models, the nonlinear response of this system is explored as the tip masses are moved resulting in different frequency spacing of the eigenvalues. For specific configurations of the tip masses modal interactions are observed within the NNMs and an imperfect bifurcation occurs between the NNMs. In the region of bifurcation, the deformation shapes experience a rapid change between the two modes describing the system.

Although good agreement is seen between the full order and nonlinear reduced order models, further comparison is needed with the experimental structure in the nonlinear regime. Using forced responses and free decays, the NNMs will be identified and compared with the predicted NNMs to further validate the structural models.

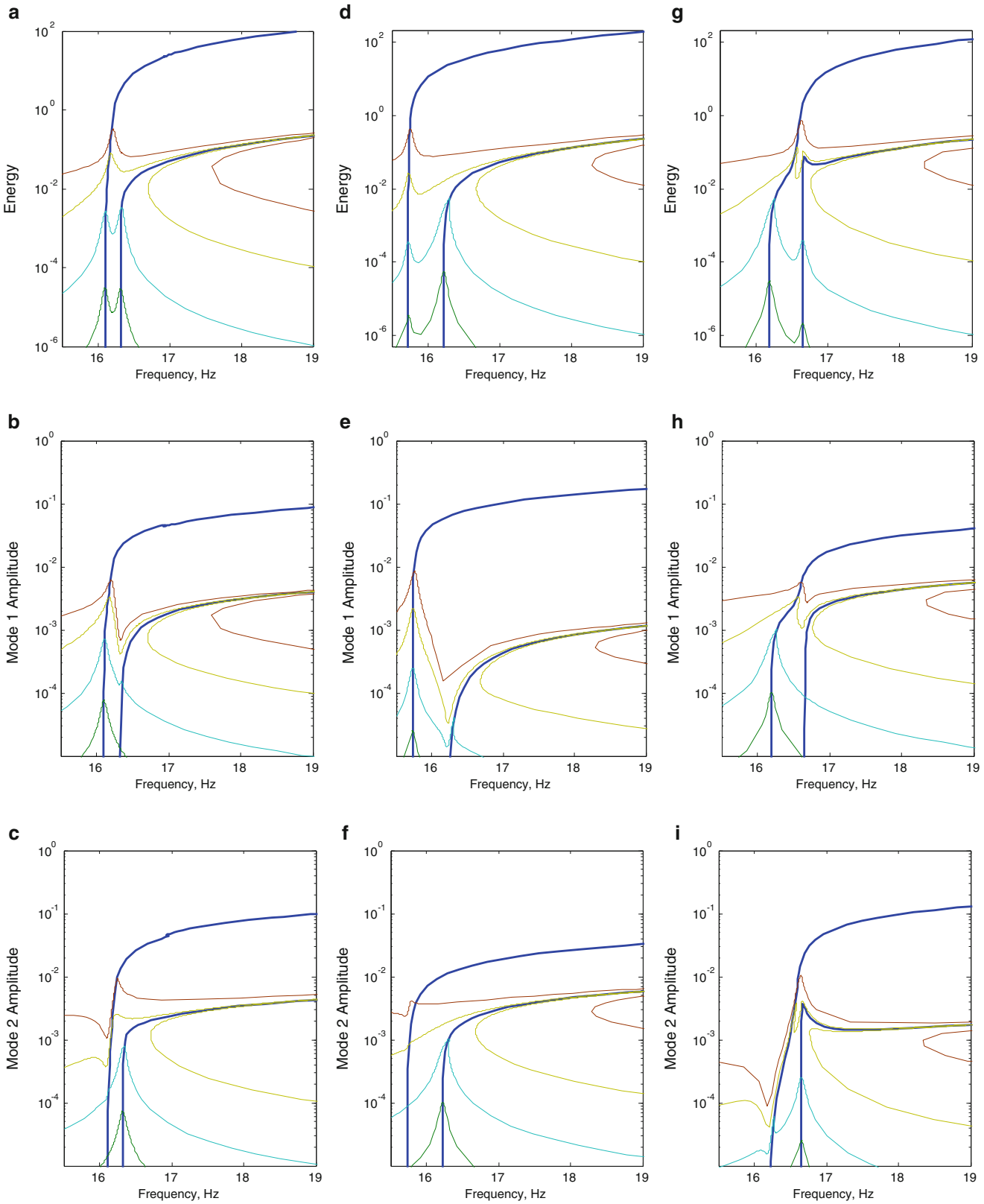

Fig. 10.6 Nonlinear normal modes (*blue line*) and forced responses (*green line* 0.01 N, *aqua line* 0.1 N, *light green line* 1 N, and *brown line* 10 N) of the asymmetric system when $L_2 = 0.95*L_1$ at (**a–c**) Change in Length = 0 mm. (**b–f**) Change in length = 10 mm, (**g–i**) Change in length = −10 mm

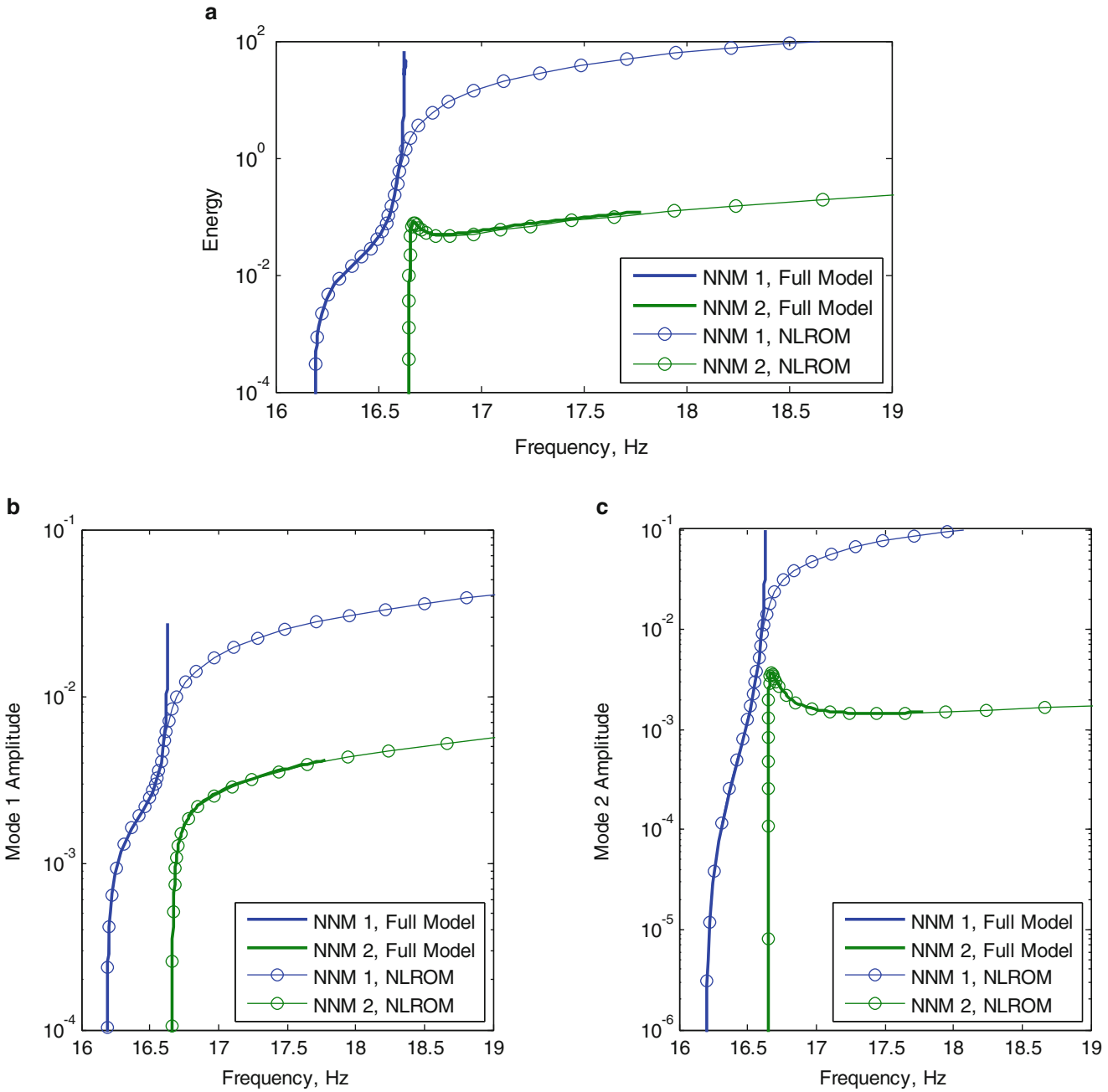

Fig. 10.7 Nonlinear normal modes and forced responses of full and reduced order model. (**a**) Energy domain, (**b**, **c**) Modal domain

References

1. Brincker, R., Lopez-Aenlle, M.: Mode shape sensitivity of two closely spaced eigenvalues. J. Sound Vib. **334**, 377–387 (2015)
2. Perkins, N.C., Mote, C.D.: Comments on curve veering in eigenvalue problems. J. Sound Vib. **106**(3), 451–463 (1986)
3. Leissa, A.W.: On a curve veering aberration. J. Appl. Math. Phys. **25** (1974)
4. Kuether, R.J., Brake, M.R., Allen, M.S.: Evaluating convergence of reduced order models using nonlinear normal modes. In: 32nd International Modal Analysis Conference (IMAC XXXII), Orlando, Florida, 2014
5. Doll, R.W., Mote, C.D.: On the dynamic analysis of curved and twisted cylinders transporting fluids. ASME J. Press. Vessel Technol. **98**(143–150), (1976)
6. Triantafyllou, M.S.: The dynamics of taut inclined cables. Q. J. Mech. Appl. Math. **37**, 421–440 (1984)
7. Behbahani-Nejad, M., Perkin, N.C.: Freely propagating waves in elastic cables. J. Sound Vib. **196**(189–202), (1996)

8. Du Bois, J.L., Adhikari, S., Lieven, N.A.J.: Experimental and numerical investigation of mode veering in a stressed structure. In: IMAC XXV, Orlando, FL, 2007
9. Lacarbonara, W., Arafat, H.N., Nayfeh, A.H.: Nonlinear interactions in imperfect beams at veering. Int. J. Nonlinear Mech. **40**, 987–1003 (2005)
10. Nayfeh, A.H.: Nonlinear Interactions: Analytical, Computational, and Experimental Methods. Wiley Series in Nonlinear Science. Wiley, New York (2000)
11. Nayfeh, A.H., Arafat, H.N., Chin, C.M., Lacarbonara, W.: Multimode interactions in suspended cables. J. Vib. Control **8**(202), (2002)
12. Emam, S.A., Nayfeh, A.H.: Nonlinear response of buckled beams to 1:1 and 3:1 internal resonances. Int. J. Nonlinear Mech. **52**, 12–25 (2013)
13. Lacarbonara, W., Rega, G.: Resonant nonlinear normal modes. Part II: activation/orthogonality conditions for shallow structural systems. Int. J. Nonlinear Mech. **38**, 873–887 (2003)
14. Allen, M.S.: Global and Multi-Input-Multi-Output (MIMO) Extensions of the Algorithm of Mode Isolation (AMI). In: George W. Woodruff School of Mechanical Engineering. Georgia Institute of Technology, Atlanta, Georgia (2005)
15. Gordon, R.W., Hollkamp, J.J.: Reduced Order Models for Acoustic Response Prediction. Air Force Research Lab (2011)
16. Kuether, R.J., Allen, M.S.: A numerical approach to directly compute nonlinear normal modes of geometrically nonlinear finite element models. Mech. Syst. Signal Process. **46**(1), 1–15 (2014)
17. Gordon, R.W., Hollkamp, J.J.: Reduced Order Models for Acoustic Response Prediction. Air Force Research Laboratory (2011)

Chapter 11
Tracking of Backbone Curves of Nonlinear Systems Using Phase-Locked-Loops

Simon Peter, Robin Riethmüller, and Remco I. Leine

Abstract In nonlinear systems the resonance frequency depends on the energy in the system. This change in resonance frequency contains valuable information about the systems behavior and the nonlinear normal modes (NNMs) associated with each point of the backbone curve. This information can e.g. be used for system identification. However, the accurate and efficient measurement of the backbone curve in nonlinear systems is still challenging. This contribution proposes a new method to measure the backbone curve which is based on the control concept of a Phase-Locked-Loop (PLL) which is well known in electronics applications. A properly designed PLL is capable of finding linear resonances but it can also be used for the tracking of energy dependent backbone curves. The new method provides very accurate results by using steady state responses in the nonlinear mode. In contrast to commonly used free decay measurements this approach eliminates transient effects. Yet, it is also very efficient and user friendly as an automated testing can be performed. The method is experimentally demonstrated on a beam structure with cubic nonlinearity. Furthermore the capability of tracking through internal resonant NNMs will be examined and new possibilities for quantitative measurements of these effects will be discussed.

Keywords Phase-locked-loop • Nonlinear normal modes • Nonlinear system identification

11.1 Introduction

For the identification of linear vibrating systems experimental modal analysis (EMA) is the standard procedure, not only because it provides extensive information about the system in a very condensed form, but also because it is a very fast and user friendly procedure. In recent years an increasing number of researchers have worked on developing an extension of modal analysis to nonlinear systems. Starting with the theoretical developments of Rosenberg [1], the concept of Nonlinear Normal Modes (NNMs) emerged as a promising approach within this development. Rosenberg's definition of NNMs as the synchronous periodic motion of a conservative system provides interesting insights into the nonlinear dynamics of conservative systems and provides a clear relation to linear modes. Extending the concept of nonlinear modes, Shaw and Pierre [2] proposed the invariant manifold approach showing that a motion of a dynamic system in a nonlinear mode can be described as a motion on a two dimensional manifold. However, for complex structures and experimental approaches the invariant manifold approach poses practical difficulties and many systems can be characterized based on the dynamics of an underlying conservative system. Hence, most research in the area of nonlinear modal analysis relies basically on Rosenberg's definition [3]. A slight change of this definition was proposed by Kerschen [4] explicitly including internal resonances by dropping the requirement of a synchronous motion. Numerous publications have shown the usefulness of this concept for understanding nonlinear dynamics even of complex structures like for example aerospace engineering [5, 6]. It also provides a clear relation to linear modes and can also be related to forced response analysis of damped systems [7, 8]. On the one hand reliable numerical algorithms such as shooting [9] and the Harmonic Balance Method (HBM) [10] have been proposed and on the other hand some effort has been made in experimentally determining NNMs. The first approach of experimentally determining the nonlinear modes of lightly damped structures was the phase resonance method proposed by Peeters [11]. For determining the NNMs a system is driven to resonance at a high excitation level, then the excitation is turned off and a time frequency analysis of the free decay is carried out. This method proved its robustness and accuracy in experimental applications [12, 13] and can still be regarded as the standard method for nonlinear modal testing. Even though more recently a phase separation concept has been proposed [14] the phase resonance approach remains an important basis for nonlinear modal analysis. However, there are some practical issues arising from this procedure. The tuning of the

S. Peter (✉) • R. Riethmüller • R.I. Leine
Institute for Nonlinear Mechanics, University of Stuttgart, Pfaffenwaldring 9, 70550 Stuttgart, Germany
e-mail: peter@inm.uni-stuttgart.de

G. Kerschen (ed.), *Nonlinear Dynamics, Volume 1*, Conference Proceedings of the Society for Experimental Mechanics Series,
DOI 10.1007/978-3-319-29739-2_11

excitation is troublesome especially in the case of strong nonlinearity where a jump in the Frequency Response Function (FRF) occurs. Close to resonance, even for small disturbances, the jump can occur prematurely. Also the tuning, which is usually done manually, is time consuming and the estimation of an excitation level driving the system in a nonlinear range requires some a priori knowledge about the system or several trial and error runs. Additionally, by using the time frequency analysis of a free decay, sophisticated signal processing such as wavelet transforms [15] is required and some inaccuracy might be induced due to transient effects.

This paper presents a novel method for phase resonance testing to overcome these practical issues by an automated procedure using a PLL. The PLL is originally an analogue circuit used in radio technology in the 1930s [16] and is nowadays widely used in electronics applications like radios, TVs or smart phones [17]. The general idea of PLL concepts is to generate a harmonic signal with a frequency which is tuned based on the phase difference to a reference signal. There are many different designs of PLLs which are all essentially nonlinear oscillators generating a harmonic output dependent on this phase difference. The design of the PLL has to be adapted to its application which can be the tuning of digital or analogue signals originating from linear or nonlinear systems [18, 19]. Yet, only few attempts have been made to use these concepts for the measurement of mechanical structures. Most of them remain theoretical and the examples are mostly numerical ones [20]. There have been attempts to use PLLs in nonlinear micro systems modeled with one DOF [21] but the applicability for testing macro scale mechanical systems or continuous structures is mostly unclear. A publication by Mojrzisch [22] showed the usefulness of the PLL experimentally for the measurement of nonlinear FRFs of a macro scale single DOF Duffing type system by phase sweeping. However, to the authors knowledge there have no attempts been made to use the PLL for tracking of backbone curves of nonlinear continuous structures and exploit its potential for the measurement of NNMs.

The paper is organized as follows. In Sect. 11.2 some basics of phase resonance testing for nonlinear structures are briefly reviewed. In the subsequent Sect. 11.3 some more specific aspects of phase resonance method using the PLL including some design aspects of the PLL used within this paper are explained. In Sect. 11.4 a numerical example is used to illustrate the method and highlight some of its characteristics. The numerical example is followed by an experimental demonstration of its functionality in Sect. 11.5. The paper closes with a conclusion and some aspects of future work in Sect. 11.6.

11.2 Nonlinear Modal Analysis Using the Phase Resonance Method

A general mechanical system with conservative nonlinearities can be described in a spatially discretized form by the differential equation

$$\boldsymbol{M}\ddot{\boldsymbol{x}} + \boldsymbol{D}\dot{\boldsymbol{x}} + \boldsymbol{K}\boldsymbol{x} + \boldsymbol{F}_{\mathrm{nl}}(\boldsymbol{x}) = \boldsymbol{F}_{\mathrm{exc}}(t), \tag{11.1}$$

where $\boldsymbol{M}$ denotes the mass matrix, $\boldsymbol{D}$ the viscous damping matrix, $\boldsymbol{K}$ the linear stiffness matrix and $\boldsymbol{F}_{\mathrm{nl}}(\boldsymbol{x})$ represents a vector of nonlinear, conservative forces. The vector of external excitation is represented $\boldsymbol{F}_{\mathrm{exc}}$. In contrast, the NNMs of an autonomous conservative system are governed by a differential equation of the form

$$\boldsymbol{M}\ddot{\boldsymbol{x}} + \boldsymbol{K}\boldsymbol{x} + \boldsymbol{F}_{\mathrm{nl}}(\boldsymbol{x}) = \boldsymbol{0}. \tag{11.2}$$

For numerical systems periodic solutions of this differential equation can be obtained in a straightforward way using shooting or the HBM. These periodic solutions provide the NNMs of the system and can for example be visualized in Frequency Energy Plots (FEPs) [4]. Due to its high efficiency and its filtering property, which is particularly interesting in conjunction with measurements, the numerical NNM calculations throughout this paper are obtained by the HBM. The details of the numerical method are described in a previous publication [23]. The experimental realization of periodic motions of systems which motions are governed by differential Eq. (11.2) is more difficult as undamped systems cannot be realized practically as there are always sources of material damping or damping in interfaces of coupled structures. Hence, the forced and damped system described by Eq. (11.1) has to be considered as a representation of real systems. For lightly damped structures the assumption of proportional damping can provide a reasonable approximation. For the realization of a NNM motion of the underlying conservative system, the non-conservative system is sought to behave like a system described by Eq. (11.2). By comparing Eqs. (11.2) and (11.1) it can be seen that theoretically the forcing should exactly balance out the damping for all points of the structure and for all times i.e.

$$\boldsymbol{D}\dot{\boldsymbol{x}}(t) = \boldsymbol{F}_{\mathrm{exc}}(t), \forall t. \tag{11.3}$$

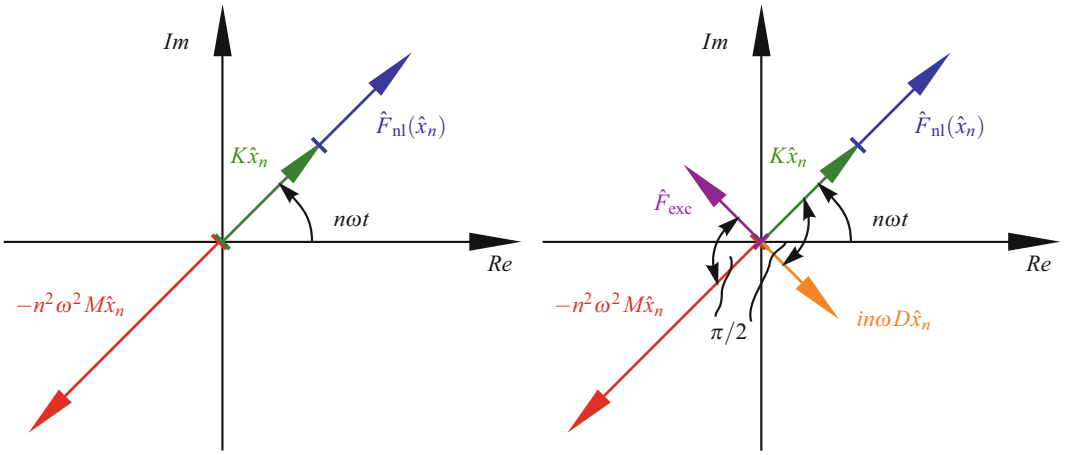

Fig. 11.1 *Left*: Pointer diagram for the n-th harmonic of a steady state NNM motion. *Right*: Pointer diagram for the n-th harmonic of a steady state NNM motion in a forced and damped system

For the realization of this state Peeters [11] derived a nonlinear mode indicator function similar to the mode indicator functions used in linear EMA. The derivation can be done by developing the displacements into an infinite cosine series and practically regarding the system's motion in the frequency domain. Similarly, the same mode indicator function can also be derived graphically using pointer diagrams. The application of pointers as a graphical representation of a signal is more common in electrical engineering but was also used e.g. in [24] in the context of multi-harmonic excitation of linear mechanical systems. As the NNMs represent a periodic motion of all DOFs, they can be transformed into the frequency domain using an infinite Fourier transform. Hence, the motion of the system can be represented by a fundamental frequency ω plus an infinite number of higher harmonics. For every harmonic the dynamic force equilibrium yielding the periodic motion can then be graphically represented as a family of pointers in the complex plane. To obtain a periodic motion the dynamic forces have to balance out for every harmonic. In Fig. 11.1 on the left this dynamic force equilibrium for the n-th harmonic is depicted symbolically for an autonomous conservative system. If this equilibrium condition is fulfilled for every harmonic, the system moves in a periodic NNM motion. This approach can be also viewed as a graphical representation of the HBM on a signal processing level. The same condition holds for a forced and damped system executing a steady state motion, simply adding two more pointers, namely the pointer of the n-th harmonic excitation force and damping force. It can be clearly seen that the pointer of the damping forces must be fully compensated by the pointer of the excitation forces, to ensure the NNM motion which is depicted in the left pointer diagram. As in the case of viscous damping, the damping force has a phase lag of $\pi/2$ with respect to the conservative restoring forces, or the displacement respectively. This means that the phase lag between the excitation force F_{exc} and the displacement must be $\pi/2$ for every harmonic n to generate an NNM motion.

Practically, the exact phase condition is impossible to maintain as it implies a fully populated forcing vector $\hat{\boldsymbol{F}}_{\mathrm{exc}}$ with higher harmonic amplitudes and phases that have to be adjusted dynamically for every point on an NNM branch. This issue was addressed in several publication [8, 11, 12] and it was shown that a single harmonic forcing mostly provides a sufficient approximation for the NNM measurement in the case of light damping. This behavior can be explained as in most systems the majority of the NNM motions are governed by the fundamental harmonic and also the NNM frequency can in most cases be estimated accurately by a single harmonic approximation. However, especially near internal resonances the higher harmonics are amplified by higher modes and have significant influence on the systems motion. In this case the appropriate forcing has to be regarded more closely. In the following, a single harmonic force at a single point of the structure will be used to realize an approximate appropriate excitation. Some issues related to the accuracy of this approach and the presence of internal resonances are addressed in the numerical study in Sect. 11.4.

11.3 Phase Resonance Testing Using the Phase-Locked-Loop

Based on the phase criterion, derived in the previous section the NNM motion of a system can be approximately excited by an appropriate harmonic forcing with a phase lag of $\pi/2$ with respect to the response. In previous publications the tuning of the phase was done manually comparing the phase of the excitation with the phase of the response. This task can be

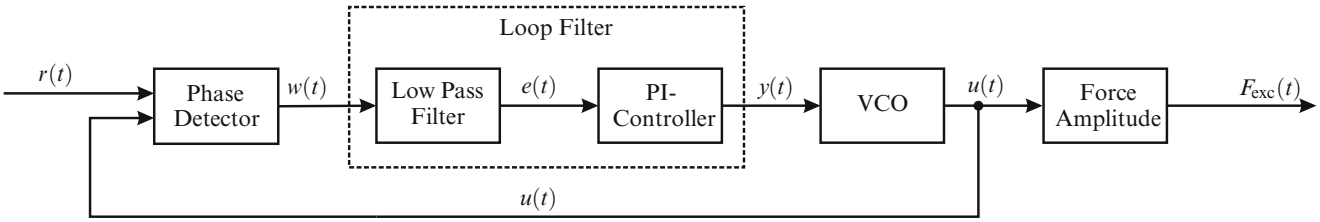

Fig. 11.2 Schematic structure of the PLL for force generation

automated by the use of a PLL which is a concept for the control of the phase between a reference and a harmonic output signal. There are different implementations of the PLL for different applications such as digital or analogue PLLs. Both versions of PLLs can be implemented electronically e.g. using Simulink. In the following, the design of an analogue PLL, which was implemented for the tuning of the phase in the context of NNM testing, is briefly described.

For this purpose a reference signal $r(t)$ of the system has to be connected to the PLL. The PLL synchronizes the phase of its output with this reference signal except for a desired phase difference. The reference signal can for instance be chosen based on the displacement of a reference point which then means that the phase difference of the output signal should be $\pi/2$. The equations for the PLL controller are derived in the following for this specific case. In an experimental setup it is reasonable to chose a reference signal based on the quantity that can directly be measured. Since in the experiments in Sect. 11.5 accelerometers are used, the reference signals in the experiments are based on the system's acceleration and the phase difference is set to $-\pi/2$. This can be achieved by simply multiplying the reference signal with a factor of -1 compared to the case of the displacement based measurements. Generally, a PLL used for the excitation of a structure consists of the blocks displayed schematically in Fig. 11.2.

The first block is the phase detector that extracts the phase of the output of the system with respect to the reference signal. There are different implementations of phase detectors [18]. In the following a mixing phase detector is used which is comparing a reference signal $r(t)$ with the output of the VCO $u(t)$ by a multiplication yielding

$$w(t) = r(t)u(t). \tag{11.4}$$

For the nonlinear modal analysis as a reference signal the displacement $x(t)$, velocity $\dot{x}(t)$ or acceleration $\ddot{x}(t)$ can directly be used depending on which quantity is measured. However, as was shown by Fan [20] it is advantageous to modify the signal of for instance the displacement by replacing it with its sign

$$r(t) = sign(x(t)) = \begin{cases} -1 & x(t) < 0 \\ 1 & x(t) \geq 0. \end{cases} \tag{11.5}$$

This modification leads to a faster and more robust PLL, as on the one hand the signal is amplified in regions which are far from resonance. On the other hand the stability criterion for the controller derived in [20] becomes independent of the forcing amplitude. For the phase detector both signals are expressed in form of Fourier series and their product can be written as

$$w(t) = \hat{r}sin(\omega_r t + \phi_r)cos(\omega_v t + \phi_v) + higher\ order\ terms\ (HOT), \tag{11.6}$$

where ω_r and ω_v denote the frequency and ϕ_r and ϕ_v the phase of the fundamental frequency of the reference signal and the VCO respectively. It should be noted that the fundamental of the reference signal is generally different to the fundamental harmonic of the displacement or acceleration, respectively. This hold especially for the amplitude providing previously mentioned advantages. However, it should also be kept in mind that, if there is a phase shift between the fundamental harmonic and higher harmonics, there can also be a slight shift in the sign function in Eq. (11.4) and the phase of its fundamental harmonic. This effect will be illustrated in the numerical example in Sect. 11.4. After some trigonometric manipulations of Eq. (11.6) and the assumption that the frequency error is small $\omega_r \approx \omega_v \approx \omega$ the output of the phase detector can be expressed as a function of the phase error $\theta_e = \phi_v - \phi_r$ and higher frequency terms

$$w(t) = \frac{1}{2}\hat{r}(sin(\theta_e) + sin(2\omega t + \phi_v + \phi_r)) + HOT. \tag{11.7}$$

The output of the phase detector is passed to the second part of the PLL, which is the loop filter consisting of a low pass filter and a PI-controller. The low pass filter that can be described by the differential equation

$$\omega_l \dot{e} + e = w(t), \tag{11.8}$$

with the cutoff frequency ω_l. This means that the output of the low pass filter is a function of the phase error θ_e if the higher frequency terms in Eq. (11.7) are suppressed sufficiently. The output of the low pass filter is the control input of the PI-controller that can be described by the state space model

$$\begin{aligned} \dot{z} &= e \\ y &= K_p e + \frac{K_p}{T_i} z. \end{aligned} \tag{11.9}$$

The parameters K_p and T_i are the tuning parameters of the proportional and integral part of the controller. The exact tuning of these parameters is rather uncritical in the PLL as long as the stable low pass property of the PI-controller is retained. The PI-controller provides the control signal for the third part of the PLL, namely the Voltage-Controlled-Oscillator (VCO), that generates the excitation signal for the structure. The VCO uses the fact that the frequency is the derivative of the phase, and hence can be realized as an integrator

$$\theta_v = \int_0^t \omega_c + K_v y(\tau) d\tau, \tag{11.10}$$

with the center frequency ω_c and tuning parameter K_v. The center frequency ω_c is the frequency with which the VCO oscillates when no reference signal is attached and the tuning factor K_v adjusts the influence of the control input coming from the loop filter. Hence, the cosine output of the VCO is generated

$$u(t) = cos(\theta_v). \tag{11.11}$$

This output signal is then fed back to the phase detector and the phase difference is minimized until the VCO creates a cosine signal with the same phase as the reference signal. Once this is the case the PLL is said to be in a locked state. The output of the VCO is multiplied by the excitation amplitude yielding

$$F_{\text{exc}}(t) = \hat{F}_{\text{exc}} u(t). \tag{11.12}$$

This force signal is then used for the excitation of the structure i.e. the created cosine shaped force signal is shifted by an angle of $\pi/2$ with respect to the sinusoidal reference signal in Eq. (11.6).

For a more detailed discussion of the design of PLLs there are numerous references [17, 18, 25]. Regarding the stability properties of the PLL, criteria can be derived using linear analysis methods like the Routh-Hurwitz criterion [20, 26] and nonlinear analysis methods like Lyapunov functions and La Salle's theorem [27]. It should be noted at this point that parameters can be found for this specific design of the PLL that ensure the stability of the PLL controller independent of the parameters of the attached system [27], which is essential when the PLL is used for the measurement of unknown structures.

With the PLL the backbone curve of a system can be measured in an automated two step methodology. In the first step the linear resonance is detected with low level excitation. Once the PLL is in a locked state the forcing level is incrementally increased such that the energy in the system increases. In nonlinear systems the resonance frequency changes with increasing energy and the PLL has to adjust the frequency of the VCO output with increasing energy to maintain the phase resonance criterion. The steady state vibration in resonance can be analyzed e.g. with an FFT or wavelet transform to extract the frequency amplitude dependence of the system. The use of the PLL for the measurement of NNM branches has several consequences compared to classical phase resonance testing:

1. There is no need for manual tuning of the phase as the PLL tunes the VCO and therefore the frequency of the excitation signal automatically.
2. The forcing is increased from a low to a high level in resonance until a desired level of vibration is reached such that the linear and nonlinear range is covered but the structure is not damaged. No a priori knowledge about nonlinear range or maximum forcing amplitude is required.

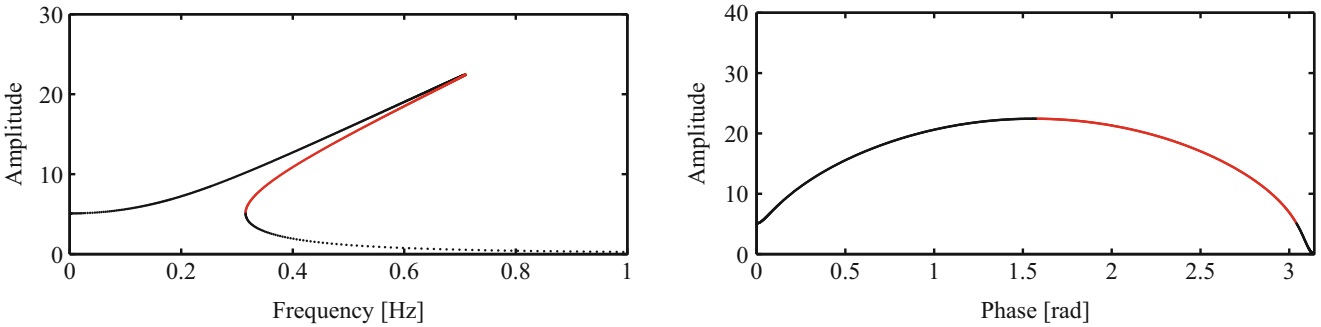

Fig. 11.3 FRF (*left*) and phase-amplitude-relation (*right*) for Duffing type example system (*black*: stable solutions, *red*: unstable solutions)

3. All measurements are carried out in steady state. No transient effects are present and signals can be analyzed with a simple FFT.
4. For low level excitation the linear resonance frequency is found and higher harmonics are negligible during resonance detection. Depending on the center frequency the VCO will lock to the corresponding mode.
5. In the nonlinear range small changes in excitation result in small changes of resonance frequency. Thus, the PLL reaches the locked state very fast and safely after increasing the excitation amplitude.
6. The PLL stabilizes unstable branches of the system such that premature jumps during the tuning in highly nonlinear systems are avoided. Because the control is based on the phase and the phase-amplitude relation is unique in the neighborhood of a mode as depicted in Fig. 11.3 all points of the phase-amplitude plane can be measured applying phase control [22].

These features will be illustrated in the following section by numerical examples before the method is applied to an experimental benchmark.

11.4 Parametric Study of a Numerical Example System

In this section the characteristics of the nonlinear modal test using the PLL are illustrated by a numerical example. Therefore, a beam structure similar to the ECL benchmark beam [28] is used as an example system. As illustrated in Fig. 11.4 the system consists of seven linear Eurler-Bernoulli beam elements and has in total 14 DOFs. The beam is clamped on the left-hand side and is supported by a cubic and linear spring on the right-hand side. The system is excited at the second node and its parameters are listed in Table 11.1.

In the following mainly the first two NNMs of the system are considered which originate from the linear eigenfrequencies at 22.4 and 121.1 Hz respectively. Both of these modes are affected by the nonlinearity as it can be seen in the frequency energy plot (FEP) in Fig. 11.5. The FEP was calculated using the HBM taking into account three harmonics which is sufficient to represent a 1:3 internal resonance, which is the only internal resonance practically playing a role in the energy range of interest.

For the tests with the PLL the damped and forced system has to be regarded. The damping in the system is assumed to be light and the hypothesis of proportional damping of the form

$$\boldsymbol{D} = \alpha_1 \boldsymbol{M} + \alpha_2 \boldsymbol{K} \tag{11.13}$$

is chosen. The coefficients are set to $\alpha_1 = 1$ and $\alpha_2 = 3 \times 10^{-4}$ which is similar to the damping observed in experiments. In the first parametric study the functionality of the PLL method for tracking of the backbone curve is illustrated. The structure is excited at the second node with a harmonic force and the displacement of the same node is also chosen as reference for the PLL tuning. Generally, the choice of the reference node is arbitrary as the NNM motion is assumed to be a monophase motion. However, this assumption does not necessarily hold in the damped and forced system as there might be a small phase difference between different DOFs. Additionally, the phase and amplitude of higher harmonics can have some influence on the phase of the reference signal in Eq. (11.6). To get started, it seems to be a natural choice to use the node of the excitation as reference. The system is modeled in Matlab/Simulink and time integration is used to study the closed loop behavior of the system including the PLL. The amplitude of the excitation force is incrementally increased as shown in Fig. 11.6 starting

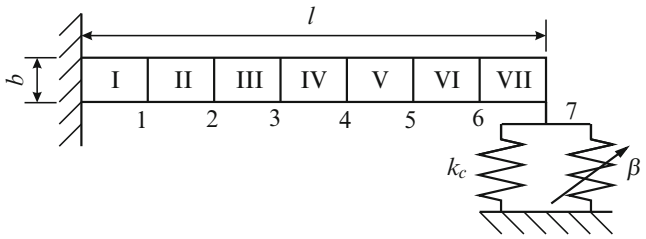

Fig. 11.4 Schematic sketch of the experimental beam

Table 11.1 Parameters of numerical beam structure

Parameter	Value	Unit
E	185	GPa
ρ	7830	kg/m^3
β	8×10^9	N/m^3
k_c	1000	N/m
l	700	mm
b	12	mm

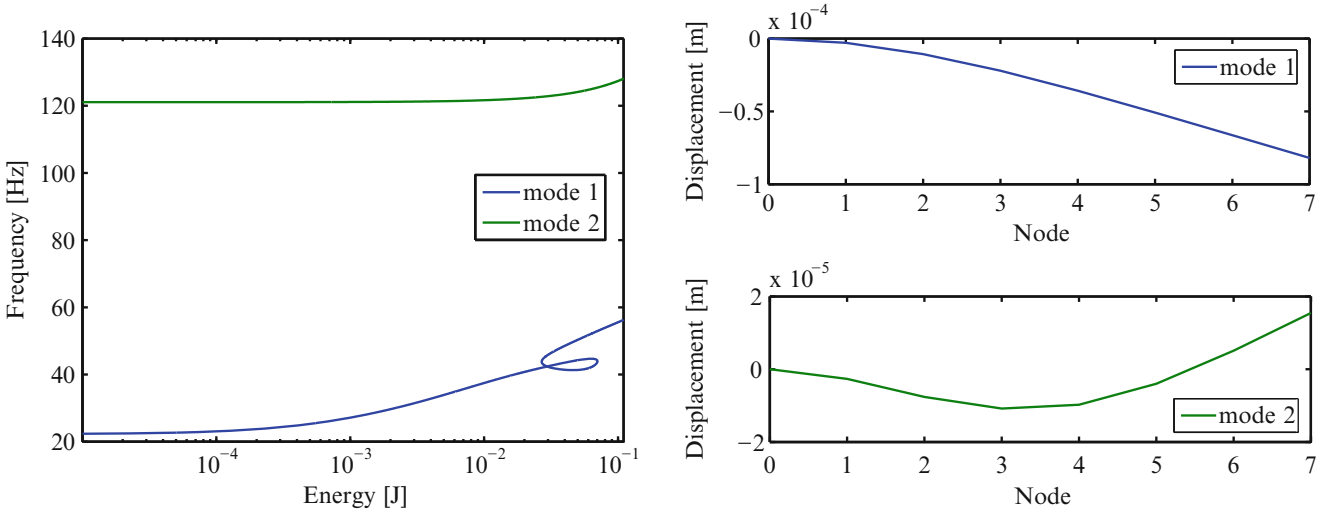

Fig. 11.5 *Left*: FEP of first two modes of the beam. *Right*: Mode shapes in linear range of the first two modes

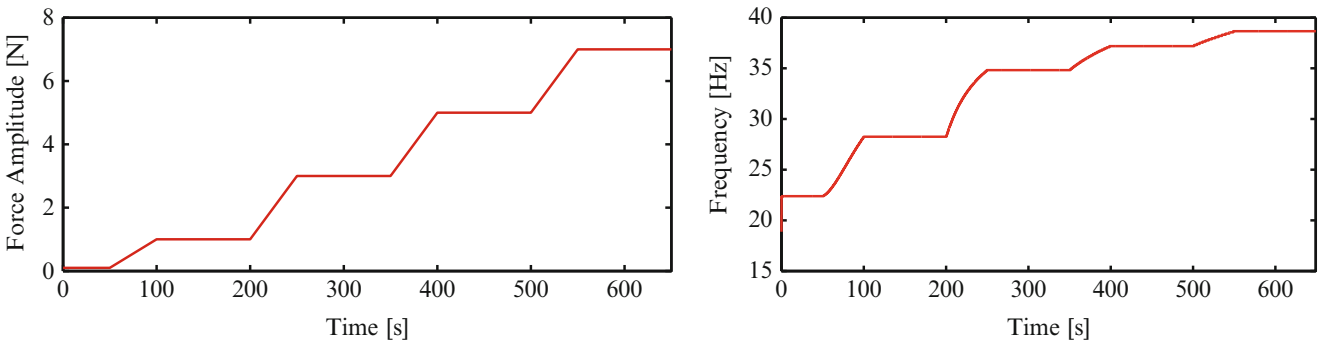

Fig. 11.6 *Left*: Amplitude of harmonic forcing. *Right*: Frequency of maximum wavelet coefficient of the force signal

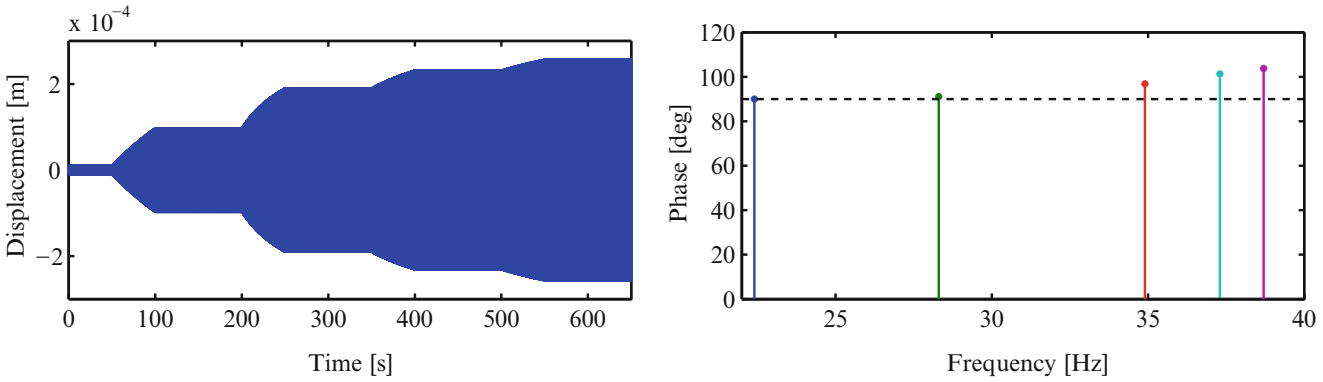

Fig. 11.7 *Left*: Time signal of the acceleration at the reference node. *Right*: Phase of first harmonic with respect to the forcing

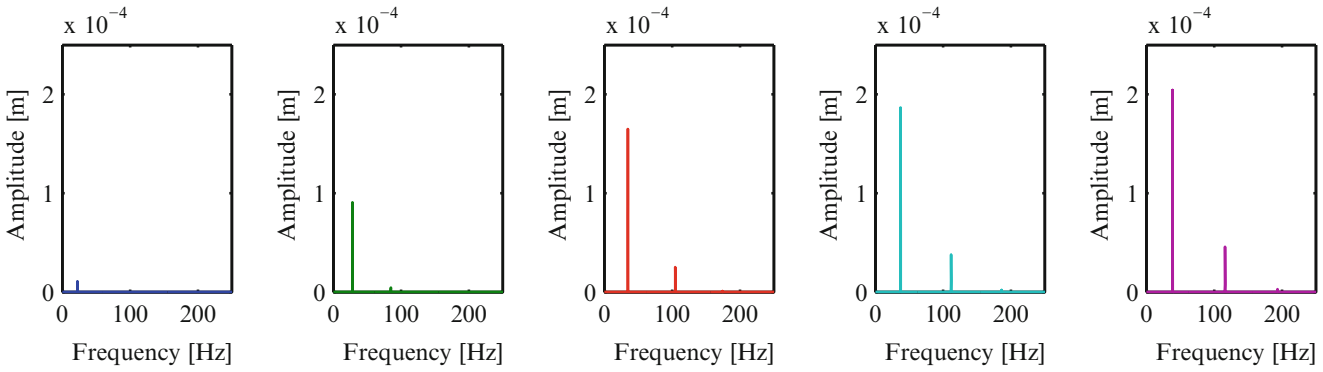

Fig. 11.8 Amplitude spectrum of response for increasing forcing amplitude $\hat{F}_{\text{exc}} = \{0.1, 1, 3, 5, 7\}$ N

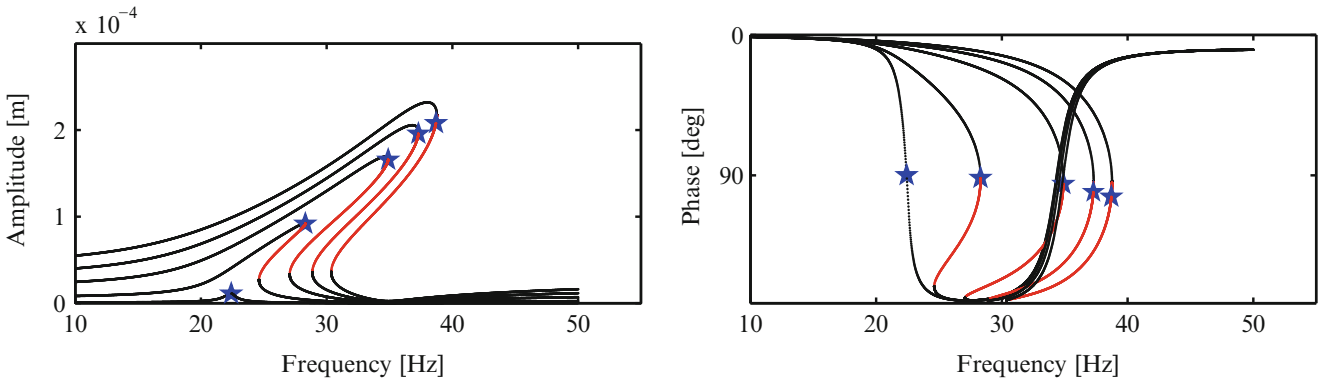

Fig. 11.9 *Left*: First harmonic FRF for system with harmonic excitation (*black*: stable; *red*: unstable). *Right*: Phase lag of first harmonic with respect to the forcing (*black*: stable; *red*: unstable)

from an initial value of 0.1 N, where the structure behaves almost linearly. The instantaneous frequency of the forcing which was extracted by the wavelet transform is plotted in Fig. 11.6. It can be observed that the linear eigenfrequency is found quickly and the PLL reaches the locked state. By increasing the forcing level up to 7 N the resonance frequency is shifted and the PLL tunes the excitation frequency.

The displacement at the reference node is displayed in Fig. 11.7. For the analysis of the results, this displacement is transformed into the frequency domain using an FFT such that the amplitudes (Fig. 11.8) and phases (Fig. 11.7) can be compared to the calculated FRFs of the system (Fig. 11.9). The FRFs are calculated using the HBM taking into account five harmonics and the stability of the FRF is determined using Hill's method [29].

In comparison, the amplitude and frequency of the first harmonic of the time signal obtained by the PLL is in very good agreement with the first harmonic of the FRF. The same also holds for higher harmonics which are not studied in a more detailed way at this point. However, an interesting aspect of the PLL testing can be observed regarding the phase lag of the

first harmonic with respect to the force. For low level excitation the phase lag is maintained at exactly 90° but for increasing excitation levels there is an increasing deviation. This effect is caused by the increase of the third harmonic, which is not in phase with the fundamental harmonic if only an imperfect force appropriation is applied. The phase detector basically relies on the first harmonic of the reference signal. As the sign detection in Eq. (11.4) is used to generate the reference signal, the phase of its first harmonic is shifted if the displacement signal contains higher harmonics with a shifted phase with respect to the fundamental. Still, this effect plays a minor role especially as the appropriate excitation is approximated by a single harmonic single point force, anyway. In the present example this can be observed when the system is driven close to the 1:3 internal resonance, where the third harmonic is amplified by the second mode. Another interesting aspect of the PLL method can herein be observed regarding the stability calculations of the FRF in Fig. 11.9. The points in which the system is driven by the PLL controller are marked with the blue star in the FRF and phase response. It can be seen that due to the small phase deviation induced by higher harmonics the PLL drives the system in a region which is unstable in the FRF. This illustrates the stabilizing effect of the close loop on the system that also helps to drive the system near jumps without facing the problem of premature jumping.

11.4.1 Effect of Internal Resonance on PLL Measurements

In the FEP it was observed that the parameters of the beam are chosen in a way that a 1:3 internal resonance can strongly affect the system's behavior when the energy exceeds a certain level. Once the system is excited at a certain level the third harmonic becomes strongly amplified by the second mode. As previously shown the strong third harmonic component may lead to a small shift in the detected phase, which depends on the amplitude and the phase of the third harmonic component relative to the fundamental. To study this effect, the forcing amplitude is increased further as it is shown in Fig. 11.10 and the robustness of the PLL method is investigated. The FRF in Fig. 11.10 shows that due to the internal resonance the amplitude of the third harmonic can be up to one third of the fundamental harmonic. The tests with the PLL method show that nevertheless the phase, frequency and amplitude errors remain small. For illustration, the test results for this specific test case are shown in Figs. 11.11 and 11.12 respectively.

It is also interesting to observe that for the highest forcing the region of the internal resonance is already passed, which results in a vanishing phase deviation. Generally, it was observed that the method is very robust even in the presence of strong higher harmonics. Even though there is some inaccuracy in the region of the internal resonance the PLL is capable of keeping track of the NNM branch. For motions which are dominated by a higher mode due to an internal resonance, first numerical experiments showed that the PLL can lock to the higher mode and tune the excitation frequency based on this mode. In this context the choice of the reference node seems to be an interesting factor, as at different points of the structure different modes can be measured. A more detailed discussion of these cases is beyond the scope of this paper since these effects were also not observed in the subsequent experimental test.

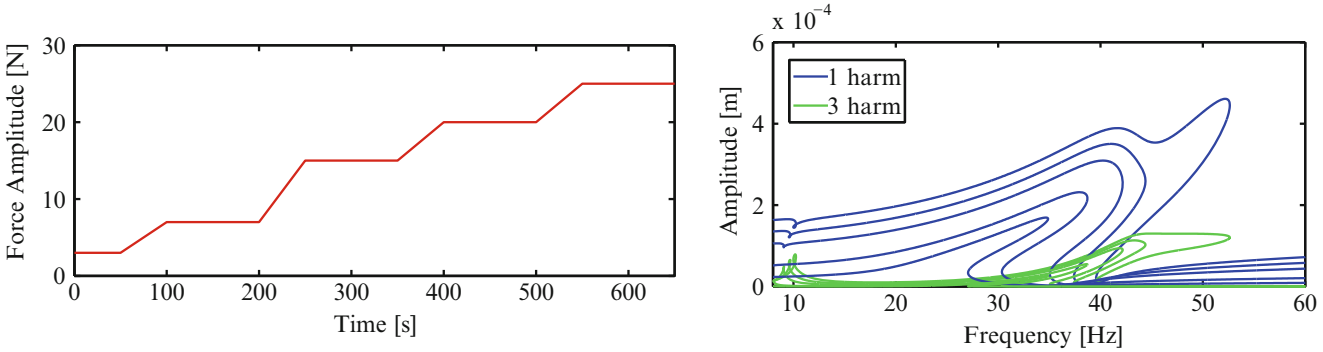

Fig. 11.10 *Left*: Amplitude of harmonic forcing. *Right*: First and third harmonic FRF at reference node

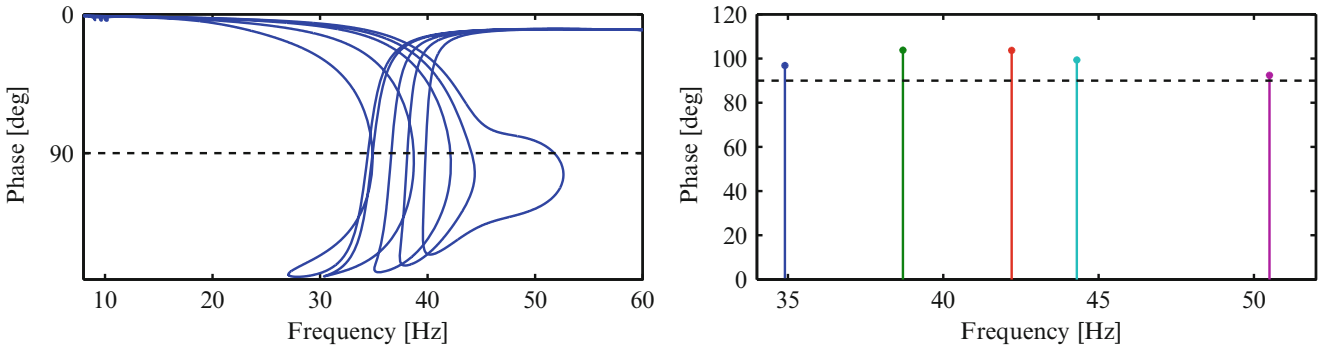

Fig. 11.11 *Left*: Phase first harmonic of calculated FRF. *Right*: Phase of first harmonic of PLL test

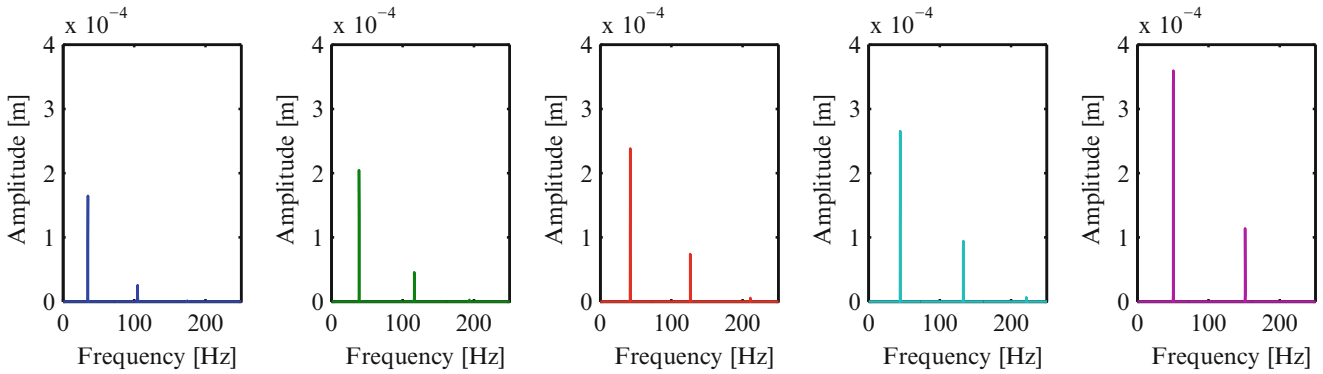

Fig. 11.12 Amplitude spectrum of response for increasing forcing amplitude $\hat{F}_{\text{exc}} = \{3, 7, 15, 20, 25\}$ N

11.5 Experimental Demonstration for a Beam with Cubic Nonlinearities

The experimental setup is similar to the numerical example in the previous section with some different parameters. It consists of a clamped steel beam with a thin beam at the tip which is also clamped. The clamping of the thin beam can be moved by an adjusting screw and the pretension of the specimen can be measured with a strain gauge located on the thick beam. Due to the clamped-clamped setup of the beam structure a geometric nonlinearity can be observed in the case of large deflection. A photo of the setup is displayed in Fig. 11.13 and a schematic sketch where the small beam and its nonlinearity is represented by a three parameter model is shown in Fig. 11.14.

The parameters for the beam without pretension, that were obtained through a model updating procedure based on the NNMs of the system which was presented in a previous publication [30], are listed in Table 11.2. The differences compared to the numerical example mainly have two consequences. Firstly, the 1:3 internal resonance is not observed in the practical experiment as even for the setup without pretension the first eigenfrequency is higher than one third of the second one. For this setup the FRF in the linear range is shown in Fig. 11.15. The higher resonance frequencies that appear in the FRF also do not lead to significant internal resonances. Secondly, the adjustment of the pretension in the beam shifts the linear eigenfrequencies as it can be seen in Fig. 11.15. It can be observed that the first eigenfrequency is affected most by an increasing pretension, which means that also for higher pretension no 1:3 internal resonance will play a role.

The PLL is implemented on a DSPACE rapid prototyping system and the force is measured with a load cell at the point of the shaker excitation. The reference signal for the PLL is obtained based on accelerometer measurements. In the first experimental test, a parametric study for the detection of the linear resonance frequency using the PLL is carried out. Therefore, the beam without pretension is excited on the second node with a small excitation amplitude of 0.5 N and the effect of different center frequencies of the VCO is investigated. The second node was also used as reference for the phase criterion. The wavelet transform was used to extract the instantaneous frequency of the excitation force over time. This frequency is plotted for the different center frequencies in Fig. 11.16. It can be observed that the VCO starts oscillating at its center frequency and therefore generates a harmonic force signal with this frequency at the very beginning of the measurement. Then the frequency changes until the PLL is in a locked state, generating a steady state harmonic signal with a certain frequency. For the first five center frequencies, the PLL locks to the first eigenfrequency even for starting frequencies

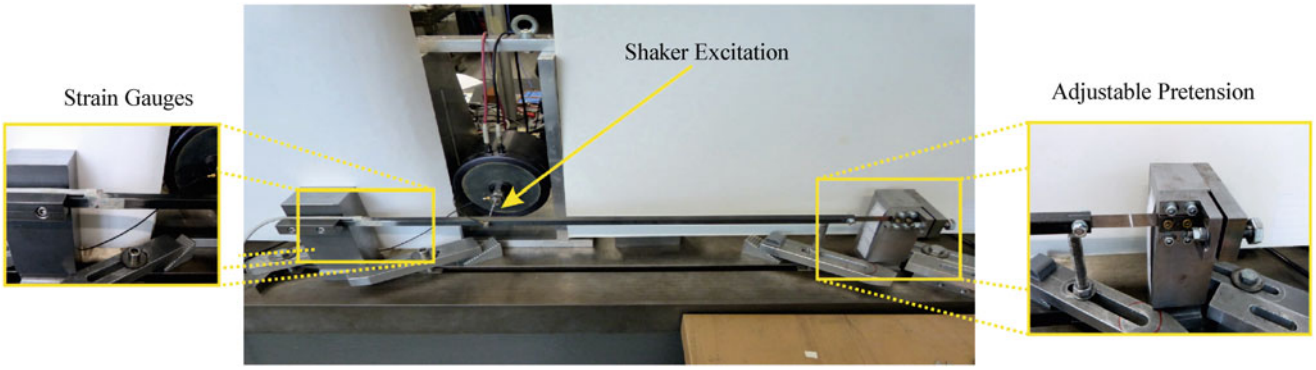

Fig. 11.13 Experimental setup of the benchmark beam

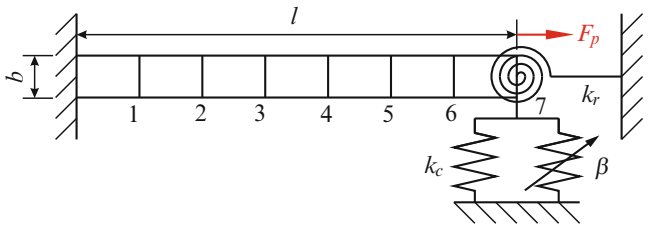

Fig. 11.14 Schematic sketch of the experimental beam

Table 11.2 Parameters of beam without pretension

Parameter	Value	Unit
E	186	GPa
k_c	5525	N/m
k_r	217	Nm/rad
β	203×10^6	N/m^3
l	700	mm
b	12	mm

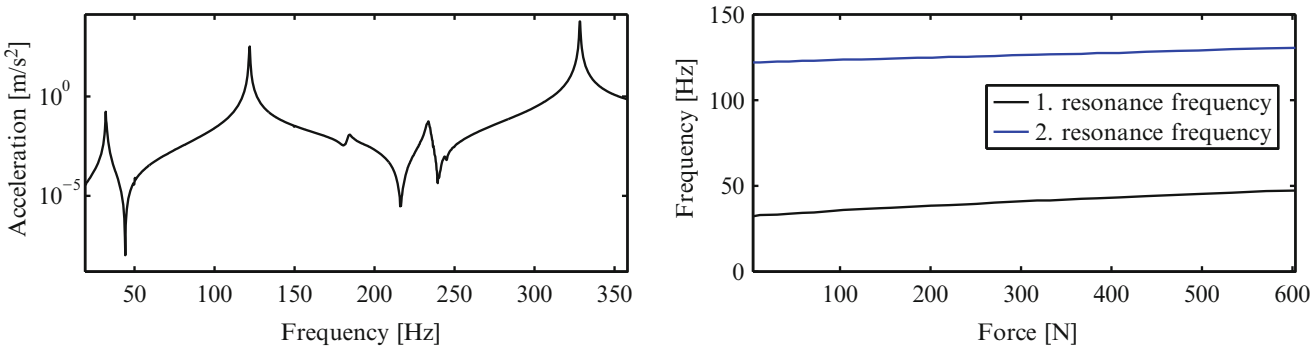

Fig. 11.15 *Left*: FRF for beam without pretension. *Right*: Resonance frequencies of the beam dependent on pretension

which are up to 70 % off the actual eigenfrequency. It can also be seen that the detection of the eigenfrequency works for an initial center frequency which is higher or lower than the eigenfrequency. However, if the initial frequency is too high, the motion is dominated by the second mode and the PLL locks to this mode as can be observed in the last figure. The parametric study clearly shows that the center frequency of the VCO is uncritical for the detection of the modes such that no a priori knowledge of the linear eigenfrequencies is required.

After detection of the linear eigenfrequency, the excitation amplitude is incrementally increased and the capability of the PLL to track the backbone curve in the nonlinear range is investigated. For this test, the pretension is increased to 300 N,

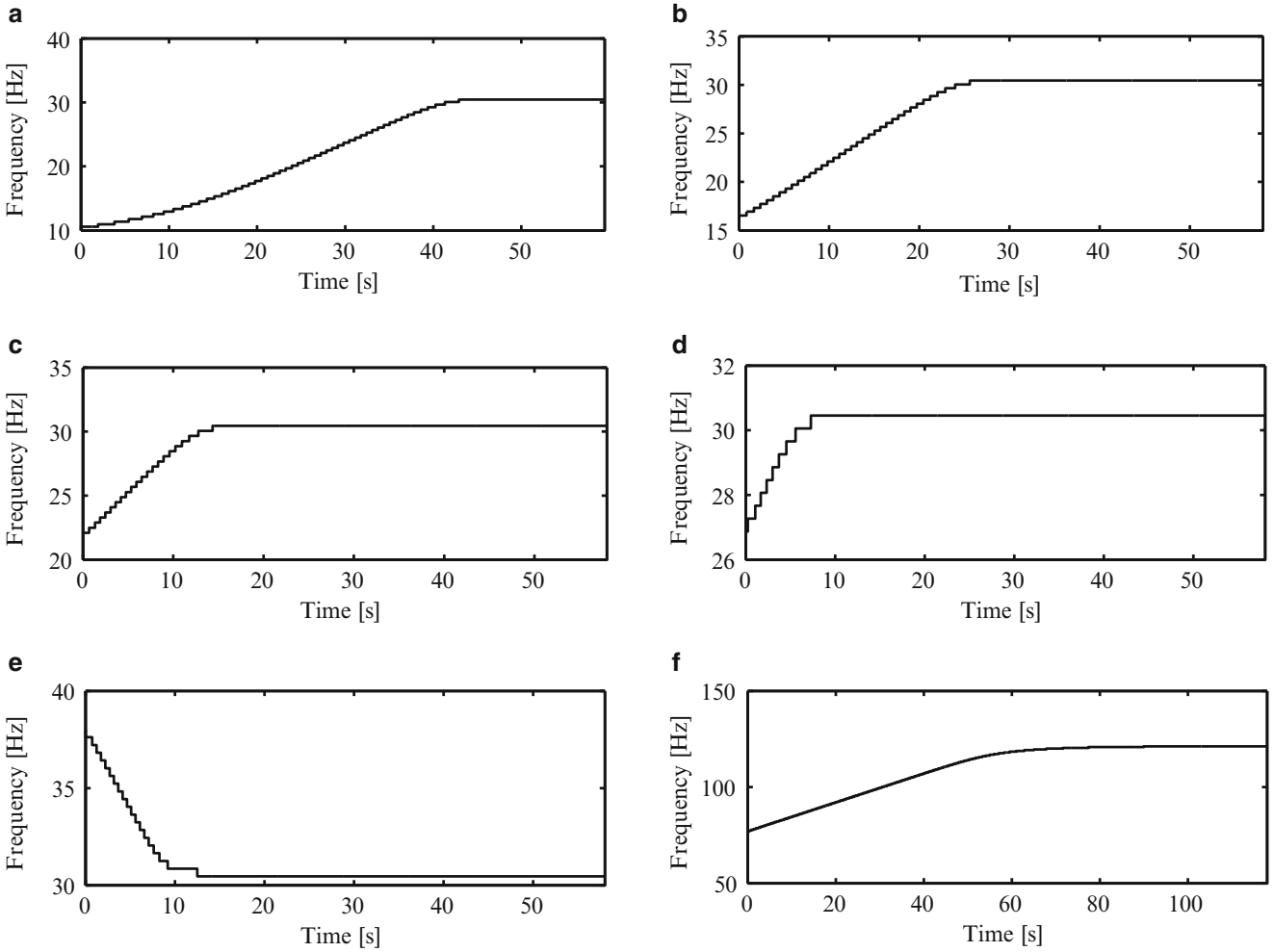

Fig. 11.16 Frequency with maximum forcing amplitude for different VCO center frequencies $f_c = \{10, 15, 20, 25, 37, 75\}$ Hz

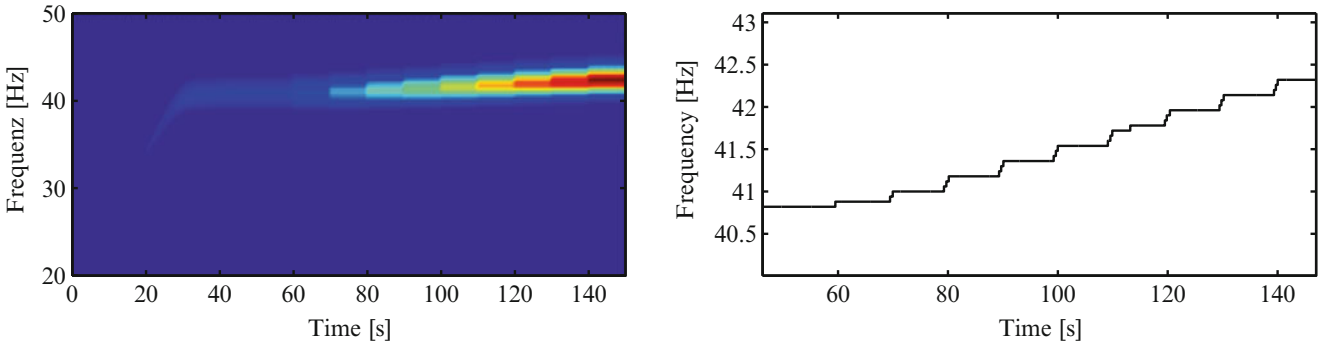

Fig. 11.17 *Left*: Wavelet transform of the acceleration signal. *Right*: Frequency of the maximum wavelet coefficient

leading to a linear eigenfrequency of 40.8 Hz. Especially for longer experiments with high deflection, the temperature in the small beam increases, which can lead an expansion and therefore to buckling in the small beam resulting in dramatic changes in the behavior of the setup. The pretension in the beam helps to avoid this phenomenon and enhances the repeatability of the measurements. For the tracking of the backbone curve in the nonlinear range, the forcing amplitude is increased from 1 to 10 N in steps of 1 N. The forcing is held constant for 60 s during the initial detection of the linear eigenfrequency. When the PLL is in the locked state in the linear eigenfrequency the forcing is increased after intervals of 10 s. The wavelet transform of the acceleration signal is shown in Fig. 11.17.

It can be observed that with each increment of the forcing, the amplitude and therefore the wavelet coefficient increases. Due to the stiffening behavior of the system the resonance frequency increases with higher amplitude such that the maximum of the wavelet transform is shifted to higher frequencies. The PLL automatically adjusts the frequency of the forcing to maintain the resonance criterion to be fulfilled. In laboratory experiments, the testing with the PLL turns out to be very user-friendly, as during the testing no manual action is necessary. Furthermore, the incremental increase of the forcing from low level to high level in resonance does not require any a priori knowledge of maximum forcing amplitude. The test can automatically be stopped once a maximum acceleration is exceeded and all previously recorded points of the backbone curve are retained.

11.6 Conclusion and Future Work

This paper presents a new method, simplifying phase resonance testing of nonlinear structures. A PLL controller is used to automatically maintain the phase criterion during the nonlinear modal test. The design of the PLL implemented for this purpose has briefly been discussed and the differences to classical phase resonance tests have been highlighted. The features of the proposed method have been studied in an extensive numerical example comparing NNM computations with the HBM with time integrations results of systems driven by the PLL controlled excitation force. It has been illustrated that the method is robust even in the presence of strong higher harmonics. The PLL is implemented in a real experimental setup and has successfully been demonstrated for an experimental benchmark structure with strong geometric nonlinearity. The new method provides several advantages compared to classical phase resonance testing. With the automated procedure, the energy dependent modes of nonlinear systems can be tracked in a fast and user-friendly way. No manual action during the testing is necessary reducing the chance of operator errors and improving the repeatability of the measurements. The testing from a low level to a high level excitation is beneficial for unknown structures. Additionally, the influence of transient effects can be eliminated as steady state measurements are used to identify the backbone curve. Due to the stabilizing effect of the PLL small phase inaccuracies do not affect the robustness of the method and the frequency amplitude relation can be extracted accurately. The method proved its robustness even in the case of an internal resonance amplifying higher harmonics.

In future research the PLL method will be applied to more complex structure with different nonlinearities. The behavior of the method in regions of internal resonances will be studied in a more detailed way. Additionally experimental studies with systems exhibiting internal resonances will be carried out and the effect of inaccuracies in the appropriate excitation is investigated. In this context, it will also be interesting to take the shaker-structure interaction into account, which naturally leads to higher harmonics in the forcing function. The extension to non-conservative systems, e.g. using the concept of complex nonlinear modes will be another future challenge.

References

1. Rosenberg, R.M.: Normal modes of nonlinear dual-mode systems. J. Appl. Mech. **27**, 263–268 (1960)
2. Shaw, S.W., Pierre, C.: Normal modes for non-linear vibratory systems. J. Sound Vib. **164**, 85–124 (1993)
3. Vakakis, A.F., Manevitch, L.I., Mikhlin, Y.V., Pilipchuk, V.N., Zevin, A.A.: Normal Modes and Localization in Nonlinear Systems. Wiley, New York (1996)
4. Kerschen, G., Peeters, M., Golinval, J.-C., Vakakis, A.F.: Nonlinear normal modes, part I: a useful framework for the structural dynamicist. Mech. Syst. Signal Process. **23**, 170–194 (2009)
5. Kerschen, G., Peeters, M., Golinval, J.-C., Stéphan, C.: Nonlinear modal analysis of a full-scale aircraft. J. Aircr. **50**, 1409–1419 (2013)
6. Detroux, T., Renson, L., Kerschen, G.: The harmonic balance method for advanced analysis and design of nonlinear mechanical systems. In: Proceedings of the IMAC-XXXII, Orlando, FL (2014)
7. Krack, M., Panning-von Scheidt, L., Wallaschek, J.: A method for nonlinear modal analysis and synthesis: application to harmonically forced and self-excited mechanical systems. J. Sound Vib. **332**, 6798–6814 (2013)
8. Kuether, R.J., Renson, L., Detroux, T., Grappasonni, C., Kerschen, G., Allen, M.S.: Prediction of isolated resonance curves using nonlinear normal modes. In: Proceedings of ASME IDETC 2015, Boston, MA (2015)
9. Peeters, M., Vigui, R., Srandour, G., Kerschen, G., Golinval, J.-C.: Nonlinear normal modes, part II: toward a practical computation using numerical continuation techniques. Mech. Syst. Signal Process. **23**, 195–216 (2009)
10. Laxalde, D., Thouverez, F.: Complex non-linear modal analysis for mechanical systems: application to turbomachinery bladings with friction interfaces. J. Sound Vib. **322**, 1009–1025 (2009)
11. Peeters, M., Kerschen, G., Golinval, J.C.: Dynamic testing of nonlinear vibrating structures using nonlinear normal modes. J. Sound Vib. **330**, 486–509 (2010)
12. Peeters, M., Kerschen, G., Golinval, J.C.: Modal testing using nonlinear normal modes: an experimental demonstration. In: Proceedings of ISMA 2010, Leuven (2010)

13. Londono, J.M., Cooper, J.E. , Neild, S.A.: Vibration testing of large scale nonlinear structures. In: Proceedings of ISMA 2014, Leuven (2014)
14. Noël, J.P., Renson, L., Grappasonni, C., Kerschen, G.: A rigorous phase separation method for testing nonlinear structures. In: Proceedings of ISMA 2014, Leuven (2014)
15. Staszewski, W.J.: Identification of non-linear systems using multi-scale ridges and skeletons of the wavelet transform. J. Sound Vib. **214**, 639–658 (1998)
16. de Bellescize, H.: La réception synchrone. L'Onde Électrique **11**, 230–240 (1932)
17. Best, R.E.: Phase-Locked Loops - Design, Simulation and Applications, 6th edn. McGraw Hill, New York (2007)
18. Abramovitch, D.Y.: Phase-locked loops: a control centric tutorial. In: Proceedings of the American Control Conference, Anchorage, AK (2002)
19. Hsieh, G.-C., Hung, J.C.: Phase-locked loop techniques - a survey. IEEE Trans. Ind. Electron. **43**(6), 609–615 (1996)
20. Fan, M., Clark, M., Feng, Z.C.: Implementation and stability study of phase-locked-loop nonlinear dynamic measurement systems. Commun. Nonlinear Sci. Numer. Simul. **12**, 1302–1315 (2007)
21. Sun, X., Horowitz, R., Komvopoulos, K.: Stability and resolution analysis of a phase-locked loop natural frequency tracking system for MEMS fatigue testing. J. Dyn. Syst. Meas. Control **124**, 599–605 (2002)
22. Mojrzisch, S., Ille, I., Wallascheck, J.: Phase controlled frequency response measurement for nonlinear vibration systems. In: Proceedings of ICSV 2013, Bangkok (2013)
23. Peter, S., Schreyer, F., Reuss, P., Gaul, L.: Consideration of local stiffening and clearance nonlinearities in coupled systems using a generalized harmonic balance method. In: Proceedings of ISMA 2014, Leuven (2014)
24. Gasch, R., Knothe, K., Liebich, R.: Strukturdynamik. Springer, Berlin (2012)
25. Gardner, F.M.: Phaselock Techniques. Wiley, New York (2005)
26. Lunze, J.: Systemtheoretische Grundlagen, Analyse und Entwurf einschleifiger Regelungen. Springer, Berlin (2014)
27. Abramovitch, D.Y.: Lyapunov redesign of analog phase-lock loops. IEEE Trans. Commun. **38**(12), 2197–2202 (2002)
28. Thouverez, F.: Presentation of the ECL benchmark. Mech. Syst. Signal Process. **17**, 195–202 (2003)
29. Lazarus, A., Thomas, O.: A harmonic-based method for computing the stability of periodic solutions of dynamical systems. C. R. Méc. **338**, 510–517 (2010)
30. Peter, S., Grundler, A., Reuss, P., Gaul, L., Leine, R.I.: Towards finite element model updating based on nonlinear normal modes. In: Proceedings of the IMAC-XXXIII, Orlando, FL (2015)

Chapter 12
The Importance of Phase-Locking in Nonlinear Modal Interactions

T.L. Hill, A. Cammarano, S.A. Neild, and D.J. Wagg

Abstract In nonlinear systems the constituent linear modes may interact due to internal resonance. In this paper we classify two distinct classes of modal interactions: *phase-locked* interactions, in which there is a specific phase between the interacting modes; and *phase-unlocked* interactions, in which the modes may interact regardless of their phase. This discussion is accompanied by the study of an example structure in which both classes of interaction may be observed. The structure is used to demonstrate the differences between phase-locked and phase-unlocked interactions, both in terms of their individual influence on the response, and in terms of their influence on each other when both classes of interactions are present.

Keywords Backbone curves • Second-order normal forms • Modal analysis • Modal interaction • Phase locking

12.1 Introduction

Nonlinear dynamic behaviour poses a significant challenge in the modelling, design and optimisation of engineering structures. This is due to the complexity of such behaviours, in terms of both the wide variety of phenomena a structure may exhibit, and the number of degrees-of-freedom than may interact to produce these phenomena. One phenomenon that is of particular importance is internal resonance, where coupling within the system is achieved at resonance. This phenomenon is unique to nonlinear interactions, and is seen in a variety of physical structures [1, 2].

Typically, the design of engineering structures requires an understanding of the forced responses. However, when these responses exhibit nonlinear behaviour they can be highly complex to compute and interpret. As a result, many approaches to nonlinear analysis begin by modelling the responses of the underlying conservative systems; for example nonlinear normal modes [3] and backbone curves [4] (note that the study of nonlinear normal modes has also been extended to nonconservative systems [5, 6], and it has been shown that backbone curves can be used to directly interpret the forced responses [7]). Both backbone curves and nonlinear normal modes provide a useful tool for understanding the underlying behaviour of forced responses, and can be used to predict the existence of internal resonances [8, 9]. However, the relative importance of different backbone curves can vary, as the underlying behaviours they describe may not always manifest themselves in the forced responses; for example, if the forcing amplitude is insufficient to reach a backbone curve, the influence of that backbone curve will not be observed [7].

In this paper we investigate the significance of *phase-locking* in backbone curve models. Phase-locking is defined as a condition imposed upon the phase relationship between the underlying linear modes of a system. Although the backbone curves may exhibit a variety of different phase relationships [8], these relationships are typically fixed for all responses represented by the backbone curves. However, as will be shown here, there also exist phase-unlocked backbone curves, where the modes may exhibit *any* phase relationship. To demonstrate this, we consider a pinned-pinned beam that with a geometric nonlinearity, as considered in [10].

Two separate configurations of this beam are considered: one with an additional rotational stiffness at one end, leading to an asymmetry in the beam; and one without any additional rotational stiffness, and hence with a symmetric structure. The backbone curves of this beam are found using the second-order normal form technique [11, 12], and it is shown that the

T.L. Hill (✉) • S.A. Neild
Department of Mechanical Engineering, University of Bristol, Queen's Building, University Walk, Bristol BS8 1TR, UK
e-mail: tom.hill@bristol.ac.uk

A. Cammarano
School of Engineering, University of Glasgow, Glasgow G12 8QQ, UK

D.J. Wagg
Department of Mechanical Engineering, University of Sheffield, Sir Frederick Mappin Building, Mappin Street, Sheffield S1 3JD, UK

G. Kerschen (ed.), *Nonlinear Dynamics, Volume 1*, Conference Proceedings of the Society for Experimental Mechanics Series,
DOI 10.1007/978-3-319-29739-2_12

asymmetric case has phase-locked backbone curves, whilst the symmetric case only has phase-unlocked backbone curves. By examining the forced responses of the beam it is shown that the behaviour described by the phase-locked backbone curves leads to internal resonance in the forced responses, whilst the phase-unlocked backbone curves do not lead to internal resonance. Finally, it is demonstrated that, whilst the phase-unlocked backbone curves do not predict the existence of internal resonance, they do still describe fundamental behaviours of the system when the system is subjected to particular forcing configurations. These observations indicate an important difference between these two classes of behaviour.

12.2 The Second-Order Normal Form Technique

12.2.1 The Example System

In this paper we consider the pinned-pinned beam with an additional rotational stiffness at one end, as shown in Fig. 12.1. Two specific cases are considered here: one in which the additional rotational stiffness, k, is zero (such that the beam is symmetric); and one in which $k = 10\,\mathrm{N\,m\,rad^{-1}}$, such that the beam is asymmetric. In both cases, the beam has dimensions $L = 500\,\mathrm{mm}$, $w = 30\,\mathrm{mm}$ and $h = 1\,\mathrm{mm}$. Additionally, the beam has a density and Young's modulus of $\rho = 7800\,\mathrm{kg\,m^{-3}}$, $E = 200 \times 10^9\,\mathrm{N\,m^{-2}}$ respectively. A similar configuration of a beam has previously discussed in [10], where it is shown that the unforced and undamped behaviour of the beam may be modelled using the first two linear modes, using the equations of motion, written

$$\ddot{q}_1 + \omega_{n1}^2 q_1 + \mu^2 \left(\gamma_{11} q_1^2 + 2\gamma_{12} q_1 q_2 + \gamma_{22} q_2^2\right)\left(\gamma_{11} q_1 + \gamma_{12} q_2\right) = 0\,, \tag{12.1a}$$

$$\ddot{q}_2 + \omega_{n2}^2 q_2 + \mu^2 \left(\gamma_{11} q_1^2 + 2\gamma_{12} q_1 q_2 + \gamma_{22} q_2^2\right)\left(\gamma_{12} q_1 + \gamma_{22} q_2\right) = 0\,, \tag{12.1b}$$

where: q_i represents the displacement of the ith linear mode; ω_{ni} represents ith linear natural frequency; and μ, γ_{11}, γ_{12} and γ_{22} are nonlinear parameters. These expressions may be written in the form

$$\ddot{\mathbf{q}} + \mathbf{\Lambda q} + \mathbf{N}_q\left(\mathbf{q}\right) = 0\,, \tag{12.2}$$

where: $\mathbf{q}$ is a vector of modal displacements, in which the ith element in $\mathbf{q}$ is q_i; $\mathbf{\Lambda}$ is a diagonal matrix whose ith leading diagonal element is the square of the ith linear natural frequency, ω_{ni}^2; and $\mathbf{N}_q$ is a vector of nonlinear terms, written

$$\mathbf{N}_q\left(\mathbf{q}\right) = \begin{pmatrix} \alpha_1 q_1^3 + 3\alpha_2 q_1^2 q_2 + \alpha_3 q_1 q_2^2 + \alpha_4 q_2^3 \\ \alpha_2 q_1^3 + \alpha_3 q_1^2 q_2 + 3\alpha_4 q_1 q_2^2 + \alpha_5 q_2^3 \end{pmatrix}, \tag{12.3}$$

where

$$\begin{aligned} &\alpha_1 = \mu^2\gamma_{11}^2\,, \quad \alpha_2 = \mu^2\gamma_{11}\gamma_{12}\,, \quad \alpha_3 = \mu^2\left(\gamma_{11}\gamma_{22} + 2\gamma_{12}^2\right)\,, \\ &\alpha_4 = \mu^2\gamma_{12}\gamma_{22}\,, \quad \alpha_5 = \mu^2\gamma_{22}^2\,. \end{aligned} \tag{12.4}$$

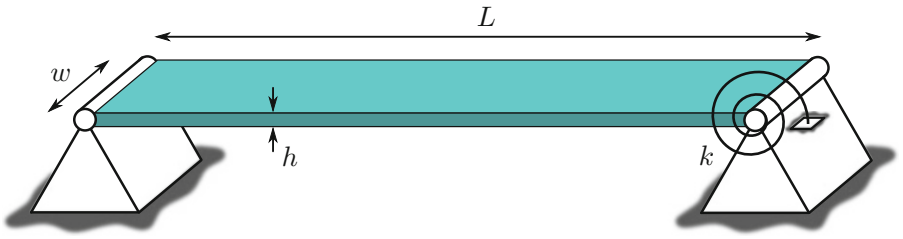

Fig. 12.1 Schematic of a pinned-pinned beam with a rotational constraint at one end

Table 12.1 The linear natural frequencies and nonlinear parameters for the two different configurations of the beam

	ω_{n1}	ω_{n2}	α_1	α_2	α_3	α_4	α_5
	(rad s^{-1})		($\times 10^{10}$)				
Symmetric case ($k = 0$)	57.71	230.83	2.00	0	8.00	0	31.98
Asymmetric case ($k = 10$)	125.91	418.41	8.81	−1.31	34.7	−5.12	133.63

From [10], it is found that, for the two different cases considered here (i.e. when the beam is symmetric, and when the beam is asymmetric) the linear natural frequencies and nonlinear parameters have the values given in Table 12.1. It can be seen that, when the beam is symmetric, i.e. when $k = 0$, then $\alpha_2 = \alpha_4 = 0$.

12.2.2 Applying the Second-Order Normal Form Technique to the Example System

The backbone curves of a system describe the loci of unforced, undamped dynamic responses of a system. In order to find the backbone curves of the example system considered here, we apply the second-order normal form technique to the unforced, undamped equations of motion, Eq. (12.2). This technique is detailed in [11], and it was first demonstrated how the technique may be used to find the backbone curves of nonlinear systems in [4].

The second-order normal form technique typically consists of three steps: the linear modal transform, which transforms the equations of motion from physical into linear modal coordinates; the forcing transform, which removes any non-resonant forcing terms from the equations of motion; and the nonlinear near-identity transform, which removes any non-resonant (i.e. harmonic) terms from the equations of motion. This results in a set of approximate, analytical expressions containing only the resonant components of the motion, which may then be solved using an assumed solution. For the case considered here, the equations of motion, Eq. (12.2), are expressed in terms of the linear modal coordinates and therefore the linear modal transform is not necessary. Additionally, the system is unforced (as we are considering the backbone curves) and hence the forcing transform is also not needed. Thus, in this case, the second-order normal form technique consists only of the nonlinear near-identity transform, applied directly to Eq. (12.2).

The nonlinear near-identity transform involves the substitution $\mathbf{q} = \mathbf{u} + \mathbf{h}$ where $\mathbf{u}$ and $\mathbf{h}$ represent the fundamental and harmonic components of $\mathbf{q}$ respectively. It is assumed that the harmonics are small and, as the nonlinear terms are also assumed to be small, the approximation $\mathbf{N}_q(\mathbf{q}) = \mathbf{N}_q(\mathbf{u})$ is made. Additionally, as non-resonant terms are removed, the fundamental component of the response, $\mathbf{u}$, is sinusoidal, and therefore the ith element of $\mathbf{u}$ may be written

$$u_i = \cos(\omega_{ri} t - \phi_i) , \tag{12.5a}$$

$$= u_{pi} + u_{mi} = \frac{U_i}{2} \mathrm{e}^{+\mathrm{j}(\omega_{ri} t - \phi_i)} + \frac{U_i}{2} \mathrm{e}^{-\mathrm{j}(\omega_{ri} t - \phi_i)} , \tag{12.5b}$$

where U_i, ω_{ri} and ϕ_i are the amplitude, response frequency and phase respectively. Note that the subscripts "p" and "m" in Eq. (12.5b), correspond to the positive and negative, i.e. *plus* and *minus*, signs in the exponents respectively. Now, substituting $\mathbf{q} = \mathbf{u}$ into Eq. (12.3), along with the assumed solutions, Eq. (12.5b), gives

$$\mathbf{N}_q(\mathbf{u}) = \begin{pmatrix} \alpha_1 (u_{p1} + u_{m1})^3 + 3\alpha_2 (u_{p1} + u_{m1})^2 (u_{p2} + u_{m2}) + \\ \alpha_2 (u_{p1} + u_{m1})^3 + \alpha_3 (u_{p1} + u_{m1})^2 (u_{p2} + u_{m2}) + \\ \qquad \alpha_3 (u_{p1} + u_{m1}) (u_{p2} + u_{m2})^2 + \alpha_4 (u_{p2} + u_{m2})^3 \\ \qquad 3\alpha_4 (u_{p1} + u_{m1}) (u_{p2} + u_{m2})^2 + \alpha_5 (u_{p2} + u_{m2})^3 \end{pmatrix} . \tag{12.6}$$

After expanding the terms in Eq. (12.6), $\mathbf{N}_q$ may be written

$$\mathbf{N}_q(\mathbf{u}) = \left[N_q \right] \mathbf{u}^* (\mathbf{u}_p, \mathbf{u}_m) , \tag{12.7}$$

where: $\mathbf{u}^*$ is a vector containing all unique combinations of the variables u_{pi} and u_{mi} (expressed in the vectors $\mathbf{u}_p$ and $\mathbf{u}_m$); and $\left[N_q\right]$ is a matrix of the coefficients corresponding to those variables. As the elements in $\mathbf{u}^*$ are composed only of u_{pi} and u_{mi}, the ℓth element of $\mathbf{u}^*$ may be written

$$u_\ell^* = \prod_{n=1}^{N} u_{pn}^{s_{p,\ell,n}} u_{mn}^{s_{m,\ell,n}}, \tag{12.8}$$

where N is the number of degrees-of-freedom of the system (i.e. $N = 2$ in the case considered here). Using Eq. (12.8), the exponents $s_{p,\ell,n}$ and $s_{m,\ell,n}$ can be found, allowing the matrix $\boldsymbol{\beta}$ to be defined, where element $\{i,\ \ell\}$ of $\boldsymbol{\beta}$ is given by

$$\beta_{i,\ell} = \left[\sum_{n=1}^{N} \left(s_{p,\ell,n} - s_{m,\ell,n}\right) \omega_{rn}\right]^2 - \omega_{ri}^2 . \tag{12.9}$$

It is the matrix $\boldsymbol{\beta}$ which allows us to determine which nonlinear terms are resonant, and thus appear in the resonant equation of motion. However, it can be seen from Eq. (12.9) that $\boldsymbol{\beta}$ is dependent on the fundamental response frequencies, ω_{ri}, and therefore the ratios between these frequencies must be known in order to determine which terms are resonant. Typically, as discussed in [11], the ratios between the response frequencies are chosen based upon the ratios between the linear natural frequencies, i.e. if $\omega_{n1} \approx \omega_{n2}$, then it is assumed that the modes will respond at the same frequency. However, here we wish to investigate how this ratio influences which terms are resonant, and hence it is assumed that the fundamental component of q_2 responds at r times that of q_1, i.e. $\omega_{r2} = r\omega_{r1}$. Substituting this into Eq. (12.9) allows $\boldsymbol{\beta}$ to be defined, for this case, as

$$\beta_{1,\ell} = \left\{\left[s_{p,\ell,1} - s_{m,\ell,1} + r\left(s_{p,\ell,2} - s_{m,\ell,2}\right)\right]^2 - 1\right\} \omega_{r1}^2 , \tag{12.10a}$$

$$\beta_{2,\ell} = \left\{\left[s_{p,\ell,1} - s_{m,\ell,1} + r\left(s_{p,\ell,2} - s_{m,\ell,2}\right)\right]^2 - r^2\right\} \omega_{r1}^2 . \tag{12.10b}$$

Now, Eqs. (12.6)–(12.8) and (12.10) may be used to write $\left[N_q\right]$, $\mathbf{u}^*$ and $\boldsymbol{\beta}$ as

$$\left[N_q\right]^\mathsf{T} = \begin{bmatrix} \alpha_1 & \alpha_2 \\ 3\alpha_1 & 3\alpha_2 \\ 3\alpha_1 & 3\alpha_2 \\ \alpha_1 & \alpha_2 \\ 3\alpha_2 & \alpha_3 \\ 6\alpha_2 & 2\alpha_3 \\ 3\alpha_2 & \alpha_3 \\ 3\alpha_2 & \alpha_3 \\ 6\alpha_2 & 2\alpha_3 \\ 3\alpha_2 & \alpha_3 \\ \alpha_3 & 3\alpha_4 \\ 2\alpha_3 & 6\alpha_4 \\ \alpha_3 & 3\alpha_4 \\ \alpha_3 & 3\alpha_4 \\ 2\alpha_3 & 6\alpha_4 \\ \alpha_3 & 3\alpha_4 \\ \alpha_4 & \alpha_5 \\ 3\alpha_4 & 3\alpha_5 \\ 3\alpha_4 & 3\alpha_5 \\ \alpha_4 & \alpha_5 \end{bmatrix}, \mathbf{u}^* = \begin{bmatrix} u_{p1}^3 \\ u_{p1}^2 u_{m1} \\ u_{p1} u_{m1}^2 \\ u_{m1}^3 \\ u_{p1}^2 u_{p2} \\ u_{p1} u_{m1} u_{p2} \\ u_{m1}^2 u_{p2} \\ u_{p1}^2 u_{m2} \\ u_{p1} u_{m1} u_{m2} \\ u_{m1}^2 u_{m2} \\ u_{p1} u_{p2}^2 \\ u_{p1} u_{p2} u_{m2} \\ u_{p1} u_{m2}^2 \\ u_{m1} u_{p2}^2 \\ u_{m1} u_{p2} u_{m2} \\ u_{m1} u_{m2}^2 \\ u_{p2}^3 \\ u_{p2}^2 u_{m2} \\ u_{p2} u_{m2}^2 \\ u_{m2}^3 \end{bmatrix}, \tag{}$$

$$\boldsymbol{\beta}^{\mathsf{T}} = \omega_{r1}^2 \begin{bmatrix} 8 & 9-r^2 \\ 0 & 1-r^2 \\ 0 & 1-r^2 \\ 8 & 9-r^2 \\ (r+1)(r+3) & 4(1+r) \\ r^2-1 & 0 \\ (r-1)(r-3) & 4(1-r) \\ (r-1)(r-3) & 4(1-r) \\ r^2-1 & 0 \\ (r+1)(r+3) & 4(1+r) \\ 4r(r+1) & (3r+1)(r+1) \\ 0 & 1-r^2 \\ 4r(r-1) & (3r-1)(r-1) \\ 4r(r-1) & (3r-1)(r-1) \\ 0 & 1-r^2 \\ 4r(r+1) & (3r+1)(r+1) \\ 9r^2-1 & 8r^2 \\ r^2-1 & 0 \\ r^2-1 & 0 \\ 9r^2-1 & 8r^2 \end{bmatrix}. \tag{12.11}$$

The resonant equation of motion is written

$$\ddot{\mathbf{u}} + \boldsymbol{\Lambda}\mathbf{u} + \mathbf{N}_u(\mathbf{u}) = 0\,, \tag{12.12}$$

where $\mathbf{N}_u$ is a vector of resonant nonlinear terms, defined using

$$\mathbf{N}_u(\mathbf{u}) = [n_u]\,\mathbf{u}^*\left(\mathbf{u}_p,\, \mathbf{u}_m\right), \tag{12.13}$$

where $[n_u]$ is a matrix of the coefficients of the resonant nonlinear terms. The nonlinear terms represented by $\left[N_q\right]$ are defined as resonant if they correspond to an element in $\boldsymbol{\beta}$ that contains a zero; hence such a term is also represented in $[n_u]$. Conversely, if a term is non-resonant (i.e. it contributes to a harmonic) then the corresponding element in $\boldsymbol{\beta}$ is non-zero, and hence the element in $[n_u]$ must be zero. This is expressed by the relationship defining element $\{i,\, \ell\}$ of $[n_u]$ as

$$[n_u]_{i,\ell} = \begin{cases} \left[N_q\right]_{i,\ell} & \text{if}: \quad \beta_{i,\ell} = 0\,, \\ 0 & \text{if}: \quad \beta_{i,\ell} \neq 0\,. \end{cases} \tag{12.14}$$

Note that, whilst the harmonics are neglected here, they may be computed using the second-order normal form technique—see [13] for further details.

It can be seen from Eq. (12.11) that the terms in $\boldsymbol{\beta}$ may be separated into three categories:

- *Non-resonant*, which are non-zero, regardless of the value of r,
- *Unconditionally-resonant*, which are zero for all values of r,
- *Conditionally-resonant*, which are only zero for specific values of r.

Furthermore, from Eq. (12.11), it can be seen that, for this case, the conditionally-resonant terms become resonant for three different values of r, namely $r = 1/3$, $r = 1$ and $r = 3$. Therefore, using Eqs. (12.11) and (12.14), the matrix of resonant coefficients, $[n_u]$, may be found, from which Eq. (12.13) may be used to write

$$\mathbf{N}_u = \begin{pmatrix} 3\alpha_1 u_{p1} u_{m1} u_1 + 2\alpha_3 u_{p2} u_{m2} u_1 \\ 2\alpha_3 u_{p1} u_{m1} u_2 + 3\alpha_5 u_{p2} u_{m2} u_2 \end{pmatrix} + \delta\left\{r - \frac{1}{3}\right\} \begin{pmatrix} \alpha_4 \left(u_{p2}^3 + u_{m2}^3\right) \\ 3\alpha_4 \left(u_{p1} u_{m2}^2 + u_{p1} u_{m2}^2\right) \end{pmatrix} + \tag{12.15}$$

$$\delta\{r-1\} \begin{pmatrix} 3\alpha_2 \left(2u_{p1} u_{m1} u_2 + u_{p1}^2 u_{m2} + u_{m1}^2 u_{p2}\right) + \alpha_3 \left(u_{m1} u_{p2}^2 + u_{p1} u_{m2}^2\right) + 3\alpha_4 u_{p2} u_{m2} u_2 \\ 3\alpha_4 \left(2u_1 u_{p2} u_{m2} + u_{m1} u_{p2}^2 + u_{p1} u_{m2}^2\right) + \alpha_3 \left(u_{p1}^2 u_{m2} + u_{m1}^2 u_{p2}\right) + 3\alpha_2 u_{p1} u_{m1} u_1 \end{pmatrix} +$$

$$+\delta\{r-3\} \begin{pmatrix} 3\alpha_2 \left(u_{m1}^2 u_{p2} + u_{p1}^2 u_{m2}\right) \\ \alpha_2 \left(u_{p1}^3 + u_{m1}^3\right) \end{pmatrix},$$

where δ represents the Dirac-delta function.

12.3 The Backbone Curves of the Example System

In order to find the backbone curves, we must solve the time-dependent resonant equations of motion, Eq. (12.12), which first requires that the time-dependence is removed from these equations. In [8] it is shown that the ith element of the vector of resonant nonlinear terms, $\mathbf{N}_u$, may be written

$$N_{ui} = N_{ui}^+ \mathrm{e}^{+\mathrm{j}\omega_{ri} t} + N_{ui}^- \mathrm{e}^{-\mathrm{j}\omega_{ri} t}\,, \tag{12.16}$$

therefore, substituting Eqs. (12.5) and (12.16), the resonant equation of motion, Eq. (12.12), for the ith mode may be written

$$\left[\left(\omega_{ni}^2 - \omega_{ri}^2\right) \frac{U_i}{2} \mathrm{e}^{-\mathrm{j}\phi_i} + N_{ui}^+\right] \mathrm{e}^{+\mathrm{j}\omega_{ri} t} + \left[\left(\omega_{ni}^2 - \omega_{ri}^2\right) \frac{U_i}{2} \mathrm{e}^{+\mathrm{j}\phi_i} + N_{ui}^-\right] \mathrm{e}^{-\mathrm{j}\omega_{ri} t} = 0\,, \tag{12.17}$$

where the contents of the square brackets form a complex conjugates pair. Therefore, the contents of these brackets may each be equated to zero, i.e.

$$\left(\omega_{ni}^2 - \omega_{ri}^2\right) U_i + 2N_{ui}^+ \mathrm{e}^{+\mathrm{j}\phi_i} = 0\,, \tag{12.18}$$

where it can be seen that Eq. (12.18) is independent of time.

Now, substituting Eq. (12.5) into Eq. (12.15) allows the complex components N_{ui}^+ to be identified. These may then be substituted into Eq. (12.18) to give

$$4\left(\omega_{n1}^2 - \omega_{r1}^2\right) U_1 + 3\alpha_1 U_1^3 + 2\alpha_3 U_1 U_2^2 + \delta_{1/3}\alpha_4 U_2^3 \mathrm{e}^{+\mathrm{j}\phi_{d1,3}} + \delta_3 3\alpha_2 U_1^2 U_2 \mathrm{e}^{+\mathrm{j}\phi_{d3,1}}$$
$$+\delta_1 \left[3\alpha_2 U_1^2 U_2 \left(2 + \mathrm{e}^{-\mathrm{j}2\phi_{d1,1}}\right) + \alpha_3 U_1 U_2^2 \mathrm{e}^{+\mathrm{j}\phi_{d1,1}} + 3\alpha_4 U_2^3\right] \mathrm{e}^{+\mathrm{j}\phi_{d1,1}} = 0\,, \tag{12.19a}$$

$$4\left(\omega_{n2}^2 - r^2\omega_{r1}^2\right) U_2 + 2\alpha_3 U_1^2 U_2 + 3\alpha_5 U_2^3 + \delta_{1/3} 3\alpha_4 U_1 U_2^2 \mathrm{e}^{-\mathrm{j}\phi_{d1,3}} + \delta_3 \alpha_2 U_1^3 \mathrm{e}^{-\mathrm{j}\phi_{d3,1}}$$
$$+\delta_1 \left[3\alpha_2 U_1^3 + \alpha_3 U_1^2 U_2 \mathrm{e}^{-\mathrm{j}\phi_{d1,1}} + 3\alpha_4 U_1 U_2^2 \left(2 + \mathrm{e}^{+\mathrm{j}2\phi_{d1,1}}\right)\right] \mathrm{e}^{-\mathrm{j}\phi_{d1,1}} = 0\,, \tag{12.19b}$$

where the phase difference, $\phi_{di,j}$, is defined as $\phi_{di,j} = i\phi_1 - j\phi_2$, and the Dirac-delta function is denoted $\delta_k = \delta\{r-k\}$. Note that $\omega_{r2} = r\omega_{r1}$ has been used.

Equation (12.19) demonstrate that some terms are a function of the phase difference between the two modes (where the phase difference is dependent on r). As will be shown in the following sections, such terms enforce a specific phase-relationship for resonant responses described by the backbone curve, known as *phase-locking*. It therefore follows that backbone curves that are described by expressions which are not a function of the phase difference do not have a specific phase-relationship, and the responses they describe may therefore exhibit any phase value between the modes. Furthermore, it can be seen in Eq. (12.19) that the terms which exhibit a phase-dependence are also those that are dependent on r i.e. are conditionally resonant terms, suggesting a relationship between conditional resonance and phase-locking.

12.3.1 The Backbone Curves of the Asymmetric Case

From Table 12.1 it can be seen that, for the asymmetric case, all nonlinear parameters, α_i, are non-zero. Additionally, the ratio between the linear natural frequencies, $\omega_{n1}{:}\omega_{n2}$, is approximately 1:3 . Therefore, it seems likely that a similar ratio will exist between the response frequencies, and hence the case where $r = 3$ is considered. From Eq. (12.19) this leads to

$$4\left(\omega_{n1}^2 - \omega_{r1}^2\right) U_1 + 3\alpha_1 U_1^3 + 2\alpha_3 U_1 U_2^2 + 3\alpha_2 U_1^2 U_2 \mathrm{e}^{+\mathrm{j}\,(3\phi_1 - \phi_2)} = 0\,, \tag{12.20a}$$

$$4\left(\omega_{n2}^2 - 9\omega_{r1}^2\right) U_2 + 2\alpha_3 U_1^2 U_2 + 3\alpha_5 U_2^3 + \alpha_2 U_1^3 \mathrm{e}^{-\mathrm{j}\,(3\phi_1 - \phi_2)} = 0\,. \tag{12.20b}$$

As we are concerned with the phase difference between the modes, we consider the case where both modal amplitudes are non-zero. Therefore, the imaginary components of Eq. (12.20) both lead to $\sin(3\phi_1 - \phi_2) = 0$, which may be satisfied by $3\phi_1 - \phi_2 = 0,\ \pi,\ \ldots$, thus enforcing phase-locking between the modes. The real components of Eq. (12.20) may then be written

$$4\left(\omega_{n1}^2 - \omega_{r1}^2\right) + 3\alpha_1 U_1^2 + 2\alpha_3 U_2^2 + p3\alpha_2 U_1 U_2 = 0\,, \tag{12.21a}$$

$$4\left(\omega_{n2}^2 - 9\omega_{r1}^2\right) U_2 + 2\alpha_3 U_1^2 U_2 + 3\alpha_5 U_2^3 + p\alpha_2 U_1^3 = 0\,, \tag{12.21b}$$

where

$$p = \begin{cases} +1 & \text{when}: \quad 3\phi_1 - \phi_2 = 0\,, \\ -1 & \text{when}: \quad 3\phi_1 - \phi_2 = \pi\,. \end{cases} \tag{12.22}$$

Here, the backbone curves associated with the solutions to the $p = +1$ case (i.e. where the linear modes are in-phase) are denoted S_1^+, and the solutions to the $p = -1$ case (i.e. where the linear modes are in anti-phase) are denoted S_1^-.

The backbone curves S_1^+ and S_1^-, found using Eq. (12.21) are shown in Fig. 12.2, along with the response of the system when subject to forcing in the first linear mode (i.e. the second mode is unforced). A linear, proportional damping model is used for this forcing case, i.e. the damping term in the ith linear equation of motion is $2\zeta\omega_{ni}\dot{q}_i$, where ζ is the modal damping ratio, which is equal for both modes. The forcing applied to the first linear mode is sinusoidal, at amplitude P_1. In the case

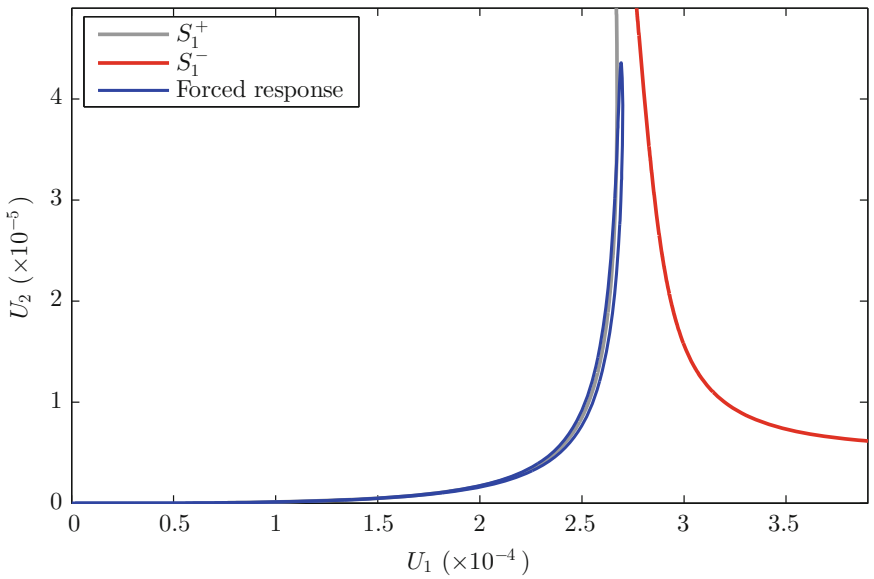

Fig. 12.2 The backbone curves and a forced response of the asymmetric beam. This is shown in the projection of the amplitude of the fundamental component of first linear mode, U_1, against that of the second linear mode, U_2. The backbone curves S_1^+ and S_1^- are represented by a *grey line* and a *red line* respectively, whilst the forced response is represented by a *blue line*

shown in Fig. 12.2, the modal damping ratio is $\zeta = 0.1\,\%$, and the forcing amplitude is $P_1 = 0.0175$. These forced responses have been computed using the numerical continuation software AUTO-07p [14].

Figure 12.2 shows that, whilst the forcing is applied directly to the first linear mode, the second mode also exhibits a response, due to internal resonance. Furthermore it can be seen that the forced response branch closely follows the backbone curves; although some deviation can be seen, due to both the approximate nature of the analytical descriptions of the backbone curves, and due to the internal energy transfer required to balance the energy lost through damping, as discussed in [7].

12.3.2 The Backbone Curves of the Symmetric Case

We now consider the symmetric case, where the rotational stiffness at the end of the beam, k, is zero. From Table 12.1, the nonlinear parameters α_2 and α_4 are zero; hence Eq. (12.19) are simplified to

$$4\left(\omega_{n1}^2 - \omega_{r1}^2\right) U_1 + 3\alpha_1 U_1^3 + 2\alpha_3 U_1 U_2^2 + \delta_1 \alpha_3 U_1 U_2^2 \mathrm{e}^{-\mathrm{j}2\left(\phi_1 - \phi_2\right)} = 0\,, \tag{12.23a}$$

$$4\left(\omega_{n2}^2 - r^2\omega_{r1}^2\right) U_2 + 2\alpha_3 U_1^2 U_2 + 3\alpha_5 U_2^3 + \delta_1 \alpha_3 U_1^2 U_2 \mathrm{e}^{-\mathrm{j}2\left(\phi_1 - \phi_2\right)} = 0\,. \tag{12.23b}$$

Equation (12.23) show that the phase-locking only occurs in the symmetric system when $r = 1$; however, it is found that substituting $r = 1$ into Eq. (12.23) does not lead to any valid solutions. This suggests that phase-locking is not possible in the symmetric case.

In [10], a similar case is also discussed (although the phase is not considered) and it is assumed that, as the ratio between the linear natural frequencies is close to 1:3, the response frequencies will also exhibit a 1:3 ratio. Therefore, substituting $r = 3$ into Eq. (12.23) gives

$$\left[4\left(\omega_{n1}^2 - \omega_{r1}^2\right) + 3\alpha_1 U_1^2 + 2\alpha_3 U_2^2\right] U_1 = 0\,, \tag{12.24a}$$

$$\left[4\left(\omega_{n2}^2 - 9\omega_{r1}^2\right) + 2\alpha_3 U_1^2 + 3\alpha_5 U_2^2\right] U_2 = 0\,. \tag{12.24b}$$

It can be seen from Eq. (12.24) that two single-mode solutions exist: one in which $U_2 = 0$, denoted S_1; and another in which $U_1 = 0$, denoted S_2. Additionally a mixed-mode solution exists, in which $U_1 \neq 0$ and $U_2 \neq 0$, denoted S_3. However, unlike the mixed-mode solutions in the asymmetric case, this has no phase-locking. Therefore, whilst the S_1^+ and S_1^- backbone curves of the asymmetric case have specific phase relationships, it appears that the mixed-mode backbone curves described by Eq. (12.24) may exist for any phase difference between the modes.

The backbone curves S_1 and S_3 are shown in Fig. 12.3, along with the response of the system when forced in the shape of the first linear mode. As with Fig. 12.2, a linear proportional damping model is used; however the modal damping ratio is higher, at $\zeta = 0.5\,\%$. The first linear mode is subjected to a sinusoidal forcing at amplitude $P_1 = 0.035$, whilst the second mode is unforced. As in the previous example, this forced response has been computed using numerical continuation, whilst the backbone curves have been calculated using the analytical expressions Eq. (12.24).

Figure 12.3 clearly shows that the forced response follows the backbone curve S_1 (which is composed of only the first mode). The S_3 backbone curve does not appear to influence this forced branch and inspection of the U_2 component reveals that there is no response in the second mode. Additionally, stability analysis of the forced branch reveals that there is no loss of stability in the region surrounding the bifurcation from S_1 onto S_3. Typically, such bifurcations are associated with internally resonant behaviour [15] and lead to bifurcations in the forced branches, along with a loss of stability. Therefore, the backbone curve bifurcation, seen in Fig. 12.3, appears to reveal a special case. This highlights an important difference between the behaviour of phase-locked backbone curves, such as those shown in Fig. 12.2 which exhibit internal resonance, and phase-unlocked backbone curves, such as S_3 in Fig. 12.3 which does not lead to internal resonance.

Although phase-unlocked backbone curves do not lead to internally-resonant behaviour, they may still be used to represent fundamental behaviours in the forced responses. This is demonstrated in Fig. 12.4, where the symmetric case shown in Fig. 12.3 (i.e. with modal damping ratio $\zeta = 0.5\,\%$ and a forcing amplitude $P_1 = 0.035$ applied to first mode) is reconsidered. However, in this case, a forcing is also applied to the second linear mode, with amplitude P_2, and with a frequency that is three times that of the first. As internal resonance is not exhibited by this system, this forcing configuration enforces a 1:3 response ratio, as assumed in the derivation of the backbone curve expressions.

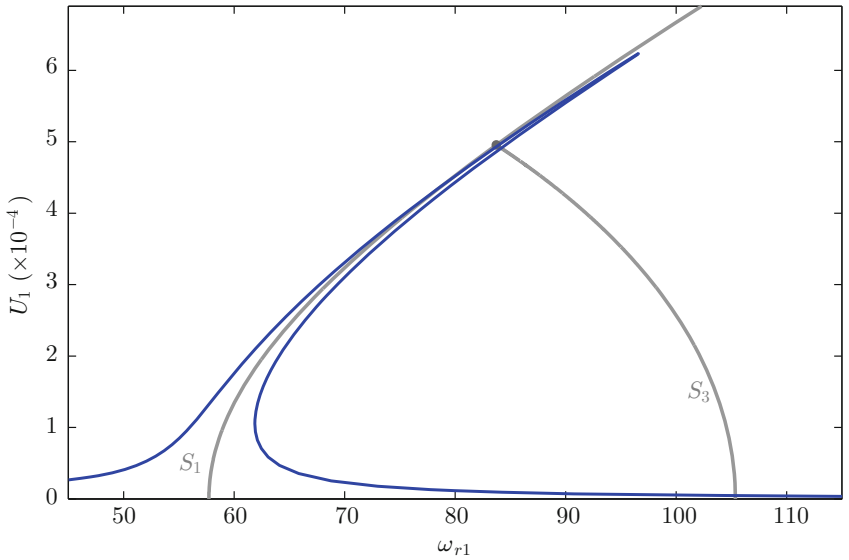

Fig. 12.3 The backbone curves S_1 and S_3, along with a forced response curve of the symmetric beam. This is shown in the projection of the fundamental response frequency of the first linear mode, ω_{r1}, against the fundamental response amplitude of the first linear mode, U_1. Note that it is assumed that ω_{r1} is equal to the forcing frequency. The backbone curves S_1 and S_3 are represented by *grey lines*, and a *grey dot* shows the bifurcation between these two backbone curves. The forced response curve is represented by a *blue line*

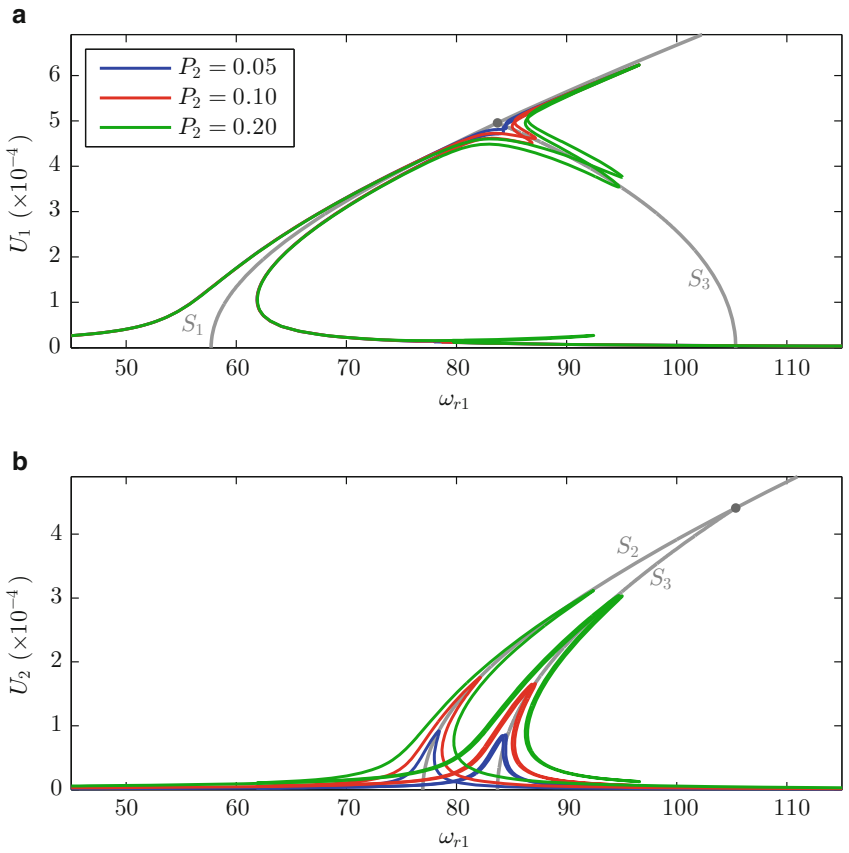

Fig. 12.4 The backbone curves and forced response curves of the symmetric beam when subjected to first and second linear modal forcing. The forcing applied to the second mode is at three times the frequency of the first, and three different forcing amplitudes are used—as shown in the legend in panel **(a)**. Panel **(a)** is shown in the projection of the fundamental response frequency of the first linear mode, ω_{r1}, against the fundamental response amplitude of the first linear mode, U_1, whilst panel **(b)** is shown in the projection of ω_{r1} against U_2. The backbone curves are represented by *grey lines*, and a *grey dot* shows the bifurcation between these two backbone curves

Figure 12.4 shows that, when a 1:3 response ratio is enforced via external forcing, the forced response branches follow the phase-unlocked backbone curve. It has also been confirmed that, as these backbone curves represent responses that may exhibit any phase between the modes, altering the phase between the external forcing does not lead to any significant changes in the forced responses. This demonstrates that such backbone curves represent fundamental underlying behaviours; however, they do not appear to predict internal resonance. As such, it appears that external forcing, or interactions with other modes, is required for the behaviour represented by phase-unlocked backbone curves to manifest.

12.4 Conclusions

In this paper we have demonstrated the difference between phase-locked and phase-unlocked backbone curves. It has been seen that a symmetric beam with nonlinear behaviour, does not have any phase-locked backbone curves. Therefore, the backbone curve of this system describing the 1:3 resonant interaction between the modes, previously discussed in [10], does not exhibit phase-locking. It has been demonstrated that this backbone curve does not lead to internal resonance when the system is forced in only one mode. This is compared to the phase-locked backbone curves of the asymmetric case, where both modes exhibit a response when only one mode is directly forced. This suggests phase-unlocked backbone curves do not describe internally-resonant behaviour, indicating an important difference between these two classes of backbone curves.

It has also been demonstrated that the presence of phase-locking terms may be predicted if the general form of the backbone curves is derived, without the need to assume a specific ratio between the response frequencies. This enables the prediction of those ratios that will lead to phase-locked backbone curves, and those that will not. This feature of the second-order normal form technique represents a significant advantage when compared to analytical techniques that require the response frequency ratio to be selected before such information is known.

References

1. Rao, G.V., Iyengar, R.: Internal resonance and non-linear response of a cable under periodic excitation. J. Sound Vib. **149**(1), 25–41 (1991)
2. Lewandowski, R.: On beams membranes and plates vibration backbone curves in cases of internal resonance. Meccanica **31**(3), 323–346 (1996)
3. Kerschen, G., Peeters, M., Golinval, J.C., Vakakis, A.F.: Nonlinear normal modes, part I: a useful framework for the structural dynamicist. Mech. Syst. Signal Process. **23**(1), 170–194 (2009). Special Issue: Non-linear Structural Dynamics
4. Cammarano, A., Hill, T.L., Neild, S.A., Wagg, D.J.: Bifurcations of backbone curves for systems of coupled nonlinear two mass oscillator. Nonlinear Dyn. **77**(1–2), 311–320 (2014)
5. Shaw, S.W., Pierre, C.: Non-linear normal modes and invariant manifolds. J. Sound Vib. **150**(1), 170–173 (1991)
6. Renson, L., Kerschen, G.: Nonlinear normal modes of nonconservative systems. In: Proceedings of the SEM IMAC XXXI Conference, February 2013
7. Hill, T.L., Cammarano, A., Neild, S.A., Wagg, D.J.: Interpreting the forced responses of a two-degree-of-freedom nonlinear oscillator using backbone curves. J. Sound Vib. **349**, 276–288 (2015)
8. Hill, T.L., Cammarano, A., Neild, S.A., Wagg, D.J.: Out-of-unison resonance in weakly nonlinear coupled oscillators. Proc. R. Soc. Lond. A: Math. Phys. Eng. Sci. **471**(2173) (2014)
9. Jiang, D., Pierre, C., Shaw, S.W.: The construction of non-linear normal modes for systems with internal resonance. Int. J. Non-Linear Mech. **40**(5), 729–746 (2005)
10. Lewandowski, R.: Solutions with bifurcation points for free vibration of beams: an analytical approach. J. Sound Vib. **177**(2), 239–249 (1994)
11. Neild, S.A., Wagg, D.J.: Applying the method of normal forms to second-order nonlinear vibration problems. Proc. R. Soc. A: Math. Phys. Eng. Sci. **467**, 1141–1163 (2011)
12. Wagg, D.J., Neild, S.A.: Approximate methods for analysing nonlinear vibrations. In: Nonlinear Vibration with Control. Solid Mechanics and Its Applications, vol. 218, pp. 145–209. Springer International Publishing, Cham (2015)
13. Neild, S.A., Champneys, A.R. , Wagg, D.J., Hill, T.L., Cammarano, A.: The use of normal forms for analysing nonlinear mechanical vibrations. Philos. Trans. R. Soc. Lond. A: Math. Phys. Eng. Sci. **373**(2051) (2015)
14. Doedel, E.J., with major contributions from A. R. Champneys, Fairgrieve, T.F., Kuznetsov, Y.A., Dercole, F., Oldeman, B.E., Paffenroth, R.C., Sandstede, B., Wang, X.J., Zhang, C.: AUTO-07P: Continuation and Bifurcation Software for Ordinary Differential Equations. Concordia University, Montreal (2008). Available at: http://cmvl.cs.concordia.ca/
15. Hill, T.L., Cammarano, A., Neild, S.A., Wagg, D.J. Relating backbone curves to the forced responses of nonlinear systems. In: Kerschen, G.(ed.) Nonlinear Dynamics, Volume 1, Conference Proceedings of the Society for Experimental Mechanics Series, pp. 113–122. Springer International Publishing, Cham (2016)

Chapter 13
A Study of the Modal Interaction Amongst Three Nonlinear Normal Modes Using a Backbone Curve Approach

X. Liu, A. Cammarano, D.J. Wagg, and S.A. Neild

Abstract In this paper, a three degree-of-freedom oscillator with cubic elastic nonlinearities is considered. For this system, the natural frequencies of its underlying linear modes are set to be approximately equal so that $\omega_{n1}:\omega_{n2}:\omega_{n3} \approx 1:1:1$. As a result, the nonlinear normal modes in the system are able to potentially interact with each other. In this study, the underlying unforced and undamped system is considered. The second-order normal forms technique is used to estimate the backbone curves of the system, which give information on the frequency and modal response amplitudes and phases. Then, through choosing the activate modes and their specific phase differences, the single-, double- and triple-mode backbone curves are computed. The results show the effect of nonlinear multi-mode interactions on the dynamic response of nonlinear oscillators. These insights will be beneficial when considering how a structure will respond and for the system identification of nonlinear multi-degree-of-freedom systems.

Keywords Backbone curve • 3-DoF nonlinear oscillator • Nonlinear modal interaction • Cubic nonlinearity • Second-order normal form method

13.1 Introduction

The dynamic response of lightly damped and weakly nonlinear multi-degree-of-freedom (M-DoF) systems are of great interest as a vibration problem in the engineering field. Due to the weak nonlinearities, the fundamental modes of these M-DoF systems cannot be decoupled and then the internal resonance effects become significant. This significantly increases the difficulties of the response prediction and system identification. In this paper, the example of a three-degree-of-freedom (3-DoF) lumped mass system with cubic stiffness nonlinearities is considered. In particular we consider the potential modal interactions that can occur by analysing the backbone curves, i.e. the response of the equivalent undamped, unforced system. This is because, in common with the majority of vibration examples that lend themselves to modal analysis, the lightly damped dynamic behaviour is largely determined by the properties of the underlying Hamiltonian dynamic system. There are many studies about the dynamic response of nonlinear systems based on backbone curves, see for example [3–5, 10, 11]. Moreover, the response of nonlinear M-DoF systems has been extensively studied because they are often related to unwanted vibration effects in structures. Most of the literature is for undamped, unforced systems, and includes beams, cables, membranes, plates and shells—see for example [1, 9, 15, 17]. Several different analytical approaches have been used to approach this type of problem, such as perturbation methods, [12] nonlinear normal modes (NNMs) [8, 14, 16] or normal form analysis [2, 6, 13]. Similar 3-DoF systems have been analysed using NNMs in the context of nonlinear vibration suppression [7].

In this paper we demonstrate different kinds of modal interactions by considering an in-line 3-DoF nonlinear oscillators. In Sect. 13.2, after generally describing the nonlinear 3-DoF system, we apply the normal form transformation method to obtain a equation set governing the response frequency and amplitudes. Based on the obtained equation set, in Sect. 13.3, the potential occurrence of different kinds of backbone curves with the specific number of activated modes is discussed and

X. Liu (✉) • D.J. Wagg
Department of Mechanical Engineering, University of Sheffield, Sheffield S1 3JD, UK
e-mail: xuanang.liu@sheffield.ac.uk

A. Cammarano
School of Engineering, University of Glasgow, Glasgow G12 8QQ, UK

S.A. Neild
Department of Mechanical Engineering, University of Bristol, Bristol BS8 1TR, UK

G. Kerschen (ed.), *Nonlinear Dynamics, Volume 1*, Conference Proceedings of the Society for Experimental Mechanics Series,
DOI 10.1007/978-3-319-29739-2_13

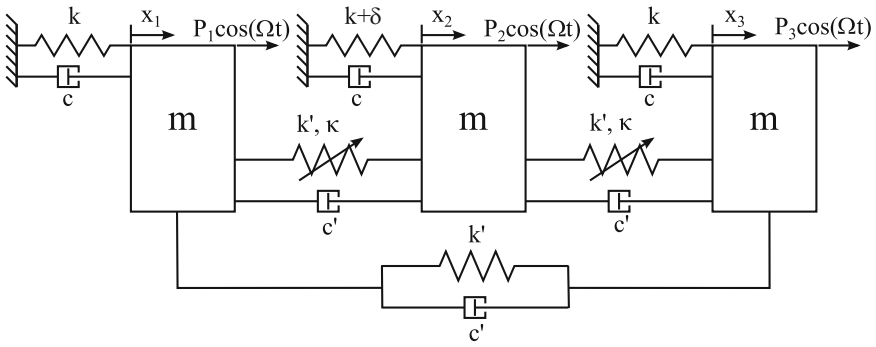

Fig. 13.1 In-line, 3-DoF nonlinear oscillator. Three lumped masses are grounded via linear springs and linear viscous damper. Masses are also coupled with each other via linear and nonlinear springs. All three masses are excited by the single-frequency-sinusoidal forces

their corresponding expressions are obtained. In Sect. 13.4, the certain system physical parameter values for both hardening and softening cases are chosen for computing the backbone curves results. Based on the results, the modal interactions are discussed. Conclusions are drawn in Sect. 13.5.

13.2 The Nonlinear 3-DoF Oscillators Considered and Normal Form Method Application

The nonlinear 3-DoF oscillating system considered here is shown in Fig. 13.1. The system consists of three identical lumped masses which are forced sinusoidally at amplitudes P_1, P_2 and P_3 respectively at the frequency Ω. Their displacements are denoted by x_1, x_2 and x_3. For this system, all three masses are linked to the ground via linear viscous dampers, with a damping constant c, and linear springs, with a stiffness k or $k + \delta$. The middle mass connects the two masses at the sides via linear viscous dampers, with damping coefficients c', and nonlinear cubic springs with the linear stiffness k' and cubic stiffness κ. The two side masses are also coupled via a linear spring, k', and a viscous damper, c'. Here, the masses are weakly linear or nonlinear coupled with each other, thus the coupled spring stiffness is very small compared with the grounded one, i.e. $k' \ll k$ and $\kappa \ll k$. Meanwhile, a small part δ ($\delta \ll$ k) is added to the grounded spring stiffness of the 2nd mass. This leads to the equivalent linear structure of this system to be mistuned.

The equation of motion (EoM) for the 3-DoF system can be written in the general form,

$$\mathbf{M}\ddot{\mathbf{x}} + \mathbf{C}\dot{\mathbf{x}} + \mathbf{K}\mathbf{x} + \mathbf{N}_{\mathbf{x}}(\mathbf{x}) = \mathbf{P}\cos(\Omega t), \tag{13.1}$$

where $\mathbf{M}$, $\mathbf{C}$ and $\mathbf{K}$ are matrices of mass, damping and stiffness respectively; $\mathbf{x}$ is a vector of physical displacement; $\mathbf{N}_{\mathbf{x}}$ is a vector of nonlinear and damping terms and $\mathbf{P}$ is the external force amplitudes vector.

Here the backbone curves are used to help illustrate the modal interactions of the nonlinear system. So to reach this, the second-order normal form method [13, 18] is chosen to obtain the backbone curves. Firstly based on the definition of the backbone curve that it describes the loci of dynamic responses of a system when unforced and undamped, Eq. (13.1) without damping and forcing terms, as,

$$\mathbf{M}\ddot{\mathbf{x}} + \mathbf{K}\mathbf{x} + \mathbf{N}_{\mathbf{x}}(\mathbf{x}) = \mathbf{0}, \tag{13.2}$$

is under consideration. Through the linear modal transformation for decoupling the linear terms, the EoM in terms of the modal coordinates $\mathbf{q}$ is obtained,

$$\ddot{\mathbf{q}} + \Lambda\mathbf{q} + \mathbf{N}_{\mathbf{q}}(\mathbf{q}) = \mathbf{0}, \tag{13.3}$$

where $\mathbf{q}$ is a vector of modal displacements and $\mathbf{\Lambda}$ is a diagonal matrix of the squares of the corresponding linearised natural frequencies ω_{n1}, ω_{n2} and ω_{n3}, and the $\mathbf{N}_{\mathbf{q}}$ is a vector of modal nonlinear terms. Here, expressions of the linear modal natural frequencies and linear modeshape matrix used are,

$$\omega_{n1} = \sqrt{1 + \frac{1}{2}(\lambda + 3k' - \sqrt{\Delta})}, \quad \omega_{n2} = \sqrt{1 + 3k'},$$

$$\omega_{n3} = \sqrt{1 + \frac{1}{2}(\lambda + 3k' + \sqrt{\Delta})}, \tag{13.4}$$

and,

$$\mathbf{V} = \begin{bmatrix} 1 & 1 & 1 \\ a & 0 & b \\ 1 & -1 & 1 \end{bmatrix}, \tag{13.5}$$

where $a, b = -(\delta + k' \pm \sqrt{\Delta})/2k'$ and $\Delta = (\delta + k')^2 + 8k'^2$. Note that for simplifying the symbol manipulation, $k = 1$ and $m = 1$ are used here without sacrifice of the problem generality. Meanwhile, the nonlinear terms vector $\mathbf{N_q}$ can be written in the form,

$$\mathbf{N_q}(\mathbf{q}) = \mathbf{n_q}\mathbf{q}^*, \tag{13.6}$$

where nonlinear element vector $\mathbf{q}^*$ and its coefficient matrix $\mathbf{n_q}$ are,

$$\mathbf{q^*} = [q_1^3,\ q_1^2 q_2,\ q_1 q_2^2,\ q_2^3,\ q_2^2 q_3,\ q_2 q_3^2,\ q_3^3,\ q_1 q_3^2,\ q_1^2 q_3,\ q_1 q_2 q_3]^T, \tag{13.7}$$

and,

$$\mathbf{n_q^T} = \begin{bmatrix} \alpha_1^{(1)} & \alpha_1^{(2)} & \alpha_1^{(3)} \\ \alpha_2^{(1)} & \alpha_2^{(2)} & \alpha_2^{(3)} \\ \alpha_3^{(1)} & \alpha_3^{(2)} & \alpha_3^{(3)} \\ \alpha_4^{(1)} & \alpha_4^{(2)} & \alpha_4^{(3)} \\ \alpha_5^{(1)} & \alpha_5^{(2)} & \alpha_5^{(3)} \\ \alpha_6^{(1)} & \alpha_6^{(2)} & \alpha_6^{(3)} \\ \alpha_7^{(1)} & \alpha_7^{(2)} & \alpha_7^{(3)} \\ \alpha_8^{(1)} & \alpha_8^{(2)} & \alpha_8^{(3)} \\ \alpha_9^{(1)} & \alpha_9^{(2)} & \alpha_9^{(3)} \\ \alpha_0^{(1)} & \alpha_0^{(2)} & \alpha_0^{(3)} \end{bmatrix}$$

$$= \frac{2\kappa}{|\mathbf{V}|} \begin{bmatrix} (a-1)^3(b+2) & 0 & (1-a)^3(a+2) \\ 0 & 3(a-1)^2(a-b) & 0 \\ 3(a-1)(b+2) & 0 & 3(1-a)(a+2) \\ 0 & a-b & 0 \\ 3(b-1)(b+2) & 0 & 3(1-b)(a+2) \\ 0 & 3(b-1)^2(a-b) & 0 \\ (b-1)^3(b+2) & 0 & (1-b)^3(a+2) \\ 3(a-1)(b-1)^2(b+2) & 0 & 3(1-a)(1-b)^2(a+2)) \\ 3(a-1)^2(b-1)(b+2) & 0 & 3(1-a)^2(1-b)(a+2) \\ 0 & 6(a-1)(b-1)(a-b) & 0 \end{bmatrix}. \tag{13.8}$$

Lastly, the nonlinear near-identity transform, $\mathbf{q} = \mathbf{u} + \mathbf{h}$, is applied, where $\mathbf{u}$ and $\mathbf{h}$ are the fundamental and harmonic components of $\mathbf{q}$ respectively. As the harmonic components are so small that can be negligible, $\mathbf{q} = \mathbf{u}$ are used here. Assuming that the fundamental response of the ith mode is sinusoidal, u_i may be written as,

$$u_i = u_{ip} + u_{im} = \frac{U_i}{2}\left[e^{j(\omega_{ri}t - \phi_i)} + e^{-j(\omega_{ri}t - \phi_i)}\right], \tag{13.9}$$

where U_i, ω_{ri} and ϕ_i is the fundamental response amplitude, frequency and phase of the ith mode respectively. As the linear natural frequencies of the three underlying modes are close, i.e. ω_{n1}:ω_{n2}:$\omega_{n3} \approx 1$:1:1, the fundamental response frequencies of the three modes are assumed to be same, so we may write $\Omega = \omega_{n1} = \omega_{n2} = \omega_{n3}$. By picking out the resonant nonlinear terms from $\mathbf{N_q}$ to be left in $\mathbf{N_u}$ based on the rule discussed in [18], we obtain the resonant EoM as,

$$\ddot{\mathbf{u}} + \mathbf{\Lambda u} + \mathbf{N_u}(\mathbf{u}) = 0, \tag{13.10}$$

where $\mathbf{N_u}$ is a vector of resonant nonlinear terms. Substituting Eq. (13.9) into Eq. (13.10) and balancing the coefficients of $e^{j\Omega t}$ and $e^{-j\Omega t}$, we get the time-independent equations relating the modal response amplitudes and frequency,

$$(\omega_{n1}^2 - \Omega^2)U_1 + \frac{1}{4}\Big[3\alpha_1^{(1)}U_1^3 + (2+p_{12})\alpha_3^{(1)}U_1U_2^2 + 3q_{13}\alpha_5^{(1)}U_2^2U_3 + 3q_{13}\alpha_7^{(1)}U_3^3 + (2+p_{13})\alpha_8^{(1)}U_1U_3^2 + 3q_{13}\alpha_9^{(1)}U_1^2U_3\Big] = 0, \tag{13.11a}$$

$$(\omega_{n2}^2 - \Omega^2)U_2 + \frac{1}{4}\Big[(2+p_{12})\alpha_2^{(2)}U_1^2 + 3\alpha_4^{(2)}U_2^2 + (2+p_{23})\alpha_6^{(2)}U_3^2 + 3q_{13}\alpha_0^{(2)}U_1U_3\Big]U_2 = 0, \tag{13.11b}$$

$$(\omega_{n3}^2 - \Omega^2)U_3 + \frac{1}{4}\Big[3q_{13}\alpha_1^{(3)}U_1^3 + 3q_{13}\alpha_3^{(3)}U_1U_2^2 + (2+p_{23})\alpha_5^{(3)}U_2^2U_3 + 3\alpha_7^{(3)}U_3^3 + 3q_{13}\alpha_8^{(3)}U_1U_3^2 + (2+p_{13})\alpha_9^{(3)}U_1^2U_3\Big] = 0, \tag{13.11c}$$

where $p_{ij} = e^{2j|\phi_i-\phi_j|}$, $q_{ij} = e^{j|\phi_i-\phi_j|}$ and $|\phi_i - \phi_j|$ denotes the modal phase difference. By solving Eq. (13.11) with choosing specific presenting modes and their phase differences, i.e. valid values of p_{ij} and q_{ij}, the backbone curves of this nonlinear system can be calculated.

13.3 Backbone Curve Calculating

For the nonlinear 3-DoF oscillating system considered here, its three mode can be potentially interacting with each other. Thus, its backbone curves can be classified into three groups of backbone curves based on the number of present modes: single-, double- and triple-mode backbone curves labelled $S(i)$, $D(ij)$ and $T(ijk)$ respectively.

Firstly, we consider the single-mode backbone curves where the response of only one mode is present. There may be potentially three single-mode backbone curves, $S1$, $S2$ and $S3$. When only mode 2 is activated which corresponds to the backbone branch $S2$, substituting $U_1 = U_3 = 0$ into Eq. (13.11) gives its governing equation as,

$$S2 : U_2 \neq 0, \qquad \Omega^2 = \omega_{n2}^2 + \frac{3}{4}\alpha_4^{(2)}U_2^2. \tag{13.12}$$

When only mode 1 or mode 3 is activated which corresponds to the backbone curve $S1$ (and curve $S3$ respectively), substituting $U_2 = U_3 = 0$ ($U_1 = U_2 = 0$) into Eq. (13.11c) (Eq. (13.11a)) leads to,

$$\alpha_1^{(3)}U_1^3 = 0 \qquad (\alpha_7^{(1)}U_3^3 = 0). \tag{13.13}$$

This can be satisfied only when $\alpha_1^{(3)} = 0$ ($\alpha_7^{(1)} = 0$) which is not the general case. Therefore, single-mode backbone curves $S1$ and $S3$ do not generally exist here.

Secondly, double-mode backbone curves are considered. Potentially they may include the branches labelled $D12_i^{\pm}$ & $D12_o^{\pm}$, $D23_i^{\pm}$ & $D23_o^{\pm}$, and $D13_i^{\pm}$ & $D13_o^{\pm}$. The subscripts i and o denote the in-unison and out-of-unison resonant[5] interaction between the activated two modes and the superscript $+$ and $-$ indicate 0 and π modal phase difference for the in-unison resonance and $+\pi/2$ and $-\pi/2$ for the out-of-unison resonance respectively. For backbone curves $D12$, mode 1 and 2 contribute to the response, thus setting $U_3 = 0$ in Eq. (13.11) gives,

$$\begin{aligned} &3\alpha_1^{(1)}U_1^2 + (2+p_{12})\alpha_3^{(1)}U_2^2 = 4(\Omega^2 - \omega_{n1}^2), \\ &(2+p_{12})\alpha_1^{(2)}U_1^2 + 3\alpha_4^{(2)}U_2^2 = 4(\Omega^2 - \omega_{n2}^2), \\ &\alpha_1^{(3)}U_1^2 + \alpha_3^{(3)}U_2^2 = 0. \end{aligned} \tag{13.14}$$

Equation (13.14) is overdetermined as there are two unknowns, U_1 and U_2 with three equations (note that Ω is a constant when considering the responses at a certain frequency). Thus Eq. (13.14) can have solutions only if $\alpha_1^{(3)} = \alpha_3^{(3)} = 0$ which is not the general situation. Similarly, it is also the case for backbone curves $D23$. Therefore, double-mode backbone curves $D12$ and $D23$ do not exist for the nonlinear system considered for the general situation. When only mode 1 and 3 are present which corresponds to backbone curves $D13$, substituting $U_2 = 0$ into Eq. (13.11) leads to,

$$\begin{aligned}(\omega_{n1}^2 - \Omega^2)U_1 + \frac{3}{4}\Big[\alpha_1^{(1)}U_1^3 + q_{13}\alpha_7^{(1)}U_3^3 + \alpha_8^{(1)}U_1U_3^2 + q_{13}\alpha_9^{(1)}U_1^2U_3\Big] = 0,\\ (\omega_{n3}^2 - \Omega^2)U_3 + \frac{3}{4}\Big[q_{13}\alpha_1^{(3)}U_1^3 + \alpha_7^{(3)}U_3^3 + q_{13}\alpha_8^{(3)}U_1U_3^2 + \alpha_9^{(3)}U_1^2U_3\Big] = 0.\end{aligned} \tag{13.15}$$

Here, due to the existence of $q_{13} = e^{j|\phi_1-\phi_3|}$, the value of $p_{13} = e^{2j|\phi_1-\phi_3|}$ has to be equal to 1 to ensure valid physical solutions of Eq. (13.15). Therefore the phase difference between mode 1 and 3 cannot be: $\pm\pi/2$, which means the out-of-unison backbone curves $D13_o^{\pm}$ do not exist here. Further rearranging Eq. (13.15), we obtain a quartic equation in U_3 which relates the response amplitudes of modes 1 and 3 as,

$$D13_i^{\pm}: \begin{Bmatrix} U_1 \neq 0, \\ U_3 \neq 0, \end{Bmatrix} \begin{array}{l} \alpha_7^{(1)}U_3^4 + q_{13}(\alpha_8^{(1)} - \alpha_7^{(3)})U_1U_3^3 + (\alpha_9^{(1)} - \alpha_8^{(3)})U_1^2U_3^2 \\ \quad + q_{13}[(\alpha_1^{(1)} - \alpha_9^{(3)})U_1^3 + \frac{4}{3}(\omega_{n1}^2 - \omega_{n3}^2)U_1]U_3 - \alpha_1^{(3)}U_1^4 = 0. \end{array} \tag{13.16}$$

Combined with the response frequency equation,

$$\Omega = \sqrt{\omega_{n1}^2 + \frac{3}{4}\{\alpha_1^{(1)}U_1^2 + q_{13}\alpha_7^{(1)}U_3^3/U1 + \alpha_8^{(1)}U_3^2 + q_{13}\alpha_9^{(1)}U_1U_3\}}, \tag{13.17a}$$

or

$$\Omega = \sqrt{\omega_{n3}^2 + \frac{3}{4}\{q_{13}\alpha_1^{(3)}U_1^3/U_3 + \alpha_7^{(3)}U_3^2 + q_{13}\alpha_8^{(3)}U_1U_3 + \alpha_9^{(1)}U_1^2\}}, \tag{13.17b}$$

we can compute the in-unison backbone curves $D13_i^{\pm}$. Note that the existence of the backbone curve branches $D13_i^{\pm}$ are still based on the valid solutions of Eqs. (13.16) and (13.17) which are further decided by the values of the coefficients of nonlinear terms, $\alpha_l^{(i)}$.

Lastly, we analyse the existence of triple-mode backbone curves. For the nonlinear 3-DoF system here, there may be triple-backbone backbone curves: $T123_{i,\,i}^{\pm,\pm}$, $T123_{i,\,o}^{\pm,\pm}$, $T123_{o,\,i}^{\pm,\pm}$ and $T123_{o,\,o}^{\pm,\pm}$. Again the subscripts denote type of resonance interaction with mode 1 and superscripts denote their phase differences. By observing Eq. (13.11), the backbone curves $T123_{i,o}$ and $T123_{o,o}$ do not exist here due to the same reason of the nonexistence of double-mode backbone curves $D13_o$ (i.e. the existence of q_{13}). For backbone curves $T123_{i,i}$ where the phase difference between mode 1, 2 and mode 1, 3 are $|\phi_1 - \phi_2| = 0$ or π and $|\phi_1 - \phi_3| = 0$ or π respectively, substituting $p_{12} = p_{23} = p_{13} = 1$ into Eq. (13.11) and rearranging gives,

$$\begin{aligned}&(\alpha_1^{(1)} - \alpha_2^{(2)})U_1^3 + (\alpha_3^{(1)} - \alpha_4^{(2)})U_1U_2^2 + q_{13}\alpha_5^{(1)}U_2^2U_3 + q_{13}\alpha_7^{(1)}U_3^3 \\ &\quad + (\alpha_8^{(1)} - \alpha_6^{(2)})U_1U_3^2 + q_{13}(\alpha_9^{(1)} - \alpha_0^{(2)})U_1^2U_3 \\ &\quad + \frac{4}{3}(\omega_{n1}^2 - \omega_{n2}^2)U_1 = 0,\end{aligned} \tag{13.18a}$$

$$\begin{aligned}&q_{13}\alpha_1^{(3)}U_1^3 + q_{13}\alpha_3^{(3)}U_1U_2^2 + (\alpha_5^{(3)} - \alpha_4^{(2)})U_2^2U_3 + (\alpha_7^{(3)} - \alpha_6^{(2)})U_3^3 \\ &\quad + q_{13}(\alpha_8^{(3)} - \alpha_0^{(2)})U_1U_3^2 + (\alpha_9^{(3)} - \alpha_2^{(2)})U_1^2U_3 \\ &\quad + \frac{4}{3}(\omega_{n3}^2 - \omega_{n2}^2)U_3 = 0.\end{aligned} \tag{13.18b}$$

By treating U_2 as a constant, Eq. (13.18) is a cubic equation set in U_1 and U_3 which can be solved for the response amplitudes. Then substitute the valid solutions of U_1, U_2 and U_3 into the rearranged Eq. (13.11b) as,

$$\Omega = \sqrt{\omega_{n2}^2 + \frac{3}{4}\left[\alpha_2^{(2)} U_1^2 + \alpha_4^{(2)} U_2^2 + \alpha_6^{(2)} U_3^2 + \alpha_8^{(1)} U_1 U_3\right]} \tag{13.19}$$

to calculate the response frequency. Similarly, substituting $p_{12} = p_{23} = -1$ and $p_{13} = 1$ into Eq. (13.11) gives the response amplitude equation set for backbone curves $T123_{o,i}$ as,

$$\begin{aligned}(3\alpha_1^{(1)} - \alpha_2^{(2)})U_1^3 + (\alpha_3^{(1)} - 3\alpha_4^{(2)})U_1 U_2^2 + 3q_{13}\alpha_5^{(1)} U_2^2 U_3 + 3q_{13}\alpha_7^{(1)} U_3^3 \\ + (3\alpha_8^{(1)} - \alpha_6^{(2)})U_1 U_3^2 + 3q_{13}(\alpha_9^{(1)} - \alpha_0^{(2)})U_1^2 U_3 \\ + 4(\omega_{n1}^2 - \omega_{n2}^2)U_1 = 0,\end{aligned} \tag{13.20a}$$

$$\begin{aligned}3q_{13}\alpha_1^{(3)} U_1^3 + 3q_{13}\alpha_3^{(3)} U_1 U_2^2 + (\alpha_5^{(3)} - 3\alpha_4^{(2)})U_2^2 U_3 + (3\alpha_7^{(3)} - \alpha_6^{(2)})U_3^3 \\ + 3q_{13}(\alpha_8^{(3)} - \alpha_0^{(2)})U_1 U_3^2 + (3\alpha_9^{(3)} - \alpha_2^{(2)})U_1^2 U_3 \\ + 4(\omega_{n3}^2 - \omega_{n2}^2)U_3 = 0,\end{aligned} \tag{13.20b}$$

and its response frequency equation is,

$$\Omega = \sqrt{\omega_{n2}^2 + \frac{1}{4}\left[\alpha_2^{(2)} U_1^2 + 3\alpha_4^{(2)} U_2^2 + \alpha_6^{(2)} U_3^2 + 3\alpha_8^{(1)} U_1 U_3\right]} \tag{13.21}$$

Note that the above obtained backbone curve equations relate the response frequency and amplitudes in modal coordinates, by applying the inverse linear modal transform with the assumption $\mathbf{q} = \mathbf{u}$, i.e. assuming the harmonics can be neglected, we can get the backbone curves in the physical space.

13.4 Backbone Results

Now we choose specific values of the system parameters for the equations obtained in Sect. 13.3 to compute the backbone curves to help illustrate the modal interactions. Figures 13.2 and 13.3 shows the backbone curves for the hardening and softening nonlinear cases respectively. All panels show the backbone curves in the projection of response frequency against

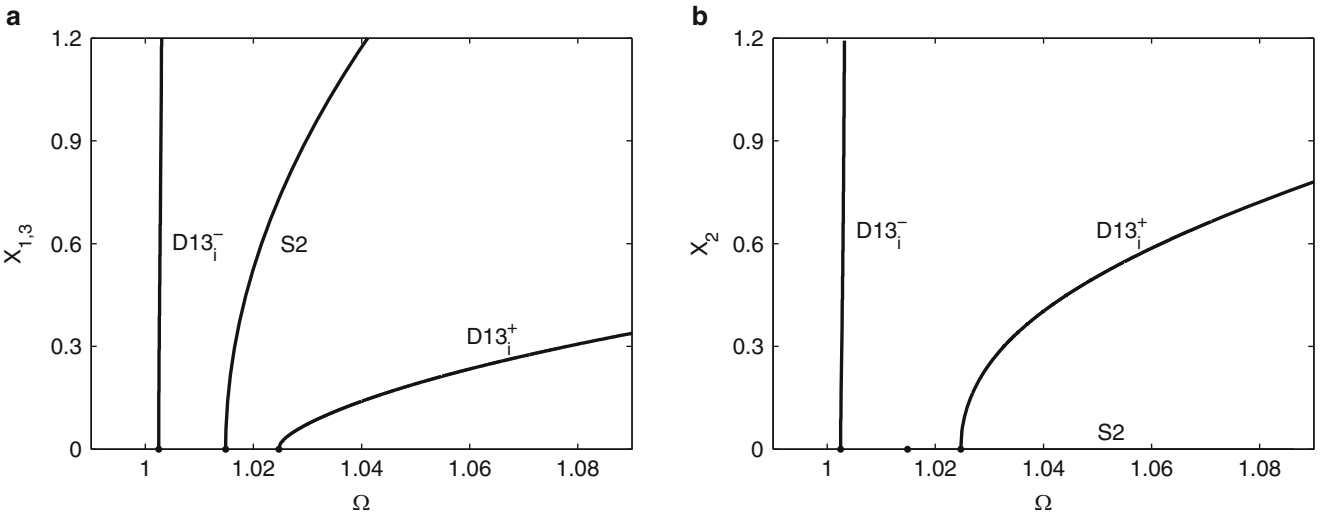

Fig. 13.2 Backbone curves for the hardening nonlinear 3-DoF oscillator with the physical parameters $m = 1$, $k = 1$, $k' = 0.01$, $\delta = 0.025$ and $\kappa = 0.025$, so the modal natural frequencies are $\omega_{n1} = 1.0025$, $\omega_{n2} = 1.0150$ and $\omega_{n3} = 1.0250$. The corresponding backbone curves are labelled as discussed in Sect. 13.3

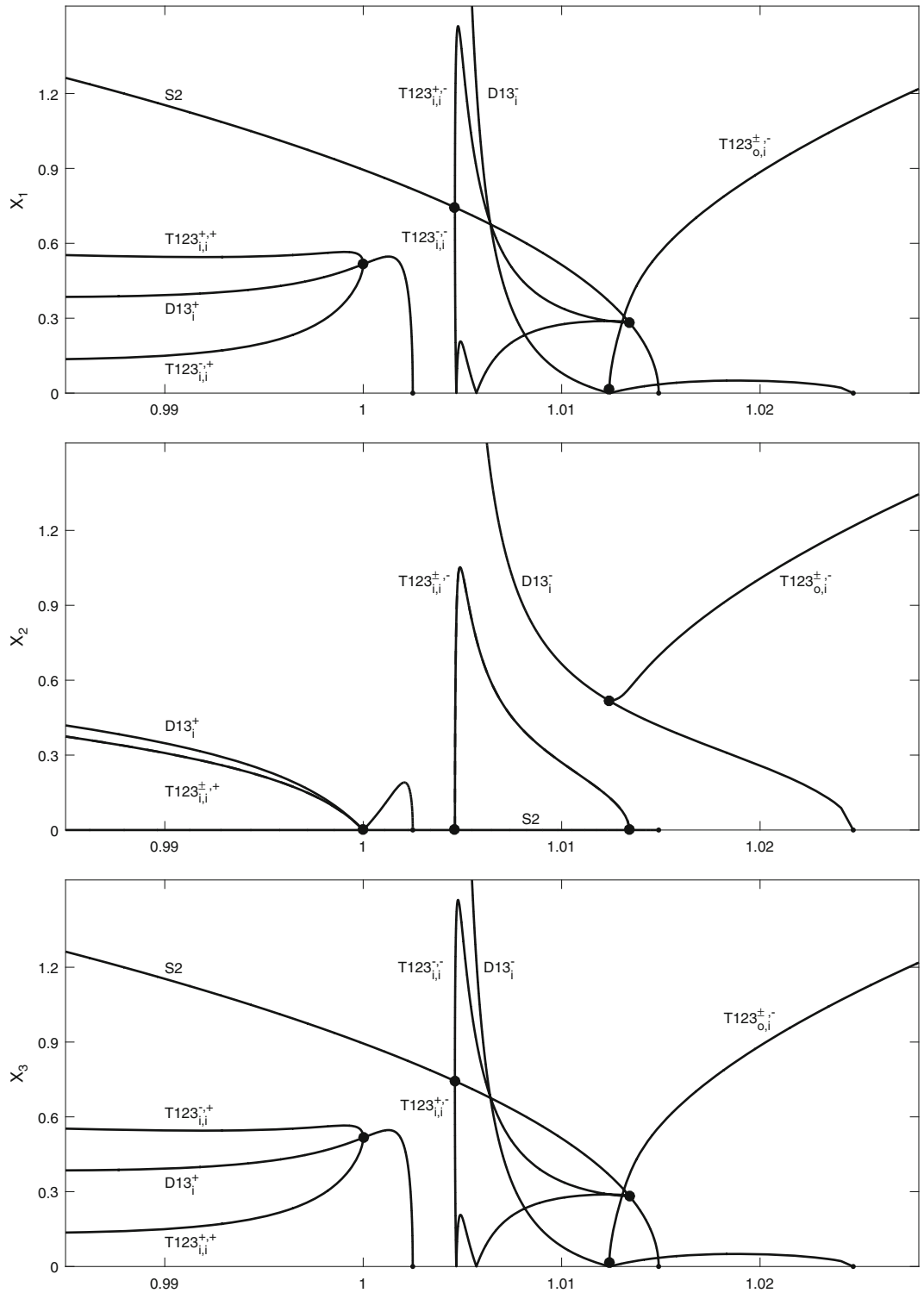

Fig. 13.3 Backbone curves for the softening nonlinear oscillator with the physical parameters $m = 1$, $k = 1$, $k' = 0.01$, $\delta = 0.025$ and $\kappa = -0.025$. Specific backbone curves are labelled as discussed in Sect. 13.3 and bifurcation points are noted by *black dots*

a displacement. For both cases, their linear modal natural frequencies are $\omega_{n1} = 1.0025$, $\omega_{n2} = 1.0150$ and $\omega_{n3} = 1.0250$ with linear parameters $k = 1$, $k' = 0.01$ and $\delta = 0.025$ and the cubic stiffness are $\kappa = \pm 0.025$ respectively.

In Fig. 13.2, it can be seen that there are three backbone curves, one single-mode backbone curve $S2$ and two double-mode backbone curves $D13_i^{\pm}$, for the hardening situation. The single-mode backbone curve, $S2$, starts from the point $[\omega_{n2},\ 0]$ and the double-mode backbone curves, $D13_i^{\pm}$, are emanating from the points $[\omega_{n3},\ 0]$ and $[\omega_{n1},\ 0]$ respectively. There is no triple-mode backbone curve as there is no valid solution for Eqs. (13.18)–(13.21). Note that due to the symmetry of the structure the backbone curves of mass 1, x_1, and mass 3, x_3, are same. For the hardening nonlinear case, although there exist two-mode interactions in the modal space its backbone curves of the physical displacements of masses are as the same as the simple nonlinear 3-DoF systems without nonlinear modal interaction.

Figure 13.3 shows the backbone curves for the softening case which are far more complicated than the results in Fig. 13.2. Here there are ten branches which includes all three kinds of backbone curves. The same as that of the hardening case, single- and double-mode backbone curves are directly starting from the points at the response frequency axis with the coordinates of the linear modal natural frequencies. All the triple-mode backbone curves are bifurcating from either single- or double-mode backbone curves: branches $T123_{i,\,i}^{\pm,+}$ bifurcate from $D13_i^{+}$; $T123_{i,\,i}^{\pm,-}$ bifurcate from $S2$ and $T123_{o,\,i}^{\pm,-}$ bifurcate from $D13_i^{-}$. Here backbone curves $T123_{o,\,i}^{\pm,+}$ do not exist. Note that here the backbone curves of mass 1 and 3 are no longer the same as the positions of branches $T123_{i,\,i}^{-,+}$ & $T123_{i,\,i}^{+,+}$ and $T123_{i,\,i}^{+,-}$ & $T123_{i,\,i}^{-,-}$ are swapping respectively. Furthermore, there are several unique features about the triple-mode backbone curves here. Firstly, as the frequency reduces, the out-of-phase backbone curves $T123_{i,\,i}^{\pm,-}$ initially start from and then finally terminate at the same backbone curve, $S2$. This means that the three-mode interaction may not occur out of the interaction frequency band even if the external input energy is enough for triggering it. The other interesting feature is that the out-of-unison backbone curves $T123_{o,\,i}^{\pm,-}$ show a hardening nonlinearity that the response frequency increases with the response amplitude even if the nonlinear stiffness are negative.

13.5 Conclusions

In this paper, a nonlinear modal behaviour of a three-degree-of-freedom coupled oscillator with cubic stiffness nonlinearities has been considered. In particular, the backbone curves of its corresponding equivalent undamped and unforced system have been analysed to help illustrate the occurrence of potential modal interactions This is an important topic because the majority of vibration examples that relate to modal analysis are lightly damped and therefore the dynamic behaviour is largely determined by the properties of the underlying undamped dynamic system.

First we considered the undamped, unforced case where all the underlying linear modal frequencies are close, i.e. ω_{n1}:ω_{n2}:$\omega_{n3} \approx 1$:1:1. Through the application of the second-order normal form method, we obtained the time-independent equations relating the modal response frequency and amplitudes based on the assumption that the modal response frequencies are same, i.e. $\Omega = \omega_{r1} = \omega_{r2} = \omega_{r3}$. Then discussing the number of contributing modes and their corresponding phase difference, we have obtained the backbone curve expressions for the single-, double- and triple-mode backbone curves. We have shown the results of the nonlinear system considered with specific physical parameters values for both hardening and softening cases. For the hardening case, the three-mode interaction does not happen. For the softening case, both two- and three-mode interactions occur. All triple-mode backbone curves are bifurcating from either single- or double-mode backbone curves. Besides, there are some unique features about the triple-mode backbone curves: (a) some of the in-unison branches only have values within a limited frequency range and, (b) the out-of-unison ones show a hardening nonlinearity for the softening situation. From the backbone curve results of the nonlinear unforced and undamped system, it can be seen that the occurrence of the three-mode interaction makes dynamic response of the weakly nonlinear multi-degree-of-freedom systems more complicated.

Acknowledgements The authors would like to acknowledges the support of the Engineering and Physical Sciences Research Council. S.A.N is supported by EPSRC Fellowship EP/K005375/1. D.J.W is supported by EPSRC grant EP/K003836/1.

References

1. Amabili, M.: Nonlinear Vibrations and Stability of Shells and Plates. Cambridge University Press, Cambridge (2008)
2. Arnol'd, V.I.: Geometrical Methods in the Theory of Ordinary Differential Equations, vol. 250. Springer Science & Business Media, New York (2012)

3. Cammarano, A., Hill, T., Neild, S., Wagg, D.: Bifurcations of backbone curves for systems of coupled nonlinear two mass oscillator. Nonlinear Dyn. **77**(1–2), 311–320 (2014)
4. Hill, T., Cammarano, A., Neild, S., Wagg, D.: Interpreting the forced responses of a two-degree-of-freedom nonlinear oscillator using backbone curves. J. Sound Vib. **349**, 276–288 (2015)
5. Hill, T.L., Cammarano, A., Neild, S.A., Wagg, D.J.: Out-of-unison resonance in weakly nonlinear coupled oscillators. Proc. Roy. Soc. Lond. A Math. Phys. Eng. Sci. **471**, 20140659 (2015)
6. Jezequel, L., Lamarque, C.H.: Analysis of non-linear dynamical systems by the normal form theory. J. Sound Vib. **149**(3), 429–459 (1991)
7. Kerschen, G., Kowtko, J.J., McFarland, D.M., Bergman, L.A., Vakakis, A.F.: Theoretical and experimental study of multimodal targeted energy transfer in a system of coupled oscillators. Nonlinear Dyn. **47**(1–3), 285–309 (2007)
8. Kerschen, G., Peeters, M., Golinval, J.C., Vakakis, A.F.: Nonlinear normal modes, part i: a useful framework for the structural dynamicist. Mech. Syst. Signal Process. **23**(1), 170–194 (2009)
9. Lewandowski, R.: On beams membranes and plates vibration backbone curves in cases of internal resonance. Meccanica **31**(3), 323–346 (1996)
10. Liu, X., Cammarano, A., Wagg, D. J., Neild, S. A., & Barthorpe, R. J: N-1 modal interactions of a three-degree-of-freedom system with cubic elastic nonlinearities. Nonlinear Dyn. **83**(1-2), 497–511 (2016)
11. Liu, X., Cammarano, A., Wagg, D., Neild, S., Barthorpe, R.: Nonlinear modal interaction analysis for a three degree-of-freedom system with cubic nonlinearities. Nonlinear Dyn. **1**, 123–131 (2016)
12. Nayfeh, A.H., Mook, D.T.: Nonlinear Oscillations. Wiley, New York (2008)
13. Neild, S.A., Wagg, D.J.: Applying the method of normal forms to second-order nonlinear vibration problems. Proc. R. Soc. Lond. A Math. Phys. Eng. Sci. **467**, 1141–1163 (2011)
14. Pierre, C., Jiang, D., Shaw, S.: Nonlinear normal modes and their application in structural dynamics. Math. Probl. Eng. **2006**, 10847, 1–15 (2006)
15. Rega, G., Lacarbonara, W., Nayfeh, A., Chin, C.: Multiple resonances in suspended cables: direct versus reduced-order models. Int. J. Non-Linear Mech. **34**(5), 901–924 (1999)
16. Touzé, C., Amabili, M.: Nonlinear normal modes for damped geometrically nonlinear systems: application to reduced-order modelling of harmonically forced structures. J. Sound Vib. **298**(4), 958–981 (2006)
17. Touzé, C., Thomas, O., Chaigne, A.: Asymmetric non-linear forced vibrations of free-edge circular plates. part 1: theory. J. Sound Vib. **258**(4), 649–676 (2002)
18. Wagg, D., Neild, S.: Nonlinear Vibration with Control. Springer, Berlin (2014)

Chapter 14
Investigating Nonlinear Modal Energy Transfer in a Random Load Environment

Joseph D. Schoneman and Matthew S. Allen

Abstract When a structure is subjected to an extreme environment, its linear normal modes, which are uncoupled under small loads, begin to influence each other and exchange energy. This is easily explained when the nonlinear normal modes of the structure are computed, since they show internal resonances where the underlying linear modes combine to produce the NNM solution at each excitation level. This paper examines the degree to which nonlinear modal coupling can serve as an energy transfer mechanism in order to reduce the vibration levels of a structure subjected to a broadband, random forcing. The structure in question is a beam with an intermediate support that is adjusted in order to vary the frequency ratios between modes. To explore the significance of modal coupling, two types of reduced order models are examined: A customary model including all of the coupling terms between the linear modes, and an uncoupled reduced order model which contains nonlinear stiffness terms in single modes only. The differences in response between the two models are used to quantify the effect of nonlinear modal coupling in the structure.

Keywords Nonlinear reduced order modeling • Nonlinear normal modes • Random response

14.1 Introduction

Linear analysis techniques are the foundation of modern structural dynamics. Most structures behave linearly at low levels of dynamic excitation, but certain high performance applications require a combination of low structural weight and high environmental loads, causing responses in the nonlinear regime. Specific motivating cases include skin panels of hypersonic vehicles [1], which undergo severe thermo-acoustic loadings at cruising speeds in excess of Mach 5, as well as the ducted engine assemblies of stealth aircraft, where jet exhaust impinges directly on the structure. Geometric nonlinearity is also prevalent in the design of joined-wing concepts [2], and in the behavior of extremely lightweight space structures such as solar sails [3].

It has long been possible to compute the response of geometrically nonlinear structures in finite element software, but the computational cost is orders of magnitude higher than that for linear analysis of the same structure. State-of-the-art finite element software combined with high performance computing clusters allow for multi-physics simulations with extremely complicated models—millions of degrees of freedom—in a reasonable amount of time: several hours to several days, depending on the model complexity and physics involved. This capability is extremely powerful, but such analysis times still limit the amount of design insight which can be obtained from a model. For applications requiring hundreds or thousands of analyses, such as optimization studies, day-long simulation times are not acceptable. Another application of interest is the "digital twin" concept under examination by the United States Air Force, which proposes the simulation of an entire aircraft over its flight history in near-real-time [4]. Full-order coupled simulation of the thermal, aerodynamic, and nonlinear structural physics of an aircraft is still barely (if at all) feasible, let alone achievable in real-time.

One key strategy for addressing these concerns is the use of reduced order modeling (ROM) or, more specifically, nonlinear reduced order modeling (NLROM) techniques. Over the past three decades, NLROM techniques have emerged which allow efficient simulation of geometric nonlinearity in beams and plates experiencing large deformations relative to their thickness. This type of nonlinearity occurs due to the axial "membrane" stretching when thin members deflect on the order of their thickness; a schematic is given for a clamped-clamped beam in Fig. 14.1.

The earliest known presentation of NLROM techniques is that by Nash [5], with other early work in the field put forward by Segalman and Dorhmann [6, 7], McEwan [8], and Muravyov and Rizzi [9]. A review of work in the field was performed

J.D. Schoneman (✉) • M.S. Allen
Department of Engineering Physics, University of Wisconsin, 1500 Engineering Drive, Madison, WI 53706, USA
e-mail: schoneman@wisc.edu; matt.allen@wisc.edu

G. Kerschen (ed.), *Nonlinear Dynamics, Volume 1*, Conference Proceedings of the Society for Experimental Mechanics Series,
DOI 10.1007/978-3-319-29739-2_14

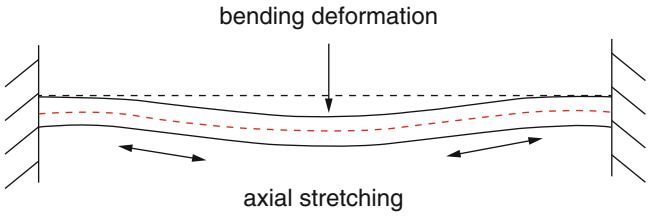

Fig. 14.1 Illustration of axial stretching effects for a clamped-clamped beam. At low deflections, deformation along the neutral axis is negligible; as the deflection increases towards one beam thickness, the axial deformation increases nonlinearly and must be included in the analysis

by Mignolet et al. [10] in 2013. Nonlinearities are almost always represented as a series of quadratic and cubic terms in the modal coordinates, which are usually obtained by leveraging the nonlinear analysis capabilities of commercial finite element (FE) software. A low-order subset (usually below ten) of linear modes is selected for inclusion in the NLROM; a series of static (FE) analyses then characterizes the nonlinear effects of membrane stretching. Forces (or deflections) are applied in the shapes of the selected modal basis, and the resulting deflections (or forces) from the finite element analysis are used to determine suitable coefficients for nonlinear terms in the NLROM. The technique used for this study is given by Gordon and Hollkamp in [1] and [11], and described in further detail in Sect. 14.3.1.

While quite a few works have discussed how to compute accurate and efficient NLROMs, little has been done to explore how these techniques can be leveraged to optimize the design of a structure. However, several works have explored optimization of geometrically nonlinear structures. With energy harvesters as a target application, Dou and Jensen seek to maximize the response of a nonlinear beam at resonance [12]; focusing on nonlinear tuned vibration absorbers, which maintain robustness in the presence of base structure nonlinearity, Grappasonni describes an optimization process used to match the characteristics of a tuned nonlinear vibration absorber to the nonlinearity of the base structure [13]. In these works the Galerkin method was used to create simple low-order models of the structures of interest; higher fidelity finite element models were not considered.

Structural loads during hypersonic flight regimes can be represented as broadband, random forcings. Random response computations are a particularly attractive use of NLROMs due to the long time histories required to obtain response statistics in a nonlinear model and the ensuing high computational costs of a full-order model. There are two key mechanisms which may reduce (or increase) the response level of a structure relative to a linear analysis:

- As displacements increase, the structure stiffens as a result of membrane stretching. This is primarily a static effect.
- Coupling between nonlinear normal modes—discussed in Sect. 14.3.3—transfers energy from excited modes to non-excited modes. Often, lower frequency modes will transfer energy to higher frequency modes acting to increase the effective damping of some modes; however, this can also cause unexpected response levels at higher frequencies.

The objective of this study is to examine specifically the reduction in response which results from nonlinear modal coupling. It is difficult to precisely decouple the effects of increased stiffness and the effects of modal energy transfer, but as a proxy, the response of fully coupled NLROMs is compared with that predicted by uncoupled NLROMs. Using the efficient analysis capability of these NLROMs, the structural response over a range of parameters is examined in a two-dimensional design space, in order to better understand the topology of the stress and displacement response surfaces.

A key concept in the analysis of nonlinear structures is that of the nonlinear normal mode, a generalization of the linear normal mode to nonlinear structures. The NNM concept in use here defines a nonlinear normal mode as a *not-necessarily synchronous periodic response of the conservative nonlinear system* [14]; since the system is nonlinear, its periodic response is a function of the amplitude of its state variables. Both the frequency of the periodic response and its shape evolve based on the amplitude of these variables.

A common visualization for the NNM is the frequency-energy plot (FEP), which tracks the variation of the resonant frequency as a function of energy present in the structure—see Fig. 14.5 for an example. FEP's allow an easy understanding of the basic characteristics of a nonlinear system and also allow ready identification of any "internal resonances" present in the system. These resonances typically occur when a lower mode's frequency reaches an integer multiple of a higher mode's frequency, and it is theorized that they may play a significant role in modal energy transfer. In much of the classical literature (see, e.g. Nayfeh [15]) internal resonances occur only when the linear natural frequencies have certain ratios. In the NNM framework, they may also occur as the frequency of one NNM backbone becomes a multiple of another NNM backbone. By adjusting the ratio of linear natural frequencies, the energy level at which an internal resonance appears can be adjusted.

The framework of the paper is as follows: First, the structure and load case of interest are described, and a reference condition is developed using linear analysis techniques. The NLROM technique in use is then described, and full-order

simulations of the model are generated and compared to reduced-order results. Finally, a two-dimensional parameter sweep is performed in order to visually examine the response of the structure as a function of the varied parameters. The accuracy of fully coupled and uncoupled NLROM's is compared, and a hypothetical optimum is chosen for the model. A discussion of the results and their implications follows.

14.2 Example Structure and Linear Analysis

The structure of interest for this study is a clamped-clamped beam with an intermediate support. The intermediate support is constrained vertically but left free in the horizontal and rotational coordinates; a schematic is shown in Fig. 14.2. The location of this support can be adjusted to modify the ratios of natural frequencies in the model. These ratios determine the location in frequency-energy space of any internal resonances in the structure. All of the simulations presented in this study use a uniform pressure loading applied to the left half of the beam; the pressure amplitude is a broadband, random variable with a flat power spectral density (PSD) level from 0 to 1000 Hz. The half-beam, rather than a full-beam, loading is used in order to spatially excite as many modes of the structure as possible and to break the symmetry of the configuration.

In addition to affecting the natural frequency ratios, adjusting the support location also adjusts the bending stiffness of the beam with respect to a given loading. As such, only beam configurations which are near the maximum-stiffness support ratio location will be examined. This location can be determined using traditional linear structural dynamics techniques. A "reference beam" is used for this calculation, with properties given in Table 14.1.

To obtain a structural model of the beam, a MATLAB-based beam finite element tool is used to generate mass and stiffness matrices; the response of the structure is then calculated in the modal domain. The process is briefly demonstrated below. The equations of motion for a linear structure with n degrees of freedom are

$$\mathbf{M}\ddot{\mathbf{x}} + \mathbf{C}\dot{\mathbf{x}} + \mathbf{K}\mathbf{x} = \mathbf{f} \tag{14.1}$$

with $\mathbf{M}$, $\mathbf{C}$, and $\mathbf{K}$ the respective mass, damping, and stiffness matrices (all size $n \times n$), $\mathbf{x}$ the displacements of the structure, $\mathbf{f}$ the vector of applied forces, (both size $n \times 1$), and the overdot representing a derivative with respect to time. The structure's linear normal modes are obtained by performing a coordinate transformation $\mathbf{x} = \mathbf{\Phi q}$ in which $\mathbf{q}$ are "modal coordinates" representing the response level of the normal modes which are contained in the columns of the modal matrix $\mathbf{\Phi}$. The modes themselves are found by solving the generalized eigenvalue problem for the undamped structure,

$$[\mathbf{K} - \omega_r^2 \mathbf{M}]\boldsymbol{\phi}_r = 0 \tag{14.2}$$

in which each eigenvector $\boldsymbol{\phi}_r$ corresponds to a circular natural frequency ω_r. The modal matrix is normalized such that it is orthogonal with respect to the mass matrix, i.e. $\mathbf{\Phi}^T\mathbf{M}\mathbf{\Phi} = \mathbf{I}$; this also requires that $\mathbf{\Phi}^T\mathbf{K}\mathbf{\Phi} = \mathbf{\Lambda}$ where $\mathbf{\Lambda}$ is a diagonal matrix with $\Lambda_{rr} = \omega_r^2$. Taking all this together, the equation of motion (14.1) becomes

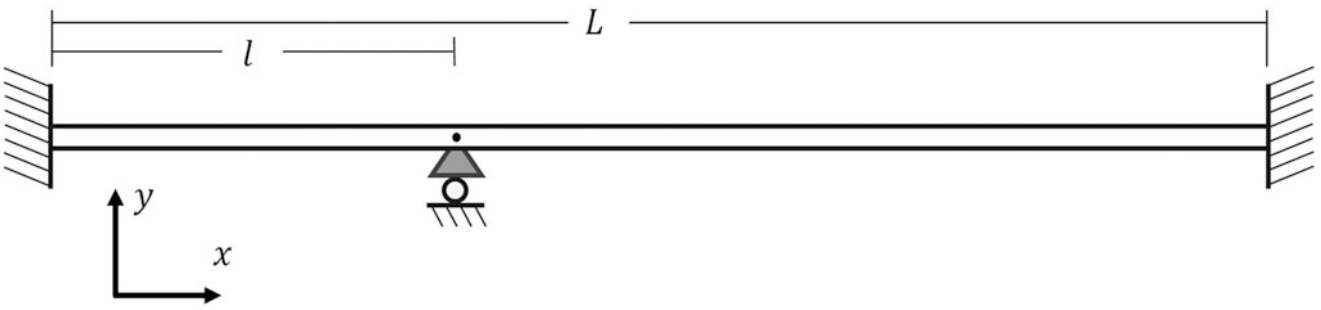

Fig. 14.2 A schematic of the beam under consideration for the present study

Table 14.1 Properties of the beam used for linear support optimization

Thickness (mm)	Length (mm)	Width (mm)	Young's modulus (MPa)	Density (Tonne/mm^3)
2	250	25	71,000	$2.7 \cdot 10^{-9}$

$$\ddot{\mathbf{q}} + \bar{\mathbf{C}}\dot{\mathbf{q}} + \mathbf{\Lambda}\mathbf{q} = \mathbf{\Phi}^T\mathbf{f} \tag{14.3}$$

The modal damping matrix is specified using critical damping ratios for each mode such that $\bar{C}_{rr} = 2\zeta_r\omega_r$. A ratio of 0.01 % is used throughout this work for all modes.

It is usually not practical or necessary to retain all n linear normal modes for simulation of a linear response. By considering only a subset m of dynamically important modes, a linear reduced order model (ROM) is created. Selection of dynamically important modes is performed by considering the frequency content of the loading; in this case, with no excitation above 1000 Hz, the first four modes of the structure are included: For the properties given above, the lowest possible fourth bending mode has a natural frequency of 1507 Hz.

Finally, the linear response to a random excitation is considered. The frequency-domain solution to Eq. (14.3) is

$$\mathbf{Q} = [-\omega^2\mathbf{I} + i\omega\bar{\mathbf{C}} + \mathbf{\Lambda}]^{-1}\mathbf{\Phi}^T\mathbf{F} \tag{14.4}$$

with $\mathbf{Q}$ and $\mathbf{F}$ the frequency-domain realizations of $\mathbf{q}$ and $\mathbf{f}$. Note that the matrix inversion is trivial due to the diagonal nature of the equations. The frequency-domain solution to $\mathbf{x}$ can then be written as $\mathbf{X} = \mathbf{\Phi}\mathbf{Q} = \mathbf{H}\mathbf{F}$ where $\mathbf{H}$ is the transfer function given by

$$\mathbf{H} = \mathbf{\Phi}[-\omega^2\mathbf{I} + i\omega\bar{\mathbf{C}} + \mathbf{\Lambda}]^{-1}\mathbf{\Phi}^T \tag{14.5}$$

The frequency response $\mathbf{X}$ due to an arbitrary random excitation $\mathbf{F}$ cannot be uniquely specified. Instead, the response is quantified using the (PSD) of $\mathbf{X}$, $\mathbf{S}_{xx}$

$$\mathbf{S}_{xx} = \mathbf{X}\mathbf{X}^* = \mathbf{H}\mathbf{S}_{ff}\mathbf{H}^* \tag{14.6}$$

where the $()^*$ operator denotes the Hermitian transpose. Integrating the PSD across the frequency axis yields the variance of the response, and taking the square root of the variance yields the standard deviation. The objective function for the optimization is the maximum standard deviation of the response at any location on the beam.

The values shown in Table 14.1 along with a random force with a flat PSD ceiling of $1 \cdot 10^{-7}$ MPa^2/Hz over 0–1000 Hz were used for linear optimization. MATLAB's *fmincon* routine, which finds the minimum of a multivariable function subject to constraints on the inputs, was used to obtain an optimum support location of $r = 35.43$ %. A plot of displacement standard deviation against support location is shown in Fig. 14.3. The maximum response standard deviation for this support location is 0.108 mm; for the given beam thickness of 2 mm, the beam remains in the linear response regime.

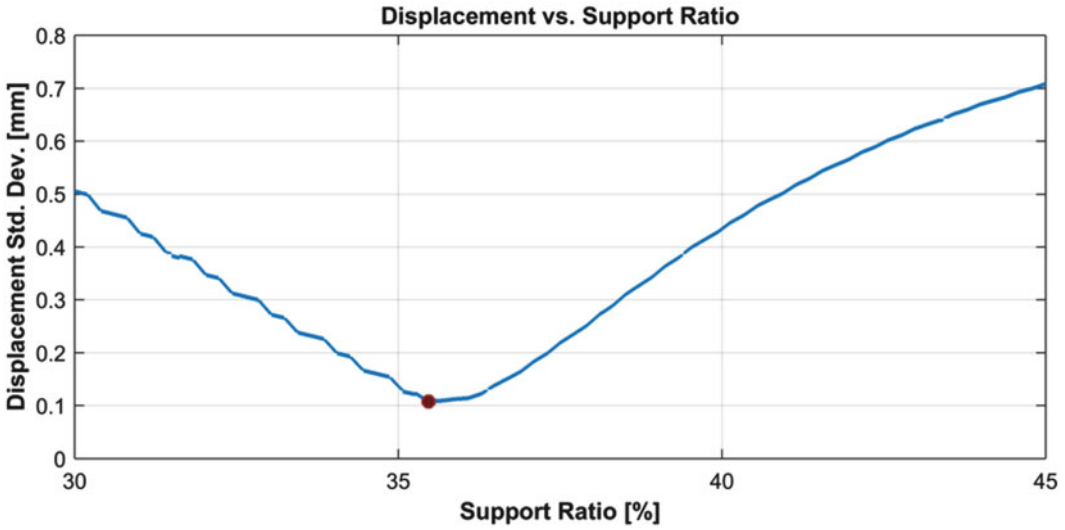

Fig. 14.3 A schematic of the beam under consideration for the present study

14.3 Nonlinear Model Development

Development of the nonlinear model consists of three main steps: Specification of a nonlinear reduced order model, development of a full-order "truth" solution for comparison, and validation. Each of the steps are described in turn below.

14.3.1 Nonlinear Reduced Order Models

As load levels are increased, beam deflections begin to exceed one beam thickness. At and above this level, significant nonlinearities are evident in the response. A linear analysis will significantly overestimate both the resulting deflection and stresses in the beam. It is possible to integrate the full-order finite element model in the FEM software to compute the response to a random load, however, the computational costs are many orders of magnitude higher than for the frequency domain analysis used for a linear system. The previously mentioned NLROM technique [11] can be used to reduce the computational cost while maintaining the accuracy of a nonlinear model. A nonlinear stiffness term, $\mathbf{f}_{nl}(\mathbf{x})$, is added to the linear model

$$\mathbf{M}\ddot{\mathbf{x}} + \mathbf{C}\dot{\mathbf{x}} + \mathbf{K}\mathbf{x} + \mathbf{f}_{nl}(\mathbf{x}) = \mathbf{f} \tag{14.7}$$

The structure is transformed to modal space using a subset of m modes

$$\ddot{\mathbf{q}} + \bar{\mathbf{C}}\dot{\mathbf{q}} + \boldsymbol{\Lambda}\mathbf{q} + \boldsymbol{\theta}(\mathbf{q}) = \boldsymbol{\Phi}^T\mathbf{f} \tag{14.8}$$

with $\boldsymbol{\theta}(\mathbf{q})$ the modal counterpart to the physical stiffness nonlinearity. This behavior can be realized using a combination of quadratic and cubic polynomials in the modal coordinates—an approach justified by use of the Green-Lagrange strain measure as applied to beams and plates in bending [16]. The rth term in the nonlinear restoring force is written as follows:

$$\theta_r(q_1, q_2, \ldots, q_m) = \sum_{i=1}^{m}\sum_{j=1}^{m} B_r(i,j)q_i q_j + \sum_{i=1}^{m}\sum_{j=1}^{m}\sum_{k=1}^{m} A_r(i,j,k)q_i q_j q_k \tag{14.9}$$

The arrays A_r and B_r contain quadratic and cubic stiffness coefficients of the nonlinear model; specification of these coefficients forms the essence of the NLROM. Several approaches exist to perform this task; that used here is the Implicit Condensation and Expansion (ICE) method [17], in which a series of static loads are applied to the full order model, each one having the shape

$$\mathbf{f} = c_r M\boldsymbol{\phi}_r \tag{14.10}$$

with a separate scaling term c_r for each mode in the basis. Were the system linear, this would cause a deformation in the rth mode only. Due to the nonlinearity, however, the applied force excites a response in other modes of the structure. Kuether, Brake, and Allen [18] showed that an effective rule of thumb for selecting force amplitudes c_r is to scale them such that the nonlinear static FE solution deflects 15–20 % less (more) than a purely linear static solution due to the hardening (softening) characteristic of the nonlinearity. Combinations of up to three modal forces are applied to the full-order model, exercising all of the nonlinear modal couplings. Then, the nonlinear response of the structure is obtained from the FE software. This response is used to form a least squares problem in terms of the stiffness coefficients, which is solved to find the required coefficients.

Equation (14.9) features inherent coupling between the normal modes. To isolate the effects of nonlinear stiffening from those of nonlinear energy transfer, it is possible to approximate the nonlinear force expression $\theta_r(\mathbf{q})$ as

$$\theta_r(q_1, q_2, \ldots, q_m) = B_r q_r^2 + A_r q_r^3 \tag{14.11}$$

This is equivalent to collecting a set of single-mode NLROMs into an uncoupled, nonlinear dynamic system. Note that the implicit coupling between bending and membrane modes is still present; it is only the coupling between bending modes that is lost.

14.3.2 Full-Order Computations

Numerous techniques exist for validating NLROM's. Since the nonlinearity appears in the static stiffness terms only, a simple first check can be made by checking the static deflection of the beam to a given load; this allows easy comparison with the full-order model. A more representative check involves comparing a transient response history of the full-order and reduced-order models. A more universal (independent of loading and initial conditions) picture of the dynamics is obtained through the use of nonlinear normal modes (NNMs) [14], which depict the frequency of the structure's periodic motion as a function of energy. The NNMs are independent of the loading, and yet they are tightly connected to the transient and forced response, providing an excellent means of comparing two NLROMs. They also provide insight into the dynamics that each ROM captures, i.e. to what extent the nonlinearity causes "stiffening" or "softening" of the linear modes [19]. A comparison of NNM's is performed in Sect. 14.3.3.

For steady-state random response, however, the ideal comparison is another steady-state random response. While expensive to compute, it allows simultaneous verification of the structural model and the integration technique used, both of which will dramatically impact the results obtained. Abaqus® finite element software was used to perform such a full-order simulation. The model was discretized using 50 3-node quadratic Euler-Bernoulli beam elements (B32 in Abaqus nomenclature) which include membrane stretching effects for large displacements.

Abaqus features two direct integration methods: "Abaqus/Standard" is the traditional solver, which features an implicit Hilber-Hughes-Taylor (HHT, also "α-method") integrator [20]. The HHT integrator is a generalization of the Newmark method with the capability of adjustable numerical damping. While the Newmark method allows specification of two independent numerical parameters γ_n and β_n, behavior of the HHT method is specified by a single parameter α_n with $-\frac{1}{3} \leq \alpha_n \leq 0$; $\alpha_n = -\frac{1}{3}$ corresponds to maximum numerical damping, while $\alpha_n = 0$ corresponds to no numerical damping—this last case is also referred to as the "average acceleration" method. The Newmark parameters γ_n and β_n are related to α_n as $\gamma_n = \frac{1}{2}(1 - 2\alpha_n)$ and $\beta_n = \frac{1}{4}(1 - \alpha_n)^2$.

The HHT method is unconditionally stable with a displacement error of $O(\Delta t^2)$ [21]. The availability of numerical damping, which applies in addition to any physical damping present in the model, is useful in structural dynamics problems to reduce high-frequency activity in the model that causes an automatic time-stepping routine to dramatically cut the time step. In most cases, the high-frequency activity is simply numerical noise due to the adjustment of the time step. The default setting in the Abaqus/Standard dynamic solver is $\alpha_n = -0.05$ for slight numerical damping. It is also possible to manually specify a value of $\alpha = 0$ to eliminate numerical damping in the procedure. This results in a significantly longer integration time, but avoids the numerical damping of higher modes.

Abaqus also features Abaqus/Explicit, an explicit dynamic solver which uses the central difference rule for integration. Several factors make the explicit integrator attractive for high speed, nonlinear dynamics: It uses a diagonal mass matrix which allows trivial inversion to compute accelerations, it requires no iterations for accuracy, and it does not require a tangent stiffness matrix. The key disadvantage of the explicit method is its conditional stability, with a time step requirement of

$$\Delta t \leq \frac{2}{\omega_{max}} \left(\sqrt{1 + \zeta^2} - \zeta \right) \tag{14.12}$$

where ω_{max} is the highest natural frequency in the model and ζ the damping in that mode. Whereas the implicit integration technique is characterized by relatively large timesteps that each take a significant amount of time to compute, the explicit technique is characterized by extremely small timesteps (often below $1 \cdot 10^{-7}$ s for models requiring any type of stress fidelity) which take an insignificant amount of time to compute. Explicit methods are not often applied to problems in structural dynamics, but can be used for the problem at hand with no re-configuration of the finite element model.

It is not possible to specify modal damping parameters for general full-order problems. In Abaqus, the simplest way to apply damping to a model is through the use of mass and stiffness-proportional damping matrices, i.e.

$$\mathbf{C} = \alpha \mathbf{M} + \beta \mathbf{K} \tag{14.13}$$

The modal transformation then causes the modal damping matrix $\bar{\mathbf{C}}$ to become diagonal. The mass term α contributes to damping at low frequencies, while the stiffness term β contributes to damping at high frequencies. For the explicit integration routine, a non-zero β can cause extremely slow integrations due to its effect on the stable time increment. As such, only α is specified for the full-order integrations. Using a value of $\alpha = 19.54$ provides a critical damping value of $\zeta = 1\,\%$ at 330 Hz, near the first mode of the reference beam.

A load level of $5 \cdot 10^{-6}\,\mathrm{MPa}^2/\mathrm{Hz}$ was specified over the frequency band of 0–1000 Hz, for an overall RMS of 70.7 kPa. This was sufficient to induce nonlinear displacements in the reference beam. The structure was integrated over a 5 s period

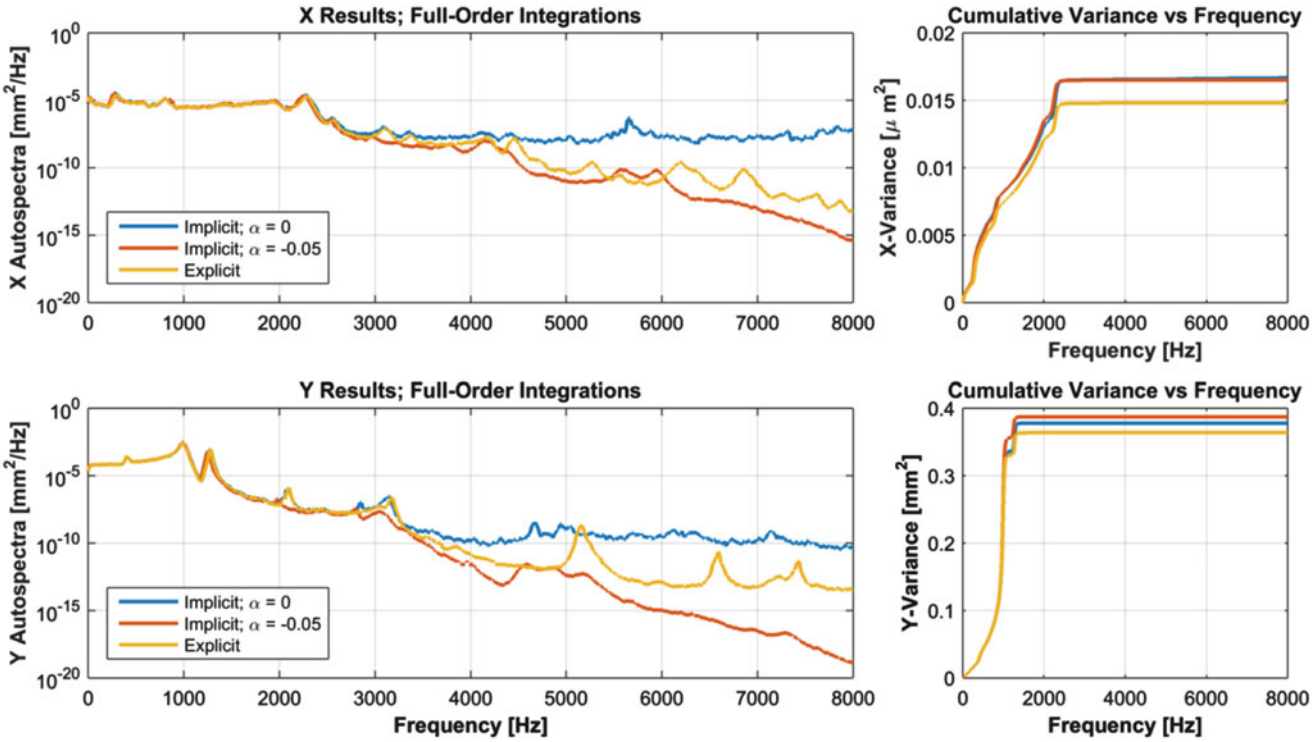

Fig. 14.4 Displacement at $x = 44.29$ mm of the beam using Abaqus/Standard (implicit) and Abaqus/Explicit integration routines

Table 14.2 Simulation times and increment counts for the implicit and explicit runs, integrated for a random load over a period of 5 s

	Implicit; $\alpha_n = -0.05$ [default]	Implicit; $\alpha_n = 0$	Explicit
Time	2 h, 53 min	16 h, 46 min	6 h, 38 min
Increments	80,006	274,285	179,480,825

at a minimum sample rate of 16 kHz (the actual sample rate for each run was, in general, much higher—see Table 14.2) with three different techniques: Implicit with default settings, implicit with $\alpha_n = 0$, and explicit. Using displacement at a single node (corresponding to $x = 44.29$ mm, approximately midway between the left and intermediate supports), as a metric, the three integrations are compared in Fig. 14.4.

The response spectra agree well up to roughly 2000 Hz, after which the results diverge. The plots on the right-hand side of Fig. 14.4 show, however, that the variance differences occur in the first few modes, with the implicit solutions showing displacement variance roughly 10 % higher than the explicit solution. The higher-frequency peaks are so low that they contribute negligibly to the overall variance. This does not mean, however, that the high-frequency response is unimportant. Indeed, this example shows the importance of high-frequency dynamics as a mechanism for nonlinear interactions between the modes.

In the implicit case with numerical damping, high-frequency dynamics are suppressed, and the lower modes are apparently unable to transfer energy to teach other by means of high-frequency axial deformations. As a result, the lower mode response levels are overpredicted. The implicit case without numerical damping does not suppress the high-frequency dynamics, but it also seems to obtain inaccurate results above roughly 4 kHz: the autospectrum profile resembles a flat noise spectrum rather than the response of a structure. In contrast, the explicit solver shows well-defined dynamic behavior over the entire observed spectrum, in addition to lower levels of response variance. For the remaining comparisons in this study, the Abaqus/Explicit results are used as "truth" data.

These results demonstrate that care must be taken to accurately model high-frequency dynamics and obtain an accurate response, even in a full-order model. As a consequence, the already-expensive time integration grows even more computationally intensive. Table 14.2 describes the total integration time for each method. Simulations were performed on four Intel i7-2600 CPU's, each with a clock speed of 3.4 GHz; 12 GB of RAM were available and the computations were not bottlenecked by memory restrictions.

14.3.3 NLROM Creation and Validation

With a full-order model and its associated random response solutions obtained, NLROM validation can take place. An NLROM including the first five modes of the structure was used for all of the following computations. In constructing the NLROM, load levels causing a 50 % thickness displacement in each mode were sufficient to meet the nonlinear activation criteria mentioned in Sect. 14.3.1. (At a displacement of 50 % the beam thickness, the nonlinear response was approximately 80 % of the linear response for each mode.) Both a fully-coupled NLROM (as per Eq. (14.9)) and a diagonalized NLROM (Eq. (14.11)) are used in the validation plots below.

The NNMs of the coupled and uncoupled NLROMs were computed in order to examine any immediate differences between the two nonlinear models. A frequency-energy plot of the comparison is shown in Fig. 14.5. The "backbone" curves of the two models are very similar, however, there is an internal resonance visible in the NNM of the coupled NLROM, which corresponds to an interaction between the first and fourth normal modes of the structure.

Next, the direct integration results are compared to further evaluate the NLROMs. Each model was integrated in MATLAB using a fixed time-step HHT routine with no numerical damping. An integration sample rate of 48 kHz was necessary to achieve convergence with the Abaqus results. (The average sampling rate that each Abaqus routine used can be inferred from Table 14.2.) Figure 14.6 compares the NLROMs with Abaqus/Explicit results using the vertical displacement at a single node of the beam. The coupled NLROM matches Abaqus very well; the diagonal NLROM proves to be surprisingly accurate, although it does overpredict the response by 15 % relative to the full-order solution. Note that the result for the linear case with this loading yields an RMS response of 0.76 mm, more than twice the nonlinear solution.

The stresses in the various models were also compared over all of the integration points in the full-order model (the stress at these locations is available from the ROMs). In Fig. 14.7, contour plots of stress are shown as functions of position vs. frequency. At right, the standard deviation and mean of the stress fields are compared. The largest differences in the stress autospectra are seen in the higher frequencies; for example, near 2000 and 3000 Hz, the diagonal NLROM predicts peak stress near the linear natural frequencies, whereas the other two models predict that these frequencies stiffen due to the large response of the lower frequency modes. This presumably causes the peak stress, near 1000 Hz, to be too large in the diagonal NLROM.

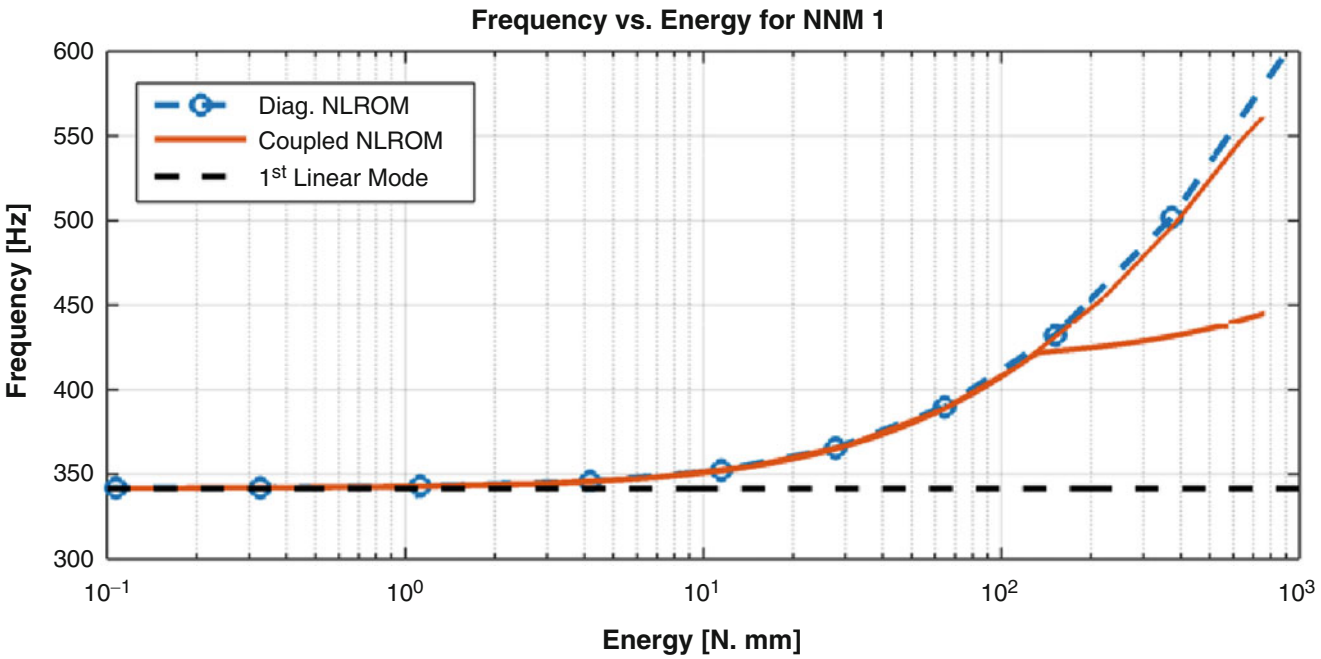

Fig. 14.5 Comparison of the beam's 1st NNM computed from a coupled 5-mode NLROM and an uncoupled NLROM

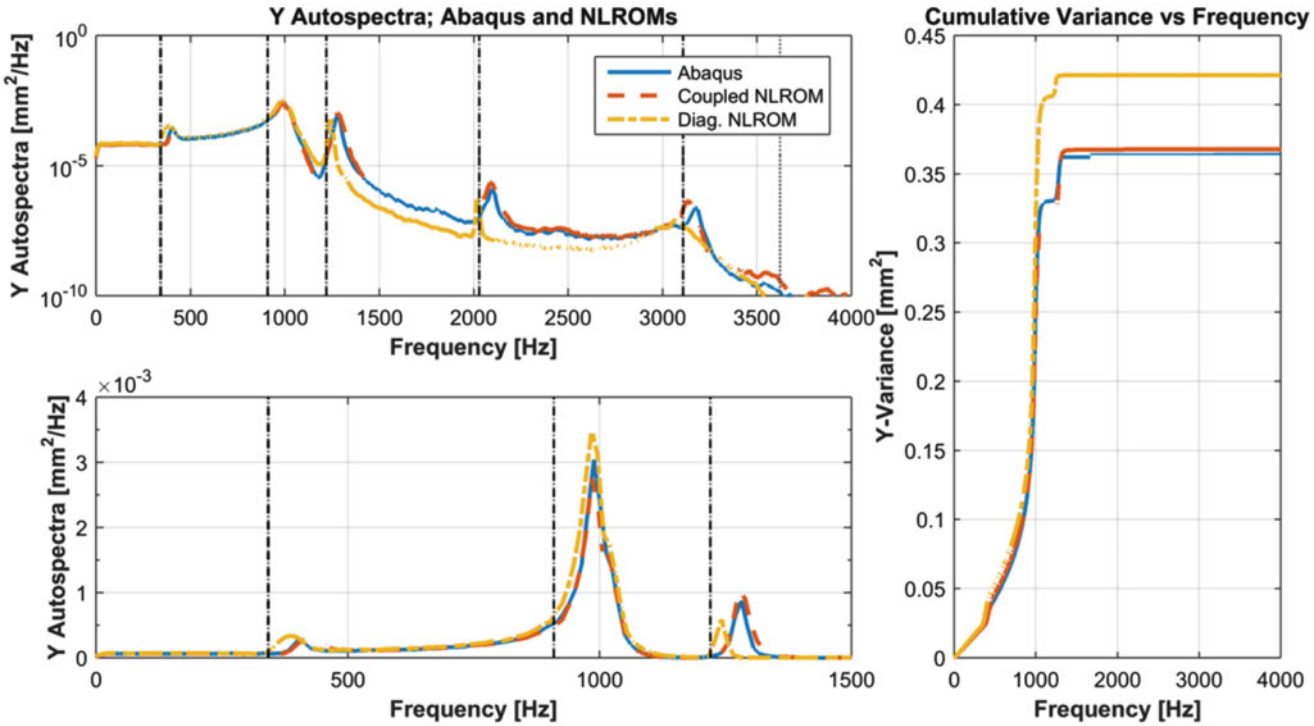

Fig. 14.6 Displacement at $x = 44.29$ mm of the beam using Abaqus/Explicit results, a coupled five mode NLROM, and a diagonal five mode NLROM. *Vertical dash/dot lines* correspond to linear natural frequencies of modes included in the NLROM; *dotted lines* indicate linear natural frequencies of modes not included in the NLROM. *Top left*: Log scale response PSD. *Right*: Cumulative response variance. *Bottom left*: Linear scale response PSD zoomed to show three lowest modes

14.4 Parameter Sweep

Once the reduced order models were obtained and validated, a two-dimensional numerical parameter sweep was performed. This technique is not generally applicable to optimization problems due to its high computational cost, but in this study it is valuable because it provided a view of how displacement and stress varied over a wide parameter range. The modified parameters were the uniform thickness of the beam t and the location of the support given by the ratio r, over the range $1.5\,\text{mm} \leq t \leq 3.5\,\text{mm}$ and $25\,\% \leq r \leq 40\,\%$. Twenty thickness values and 18 support locations were simulated, for a total of 360 points in the grid. Each point took roughly 2 min to compute between NLROM construction, time integration, and stress extraction.

Figure 14.8 shows the results for the coupled NLROM. The maximum root mean square (RMS) values of stress and displacement are shown for each configuration. With full time histories available for each response, condensation into the RMS value is not necessarily the best choice of objective function. For example, a designer might be more interested in the estimated lifetime of the component, and substitute the results into a fatigue-life estimation routine; one might also use the results to estimate the likelihood of exceeding a certain threshold. (The non-Gaussian nature of the nonlinear response complicates this task). The RMS value is used here purely for its simplicity.

First, examine the coupled contours in Fig. 14.8. At high beam thicknesses, both stress and displacement contours show that the optimal design tends towards the support location at 34 %, which was the linear optimum. As the thickness of the beam decreases and the response enters the nonlinear regime, the optimal location for minimum stress shifts markedly leftward, while the optimal location for minimum displacement remains essentially unchanged. Increases in thickness seem to lead to monotonic decreases in stress, again as would be expected for a linear optimization. The topology of the response is, at large scales, smooth and convex, with no observable local minima. This suggests that, for nonlinear stiffening structures in a random load environment, any number of traditional stochastic optimization techniques could be appropriate, and global optimization techniques (e.g. a genetic algorithm, particle swarm optimization, etc.) need not be applied. Future work will explore the applicability of common stochastic optimization techniques, such as the use of response surface methods or stochastic finite differences.

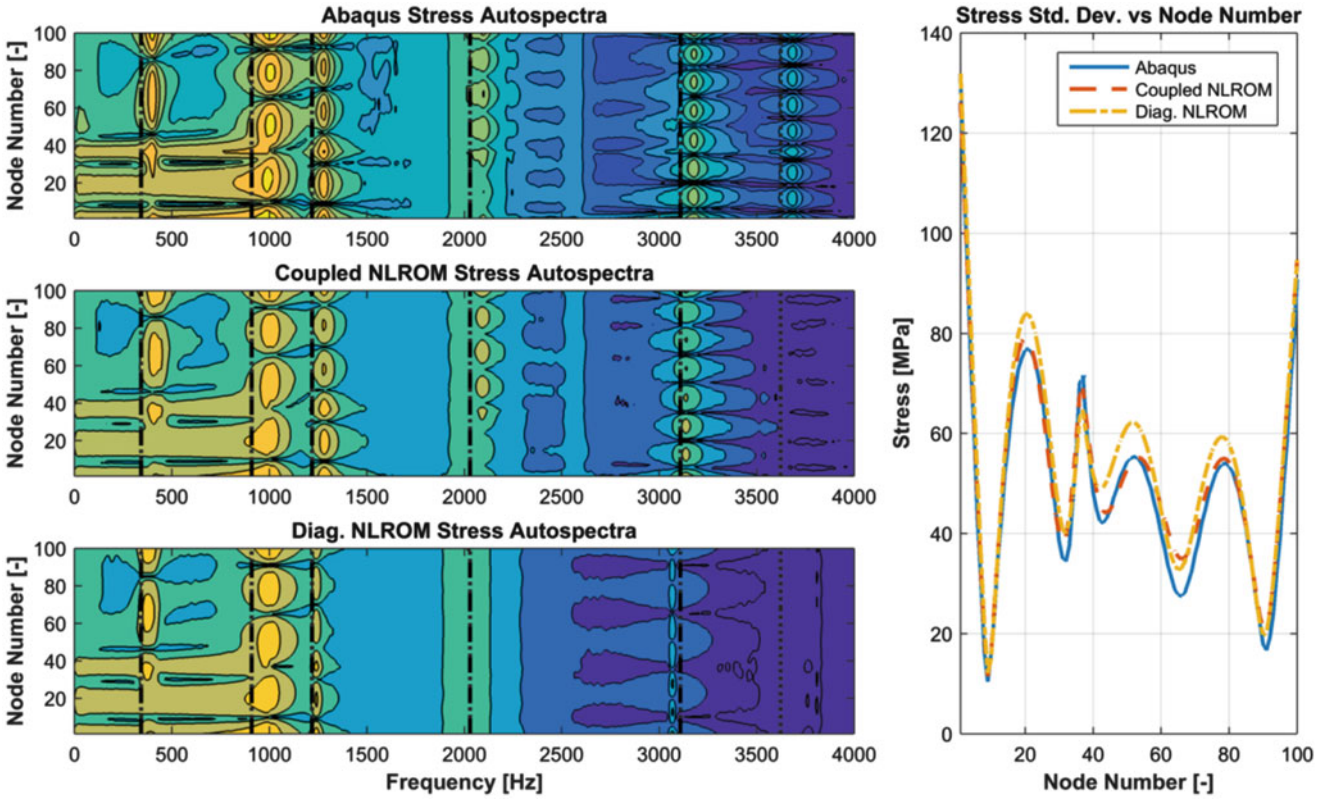

Fig. 14.7 Stress autospectra of the beam at all element integration points (*left*) and the resulting standard deviation (*right*) levels using Abaqus/Explicit results, a coupled five mode NLROM, and a diagonal five mode NLROM. *Vertical dash/dot lines* correspond to linear natural frequencies of modes included in the NLROM; *dotted lines* indicate linear natural frequencies of modes not included in the NLROM

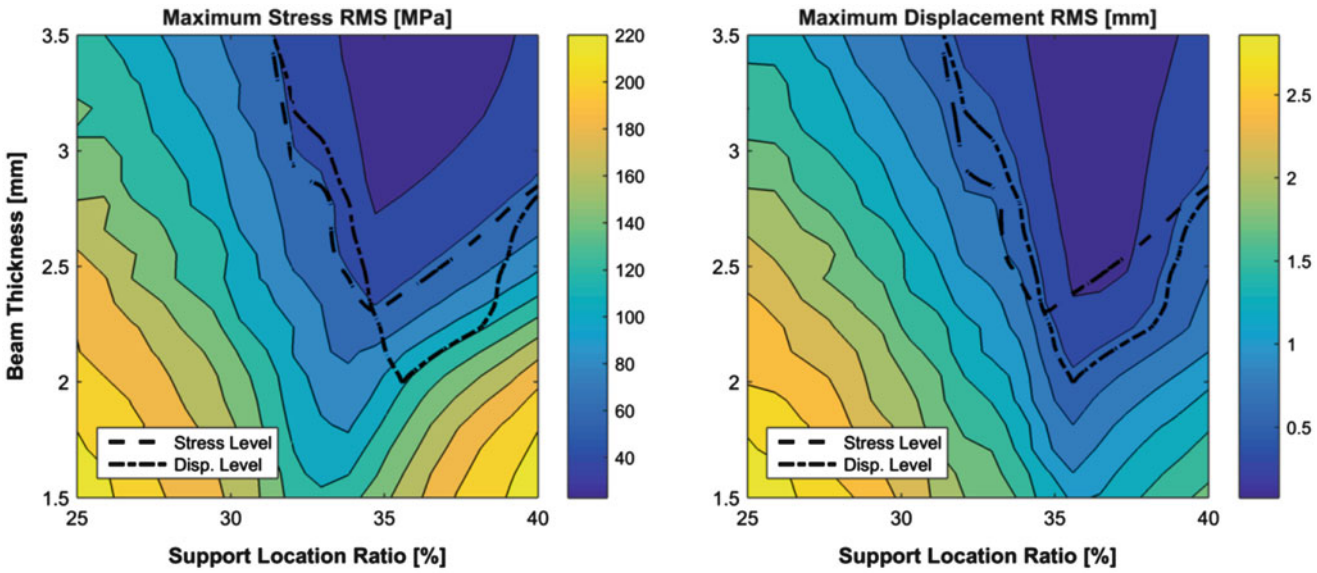

Fig. 14.8 Stress and displacement contours for five-mode coupled NLROM. *Dashed* and *dash/dot lines* indicate RMS displacement of 0.7 mm and RMS stress of 65 MPa

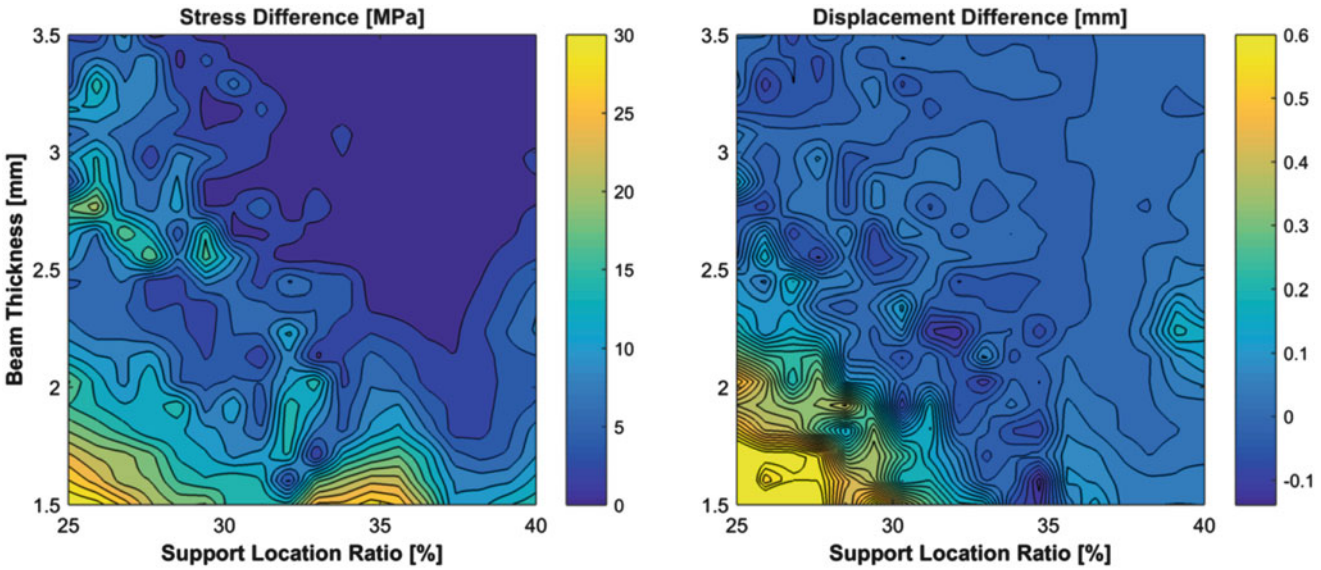

Fig. 14.9 Stress and displacement contours of the five-mode diagonal NLROM in terms of a departure from the five mode coupled NLROM

The parameter sweep results can be used to perform a representative optimization through the use of interpolating contours. Consider the problem of minimizing thickness with constraints on stress and displacement. Contours of level stress and displacement can be inscribed on the $t - r$ plane as in Fig. 14.8 for a displacement RMS of $\delta = 0.7$ mm and a stress RMS of $\sigma = 65$ MPa, such that the minimum-thickness design which meets the constraints can be found at $t = 2.33$ mm, $r = 34.6\,\%$.

Now consider the diagonal contours in Fig. 14.9. For ease of comparison, the results of the diagonal NLROM are shown in terms of departure from the coupled NLROM, with positive values of stress and displacement standard deviation corresponding to a higher prediction of the diagonal NLROM. Absolute difference, rather than percentage difference, is used in order to mitigate further noise in the (already quite noisy) results.

Unfortunately, no clear narrative on the effect of modal energy transfer emerges from these plots. Variations in the stress and displacement fields are too large to be caused by sampling error from the response statistics, but follow no discernible pattern based on the configuration of the beam. As the support location is shifted leftward and the thickness lessened, the overall stiffness of the beam is reduced and energy transfer effects become more apparent. The highest levels of energy transfer seen in the configuration space occur at the bottom left corner of the plot. Re-simulating this configuration in Abaqus/Explicit and in MATLAB using each NLROM leads to the displacement autospectrum plot of Fig. 14.10.

This location does not correspond to the maximum displacement point of the beam, but still provides insight into the dynamics in play: The Abaqus/Explicit and coupled NLROM results have degenerated into a nearly flat response across the frequency spectrum, with significant activation of modes lying outside the 1000 Hz forcing bandwidth. The uncoupled NLROM, on the other hand, drops off in response immediately after 1000 Hz, with modes above this level behaving in a linear manner. This is exactly the large-scale energy transfer behavior that is of interest, however, the response of the structure at this load level is too high to be of practical use.

14.5 Conclusion

The effect of modal energy transfer normal modes was examined in the context of a flat beam structure with a variable configuration. While generating truth data through direct integration of the full finite element model, the importance of energy transfer was indirectly demonstrated by varying the parameters of a full-order finite element integration; different procedures and settings yielded significantly different displacement statistics due to the suppression of high-frequency membrane effects through numerical damping, producing response errors on the order of 10 %. Since the power transferred to a mode is a product of the applied force and the modal velocity, it seems that if the high frequency modes are suppressed by numerical damping, they cannot absorb as much power from the low frequency modes. As a result, the response amplitude at low frequencies is over-predicted.

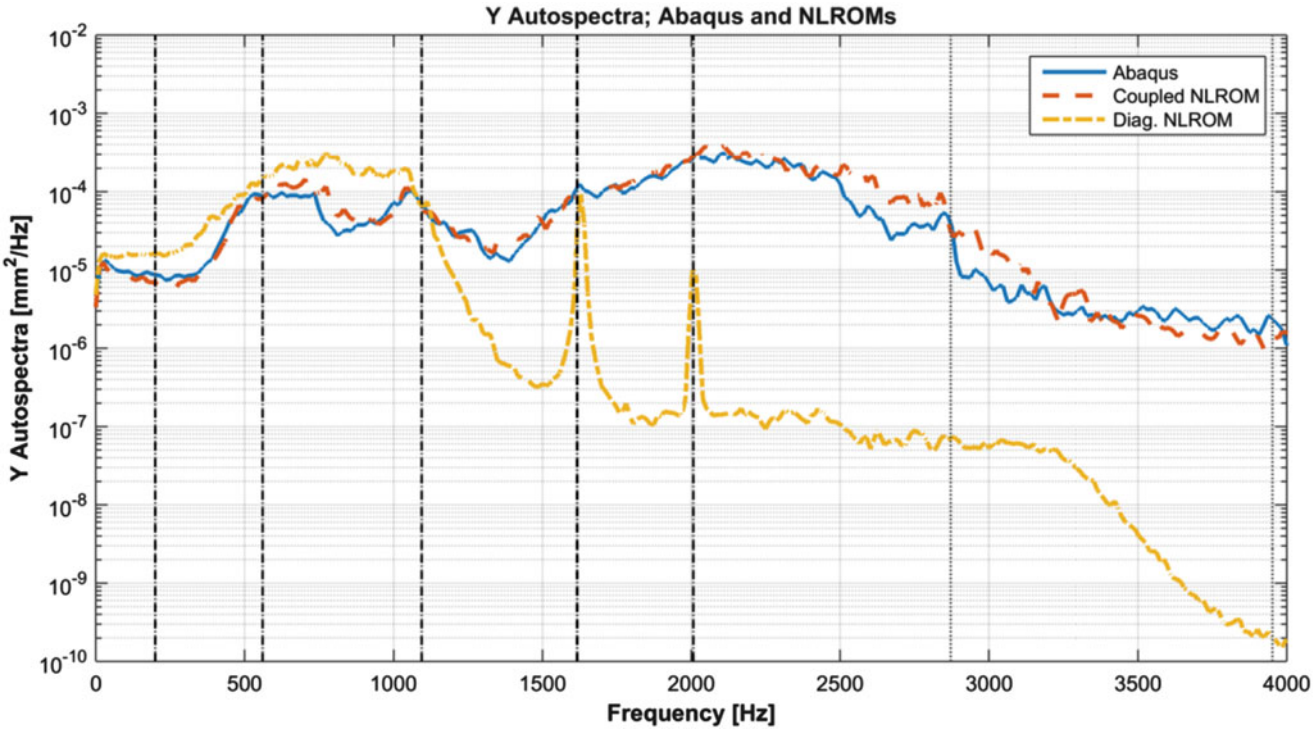

Fig. 14.10 Displacement at $x = 44.29$ mm of the beam using Abaqus/Explicit results, a coupled five mode NLROM, and a diagonal five mode NLROM. *Vertical dash/dot lines* correspond to linear natural frequencies of modes included in the NLROM; *dotted lines* indicate linear natural frequency of modes not included in the NLROM

The requirement to include such high-frequency effects also demonstrates the futility of random response and other long-time-history prediction through full-order simulation: Not only are long time histories required, but extremely small time increments are necessary to accurately predict nonlinear response. In this case, the explicit integration method, often considered too expensive for structural dynamics problems, had the best combination of accuracy and efficiency relative to the Newmark/HHT method with no numerical damping.

To obtain a quantitative understanding of the effects of modal energy transfer across multiple configurations of the beam, two sets of nonlinear reduced order models were developed: The first featured a full set of modal coupling terms between the modes, while the second was "diagonalized" and featured quadratic and cubic terms of single modes only. Comparing the displacement, energy, and stress results of these two NLROMs at a single design point showed that, as expected, the coupled NLROM closely matched full-order Abaqus results, while the diagonalized ROM overpredicted both stress and displacement levels. Using the efficient analysis capabilities of the NLROMs, a grid of 360 design points was evaluated for maximum stress and displacement RMS over a 7.5 s time history. This "parameter sweep," though not an effective means of optimization in general, provided a general overview of the topology of this type of design space, showing largely convex behavior without the prevalence of local minima that would require a global optimization technique.

Finally, the difference in response between the coupled and diagonal NLROMs was investigated. For this structure, no discernible pattern or preferential behavior was observable in the response contours. Examining a single solution for which nonlinear energy transfer was a major factor did show the prevalence of modal interaction in that particular example, but was at too high a response level to be of any practical use. The results here are inconclusive as to the feasibility of leveraging nonlinear energy transfer within a structure to reduce the response levels. A key difficulty in attempting to maximize the internal energy transfer within a structure is that the primary mechanism governing the transfer seems to be the ratios between linear natural frequencies; there is no apparent method to modify these natural frequency ratios without also modifying the stiffness of the structure with respect to a dynamic forcing. In this case, modifying the natural frequency ratios by shifting the support also led to a reduction in overall stiffness as the support moved away from the 34 % location corresponding to maximum bending stiffness.

Future work on this topic will include a consideration of applicable optimization techniques for the nonlinear random response problem and evaluation of substructuring and reduced order modeling techniques for more complex, built-up structures. A similar investigation of energy transfer effects in curved structures, which exhibit stronger coupling between axial and bending modes, is also of interest. A less computationally-intensive and more exact method of quantifying energy transfer between a structure's modes will also be examined.

Overall, the use of nonlinear analysis techniques for design optimization shows great promise in terms of achievable weight reduction for a given set of constraints on stress and displacement. Modal interactions in nonlinear structures are still not well understood, but it is clear from this and other studies that they play a key role in nonlinear dynamic response. Even if it is not possible to target high energy transfer levels as a design goal, they still enable the reduction of a nonlinear response by sending energy outward from excited modes to those out of the excitation bandwidth; a behavior which can be either beneficial or detrimental. An understanding of these effects will be invaluable in the pursuit of efficient nonlinear structures.

Acknowledgements This material is based upon work supported by the National Science Foundation Graduate Research Fellowship under Grant No. DGE-1256259. Any opinion, findings, and conclusions or recommendations expressed in this material are those of the authors(s) and do not necessarily reflect the views of the National Science Foundation.

The authors also acknowledge Joseph Hollkamp from the Air Force Research Laboratory's Structural Sciences Center, for the insights that he shared and for providing the Abaqus interface that was used in this work.

References

1. Gordon, R.W., Hollkamp, J.J.: Reduced-order models for acoustic response prediction. Technical Report, AFRL-RBWP-TR-2011-3040, Air Force Research Laboratory (2011)
2. Teunisse, N., Tiso, P., Demasi, L., Cavallaro, R.: Computational reduced order methods for structurally nonlinear joined wings. In: 56th AIAA/ASCE/AHS/ASC Structures, Structural Dynamics, and Materials Conference, Kissimmee, FL (2015)
3. Wang, J., Tzikang, C., Sleight, D.W., Tessler, A.: Simulating nonlinear deformations of solar sail membranes using explicit time integration. In: 45th AIAA/ASCE/AHS/ASC Structures, Structural Dynamics, and Materials Conference, Palm Springs, CA (2004)
4. Tuegel, E.J., Ingraffea, A.R., Eason, T.G., Spottswood, M.S.: Reengineering aircraft structural life prediction using a digital twin. Int. J. Aerosp. Eng. **2011** (2011)
5. Nash, M.: Nonlinear structural dynamics by finite element modal synthesis. Ph.D thesis, Department of Aeronautics, Imperial College (1977)
6. Segalman, D.J., Dohrmann, C.R.: Method for calculating the dynamics of rotating flexible structures, part 1: derivation. Trans. ASME J. Vib. Acoust. **118**, 313–317 (1996)
7. Segalman, D.J., Dohrmann, C.R.: Method for calculating the dynamics of rotating flexible structures, part 2: example calculations. Trans. ASME J. Vib. Acoust. **118**, 318–322 (1996)
8. McEwan, M.I., Wright, J., Cooper, J.E., Leung, A.Y.T.: A combined modal/finite element analysis technique for the dynamic response of a non-linear beam to harmonic excitation. J. Sound Vib. **243**, 601–624 (2001)
9. Muravyov, A.A., Rizzi, S.A.: Determination of nonlinear stiffness with application to random vibration of geometrically nonlinear structures. Comput. Struct. **81**, 1513–1523 (2003)
10. Mignolet, M.P., Przekop, A., Rizzi, S.A., Spottswood, S.M.: A review of indirect/non-intrusive reduced order modeling of nonlinear geometric structures. J. Sound Vib. **332**, 2437–2460 (2013)
11. Hollkamp, J.J., Gordon, R.W., Spottswood, S.M.: Nonlinear modal models for sonic fatigue response prediction: a comparison of methods. J. Sound Vib. **284**, 1145–1163 (2005)
12. Suguang, D., Jensen, J.S.: Optimization of nonlinear structural resonance using the incremental harmonic balance method. J. Sound Vib. **334**, 239–254 (2015)
13. Grappasonni, C., Habib, G., Detroux, T., Wang, F., Kerschen, G., Jensen, J.S.: Practical design of a nonlinear tuned vibration absorber. In: International Conference on Noise and Vibration Engineering, Leuven (2014)
14. Kerschen, G., Peeters, M., Golinval, J., Vakakis, A.F.: Nonlinear normal modes, part i: a useful framework for the structural dynamicist. Mech. Syst. Signal Process. **23**(1), 170–194 (2009)
15. Nayfeh, A.H.: Introduction to Perturbation Techniques. Wiley, New York (2011)
16. Rutzmoser, J.B., Rixen, D.J.: Model order reduction for geometric nonlinear structures with variable state-dependent basis. Dyn. Coupled Struct. **1**, 455–462 (2014)
17. Hollkamp, J.J., Gordon, R.W.: Reduced-order models for nonlinear response prediction: implicit condensation and expansion. J. Sound Vib. **318**, 1139–1153 (2008)
18. Allen, M.S., Kuether, R.J., Deaner, B., Sracic, M.W.: A numerical continuation method to compute nonlinear normal modes using modal reduction. In: 53rd AIAA/ASCE/AHS/ASC Structures, Structural Dynamics, and Materials Conference, Honolulu, HI (2012)
19. Kuether, R.J., Brake, M.R., Allen, M.S.: Evaluating convergence of reduced order models using nonlinear normal modes. Model Validation Uncertain. Quantif. **3**, 287–300 (2014)
20. Dassault Systems Simulia Corp.: Abaqus Theory Manual (2012)
21. Cook, R.D., Malkus, D.S., Plesha, M.E., Witt, R.J.: Concepts and Applications of Finite Element Analysis, 4th edn. Wiley, New York

Chapter 15
Nonlinear Modal Testing Performed by Pulsed-Air Jet Excitation System

M. Piraccini, D. Di Maio, and R. Di Sante

Abstract This paper presents a novel approach for testing structural component to nonlinear vibrations. Nowadays, nonlinear testing is mainly carried out by using electromagnetic shakers. These are efficient and powerful excitation systems which transmit the force by a rigid stinger and can be driven by different excitation signals. The rigid connection contributes to create mechanical impedance mismatch between the shaker and the test structure thus reducing the efficiency of the driving force. An alternative solution to shakers is represented by use of a pulsed air jet excitation method, which drives the force by a pulsed air-jets and therefore contactless. This condition eliminates the mechanical impedance mismatch with the test structure and the excitation can be more efficient than the one created by shakers. The pulsed air-jet excitation system is used to study nonlinear vibrations of composites components. These were designed to be mock-ups of fan blades the layup of which was varied for the three types of components used in this work. Tests were carried out by performing forced response and free decay measurements. The free decay type of test revealed interesting results and the novelty of using such an exciter for nonlinear testing. The major novelty consists of interrupting the air flow from a steady state condition and let happen the free decay, all these without experiencing undesired dynamics as experienced by contact excitation.

Keywords Pulsed air-jet exciter • Nonlinear vibrations • Composites

15.1 Introduction

In recent years, there has been an increasing interest in studying the behaviour of structures presenting nonlinearities [1]. This is primarily due to the increased use of new materials such as composites. For example, over 50 % of the structural components of the Boeing 787 and Airbus 350 XWB are made of composite materials [2], which are inherently more flexible and less damped, being therefore more prone to nonlinear behaviour. Hence, the understanding of their performance under operating conditions, especially when extreme loads are present, has become increasingly important. Different methodologies have been used to get a deeper insight into the dynamics of nonlinear systems [3]. This paper focuses in particular on the nonlinear resonant method (NL-RDM) and on the experimental testing apparatus and procedure supporting this identification method. The NL-RDM was firstly presented in 2001 [4] and refined in subsequent works [5, 6]. The method uses responses obtained from burst or narrowband excitation of the structure at the natural frequency of the mode of interest. When the excitation ends, the responses are allowed to decay freely. Only the concerned mode and the modes nonlinearly coupled to it contribute to the response, allowing the nonlinear identification of the mode itself. Such an approach proves effective to analyse structures that are linear at low vibration amplitudes, but show increasingly larger active elements of nonlinearity at higher excitation levels. This is the case of many industrial structures. The nonlinear resonant method has been applied experimentally to different structures. In [5] Platten et al. characterised successfully the first three modes of a clamped panel structure, in which they had introduced a distributed nonlinearity by stretching the panel's middle surface. In [6] the same authors identified the first five modes of an aircraft like wing/store/pylon structure with discrete hardening stiffness nonlinearity introduced in the pylon. In these works, electrodynamic shakers were rigidly connected to the test structures to provide the burst excitation required by the method. More recently, Londono et al. [7] applied a modified version of the method to a single-degree-of-freedom system represented by a base-excited mass mounted on bearings sliding with low friction along steel shafts. The mass was also connected to two preloaded transversal springs which produced nonlinear

M. Piraccini • D. Di Maio (✉)
Department of Mechanical Engineering, University of Bristol, University Walk, BS8 1TR Bristol, UK
e-mail: dario.dimaio@bristol.ac.uk

R. Di Sante
Department of Mechanical Engineering, University of Bologna, Bologna, Italy

G. Kerschen (ed.), *Nonlinear Dynamics, Volume 1*, Conference Proceedings of the Society for Experimental Mechanics Series,
DOI 10.1007/978-3-319-29739-2_15

stiffness. In all these cases, contact excitation provided by shakers is employed to drive each mode separately. This can be an issue [5] since the force is not in phase with the driving voltage and tuning is affected by the severe shaker-structure interaction. Consequently, second harmonics appear in the force signal. Furthermore, when the excitation ends, the stinger is still attached to the structure thus possibly affecting its dynamic behaviour. In order to overcome the problems related to the interaction between the test structure and the excitation device, in this paper a different contactless excitation method is proposed. Compressed air is used to generate a flow which is then chopped by a spinning disc with a series of holes drilled in it. The excitation frequency is therefore given by the number of holes and the rotation speed. After the sudden interruption of the airflow, the responses are allowed to decay freely and without constraint to the excitation system. The paper is organised as follows. Section 16.2 describes the pulsed-air excitation system proposed in this work. Section 16.3 reports the design and realisation of the composite blades used in the experiments. Forced and free-decay responses obtained during the tests are presented in Sect. 16.4 together with a description of the procedure used for signal processing.

15.2 Pulsed Air Jet Excitation System

This section will present a contactless excitation system which works by using compressed air. Figure 15.1 shows the schematic of the excitation system. It is rather simple mechanism based on compressed air flowing into a plenum chamber throughout an orifice. A spinning disc, designed with several holes, opens and closes the orifice thus generating air-jets. The dynamic range of the exciter is given by the capacity of electric motor (max velocity) and by the number of holes on the disc. The actual excitation frequency is given by the following equation:

$$\omega_n = \frac{\Omega}{60} n_{DH}$$

where, ω_n is the excitation frequency, Ω rotational speed of the disc and n_{DH} the number of holes designed for the disc.

Several measurements to experimentally quantify the influence of some design parameters were carried out. For example, the ducting (comprising of orifice, sampling hole and nozzle) or the addition of a double nozzle were presented in [8]. To characterize the excitation force with respect of the measured pressure at the nozzle and the excitation frequency, a small test rig was configured as shown in Fig. 15.2. The nozzle was once addressed over the pressure gauge and once over the load cell. The test was repeated at different excitation frequencies. The results are plotted in Fig. 15.3.

The excitation system, as presented in here, has got some useful features but also some disadvantages. In fact, the pulsed excitation generates harmonics at multiple of the fundamental one. This can determine some undesired effects like parasitic excitation, where some vibration contents can be summed to the one excited by the fundamental tone. However, this is expected and can be monitored accordingly.

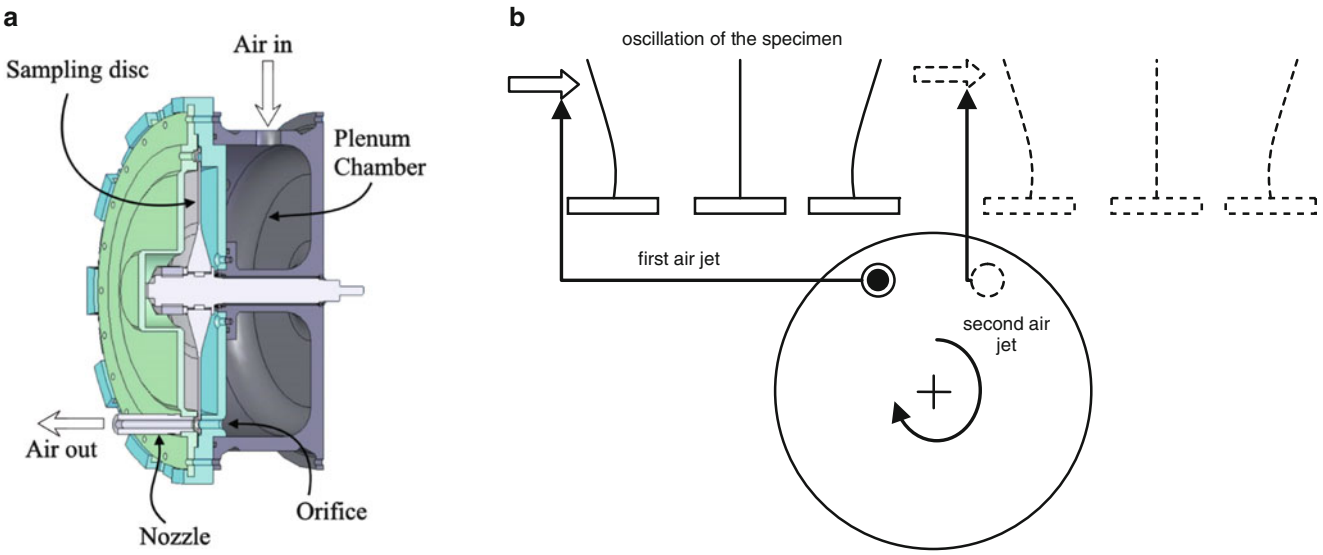

Fig. 15.1 (**a**) Mechanical scheme of pulsed air-jet system and (**b**) the operating principle

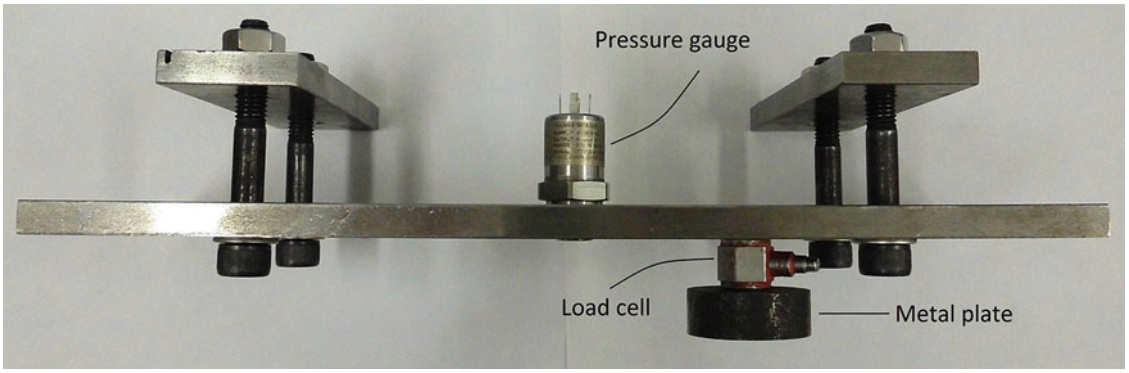

Fig. 15.2 Test rig for force vs. pressure characterization

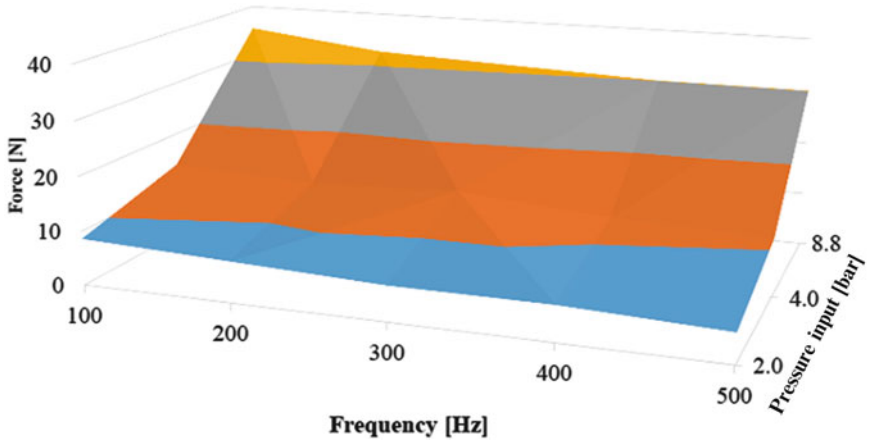

Fig. 15.3 Relationship between excitation force, pressure and excitation frequency

The goodness is in its contactless feature which can make the system very convenient when a ramp-down test is aimed. The exciter can generate a steady-state vibration and that is sustained as long as the compressed air flows throughout the system. A free decay can be therefore obtained by abruptly interrupting the airflow, thus letting the vibration of the component to decay. This approach was used to characterize the nonlinear response of cantilever composite blades. The free decay is inherently a challenging type of testing because the excitation source cannot be disconnected so easily from the test structure. If the exciter, such as a shaker, is left connected then its dynamics can influence the results. This is more plausible when high amplitude levels are aimed for.

15.3 Design and Manufacturing of the Composite Blades

In this section an outline of the considerations, analyses, constraints, and decisions made about how to design the composite blades object of this work is presented. Manual envelope bagging technique is explained as applied to the actual manufacturing of the components. Difficulties encountered in manufacturing the blades are explained and the methods used to solve them are detailed.

15.3.1 Design Considerations

The objective was to excite geometrically nonlinear vibration and so one side of the blade was thought to be straight, whereas the other one was designed so as to create an angle of $90° + \beta$ between the edge and the base. Different twisting angles θ, thicknesses s, and blade length L were examined in finite element analyses. The following values of the aforementioned parameters were all modelled, see Table 15.1.

Table 15.1 Design parameters

Parameters	Value-1	Value-2	Value-3
Trapezoidal angle (β)	5°	10°	15°
Twisting angle (θ)	10°	20°	–
Thickness (s)	2 mm	3 mm	–
Length (L)	100 mm	300 mm	500 mm

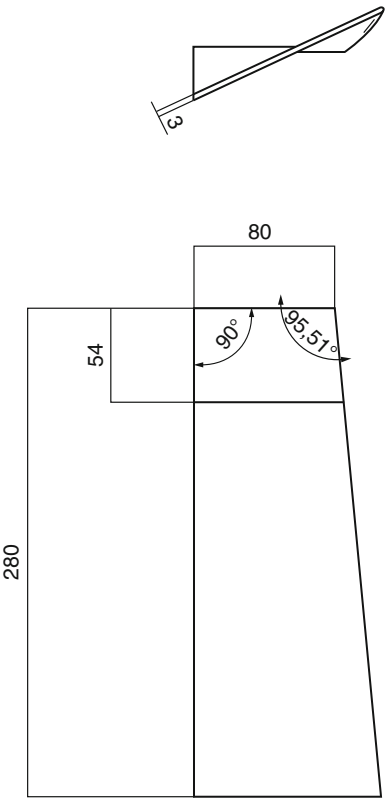

Fig. 15.4 Definitive dimensions for the composite blade

The mode shapes of interest in the analyses were the 1st flexural, the 1st torsional, and the 2nd flexural. From finite element analyses it was possible to notice that a blade long 100 mm would be too stiff and have too high natural frequencies as the frequency range of interest was up to 400–500 Hz because of the difficulties to properly excite the vibration and measure it with higher natural frequencies. Moreover some combinations of parameters led to natural frequencies that were too close one another; it would be then difficult to analyse the dynamics of such a structure as it would not be allowed to use the 1DOF approximation. Since it was subsequently known the composite roll was 300 mm in width it was evident that a blade long 500 mm would not optimise the nesting during the cutting of the composite plies. A flat area long 54 mm was thought to be adequate to properly clamp the blade during vibration tests. The length of 280 mm optimised the cutting process by reducing the waste during cutting. Thus, either to reduce the composite waste or to have natural frequencies of the first three mode shapes in the range of interest, the possible length had to be close to 300 mm. A 10°-twisting-angle was deemed too small to be practically realised and the 20° value for the twisting angle was chosen. The trapezoidal angle was chosen to be 5° as it seemed to lead to better mode shapes. Since the blade had to contain 4 ply drops, with a consequently change in thickness of 0.5 mm (being each ply 0.125-thick), a 3 mm-thickness was more adequate to experience such a change; moreover the flat rectangular specimens with ply drops previously tested during another research project were 3 mm-thick and the thickness change created no problems so that it was thought to be expedient to use such a previous validation. Final choices for the parameters of the blade can be seen in Fig. 15.4.

Three different layups were made so as to test the different dynamics with varying fibre directions. Since subsequent fatigue tests would be carried out by exciting the specimens at the 2nd flexural mode, the ply drops were not located on the surface of the blade as the bending normal stress is maximum in that area, but two full plies were allowed to be present in the zone of maximum stress. Since each ply has an after-cured-thickness of 0.125 mm, 24 plies were used for the three specimens. The chosen stacking sequences were symmetric across their mid-plane in order to exhibit no coupling between bending and extensional responses; one important practical implication is that such laminates do not have a tendency to bend

or twist from the inevitable thermally induced contractions that occur during cooling following the curing process. The fibre orientations were unidirectional 0°, cross-ply [0/90]s and balanced angle-ply [+45/−45]s. Cross-ply laminates exhibit no coupling either between shear and extensional response and between bending and twisting response. A symmetric angle-ply laminates does not have shear-extensional coupling effects.

After making the first blade a problem became evident; the area designed to be flat so as to be properly clamped during vibration tests was not sufficiently flat. In fact, the bottom surface, which was in contact with the mould, appeared completely flat whereas the top surface experienced a slight curvature that impeded a correct clamp of the blade. Thus, the first blade manufactured was not deemed adequate to be experimentally tested. In a second attempt the aforementioned problem was solved by means of a top plate that was cut and applied on the composite during the curing cycle in order for the blade to have both surfaces under compression. In this way, a uniform pressure could be exerted on the root of the blade during the autoclave cycle and both bottom and top surfaces were perfectly flat.

15.4 Experimental Work

In order to carry out forced response analyses it was decided to use only contactless methods for both the excitation and the measurement systems. The test rig was made as shown in Fig. 15.5 where the exciter is positioned at the top left corner of the specimen. This way all 3 modes could be excited. As can be seen from Fig. 15.5, the blade was clamped to a specific base designed in order to provide very accurate clamp, hence reducing the possibilities of the presence of contact nonlinearities and energy dissipation in the clamp. A guillotine was placed in front of the airflow in order to cut the air in following decay analyses. A nozzle was used to bring the flow as close as possible to the excitation point so as to create as much a homogeneous fluid dynamics as possible. The vibration velocity was measured by means of a Polytec PSV400 Laser Doppler Vibrometer with sensitivity of 2 m/s/V in the single-point mode of use.

The scanning head was set outside the anechoic chamber containing the blade and exciter. Since detection of superharmonics in nonlinear vibration was one of the goals of the subsequent decay analyses, a low pass filter was set at a high frequency (20 kHz) to allow the investigation of a wide range of frequency content in the signal.

Fig. 15.5 Text fixture, blade and exciter's nozzle

In order to increase the reflection from the surface of the blade, reflective tape was used at the point of measurement. The forced response was acquired by using a LabVIEW programme and the frequency of excitation was set by using a control panel for regulating the speed of the electric motor of the exciter. By regulating the airflow by means of opening or closing the flow control valve of the chopped air machine, different excitation intensities were adopted in order to characterise the behaviour of the 1st flexural, 1st torsional, and 2nd flexural mode shapes of the three different layups at increasing displacements. After localising the resonant frequencies, tests were carried out on each of the first three mode shapes by exciting each blade in a frequency range around its natural frequencies and repeating the tests at different levels of excitation (i.e. different airflow intensities).

15.4.1 Experimental Results

The following graphs summarise the global measured forced responses and give the natural frequency change with regard to the measured amplitude of the displacement.

15.4.1.1 Unidirectional: 1st Flexural Mode

The 1st flexural vibration of the unidirectional 0°-angled blade has been studied by means of exciting the component around its linear natural frequency (74 Hz) with six increasing airflow intensities. From forced responses (Fig. 15.6a) it can be seen that even with the lowest excitation intensities the amplitude of the vibration of the unidirectional blade at the first mode shape was extremely high. The behaviour of the blade vibrating with the 1st flexural mode shape is evidently linear as there is no significant frequency variation with varying amplitude even if the displacement becomes very large as can be seen from backbone curve in Fig. 15.6b.

15.4.1.2 Unidirectional: 1st Torsional Mode

The vibration of the 1st torsional mode of the 0° blade is extremely singular and markedly nonlinear. Nine increasing airflow intensities were investigated so as to be able to fully characterise such a varying behaviour. From Fig. 15.7a it can be seen that jump phenomena start to appear when the peak of the vibration approaches the value of the thickness of the blade (i.e. 3 mm) and the vibration abruptly changes its intensity. This is coherent with the known consideration that significant nonlinearities

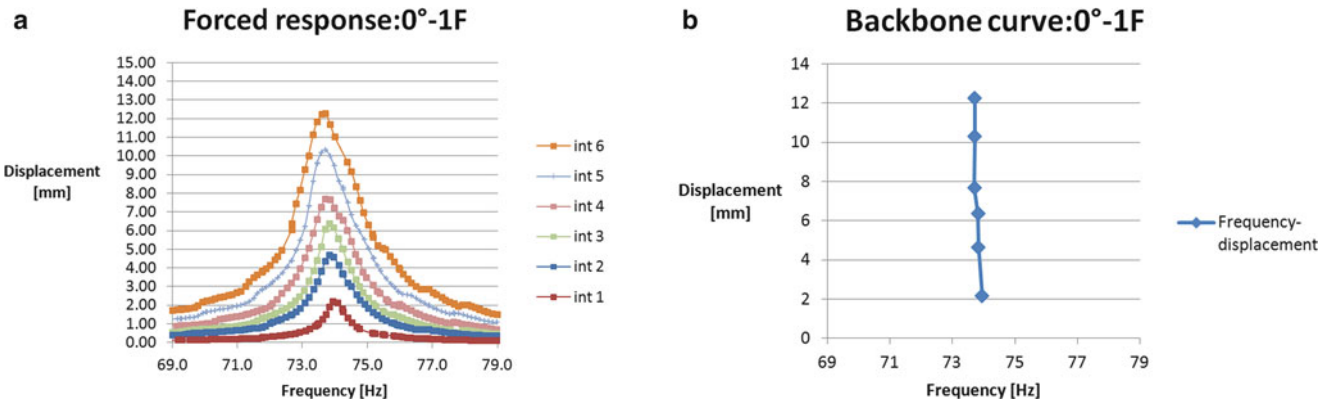

Fig. 15.6 First bending mode. (**a**) Forced responses of the unidirectional blade during vibration at its first flexural mode with six increasing intensities of airflow (labelled "int"). (**b**) Backbone curve of the unidirectional blade undergoing linear vibration at its first flexural mode with six increasing loading intensities

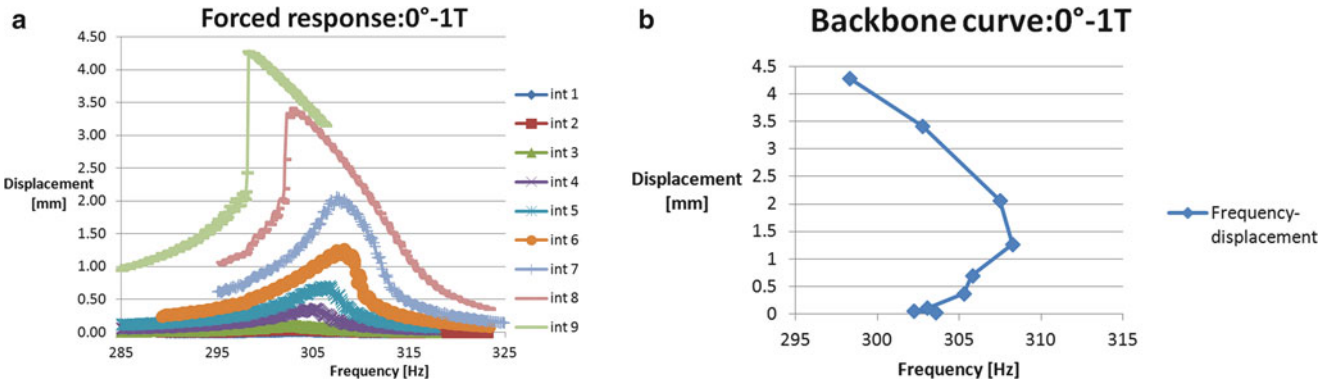

Fig. 15.7 First torsional mode. (**a**) Forced responses of the unidirectional blade during vibration at its first torsional mode with nine increasing intensities of airflow. (**b**) Backbone curve of the unidirectional blade undergoing nonlinear vibration at its first torsional mode with nine increasing loading intensities

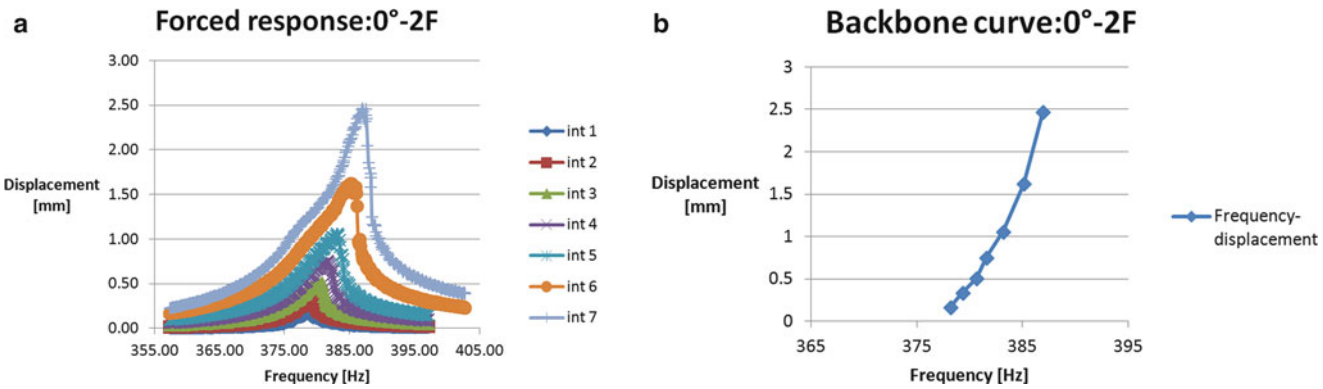

Fig. 15.8 Second bending mode. (**a**) Forced responses of the unidirectional blade during vibration at its second flexural mode with seven increasing intensities of airflow. (**b**) Backbone curve of the unidirectional blade undergoing nonlinear vibration at its second flexural mode with seven increasing loading intensities

most often appear when displacement is comparable to the thickness. From Fig. 15.7b, which represents the backbone curve of the vibration, it can be noted that vibration changes its behaviour as displacement approaches 1.5 mm from a hardening nonlinear type of vibration to a softening nonlinearity underlining a change in the laminate stiffness.

15.4.1.3 Unidirectional: 2nd Flexural Mode

Differently from the first flexural mode the 2nd flexural mode exhibits a strong hardening behaviour; in Fig. 15.8a jump phenomena are also evident starting at around 1.5 mm. Backbone curve in Fig. 15.8b shows natural frequency increasing with increasing vibration amplitude.

15.4.2 Free Decay Procedure and Signal Processing

The following experimental procedure was used in order to characterise the behaviour of free decay responses. By using the same experimental equipment as those used for the forced response tests, the airflow was cut by using a guillotine and the vibration was acquired via LDV system during free decay. The so-acquired velocity signal was integrated to give the displacement and then analysed by using a spectrogram, also called sliding Discrete Fourier Transform, meaning that the frequency content was derived by using Fast Fourier Transform algorithm applied to a sliding window over time. Thus, it is possible to visualise either the frequency content and how different frequencies appear and disappear in the signal during the decay. Discrete Fourier Transform over the entire decay time was also applied to have an idea of how strong each frequency

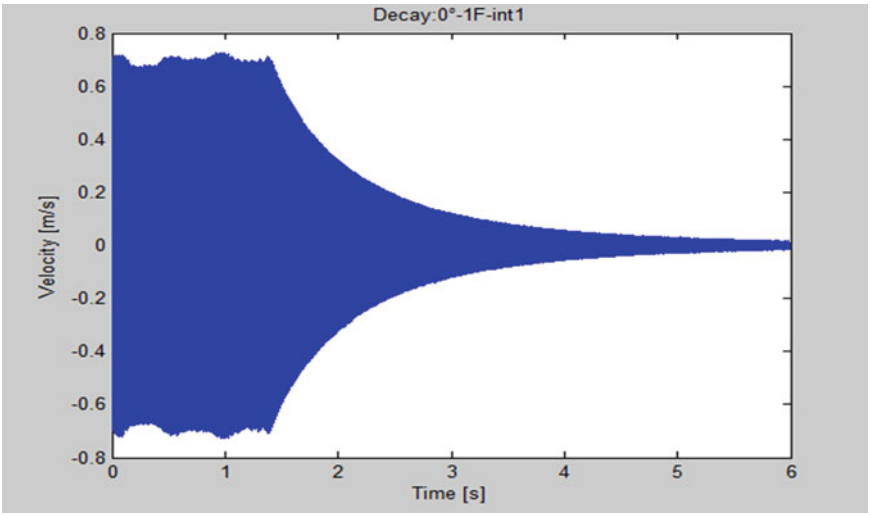

Fig. 15.9 Acquisition of the velocity decay from Laser Doppler Vibrometer

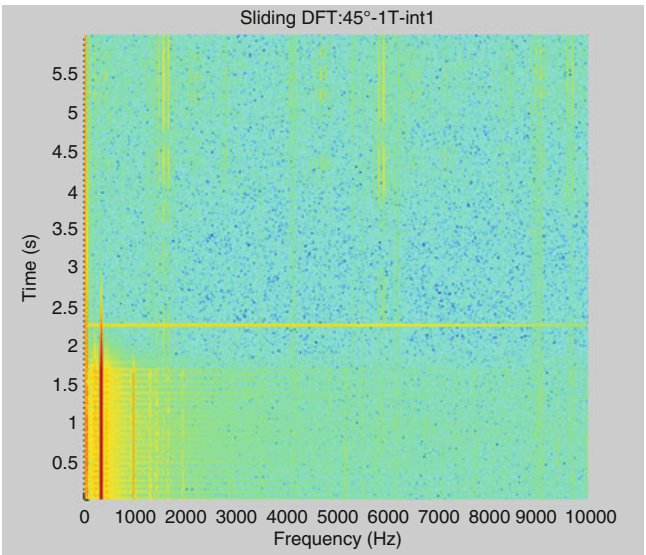

Fig. 15.10 Sliding DFT computation with Hamming windowing

component in the signal was. After isolating the fundamental frequency of vibration by means of a second-order band-pass filter to adopt a one-degree-of-freedom model, the logarithmic decrement of the decay was computed and the damping ratio associated with the excited mode shape was analysed as a function of amplitude for those modes which had a viscous-like damping. The entire procedure was made up of the following steps and repeated at different levels of excitation.

Acquiring the decay signal of the velocity from Polytec LDV system as shown in Fig. 15.9.

Integration of the velocity in order to obtain the displacement signal. Computing the spectrogram (i.e. sliding Discrete Fourier Transform with Hamming windowing) of the signal to visualise the frequency content present during the decay, see Fig. 15.10. Computing DFT over the entire signal to visualise the strength of each frequency component in the signal, see Fig. 15.11.

Applying a band-pass filter to isolate the fundamental frequency associated with the externally excited mode shape, see Fig. 15.12.

Dividing the filtered signal in its positive and negative branches and envelope detection by means of peak recognition, see Fig. 15.13.

Computation of the logarithmic decrement and subsequently the damping ratio as shown in Fig. 15.14.

The proposed procedure was applied to different excitation levels. The following section will present some results obtained by using this procedure.

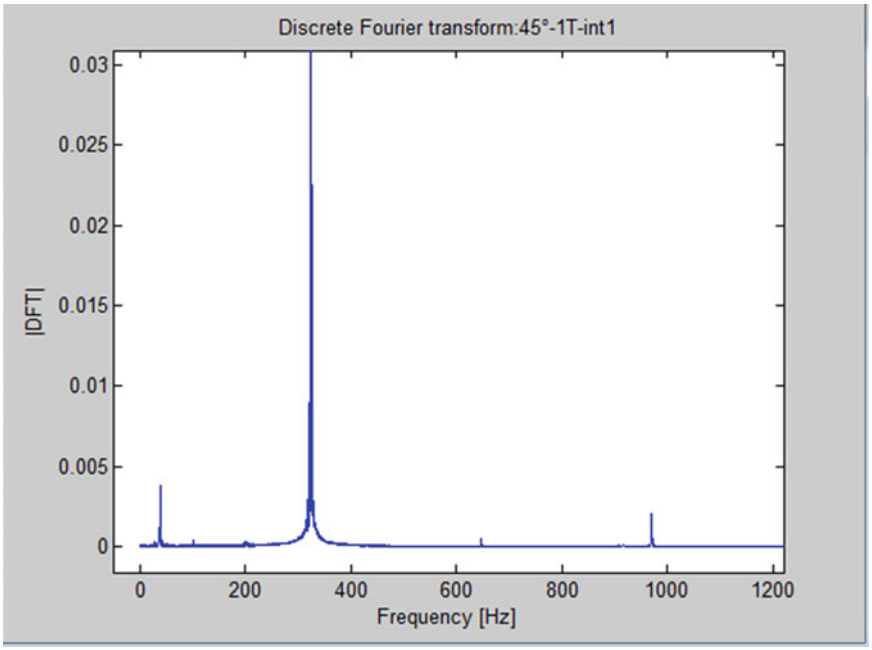

Fig. 15.11 Computation of the Discrete Fourier Transform of the acquired signal to visualise how strong frequency component are

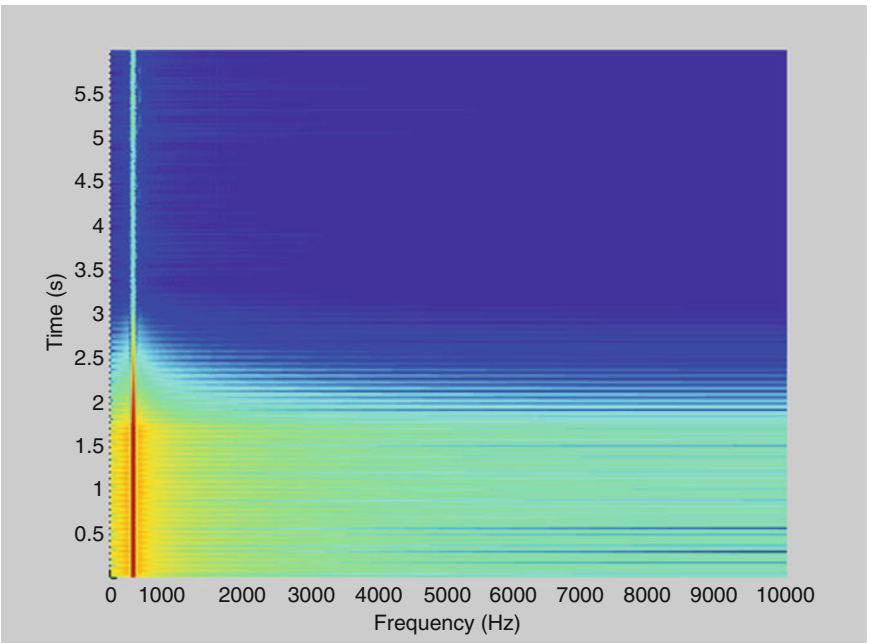

Fig. 15.12 Application of band-pass filter to isolate the fundamental resonant frequency associated with the excited mode

15.4.3 Free Decay Experimental Results

15.4.3.1 Unidirectional: 1st Flexural Mode

Figures 15.15, 15.16 and 15.17 show the time decay signal for three different excitation forces. The 1st flexural mode associated with the unidirectional blade is confirmed to be strongly linear as no superharmonics appear in the frequency spectrum (Fig. 15.18) and damping phenomenon is uniquely viscous-like damping (i.e. exponential decay). The logarithmic decrement and subsequent damping ratio underline a tendency to an increase in the damping values with increasing amplitude level (Fig. 15.19).

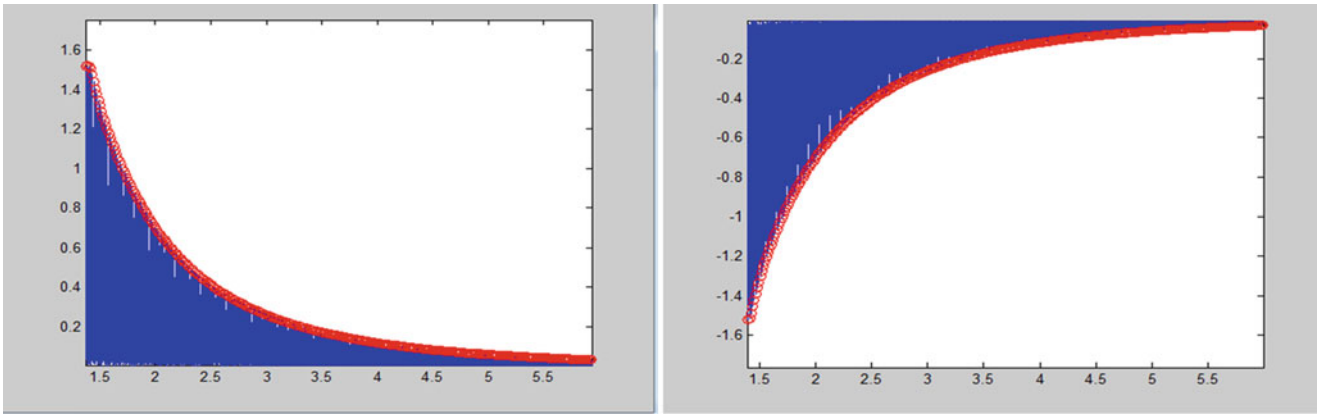

Fig. 15.13 The signal is divided in its positive and negative part in order to compute both the decay rates by means of peaks detection

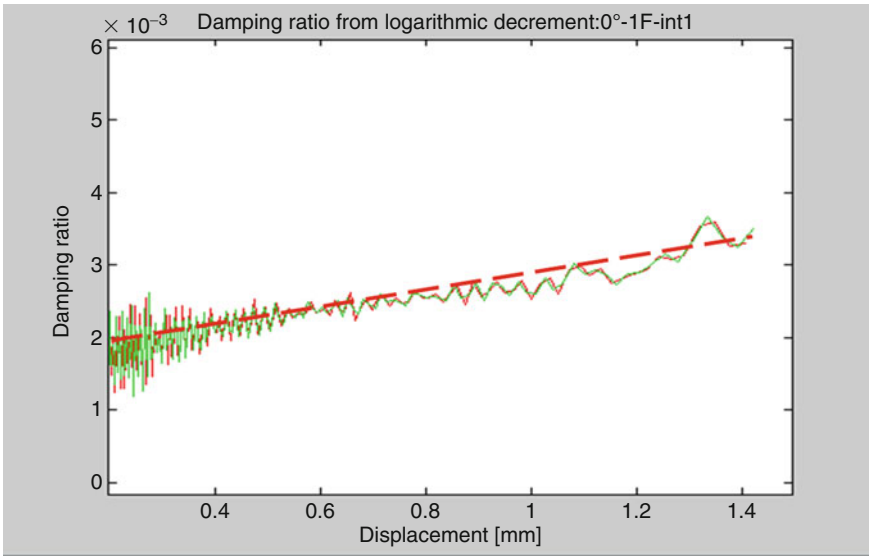

Fig. 15.14 Damping ratio computation as a function of the amplitude of vibration

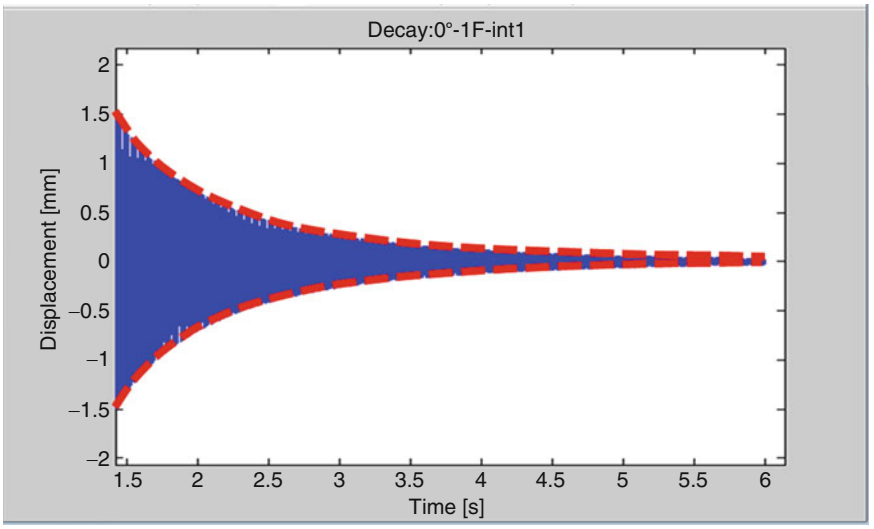

Fig. 15.15 Displacement decay of the unidirectional blade vibrating at first flexural mode. Decay intensity 1

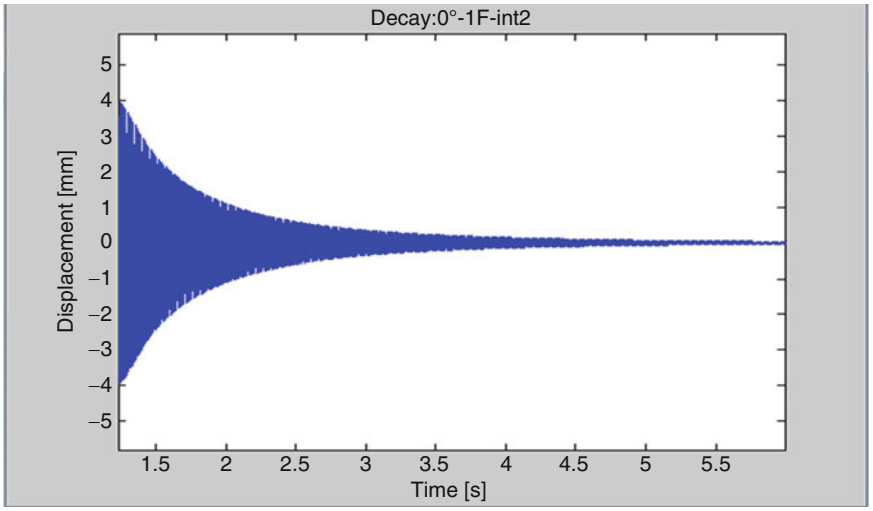

Fig. 15.16 Displacement decay of the unidirectional blade vibrating at first flexural mode. Decay intensity 2

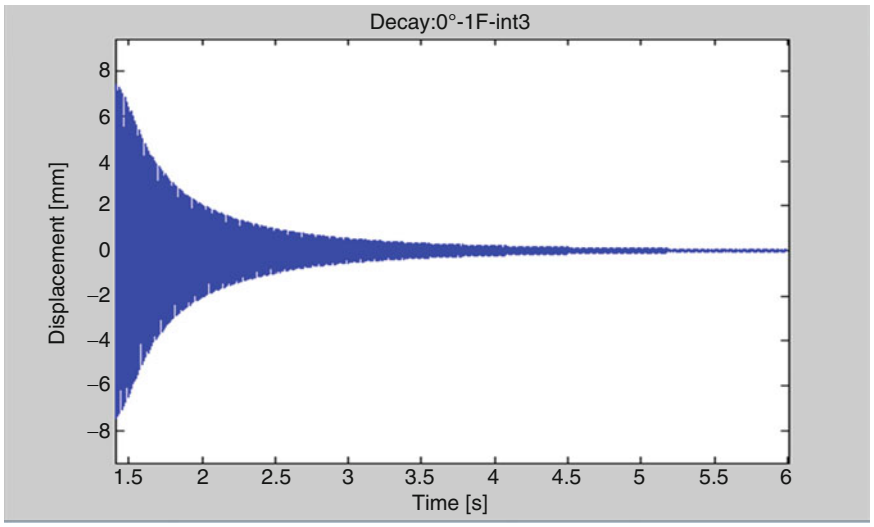

Fig. 15.17 Displacement decay of the unidirectional blade vibrating at first flexural mode. Decay intensity 3

15.4.3.2 Unidirectional: 1st Torsional Mode

The first torsional mode associated with the unidirectional blade is confirmed to be strongly nonlinear by the presence of at least four superharmonics in the decay signal at the highest intensity, as shown in Fig. 15.20. The intense presence of the frequency associated with the first flexural mode in the frequency spectrum of the signal (Fig. 15.21) may indicate a 1:4 internal resonance phenomenon between the torsional (305 Hz) and flexural (74 Hz) modes in which energy is transferred by means of a nonlinear coupling from external resonance of the torsional motion to internal resonance of the flexural motion. From Fig. 15.22 it can be seen that as the time elapses and vibration amplitude is successively damped out causing the displacement to decrease over time, only the first flexural resonance appears. This indicates that even if the forcing frequency from which the decay starts was set at the torsional resonance, at small displacements energy is transferred to lower mode shapes.

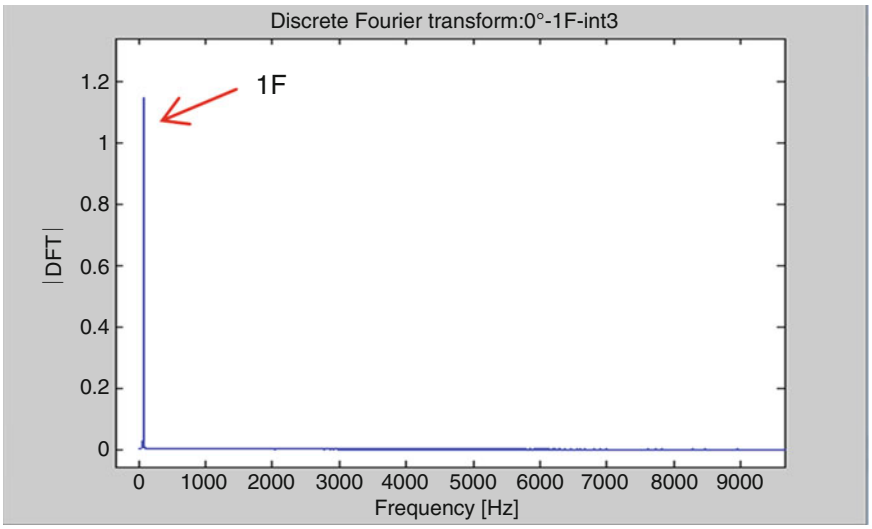

Fig. 15.18 Frequency spectrum shows no nonlinearities. Decay intensity 3

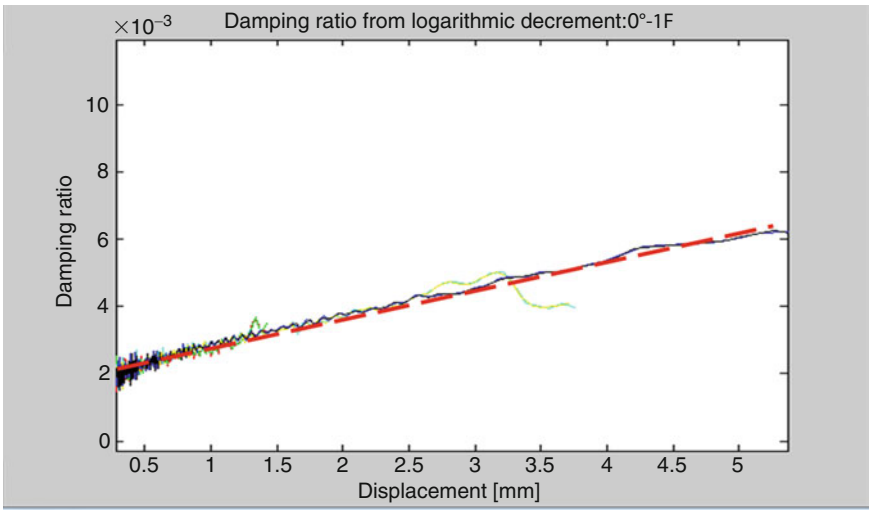

Fig. 15.19 Damping ratio linearly increases with increasing vibration amplitude

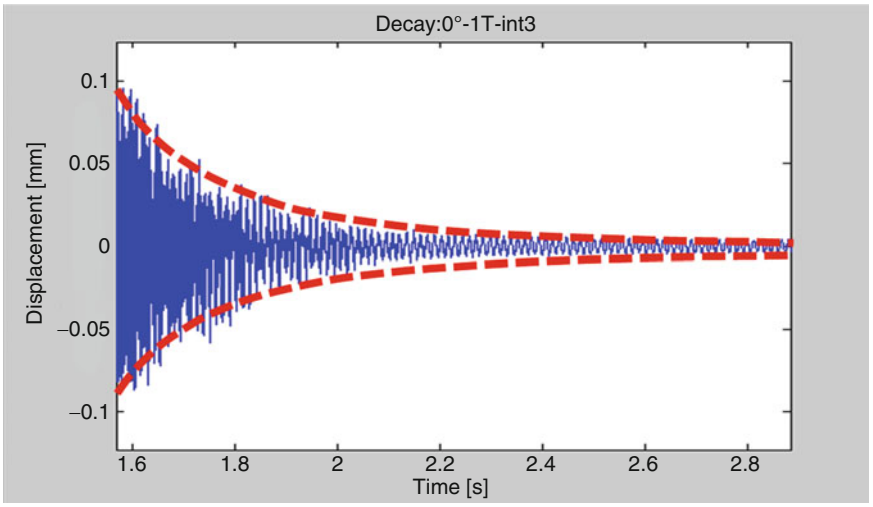

Fig. 15.20 Velocity decay of the unidirectional blade vibrating at first flexural mode. Decay intensity 4

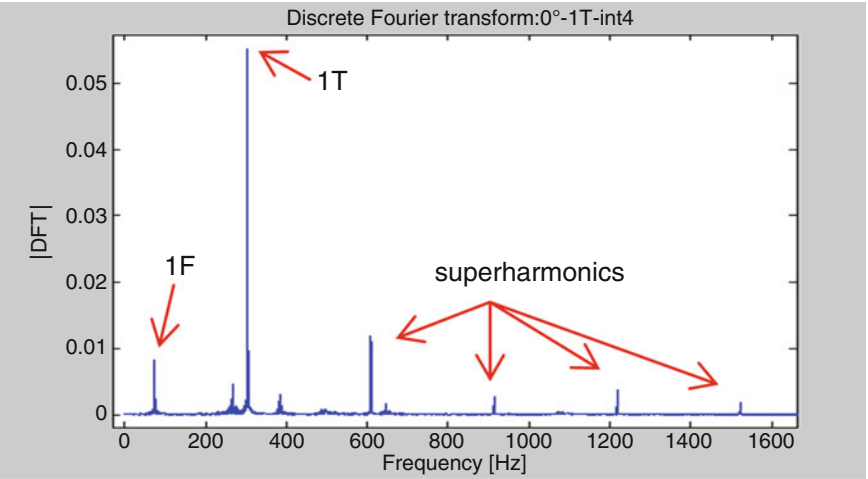

Fig. 15.21 Frequency spectrum shows four superharmonics of the torsional fundamental frequency and an intense presence of the first flexural natural frequency. Decay intensity 4

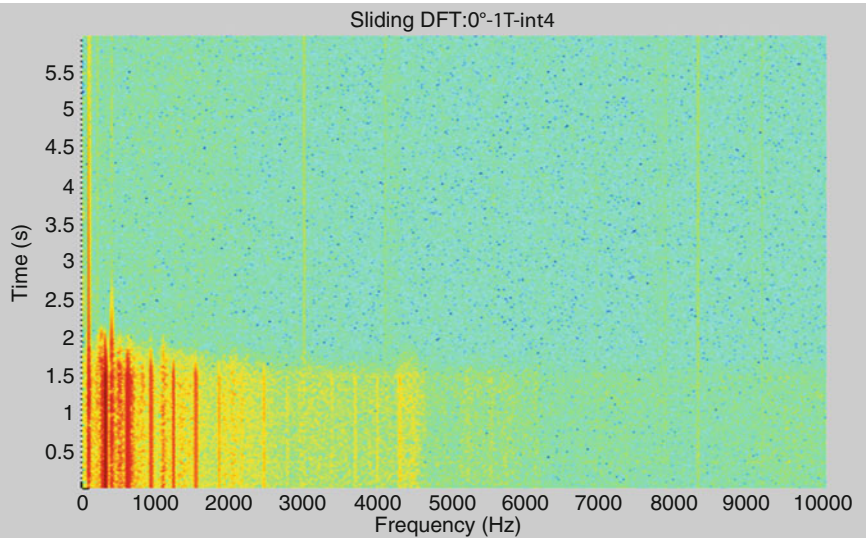

Fig. 15.22 Sliding frequency spectrum over time clearly shows vibration damps out the superharmonics during the decay as time elapses and vibration amplitude decrease. Decay intensity 4

15.4.3.3 Unidirectional: 2nd Flexural Mode

The 2nd flexural mode of the 0° blade is confirmed highly nonlinear by the presence of four superharmonics in the signal at the highest excitation intensities (Figs. 15.23 and 15.24). Interestingly, the damping phenomenon changes from viscous damping at small amplitude vibration (Fig. 15.25) to Coulomb-like damping at high displacement (Fig. 15.26) introducing further nonlinear behaviour.

15.5 Conclusions

The pulsed air-jet excitation system is used in this work for inducing high vibration amplitudes of composites components. Despite this system was designed for High Cycle Fatigue testing thanks to its contactless feature, it was understood that such a feature could be well exploited for nonlinear testing. The major advantage is to allow steady state conditions at any excitation frequency and from which a free decay can be initiated. The same system can be also used for forced

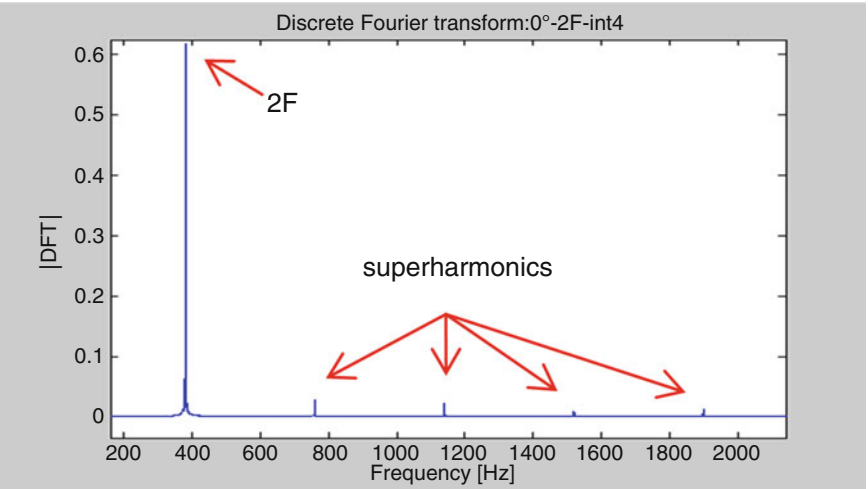

Fig. 15.23 Frequency spectrum shows four superharmonics of the second flexural fundamental frequency. Decay intensity 4

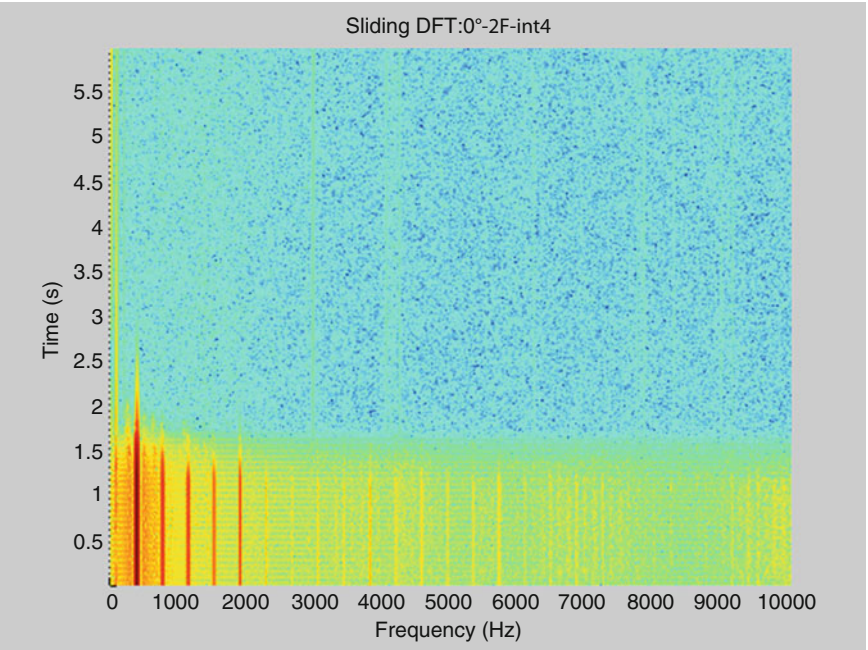

Fig. 15.24 Sliding frequency spectrum over time clearly shows vibration damps out the four superharmonics during the decay as time elapses and vibration amplitude decreases. A wide frequency range is present in the signal indicating extremely strong nonlinear behaviour. Decay intensity 4

response testing. Some staggered composite blades were manufactured and tested in both free-free decay and forced response measurements. The bladed were manufactured by creating three different layups and results of experiments were presented in here. Few drawbacks can be pinpointed and these are the excitation type which is pulsed and not harmonic. This can determine additional excitation components to the fundamental one. The other pitfalls could be seen in the air-jet which is only push and therefore this system would not be suitable for testing under free-free conditions. Nevertheless, the authors believe that the dynamic community should be informed of such an excitation so as to encourage further developments.

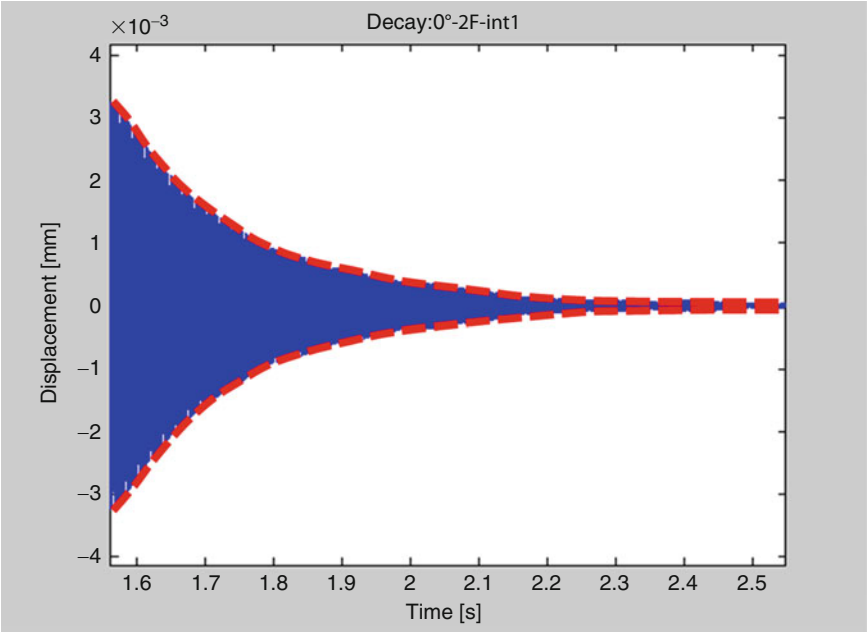

Fig. 15.25 Displacement decay of the unidirectional blade vibrating at second flexural mode with small amplitude. Damping can be approximated by a viscous model. Decay intensity 1

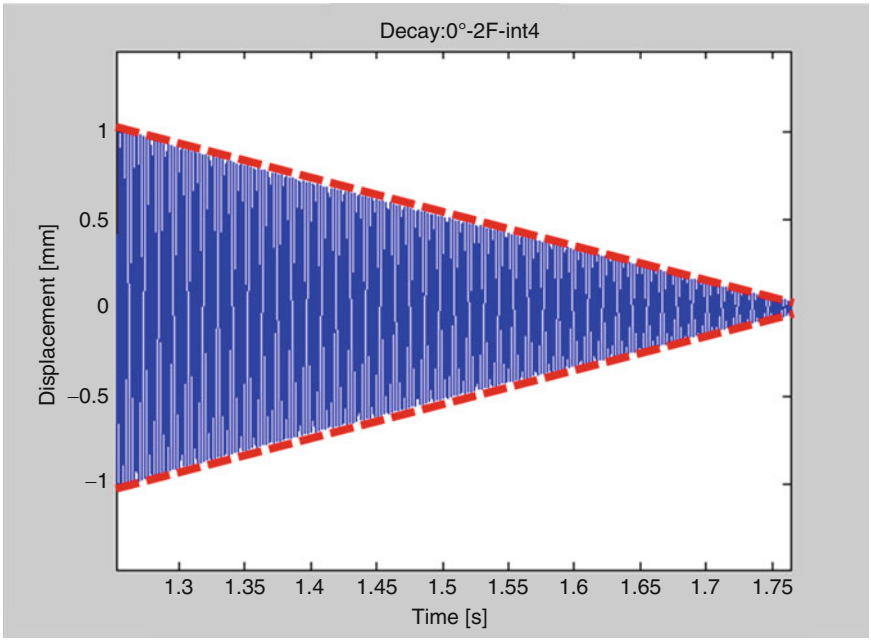

[t!]

Fig. 15.26 Displacement decay of the unidirectional blade vibrating at second flexural mode with large amplitude. Damping can be approximated by a dry friction model. Decay intensity 4

References

1. Worden, K., Tomlinson, G.: Nonlinearity in Structural Dynamics: Detection, Identification and Modelling. IOP Publishing Ltd, Bristol, Philadelphia (2001)
2. Di Sante, R.: Fibre optic sensors for structural health monitoring of aircraft composite structures: recent advances and applications. Sensors **15**, 18666–18713 (2015)

3. Carri, A., Ewins, D.: A systematic approach to modal testing of nonlinear structures. In: Allemang, R., De Clerck, J., Niezrecki, C., Wicks, A. (eds.) Topics in Modal Analysis Conference Proceedings of the Society for Experimental Mechanics Series, vol. 7, pp. 273–286. Springer, New York (2014)
4. Wright, J.R., Platten, M.F., Cooper, J.E., Sarmast, M.: Identification of multi degree of freedom weakly nonlinear systems using a model based in modal space. In: Proceedings of the COST International Conference on Structural System Identification, pp. 49–68. Universitätsbibliothek Kassel, Kassel, Germany (2001)
5. Platten, M.F., Wright, J.R., Dimitriadis, G., Cooper, J.E.: Identification of multidegree of freedom nonlinear systems using an extended modal space model. Mech. Syst. Signal Process. **23**(1), 8–29 (2009)
6. Platten, M.F., Wright, J.R., Cooper, J.E., Dimitriadis, G.: Identification of a nonlinear wing structure using an extended modal model. J. Aircr. **46**(5), 1614–1626 (2009)
7. Londono, J.M., Neild, S.A., Cooper, J.E.: Identification of backbone curves of nonlinear systems from resonance decay responses. J. Sound Vib. **348**, 224–238 (2015)
8. Di Maio, D., Magi, F.: Development of testing methods for endurance trials of composites components. J. Compos. Mater. **49**(24), 2977–2991 (2015)

Chapter 16
EMA-FEA Correlation and Updating for Nonlinear Behaviour of an Automotive Heat-Shield

Elvio Bonisoli, Marco Brino, and Giuseppe Credo

Abstract This paper focuses on the correlation between Experimental Modal Analysis (EMA) and Finite Element Analysis (FEA) of an automotive component where different parameters can affect the simplicity of a linear approach.

The component is a heat-shield that covers the catalytic converter through rigid brackets and fasteners. Thermal refractory, viscous and vibration absorber material is interposed between two steel sheet layers. This filler material and the wafer-like structure of the shield are thought of being the main cause of nonlinear behaviour. Shaker tests with force-controlled sine sweep excitation are performed for obtaining linearised data on different force levels for the updating step on the model. In particular the system presents complex bending dynamics of the shield coupled to the entire structure. Due to the constraints and the added masses of instruments to measure it, veering phenomena are evinced.

A One Factor At Time (OFAT) study on the numerical model is performed for tuning unknown parameters and build an effective and reliable model that could fit the experimental results. Several modelling techniques for the filler are considered to investigate its effect on the dynamic response and the sensitivity to the factors involved. Modal Assurance Criterion (MAC) and frequency comparisons are used for evaluating the discrepancies between model and experiment.

Keywords Heat-shield • Updating • Nonlinear system • Experimental modal analysis • Finite element model

16.1 Introduction

Numerical simulations of components and systems are now a common use in automotive fields and very often they are a powerful tool for improving the design phase.

Experimental Modal Analysis and other tests [1] are used to validate the numerical models and to check the actual operating conditions.

In most of the cases a Model Updating [2] is necessary, because the wide range of values related to standard table-based material properties (in particular Young's modulus and density, which are necessary in modal analysis) do not represent well the actual properties of the material used during the production process, with the possibility of tuning the model and fitting it to the experimental results obtained.

The comparison of EMA-FEA is not only performed with a frequency-based fit, but the modeshape is very important in the correlation, thus the Modal Assurance Criterion (MAC) [3] is now one of the most used standard for this purpose, other than the method used in this work, with all its interpretations and applications presented in [4].

Another use of MAC is for comparing two experimental models or two numerical models for following mode paths on structures with modifications, in particular when studying crossing and veering phenomena, firstly investigated by Leissa in [5] and then analysed on component-to-system behaviour in [6].

In this work the investigated component is a heat-shield that is connected to the catalytic converter in order to protect neighbour components from its heat during operative conditions.

E. Bonisoli (✉) • M. Brino
Department of Management and Production Engineering, Politecnico di Torino, Corso Duca degli Abruzzi 24, 10129 Torino, Italy
e-mail: elvio.bonisoli@polito.it

G. Credo
General Motors Powertrain, NVH & Dynamics Engineering Group, Corso Castelfidardo 36, 10129 Torino, Italy

G. Kerschen (ed.), *Nonlinear Dynamics, Volume 1*, Conference Proceedings of the Society for Experimental Mechanics Series,
DOI 10.1007/978-3-319-29739-2_16

The shield is composed of three layers:

- steel upper sheet;
- refractory and sound-absorbent material filler;
- steel lower sheet.

The overall thickness is practically constant for the entire surface, although the refractory material is not present along the external boundaries, due to the folding process on one of the two metal sheets.

16.2 Experimental Setup

The heat-shield test has been performed considering the component assembled to its neighbour components, the catalytic converter in particular, with free-free boundary conditions applied and simulated through low stiffness elastic springs and considering sine sweep shaker excitation with force-controlled input, in order to reduce the nonlinear contribution and consider a linearisation about a certain force load and being able to perform correlation with numerical linear models.

The actual assembled structure and its test setup are shown in Figs. 16.1 and 16.2.

For the acceleration acquisition two possible accelerometers were available:

- triaxial accelerometer, 14g of weight;
- monoaxial accelerometer, 2g of weight.

The triaxial accelerometer allows the acquisition of more information on the three orthogonal directions, but its mass contribution to the structure might change too much the dynamic behaviour, while the monoaxial is much lighter but it only allows the acquisition along the normal direction of the shield surface.

For the choices a parametric analysis on a numerical FE model have been performed, for evaluating the frequencies and modeshapes contribution of increasing added mass on the structure. Figure 16.3 shows the dependency of the resonant frequencies with respect to the accelerometers mass, while Fig. 16.4 demonstrates that effect on the modeshapes. The modeshapes are compared using Modal Assurance Criterion (MAC) index, defined in Eq. (16.1)

$$MAC_{i,j} = \frac{\left(\Phi_i^T \Phi_j\right)^2}{\left(\Phi_i^T \Phi_i\right)\left(\Phi_j^T \Phi_j\right)} = \cos^2 \alpha_{i,j} \tag{16.1}$$

where Φ_i, Φ_j are the eigenvectors of mode i, and j respectively.

On both frequency and modeshape contribution, the 14g case shows significant influence. In particular, the frequencies not only vary in absolute value, with non-constant trend, but crossing/veering and modes switch occur. Moreover, the MAC plot for modeshapes shows mode mixing, typical of mode veering behaviour, bringing to the conclusion that the mass contribution of the accelerometers is significant and the 2g sensor must be chosen. Thus, only normal vibration for each acquisition point will be taken into account.

Fig. 16.1 Constrained heat-shield

Fig. 16.2 Test setup with springs and shaker

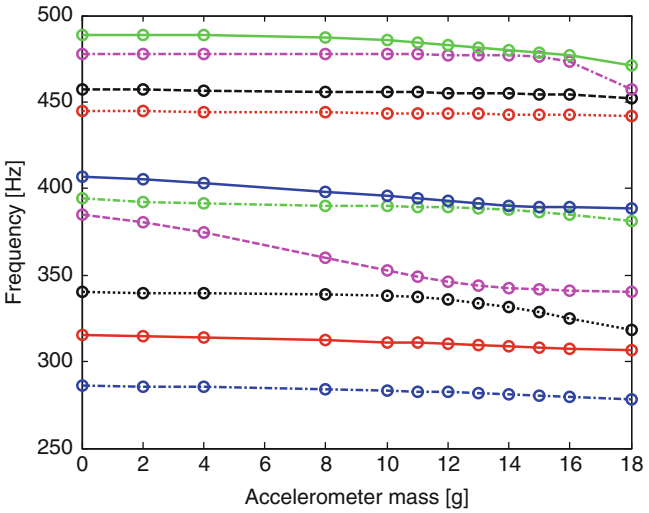

Fig. 16.3 Dependency of natural frequencies with respect to accelerometers mass

The experimental points considered are shown in Fig. 16.5, and thay are arranged in order to cover the most relevant points of the structure, based on the requests of the company.

The system has been excited with sine sweep force-controlled load, in the 250–640 Hz range with a speed of 2 Hz/s. For confirming the nonlinear behaviour of the system, a check on the acceleration variability with respect to the load level has been performed, and the result is shown in Fig. 16.6.

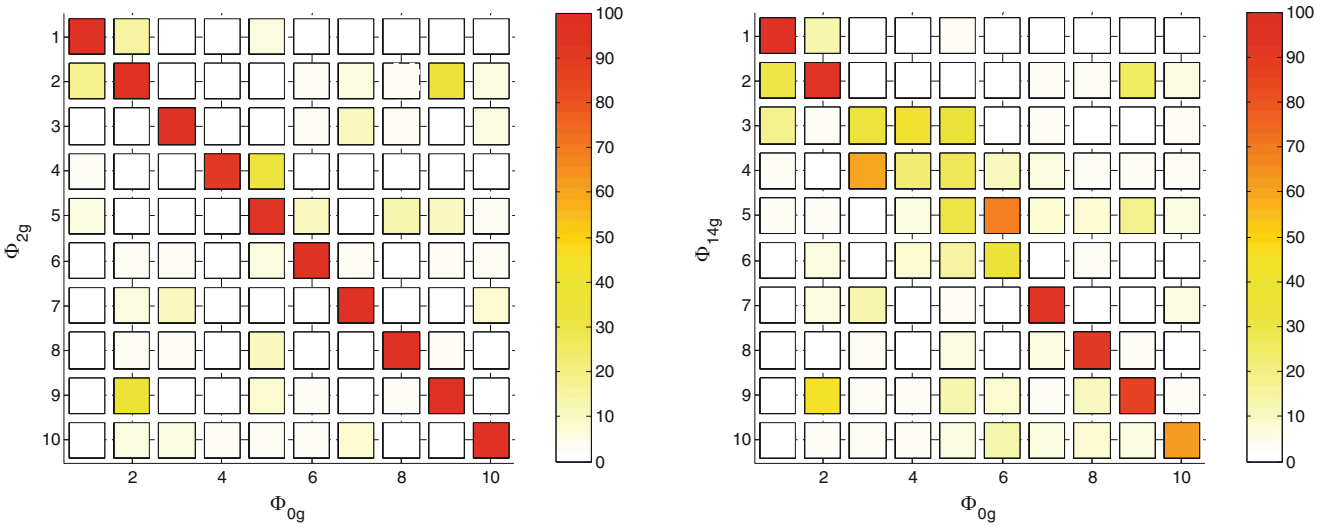

Fig. 16.4 Dependency of modeshapes with respect to accelerometers mass, using MAC index, between 0g and 2g configuration (*left*), and between 0g and 14g configuration (*right*)

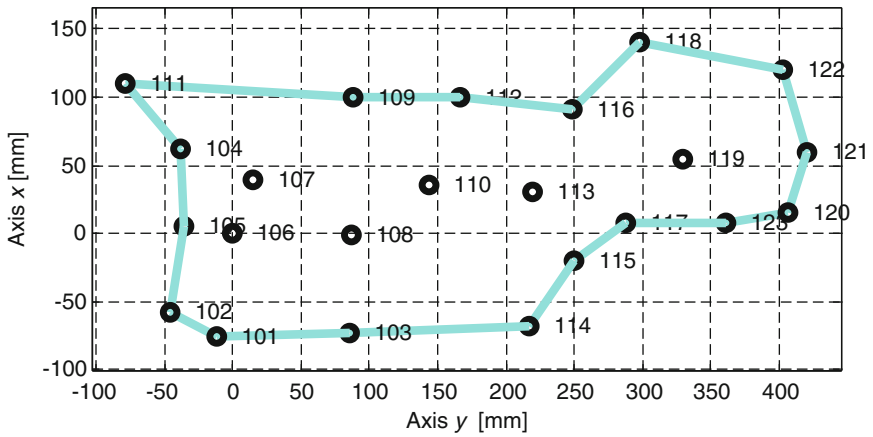

Fig. 16.5 Position of the experimental points acquired

The three curves are at different levels, because of the different excitation, and the peaks occur at different frequencies, in particular they tend to lower frequencies with increasing load. This is a classic softening behaviour in thin shells [7].

Full EMA has been performed on 0.5 N and 1.0 N levels (0.25 N has not been taken into account because of poor acquisition quality due to too low response of the structure to the excitation), and the results are shown in Fig. 16.7.

The acquisition quality was better on the 1.0 N case, and thus it is the configuration considered as a reference for the correlation with the numerical FE model.

16.3 Numerical Model

A Finite Element model (named *Model 0*) was used as a starting model for performing numerical analyses that could fit the experimental test.

The model included all the components of the experimental structure, as shown in Fig. 16.8, but in all the subsequent figures only the heat-shield component is visualised.

Some improvements have been carried out on this model before running the modal analysis and comparing the results with EMA. First, a minimum distance search among the nodes allowed the choice of the nearest nodes with respect to the actual experimental points, and they were renumbered for quick check. Then, local reference frames have been added in

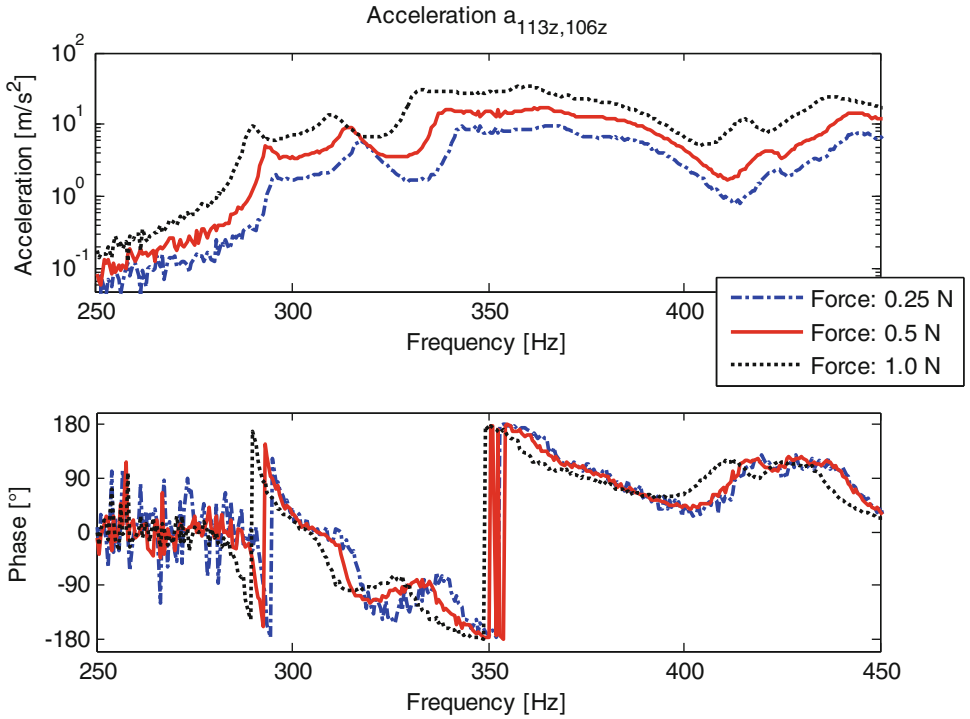

Fig. 16.6 Acceleration acquisition at different excitation levels

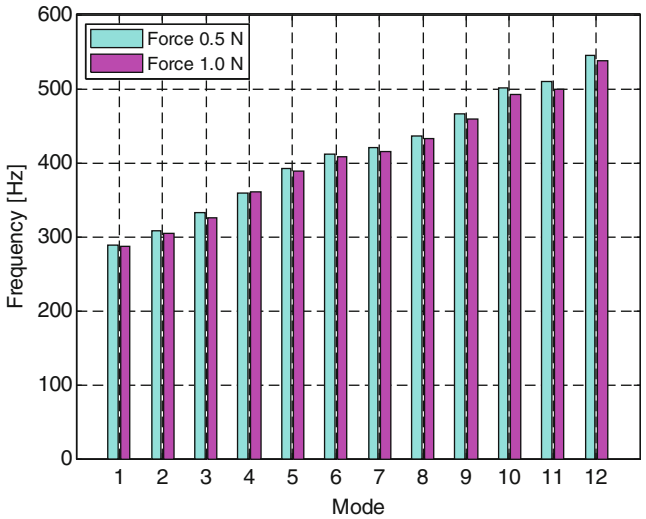

Fig. 16.7 Identified frequency comparison between 0.5 N and 1.0 N input force levels

correspondence of those nodes in order of imposing the z-direction collinear with the normal of the surface at the nodes, and thus collinear with the impact/accelerometer acquisition axis and direction. This improvement allows one-to-one comparison of eigenvectors with the experimental results.

The mass simulators used for maintaining constant mass during roving accelerometer test have been modelled as non structural masses (CONM2) and linked to the external surface of the shield with RBE3 elements. The RBE3 have been chosen with respect to the RBE2 for avoiding stiffening contribution on the shield element involved in the link. This improved model is named *Model 1*.

Figure 16.9 shows the visual comparison of the two models, with a detail of the described features of Model 1 in Fig. 16.10.

The modal results of this model have been compared with the experiments using a frequency comparison and a MAC index for the correlation of numerical and experimental modeshapes.

Fig. 16.8 Full FEM model of the constrained heat-shield

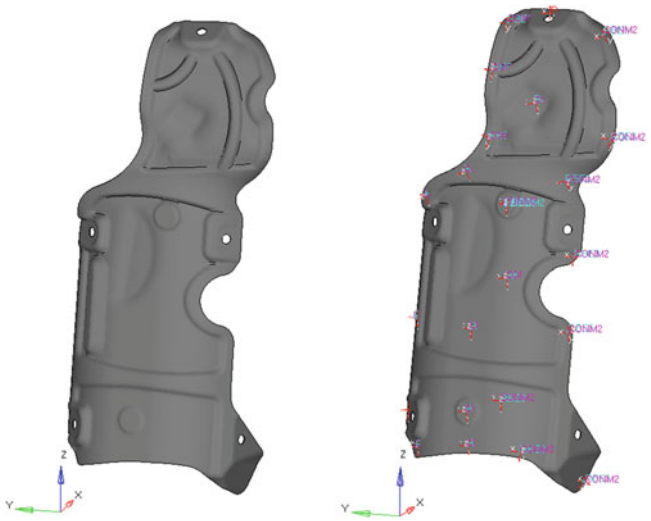

Fig. 16.9 Model comparison between Model 0 and Model 1

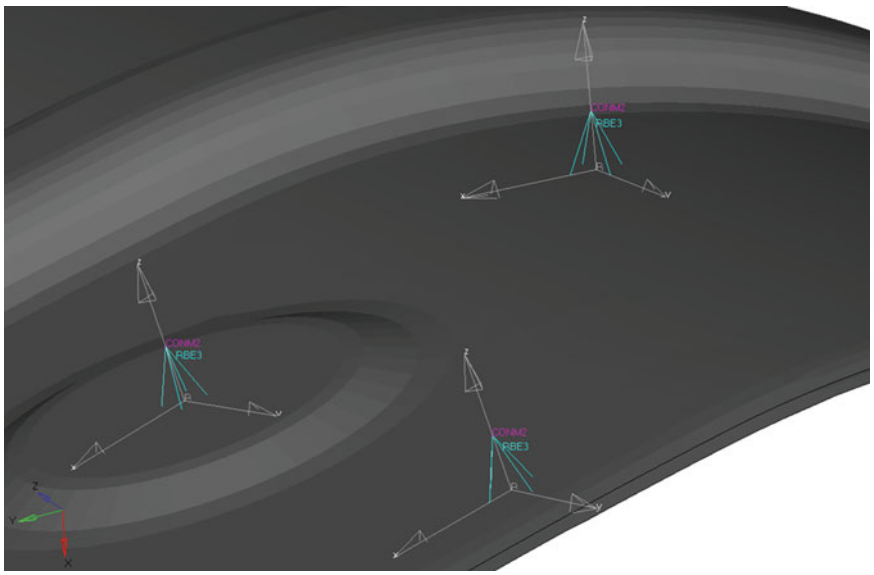

Fig. 16.10 Detail of Model 1

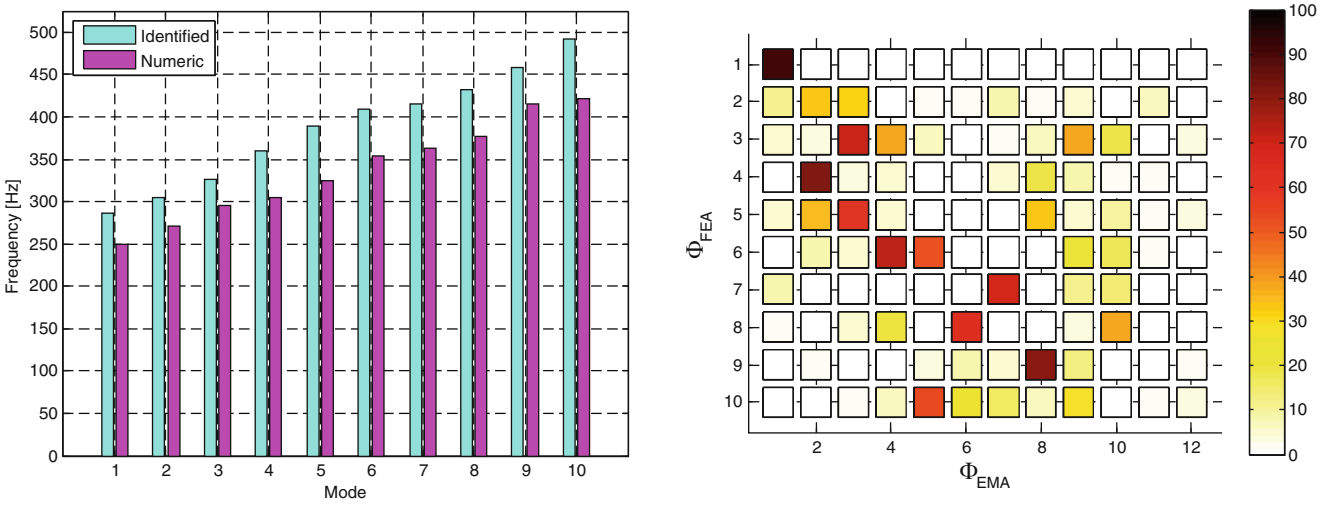

Fig. 16.11 Comparison of natural frequencies (*left*) and MAC (*right*) between Test and Model 1

Table 16.1 Description of model OFAT evolutions

Model ID	Characteristics
2	Larger load cell RBE3 spider
3	Solid viscous filler
4	Solid viscous filler, no external border
5	Solid viscous filler, steel external border

Figure 16.11 shows the comparison results, where large difference between the experimental and numerical resonant frequencies (in particular, numerical modes are lower) and, moreover, the modeshapes are not in general well correlated, except some modes which are not in the same mode order.

The possible weaknesses of this model are in the differences with respect to reality, and in particular the viscous filler which in not modelled (there are only two independent shells connected one another at the boundaries with RBE2 elements), the influence area of the load cell (much wider). Those improvements can be applied on the model for getting more reliable solution.

16.4 OFAT on FE Model and Validation

In order of being able to evaluate the possible improvements from the model modifications suggested in the previous section, a One Factor At Time (OFAT) sensitivity analysis have been performed. This strategy allows a direct evaluation of the effect of the modifications applied. Several models have been built and their characteristics are summarised in Table 16.1.

16.4.1 Model 2

The first improvement factor to be analysed is the effect of the actual area of influence of the load cell. A better solution is to take into account a larger RBE3 spider, in order to involve more elements in the connection and simulate the actual width of the sensor, as shown in Fig. 16.12.

The results of this model are shown in Fig. 16.13.

The improvement is verified on both frequency side, with numerical results closer to the experimental ones, and mode-shape side, with correlation MAC values that are now arranged showing a weak diagonal. The single values might seem in general lower, but the improvement is verified.

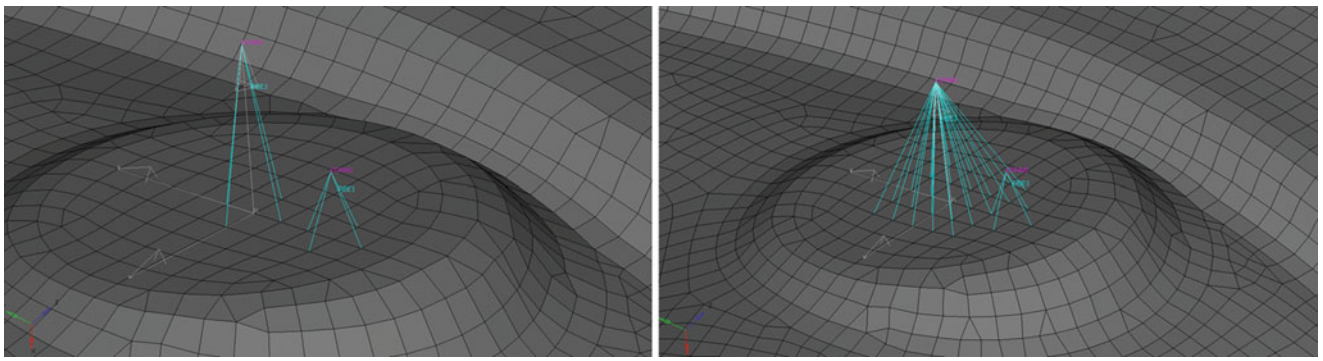

Fig. 16.12 Detail of load cell connection in Model 1 (*left*) and Model 2 (*right*)

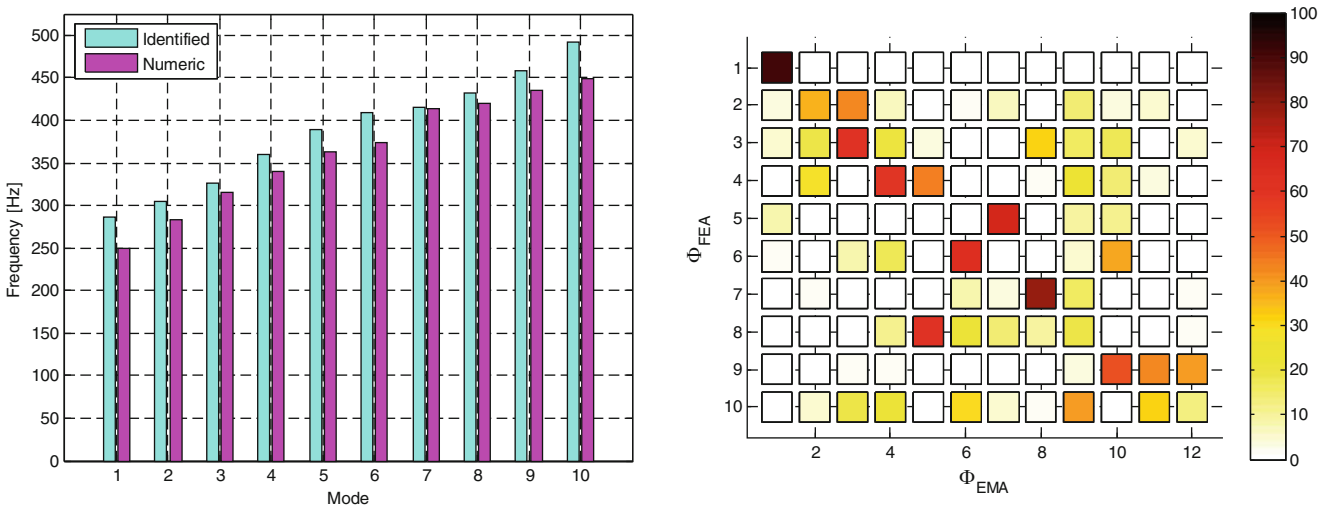

Fig. 16.13 Comparison of natural frequencies (*left*) and MAC (*right*) between Test and Model 2

16.4.2 Model 3

The missing of the actual modelling of the viscous filler, considered not involved in the undamped dynamic behaviour, due to its very low elastic contribution, is considered another possible cause of the lack of correlation of Model 1.

Thus, a layer of solid elements has been added to the model, generating a direct connection between the two steel layers, modelled as shells. A material has been associated to that set of solid elements, using the total mass of the shield as a reference to compute a bulk density to be associated to the viscous filler. The elasticity modulus has been empirically chosen and might be one of the possible updating parameters. In addition, the RBE2 set of elements that connects the two sheet layers together is replaced with QUAD4 elements that are considered more physically consistent. A visual effect of the modification on the model is shown in Fig. 16.14.

Analysing the results in Fig. 16.15, the numerical frequencies are closer to the experimental, while the mode-shapes do not improve significantly with respect to Model 1.

16.4.3 Model 4

Taking into account the actual shield and the manufacturing step of superimposition of the sheet metals at the border, close to the external zone the viscous filler is not present.

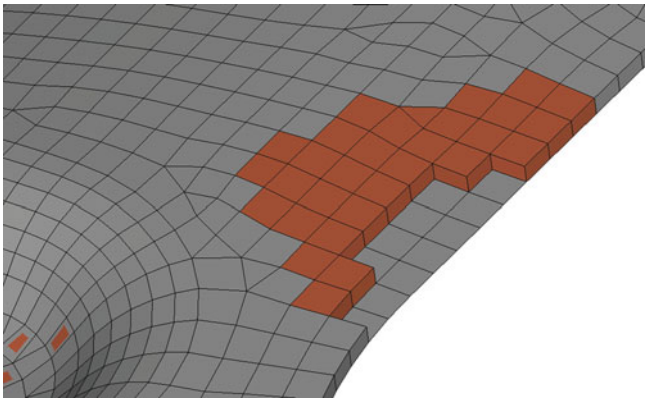

Fig. 16.14 Detail with broken-out section, with solid elements for the viscous filler

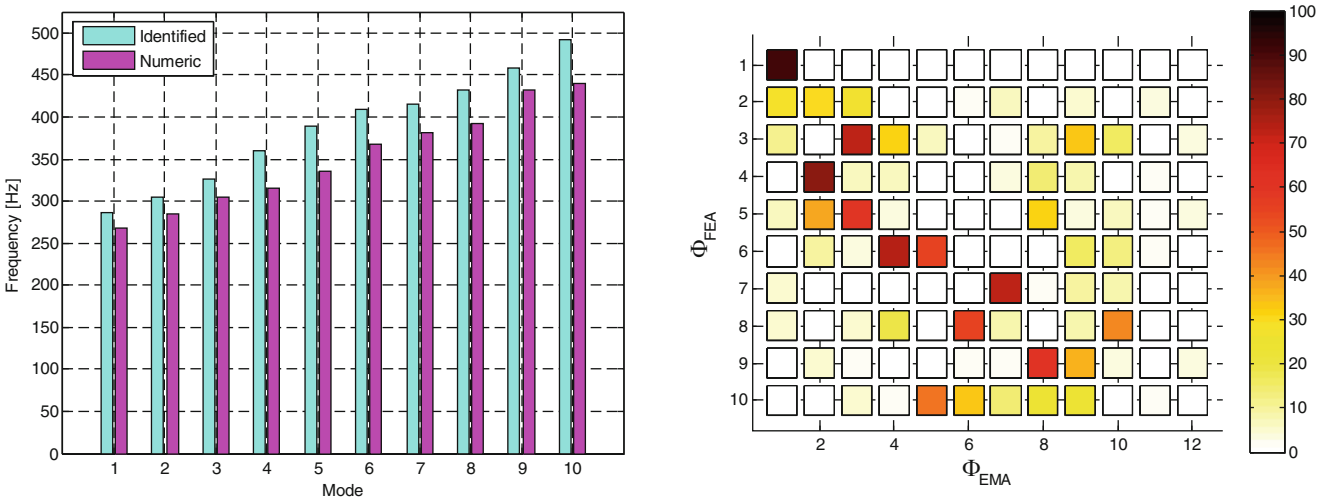

Fig. 16.15 Comparison of natural frequencies (*left*) and MAC (*right*) between Test and Model 3

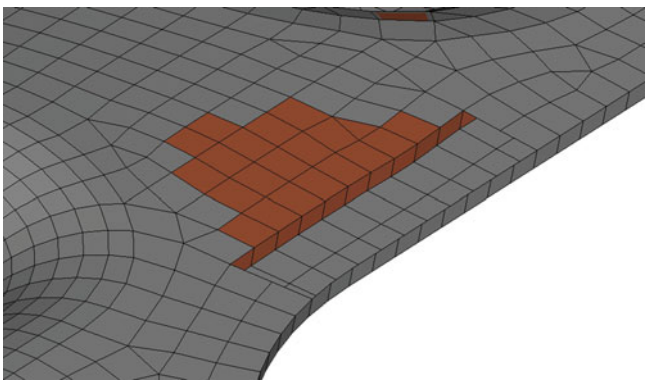

Fig. 16.16 Detail with broken-out section, with solid elements without external border

One possibility to model this detail is to remove layers of solid elements at the external borders, as shown in Fig. 16.16.

The external transversal shells are kept, as in the case of Model 3.

The results for Model 4, are shown in Fig. 16.17.

Considering the frequencies, there is no significant improvement, in particular with respect to Model 3, and for some modes the frequencies are lower. Considering the modeshapes, the results are the same as Model 4.

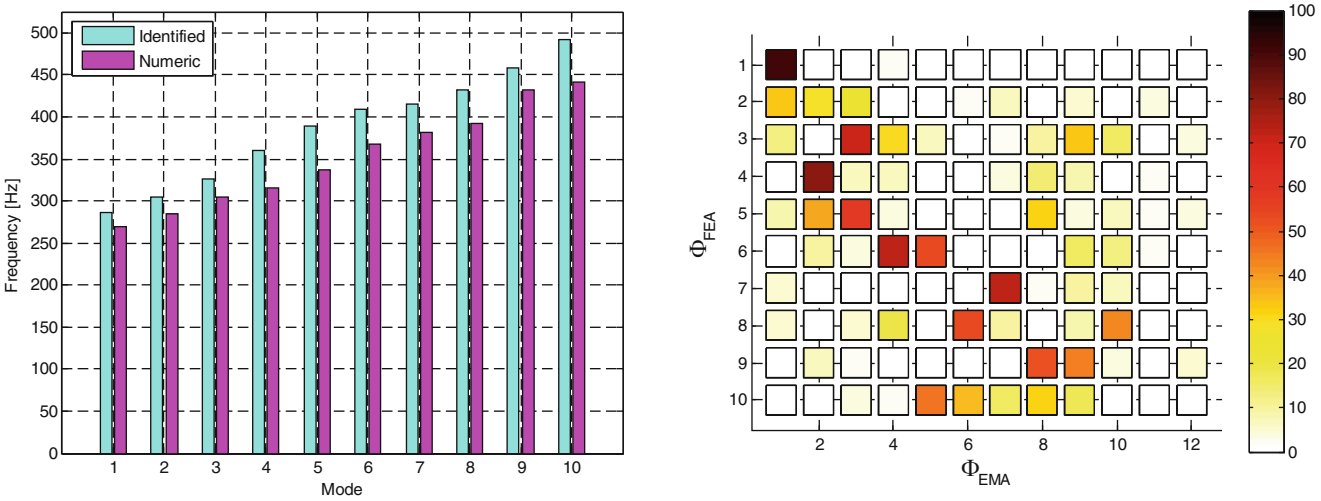

Fig. 16.17 Comparison of natural frequencies (*left*) and MAC (*right*) between Test and Model 4

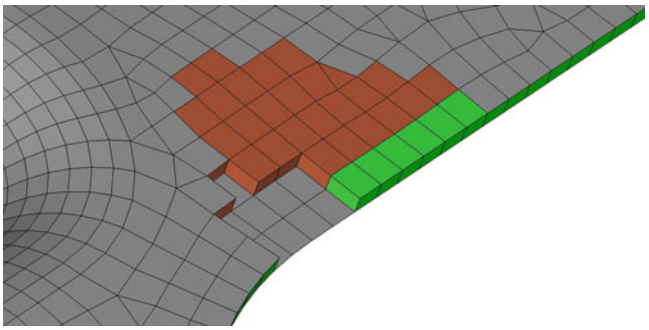

Fig. 16.18 Detail with broken-out section, with solid elements with steel external border

16.4.4 Model 5

The lack of improvements of Model 4, in particular considering the lower frequencies, helped to check the possibility that the stiffness contribution of the two superimposed layers of sheet metal at the component borders were higher than expected. Thus the choice for another model, Model 5, has been to substitute the first row of solid elements of the filler of Model 3, with steel material properties. The visual modification can be checked in Fig. 16.18.

The results for Model 5 are shown in Fig. 16.19.

Looking at the frequency bar chart, the impression is that there is an improvement, because the numerical frequencies are closer to the experimental ones, but the MAC plot shows that the eigenvectors poorly match and, even though the frequencies are increased, the modeshapes are further with respect to the previous cases.

16.5 Final Model Updating and FRF Validation

The OFAT analysis has shown which parameter brings to an improvement and that a combination of Model 2 with Model 3, leading to Model 6, could give an increased improvement with respect to the two contributions separately.

The results of this combined model are shown in Fig. 16.20.

The improvements are significant in both frequency (the numerical frequencies are now very close to the experimental) and MAC (the diagonal trend is clearer and the single correlation values are increased) charts, validating this model with respect to the previous, and considering it as a master model for preforming updating operations.

For deep model updating the resonant frequencies discrepancies and the modeshapes correlation are not the only evaluation characteristics, but also FRF superimposition of experimental and numerical is taken into account. The numerical

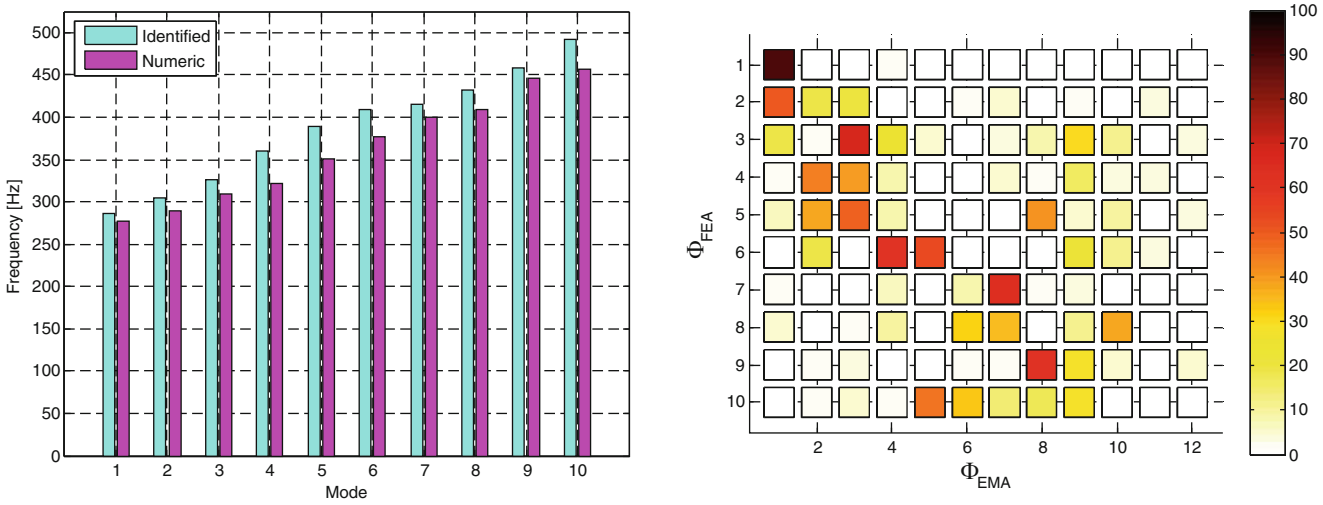

Fig. 16.19 Comparison of natural frequencies (*left*) and MAC (*right*) between Test and Model 5

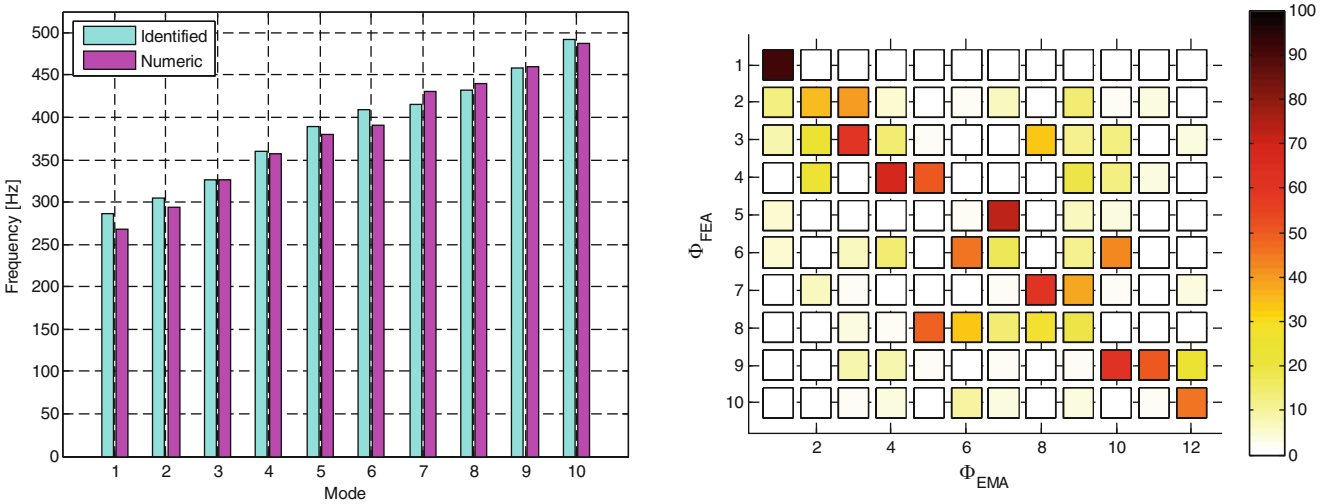

Fig. 16.20 Comparison of natural frequencies (*left*) and MAC (*right*) between Test and Model 6

FRF are computed with modal superposition, using the modal basis computed and assuming modal damping ratios, and with direct integration of frequency response assuming viscous damping to the material properties. The comparison of some FRF is shown in Fig. 16.21.

The offset between the two numeric techniques confirms that the modal superposition method is enough and reliable, assuming constant modal damping ratio as $\zeta = \frac{\eta}{2}$ for first approximation, which is much faster than a direct numeric solution, which could take hours to compute.

While some FRF reasonably fit, with frequency difference but with consistent general trend, some functions do not fit well the same. Model 6 is a very good model to start with, performing updating methods for a closer general fit.

16.6 Conclusions

In this paper the study of nonlinear dynamic behaviour of an automotive heat-shield was carried out, starting from experimental tests with modal analysis, using shaker testing on different excitation levels, and then building a numerical model on which several OFAT analysis were performed in order to find the right modelling choices for the best experimental-numerical correlation.

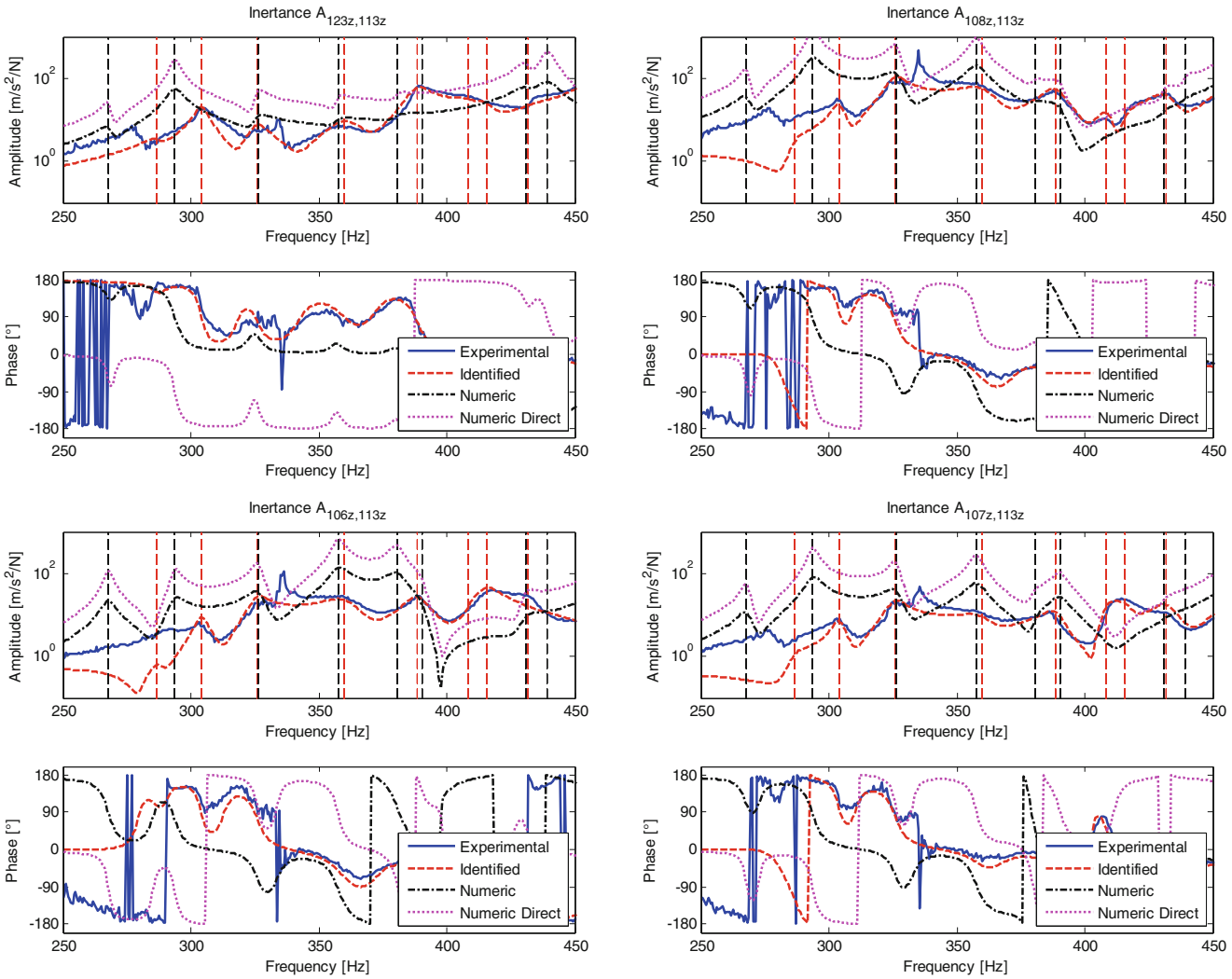

Fig. 16.21 FRFs comparisons of output points #106z, #107z, #108z, #113z, #120z, #123z considering raw experimental data, identified data from test, numeric obtained through modal superposition and numeric directly obtained

The above mentioned Model 6 (which presents, starting from Model 1 and its accelerometers mass modelling, a wider RBE3 spider for the load cell connection and solid filler material mesh between the two metallic shells, with external borders of filler removed) is found being the best compromise and with the best correlation with respect to the experiments, even though some critical points still remain.

A one-to-one EMA-FEA correlation regarding both natural frequencies and mode-shapes is still hard to detect, and a deeper study and optimisation of the filler material properties is one of the further investigation paths, together with possible improvements on the experimental side, such as a test on operating conditions or using the full constrained system attached to a large shaker (then with excitation loads on the connections, as in the operating conditions), with operative loads (thus with operative load level with its non-linear effect).

Acknowledgment This work was performed under a research project with General Motors. The authors would like to thank Dr. Michele Belluscio for his enthusiasm and driving force in the project.

References

1. Maia, M.M.N., Silva, J.M.M.: Theoretical and Experimental Modal Analysis. Wiley, New York, USA (1997)
2. Friswell, M.I., Mottershead, J.E.: Finite Element Model Updating in Structural Dynamics. Kluwer, Dordrecht (1995)
3. Allemang, R.J., Brown, D.L.: A correlation coefficient for modal vector analysis. In: Proceedings of the I IMAC, pp. 110–116 (1982)
4. Allemang, R.J.: The modal assurance criterion - twenty years of use and abuse. Sound Vib. 14–20 (2003)
5. Leissa, W.: On a curve veering aberration. J. Appl. Math. Phys. (ZAMP) **25**, 99–111 (1974)
6. Bonisoli, E., Marcuccio, G., Rosso, C.: Crossing and veering phenomena in crank mechanism dynamics. In: Proceedings of the XXXI IMAC, pp. 1–11. Garden Grove, California, February 11–14, Paper 376 (2013)
7. Amabili, M.: Nonlinear Vibrations and Stability of Shells and Plates. Cambridge University Press, Cambridge, UK (2008)

Chapter 17
Tutorial on Nonlinear System Identification

G. Kerschen

Abstract Because nonlinearity is now a frequent occurrence in real-life applications, the practitioner should understand the resulting dynamical phenomena and account for them in the design process. This tutorial focuses on nonlinear system identification, which extracts relevant information about nonlinearity directly from experimental measurements. Specifically, the identification process is a progression through three steps, namely detection, characterization and parameter estimation. The tutorial presents these steps in detail and illustrates them using real aerospace structures.

Keywords Nonlinear vibrations • System identification • Detection • Characterization • Parameter estimation

17.1 Introduction

Mathematical modeling refers to the use of mathematical language to simulate the behavior of a 'real world' (practical) system. Its role is to provide a better understanding and characterization of the system. Theory is useful for drawing general conclusions from simple models, and computers are useful for drawing specific conclusions from complicated models. In the theory of mechanical vibrations, mathematical models—termed structural models—are helpful for the analysis of the dynamic behavior of the structure being modeled.

The demand for enhanced and reliable performance of vibrating structures in terms of weight, comfort, safety, noise and durability is ever increasing while, at the same time, there is a demand for shorter design cycles, longer operating life, minimization of inspection and repair needs, and reduced costs. With the advent of powerful computers, it has become less expensive both in terms of cost and time to perform numerical simulations, than to run a sophisticated experiment. The consequence has been a considerable shift toward computer-aided design and numerical experiments, where structural models are employed to simulate experiments, and to perform accurate and reliable predictions of the structure's future behavior.

Even if we are entering the age of virtual prototyping [1], *experimental testing* and *system identification* still play a key role because they help the structural dynamicist to reconcile numerical predictions with experimental investigations. The term 'system identification' is sometimes used in a broader context in the technical literature and may also refer to the extraction of information about the structural behavior directly from experimental data, i.e., without necessarily requesting a model (e.g., identification of the number of active modes or the presence of natural frequencies within a certain frequency range). In this tutorial, system identification refers to the development (or the improvement) of structural models from input and output measurements performed on the real structure using vibration sensing devices.

Linear system identification is a discipline that has evolved considerably during the last 30 years [2, 3]. Modal parameter estimation—termed *modal analysis*—is indubitably the most popular approach to performing linear system identification in structural dynamics. The model of the system is known to be in the form of modal parameters, namely the natural frequencies, mode shapes and damping ratios. The popularity of modal analysis stems from its great generality; modal parameters can describe the behavior of a system for any input type and any range of the input. Numerous approaches have been developed for this purpose: *Ibrahim time domain* method [4], *eigensystem realization algorithm* [5], *stochastic subspace identification* method [6], *polyreference least-squares complex frequency domain* method [7] to name a few. It is, however, important to note that modal identification of highly damped structures or complex industrial structures with high modal density and

G. Kerschen (✉)
Department of Aerospace and Mechanical Engineering, Space Structures and Systems Laboratory (S3L),
Structural Dynamics Research Group, University of Liège, Liège, Belgium
e-mail: g.kerschen@ulg.ac.be

G. Kerschen (ed.), *Nonlinear Dynamics, Volume 1*, Conference Proceedings of the Society for Experimental Mechanics Series,
DOI 10.1007/978-3-319-29739-2_17

large modal overlap are now within reach. Unification of the theoretical development of modal identification algorithms was attempted in [8, 9], which is another sign of the maturity of this research field.

The focus in this tutorial is on structural system identification in the presence of nonlinearity. Nonlinearity is generic in Nature, and linear behavior is an exception. In structural dynamics, typical sources of nonlinearities are:

- Geometric nonlinearity results when a structure undergoes large displacements and arises from the potential energy. An illustration is the simple pendulum, the equation of motion of which is $\ddot{\theta} + \omega_0^2 \sin\theta = 0$; the nonlinear term $\omega_0^2 \sin\theta$ represents geometric nonlinearity, since it models large angular motions. Large deformations of flexible elastic continua such as beams, plates and shells are also responsible for geometric nonlinearities [see, e.g., [10, 11].
- Inertia nonlinearity derives from nonlinear terms containing velocities and/or accelerations in the equations of motion, and takes its source in the kinetic energy of the system (e.g., convective acceleration terms in a continuum and Coriolis accelerations in motions of bodies moving relative to rotating frames).
- A nonlinear material behavior may be observed when the constitutive law relating stresses and strains is nonlinear. This is often the case in foams [12–14] and in resilient mounting systems such as rubber isolators [15].
- Damping dissipation is essentially a nonlinear and still not fully modeled and understood phenomenon. The modal damping assumption is not necessarily the most appropriate representation of the physical reality, and its widespread use is to be attributed to its mathematical convenience. Dry friction effects (bodies in contact, sliding with respect to each other) and hysteretic damping are examples of nonlinear damping, see, e.g., [16–19]. It is important to note that dry friction affects the dynamics especially for small-amplitude motion, which is contrary to what might be expected by conventional wisdom.
- Nonlinearity may also result due to boundary conditions (for example, free surfaces in fluids, vibro-impacts due to loose joints or contacts with rigid constraints, clearances, imperfectly bonded elastic bodies), or certain external nonlinear body forces (e.g., magnetoelastic, electrodynamic or hydrodynamic forces). Clearance and vibro-impact nonlinearity possesses nonsmooth force-deflection characteristic and generally requires a special treatment compared with other types of nonlinearities [20].

Many practical examples of nonlinear dynamic behavior have been reported in the engineering literature. In the automotive industry, brake squeal which is a self-excited vibration of the brake rotor related to the friction variation between the pads and the rotor is an irritating but non-life-threatening example of an undesirable effect of nonlinearity [21]. Many automobiles have viscoelastic engine mounts which show marked nonlinear behavior: dependence on amplitude, frequency and preload. In an aircraft, besides nonlinear fluid-structure interaction, typical nonlinearities include backlash and friction in control surfaces and joints, hardening nonlinearities in the engine-to-pylon connection, and saturation effects in hydraulic actuators. In [22], a commercial airplane is described in which the propellers induced a subharmonic vibration of order $1/2$ in the wings which produced a subharmonic of order $1/4$ in the rudder. The oscillations were so violent that the effects on the airplane were catastrophic [23]. In mechatronic systems, sources of nonlinearities are friction in bearings and guideways, as well as backlash and clearances in robot joints. In civil engineering, many demountable structures such as grandstands at concerts and sporting events are prone to substantial structural nonlinearity as a result of looseness of joints. This creates both clearances and friction and may invalidate any linear model-based simulations of the behavior created by crowd movement. Nonlinearity may also arise in a damaged structure: fatigue cracks, rivets and bolts that subsequently open and close under dynamic loading or internal parts impacting upon each other.

With continual interest to expand the performance envelope of structures at ever increasing speeds, there is the need for designing lighter, more flexible, and consequently, more nonlinear structural elements. It follows that the demand to utilize nonlinear (or even strongly nonlinear) structural components is increasingly present in engineering applications. It is, therefore, rather paradoxical to observe that very often linear behavior is taken for granted in structural dynamics. Why is it so? It should be recognized that at sufficiently small-amplitude motions, linear theory may be accurate for modeling, although it is not always the case (e.g., dry friction). However, the main reason is that nonlinear dynamical systems theory is far less established than its linear counterpart. Indeed, the basic principles that apply to a linear system and that form the basis of modal analysis are no longer valid in the presence of nonlinearity. In addition, even weak nonlinear systems can exhibit extremely interesting and complex phenomena which linear systems cannot. These phenomena include jumps, bifurcations, saturation, subharmonic, superharmonic and internal resonances, resonance captures, limit cycles, modal interactions and chaos. Readers who look for an introduction to nonlinear oscillations may consult [23–26]. More mathematically inclined readers may refer to [27, 28].

This is not to say that nonlinear systems have not received considerable attention during the last decades. Even if, for years, one way to study nonlinear systems was the *linearization approach* [29, 30], many efforts have been spent in order to develop theories for the investigation of nonlinear systems in structural dynamics. A nonlinear extension of the concept of mode shapes was proposed in [31, 32] and further investigated in [33–36]. Weakly nonlinear systems were thoroughly analyzed

using perturbation theory [23, 37–39]. Perturbation methods include for instance the method of *averaging*, the *Lindstedt-Poincaré* technique and the method of *multiple scales* and aim at obtaining asymptotically uniform approximations of the solutions. During the last decade or so, one has witnessed a transition from weakly nonlinear structures to strongly nonlinear structures (by strongly nonlinear systems, a system for which the nonlinear terms are the same order as the linear terms is meant) thanks to the extension of classical perturbation techniques [40, 41] and the development of new methodologies [20, 42–44].

Recently, a few studies proposed to take advantage of nonlinearities instead of ignoring or avoiding them, which represents an interesting shift in paradigm. For example, the concept of parametric resonance is exploited to design microelectromechanical oscillators with filtering capabilities in [45]. In [46–48], it is shown that essential (i.e., nonlinearizable) nonlinearity leads to irreversible nonlinear energy transfer phenomena between subsystems—termed *nonlinear energy pumping*. In [49], chaotic interrogation and phase space reconstruction are used to assess the strength of a bolted connection in a composite beam. In [50], the geometric shape of dynamic attractors is exploited to enhance small parametric variations in a system.

Focusing now on the development (or the improvement) of structural models from experimental measurements in the presence of nonlinearity, i.e., *nonlinear system identification*, one is forced to admit that there is no general analysis method that can be applied to all systems in all instances [see, e.g, previous overviews [51, 52]], as it is the case for modal analysis in linear structural dynamics. In addition, many techniques which are capable of dealing with systems with low dimensionality collapse if they are faced with system with high modal density. Two reasons for this failure are the inapplicability of various concepts of linear theory and the highly 'individualistic' nature of nonlinear systems. A third reason is that the functional $S[\bullet]$ which maps the input $x(t)$ to the output $y(t)$, $y(t) = S[x(t)]$, is not known beforehand. For instance, the ubiquitous *Duffing oscillator* [53], the equation of motion of which is $m\ddot{y}(t) + c\dot{y}(t) + ky(t) + k_3y^3(t) = x(t)$, represents a typical example of polynomial form of restoring force nonlinearity, whereas hysteretic damping is an example of nonpolynomial form of nonlinearity. This represents a major difficulty compared with linear system identification for which the structure of the functional is well defined.

Even if there is a difference between the way one did nonlinear system identification 'historically' and the way one would do it now, the identification process may be regarded as a progression through three steps, namely detection, characterization and parameter estimation, as outlined in Fig. 17.1. Once nonlinear behavior has been detected, a nonlinear system is said to be characterized after the location, type and functional form of all the nonlinearities throughout the system are determined. The parameters of the selected model are then estimated using linear least-squares fitting or nonlinear optimization algorithms depending upon the method considered.

Nonlinear system identification is an integral part of the *verification and validation* (V&V) process. According to [54], verification refers to *solving the equations correctly*, i.e., performing the computations in a mathematically correct manner, whereas validation refers to *solving the correct equations*, i.e., formulating a mathematical model and selecting the coefficients such that physical phenomenon of interest is described to an adequate level of fidelity. As stated in [55], one definition that captures many of the important aspects of model validation is taken from the simulation sciences literature:

> The substantiation that a model within its domain of applicability possesses a satisfactory range of accuracy consistent with the intended application of the model [56]

Scope of the Presentation

The motivation behind this tutorial presentation is threefold. First, it is meant to provide a concise point of departure for researchers and practitioners alike wishing to assess the current state of the art in the identification of nonlinear structural models. Second, the tutorial intends to review several methods that have been proposed in the technical literature and to highlight some of the reasons that prevent these techniques from being applied to complex structures. The last goal is to identify future research needs which would help to 'push the envelope' in nonlinear system identification.

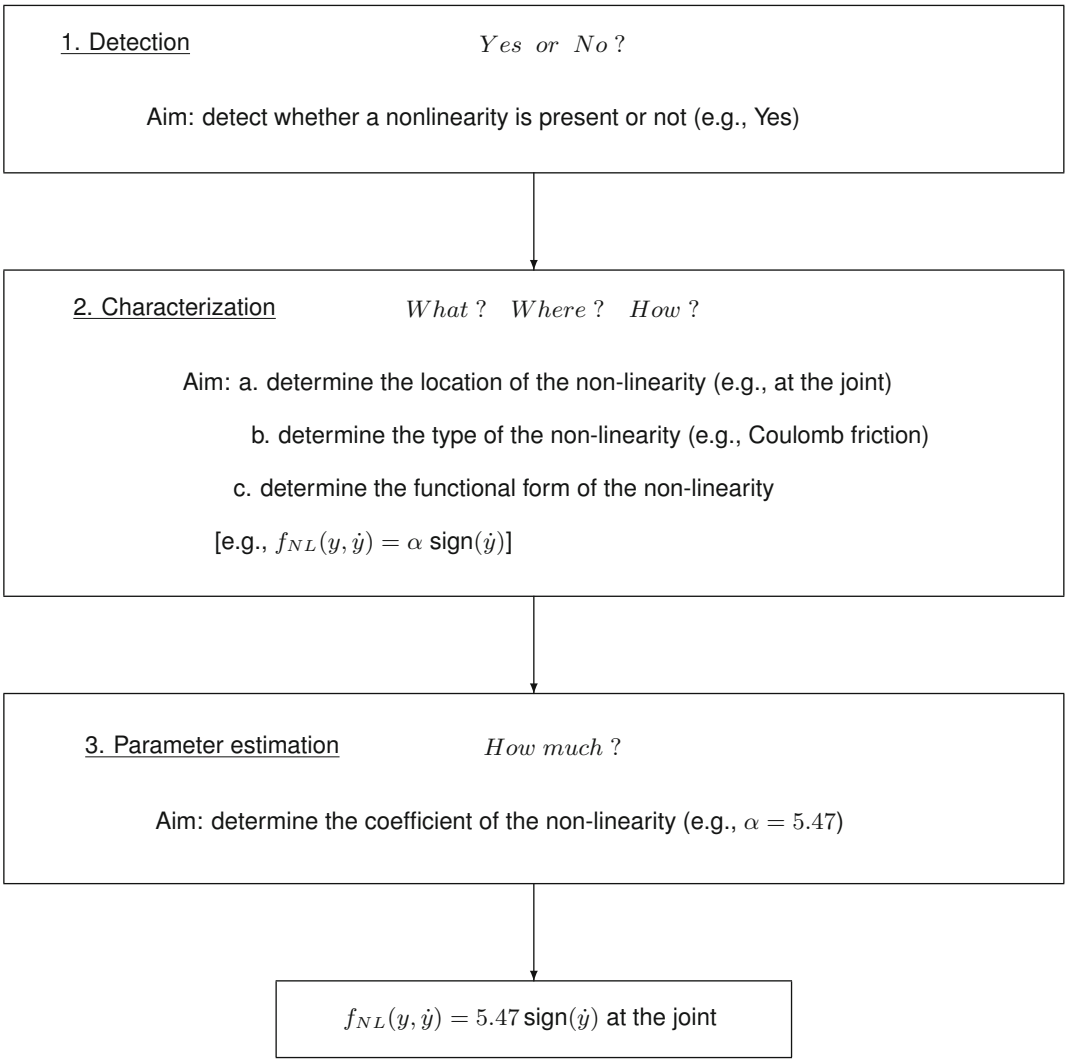

Fig. 17.1 Identification process

References

1. Van Der Auweraer, H.: Testing in the age of virtual prototyping. In: Proceedings of International Conference on Structural Dynamics Modelling, Funchal (2002)
2. Ljung, L.: System Identification - Theory for the User. Prentice-Hall, Englewood Cliffs (1987)
3. Soderstrom, T., Stoica, P.: System Identification. Prentice-Hall, Englewood Cliffs (1989)
4. Ibrahim, S.R., Mikulcik, E.C.: A time domain modal vibration test technique. Shock Vib. Bull. **43**, 21–37 (1973)
5. Juang, J.S., Pappa, R.S.: An eigensystem realization algorithm for modal parameter identification and model reduction. AIAA J. Guid. Control Dyn. **12**, 620–627 (1985)
6. Van Overschee, P., De Moor, B.: Subspace Identification for Linear Systems: Theory, Implementation, Applications. Kluwer Academic Publishers, Dordrecht (1996)
7. Peeters, B., Van Der Auweraer, H., Guillaume, P.: The PolyMAX frequency domain method: a new standard for modal parameter estimation. Shock Vib. **11**, 395–409 (2004)
8. Allemang, R.J., Brown, D.L.: A unified matrix polynomial approach to modal identification. J. Sound Vib. **211**, 301–322 (1998)
9. Allemang, R.J., Phillips, A.W.: The unified matrix polynomial approach to understanding modal parameter estimation: an update. In: Proceedings of the International Seminar on Modal Analysis (ISMA), Leuven (2004)
10. Amabili, M., Paidoussis, M.: Review of studies on geometrically nonlinear vibrations and dynamics of circular cylindrical shells and panels, with and without fluid-structure interaction. Appl. Mech. Rev. **56**, 349–381 (2003)
11. Nayfeh, A.H., Pai, P.F.: Linear and Nonlinear Structural Mechanics. Wiley-Interscience, New York (2004)
12. White, S.W., Kim, S.K., Bajaj, A.K., Davies, P., Showers, D.K., Liedtke, P.E.: Experimental techniques and identification of nonlinear and viscoelastic properties of flexible polyurethane foam. Nonlinear Dyn. **22**, 281–313 (2000)

13. Schultze, J.F., Hemez, F.M., Doebling, S.W., Sohn, H.: Application of non-linear system model updating using feature extraction and parameter effect analysis. Shock Vib. **8**, 325–337 (2001)
14. Singh, R., Davies, P., Bajaj, A.K.: Identification of nonlinear and viscoelastic properties of flexible polyurethane foam. Nonlinear Dyn. **34**, 319–346 (2003)
15. Richards, C.M., Singh, R.: Characterization of rubber isolator nonlinearities in the context of single- and multi-degree-of-freedom experimental systems. J. Sound Vib. **247**, 807–834 (2001)
16. Caughey, T.K., Vijayaraghavan, A.: Free and forced oscillations of a dynamic system with linear hysteretic damping. Int. J. Non-Linear Mech. **5**, 533–555 (1970)
17. Tomlinson, G.R., Hibbert, J.H.: Identification of the dynamic characteristics of a structure with Coulomb friction. J. Sound Vib. **64**, 233–242 (1979)
18. Sherif, H.A., Abu Omar, T.M.: Mechanism of energy dissipation in mechanical system with dry friction. Tribol. Int. **37**, 235–244 (2004)
19. Al-Bender, F., Symens, W., Swevers, J., Van Brussel, H.: Theoretical analysis of the dynamic behavior of hysteresis elements in mechanical systems. Int. J. Non-Linear Mech. **39**, 1721–1735 (2004)
20. Babitsky, V.I., Krupenin, V.L.: Vibrations of Strongly Nonlinear Discontinuous Systems. Springer, Berlin (2001)
21. Rhee, S.H., Tsang, P.H.S., Yen, S.W.: Friction-induced noise and vibrations of disc brakes. Wear **133**, 39–45 (1989)
22. Von Karman, T.: The engineer grapples with nonlinear problems. Bull. Am. Math. Soc. **46**, 615–683 (1940)
23. Nayfeh, A.H., Mook, D.T.: Nonlinear Oscillations. Wiley-Interscience, New York (1979)
24. Strogatz, S.H.: Nonlinear Dynamics and Chaos: With Applications to Physics, Biology, Chemistry, and Engineering. Addison-Wesley, Reading (1994)
25. Verhulst, F.: Nonlinear Differential Equations and Dynamical Systems, 2nd edn. Springer, Berlin (1999)
26. Rand, R.: Lecture Notes on Nonlinear Vibrations, Cornell, Ithaca, NY (2003). Notes freely available at http://tam.cornell.edu/Rand.html.
27. Guckenheimer, J., Holmes, P.: Nonlinear Oscillations, Dynamical Systems and Bifurcation of Vector Fields. Springer, New York (1983)
28. Wiggins, S.: Introduction to Applied Nonlinear Dynamical Systems and Chaos. Springer, New York (1990)
29. Caughey, T.K.: Equivalent linearisation techniques. J. Acoust. Soc. Am. **35**, 1706–1711 (1963)
30. Iwan, W.D.: A generalization of the concept of equivalent linearization. Int. J. Non-Linear Mech. **8**, 279–287 (1973)
31. Rosenberg, R.M.: The normal modes of nonlinear n-degree-of-freedom systems. J. Appl. Mech. **29**, 7–14 (1962)
32. Rosenberg, R.M.: On nonlinear vibrations of systems with many degrees of freedom. Adv. Appl. Mech. **9**, 155–242 (1966)
33. Rand, R.: A direct method for nonlinear normal modes. Int. J. Non-Linear Mech. **9**, 363–368 (1974)
34. Shaw, S.W., Pierre, C.: Normal modes for non-linear vibratory systems. J. Sound Vib. **164**, 85–124 (1993)
35. Vakakis, A.F., Manevitch, L.I., Mikhlin, Y.V., Pilipchuk, V.N., Zevin, A.A.: Normal Modes and Localization in Nonlinear Systems. Wiley, New York (1996)
36. Vakakis, A.F.: Non-linear normal modes and their applications in vibration theory: an overview. Mech. Syst. Signal Process. **11**, 3–22 (1997)
37. Nayfeh, A.H.: Introduction to Perturbation Techniques. Wiley-Interscience, New York (1981)
38. O'Malley, R.E.: Singular Perturbation Methods for Ordinary Differential Equations. Springer, New York (1991)
39. Kevorkian, J., Cole, J.D.: Multiple Scales and Singular Perturbation Methods. Springer, New York (1996)
40. Chan, H.S.Y., Chung, K.W., Xu, Z.: A perturbation-incremental method for strongly non-linear oscillators. Int. J. Non-Linear Mech. **31**, 59–72 (1996)
41. Chen, S.H., Cheung, Y.K.: A modified Lindstedt-Poincaré method for a strongly nonlinear two degree-of-freedom system. J. Sound Vib. **193**, 751–762 (1996)
42. Pilipchuk, V.N.: The calculation of strongly nonlinear systems close to vibration-impact systems. Prikl. Mat. Mech. (PMM) **49**, 572–578 (1985)
43. Manevitch, L.I.: Complex representation of dynamics of coupled oscillators. In: Mathematical Models of Nonlinear Excitations, Transfer Dynamics and Control in Condensed Systems. Kluwer Academic/Plenum Publishers, New York (1999)
44. Qaisi, M.I., Kilani, A.W.: A power-series solution for a strongly non-linear two-degree-of-freedom system. J. Sound Vib. **233**, 489–494 (2000)
45. Rhoads, J.F., Shaw, S.W., Turner, K.L., Baskaran, R.: Tunable MEMS filters that exploit parametric resonance. J. Vib. Acoust. **127**, 423–430 (2005)
46. Vakakis, A.F., Gendelman, O.: Energy pumping in nonlinear mechanical oscillators: part II — resonance capture. J. Appl. Mech. **68**, 42–48 (2001)
47. Vakakis, A.F., McFarland, D.M., Bergman, L.A., Manevitch, L.I., Gendelman, O.: Isolated resonance captures and resonance capture cascades leading to single- or multi-mode passive energy pumping in damped coupled oscillators. J. Vib. Acoust. **126**, 235–244 (2004)
48. Kerschen, G., Lee, Y.S., Vakakis, A.F., McFarland, D.M., Bergman, L.A.: Irreversible passive energy transfer in coupled oscillators with essential nonlinearity. SIAM J. Appl. Math. **66**, 648–679 (2005)
49. Nichols, J.M., Nichols, C.J., Todd, M.D., Seaver, M., Trickey, S.T., Virgin, L.N.: Use of data-driven phase space models in assessing the strength of a bolted connection in a composite beam. Smart Mater. Struct. **13**, 241–250 (2004)
50. Epureanu, B.I., Hashmi, A.: Parameter reconstruction based on sensitivity vector fields. J. Vib. Acoust. **128**, 732–740 (2006)
51. Adams, D.E., Allemang, R.J.: Survey of nonlinear detection and identification techniques for experimental vibrations structural dynamic model through feedback. In: Proceedings of the International Seminar on Modal Analysis (ISMA), Leuven, pp. 269–281 (1998)
52. Worden, K.: Nonlinearity in structural dynamics: the last ten years. In: Proceedings of the European COST F3 Conference on System Identification and Structural Health Monitoring, Madrid, pp. 29–52 (2000)
53. Duffing, G.: Erzwungene Schwingungen bei Veranderlicher Eigenfrequenz (Forced Oscillations in the Presence of Variable Eigenfrequencies). Vieweg, Braunschweig (1918)
54. Roache, P.J.: Verification and Validation in Computational Science and Engineering. Hermosa Publications, Albuquerque (1998)
55. Doebling, S.: Structural dynamics model validation: pushing the envelope. In: Proceedings of International Conference on Structural Dynamics Modelling, Funchal (2002)
56. Schlesinger, S., Crosbie, R.E., Gagne, R.E., Innis, G.S., Lalwani, C.S., Loch, J., Sylvester, R.J., Wright, R.D., Kheir, N., Bartos, D.: Terminology for model credibility. Simulation **32**, 103–104 (1979)

Chapter 18
Higher-Order Frequency Response Functions for Hysteretic Systems

G. Manson and K. Worden

Abstract Volterra analysis for nonlinear systems has long been established as an informative means of investigating nonlinear system behaviour; in particular, the Volterra kernels can be directly transformed into Higher-order Frequency Response Functions (HFRFs) which allow direct visualisation of nonlinear frequency interactions in system responses. Unfortunately, Volterra analysis is restricted to certain (smooth, without memory) classes of systems which exclude many which are of major interest in structural dynamics. In the current paper, it is demonstrated that, by considering non-smooth systems as a combination of smooth systems, it is possible to develop a Volterra series representation for such systems. The paper also presents an approach for rewriting the equation of motion of the Bouc-Wen model of hysteresis so as to remove the hidden state thereby permitting further analysis using the Volterra series.

Keywords Nonlinear systems • Volterra series • Non-smooth systems • Systems with memory • Bouc-Wen hysteresis model

18.1 Introduction

In 1887 Vito Volterra [1] developed the functional representation of the Taylor Series which bears his name. The series extended the standard convolution integral for linear systems to permit characterisation of a range of nonlinear systems. From that date, there has developed a large body of research, across many diverse areas, into systems whose behaviour can be accurately represented using the Volterra series. There are limitations associated with the Volterra series and these are well documented [2, 3]. Alongside the related issues of series convergence and series truncation, there is also the issue regarding the types of nonlinear system which may be represented using the Volterra series. It is usually stated that the Volterra series representation is only valid for those systems that are smooth and have finite memory. This clearly precludes representation of hysteretic systems which are neither smooth nor possess finite memory. The purpose of the current paper is to demonstrate that it may be possible to develop a Volterra series representation of such systems.

The phenomenon of hysteresis or memory-dependency is observed throughout many areas of engineering and science such as liquid–solid phase transitions, elasto-plasticity of materials and superconductivity [4]. In the specific case of the dynamic response of mechanical systems, hysteretic behaviour is often observed due to the dynamic response of elasto-plastic components. There exist many mathematical models for describing hysteretic behaviour but one which is often used in the context of dynamical systems, and the one studied in this work, is the Bouc-Wen model [5, 6].

The layout of the paper is as follows: Sect. 19.2 briefly describes the form of the Bouc-Wen model considered in this work. Section 19.3 demonstrates an approach for removing the hidden, unmeasurable state from the Bouc-Wen model equation of motion. Section 19.4 briefly introduces the Volterra series, before calculating and plotting the Higher-Order Frequency Response Functions (HFRFs) for the Bouc-Wen system. Section 19.5 discusses how these HFRFs may be employed in the calculation of hysteretic system responses and for parameter identification purposes. Section 19.6 rounds off with some conclusions.

G. Manson (✉) • K. Worden
Dynamics Research Group, Department of Mechanical Engineering, University of Sheffield, Mappin Street, Sheffield S1 3JD, UK
e-mail: graeme.manson@sheffield.ac.uk

G. Kerschen (ed.), *Nonlinear Dynamics, Volume 1*, Conference Proceedings of the Society for Experimental Mechanics Series,
DOI 10.1007/978-3-319-29739-2_18

18.2 Bouc-Wen Model of Hysteresis

The response of hysteretic systems lag behind the inputs and these systems are often described as having 'memory'. One of the most-commonly used mathematical models for describing hysteretic behaviour is the general Bouc-Wen model [5, 6]. The model considers a single-degree-of-freedom (SDOF) system with a restoring force model which consists of a polynomial non-hysteretic component and a hysteretic component based upon the time histories of the system's velocity and displacement. Mathematically, this may be written:

$$m\ddot{y} + g\left(y, \dot{y}\right) + z\left(y, \dot{y}\right) = x \tag{18.1}$$

where y, $\dot{y}$ and $\ddot{y}$ are the displacement, velocity and acceleration responses, respectively, to an excitation force, x. $g\left(y, \dot{y}\right)$ is the polynomial non-hysteretic component of the restoring force, $z\left(y, \dot{y}\right)$ is the hysteretic component of the restoring force and m is the mass of the system.

In the current work, the non-hysteretic component of the restoring force was assumed to be linear, so that

$$g\left(y, \dot{y}\right) = c\dot{y} + ky \tag{18.2}$$

where c and k are the linear viscous damping and linear stiffness parameters respectively. It is worth stating that this assumption of linearity of the non-hysteretic component is not required for the work that follows: it would be possible to construct expressions for HFRFs of the Bouc-Wen model even if the non-hysteretic component was represented by a polynomial nonlinearity. Wen [6] defined the hysteretic component via a second equation of motion

$$\dot{z} = A\dot{y} - \alpha\left|\dot{y}\right||z|^{n-1}z - \beta\dot{y}|z|^{n} \tag{18.3}$$

The parameters α, β and n will govern the hysteresis loop parameters. It may be observed that the ky term in Eq. (18.2) and the $A\dot{y}$ term in Eq. (18.3) are both linear spring force terms and therefore may be combined (this is not essential for the following analysis to hold however) to give the following system equations:

$$m\ddot{y} + c\dot{y} + z\left(y, \dot{y}\right) = x \tag{18.4}$$

where

$$\dot{z} = A\dot{y} - \alpha\left|\dot{y}\right||z|^{n-1}z - \beta\dot{y}|z|^{n} \tag{18.5}$$

In the next section, the above formulation will be used as the starting point for removal of the unmeasurable, hidden state $z\left(y, \dot{y}\right)$ from the system's equation of motion.

18.3 Removing the Hidden State from the Bouc-Wen Hysteretic Model

The general Bouc-Wen model was introduced in the previous section. Whilst the input force, x, and output displacement, velocity and acceleration, y, $\dot{y}$ and $\ddot{y}$ respectively, will generally be measurable, the hidden state, z, will not be measurable. The presence of this hidden-state in the Bouc-Wen representation can often limit its usefulness. In this section, it will be demonstrated that it is possible to represent the Bouc-Wen formulation without the explicit presence of the hidden state term.

Equation (18.4) may be rewritten as a first-order equation by substituting $\dot{y}$ for v to give:

$$m\dot{v} + cv + z = x \tag{18.6}$$

which allows the representation of the hidden state, z, in terms of the measurable forces and states:

$$z = x - m\dot{v} - cv \tag{18.7}$$

Differentiating Eq. (18.6) with respect to time, substituting in Eq. (18.5) and using the representation of the hidden state given in Eq. (18.7) gives the following Bouc-Wen representation only in terms of measurable states:

$$m\ddot{v} + c\dot{v} + Av - \alpha\,|v|\,\left|x - m\dot{v} - cv\right|^{n-1}\left(x - m\dot{v} - cv\right) - \beta v\left|x - m\dot{v} - cv\right|^{n} = \dot{x} \tag{18.8}$$

The above expression may appear over-complicated, at first glance, but it will be shown in the next section that this process opens up the possibility of calculating Higher-Order Frequency Response Function (HFRF) expressions for the Bouc-Wen model.

18.4 Higher-Order Frequency Response Functions for the Bouc-Wen Hysteretic Model

18.4.1 Volterra Series Representation of Nonlinear Systems

It is well-known that many nonlinear systems or input–output processes $x(t) \rightarrow y(t)$ can be realised as a mapping [1, 7],

$$y(t) = y_1(t) + y_2(t) + y_3(t) + \cdots + y_p(t) + \ldots \tag{18.9}$$

where

$$y_p(t) = \int_{-\infty}^{+\infty} \ldots \int_{-\infty}^{+\infty} d\tau_1 \ldots d\tau_p \;\; h_p\left(\tau_1, \ldots, \tau_p\right) x\left(t - \tau_1\right) \ldots x\left(t - \tau_p\right) \tag{18.10}$$

This is the *Volterra series* and the functions h_p are the *Volterra kernels*. The dual frequency-domain representation is based on the Higher-Order Frequency Response Function (HFRFs) or *Volterra kernel transforms*, $H_p(\omega_1, \ldots, \omega_p)$, which are defined as the multi-dimensional Fourier transforms of the kernels. The dual time-frequency relationships are shown below:

$$H_p\left(\omega_1, \ldots, \omega_p\right) = \int_{-\infty}^{\infty} \ldots \int_{-\infty}^{\infty} d\tau_1 \ldots d\tau_p \; h_n\left(\tau_1, \ldots, \tau_p\right) e^{-i\left(\omega_1\tau_1 + \cdots + \omega_p\tau_p\right)} \tag{18.11}$$

18.4.2 HFRFs for Bouc-Wen Models

The system which will be studied here is the Bouc-Wen representation given in Eq. (18.8). For the time being, it is only possible to develop expressions for HFRFs for Bouc-Wen systems with integer values of n. For the purposes of the current work, this will be conducted for values of $n = 1$ and $n = 2$. If only integer values of n are being considered, it is possible to simplify the Bouc-Wen representation given in Eq. (18.8) to give:

$$m\ddot{v} + c\dot{v} + Av + \gamma v\left(x - m\dot{v} - cv\right)^{n} = \dot{x} \tag{18.12}$$

where $\gamma = \pm\alpha \pm \beta$. The sign before α and β will be dependent upon the value of n and the signs of v and $\left(x - m\dot{v} - cv\right)$.

For the case where $n = 1$, the equation of motion will be

$$m\ddot{v} + c\dot{v} + Av + \gamma v\left(x - m\dot{v} - cv\right) = \dot{x} \tag{18.13}$$

where

$$\gamma = \begin{cases} -\alpha - \beta \text{ if } v \geq 0 \text{ and } \left(x - m\dot{v} - cv\right) \geq 0 \\ -\alpha + \beta \text{ if } v \geq 0 \text{ and } \left(x - m\dot{v} - cv\right) < 0 \\ \alpha - \beta \text{ if } v < 0 \text{ and } \left(x - m\dot{v} - cv\right) \geq 0 \\ \alpha + \beta \text{ if } v < 0 \text{ and } \left(x - m\dot{v} - cv\right) < 0 \end{cases} \tag{18.14}$$

For the case where $n = 2$, the equation of motion will be

$$m\ddot{v} + c\dot{v} + Av + \gamma v\left(x - m\dot{v} - cv\right)^2 = \dot{x} \tag{18.15}$$

where

$$\gamma = \begin{cases} -\alpha - \beta \text{ if } v \geq 0 \text{ and } \left(x - m\dot{v} - cv\right) \geq 0 \\ \alpha - \beta \text{ if } v \geq 0 \text{ and } \left(x - m\dot{v} - cv\right) < 0 \\ \alpha - \beta \text{ if } v < 0 \text{ and } \left(x - m\dot{v} - cv\right) \geq 0 \\ -\alpha - \beta \text{ if } v < 0 \text{ and } \left(x - m\dot{v} - cv\right) < 0 \end{cases} \tag{18.16}$$

The above essentially means that, for the $n = 1$ case, there can be up to four different forms for each $H_p(\omega_1, \ldots, \omega_p)$, depending upon the signs of v and $\left(x - m\dot{v} - cv\right)$, whilst there can be two different forms for each $H_p(\omega_1, \ldots, \omega_p)$ for the $n = 2$ case, depending upon the signs of v and $\left(x - m\dot{v} - cv\right)$. This means that, in order to obtain predicted responses from the Volterra series approximation, it will be necessary to switch between the different HFRF forms depending upon the signs of v and $\left(x - m\dot{v} - cv\right)$. This will be discussed in more detail at the end of the paper.

For now, the HFRF expressions, up to and including $H_3(\omega_1, \omega_2, \omega_3)$, for these two values of n will now be calculated. When the equations of motion are available, the method of harmonic probing [8] is both simple and effective and is the method applied here. In order to calculate the linear FRF, $H_1(\omega)$, a probing input of a single harmonic is applied:

$$x_{p_1} = \mathrm{e}^{i\omega t} \tag{18.17}$$

The expression required for the right-hand side of Eqs. (18.13) and (18.15) is the first derivative which gives a probing expression of:

$$\dot{x}_{p_1} = i\omega \mathrm{e}^{i\omega t} \tag{18.18}$$

Assuming that v is the output response to the input, x, gives the following first-order probing expressions for v, $\dot{v}$ and $\ddot{v}$:

$$\begin{aligned} v_{p_1} &= H_1(\omega)\, \mathrm{e}^{i\omega t} \\ \dot{v}_{p_1} &= i\omega H_1(\omega)\, \mathrm{e}^{i\omega t} \\ \ddot{v}_{p_1} &= -\omega^2 H_1(\omega)\, \mathrm{e}^{i\omega t} \end{aligned} \tag{18.19}$$

Note, the reason that a first-order probing expression is not required for $\left(x - m\dot{v} - cv\right)$ is because it would always be multiplied by v in Eqs. (18.13) and (18.15) and would therefore be unable to produce an $\mathrm{e}^{i\omega t}$ term which is required to contribute to an expression for $H_1(\omega)$.

Substituting the expressions in Eqs. (18.18) and (18.19) into either Eq. (18.13) or (18.15) and equating $\mathrm{e}^{i\omega t}$ terms gives the same expression for $H_1(\omega)$, namely:

$$H_1(\omega) = \frac{i\omega}{-m\omega^2 + i\omega c + A} \tag{18.20}$$

which is simply the linear mobility FRF for a SDOF system relating the linear component of the velocity output ($v = \dot{y}$) to the input force, x.

The process for obtaining $H_2(\omega_1, \omega_2)$ is similar but the probing expressions are a little more involved. A dual harmonic probing input is applied:

$$\begin{aligned} x_{p_2} &= \mathrm{e}^{i\omega_1 t} + \mathrm{e}^{i\omega_2 t} \\ \dot{x}_{p_2} &= i\omega_1 \mathrm{e}^{i\omega_1 t} + i\omega_2 \mathrm{e}^{i\omega_2 t} \end{aligned} \tag{18.21}$$

The second-order probing expressions for v, $\dot{v}$ and $\ddot{v}$ are:

$$\begin{aligned} v_{p_2} &= H_1(\omega_1)\, \mathrm{e}^{i\omega_1 t} + H_1(\omega_2)\, \mathrm{e}^{i\omega_2 t} + 2H_2(\omega_1, \omega_2)\, \mathrm{e}^{i(\omega_1+\omega_2)t} \\ \dot{v}_{p_2} &= i\omega_1 H_1(\omega_1)\, \mathrm{e}^{i\omega_1 t} + i\omega_2 H_1(\omega_2)\, \mathrm{e}^{i\omega_2 t} + 2i(\omega_1 + \omega_2) H_2(\omega_1, \omega_2)\, \mathrm{e}^{i(\omega_1+\omega_2)t} \\ \ddot{v}_{p_2} &= -\omega_1^2 H_1(\omega_1)\, \mathrm{e}^{i\omega_1 t} - \omega_2^2 H_1(\omega_2)\, \mathrm{e}^{i\omega_2 t} - 2(\omega_1 + \omega_2)^2 H_2(\omega_1, \omega_2)\, \mathrm{e}^{i(\omega_1+\omega_2)t} \end{aligned} \tag{18.22}$$

On this occasion, it will be necessary to produce a second-order probing expression for $\left(x - m\dot{v} - cv\right)$. This is given by:

$$\begin{aligned}\left(x_{p_2} - m\dot{v}_{p_2} - cv_{p_2}\right) = &\left(1 - i\omega_1 mH_1\left(\omega_1\right) - cH_1\left(\omega_1\right)\right)\mathrm{e}^{i\omega_1 t} + \left(1 - i\omega_2 mH_1\left(\omega_2\right) - cH_1\left(\omega_2\right)\right)\mathrm{e}^{i\omega_2 t} \\ &+2\left(-i\left(\omega_1 + \omega_2\right)m - c\right)H_2\left(\omega_1, \omega_2\right)\mathrm{e}^{i(\omega_1+\omega_2)t}\end{aligned} \tag{18.23}$$

Substituting the expressions in Eqs. (18.21), (18.22) and (18.23) into Eq. (18.13) and equating $\mathrm{e}^{i(\omega_1+\omega_2)t}$ terms gives the following expression for $H_2(\omega_1, \omega_2)$ for the $n = 1$ case:

$$\begin{aligned}H_2\left(\omega_1, \omega_2\right) &= \frac{-\gamma\{H_1(\omega_1)[1-i\omega_2 mH_1(\omega_2)-cH_1(\omega_2)]+H_1(\omega_2)[1-i\omega_1 mH_1(\omega_1)-cH_1(\omega_1)]\}}{2\left[-m(\omega_1+\omega_2)^2+i(\omega_1+\omega_2)c+A\right]} \\ &= \frac{-\gamma H_1(\omega_1+\omega_2)\{H_1(\omega_1)[1-i\omega_2 mH_1(\omega_2)-cH_1(\omega_2)]+H_1(\omega_2)[1-i\omega_1 mH_1(\omega_1)-cH_1(\omega_1)]\}}{2i(\omega_1+\omega_2)}\end{aligned} \tag{18.24}$$

It is often the case (e.g. when the input force is sinusoidal) that the diagonals of the HFRFs are the components of interest. For the $n = 1$ case, $H_2(\omega, \omega)$ is given by:

$$H_2\left(\omega, \omega\right) = \frac{-\gamma H_1\left(2\omega\right)H_1\left(\omega\right)\left[1 - i\omega mH_1\left(\omega\right) - cH_1\left(\omega\right)\right]}{2i\omega} \tag{18.25}$$

It may observed however that setting $\omega_1 = \omega$ and $\omega_2 = -\omega$ in Eq. (18.24) results in both the denominator and numerator being zero. In the current case, the HFRFs relate the velocity output, which cannot contain a D.C. component, to the forcing input and therefore the diagonal $H_2\left(\omega, -\omega\right)$, which is concerned with the zero frequency (D.C.) component, must be zero for all ω:

$$H_2\left(\omega, -\omega\right) = 0 \tag{18.26}$$

Substituting the expressions in Eqs. (18.21), (18.22) and (18.23) into Eq. (18.15) and equating $\mathrm{e}^{i(\omega_1+\omega_2)t}$ terms gives the following expression for $H_2(\omega_1, \omega_2)$ for the $n = 2$ case:

$$H_2\left(\omega_1, \omega_2\right) = 0 \tag{18.27}$$

The above results from the fact the $\gamma v\left(x - m\dot{v} - cv\right)^2$ term is unable to produce any $\mathrm{e}^{i(\omega_1+\omega_2)t}$ terms. The first non-zero HFRF for the $n = 2$ Bouc-Wen system will be $H_3(\omega_1, \omega_2, \omega_3)$.

In order to obtain expressions for $H_3(\omega_1, \omega_2, \omega_3)$ for the two Bouc-Wen cases, the harmonic probing is extended to a three harmonic input:

$$\begin{aligned}x_{p_3} &= \mathrm{e}^{i\omega_1 t} + \mathrm{e}^{i\omega_2 t} + \mathrm{e}^{i\omega_3 t} \\ \dot{x}_{p_3} &= i\omega_1\mathrm{e}^{i\omega_1 t} + i\omega_2\mathrm{e}^{i\omega_2 t} + i\omega_3\mathrm{e}^{i\omega_3 t}\end{aligned} \tag{18.28}$$

The third-order probing expression for v is:

$$\begin{aligned}v_{p_3} = &H_1\left(\omega_1\right)\mathrm{e}^{i\omega_1 t} + H_1\left(\omega_2\right)\mathrm{e}^{i\omega_2 t} + H_1\left(\omega_3\right)\mathrm{e}^{i\omega_3 t} + 2H_2\left(\omega_1, \omega_2\right)\mathrm{e}^{i(\omega_1+\omega_2)t} \\ &+2H_2\left(\omega_1, \omega_3\right)\mathrm{e}^{i(\omega_1+\omega_3)t} + 2H_2\left(\omega_2, \omega_3\right)\mathrm{e}^{i(\omega_1+\omega_2)t} + 6H_3\left(\omega_1, \omega_2, \omega_3\right)\mathrm{e}^{i(\omega_1+\omega_2+\omega_3)t}\end{aligned} \tag{18.29}$$

with the third-order probing expressions for $\dot{v}$ and $\ddot{v}$ simply being the first and second derivatives with respect to time of the above expression. The third-order probing expression for $\left(x - m\dot{v} - cv\right)$ is given by:

$$\begin{aligned}\left(x_{p_3} - m\dot{v}_{p_3} - cv_{p_3}\right) = &\left(1 - i\omega_1 mH_1\left(\omega_1\right) - cH_1\left(\omega_1\right)\right)\mathrm{e}^{i\omega_1 t} + \left(1 - i\omega_2 mH_1\left(\omega_2\right) - cH_1\left(\omega_2\right)\right)\mathrm{e}^{i\omega_2 t} \\ &+\left(1 - i\omega_3 mH_1\left(\omega_3\right) - cH_1\left(\omega_3\right)\right)\mathrm{e}^{i\omega_3 t} + 2\left(-i\left(\omega_1 + \omega_2\right)m - c\right)H_2\left(\omega_1, \omega_2\right)\mathrm{e}^{i(\omega_1+\omega_2)t} \\ &+2\left(-i\left(\omega_1 + \omega_3\right)m - c\right)H_2\left(\omega_1, \omega_3\right)\mathrm{e}^{i(\omega_1+\omega_3)t} + 2\left(-i\left(\omega_2 + \omega_3\right)m - c\right)H_2\left(\omega_2, \omega_3\right)\mathrm{e}^{i(\omega_2+\omega_3)t} \\ &+6\left(-i\left(\omega_1 + \omega_2 + \omega_3\right)m - c\right)H_3\left(\omega_1, \omega_2, \omega_3\right)\mathrm{e}^{i(\omega_1+\omega_2+\omega_3)t}\end{aligned} \tag{18.30}$$

Substituting the expressions in Eqs. (18.28), (18.29) and (18.30) Eq. (18.13) and equating $e^{i(\omega_1+\omega_2+\omega_3)t}$ terms gives the following expression for $H_3(\omega_1, \omega_2, \omega_3)$ for the $n = 1$ case:

$$H_3(\omega_1, \omega_2, \omega_3) = \frac{-\gamma H_1(\omega_1 + \omega_2 + \omega_3) B}{6i(\omega_1 + \omega_2 + \omega_3)} \tag{18.31}$$

where B is given by:

$$\begin{aligned} B = {} & 2H_1(\omega_1) H_2(\omega_2, \omega_3) [-i(\omega_2 + \omega_3) m - c] + 2H_1(\omega_2) H_2(\omega_1, \omega_3) [-i(\omega_1 + \omega_3) m - c] \\ & + 2H_1(\omega_3) H_2(\omega_1, \omega_2) [-i(\omega_1 + \omega_2) m - c] + 2H_2(\omega_1, \omega_2) [1 - i\omega_3 m H_1(\omega_3) - cH_1(\omega_3)] \\ & + 2H_2(\omega_1, \omega_3) [1 - i\omega_2 m H_1(\omega_2) - cH_1(\omega_2)] + 2H_2(\omega_2, \omega_3) [1 - i\omega_1 m H_1(\omega_1) - cH_1(\omega_1)] \end{aligned} \tag{18.32}$$

Similarly, substituting the expressions in Eqs. (18.28), (18.29) and (18.30) Eq. (18.15) and equating $e^{i(\omega_1+\omega_2+\omega_3)t}$ terms gives the following expression for $H_3(\omega_1, \omega_2, \omega_3)$ for the $n = 2$ case:

$$H_3(\omega_1, \omega_2, \omega_3) = \frac{-\gamma H_1(\omega_1 + \omega_2 + \omega_3) C}{6i(\omega_1 + \omega_2 + \omega_3)} \tag{18.33}$$

where C is given by:

$$\begin{aligned} C = {} & 2H_1(\omega_1) [1 - i\omega_2 m H_1(\omega_2) - cH_1(\omega_2)] [1 - i\omega_3 m H_1(\omega_3) - cH_1(\omega_3)] \\ & + 2H_1(\omega_2) [1 - i\omega_1 m H_1(\omega_1) - cH_1(\omega_1)] [1 - i\omega_3 m H_1(\omega_3) - cH_1(\omega_3)] \\ & + 2H_1(\omega_3) [1 - i\omega_1 m H_1(\omega_1) - cH_1(\omega_1)] [1 - i\omega_2 m H_1(\omega_2) - cH_1(\omega_2)] \end{aligned} \tag{18.34}$$

The diagonals of $H_3(\omega_1, \omega_2, \omega_3)$ are a little more concise than the above general expressions. For the $n = 1$ case, $H_3(\omega, \omega, \omega)$ is given by:

$$H_3(\omega, \omega, \omega) = \frac{-\gamma H_1(3\omega) \{H_1(\omega) H_2(\omega, \omega) [-i2\omega m - c] + H_2(\omega, \omega) [1 - i\omega m H_1(\omega) - cH_1(\omega)]\}}{3i\omega} \tag{18.35}$$

which may be rewritten solely in terms of the linear FRF and the nonlinear parameters by substituting Eq. (18.25) for $H_2(\omega, \omega)$ in the previous expression to give:

$$H_3(\omega, \omega, \omega) = \frac{\gamma^2 H_1(3\omega) H_1(2\omega) H_1(\omega) [1 - i\omega m H_1(\omega) - cH_1(\omega)] [1 - i3\omega m H_1(\omega) - 2cH_1(\omega)]}{-6\omega^2} \tag{18.36}$$

The $H_3(\omega, \omega, -\omega)$ diagonal for the $n = 1$ case is given by:

$$\begin{aligned} H_3(\omega, \omega, -\omega) &= \tfrac{-\gamma H_1(\omega) H_2(\omega, \omega) [1 - i\omega m H_1(-\omega) - 2cH_1(-\omega)]}{3i\omega} \\ &= \frac{\gamma^2 H_1(\omega)^2 H_1(2\omega) [1 - i\omega m H_1(\omega) - cH_1(\omega)] [1 - i\omega m H_1(-\omega) - 2cH_1(-\omega)]}{-6\omega^2} \end{aligned} \tag{18.37}$$

The occurrence of the γ^2 term in Eqs. (18.36) and (18.37) means that, for the $n = 1$ case, only two forms of $H_3(\omega, \omega, \omega)$ and $H_3(\omega, \omega, -\omega)$ exist, unlike the four forms of $H_2(\omega, \omega)$ which existed for the $n = 1$ case.

For the $n = 2$ case, $H_3(\omega, \omega, \omega)$ is given by:

$$H_3(\omega, \omega, \omega) = \frac{-\gamma H_1(3\omega) H_1(\omega) [1 - i\omega m H_1(\omega) - cH_1(\omega)]^2}{i3\omega} \tag{18.38}$$

and the $H_3(\omega, \omega, -\omega)$ diagonal for the $n = 2$ case is given by:

$$\begin{aligned} & H_3(\omega, \omega, -\omega) \\ & = \frac{-\gamma H_1(\omega) [1 - i\omega m H_1(\omega) - cH_1(\omega)] \{2H_1(\omega) + H_1(-\omega) + H_1(\omega) H_1(-\omega) [i\omega m - 3c]\}}{3i\omega} \end{aligned} \tag{18.39}$$

18.4.3 Example Bouc-Wen HFRFs

In order to visualise some of the HFRF surfaces and diagonals whose expressions were developed in the previous sub-section, an example will be considered. The Bouc-Wen expression under consideration is given by Eqs. (18.4) and (18.5) and the following parameters were chosen for both cases i.e. when $n = 1$ or $n = 2$:

$$m = 1\ \text{kg},\ c = 20\ \text{N/ (m/s)}\,,\ A = 1 \times 10^4\ \text{N/m},\ \alpha = 20,\ \beta = 5$$

Inserting these parameters into Eq. (18.20) gives the mobility FRF for the underlying linear system which is shown in Fig. 18.1. As $H_1(\omega)$ only depends upon the linear parameters, it will be the same for both the $n = 1$ and $n = 2$ cases.

As stated above, the $H_2(\omega_1, \omega_2)$ FRF is zero for the $n = 2$ case but will be non-zero for the $n = 1$ case. Figure 18.2 shows contour representations, calculated using Eq. (18.24), of the amplitude and phase of the $H_2(\omega_1, \omega_2)$ surface for the situation where $\gamma = (-\alpha - \beta)$. This was the required form of the HFRF when $v \geq 0$ and $\left(x - m\dot{v} - cv\right) \geq 0$. The three other $H_2(\omega_1, \omega_2)$ forms (given using the three other γ values given in Eq. (18.14)) would be required but these would simply be scaled versions of that shown in Fig. 18.2.

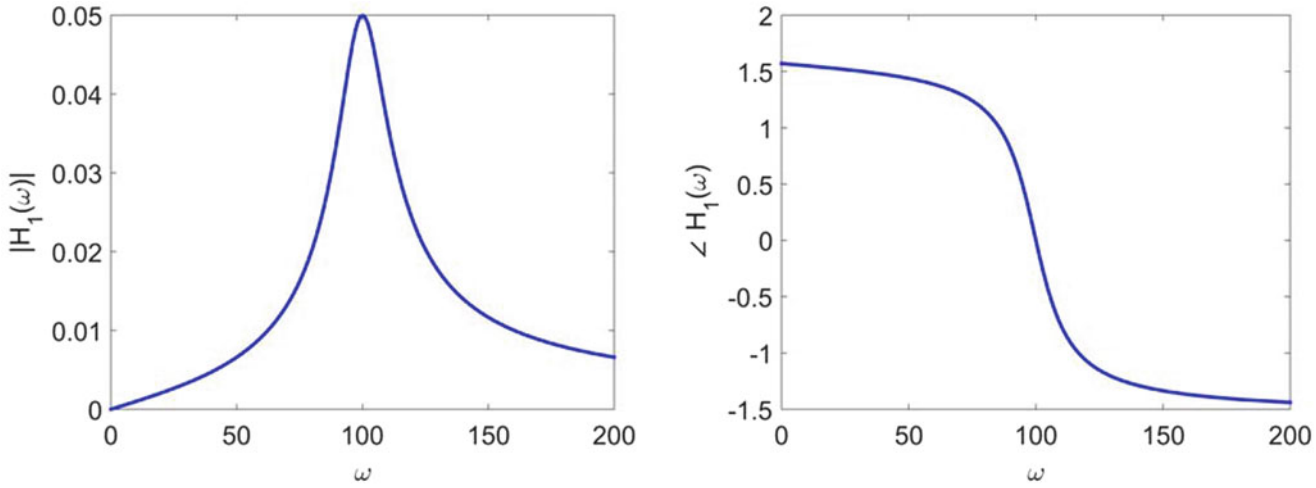

Fig. 18.1 Amplitude (*left*) and phase (*right*) of $H_1(\omega)$ for both the $n = 1$ and $n = 2$ cases

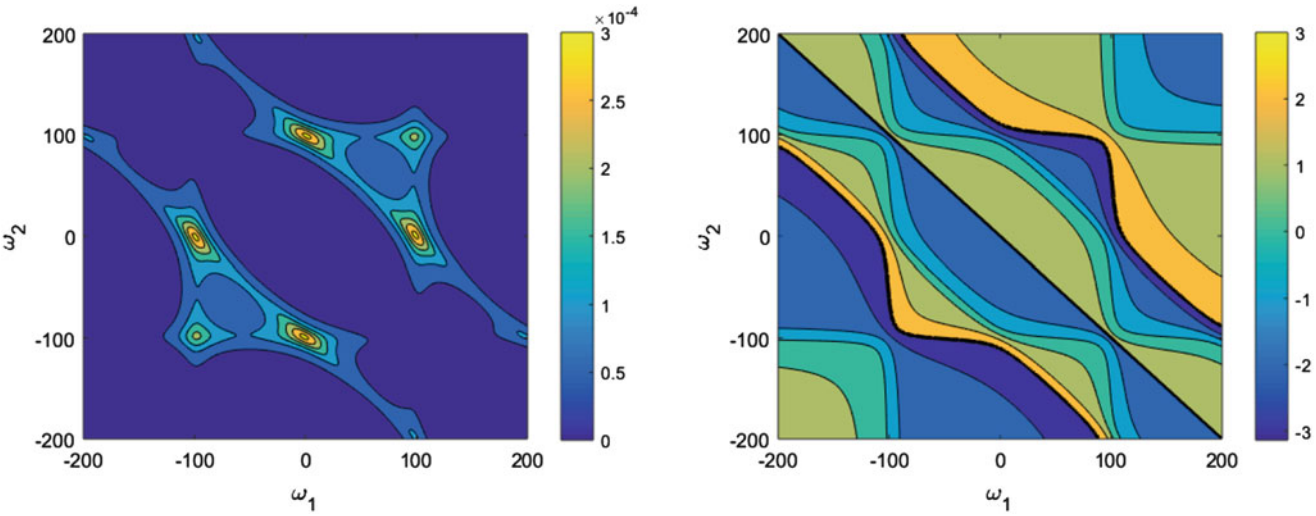

Fig. 18.2 Amplitude (*left*) and phase (*right*) of one of the four $H_2(\omega_1, \omega_2)$ HFRFs for the $n = 1$ case. The example shown is for $\gamma = (-\alpha - \beta)$ i.e. when $v \geq 0$ and $\left(x - m\dot{v} - cv\right) \geq 0$

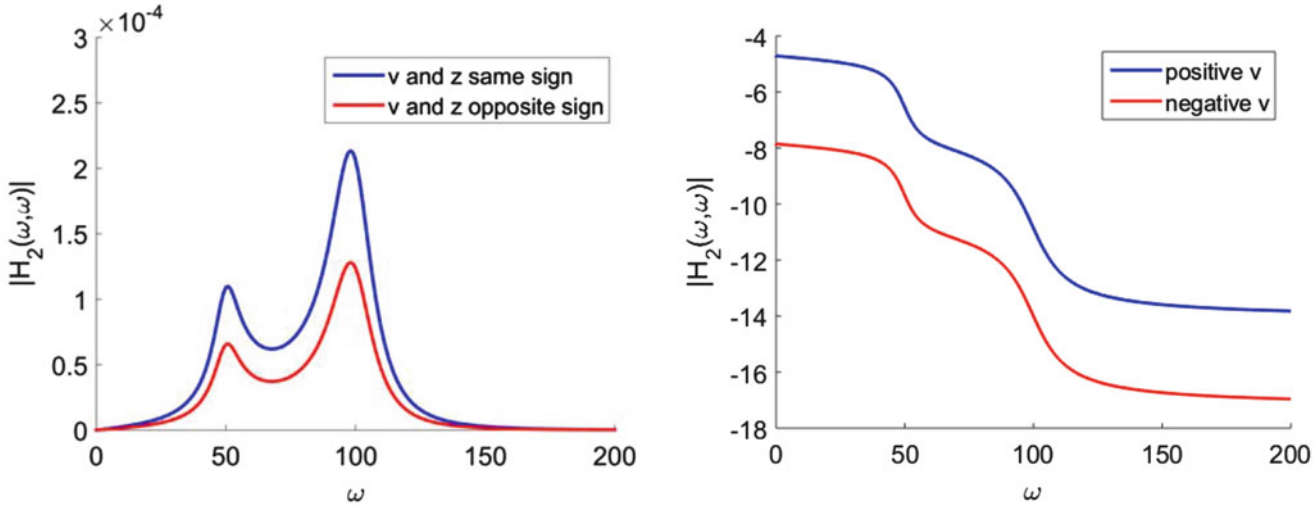

Fig. 18.3 Amplitude (*left*) and phase (*right*) of the $H_2(\omega, \omega)$ diagonals for the $n = 1$ case

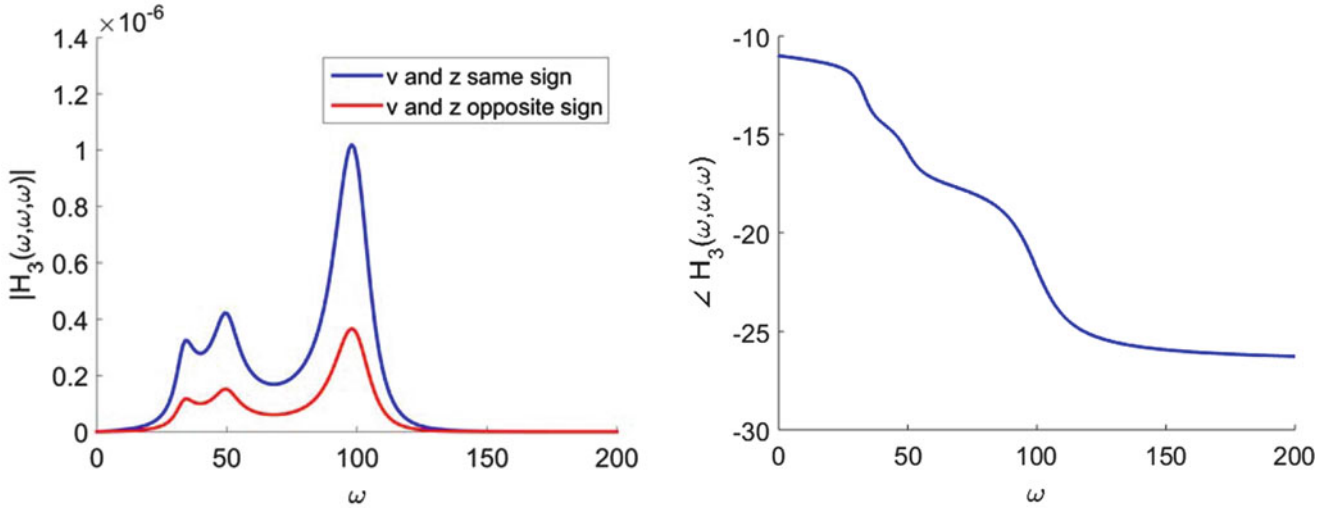

Fig. 18.4 Amplitude (*left*) and phase (*right*) of the $H_3(\omega, \omega, \omega)$ diagonals for the $n = 1$ case

The principal diagonals of all four of the $H_2(\omega, \omega)$ forms are plotted together in Fig. 18.3. Whilst it may initially appear that only two plots are depicted, there are four cases shown but there are simply two different amplitude plots (the $\gamma = (-\alpha - \beta)$ diagonal will overlay the $\gamma = (\alpha + \beta)$ diagonal and the $\gamma = (-\alpha + \beta)$ diagonal will overlay the $\gamma = (\alpha - \beta)$ diagonal). Similarly there are only two different phase plots (the $\gamma = (-\alpha - \beta)$ diagonal will overlay the $\gamma = (-\alpha + \beta)$ diagonal and the $\gamma = (\alpha + \beta)$ diagonal will overlay the $\gamma = (\alpha - \beta)$ diagonal). Examination of these plots shows that there are peaks at the undamped natural frequency of the underlying linear system and one-half of this value. This is typical of the behaviour observed in systems with a quadratic nonlinearity component. Note that phase plot was plotted using MATLAB's *unwrap* function to highlight the constant difference of π radians between the two lines.

As demonstrated in the previous sub-section, for both the $n = 1$ and $n = 2$ cases, the $H_3(\omega_1, \omega_2, \omega_3)$ FRF will be non-zero. It is not possible to plot the full amplitude and phase $H_3(\omega_1, \omega_2, \omega_3)$ surfaces, due to them being four-dimensional and so only the diagonals of the surfaces will be considered here. Figures 18.4 and 18.5 show the $H_3(\omega, \omega, \omega)$ and $H_3(\omega, \omega, -\omega)$ diagonals for the $n = 1$ case. As stated above (after Eq. (18.37)) the occurrence of γ^2 in the expression means that only two different forms of the $H_3(\omega_1, \omega_2, \omega_3)$ FRF exists for the $n = 1$ case. Examination of Figs. 18.4 and 18.5 show that this difference only occurs in the relative amplitudes in the amplitude plot. Figure 18.4 shows that there are peaks at the undamped natural frequency of the underlying linear system and one-half and one-third of this value. Figure 18.5 only shows peaks at the undamped natural frequency of the underlying linear system and one-half of this value. Both of these observations are in keeping with expected third-order FRF behaviour observed in systems with a quadratic nonlinearity component.

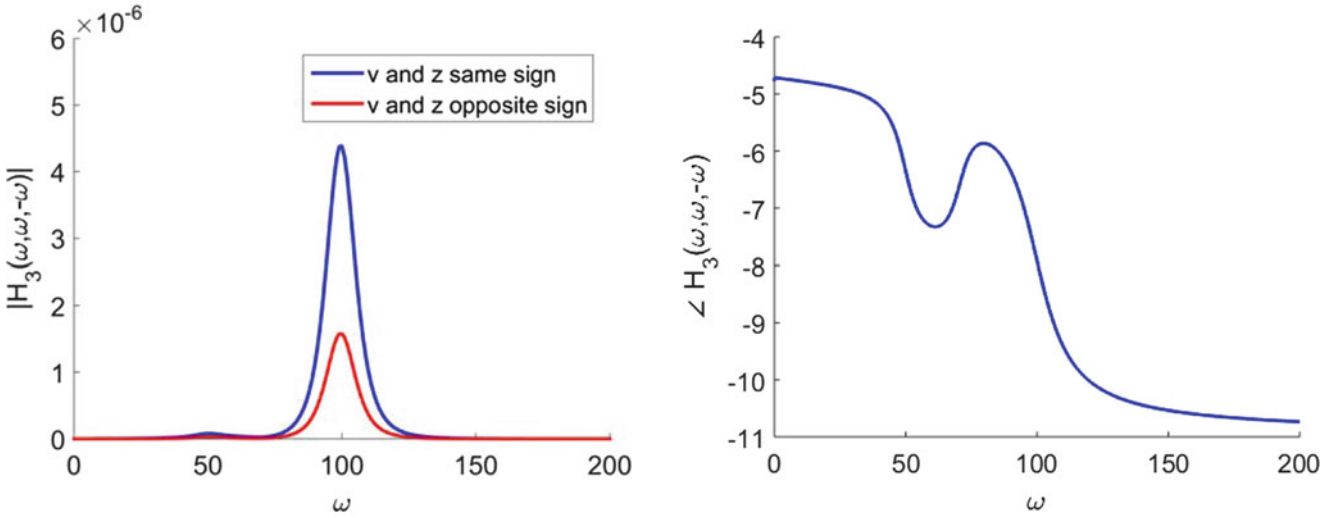

Fig. 18.5 Amplitude (*left*) and phase (*right*) of the $H_3(\omega, \omega, -\omega)$ diagonals for the $n = 1$ case

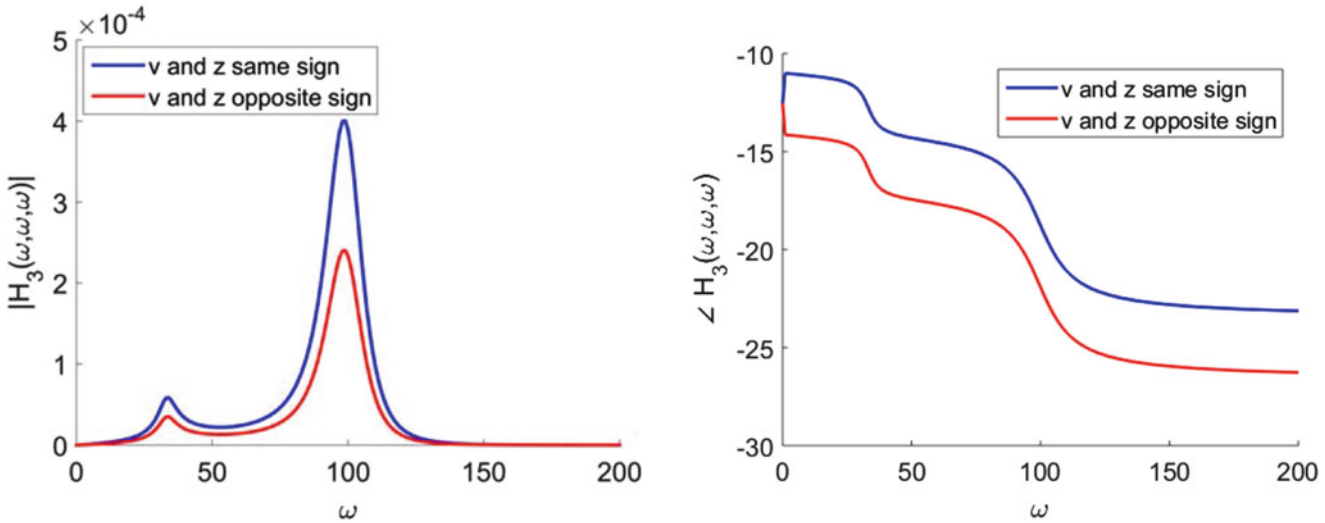

Fig. 18.6 Amplitude (*left*) and phase (*right*) of the $H_3(\omega, \omega, \omega)$ diagonals for the $n = 2$ case

Figures 18.6 and 18.7 show the $H_3(\omega, \omega, \omega)$ and $H_3(\omega, \omega, -\omega)$ diagonals for the $n = 2$ case. For both diagonals, two distinct HFRF forms may be seen (in both amplitude and phase). Figure 18.6 shows that there are peaks at the undamped natural frequency of the underlying linear system and one-third of this value whilst Fig. 18.7 only shows a single peak at the undamped natural frequency of the underlying linear system. This is in keeping with the $H_3(\omega_1, \omega_2, \omega_3)$ behaviour which is observed in systems with a cubic nonlinearity but no quadratic component.

18.5 Switching Between Higher-Order Frequency Response Functions for Non-Smooth Systems or Systems with Memory

In the previous section, expressions were developed for the first three HFRFs for two Bouc-Wen models along with figures displaying the nature of these HFRFs for a numerical example. Whilst it is novel to show that it is possible to develop HFRF expressions for non-smooth systems (especially those with hidden states), it is reasonable to ask how these different forms of the HFRFs may be used in the prediction of the response of such systems.

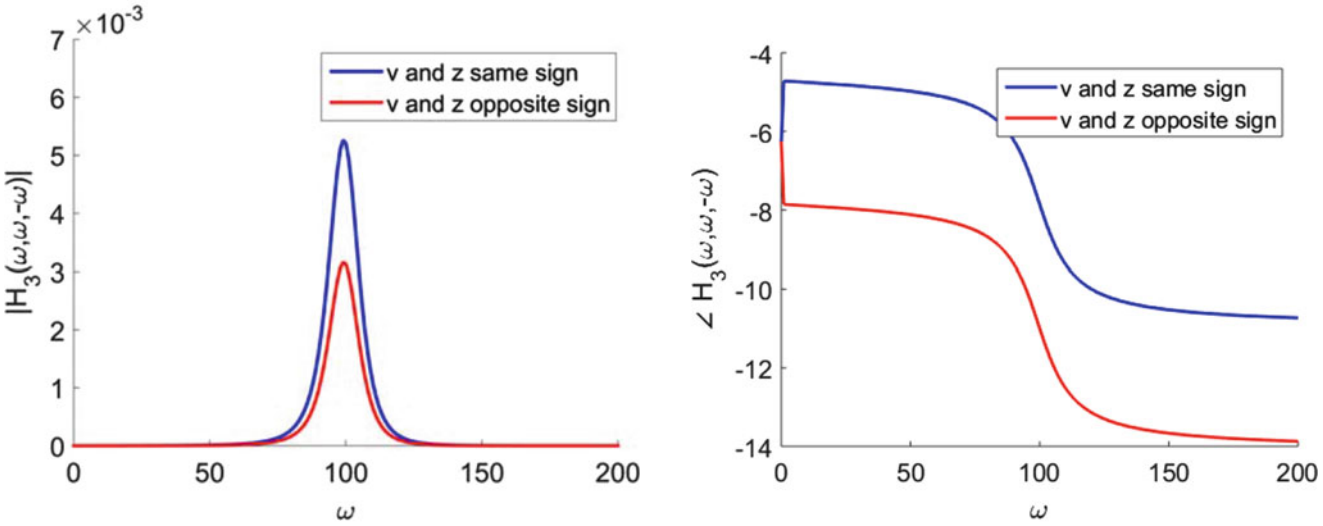

Fig. 18.7 Amplitude (*left*) and phase (*right*) of the $H_3(\omega, \omega, -\omega)$ diagonals for the $n = 2$ case

Consider the case where a cosinusoidal forcing input is being applied to a smooth system with finite memory. The forcing input will be given by:

$$x(t) = X\cos(\Omega t) \tag{18.40}$$

and the Volterra series representation of the steady-state displacement response of the system would be given by:

$$\begin{aligned} y(t) &= y_1(t) + y_2(t) + y_3(t) + \ldots \\ &= X\,|H_1(\Omega)|\cos(\Omega t + \angle H_1(\Omega)) \\ &\quad + \tfrac{X^2}{2}\{|H_2(\Omega,\Omega)|\cos(2\Omega t + \angle H_2(\Omega,\Omega)) + H_2(\Omega,-\Omega)\} \\ &\quad + \tfrac{X^3}{4}\{|H_3(\Omega,\Omega,\Omega)|\cos(3\Omega t + \angle H_3(\Omega,\Omega,\Omega)) \\ &\quad + 3\,|H_3(\Omega,\Omega,-\Omega)|\cos(\Omega t + \angle H_3(\Omega,\Omega,-\Omega))\} + \ldots \end{aligned} \tag{18.41}$$

If, however, the system of interest were one of the two Bouc-Wen models discussed in the previous section, the calculation of the system response would not be quite so straightforward. As discussed previously, with the non-smooth system there is no longer only a single form of each of the HFRFs but rather multiple forms which depend upon the signs of the measured forces and states. One cannot simply calculate a steady-state response of the type given in Eq. (18.41) for each of the different sign combinations and switch between the different responses depending upon the signs of the measured forces and states. Each switch will introduce a transient response which will also have to be calculated: this will be the next stage of this work.

It is anticipated that, if it is possible to estimate these different HFRF forms from simulated or experimental data, it may also be possible to identify the linear and nonlinear system parameters.

18.6 Discussion and Conclusions

There were two new findings presented in the current paper. The first was that it is possible to re-formulate the equation of motion of a well-studied system with a hidden, unmeasurable state so that it was only written in terms of its measurable forces and states. It is expected that there are many other systems with hidden states which may be amenable to a similar treatment. The second finding directly followed from the first and demonstrated that it is possible to calculate HFRFs for non-smooth systems with memory. The first three HFRFs for a pair of Bouc-Wen models were calculated and plotted for a numerical example. As mentioned above, the next phase of this work will be to ascertain whether "switching" between the different forms of the HFRFs, in combination with a transient response calculation, is capable of representing the actual response behaviour of the Bouc-Wen model. To the authors' knowledge, this would be the first Volterra series representation of a non-smooth system with memory.

References

1. Volterra, V.: Theory of Functionals and Integral equations. Dover Publications, New York (1959)
2. Palm, G., Poggio, T.: The Volterra representation and the Wiener expansion: validity and pitfalls. SIAM J. Appl. Math. **33**(2), 195–216 (1977)
3. Rugh, W.J.: Nonlinear System Theory. The Volterra/Wiener Approach. John Hopkins University Press (1981)
4. Visitin, A.: Differential Models of Hysteresis. Springer, Berlin (1994)
5. Bouc, R.: Forced vibration of mechanical systems with hysteresis. In: Proc. of 4th Conference on Nonlinear Oscillations, Prague, Czechoslovakia, 1967
6. Wen, Y.: Method for random vibration of hysteretic systems. ASCE J. Eng. Mech. Div. 249–263 (1976)
7. Schetzen, M.: The Volterra and Wiener Theories of Nonlinear Systems. John Wiley Interscience Publication, New York (1980)
8. Bedrosian, E., Rice, S.O.: The output properties of Volterra systems driven by harmonic and Gaussian inputs. Proc. IEEE **59**, 1688–1707 (1971)

Chapter 19
Model Upgrading T0 Augment Linear Model Capabilities into Nonlinear Regions

S.B. Cooper, A. delli Carri, and D. Di Maio

Abstract Identification of nonlinear dynamical systems have enjoyed significant progression over the past few years with the outcome of various developed identification methods, however there is still no generalised method applicable to structures with arbitrary nonlinearity. In the analysis of nonlinear dynamical system, it is essential to establish accurate and reliable tools that are capable of estimating the parameters from measured data for both the linear and nonlinear system. This paper presents a modular framework approach for upgrading a valid linear finite element structural model to accommodate any nonlinearities present in a system. To validate the efficiency of the proposed method, numerical and experimental studies are conducted on a "Multiple Beam Test Structure", the method uses an iterative process to upgrade the nonlinear terms in the system. The results are verified by comparing predicted new response with measured data.

Keywords Nonlinearities • Model upgrading • Finite element • Structural models and framework

19.1 Introduction

Nonlinear system identification has received a lot of attention over the last few years up till date with examples such as continuous structures with localised geometrical nonlinearity [1, 2], a compressive review on the types of nonlinearity and methods of nonlinear system identification can be found in [3]. Identification of nonlinear multi-degree-of-freedom (MDOF) lumped parameters was also presented in [4, 5]. The identification of weak nonlinearities was also studied on more complex structures, example of this can be found [6] where a strategy for non-linear modal identification of weak nonlinear effects on large aircraft structures was presented. An aluminium plate attached with two stores used to illustrate the behaviour of a wing and an engine suspended by a means of nonlinear pylon also displayed a presence of weak nonlinearities during a vibration test, the results obtained illustrated some hardening characteristics as show in [7]. Similar study was also carried out on a large helicopter with the identification of a weak nonlinear softening behaviour on one of the vibration modes as shown in [8]. The current process of modelling nonlinearity in engineering structures is by including some corresponding nonlinear elements in the mathematical models which describes the nonlinear system. For this type of case study, the parameters of these nonlinear elements are usually specific and can only be obtained from an experimental test or through an updating process.

However, engineers today are frequently being challenged and confronted with the presence of nonlinear behaviour in large structures where they are not easy to locate. Examples of case studies where nonlinearity have been noticed in aerospace structures can be found in [9] where nonlinearity was detected and reported at the elastomeric mounts supporting the four turboprop engines of the aircraft during the Ground Vibration Test (GVT) of the Airbus A400M aircraft designed for military purpose. The F-16 fighter aircraft also showed some nonlinearity behaviour at wing-to-payload mounting interface of the aircraft when a similar GVT was conducted [10]. Nonlinearities were also detected on the Cassini spacecraft due to the presence of gaps in the support of the Huygens probe [11]. More case studies on the presences of nonlinearities in engineering structures can be found in the literature, this shows that there is a requirement in designing appropriate tools, or framework, which are capable of dealing with cases where nonlinearities are present in today's engineering structures.

In this paper authors seek to propose a modular framework for upgrading a linear system to capture any nonlinearities present in a structure, the framework is based on establishing an underlying linear model or properties of the structure through an optimisation process. The nonlinear identification is conducted by using a process which entails *detection, localisation,*

S.B. Cooper • A. delli Carri • D. Di Maio (✉)
University of Bristol, University Walk, BS8 1TR Bristol, UK
e-mail: dario.dimaio@bristol.ac.uk

G. Kerschen (ed.), *Nonlinear Dynamics, Volume 1*, Conference Proceedings of the Society for Experimental Mechanics Series,
DOI 10.1007/978-3-319-29739-2_19

characterisation and quantification of the nonlinearity in the system. The upgrading process regards the inclusion of missing physical terms which enable a finite element model to predict responses for any loading conditions.

19.1.1 Review on Nonlinear Identification Methods

In a comprehensive review presented by Kerschen et al. in [3], seven methods have been identified as the most popular methods used in the analysis of nonlinear system. These methods are:

- Time domain methods
- Frequency domain methods,
- Modal methods,
- Linearization methods,
- Time-frequency analysis,
- Black-box modelling
- Structural modelling updating

A survey of these seven identification methods are discussed fully in [3], in addition the authors of this paper have undertaken a statistical analysis on the practical application of these methods most especially in the field of structural dynamics. In the analysis small structures are categorised as examples of simulation or experimental work which has been carried out on beams, plates, lap joints and small masses connected together with a nonlinear device using the associated technique. Large structures are categorised as automotive shock absorbers, full scales shear wall structures, helicopter blades, aircraft wings, ailerons, SmallSat Spacecraft, and a full-scaled small aircraft.

Despite the level of development in nonlinear identification methods, the chart presented in Fig. 19.1 indicates that only a small percentage of these methods are practically suitable for structures modelled with large degrees of freedom (DOF) and localised nonlinearity. For clarity, the above chart is intended to show a comparison of how each method has been applied in the identification of nonlinearity in different industrial application. An important criterion in the industrial environment is that a method is acknowledged as a good method if it can be applied to a real life structure or system. In most cases the direct application of these methods are not always straightforward due to the level of mathematical algorithms that these methods are founded upon.

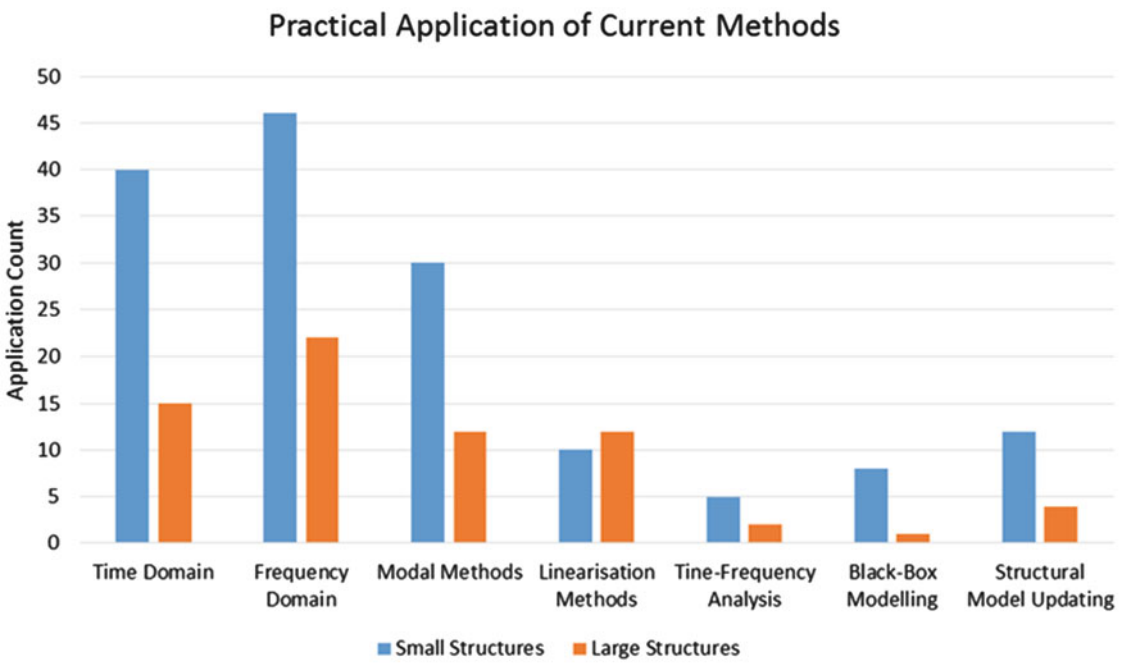

Fig. 19.1 Practical application of current identification methods, subcategorised by small and large structures

In the field of structural dynamics, the basic concept behind nonlinear identification is that every structure is considered to have an underlying linear model (ULM) where the response of a structure obeys the homogeneity principle up to a certain level before shifting into nonlinear region where superposition is no longer valid. Regardless of the extensive literature on linear and nonlinear identification, there is little or no work on developing methodologies that are capable of enhancing validated linear structural models to accommodate discrete and localised nonlinearities. Hence this paper is aimed at presenting a practical application of a modular framework where an optimised linear FE structural model is upgraded to operate normally in the presence of discretized and localised nonlinearities.

19.2 Identification Process of Nonlinear System

Another way to classify the current literature on nonlinear identification is based on the processes involved in the identification of a nonlinear system. In this context, *Identification* process is defined as the number of steps or procedures required for the complete identification of a nonlinear system. Arguably, in structural dynamics, the identification process is often developed based on the type and source of nonlinearity associated with the structure or system. This aspect of nonlinear identification has also received the development of several procedures and strategies that is capable of providing a successful nonlinear identification. A more generic identification process which seeks to provide answers to some typical questions concerning nonlinear structures is presented in [3], with the aim to tackle some of these challenges.

(a) Does the structure exhibit a nonlinear behaviour?
(b) What is the type and source of nonlinearity?
(c) What is the strength of the nonlinearity?

However an updated version of this process which incorporates modal testing into each step definition is presented in an opinion paper in [12]. This new updated process is tailored to answer industrial practical problems where structural integrity is of great concern. More often industries are being challenged with cases where their proposed structural linear FE model fails to produce reliable predicted response due to the presence of some nonlinear features in the structure. The underlying principle for this new updated process is that an improved modal testing and analysis identification process might be an appropriate way of solving some of the challenges that industries are currently facing in this area. The major definition of these processes are:

1. *Modal Testing* + **Detection**: to determine the strength of nonlinearity from measured response.
2. *Modal Testing* + **Characterisation**: to determine the type of nonlinearity.
3. *Modal Testing* + **Location**: to locate regions containing nonlinear features.
4. *Modal Testing* + **Quantification**: to quantify the nonlinear features.

In this context detection, characterisation, location and quantification are defined as:

Detection is used as a form of indicator based on the measured response to ascertain that there is some effect of nonlinearity which cannot be neglected and at that stage the structural model is no longer classified as a linear model.

Location is mainly to determine where the nonlinear features are located in the structural model and also which are the corresponding degrees of freedom (DOF) in the FE model.

Characterisation is referred to the physical origins of the nonlinear features in the structure and most importantly the source of the nonlinear effect i.e. stiffness or damping of the structural model.

Quantification involves searching for the coefficient of the characterised nonlinear term.

19.3 Modular Framework and Upgrading Approach

In this era of structural modelling where finite element method is widely used, there is still a great concern with incorporating valid linear FE models with identified nonlinearities in a structure. This modular framework is structured mainly to enhance an optimised linear structural model to accommodate any form of nonlinearities. A large majority of the procedure in this framework is based on the physical modelling approach while some subsection like the damping ratio estimation is based on the traditional modal space approach. The physical modelling approach has the abilities to identify nonlinearities in a modular form by using different developed toolbox to answer the three main questions, as presented in Sect. 19.2. The framework is intended to integrate the classic finite element modelling and experimental modal testing used in most industrial application

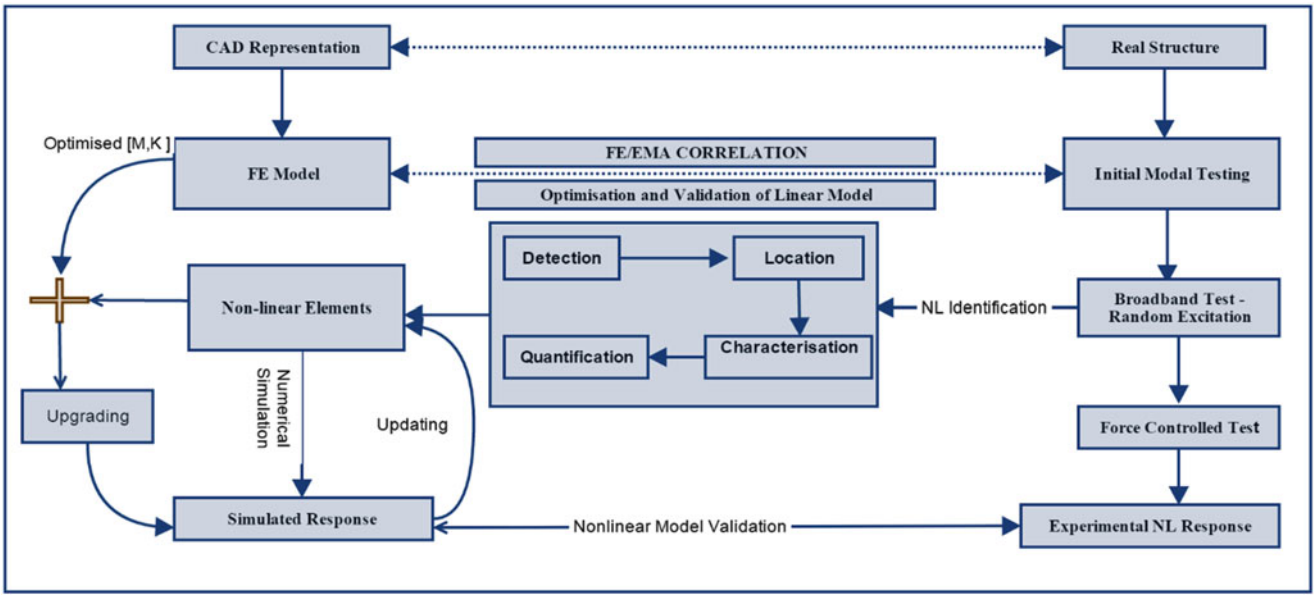

Fig. 19.2 Modular framework for model upgrading

to obtain a successful nonlinear identification. The last phase of the framework seeks to validate the identified nonlinearity through an upgrading approach, where upgrading involves adding valid linear FE models to the nonlinear term to make it complete before updating the coefficients of the parameters. Since there is a need for a comprehensive validation of the nonlinear identification, the upgrading process helps to generate nonlinear models which can be validated by using forced controlled simulation and experimental tests. A schematic of the process is presented in Fig. 19.2.

19.4 The Multiple Beam Structure

The test structure used for this analysis is represented in Fig. 19.3, it is made up of five rectangular steel beams bolted on a large steel frame with M6 bolts. Each beam is connected to each other with the aid of a flexible spring bolted with M4 bolts, the structure is instrumented with an accelerometer close to the tip of each beam and a force gauge attached to beam 3. The structure is designed to display some nonlinear behaviour by tuning the springs with different heights, extra block masses of different weight are added to beam 2–5 to introduce different dynamics into the system. The double spring connection, between beam 1 and 2, and the flattened spring, between beam 3 and 4, act as sources of nonlinearity.

19.4.1 Experimental Testing

Two different tests were performed on the structure, the first test was a broadband test. The aim of the broadband test is to identify the number of modes present inside a selected frequency range. The second test performed on the structure is a forced control test, the results obtained from this test are used to validate the nonlinear forced simulated model. Low and high level broadband test, using random excitation, were performed on the structure the results of which were able to provide an initial assessment of the structure. Figures 19.4 and 19.5 present both the FRF and the coherence for low level of excitation. Figures 19.6 and 19.7 present both FRF and coherence for high level of excitation. In this high vibratory state both coherences show clear signs that nonlinearities are being activated.

In total 19 modes were identified within the first 1000 [Hz] of the structure. It is also worth mentioning that there other broadband test results for beam 1, 4 and 5 but these results are not included in this paper, in addition as we move further away from the excited beam the energy drops so there the energy that reaches beam 1 and 5 are not as high as the other beams.

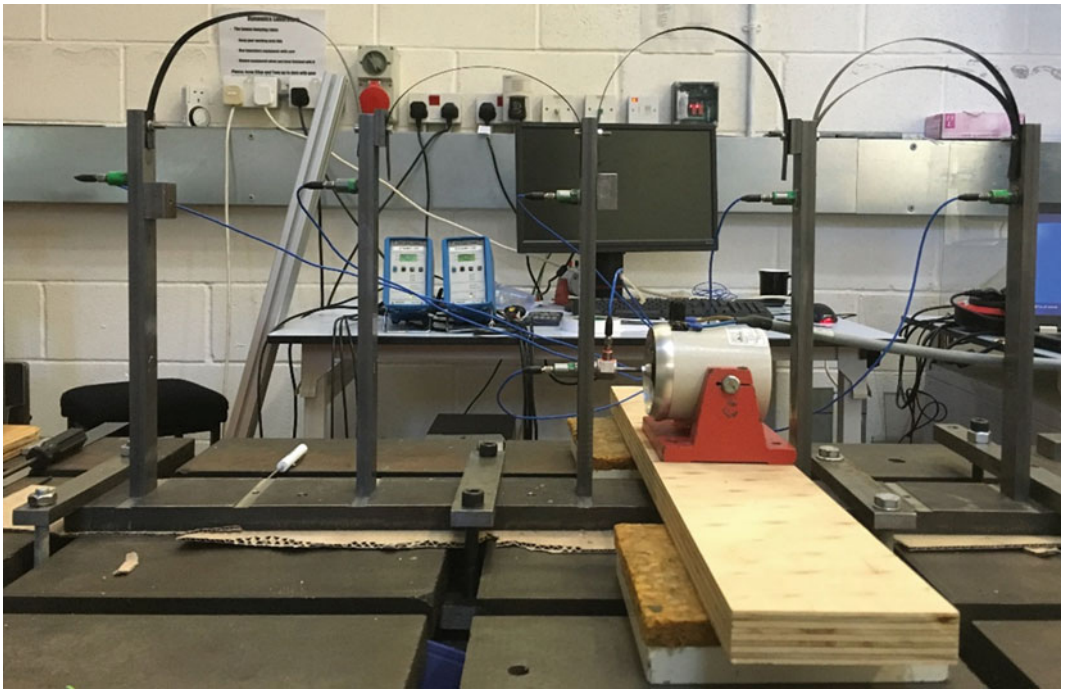

Fig. 19.3 Multiple beam test structure

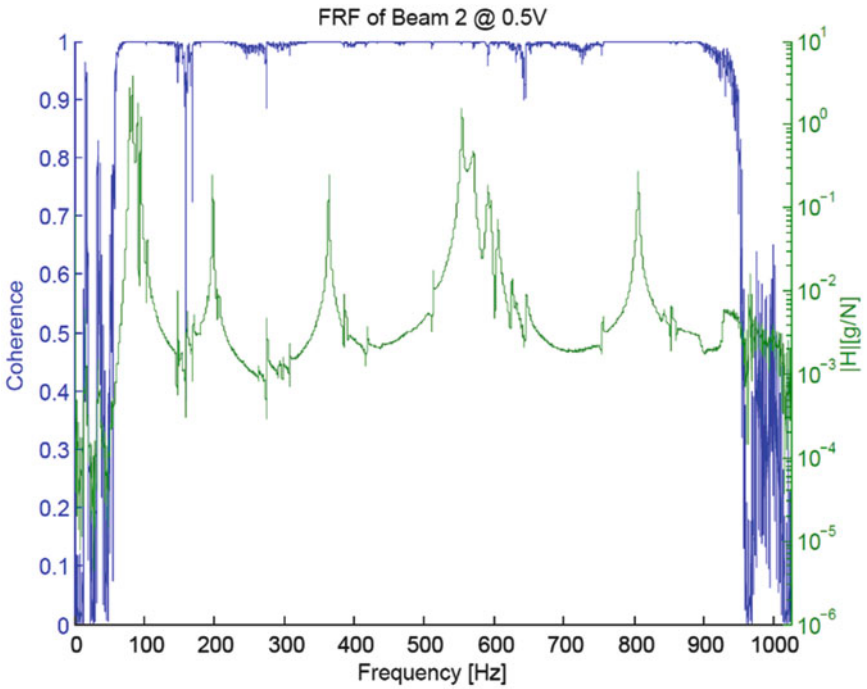

Fig. 19.4 FRF and coherence at low level of excitation beam 2

19.4.2 Linear FE Model Validation

The first phase in the modular frame presented in Fig. 19.2 is to obtain some properties that can represent a valid linear model of the structure, an FE model of the structure was created using the standard ABAQUS software package. The beams were modelled using beam elements in ABAQUS, the flexible springs connecting the beams are modelled using the standard

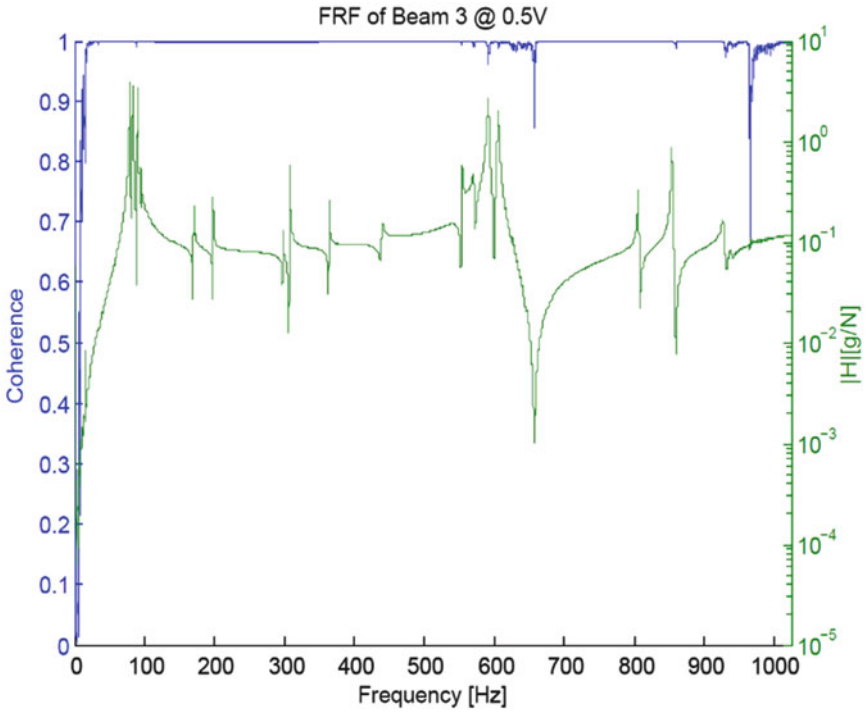

Fig. 19.5 FRF and coherence at low level of excitation beam 3

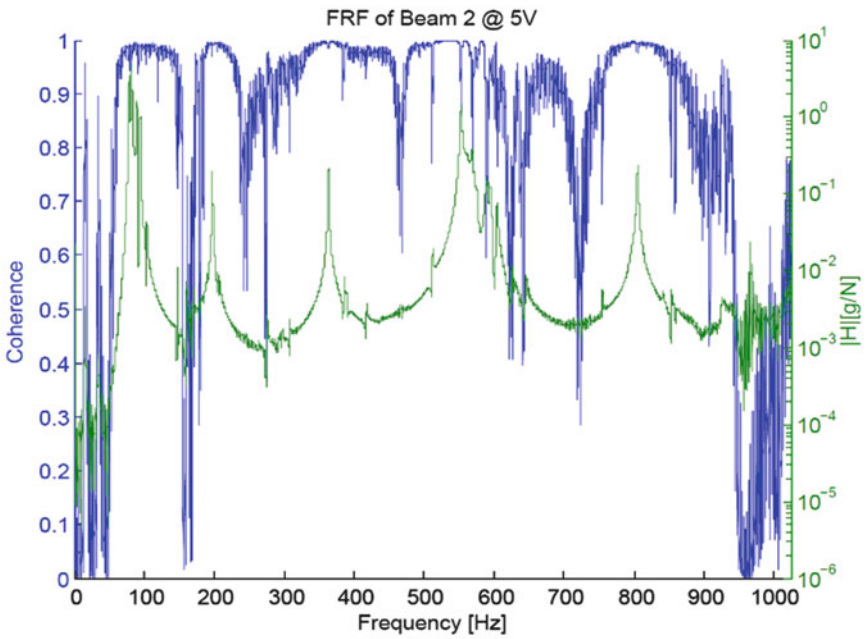

Fig. 19.6 FRF and coherence at high level of excitation beam 2

spring and dashpots in ABAQUS toolbox. Initial values of Young's modulus and spring stiffness were assigned to get an initial finite element model before the optimisation process, standard modal analysis was conducted to get the FE frequency values and mode shapes.

Figures 19.8, 19.9 and 19.10 shows the first three FE modes of the structure with their corresponding natural frequencies (see Table 19.1), although the real springs are modelled as springs and dashpot in the FE model the discrepancy between the FE and experimental natural frequencies are within 3 %. The first three modes are mainly considered due to their high resonant peak as shown in Figs. 19.4, 19.5, 19.6 and 19.7.

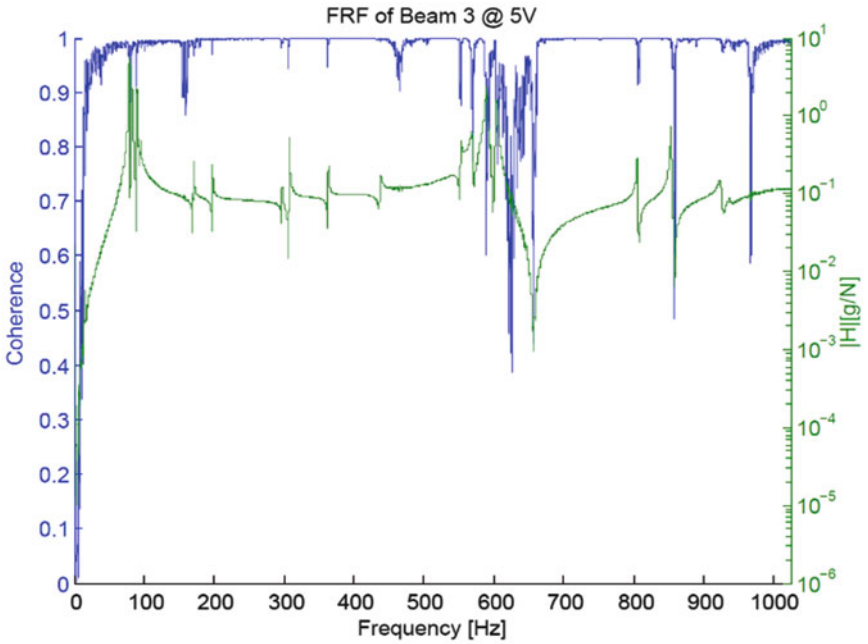

Fig. 19.7 FRF and coherence at high level of excitation beam 3

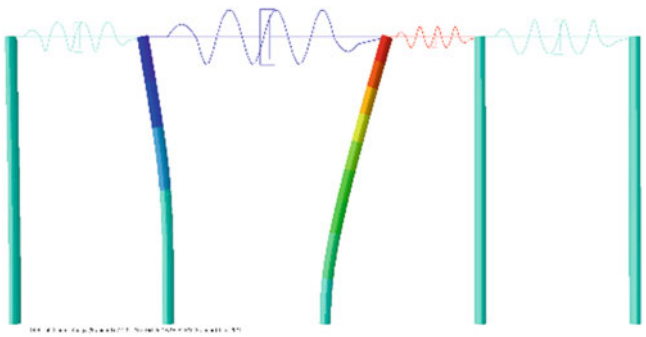

Fig. 19.8 FE mode 1 at 79.07 [Hz]

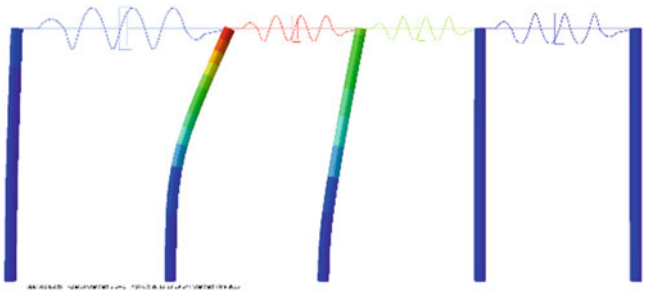

Fig. 19.9 FE mode 2 at 83.02 [Hz]

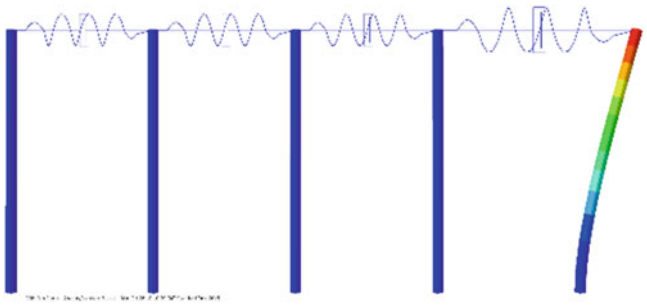

Fig. 19.10 FE mode 3 at 92.3 [Hz]

Table 19.1 Natural frequencies

Modes	Frequency value
Mode 1	79.07 Hz
Mode 2	83.02 Hz
Mode 3	92.30 Hz

Table 19.2 Updated natural frequencies and MAC percentage values

Pair	FE Freq. (Hz)	EMA Freq. (Hz)	Diff (%)	MAC (%)
1	78.52	78.59	−0.07	64.5
2	83.03	82.95	0.10	52.1
3	92.66	92.55	0.13	74.8
4	103.73	103.74	−0.01	94.8
5	307.98	307.98	0.00	50.5
6	573.61	570.66	0.52	95.9
7	590.90	590.89	0.00	99.5
8	625.82	625.09	0.12	97.0
9	646.03	646.07	−0.01	96.3

19.5 FE and EMA Correlation

To update the mode shapes and natural frequencies of the FE model, standard optimisation software (FEMtools) was used to pair the FE and experimental natural frequencies of the first few modes. The modal assurance criterion (MAC) was used to measure the accuracy of the updated modes with the experimental modes. Table 19.2 shows the FEA and EMA paired values with their corresponding MAC percentage values.

The nature of the joints between the beams (bent steel rulers) makes the system prone to exhibit complex mode shapes which, in turn, make the match of MAC values a much more difficult task to handle, and will lead to bigger MAC errors. These errors, while relatively harmless in a linear environment, will become important when the nonlinear terms are included. As an example, one can think about a nonlinear spring that sits between two degrees of freedom: in a real mode shape there is always a point in which the two degrees of freedom are in their un-deformed position, with the nonlinear spring at rest. In a complex mode shape there is no such point, and the nonlinear spring is always excited in some way. An error on the MAC values means that the mode shapes of the model are not matching the ones of the system, thus the FRF residuals will be off. One can likely find a nonlinear coefficient that accounts for these discrepancies, but in this case its value will not account solely for the nonlinear stiffness of the real joint.

19.6 Nonlinear Identification

Referring back to the modular framework in Fig. 19.2, the second phase involves the identification of nonlinearities present in the system using the results obtained from the broadband test.

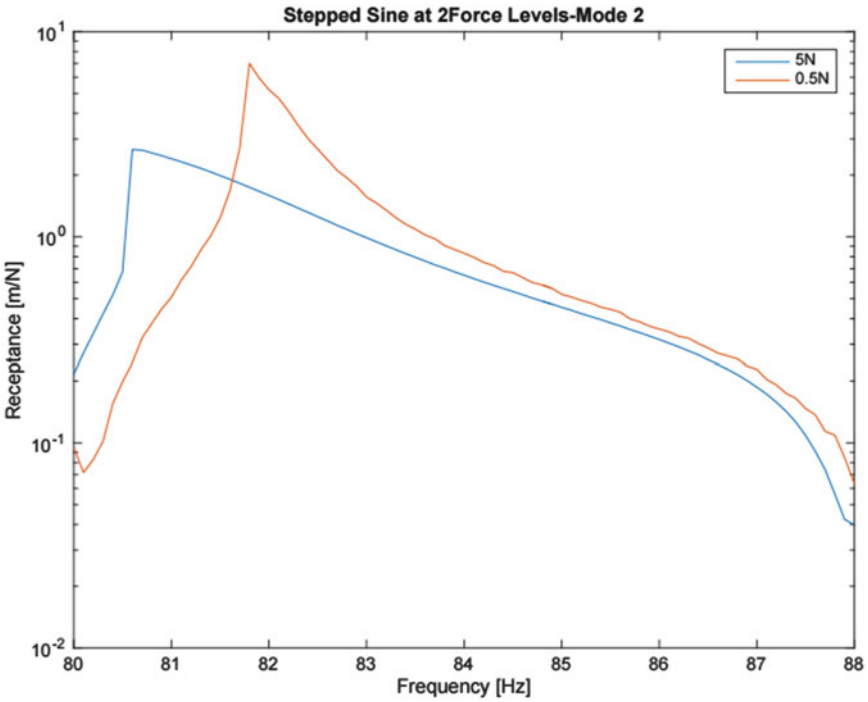

Fig. 19.11 Stepped sine FRF at 2 force levels for mode 2-beam 3

19.6.1 Detection

The first step in the identification process is the detection of nonlinearity, several methods and toolbox have been developed for the detection of nonlinearity but the homogeneity method is by far the most instinctive method using experimental measurement. The method operates by directly comparing 2 FRFs and also relies on the fact that the FRFs of a linear system is independent of its input amplitude. However for a nonlinear system the FRF is dependent on its input force, in this case the results from the stepped-sine and broadband test have shown some evidence of nonlinearity in the structure. Figures 19.11 and 19.12 shows FRF of beam 3 at mode 1 and its corresponding cross correlation shift, the homogeneity method must be applied to a mode at a time to return a reliable result hence mode 1 has been chosen for this example.

While the homogeneity method has some challenges with quantifying the distortion of the FRF and also providing a physical measure of the nonlinearity in the system, the correlation function in Fig. 19.12 indicates a frequency shift of 1.8 [Hz] in addition to a nonlinearity index.

19.6.2 Location and Characterisation

The reverse path method is arguable the most applicable method for locating and characterising nonlinearities based on physical modelling approach, it assumes the nonlinearities as a force feedback terms acting on an underlying linear system [13]. The parameter estimation is performed in the frequency domain using the conventional Multiple-Input-Single-Output (MISO) techniques. Since the overall aim of the modular framework is to conduct all the steps using a physical modelling the reverse path was adopted for this stage of the paper, collecting the broadband time histories responses at high level and treating the nonlinearities as feedback terms the location method is to run a sensitivity analysis about the locations that have the most influence on the coherence of the under-lying linear system. The reverse path relies on the multiple coherence function as an indication for the goodness estimation, Fig. 19.13 shows the coherence sensitivity associated with all the potential nonlinear locations.

From the chart one can conclude that the most affected DOF is #3, #1 and #2 hence the nonlinearity is located between beams 1 2 and 3. Once an idea of the nonlinear element has been located the reverse path is also used to determine the functional form of nonlinearity in the system, Fig. 19.14 shows the plot for the best iteration of the reverse path where the

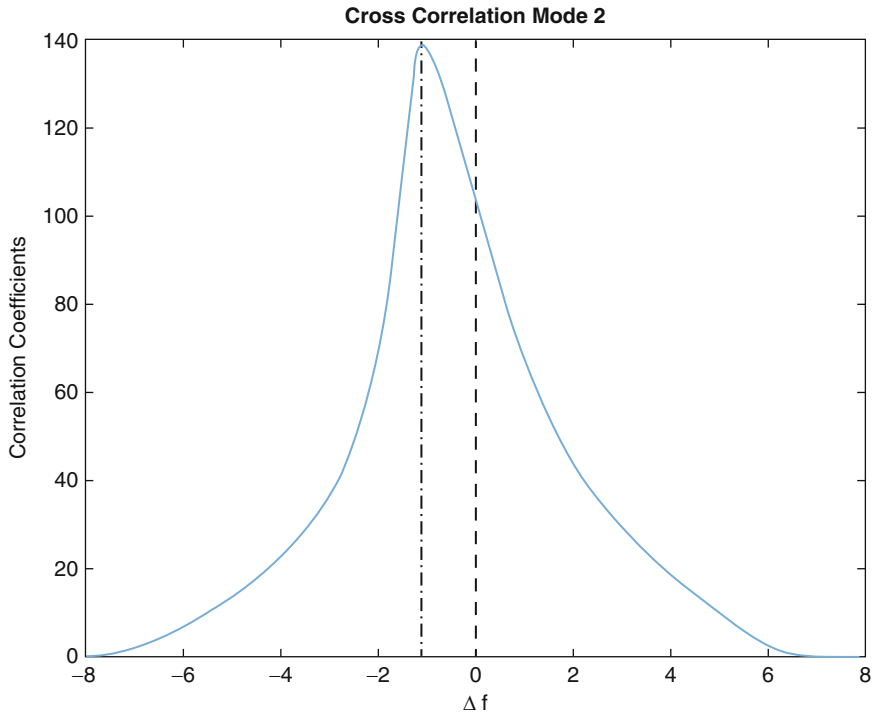

Fig. 19.12 Cross correlation plot for mode 2 at beam 3

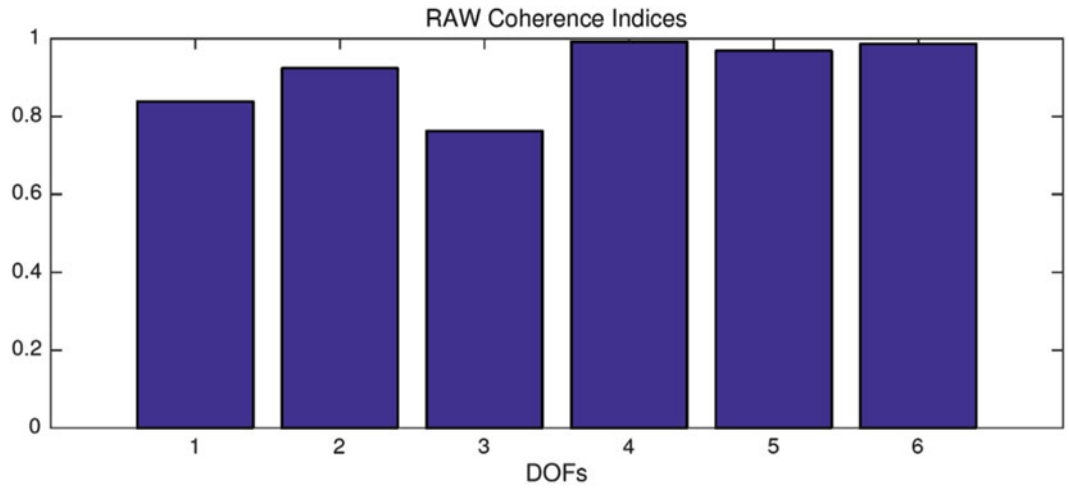

Fig. 19.13 Location plot with all potential nonlinear location

nonlinear term is characterised to have a forth order function of $F_{NL1} = \text{sign}(x).|x|^2$ and $F_{NL2} = X^2$ between DOF#1 and DOF#2. It is important to note that more iteration can be carried out to improve the coherence but at a cost to an increase in the order functional form at the characterisation stage.

19.6.3 Quantification

After a number of iterations it is possible to plot the final coherence improvement archived during the simulation, Fig. 19.15 shows the coherence indices for each degree of freedom, i.e. the indices of each beam and the driving point before and after the identification. The coherence function before and after the identification can also be obtained in the bandwidth of interest 80–280 [Hz] for DOF #3 which is the worst coherent point as shown in Fig. 19.16.

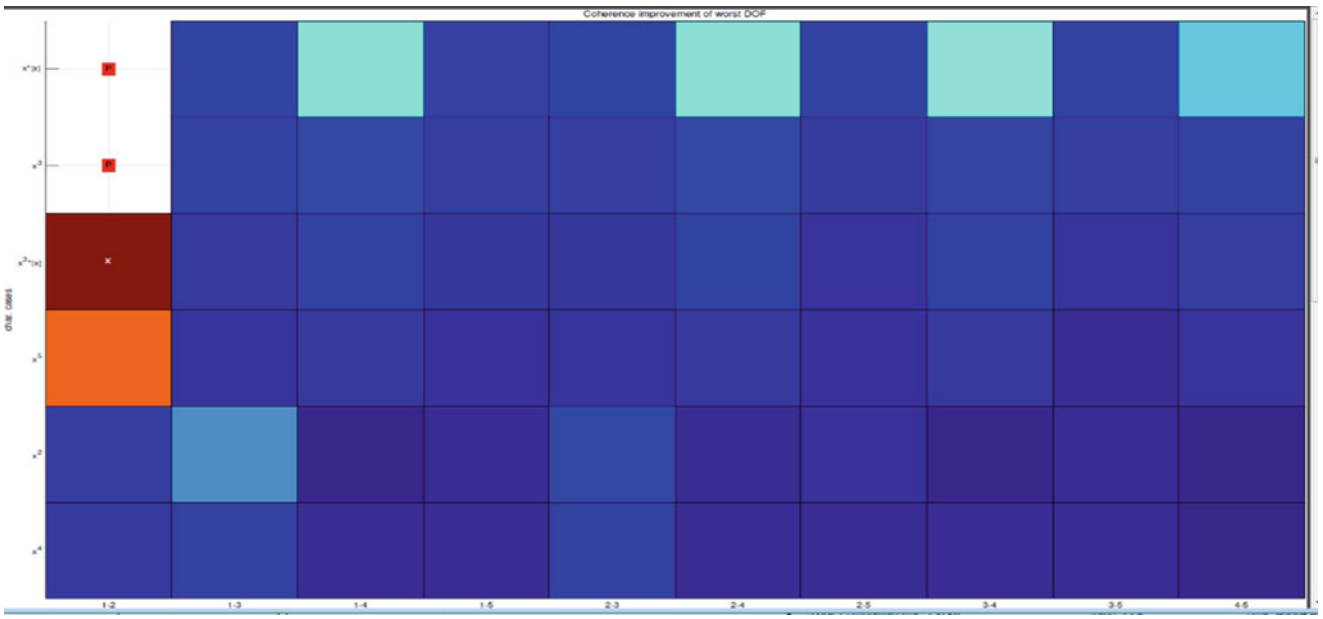

Fig. 19.14 Iteration of characterisation-localisation step using the reverse path

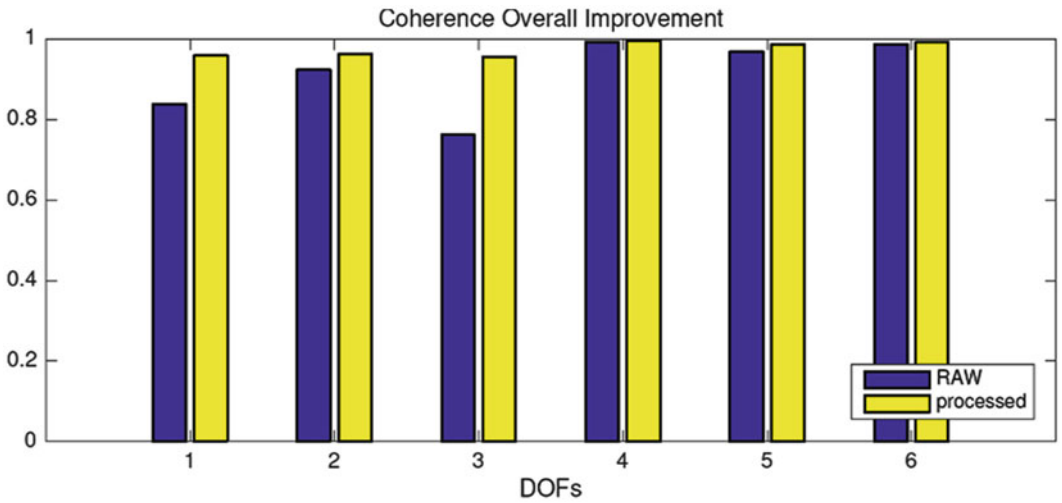

Fig. 19.15 Coherence improvement after identification

The first initial coefficients of the nonlinearities are also obtainable using the reverse path method as a starting point before going through the process of manual updating. The nonlinear coefficients are expected to be constant and real valued however the reverse path operates in the frequency dependent complex values, therefore the retrieved coefficients are averaged real values. It is worth noting that the retrieved values is obtained based on the information of the underlying linear model and its corresponding averages.

19.7 Model Upgrading

This section of the modular framework is what brings together all the previous work that has been conducted on the structure, it is often disregarded but it is arguable one of the most important process which helps to complete the structural model in the simulation aspect. The upgrading process entails adding the identified parameters that describe the nonlinear stiffness and damping in the structure to the original validated linear FE model, this is essential to make up a complete model that would describe the nonlinear behaviour within a set range of simulated force values.

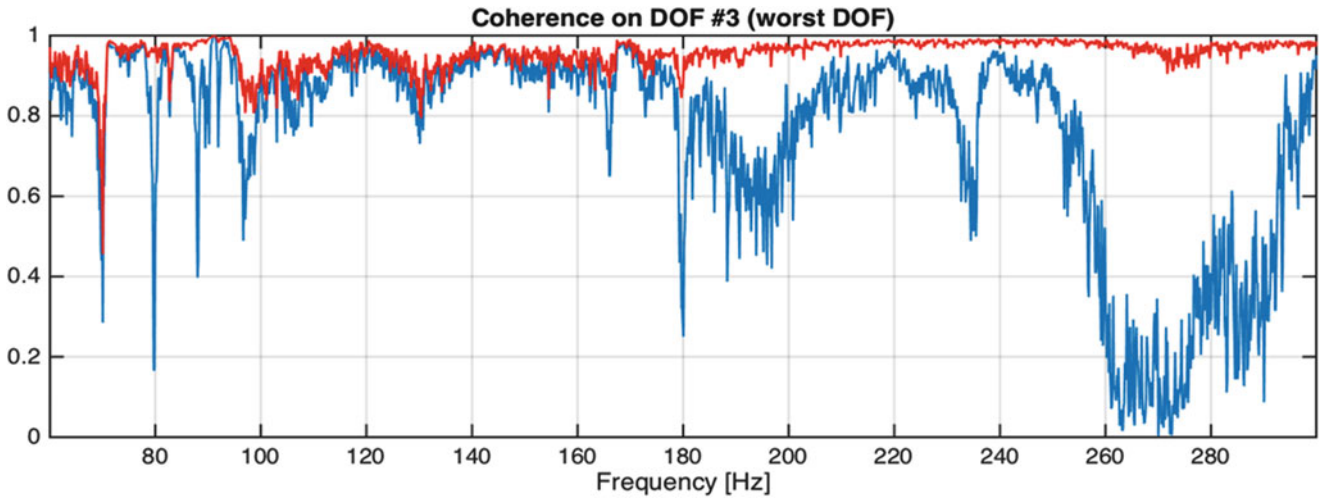

Fig. 19.16 Coherence function at the worst DOF #3

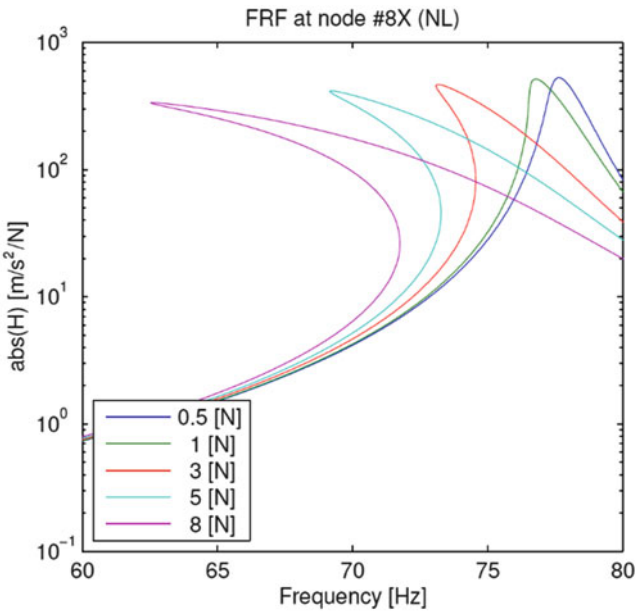

Fig. 19.17 Forced response simulation FRF beam 1 @node 8

The model upgrading was performed on the multiple beam test structure by extracting the optimised mass and stiffness matrices of the linear model and manually added the identified nonlinear terms into the equations of motion used for the numerical simulation. A range of forced controlled simulation was carried out at 0.5N, 3N, 5N, and 8N with the full DOF of the FE model, the simulation was conducted in MATLAB using AUTO continuation code. The responses of the model are plotted in units of acceleration and frequency to obtain better curves and continuation path. Figures 19.17 and 19.18 shows some example of the response plot of selected nodes from the FE and numerical simulation.

19.8 Model Updating

Now that the model has been upgraded, it is still not possible to refer to the model as an exact model but has it now has integrated parameters which can describe the nonlinear behaviour of the real structure. This stage involves matching the initial nonlinear simulated response with the measured response. It is worthing noting that at this stage the functional form

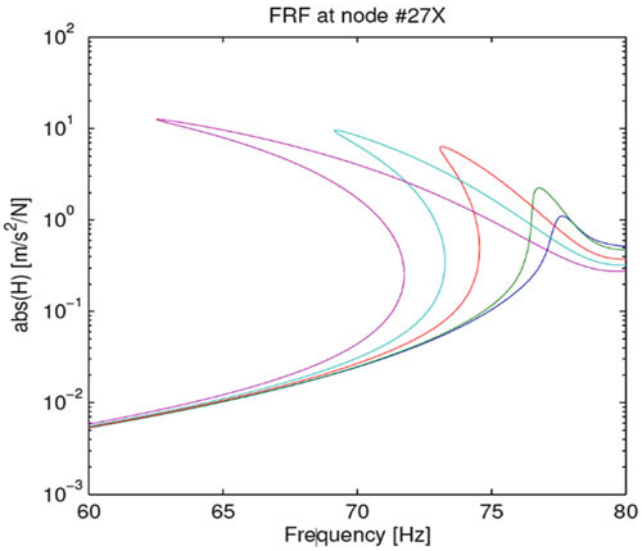

Fig. 19.18 Forced response simulation FRF beam 2 @node 27

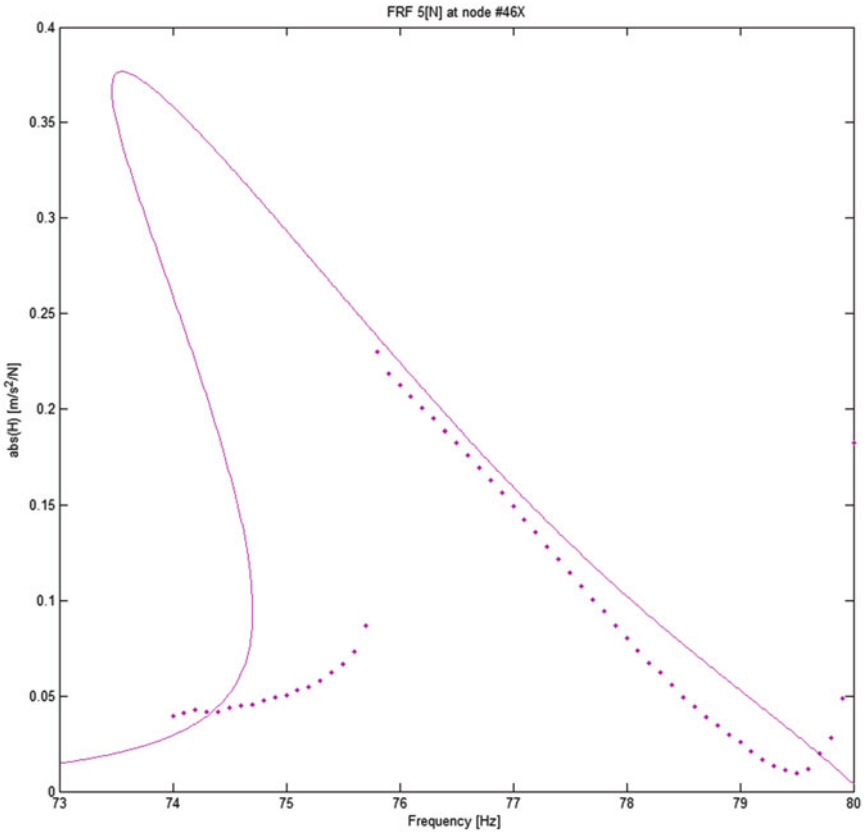

Fig. 19.19 FRF beam 3 measured response and updates simulated response

of nonlinearity is kept constant and only the coefficients of the nonlinear terms are updated iteratively to match the measured response. To conduct the updating on the structure, forced response simulation was conducted with a frequency range of the first mode using the harmonic balance method at a force level of 8 N. A corresponding force control test was conducted on the structure to correlate and update the simulated response. Figure 19.19 shows the result of the updated response.

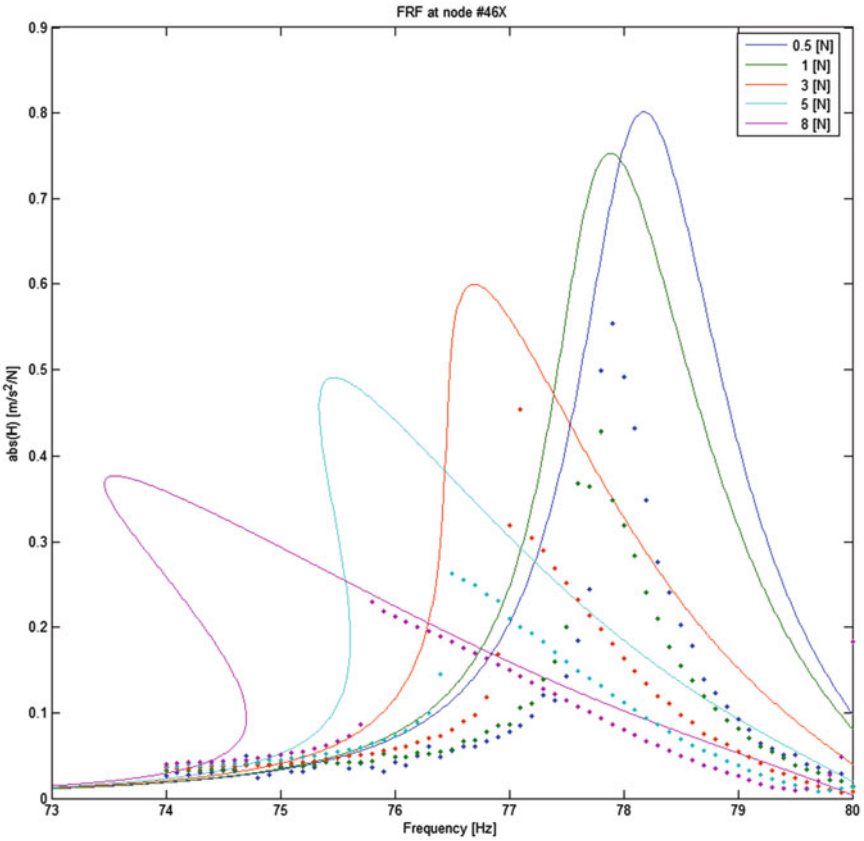

Fig. 19.20 FRF of beam 3 at several forcing levels for model validation

19.9 Nonlinear Model Validation

The final step in the modular framework is to validate the identified nonlinear model, this done by generating new forced response simulations using the new coefficients obtained from the updating process. Several forcing levels of [0.5 N, 1 N, 3 N, 5 N and 8 N] were simulated, the corresponding force control experiment was conducted to obtain measured data. The comparison of these results are shown in Fig. 19.20.

In Fig. 19.20 one can observe that there is a frequency shift and the dotted lines which are the measured response are not matching exactly with the continuous line which are the simulated response. This small error can be narrowed back to the underlying linear FE model of the structure, referring back to Table 19.1 which shows the underlying linear frequency and MAC updated values. Although the frequency values have almost zero percent error the MAC values which relates to the mode shapes of the structure are not properly paired during the model updating of linear FE model. Hence this suggests that it is important to have well updated linear model where the mode shapes and frequencies are paired to high degree of accuracy to obtain a well predicted nonlinear model.

19.10 Conclusion

This paper presents the application of a modular framework for upgrading a valid linear FE model and to accommodate a form of nonlinearity present in the structure. The approach used in the framework were highlighted in three different phases which entails FE/EMA correlation to obtain an underlying linear FE model, nonlinear identification process and model upgrading. The final stage of the application was to validate the identified nonlinear model through simulation and new experimental data. Only a selected number of methods were chosen for the nonlinear identification phase due to the physical modelling approach as adopted for the proposed framework. The error between the simulated and experimental forced responses can be

associated to the goodness of the underlying linear FE model and the accuracy of the characterised nonlinear elements. The nonlinear identification and validation phase still remain an area that could benefit from further development most especially using the physical modelling approach.

References

1. Trickey, S.T., Virgin, L.N., Dowell, E.H.: The stability of limit-cycle oscillations in a nonlinear aeroelastic system. In: Proceedings of the Royal Society of London, 2002
2. Kerschen, G., Lenaerts, V., Golinval, J.C.: Identification of a continuous structure with a geometrical non-linearity. Part I: Conditioned reverse path method. J. Sound Vib. **262**(4), 889–906 (2003)
3. Kerschen, G., et al.: Past, present and future of nonlinear system identification in structural dynamics. Mech. Syst. Signal Process. **20**(3), 505–592 (2006)
4. Özer, M.B., Özgüven, H.N., Royston, T.J.: Identification of structural non-linearities using describing functions. Mech. Syst. Signal Process. **23**, 30–44 (2009)
5. Dimitriadis, G.: Experimental validation of the constant level method for identification of non-linear multi-degree-of-freedom systems. J. Sound Vib. **258**(5), 829–845 (2002)
6. Fuellekrug, U., Goege, D.: Identification of weak non-linearities within complex aerospace structures. Aerosp. Sci. Technol. **23**(1), 53–62 (2012)
7. Platten, M.F., Wright, J.R., Cooper, J.E., Dimitriadis, G.: Identification of a nonlinear wing structure using an extended modal model. J. Aircr. **46**(5), 1614–1626 (2009)
8. Carrella, A., Ewins, D.J.: Identifying and quantifying structural nonlinearities in engineering applications from measured frequency response functions. Mech. Syst. Signal Process. **25**(3), 1011–1027 (2011)
9. Peeters B., Debille J., Climent H.: Modern solutions for ground vibration and modal survey Testing_LMS. In: LMS Ground Vibration Test Workshop, Spain, 2010
10. Noel, J.P., Renson, L., Kerschen, G., Peeters, B., Manzato, S., Debille, J.: Nonlinear dynamic analysis of an F-16 aircraft using GVT data. In: Proceedings of the International Forum on Aeroelasticity and Structural Dynamics (IFASD), Bristol, 2013
11. Carney, K., Yunis, I., Smith, K., Peng, C.Y.: Nonlinear-Dynamic-Behavior-Cassini-Spacecraft-Modal-Survey. In: Proceedings of the 15th International Modal Analysis Conference (IMAC), Orlando, FL, 1997
12. Ewins, D.J., Weekes, B., delli Carri, A.: Modal testing for model validation of structures with discrete nonlinearities. J. Philos. Trans. **373**, 1–20 (2015)
13. Richards, C.M., Singh, R.: Identification of multi-degree-of-freedom non-linear system under random excitations by the reverse path spectral method. J. Sound Vib. **213**(4), 673–708 (1998)

Chapter 20
Obtaining Nonlinear Frequency Responses from Broadband Testing

Etienne Gourc, Chiara Grappasonni, Jean-Philippe Noël, Thibaut Detroux, and Gaëtan Kerschen

Abstract The objective of the paper is to obtain the frequency response curves of nonlinear mechanical systems from broadband testing. The proposed approach consists in coupling an identification method with a continuation method. Specifically, the frequency-domain nonlinear subspace identification (FNSI) method is first used to derive an experimental model of the structure in state space from broadband measurements. The harmonic balance method coupled with arclength continuation then utilizes this experimental model to compute the frequency response curves of the system. The method is demonstrated using a numerical example.

Keywords Subspace identification • Continuation • Harmonic balance • Nonlinear • Random excitation

20.1 Introduction

Nonlinear dynamical systems may exhibit complex behavior such as bifurcations, jump phenomenon or sensitivity to motion amplitude. When investigated using linear system identification method, these dynamical phenomena can be erroneously interpreted and lead to an inaccurate model.

Because nonlinearity is a frequent occurrence in engineering structures, there is a need for embedded methods that can be used to characterize the nonlinear behavior of a structure from experimental data [8].

Among existing identification methods, subspace methods, developed for linear system identification [10, 13], are able to deal with multiple-input, multiple-output systems, were successfully applied for real-life applications [7]. Thanks to the feedback interpretation of the nonlinear structural dynamics [1], Marchesiello and Garibaldi proposed a time domain nonlinear subspace identification (TNSI) method able to estimate the frequency response function (FRF) of the underlying linear system as well as the nonlinear coefficients [9]. It has been shown that the method is sufficiently robust to identify appropriate nonlinear behavior from a set of basis functions. Later a frequency-domain version of the method, termed FNSI, was introduced [11]. Frequency-domain approaches are useful to reduce computational burden by selecting appropriate frequency bandwidth in the response spectrum for the identification. For greater flexibility allowing identification of complex nonlinearity, nonlinear basis function were replaced by cubic splines and the method was applied to the identification of bolted connections of a solar array panel [12].

The previous mentioned references aim at characterizing nonlinear systems using input-output data. The identified model is in the state-space form and the estimated matrices cannot be directly related to the system physical mass, damping and stiffness matrices. Therefore, as pointed out by Ewins et al., there is a need for a simulation tool to simulate directly the estimated model in the state-space frequency domain [6].

Different algorithms for the computation of periodic solutions and bifurcations of nonlinear structure can be found in the literature. Most of them rely on a continuation procedure to track periodic solutions along branches with respect to a control parameter (frequency of excitation or a system parameter) [2]. Among all the methods for computing periodic solutions in frequency domain, the harmonic balance (HB) is arguably the most used. The periodic signals are approximated by their Fourier coefficients, which become the new unknowns of the problem.

This method was applied to several industrial cases such as rotor-stator contact problems in turbo-machinery [14], or to large-scale structures such as the nonlinear behavior of a full-scale vehicle [3]. Recently, the harmonic balance method

E. Gourc (✉) • C. Grappasonni • J.-P. Noël • T. Detroux
Department of Aerospace and Mechanical Engineering, Space Structure and Systems Laboratory (S3L), University of Liège, Liège, Belgium
e-mail: etienne.gourc@ulg.ac.be

G. Kerschen
University of Liege in Belgium Liege, Belgium

G. Kerschen (ed.), *Nonlinear Dynamics, Volume 1*, Conference Proceedings of the Society for Experimental Mechanics Series,
DOI 10.1007/978-3-319-29739-2_20

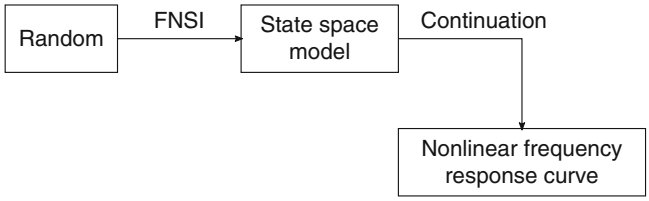

Fig. 20.1 Diagram of the system identification methodology as addressed in the present paper

has been used for the detection and tracking of codimension-1 bifurcations and applied to the analysis of the SmallSat spacecraft [5].

In this paper, an embedded approach coupling the FNSI method with a state-space harmonic-balance based continuation method is proposed and summarized in Fig. 20.1.

20.2 Frequency-Domain Nonlinear Subspace Identification

In this section, the frequency nonlinear subspace identification method (FNSI) is briefly recalled [11].

20.2.1 Identification Problem Formulation

The behavior of a mechanical system with discrete nonlinearities may be described by the following equation of motion

$$M\ddot{q}(t) + C\dot{q}(t) + Kq(t) + f(q(t), \dot{q}(t)) = p(t) \tag{20.1}$$

where $M, C, K \in \mathbb{R}^{r\times r}$ are the linear mass, viscous damping and stiffness matrices, $q(t), p(t) \in \mathbb{R}^r$ are the generalized displacement and external force vector. $f(t) \in \mathbb{R}^r$ is the nonlinear restoring force vector. The effect of the s lumped nonlinearities is expressed as

$$f(q(t), \dot{q}(t)) = \sum_{j=1}^{s} \mu_j b_j g_j(q(t), \dot{q}(t)) \tag{20.2}$$

where μ_j are the nonlinear coefficients, $b_j \in \mathbb{R}^r$ is a Boolean vector indicating the location of the nonlinearity and $g_j(q(t), \dot{q}(t))$ is the nonlinear functional form. Defining the state vector $x = [q^T, \dot{q}^T]^T \in \mathbb{R}^n$ ($n = 2r$), system (20.1) is rewritten in state space form as

$$\begin{aligned} \dot{x}(t) &= A_c x(t) + B_c e(p(t), q(t), \dot{q}(t)) \\ q(t) &= Cx(t) + De(p(t), q(t), \dot{q}(t)) \end{aligned} \tag{20.3}$$

here, the subscript c stands for continuous space. $e(t) = [p(t)^T, g_1(t), \ldots, g_s(t)]^T \in \mathbb{R}^{r+s}$ is the extended input vector which comes from the feedback interpretation of the nonlinear terms [11]. State space matrices $A_c \in \mathbb{R}^{n\times n}$, $B_c \in \mathbb{R}^{n\times(r+s)}$, $C \in \mathbb{R}^{r\times n}$, $D \in \mathbb{R}^{r\times(r+s)}$ are related to physical matrices as

$$A_c = \begin{bmatrix} 0^{r\times r} & I^{r\times r} \\ -M^{-1}K & -M^{-1}C \end{bmatrix}, \quad B_c = \begin{bmatrix} 0^{r\times r} & 0^{r\times 1} & \ldots & 0^{r\times 1} \\ M^{-1} & -\mu_1 M^{-1} b_1 & \ldots & -\mu_s M^{-1} b_s \end{bmatrix} \tag{20.4}$$

$$C = \begin{bmatrix} I^{r\times r} & 0^{r\times r} \end{bmatrix}, \quad D = 0^{r\times(r+s)}$$

In order to reduce computational burden, the identification is performed in frequency domain. For improved numerical conditioning, a discrete-time translation is considered [9] before applying the discrete Fourier transform to system (20.3)

$$\begin{aligned} z_k X(k) &= A_d X(k) + B_d E(k) \\ Q(k) &= CX(k) + DE(k) \end{aligned} \tag{20.5}$$

where $z_k = e^{2j\pi k/N_s}$, N_s is the number of recorded samples in the time series. Knowing the extended input E and output Q, we want to determine the order of the system n and the system matrices A_d, B_d, C end D.

20.2.2 The Output-State-Input Equation

In practical applications, only a limited set of degree of freedom (DOF) in $p(t)$ and $q(t)$ are excited and observed, respectively. Therefore, the problem is preferably stated in terms of measured applied force $u(t) \in \mathbb{R}^{m \leq r}$ and displacement $y(t) \in \mathbb{R}^{l \leq r}$, so that $e(t) \in \mathbb{R}^{s+m}$. Equation (20.5) is rewritten as

$$\begin{aligned} z_k X(k) &= A_d X(k) + B_d^e E(k) \\ Y(k) &= C_d X(k) + D_d^e E(k) \end{aligned} \tag{20.6}$$

where $Y(k)$ is the discrete Fourier transform of $y(t)$ and the state space matrices are now a projection of the original matrices onto the observed and controlled DOFs. In what follows, the subscript d is dropped for brevity. The measured input and output spectra are rearranged in block Hankel matrices

$$Y_i = \begin{bmatrix} Y(1) & Y(2) & \dots & Y(N) \\ z_1 Y(1) & z_2 Y(2) & \dots & z_N Y(N) \\ z_1^2 Y(1) & z_2^2 Y(2) & \dots & z_N^2 Y(N) \\ \vdots & \vdots & \ddots & \vdots \\ z_1^{i-1} Y(1) & z_2^{i-1} Y(2) & \dots & z_N^{i-1} Y(N) \end{bmatrix} \in \mathbb{R}^{li \times N} \tag{20.7}$$

where i is a user-defined index which must be chosen to encompass sufficient information to identify the system. N is the number of non-necessary equidistant frequency lines taken for the identification procedure. The extended observability matrix Γ_i and the lower block Toeplitz matrix H_i are defined as

$$\begin{aligned} \Gamma_i &= \begin{bmatrix} C^T & CA^T & CA^{2^T} & \dots & CA^{i-1^T} \end{bmatrix}^T \in \mathbb{R}^{li \times n} \\ H_i &= \begin{bmatrix} D^e & 0 & 0 & \dots & 0 \\ CB^e & D^e & 0 & \dots & 0 \\ CAB^e & CB^e & D^e & \dots & 0 \\ \vdots & \vdots & \vdots & \ddots & \vdots \\ CA^{i-2}B^e & CA^{i-3}B^e & CA^{i-4}B^e & \dots & D^e \end{bmatrix} \in \mathbb{R}^{li \times (s+m)i} \end{aligned} \tag{20.8}$$

By making recursive use of Eq. (20.6), the output-state-input matrix equation is obtained

$$Y_i = \Gamma_i X + H_i E_i \tag{20.9}$$

here $X \in \mathbb{R}^{n \times N}$ is the unknown state spectrum.

20.2.3 Estimation of the State Matrices and the Order of the System

The subspace identification method can now be applied to (20.9) to determine the order of the system and the matrices of the state space system (20.6). The algorithm consists of two main steps.

- First, the term depending on the input and the nonlinearities, namely $H_i E_i$ is eliminated. This task is achieved through an orthogonal projection onto the orthogonal complement of E_i. Then a singular value decomposition (SVD) of the result of the projection is performed. The order of the system and the estimated extended observability matrix are determined from the result of the SVD.

- The next step consist in computing the matrices of the state space system. Matrices A and C are easily computed by making use of the shift property of Γ_i. The procedure for computing matrices B and D is discussed in [11] (or in [13] for a general presentation of subspace-based identification methods).

Note that the state space matrices are obtained only within a similarity transformation matrix T, so that

$$A_c = T\hat{A}_c T^{-1}, \quad B_c = T\hat{B}_c, \quad C = \hat{C}T^{-1}, \quad D = \hat{D} \tag{20.10}$$

It is possible to define a similarity transformation matrix to express the identified matrices in the physical state-space domain (i.e. $x = [q^T, \dot{q}^T]^T$). Using Eq. (20.10), the problem is formulated as follows

$$\begin{aligned} T\hat{A}_c &= \begin{bmatrix} T_1 & T_2 \\ T_3 & T_4 \end{bmatrix} \begin{bmatrix} A_1 & A_2 \\ A_3 & A_4 \end{bmatrix} = \begin{bmatrix} 0^{r\times r} & I^{r\times r} \\ -M^{-1}K & -M^{-1}C \end{bmatrix} \begin{bmatrix} T_1 & T_2 \\ T_3 & T_4 \end{bmatrix} \\ \hat{C} &= \begin{bmatrix} C_1 & C_2 \end{bmatrix} = \begin{bmatrix} I^{r\times r} & 0^{r\times r} \end{bmatrix} \begin{bmatrix} T_1 & T_2 \\ T_3 & T_4 \end{bmatrix} \end{aligned} \tag{20.11}$$

which gives

$$\begin{aligned} T_1A_1 + T_2A_3 &= T_3 \\ T_1A_2 + T_2A_4 &= T_4 \\ C_1 &= T_1 \\ C_2 &= T_2 \end{aligned} \tag{20.12}$$

Therefore the obtained similarity transformation matrix reads

$$T = \begin{bmatrix} \hat{C} \\ \hat{C}\hat{A}_c \end{bmatrix} \tag{20.13}$$

Usually, a last procedure to compute the nonlinear coefficients μ_j from the estimated matrices is performed. However, this step is not necessary for the continuation procedure.

20.3 Harmonic Balance-Based Continuation Method

In this section, the computation of the periodic solution using the harmonic balance method is presented.

20.3.1 Harmonic Balance Formulation

The harmonic balance method is applied directly to the state-space system (20.3), where the state space matrices are those obtained using the FNSI method ($\hat{A}_c$, $\hat{B}_c$, $\hat{C}$ and $\hat{D}$). In what follows, the hats are dropped for simplicity of notation. The state, output and input variables are approximated by Fourier series truncated to the N-th harmonic

$$\begin{aligned} x(t) &= \frac{X_0}{\sqrt{2}} + \sum_{j=1}^{N} X_{cj}\cos(k_j\theta) + X_{sj}\sin(k_j\theta) \\ q(t) &= \frac{Q_0}{\sqrt{2}} + \sum_{j=1}^{N} Q_{cj}\cos(k_j\theta) + Q_{sj}\sin(k_j\theta) \\ e(t) &= \frac{E_0}{\sqrt{2}} + \sum_{j=1}^{N} E_{cj}\cos(k_j\theta) + E_{sj}\sin(k_j\theta) \end{aligned} \tag{20.14}$$

where $\theta = \omega t$, ω is the pulsation of excitation. Q_{cj} and Q_{sj} are the unknown Fourier coefficients related to the cosine and sine terms, respectively. Note that the Fourier coefficients of $e(t)$, depends on the Fourier coefficients of $q(t)$ due to the nonlinear basis functions g_j. $k \in \mathbb{R}^N$ is the vector containing the different harmonics. The Fourier coefficients are gathered into vectors as follow

$$\begin{aligned} Q &= \left[Q_0\ Q_{c1}\ Q_{s1}\ \ldots\ Q_{cN}\ Q_{sN}\right] \in \mathbb{R}^{(2N+1)l} \\ X &= \left[X_0\ X_{c1}\ X_{s1}\ \ldots\ X_{cN}\ X_{sN}\right] \in \mathbb{R}^{(2N+1)n} \\ E &= \left[E_0\ E_{c1}\ E_{s1}\ \ldots\ E_{cN}\ E_{sN}\right] \in \mathbb{R}^{(2N+1)(s+m)} \end{aligned} \tag{20.15}$$

Using (20.15), the variables are rewritten in compact form as follow

$$\begin{aligned} x(t) &= (T(\theta) \otimes I_n)X \\ q(t) &= (T(\theta) \otimes I_l)Q \\ e(t) &= (T(\theta) \otimes I_{s+m})E \end{aligned} \tag{20.16}$$

where $T(\theta)$ is a vector gathering the trigonometric functions as

$$T(\theta) = \left[\frac{1}{\sqrt{2}}\ \ \cos(k_1\theta)\ \ \sin(k_1\theta)\ \ldots\ \ \cos(k_N\theta)\ \ \sin(k_N\theta)\right] \in \mathbb{R}^{(2N+1)} \tag{20.17}$$

The time derivative of $x(t)$ can be written using a linear operator as

$$\frac{dx}{dt} = \omega\frac{d}{d\theta} = \omega\left(\frac{dT(\theta)}{d\theta} \otimes I_n\right)X = \omega[(T(\theta)\nabla) \otimes I_n]X \tag{20.18}$$

with

$$\nabla = \begin{bmatrix} 0 & & & \\ & \nabla_1 & & \\ & & \ddots & \\ & & & \nabla_N \end{bmatrix} \quad \text{with } \nabla_j = \begin{bmatrix} 0 & k_j \\ -k_j & 0 \end{bmatrix} \tag{20.19}$$

Substituting Eqs. (20.16), (20.18) into (20.3) and applying Galerkin procedure gives

$$\begin{aligned} \omega(\nabla \otimes I_n)X &= (I_{(2N+1)} \otimes A_c)X + (I_{(2N+1)} \otimes B_c)E \\ Q &= (I_{(2N+1)} \otimes C)X + (I_{(2N+1)} \otimes D)E \end{aligned} \tag{20.20}$$

Rearranging, the following residue equation is obtained

$$h(Q, \omega) \equiv Q - G(\omega)E(Q) = 0 \tag{20.21}$$

with

$$\begin{aligned} G(\omega) &= (I_{(2N+1)} \otimes C)\Lambda^{-1}(I_{(2N+1)} \otimes B_c) + (I_{(2N+1)} \otimes D) \\ \Lambda &= \omega(\nabla \otimes I_n) - (I_{(2N+1)} \otimes A_c) \end{aligned} \tag{20.22}$$

The Fourier coefficients of the nonlinear terms are computed using alternating-time-frequency method (AFT) [4], that takes advantage of the fast Fourier transform to compute E

$$Q \xrightarrow{FFT^{-1}} q(t) \rightarrow e(p(t), q(t), \dot{q}(t)) \xrightarrow{FFT} E \tag{20.23}$$

20.3.2 Continuation of Periodic Solutions

In order to track a branch of periodic solutions, a predictor-corrector method based on pseudo-arclength parametrization is used. Denoting J_Q and J_ω the Jacobian matrices with respect to Q and ω, respectively, the tangent vector $t_{(i)}$ at a point $(Q_{(i-1)}, \omega_{(i-1)})$ along the branch reads

$$\begin{bmatrix} J_Q \; J_\omega \\ t_{(i-1)}^T \end{bmatrix} t_{(i)} = \begin{bmatrix} 0 \\ 1 \end{bmatrix} \tag{20.24}$$

The last equation from (20.24) prevents the continuation procedure from turning back. The tangent vector is used to compute a prediction for the next step $(Q_{(i)}^{(0)}, \omega_{(i)}^{(0)})$ using the step length δ_s. Generally, the predicted value does not satisfy Eq. (20.21). Therefore a correction stage based on Newton's method is performed. In order to be able to deal with turning points, we seek corrections in a direction orthogonal to the tangent vector

$$\begin{bmatrix} J_Q \; J_\omega \\ t_{(i)}^T \end{bmatrix} \begin{bmatrix} \Delta Q^{(k+1)} \\ \Delta\omega^{(k+1)} \end{bmatrix} = \begin{bmatrix} -h(Q_{(i)}^{(k)}, \omega_{(i)}^{(k)}) \\ 0 \end{bmatrix} \tag{20.25}$$

with $Q_{(i)}^{(k+1)} = Q_{(i)}^{(k)} + \Delta Q^{(k+1)}$, $\omega_{(i)}^{(k+1)} = \omega_{(i)}^{(k)} + \Delta\omega^{(k+1)}$. Corrections are performed until the convergence criterion is satisfied.

20.4 Numerical Example

In this section, a numerical application of the method based on synthetic data is presented. The studied system consists of two coupled Duffing oscillators. The corresponding equations of motion are given by

$$\begin{aligned} \ddot{q}_1(t) + c\dot{q}_1(t) + kq_1(t) + \mu_1 q_1(t)^3 + d(q_1(t) - q_2(t)) &= p(t) \\ \ddot{q}_2(t) + c\dot{q}_2(t) + kq_2(t) + \mu_2 q_2(t)^3 + d(q_2(t) - q_1(t)) &= 0 \end{aligned} \tag{20.26}$$

where $\mu_1 = \mu_2 = k = 1, c = 0.1$ and $d = 5$. From Eq. (20.26), the nonlinearities are defined by the nonlinear coefficients μ_i, $g_i = q_i(t)^3$ $(i = 1, 2)$, $b_1 = [1, 0]^T$ and $b_2 = [0, 1]^T$. Therefore, the extended input vector reads $e(t) = [p(t), 0, q_1(t)^3, q_2(t)^3]^T$. The first mass is excited by a single band-limited (0–80 rad/s) normally distributed random signal (5000 points) repeated 8 times. Its root-mean-square (r.m.s.) value is equal to 3 N. Numerical integration of the equations of motion was performed using fourth order Runge-Kutta method. The last 5000 points of the result of the numerical integration, resampled at 200 rad/s, are used as input to generate the extended input vector. Remark that the input band was chosen to encompass the third harmonic of the highest natural frequency. The model order $n = 4$ is determined from the inspection of the singular value plot depicted in Fig. 20.2 with $i = 40$ block rows. A jump of four orders of magnitude between model order four and five is observed. Also, as shown in Fig. 20.2, an excellent agreement between the theoretical and identified FRF of the underlying linear system is observed.

Figure 20.3 displays the complex and frequency-dependent estimation of the nonlinear coefficients determined from the extended FRF [9]. Note that this step is unnecessary for the continuation procedure and only serves as an indicator of the quality of the identification. Effectively, a correctly estimated system should lead to an almost constant nonlinear coefficient over the frequency range of interest and an imaginary part several orders of magnitude below the real part. In this case, a variation of less than 1 % of the real part of the nonlinear coefficients in the frequency range of interest is observed. The imaginary parts are three and four orders of magnitude lower that the real parts for the first and second nonlinear coefficient, respectively.

The identified B_c matrix in the physical state-space domain, denoted $\tilde{B}_c$, computed using Eqs. (20.10), (20.13) yields

$$\tilde{B}_c = \begin{bmatrix} 0.016 & 0 & 0.016 & 0 \\ 0 & 0 & 0 & 0.016 \\ 0.997 & 0 & 0.998 & 0 \\ 0 & 0 & 0 & 0.998 \end{bmatrix} \tag{20.27}$$

The values of the nonlinear coefficients are close to the original model in Eq. (20.4). However, the structure of $\tilde{B}_c$ is not conform with the theoretical expectation, since undesired terms that are approximatively two orders of magnitude smaller than the nonlinear and the forcing coefficients are present in the first block row of $\tilde{B}_c$. The effect of these undesired terms can be apprehended by rewriting the identified physical state-space model into the physical space. The identified system reads

$$\begin{bmatrix} \dot{x}_1 \\ \dot{x}_2 \\ \dot{x}_3 \\ \dot{x}_4 \end{bmatrix} = \begin{bmatrix} 0 & 0 & 1 & 0 \\ 0 & 0 & 0 & 1 \\ -\tilde{k}-\tilde{d} & \tilde{d} & -\tilde{c} & 0 \\ \tilde{d} & -\tilde{k}-\tilde{d} & 0 & -\tilde{c} \end{bmatrix} \begin{bmatrix} x_1 \\ x_2 \\ x_3 \\ x_4 \end{bmatrix} + \begin{bmatrix} B_1 & 0 & B_2 & 0 \\ 0 & 0 & 0 & B_3 \\ \tilde{\mu}_f & 0 & \tilde{\mu}_1 & 0 \\ 0 & 0 & 0 & \tilde{\mu}_2 \end{bmatrix} \begin{bmatrix} p \\ 0 \\ q_1^3 \\ q_2^3 \end{bmatrix} \tag{20.28}$$

where the tildes denote the coefficients identified using the FNSI method and expressed in the physical state-space domain. The terms B_i ($i = 1..3$) denote the undesired terms of the $\tilde{B}_c$ matrix. Using the matrix C [which is the exact due to (20.11)], the reconstructed model in the physical-domain is written by

$$\begin{aligned} &\ddot{q}_1 + \tilde{c}\dot{q}_1 + \tilde{k}q_1 + \tilde{\mu}_1 q_1^3 + \tilde{d}(q_1 - q_2) - 3B_2 q_1^2 \dot{q}_1 = \tilde{\mu}_f p(t) + B_1 \dot{p}(t) \\ &\ddot{q}_2 + \tilde{c}\dot{q}_2 + \tilde{k}q_2 + \tilde{\mu}_2 q_2^3 + \tilde{d}(q_2 - q_1) - 3B_3 q_2^2 \dot{q}_2 = 0 \end{aligned} \tag{20.29}$$

It is seen that the term B_1 modify the excitation while the terms B_2 and B_3 constitute spurious nonlinearities corresponding to Van der Pol damping added to the identified model. These terms are conform with the assumed nonlinear basis functions and must be forced to zero in order to recover a coherent identified system.

The result of the numerical continuation is depicted in Fig. 20.4 for a forcing amplitude of $2N$. Solid and dotted lines correspond to stable and unstable periodic responses, respectively. Black and blue lines correspond to the theoretical and identified frequency response curves of the system, respectively. The circles and the squares represent fold and Neimark-Sacker bifurcations, respectively. Both responses of the theoretical and identified model were obtained using the continuation procedure. The frequency response curve of the identified model without and with the undesired terms B_i are depicted in the left and the right graph, respectively.

The frequency response curve of the identified model when the spurious terms (termed FNSI updated) have been removed matches almost exactly the theoretical predictions. Both fold and Neimark-Sacker bifurcations are identified in agreement with the theoretical prediction. On the contrary, as observed on the right plot, even if these spurious terms are small compared to the identified nonlinear coefficients, they lead to strongly erroneous results and therefore must be removed from $\tilde{B}_c$.

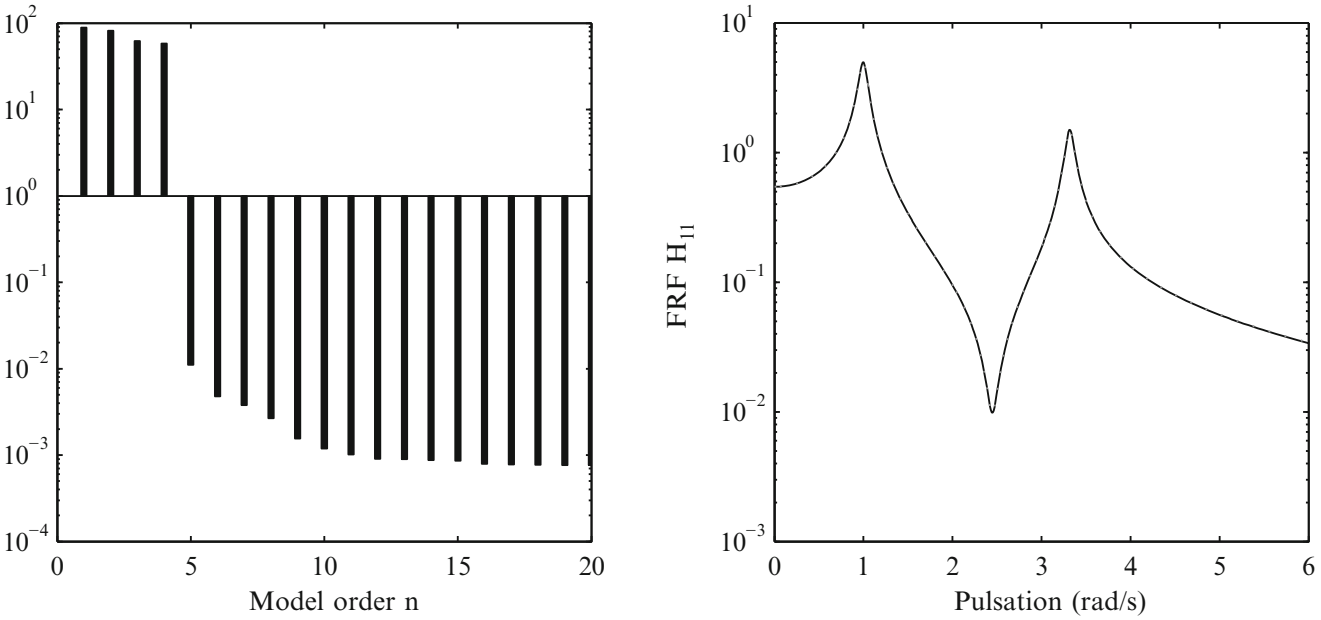

Fig. 20.2 *Left*: plot of the twenty first singular values with $i = 30$. *Right*: theoretical (*grey dotted line*) and identified (*black solid line*) FRF of the underlying linear system

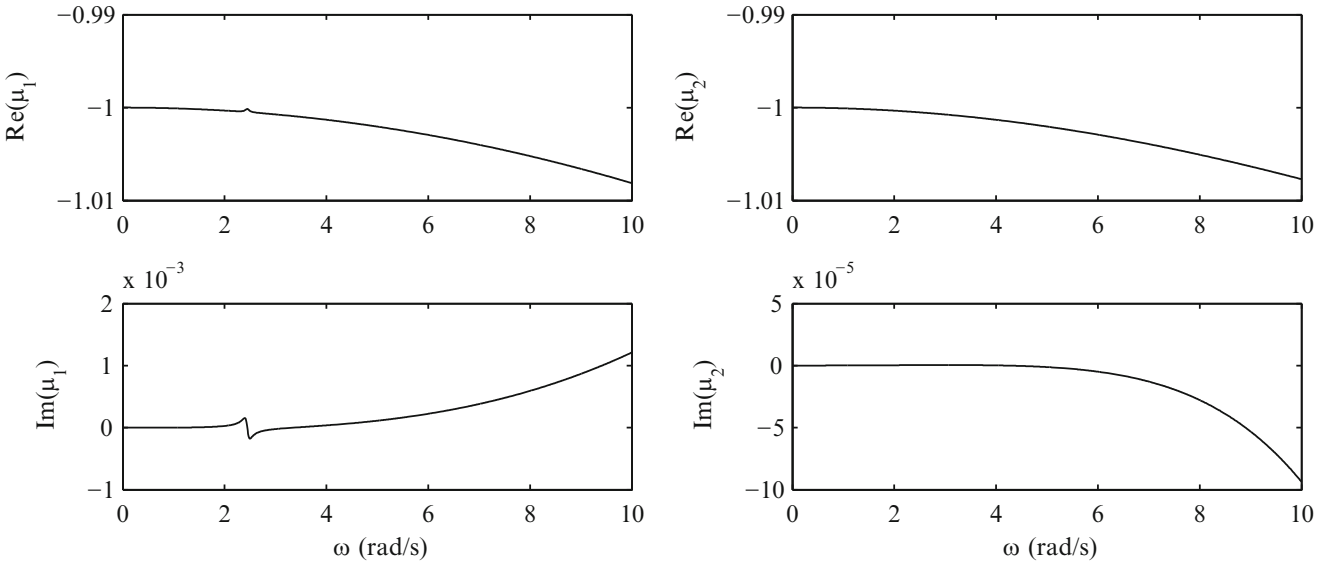

Fig. 20.3 Real and imaginary parts of the estimated nonlinear coefficients μ_1 and μ_2

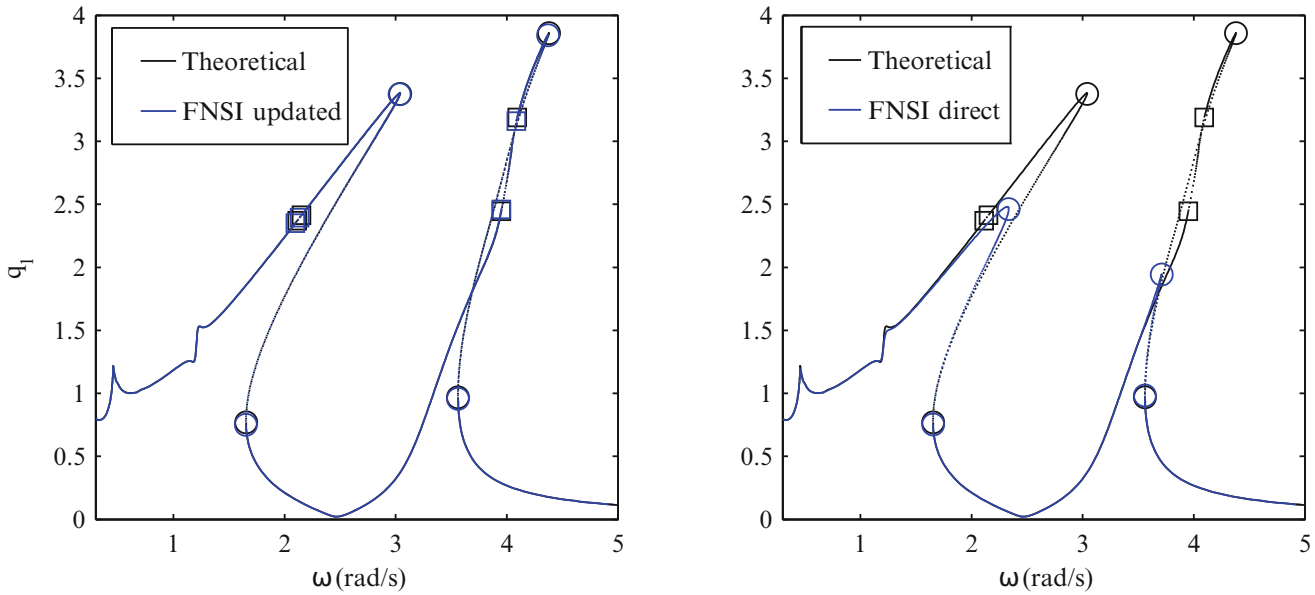

Fig. 20.4 Frequency response curves of the theoretical (*black*) and identified model (*blue*). *Left*: updated FNSI model. *Right*: original FNSI model

20.5 Conclusion

In this paper, an algorithm coupling the frequency nonlinear subspace identification method and a harmonic balance based continuation method for the simulation has been presented. The objective of this procedure is to obtain the nonlinear frequency response curves of a nonlinear system directly from random measurements. Since the identification procedure is carried out in the state space domain, the simulation is also performed in the state space domain, which prevents from reconstructing the identified model in physical space. An expression of the similarity transformation matrix which allows the identification of spurious nonlinearity has been presented. The method has been tested on a numerical application with a two degree of freedom Duffing oscillator. The theoretical and identified frequency response curves are in good agreement. The nature and location of the bifurcations is also recovered. The origin of the spurious terms in the identified matrix B_c has not been yet identified, which will be the object of further work.

References

1. Adams, D.E., Allemang, R.J.: A new derivation of the frequency response function matrix for vibrating non-linear systems. J. Sound Vib. **227**(5), 1083–1108 (1999)
2. Allgower, E.L., Georg, K.: Numerical Continuation Methods: An Introduction, vol. 13. Springer Science & Business Media, Berlin (2012)
3. Barillon, F., Sinou, J.-J., Duffal, J.-M., Jézéquel, L.: Non-linear dynamics of a whole vehicle finite element model using a harmonic balance method. Int. J. Veh. Des. **63**(4), 387–403 (2013)
4. Cameron, T.M., Griffin, J.H.: An alternating frequency/time domain method for calculating the steady-state response of nonlinear dynamic systems. J. Appl. Mech. **56**(1), 149–154 (1989)
5. Detroux, T., Renson, L., Kerschen, G.: The harmonic balance method for advanced analysis and design of nonlinear mechanical systems. In: Nonlinear Dynamics, vol. 2, pp. 19–34. Springer, Berlin (2014)
6. Ewins, D.J., Weekes, B., delli Carri, A.: Modal testing for model validation of structures with discrete nonlinearities. Philos. Trans. R. Soc. A **373**(2051), 20140410 (2015)
7. Garibaldi, L., Marchesiello, S., Bonisoli, E.: Identification and up-dating over the z24 benchmark. Mech. Syst. Signal Process. **17**(1), 153–161 (2003)
8. Kerschen, G., Worden, K., Vakakis, A.F., Golinval, J.-C.: Past, present and future of nonlinear system identification in structural dynamics. Mech. Syst. Signal Process. **20**(3), 505–592 (2006)
9. Marchesiello, S., Garibaldi, L.: A time domain approach for identifying nonlinear vibrating structures by subspace methods. Mech. Syst. Signal Process. **22**(1), 81–101 (2008)
10. McKelvey, T., Akçay, H., Ljung, L.: Subspace-based multivariable system identification from frequency response data. IEEE Trans. Autom. Control **41**(7), 960–979 (1996)
11. Noël, J.-P., Kerschen, G.: Frequency-domain subspace identification for nonlinear mechanical systems. Mech. Syst. Signal Process. **40**(2), 701–717 (2013)
12. Noël, J.-P., Kerschen, G., Foltête, E., Cogan, S.: Grey-box identification of a non-linear solar array structure using cubic splines. Int. J. Non Linear Mech. **67**, 106–119 (2014)
13. Van Overschee, P., De Moor, B.L.: Subspace Identification for Linear Systems: Theory — Implementation — Applications. Springer Science & Business Media, Berlin (2012)
14. Von Groll, G., Ewins, D.J.: The harmonic balance method with arc-length continuation in rotor/stator contact problems. J. Sound Vib. **241**(2), 223–233 (2001)

Chapter 21
Experimental Study of Isolated Response Curves in a Two-Degree-of-Freedom Nonlinear System

T. Detroux, J.P. Noël, G. Kerschen, and L.N. Virgin

Abstract In the present paper, the observation and characterization of isolated response curves (IRCs) are experimentally reported in the case of a nonlinear system consisting of two masses sliding on an horizontal guide. Transverse springs are attached to one mass to provide the nonlinear restoring force, and a harmonic motion of the complete system is imposed by prescribing the displacement of their supports. The existence of an IRC is related to a 3:1 internal resonance between the two modes of the system. The observed IRC is studied in detached and merged conditions using swept-sine excitations and system perturbations.

Keywords Isolated response curve • Internal resonance • Experimental observation • Two-degree-of-freedom system • Sine-sweep excitation • Perturbations

21.1 Introduction

Isolated response curves (IRCs) are an intriguing feature of nonlinear dynamics. They correspond to closed loops of solutions emerging in nonlinear frequency responses and which are, by definition, detached from the main response branch [1]. IRCs may thus go easily undetected in the analysis of the forced response of a nonlinear system, whether it be numerically employing classical continuation techniques, or experimentally applying sine-sweep excitations. However, an increase in forcing amplitude may cause the merging of the main branch and the IRC, resulting in dramatic frequency and amplitude shifts of the resonance location. This renders IRCs potentially dangerous in practice for engineers designing systems likely to operate in nonlinear regimes of motion [2, 3].

In [4], the authors investigated numerically a series of intrinsic features of IRCs, in particular their creation mechanism, the evolution of their bifurcations according to parameter variations and their basins of attraction. In the present paper, the observation and characterization of IRCs are experimentally reported in the case of a two-degree-of-freedom, base-excited mechanical system with nonlinear hardening springs. As it is conjectured that interactions between nonlinear modes underlie the existence of IRCs [5, 6], potential 3:1 internal resonances between the in-phase and out-of-phase modes of the system are specifically studied. Section 21.2 details the experimental setup of interest. In Sect. 21.3, the forced response of the setup to swept-sine excitations of various amplitudes is analyzed. The existence of an IRC is revealed through the sudden shift undergone by the resonance frequency of the in-phase mode. Perturbations are also applied to the system to observe the IRC when detached. Conclusions of the paper are summarized in Sect. 21.4.

21.2 An Experimental Two-Degree-of-Freedom System with Hardening Springs

The experimental setup consists of two masses sliding on an horizontal guide, as shown in Fig. 21.1a, b. The masses are connected together and to the ground through extension springs, whose lengths and stiffnesses determine the static equilibrium of the system. Motion of the masses is recorded by means of uniaxial accelerometers. Two transverse bungee

T. Detroux • J.P. Noël (✉) • G. Kerschen
Aerospace and Mechanical Engineering Department, Space Structures and Systems Laboratory, University of Liège, Liège, Belgium
e-mail: jp.noel@ulg.ac.be

L.N. Virgin
Nonlinear Dynamics Group, School of Engineering, Duke University, Durham, NC, USA

G. Kerschen (ed.), *Nonlinear Dynamics, Volume 1*, Conference Proceedings of the Society for Experimental Mechanics Series,
DOI 10.1007/978-3-319-29739-2_21

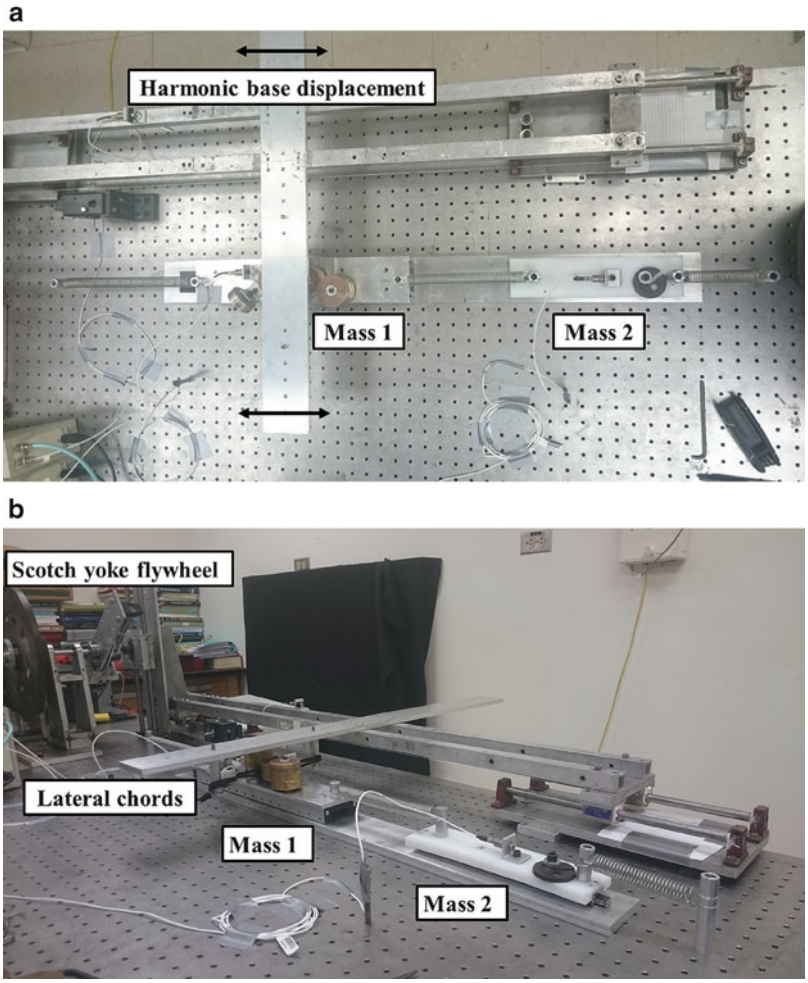

Fig. 21.1 Experimental setup. (**a**) Top view; (**b**) Side view

chords are attached to mass 1 (see Fig. 21.1b) to provide a nonlinear restoring force in the direction of motion. The displacements of the transverse spring supports are prescribed to impart motion to the two masses using a Scotch yoke flywheel [7]. The Scotch yoke converts rotational motion into an unidirectional harmonic displacement $d = D\sin(\omega t)$. The frequency $\omega/2\pi$ was limited to 2.7 Hz in the present experimental test rig, and the amplitude D was set manually, but could be accurately estimated.

The restoring force in the system caused by the transverse bungee chords can be theoretically written as [4]

$$F_{nl}(x) = 2k\left(1 - \frac{\lambda}{\sqrt{1 + (x/l)^2}}\right) \tag{21.1}$$

where $x = x_1 - d$ is the displacement of mass 1 x_1 relative to the displacement of the base d, k, l and l_0 denote the stiffness, length and natural length of the lateral springs, respectively, and $\lambda = l/l_0$ is the pre-stress parameter. The Taylor series expansion of Eq. (21.1) around 0 reads

$$F_{nl}(x) = (1 - \lambda)x + \frac{\lambda}{2l^2}x^3 + R_3(x). \tag{21.2}$$

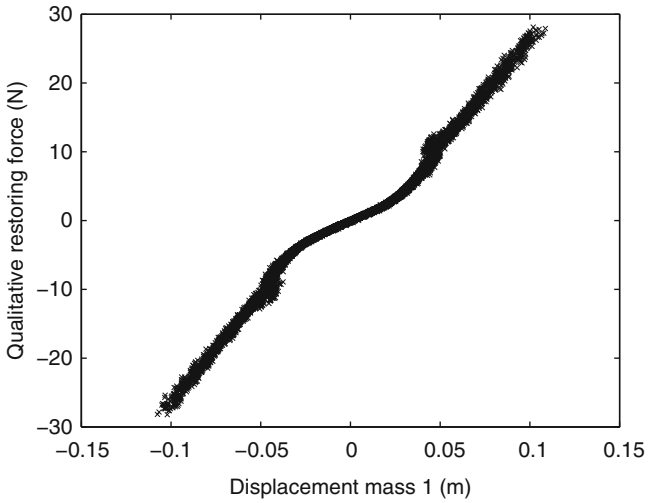

Fig. 21.2 Qualitative restoring force of the lateral spring connection

Equation (21.2) indicates that the third-order term in the restoring force increases with the pre-stress parameter λ. In the present work, transverse bungee chords with no pre-stress, i.e. $\lambda = 1$, were considered in order to facilitate the creation of IRCs, as suggested in [4]. Figure 21.2 shows a qualitative estimate of the restoring force in the system calculated using the restoring force surface (RFS) method [8], confirming the highly nonlinear behavior of the lateral spring connection.

The estimation of the linear resonance frequencies of the setup is central in this study, as the potential existence of IRCs is conditional upon their ratio [4, 5]. For that purpose, high-amplitude impacts were manually applied to the two masses, as illustrated in Fig. 21.3a. In this plot, three impacts on mass 2 are followed by three impacts on mass 1. The resulting free decays can be analyzed to extract resonance frequencies. This is achieved in Fig. 21.3b by plotting the wavelet transform of the acceleration measured on mass 1. The first three impacts mostly feature the second mode response around 6.45 Hz. No amplitude-dependence is noticed for this mode proving its linearity. Conversely, the in-phase mode of the system, clearly observed during the three final impacts, exhibits a strong, hardening dependence upon the amplitude of motion. For sufficiently large response amplitudes, its third harmonic is seen to coincide with the second mode frequency, which is a necessary condition for the creation of an IRC via a 3:1 modal interaction [4]. Focusing on the tip of the free-decay behavior of mode 1, its resonance frequency is estimated at 1.75 Hz, yielding a ratio of 3.7 between the two mode linear frequencies. This favorable ratio was achieved by tuning the masses of the setup, which were eventually fixed to 3.67 (mass 1) and 0.45 (mass 2) kg.

21.3 Experimental Forced Responses

In this section, the forced response of the system to swept-sine base excitations of various amplitudes is studied. Throughout the section, a sweep rate of 0.13 Hz/min is considered. Figure 21.4 depicts the sweep-up (in black) and sweep-down (in blue) responses of mass 1 for a base amplitude of 5.9 mm. Clear jumps down and up occur around 2.55 and 1.8 Hz, respectively. This large bi-stability region is a result of the strong nonlinearity in the system.

In Fig. 21.5, the displacement of mass 1 in response to swept-sine forcing profiles of increasing amplitudes, namely 5, 5.7, 5.9 and 6 mm, is represented. A dramatic modification of the first mode resonance frequency from 2.15 to 2.55 Hz, that is a nearly 20 % rise, is observed when increasing the base amplitude from 5.7 to 5.9 mm. This phenomenon, which also implies an increase of the response amplitude from 0.05 to 0.11 m, is to be attributed to the merging of an IRC with the main response branch. The merging mechanism of an IRC is discussed in detail in [4] through analysis and tracking of limit-point bifurcations.

It should be emphasized that the IRC merging in Fig. 21.5 occurs near 2.15 Hz, that is, in the neighborhood of the 3:1 interaction between the in-phase and out-of-phase modes of the system. This merging frequency region is closely studied in Fig. 21.6a–f. Figure 21.6a, b display the acceleration of mass 1 recorded for base displacements of 5.7 and 5.9 mm, respectively. In the former case, the IRC is detached, and the system jumps down to a low-amplitude solution around 2.15 Hz. In the latter case, the IRC is merged, and a high-amplitude solution is continuously attainable when sweeping

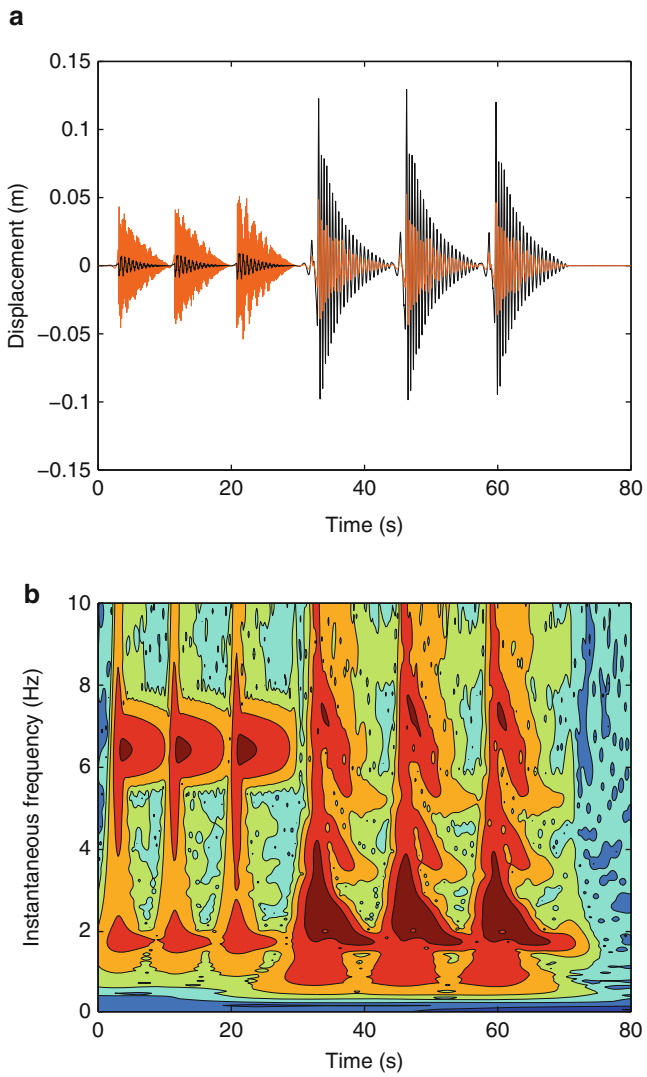

Fig. 21.3 Free-decay analysis. (**a**) Displacements measured on mass 1 (in *black*) and mass 2 (in *orange*) in response to three impacts applied to mass 2 followed by three impacts applied to mass 1. (**b**) Wavelet transform of mass 1 acceleration

up the excitation frequency. The corresponding accelerations of mass 2 plotted in Fig. 21.6c–d show that it undergoes greater acceleration levels than mass 1. Both mass accelerations also exhibit a strong beating behavior in the merging region in Fig. 21.6b, d. Finally, the existence of a 3:1 internal resonance in the system is highlighted in Fig. 21.6e and f, where the wavelet transform of Fig. 21.6c and d is plotted, respectively. A strong third harmonic component is clearly seen to emerge in the vicinity of the out-of-phase mode frequency.

The possibility the realize a periodic solution on the detached IRC by perturbing the system is eventually investigated. For that purpose, a base excitation of 5 mm and 2.38 Hz is considered in Fig. 21.7. Initially, the system vibrates at low amplitude. A series of perturbations is applied until the IRC is reached and the motion stabilizes at high amplitude. A subsequent sweep up on the IRC permits to determine its domain of existence. A jump down around 2.47 Hz locates the right tip of its stable part. The excitation is then swept back to 2.38 Hz, where new perturbations are applied. A sweep down along the stabilized IRC finally specifies the left tip of its stable part around 2.16 Hz.

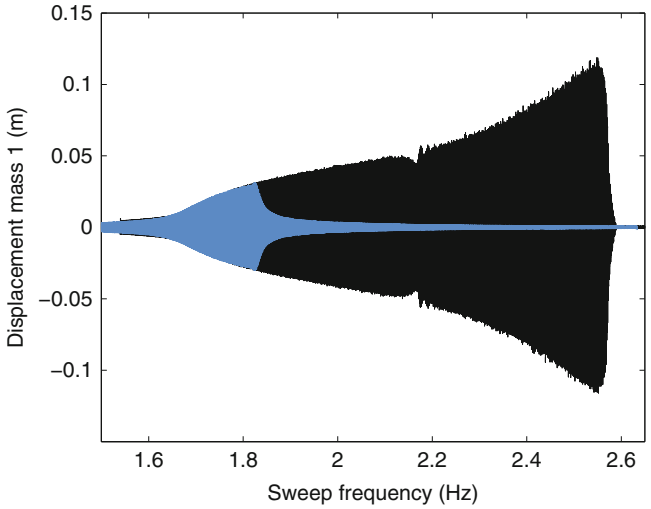

Fig. 21.4 Response of mass 1 to a swept-sine excitation with an amplitude of 5.9 mm. Sweep up (*black*); sweep down (*blue*)

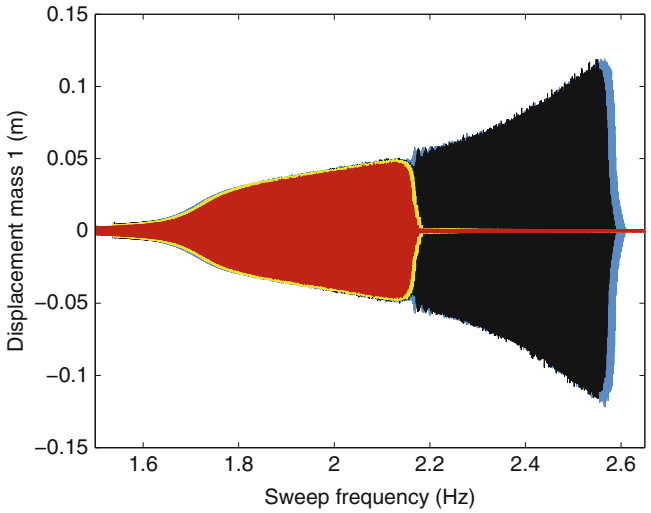

Fig. 21.5 Response of mass 1 to swept-sine excitations of increasing amplitude: 5 mm (*red*); 5.7 mm (*yellow*); 5.9 mm (*black*); 6 mm (*blue*)

21.4 Conclusions

The objective of this paper was to investigate experimentally isolated response curves (IRCs) in a two-degree-of-freedom nonlinear system. More specifically, the paper intended to relate the existence of an IRC to a 3:1 internal resonance between the two modes of the system. To this end, swept-sine base excitations of various amplitudes were applied to the system. A dramatic modification of the first mode resonance frequency was noticed for small excitation amplitude increments. This frequency jump is the likely manifestation of the presence of an IRC, which expands and merges with the main frequency response as the excitation amplitude is increased. Nonetheless, the results reported in this paper deserve further investigation. In particular, a reliable numerical model of the setup should be developed in order to achieve a complete understanding of the observed phenomena.

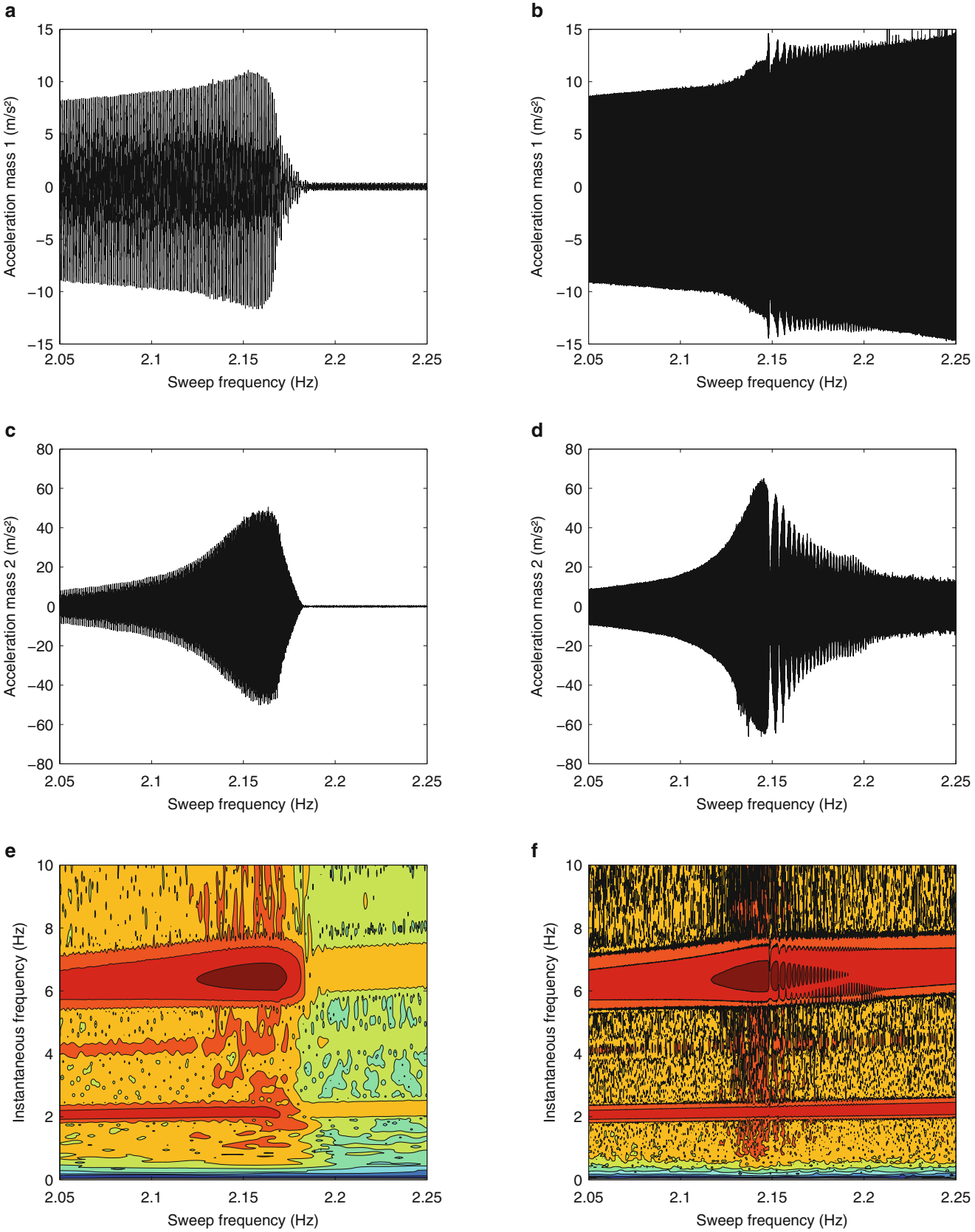

Fig. 21.6 Merging of the IRC. Accelerations of mass 1 (**a**–**b**) and mass 2 (**c**–**d**) and wavelet transform of mass 2 acceleration (**e**–**f**) in response to swept-sine excitations with amplitudes of 5.7 mm (first column) and 5.9 mm (second column)

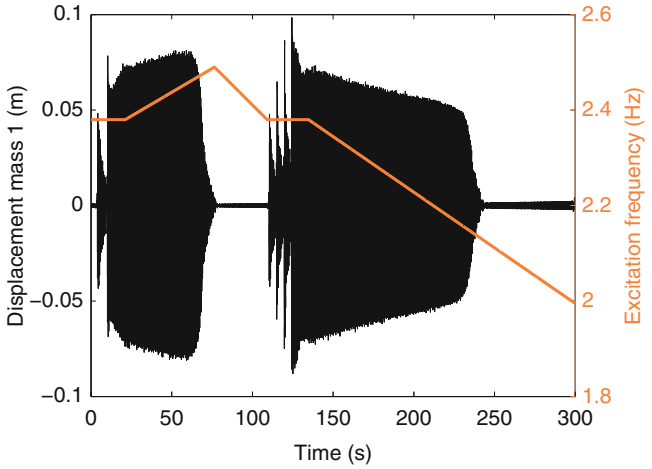

Fig. 21.7 Realization of periodic solutions on the detached IRC by perturbations. The amplitude and initial frequency of the base excitation are 5 mm 2.38 Hz, respectively. The *black* and *orange lines* depict the displacement of mass 1 and the excitation frequency, respectively

Acknowledgements The authors T. Detroux and G. Kerschen would like to acknowledge the financial support of the European Union (ERC Starting Grant NoVib 307265). The author J.P. Noël is a Postdoctoral Researcher of the *Fonds de la Recherche Scientifique—FNRS* which is also gratefully acknowledged.

References

1. Gatti, G., Brennan, M. Kovacic, I.: On the interactions of the responses at the resonance frequencies of a nonlinear two degrees-of-freedom system. Physica D **239**, 591–599 (2010)
2. Duan, C., Singh, R.: Isolated sub-harmonic resonance branch in the frequency response of an oscillator with slight asymmetry in the clearance. J. Sound Vib. **314**, 12–18 (2008)
3. Alexander, N., Schilder, F.: Exploring the performance of a nonlinear tuned mass damper. J. Sound Vib. **319**, 445–462 (2009)
4. Noël, J., Detroux, T., Kerschen, G., Virgin, L.: Isolated response curves in a base-excited, two-degree-of-freedom, nonlinear system. In: Proceedings of the ASME 2015 International Design Engineering Technical Conferences & Computers and Information in Engineering Conference (IDETC/CIE), Boston, MA (2015)
5. Kuether, R., Renson, L., Detroux, T., Grappasonni, C., Kerschen, G., Allen, M.: Nonlinear normal modes, modal interactions and isolated resonance curves. J. Sound Vib. **351**, 299–310 (2015)
6. Hill, T., Green, P., Cammarano, A., Neild, S.: Fast Bayesian identification of multi-mode systems using backbone curves. J. Sound Vib. (2015, in press)
7. Virgin, L.: Introduction to Experimental Nonlinear Dynamics: A Case Study in Mechanical Vibration. Cambridge University Press, Cambridge (2000)
8. Noël, J., Renson, L., Kerschen, G.: Complex dynamics of a nonlinear aerospace structure: experimental identification and modal interactions. J. Sound Vib. **333**, 2588–2607 (2014)

Chapter 22
Nonlinear Response of a Thin Panel in a Multi-Discipline Environment: Part I—Experimental Results

T.J. Beberniss, S.M. Spottswood, R.A. Perez, and T.G. Eason

Abstract High-speed aircraft structures are susceptible to the extreme and transient effects of the associated aerodynamic environment. These structures can experience a myriad of limit states—yield, fatigue, creep, buckling, and the response is very often path-dependent. Hypersonics, defined as flight speeds greater than Mach 5 (Heppenheimer, NASA Technical Report, NASA SP-2007-4232, September 2007) where aerodynamic heating drives the analysis and design, often causing appreciable structural concerns, is a flight regime with very little practical experience. While the NASA Space Shuttle Orbiter and other space-access vehicles routinely transit the Mach 5 barrier, long-duration air-breathing flights represent but a scant portion of past flight-test programs. As a result, the aerospace industry accounts for the associated uncertainties in the structural response through overly-conservative, and often program-deleterious, design assumptions. The USAF Research Laboratory, Structural Sciences Center (SSC), is investigating and developing analysis methods to predict the changing, nonlinear response of hypersonic hot-structures; however, there is a lack of relevant flight-test and experimental data useful for validating these developing structures-centric methods. The SSC recently began a series of thorough wind-tunnel experiments to provide quality, full-field experimental data for a simple, clamped nominally flat panel exposed to supersonic flow, shock boundary-layer interactions (SBLI) and heated flow. External heating sufficient to buckle the test article during supersonic wind tunnel experiments is being explored. Early results are presented in the present study. Additionally, wind tunnel conditions will be sought that lead to panel snap-through dynamics. The present study documents the evolution of the experiments, emphasizing the nonlinear response of the panel in preparation for upcoming wind-tunnel experiments. Also discussed are the characteristics of the experimental conditions leading to the nonlinear structural response, and the full-field displacement, pressure and thermal results necessary for model validation. Part II of this study will present the results of a numerical study of the same structure in the supersonic environment.

Keywords Hypersonics • Thermal buckling • Nonlinear • Dynamics • Aeroacoustics • Digital image correlation

22.1 Introduction & Background

High-performance, extreme-environment [2] and hypersonic hot-structures are exposed to severe thermal gradients. When combined with broadband boundary layer and engine exhaust noise, the results can be severely life-limiting. The structural response to this combination of loading is often counter-intuitive underlying the nonlinear nature of the problem. In Fig. 22.1, the aft region of a notional, reusable hypersonic vehicle is highlighted, where this combination of aerodynamic, thermal and flight-loading leads to challenging structural design problems [3]. The relatively small aircraft region shown in Fig. 22.1 exhibits a thermal gradient of nearly 370 °C (700°F). This region has become a point of intense study, and the Panel 1 structure identified in Fig. 22.1 is currently being manufactured for testing. A finite element model (FEM) of that Panel 1 test article is shown in Fig. 22.2, with expected test thermal gradients for one test condition. Of course these are only single trajectory analysis/test points, while the loading and resulting structural response are largely transient throughout the trajectory. Capturing the transient and combined loading in a laboratory setting is a major focus of SSC research.

This aircraft region also has the added complication of having a nearby control surface which when deflected can cause a shock boundary-layer interaction and fuselage impingement. The shock impingement scenario is a troublesome one for aerospace designers because it amplifies both the aerodynamic loading and heating, and the conditions leading to such a loading scenario are difficult to identify making a conservative design approach necessary. Additionally, and perhaps most interesting from a dynamic perspective, the impinging shock will also contain a relatively low frequency oscillatory

T.J. Beberniss • S.M. Spottswood (✉) • R.A. Perez • T.G. Eason
Air Force Research Laboratory, Structural Sciences Center, 2790 D Street, Building 65, WPAFB, OH 45433-7402, USA
e-mail: stephen.spottswood.1@us.af.mil

G. Kerschen (ed.), *Nonlinear Dynamics, Volume 1*, Conference Proceedings of the Society for Experimental Mechanics Series,
DOI 10.1007/978-3-319-29739-2_22

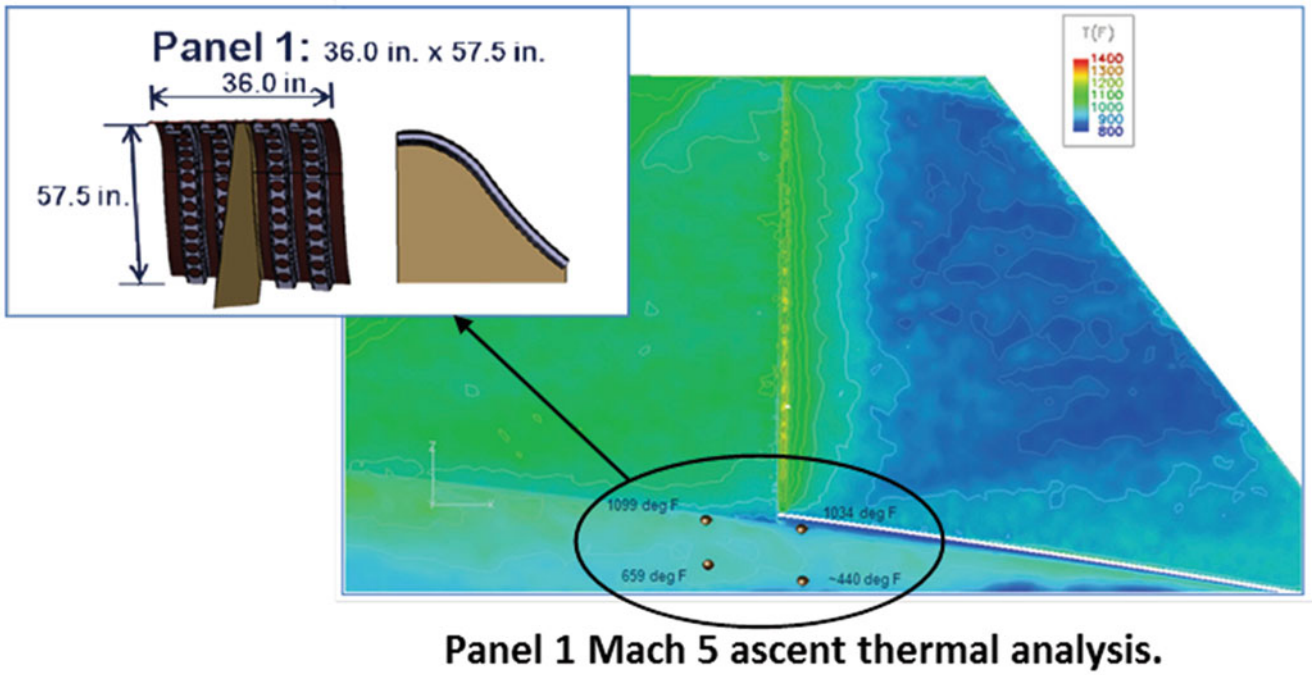

Fig. 22.1 Thermal analysis of Lockheed-Martin hypersonic vehicle extreme-environment tail structure

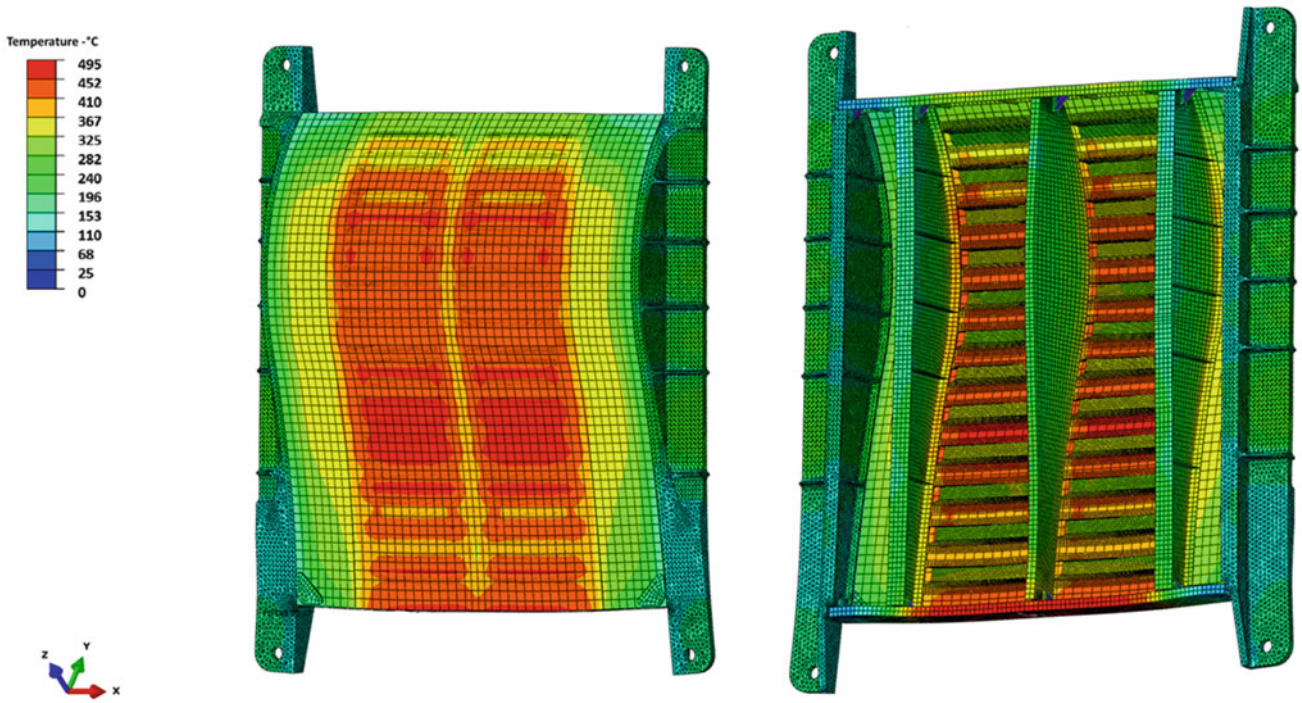

Fig. 22.2 Representative test article from the aircraft region denoted in Fig. 22.1, (**a**) Front-side thermal gradients and (**b**) back-side thermal gradients through the substructure

component that may even couple with the structural panel dynamics. In Fig. 22.3, Beresh, Clemens and Dolling note the case of a shock foot oscillation upstream of a 28° compression ramp [4, 5]. The surface pressure time history is obviously unsteady, with oscillation frequencies between 1 and 10 kHz, and possibly even lower, increasing the likelihood of damaging fluid-structural coupling.

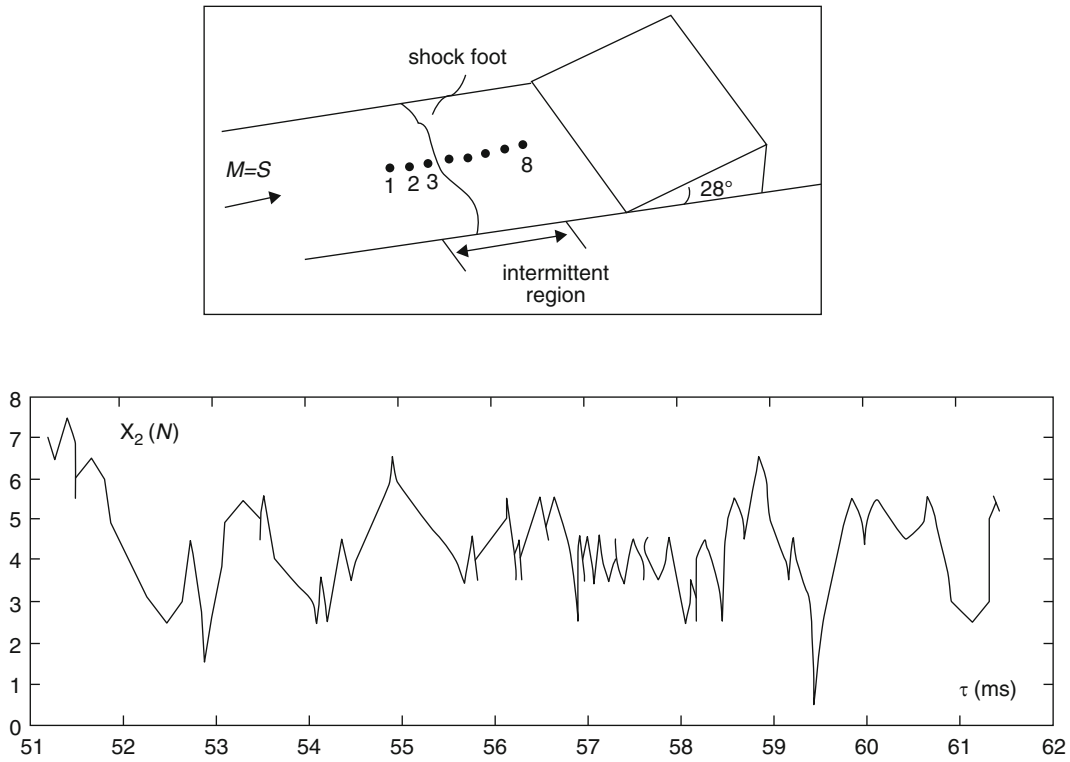

Fig. 22.3 Shock foot unsteadiness at Mach 5 (used with permission [4, 5])

Fig. 22.4 SR-71 skin panel buckling

In addition to the extreme aerodynamic loading, the combination of aeroheating and structural boundary conditions often conspire to induce aircraft panel deformation or even buckling. Aerospace structures are generally thin-gauge with stiffener/sub-structure spacing determined to best balance weight and strength/stiffness requirements. Understanding what loading and boundary condition combinations lead to excessive panel deformation is a challenge. In Fig. 22.4, the titanium underside of the SR-71 is shown, with appreciable waviness. It is not known whether this deformation, and the impact to local heating, e.g., the state of the boundary layer and vehicle drag for instance, was ever considered in the vehicle design.

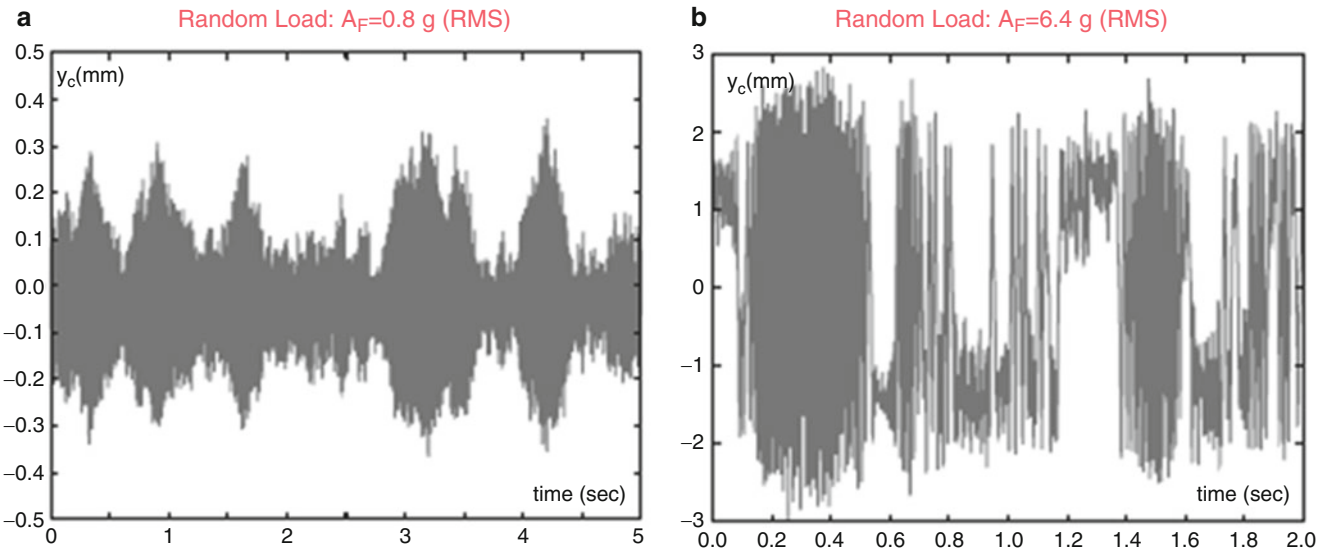

Fig. 22.5 Post-buckled beam response to random loading: (**a**) single well, and (**b**) cross-well behavior [6]

Once an aerospace panel deforms beyond a buckled state, it is susceptible to co-existing or snap-through type response. In Fig. 22.5, Wiebe and Spottswood investigated this nonlinear behavior using a post-buckled, clamped-clamped beam as a surrogate for constrained aerospace structures [6]. In the paper, the authors predicted the system embedding dimension using a novel approach to the method of false nearest neighbors (FNN). The embedding dimension, itself a function of the system response type, i.e., single-well or cross-well dynamics, provides guidance towards assembling a nonlinear reduced order model (NLROM). More on the coupling and NLROM modeling aspects are discussed in [7] and will be discussed in Part II of this study [8].

All of these scenarios describe conditions that aerospace analysts must account for when designing hot-structures for hypersonic vehicles. Unfortunately, aerothermoelastic analysis methods are largely relegated to research groups, and a quick review of past hypersonic programs will underscore the often untenable conservative design approach that industry designers must take without methods that can capture coupled and nonlinear responses. In response, the SSC has embarked on a multi-year experimental effort to (1) study the response of a simple, compliant panel to turbulent/SBLI, (2) develop and/or modify full-field experimental techniques to simultaneously measure the unsteady pressure and dynamic response, and (3) refine and develop an experimental dataset for the validation of aerothermoelastic analysis techniques. In addition to these three goals, the SSC is also intent on exploring the experimental conditions that would allow for the study of interesting, nonlinear behavior like the described post-buckled response.

22.2 Experimental History and Overview

The compliant panel, wind tunnel experiments are being conducted in the AFRL Aerospace Systems Directorate large-scale RC-19 supersonic combustion research cell [9]. The RC-19 facility is a continuous flow wind tunnel designed to study the mechanisms that govern the mixing and combustion process for supersonic combustor geometries. The facility was modified starting in 2011 to accommodate the present, and ongoing, series of aerothermoelastic experiments. A sectional view of the tunnel arrangement in its present form is shown in Fig. 22.6.

All of the testing was conducted at Mach 2.0, free-stream dynamic pressures (q_∞) of 61.7, 91.4, and 123 kPa, and total pressures of 172, 255, and 345 kPa. Free-stream and stagnation conditions are referenced to the tunnel nozzle exit. The Mach 2 nozzle is located upstream of the test section, while the test section consists of interchangeable walls that can be configured to meet a variety of experimental requirements.

In the first year of testing, the tunnel was modified to accommodate the compliant test article and a shock generating wedge that could be raised continuously from flush with the tunnel bottom surface to an angle of 10°. The test article and frame were manufactured from AISI 4140 alloy steel. The dimensions of the frame were 305 mm × 152 mm × 12.7 mm. The 0.635 mm panel specimen was bonded to the frame, leaving 254 mm by 127 mm for the compliant panel specimen.

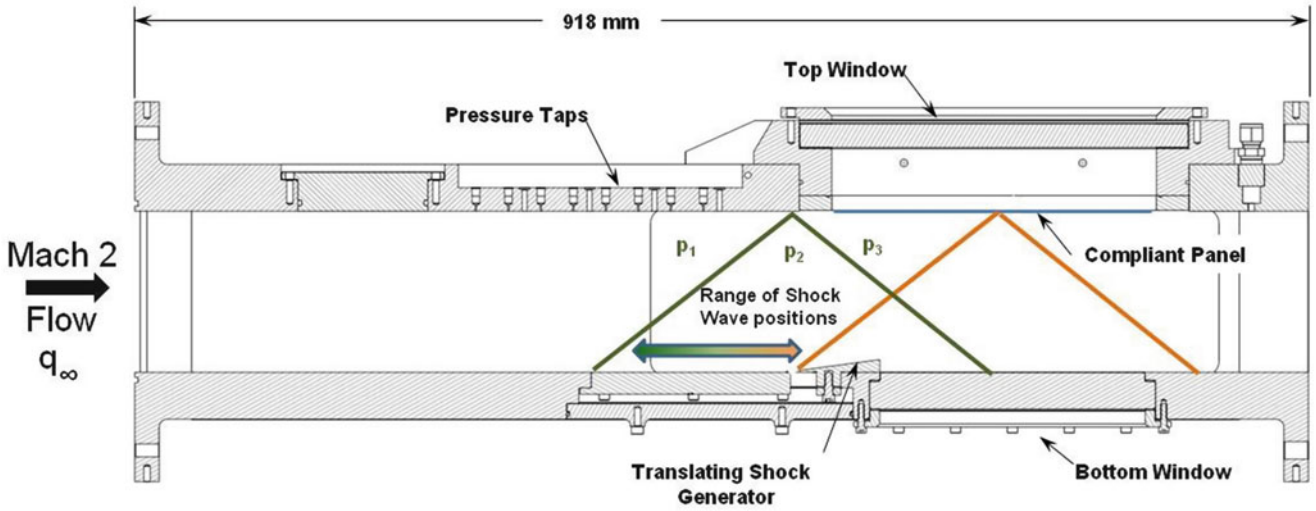

Fig. 22.6 RC-19 tunnel test-section [10]

The flexible panel specimen was designed so that an appreciable number of the structural dynamic modes would be below 1000 Hz, just like a traditional aircraft panel. To accommodate this test article arrangement, the RC-19 top tunnel test section was replaced with three-sections. The first section, containing pressure ports, was located upstream of the test article. The second section included the compliant panel. The last section connected the modified test section to the tunnel exhaust section and, importantly, was ported to a cavity with the top window (see Fig. 22.6) behind the compliant panel. These pressure ports were added to the top section of the tunnel wall downstream of the compliant panel to equalize the pressure between the panel and the top window. Equalization of the pressure was necessary to prevent yielding of the panel during tunnel start-up. The top window allowed for the use of 3D Digital Image Correlation (DIC) to obtain the full field displacements of the panel during testing. The sides of the tunnel also contained large windows to allow for pressure sensitive paint (PSP) illumination and implementation of a shadowgraph set-up to visualize the flow over the test panel. During testing, and to characterize the fluctuating pressure on the compliant panel, a fast reacting pressure sensitive paint was applied to the flow side.

The experimental procedure, described in greater detail in [11], began as follows. First the exhaust section was used to reduce the tunnel pressure to approximately 0.2 atm, and then the tunnel was started by allowing an inflow of air and setting the inlet total pressure to 2.65 atm. This resulted in a static pressure on the panel of 0.34 atm with the shock generator at 0°. The inflowing air was generally unheated thus creating a static temperature of −112 °C and panel equilibrium temperature of 0.5 °C. The frame and panel temperatures were monitored at single locations each on the compliant panel and frame throughout the test using K-type thermocouples. Test measurements did not begin until the differential temperature between the frame and test panel, initially at room temperature, reached 6.5 °C. The temperature difference resulted in a tensile preload on the panel, slightly altering the dynamic response. Once a stable temperature difference was achieved, the DIC cameras were triggered and images were recorded for 20.8 s at a sampling frequency of 5 kHz. The PSP was recorded for 5 s at 500 Hz. At the same time, the laser vibrometry data and strain gage data were recorded on a separate data acquisition system for 60 s at a sampling rate of 10 kHz. The shock generator angle was increased in 2° increments, and the process was repeated until the shock generator reached 10°. The boundary layer thickness without the shock generator is approximately 7.6 mm where the flow first meets the panel and grows to 10.2 mm at the end of the panel.

Some changes were necessary for the second year of testing. First, the frame and panel were machined from a single block of ANSI 4150 alloy steel. A panel/frame bond-line failure during the first year of test spurred this redesign. This time the integral frame/test panel was machined from a steel block leaving the same frame/specimen dimensions as in the first year of testing. At the same time, a rigid 12.7 mm control specimen was also procured. A window was added to the bottom wall test section to allow for viewing the PSP on the flow-side surface of the compliant panel. One other major change to the testing set-up was the move from a variable angle shock generator to a fixed, 8° angled wedge. The shock generator was placed in the bottom wall of the tunnel turning the flow, resulting in an oblique shock-wave angle of 39° emanating from the tunnel bottom wall. The shock generator could translate 170 mm in the flow direction allowing the shock to impinge from the compliant panel leading edge to near the panel mid-point as shown in Fig. 22.6. Additional lighting was added to the test so that the high-speed camera dedicated to the PSP measurement could sample at a higher frequency. This improvement allowed for both longer PSP measurement and a greater sampling frequency. Specifically, the cameras used for the DIC and

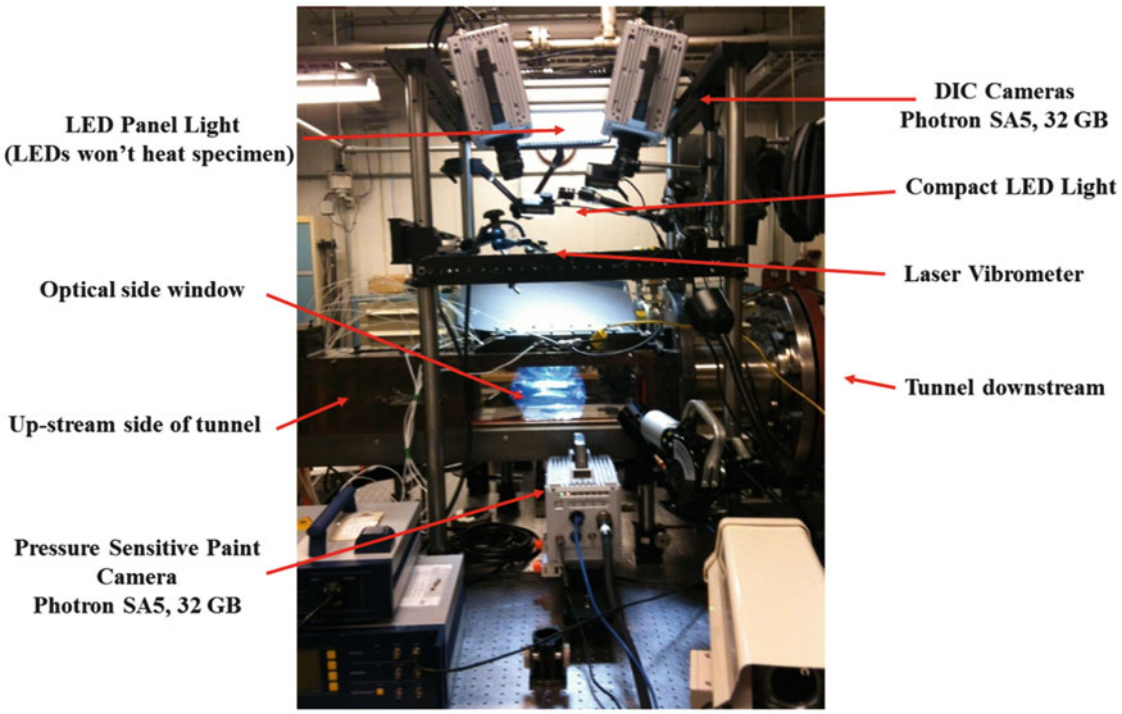

Fig. 22.7 Experimental set-up for second wind tunnel entry in 2012 [10]

PSP (Photron SA5) were triggered simultaneously and images are recorded for approximately 22.5 s at a sampling frequency of 4 kHz for the DIC and 14.5 s at 4 kHz for the PSP images. The PSP sampling was a significant improvement over the previous year of testing. Again, laser vibrometry data and strain gage data are recorded for 60 s sampled at 20 kHz. The tunnel test set-up, with the myriad of cameras, one Litepanel 1 × 1 Bi-Focus LED lights (305 mm × 305 mm, 1152 LED bulbs) for the DIC measurements, and the dual-beam Polytec OFV-552 laser-Doppler vibrometer (LDV), is shown in Fig. 22.7 [10].

In the upcoming series of RC-19 experiments, planned for the winter of 2016, several important changes will be made to this already complex arrangement. Great care will be taken to characterize the flow environment, including a boundary-layer study using a rigid article and moveable rake. The boundary layer height will be measured at two locations along the panel length and at one position near the tunnel wall to quantify edge/corner effects. New high-speed Photron SA-Z DIC cameras with increased memory (from 32 to 64 GB) were purchased that allow for an increase in sampling rate, longer time records, less required lighting, and a 4X reduction in download time. New rigid test articles were also fabricated that will provide discrete, high speed Kulite and PCB pressure transducer measurements, providing a direct comparison with simultaneous PSP measurements. It was noted in a companion, computational study [12], that knowledge of the full-field temperature is necessary, and so temperature sensitive paint (TSP) and PSP will be applied to the flow-side of the test panels. Originally, full-field temperature was to be measured using a forward looking infrared camera (FLIR), but the quartz window above the specimen in Fig. 22.6 significantly filters the IR signature (see Fig. 22.8).

Narrower test panels (102 mm versus the original 127 mm wide ones) have also been prepared to allow for greater understanding of the tunnel corner/wall effects on the panel. Specifically, are there appreciable tunnel corner effects, and can the mean pressure loading be assumed uniform (two-dimensional) across the panel surface? This level of loading characterization is important for validation purposes. A fourth camera will be used to record the SBLI and panel interactions via high-speed shadowgraph. Finally, the cavity back pressure will be manipulated to reduce the tunnel/cavity pressure differential, and external heating via halogen lamps will be applied, to create interesting post-buckled and snap-through dynamic conditions. Higher-temperature experiments were conducted during the last series of RC-19 tunnel experiments, and panel buckling was observed. Unfortunately, the heated flow quickly destroyed the PSP and so the dynamic surface pressure was not measured.

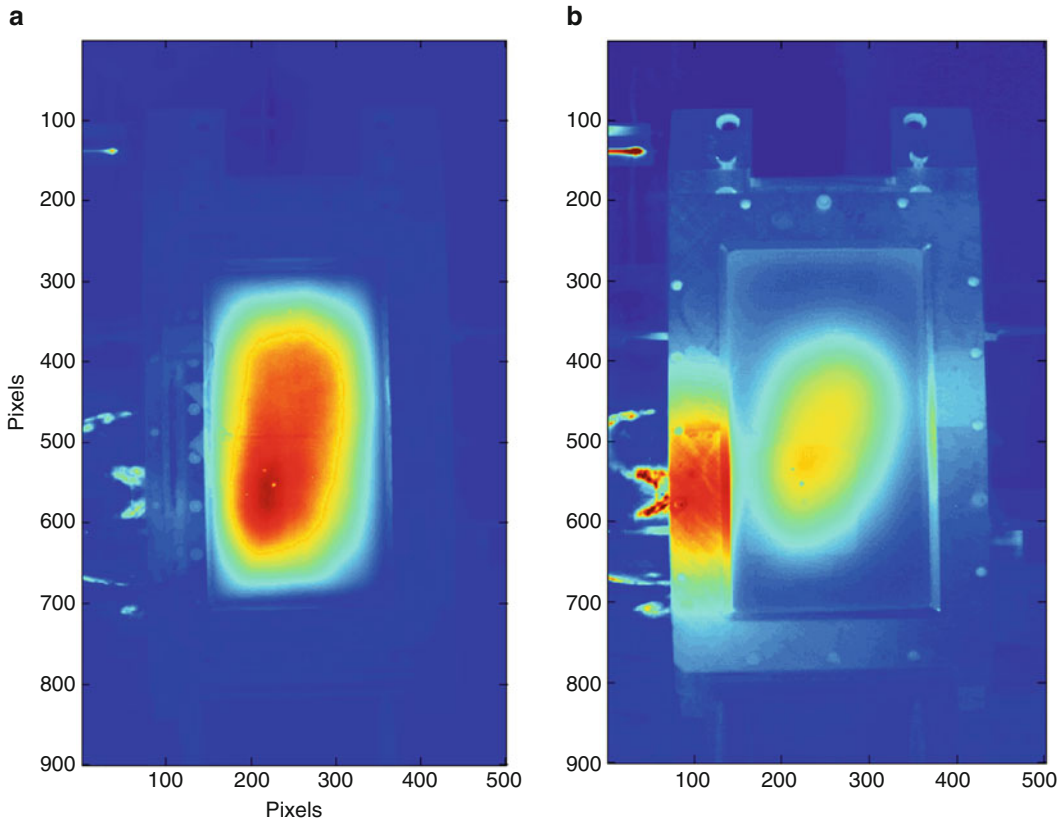

Fig. 22.8 Full field measurement of panel temperature using FLIR: (**a**) without the quartz window, and (**b**) with the quartz window. Note that the temperature scales are different and that the maximum panel temperature in (**a**) is 77 °C and approximately 22 °C in (**b**) due to the IR filter effect of the quartz window

To prepare for this last test objective, the exploration of interesting post-buckled nonlinear behavior, an integral frame/panel test specimen from the second year of testing was used to study panel buckling and post-buckling behavior. This thermal testing was also used to assess the halogen lamp heating arrangement required for panel buckling during RC-19 experiments. This thermal experimental setup for the heating test is shown in Fig. 22.9. The panel is bolted to a section of the RC-19 tunnel wall to better represent the upcoming wind tunnel experiments. Two Lowel Pro-light TM halogen lamps were used to heat the surface of the panel. As shown in Fig. 22.8, the heat from the lamps led to a non-uniform temperature field on the surface of the panel; however, the panel/frame temperature differential did lead to buckling. The full-field static deflections were measured using a pair of high-resolution (6 Megapixel) Allied Vision Prosilica GT 2750 DIC cameras.

The full-field temperatures were measured using a high-resolution FLIR Systems SC6000 infrared camera shown in Fig. 22.9. The accumulated experience from the two previous RC-19 wind tunnel experiments, and the more recent thermal experiments, are providing the foundation for the upcoming, final RC-19 experiments. A sampling of results, emphasizing the nonlinear nature of the experiments, will be presented and discussed in the following section.

22.3 Preliminary Results and Discussion

The principal purpose of the experiment was to measure the effects of the turbulent boundary layer and shock impingement on the response of the panel specimen while simultaneously recording the full-field surface pressure and panel dynamic displacement. It is the goal of the SSC to provide a relevant experimental data set for the validation of this class of aero-structural problem. It has also always been the intent to explore interesting nonlinear experimental behavior, and the following examples elucidate this last objective. In the first year of testing, two experimental configurations demonstrate both the sensitivity of the panel response to SBLI and the potential for the panel to behave nonlinearly. In Fig. 22.10, two different experimental cases are examined, where the shock generator is first flush with the tunnel bottom wall, e.g., no SBLI effect, and

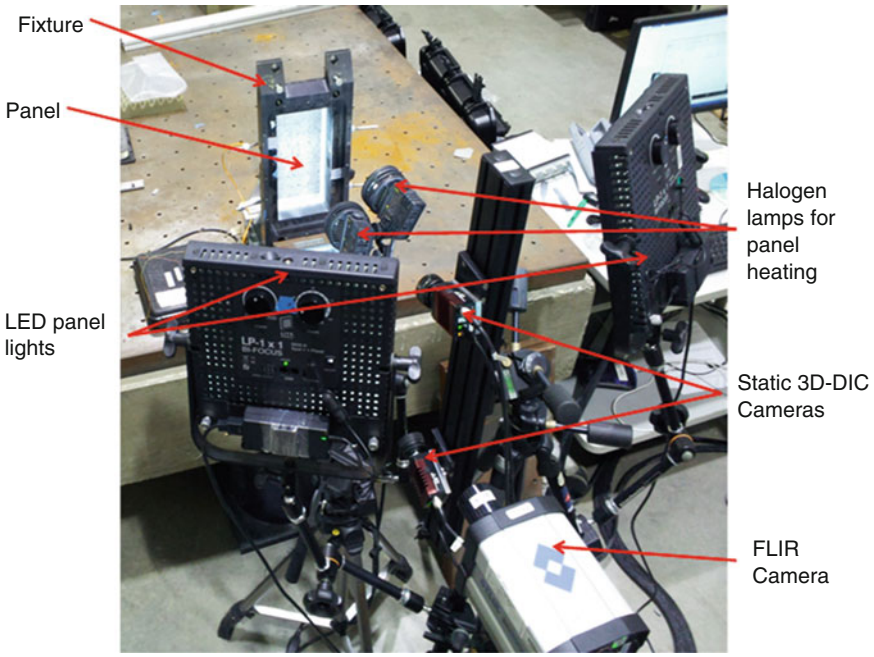

Fig. 22.9 Laboratory testing arrangement for static buckling test [7]

then raised to 10°. Observe in Fig. 22.10(a) the marked difference in the dynamic displacement due to loading changes caused by the impinging shock. In Fig. 22.10(b) the displacement power spectral density (PSD) exhibits all the signs of a hardening geometric nonlinearity—the positive shift in frequency and the broadening of the response peaks in the frequency domain. The frequency broadening stems from the stochastic (turbulent boundary layer) input to a structural system where stiffness is a function of displacement. Finally, in Fig. 22.10(c, d), images of the surface pressure (PSP) for the no-shock/shock cases are included to show the spatially disparate pressure loading. These PSP images were captured by looking through a window in the tunnel sidewall, thus the skewed perspective. In the second year of testing a window was added to the bottom tunnel wall and the images were much less skewed.

Next, consider a case (Fig. 22.11) from the second year of testing, where the panel response to SBLI and heated flow conditions was studied using a fixed 8° shock generator. In Fig. 22.11(a), the panel center displacement time history is shown for both heated and unheated flow conditions. The corresponding displacement PSD is displayed in Fig. 22.11(b). The heated wind tunnel flow quickly overwhelmed the PSP and so the surface pressure image of Fig. 22.11(c) is for the unheated case only. Interestingly, the panel center displacement PSD of the post-buckled panel does not differ appreciably from the unheated/non-buckled case. In the heated flow condition, the panel was buckled 2 mm (approximately 3 panel thicknesses) into the flow; however, the dynamic response is clearly not as great as was exhibited in previous experiments.

One new variable in the upcoming experiments will be the ability to adjust the cavity back pressure to accentuate/tune the panel dynamic response. Ideally, the conditions leading to dynamic snap-through will also be identified. To that end, new external sources of heating are being explored to (1) exert greater control over the magnitude of panel buckling, and (2) continue to use the PSP (and TSP) during the experiments. The results of this early experimentation can be seen in Fig. 22.12, which displays (a) the full-field temperature field and (b) the state of the panel (displacement) from nearly 80 °C to room temperature. Full-field DIC images of the panel displacement field correspond to several discrete temperature points are also denoted in Fig. 22.12(b). These results were obtained by first heating the panel using the halogen lamps and associated testing arrangement shown in Fig. 22.9, and then taking DIC and FLIR images as the panel cooled to room temperature. The panel is initially (nominally) flat but the effect of imperfections can be observed by considering the panel center displacement (black curve), of Fig. 22.12(b). In contrast to a perfectly-flat panel reaching a critical point beyond which symmetric buckling occurs, the imperfect panel deflects with temperature beyond the critical point until another stable, asymmetric equilibrium is realized. A good discussion of this very issue for panel buckling/acoustic experiments is discussed by Murphy [13]. At maximum temperature (approx. 80 °C) the panel did exhibit multiple (asymmetric) stable equilibria during the experimentation and so had reached the point where the secondary branch, described by Murphy, had appeared.

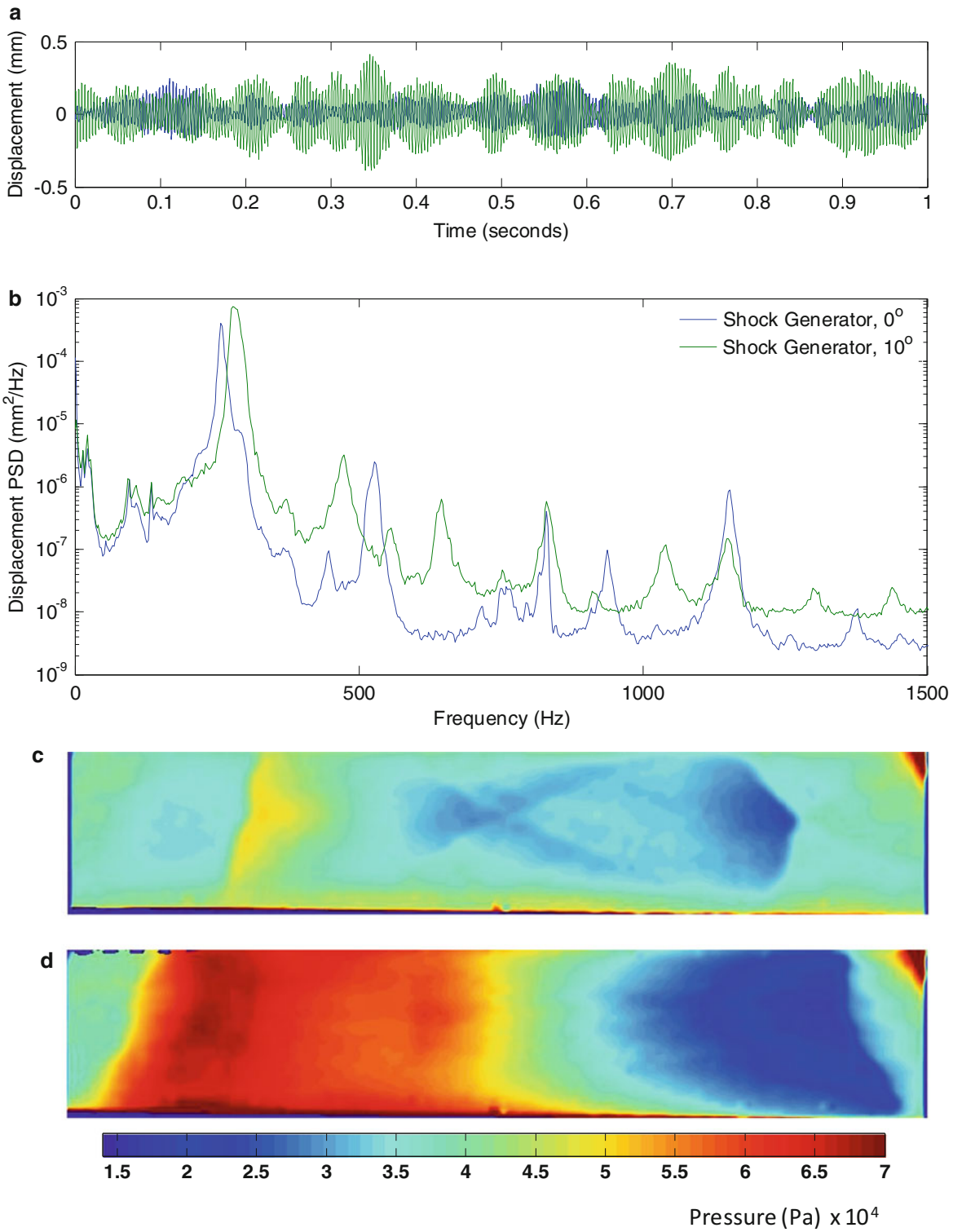

Fig. 22.10 Year 1 RC-19 experimentation showing impact of shock generator setting, flush (0°) and 10° (SBLI): (**a**) panel center displacement time history, (**b**) displacement PSD, and accompanying surface pressure (PSP) for (**c**) shock generator at 0° and (**d**) shock generator at 10°

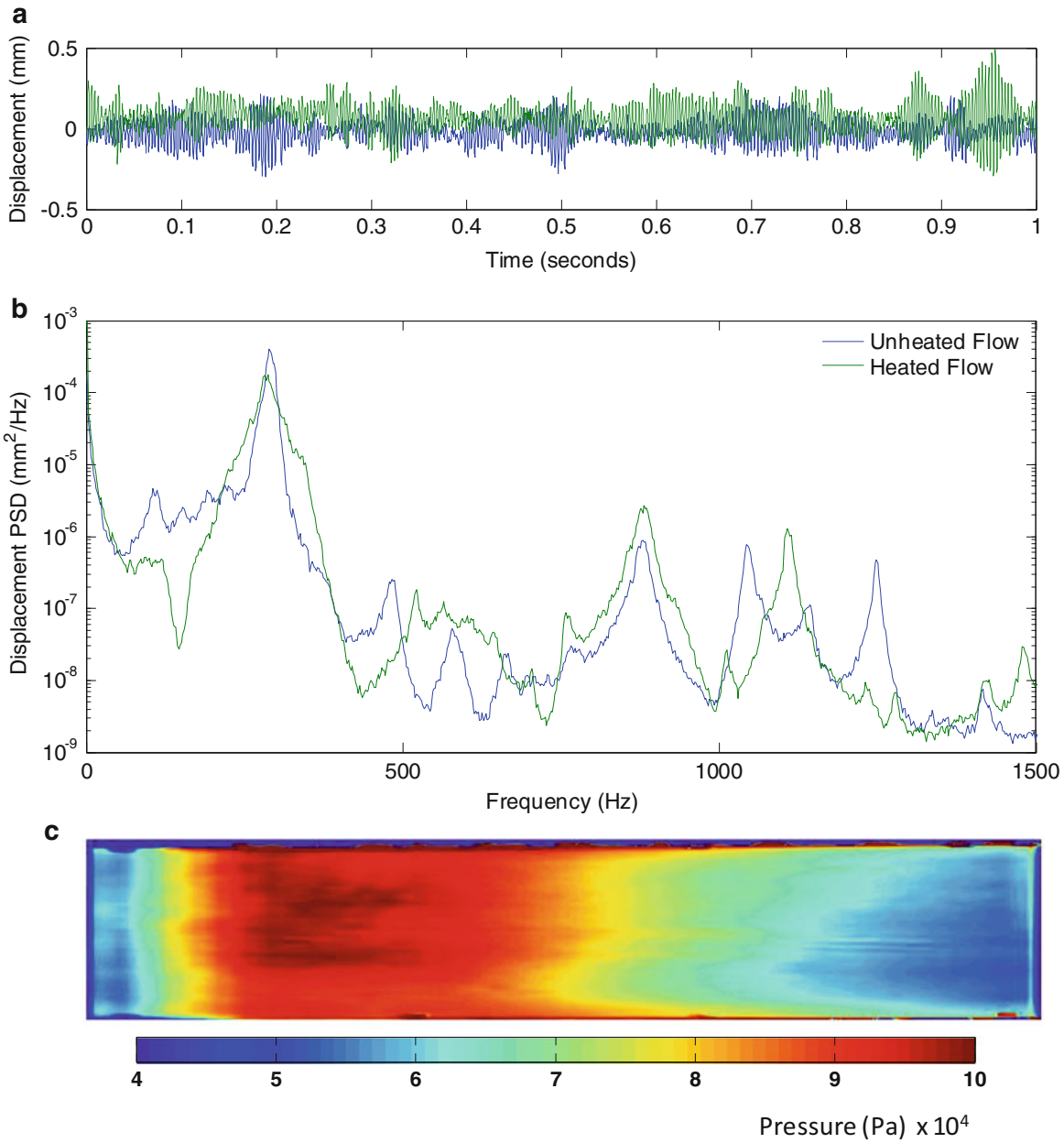

Fig. 22.11 Year 2 RC-19 experimentation showing impact of heated flow for constant 8° shock generator setting/SBLI: (**a**) panel center displacement time history, (**b**) displacement PSD for heated and unheated flow, and (**c**) accompanying surface pressure (PSP) for the case without heated flow

This behavior was also observed in the numerical results shown in Fig. 22.13. The FE model of the panel displays both the principal and asymmetric path, along with the full panel displacement at discrete locations. Future work will include measuring this phenomena experimentally and using that data to calibrate the modal model to predict and define future RC-19 experimental conditions.

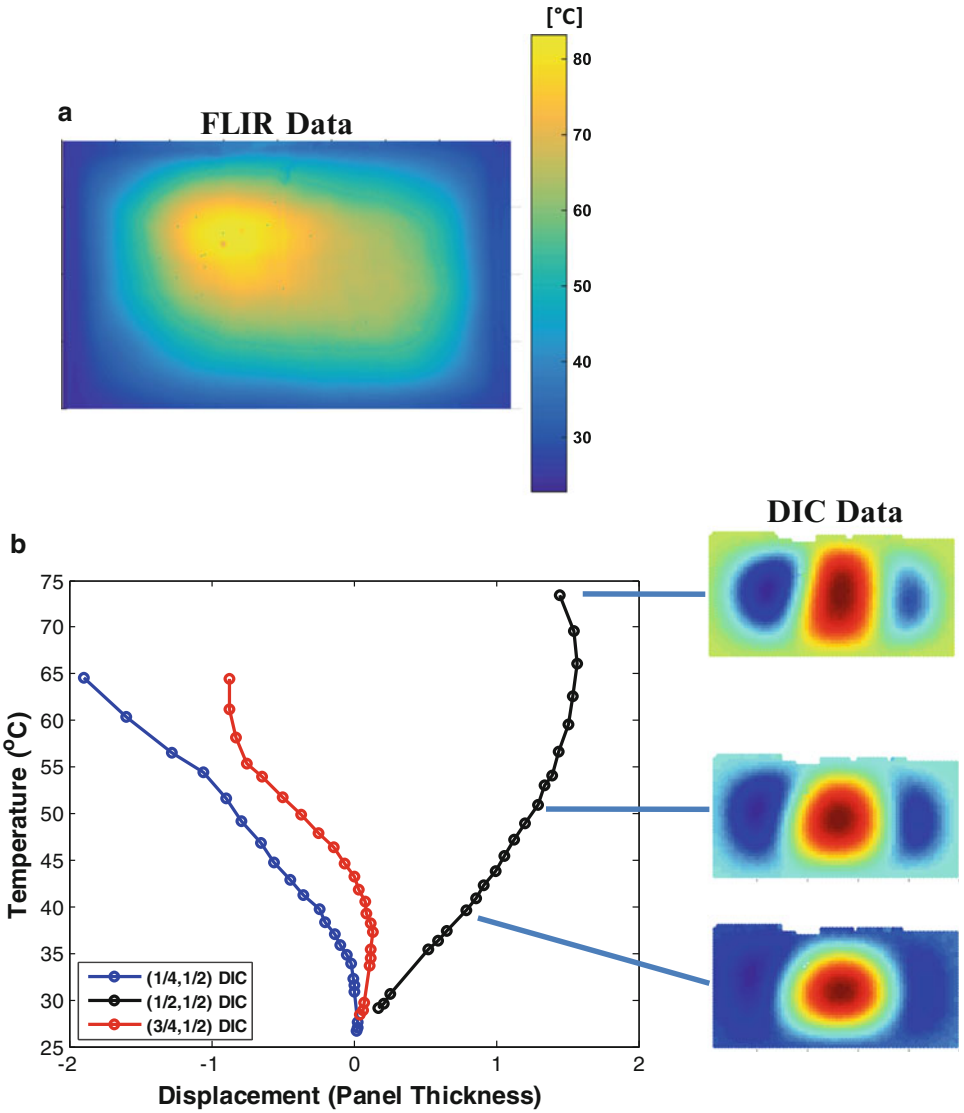

Fig. 22.12 Full-field temperatures and corresponding out-of-plane experimental displacements of the RC-19 panel specimen, (**a**) FLIR full-field temperature, (**b**) out-of-plane displacements at the ¼ and ½-points and corresponding DIC images [7]

22.4 Conclusions and Future Work

The present investigations were started by the AFRL Structural Sciences Center to better understand the impact of turbulent flow/shock boundary layer interaction on the dynamic response of an aircraft-like panel. A number of developing (dynamic 3D DIC and fast reacting PSP) and available (FLIR) full-field experimental techniques were used to measure both the full-field input (surface pressures and temperatures) and response (displacement). The results demonstrated the sensitivity of thin, constrained aircraft-like panels to SBLI and to heated flow. In addition, these panels will often behave nonlinearly which can obfuscate the structural response prediction. Future experiments will further explore post-buckled response including the identification of conditions necessary to both buckle the panel and induce snap-through response.

Acknowledgments The authors gratefully acknowledge the support of Dr. David Stargel of the Air Force Office of Scientific Research (AFOSR), LRIR number 12RB04COR.

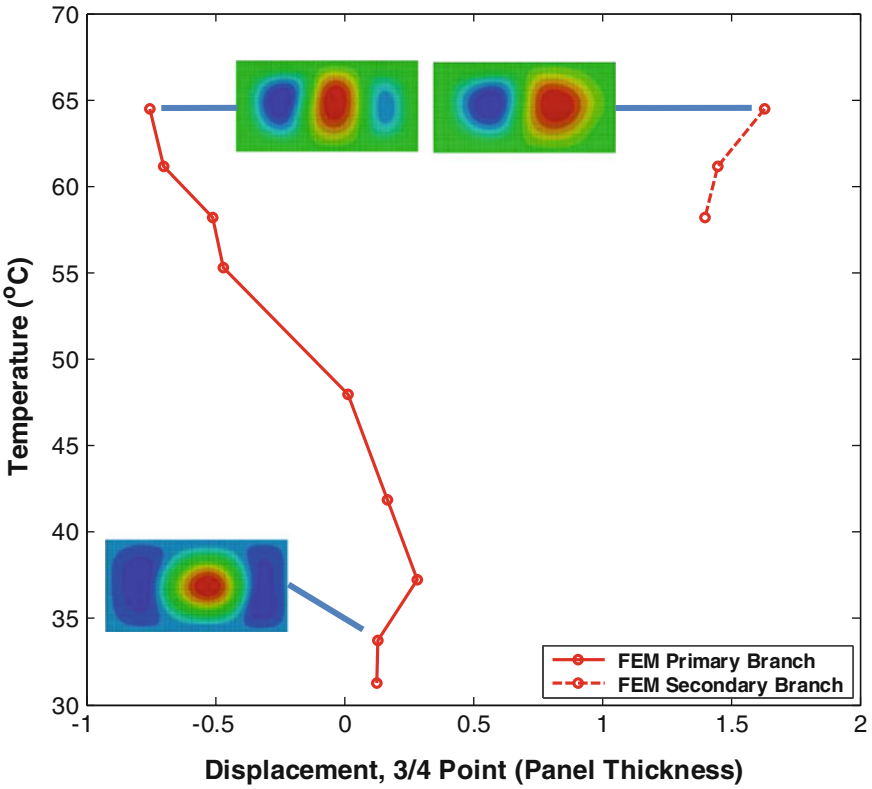

Fig. 22.13 RC-19 panel FE model static equilibrium paths

References

1. Heppenheimer, T.A.: Facing the heat barrier: a history of hypersonics. NASA Technical Report, NASA SP-2007-4232, Sept 2007
2. Coates, J., Meltzer, Jr. P.: AFRL examines technology used to test B-2 aft deck performance. http://www.wpafb.af.mil/news/story.asp?id=123104052, 6/24/2008
3. Zuchowski, B.: Predictive capability for hypersonic structural response and life prediction: phase II—detailed design of hypersonic cruise vehicle hot-structure. Technical Report, AFRL-RB-WP-TR-2012-0280, May 2012
4. Beresh, S.J., Clemens, N.T., Dolling, D.S.: The relationship between upstream turbulent boundary layer velocity fluctuations and separation shock unsteadiness. In: 37th AIAA Aerospace Sciences Meeting and Exhibit, Reno, NV, 11–14 Jan 1999, AIAA Paper 99-0295
5. Dolling, D.S.: Fluctuating loads in shock wave/turbulent boundary layer: tutorial and update. January 1993, AIAA Paper 93-0284
6. Wiebe, R., Spottswood, S.M.: On the response dimension of nonlinear structural vibrations. Submitted to the Journal of Sound and Vibration, August 2015
7. Perez, R., Bartram, G., Beberniss, T., Wiebe, R., Spottswood, S.M.: Calibration of aero-structural reduced order models using full-field experimental measurements. Submitted to the Journal of Mechanical Systems and Signal Processing, September 2015
8. Perez, R.A., Spottswood, S.M., Beberniss, T.J., Bartram, G.W., Eason, T.G.: Nonlinear dynamic response prediction of a thin panel in a multi-discipline environment: part II—numerical predictions. In: IMAC XXXIV Conference and Exposition on Structural Dynamics, Orlando, FL, Jan 2016
9. Gruber, M.R., Nejad, A.S.: Development of a large-scale supersonic combustion research facility. In: 32nd Aerospace Sciences Meeting & Exhibit, Reno, NV, 1–13 Jan 1994, AIAA Paper 94-0544
10. Spottswood, S.M., Beberniss, T.J., Eason, T.G.: Full-field, dynamic pressure and displacement measurements of a panel excited by shock boundary-layer interaction. In: 19th AIAA/CEAS Aeroacoustics Conference, Berlin, Germany, 27–29 May 2013, AIAA Paper 2013-2016
11. Beberniss, T., Eason, T., Spottswood, M.: High speed DIC measurements of random nonlinear dynamic response. 2011 SEM Annual Conference, Uncasville, CT, 13–16 June 2011
12. Gogulapati, A., Deshmukh, R., Crowell, A.R., McNamara, J.J., Vyas, V., Wang, X.Q., Mignolet, M., Beberniss, T., Spottswood, S.M., Eason, T.G.: Response of a panel to shock impingement: modeling and comparison with experiments. In: AIAA SciTech Conference 2014, National Harbor, MD, 13–17 Jan 2014, AIAA Paper 2014-0148
13. Murphy, K.D., Virgin, L.N., Rizzi, S.A.: Characterizing the dynamic response of a thermally loaded, acoustically excited panel. J. Sound Vib. **196**(5), 635–658 (1996)

Chapter 23
Nonlinear Dynamic Response Prediction of a Thin Panel in a Multi-Discipline Environment: Part II—Numerical Predictions

R.A. Perez, S.M. Spottswood, T.J. Beberniss, G.W. Bartram, and T.G. Eason

Abstract Hypersonic aircraft structures must operate in a complex loading environment, where the coupling of the aircraft structural response with the aerodynamics will lead to conditions involving rich nonlinear dynamics. The modeling of these fluid-thermal-structural interactions is complex and prohibitively expensive when high fidelity models are used (i.e., CFD and FEA). This aspect, and the lack of relevant flight-test and experimental data, have resulted in knowledge gaps, which have led to the design of overly-conservative structures in the past. Work at the Structural Sciences Center (SSC) of the USAF Research Laboratory has focused on addressing these knowledge gaps from a structures perspective. As discussed in Part I of this paper, 3 years ago the SSC began a series of wind-tunnel experiments to provide full-field experimental data for a clamped nominally flat panel exposed to supersonic flow. The present work will focus on numerical predictions of the panel dynamic response using a reduced order model (ROM) for the structural response and full-field measurement data to represent the loads on the panel.

Keywords Fluid-structure interaction • Reduced order model • Full-field measurement techniques • Structural dynamics • Finite element analysis

23.1 Introduction

The design and operation of reusable hypersonic aircraft have presented new challenges in all areas of aerospace engineering. The Air Force Research Laboratory (AFRL) Structural Sciences Center (SSC) at Wright-Patterson Air Force Base, Ohio, is focused on the development of a computational framework to simulate the evolution of hypersonic aircraft structures. As discussed by Blevins and Holehouse [1], the hypersonic environment can include significant aerothermal heating, shock-boundary-layer interaction (SBLI) resulting in an amplification of the heating and the aeroacoustic loading, flow separation resulting in amplification of the fluctuating pressures, or a combination of these scenarios. Therefore, the successful simulation of the structural response requires not only a proper modeling of the structural characteristics, but also a good characterization of the loading environment. Furthermore, design of a light-weight structure will require the designer to step outside of the traditional aircraft design perspective of superposing the worst loading conditions to produce the most conservative design [2, 3].

These challenges motivated a series of discovery experiments by the SSC at the large-scale supersonic combustion research facility abbreviated herein as the RC-19 wind-tunnel [4, 5]. The purpose of these experiments was to investigate, through full-field 3D-digital image correlation (DIC) and pressure sensitive paint (PSP), the interaction between a flexible panel and high-speed flow, including shock-boundary layer interactions. The full-field measurement techniques allowed Spottswood et al. [4, 5] to study the coherent structures of the flow on the panel as well as the dominant shapes of deformation of the panel.

Inspired by the results from the RC-19 tests, Gogulapati et al. [6, 7] applied a coupled fluid-structure interaction computational framework in an effort to model the complex response of the panel and the loading environment in the RC-19 wind tunnel. The authors of this work focused on two cases: Heated and unheated flow with shock impingement on the panel. Their framework combined a CFD surrogate model to capture the steady surface pressure and approximate models for the unsteady pressure fluctuations due to panel vibration and boundary layer turbulence. The structural response of the panel

R.A. Perez (✉) • G.W. Bartram
Universal Technology Corporation, 1270 North Fairfield Road, Dayton, OH 45432, USA
e-mail: ricardo.perez.10.ctr.mx@us.af.mil

S.M. Spottswood • T.J. Beberniss • T.G. Eason
Structural Sciences Center, Aerospace Systems Directorate, Air Force Research Laboratory, Wright-Patterson AFB, OH 45433, USA

G. Kerschen (ed.), *Nonlinear Dynamics, Volume 1*, Conference Proceedings of the Society for Experimental Mechanics Series,
DOI 10.1007/978-3-319-29739-2_23

was modeled using finite element analysis (FEA) and reduced order models (ROM) built from the FEA. In a preliminary assessment [6], they obtained good agreement between measured and computed mean distributions of the panel pressure, in particular the location and magnitude of the peak pressure due to the shock impingement. However, the simulations underpredicted the dynamic response of the panel in both heated and unheated flow cases. Some of the dominant sources of uncertainty they reported included discrepancies in the natural frequencies between the FEA model and experiment, the temperature of the panel, and interpolation of the aero-induced loading to the FEA mesh. In the second part of their study [7], a series of sensitivity analyses were carried out to understand the impact of several sources of uncertainty on the prediction of the response of the panel. Two main conclusions were that more information was needed to determine the temperature state of the panel and the existence of shock unsteadiness.

In this work, numerical predictions of the RC-19 panel response will be presented. The models pertaining to the loading environment will be replaced with the PSP data obtained from the test. This approach will enable to focus the analysis on the model uncertainties pertaining to the structure alone. The overall objective is to assess the feasibility of replacing the models of the complex loading environment with the PSP data. The success of this approach relies on the turbulent boundary layer (TBL) loading being the dominant source of excitation on the panel over any two-way fluid-structure interactions, which would require the solution of a coupled system of equations. Another potential problem with this approach is that an uncertainty analysis of the PSP data has not been performed, so the measurement could over or underpredict the actual pressure on the panel. Work on understanding and quantifying this measurement uncertainty will be performed in the second round of wind tunnel tests.

The outline of this paper is as follows. Section 24.2 describes the computational models: FEA and ROM. In Sect. 24.3, the post-processing of the RC-19 PSP and DIC data will be described. Section 24.4 will deal with the simulation of the panel response.

23.2 Computational Model

The response of the panel was obtained using a structural ROM built from an FEA model in Abaqus®. This section will first describe the finite element model of the panel. Then, a summary of the formulation of the ROM governing equations and the construction of the ROM will be presented.

23.2.1 Finite Element Model

The RC-19 panel was machined from a 305 mm × 152 mm × 12.7 mm block of AISI 4140 alloy steel, the material properties are shown in Table 23.1. A pocket was machined into the block leaving 0.635 mm for the compliant panel thickness over an effective vibration dimension of 254 mm × 127 mm. The panel was modeled using S4R shell elements in Abaqus®. The mesh consisted of 100 elements in the spanwise direction (along the length of the panel) and 50 in the chordwise direction (along the width of the panel).

The initial configuration of the FEA mesh was set according to the results from [8], where the geometric imperfection of the panel was measured with DIC. This geometric imperfection included the initial imperfection and the deformation induced by the installation of the panel in the wind-tunnel wall.

Table 23.1 Panel geometric and material properties

Property	Value
Length	0.254 m
Width	0.127 m
Thickness	6.35×10^{-4} m
Density	7850 kg/m^3
Young's modulus	205 GPa
Poisson's ratio	0.29
Coefficient of thermal expansion	1.22×10^{-5}/K

23.2.2 ROM Formulation

The structural ROMs considered in this study are based on a representation of the nonlinear geometric response in terms of a set of basis functions,

$$\mathbf{u}(t) = \sum_{n=1}^{M} \eta_n(t)\, \boldsymbol{\psi}^{(n)} \tag{23.1}$$

where $\mathbf{u}(t)$ represents the displacement field, $\boldsymbol{\psi}^{(n)}$ are specified, constant basis functions, and $\eta_n(t)$ are the time dependent generalized coordinates.

Following the work by Kim et al. [9] the governing equations of the ROM can be obtained from finite deformation elasticity and a Galerkin approach (i.e. enforcing the condition that the error introduced by the representation of the displacement field in terms of a set of basis function be orthogonal to the same basis functions). Shown in Eq. (23.2) are the governing equations of the ROM:

$$M_{ij}\ddot{\eta}_j + D_{ij}\dot{\eta}_j + K_{ij}^{(1)}\ \eta_j + K_{ijl}^{(2)}\eta_j\eta_l + K_{ijlp}^{(3)}\eta_j\eta_l\eta_p = F_i \tag{23.2}$$

where a linear damping term $D_{ij}\ \dot{\eta}_j$ has been added to collectively represent various dissipation mechanisms. Furthermore, M_{ij} denotes the elements of the mass matrix, $K_{ij}^{(1)}$, $K_{ijl}^{(2)}$, $K_{ijlp}^{(3)}$ are the linear, quadratic, and cubic stiffness coefficients and F_i are the modal forces. The method for indirect evaluation of the coefficients in Eq. (23.2) by Hollkamp and Gordon [10] using a finite element model was used here.

The selection of the basis $\boldsymbol{\psi}^{(n)}$ represents a key step in the formulation of the reduced order modeling strategy. Following the discussions of Hollkamp and Gordon [10], Kim et al. [9], Muravyov and Rizzi [11] and Mignolet et al. [12], the core of the basis is formed by the linear modes of the structure, hereafter referred to as out-of-plane or bending modes, which would appear significantly in the linear response.

23.2.3 ROM of RC-19 Panel

A nonlinear ROM of the RC-19 panel was generated using the FEA model described in Sect. 24.2.1 with the implicit condensation approach of Hollkamp and Gordon [10]. The modes forming the basis were selected by projecting the measured DIC displacement field on the first 12 modes of the panel. As described by Spottswood et al. [4, 5], 22 s of the response were recorded with DIC at a sampling frequency of 4000 Hz. The resulting projection coefficients were used to reconstruct the response, and the power spectral density (PSD) of the reconstructed response was compared against the PSD of the DIC data at the center point of the panel. The good matching of the PSD of the DIC data, shown in Fig. 23.1, indicates that the basis is rich enough to represent the displacement field from the DIC data. Therefore, the nonlinear stiffness coefficients of the ROM were identified for the first 12 modes of the panel.

The measured first nine natural frequencies of the installed panel are shown in Table 23.2 along with the natural frequencies computed with the FEA model. Also shown in Table 23.2 are the experimental modal damping ratios of the panel obtained from a modal test of the uninstalled panel (i.e., free-free boundary conditions). The effect of the prestress introduced after installing the panel can be clearly seen by the discrepancy in the frequencies between the measured and predicted results. The ROM stiffness matrix is diagonal with elements equal to $(2\pi f_i)^2$, where f_i is the *ith* natural frequency. Therefore, the predicted elements of the linear stiffness terms were replaced with the measured ones. The elements of the ROM damping matrix were set equal to their corresponding measured modal damping ratio. Time integration was performed using the Newmark-beta method with a time step equal to 2.5×10^{-5} s.

In this work, pressure data measured during the test using PSP will be used instead of a model of the loading environment. As described by Spottswood et al. [4, 5], the following different flow configurations were explored: no shock impingement, shock impingement 1/3 of the length of the panel downstream of the leading edge, and shock impingement near the center of the panel. Only the case with no shock impingement will be discussed in this paper.

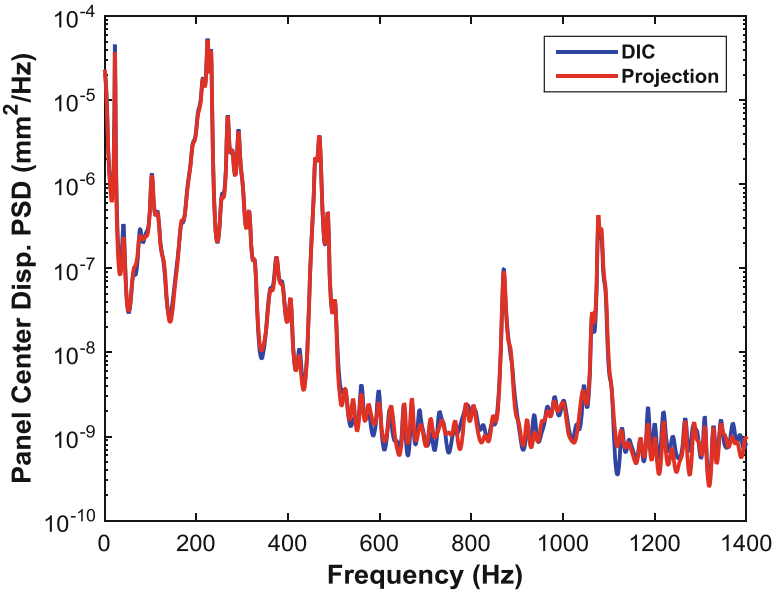

Fig. 23.1 PSD of the panel center response, DIC vs. projection results

Table 23.2 Natural frequencies and damping ratios of the uninstalled panel

Mode #	Frequency Abaqus® (Hz)	Frequency installed panel (Hz)	Damping ratio (Free-free panel) (%)
(1.1)	250	227	0.22
(1.2)	313	285	0.21
(1.3)	450	422	0.13
(1.4)	628	454	0.11
(2.1)	624	570	0.11
(2.2)	697	660	0.09
(1.5)	856	791	0.10
(2.3)	816	806	0.11
(2.4)	985	950	0.07

23.3 PSP Data Post-Processing

The PSP measurement space did not cover the entire surface of the panel, but only for the subsection shown in Fig. 23.2. The center of the PSP data measurement region is approximately equal to the center of the panel. The pressure values in the areas outside of the measurement region were obtained by performing a nearest neighbor extrapolation.

In order to transfer the load data to the FEA model, the pressure values from the pixels within one finite element were averaged leading to a constant pressure within every finite element; this is shown in Fig. 23.3 where a finite element contains 81 pixels.

A challenge of working with full-field measurements is the size of the data files. For the PSP grid of the case with no shock (526×654 pixels) 10 GB were required to store 1 s of data. The structural response predictions will be performed using 1 s of PSP data.

A cavity located on the back side of the panel was used to equalize the front and back side pressure on the panel, thereby mitigating the possibility of yielding the panel during tunnel start-up. Therefore, the pressure load applied on the panel was equal to the pressure differential between the front (PSP data) and back (measured with a pressure transducer located in the cavity).

In the next section the response of the panel due to the pressure loading obtained from the PSP data is discussed.

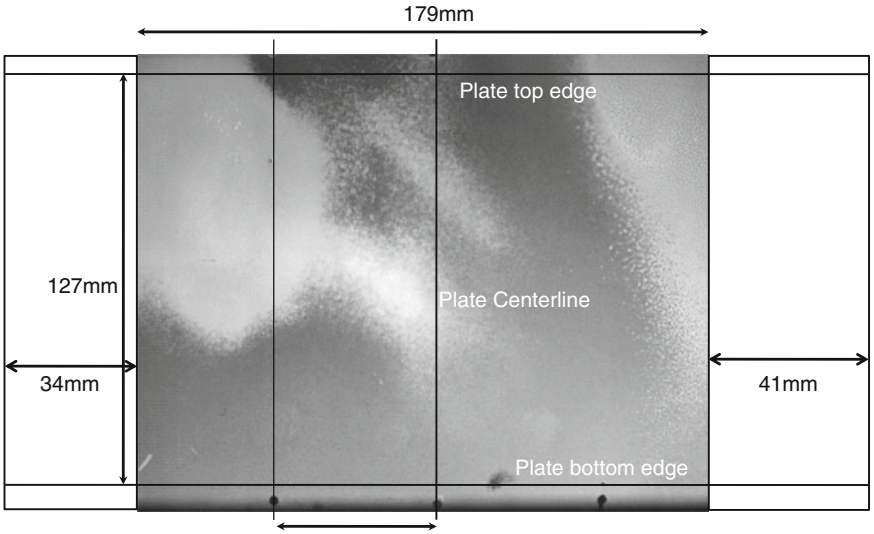

Fig. 23.2 Schematic showing PSD measurement space relative to the area of the panel for the case with no shock impingement

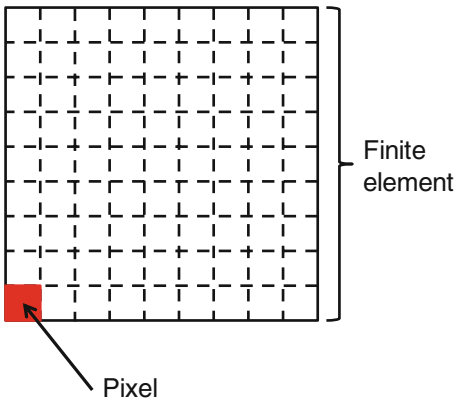

Fig. 23.3 Schematic showing PSD averaging of pressure within a finite element

23.4 Simulation of Structural Response

Test results from the DIC measurements are compared against ROM predictions in this section. Updating of the ROM was necessary in order to improve the matching of the experimental data. These modifications and the results will be discussed in this section.

Shown in Fig. 23.4 is a comparison of the PSD of the predicted and measured panel response at the center point of the panel. The ROM in its current state overpredicted the panel response. There is also a discrepancy in the frequencies of the last two peaks in the PSD.

In order to understand the source of the discrepancy in the ROM prediction, operational modal analysis (OMA) was applied to the full-field DIC data for the dominant peaks of the PSD. The DIC speckled pattern for this case is shown in Fig. 23.5. The pattern consists of an array of 45 points. In subsequent cases, the pattern was extended to cover most of the area of the panel. The coarse grid sets a limit on the modes that can be explored with OMA.

Shown in Fig. 23.6 is the PSD of the panel center point response. The deflected shapes are the singular vectors resulting from the decomposition of the Hermitian auto and cross-spectral density matrix. The shapes shown in Fig. 23.5 correspond to the maximum singular vector for a particular frequency. This approach was used by Spottswood et al. [4, 5] in order to observe the dominant aspects of the response at a given frequency. The ODS of the dominant peak, located at 230 Hz, is a combination of modes 1 and 2. The response at 470 Hz is dominated by mode 3 and the response at 870 and 1080 Hz is dominated by modes 8 and 12, respectively.

Based on the observations made from the ODS, the linear stiffness terms corresponding to modes 3, 8, and 12 were modified with the frequencies from the PSD of the DIC data. Shown in Fig. 23.7 is the response at the center point of the panel with the updated linear stiffness terms. While the updated ROM still overpredicts the response, the matching of the location of the peaks improved.

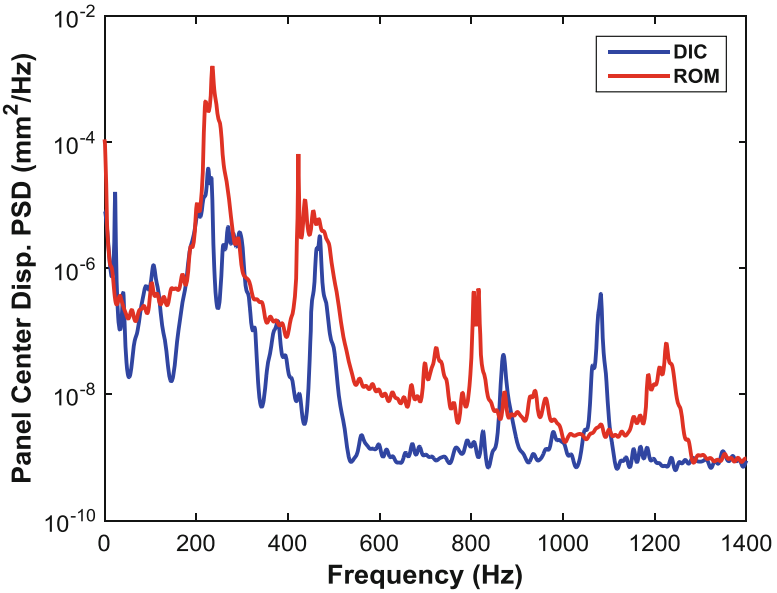

Fig. 23.4 PSD of panel center point response, DIC vs. ROM

Fig. 23.5 Panel top-surface and frame with DIC speckled pattern for the case with no shock impingement

Spottswood et al. [4] observed that the panel vibration has an effect in the flow near-field. This can be seen in Fig. 23.8, which shows the PSD of the pressure data at the panel quarter, middle, and three-quarter points. The effect of the panel vibration can be observed by the peaks in the PSD at frequencies that match the frequencies of the dominant peaks in the panel response. The exact physical mechanism leading to those peaks has not been determined yet.

Next, pressure data obtained for the same nominal flow conditions, but with a rigid specimen instead of the compliant panel, was used. Shown in Fig. 23.9 is the updated PSD of the panel center point response. There is a clear decrease in the response level when compared to the results obtained using the pressure data for the compliant panel. However, the level of the predicted response is still higher than the test data. As discussed by Hollkamp et al. [13] coupling between the structure and acoustics can lead to additional damping.

Next, the damping of modes 1, 3, and 8 was increased. Shown in Fig. 23.10 is the PSD of the panel center response obtained with the updated damping matrix. The resulting damping ratios as well as the original ones are shown in Table 23.3. Shown in Fig. 23.10 is the PSD of the response at the center point of the panel. The prediction of the ROM with updated damping agrees well with the test data.

As it was mentioned in the Introduction, quantification of the measurement error in the PSP data will be performed in the upcoming wind tunnel tests. This will help clarify if extra damping required to improve the ROM predictions is necessary or if measurement error in the PSP is leading to a higher pressure than the one actually seen by the panel in the test.

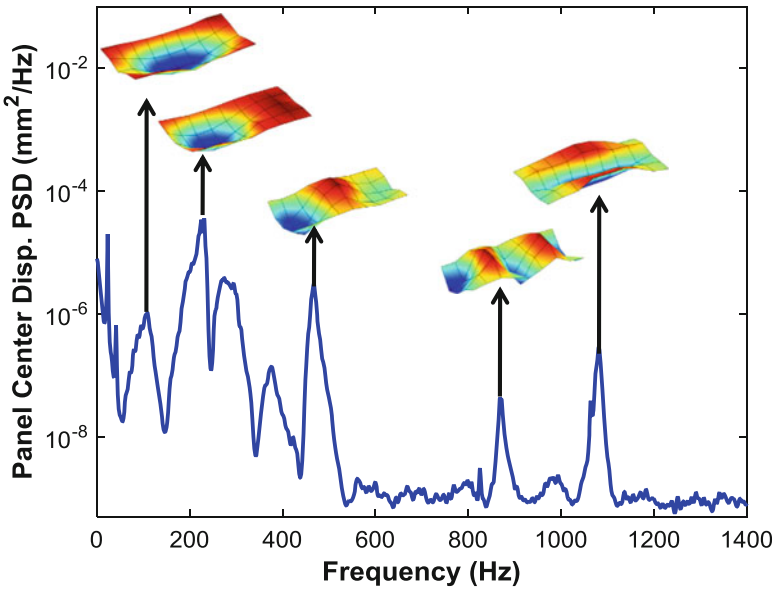

Fig. 23.6 PSD of panel center point response and displacement operational deflected shapes

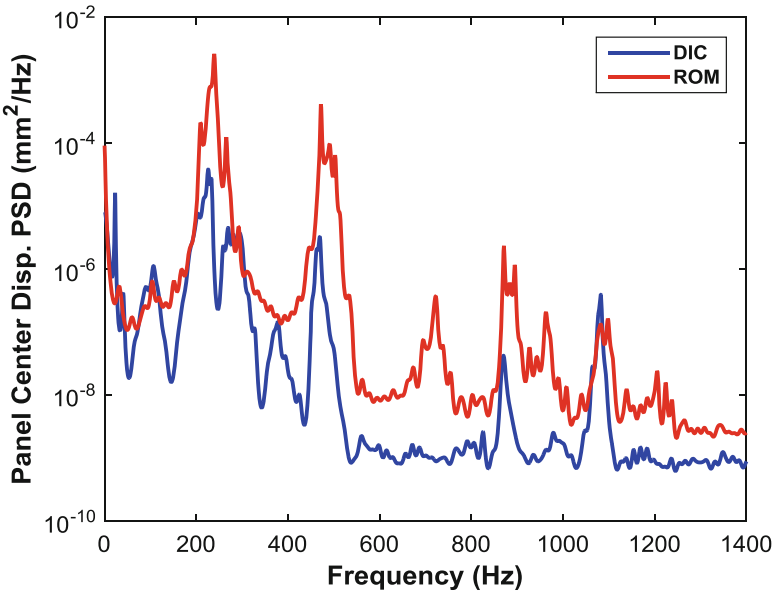

Fig. 23.7 PSD of panel center point response, DIC vs. ROM

23.5 Summary

The results from a modeling effort of the dynamic response of a compliant panel in a supersonic wind tunnel were presented. The aero-induced loading was obtained from PSP data measured during the wind tunnel test. The response of the panel was computed using a ROM that includes geometric nonlinear effects and the ROM predictions were compared against data measured using DIC.

The case considered consisted of turbulent flow over a compliant panel with no shock impingement. The response for this case was seen to be in the nonlinear regime, but the shift in the natural frequency of some of the peaks was considered to be too large to be attributed to the geometric nonlinear stiffening due to the vibration of the panel. Computation of the ODS revealed that the three peaks in the PSD of the response that shifted to higher frequencies were dominated by modes 3, 8, and 12, respectively. Modification of the linear stiffness terms corresponding to these modes led to an improvement in the ROM predicted response. Increasing the modal damping led to an excellent matching of the test data. The effect of the panel

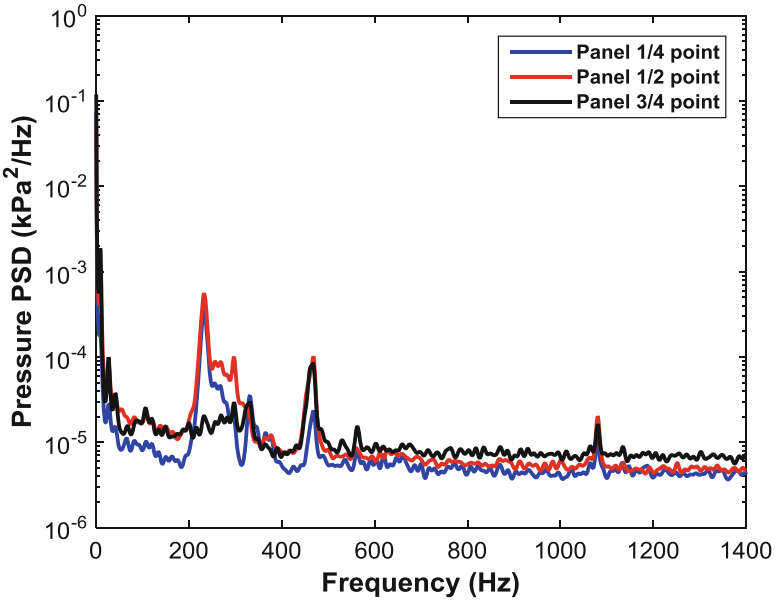

Fig. 23.8 PSD of PSP data at panel quarter, center, and three-quarter points

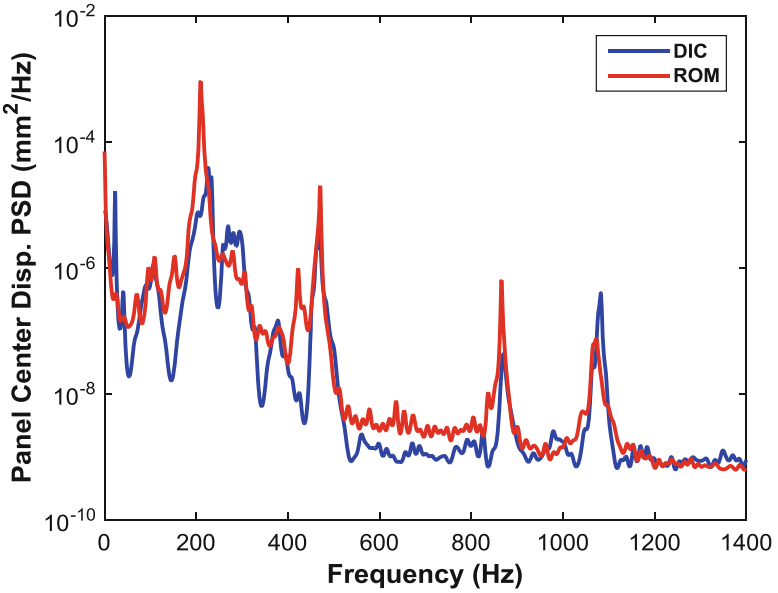

Fig. 23.9 PSD of panel center point response, DIC vs. ROM

Table 23.3 Original and updated damping ratios for case with no shock

Mode #	Original damping ratio (%)	Updated damping ratio (%)
(1.1)	0.22	3.4
(1.3)	0.13	0.6
(2.3)	0.10	0.5

vibration on the flow was seen in the PSP data. This could be due to coupling between the structure and acoustics that leads to increased damping in the response. Use of the PSP data obtained from a rigid specimen without the shock impingement led more reasonable modal damping ratios.

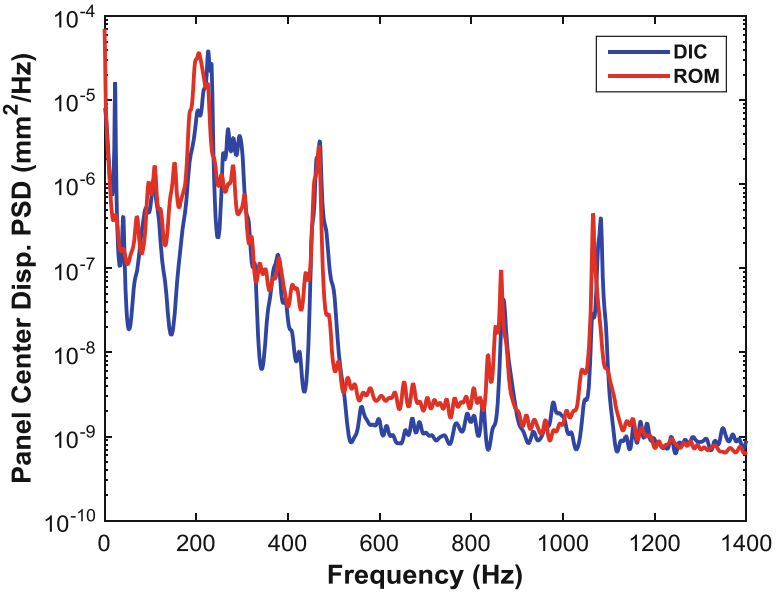

Fig. 23.10 PSD of panel center point response, DIC vs. ROM

Acknowledgements The authors gratefully acknowledge the support of Dr. David Stargel of the Air Force Office of Scientific Research (AFOSR), LRIR number 12RB04COR.

References

1. Blevins, R.D., Holehouse, I.: Thermoacoustic loads and fatigue of hypersonic vehicle skin panels. J Aircr **30**, 971–978 (1993)
2. Quiroz, R., Embler, J., Jacobs, R., Tzong, G., Liguore, S.: Predictive capability for hypersonic structural response and life prediction: phase II—detailed design of hypersonic cruise vehicle hot-structure. Technical Report, AFRL-RQ-WP-TR-2012-0265, Feb 2012
3. Zuchowski, B.: Predictive capability for hypersonic structural response and life prediction: phase II—detailed design of hypersonic cruise vehicle hot-structure. Technical Report, AFRL-RB-WP-TR-2012-0280, May 2012
4. Spottswood, S.M., Easton, T., Beberniss, T.: Influence of shock-boundary layer interactions on the dynamic response of a flexible panel. In: ISMA 2012 International Conference on Noise and Vibration Engineering, 2012
5. Spottswood, S.M., Beberniss, T., Eason, T.: Full-field dynamic pressure and displacement measurements of a panel excited by shock boundary-layer interaction. In: 19th AIAA/CEAS Aeroacoustics Conference, 2013
6. Gogulapati, A., Deshmukh, R., Crowell, A.R., McNamara, J.J., Vyas, V., Wang, X.Q., Mignolet, M., Beberniss, T., Spottswood, S.M., Eason, T.G.: Response of a panel to shock impingement: modeling and comparison with experiments. In: 55th AIAA/ASME/ASCE/AHS/SC Structures, Structural Dynamics, and Materials Conference, 2014
7. Gogulapati, A., Deshmukh, R., McNamara, J.J., Vyas, V., Wang, X.Q., Mignolet, M., Beberniss, T., Spottswood, S.M., Eason, T.G.: Response of a panel to shock impingement: modeling and comparison with experiments—Part 2. In: 56th AIAA/ASME/ASCE/AHS/ASC Structures, Structural Dynamics, and Materials Conference, 2015
8. Perez, R., Bartram, G., Beberniss, T., Wiebe, R., Spottswood, S.M.: Calibration of aero-structural reduced order models using full-field experimental measurements, mechanical systems and signal processing. Under Rev
9. Kim, K., Radu, A.G., Wang, X.Q., Mignolet, M.P.: Nonlinear reduced order modeling of isotropic and functionally graded plates. Int J Nonlinear Mech **49**, 100–110 (2013)
10. Hollkamp, J.J., Gordon, R.W.: Modeling membrane displacements in the sonic fatigue response prediction problem. AIAA-2005-2095, 2005
11. Muravyov, A.A., Rizzi, S.A.: Determination of nonlinear stiffness with application to random vibration of geometrically nonlinear structures. Comput Struct **81**, 1513–1523 (2003)
12. Mignolet, M.P., Przekop, A., Rizzi, S.A., Spottswood, S.M.: A review of indirect/non-intrusive reduced order modeling of nonlinear geometric structures. J Sound Vib **10**(332), 2437–2460 (2013)
13. Hollkamp, J., Gordon, R., Beberniss, T.: Coupling acoustics to nonlinear structural models: predictions and experiments, In: 51st AIAA/ASME/ASCE/AHS/ASC Structures, Structural Dynamics, and Materials Conference, 2010

Chapter 24
Stability Analysis of Curved Panels

Ilinca Stanciulescu, Yang Zhou, and Mihaela Nistor

Abstract Aerospace, mechanical and civil engineering systems extensively use curved panels as structural components. The curved panels exhibit high risk of loss of stability especially with modern requirements for increasingly lighter designs. Correct identification of the load-carrying capabilities and thorough understanding of the stability behavior under transient excitations provide necessary information to safely design such structural components. In this work we use the arclength and branch-switching methods to correctly identify the buckling load and all equilibria. Compared to other methods, prior knowledge of the bifurcation modes is not required and the same mesh is used for tracing all secondary equilibrium paths. This method can identify secondary branches that other procedures failed to retrieve. Finally, the transient behavior of curved panels is also examined; in particular we seek to identify the dynamic snap-through boundary that separates small amplitude non-snap from large amplitude post-snap vibrations. Typically, analytical solutions for such highly nonlinear behavior are not available, and extensive parametric studies are usually required leading to very high computational cost. We examine the connections between different dynamic snap-through boundaries and seek to correlate them with features of the equilibrium manifold to identify computationally more efficient ways for their estimation.

Keywords Nonlinear stability analysis • Critical points • Arclength and branch-switching methods • Stability boundaries • Snap-through

24.1 Introduction

Cylindrical shells are used in engineering applications as structural components in a variety of systems such as aircraft, tanks, pipelines, and offshore platforms. As structural components, curved panels have efficient load-carrying capabilities but also exhibit high risk of buckling failures.

Safe design of the structural components requires correct identification of the critical load and thorough understanding of the stability behavior under transient excitations. In the literature a variety of methods were adopted for the stability analysis. For example, early studies used the classical buckling theory to approximate buckling loads [1–4]. This approach usually overestimates the buckling load, ignores bending effects before buckling and does not retrieve postbuckling responses. In order to conduct postbuckling analysis, the perturbation approach was introduced [5]. However, this method is typically valid only in the vicinity of critical points. Widely used to perform nonlinear postbuckling analysis are path following schemes such as Newton-Raphson or arclength methods. The major disadvantage of these approaches is that they are unable to trace secondary equilibrium paths. The asymmetric meshing technique [6, 7] revealed on a benchmark problem the existence of a bifurcation buckling in asymmetric mode, which was previously unidentified. Nevertheless, some features of the postbuckling behavior still remained unnoticed. In [11], using an arclength method combined with a branch-switching method [8, 9] we found two previously undetected pairs of bifurcation points and consequently two other pairs of secondary paths for the benchmark problem. One of the secondary paths contains equilibrium configurations that are stable. While these equilibria cannot be reached through a continuous stable path, they are still important: perturbations in the system may lead to dynamic jumps to these states. The identification of additional unstable equilibria also reveals that the degree of instability of the system is higher than what researchers previously found.

I. Stanciulescu (✉) • Y. Zhou • M. Nistor
Department of Civil and Environmental Engineering, Rice University, 6100 Main Street, Houston, TX 77005, USA
e-mail: ilinca.s@rice.edu

G. Kerschen (ed.), *Nonlinear Dynamics, Volume 1*, Conference Proceedings of the Society for Experimental Mechanics Series,
DOI 10.1007/978-3-319-29739-2_24

Curved thin panels are also subject to dynamic instabilities, in particular to snap through buckling (jumps between remote configurations) characterized by sudden curvature reversals and resulting into increased fatigue risk. Identification of stability boundaries is an important step towards safe design and requires a thorough examination of the parameter space. Two loading parameters will be considered in this study (the amplitude and frequency of the load) and methods for the efficient identification of the stability boundaries will be examined.

24.2 Static Stability Analysis

In this section, we first briefly describe the numerical procedure that combines arclength and branch-switching methods to find the critical points and corresponding postbuckling equilibrium paths. Then the numerical procedure is applied to a benchmark cylindrical panel [10] to show its advantages and lastly is used for comparing the differences between a panel with constant thickness and an orthogrid panel that has the same volume of material and the same length and width dimensions.

24.2.1 Numerical Procedure

Nonlinear buckling and postbuckling analysis requires identification of critical points on the equilibrium path. Critical points are points where a system has qualitative changes in its response, of which we are primarily interested in the loss of stability. For an elastic system, at a critical point the tangent stiffness matrix becomes singular. These points can be differentiated into limit or bifurcation points (Fig. 24.1). After the detection of the critical points, the branch-switching method proposed in [8, 9] is adopted to switch at a bifurcation point from the primary equilibrium path to the secondary equilibrium path.

The combined numerical procedure used to perform a thorough nonlinear buckling and postbuckling analysis can be summarized as follows: (1) the primary equilibrium path is traced by an arc-length method while monitoring the lowest eigenvalues of the tangent stiffness; (2) all critical points on the primary path are found by identifying the configurations for which eigenvalues change sign; (3) the critical points are classified into limit and bifurcation points; (4) the bifurcation points are differentiated into simple and multiple bifurcation points by the multiplicity of zero eigenvalues; (5) the branch-switching method is used to switch from the primary path to a secondary path at a bifurcation point; (6) the remaining solutions on every secondary path are traced using the arclength method. The process is recursive and each secondary path can be further examined to identify the presence of other limit points and /or of branching. For a detailed description of the method, the interested reader is referred to [11].

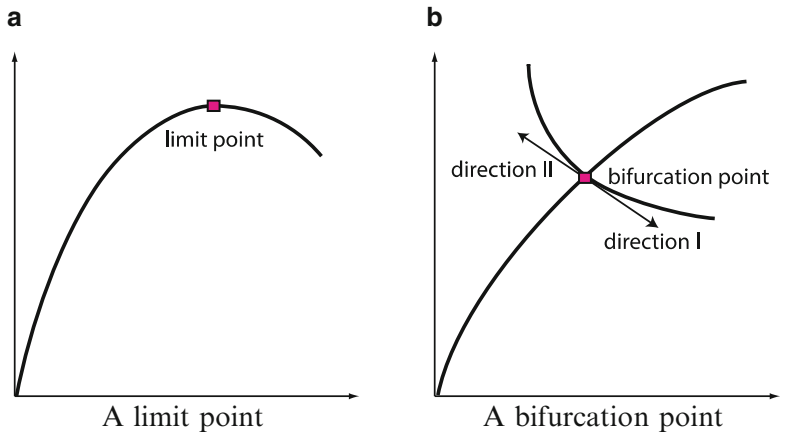

Fig. 24.1 Critical points on equilibrium path. (**a**) A limit point; (**b**) A bifurcation point

24.2.2 Benchmark Panel

The benchmark example is a circular cylindrical panel (radius R = 2540 mm and thickness t = 6.35 mm) with simply supported longitudinal edges of length a = 508 mm and free curved circumferential edges of projected length b = 507.15 mm (Fig. 24.2). The material is isotropic with Young's modulus E = 3102.75 MPa, and Poisson's ratio $\nu = 0.3$. P_C represents the symmetry plane perpendicular to the circumferential edge and P_L is the symmetry plane perpendicular to the longitudinal edge. A point load is applied in positive z direction at the center of the panel. The numerical simulations are performed with the Finite Element Analysis Program (FEAP) [12].

Using the numerical procedure described in [11] we find the primary equilibrium path (solutions symmetric with respect to both P_C and P_L) and three secondary equilibrium branches containing solutions with different asymmetries (Fig. 24.3a). The secondary path C was previously identified with the asymmetric meshing technique [6], but the numerical procedure adopted in [11] also identified path L and path B.

The primary equilibrium path (Fig. 24.3a, solid line) is traced by the arclength method, while monitoring several lowest eigenvalues of the tangent stiffness matrix **K**. On this equilibrium path a pair of limit points (points with horizontal tangents) is detected and the limit point critical load is $P_{cr} = 595.20$ N. Figure 24.3b shows the lowest five eigenvalues of the tangent stiffness matrix on this primary equilibrium path. The critical points are found by identifying all zero eigenvalues. If we monitor λ_1 (dashed line), the lowest eigenvalue of the tangent stiffness matrix, its positive value at zero load decreases as the load is increased, becomes zero and then negative. The point where it becomes zero indicates the existence of a critical point. This point is a bifurcation point, because there is no horizontal tangency here. Similarly, if we trace λ_2 (solid line), the second

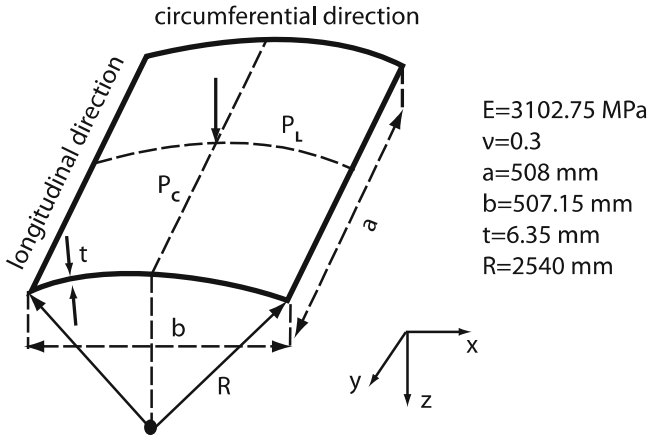

Fig. 24.2 Benchmark cylindrical problem geometry and material properties

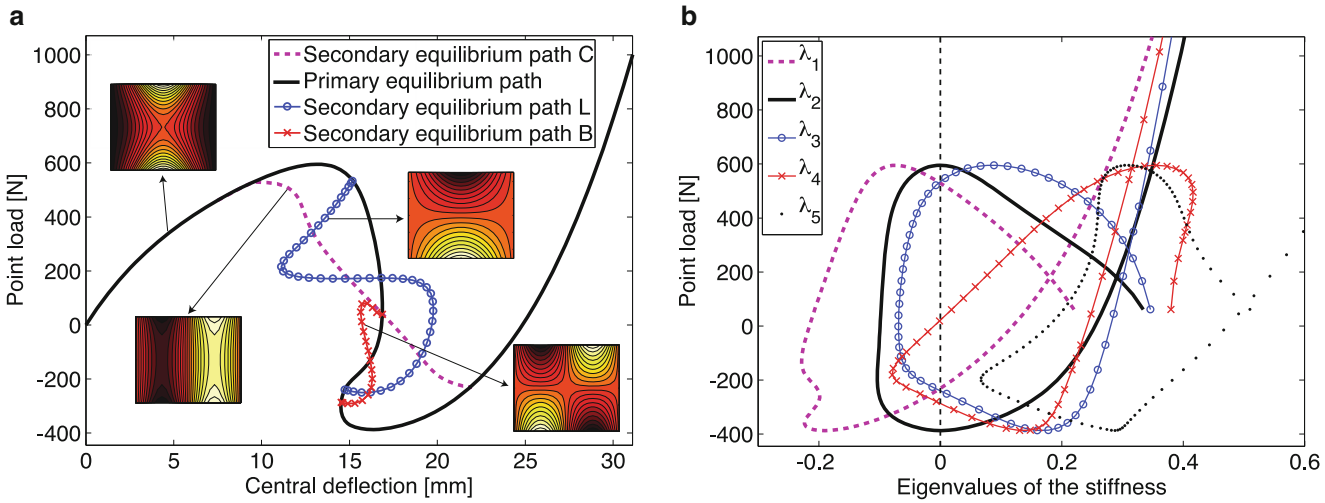

Fig. 24.3 Solution of the benchmark example. (**a**) All connected equilibrium paths; (**b**) Five lowest eigenvalues

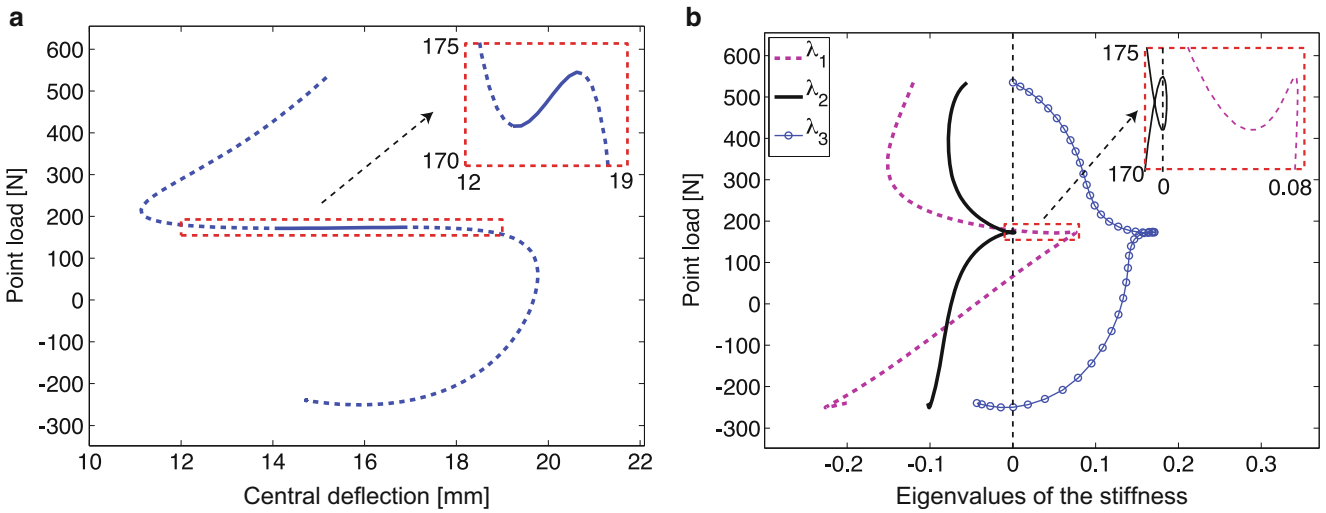

Fig. 24.4 Stability of equilibria on secondary path L. (**a**) Secondary equilibrium path L; (**b**) Three lowest eigenvalues

lowest eigenvalue of the tangent stiffness matrix, its positive value decreases as the load increases, becomes zero and then negative. The point where it becomes zero corresponds to a critical point, which is a limit point in this case. If we continue on the path, we find that λ_3 and λ_4 also become zero and they correspond to bifurcation points. The fifth lowest eigenvalue of the tangent stiffness matrix, λ_5, is positive all the time, an indication that all critical points on the primary equilibrium path were identified. Looking at the four lowest eigenvalues of the tangent stiffness matrix, after they become negative, at certain load levels they cross once more the zero value, indicating the existence of paired critical points where the bifurcated branches rejoin the primary path. Figure 24.3a also shows the deformed shapes on each of the equilibrium paths.

The stability for each of the equilibrium paths can be assessed with the aid of the eigenvalues of the tangent stiffness matrix. If all eigenvalues are positive, then the equilibrium path is stable, while if at least one is negative, then the equilibrium is unstable. Figure 24.4 reveals an interesting feature of the secondary equilibrium path L. For instance, for loads from 171.6N to 173.8N all eigenvalues on path L are positive (Fig. 24.4b), indicating that within this load interval the secondary equilibrium path in stable. Note that a detailed examination of paths C, L and B was not performed and further branching from these paths is still possible but did not make the object of this study.

24.2.3 Orthogrid Panels

The ability to find all critical points on the primary equilibrium path and the secondary equilibrium branches, allows the assessment of the degree of instability for a structural element subject to static loads. Orthogrid panels (grid stiffened shells) are known to have superior strength and stiffness to weight ratios. To verify the better performance of orthogrid panels compared to panels with constant thickness, consider the following example. An orthogrid panel and a constant thickness panel (Fig. 24.5) having the same material properties, the same length $a = 180.3$ mm and width $b = 152.4$ mm, and the same volume of material. The thickness of the constant thickness panel is $t_p = 1.8$ mm, while the thickness of the membrane (backing) of the orthogrid is $t_{og} = 1.4$ mm and of the height of its stiffening ribs is $t_r = 3.8$ mm. The material is isotropic with Young's modulus $E = 2400$ MPa, and Poisson's ratio $\nu = 0.33$.

Unlike the initially curved panel discussed in Sect. 24.2.2, in this section we examine panels that are initially flat, buckle to a certain buckling level due to axial loads and then are subject to transverse loadings that can induce snap-through. The sequence of loading is thus applied in two stages (Fig. 24.6). In the first step the panels are axially compressed until a certain buckling level (rise) is reached and in the second step lateral loading is applied. The response of a structure under this type of loading will vary with the buckling level, in the same manner in which the behaviour of initially curved panels depends on the panel rise.

The responses for the orthogrid and the constant thickness panels when buckled to a rise of 3.5 mm are shown in Fig. 24.7. The constant thickness panel has three secondary equilibrium branches, while the orthogrid panel has only one, indicating

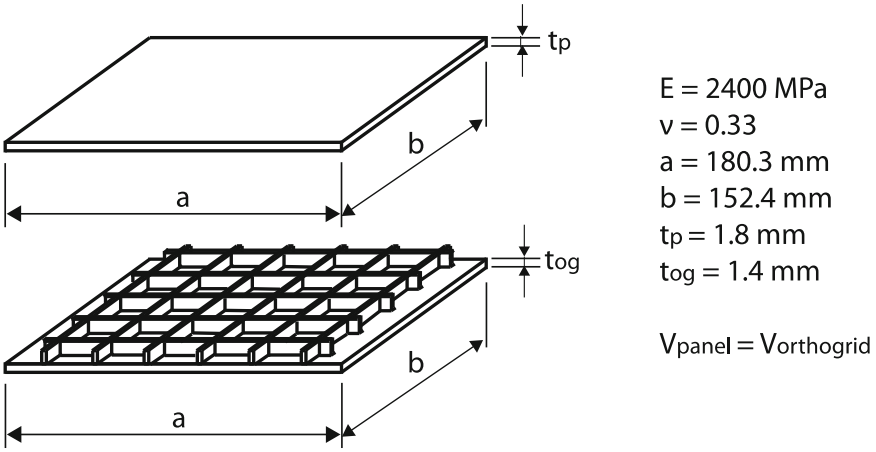

Fig. 24.5 Orthogrid and constant thickness panel geometry and material properties

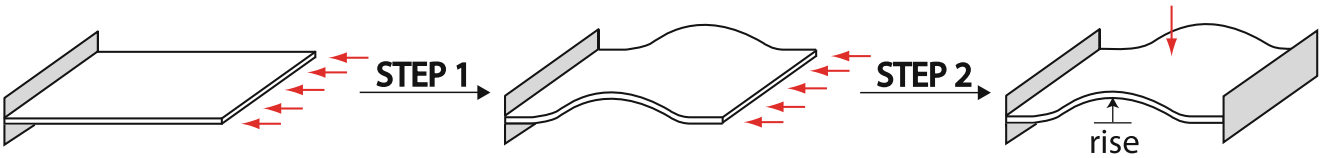

Fig. 24.6 Loading sequence for the orthogrid and constant thickness panel

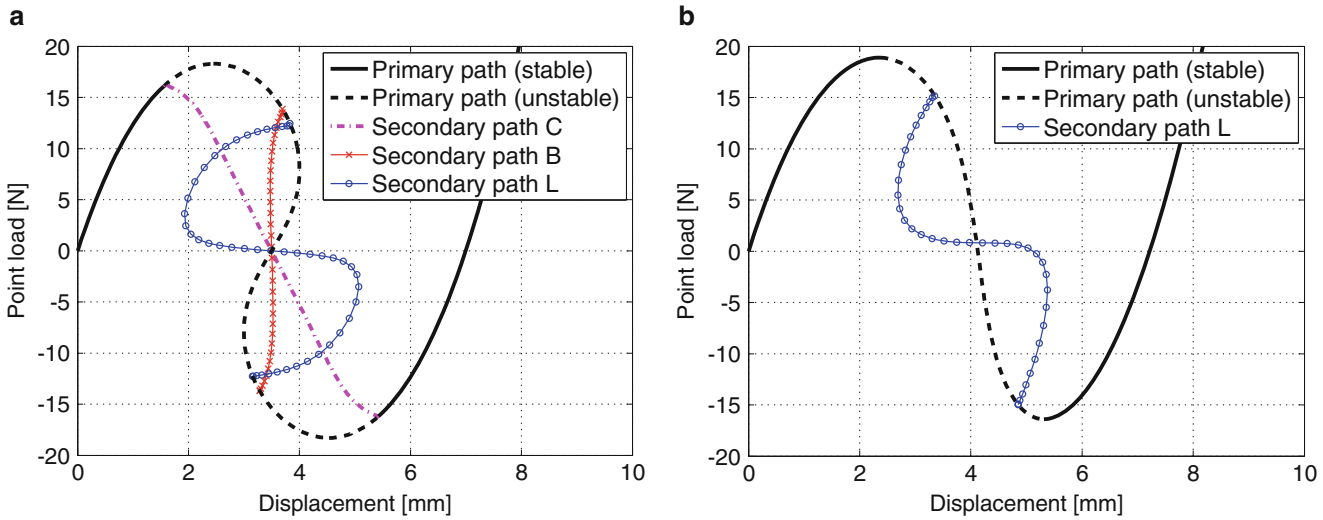

Fig. 24.7 Equilibrium paths for constant thickness panel and orthogrid panel that were buckled to a rise of 3.5 mm. (**a**) Constant thickness panel; (**b**) Orthogrid panel

that the degree of instability for the constant thickness panel is higher than for the orthogrid. Also, the value at which the loss of stability occurs is lower for the constant thickness panel. The loss of stability occurs at a bifurcation point for the constant thickness panel and at a limit point for the orthogrid panel.

For the orthogrid panel, the loss of stability will eventually move from a limit point to a bifurcation point, but this happens at higher rises than for the constant thickness panel. Figure 24.8 shows with solid line the load values at which loss of stability occurs for the constant thickness panel, and with dashed line the load values for the orthogrid panel. The figure also illustrates the rise at which the loss of stability switches from a load corresponding to a limit point to a load corresponding to a bifurcation point. This switch takes place at lower rises for the constant thickness panel. Although at lower rises both the orthogrid and the constant thickness panels have similar critical force values, as the rise increases the load at which loss of stability happens increases significantly faster for the orthogrid panel.

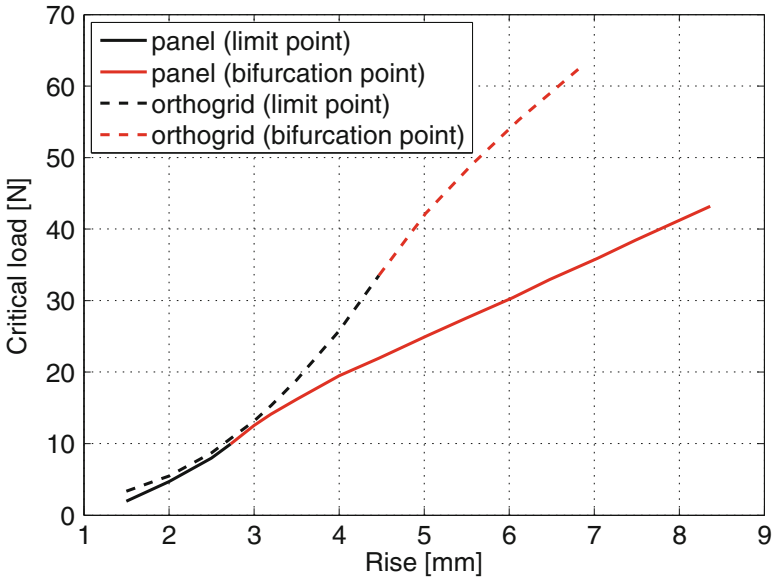

Fig. 24.8 Load at which loss of stability occurs at various rises for the orthogrid and constant thickness panels

24.3 Dynamic Analysis

To understand the stability behavior under transient loading, it is of interest to identify the dynamic snap-through boundary. This boundary separates the small amplitude non-snap from large amplitude post-snap vibrations. Obtaining it requires a high computational cost because of the extensive parametric studies that are involved.

For this section we consider again a simple curved cylindrical panel but shallower than the benchmark example (rise 5.08 mm). All other material and geometrical properties are the same as for the benchmark panel (Fig. 24.2) discussed in Sect. 24.2.2. Distributed load is applied statically and dynamically. Figure 24.9a shows the primary equilibrium path obtained, on which, except for the limit points, there are no other critical points. This indicates that no branching takes place for this system and that snap-through will always be controlled by the limit point. For the transient analysis we investigate the loading space by performing simulations with different forcing frequency and amplitude. The snap-through boundary obtained from sweeping the parameter space is shown in Fig. 24.9b.

Pairs of forcing amplitude and frequencies above the snap-boundary (gray) correspond to loading cases that result in responses exhibiting snap-through, and the ones below the snap-boundary (white) to responses that do not experience snap-through. Figure 24.10a shows the small amplitude (no snap) response for a forcing amplitude of $P = 213.348$ Pa and a frequency of $\omega = 116.3018$ rad/s (blue square in Fig. 24.9b) with a displacement range in the interval $[-1.5, 1]$ mm. Similarly, Fig. 24.10b shows the large amplitude response for a forcing amplitude of $P = 240.0165$ Pa and the same frequency of $\omega = 116.3018$ rad/s (red circle in Fig. 24.9b). The range of the displacement in this case is $[-12, 5]$ mm, or approximately seven times larger, indicating that the system is visiting the region of remote equilibria (snap-through behavior). Also note that the snap through events are persistent in this case and the system does not settle into small amplitude oscillations.

Similar parametric investigations of shallow panels with varied geometrical properties and identical material properties and boundary conditions indicate that the V shape of the boundary in Fig. 24.9b is typical and that the boundary scales with the change in geometry (and the induced changes in the critical load value and natural frequencies). Work is currently in progress to identify the regimes for which such scaling is possible, which may offer opportunities for a more efficient computation of the dynamic stability boundaries.

24.4 Concluding Remarks

Critical points and all postbuckling responses are identified for curved panels using a numerical procedure that requires no prior knowledge of the bifurcation modes and uses the same mesh to compute all secondary paths. The performance of orthogrid panels is then compared to that of constant thickness panels, with similar length and width, and the same volume

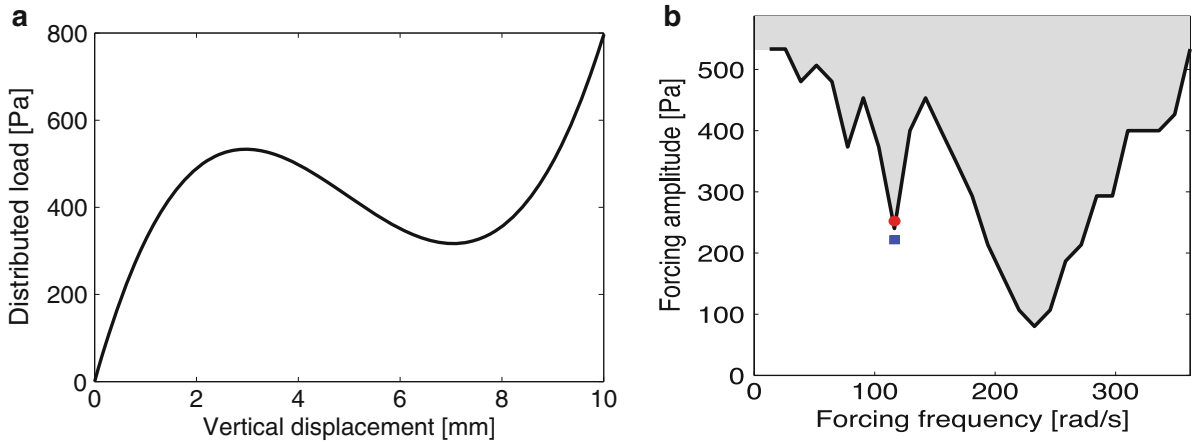

Fig. 24.9 Static and dynamic responses for cylindrical panel. (**a**) Static primary equilibrium path; (**b**) Snap-through boundary

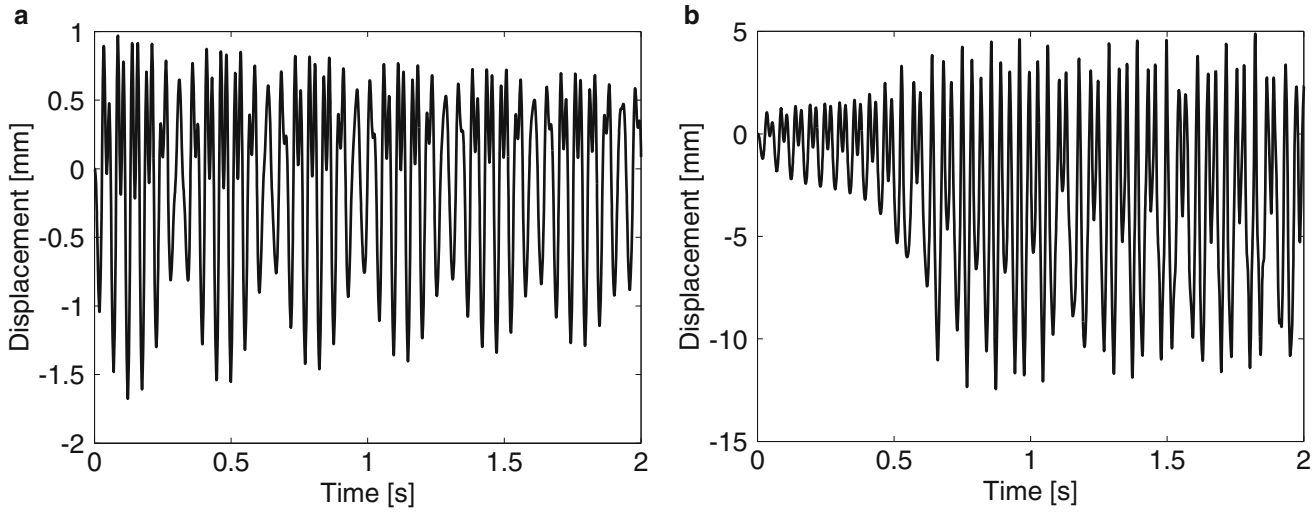

Fig. 24.10 Examples of transient responses. (**a**) Small amplitude (no snap) response (P = 213.348 Pa, ω = 116.3018 rad/s); (**b**) Persistent snap-through response (P = 240.0165 Pa, ω = 116.3018 rad/s)

of material. The rise is shown to influence the number and location of critical points, and also the postbuckling behavior. The orthogrid showed better performance with higher stiffness, increased critical forces and fewer critical surfaces.

The transient responses of curved structural components can be classified in small amplitude or large amplitude snap-through oscillations that correspond to increased fatigue risk. The variation of loading frequencies and loading amplitudes is thoroughly investigated to obtain the snap through boundary. Numerically, this is a costly process that requires completion of numerous simulations to sweep the parameter space. Further investigations are necessary to develop techniques that will allow faster evaluation of the dynamic boundaries.

Acknowledgments The work has been funded by AFOSR under Grant no. FA9550-121-1-0130 and by HPTI under Grant nos. BY11020SP, BY12020SP, and BY13020SP. These supports are greatly appreciated. Support was also received from the Data Analysis and Visualization Cyber-infrastructure funded by NSF under Grant OCI-0959097.

References

1. Sobel, L.H.: Effects of boundary conditions on the stability of cylinders subject to lateral and axial pressures. AIAA J. **2**(8), 1437–1440 (1964)
2. Batdorf, S.B.: A simplified method of elastic-stability analysis for thin cylindrical shells. 2-modified equilibrium equation, NACA technical note 1342 (1947)

3. Hoff, N., Soong, T.-C.: Buckling of circular cylindrical shells in axial compression. Int. J. Mech. Sci. **7**(7), 489–520 (1965)
4. Sobel, L.H., Weller, T., Agarwal, B.L.: Buckling of cylindrical panels under axial compression. Comput. Struct. **6**(1), 29–35 (1976)
5. Koiter, W.T.: The stability of elastic equilibrium, Technical report AFFDL-TR-70-25, (1970)
6. Wardle, B.L.: Solution to the incorrect benchmark shell-buckling problem, AIAA J. **46**(2), 381–387, (2008)
7. Tudela, M., Lagace, P., Wardle, B.: "Buckling response of transversely loaded composite shells", 39th AIAA/ASME/ASCE/AHS/ASC Structures, Structural Dynamics, and Materials Conference and Exhibit, Long Beach, CA, U.S.A., April 20–23, (1998)
8. Wriggers, P., Simo, J.C.: A general procedure for the direct computation of turning and bifurcation points. Int. J. Numer. Methods Eng. **30**(1), 155–176 (1990)
9. Wagner, W., Wriggers, P.: A simple method for the calculation of postcritical branches. Eng. Comput. **5**(2), 103–109 (1988)
10. Crisfield, M.A.: A fast incremental/iterative solution procedure that handles 'snap-through'. Comput. Struct. **13**, 55–62 (1981)
11. Zhou, Y., Stanciulescu, I., Eason, T., Spottswood, M.: Nonlinear elastic buckling and postbuckling analysis of cylindrical panels. Finite Elem. Anal. Des. **96**, 41–50 (2015)
12. Taylor, R.L.: FEAP—Finite Element Analysis Program. University of California, Berkeley, CA (2014)

Chapter 25
Optimal Representation of a Varying Temperature Field for Coupling with a Structural Reduced Order Model

Raghavendra Murthy, Andrew K. Matney, X. Q. Wang, and Marc P. Mignolet

Abstract This investigation focuses on determining how to optimally represent the temperature distribution of a structure to capture at best its effects on the nonlinear geometric response of the structure expressed in a given modal expansion format. More specifically, with the temperature assumed in an expansion form, it is desired to find thermal basis functions most adapted for the ensuing structural computations. Under the assumptions that the tensor of elasticity and coefficient of thermal expansion are independent of temperature, it is justified that these thermal basis functions should be proportional to linear and nonlinear stress distributions induced by each structural mode and linear combinations of two such modes in the absence of temperature. The implementation of this finding in the context of structural and thermal finite element models is described and validated on a hypersonic panel under strong coupling between structural, thermal, and aerodynamic analyses. It is observed that the effects of the temperature on the structural response are indeed accurately captured without requiring a full modeling of the temperature field.

Keywords Reduced order modeling • Cracked structure • Generalized finite element modeling • Local enrichment • Nonlinear geometric response • Structural model • Thermal model • Basis functions

25.1 Introduction

The heating of a structure results in changes in natural frequencies, mode shapes, and modal forces which are quite straightforward to determine in finite element analyses for a particular temperature distribution. Relying on such "hot" modal models to predict the structural response is appropriate when the temperature distribution does not change and/or is known in advance. This distribution could however vary with operating conditions and/or be dependent on the structural response itself. These situations occur in particular in connection with high speed aircraft/aerospace vehicles in which the temperature results from convection and is dependent on flight conditions but also may be coupled to the structural response through changes in the aerodynamics. For such situations, it has been proposed to construct reduced order models (ROMs) of both structural motions and temperature [1–9].

A key issue in this construction is the selection, preferably a priori/without prior knowledge, of a limited set of basis functions to represent the structural motions, the temperature, and their coupling. For the structural response, this selection is reasonably clear at this point (e.g., see [7–9]): use the linear modes to which are added enrichments to capture (1) the nonlinear geometric effects (such as the dual modes of [10, 11]) if they are present and (2) the thermally induced extension of the panel (if not already represented by the linear and dual modes).

The selection of an appropriate thermal basis is however less obvious because the heat conduction is a much more local problem than the structural one; the temperature distribution being strongly dependent on the heat flux. If prior information is available and snapshots of the temperature distribution in the structure are known, a proper orthogonal decomposition (POD) strategy is appropriate as well demonstrated in [1, 2]. When no such a priori data is available, one must proceed differently, e.g. by relying on the eigenvectors of the conductance or conductance/capacitance eigenvalue problem as done in particular in [3–5, 7]. While mathematically well founded, this approach may require that a large number of eigenvectors be included to capture the wide range of temperature distributions that arise depending on the applied heat flux.

R. Murthy • A.K. Matney • X.Q. Wang • M.P. Mignolet (✉)
SEMTE, Faculties of Mechanical and Aerospace Engineering, Arizona State University, 501 E. Tyler Mall, Tempe, AZ 85287-6106, USA
e-mail: marc.mignolet@asu.edu

G. Kerschen (ed.), *Nonlinear Dynamics, Volume 1*, Conference Proceedings of the Society for Experimental Mechanics Series,
DOI 10.1007/978-3-319-29739-2_25

In this light, the present investigation focuses on (1) the determination of the temperature distributions which most significantly affect the structural response along a given set of structural modes, and (2) the use of these distributions as basis functions for the representation of the temperature field. The application of these concepts is demonstrated on a representative panel model.

25.2 Structural-Thermal Nonlinear Reduced Order Modeling

The reduced order models considered here are based on a representation of the temperature and displacement fields in the continuum structure in a "modal expansion" form, i.e. as

$$T\left(\mathbf{X},t\right)=\sum_{n=1}^{\mu}\tau_n(t)\;T^{(n)}\left(\mathbf{X}\right) \tag{25.1}$$

for the temperature, and

$$u_i\left(\mathbf{X},t\right)=\sum_{n=1}^{M}q_n(t)\;U_i^{(n)}\left(\mathbf{X}\right) \tag{25.2}$$

for the displacement. Note that $U_i^{(m)}$ and $T^{(m)}$ are specified functions of the position vector $\boldsymbol{X}$ in the *undeformed* configuration of the structure, chosen to satisfy the necessary boundary conditions. In the context of finite elements, the analogous representations of the displacement and temperature vectors, $\boldsymbol{w}$ and $\boldsymbol{T}$, are

$$\mathbf{T}(t)=\sum_{n=1}^{\mu}\tau_n(t)\;\mathbf{T}^{(n)} \tag{25.3}$$

and

$$\mathbf{w}(t)=\sum_{n=1}^{M}q_n(t)\;\boldsymbol{\Psi}_i^{(n)}. \tag{25.4}$$

A set of nonlinear ordinary differential equations governing the evolution of the generalized coordinates $q_n(t)$ and $\tau_n(t)$ can be obtained in a Galerkin format from the governing field equations for the displacements $u_i(\mathbf{X},t)$ and temperature $T(\mathbf{X},t)$ in the undeformed configuration, see [3]. Specifically, assuming a Duhamel-Neumann form of the Helmholtz free energy in terms of the temperature and Green strain tensors with temperature independent elasticity tensor and coefficient of thermal expansion, it is found that (summation implied over repeated indices)

$$M_{ij}\;\ddot{q}_j+D_{ij}\;\dot{q}_j+K_{ij}^{(1)}\;q_j-K_{ijl}^{(th)}\;q_j\;\tau_l+F_i^{(NL)}\;\left(q_j\right)=F_i+F_{il}^{(th)}\tau_l \tag{25.5}$$

and

$$B_{ij}\;\;\dot{\tau}_j+\tilde{K}_{ij}\tau_j+K_{ijl}^{(st)}\;\dot{q}_j\;\tau_l=P_i. \tag{25.6}$$

In Eq. (25.5), the elements of the mass and linear stiffness matrices are denoted by M_{ij} and $K_{ij}^{(1)}$ while F_i denote the modal mechanical forces. Further, the components of the matrices $K_{ijl}^{(th)}$ and $F_{il}^{(th)}$ provide the influence of temperature on the structural response, thereby coupling the structural problem to the thermal one. The vector $F_i^{(NL)}\left(q_j\right)$ denotes the nonlinear forces arising from large displacements (geometric nonlinearity) as appropriate. Following [3, 10, 13] these forces are modeled as

$$F_i^{(NL)}\;\left(q_j\right)=K_{ijl}^{(2)}\;q_j\;q_l+K_{ijlp}^{(3)}\;q_j\;q_l\;q_p \tag{25.7}$$

where $K^{(2)}_{ijl}$ and $K^{(3)}_{ijlp}$ denote quadratic and cubic stiffness coefficients independent of temperature. Equations (25.5) and (25.7) have also been generalized to account for a linear dependence of the elasticity tensor and coefficient of thermal expansion with respect to temperature [5], a commonly observed behavior. In that case, $K^{(2)}_{ijl}$ and $K^{(3)}_{ijlp}$ depend linearly on the temperature generalized coordinates τ_n while the terms $K^{(th)}_{ijl}\ \tau_l$ and $F^{(th)}_{il}\tau_l$ are replaced by cubic polynomials in τ_n.

Present in the heat conduction equation, Eq. (25.6), are B_{ij} and $\tilde{K}_{ij}$, the elements of the capacitance and conductance matrices, which may depend on temperature, and therefore, on time. The source term P_i includes all heat fluxes including, as appropriate, the heat convection with the fluid, radiation effects, external heating, etc. Finally, the term $K^{(st)}_{ijl}\ \dot{q}_j\ \tau_l$ represents the latency effect which provides a direct effect of the structural response on the temperature distribution. Note however that this term is in general very small and is typically neglected.

With the parametric form of the reduced order model governing equations expressed above, it is next necessary to determine the parameters M_{ij}, $K^{(1)}_{ij}$, $K^{(2)}_{ijl}$, $K^{(3)}_{ijlp}$, $K^{(th)}_{ijl}$, $F^{(th)}_{il}$, B_{ij} and $\tilde{K}_{ij}$ using the structural and thermal finite element models of the panel. This procedure will not be described here for brevity, it is detailed in [3], see also [5, 13], when the elasticity tensor and coefficient of thermal expansion depend on temperature.

25.3 Optimum Thermal Modes

Equation (25.5) demonstrates that the effect of temperature on the structural response arises from two set of coupling terms, one on its left-hand-side, TE_1, (a matrix) and the other one on its right-hand-side, TE_2, (a vector) defined as

$$TE_1 = K^{(th)}_{ijl}\ \tau_l \tag{25.8a}$$

and

$$TE_2 = F^{(th)}_{il}\ \tau_l \tag{25.8b}$$

For an improved perspective in the nature of these terms, assume that $K^{(th)}_{ijl}$ and $F^{(th)}_{il}$ are represented by the expressions derived in [3], i.e.,

$$K^{(th)}_{ijl} = \int_{\Omega_0} \frac{\partial U^{(i)}_s}{\partial X_k}\frac{\partial U^{(j)}_s}{\partial X_p}\ C_{pkvr}\ \alpha_{vr}\ T^{(l)}\ d\mathbf{X} \tag{25.9}$$

and

$$F^{(th)}_{il} = \int_{\Omega_0} \frac{\partial U^{(i)}_s}{\partial X_k}\ C_{skvr}\ \alpha_{vr}\ T^{(l)}\ d\mathbf{X} \tag{25.10}$$

where α and C are the thermal expansion and elasticity tensors and Ω_0 denotes the domain of the structure in the undeformed space. Then,

$$TE_1 = K^{(th)}_{ijl}\ \tau_l = \int_{\Omega_0} \frac{\partial U^{(i)}_s}{\partial X_k}\frac{\partial U^{(j)}_s}{\partial X_p}\ C_{pkvr}\ \alpha_{vr}\ T^{(l)}\ \tau_l\ d\mathbf{X} = \int_{\Omega_0} \frac{\partial U^{(i)}_s}{\partial X_k}\frac{\partial U^{(j)}_s}{\partial X_p}\ C_{pkvr}\ \alpha_{vr}\ T\ d\mathbf{X} \tag{25.11}$$

and

$$TE_2 = F^{(th)}_{il}\ \tau_l = \int_{\Omega_0} \frac{\partial U^{(i)}_s}{\partial X_k}\ C_{skvr}\ \alpha_{vr}\ T^{(l)}\ \tau_l\ d\mathbf{X} = \int_{\Omega_0} \frac{\partial U^{(i)}_s}{\partial X_k}\ C_{skvr}\ \alpha_{vr}\ T\ d\mathbf{X} \tag{25.12}$$

which demonstrate that $K^{(th)}_{ijl}$ and $F^{(th)}_{il}$ are the projections of the temperature distribution on the two fields

$$G_{ij} = \frac{\partial U^{(i)}_s}{\partial X_k}\frac{\partial U^{(j)}_s}{\partial X_p}\ C_{pkvr}\ \alpha_{vr} \tag{25.13}$$

and

$$H_i = \frac{\partial U_s^{(i)}}{\partial X_k} C_{skvr} \alpha_{vr}. \tag{25.14}$$

Accordingly, the temperature distribution can be written as

$$T(\mathbf{X}, t) = \sum_{n=1}^{\widehat{\mu}} \widehat{\tau}_n(t) \widehat{T}^{(n)}(\mathbf{X}) + T_\perp(\mathbf{X}, t) \tag{25.15}$$

where the basis functions $\widehat{T}^{(n)}(\mathbf{X})$ span the space of the fields G_{ij} and H_i, $\widehat{\tau}_n(t)$ are their corresponding generalized coordinates, and $T_\perp(\mathbf{X}, t)$ is at all times perpendicular to all functions $\widehat{T}^{(n)}(\mathbf{X})$. Furthermore, the effect of the temperature field on the structure is only dependent on the values of $\widehat{\tau}_n(t)$. Thus, the functions $\widehat{T}^{(n)}(\mathbf{X})$ represent a natural basis to include in the representation of the temperature field as it captures exactly the thermal-structural coupling. However, it is clear from Eq. (25.15) that this basis is not complete, it is only one component of a rational representation of the temperature distribution.

Having demonstrated the interest of the basis $\widehat{T}^{(n)}(\mathbf{X})$, the next step is to devise its construction. To this end, note that

$$S_i^L(\mathbf{X}) = C_{skvr} \frac{\partial U_s^{(i)}}{\partial X_k} \tag{25.16}$$

is the linear stress induced by structural mode i at point $\mathbf{X}$. Thus, the functions H_i can be obtained by computing the distribution of the linear stress on the structure induced by mode i displacements multiplied at each point by the local thermal expansion tensor. This perspective thus provides an approach to determining H_i from a finite element model.

The total Lagrangian formulation of [10] demonstrates that any component of the 2nd Piola-Kirchhoff stress tensor at each point of the structure is a quadratic function of the generalized coordinates, i.e.,

$$S(\mathbf{X}) = S_0(\mathbf{X}) + q_i S_i^L(\mathbf{X}) + q_i q_j S_{ij}^{NL}(\mathbf{X}) \tag{25.17}$$

with $S_0(\mathbf{X})$ the stress component due to the thermal expansion, $S_i^L(\mathbf{X})$ defined as above, and

$$S_{ij}^{NL}(\mathbf{X}) = C_{pkvr} \frac{\partial U_s^{(i)}}{\partial X_k} \frac{\partial U_s^{(j)}}{\partial X_p}. \tag{25.18}$$

Accordingly, the functions G_{ij} can also be evaluated from a finite element model. Specifically, the terms corresponding to $j = i$ are first determined by subjecting the nonlinear structure to displacements along mode i alone without temperature, determining the (2nd Piola-Kirchhoff) stress distribution, and removing the linear part of the stress, Eq. (25.16), leaving $S_{ii}^{NL}(\mathbf{X})$. Finally, the structure is displaced according to a linear combination of modes i and j and the stresses are determined. From them $S_{ij}^{NL}(\mathbf{X})$ is computed as (no sum on i nor j)

$$S_{ij}^{NL}(\mathbf{X}) = \frac{1}{q_i q_j} \left[S(\mathbf{X}) - q_i S_i^L(\mathbf{X}) - q_i^2 S_{ii}^{NL}(\mathbf{X}) - q_j S_j^L(\mathbf{X}) - q_j^2 S_{jj}^{NL}(\mathbf{X}) \right]. \tag{25.19}$$

Next, the distributions $S_i^L(\mathbf{X})$ and $S_{ij}^{NL}(\mathbf{X})$ are regrouped to form a first approximation, $T'^{(n)}(\mathbf{X})$, of the basis $\widehat{T}^{(n)}(\mathbf{X})$ and the corresponding values of the coefficients $K_{ijl}^{(th)}$, denoted as $K'^{(th)}_{ijl}$, are determined for all functions $T'^{(n)}(\mathbf{X})$. The first group of basis functions $\widehat{T}^{(n)}(\mathbf{X})$ is then obtained as the linear combinations of the $T'^{(n)}(\mathbf{X})$ that give maximum values of the resulting coefficients $K_{ijl}^{(th)}$ and $F_{il}^{(th)}$, denoted as $\widehat{K}_{ijl}^{(th)}$ and $\widehat{F}_{il}^{(th)}$, for an ensemble of values of i and j (potentially all structural modes). This problem in fact reduces to the eigenvalue problem

$$\mathbf{V} \boldsymbol{\varphi}_i = \lambda_i \boldsymbol{\varphi}_i \tag{25.20}$$

where the vector $\boldsymbol{\varphi}_i$ contains the coordinates of the representation of $\widehat{T}^{(n)}(\mathbf{X})$ on $T'^{(n)}(\mathbf{X})$ and the matrix $\mathbf{V}$ is defined by its elements as

$$V_{Il} = K'^{(th)}_{ijl} \tag{25.21}$$

where the values of the structural index I are reshaped from the mode numbers i and j of interest. An analysis of the sorted eigenvalues λ_i is then carried out and the $\widehat{\mu}_1$ eigenvectors with largest eigenvalues are retained. Stacking them by columns in the matrix

$$\boldsymbol{\Phi} = \left[\boldsymbol{\varphi}_1\ \boldsymbol{\varphi}_2 \ldots \boldsymbol{\varphi}_{\widehat{\mu}_1}\right] \tag{25.22}$$

yields the first group of "optimum thermal modes"

$$\widehat{T}^{(n)}(\mathbf{X}) = \boldsymbol{\Phi}\ T'^{(n)}(\mathbf{X}). \tag{25.23}$$

Utilizing these modes will give an accurate and compact representation of the coupling term

$$TE_1 = K^{(th)}_{ijl}\ \tau_l \approx \widehat{K}^{(th)}_{ijl}\ \widehat{\tau}_l \tag{25.24}$$

but may not lead to an equal good match of the other coupling term TE_2. To address the issue, a second group of optimum thermal modes is determined to ensure a good matching of these terms. Its construction proceeds as follows. The residuals $F''^{(th)}_{il}$ of the projections of the coefficients $F^{(th)}_{il}$ on the basis functions $\widehat{T}^{(n)}(\mathbf{X})$ are first determined and are assembled in the matrix $\mathbf{W}$ of elements

$$W_{il} = F''^{(th)}_{il}. \tag{25.25}$$

The eigenvalues and eigenvectors of $\mathbf{W}$ are next determined from

$$\mathbf{W}\ \overline{\boldsymbol{\varphi}}_i = \overline{\lambda}_i\ \overline{\boldsymbol{\varphi}}_i. \tag{25.26}$$

Keeping again the $\widehat{\mu}_2$ eigenvectors with largest eigenvalues $\overline{\lambda}_i$ are retained. Stacking them by columns in the matrix

$$\overline{\boldsymbol{\Phi}} = \left[\overline{\boldsymbol{\varphi}}_1\ \overline{\boldsymbol{\varphi}}_2 \ldots \overline{\boldsymbol{\varphi}}_{\widehat{\mu}_2}\right] \tag{25.27}$$

yields the second group of "optimum thermal modes"

$$\widehat{T}^{(n)}(\mathbf{X}) = \overline{\boldsymbol{\Phi}}\ T'^{(n)}(\mathbf{X}). \tag{25.28}$$

25.4 Validation Example

The representative hypersonic panel used by Culler and McNamara [12], and shown in Fig. 25.1 is an excellent test case to validate the concept and construction of the optimum thermal modes given the complexity of the structural and thermal interactions through aerodynamics.

The structural finite element model [12] is composed of 2400 CQUAD4 (4 node plate) elements, resulting in 2499 nodes. In both the structural and thermal problems the dimensions of the element were 0.25 in. by 0.25 in. The panel has the following structural boundary conditions

1. At the leading edge, $x = 0$ and $z = 0$, zero displacements are enforced for all degrees of freedom but the y translations, which are free.

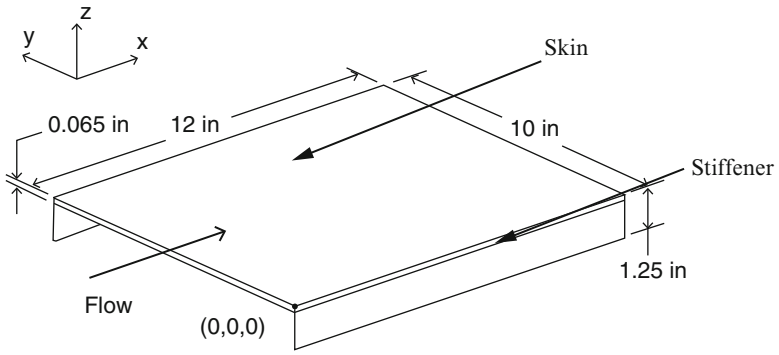

Fig. 25.1 Representative hypersonic ramp panel

Table 25.1 Material properties of panel

Young's moduli (psi)	15×10^6	Density (lbm/in^3)	0.065	Coeff. Therm. Exp. (1/°F) at 30°F	0.556×10^{-6}
Shear modulus$_{12}$	2.5×10^6	Poisson's ratio$_{12}$	0.30	Coeff. Therm. Exp. (1/°F) at 2500°F	2.334×10^{-6}

Table 25.2 Specific heat (c) and in-plane conductivity (k) vs. temperature (T)

T (°F)	c (BTU/lbm/°F)	k (BTU/h/ft/°F)	T (°F)	c (BTU/lbm/°F)	k (BTU/h/ft/°F)
0	0.170	17.5	1500	0.330	23.3
200	–	20.9	1750	–	23.1
500	0.242	23.6	2000	0.360	22.5
750	–	24.2	2250	–	21.9
1000	0.295	24.2	2500	0.390	21.4
1250	–	23.9	2750	–	20.9

2. At the trailing edge, $x = 12$ in and $z = 0$, zero displacements are enforced for all degrees of freedom except x and y translations, which are free. Springs also act on the nodes of the trailing edge in the x direction with a spring constant of 2378 lb/in.
3. At the panel center, $x = 6$ in, $y = 5$ in, and $z = 0$, zero displacement is enforced for y translations.

The structural properties of the composite material used in this model, advanced carbon–carbon 4, are provided in Table 25.1 [15]. These properties, except for the coefficient of thermal expansion will remain constant since there is no significant change over the range of temperatures experienced in this analysis. Moreover, the coefficient of thermal expansion was assumed to vary linearly between the data given in Table 25.1.

The thermal finite element model [12] consisted of 8-node brick elements (CHEXA) on the skin and plane elements (CQUAD4) on the stiffeners for a total to 2400 elements and 4508 nodes. The CHEXA elements allowed for the through thickness temperature gradient to be calculated while the CQUAD4 elements yielded a constant temperature through thickness. This choice of elements resulted from the boundary conditions which were adiabatic on the stiffeners and the bottom of the skin while on its top a flux boundary condition was imposed accounting for both convection and radiation. With these boundary conditions, a near constant temperature through the thickness of the stiffeners could be expected while a variation of temperature through the skin thickness would take place. Since the structural elements on the skin permit only the imposition of a linear temperature profile, a single thermal element through the thickness of the skin was adopted. The thermal properties of the panel are defined as a function of temperature in Table 25.2 except for the emissivity (=0.8) and the 33 component of the thermal conductivity (=3.0 BTU/h/ft/°F).

Finally, the aerodynamic pressure and aerodynamic heating were modeled using piston theory and Eckert's reference enthalpy method, respectively. The vehicle was accelerated from Mach 2 to Mach 12 over 300 s, while the dynamic pressure was held constant at 2000 psf. The structural, thermal and aerodynamic solutions were marched in time in a process described in detail in [12]. One-way coupling refers to the analysis in which the thermal problem is executed independently of the structural deformation. The temperature fields are fed to the structural solver and influence its response, but the structural displacement does not affect the heating on the panel. Two-way coupling refers to analyses in which the heating on the panel is influenced by the structural displacement. It is this latter format that more closely resembles reality, and is the subject of the work presented here.

The development of an accurate ROM of the two-way coupled situation was achieved through a series of steps in [7–9, 14] which serves as baseline for the present investigation, the 38 structural modes and the thermal modes and the corresponding generalized coordinates time histories more specifically.

The procedure described above was mostly followed to construct the optimum thermal modes with the linear and nonlinear stress distributions $S_i^L(\mathbf{X})$ and $S_{ij}^{NL}(\mathbf{X})$ obtained from the Nastran finite element model of the panel. Two variations of the stated procedure were however implemented. The first relates to the set of tentative modes $T'^{(n)}(\mathbf{X})$. Specifically, the derivation of Eq. (25.15) from Eqs. (25.13) and (25.14) assumes that the temperature distribution can be arbitrarily varied on the surface and through the thickness of the panel to match the stress distributions. While it is true for the former (within the limits of the finite elements construct), only a linear temperature through thickness can be imposed on the structural plate elements of the skin and only a constant temperature through thickness results from the choice of plate thermal elements on the stiffeners. So, one might expect that Eq. (25.15) does not capture correctly the through thickness aspects and thus not only were the original nonlinear stress modes retained, but the modes obtained by flipping the sign of the stress mode in the bottom of the panel only were also taken as part of the basis. Combining these two groups of modes allows to obtain any linear through thickness behavior.

The second modification of the process concerns the matrix $\mathbf{V}$ the elements of which were normalized by the linear stiffness matrix, i.e.,

$$V_{Il} = \frac{K'^{(th)}_{ijl}}{\sqrt{K^{(1)}_{ii} K^{(1)}_{jj}}} \tag{25.29}$$

to better quantify the temperature effects with respect to the natural stiffness of the panel.

To validate the appropriateness of the optimum thermal modes, the temperature distributions obtained in [9] for the two-way coupled problem were adopted and the present focus was on first demonstrating that the terms TE_1 and TE_2 obtained with the optimum thermal modes accurately matched those obtained from the ROM computations of [9]. For this check, the temperatures of [9] were projected on the optimum thermal modes to obtain the corresponding generalized coordinates $\widehat{\tau}_n(t)$. Second, it was also of interest to assess how well the temperature distribution could be captured by just the optimum thermal modes and their generalized coordinates. A close representation is not necessarily expected but it would be desirable that the optimum thermal modes provide a good start on the representation of the temperature.

Shown in Fig. 25.2 are the sorted eigenvalues of the optimum thermal mode eigenvalue problem, Eq. (25.20). 35 optimum thermal modes were chosen to be retained based on the eigenvalues dropping to 0.1 % of the maximum eigenvalue. A final addition to this basis was the uniform temperature.

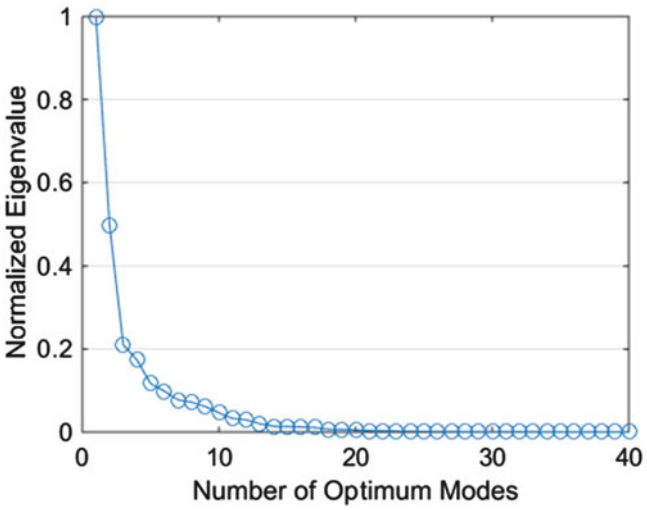

Fig. 25.2 Eigenvalues vs. eigenvector number, Eq. (25.20)

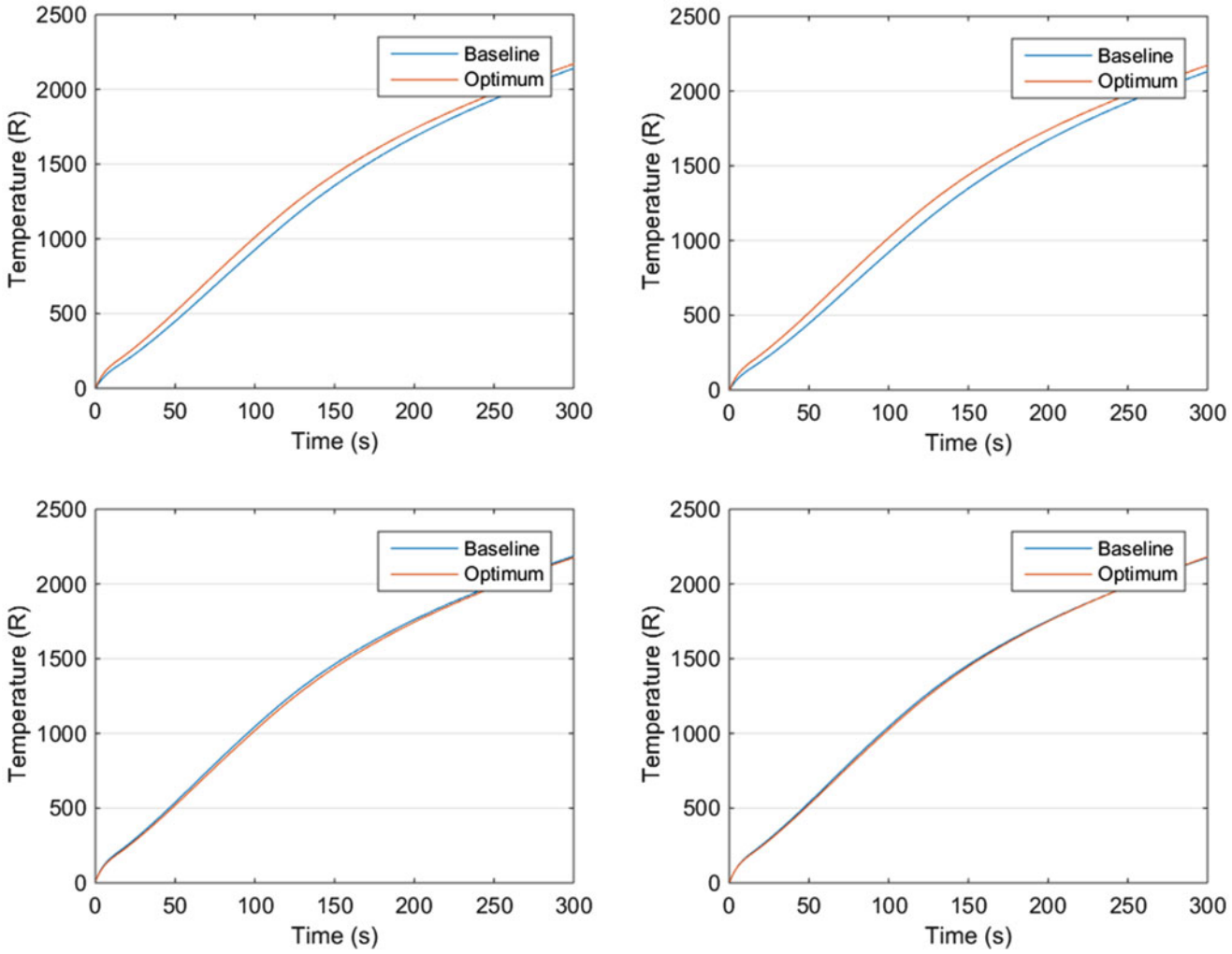

Fig. 25.3 Comparisons of the temperature vs. time at several nodes as computed from the reduced order model of [9] (curves "Baseline") and using the optimum thermal modes (curves "Optimum")

Shown in Fig. 25.3 are some representative temperature time histories on selected nodes on the panel. It can be observed that the optimum modes provide a good first approximation of the temperature distribution obtained from [9] even though they were not designed to this end.

Next, shown in Fig. 25.4 is the evolution over time of some of the components of the matrix TE_1 as computed directly from the reduced order model of [9] and using the optimum thermal modes. Clearly, the matching is very good for the dominant components of this matrix demonstrating the optimum thermal modes do accomplish what they were designed for, i.e., capture the effects of temperature on structural response.

Considering the temperature effect term TE_2, it was desired to assess whether this vector can be accurately captured by a the linear stress mode distribution H_i alone as suggested by Eq. (25.12). To this end, the eigenvalue problem of Eq. (25.26) was modified to include directly the terms $F_{il}^{(th)}$ of the projections of the coefficients as opposed to their residues $F''^{(th)}_{il}$.

Shown in Fig. 25.5 are the corresponding sorted eigenvalues from which it was decided to select the first 35 eigenvectors as other optimum thermal modes. As done in connection with TE_1, a final addition to this basis was the uniform temperature. Then, shown in Fig. 25.6 is the evolution over time of some of the components of the vector TE_2 as computed directly from the reduced order model of [9] and using the optimum thermal modes. While the matching is not as close as seen in Fig. 25.4, it is clear that the overall trends of these components is captured by the basis.

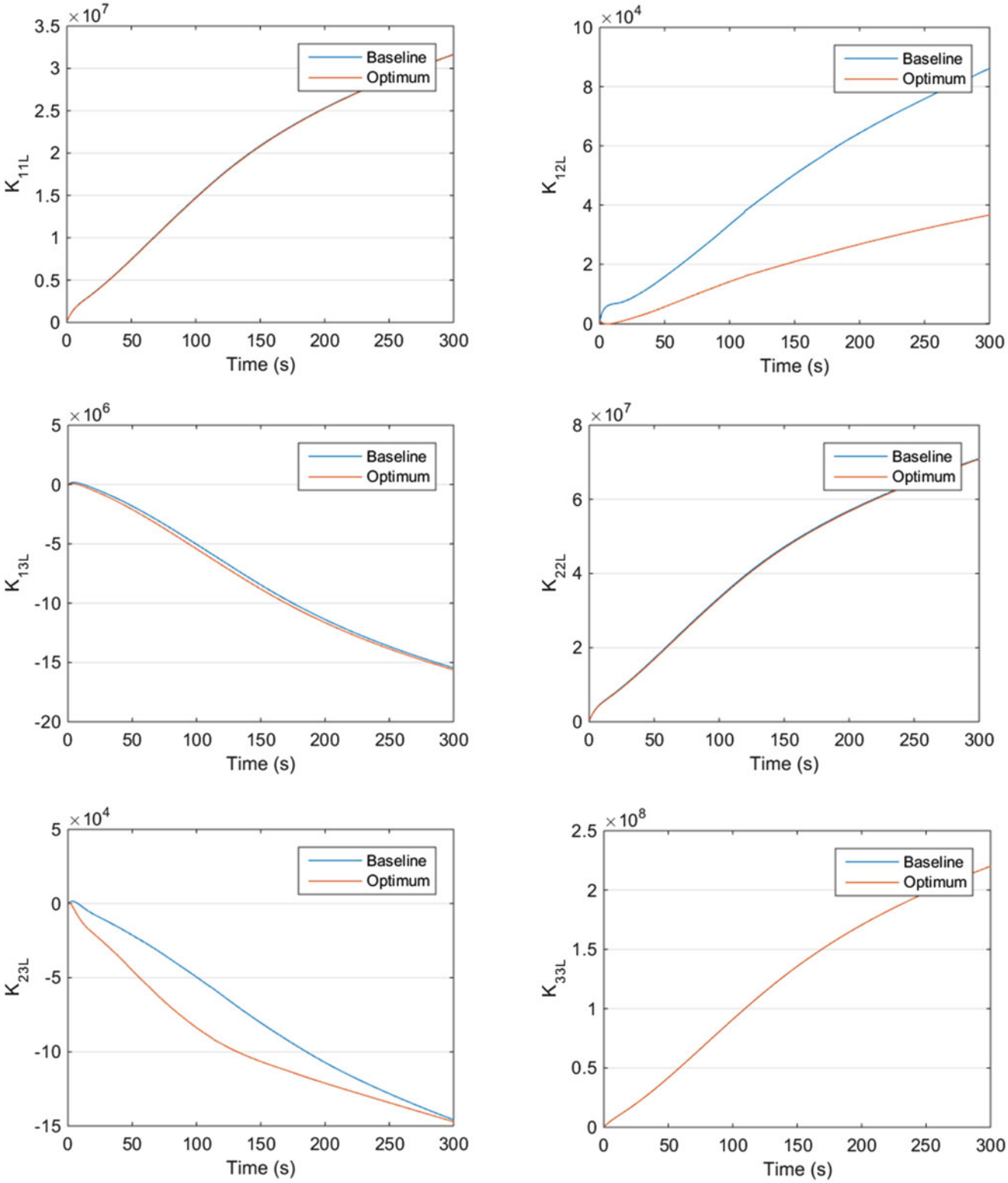

Fig. 25.4 Comparisons of selected elements of the matrix TE_1 vs. time as computed from the reduced order model of [9] (curves "Baseline") and using the optimum thermal modes (curves "Optimum")

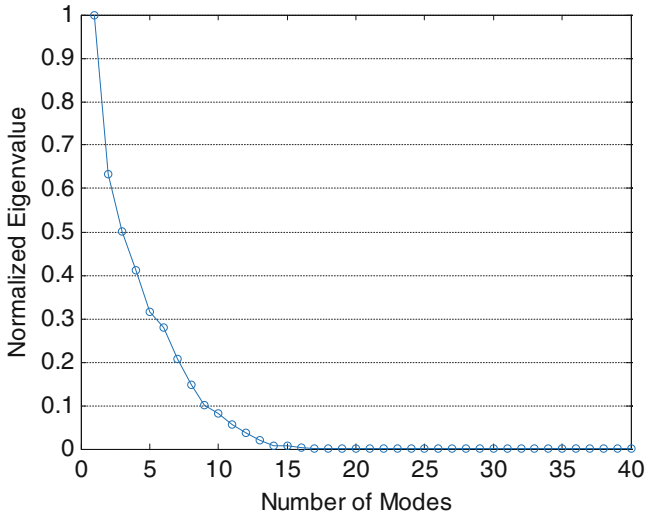

Fig. 25.5 Eigenvalues vs. eigenvector number, Eq. (25.26)

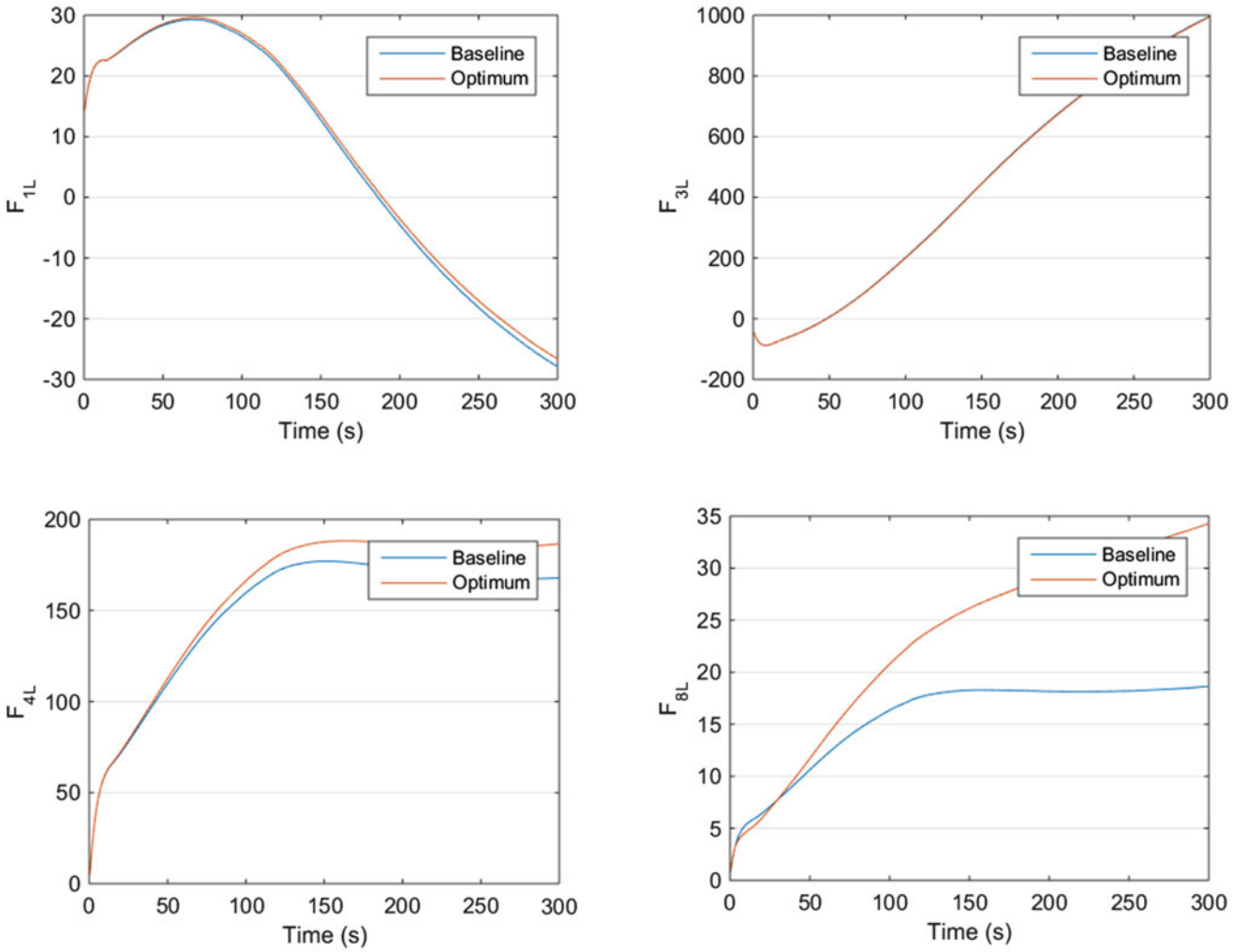

Fig. 25.6 Comparisons of selected elements of the vector TE_2 vs. time as computed from the reduced order model of [9] (curves "Baseline") and using the optimum thermal modes (curves "Optimum")

25.5 Summary

The context of the present investigation is the construction of coupled structural-thermal ROMs for the analysis of hot structures. A challenging question has been the a priori selection of thermal basis functions for the representation of the temperature and its ensuing effects on the structural response. The present effort adopts a structure-centric perspective, i.e., addresses the determination of the temperature distributions that affect most strongly the structural response as quantified by the thermal effects terms TE_1 and TE_2, see Eq. (25.8a) and (25.8b), under the assumptions that the tensor of elasticity and coefficient of thermal expansion are independent of temperature. Relying on a Lagrangian finite deformation elasticity analysis, integral expressions for TE_1 and TE_2 are first derived which show those terms as projections of the thermal strains, the product of the temperature by the thermal expansion tensor, on the linear and nonlinear stresses (2nd Piola-Kirchhoff) induced by structural deformations in its assumed modes. This interpretation then demonstrates that the "optimum thermal modes" should be proportional to the distributions of those stresses. The transposition of this result to plate/shell finite element models of the structural and thermal response of the structure is described and a detailed validation is carried out on a hypersonic panel under strong coupling between structural, thermal, and aerodynamic analyses. It is observed, see Figs. 25.4 and 25.6, that the effects of the temperature on the structural response, TE_1 and TE_2, are indeed captured without requiring a full modeling of the temperature field. Finally, it is seen, Fig. 25.3, that the combination of the optimum thermal modes and a uniform temperature (in this case, given the adiabatic boundary conditions) leads to a good first approximation of the temperature distribution. Further efforts will focus on complementing these basis functions for an accurate representation of the entire temperature distribution as well, not just of its effects on the structural response.

Acknowledgements The authors gratefully acknowledge the support of this work by the AFRL-University Collaborative Center in Structural Sciences (Cooperative Agreement FA8650-13-2-2347), with Dr. Ravi Penmetsa as program manager.

References

1. Falkiewicz, N.J., Cesnik, C.E.S.: Proper orthogonal decomposition for reduced-order thermal solution in hypersonic aerothermoelastic simulations. AIAA J. **49**(5), 994–1009 (2011)
2. Falkiewicz, N.J., Cesnik, C.E.S., Crowell, A.R., McNamara, J.J.: Reduced order aerothermoelastic framework for hypersonic vehicle control simulation. AIAA J. **49**(8), 1625–1646 (2011)
3. Perez, R., Wang, X.Q., Mignolet, M.P.: Nonlinear reduced order models for thermoelastodynamic response of isotropic and FGM panels. AIAA J. **49**, 630–641 (2011)
4. Perez, R., Wang, X.Q., Mignolet, M.P.: Steady and unsteady nonlinear thermoelastodynamic response of panels by reduced order models. In: Proceedings of the 51st Structures, Structural Dynamics, and Materials Conference, Orlando, Florida, 12–15 Apr 2010, Paper AIAA-2010-2724
5. Matney, A., Perez, R., Mignolet, M.P.: Nonlinear unsteady thermoelastodynamic response of a panel subjected to an oscillating flux by reduced order models. In: Proceedings of the 52nd Structures, Structural Dynamics and Materials Conference, Denver, Colorado, 4–7 Apr 2011, AIAA 2011-2016
6. Hollkamp, J., Gordon, R.: Application of reduced-order models for thermoelastic trajectory simulation. In: Proceedings of the 53nd Structures, Structural Dynamics and Materials Conference, Honolulu, Hawaii, 23–26 Apr 2012, AIAA-2012-1550
7. Matney, A., Spottswood, S.M., Mignolet, M.P., Culler, A.J., McNamara, J.J.: Coupled reduced order model-based structural-thermal prediction of hypersonic panel response. In: Proceedings of the 11th International Conference on Recent Advances in Structural Dynamics, Pisa, Italy, 1–3 July 2013
8. Matney, A., Mignolet, M.P., Spottswood, S.M., Culler, A.J., McNamara, J.J.: Thermal reduced order model adaptation to aero-thermo-structural interactions. In: Proceedings of the 55th Structures, Structural Dynamics and Materials Conference (SciTech 2014), National Harbor, Maryland, 13–17 Jan 2014
9. Matney, A., Mignolet, M.P., Culler, A.J., McNamara, J.J., Spottswood, S.M.: Panel response prediction through reduced order models with application to hypersonic aircraft. In: Proceedings of the AIAA Science and Technology Forum and Exposition (SciTech 2015), Orlando, FL, 5–9 Jan 2015, AIAA Paper AIAA 2015-1630
10. Kim, K., Radu, A.G., Wang, X.Q., Mignolet, M.P.: Nonlinear reduced order modeling of isotropic and functionally graded plates. Int. J. Non Linear Mech. **49**, 100–110 (2013)
11. Perez, R.A., Wang, X.Q., Mignolet, M.P.: Non-intrusive structural dynamic reduced order modeling for large deformations: enhancements for complex structures. J. Comput. Nonlinear Dyn. **9**(3), 031008-1–031008-12 (2014)

12. Culler, A., McNamara, J.: Impact of fluid-thermal-structural coupling on response prediction of hypersonic skin panels. AIAA J. **49**, 2393–2406 (2011)
13. Mignolet, M.P., Przekop, A., Rizzi, S.A., Spottswood, S.M.: A review of indirect/non-intrusive reduced order modeling of nonlinear geometric structures. J Sound Vib. **332**(10), 2437–2460 (2013)
14. Matney, A., Perez, R.A., Spottswood, S.M., Wang, X.Q., Mignolet, M.P.: Nonlinear structural reduced order modeling methods for hypersonic structures. In: Proceedings of the 53nd Structures, Structural Dynamics and Materials Conference, Honolulu, Hawaii, 23–26 Apr 2012, AIAA -2012-1972
15. Blevins, R.D., Holehouse, I., Wentz, K.R.: Thermoacoustic loads and fatigue of hypersonic vehicle skin panels. J. Aircr. **30**(6), 971–978 (1993)

Chapter 26
Basis Identification for Nonlinear Dynamical Systems Using Sparse Coding

Rohit Deshmukh, Zongxian Liang, and Jack J. McNamara

Abstract Basis identification is a critical step in the construction of accurate reduced order models using Galerkin projection. This is particularly challenging in unsteady nonlinear flow fields due to the presence of multi-scale phenomena that cannot be ignored and are not well captured using the ubiquitous Proper Orthogonal Decomposition. This study focuses on this issue by exploring an approach known as sparse coding for the basis identification problem. Compared to Proper Orthogonal Decomposition, which seeks to truncate the basis spanning an observed data set into a small set of dominant modes, sparse coding is used to select a compact basis that best spans the entire data set. Thus, the resulting bases are inherently multi-scale, enabling improved reduced order modeling of unsteady flow fields. The approach is demonstrated for a canonical problem of an incompressible flow inside a 2-D lid-driven cavity. Results indicate that Galerkin reduction of the governing equations using sparse modes yields significantly improved fluid predictions.

Keywords Post-execution basis identification • Sparse coding • Multi-scale • POD • ROM

26.1 Introduction and Problem Statement

The advancement of computational fluid dynamics (CFD), parallel computing algorithms, and computing hardware, has enabled unprecedented insight into complex flow physics through numerical analysis. However, the computational expense associated with such analysis tools has restricted their application to relatively small spatial and temporal scale studies on simplistic configurations. Thus, the advances in CFD methodologies have not yet enabled the broad consideration of nonlinear, multi-scale, unsteady flows, in systems level studies—e.g. fluid-structure interaction, flow control, aerodynamic design, structural design, etc. Yet the critical need for high fidelity flow modeling in such problems motivates the pursuit of tractable and robust reduced order models (ROMs).

A common ROM approach is to project the governing equations onto a reduced dimensional space comprised of characteristic bases [1–6]. These can be based on orthogonal (e.g., Galerkin) or non-orthogonal (e.g., Petrov-Galerkin) projections [1–6]. However, the accuracy of such approaches is intimately bound to the quality of the chosen bases. This is challenging for nonlinear problems, due to the need to carry out basis identification from post execution data of representative system dynamics. In the context of highly unsteady nonlinear flows, this is further complicated by the fact that generally: (1) the gathering of the data is computationally expensive, (2) the data is very large and high dimensional, and (3) the scope of the data is narrow. Thus, identifying a compact set of prominent and dynamically important flow features to fundamentally characterize the fluid dynamics is a non-trivial problem.

Proper Orthogonal Decomposition (POD), or Principal Components Analysis (PCA) [1, 7–10], is a widely used and explored technique aimed at meeting this need. The approach is based on identifying and ordering principal components in observed data. The POD modes are optimal in terms of capturing the energy of an observed flow response, thus a reduced dimensional basis of the system is often identified by truncating the modes based on energy contribution to the response [1, 7–10]. However, there are several issues with this approach. First, the POD modes are only optimal in the sense of reconstructing the observed flow responses [1, 11, 12]. Thus, they may not generalize well for model predictions that deviate from observed conditions. From a fluid physics perspective, a truncated set of POD modes is biased towards the high-energy, large-scale, dominant structures and ignores the small-scale, low-energy structures [1, 11, 13]. The large-scale structures are formed as a result of disturbances in the flow- obtaining energy from the mean flow, and then subsequently breaking down into smaller scales [14]. The small-scale structures then cause energy dissipation and result in viscosity in the fluid-flow.

R. Deshmukh • Z. Liang • J.J. McNamara (✉)
Department of Mechanical and Aerospace Engineering, The Ohio State University, Columbus, OH 43210, USA
e-mail: mcnamara.190@osu.edu

G. Kerschen (ed.), *Nonlinear Dynamics, Volume 1*, Conference Proceedings of the Society for Experimental Mechanics Series,
DOI 10.1007/978-3-319-29739-2_26

Thus, POD based Galerkin ROMs do not account for sufficient energy dissipation, resulting in over-prediction of kinetic energy [1, 11, 13]. Moreover, the energy accumulation over a period of time may also cause the ROM to become unstable [11, 13, 15]. Related to this, it is now well-established that POD modes are ineffective in capturing the local dynamics (or transience) of full-order systems [11, 12]. This is because the POD modes are always active, or have nonzero coefficients for all time windows. For these reasons it is clear that the optimality of POD modes, in terms of energy capture, is non-ideal for model reduction of highly unsteady, nonlinear flow fields.

Techniques such as Balanced Truncation [16], Balanced POD (BPOD) [2], and Eigensystem Realisation Algorithm (ERA) [17] have addressed some of the limitations identified earlier. However, balanced truncation is intractable for large data (for more than 10,000 degrees of freedom) [3], BPOD is only applicable to response data of linear systems as it requires adjoint system information [2, 17], and modes generated by ERA cannot be used for projection of non-linear dynamics [17]. In a recent study, a technique is developed to generate a stable Galerkin projection based ROM [11]. However, building the ROM is an iterative process, and requires multiple time-integrations until an energy-balance is achieved. These issues highlight the need to explore alternative basis identification techniques that not only generalize well to changing flow conditions, but also accurately capture essential multi-scale features.

Olshausen and Field [18] argue that most naturally occurring phenomena are conveniently represented using non-Gaussian distributions, whereas the PCA approach is suitable when the structure of the data can be represented using Gaussian distributions. In Gaussian distributions, the linear correlation between statistical structures is the most important relation. Observations from a naturally occurring phenomena, such as natural images, contain higher order statistics. To this end, a technique based on sparse coding was proposed to extract the higher order features from natural image data [18]. This approach, which is also referred to as sparse dictionary learning [19], generates a finite dictionary of modes in which only a subset is active—i.e. has nonzero coefficients—for a given time window. Furthermore, sparse coding describes a nonlinear system in a locally linear manner by tailoring the modes to local behavior of the system [20]. Thus, compared to the POD approach—where the principal components of the observed data are identified, ordered and then truncated to a compact set—sparse coding is formulated as a procedure to identify a compact representation that best spans the entire observed data. The sparse coding approach has been successfully applied in a number of topics, such as in image processing [21], audio analysis [22], neuroscience [18, 23, 24], and electrical power disaggregation [25].

In a previous study conducted by the authors, sparse coding approach was examined in the context of reduced order modeling of dynamical systems [26]. The ROMs generated using sparse bases were compared against the standard POD ROMs in terms of stability and accuracy. The sparse ROMs were found to perform better than the POD ROMs when the same number of modes were used. This paper is a continuation of that study, where the performance of the sparse and POD bases are assessed in the context of different energy components of the dynamical system—in this case turbulent kinetic energy of a lid driven cavity.

The remainder of this extended abstract is organized as follows. The POD and the sparse coding approaches are presented in Sect. 26.2. Results describing the application of POD and sparse modes to model the unsteady flow fields are presented in Sect. 26.3. Concluding remarks are presented in Sect. 26.4.

26.2 Method of Solution

High resolution data are computed by solving the 2-D incompressible Navier Stokes (NS) equations using a Direct Numerical Simulation (DNS) CFD solver. The POD approach is based on the method of snapshots developed by Sirovich [10]. Sparse modes are evaluated using the algorithm developed by Friedman et al. [27]. These approaches are detailed next.

26.2.1 Full Order Models

The DNS solution to the non-dimensionalized NS equations given by (26.1) is generated using the PICar3D code [28].

$$\nabla \cdot \boldsymbol{u} = 0, \quad \frac{\partial \boldsymbol{u}}{\partial t} + (\boldsymbol{u}.\nabla)\boldsymbol{u} = -\nabla p + \frac{1}{Re}\nabla^2 \boldsymbol{u} \tag{26.1}$$

where ∇ is the gradient operator, t is non-dimensional time, Re is Reynolds number, p is pressure, and $\boldsymbol{u}$ is velocity.

The PICar3D code uses a second order central difference spatial scheme and a second-order fractional-step method for time marching. The equations are discretized on a Cartesian mesh and boundary conditions are imposed using a ghost-cell procedure [28].

26.2.2 Generation of the Reduced Order Modes

The full order solution is decomposed into mean ($\bar{\boldsymbol{U}}(\mathbf{x})$) and fluctuating components ($\boldsymbol{q}(\boldsymbol{x}, t)$) of velocity. The component $\bar{\boldsymbol{U}}(\boldsymbol{x})$ is evaluated as time average of velocity field. The component ($\boldsymbol{q}(\boldsymbol{x}, t)$) is approximated as a linear combination of the reduced order modes:

$$\boldsymbol{q}(\boldsymbol{x}, t) = \tilde{\mathbf{u}}(\mathbf{x}, t) \approx \sum_{i=1}^{N} s^i(t)\boldsymbol{\Phi}_i(\boldsymbol{x}), \tag{26.2}$$

where $\boldsymbol{\Phi_i}$ is the ith mode, $\tilde{u}$ is the fluctuating component of the velocity field, N is the number of modes, $s^i(t)$ is the coefficient corresponding to the ith mode at time t, and $x \in \Omega$, Ω being the flow domain. The computation of POD and sparse modes are discussed next.

26.2.2.1 Proper Orthogonal Decomposition

The procedure to extract POD modes from a snapshot matrix $\boldsymbol{Q} = [\boldsymbol{q_1 q_2 \cdots q_k \cdots q_m}]$ has been extensively documented [8, 10] and therefore is not repeated here. However, for comparative discussion with the sparse coding procedure, it is convenient to note that the POD modes fundamentally represent the solution to the following minimization problem [29]:

$$\min_{\boldsymbol{\Phi},\boldsymbol{S}} \frac{1}{2} \|\boldsymbol{Q} - \boldsymbol{\Phi S}\|_F^2 \quad \text{such that} \quad \|\boldsymbol{\Phi}_i\| \leq 1 \ \text{ for all } \ i, \tag{26.3}$$

where the columns of $\boldsymbol{\Phi}$ are the POD modes, $\boldsymbol{S}$ is the coefficient matrix, and $\|\cdot\|_F^2$ is the square Frobenius norm of '$\cdot$'. The POD modes are arranged in the descending order of eigenvalues, where the first few modes represent the most energetic structures in the snapshots data [8]. Note that the complete set of POD modes exactly reproduces the snapshot matrix.

26.2.2.2 Sparse Coding

In its general formulation, sparse coding aims to solve the following minimization problem:

$$\min_{\boldsymbol{S},\boldsymbol{\Phi}} \ \frac{1}{2} \sum_{k=1}^{m} \left(\|\boldsymbol{q}_k - \boldsymbol{\Phi s}_k\|_F^2 + \beta \|\boldsymbol{s}_k\|_0 \right), \quad \|\boldsymbol{\Phi}_i\| \leq 1 \ \text{ for all } \ i \tag{26.4}$$

where the columns of $\boldsymbol{\Phi}$ are the sparse modes; $\boldsymbol{S}$ is a matrix of activation coefficients; each column $\boldsymbol{s}_k$ is encouraged to be sparse by a penalty on the L0 "norm" of $\boldsymbol{s}_k$ (the count of the non-zero elements of the vector); and $\beta > 0$ is the regularization (or penalty) parameter, denoted here as the *sparsity coefficient*. Note that if the penalty term is ignored, (26.4) reduces to the PCA problem (26.3) and yields the POD modes. The L0 penalty forces some of the entries in $\boldsymbol{s}_k$ to be zero, thereby resulting in a sparse coefficient matrix. The level of sparsity is controlled using β, where increasing the value of β increases the number of zero entries in $\boldsymbol{s}_k$, thus producing a "sparser" coefficient matrix $\boldsymbol{S}$. Yang et al. [21] recommend that a value of $0 < \beta < 0.5$ is typically adequate for most cases.

In practice, the solution of (26.4) is challenging due to its non-convexity [30], both due to the fact that the objective is not jointly convex in $\boldsymbol{\Phi}$ and $\boldsymbol{S}$, and due to the non-convexity of the L0 norm. To address the latter problem, the L0 penalty in (26.4) is replaced with a L1 penalty, making the problem convex in nature [30]. Optimisation problem is then given as:

$$\min_{\boldsymbol{S},\boldsymbol{\Phi}} \ \frac{1}{2} \sum_{k=1}^{m} \left(\|\boldsymbol{q}_k - \boldsymbol{\Phi s}_k\|_F^2 + \beta \|\boldsymbol{s}_k\|_1 \right), \quad \|\boldsymbol{\Phi}_i\| \leq 1 \ \text{ for all } \ i \tag{26.5}$$

where $\|.\|_1$ is the L1 norm. Although this problem is still not jointly convex in $\boldsymbol{S}$ and $\boldsymbol{\Phi}$, it can be approximately optimized by alternating minimization over these two matrices, which lead to convex problems in both cases. In particular, optimizing (26.5) over $\boldsymbol{S}$ is known as a least absolute shrinkage and selection operator (LASSO) problem [31], and has been widely studied by the Statistics and Machine Learning communities, among others [27, 31, 32]. A number of algorithms have been devised to solve (26.5). In the current study, an algorithm [27] based on the coordinate descent technique is adopted. Likewise, optimizing (26.5) over $\boldsymbol{\Phi}$ is a constrained least-squares problem, and is solved by using the Method of Optimal Directions (MOD) approach [33]. The MOD approach is equivalent to post-multiplying $\boldsymbol{Q}$ with the pseudo-inverse of matrix $\boldsymbol{S}$ to obtain the updated dictionary elements.

It is important to recognize that the use of L1 penalty eliminates the condition of orthogonality of the modes. Consequently, the sparse modes are not 'ordered' in terms of energy content. Therefore, the desired number of sparse modes are generated by varying β between 0 and 0.5 in a trial and error manner. In the current approach, all the sparse modes generated from the sparse coding process are used to build a ROM. This approach is only efficient when a small set of bases can approximate the entire solution manifold. However, sparse coding process has been used to generate large dictionaries of bases [34, 35]. Adaptive selection of bases from a large dictionary is proposed in order to approximate nonlinear solution manifolds.

Additionally, sparsity within the computed sparse coefficient matrix is also found to affect the performance of the ROM generated using the previous approach [26]. Sparsity levels of 50–80 % are found to result in stable and reasonably accurate sparse ROMs. The sparsity in the coefficient matrix is ensured to fall in this range by varying the β value before building a ROM. Estimating an exact value for β prior to computing the sparse modes and sparse coefficient matrix, that will satisfy the sparsity constraints, is not feasible when using the previous sparse coding approach. This issue will also be addressed in the proposed study.

26.2.2.3 Galerkin Projection

The reduced order solution to the unsteady fluid system is obtained by computing the time histories of the modal weights (also called prediction coefficients) using a Galerkin projection framework. In Galerkin projection [1–4], the governing partial differential equations are projected onto the space spanned by a set of basis functions to yield a system of ordinary differential equations. The implementation of Galerkin projection involves the following steps. First, the fluctuating component of each snapshot ($\boldsymbol{q}_k$) is expanded as a linear combination of reduced order modes as shown in (26.2). Next, the expansion is substituted into the governing equations, (26.1). Subsequently, the residual term is minimized by constraining it to be orthogonal to the space spanned by the modes. This process results in following set of ordinary differential equations:

$$\left(\boldsymbol{\Phi}_i, \frac{\partial(\tilde{\boldsymbol{u}}+\bar{\boldsymbol{U}})}{\partial t} + \left((\tilde{\boldsymbol{u}}+\bar{\boldsymbol{U}})\cdot\nabla\right)(\tilde{\boldsymbol{u}}+\bar{\boldsymbol{U}})\right) = \frac{1}{Re}\left(\boldsymbol{\Phi}_i, \nabla^2(\tilde{\boldsymbol{u}}+\bar{\boldsymbol{U}})\right) \tag{26.6}$$

where $i = 1, 2, \cdots, N$, and $\tilde{\boldsymbol{u}}$ is expressed as a linear combination of the reduced order modes, as shown in (26.2). The dot product between any vectors $\boldsymbol{f}$ and $\boldsymbol{g}$ is given as:

$$(\boldsymbol{f}, \boldsymbol{g}) = \int_{\Omega} \boldsymbol{f}\cdot\boldsymbol{g}\, d\Omega \tag{26.7}$$

where Ω is the flow domain. Equation (26.6) yields the following set of evolution equations for the mode amplitudes $s^i(t)$:

$$\begin{bmatrix} \frac{s^1(t)}{dt} \\ \vdots \\ \frac{s^i(t)}{dt} \\ \vdots \\ \frac{s^N(t)}{dt} \end{bmatrix} = \left[d_{ij}\right]^{-1} \begin{bmatrix} a_1 + \sum_{j=1}^{N} b_{1j}s^j(t) + \sum_{j=1}^{N}\sum_{k=1}^{N} c_{1jk}s^j(t)s^k(t) \\ \vdots \\ a_i + \sum_{j=1}^{N} b_{ij}s^j(t) + \sum_{j=1}^{N}\sum_{k=1}^{N} c_{ijk}s^j(t)s^k(t) \\ \vdots \\ a_N + \sum_{j=1}^{N} b_{Nj}s^j(t) + \sum_{j=1}^{N}\sum_{k=1}^{N} c_{Njk}s^j(t)s^k(t) \end{bmatrix} \tag{26.8}$$

where the coefficients are given as:

$$a_i = -\left(\boldsymbol{\Phi}_i, \left(\bar{\boldsymbol{U}}.\boldsymbol{\nabla}\right)\bar{\boldsymbol{U}}\right) + \frac{1}{Re}\left(\boldsymbol{\Phi}_i, \boldsymbol{\nabla}^2\bar{\boldsymbol{U}}\right) \tag{26.9}$$

$$b_{ij} = -\left(\boldsymbol{\Phi}_i, \left(\boldsymbol{\Phi}_j.\boldsymbol{\nabla}\right)\bar{\boldsymbol{U}}\right) - \left(\boldsymbol{\Phi}_i, \left(\bar{\boldsymbol{U}}.\boldsymbol{\nabla}\right)\boldsymbol{\Phi}_j\right) + \frac{1}{Re}\left(\boldsymbol{\Phi}_i, \boldsymbol{\nabla}^2\boldsymbol{\Phi}_j\right) \tag{26.10}$$

$$c_{ijk} = -\left(\boldsymbol{\Phi}_i, \left(\boldsymbol{\Phi}_j.\boldsymbol{\nabla}\right)\boldsymbol{\Phi}_k\right) \tag{26.11}$$

$$d_{ij} = \left(\boldsymbol{\Phi}_i, \boldsymbol{\Phi}_j\right) \tag{26.12}$$

The system of ordinary differential equations is then time marched using the fourth order Runge-Kutta scheme to obtain the prediction coefficients. In the case studies presented in this paper, including the pressure terms in the Galerkin projection approach is established to have a negligible effect on the computed velocity field [36–38]. Therefore, the projection of pressure was ignored when computing the solution.

26.2.2.4 Energy Balance Equations

As a metric of comparison for the full and reduced order models, the following energy balance equation[39] is used:

$$\frac{\partial \mathcal{E}}{\partial t} = \mathcal{L} + \mathcal{P} + \mathcal{T} + \mathcal{D} + \mathcal{G} \tag{26.13}$$

where $\mathcal{E}$ is the turbulent kinetic energy, and $\mathcal{L}$, $\mathcal{P}$, $\mathcal{T}$, $\mathcal{D}$, $\mathcal{G}$ are time rates of change of convection, production, transfer, dissipation, and terms that are linear in fluctuating components, respectively. These terms are given as:

$$\frac{\partial \mathcal{E}}{\partial t} = \frac{1}{2}\frac{\partial(\tilde{\boldsymbol{u}}, \tilde{\boldsymbol{u}})}{\partial t} \tag{26.14}$$

$$\mathcal{L} = -\left(\tilde{\boldsymbol{u}}, \left(\bar{\boldsymbol{U}}.\boldsymbol{\nabla}\right)\tilde{\boldsymbol{u}}\right) \tag{26.15}$$

$$\mathcal{P} = -\left(\tilde{\boldsymbol{u}}, \left(\tilde{\boldsymbol{u}}.\boldsymbol{\nabla}\right)\bar{\boldsymbol{U}}\right) \tag{26.16}$$

$$\mathcal{T} = -\left(\tilde{\boldsymbol{u}}, \left(\tilde{\boldsymbol{u}}.\boldsymbol{\nabla}\right)\tilde{\boldsymbol{u}}\right) \tag{26.17}$$

$$\mathcal{D} = \frac{1}{Re}\left(\tilde{\boldsymbol{u}}, \boldsymbol{\nabla}^2\tilde{\boldsymbol{u}}\right) \tag{26.18}$$

$$\mathcal{G} = \frac{1}{Re}\left(\tilde{\boldsymbol{u}}, \boldsymbol{\nabla}^2\bar{\boldsymbol{U}}\right) - \left(\tilde{\boldsymbol{u}}, \left(\bar{\boldsymbol{U}}.\boldsymbol{\nabla}\right)\bar{\boldsymbol{U}}\right). \tag{26.19}$$

The time rate of change of TKE ($\mathcal{E}$) account for the changes in TKE at any instant in time, $\mathcal{L}$ accounts for variations in TKE due to convection, $\mathcal{P}$ is the rate at which energy is being added to the system from the mean flow, $\mathcal{D}$ is the rate dissipation of energy due to the small scale turbulent structures, and $\mathcal{T}$ is the rate of transfer of energy between different turbulent structures [39, 40]. Integrating (26.13) in time, we get:

$$\int_{t=0}^{t_0} \frac{\partial \mathcal{E}}{\partial t} dt = \int_{t=0}^{t_0} \left(\mathcal{L} + \mathcal{P} + \mathcal{T} + \mathcal{D} + \mathcal{G}\right) dt \tag{26.20}$$

where t_0 is the length of time window over which the data are collected. Assuming statistically stationary process, the net rate of change of TKE over time is:

$$\int_{t=0}^{t_0} \frac{\partial \mathcal{E}}{\partial t} dt \approx 0 \tag{26.21}$$

Moreover, because $\mathcal{G}$ is linear in fluctuating component, and time integral of fluctuating component is zero,

$$\int_{t=0}^{t_0} \mathcal{G} dt = 0 \tag{26.22}$$

Thus, for a statistically stationary process, the time integral of energy balance equation (26.13) reduces to:

$$\int_{t=0}^{t_0} (\mathcal{L} + \mathcal{P} + \mathcal{T} + \mathcal{D})\, dt \approx 0 \tag{26.23}$$

Finally, the energy balance equation for a ROM is obtained by substituting the basis expansion (26.2) in (26.13). As a stable and accurate ROM for a statically stationary system will not add or deduct TKE, it will satisfy (26.23).

26.3 Results

A case study describing the application of POD and sparse approaches to model 2-D incompressible unsteady flow is presented. Performances of ROMs generated by using POD and sparse modes within a Galerkin projection framework are compared. The unsteady response of a fluid enclosed in a cavity and actuated using a moving surface (lid) is examined. This configuration, widely referred to as 'the lid-driven cavity flow' has been used in several studies [11, 41, 42] for benchmarking purposes. The cavity considered in this study is a 2-D square, enclosed region, with three rigid stationary walls and one rigid lid translating in x direction with constant velocity. The lid velocity is prescribed as $\left(1 - (2x - 1)^2\right)^2$, where x varies from 0 to 1. The DNS solutions are obtained using a 512×512 uniform grid at Re of 30,000, where the Re is computed based on the maximum lid velocity. A total of 50,000 uniformly sampled observations are collected from 500 units of non-dimensional time once the flow had reached a statistically stationary state. A snapshot matrix spanning first 25 time units is constructed using 1250 snapshots sampled at a uniform frequency of 50 units. Comparison between extracted POD modes, sparse modes, and original snapshots is provided next.

26.3.1 Comparison Between POD and Sparse Modes

The velocity components of the POD modes numbered 1, 10, 50 and 100, and four modes taken arbitrarily from a set of 100 sparse modes are shown in Figs. 26.1 and 26.2, respectively. For reference, the velocity components from the full order solution are displayed in Fig. 26.3. The POD approach produces a set of orthogonal modes, that are ordered from highest to lowest energy. The spatial variance of the POD modes increases with increasing the mode number, where lower order modes capture the high energy structures. Thus, a truncated set of POD modes discards the low-energy structures. In contrast, sparse modes resemble the snapshots of the original flow field and yield physically representative multi-scale features.

The energy content in the modes is computed as the sum of the squares of the projection coefficients corresponding to the snapshot matrix. The energies of the modes are shown in Fig. 26.4. The energy contained in the POD decreases rapidly with increase in mode number, with first 17 modes accounting for approximately 90 % of the total energy. In comparison, the energy distribution in the sparse modes is much more uniform, or "leveled", and does not exhibit any monotonic trend. This is because the POD modes are arranged in the order of decreasing energy content; consequentially, the lower order POD modes contain majority of the dominant, high-energy structures. On the other hand, all the sparse modes contain multi-scale features, and therefore capture relatively equal amount of flow energy.

The time varying projection coefficients of the sparse and POD modes for first 25 units of time history, are shown in Fig. 26.5. The POD coefficients are almost always non-zero. However, a subset of the sparse coefficients are zero for a given snapshot. This indicates that only a subset of sparse modes is active at given time. The active sparse modes within a small window in time are therefore more tailored to the dynamics of the system in that time window. On the contrary, the POD approach is not designed to capture the local dynamics; this is because the POD modes are optimal in terms of capturing energy, and are always active.

The ability of a set of sparse modes to account for the multi-scale features is further studied. Transformation matrix between 20 sparse modes and 200 POD modes is computed. Next, log_{10} of the absolute of the transformation matrix is computed to obtain the 'modified' transformation matrix, as shown in Fig. 26.6. A relatively large value of an element of the transformation matrix represents existence of higher correlation between corresponding POD mode and sparse mode. For example, a value of 0 in the modified transformation matrix represents 100 % correlation between corresponding pair of POD and sparse modes, a value of $-\infty$ represents zero correlation. It is apparent that the 20 sparse modes contain combinations of all the 200 POD modes. Thus, a set of sparse modes contain both the large energy (low order POD modes) and small energy (higher order POD modes) information.

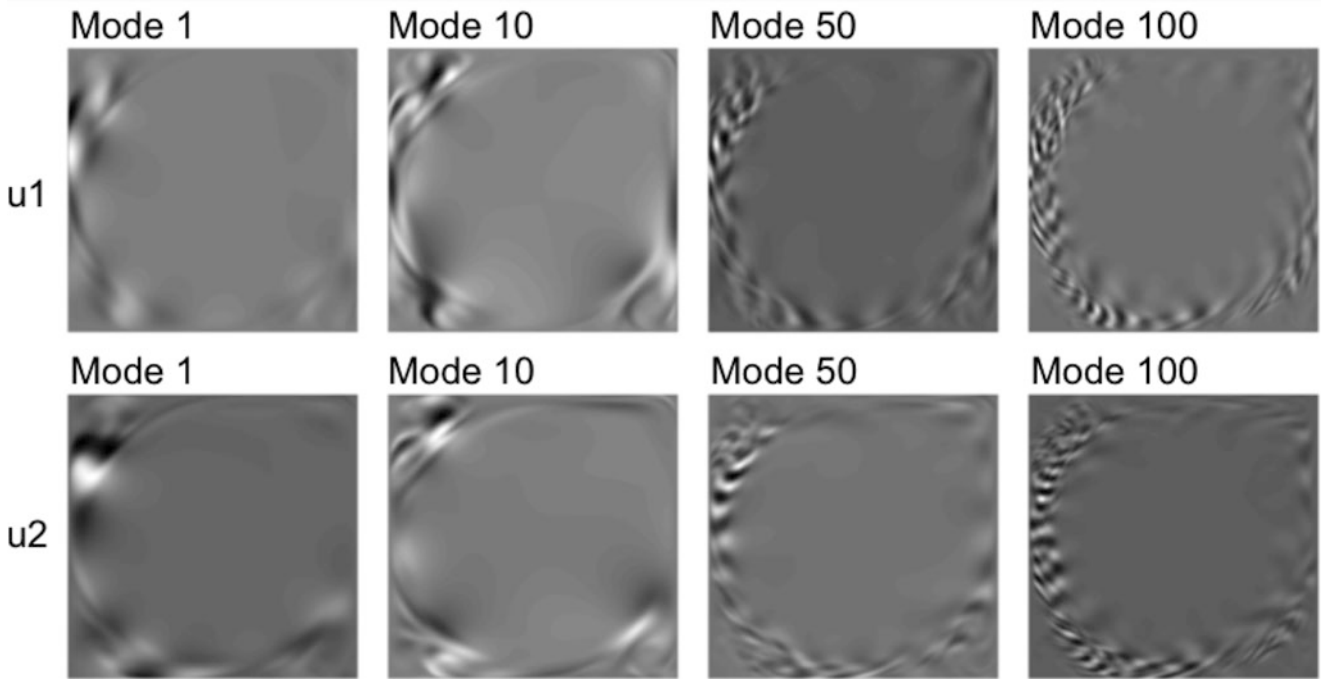

Fig. 26.1 The u1 and u2 components of the POD modes numbered 1, 10, 50 and 100 of the lid-driven cavity

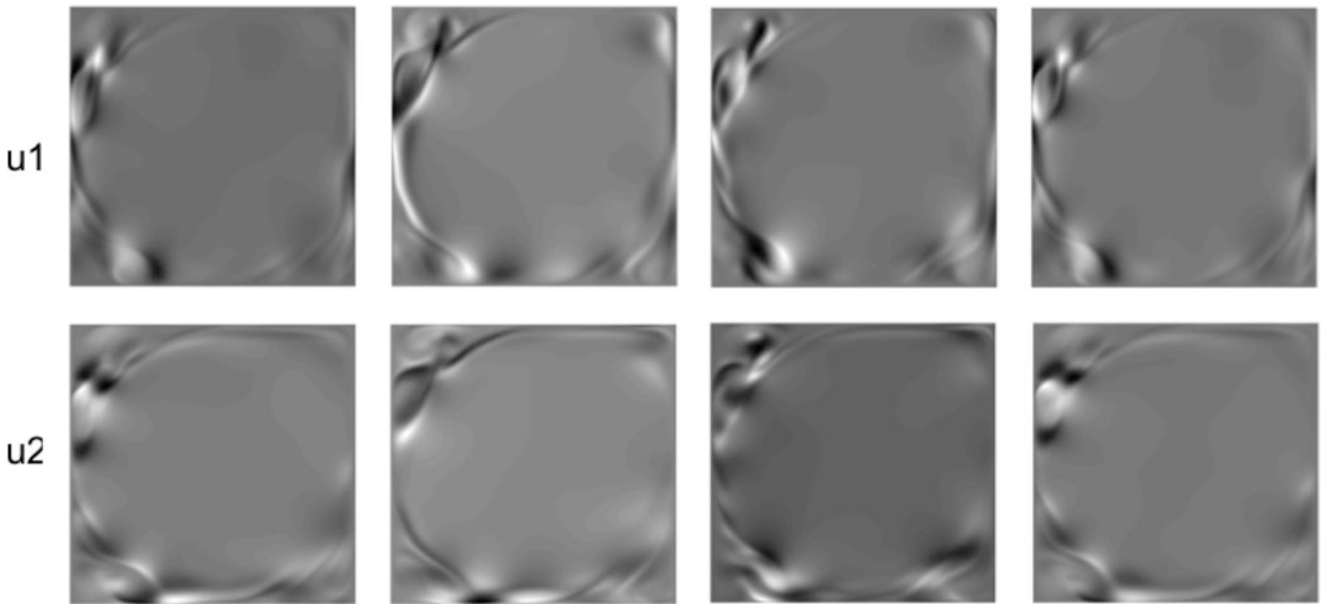

Fig. 26.2 The u1 and u2 components of four of the sparse modes of the lid-driven cavity

26.3.2 Predicted Instantaneous TKE

Next, ROMs are constructed using different numbers of POD and sparse modes. The flow predictions obtained from the ROMs are compared to the full order solutions for the 500 time units. The instantaneous TKE predicted by the ROMs is shown in Fig. 26.7. When the same number of modes are used, the sparse ROMs capture the energy levels with greater accuracy compared to the POD ROMs. The 10 and 20-mode POD models over-predict the energy by two orders of magnitude, averaged over first 500 time units, whereas, the 10-mode sparse model over-predicts the energy by a factor of 1.2 over the same duration. Moreover, as many as 80 POD modes are required to capture the TKE levels with accuracy; whereas, all the

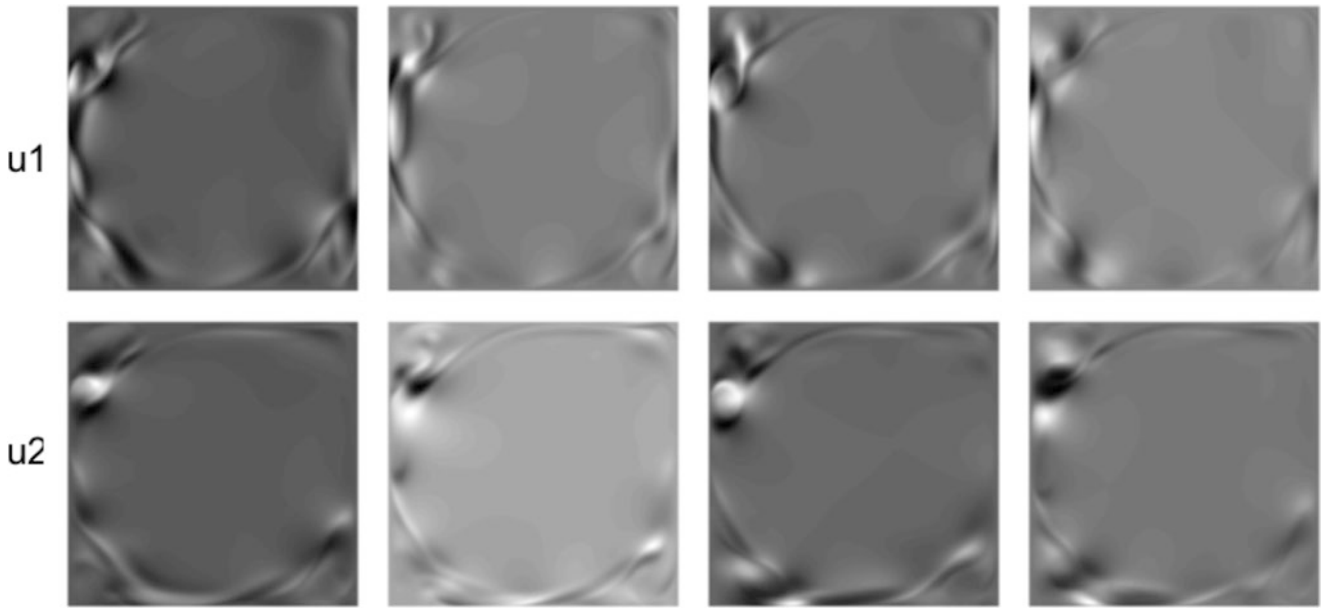

Fig. 26.3 The u1 and u2 components of four different snapshots of the lid-driven cavity

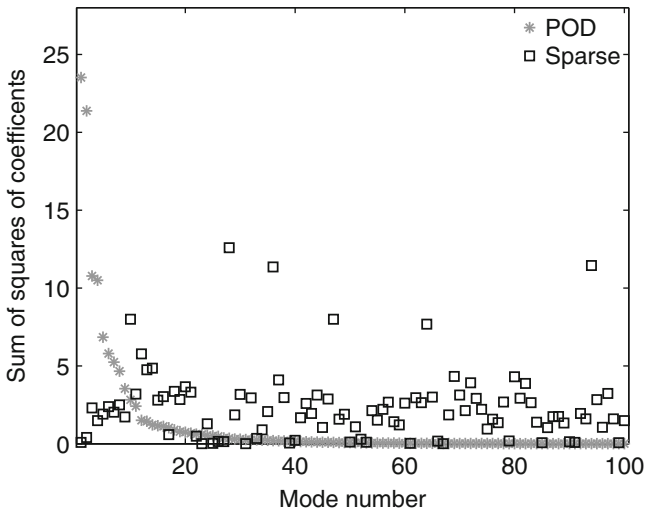

Fig. 26.4 Energy content in the first 100 POD modes and the sparse modes of a 100-mode model of the lid-driven cavity, expressed in terms of the sum of squares of projection coefficients evaluated over 25 time units

sparse models capture the TKE levels with good accuracy. These results are consistent with the previous findings [1, 11, 13] that ignoring small-scale, low-energy information in a truncated POD set may result in over-prediction of turbulent kinetic energy, and therefore result in an inaccurate flow prediction. The sparse modes include low energy, dynamically important, features that may provide the appropriate dissipation to balance the large scale dominant structures.

26.3.3 Energy Balance Analysis

In order to further analyze the stabilizing property of sparse modes, energy balance analyses of DNS, POD ROMs and sparse ROMs are carried out. The energy balance terms are computed using Eqs. (26.14)–(26.19). The energy balance terms for DNS are shown in Fig. 26.8. The TKE ($\mathcal{E}$), time rate of change of TKE ($\partial\mathcal{E}/\partial t$), production ($\mathcal{P}$), and dissipation ($\mathcal{D}$) are shown in Fig. 26.8a, b (zoomed-in view). It is observed that there is a positive correlation between ($\mathcal{P}$) and ($\partial\mathcal{E}/\partial t$), and a

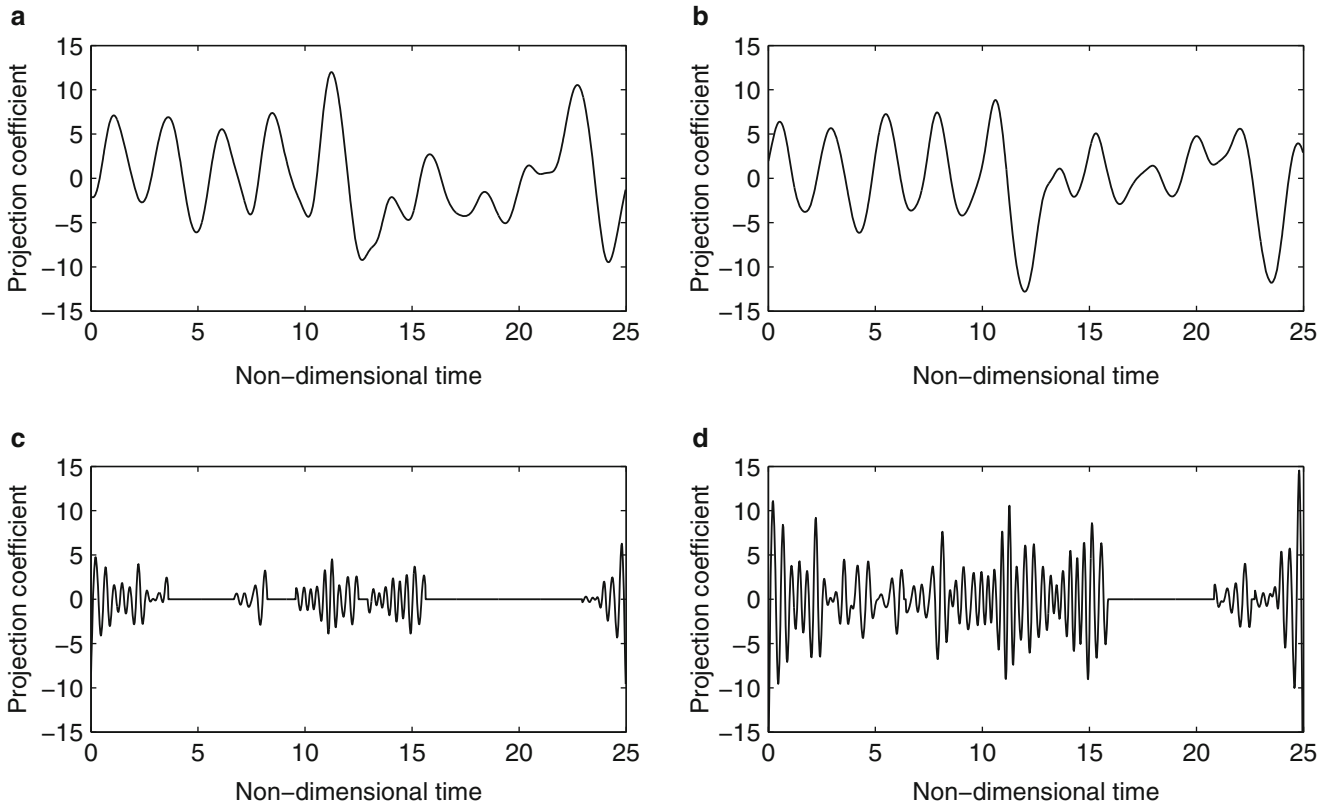

Fig. 26.5 The time history of projection coefficients corresponding to two of the modes from 100-mode POD and 100-mode sparse model of the lid-driven cavity. (**a**) POD mode 1. (**b**) POD mode 2. (**c**) Sparse mode 1. (**d**) Sparse mode 2

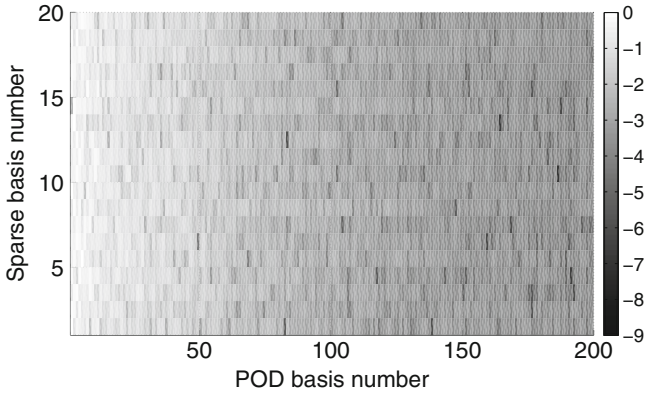

Fig. 26.6 Transformation matrix between the 20 sparse modes and 200 POD modes

negative correlation between ($\mathcal{D}$) and ($\partial\mathcal{E}/\partial t$). This result is in agreement with the theory that an increase in rate of production will result in increase in rate of TKE; whereas, increase in magnitude of rate of dissipation will have opposite effect of rate if TKE. Moreover, positive values of TKE rate result in increase in TKE, and vice versa. Also notice that there is no net gain in TKE over time for the statistically stationary DNS data. Furthermore, terms $\mathcal{L}$, $\mathcal{T}$, and $\mathcal{G}$ are negligible compared to rest of the energy balance terms. The rate of convection ($\mathcal{L}$) is negligible as there is no net flow in or out of the considered control volume of a closed lid-driven cavity. The negligible transfer rate term ($\mathcal{T}$) is consistent with the study carried out by Noack et al. [40]. The $\mathcal{G}$ term is small because of the reasons discussed earlier.

Next, energy balance analysis is carried out for POD and Sparse ROMs. Energy balance terms for 10-mode, 20-mode, and 200-mode ROMs are shown in Figs. 26.9, 26.10, and 26.11, respectively. The production term is found to be much larger than the dissipation term for first 70 time-units for 10 and 20-mode POD ROMs. This results in initial increase in TKE,

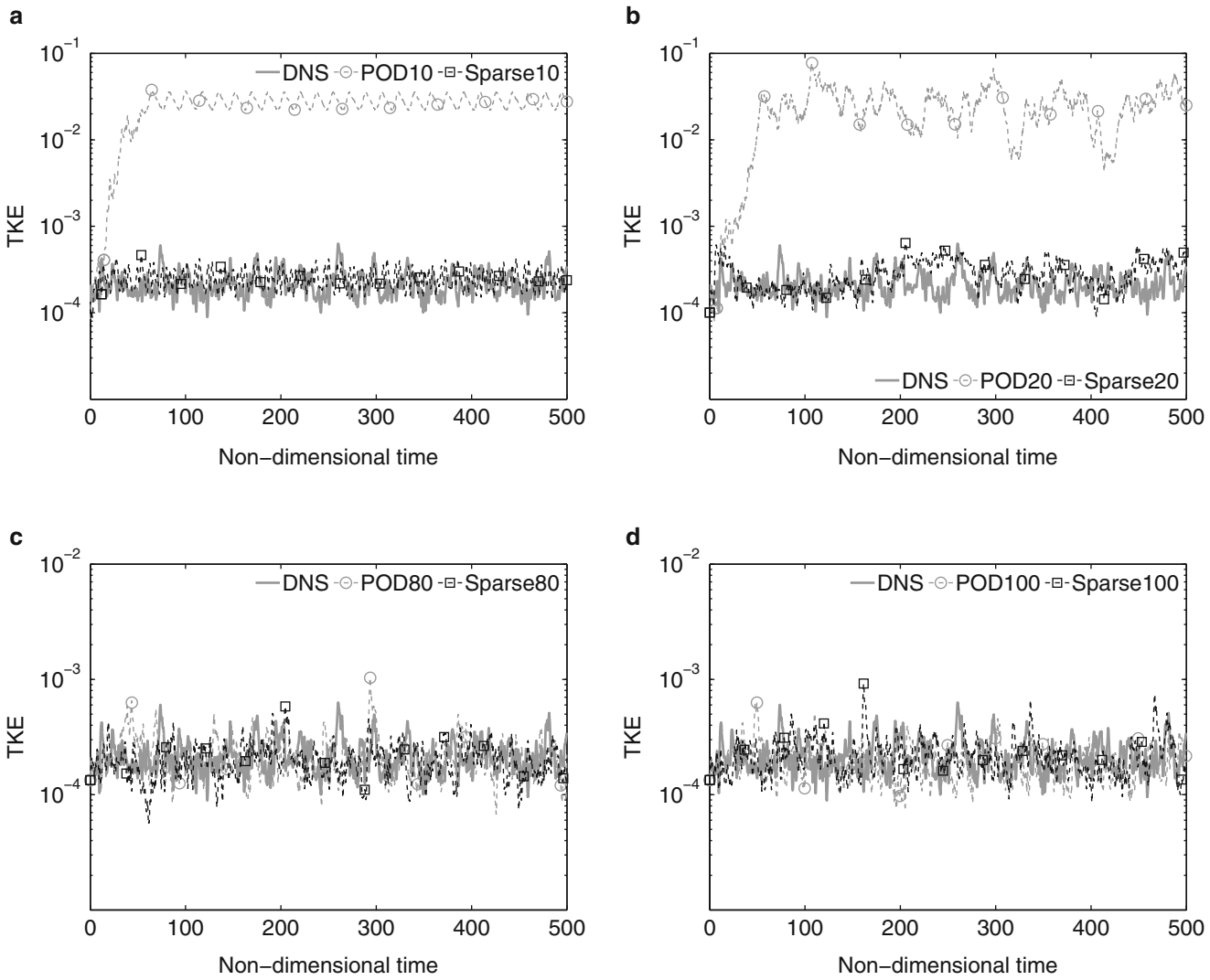

Fig. 26.7 Time history of the instantaneous TKE of the lid-driven cavity as predicted by DNS, and the computed POD and sparse ROMs constructed using (**a**) 10 modes, (**b**) 20 modes, (**c**) 80 modes, and (**d**) 100 modes. The snapshot matrix used to compute the modes spans first 25 time units, and ROMs are integrated for 500 time units

the TKE values settle down within a band past 70 time-units; however, the TKE levels are much higher as compared to the DNS. This initial, sharp increase in TKE values is missing in case of sparse ROMs, as the production and dissipation terms are comparable. Thus, the sparse ROMs seem to maintain energy balance right from $t = 0$. The energy balance terms for 200-mode POD and sparse ROMs are comparable to that of DNS, which is expected as the 200-mode ROMs predict the TKE levels with good accuracy.

26.4 Conclusions

The generation of the sparse and POD modes is described with an example of a flow inside a 2-D lid-driven cavity. The computed POD and sparse modes are compared in terms of the energy content in the modes, time history of the projection coefficients, and spatial structure of the $u1$ and $u2$ components of the modes. Several Galerkin projection based ROMs are developed for the lid-driven cavity problems. The sparse ROMs are generated following the methodology developed by the authors in the previous work. Whereas, the POD ROMs are generated using the standard Galerkin-POD approach. It is found that the sparse ROMs perform better as compared to the POD ROMs when the same number of modes are used.

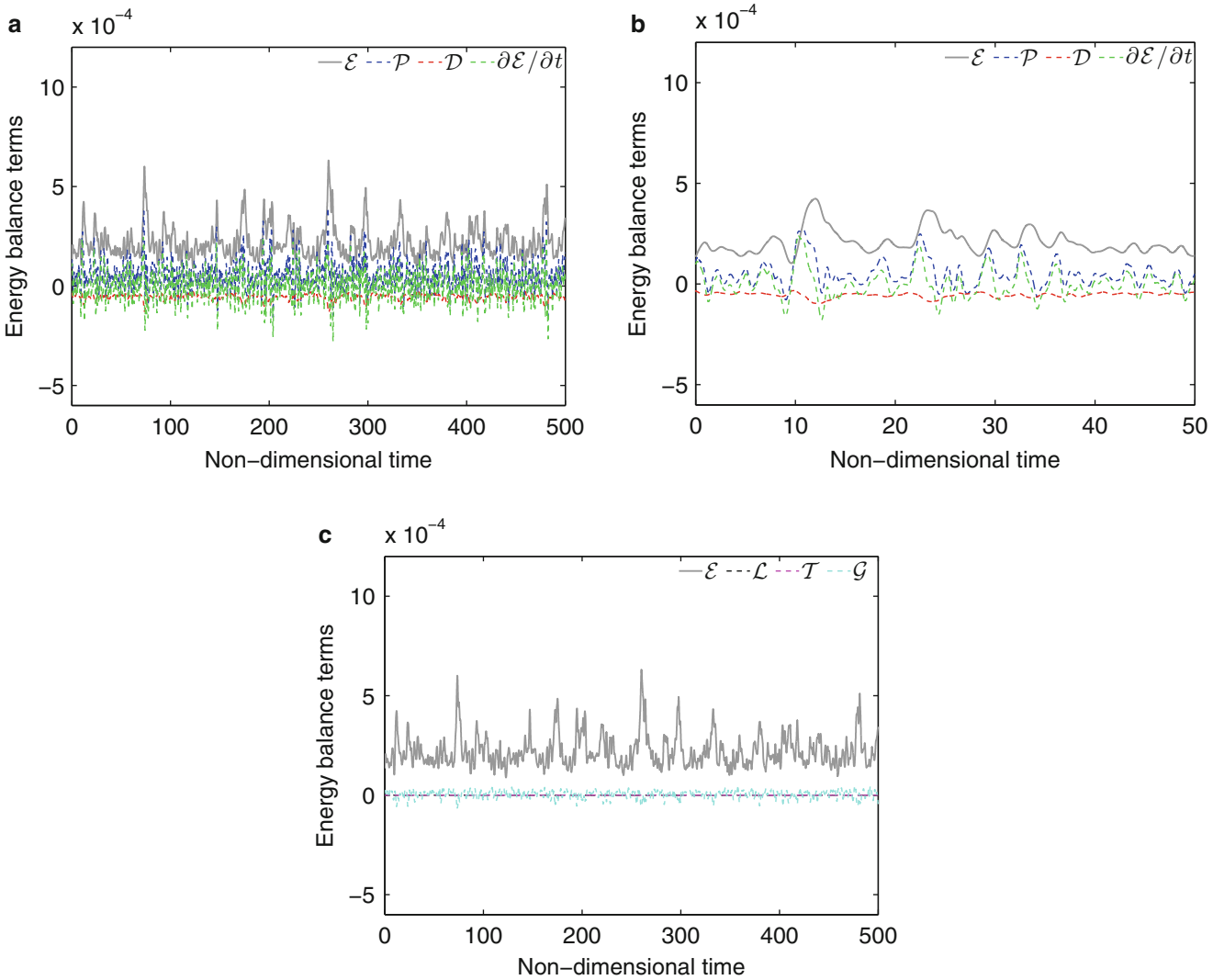

Fig. 26.8 Energy balance terms for DNS. (**a**) Energy balance terms considered in analysis. (**b**) Zoomed-in time window. (**c**) Neglected terms—$\mathcal{L}$, $\mathcal{T}$, and $\mathcal{G}$

Acknowledgements The authors gratefully acknowledge the support of ONR grant N00014-14-1-0018, under the direction of Dr. Judah Milgram, an HPCMPO Frontier PETTT Project Grant, under the direction of David Bartoe, and an allocation of computing time from the Ohio Supercomputer Center. The authors thank Dr. Lionel Agostini, Mr. Kalyan Goparaju, Mr. S. Unnikrishnan, and Dr. Datta Gaitonde, Mechanical & Aerospace Engineering, The Ohio State University for providing technical guidance in the study of local flow dynamics.

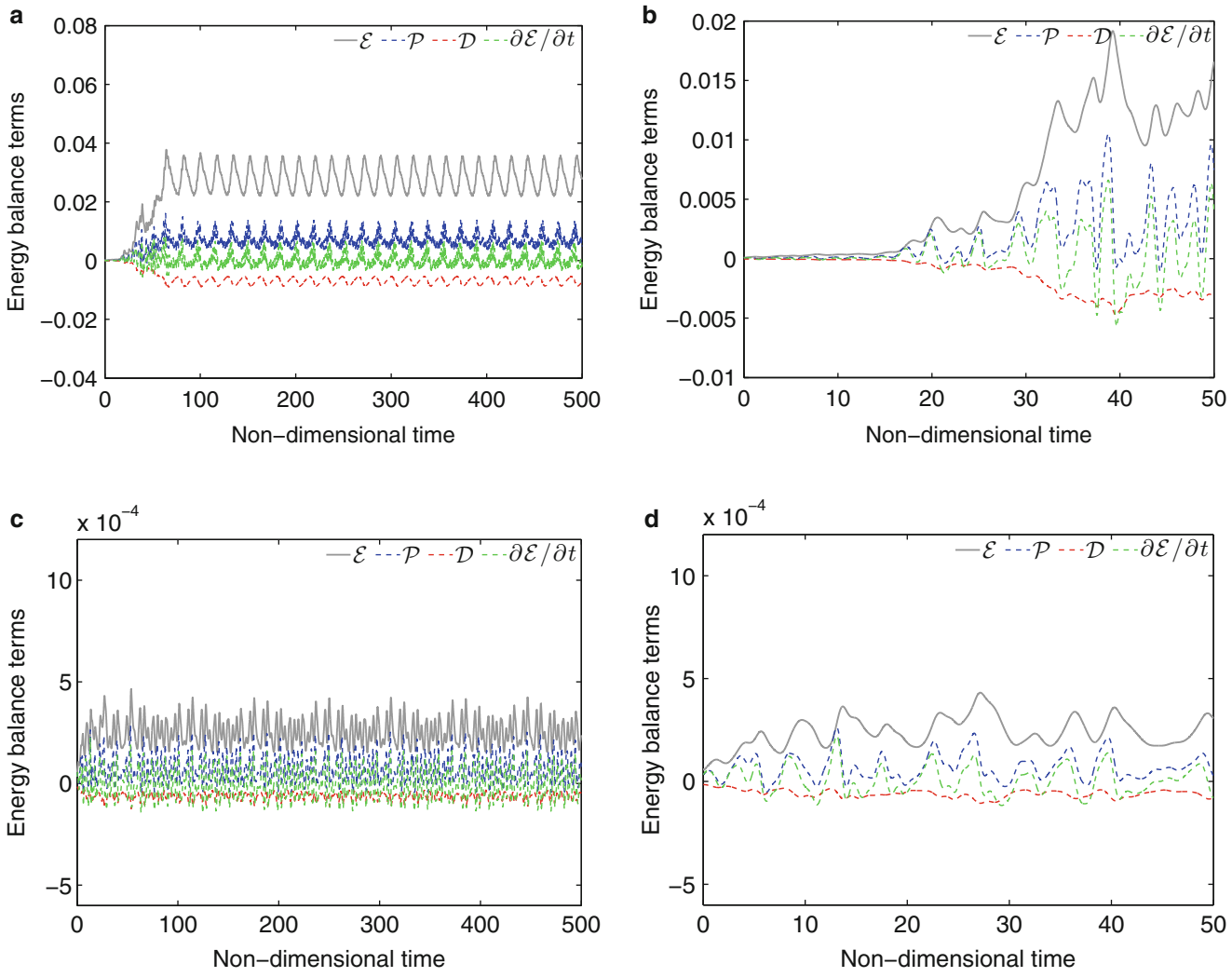

Fig. 26.9 Energy balance terms for 10-mode POD and sparse ROMs. (**a**) 10-mode POD. (**b**) 10-mode POD, zoomed-in. (**c**)10-mode sparse. (**d**) 10-mode sparse, zoomed-in

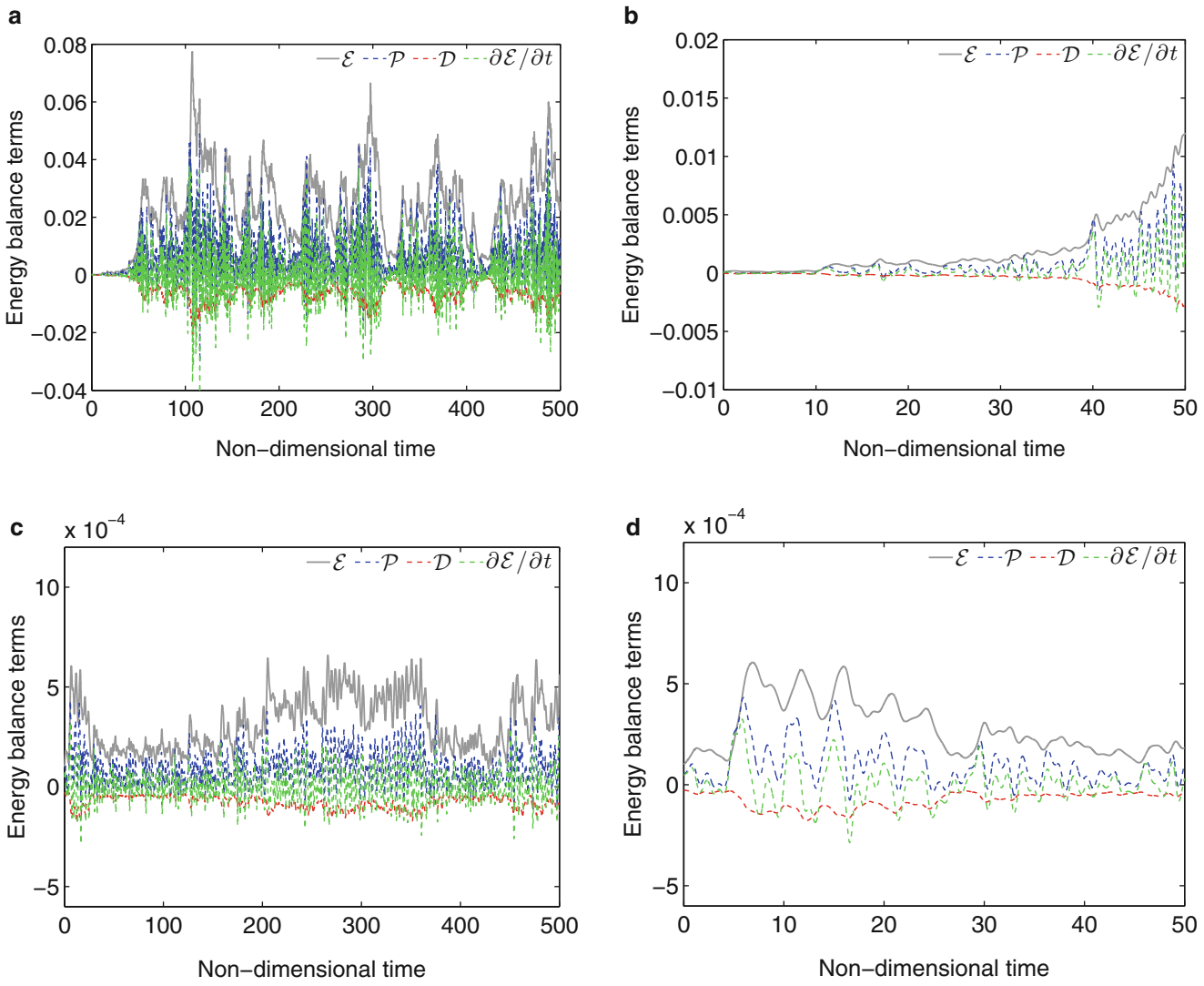

Fig. 26.10 Energy balance terms for 20-mode POD and sparse ROMs. (**a**) 20-mode POD. (**b**) 20-mode POD, zoomed-in. (**c**) 20-mode sparse. (**d**) 20-mode sparse, zoomed-in

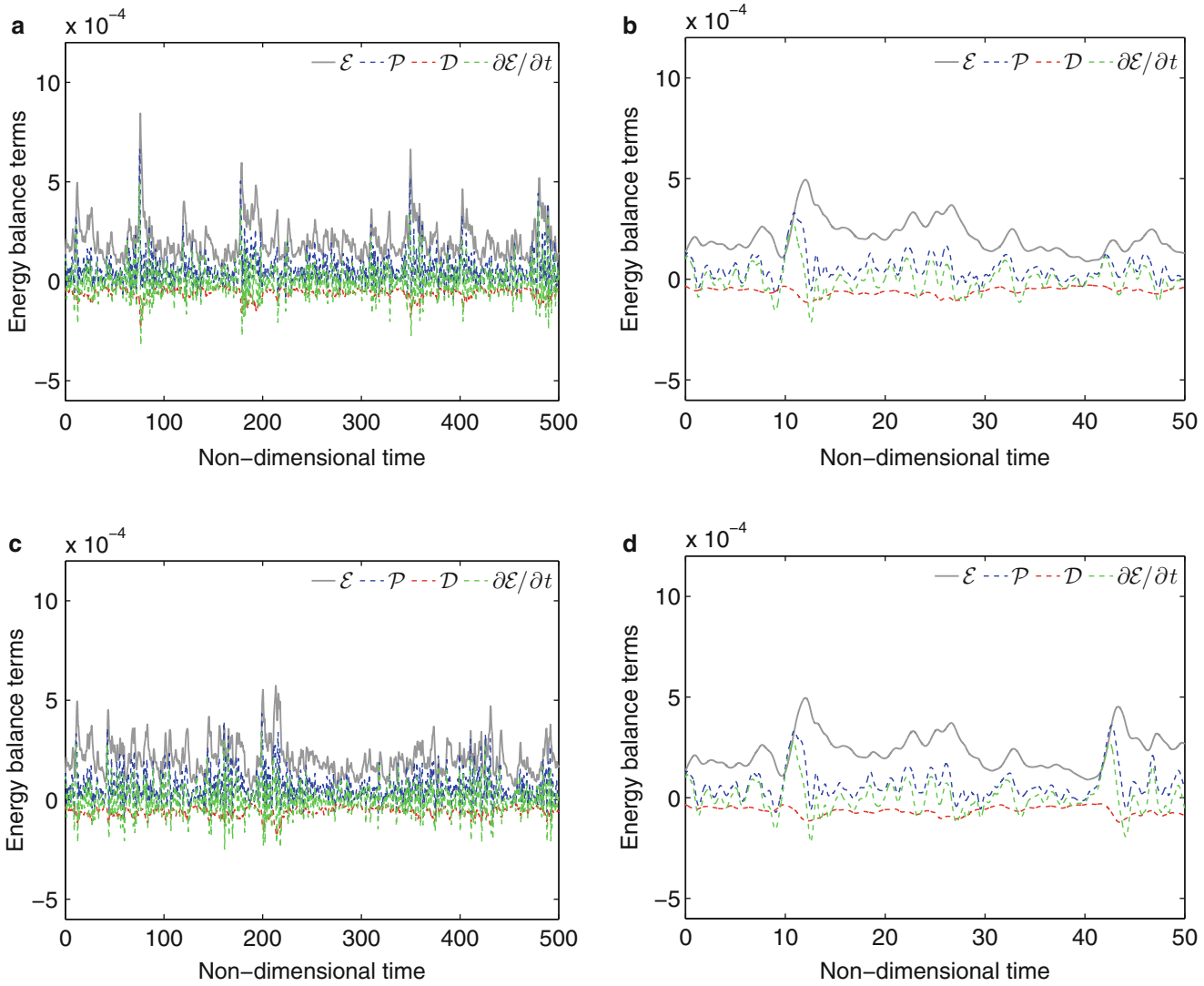

Fig. 26.11 Energy balance terms for 200-mode POD and sparse ROMs. (**a**) 200-mode POD. (**b**) 200-mode POD, zoomed-in. (**c**) 200-mode sparse. (**d**) 200-mode sparse, zoomed-in

References

1. Holmes, P., Lumley, J.L., Berkooz, G., Rowley, C.: Turbulence, Coherent Structures, Dynamical Systems and Symmetry, 2nd edn. Cambridge University Press, New York (2012)
2. Ilak, M., Bagheri, S., Brandt, L., Rowley, C.W., Henningson, D.S.: Model reduction of the nonlinear complex Ginzburg-Landau equation. SIAM J. Appl. Dyn. Syst. **9**(4), 1284–1302 (2010)
3. Kalashnikova, I., van Bloemen, W.B., Arunajatesan, S., Barone, M.: Stabilization of projection-based reduced order models for linear time-invariant systems via optimization-based eigenvalue reassignment. Comput. Methods Appl. Mech. Eng. **272**, 251–270 (2014)
4. Rowley, C.: Model reduction for fluids, using balanced proper orthogonal decomposition. Int. J. Bifurcation Chaos **15**(3), 997–1013 (2005)
5. Noack, B.R., Afanasiev, K., Morzynski, M., Tadmor, G., Thiele, F.: A hierarchy of low-dimensional models for the transient and post-transient cylinder wake. J. Fluid Mech. **497**, 335–363 (2003)
6. Noack, B.R., Eckelmann, H.: A low-dimensional Galerkin method for the three-dimensional flow around a circular cylinder. Phys. Fluids (1994–present) **6**(1), 124–143 (1994)
7. Lucia, D.J., Beran, P.S., Silva, W.A.: Reduced-order modeling: new approaches for computational physics. Prog. Aerosp. Sci. **40**(1), 51–117 (2004)
8. Berkooz, G., Holmes, P., Lumley, J.L.: The proper orthogonal decomposition in the analysis of turbulent flows. Annu. Rev. Fluid Mech. **25**(1), 539–575 (1993)
9. Chatterjee, A.: An introduction to the proper orthogonal decomposition. Curr. Sci. **78**(7), 808–817 (2000)

10. Sirovich, L.: Turbulence and the dynamics of coherent structures. I-Coherent structures. II-symmetries and transformations. III-Dynamics and scaling. Q. Appl. Math. **45**, 561–571 (1987)
11. Balajewicz, M.J., Dowell, E.H., Noack, B.R.: Low-dimensional modelling of high-Reynolds-number shear flows incorporating constraints from the Navier–Stokes equation. J. Fluid Mech. **729**, 285–308 (2013)
12. Ilak, M., Rowley, C.W.: Modeling of transitional channel flow using balanced proper orthogonal decomposition. Phys. Fluids (1994–present) **20**(3), 034103 (2008)
13. Amsallem, D., Farhat, C.: Stabilization of projection-based reduced-order models. Int. J. Numer. Methods Eng. **91**(4), 358–377 (2012)
14. Pope, S.B.: Turbulent Flows, 6th edn. Cambridge University Press, New York (2009)
15. Amsallem, D., Zahr, M.J., Farhat, C.: Nonlinear model order reduction based on local reduced-order bases. Int. J. Numer. Methods Eng. **92**(10), 891–916 (2012)
16. Zhou, K., Doyle, J.C., Glover, K.: Robust and Optimal Control, 1st edn. Prentice Hall, Upper Saddle River (1996)
17. Ma, Z., Ahuja, S., Rowley, C.W.: Reduced-order models for control of fluids using the eigensystem realization algorithm. Theor. Comput. Fluid Dyn. **25**(1–4), 233–247 (2010)
18. Olshausen, B., Field, D.: Emergence of simple-cell receptive field properties by learning a sparse code for natural images. Nature **381**(6583), 607–609 (1996)
19. Kreutz-Delgado, K., Murray, J.F., Rao, B.D., Engan, K., Lee, T., Sejnowski, T.J.: Dictionary learning algorithms for sparse representation. Neural Comput. **15**(2), 349–396 (2003)
20. Yang, J., Yu, K., Huang, T.: Efficient highly over-complete sparse coding using a mixture model. In: Computer Vision—ECCV 2010, pp. 113–126. Springer, Berlin (2010)
21. Yang, J., Yu, K., Gong, Y., Huang, T.: Linear spatial pyramid matching using sparse coding for image classification. In: IEEE Computer Vision and Pattern Recognition, pp. 1794–1801 (2009)
22. Grosse, R., Raina, R., Kwong, H., Ng, A.: Shift-invariance sparse coding for audio classification (2012). arXiv preprint arXiv:1206.5241
23. Lee, H., Battle, A., Raina, R., Ng, A.: Efficient sparse coding algorithms. In: Advances in Neural Information Processing Systems, pp. 801–808 (2006)
24. Olshausen, B., Field, D.: Sparse coding of sensory inputs. Curr. Opin. Neurobiol. **14**(4), 481–487 (2004)
25. Kolter, J., Batra, S., Ng, A.: Energy disaggregation via discriminative sparse coding. In: Advances in Neural Information Processing Systems, pp. 1153–1161 (2010)
26. Deshmukh, R., Liang, Z., Gogulapati, A., McNamara, J.J., Kolter, J.Z.: Basis identification for reduced order modeling of unsteady flows using sparse coding. In: Proceedings of the 56th AIAA/ASCE/AHS/ASC Structures, Structural Dynamics, and Materials Conference (SciTech 2015), No. AIAA 2015-0688, Kissimmee, FL, 5–9 Jan 2015
27. Friedman, J., Hastie, T., Tibshirani, R.: Regularization paths for generalized linear models via coordinate descent. J. Stat. Softw. **33**(1), 1–22 (2010)
28. Mittal, R., Dong, H., Bozkurttas, M., Najjar, F., Vargas, A., von Loebbecke, A.: A versatile sharp interface immersed boundary method for incompressible flows with complex boundaries. J. Comput. Phys. **227**(10), 4825–4852 (2008)
29. Abdi, H., Williams, L.: Principal component analysis. Wiley Interdiscip. Rev. Comput. Stat. **2**(4), 433–459 (2010)
30. Zuo, W., Meng, D., Zhang, L., Feng, X., Zhang, D.: A generalized iterated shrinkage algorithm for non-convex sparse coding. In: Proceedings of the IEEE International Conference on Computer Vision, pp. 217–224 (2013)
31. Tibshirani, R.: Regression shrinkage and selection via the lasso. J. R. Stat. Soc. Ser. B Methodol. **58**, 267–288 (1996)
32. Friedman, J., Hastie, T., Tibshirani, R.: Sparse inverse covariance estimation with the graphical lasso. Biostatistics **9**(3), 432–441 (2008)
33. Engan, K., Aase, S.O., Hakon Husoy, J.: Method of optimal directions for frame design. In: Proceedings of the IEEE International Conference on Acoustics, Speech, and Signal Processing, vol. 5, pp. 2443–2446. IEEE, New York (1999)
34. Olshausen, B.A., Field, D.J.: Sparse coding with an overcomplete basis set: a strategy employed by V1? Vis. Res. **37**(23), 3311–3325 (1997)
35. Xiang, Z.J., Xu, H., Ramadge, P.J.: Learning sparse representations of high dimensional data on large scale dictionaries. In: Advances in Neural Information Processing Systems, pp. 900–908 (2011)
36. Ullmann, S., Lang, J.: A POD-Galerkin reduced model with updated coefficients for Smagorinsky LES. In: Proceeding of V. European Conference on Computational Fluid Dynamics, ECCOMAS CFD (2010)
37. Graham, W., Peraire, J., Tang, K.: Optimal control of vortex shedding using low-order models. Part 1 – open-loop model development. Int. J. Numer. Methods Eng. **44**, (7), 945–972 (1999)
38. Bergmann, M., Cordier, L., Brancher, J.: Optimal rotary control of the cylinder wake using proper orthogonal decomposition reduced-order model. Phys. Fluids (1994–present) **17**(9), 097–101 (2005)
39. Monin, A.S., Lumley, J.L., Yaglom, A.M.: Statistical Fluid Mechanics: Mechanics of Turbulence, vol. 1. MIT Press, New York (1971)
40. Noack, B.R., Papas, P., Monkewitz, P.A.: The need for a pressure-term representation in empirical Galerkin models of incompressible shear flows. J. Fluid Mech. **523**, 339–365 (2005)
41. Leblond, C., Allery, C., Inard, C.: An optimal projection method for the reduced-order modeling of incompressible flows. Comput. Methods Appl. Mech. Eng. **200**(33), 2507–2527 (2011)
42. Terragni, F., Valero, E., Vega, J.: Local POD plus Galerkin projection in the unsteady lid-driven cavity problem. SIAM J. Sci. Comput. **33**(6), 3538–3561 (2011)

Chapter 27
Interaction Between Aerothermally Compliant Structures and Boundary Layer Transition

Zachary B. Riley and Jack J. McNamara

Abstract The inherent relationship between boundary layer stability, aerodynamic heating, and surface conditions make the potential for interaction between the structural response and boundary layer transition an important and challenging area of study in high speed flows. This interdependence implies that accurate structural response prediction of a hypersonic vehicle necessitates an aerothermoelastic analysis that accounts for boundary layer stability in regions where transition is likely to occur. This study focuses on this problem by incorporating a time-varying boundary layer state into the aerothermoelastic response prediction of a structural panel in hypersonic flow. Results demonstrate that rearward movement of the boundary layer transition front reduces thermal loading to the panel and peak deformation, potentially extending the life of the structure.

Keywords Fluid-thermal-structural-interactions • Boundary layer transition • Hypersonic • Aerothermoelastic • Hot structure

27.1 Introduction

Load bearing thermal protection systems, in the form of thin-gauge metallic airframes, provide a means to minimize the weight and improve the serviceability of reusable, long duration cruise hypersonic aircraft [1–5]. However, the compliant nature of these structures, in combination with the severe aerothermodynamic loading, results in a propensity for nonlinear fluid-structural interactions. Due to this interaction, the boundary layer state (laminar, transitional, or turbulent) is dependent on the structural response. Accurate determination of the aerodynamic heat load, which varies significantly with the state of the boundary layer, is detrimental to structural life prediction and optimal weight design [2–5]. Therefore, the future design of hypersonic aircraft may necessitate aerothermoelastic analysis which accounts for the state of the boundary layer.

Boundary layer stability is highly dependent on wall temperature [6, 7] and surface geometry [7–17], both of which vary during flight for hot structure hypersonic vehicles. Previous studies have examined how aerothermoelastic effects, such as thermally induced deformations, can augment aerothermal loads [18, 19] and impact boundary layer transition [20, 21]. Through wind-tunnel testing of X-33 configurations, Berry et al. [20] concluded that a three-dimensional array of bowed panels was less effective at forcing transition onset than discrete roughness. In a recent study, Riley et al. [21] numerically assessed the boundary layer stability of flow past large-scale, two-dimensionally (2-D) varying surface topologies resembling deformations of surface panels using the linear Parabolized Stability Equations. This study indicated that series of panels, deformed into the flow, significantly disrupts the unstable growth of disturbances excited in the absence of the deformations. The potential for 2-D wavy walls to stabilize hypersonic boundary layers has also been observed for roughness scale deformations [12–17]. As the vehicle response alters the boundary layer state, this in turn affects the aerothermal loads acting on the structure.

A few studies have examined how transitional fluid loading impacts structural response. Lamorte and Friedmann [22] assessed how transition location, and its associated uncertainty, impacts the aerothermoelastic stability of a wing structure subject to transitional aerodynamic heating. Additionally, Riley et al. [23] examined how transition onset location, transition length, and transitional heat flux and fluctuating pressure that exceed (or *overshoot*) turbulent values affect the structural response of surface panels. These studies found that transitional flows can result in aerothermal loads and structural responses which exceed that predicted assuming turbulent loading conditions.

These previous studies indicate that boundary layer stability is sensitive to changes in surface conditions and that the structural response is strongly dependent on the boundary layer state (laminar, transitional, turbulent). This interdependence

Z.B. Riley • J.J. McNamara (✉)
The Ohio State University, Columbus, OH 43210-1276, USA
e-mail: mcnamara.190@osu.edu

G. Kerschen (ed.), *Nonlinear Dynamics, Volume 1*, Conference Proceedings of the Society for Experimental Mechanics Series,
DOI 10.1007/978-3-319-29739-2_27

implies that accurate structural response prediction of a hypersonic vehicle necessitates an aerothermoelastic analysis that incorporates boundary layer stability analysis in transitional flow regions. Thus, this paper focuses on examination of the coupled problem by carrying out an aerothermoelastic analysis of a panel for the case of a time-varying boundary layer transition location. Completion of this study provides improved insight into the degree of aerothermoelastic coupling required in the design and analysis of hypersonic vehicles.

27.2 Methodology

An overview of the aerothermoelastic framework used to obtain the panel response is provided in Sect. 27.2.1. The transitional aerothermodynamic load models are discussed in Sect. 27.2.2. Finally, the specific problem examined in this paper is described in Sect. 27.2.3.

27.2.1 Aerothermoelastic Model

The aerothermoelastic model, depicted in Fig. 27.1, has three primary components: (1) aerothermodynamic loads, (2) structural dynamics, and (3) heat transfer. The aerothermodynamics drive the thermo-structural response through the application of a pressure load (composed as the summation of mean and fluctuating components) and a surface heat flux. The mean flow pressure is modeled using third-order piston theory [24–26] which accounts for changes in the mean pressure due to structural deformations. The fluctuating pressure load (FPL) is computed using the model discussed in Sect. 27.2.2.3. This framework was previously used to assess the impact of transitional heat flux and fluctuating pressure loads on panel response, where the transition onset and length were prescribed prior to the simulation [23]. The heat flux is modeled using Eckert's reference enthalpy method [27]. Note that the FPL and heat flux are dependent on the boundary layer edge properties, which are obtained from the mean flow pressure in conjunction with isentropic flow relations [24]. The aerothermoelastic model is currently being modified, as shown by the dashed lines in Fig. 27.1, to incorporate a transition prediction surrogate such that the transition onset location may vary in time; either with a prescribed variation or as a function of the structural response. For this study, only the prescribed variation in time is considered.

The structure is modeled as cylindrical bending of an isotropic plate with the assumptions of von Kármán moderate deflection plate theory [24]. The formulation includes the effects of thermal loading due to non-uniform (in-plane and through-thickness) temperature distributions, chord-wise variation of the modulus of elasticity and thermal expansion coefficient, rotary inertia, and Rayleigh damping. The structural equation of motion is discretized using Galerkin's method. The transverse displacement is approximated as a series of free-vibration mode shapes of the panel that satisfy pinned boundary conditions. Note that due to the kinematic constraints, the in-plane thermal effects are primarily driven by the chord-wise average temperature [28].

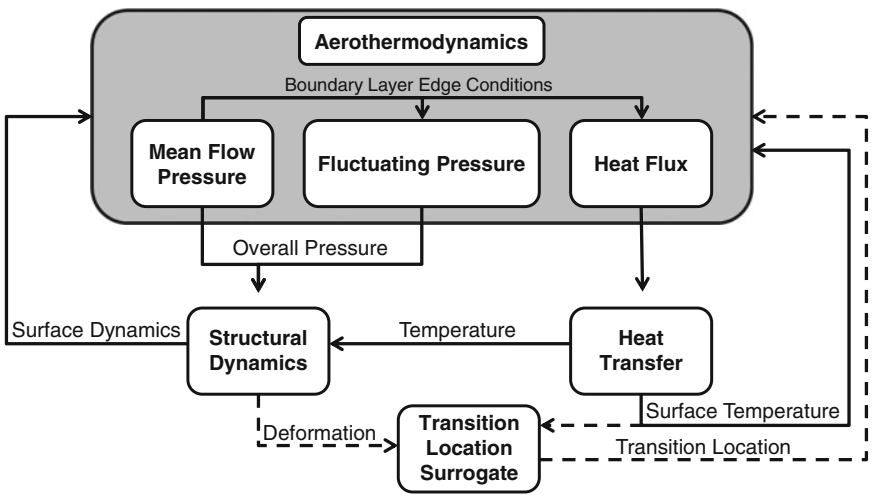

Fig. 27.1 Enhanced aerothermoelastic model

As shown in Fig. 27.1, the structural temperature is computed from a heat transfer analysis. This is carried out by solving a finite element formulation of the transient, 2-D heat transfer equation with temperature-dependent specific heat and thermal conductivity [28]. The 2-D formulation allows for heat conduction through both the thickness and length of the panel. An adiabatic wall condition is prescribed for each boundary of the panel, except the upper surface where the aerodynamic heat flux is applied.

The aerothermal and aeroelastic solvers are linked using a loosely coupled partitioned approach. This scheme is advantageous in terms of computational efficiency as the individuals solvers can use different time steps and information is exchanged between the solvers only once per time step [29]. In-depth descriptions of the aerothermoelastic model formulation are provided in [24, 28]. Further information regarding the coupling procedure and numerical schemes implemented in the aerothermoelastic model is given in [29, 30].

27.2.2 Transitional Aerothermodynamic Loads

In this study, the aerothermodynamic loads acting on the panel are heat flux and an overall pressure load (comprised of a mean and fluctuating component). Transitional boundary layer effects are incorporated into the heat flux and fluctuating pressure through blending laminar and turbulent profiles in proportion to an intermittency function, which represents the fraction of time any spatial location spends in turbulent flow [31]. A brief description of the intermittency function is given in Sect. 27.2.2.1. Details on the transitional heat flux and fluctuating pressure models are provided in Sects. 27.2.2.2 and 27.2.2.3.

27.2.2.1 Intermittency

Transition from laminar to turbulent flow is, in general, not an abrupt process. It occurs over a finite length due to the growth, propagation, and interaction of turbulent spots [32]. As a result, the flow during transition can be characterized as a laminar boundary layer subject to intermittent patches of turbulence. Thus, the statistical flow properties in the transition region can be described using an intermittency function which represents the fraction of time any spatial location spends in turbulent flow. The intermittency throughout the transition region is computed using Eq. (27.1), which is derived from Emmon's probabilistic model [32, 33] with the assumption that the burst source-rate density can be described as a Dirac delta function. This form of the source-rate density function assumes the hypothesis of concentrated breakdown is valid [34], implying that turbulent spots are formed only at the transition onset location x_t. However, at the transition onset location turbulent spots may form randomly in time and in the spanwise direction. The intermittency distribution in Eq. (27.1) is a function of the edge velocity U_e (assumed constant over the transition region), the transition onset location x_t, the number of turbulent spots per unit time and spanwise distance n, and a spot propagation parameter σ. The spot propagation parameter is defined in Eq. (27.2), where $u_g = u_l - u_t$, $u_c = 1/2(u_l + u_t)$, u_l and u_t are the leading and trailing edge velocities of the turbulent spot, and α is the half angle.

$$\gamma(x) = 1 - \exp\left[-\frac{\sigma n}{U_e}(x - x_t)^2\right] \tag{27.1}$$

$$\sigma = \frac{u_g U_e}{u_c u_t} \tan\alpha \tag{27.2}$$

From the definition of intermittency, the length of the transition region Δx_t can be expressed as shown in Eq. (27.3). Introducing Δx_t into the exponent in Eq. (27.1), results in an expression for the intermittency which is a function of the transition onset and length alone.

$$\Delta x_t = (x - x_t)|_{\gamma=0.99} - (x - x_t)|_{\gamma=0.01} = 2.0457\sqrt{\frac{U_e}{\sigma n}} \tag{27.3}$$

$$\gamma(x) = 1 - \exp\left[-\frac{4.1850}{\Delta x_t^2}(x - x_t)^2\right] \tag{27.4}$$

27.2.2.2 Heat Flux

The transitional heat flux is approximated by using the intermittency to blend the laminar and turbulent values as shown in Eq. (27.5). If the laminar and turbulent boundary layers originate at the same location, the blending in Eq. (27.5) can not account for transitional overshoot in heat flux [34]. Overshoot can be incorporated by assuming the turbulent boundary layer begins at a virtual origin $turb_{VO}$ corresponding to the transition onset location [31]. Applying the linear blending in Eq. (27.5) and assuming the turbulent boundary layer originates at x_t, Dhawan and Narasimha [31] matched experimental skin friction coefficients and displacement thickness during transition.

$$Q_{tran} = (1-\gamma)Q_{lam} + \gamma Q_{turb_{VO}} \tag{27.5}$$

Previous experiments, which have observed transitional overshoot in heat flux [35], demonstrate that heating rates decrease back to fully turbulent conditions beyond the overshoot region. To model this, the transitional heat flux [computed using Eq. (27.5)] is blended with the fully turbulent heating rates as shown in Eq. (27.6), where Λ is a Gaussian function, defined in Eq. (27.7). The peak of the Gaussian function coincides with the end of transition x_{te}, and the Full Width at Half Maximum β is specified such that the function decreases to negligible values prior to the end of the geometry x_{end}. This ensures that fully turbulent heating rates are obtained on the end of the geometry.

$$Q(x) = (1-\Lambda)Q_{turb} + \Lambda Q_{tran} \ (x_{te} \leq x \leq x_{end}) \tag{27.6}$$

$$\Lambda(x) = \exp\left[\frac{-\left(\frac{x-x_{te}}{x_{end}-x_{te}}\right)^2}{2\beta^2}\right] \tag{27.7}$$

$$\beta = \frac{0.5}{2\sqrt{2\ln 2}} \tag{27.8}$$

An example of the transitional heat flux generated using this model is provided in Fig. 27.2 for transition beginning at $x/L = 0.3$ and ending at $x/L = 0.5$. The "*No overshoot*" line in Fig. 27.2 corresponds to the transitional heat flux profile obtained using Eq. (27.5) if the laminar and turbulent boundary layers have the same origin. The "*Overshoot*" heat flux was generated assuming the turbulent boundary layer originates at $x/L = 0.3$ with the Gaussian blending applied in the turbulent region ($x/L \geq 0.5$). The heat flux profiles in Fig. 27.2 demonstrate that, through shifting the turbulent boundary layer origin, this model can be used to generate heat flux profiles which either account for or neglect the effect of transitional overshoot.

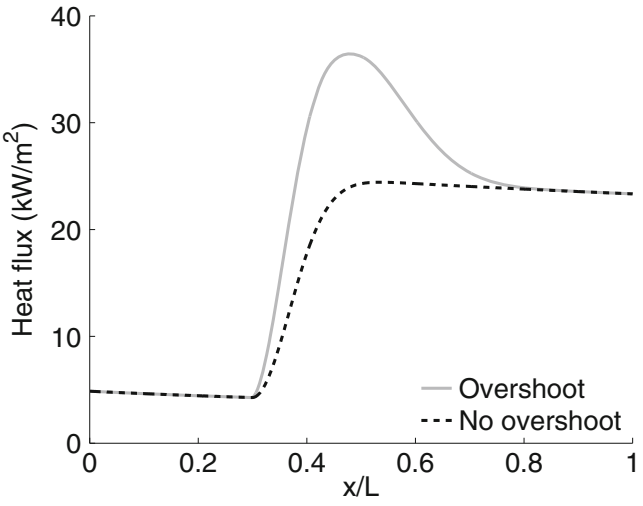

Fig. 27.2 Transitional heat flux model $x_t = 0.30\,\text{m}$ and $\Delta x_t = 0.20\,\text{m}$

27.2.2.3 Fluctuating Pressure

The fluctuating pressure load model currently implemented in the aerothermoelastic solver is a modified version of the semi-empirical model developed by Deshmukh et al. [36]. The unsteady pressure is expressed as shown in Eq. (27.9), where $f(x,t)$ and $\Theta(x,t)$ represent the magnitude and phase angle of the pressure load.

$$p = f(x,t)e^{i\Theta(x,t)} \tag{27.9}$$

As denoted in Eq. (27.10), the phase angle is decomposed into separate temporal τ and spatial ψ components where the spatial variation is assumed relative to the leading edge of the panel. The temporal phase angles account for the phase lag between disturbances of different frequency at the same spatial location. Conversely, the spatial phase angles account for the phase lag between disturbances of the same frequency at different spatial locations. In this study, the phase angles (τ and ψ) are assumed to vary randomly with x and t, respectively. Recent work indicates that the impact of the boundary layer induced pressure fluctuation on structural response is dependent on the spatial phase angle model [36]. Therefore, the assumption of a random spatial phase angle, which neglects coherence in the boundary layer, introduces uncertainty into the predicted structural responses. The amplitude $f(x,t)$ is described as the combination of a root mean square (RMS) value, corresponding to the magnitude, and a power spectral density (PSD), corresponding to the frequency content [37–39].

$$\Theta(x,t) = \tau(t) + \psi(x) \tag{27.10}$$

The transitional boundary layer RMS pressure $\tilde{p}$ is modeled using Eq. (27.11), which is a modified version of Laganelli's relation for turbulent boundary layer attached flow [37–39]. As shown in Eq. (27.11), the RMS pressure is a function of the dynamic pressure at the boundary layer edge q_e, a compressible flow transformation function F_c, a viscosity/velocity power law exponent λ, and a compressibility exponent b. Laganelli's relation was modified to increase the incompressible fluctuating pressure intensity from 0.006 to 0.009, as recommended by Bull [40] and Beresh et al. [41]. The second modification introduces an $Re_\theta^{-0.1}$ dependence into the RMS pressure calculation, which Beresh et al. [41] found to exist for Mach numbers between 2 to 3. Note that, $Re_\theta\big|_{\bar{x}^*}$ represents a normalization constant that specifies the spatial location at which the Re_θ dependence begins. The final modification incorporates a dependence on the local skin friction coefficients corresponding to transitional $c_{f_{tran}}$ and fully turbulent $c_{f_{turb}}$ boundary layers. The relationship in Eq. (27.11) is similar to Laganelli's model for turbulent boundary layer pressure fluctuations on rough surfaces [38], which scales the smooth wall RMS pressure based off the skin friction ratio to obtain the rough wall RMS pressure. As shown in Eq. (27.12), the transitional skin friction coefficient is computed in the same manner as the heat flux. To remove leading edge effects, the RMS pressure in the laminar region is specified as the minimum RMS value prior to transition onset.

$$\frac{\tilde{p}}{q_e} = 0.009F_c^{\lambda(1+b)}\left(\frac{Re_\theta}{Re_\theta\big|_{\bar{x}^*}}\right)^{-0.1}\frac{c_{f_{tran}}}{c_{f_{turb}}} \tag{27.11}$$

$$c_{f_{tran}} = (1-\gamma)c_{f_{lam}} + \gamma c_{f_{turb_{VO}}} \tag{27.12}$$

The PSD ϕ is computed using Eq. (27.13), where δ_1 represents the boundary layer displacement thickness and ω corresponds to angular frequency. The fluctuating pressure load, acting on the panel, is obtained by converting the frequency domain PSD values and phase angles to a time domain signal using the analytical function provided in Eq. (27.14). This function is the real component of a one-sided Inverse Fourier Transform, where the upper limit of integration ω_{max} corresponds to the largest frequency expected to impact the structure. As energy is removed due to the frequency truncation, the pressure signal must be computed using a scaled PSD [Eq. (27.15)] in order to reproduce a fluctuating pressure which matches the input RMS values.

$$\frac{\phi(x,\omega)U_e}{q_e^2\delta_1} = \frac{(\tilde{p}/q_e)^2F_c^{-2\lambda}(2/\pi)}{1+\left(F_c^{-2\lambda}\omega\delta_1/U_e\right)^2} \tag{27.13}$$

$$p(x,t) = \int_0^{\omega_{max}} \sqrt{2\phi^*(x,\omega)\Delta\omega}\cos(\omega t + \Theta(x,\omega))\,d\omega \tag{27.14}$$

$$\phi^*(x,\omega) = \frac{\tilde{p}^2}{\int_0^{\omega_{max}}\phi(x,\omega)\,d\omega}\phi(x,\omega) \tag{27.15}$$

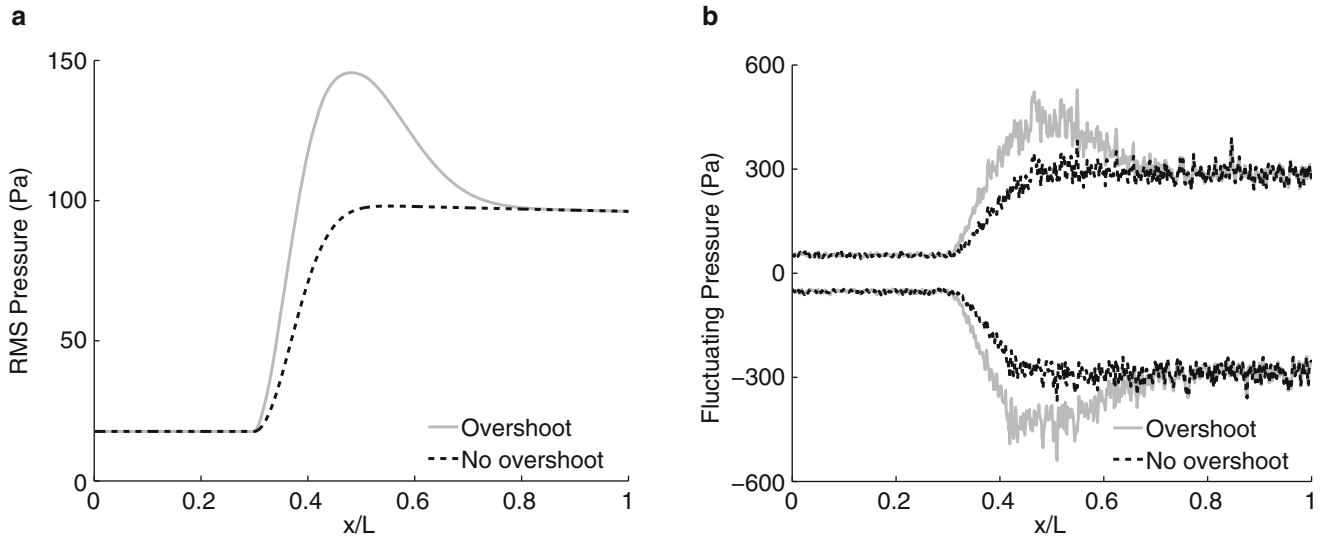

Fig. 27.3 Transitional fluctuating pressure load model. (**a**) RMS of fluctuating pressure. (**b**) Fluctuating pressure snapshot envelope

Table 27.1 Freestream conditions and panel geometry

Mach number	4.0
Altitude	30 km
Unit Reynolds number	1.461e6 m^{-1}
Turn angle	5.0 °
Length	1.00 m
Thickness	2.50 mm
Material	Aluminum 7075

An example of the transitional pressure load is provided in Fig. 27.3 in terms of the RMS pressure (Fig. 27.3a) and a snapshot of the fluctuating pressure envelope (Fig. 27.3b), for transition beginning at $x/L = 0.3$ and ending at $x/L = 0.5$. As with the heat flux profiles in Fig. 27.2, results are presented for shifted and unshifted turbulent boundary layers to demonstrate the effect of accounting for or neglecting transitional overshoot. The RMS pressure in Fig. 27.3a demonstrates that the present formulation results in a smooth spatial variation in the RMS pressure throughout transition, with peak magnitudes occurring at the end of transition. The fluctuating pressure envelope in Fig. 27.3b represents the minimum and maximum bounds of the instantaneous pressure load acting on the panel.

27.2.3 Problem Description

The freestream conditions and panel geometry considered in this study are listed in Table 27.1. It is assumed that the panel lies 1 m downstream of the leading edge of a wedge with a 5.0 ° half angle. Therefore, the flow the panel experiences corresponds to the post oblique shock conditions (i.e. $M = 3.64$). The material properties of the panel are listed in Table 27.2. Note that the modulus of elasticity, specific heat capacity, thermal conductivity, and thermal expansion coefficient are temperature-dependent properties where the listed values correspond to a temperature of 300 K. The numerical parameters used in this study, listed in Table 27.3, were determined through a convergence study of the post-instability, limit cycle response of the panel. This configuration (geometry, material, freestream conditions) is selected for this study as it has been thoroughly examined in past works [23, 28, 29]. While this configuration does not represent an actual structure intended for use on a hypersonic vehicle, it provides the means to study a representative coupled response over a relatively short time record [28].

Table 27.2 Material properties of Al-7075 at 300 K

Density	2768 kg/m^3
Poisson's ratio	0.325
Modulus of elasticity	71.345 GPa
Specific heat capacity	850.99 J/kg K
Thermal conductivity	132.05 W/m K
Thermal expansion coefficient	22.184 μm/m K

Table 27.3 Numerical parameters of the aerothermoelastic solution

Structural mode shapes	25
Aeroelastic time step	12.5 μs
Aerothermal time step	125 μs

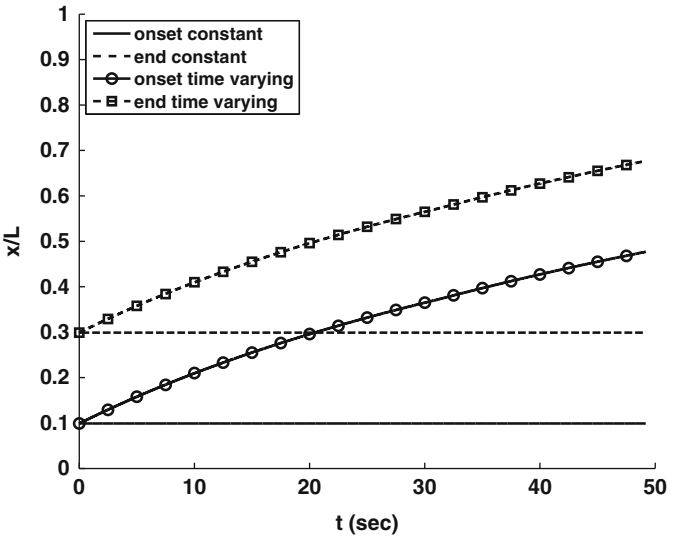

Fig. 27.4 Transition region as a function of time

27.3 Results and Analysis

A preliminary analysis was performed to demonstrate the importance of accounting for time-varying, fluid stability in aerothermoelastic response prediction. Results are presented for panel responses obtained assuming a constant transition length ($\Delta x_t = 0.2\,\text{m}$) and an initial transition onset location of $x_t = 0.1\,\text{m}$. The onset location either remains constant or varies in time as a function of the average wall temperature, according to Eq. (27.16). The relationship in Eq. (27.16) linearly interpolates between $x_t = 0.1\,\text{m}, T_w = 300\,\text{K}$ and $x_t = 0.7\,\text{m}, T_w = 495\,\text{K}$, where the later conditions are specified to ensure the last 0.1 m of the panel is subject to fully turbulent loading and to remain within the temperature range for the material property data set. Here, Eq. (27.16) is an ad hoc expression meant to approximate the stabilizing effect of elevated temperature on second mode disturbances [6] as the transition onset moves downstream with increasing wall temperature.

$$x_t(t) = 0.1\,\text{m} + \left(0.7\,\text{m} - 0.1\,\text{m}\right)\frac{T_w(t) - 300\,\text{K}}{495\,\text{K} - 300\,\text{K}} \tag{27.16}$$

The transition region definitions for the constant and time-varying cases are provided in Fig. 27.4 in terms of the locations corresponding to the onset and end of transition. At the start of the simulation ($t = 0\,\text{s}$), both cases have the same transition region ($x_t = 0.1\,\text{m}, x_{te} = 0.3\,\text{m}$). However, as the panel temperature rises, as a result of the applied heat flux, the time-varying transition region moves rearward along the panel, maintaining a transition length of $\Delta x_t = 0.2\,\text{m}$.

The impact of the time-varying transition region on the panel response is depicted in Fig. 27.5 in terms of the maximum temperature (Fig. 27.5a) throughout the panel and the three quarter chord displacement envelope (Fig. 27.5b). The results in Fig. 27.5 indicate that as the transition region moves rearward along the panel, the peak temperature decreases and the time to flutter increases, as compared to the constant transition region response. This is a product of the reduction in the thermal load, due to the increased region of the panel subject to laminar heating.

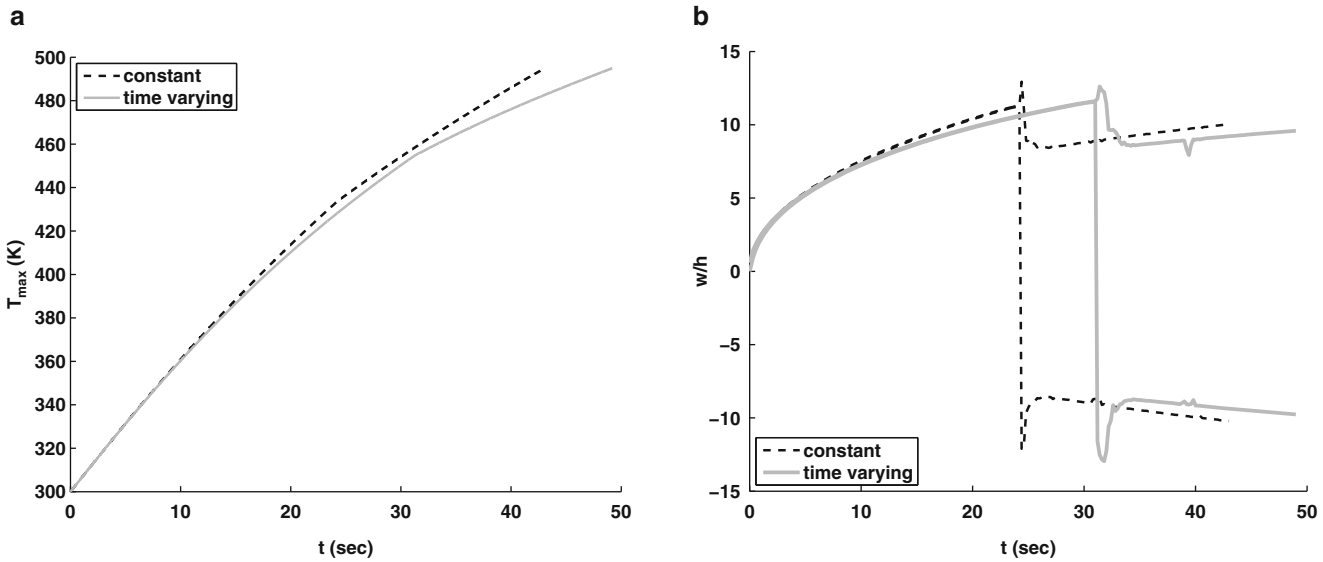

Fig. 27.5 Constant vs. time varying transition location. (**a**) Maximum temperature. (**b**) 3/4 chord displacement

The response of the panel subject to both constant and time-varying transitional loads is provided in Fig. 27.6, in terms of the average through-thickness temperature rise (Fig. 27.6a), chordwise thermal gradient (Fig. 27.6b), normalized displacement (Fig. 27.6c), and slope (Fig. 27.6d). Note that, the temperature rise in Fig. 27.6a is relative to the initial panel temperature of 300 K and the displacement in Fig. 27.6c is normalized by the panel thickness h. Comparison of the temperature profiles in Fig. 27.6a, indicates that the time-varying transition region reduces the peak temperature and shifts its spatial location further downstream in time, as compared with the constant transition definition. This reduction and shift in peak temperature greatly reduces the thermal gradient across the panel, as highlighted in Fig. 27.6b. The displacement and slope profiles in Fig. 27.6c, d illustrate that the prescribed transition region only affects the magnitude of the peak deformation. This is expected as the panel deformation is driven by the thermal loading which, as Fig. 27.6a, b highlight, is dependent on the transition region. The asymmetry of the panel is an aeroelastic effect, resulting from the interaction between the fluid pressure and the thermally induced deformation. As the profiles in Fig. 27.6c, d are similar for either transition definition, this implies that the location of the peak fluctuating pressure load does not significantly impact the structural response.

27.4 Conclusions and Future Work

This study examines the effect of time varying boundary layer transition location during aerothermoelastic analysis of a representative hypersonic vehicle panel. The results indicate that rearward movement of the transition front (i.e., relaminarization of the boundary layer) significantly reduces the thermal loading and peak deformation, potentially extending the life of the structure. These results help to quantify the degree of coupling fidelity required to accurately predict the response of a structure subject to hypersonic aerodynamic loading.

Acknowledgements This research was conducted with Government support by the DoD through a National Defense Science and Engineering Graduate Fellowship (32 CFR 168a), the AFRL-University Collaborative Center in Structural Sciences (AFRL/RQ Cooperative Agreement FA8650-13-2-2347) with Dr. Ravi Penmetsa as program manager, and through an allocation of computing time from the Ohio Super Computer Center.

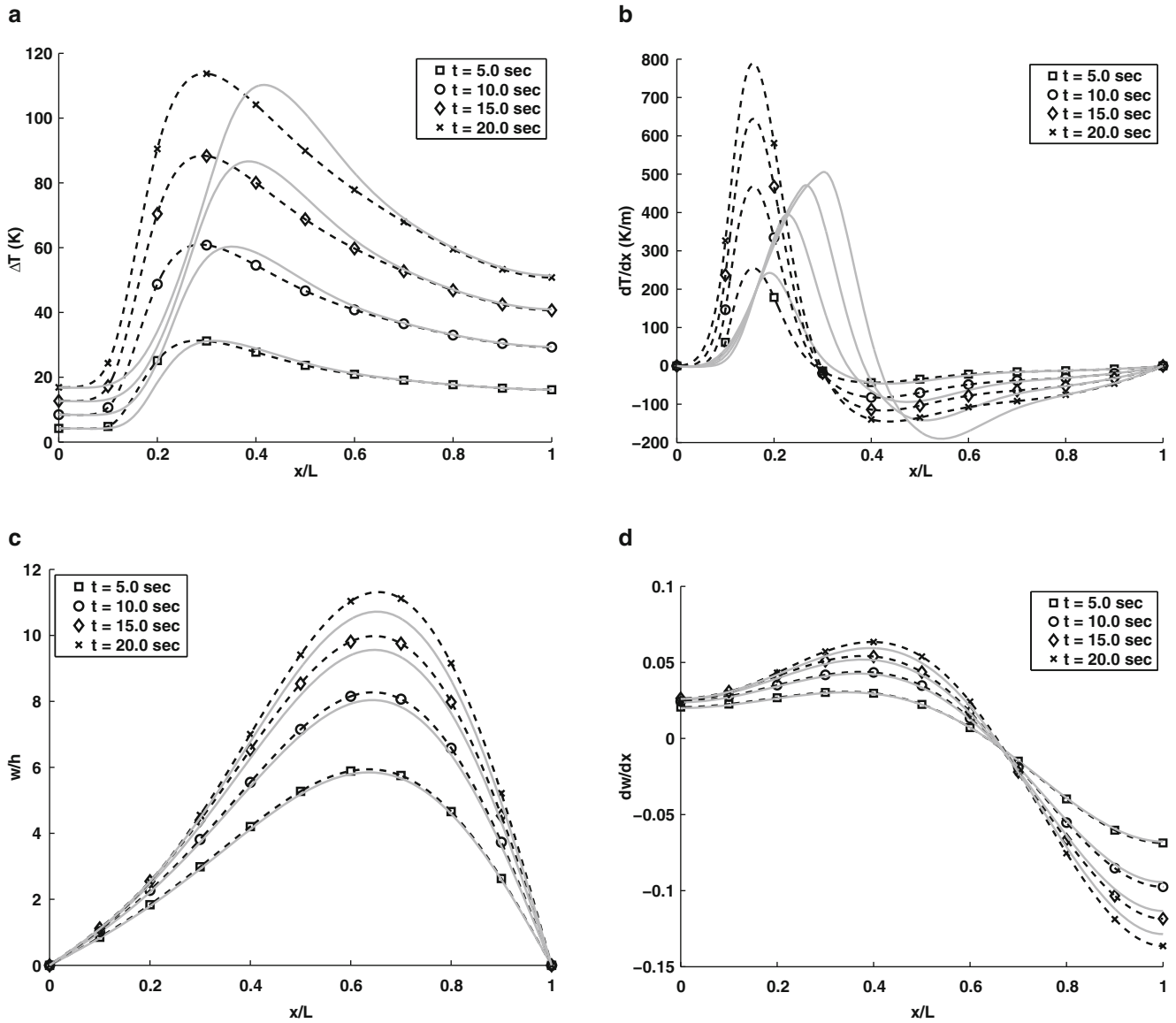

Fig. 27.6 Variation in panel response due to constant (*dashed lines*) and time varying (*solid lines*) transition onset. (**a**) Average through-thickness temperature rise. (**b**) Chordwise thermal gradient. (**c**) Displacement. (**d**) Slope

References

1. Kontinos, D., Palmer, G.: Numerical simulation of metallic thermal protection system panel bowing. J. Spacecr. Rocket **36**(6), 842–849 (1999)
2. Zuchowski, B.: Predictive capability for hypersonic structural response and life prediction, phase 1 - identification of knowledge gaps. Technical Report AFRL-RB-WP-TR-2010-3069, August 2010
3. Tzong, G., Jacobs, R., Liguore, S.: Predictive capability for hypersonic structural response and life prediction: phase 1 - identification of knowledge gaps. Technical Report AFRL-RB-WP-TR-2010-3068, September 2010
4. Zuchowski, B.: Predictive capability for hypersonic structural response and life prediction: phase ii - detailed design of hypersonic cruise vehicle hot-structure. Technical Report AFRL-RQ-WP-TR-2012-0280, May 2012
5. Quiroz, R., Embler, J., Jacobs, R., Tzong, G., Liguore, S.: Predictive capability for hypersonic structural response and life prediction: phase ii - detailed design of hypersonic cruise vehicle hot-structure. Technical Report AFRL-RQ-WP-TR-2012-0265, February 2012
6. Mack, L.M.: The stability of the compressible laminar boundary layer according to a direct numerical solution, pp. 329–362. Technical Editing and Reproduction Ltd., Harford House, 7-9 Charlotte St. London W.1., 97th edn., May 1965, AGARD-CP-97
7. Schneider, S.: Effects of roughness on hypersonic boundary layer transition. J. Spacecr. Rocket **45**(2), 193–209 (2008)
8. Fedorov, A., Khokhlov, A.: Receptivity of hypersonic boundary layer to wall disturbances. Theor. Comput. Fluid Dyn. **15**, 231–254 (2002)
9. Wang, X., Zhong, X.: Receptivity of a hypersonic flat-plate boundary layer to three-dimensional surface roughness. J. Spacecr. Rocket **45**(6), 1165–1175 (2008)

10. Berry, S., Horvath, T.: Discrete-roughness transition for hypersonic flight vehicles. J. Spacecr. Rocket **45**(2), 216–227 (2008)
11. Wang, X., Zhong, X.: Effect of wall perturbations on the receptivity of a hypersonic boundary layer. Phys. Fluids **21**(4), 19 (2009). Paper 044101. doi:10.1063/1.3103880.
12. Fujii, K.: Experiment of the two-dimensional roughness effect on hypersonic boundary-layer transition. J. Spacecr. Rocket **43**(4), 731–738 (2006)
13. Marxen, O., Iaccarino, G., Shaqfeh, E.: Disturbance evolution in a Mach 4.8 boundary layer with two-dimensional roughness-induced separation and shock. J. Fluid Mech. **648**, 435–469 (2010)
14. Bountin, D., Chimitov, T., Maslov, A.: Stabilization of a hypersonic boundary layer using a wavy surface. AIAA J. **51**(5), 1203–1210 (2013)
15. Duan, L., Wang, X., Zhong, X.: Stabilization of a Mach 5.92 boundary layer by two-dimensional finite-height roughness. AIAA J. **51**(1) (2013). doi:10.25114/I.J051643
16. Fong, K., Wang, X., Zhong, X.: Numerical simulation of roughness effect on the stability of a hypersonic boundary layer. Comput. Fluids **96**, 350–367 (2014)
17. Fong, K., Wang, X., Zhong, X.: Parametric study on stabilization of hypersonic boundary-layer waves using 2-D surface roughness. AIAA Paper 2015-0837, January 2015, 53rd AIAA Aerospace Sciences Meeting
18. Glass, C.E., Hunt, L.R.: Aerothermal tests of spherical dome protuberances on a flat plate at a Mach number of 6.5. NASA TP-2631 (1986)
19. Glass, C., Hunt, L.: Aerothermal tests of quilted dome models on a flat plate at a Mach number of 6.5, NASA TP-2804 (1988)
20. Berry, S., Horvath, T., Hollis, B., Thompson, R., Hamilton II, H.: X-33 hypersonic boundary-layer transition. J. Spacecr. Rocket **38**(5), 646–656 (2001)
21. Riley, Z., McNamara, J., Johnson, H.: Assessing hypersonic boundary layer stability in the presence of structural deformation. AIAA J. **52**(11), 2547–2558 (2014). doi: 10.2514/1.J052941
22. Lamorte, N., Friedmann, P.P.: hypersonic aeroelastic and aerothermoelastic studies using computational fluid dynamics. AIAA J. **52**(9), 2062–2078 (2014)
23. Riley, Z., Deshmukh, R., Miller, B.A., McNamara, J.: Characterization of structural response to hypersonic boundary layer transition. AIAA Paper 2015-0688, January 2015, 56th AIAA/ASCE/AHS/ASC Structures, Structural Dynamics and Materials Conference
24. Culler, A.J., McNamara, J.J.: Studies on fluid-thermal-structural coupling for aerothermoelasticity in hypersonic flow. AIAA J. **48**(8), 1721–1738 (2010)
25. Lighthill, M.: Oscillating airfoils at high Mach numbers. J. Aeronaut. Sci. **20**(6), 402–406 (1953)
26. Ashley, H., Zartarian, G.: Piston theory - a new aerodynamic tool for the aeroelastician. J. Aeronaut. Sci. **23**(12), 1109–1118 (1956)
27. Eckert, E.R.G.: Engineering relations for heat transfer and friction in high-velocity laminar and turbulent boundary-layer flow over surfaces with constant pressure and temperature. Trans. ASME **78**(6), 1273–1283 (1956)
28. Miller, B.A., McNamara, J.J., Culler, A.J., Spottswood, S.M.: The impact of flow induced loads on snap-through behavior of acoustically excited, thermally buckled panels. J. Sound Vib. **330**(23), 5736–5752 (2011)
29. Miller, B., McNamara, J.: Efficient time-marching of fluid-thermal-structural interactions. AIAA Paper 2014-0337, January 2014, 55th AIAA/ASME/ASCE/AHS/ASC Structures, Structural Dynamics and Materials Conference
30. Miller, B.A., McNamara, J.J.: Time-marching considerations for response prediction of structures in hypersonic flows. AIAA J. **53**(10), 3028–3038 (2015). doi:10.2514/1.J053872
31. Dhawan, S., Narasimha, R.: Some properties of boundary layer flow during the transition from laminar to turbulent motion. J. Fluid Mech. **3**, 418–436 (1958)
32. Emmons, H.W.: The laminar-turbulent transition in a boundary layer-Part I. (Inst. Aeronaut. Sci.) **18**, 490–498 (1951)
33. Emmons, H.W., Bryson, A.: The laminar-turbulent transition in a boundary layer-Part II. In: Proceedings of the First U.S. National Congress of Theoretical and Applied Mechanices, pp. 859–868 (1952)
34. Narasimha, R.: The laminar-turbulent transition zone in the boundary layer. Prog. Aerosp. Sci. **22**, 29–80 (1985)
35. Wadhams, T., Mundy, E., MacLean, M., Holden, M.: Ground test studies of the HIFiRE-1 transition experiment part 1: experimental results. J. Spacecr. Rocket **45**(6), 1134–1148 (2008)
36. Deshmukh, R., Culler, A., Miller, B., McNamara, J.: Response of skin panels to combined self- and boundary layer- induced fluctuating pressure. J. Fluids Struct. **58**, 216–235 (2015)
37. Laganelli, A., Howe, J.: Prediction of pressure fluctuations associated with maneuvering re-entry weapons. AFFDL-TR-77-59, July 1977
38. Laganelli, A., Wolfe, H.: Prediction of fluctuating pressure in attached and separated turbulent boundary-layer flow. J. Aircr. **30**(6), 962–970 (1993)
39. Blevins, R.D., Bofilios, D., Holehouse, I., Hwa, V.W., Tratt, M.D., Laganelli, A.L., Pozefsky, P., Pierucci, M.: Thermo-Vibro-Acoustic Loads and Fatigue of Hypersonic Flight Vehicle Structure - Phase II Report, Rohr Industries, Inc., RHR 89-202, November 1989
40. Bull, M.K.: Wall-pressure fluctuations beneath turbulent boundary layers: some reflections on forty years of research. J. Sound Vib. **190**(3), 299–315 (1996)
41. Beresh, S.J., Henfling, J.F., Spillers, R.W., Pruett, B.O.: Fluctuating wall pressures measured beneath a supersonic turbulent boundary layer. Phys. Fluids **23** (2011). Paper 075110. doi:10.1063/1.3609271

Chapter 28
Simultaneous Vibration Isolation and Energy Harvesting: Simulation and Experiment

R. Benjamin Davis and Matthew D. McDowell

Abstract Passive vibration isolators that use post-buckled beams as spring elements have received considerable research attention because the buckled beams exhibit low stiffness and less static deflection relative to similarly soft linear springs. This work considers such a vibration isolation system, but with the additional novelty of using piezoelectric film on the surface of the buckled beams. While the isolator is in operation, the piezoelectric film flexes along with the beam to produce an electric current. This electric current can then be used to passively power sensors, wireless networks, or charge batteries. The entire device operates passively on ambient vibration with no required external power or control system. The structural system is modeled using the elastica in conjunction with shooting methods. The structural response is then coupled to the circuit equation to determine the output voltage and corresponding power of the energy harvesting circuit. The simulated vibration isolation and energy harvesting performance is compared to experimental results. Both theoretical and experimental data suggest that there is not necessarily a trade-off between vibration isolation and harvested power. That is, over certain frequency ranges, improved vibration isolation will be accompanied by an increase in the harvested power.

Keywords Vibration isolation • Energy harvesting • Multiphysics modeling • Elastica • Shooting method

28.1 Introduction and Background

Vibration isolation systems are used in a variety of applications to protect sensitive equipment from excessive vibration or to attenuate the vibration transmitted by machines to their surroundings. Classical vibration isolation systems place linear springs between the source of the vibration and the mass to be isolated. (For a detailed presentation of classical vibration isolation systems, see the texts of Inman [1] or Thomson and Dahleh [2].) In classical SDOF vibration isolation systems, the amplitude ratio of the mass response to the source excitation—known as transmissibility—is less than unity for excitation frequencies exceeding $\sqrt{2}$ times the natural frequency. It is therefore generally desirable to design isolation systems such that the fundamental frequency of the system is as low as possible. For a fixed mass, this is achieved by making the spring elements as soft as practicable.

However, by Hooke's law, it is clear that soft linear springs will experience large static deflections when loaded with a large mass. In some applications, these static deflections may be unacceptable and require compromising transmissibility in favor of stiffer springs. To achieve low stiffness and small static deflections in vibration isolation, researchers have turned to the use of post-buckled structures as spring elements. The earliest experimental implementations of this concept are due to Winterflood et al. [3] and Virgin and Davis [4]. Since then, the concept has received considerable research attention, and a 2008 review of research related to passive nonlinear vibration isolators was presented by Ibrahim [5].

In parallel to these advances in vibration isolation, there has been an impressive amount of research directed toward vibrational energy harvesting. As their name suggests, vibrational energy harvesters convert otherwise wasted vibrational energy into useful power. The prototypical design consists of a metallic cantilevered beam covered on one side (unimorph) or both sides (bimorph) with a piezoelectric material. Given a known base excitation, the beams are designed to experience resonance at a dominant excitation frequency. This resonant response maximizes the voltage developed in the piezoelectric material, and with an appropriate choice of resistance, the power produced by the energy harvesting circuit can be maximized as well. While the power generated by these devices is typically low (on the order of micro-watts), the ever decreasing power

R.B. Davis (✉) • M.D. McDowell
College of Engineering, University of Georgia, Athens, GA 30602, USA
e-mail: ben.davis@uga.edu

G. Kerschen (ed.), *Nonlinear Dynamics, Volume 1*, Conference Proceedings of the Society for Experimental Mechanics Series,
DOI 10.1007/978-3-319-29739-2_28

demands of today's electronics make vibrational energy harvesters practical for charging small batteries as well as powering remote sensors and wireless networks. See the text of Erturk and Inman for an in-depth treatment of the modeling and testing of vibrational energy harvesters [6].

In this paper, we describe the theoretical modeling and experimental testing of a new device designed to simultaneously achieve vibration isolation and energy harvesting. The following sections describe the theoretical modeling and experimental testing of the device, and demonstrate that effective passive vibration isolation can be achieved while also passively harvesting useful quantities of electric power. The device employs an experimental isolator very similar to the one constructed by Virgin and Davis [4]. The key difference here is that piezoelectric film is attached to the beams to harvest some of the energy associated with beam flexure. Zhu et al. [7, 8] considered energy harvesting (but not vibration isolation) using magnetically driven buckled beams covered with a similar piezoelectric film.

28.2 Theory

The theoretical modeling of the system can be divided into three steps. In the first step, the post-buckled equilibrium of the beam is found using the elastica in conjunction with a single parameter shooting method. Next, we assume small amplitude vibration about the equilibrium position and use a three-parameter shooting method to calculate the beam's response under harmonic base excitation. Third, we solve the electric circuit equation to determine the output voltage of the energy harvesting circuit. To simplify the analysis, we assume that the structure is one-way coupled to the electric circuit. That is, the structural motion will be coupled to the circuit, but the effect that the electric circuit has on the beam dynamics is assumed to be negligible. The validity of this assumption will be assessed in Sect. 28.4.1. For the sake of brevity, the model equations are presented without derivation. For more details on the structural modeling, interested readers may consult the thesis of Sidbury [9]. Additional details on the modeling of the energy harvesting circuit can be found in the text of Erturk and Inman [6].

28.2.1 Static Equilibrium

Consider the system shown in Fig. 28.1. Under the weight of the mass, m, a slender beam with pinned ends buckles producing an end shortening, δ, and a maximum lateral deflection, w. The Euler buckling load for a beam of this type is $P_{cr} = \pi^2 EI/L^2$, where EI and L are the beam's flexural rigidity and length. Describing the system in terms of an arc length coordinate, s, and applying the static equilibrium condition gives the following system of differential equations (see Sidbury [9]):

$$\frac{d\bar{x}}{ds} = cos(\theta), \tag{28.1}$$

$$\frac{d\bar{y}}{ds} = sin(\theta), \tag{28.2}$$

$$\frac{d\theta}{ds} = \bar{m} - d_0, \tag{28.3}$$

$$\frac{d\bar{m}}{ds} = -\bar{p}sin(\theta), \tag{28.4}$$

which is in terms of the following non-dimensional parameters: $\bar{x} = x/L$, $\bar{y} = y/L$, $\bar{s} = s/L$, $\bar{p} = PL^2/EI$, $\bar{m} = ML/EI$, where P is the axial load (mg) and M is the moment induced in the beam. The parameter d_0 describes the amount of initial curvature in the beam. We have assumed here that the beam is under pure axial load.

The pinned end condition at $\bar{s} = 0$ requires that $\bar{y} = \bar{x} = \bar{m} = 0$ while the pinned-rolling connection at $\bar{s} = 1$ requires that $\bar{y} = \bar{m} = 0$. The shooting method is then used to solve this boundary value problem by treating it as an initial value problem. In this particular case, a guess is supplied as an initial condition at $\theta(0)$ then Eqs. (28.1)–(28.4) are integrated numerically using a fourth-fifth order Runge-Kutta scheme. The resulting moment at $\bar{s} = 1$ is then compared to its required boundary value of zero. The guess for $\theta(0)$ is then iteratively adjusted until the calculated end moment is sufficiently close to zero. More information on the use of shooting methods to solve the elastica can be found in the thesis of Santillan [10].

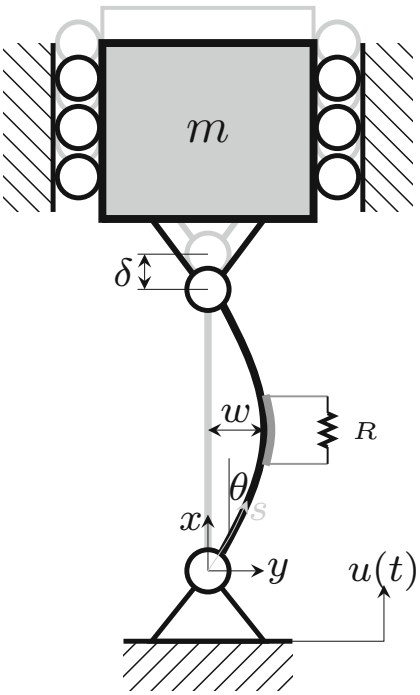

Fig. 28.1 Diagram of buckled beam with an attached piezoelectric film and subject to base motion

28.2.2 Dynamic Equations of Motion

After determining the static deflection shape of the beam, we calculate the steady-state dynamic response of the beam under harmonic base excitation assuming small amplitude vibration superimposed on the static equilibrium configuration. Using d'Alembert's Principle to enforce dynamic equilibrium, it can be shown [9] that the following spatial differential equations are established:

$$\frac{d\bar{x}_d}{ds} = -\theta_d sin(\theta_e), \tag{28.5}$$

$$\frac{d\bar{y}_d}{ds} = \theta_d cos(\theta_e), \tag{28.6}$$

$$\frac{d\theta_d}{ds} = \frac{\bar{m}_d}{(1 + i\bar{\omega}\bar{\gamma})}, \tag{28.7}$$

$$\frac{d\bar{m}_d}{ds} = (\bar{q}_d - \bar{p}\theta_d)cos(\theta_e) - \bar{p}_d sin(\theta_e), \tag{28.8}$$

$$\frac{d\bar{p}_d}{ds} = \left(\bar{\omega}^2 - i\bar{\omega}\bar{c}\right)\bar{x}_d, \tag{28.9}$$

$$\frac{d\bar{q}_d}{ds} = \left(\bar{\omega}^2 - i\bar{\omega}\bar{c}\right)\bar{y}_d, \tag{28.10}$$

where the d subscript indicates the dynamic component of a variable while the e subscript denotes the static equilibrium component and the additional non-dimensional parameters are given by

$$\bar{\omega} = \omega\sqrt{\frac{\mu L^4}{EI}}, \tag{28.11}$$

$$\bar{q}_d = \frac{q_d L^2}{EI}, \tag{28.12}$$

$$\bar{c} = \frac{cL^2}{\sqrt{\mu EI}}, \tag{28.13}$$

$$\bar{\gamma} = \frac{\gamma\sqrt{I}}{\sqrt{\mu EL^4}}. \tag{28.14}$$

Here, $\bar{\omega}$ is the non-dimensional excitation frequency, where μ is the mass per unit length of the beam, and $\bar{q}_d$ is the non-dimensional dynamic component of the transverse force in the beam. The $\bar{c}$ and $\bar{\gamma}$ parameters represent non-dimensional viscous and Kelvin-Voigt damping, respectively.

The solution of Eqs. (28.5)–(28.10) requires a three-parameter shooting method in which guesses are supplied for $\theta_d(0)$, $p_d(0)$, and $q_d(0)$ and are iteratively updated until $\bar{y}_d(1)$, $\bar{m}_d(1)$ and $\bar{p}_d(1) + r\bar{p}\bar{\omega}^2\bar{x}_d(1)$ are all sufficiently close to zero. The last of these quantities enforces axial dynamic load equilibrium at the end of the beam and includes a non-dimensional stiffness parameter, r, that is a given by $r = EI/\mu g L^3$.

Note that with the inclusion of damping, the solutions to Eqs. (28.5)–(28.10) will generally be complex, so the solution procedure requires that the complex modulus of $\bar{y}_d(1)$, $\bar{m}_d(1)$ and $\bar{p}_d(1) + r\bar{p}\bar{\omega}^2\bar{x}_d(1)$ all be near zero. To facilitate the identification of valid solutions, the problem was cast as an optimization problem in which the ℓ^2-norm of the three quantities was to be minimized. However, it was observed that it was quite common for the optimization scheme (Matlab's *fmincon*) to identify local minima as solutions to this objective function. Accepting these local minima as solutions, even if they are within a low prescribed tolerance, can result in incorrect transmissibility curves. To avoid this issue, a global search optimization algorithm was implemented. This algorithm conducts an intelligent search of the parameter space to identify only global minima. Combining this approach with the requirement that the objective function be less than $4 * 10^{-4}$ resulted in transmissibility predictions that were much more well behaved.

Once a solution to Eqs. (28.5)–(28.10) was found, transmissibility, *TR*, was calculated by comparing the complex modulus of $\bar{x}_d$ to the amplitude of base excitation, i.e.,

$$TR = \frac{\sqrt{Re(\bar{x}_d(1))^2 + Imag(\bar{x}_d(1))^2}}{u_0}, \tag{28.15}$$

where $u_0 = u_b/L$ with u_b defined as the amplitude of the base excitation.

28.2.3 Electrical Modeling

Beginning with the constitutive equations relating stress, strain, electric field, and electric displacement, it can be shown[6] that the voltage, v, generated by a thin piezoelectric beam in bending is given by

$$C_p\dot{v} + \frac{v}{R_l} = d_{31}E_p b_p h_{pc}\int_{x_{p0}}^{x_{pend}} \frac{d^3 y_d(s,t)}{ds^2 dt} ds, \tag{28.16}$$

where R_l is the resistance load of the circuit, d_{31} is the piezoelectric constant for the film in bending, E_p is the elastic modulus of the piezoelectric material, and h_{pc} is the distance from the neutral axis of the beam to the outer surface for piezoelectric film. The integral limits x_{p0} and $x_{p_{end}}$ are the x locations corresponding to the bottom and top of the piezoelectric film. The C_p parameter represents the internal capacitance of the piezoelectric material and is given by

$$C_p = \frac{\epsilon_{33} b_p l_p}{h_p}, \tag{28.17}$$

where ϵ_{33}, b_p, and l_p are the permittivity, width, and length of the piezoelectric material, respectively.

After solving for $y_d(s,t)$ using Eqs. (28.5)–(28.10), the right hand of Eq. (28.16) is computed and applied. The resulting steady-state *rms* voltage is then used to calculate harvested power with

$$\wp = \frac{v_{rms}^2}{R_l}. \tag{28.18}$$

28.3 Experiment

28.3.1 Description of Experimental Set-Up

The experimental realization of the device is shown in Fig. 28.2. The device consists of a 15.00 cm long by 11.00 cm wide by 0.95 cm thick aluminum base mounted to an electro-mechanical shaker (model 2075E manufactured by the Modal Shop, Inc.). A thin vertical aluminum arm is mounted to the base. Attached to the arm is a precision ball slide assembly (DelTron model N4) with 7.62 cm of travel. The bearing supports a carrier that can support a variable amount of additional payload mass. Aluminum L-brackets are attached to the top of the base and to the bottom of the carrier. The L-brackets are attached at their respective corners to create V-grooves that support the beams and simulate simply-supported boundary conditions. The two beams are made of spring steel and each have a length of 17.15 cm, a width of 2.00 cm, and a thickness of 0.25 mm. The mass of a single beam was found to be 6.078 g, which corresponds to a density of 7088 kg/m^3. The displacements of the base and the carrier are measured with Linear Voltage Displacement Transducers (LVDTs) that are manufactured by Schaevitz Sensors, Inc. (model DC-EC-2000). Across all experiments, the base displacement of the shaker was controlled to be $u_b = 2.5$ mm.

The piezoelectric film is manufactured by Measurement Specialties, Inc. and consists of a 3.00 cm long by 1.2 cm wide by 28 μm patch of piezoelectric material that is encapsulated by a self-adhesive plastic. The film is very inexpensive, with a single patch cost of approximately $8.00, and is nominally positioned such that its center is at the center of the beam span, though trials were conducted with the patches placed elsewhere. The leads of piezoelectric film are connected to four potentiometers in series which are capable of adjusting the circuit resistance from zero to 10 MΩ. Based on the technical data provided by the manufacturer of the piezoelectric film, the following parameters values were used in its theoretical modeling: $E_p = 3.5$ GPa, $d_{31} = 23 * 10^{-12}$ C/N, and $\epsilon_p = 1.13 * 10^{-10}$ F/m.

28.3.2 Empirically-Derived Parameters

Values for the beam's elastic modulus, initial imperfection, and system damping were determined using experimental results. Using beam geometry and material properties, the theory described in Sect. 28.2.1 was implemented to determine the axial load versus end shortening curves for different values of the imperfection parameter, d_0. In addition, end shortening data were collected as mass was added to the carrier in 3.1 g increments. As observed in Fig. 28.3, the experimental data

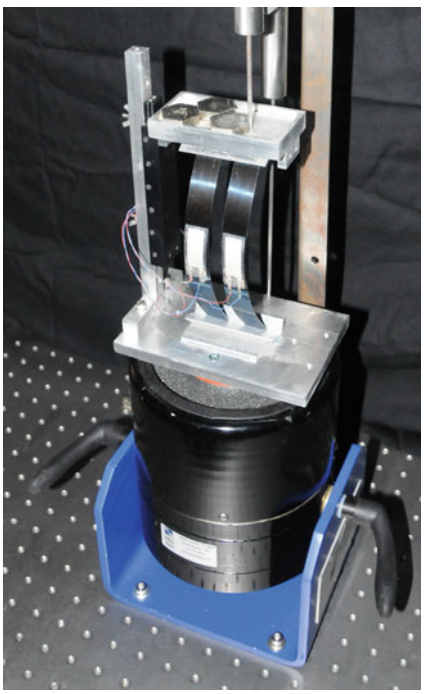

Fig. 28.2 Image of experimental system in the nominal configuration

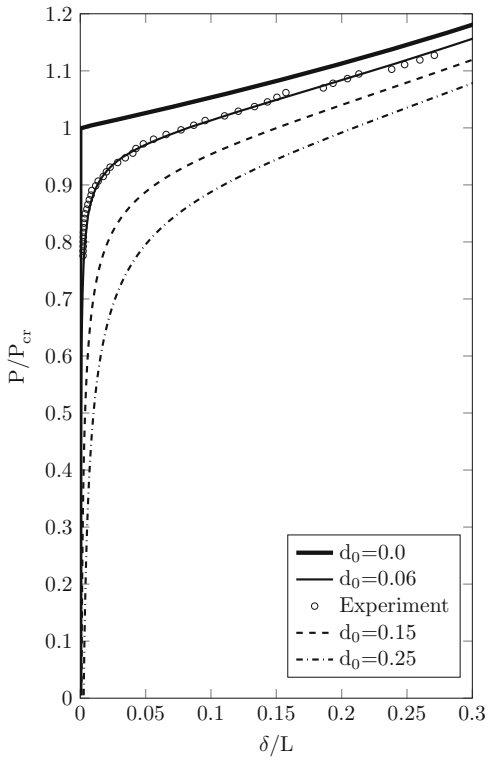

Fig. 28.3 Normalized load vs. normalized end shortening for different values of initial imperfection

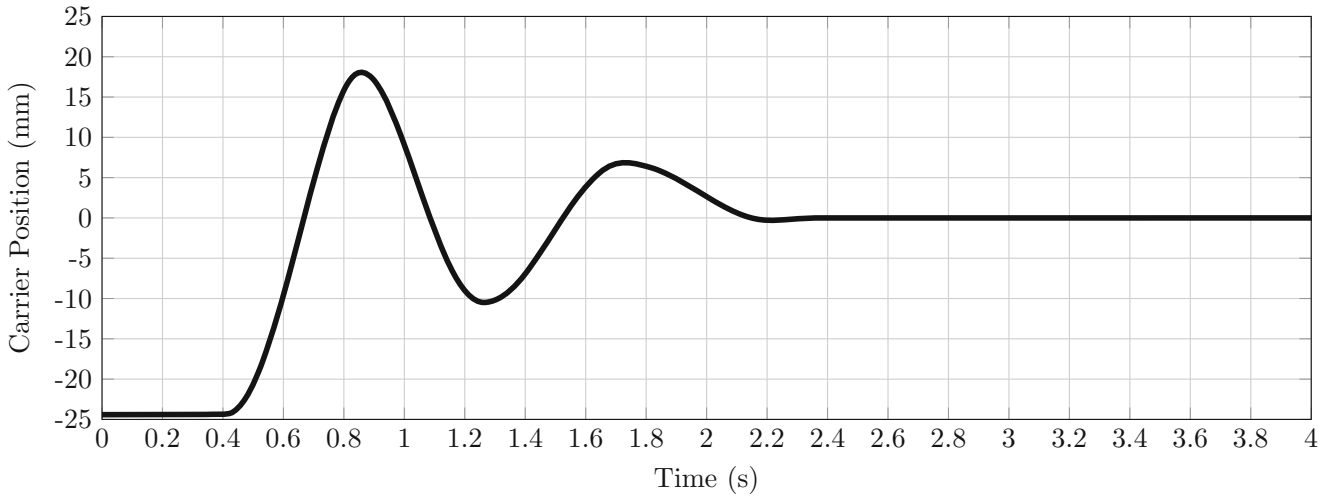

Fig. 28.4 Experimental free decay

most closely corresponds to the theoretical curve when $d_0 = 0.06$. This initial imperfection value was then used in all subsequent simulations. Additionally, the Young's modulus of the spring steel material was estimated to be 195 GPa using the experimental force-deflection data, and this value was also assumed in all simulations. This modulus along with the beam geometry detailed above results in a single beam critical buckling load of $P_{cr} = 1.782$ N. For the two-beam experimental system under gravity, this corresponds to an applied mass of 363.4 g.

To determine damping, free vibration time histories of the system were obtained and an example time history is shown in Fig. 28.4. It can be observed that the system is quite heavily damped and exhibits a damped natural frequency of approximately 1.15 Hz. Applying the log-decrement method on the two positive peaks, the viscous damping ratio was found to be approximately 0.15. However, it appears that the effective damping increases as the system approaches equilibrium. In the simulations, two damping parameters were used. A viscous damping parameter of $\bar{c} = 0.82$ was estimated by treating

the system as a SDOF oscillator with an undamped natural frequency of 1.16 Hz and a viscous damping ratio of $\zeta = 0.15$. A small non-dimensional Kelvin-Voigt damping value of $\bar{\gamma} = 0.04$ was also assumed to produce better agreement between the theoretical and experimental transmissibility results.

28.4 Results and Discussion

The following subsections present the theoretical and experimental vibration isolation and energy harvesting performance of the experimental system, and conclude with a discussion of some considerations when designing the system for optimal performance.

28.4.1 Vibration Isolation

As mentioned in Sect. 28.2, the theoretical model assumes that the presence of the piezoelectric film does not influence the structural mechanics of the system. To verify that this is a reasonable assumption, transmissibility data were collected with and without the piezoelectric film attached. A supported mass of 352.72 g ($P/P_{cr} = 0.97$) was used for both trials. For the trial in which the film was attached, a resistance of 3 MΩ was used in the energy harvesting circuit. The data are shown in Fig. 28.5 along with the corresponding simulation results. Figure 28.5 shows that the two sets of transmissibility data demonstrate good agreement with each other and with the simulation results, thus providing confidence in the modeling approach. It also indicates that the energy harvested from the beam flexure does not seem to manifest in an appreciable amount of additional system damping. Note that the experimental device is quite effective as a vibration isolator with transmissibilities below 2 % at 10 Hz.

28.4.2 Energy Harvesting

The resistance at which power is maximized in an energy harvesting circuit will depend on the properties of the piezoelectric material and was determined experimentally to be approximately 3 MΩ. Figure 28.6 shows the theoretical and experimental transmissibility and harvested power when $P/P_{cr} = 0.97$ and $R_l = 3\,\text{M}\Omega$. The experimental power results represent the

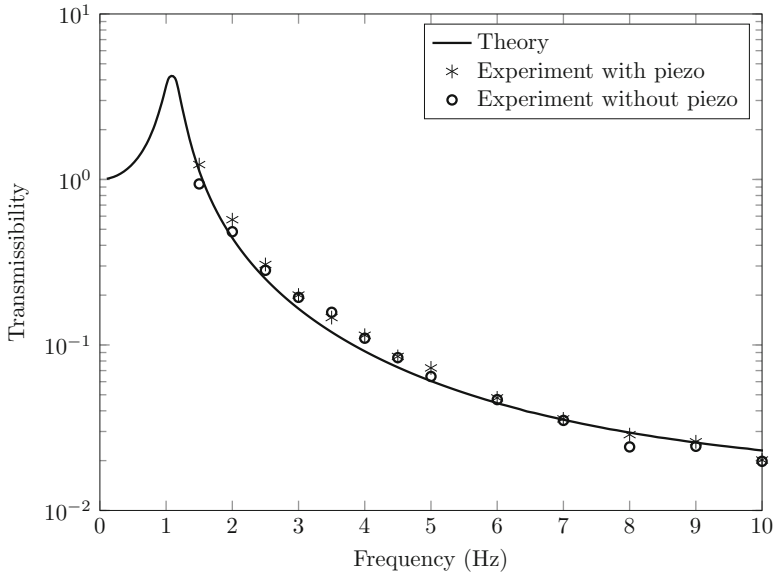

Fig. 28.5 Theoretical and experimental transmissibility ($P/P_{cr} = 0.97$)

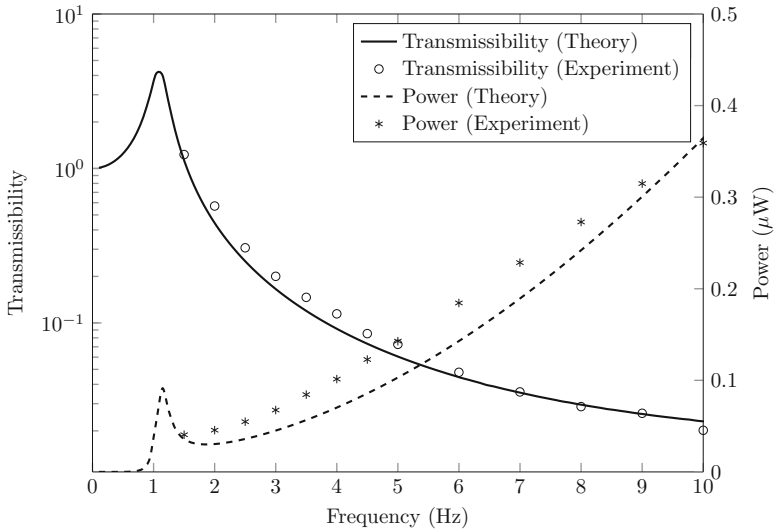

Fig. 28.6 Theoretical and experimental transmissibility and total power generated by both beams ($P/P_{cr} = 0.97$, $x_p = 0.5L$)

total power produced by both beams and are compared to two times the theoretical power predicted for a single beam. While the theory tends to under-predict the measured power, the overall agreement between theory and experiment is good. The results show that there is not necessarily a trade-off between transmissibility and harvested power as the excitation frequency is increased; power increases and transmissibility decreases with frequency, which are two desirable trends from a performance standpoint.

At 10 Hz, the total power harvested is approximately 0.35 μW, which is sufficient to operate some low-power electronic devices. However, it is noted that piezoelectric films are only covering about 8.75 % of the total (front and back) surface area of the beams, so there is considerable potential for the device to produce more power by using longer film. In addition, assuming the beams are sized to buckle under the mass requiring isolation, there is effectively no limit to the number of beams that can be used in these devices. It would therefore not be impractical to design devices capable of harvesting 10 μW or more.

While the piezoelectric film is nominally placed such that the middle of the patch is at half span ($x_p = 0.5L$), the effects of piezoelectric film placement were investigated by collecting data at $x_p = 0.7L$ and $x_p = 0.9L$. By inspection of Eq. (28.16) and reasoning that $d^2\bar{y}_d/d^2s$ is greatest at the center of the beam, it is not surprising that placing the film in the center of the beam produces the greatest power. Moving the center of the film from $x_p = 0.5L$ to $x_p = 0.7L$ represents an approximately 20 % decrease in power while the move from $x_p = 0.5$ to $x_p = 0.9L$ results in over a seven-fold reduction in power. (Given the symmetry of the beam, it is reasoned that the power harvested at $x_p = 0.7L$ and $x_p = 0.9L$ will be identical to the power harvested at $x_p = 0.3L$ and $x_p = 0.1L$, respectively.) The theoretical results in Fig. 28.7 again under-predict the experimentally determined power; however, the theoretical and experimental trends (with respect to both frequency and film placement) agree very well, which suggests that the under-prediction may be due to the choice of certain parameters associated with the piezoelectric film.

To investigate the effects of piezoelectric film coverage, Eq. (28.16) was evaluated at a fixed frequency of 8 Hz while the end point of the piezoelectric film, $x_{p_{end}}$, was varied across the span of the beam. Figure 28.8 shows the predicted power harvested with a piezoelectric patch terminating across varying fractions of span for three different values of axial load. As may be anticipated from previous results, the greatest incremental power increases occur when the film is lengthened across the middle 50 % of the beam, while there is relatively little power to be gained by lengthening the film at the beam's ends. Figure 28.8 also shows that harvested power tends to decrease with increasing axial load. This effect, combined with the relationship between axial load and transmissibility are considered presently.

28.4.3 Design Considerations

Figure 28.8 shows that power decreases significantly with increasing axial load. Similarly, Fig. 28.3 shows that the slope of the load-deflection curves (i.e., stiffness) decreases substantially with increasing axial load when $P/P_{cr} \approx 1$. Since

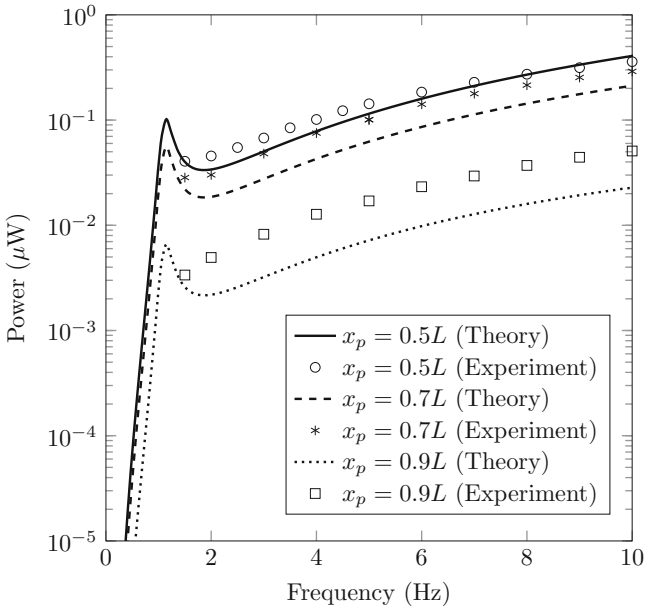

Fig. 28.7 Total power generated by both beams with the piezoelectric patches positioned at different locations along beam

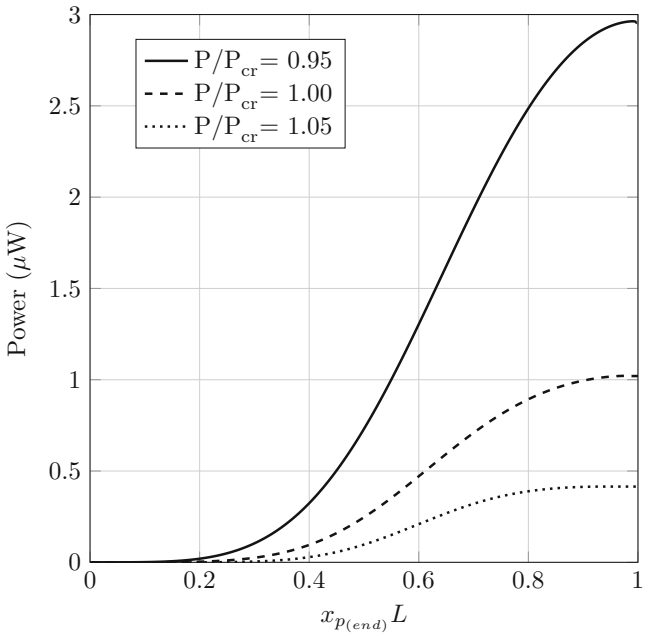

Fig. 28.8 Theoretical power harvested by a single beam with a piezoelectric patch terminating across varying fractions of span ($f = 8$ Hz, $d_0 = 0.06$)

transmissibility at a fixed frequency will decrease with decreasing stiffness, it is expected that transmissibility will tend to decrease with increasing load, provided the loads are relatively low. As loads increase into the region where the slope of the load-deflection curve is largely constant, the transmissibility will begin to level out. These effects are shown in Fig. 28.9, where the theoretical transmissibility and power of the experimental system are plotted across a range of axial loads at a fixed frequency 8 Hz. The power results are consistent with Fig. 28.8 in that they show a monotonic decrease in power with increasing axial load. The transmissibility trends do indeed show a steep decrease near $P/P_{cr} = 1$, followed by a leveling out at higher levels of axial load.

Given that it is desirable to design the devices such that harvested power is maximized and transmissibility is minimized, it is helpful to consider the ratio of power to transmissibility as a simple performance metric to be maximized. Figure 28.10

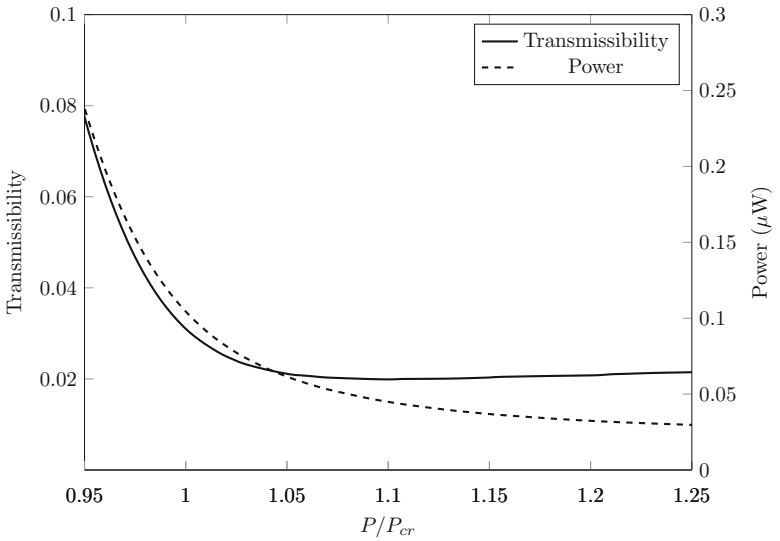

Fig. 28.9 Transmissibility and power harvested by a single beam for varying axial load ($f = 8$ Hz, $d_0 = 0.06$, $R_l = 3\,\mathrm{M}\Omega$)

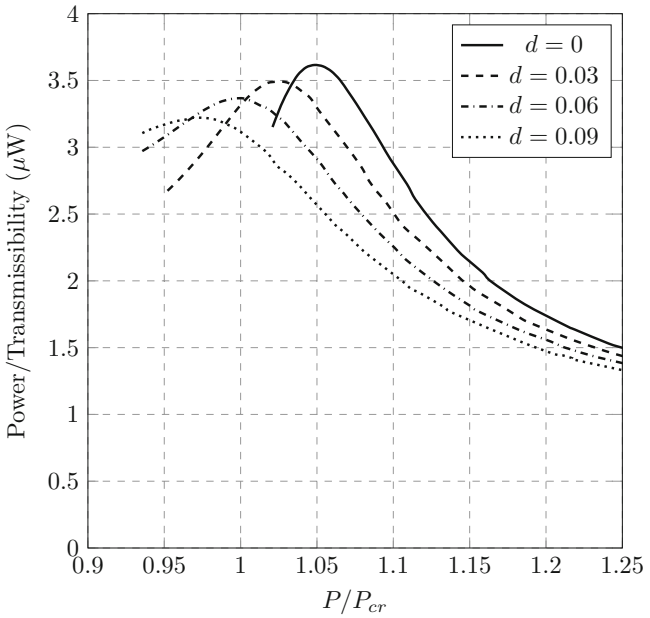

Fig. 28.10 Performance ratio of power/transmissibility for varying axial load and values of initial imperfection ($f = 8$ Hz)

plots this metric for the experimental system operating at 8 Hz. The metric is calculated across axial load and for different values of initial imperfection. The results show that for any given amount of initial imperfection, there exists an optimal load at which the performance metric is maximized and this optimal load tends to decrease with increasing levels of initial imperfection. Additionally, the maximum value of the performance metric tends to drop with increasing imperfection. For the experimental device considered here ($d_0 = 0.06$), the results suggest that the optimal performance will occur at $P/P_{cr} = 1.00$. It is also noted that the performance penalty associated with the use of imperfect beams is not especially severe with the peak performance in the $d_0 = 0$ case being only 1.12 times higher than it is in the $d_0 = 0.09$ case. Future work will include consideration of how other parameters (e.g., frequency, damping, piezoelectric placement) affect this performance metric and may also include the determination of the metric's theoretical absolute maximum value.

28.5 Conclusions

Here we describe the theoretical modeling and experimental testing of a novel device that simultaneously performs passive vibration isolation and energy harvesting. The device uses buckled beams with an inexpensive piezoelectric film attached to their outer surface. The buckled beams act as nonlinear springs offering low stiffness and less static deflection relative to similarly soft linear springs, while the piezoelectric film is used to convert the mechanical energy of beam flexure into electric energy that can potentially be used or stored for other applications. The structural mechanics of the system were modeled using the elastica in conjunction with shooting methods. The structural results were then used as input to the electric circuit equation associated with the piezoelectric film. Results indicate strong agreement between the theory and experiment in terms of both transmissibility and power. The maximum amount of harvested power that was demonstrated experimentally was about 0.35 μW, though similar devices capable of producing an order of magnitude more power seem readily realizable. One beneficial feature of this entirely passive system is that the decreases in transmissibility that occur with increases in excitation frequency are accompanied by increases in harvested power. This study also included consideration of the theoretical performance across varying axial loads. After defining a simple performance metric as the ratio of harvested power to transmissibility, it was determined that for any given amount of initial beam imperfection, there exists an axial load at which the performance metric is maximized. Future work will study how other factors such as excitation frequency and system damping affect this performance metric. This will enable engineers to better optimize the design of these useful and multi-functional devices.

Acknowledgements The authors would like to thank Nolan Williamson, an undergraduate student at the University of Georgia who assisted with the design of the experimental fixtures used in this work.

References

1. Inman, D.J.: Engineering Vibration, 2nd edn. Prentice Hall, Upper Saddle River (2001)
2. Thomson, W.T., Dahleh, M.D.: Theory of Vibration with Applications, 5th edn. Prentice Hall, Upper Saddle River (1998)
3. Winterflood, J., Barber, T., Blair, D.: Using Euler buckling springs for vibration isolation. Classical Quantum Gravity **19**(7), 1639 (2002)
4. Virgin, L., Davis, R.: Vibration isolation using buckled struts. J. Sound Vib. **260**(5), 965–973 (2003)
5. Ibrahim, R.: Recent advances in nonlinear passive vibration isolators. J. Sound Vib. **314**(3), 371–452 (2008)
6. Erturk, A., Inman, D.J.: Piezoelectric Energy Harvesting. Wiley, Chichester (2011)
7. Zhu, Y., Zu, J., Su, W.: Broadband energy harvesting through a piezoelectric beam subjected to dynamic compressive loading. Smart Mater. Struct. **22**(4), 045007 (2013)
8. Zhu, Y., Zu, J.: A magnet-induced buckled-beam piezoelectric generator for wideband vibration-based energy harvesting. J. Intell. Mater. Syst. Struct. **25**(14), 1890–1901 (2014)
9. Sidbury, J.E.: Analysis of buckled and pre-bent columns used as vibration isolators. Master's thesis, Virginia Tech (2003)
10. Santillan, S.T.: Analysis of the elastica with applications to vibration isolation. Ph.D. thesis, Duke University (2007)

Chapter 29
Nonlinear Dynamic Interaction in a Coupled Electro-Magneto-Mechanical System: Experimental Study

I.T. Georgiou and F. Romeo

Abstract The dynamic experimental response of an electro-magneto-mechanical coupled system excited by a harmonic voltage is addressed. The system mathematical model involves coupling quadratic nonlinearities due to the dependence of the inductance on the displacement of the metallic oscillator mass; as a result, a strongly nonlinear behavior characterizes the system's dynamic response. In this study we present initial experimental results that confirm the occurrence of interesting main nonlinear phenomena: The non-linear resonance related to the current quadratic nonlinearity which imposes a natural linear resonance at half the frequency of the linear oscillator and a jump, after which the mass of the mechanical oscillator undergoes large amplitude oscillations and coexisting attractors appear.

Keywords Multi-physics dynamics • Experimental nonlinear dynamics • Slow-fast dynamics • Nonlinear resonance • Coexisting attractors

29.1 Introduction

The experimental dynamic response of a system in which a mechanical linear oscillator consisting of a cantilever beam is nonlinearly coupled to a linear electric circuit through an electromagnet is presented in this work. This experimental investigation follows previous analytical and numerical investigations carried out by the authors on this type of multi-physics system [1, 2]. Based on these studies, when the mechanical oscillator is excited via harmonic voltage applied to the electric circuit, interesting nonlinear phenomena arise such as the non-linear resonance related to the current quadratic nonlinearity which imposes a natural linear resonance at half the frequency of the linear oscillator, jump phenomena and transitions to complex chaotic interaction dynamics. Aiming at verifying these peculiar regimes of the response of this system, an experimental campaign was started recently in the Nonlinear Dynamics Lab at the Department of Naval Architecture and Marine Engineering of the National Technical University of Athens. The initial experimental results are presented in this paper that is organized as follows. After the introductory section, the experimental setup is described in detail. The coupled system analytical model is then presented as it will be used to obtain numerical solutions to be compared with the experimental ones. At last, before the concluding remarks, the results of a number of experimental tests are presented.

29.2 Experimental Setup

In Fig. 29.1 the experimental setup of the dynamical system consisting of coupled mechanical and electro-magnetic subsystems is shown through a sketch and a picture. The experimental setup consists of the following components: electromagnet, metal steel cantilever beam, two acceleration sensors, sound measurement sensor, electric current recording sensor, frequency generator, power amplifier and sensor signal amplifier.

I.T. Georgiou
School of Naval Architecture and Marine Engineering, National Technical University of Athens, 9, Heron Polytechniou Ave., GR 15773 Zografou, Athens, Greece
e-mail: georgiou@central.ntua.gr

F. Romeo (✉)
Department of Structural and Geotechnical Engineering, Sapienza University of Rome, 53, Via Gramsci, 00197 Rome, Italy
e-mail: francesco.romeo@uniroma1.it

G. Kerschen (ed.), *Nonlinear Dynamics, Volume 1*, Conference Proceedings of the Society for Experimental Mechanics Series,
DOI 10.1007/978-3-319-29739-2_29

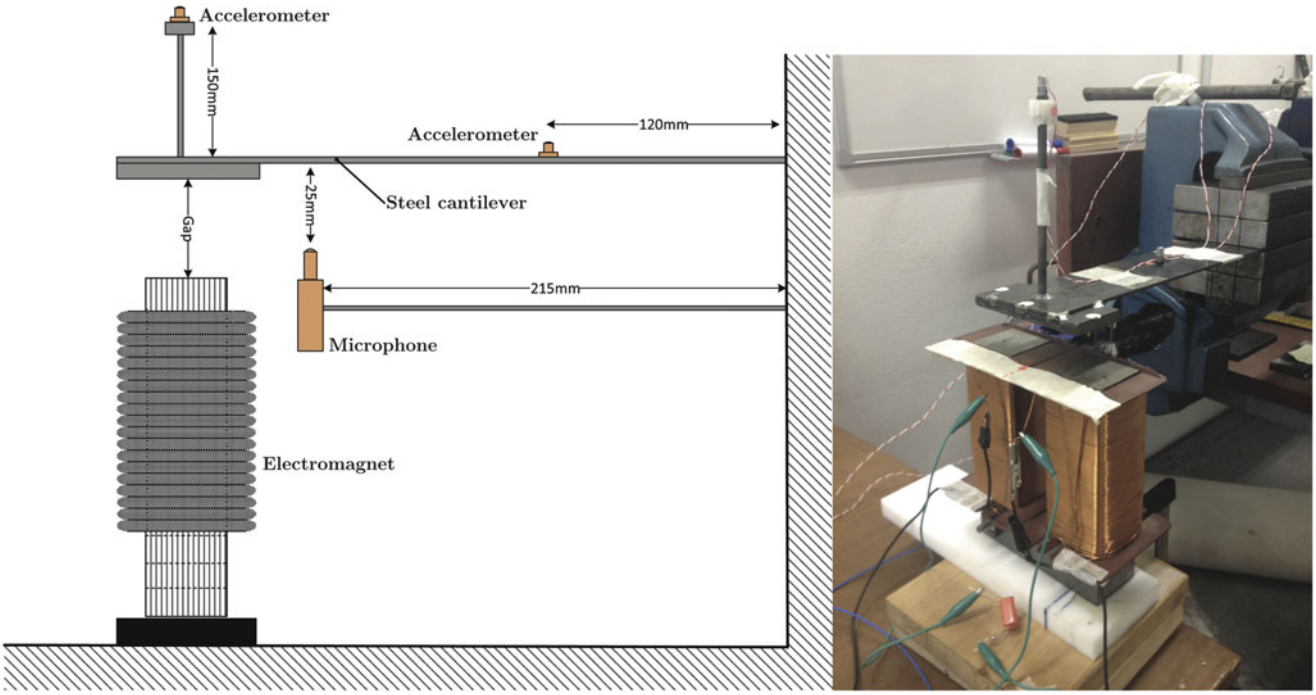

Fig. 29.1 Experimental setup of the mechanical system coupled via a magnetic field to a megneto-electrical system

The electrical circuit connecting the assembly of the electromagnet and the cantilever beam is shown in Fig. 29.2. The generator is regulated to the desired type of output signal, and then the amplitude of the output voltage and frequency are the control parameters. Then, the generator output signal is routed to the power amplifier to receive the required power to operate the electromagnet. Between the amplifier and the electromagnet, the current sensor is inserted allowing us to record the instantaneous value of the current. The current sensor output signal is then directed to one of the channels of the data acquisition card located in the computer. For recording vibration data, three sensors were placed: two accelerometers (PCB piezotronics M353B17) and one microphone (PCB piezotronics 130D21). Their position is shown in Fig. 29.1. The weight of the steel cantilever beam is 500 g.

The electromagnet consists of soft iron plates that are used as the core and a coil of insulated copper wire as sketched in Fig. 29.3. The conductor diameter is 1.024 mm, the number of turns of wire is 1030, the inductance $L_0 = 344\,\text{mH}$ and the resistance is $R = 9\,\Omega$. A capacitor is also added in the circuit with characteristics $C = 207\,\text{nF}$.

29.3 Multi-Physics Coupled Oscillators Model

The mechanical part is modeled as a linear oscillator coupled nonlinearly through an electromagnet to a linear electric circuit. The system analyzed in this paper is modeled following [3]. Let m, c, k denote respectively the mass, dissipation, spring parameters of the linear oscillator. Let L, C, R denote the inductance, capacitance, and resistance of the electrical oscillator. The variables x and q denote the mechanical and electrical displacement (charge), respectively. The velocity of the mass and the electric current are $v \equiv \dot{x}, i \equiv \dot{q}$, respectively. The variables f and e denote external mechanical forcing and voltage excitation. In particular, we assume that the inductance is approximated by a linear function of the displacement of the metallic mass, namely $L(x) = L_0 + L_1 x$. Positive-valued parameter L_0 denotes the limiting case where the metallic mass is not in the region of influence of the magnetic field. The linear natural frequencies and linear dissipation factors of the mechanical and electrical oscillators are given by: $\omega_m^2 \equiv \frac{k}{m}$, $\omega_e^2 \equiv \frac{1}{L_0 C}$, $\zeta_m \equiv \frac{c}{2\sqrt{km}}$, $\zeta_e \equiv \frac{R\sqrt{C}}{2\sqrt{L_0}}$. The electro-mechanical inertia and nonlinear inductance coupling parameters are: $\epsilon \equiv \frac{L_0}{2m}$, $\alpha \equiv \frac{L_1}{L_0}$ We also introduce the external force-per-mass and voltage-per-inductance excitations: $\hat{f} \equiv \frac{f}{m}$, $\hat{e} \equiv \frac{e}{L_0}$.

This multi-physics coupled system is a nonlinear dynamical system with its coupling nonlinearity stemming from the dependence of the inductance on the displacement and possibly velocity of the metallic oscillator mass. Having introduced

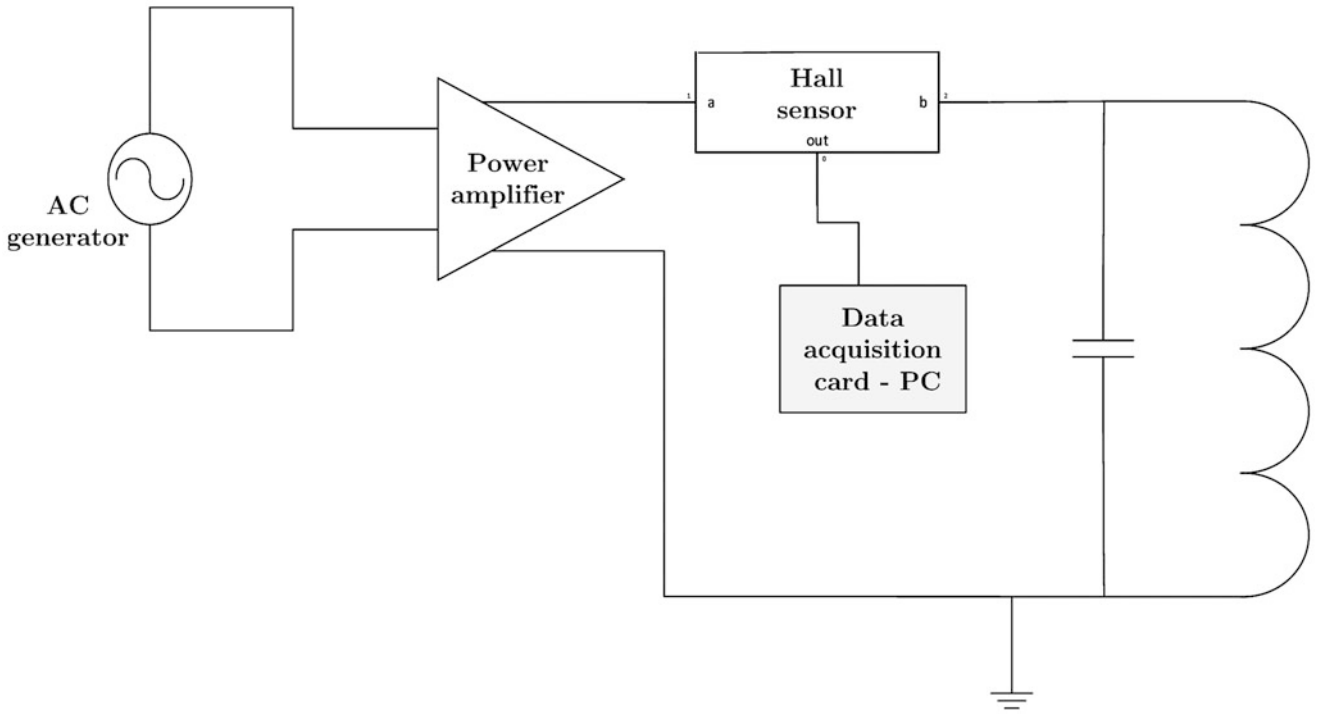

Fig. 29.2 Schematic diagram of the electrical circuit

the parameters entering the coupled electro-magneto-mechanical system, the equations of motion are given by the following two coupled second order ordinary differential equations:

$$\begin{aligned} \ddot{x} + 2\zeta_m \omega_m \dot{x} + \omega_m^2 x &= \epsilon \alpha \dot{q}^2 + \hat{f} \\ (1 + \alpha x)\ddot{q} + (2\zeta_e \omega_e + \alpha \dot{x})\dot{q} + \omega_e^2 q &= \hat{e} \end{aligned} \tag{29.1}$$

The interest lies in investigating how the mechanical part will respond when it is actuated by the electrical part; the question being to ascertain whether the steady dynamics of the former is determined by the dynamics of the latter. Over some range of the forcing parameters the long term response is a slow periodic motion with period-1 for the electromagnetic part and period-2 for the mechanical part. In the terminology of dynamics systems this is a stable periodic attractor with the peculiarity that it has a 2:1 ratio of frequencies for the part of the coupled system. Like static equilibrium states, periodic states are critical elements of the dynamical system. Thus their behavior during quasi-static sweeps of the forcing parameters is of paramount importance. Being critical states, periodic motions, as it is well known, are prone to various types of bifurcations. Previous SIM analytic approximations and numerical investigations [1] show that the system has a slow periodic response over a well-defined region of the forcing parameters. This region starts from low frequencies and includes the frequency $\omega = 0.5$ where the linear system undergoes a resonance due to the presence of the quadratic nonlinear dependence of the electromagnet inductance on the current. Note that the natural frequency of the oscillator is scaled at 1 for the numerical simulations. At some critical value the amplitude-frequency response loses its smoothness via bifurcation mechanism that creates a finite jump.

29.4 Experimental Tests

The experimental tests have been carried out by applying a constant voltage amplitude of 25 V and performing forward and backward frequency sweeps. The signals received from the sensors is instantaneous voltages and require proper conversion to the corresponding physical units. Different values of gap between the surface of the electromagnet and the beam were investigated in order to tune the strength of the nonlinear coupling. The following configurations were tested (gap is expressed

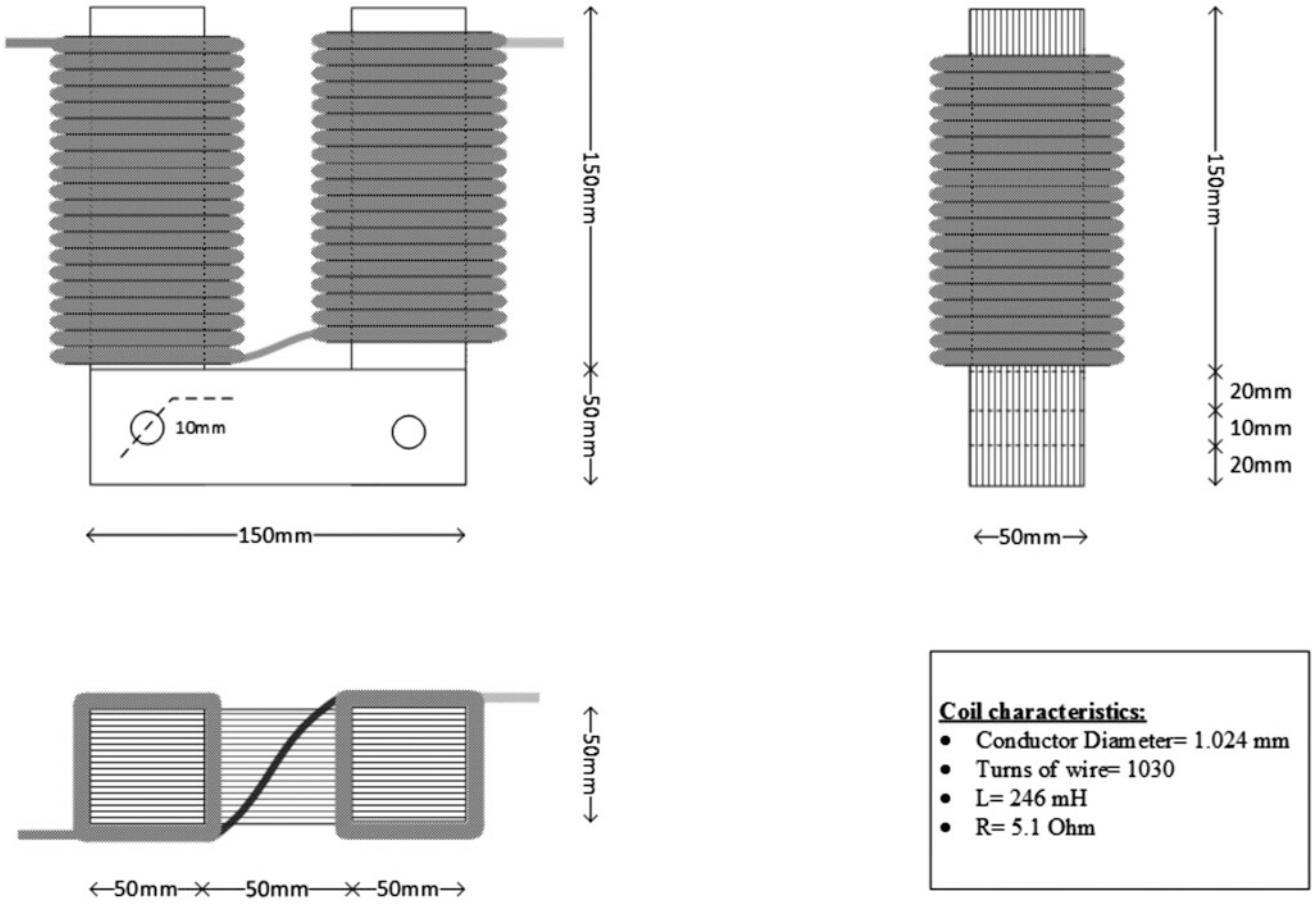

Fig. 29.3 Schematic diagram of the electromagnet

Table 29.1 Numerical and experimental systems' parameters

Parameter	Symbol	Num.	Exp.
Singular parameter	μ	0.2	0.021
Mechanical dissipation factor	ζ_m	0.01	0.01
Electrical dissipation factor	ζ_e	0.1	0.0011
Electro-mechanical coupling	ϵ	5.0	0.34
Inductance nonlinearity	α	10.0	–

in mm): 68.0, 60.0, 55.0, 40.0, 35.0, 32.0. While the two ranges of frequencies studied are: From 5.00 to 7.00 Hz and from 11.00 to 14.00 Hz. The length of the recorded data is 10 s, and measurements were taken in both the steady state of oscillation of the beam, and the transition from one frequency to another.

In the numerical investigations adopted to qualitatively compare the experimental results the system parameters are set as reported in Table 29.1. Figure 29.4a shows the frequency-mechanical response amplitude plot computed through a quasi-static forward and backward frequency sweeps for $\mu = 0.2$. For low values of μ the system would behave almost linearly, so that the forward sweep would coincide with the backward one; moreover, a stable period-1 attractor resonating around $\Omega = 0.5$ would appear. Note that low linear resonant frequency in the numerical model is at 1. In Fig. 29.4a however, the different branches corresponding to forward and backward sweeps show how the coupling nonlinearity affects the dynamics; in particular, the upper branch of the period-1 attractor is obtained from the backward sweep. As shown in [1] this branch arises from the lower bound of the chaotic region located in the frequency interval $4.0 \leq \Omega \leq 4.5$ and then, as the frequency decreases, it grows until the instability is reached around $\Omega = 1.55$; furthermore, the resonance around $\Omega = 0.5$ persists. At the critical frequency $\Omega = 0.966$ (dashed red line) the period-1 attractor suffers an abrupt downwards finite jump. Before the jump the amplitude of the period-1 attractor is much higher than the amplitude at the linear resonance $\Omega = 0.5$ (dashed blue line). These steady state dynamics evolve at a slow time scale set by the low frequency of the voltage excitation and two questions arise.

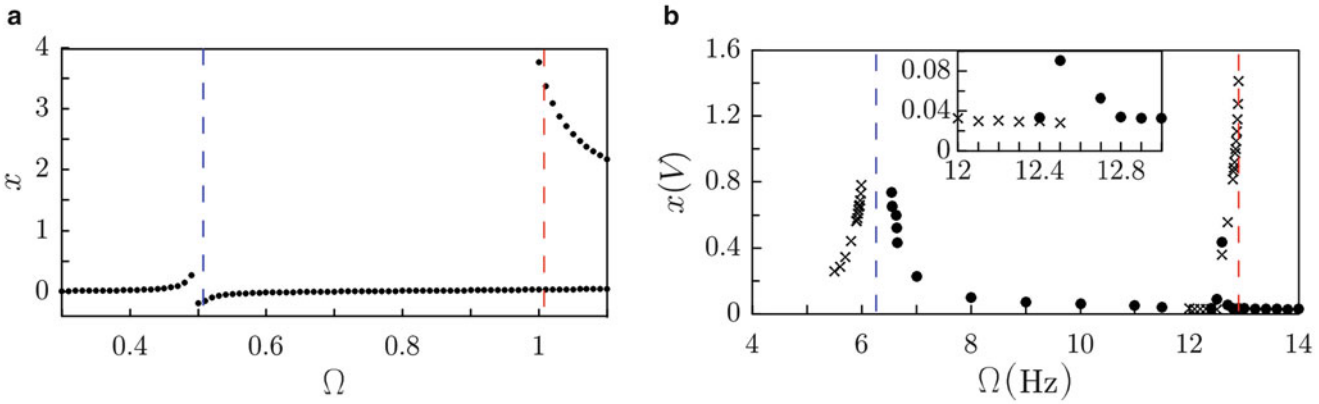

Fig. 29.4 Mechanical oscillator displacement diagram of the periodic attractor as a function of forcing frequency for a fixed value of forcing amplitude. Numerical (**a**) and experimental (**b**) results over a frequency region that contains the natural linear frequency of the mechanical oscillator (forward (x) and backward (•) sweep)

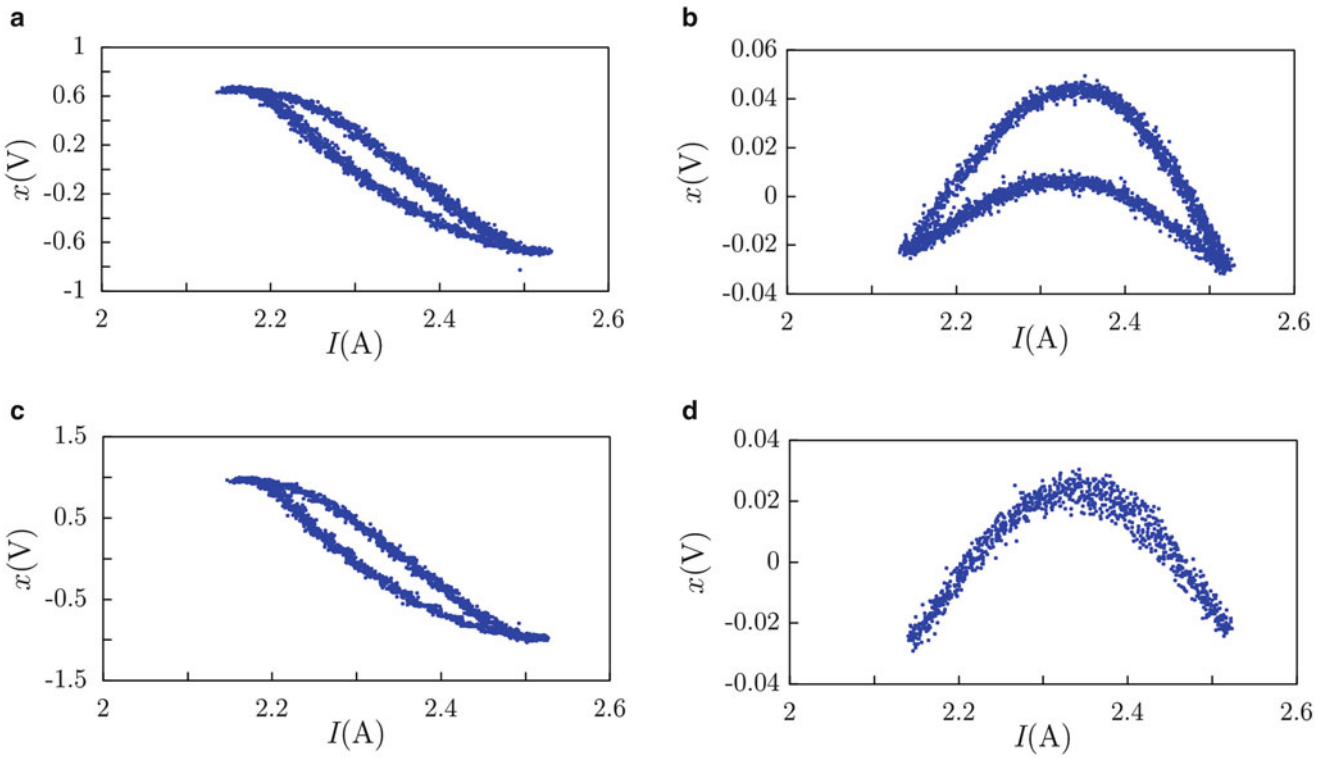

Fig. 29.5 Coexisting attractors on the current mechanical displacement plane (I-x). (**a**) and (**b**) for $\Omega = 12.70$ Hz; (**c**) and (**d**) for $\Omega = 12.80$ Hz

The experimental frequency-mechanical response amplitude plot is shown in Fig. 29.4b. The results reported refer to a gap value of 35.0 mm and forward (x) and backward (•) frequency sweeps. The qualitative agreement with the numerical results obtained by direct numerical integration of (29.1) can be seen in terms of both, the non-linear resonance related to the current quadratic nonlinearity, which imposes a natural linear resonance at half the frequency of the linear oscillator given by $\Omega = 6.4$ Hz (dashed blue line) and a jump at the cantilever natural frequency occurring at $\Omega = 12.86$ Hz (dashed red line).

Moreover, the coexistence of (at least) two periodic attractors can be seen by the experimental phase portraits reported in Fig. 29.5. In particular, in the current-mechanical displacement plane reported in Fig. 29.5a, b the two coexisting attractors shown correspond to $\Omega = 12.7$ Hz, whereas those reported in Fig. 29.5c, d refer to the case $\Omega = 12.8$ Hz.

29.5 Conclusions

The dynamics of a coupled nonlinear electro-magneto-mechanical system was addressed by means of experimental and numerical approaches. The slow time scale forced frequency-amplitude response of the full order system was numerically computed by means of Poincaré mappings. The numerical predictions were qualitatively validated experimentally in a cantilever steel beam coupled to an electromagnet driven by an harmonic voltage. The predicted nonlinear resonance related to the current quadratic nonlinearity which imposes a natural linear resonance at half the frequency of the linear oscillator was observed in the experiment. The predicted jump occurring at the mechanical oscillator natural frequency, after which the mass of the mechanical oscillator undergoes large amplitude oscillations, was also captured by the experimental test. After this jump, coexisting attractors have been found as a result of the nonlinear multi-physics interaction. Further on-going extensive experimental investigations are expected to provide a more comprehensive interpretation of the numerous dynamic phenomena involved.

References

1. Georgiou, I.T., Romeo, F.: Multi-physics dynamics of a mechanical oscillator coupled to an electro-magnetic circuit. Int. J. Nonlinear Mech. **70**, 153–164 (2015)
2. Romeo, F., Georgiou, I.T.: Multiphysics chaotic interaction in a coupled electro-magneto-mechanical system. In: ASME Proceedings IMECE 2014, 4B, Paper No. IMECE2014-38714, p. V04BT04A018 (2014)
3. Landa, P.S.: Nonlinear Oscillations and Waves in Dynamical Systems. Kluwer Academic, Dordrecht (1996)

Chapter 30
Hysteresis Identification Using Nonlinear State-Space Models

J.P. Noël, A.F. Esfahani, G. Kerschen, and J. Schoukens

Abstract Most studies tackling hysteresis identification in the technical literature follow white-box approaches, i.e. they rely on the assumption that measured data obey a specific hysteretic model. Such an assumption may be a hard requirement to handle in real applications, since hysteresis is a highly individualistic nonlinear behaviour. The present paper adopts a black-box approach based on nonlinear state-space models to identify hysteresis dynamics. This approach is shown to provide a general framework to hysteresis identification, featuring flexibility and parsimony of representation. Nonlinear model terms are constructed as a multivariate polynomial in the state variables, and parameter estimation is performed by minimising weighted least-squares cost functions. Technical issues, including the selection of the model order and the polynomial degree, are discussed, and model validation is achieved in both broadband and sine conditions. The study is carried out numerically by exploiting synthetic data generated via the Bouc-Wen equations.

Keywords Hysteresis • Dynamic nonlinearity • Nonlinear system identification • Black-box method • State-space models

30.1 Introduction

Hysteresis is a phenomenology commonly encountered in a wide variety of engineering and science disciplines, ranging from solid mechanics, electromagnetism and aerodynamics [1–3] to biology, ecology and psychology [4–6]. In structural dynamics, hysteresis is mostly featured in joints, where it results from friction between assembled parts [7]. The defining property of a hysteretic system is the persistence of an input-output loop as the input frequency approaches zero [8]. Hysteretic systems are inherently nonlinear, as the quasi-static existence of a loop requires an input-output phase shift different from 0° to 180°, which are the only two options offered by linear theory. The root cause of hysteresis is multistability [9]. A hysteretic system possesses multiple stable equilibria, attracting the output depending on the input history. In this sense, it is appropriate to refer hysteresis as system nonlinear memory.

The identification of hysteresis is challenging, primarily because it is a dynamic kind of nonlinearity governed by internal variables, which are not measurable. Most studies tackling hysteresis identification in the technical literature follow white-box approaches, i.e. they rely on the assumption that measured data obey a specific hysteretic model [10]. The Bouc-Wen model was identified in numerous works, in particular using optimisation techniques such as evolutionary [11, 12] and particle swarm [13] algorithms. In [14–16], a Bayesian framework was exploited to quantify uncertainty in Bouc-Wen identification. Specialised NARX [17], neural network [18] and Hammerstein [19] models were also developed to address Bouc-Wen systems. The experimental identification of other hysteresis models, like the Preisach equations and a stochastic

J.P. Noël (✉)
ELEC Department, Vrije Universiteit Brussel, Brussels, Belgium
Aerospace and Mechanical Engineering Department, Space Structures and Systems Laboratory, University of Liège, Liège, Belgium
e-mail: jp.noel@ulg.ac.be

A.F. Esfahani • J. Schoukens
ELEC Department, Vrije Universiteit Brussel, Brussels, Belgium
e-mail: alireza.fakhrizadeh.esfahani@vub.ac.be; johan.schoukens@vub.ac.be

G. Kerschen
Aerospace and Mechanical Engineering Department, Space Structures and Systems Laboratory, University of Liège, Liège, Belgium
e-mail: g.kerschen@ulg.ac.be

G. Kerschen (ed.), *Nonlinear Dynamics, Volume 1*, Conference Proceedings of the Society for Experimental Mechanics Series,
DOI 10.1007/978-3-319-29739-2_30

Iwan description of friction, is reported in [20] and [21], respectively. Assuming a specific model structure in a white-box philosophy may however be a hard requirement to handle in real applications, since hysteresis is a highly individualistic nonlinear behaviour.

In this paper, a black-box approach based on nonlinear state-space models is adopted to identify hysteresis dynamics. State-space identification is a powerful way to experimentally model nonlinear systems. A literature survey shows that systems as diverse as a magneto-rheological damper [22], a wet-clutch device [23], a glucoregulatory system [24], or a Li-Ion battery [25] were successfully identified using nonlinear state-space models. The approach proposed in the present paper exploits the great flexibility of a state-space representation to establish a general framework to hysteresis identification, which makes no use of a priori assumptions. Physical insight into the system behaviour can also be retrieved, ensuring a reasonable parsimony of the derived model. Nonlinear model terms are constructed as a multivariate polynomial in the state variables, and parameter estimation is performed by minimising weighted least-squares cost functions in the frequency domain. This minimisation effort guarantees maximum likelihood dispersion properties for the parameter estimates. Technical issues, including the selection of the model order and the polynomial degree, are discussed, and model validation is achieved in both broadband and sine conditions. The present study is carried out numerically by exploiting synthetic data generated via the Bouc-Wen equations. However, it is emphasised that the Bouc-Wen nature of the data will not be exploited in the identification process.

The paper is organised as follows. The synthesis of input-output data is described in Sect. 30.2, where noise assumptions are also stated. A nonparametric study of the nonlinear distortions affecting the generated data is conducted in Sect. 30.3, and parametric modelling in state space is carried out in Sect. 30.4. Model validation is eventually achieved in Sects. 30.4 and 30.5, and concluding remarks are formulated in Sect. 30.6.

30.2 Synthetic Generation of Hysteretic Data

The synthesis of noisy data exhibiting hysteresis behaviour is carried out in this section by combining the Bouc-Wen differential equations (Sect. 30.2.1), multisine excitation signals (Sect. 30.2.2) and the Newmark integration rules (Sect. 30.2.3). Noise assumptions are finally discussed in Sect. 30.2.4.

30.2.1 The Bouc-Wen Model of Hysteresis

The Bouc-Wen model [26, 27] has been intensively exploited during the last decades to represent hysteretic effects in structural dynamics, especially in the case of random vibrations. Extensive literature reviews about phenomenological and applied aspects related to Bouc-Wen modelling can be found in [28, 29]. In this work, a Bouc-Wen system with a single degree of freedom is considered to demonstrate the applicability of state-space models to hysteresis identification. In that respect, multi-degree-of-freedom systems are out of the scope of the paper.

The vibrations of a single-degree-of-freedom Bouc-Wen system is governed by Newton's law of dynamics written in the form [27]

$$m_L\,\ddot{y}(t) + r(y,\dot{y}) + z(y,\dot{y}) = u(t), \tag{30.1}$$

where m_L is the mass constant, y the displacement, u the external force, and where an over-dot indicates a derivative with respect to the time variable t. The total restoring force in the system is composed of a static nonlinear term $r(y,\dot{y})$, which only depends on the instantaneous values of the displacement $y(t)$ and velocity $\dot{y}(t)$, and of a dynamic, i.e. history-dependent, nonlinear term $z(y,\dot{y})$, which encodes the hysteretic memory of the system. In the present study, the static restoring force contribution is assumed to be linear, that is

$$r(y,\dot{y}) = k_L\,y + c_L\,\dot{y}, \tag{30.2}$$

where k_L and c_L are the linear stiffness and viscous damping coefficients, respectively. The hysteretic force $z(y,\dot{y})$ obeys the first-order differential equation

$$\dot{z}(y,\dot{y}) = \alpha\,\dot{y} - \beta\left(\gamma\ |\dot{y}|\,|z|^{\nu-1}\,z + \delta\,\dot{y}\,|z|^{\nu}\right), \tag{30.3}$$

Table 30.1 Physical parameters of the Bouc-Wen system

Parameter	m_L	c_L	k_L	α	β	γ	δ	ν
Value (in SI unit)	2	10	$5\,10^4$	$5\,10^4$	$1\,10^3$	0.8	−1.1	1

Table 30.2 Linear modal parameters of the Bouc-Wen system

Parameter	Natural frequency ω_0 (Hz)	Damping ratio ζ (%)
Value	35.59	1.12

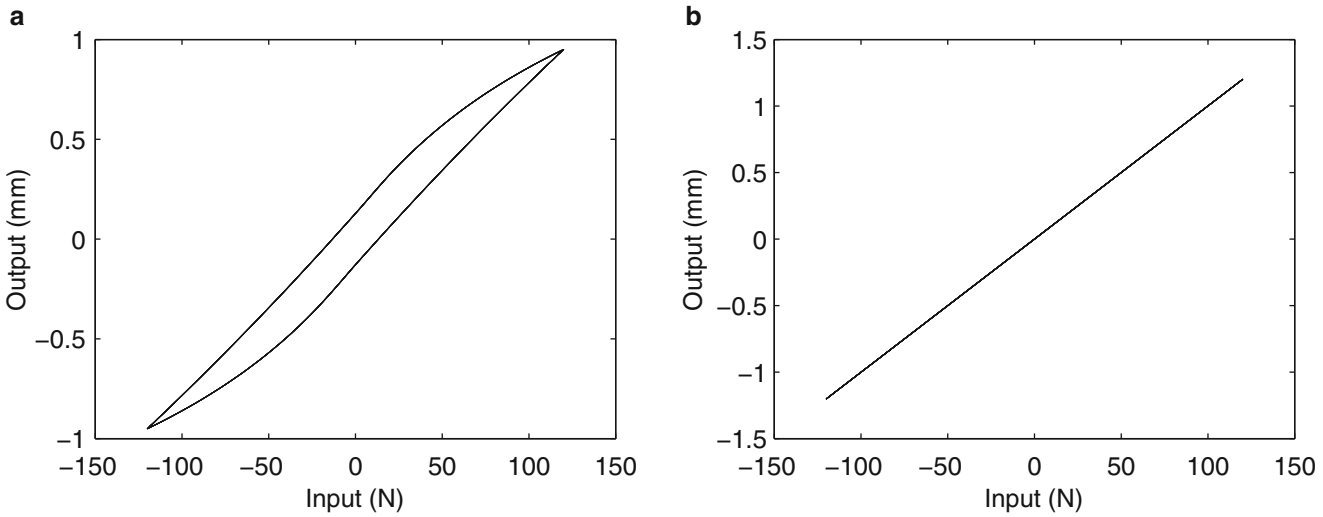

Fig. 30.1 Hysteresis loop in the system input-output plane for quasi-static forcing conditions. (**a**) Non-degenerate loop obtained for the parameters in Table 30.1; (**b**) linear behaviour retrieved when setting the β parameter to 0

where the five Bouc-Wen parameters α, β, γ, δ and ν are used to tune the shape and the smoothness of the system hysteresis loop. Note that the variable z is not measurable, which may complicate the formulation of an identification problem. Another difficulty is that Eq. (30.3) is a nonlinear relation in the parameter ν. These two issues will be addressed in Sect. 30.4.3 through a black-box state-space modelling approach.

Table 30.1 lists the values of the physical parameters selected in this work. The linear modal parameters deduced from m_L, c_L and k_L are given in Table 30.2. Figure 30.1a illustrates the existence of a non-degenerate loop in the system input-output plane for quasi-static forcing conditions. In comparison, by setting the β parameter to 0, a linear behaviour is retrieved in Fig. 30.1b. The excitation $u(t)$ in these two figures is a sine wave with a frequency of 1 Hz and an amplitude of 120 N. The response exhibits no initial condition transients as it is depicted over ten cycles in steady state.

30.2.2 Excitation Signal

Multisine excitations will be considered throughout the identification process. A multisine is a periodic signal with a user-defined amplitude spectrum and randomly-chosen phases. It is also known as a pseudo-random signal, since it features a random appearance in the time domain and deterministic amplitudes in the frequency domain. Multisines are attractive because they are periodic, broadband, and low-crest-factor signals [30]. In particular, periodicity allows leakage to be eliminated in frequency-domain identification and the covariance matrix of the noise disturbances to be estimated directly from data.

Formally, a multisine input $u(t)$ is defined by means of a sum of sine waves with related frequencies as [30]

$$u(t) = N^{-1/2} \sum_{k=-N/2+1}^{N/2-1} U_k \, e^{j\left(2\pi \, k \, \frac{f_s}{N} \, t + \phi_k\right)}, \tag{30.4}$$

where $U_k = U_{-k}$, $U_0 = 0$, and $\phi_k = -\phi_{-k}$. N is the number of time samples, $N^{-1/2}$ a scaling factor, f_s the sampling frequency, and j the imaginary unit. The amplitudes U_k are controlled by the user to meet a desired spectrum (see Sects. 30.3 and 30.4.3), and the phases ϕ_k are drawn from an uniform distribution on $[0,\ 2\pi)$. The signal $u(t)$ in Eq. (30.4) is asymptotically normally distributed in the time domain as N tends to infinity.

30.2.3 Time Integration

The Bouc-Wen dynamics in Eqs. (30.1) and (30.3) can be effectively integrated in time using a Newmark method. Newmark integration relies on one-step-ahead approximations of the velocity and displacement fields obtained by applying Taylor expansion and numerical quadrature techniques [31]. Denoting by h the integration time step, these approximation relations write

$$\begin{aligned} \dot{y}(t+h) &= \dot{y}(t) + (1-a)\ h\,\ddot{y}(t) + a\,h\,\ddot{y}(t+h) \\ y(t+h) &= y(t) + h\,\dot{y}(t) + \left(\tfrac{1}{2} - b\right)\ h^2\,\ddot{y}(t) + b\,h^2\,\ddot{y}(t+h). \end{aligned} \tag{30.5}$$

Parameters a and b are typically set to 0.5 and 0.25, respectively. Equation (30.5) is herein enriched with an integration formula for the variable $z(t)$, which takes the form

$$z(t+h) = z(t) + (1-c)\ h\,\dot{z}(t) + c\,h\,\dot{z}(t+h), \tag{30.6}$$

where c, similarly to a, is set to 0.5. Based on Eqs. (30.5) and (30.6), a Newmark scheme proceeds in two steps. First, predictions of $\dot{y}(t+h)$, $y(t+h)$ and $z(t+h)$ are calculated assuming $\ddot{y}(t+h) = 0$ and $\dot{z}(t+h) = 0$. Second, the initial predictors are corrected via Newton-Raphson iterations so as to satisfy the dynamic equilibria in Eqs. (30.1) and (30.3).

The sampling rate during integration, i.e. $1/h$, is set to 15,000 Hz. For identification use, synthesised time histories are low-pass filtered and downsampled to 750 Hz. Figure 30.2a displays the system output calculated in response to a multisine input for which all frequencies in the 5–150 Hz band are excited. The root-mean-squared (RMS) amplitude of the input is 50 N and five output periods are simulated. The exponential decay of the system transient response is plotted in Fig. 30.2b by subtracting the last synthesised period from the entire time record. This graph indicates that transients due to initial conditions only affect the first period of measurement, and that the applied periodic input results in a periodic output. It also demonstrates the high accuracy of the Newmark integration, as the transient response reaches the Matlab precision of −313 dB in steady state.

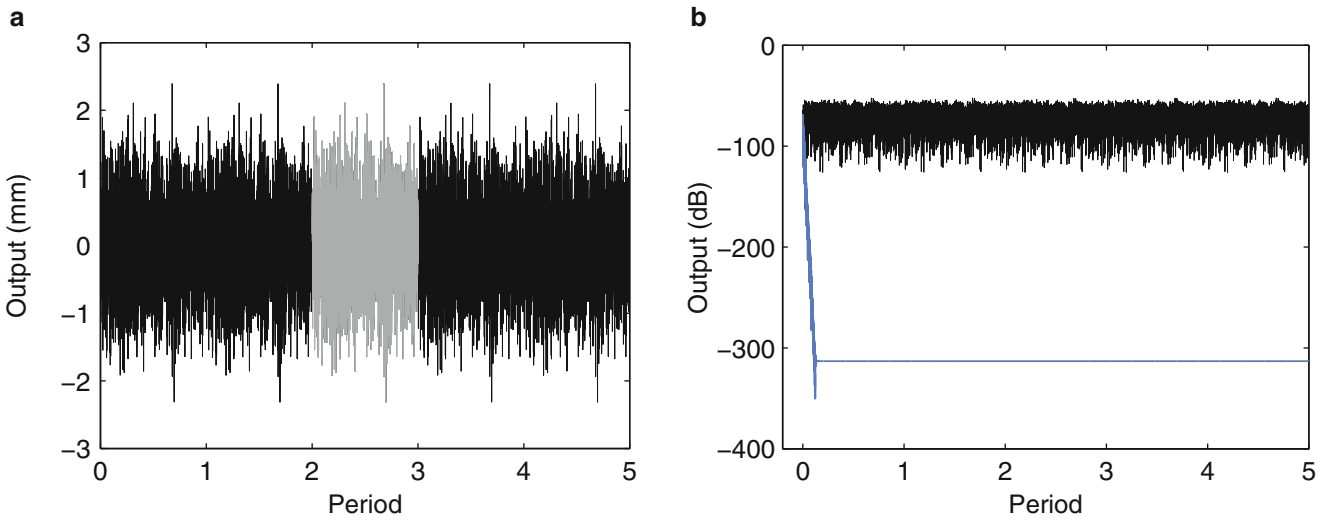

Fig. 30.2 System output calculated in response to a multisine input band-limited in 5–150 Hz. (**a**) Output over five periods, with one specific period highlighted in *grey*; (**b**) output in logarithmic scaling (in *black*) and decay of the transient response (in *blue*)

30.2.4 Noise Assumptions

White Gaussian noise is added to the synthesised output measurements $y(t)$ considering a signal-to-noise ratio (SNR) of 40 dB. The input time series $u(t)$ is assumed to be noiseless, i.e. observed without errors and independent of the output noise. In practice, electromagnetic shakers typically yield a SNR of 60–80 dB, which is coherent with a noise-free assumption. If the input noise disturbances are otherwise too important, measurements can be averaged over multiple periods.

30.3 Nonparametric Analysis of Nonlinear Distortions

In this section, a simple testing procedure is employed to gain rapid insight into the nonlinear distortions observed in output data. The procedure requires no user interaction, and no parametric modelling effort. It allows an objective, i.e. a quantitative, detection of nonlinear behaviour and separates distortions originating from odd and even nonlinearities. The basic idea of the approach is to design a multisine excitation signal comprising odd frequencies only, called measurement lines, and to assess nonlinear distortions by measuring the output level at the nonexcited frequencies, called detection lines [32]. More specifically, Fig. 30.3 shows that the adopted input amplitude spectrum possesses no even frequencies, serving as even detection lines. In addition, odd excited frequencies are grouped into sets of successive lines (for instance, 1–3–5 and 7–9–11), and one frequency is randomly rejected from each group to function as an odd detection line (for instance, 5 and 9) [33]. This specific choice of input spectrum permits the following classification of the output spectrum contributions in Fig. 30.3, assuming steady-state conditions [34]:

- at the measurement lines, linear dynamics (in black) and odd nonlinear distortions (in orange) appear;
- at the odd detection lines, only odd nonlinear distortions (in orange) are visible;
- at the even detection lines, only even nonlinear distortions (in blue) emerge.

This nonparametric analysis procedure is applied in Fig. 30.4 to the Bouc-Wen system of Sect. 30.2.1. The excitation signal is a multisine with odd excited frequencies in 5–150 Hz, and a frequency resolution $f_0 = f_s/N \cong 0.09$ Hz, given $N = 8192$. Odd detection lines are created by randomly excluding one frequency in each group of three successive measurement lines. The RMS input amplitude is equal to 1, 10, 25 and 50 N in Fig. 30.4a–d, respectively. The noise level displayed in black is obtained by averaging the measurements over four periods in steady state. Figure 30.4 proves that the system features no even nonlinearity. Conversely, substantial odd distortions are detected, including at low forcing level in Fig. 30.4a, where they lie 20 dB below the output level in the resonance vicinity. At higher forcing levels in Fig. 30.4b–d, odd distortions affect the system response throughout the input band, in particular in the resonance frequency and the third harmonic regions.

In summary, this section learns that identifying the Bouc-Wen system of Sect. 30.2.1 solely requires odd nonlinear model terms, which was retrieved by making exclusive use of output data. This is coherent with Eq. (30.3) which writes, given the choice $\nu = 1$ in Table 30.1,

$$\dot{z}(y, \dot{y}) = \alpha\, \dot{y} - \beta\, \gamma\ \ |\dot{y}|\, z - \beta\, \delta\, \dot{y}\, |z|\,, \tag{30.7}$$

where the expressions $|\dot{y}|\, z$ and $\dot{y}\, |z|$ are quadratic odd nonlinearities.

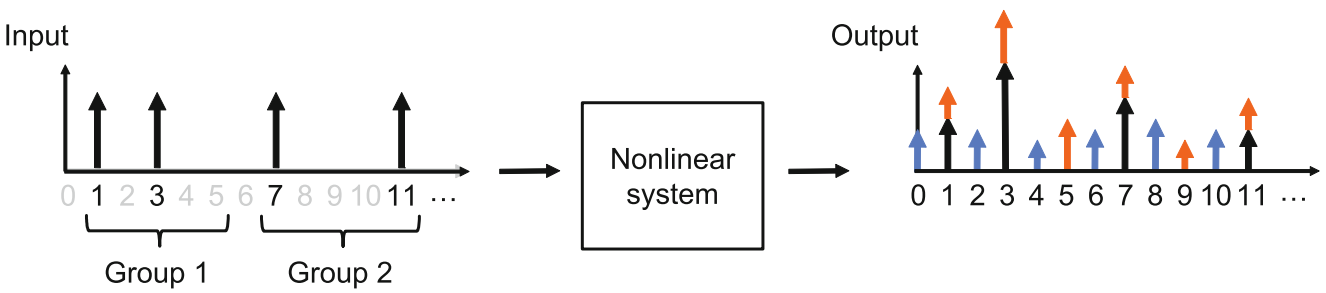

Fig. 30.3 Multisine input spectrum with well-selected measurement (in *black*) and detection (in *grey*) lines, and corresponding output spectrum where odd (in *orange*) and even (in *blue*) nonlinear distortions are quantified and separated

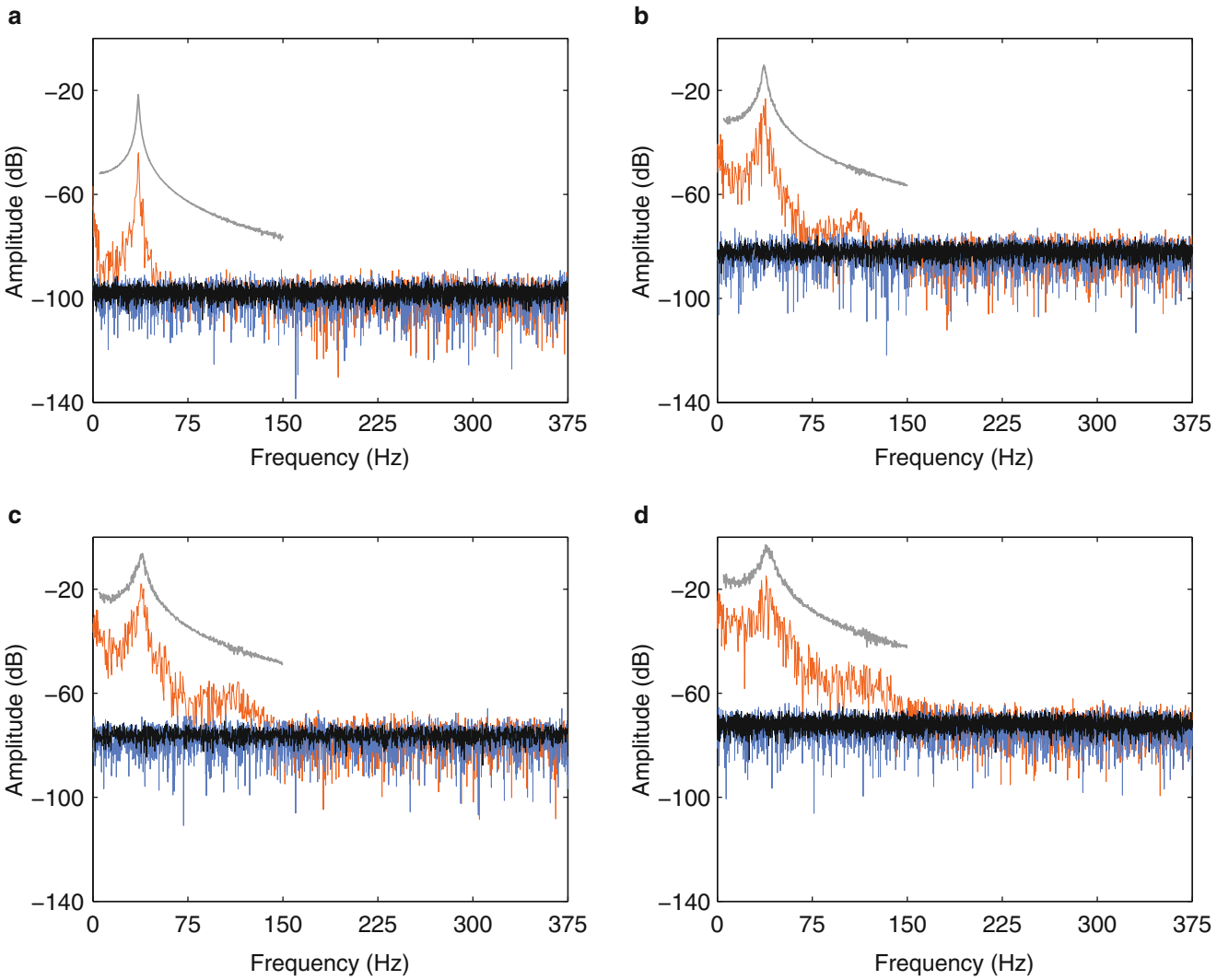

Fig. 30.4 Nonparametric analysis of the nonlinear distortions affecting the Bouc-Wen system of Sect. 30.2.1. The RMS input amplitude is equal to (**a**) 1, (**b**) 10, (**c**) 25 and (**d**) 50 N. Output level at the measurement lines (in *grey*); odd distortions (in *orange*); even distortions (in *blue*); noise level (in *black*)

30.4 Nonlinear State-Space Identification

A nonlinear state-space model can be generally expressed in discrete-time form as

$$\begin{cases} \mathbf{x}(t+1) = \mathbf{g}\left(\mathbf{x}(t), \mathbf{u}(t), \boldsymbol{\theta}\right) \\ \mathbf{y}(t) = \mathbf{h}\left(\mathbf{x}(t), \mathbf{u}(t), \boldsymbol{\theta}\right), \end{cases} \tag{30.8}$$

where $\mathbf{x} \in \mathbb{R}^n$ is the state vector, $\mathbf{u} \in \mathbb{R}^q$ the input vector, $\mathbf{y} \in \mathbb{R}^l$ the output vector, $\mathbf{g} \in \mathbb{R}^n$ and $\mathbf{h} \in \mathbb{R}^l$ two nonlinear functionals, and n the model order. The vector $\boldsymbol{\theta} \in \mathbb{R}^{n_\theta}$ contains the parameters of the model to be estimated. The first relation in Eq. (30.8) is known as the state equation, and dictates the dynamic evolution of the system. The second relation is the output equation, which translates the current system state and input into measurable output information.

30.4.1 The Polynomial Nonlinear State-Space Model Structure

The nonlinear functionals $\mathbf{g}(\mathbf{x}(t), \mathbf{u}(t), \boldsymbol{\theta})$ and $\mathbf{h}(\mathbf{x}(t), \mathbf{u}(t), \boldsymbol{\theta})$ in Eq. (30.8) can, in principle, be expanded using any basis functions. In this paper, a polynomial representation is adopted, following the original idea of Paduart et al. [22]. Polynomial expansions are attractive because they are simple, linear in their parameters, can be easily extended to the multivariate case, and possess universal approximation properties [35]. Equation (30.8) becomes

$$\begin{cases} \mathbf{x}(t+1) = \mathbf{A}\,\mathbf{x}(t) + \mathbf{B}\,\mathbf{u}(t) + \mathbf{E}\,\mathbf{e}(\mathbf{x}(t), \mathbf{u}(t)) \\ \mathbf{y}(t) = \mathbf{C}\,\mathbf{x}(t) + \mathbf{D}\,\mathbf{u}(t) + \mathbf{F}\,\mathbf{f}(\mathbf{x}(t), \mathbf{u}(t)), \end{cases} \tag{30.9}$$

where $\mathbf{A} \in \mathbb{R}^{n\times n}$, $\mathbf{B} \in \mathbb{R}^{n\times q}$, $\mathbf{C} \in \mathbb{R}^{l\times n}$ and $\mathbf{D} \in \mathbb{R}^{l\times q}$ are the linear state, input, output and feedthrough matrices, respectively. The vectors $\mathbf{e} \in \mathbb{R}^{n_e}$ and $\mathbf{f} \in \mathbb{R}^{n_f}$ include all monomial combinations of the state and input variables up to degree d. The associated coefficients are arranged in the matrices $\mathbf{E} \in \mathbb{R}^{n\times n_e}$ and $\mathbf{F} \in \mathbb{R}^{l\times n_f}$.

The number of parameters in Eq. (30.9) is [22]

$$s = \left(\frac{(n+q+d)!}{d!\ (n+q)!} - 1 \right) \times (n+l)\,. \tag{30.10}$$

This number can be reduced by probing the significance of each nonlinear term in the decrease of the model error fit evaluated on validation data. In this respect, Paduart [36] introduced several parsimonious alternatives to Eq. (30.9). This includes considering nonlinear terms in the state equation only, disregarding input variables in the monomial combinations, or selecting non-consecutive polynomial degrees. These modelling strategies will be exploited in Sect. 30.4.3 to avoid overfitting issues.

30.4.2 Identification Methodology

A two-step methodology was proposed in [22] to identify the parameters of the model structure in Eq. (30.9). First, initial estimates of the linear system matrices $(\mathbf{A}, \mathbf{B}, \mathbf{C}, \mathbf{D})$ are calculated by measuring and fitting the best linear approximation (BLA) of the system under test. Second, assuming zero initial values for the nonlinear coefficients in $(\mathbf{E}, \mathbf{F})$, a full nonlinear model is built using optimisation.

30.4.2.1 Initial Linear Model

The BLA of a nonlinear system is defined as the linear model $G_{BLA}(j\omega_k)$ which approximates best the system output in least-squares sense [30]. In general, it varies with the input frequency content and RMS value. The BLA can be measured by conducting M experiments, consisting each in applying a multisine excitation and collecting P steady-state periods of input-output data [33]. In the single-input, single-output case, the frequency response function (FRF) associated with the mth experiment is obtained as the ratio

$$G_m(j\omega_k) = \frac{\frac{1}{P}\sum_{p=1}^{P} Y_{m,p}(k)}{\frac{1}{P}\sum_{p=1}^{P} U_{m,p}(k)}, \tag{30.11}$$

where $U_{m,p}(k)$ and $Y_{m,p}(k)$ are the discrete Fourier transforms (DFTs) of the input $u(t)$ and output $y(t)$ acquired during the pth period of the mth experiment, respectively. The BLA is calculated as an averaged FRF over experiments, so that

$$G_{BLA}(j\omega_k) = \frac{1}{M}\sum_{m=1}^{M} G_m(j\omega_k). \tag{30.12}$$

A linear state-space model $(\mathbf{A}, \mathbf{B}, \mathbf{C}, \mathbf{D})$ is fitted to the nonparametric measurement of $G_{BLA}(j\omega_k)$ in Eq. (30.12) using a frequency-domain subspace identification method [37, 38]. The quality of the subspace model is evaluated through the weighted least-squares cost function

$$V_L = \sum_{k=1}^{F} \epsilon_L^H(k) W_L(k)\, \epsilon_L(k), \tag{30.13}$$

where F is the number of processed frequencies, H denotes the Hermitian transpose, and $W_L(k)$ is a weighting function. Note that the proper selection of W_L is studied in Sect. 30.4.3. The model fitting error $\epsilon_L(k)$ is defined as the difference

$$\epsilon_L(k) = G_L(j\omega_k) - G_{BLA}(j\omega_k). \tag{30.14}$$

The transfer function of the linear subspace model is constructed as

$$G_L(j\omega_k) = \mathbf{C}\ (z_k\, \mathbf{I}^n - \mathbf{A})^{-1}\ \mathbf{B} + \mathbf{D}, \tag{30.15}$$

where $z_k = e^{j(2\pi\, k/N)}$ is the z-transform variable and $\mathbf{I}^n \in \mathbb{R}^{n\times n}$ an identify matrix.

The subspace method of McKelvey et al. [37] generally yields a reasonably low value of the cost function V_L. Minimising V_L with respect to all parameters in $(\mathbf{A}, \mathbf{B}, \mathbf{C}, \mathbf{D})$ further improves the quality of the obtained linear model. As shown in Sect. 30.4.3, this also reduces its dependence upon an algorithmic dimensioning parameter i, which sizes the data matrices processed in the subspace identification [22]. Moreover, the model order n is, in practice, determined by carrying out the cost function minimisation for multiple n values, and retaining the model with the lowest validation fitting error.

30.4.2.2 Full Nonlinear Model

The second step of the identification methodology involves minimising a second weighted least-squares cost function writing

$$V_{NL} = \sum_{k=1}^{F} \epsilon_{NL}^H(k) W_{NL}(k)\, \epsilon_{NL}(k), \tag{30.16}$$

where $W_{NL}(k)$ is a weighting function discussed in Sect. 30.4.3. In Eq. (30.16), the error measure $\epsilon_{NL}(k)$ is defined as

$$\epsilon_{NL}(k) = Y_{NL}(k) - Y(k), \tag{30.17}$$

where $Y_{NL}(k)$ and $Y(k)$ are the modelled and measured output DFT spectra, respectively. All parameters of the full nonlinear model $(\mathbf{A}, \mathbf{B}, \mathbf{C}, \mathbf{D}, \mathbf{E}, \mathbf{F})$ are estimated by minimising V_{NL}, starting from the linear system matrices obtained in Sect. 30.4.2.1 and zero initial values for the nonlinear coefficients.

Note that the minimisation of the two cost functions in Eqs. (30.13) and (30.16) is performed in this work using a Levenberg-Marquardt optimisation routine, which combines the large convergence region of the gradient descent method with the fast convergence of the Gauss-Newton method [39, 40]. In this regard, technicalities related to the calculation of the Jacobian of Eqs. (30.13) and (30.16) are elaborated in [22].

30.4.3 Identification Results

This section identifies the Bouc-Wen system of Sect. 30.2.1 using a polynomial nonlinear state-space model. A multisine excitation with all odd and even frequencies excited in the 5–150 Hz band is applied to synthesise four steady-state periods of measurement. The input amplitude level is fixed to 50 N RMS, which leads to severe nonlinear effects, as visible in Fig. 30.4d. We stress the deliberate choice to select two different input signals to perform the nonparametric analysis of output distortions and the parametric modelling of input-output data. In particular, a decimated force spectrum was required to distinguish odd from even nonlinearities in Sect. 30.3, whereas a full spectrum is utilised herein to capture the system dynamics over the complete band of interest.

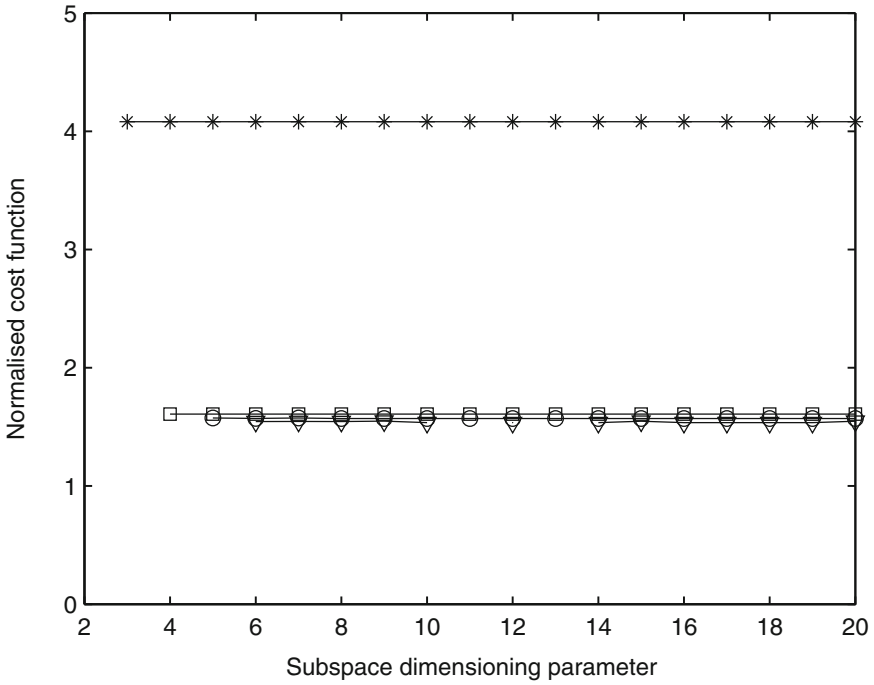

Fig. 30.5 Cost function V_L normalised by the number of processed frequencies F and plotted versus the subspace dimensioning parameter i. Model order 2 (*stars*), 3 (*rectangles*), 4 (*circles*) and 5 (*triangles*)

To calculate the BLA of the Bouc-Wen system, four data sets are generated, i.e. $M = 4$, considering different realisations of the multisine phases and noise disturbances. The nonparametric estimate $G_{BLA}(j\omega_k)$ calculated through Eq. (30.12) is transformed into a linear parametric state-space model $(\mathbf{A}, \mathbf{B}, \mathbf{C}, \mathbf{D})$ by applying subspace identification and subsequently minimising the cost function in Eq. (30.13). The weighting function $W_L(k)$ is chosen as the inverse of the total variance of $G_{BLA}(j\omega_k)$, hence encompassing the variability caused by nonlinear and noise distortions. This choice comes down to setting [41]

$$W_L(k) = \frac{1}{M\,(M-1)} \sum_{m=1}^{M} \left| G_m(j\omega_k) - G_{BLA}(j\omega_k) \right|^2 . \tag{30.18}$$

Figure 30.5 depicts the minimised cost function V_L versus the subspace dimensioning parameter i. The cost function is normalised by the number of processed frequencies $F = 1585$, and is plotted for model orders 2, 3, 4 and 5 using star, rectangular, circular and triangular labels, respectively. It is observed that V_L is virtually insensitive to i, and that the order 3 corresponds to the best trade-off between model accuracy and parameter parsimony. Note that, for $n = 3$, the minimum value of the cost function is obtained for $i = 4$.

The nonparametric and parametric BLA of the system are presented in Fig. 30.6 in grey and blue, respectively. An accurate fit based on a model of order 2 is achieved in Fig. 30.6a, except for frequencies lower than 15 Hz. In this region, the modelling error level displayed in orange becomes substantially larger than the total distortions level plotted in black. By contrast, selecting $n = 3$, as in Fig. 30.6b, results in a perfect fitting throughout the input band, confirming the analysis of Fig. 30.5. The need for a model of order 3 is substantiated by recasting the Bouc-Wen dynamics of Eqs. (30.1) and (30.7) in the form

$$\begin{cases} \begin{pmatrix} \dot{y} \\ \ddot{y} \\ \dot{z} \end{pmatrix} = \begin{pmatrix} 0 & 1 & 0 \\ -\frac{k_L}{m_L} & -\frac{c_L}{m_L} & -\frac{1}{m_L} \\ 0 & \alpha & 0 \end{pmatrix} \begin{pmatrix} y \\ \dot{y} \\ z \end{pmatrix} + \begin{pmatrix} 0 \\ \frac{1}{m_L} \\ 0 \end{pmatrix} u + \begin{pmatrix} 0 & 0 \\ 0 & 0 \\ -\beta\,\gamma & -\beta\,\delta \end{pmatrix} \begin{pmatrix} |\dot{y}|\,z \\ \dot{y}\,|z| \end{pmatrix} \\ \\ \quad y = \begin{pmatrix} 1\,0\,0 \end{pmatrix} \begin{pmatrix} y \\ \dot{y} \\ z \end{pmatrix} . \end{cases} \tag{30.19}$$

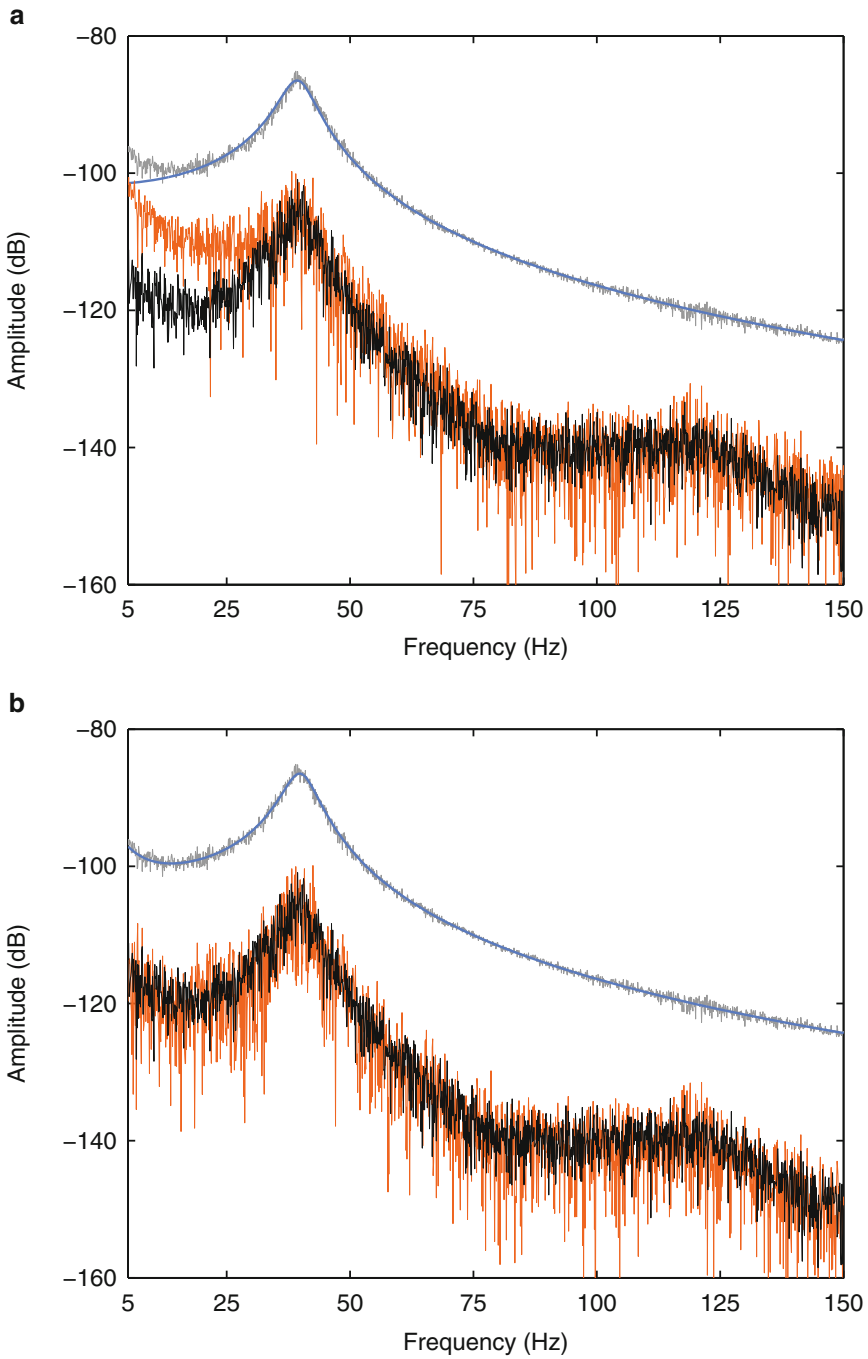

Fig. 30.6 Nonparametric (in *grey*) and parametric (in *blue*) BLA, modelling error level (in *orange*) and total distortions level (in *black*). (**a**) $n = 2$; (**b**) $n = 3$

Equation (30.19) shows that translating the Bouc-Wen equations in state space requires the definition of three state variables. It should also be noted that the state matrix $\mathbf{A}$ identified for $n = 3$ possesses a pair of complex conjugate poles and one real pole. The appearance in the fitted model of a real pole, i.e. pole with zero frequency, is consistent with the definition of hysteresis as a quasi-static phenomenon, as explained in Sect. 30.1.

Final estimates of all nonlinear state-space parameters ($\mathbf{A}, \mathbf{B}, \mathbf{C}, \mathbf{D}, \mathbf{E}, \mathbf{F}$) are obtained by minimising the cost function V_{NL}. A unit weighting $W_{NL}(k)$ is applied in Eq. (30.16), reflecting that unmodelled dynamics, which is assumed to be uniformly distributed in the frequency domain, dominates noise disturbances. Figure 30.7 plots the decrease of the RMS modelling error over 150 Levenberg-Marquardt iterations. This error is evaluated on a validation data set generated considering the

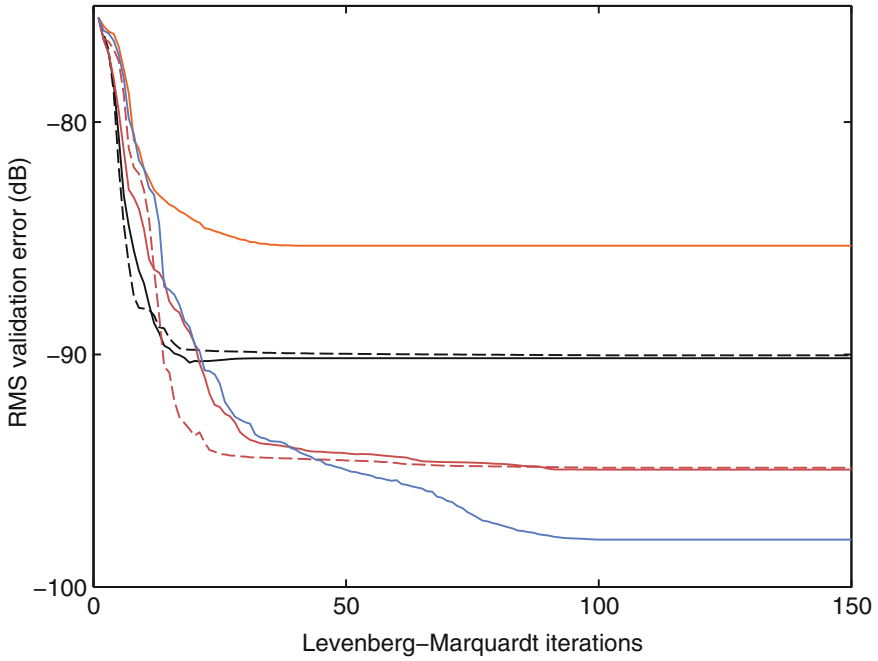

Fig. 30.7 Decrease of the RMS validation error over 150 Levenberg-Marquardt iterations. Polynomial nonlinear state-space models of degree 2 (in *orange*), 2–3 (in *solid black*), 2–3–4 (in *dashed black*), 2–3–4–5 (in *solid red*), 2–3–4–5–6 (in *dashed red*), and 2–3–4–5–6–7 (in *blue*)

Table 30.3 RMS validation error for polynomial nonlinear state-space models of various degrees together with their respective number of parameters

Polynomial degree	RMS validation error (dB)	Number of parameters
2	−85.32	34
2–3	−90.35	64
2–3–4	−90.03	109
2–3–4–5	−94.87	172
2–3–4–5–6	−94.85	256
2–3–4–5–6–7	−97.96	364
3–5–7	−98.32	217

same excitation properties as for estimation data. The converged value of the error for different nonlinear models is given in Table 30.3, together with their respective number of model parameters. As a result of the odd nature of the nonlinearities in Eqs. (30.7) and (30.19), it is found that introducing in the model even-degree monomials brings no decrease of the validation error, confirming the physical intuition gained in Sect. 30.3. The most accurate state-space model reported in Table 30.3 comprises odd monomials up to $d = 7$, for a total of 217 parameters. Note that all the models in Fig. 30.7 and Table 30.3 do neither incorporate nonlinear terms in the output equation, nor input variables in the monomial combinations, in accordance with Eq. (30.19).

The frequency-domain behaviour of the validation modelling error is studied in Fig. 30.8, where the output spectrum in grey is compared with linear and nonlinear fitting error levels in orange and blue, respectively. Using monomials of degree 2 and 3 in the state variables, as is the standard choice [22], reduces the linear error by a factor of 20 dB, as visible in Fig. 30.8a. A further decrease of 10 dB is achieved by selecting monomials of degree 3, 5 and 7, as in Fig. 30.8b. It should be remarked that an exact polynomial description of the nonlinearities $|\dot{y}|\, z$ and $\dot{y}\, |z|$ in Eq. (30.7) demands, in principle, an infinite series of terms, preventing the nonlinear errors in Fig. 30.8 from reaching the noise level depicted in black. Increasing the polynomial degree d to values higher than 7, though being manifestly possible, was not attempted in this work to limit the computational burden involved in the cost function minimisation. Finally, the time-domain errors corresponding to Fig. 30.8b are depicted in Fig. 30.9. The RMS values of the validation output time history and of the linear and nonlinear errors are equal to 0.66, 0.15 and 0.01 mm, respectively. This graph nicely illustrates the important increase of the identification accuracy obtained by introducing nonlinear black-box terms in the state-space modelling of hysteresis.

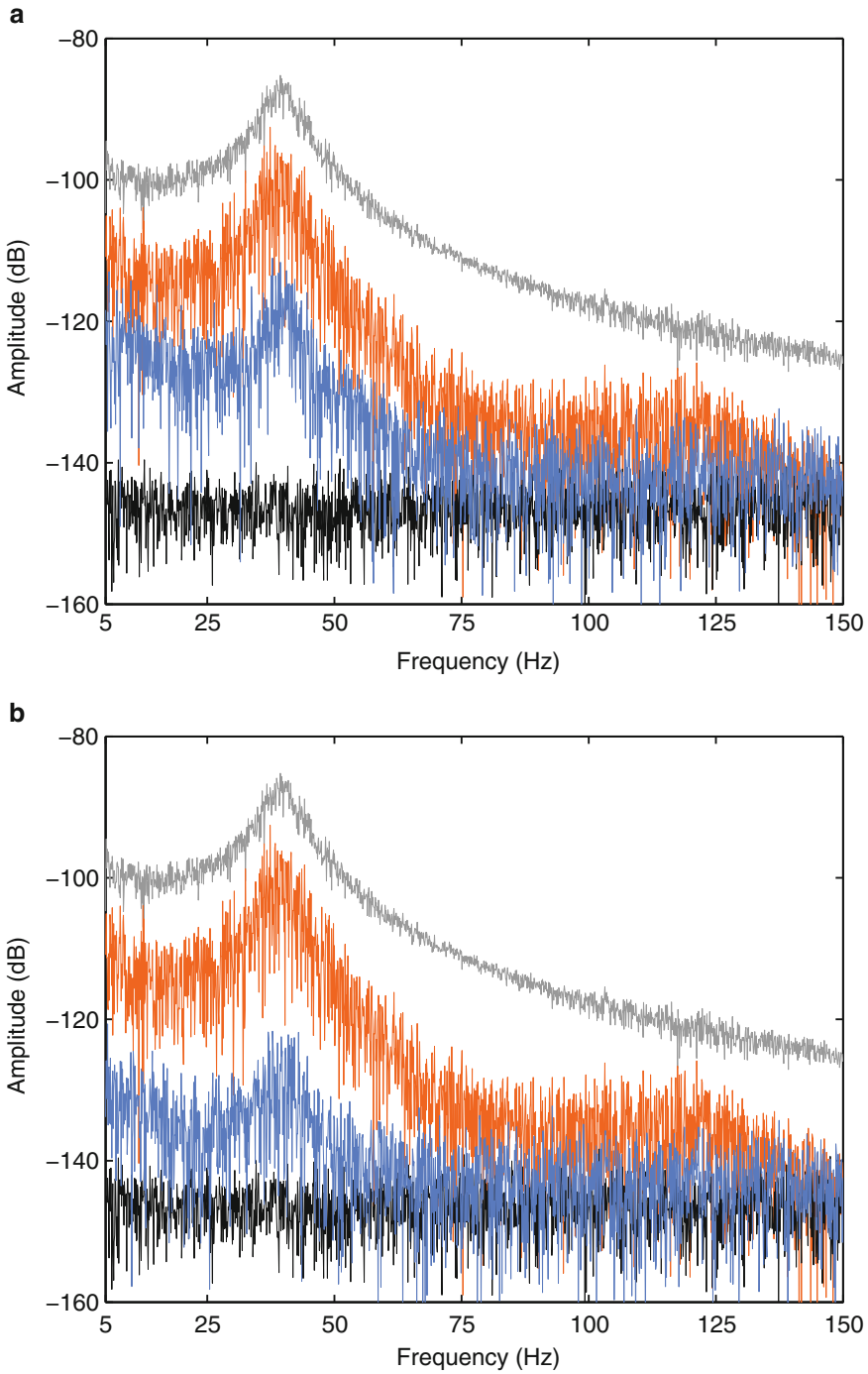

Fig. 30.8 Frequency-domain behaviour of the validation modelling error over the input band, featuring the output spectrum (in *grey*), the linear (in *orange*) and nonlinear (in *blue*) fitting error levels, and the noise level (in *black*). (**a**) Monomials of degree 2 and 3; (**b**) monomials of degree 3, 5 and 7

30.5 Model Validation Under Sine-Sweep Excitations

This final section investigates the domain of validity of the state-space models fitted in Sect. 30.4.3 under sine excitation signals. In particular, a comparison is made between the exact and reconstructed responses of the Bouc-Wen system under various sine-sweep forcing levels. Figure 30.10 presents the relative error in percent between the two responses for input amplitudes ranging from 5 to 100 N. Four different nonlinear state-space models are analysed in this figure, namely

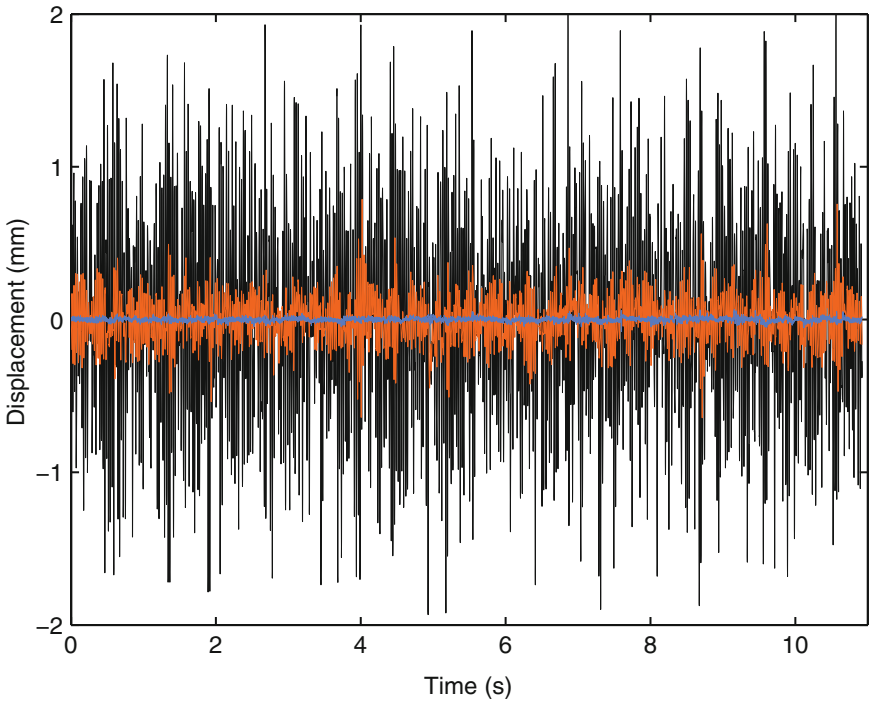

Fig. 30.9 Time-domain behaviour of the validation modelling error for monomials of degree 3, 5 and 7, featuring the output time history (in *black*) and the linear (in *orange*) and nonlinear (in *blue*) fitting error levels

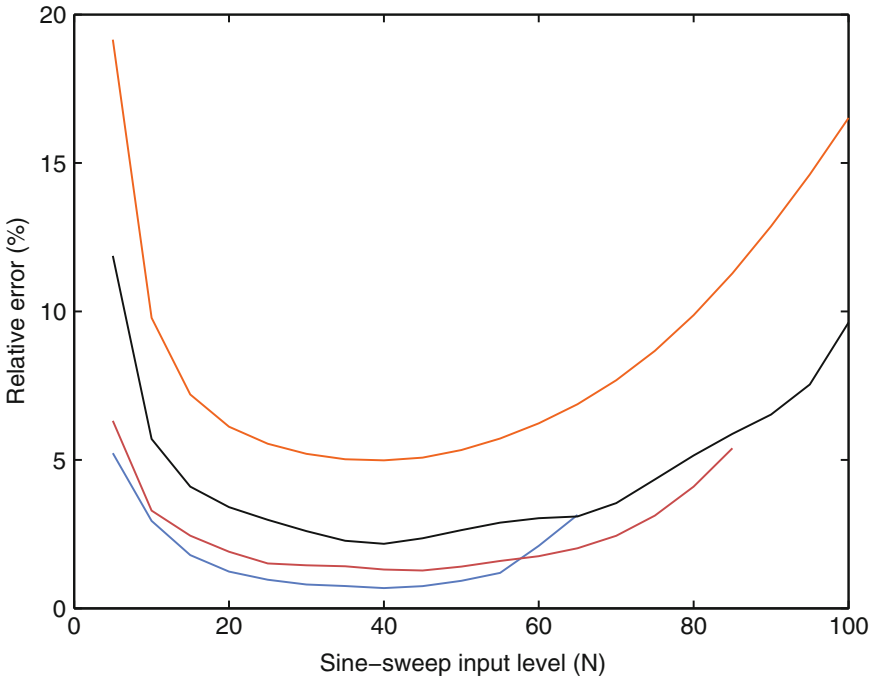

Fig. 30.10 Relative error (in %) between the exact and reconstructed responses of the Bouc-Wen system for sine-sweep forcing amplitudes ranging from 5 to 100 N. Nonlinear state-space models with monomials of degree 2 (in *orange*), 2–3 (in *black*), 2–3–5 (in *red*), 2–3–5–7 (in *blue*)

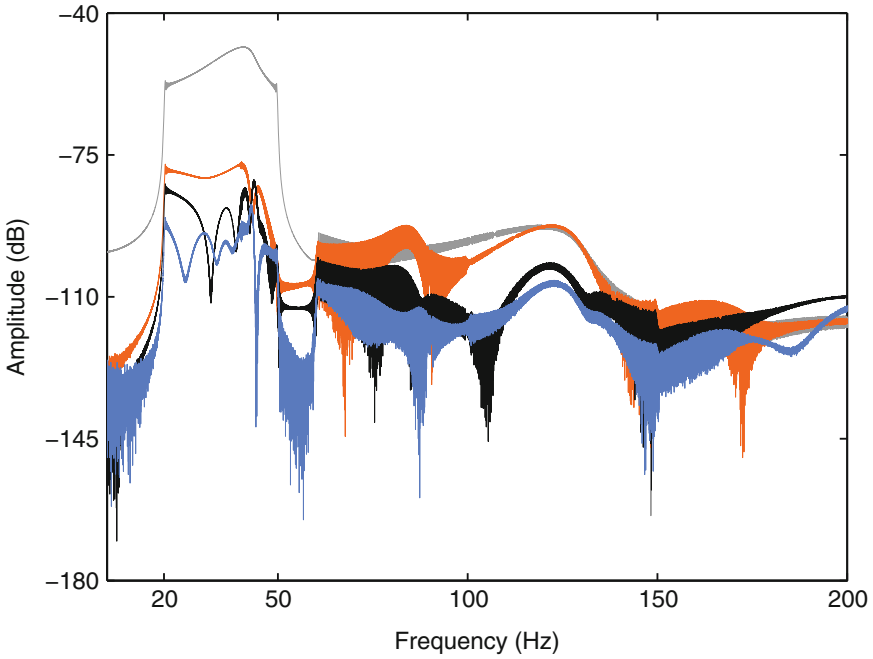

Fig. 30.11 Exact output spectrum over 5–200 Hz at 40 N sine-sweep level (in *grey*) and reconstruction error for the 2 (in *orange*), 2–3 (in *black*) and 2–3–5–7 (in *blue*) nonlinear state-space models

comprising monomials of degree 2 (in orange), 2–3 (in black), 2–3–5 (in red) and 2–3–5–7 (in blue). The chosen input signals sweep the interval from 20 to 50 Hz at a linear rate of 10 Hz/min. Reconstructed outputs are simulated in discrete time by evaluating Eq. (30.9), which are explicit relations in $\mathbf{y}(t)$. It is observed that, as the model complexity increases, the prediction capabilities improve. The minimum relative error is achieved for all tested models around 40 N, reaching 0.7 % in the case of the 2–3–5–7 model. However, complex models are likely to become unstable when extrapolated outside their fitting domain. This is visible for the blue and red models in Fig. 30.10, which do no longer predict bounded outputs for input levels higher than 65 and 85 N, respectively.

A frequency-domain error analysis is performed at 40 N input level in Fig. 30.11. The exact output spectrum is plotted in grey, and is compared with the reconstruction error for the 2 (in orange), 2–3 (in black) and 2–3–5–7 (in blue) state-space models. The error is seen to decrease in the input band for increasing model complexity. In the vicinity of the third harmonic around 120 Hz, the error similarly drops for higher polynomial degrees. Note that the cut-off frequency of 150 Hz of the multisine excitation under which the state-space models were fitted is visible in the error plots of Fig. 30.11.

30.6 Conclusions

The purpose of the present paper was to introduce a general framework to identify hysteresis in dynamic systems. State-space models with polynomial nonlinear terms were selected to support this framework. They are fitted to data using a rigorous two-step methodology involving weighted least-squares minimisation. A numerical study was conducted to demonstrate the fitting accuracy of the proposed approach. The identified black-box models were also found to be reasonably parsimonious, given that they require no a priori knowledge about the observed hysteretic behaviour. This paper paves the way for addressing the experimental modelling of hysteresis featured in real applications, especially in the dynamics of jointed structures.

Acknowledgements This work was supported in part by the Fund for Scientific Research (FWO-Vlaanderen), by the Flemish Government (Methusalem), by the Belgian Government through the Inter university Poles of Attraction (IAP VII) Program, and by the ERC advanced grant SNLSID, under contract 320378.

References

1. Morrison, D., Jia, Y., Moosbrugger, J.: Cyclic plasticity of nickel at low plastic strain amplitude: hysteresis loop shape analysis. Mater. Sci. Eng. **A314**, 24–30 (2001)
2. Bertotti, G.: Hysteresis in Magnetism: For Physicists, Materials Scientists, and Engineers. Academic, San Diego (1998)
3. Mueller, T.: The influence of laminar separation and transition on low Reynolds number airfoil hysteresis. AIAA J. Aircr. **22**(9), 763–770 (1985)
4. Angeli, D., Ferrell, J., Sontag, E.: Detection of multistability, bifurcations, and hysteresis in a large class of biological positive-feedback systems. Proc. Natl. Acad. Sci. U. S. A. **101**(7), 1822–1827 (2004)
5. Beisner, B., Haydon, D., Cuddington, K.: Alternative stable states in ecology. Front. Ecol. Environ. **1**(7), 376–382 (2003)
6. Ramachandran, V., Anstis, S.: Perceptual organization in multistable apparent motion. Perception **14**, 135–143 (1985)
7. Gaul, L., Nitsche, R.: The role of friction in mechanical joints. Appl. Mech. Rev. **54**(2), 93–106 (2001)
8. Bernstein, D.: Ivory ghost. IEEE Control Syst. Mag. **27**, 16–17 (2007)
9. Jinhyoung, O., Drincic, B., Bernstein, D.: Nonlinear feedback models of hysteresis. IEEE Control Syst. Mag. **29**(1), 100–119 (2009)
10. Hassani, V., Tjahjowidodo, T., Do, T.: A survey on hysteresis modeling, identification and control. Mech. Syst. Signal Process. **49**, 209–233 (2014)
11. Charalampakis, A., Koumousis, V.: Identification of Bouc-Wen hysteretic systems by a hybrid evolutionary algorithm. J. Sound Vib. **314**, 571–585 (2008)
12. Worden, K., Manson, G.: On the identification of hysteretic systems, Part I: fitness landscapes and evolutionary identification. Mech. Syst. Signal Process. **29**, 201–212 (2012)
13. Charalampakis, A., Dimou, C.: Identification of Bouc-Wen hysteretic systems using particle swarm optimization. Comput. Struct. **88**, 1197–1205 (2010)
14. Worden, K., Becker, W.: On the identification of hysteretic systems, Part II: Bayesian sensitivity analysis and parameter confidence. Mech. Syst. Signal Process. **29**, 213–227 (2012)
15. Worden, K., Hensman, J.: Parameter estimation and model selection for a class of hysteretic systems using Bayesian inference. Mech. Syst. Signal Process. **32**, 153–169 (2012)
16. Ortiz, G., Alvarez, D., Bedoya-Ruiz, D.: Identification of Bouc-Wen type models using the transitional Markov Chain Monte Carlo method. Comput. Struct. **146**, 252–269 (2015)
17. Worden, K., Barthorpe, R.: Identification of hysteretic systems using NARX models, Part I: evolutionary identification. In: Proceedings of the 29th International Modal Analysis Conference (IMAC), Jacksonville (2012)
18. Xie, S., Zhang, Y., Chen, C., Zhang, X.: Identification of nonlinear hysteretic systems by artificial neural networks. Mech. Syst. Signal Process. **34**, 76–87 (2013)
19. Radouane, A., Ahmed-Ali, T., Giri, F.: Parameter identification of Hammerstein systems with Bouc-Wen hysteresis input nonlinearity. In: Proceedings of the European Control Conference (ECC), Strasbourg (2014)
20. Ktena, A., Fotiadis, D., Spanos, P., Massalas, C.: A Preisach model identification procedure and simulation of hysteresis in ferromagnets and shape-memory alloys. Phys. B Condens. Matter **306**(1–4), 84–90 (2001)
21. Mignolet, M., Song, P., Wang, X.: A stochastic Iwan-type model for joint behavior variability modeling. J. Sound Vib. **349**, 289–298 (2015)
22. Paduart, J., Lauwers, L., Swevers, J., Smolders, K., Schoukens, J., Pintelon, R.: Identification of nonlinear systems using polynomial nonlinear state space models. Automatica **46**, 647–656 (2010)
23. Widanage, W., Stoev, J., Van Mulders, A., Schoukens, J., Pinte, G.: Nonlinear system identification of the filling phase of a wet-clutch system. Control Eng. Pract. **19**, 1506–1516 (2011)
24. Marconato, A., Schoukens, M., Tiels, K., Widanage, W., Abu-Rmileh, A., Schoukens, J.: Comparison of several data-driven non-linear system identification methods on a simplified glucoregulatory system example. IET Control Theory Appl. **8**(17), 1921–1930 (2014)
25. Relan, R., Vanbeylen, L., Firouz, Y., Schoukens, J.: Characterization and nonlinear modelling of Li-Ion battery. In: Proceedings of the 34th Benelux Meeting on Systems and Control, Lommel (2015)
26. Bouc, R.: Forced vibrations of a mechanical system with hysteresis. In: Proceedings of the 4th Conference on Nonlinear Oscillations, Prague (1967)
27. Wen, Y.: Method for random vibration of hysteretic systems. ASCE J. Eng. Mech. Div. **102**(2), 249–263 (1976)
28. Ismail, M., Ikhouane, F., Rodellar, J.: The hysteresis Bouc-Wen model, a survey. Arch. Comput. Methods Eng. **16**, 161–188 (2009)
29. Ikhouane, F., Rodellar, J.: Systems with Hysteresis: Analysis, Identification and Control Using the Bouc-Wen Model. Wiley, Chichester (2007)
30. Pintelon, R., Schoukens, J.: System Identification: A Frequency Domain Approach. IEEE, Piscataway (2001)
31. Géradin, M., Rixen, D.: Mechanical Vibrations: Theory and Application to Structural Dynamics. Wiley, Chichester (2015)
32. Schoukens, J., Pintelon, R., Dobrowiecki, T.: Linear modeling in the presence of nonlinear distortions. IEEE Trans. Instrum. Meas. **51**, 786–792 (2002)
33. Schoukens, J., Pintelon, R., Rolain, Y.: Mastering System Identification in 100 Exercises. IEEE, Piscataway (2012)
34. Schoukens, J., Pintelon, R., Dobrowiecki, T., Rolain, Y.: Identification of linear systems with nonlinear distortions. Automatica **41**, 491–504 (2005)
35. Fliess, M., Normand-Cyrot, D.: On the approximation of nonlinear systems by some simple state-space models. In: Proceedings of the 6th IFAC Symposium on Identification and Parameter Estimation Conference, Washington (1982)
36. Paduart, J.: Identification of nonlinear systems using polynomial nonlinear state space models. Ph.D. thesis, Vrije Universiteit Brussel, Brussels (2007)
37. McKelvey, T., Cay, H.A., Ljung, L.: Subspace-based multivariable system identification from frequency response data. IEEE Trans. Autom. Control **41**(7), 960–979 (1996)

38. Pintelon, R.: Frequency-domain subspace system identification using non-parametric noise models. Automatica **38**, 1295–1311 (2002)
39. Levenberg, K.: A method for the solution of certain problems in least squares. Q. Appl. Math. **2**, 164–168 (1944)
40. Marquardt, D.: An algorithm for least-squares estimation of nonlinear parameters. J. Soc. Ind. Appl. Math. **11**(2), 431–441 (1963)
41. D'haene, T., Pintelon, R., Schoukens, J., Van Gheem, E.: Variance analysis of frequency response function measurements using periodic excitations. IEEE Trans. Instrum. Meas. **54**(4), 1452–1456 (2005)

Chapter 31
Nonholonomically Constrained Dynamics of Rolling Isolation Systems

Karah C. Kelly and Henri P. Gavin

Abstract Rolling Isolation Systems provide a simple and effective means for protecting components from horizontal floor vibrations. In these systems a platform rolls on four steel balls which, in turn, rest within shallow bowls. The trajectories of the balls is uniquely determined by the horizontal and rotational components of the rolling platform, and thus provides nonholonomic constraints. In general, the bowls are not parabolic, so the potential energy function of this system is not quadratic. This paper presents the application of Gauss's Principle of Least Constraint to the modeling of rolling isolation platforms. The equations of motion are described in terms of a redundant set of constrained coordinates. Coordinate accelerations are uniquely determined at any point in time via Gauss's Principle by solving a linearly-constrained quadratic minimization. In the absence of any modeled damping, the equations of motion conserve energy. Simulations and experiments show that responses are highly sensitive to small changes in the initial conditions; peak responses can be predicted only statistically.

Keywords Vibration isolation • Nonlinear dynamics • Constrained dynamical systems

31.1 Introduction

Rolling isolation systems are widely used to mitigate earthquake hazards by reducing the damage caused to computing facilities, telecommunication networks, and lifeline systems. Rolling Isolation systems (RIS) have been installed in hundreds of buildings worldwide to protect such systems. However, the installations of these systems have preceded capabilities to model their behavior. The behavior of these systems are essentially nonlinear because they have a non quadratic potential and have nonholonomic constraints. Unfortunately equations of motions have been very difficult to derive and interpret [1]. Gauss's Principle of Least Constraint provides an alternative systematic method to derive and interpret the equation of motions for the constrained system.

This paper shows the application of Gauss's Principle of Least Constraint to rolling isolation systems and interprets the resulting equation of motions. This model is also the first to include the vertical component of velocity in the kinetic energy.

31.2 The Model

The rolling isolation systems modeled in this study consist of a planar horizontal platform that rolls on four rigid balls, each resting in a shallow radially-symmetric dish. As the platform rolls, its height changes according to the location of the four balls within their dishes. The model is determined uniquely from geometry: the dimensions of the platform, the x, y locations of the dish centers, and the shape of the dish-shaped rolling surfaces. The basic shape for the isolator dishes in this study is modeled after the ISO-Base Seismic Platform [1]. The motion of the isolation platform depends on the shape of the dish. The height $h(r)$ of all dishes in this system will be a variation of the following equation [2]

$$h_r = a_1 \log\left(\cosh\left(\frac{r}{a_0}\right)\right) + a_2 r^2 + a_3 r^3 \left((sign(r)\right) \tag{31.1}$$

K.C. Kelly • H.P. Gavin (✉)
Department of Civil and Environmental Engineering, Duke University, Durham, NC 27713, USA
e-mail: henri.gavin@duke.edu

G. Kerschen (ed.), *Nonlinear Dynamics, Volume 1*, Conference Proceedings of the Society for Experimental Mechanics Series,
DOI 10.1007/978-3-319-29739-2_31

where r is the radial position of the ball from the center of it's dish, in meters, and $a_0 = 0$, $a_1 = 0.1$, $a_2 = 0.01$, $a_3 = 0$, . The geometry of the platform is a rectangle with length size $2a$ where $a = 2\,\text{m}$ and width $2b$ and $b = 2\,\text{m}$. The mass of the system is $m = 20\,\text{kg}$. The four balls are located at the corners. The coordinates of balls 1, 2, 3, and 4 are (in order) (a, b), $(-a, b)$, $(-a, -b)$, $(a, -b)$. The top platform is flat while the lower platform holds shallow dishes in which the balls roll. The location of each ball with respect to the center of it's dish are given by coordinates (x_i, y_i) and the radial component of the ball location is $r_i = \sqrt{x_i^2 + y_i^2}$. In deriving the unconstrained equations of motion we consider x_i, y_i, and r_i to be independent coordinates. The constraints between x_i, y_i, and r_i, along with the constraint that the platform motion dictates the motion of the balls will be incorporated using Gauss's Principle.

31.3 Gauss's Principle of Least Constraint

In Gauss's Principle of Least Constraint, [3, 4] the accelerations $a(t)$ of n unconstrained coordinates of motion, q_i, $(i = 1, \ldots, n)$ is expressed as

$$M(q(t), t)\, a(t) = F(q(t), \dot{q}(t), t) \tag{31.2}$$

The constrained system requires additional actions, $F^c(t)$ in order to enforce the constraints, so the constrained equations of motion are

$$M(q(t), t)\, \ddot{q}(t) = F(q(t), \dot{q}(t), t) + F^c(q(t), \dot{q}(t), t) \tag{31.3}$$

Defining a quadratic form of the differences between the (true) constrained accelerations $\ddot{q}$ and the unconstrained accelerations a as

$$G = \frac{1}{2}(\ddot{q} - a)^T M(\ddot{q} - a)\,, \tag{31.4}$$

Gauss's Principle of Least Constraint states that the acceleration of the constrained system $\ddot{q}$ minimizes G subjected to a system of constraints

$$A(q(t), \dot{q}(t))\, \ddot{q}(t) = B(q(t), \dot{q}(t), t). \tag{31.5}$$

This simple minimization of a quadratic objective subject to a set of linear equality constraints is easily accomplished using Lagrange multipliers. The augmented objective is

$$G_A = \frac{1}{2}\ddot{q}^T M\ddot{q} - a^T M\ddot{q} + \frac{1}{2}a^T Ma + \lambda^T(A\ddot{q} - B) \tag{31.6}$$

and the necessary and sufficient conditions for optimality are

$$\frac{\partial G_A}{\partial \ddot{q}} = 0: \quad M\ddot{q} - F + A^T\lambda = 0 \tag{31.7}$$

$$\frac{\partial G_A}{\partial \lambda} = 0: \qquad A\ddot{q} - B = 0 \tag{31.8}$$

The constraint forces are obtained from the Lagrange multipliers as $F^c = -A^T\lambda$.

31.4 The Unconstrained Dynamics

Lagrange's equations are used here to derive the unconstrained equations of motion.

$$\frac{d}{dt}\left(\frac{\partial T}{\partial \dot{q}_j}\right) - \frac{\partial T}{\partial q_j} + \frac{\partial V}{\partial q_j} = 0 \tag{31.9}$$

where T is the kinetic energy, V is the potential energy, and q_j is a generalized coordinate. We model this system with a set of 15 independent coordinates

$$q_j \in \{X,\ Y,\ \theta,\ r_1,\ r_2,\ r_3,\ r_4,\ x_1,\ y_1,\ x_2,\ y_2,\ x_3,\ y_3,\ x_4,\ y_4\}$$

where X, Y, and θ give the translation of the platform and its rotation about a vertical axis; and x_i, y_i, and r_i give the location of the ith ball with respect to its dish center. With this definition of independent coordinates, many of the partial derivatives used in the following derivations simplify to zero:

$$\frac{\partial r_i}{\partial x_i} = 0; \quad \frac{\partial r_i}{\partial y_i} = 0; \quad \frac{\partial \dot{r}_i}{\partial \dot{x}_i} = 0; \quad \frac{\partial \dot{r}_i}{\partial \dot{y}_i} = 0.$$

Derivatives related to the vertical component of motion of the ith ball are

$$\frac{d}{dt}h_i = \dot{h}_i = h_i'\dot{r}_i; \quad \frac{\partial h_i'}{\partial r_i} = h_i''; \quad \frac{d}{dt}(h_i') = h_i''\dot{r}_i; \quad \ddot{h}_i = h_i'\ddot{r}_i; \quad \frac{d}{dt}(h_i'\dot{r}_i) = h_i''\dot{r}_i^2 + h_i'\ddot{r}_i;$$

$$\frac{\partial \dot{h}_i}{\partial r_i} = h_i''\dot{r}_i; \quad \frac{\partial \dot{h}_i}{\partial x_i} = h_i''\dot{r}_i\frac{\partial r_i}{\partial x_i} = 0; \quad \frac{\partial \dot{h}_i}{\partial y_i} = h_i''\dot{r}_i\frac{\partial r_i}{\partial y_i} = 0; \quad \frac{\partial \dot{h}_i}{\partial \dot{r}_i} = h_i';$$
$$\frac{\partial \dot{h}_i}{\partial \dot{x}_i} = h_i'\frac{\partial \dot{r}_i}{\partial \dot{x}_i} = 0; \quad \frac{\partial \dot{h}_i}{\partial \dot{y}_i} = h_i'\frac{\partial \dot{r}_i}{\partial \dot{y}_i} = 0$$

The potential energy is found from $V = mg\bar{h}$ where $\bar{h}$ is the change in height of the platform at the center of mass. Since there are four balls at equal distance from the geometric center (the assumed center of mass), $\bar{h} = \frac{1}{4}(h_1 + h_2 + h_3 + h_4)$ and the potential energy is

$$V = mg\frac{1}{4}(h_1 + h_2 + h_3 + h_4) \tag{31.10}$$

The partial derivative of the potential energy with respect to the coordinates q_j are

$$\frac{\partial V}{\partial X} = 0; \quad \frac{\partial V}{\partial Y} = 0; \quad \frac{\partial V}{\partial \theta} = 0; \quad \frac{\partial V}{\partial r_i} = \frac{1}{4}mgh_i'; \quad \frac{\partial V}{\partial x_i} = 0; \quad \frac{\partial V}{\partial y_i} = 0. \tag{31.11}$$

The kinetic energy involves components of the platform velocity in the X, Y, Z, and θ directions. The vertical velocity of the center of mass is approximated as the weighted average of the vertical velocity of the four balls. The response velocities $\dot{X}$, $\dot{Y}$, $\dot{Z}$, and $\dot{\theta}$ are *relative* to the moving floor, which has velocities $\dot{w}_x, \dot{w}_y, \dot{w}_z$ with respect to the inertial reference frame. So the kinetic energy of all components of the total velocities is

$$T = \frac{1}{2}m\left((\dot{X} + \dot{w_x})^2 + (\dot{Y} + \dot{w_y})^2 + \left(\frac{1}{4}(\dot{h}_1 + \dot{h}_2 + \dot{h}_3 + \dot{h}_4) + \dot{w}_z\right)^2\right) + \frac{1}{2}J\dot{\theta}^2 \tag{31.12}$$

The partial derivatives $\partial T/\partial q_j$ are

$$\frac{\partial T}{\partial X} = 0; \quad \frac{\partial T}{\partial Y} = 0; \quad \frac{\partial T}{\partial \theta} = 0; \quad \frac{\partial T}{\partial r_i} = \frac{1}{4}m\left(\frac{1}{4}(\dot{h}_1 + \dot{h}_2 + \dot{h}_3 + \dot{h}_4) + \dot{w}_z\right)h_i''\dot{r}_i;$$
$$\frac{\partial T}{\partial x_i} = 0; \quad \frac{\partial T}{\partial y_i} = 0. \tag{31.13}$$

The partial derivatives $\partial T/\partial \dot{q}_j$ are

$$\frac{\partial T}{\partial \dot{X}} = m(\dot{X} + \dot{w_x}); \quad \frac{\partial T}{\partial \dot{Y}} = m(\dot{Y} + \dot{w_y}); \quad \frac{\partial T}{\partial \dot{\theta}} = J\dot{\theta}; \tag{31.14}$$

$$\frac{\partial T}{\partial \dot{r}_i} = \frac{1}{4}m\left(\frac{1}{4}(\dot{h}_1 + \dot{h}_2 + \dot{h}_3 + \dot{h}_4) + \dot{w}_z\right)h_i'; \tag{31.15}$$

$$\frac{\partial T}{\partial \dot{x}_i} = 0; \quad \frac{\partial T}{\partial \dot{y}_i} = 0. \tag{31.16}$$

And the time derivatives are

$$\frac{d}{dt}\left(\frac{\partial T}{\partial \dot{X}}\right) = m(\ddot{X} + \ddot{w}_x); \quad \frac{d}{dt}\left(\frac{\partial T}{\partial \dot{Y}}\right) = m(\ddot{Y} + \ddot{w}_y); \quad \frac{d}{dt}\left(\frac{\partial T}{\partial \dot{\theta}}\right) = J\ddot{\theta}; \tag{31.17}$$

$$\frac{d}{dt}\left(\frac{\partial T}{\partial \dot{r}_i}\right) = \frac{1}{4}m\left(\frac{1}{4}(\dot{h}_1 + \dot{h}_2 + \dot{h}_3 + \dot{h}_4) + \dot{w}_z\right) h_i'' \dot{r}_i \tag{31.18}$$

$$+ \frac{1}{4}mh_i'\left(\frac{1}{4}(h_1''\dot{r}_1^2 + \cdots + h_4''\dot{r}_4^2 + h_1'\ddot{r}_1 + \cdots + h_4'\ddot{r}_4) + \ddot{w}_z\right) \tag{31.19}$$

$$\frac{d}{dt}\left(\frac{\partial T}{\partial \dot{x}_i}\right) = 0; \quad \frac{d}{dt}\left(\frac{\partial T}{\partial \dot{y}_i}\right) = 0. \tag{31.20}$$

Applying Lagrange's equation (31.9), the equations of motion for the unconstrained dynamics are found

$$m(\ddot{X} + \ddot{w}_x) = 0; \quad m(\ddot{Y} + \ddot{w}_y) = 0; \quad J\ddot{\theta} = 0; \tag{31.21}$$

$$\begin{aligned}
&\frac{1}{4}m\left(\frac{1}{4}(\dot{h}_1 + \cdots + \dot{h}_4) + \dot{w}_z\right) h_i'' \dot{r}_i \\
&+\frac{1}{4}mh_i'\left(\frac{1}{4}(h_1''\dot{r}_1^2 + \cdots + h_4''\dot{r}_4^2 + h_1'\ddot{r}_1 + \cdots + h_4'\ddot{r}_4) + \ddot{w}_z\right) \\
&-\frac{1}{4}m\left(\frac{1}{4}(\dot{h}_1 + \cdots + \dot{h}_4) + \dot{w}_z\right) h_i'' \dot{r}_i + \frac{1}{4}mgh_i' = 0
\end{aligned} \tag{31.22}$$

Note that the first and third terms of Eq. (31.22) exactly negate each other. Factoring out $(m/16)$ we obtain simplified unconstrained equations of motion for the four balls

$$(h_i'h_1'\ddot{r}_1 + \cdots + h_i'h_4'\ddot{r}_4) + (h_i'h_1''\dot{r}_1^2 + \cdots + h_i'h_4''\dot{r}_4^2) + 4gh_i' = -4h_i'\ddot{w}_z \tag{31.23}$$

however in the following we retain the $(m/16)$ factor in order to preserve the relative scaling of the unconstrained equations of motion and the constraints and to preserve the physical interpretation of the constraint forces F^c. These unconstrained equations are linear in the accelerations

$$M\,a = F \tag{31.24}$$

where

$$M = \begin{bmatrix}
m & 0 & 0 & 0 & 0 & 0 & 0 & \\
0 & m & 0 & 0 & 0 & 0 & 0 & \\
0 & 0 & J & 0 & 0 & 0 & 0 & \\
0 & 0 & 0 & \frac{mh_1'h_1'}{16} & \frac{mh_1'h_2'}{16} & \frac{mh_1'h_3'}{16} & \frac{mh_1'h_4'}{16} & 0_{7\times 8} \\
0 & 0 & 0 & \frac{mh_2'h_1'}{16} & \frac{mh_2'h_2'}{16} & \frac{mh_2'h_3'}{16} & \frac{mh_2'h_4'}{16} & \\
0 & 0 & 0 & \frac{mh_3'h_1'}{16} & \frac{mh_3'h_2'}{16} & \frac{mh_3'h_3'}{16} & \frac{mh_3'h_4'}{1} & \\
0 & 0 & 0 & \frac{mh_4'h_1'}{16} & \frac{mh_4'h_2'}{16} & \frac{mh_4'h_3'}{16} & \frac{mh_4'h_4'}{16} & \\
 & & & & 0_{8\times 7} & & & 0_{8\times 8}
\end{bmatrix} \tag{31.25}$$

and

$$F = \begin{Bmatrix} -m\ddot{w}_x \\ -m\ddot{w}_y \\ 0 \\ -\frac{1}{4}m(\frac{1}{4}(h_1'h_1''\dot{r}_1^2 + \cdots + h_1'h_4''\dot{r}_4^2) - h_1'\ddot{w}_z - gh_1') \\ -\frac{1}{4}m(\frac{1}{4}(h_2'h_1''\dot{r}_1^2 + \cdots + h_2'h_4''\dot{r}_4^2) - h_2'\ddot{w}_z - gh_2') \\ -\frac{1}{4}m(\frac{1}{4}(h_3'h_1''\dot{r}_1^2 + \cdots + h_3'h_4''\dot{r}_4^2) - h_3'\ddot{w}_z - gh_3') \\ -\frac{1}{4}m(\frac{1}{4}(h_4'h_1''\dot{r}_1^2 + \cdots + h_4'h_4''\dot{r}_4^2) - h_4'\ddot{w}_z - gh_4') \\ 0_{8\times 1} \end{Bmatrix} \tag{31.26}$$

The matrix M is non-negative definite and depends on the coordinate positions, but not their velocities. The vector F depends on positions, velocities, and time. These unconstrained dynamics describe the motions of the four balls and the platform separately. In this system the platform motion is decoupled from the ball motion (this coupling will enter as a constraint) and the ball motions are all inter-related, despite the fact that the platform is not yet explicitly coupled to the ball motions. Further, note that the ball motions are described as rectilinear radial motions only, r_i; the x_i and y_i components of the ball motions can not be determined by these unconstrained system dynamics. Also note that if the vertical component of the platform velocity, $\dot{h}$, were neglected in the expression for the kinetic energy, then $\partial T/\partial r_i = 0$, $\partial T/\partial \dot{r}_i = 0$, and the unconstrained equations of motion of the (assumed massless) balls would simply be $mgh_i' = 0$. By including the vertical component of platform's velocity as a weighted average of the ball heights, $\dot{h}_i$, we obtain a coupling between the radial dynamics of the motions of all four balls. Without constraints linking the ball velocities and the platform velocities, these unconstrained equations of motion have little physical significance.

31.5 The Constraints and the True Equations of Constrained Motion

This model involves two types of constraints. The first constraint is the relationship between x_i, y_i, and r_i.

$$r_i^2 = x_i^2 + y_i^2 \tag{31.27}$$

The second is the nonholonomic relationship between the platform motion $\dot{X}, \dot{Y}.\dot{\theta}$ and the ball motion $\dot{x}_i$, $\dot{y}_i$. Let $a_i = a, -a, -a, a$ for $i = 1, 2, 3, 4$ and let $b_i = b, b, -b, -b$ for $i = 1, 2, 3, 4$. Let $c = \cos(\theta)$ and $s = \sin(\theta)$. The two constraint equations for each ball prescribe how the velocity of the platform determines the velocities of each ball

$$\dot{x}_i = \frac{1}{2}\left(\dot{X} + \dot{\theta}(-a_i s - b_i c)\right) \qquad \dot{y}_i = \frac{1}{2}\left(\dot{Y} + \dot{\theta}(a_i c - b_i s)\right) \tag{31.28}$$

The factor of (1/2) indicates that the velocity of the center of the ball is half of the velocity of the top of the ball (the point on the ball where the rolling horizontal platform rests). This is not precisely correct. Because the lower rolling surface (the dish) is sloped, the true value of this factor is slightly less than (1/2). By differentiating the constraints, they can be expressed in a form that is linear in the accelerations:

$$r_i\dot{r}_i = x_i\dot{x}_i + y_i\dot{y}_i \tag{31.29}$$

$$r_i\ddot{r}_i = x_i\ddot{x}_i + \dot{x}_i{}^2 + y_i\ddot{y}_i + \dot{y}_i^2 - \dot{r}_i^2 \tag{31.30}$$

$$\ddot{x}_i = \frac{1}{2}\left(\ddot{X} + \ddot{\theta}(-a_i s - b_i c)\right) + \frac{1}{2}\dot{\theta}(-a_i c\dot{\theta} + b_i s\dot{\theta}) \tag{31.31}$$

$$\ddot{y}_i = \frac{1}{2}\left(\ddot{Y} + \ddot{\theta}(a_i c - b_i s)\right) + \frac{1}{2}\dot{\theta}(-a_i s\dot{\theta} - b_i c\dot{\theta}) \tag{31.32}$$

or

$$A\,\ddot{q} = B \tag{31.33}$$

where

$$A = \begin{bmatrix} -1 & 0 & -as-bc & 0 & 0 & 0 & 0 & 2 & 0 & 0 & 0 & 0 & 0 & 0 & 0 \\ 0 & -1 & ac-bs & 0 & 0 & 0 & 0 & 0 & 2 & 0 & 0 & 0 & 0 & 0 & 0 \\ -1 & 0 & as-bc & 0 & 0 & 0 & 0 & 0 & 0 & 2 & 0 & 0 & 0 & 0 & 0 \\ 0 & -1 & ac-bs & 0 & 0 & 0 & 0 & 0 & 0 & 0 & 2 & 0 & 0 & 0 & 0 \\ -1 & 0 & as+bc & 0 & 0 & 0 & 0 & 0 & 0 & 0 & 0 & 2 & 0 & 0 & 0 \\ 0 & -1 & -ac+bs & 0 & 0 & 0 & 0 & 0 & 0 & 0 & 0 & 0 & 2 & 0 & 0 \\ -1 & 0 & -as+bc & 0 & 0 & 0 & 0 & 0 & 0 & 0 & 0 & 0 & 0 & 2 & 0 \\ 0 & -1 & ac+bs & 0 & 0 & 0 & 0 & 0 & 0 & 0 & 0 & 0 & 0 & 0 & 2 \\ 0 & 0 & 0 & -r_1 & 0 & 0 & 0 & x_1 & y_1 & 0 & 0 & 0 & 0 & 0 & 0 \\ 0 & 0 & 0 & 0 & -r_2 & 0 & 0 & 0 & 0 & x_2 & y_2 & 0 & 0 & 0 & 0 \\ 0 & 0 & 0 & 0 & 0 & -r_3 & 0 & 0 & 0 & 0 & 0 & x_3 & y_3 & 0 & 0 \\ 0 & 0 & 0 & 0 & 0 & 0 & -r_4 & 0 & 0 & 0 & 0 & 0 & 0 & x_4 & y_4 \end{bmatrix} \tag{31.34}$$

and

$$B = \begin{Bmatrix} \dot{\theta}^2(-ac+bs) \\ \dot{\theta}^2(-as-bc) \\ \dot{\theta}^2(ac+bs) \\ \dot{\theta}^2(as-bc) \\ \dot{\theta}^2(ac-bs) \\ \dot{\theta}^2(as+bc) \\ \dot{\theta}^2(-ac-bs) \\ \dot{\theta}^2(-as+bc) \\ -\dot{x_1}^2 - \dot{y_1}^2 + \dot{r}_1^2 \\ -\dot{x_2}^2 - \dot{y_2}^2 + \dot{r}_2^2 \\ -\dot{x_3}^2 - \dot{y_3}^2 + \dot{r}_3^2 \\ -\dot{x_4}^2 - \dot{y_4}^2 + \dot{r}_4^2 \end{Bmatrix} \tag{31.35}$$

The matrix A depends only upon the coordinate positions and the vector B depends on positions and velocities. Following Gauss's Principle of Least Constraint, we minimize G with respect to $\ddot{q}$ such that $A\ddot{q} = B$ to obtain the constrained equations of motion

$$\begin{bmatrix} M & A^T \\ A & 0 \end{bmatrix} \begin{Bmatrix} \ddot{q} \\ \lambda \end{Bmatrix} = \begin{Bmatrix} F \\ B \end{Bmatrix} \tag{31.36}$$

Note that the solution to this equation ($\ddot{q}$ and λ) is defined and unique as long as the range space of A spans the null space of M. This condition is satisfied whether or not we include the vertical component of the platform velocity in the kinetic energy.

31.6 Simulation

We use numerical transient-response simulation to demonstrate that (in the absence of any modeled damping and any external forcing) these equations of motion conserve energy. In running any transient response simulation of the equations of motion described by Gauss's Principle, the initial conditions must satisfy the constraints. Positions and velocities of the 15 coordinates $X = 0.01$ $Y = 0.01$ $\theta = 0$ $\dot{X} = 0.07$ $\dot{Y} = 0.05$ $\dot{\theta} = 0$ $x_1 = 0.04$ $x_2 = 0.05$ $x_3 = 0.01$ $x_4 = 0.04$ $y_1 = 0.01$, $y_2 = 0.01$, $y_3 = 0.03$ and $y_4 = 0.04$. $r_i, \dot{x}_i, \dot{y}_i$ and $\dot{r}_i$ are related by Eqs. (31.27)–(31.29). If the initial conditions fail to satisfy the constraints, the ensuing responses do not conserve energy. The simulation shows each ball movement, the platform movement, and the conservation of energy. The simulation was ran using free response ($\ddot{w}_x, \ddot{w}_y, \ddot{w}_z = 0$) and non-zero initial displacements of the platform (X, Y, θ) and the ball locations x_i and y_i. The platform movement and the individual ball movements are shown in Figs. 31.1 and 31.2. The kinetic and potential energies, and their sum, are shown in Fig. 31.3.

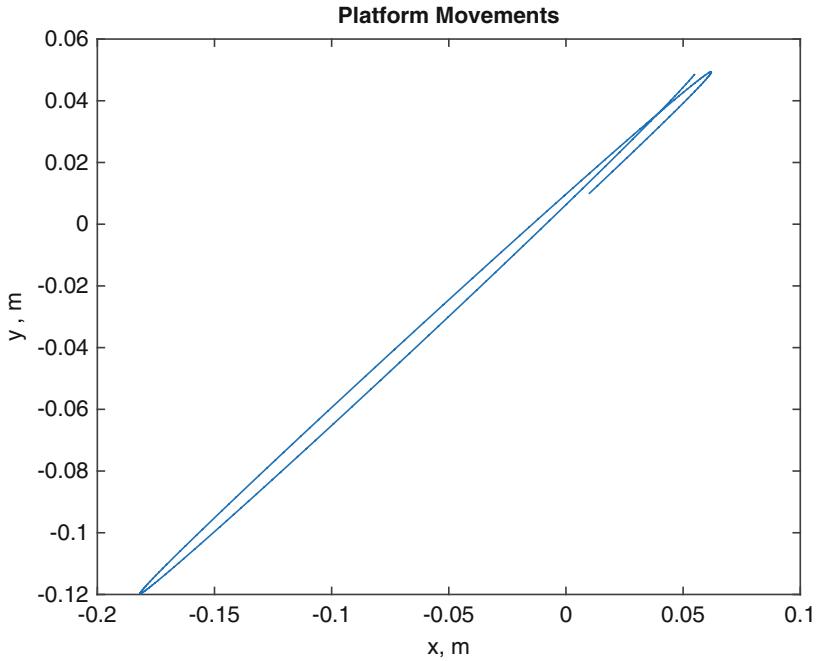

Fig. 31.1 Trajectory of the motion of the platform center

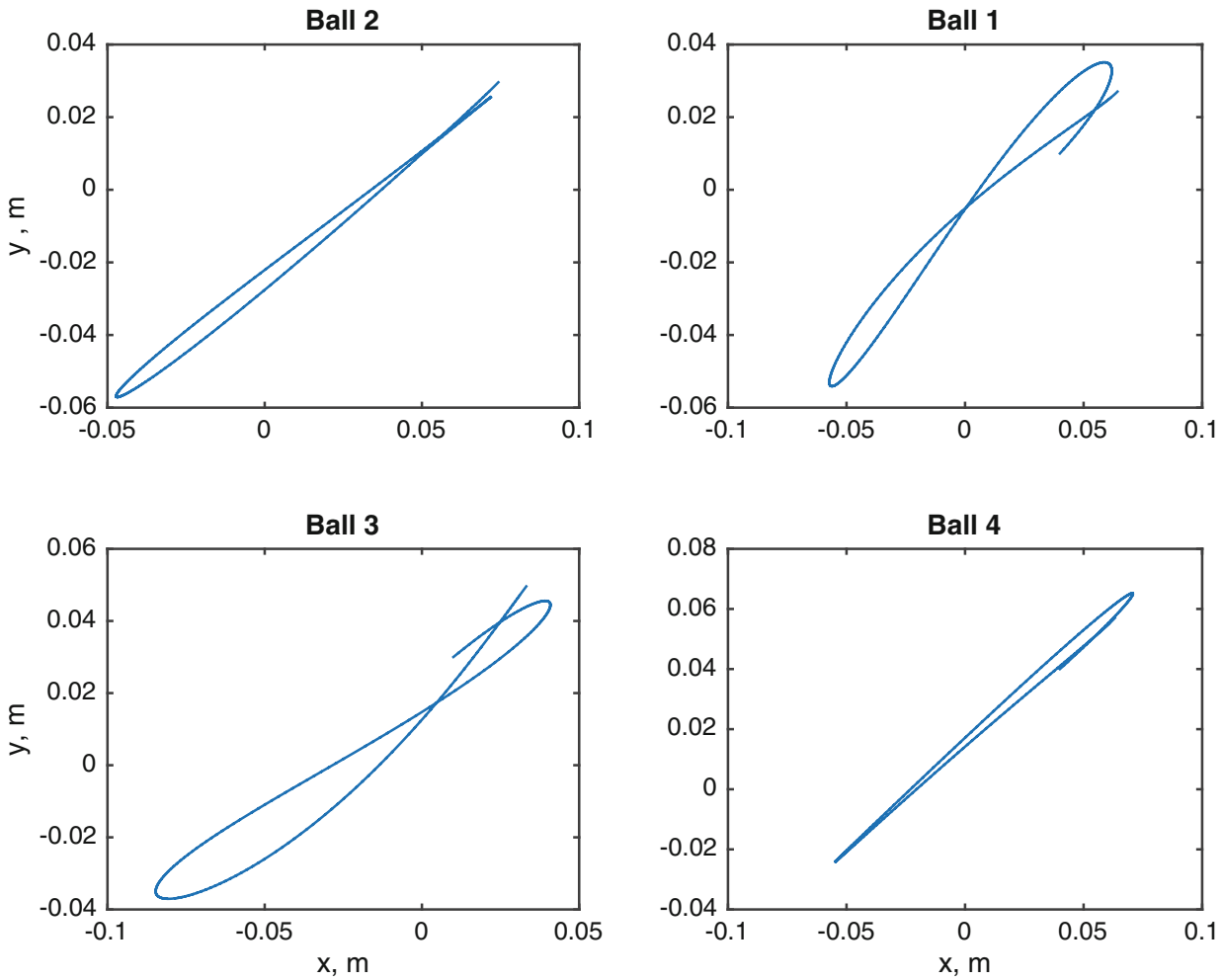

Fig. 31.2 Ball position trajectories

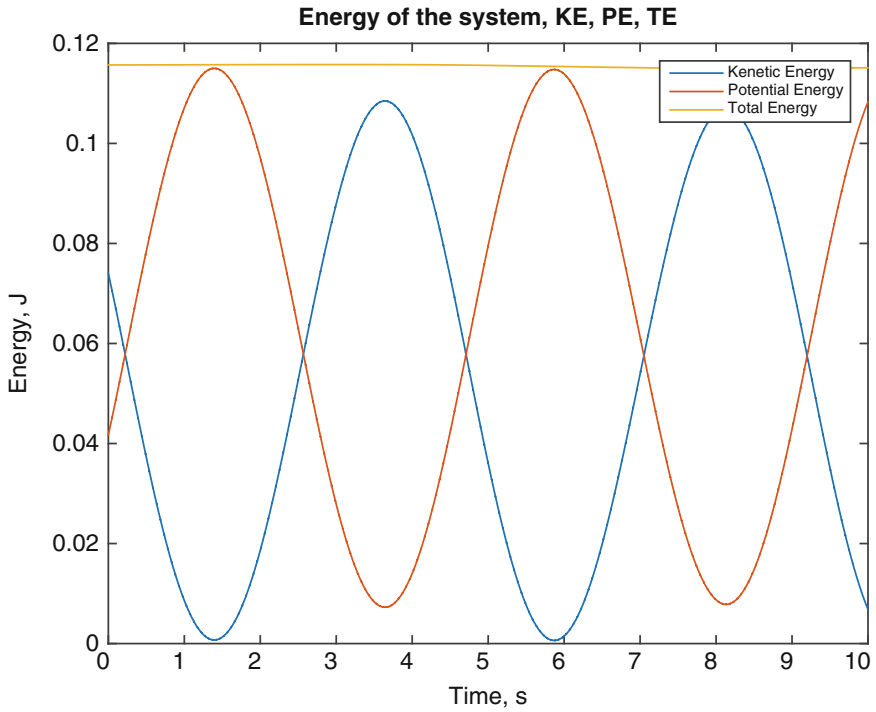

Fig. 31.3 Kinetic, potential and total energies in the system. The total energy is conserved

31.7 Conclusion

This paper illustrates the application of Gauss's Principle of Least Constraint to the modeling of a rolling isolation system. This approach to modeling the dynamics of constrained systems requires no distinction between the classification of constraints (e.g., holonomic or nonholonomic). The equations of motion for the unconstrained system are derived without regard for the constraints. The constraints are adjoined to a weighted quadratic objective minimizing the difference between the unconstrained and the constrained accelerations, and the saddle point of the adjoined system determines the equations of motion. Free response simulations of these equations of motion show that, in the absence of damping and external forcing, the total energy of this system is conserved.

Acknowledgements This material is based in part upon work supported by the National Science Foundation under Grant Number CMMI-1436015. Any opinions, findings, and conclusions or recommendations expressed in this material are those of the author(s) and do not necessarily reflect the views of the National Science Foundation.

References

1. Harvey, P.S., Jr., Gavin, H.P.: The nonholonomic and chaotic nature of a rolling isolation system. J. Sound Vib. **332**(14), 3535–3551 (2013)
2. Harvey, P.S., Jr., Wiebe, R., Gavin, H.P.: On the chaotic response of a nonlinear rolling isolation system. Phys. D Nonlinear Phenom. **256**, 36–42 (2013)
3. Hofrath, Gauss, C.F.: Über ein Neues Allgemeines Grundgesatz der Mechanik. J. Reine Angew. Math. **44**, 232–235 (1829)
4. Udwadia, F.E., Robert, E.G.: A new perspective on constrained motion. Proc. Math. Phys. Sci. **439**, 407–410 (1992)

Chapter 32
Parameter Estimation on Nonlinear Systems Using Orthogonal and Algebraic Techniques

L.G. Trujillo-Franco, G. Silva-Navarro, and F. Beltrán-Carbajal

Abstract High displacements, geometrical restrictions and complex behavior are now common in modern mechanical structures involving new materials with inherent nonlinear phenomena (e.g., stiffness, damping and excitation). In this work, we propose a novel parameter identification scheme based on signal approximation via orthogonal functions. A Hilbert transform based nonlinearity index is calculated in order to evaluate possible nonlinearities appearing into the system dynamics and then we compute the algebraic estimation of the most important parameters into the nonlinear system. We use algebraic identification techniques based on the Mikusinski's approach to operational calculus, The proposed approach is first developed for single degree-of-freedom systems and then this is generalized for some case studies considering multiple degrees-of-freedom, by using information obtained from variations in the initial conditions (free response) to get the so-called eigenstructure. The approach is validated by means of numerical simulations and experimental results.

Keywords Nonlinear mechanical systems • System identification • Algebraic identification • Orthogonal functions • Signals approximation

32.1 Introduction

In the area of system parameters identification is quite common to question about the influence of inherent nonlinearities into the system on the overall global performance of the methods used during the identification process. Historically the assumption of linear behavior on mechanical system under analysis has been an object of both, questions about the accuracy of the identified parameters and, on the other hand, a widespread acceptance specifically because of the relative simplicity besides the easy and fast application of the numerical methods involved in the process. Finally, when assuming linear behavior on the system, then it is possible to use basic approaches like least squares and autoregressive models for control purposes [6]. Despite of the numerous advantages of the linearity assumption on mechanical systems, there exist cases where the linear methods are ineffective or inoperative [2, 4, 10, 11].

In the last few decades, the interest of the structural and mechanical engineers has focused on the comprehension and prediction of the dynamic behavior on specific systems and structures, whose dynamics is inherently nonlinear, perhaps due to new characteristics of the construction materials or, in other cases, the geometry used for the basic entities or elements. This could be the case in recent engineering applications using modern structures, mechanisms and/or materials. For instance, large and lighter structures constructed with composite materials like honey comb panels and others [4, 11]. Parallel to this, the evident developments in computing sciences nowadays open the doors to the possibility of applying novel, sophisticated and previously unacceptable/complicated identification schemes, for mechanical systems.

In this work, we present a set of mathematical tools like Mikusinski's operational calculus, orthogonal functions signal approximation, algebraic identification and Hilbert transforms, working systematically to determine the parameters of a mechanical system given its free vibration response.

L.G. Trujillo-Franco (✉) • G. Silva-Navarro
Departamento de Ingeniería Eléctrica, Centro de Investigación y de Estudios Avanzados del I.P.N. Sección de Mecatrónica, Av. IPN No. 2508, Col. S.P. Zacatenco, C.P. 07360 México, D.F., Mexico
e-mail: ltrujillo@cinvestav.mx; gsilva@cinvestav.mx

F. Beltrán-Carbajal
Departamento de Energía, Universidad Autónoma Metropolitana, Unidad Azcapotzalco, Av. San Pablo No. 180, Col. Reynosa Tamaulipas, C.P. 02200 México, D.F., Mexico
e-mail: fbeltran@correo.azc.uam.mx

G. Kerschen (ed.), *Nonlinear Dynamics, Volume 1*, Conference Proceedings of the Society for Experimental Mechanics Series,
DOI 10.1007/978-3-319-29739-2_32

32.2 Nonlinear Vibrating Mechanical System

Consider the vibrating mechanical system shown in Fig. 32.1, where x is the displacement of the mass over one axis, m, k and c denote mass, stiffness and viscous damping associated to this single degree-of-freedom (SDOF) and the nonlinearities like dry friction and polynomial stiffness are concentrated into the function $q_{nl}\left(x,\dot{x}\right)$.

We can express the mathematical model of this flexible mechanical system by the ordinary differential equation

$$m\ddot{x} + c\dot{x} + kx + q_{nl}\left(x,\dot{x}\right) = f(t), \qquad x \in R \tag{32.1}$$

where $q_{nl}\left(\cdot\right)$ is a nonlinear restoring force function, possibly depending on the displacement and velocity of the mechanical system. Here the dynamic response of the linear part is determined for the parameters m, c and k whose are mass damping and stiffness respectively, the nonlinear restoring force $q_{nl}\left(x,\dot{x}\right)$ take a structure such that it contains the sum of nonlinearities like dry friction, nonlinear damping and some kind of polynomial stiffness as follows [10, 11]:

$$q_{nl}\left(x,\dot{x}\right) = k_p x^3 + f_d sign(x) + c_d sign\left(\dot{x}\right) \tag{32.2}$$

Here k_p is the cubic stiffness constant and f_d and c_d are Coulomb dry friction and nonlinear damping constants, respectively.

In previous works a time domain scheme for system parameter identification has been proposed, which involves the use of operational calculus for the algebraic manipulation of the differential equation [5, 9]. The proposed algebraic scheme allows getting, in a time domain and in an on-line fashion, fast estimations of the unknown system parameters, by using measurements of the system output and input.

Now, consider the mechanical vibrating system (32.1), where the function $q_{nl}\left(x,\dot{x}\right)$ is nonlinear. There is not a direct expression for it in terms of operational calculus, however, we can multiply Eq. (32.1) by $(\Delta t)^2 = (t-t_0)^2$ and integrate by parts two times with respect to the time, without affecting the expression, and then we have that

$$\begin{aligned} m\left(2\int_{t_0}^{(2)} x - 4\int_{t_0}(\Delta t)\,x + (\Delta t)^2 x\right) + c\left(-2\int_{t_0}^{(2)}(\Delta t)\,x + \int_{t_0}(\Delta t)^2 x\right) + k\int_{t_0}^{(2)}(\Delta t)^2 x \\ + \int_{t_0}^{(2)}(\Delta t)^2 q_{nl}\left(x,\dot{x}\right) = \int_{t_0}^{(2)}(\Delta t)^2 f(t) \end{aligned} \tag{32.3}$$

where $\Delta t = t - t_0$ and ${}_{t_0}^{(n)}\phi(t)$ are iterated integrals of the form ${}_{t_0}^{t}{}_{t_0}^{\sigma_1}\cdots{}_{t_0}^{\sigma_{n-1}}\phi\left(\sigma_n\right)d\sigma_n\cdots d\sigma_1$ with ${}_{t_0}^{(1)}\phi(t) = {}_{t_0}^{t}\phi\left(\sigma\right)d\sigma$, ${}_{t_0}^{(0)}\phi(t) = \phi(t)$ and n is a positive integer. Note that, this expression does not depend on the system initial conditions of any involved function. Here, we have an algebraic expression for the system parameters m, c, k, and the coefficients k_p, f_d, f_c, which appears algebraically in the nonlinear function $q_{nl}\left(x,\dot{x}\right)$ [5]. Notice also that, the identification of the system parameters is achieved by the algebraic manipulation of Eq. (32.3), in order to express these parameters by a system of equations or a similar expression, whose solution is precisely the set of unknown terms [9]. In fact, a set of functions are called orthogonal in the closed interval $[a,b]$ if they satisfy:

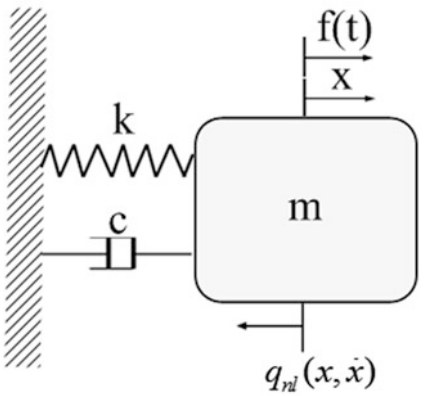

Fig. 32.1 Schematic diagram of a nonlinear SDOF system

$$\begin{aligned}\int_a^b \phi_i(t)\phi_j(t) &= 0 \text{ if } i \neq j \\ \int_a^b \phi_i(t)\phi_j(t) &= \text{constant} \neq 0 \text{ if } i = j\end{aligned} \tag{32.4}$$

It is well known that, in a certain interval, it is possible to approximate a given function by a finite sum of orthogonal functions. The orthogonal functions approximation of the integrands in Eq. (32.3) by a sum of r orthogonal functions is given by:

$$\begin{aligned}\Delta t^p x(t) &\cong X_{l(1,r)}\phi(t)_{(1,r)} \\ \Delta t^2 x(t) &\cong F_{(1,r)}\phi(t)_{(1,r)} \\ \Delta t^2 q_{nl}\left(x, \dot{x}\right) &\cong Q_{(1,r)}\phi(t)_{(1,r)}\end{aligned} \tag{32.5}$$

where $l = 0, 1, 2$. Here, X, Q and F are constant vectors with coefficients of the orthogonal functions approximation of the integrands. Here, the approximated function $Q_{(1,r)}\phi(t)_{(1,r)}$ has the following structure:

$$Q_{(1,r)}\phi(t)_{(1,r)} = k_p x_{3(1,r)} + f_{ds} s_{x(1,r)} + c_d s_{dx(1,r)} \tag{32.6}$$

with the independent approximations x_3, s_x and s_{dx} given by:

$$\begin{aligned}\Delta t^2 x^3 &\cong x_{3(1,r)} = X_{3(1,r)}\phi(t)_{(1,r)} \\ \Delta t^2 sign(x) &\cong s_{dx(1,r)} = S_{dx(1,r)}\phi(t)_{(1,r)} \\ \Delta t^2 sign(x) &\cong s_{x(1,r)} = S_{x(1,r)}\phi(t)_{(1,r)}\end{aligned} \tag{32.7}$$

As reported in [1], the orthogonal functions signal approximation is useful for the solution of integral equations due to the property which allows to compute the iterated numerical integration, as defined by the following matrix expression:

$$\int_{t0}^{(n)} \phi(\tau) d\tau^n \cong P^n \phi(t) \tag{32.8}$$

where $P \in R^{r\times r}$ is the so-called operational matrix of integration with constant elements, whose values depend on the orthogonal basis used, $\phi \in R^r$ is a vector called the basis of the orthogonal series. In [8], a unified method for the operational matrix of integration computing is reported for the most popular orthogonal functions basis for signal approximation and, therefore, we can compute numerically the iterated integral using this property. The substitution of Eq. (32.6) in Eq. (32.3) yields to:

$$m\left(2X_0\phi(t)P^2 - 4X_1\phi(t)P + X_2\phi(t)\right) + c\left(-2X_1\phi(t)P^2 + X_2\phi(t)P\right) + kX_2\phi(t)P^2 + Q_{nl}\phi(t)P^2 = F\phi(t)P^2 \tag{32.9}$$

Since we use a given orthogonal basis $\phi(t)$ we can equate this coefficients, so that, using Eqs. (32.7) and (32.8), we can obtain the following matrix equation:

$$\left[m, c, k, k_p, f_c, f_d\right]\begin{bmatrix} 2X_0P - 4X_1P + X_2 \\ -2X_1P^2 + X_2P \\ X_2P^2 \\ X_3P^2 \\ S_{dx}P^2 \\ S_xQP \end{bmatrix} = \left[FP^2\right] \tag{32.10}$$

Now, let us define

$$[\Theta]^T = \left[m, c, k, k_p, f_c, f_d\right], \quad [A] = \begin{bmatrix} 2X_0P - 4X_1P + X_2 \\ -2X_1P^2 + X_2P \\ X_2P^2 \\ X_3P^2 \\ S_{dx}P^2 \\ S_xQP \end{bmatrix}, \quad B = \left[FP^2\right] \tag{32.11}$$

Thus, in a more compact form, we can also write:

$$[\Theta]^T [A] = [B] \tag{32.12}$$

This last expression constitutes the algebraic problem for parameter identification, solved by using singular value decomposition, which allows introducing the concept of pseudo-inverse matrix, in order to solve the algebraic problem for the vector, as follows:

$$[\Theta] = [B] [A]^T \left([A] [A]^T\right)^{-1} \tag{32.13}$$

Notice that, the extension for multiple degrees of freedom (MDOF) systems is also possible by substituting the signals, $x \in R$ and $f \in R$, by the corresponding vectors $x \in R^{N_{dof} \times 1}$ and $f \in R^{N_{dof} \times 1}$ with N_{dof} the number of degrees of freedom. Therefore, Eq. (32.14) is still valid, in this new case, for the matrices *M, C, K* and *Q* for the nonlinear terms.

Remark In case of free vibrations (nonzero initial conditions and $f(t) \equiv 0$) this approach allows to determine the eigen-structure of the system and the combined nonlinear restoring force coefficients, that is, one can define: $\frac{c}{m} = 2\zeta\omega_n$, $\frac{k}{m} = {\omega_n}^2$, and $\overline{q}_{nl} = \frac{q_{nl}}{m}$. Thus, the algebraic identification expression for the case of free vibration is:

$$\left[2\zeta\omega_n, {\omega_n}^2, \overline{k}_p, \overline{f}_c, \overline{f}_d\right] \begin{bmatrix} -2X_1P^2 + X_2P \\ X_2P^2 \\ X_3P^2 \\ S_{dx}P^2 \\ S_xQP \end{bmatrix} = [-2X_0P + 4X_1P - X_2] \tag{32.14}$$

where $\overline{k}_p = \frac{k_p}{m}$, $\overline{f}_d = \frac{f_d}{m}$, and $\overline{f}_c = \frac{f_c}{m}$. For n MDOF mechanical systems, under free vibrations, the unknown parameters cannot be identified separately but as a combination of them [1], that is,

$$\left[\overline{C}, \overline{K}, \overline{K}_p, \overline{F}_c, \overline{F}_d\right] \begin{bmatrix} -2X_1P^2 + X_2P \\ X_2P^2 \\ X_3P^2 \\ S_{dx}P^2 \\ S_xQP \end{bmatrix} = [-2X_0P + 4X_1P - X_2] \tag{32.15}$$

where $\overline{C} = M^{-1}C$, $\overline{K} = M^{-1}K$, $\overline{K}_p = M^{-1}K_p$, $\overline{F}_d = M^{-1}F_d$, and $\overline{F}_c = M^{-1}F_c$.

32.3 Nonlinearity Index

From the definition of the Hilbert transform it is derived the Hilbert transform of the frequency response function (FRF) of a given system as follows [4]:

$$H\{G(\omega)\} = -\frac{1}{i\pi} PV \int_{-\infty}^{\infty} \frac{G(\omega)}{\omega - \omega_c} d\omega \tag{32.16}$$

Notice that, the Hilbert transform maps the functions under its action into the same domain. Here PV denotes the Cauchy principal value of the integral, which is needed due to the fact that the integrand has a singularity at $\omega = \omega_c$. Furthermore, when applying the Hilbert transform to a FRF (i.e., $G(\omega)$) the imaginary part and the real part of the FRF are related as follows [10]:

$$\begin{aligned} \mathrm{Re}\{G(\omega)\} &= -\tfrac{1}{i\pi} PV \int_{-\infty}^{\infty} \frac{\mathrm{Im}\{G(\omega)\}}{\omega - \omega_c} d\omega \\ \mathrm{Im}\{G(\omega)\} &= \tfrac{1}{i\pi} PV \int_{-\infty}^{\infty} \frac{\mathrm{Re}\{G(\omega)\}}{\omega - \omega_c} d\omega \end{aligned} \tag{32.17}$$

These relations are referred as the Hilbert transform pairs; nevertheless, for nonlinear systems, this pair is not generally valid and, consequently, the Hilbert transform will return a distorted version of the FRF, so that, in this order of ideas, we have a nonlinearity indicator by analyzing the level of distortion on the original FRF. For this comparison, it is useful to calculate the cross correlation coefficient:

$$\eta_{Hi} = \|R_{HG}(0)\|^2 \tag{32.18}$$

where $\|R_{HG}(0)\|$ is the normalized cross correlation coefficient. Here G is the FRF of the system and H is the Hilbert transform of G and R_{HG} is such that:

$$R_{HG}(\Delta\omega) = \int_{-\infty}^{\infty} H(\omega)\, G(\omega + \Delta\omega)\, d\omega \tag{32.19}$$

This index is an indicator of the system nonlinearity at a specific input amplitude. In this work, we use this index to study the presence of nonlinearities in the system under analysis; such that the most η_{Hi} diverges from 1 the most nonlinear behavior does the system have, that is, for a linear system the expected value of η_{Hi} is precisely 1. Moreover, due to the fact that the Hilbert transform is a numerical method then, this necessarily leads to numerical errors and, as a consequence, we need to consider some kind of linearity criteria. For example, as reported in [4], we can consider a value of $1 \geq \eta_{Hi} \geq 0.9$ for a linearity assumption of the system.

32.4 Some Illustrative Cases

The experimental setup is a rectilinear mechanical plant (Model 210a) provided by *Educational Control Products*®. The mechanical system consists of two mass carriages, interconnected by two nonlinear rubber elastic element springs. Each mass carriage suspension has anti-friction ball bearing systems. Each mass carriage has a (rotary) high-resolution optical encoder to measure its actual positions via cable-pulley systems (with effective resolutions of 2266 pulses/cm or 4.413×10^{-3} mm/pulse). This mechanical plant is easily configurable for 1° of freedom by locking the second mass carriage and decoupling the second non-linear elastic element. The signal and algebraic identification are obtained through a high-speed DSP board into a standard PC running under *Windows XP*® and *Matlab*®*/Simulink*®.

It is important to note that, it is quite difficult to have an experimental estimation of the viscous damping by using conventional techniques like Peak Picking due to the nonlinearities present in this particular system (Table 32.1).

The system response to the sinusoidal swept $f(t) = F \sin(\omega(t)t)$ [N], $\omega(t) = 1.25t$, where the amplitude F is varied (incremental) in an interval $F \in [0.15,\ \ 6.15]$ [N] with 13 different measurements in that interval. The corresponding Nyquist diagrams are shown in Fig. 32.2. Here we can observe a clear distortion on the Hilbert transforms for the original FRF (in blue), which is evident when the amplitude of the excitation force achieves a level of approximately 3 [N]. We have

Table 32.1 Mechanical system parameters for a SDOF configuration

Parameter	Value
m	2.35 kg
c	–
k	1272 N/m
k_p	-1.237×10^6 N/m^3

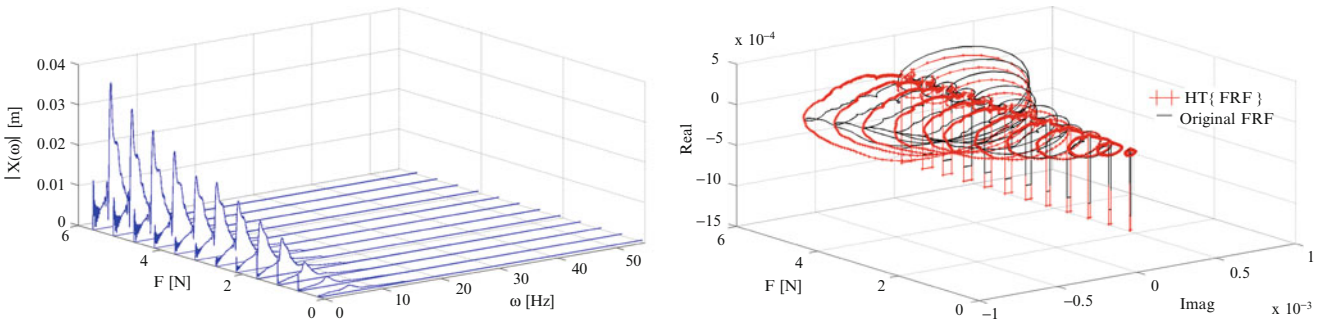

Fig. 32.2 FRF of a SDOF system at different amplitudes and distortions in the Hilbert transform due to the non-linear restoring force

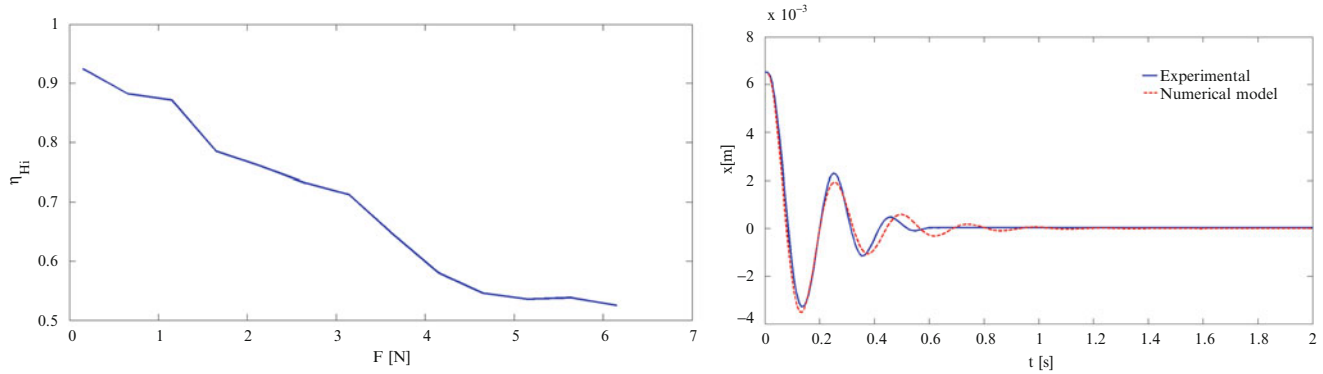

Fig. 32.3 Non-linearity index calculated when $F \in [0.15,\ \ 6.15]$ [N] for SDOF and free vibration response (numerical and experimental) of the mass carriage x

Table 32.2 Mechanical system parameters estimation for SDOF configuration

Parameter	Actual value	Estimated	Difference
$2\zeta\omega_n$	–	4.619	–
${\omega_n}^2$	541.276	529.607	2.15 %
$\overline{k}_p$ (N/m^3)	-5.2638×10^5	-5.0471×10^5	4.2936 %

made the choice of estimating the original FRF using sine swept excitation, because this kind of input to the system allows observing the system dynamic behavior in a more descriptive way, and then we compute the nonlinearity index based on the Hilbert transform as defined in (32.17) and (32.18).

The numerical and experimental transient response for the displacement x is shown in Fig. 32.3. Free vibration response of the first mass carriage x_1, where the initial conditions were $x_1(0) = 0.0065$ m and $\dot{x}_1(0) = 0$ m/s. For identification purposes, we use orthogonal functions signal approximation with the Hartley orthogonal functions basis [8], selected among the possible orthogonal sets, due to its good behavior for estimation purposes (see also [1]). Here we use $r = 100$ with a sampling period of 9 ms. The estimation of the system parameters is summarized in Table 32.2, resulting in reasonable estimated values.

The corresponding configuration for the case of a 2 DOF is shown in Fig. 32.4, while the system parameters for this configuration are those reported in Table 32.3. For the estimation of the eigenestructure of this 2 DOF system, we use the measured displacements x_1 and x_2 resulting from an initial conditions change on the system, corresponding to $x_1(0) = 0.0065$ [m], $x_2(0) = 0.0063$ [m] and $\dot{x}_1(0) = 0$ [m/s] and $\dot{x}_2(0) = 0$ [m/s]. The nonlinearity index as a function of the amplitude for the 2-DOF case is reported in Fig. 32.5, where the free vibration response of the system is also shown (right). By approximating the signals x_1 and x_2 with 100 terms of the Hartley orthogonal basis, as we did before, we obtain the combined system matrices of damping $M^{-1}\,C$, stiffness $M^{-1}\,K$ and polynomial stiffness $M^{-1}\,K_p$, whose values are reported in Table 32.4. Only the corresponding FRF's of the first mass carriage are reported, however, it is quite easy to note that the amplitude interval in which the system behavior is dominantly linear before the input amplitude reaches approximately 4 [N].

Finally, the nonlinearity index and free vibration response of the 2 DOF mechanical system are described in Fig. 32.6, where one can confirm that this system certainly exhibits high nonlinearities as far as the force input is increased.

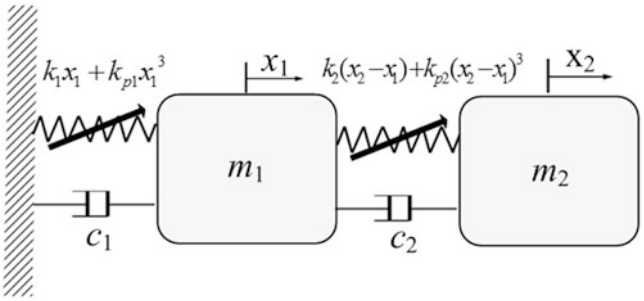

Fig. 32.4 Configuration of a 2 DOF mechanical system

Table 32.3 Mechanical system parameters for 2 DOF

Parameter	Value
m_1 (kg)	2.35
c_1 (Ns/m)	–
k_1 (N/m)	1272.1
k_{p1} (N/m^3)	-1.237×10^6
m_2 (kg)	2.754
c_2 (Ns/m)	–
k_2 (N/m)	1570
k_{p2} (N/m^3)	-1.350×10^6

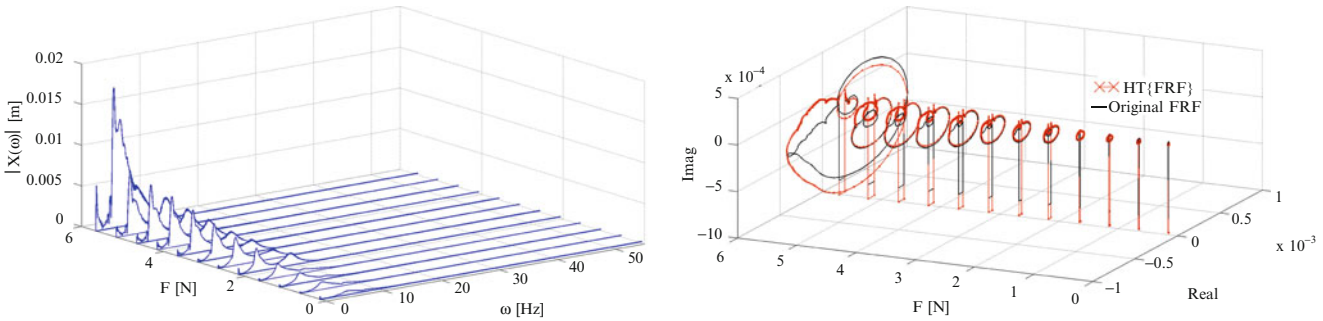

Fig. 32.5 Free vibration response of the first mass carriage x_1 and experimental FRF computed from a sine sweep from 0.1 to 10 Hz and a constant force of 1.0 N

Table 32.4 Mechanical system parameters estimation for 2 DOF

Parameter	Estimated value
$M^{-1}C$	$\begin{bmatrix} 9.7882 & -4.7765 \\ -4.3438 & 4.3438 \end{bmatrix}$
$M^{-1}K$	$1 \times 10^3 \begin{bmatrix} 1.0265 & -0.5276 \\ -0.4799 & 0.4799 \end{bmatrix}$
k_1 (N/m)	$1 \times 10^5 \begin{bmatrix} -9.8980 & 5.0471 \\ 4.5899 & -4.5899 \end{bmatrix}$

32.5 Conclusions

In this work the on-line algebraic identification, based on operational calculus, is combined with orthogonal functions approximation, thus taking advantage of their specific algebraic and computational properties. Computationally speaking, the required iterated integrations are formulated and computed by using a compact and clear matrix expression, which is well-defined and robust, due to the good structure of the operational matrix of integration in an algebraic sense. That means that the pseudo-inverse is always possible to be computed and the results are finite and bounded. The parameter estimations, however, are slower for this particular formulation. The nonlinearity indicator tested here is easy to program and compute, after some considerations reported in the literature. It is necessary to make a good analysis of the numerical methods applied

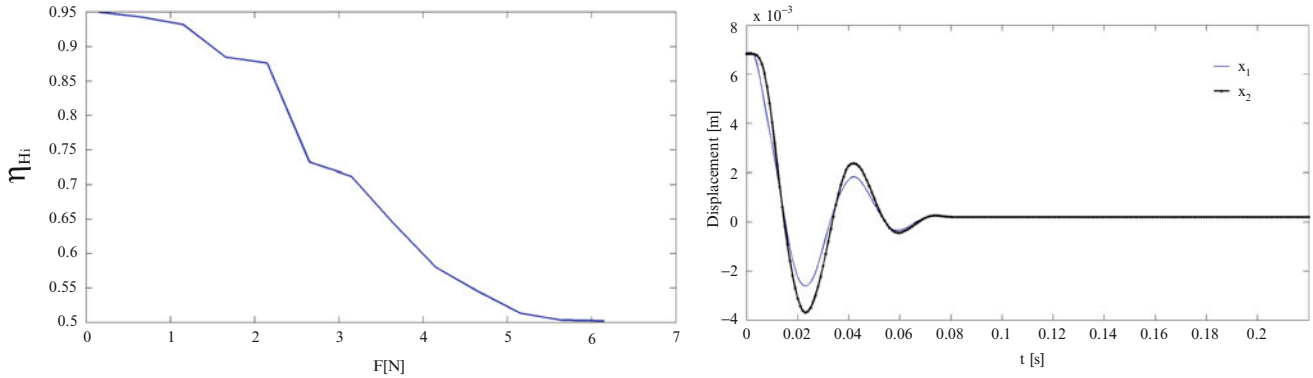

Fig. 32.6 Non-linearity index calculated when $F \in [0.15 \;\; 6.15]$ [N] for 2 DOF and free vibration response of the mass carriages x_1 and x_2

to the original data in order to have a good criterion for the final determination of presence of nonlinearities, that is, one has to be careful about what is going to be an acceptable value for η_{Hi} to consider the system as nonlinear. In particular, we have assumed a value of $\eta_{Hi} \leq 0.9$ to establish that a given system is dominantly nonlinear.

References

1. Pacheco, R.P., Steffen Jr., V.: On the identification of non-linear mechanical systems using orthogonal functions. Int. J. Non-Linear Mech. **9**, 1147–1159 (2004)
2. Simon, M., Tomlinson, G.R.: Use of the Hilbert transform in modal analysis of linear and non-linear structures. J. Sound Vib. **96**(4), 421–436 (1984)
3. Isermann, R., Münchhof, M.: Identification of Dynamic Systems: An Introduction with Applications. Springer, Berlin (2011)
4. Feldman, M.: Hilbert Transform Applications in Mechanical Vibration. Wiley, Chichester (2011)
5. Fliess, M., Sira-Ramírez, H.: An algebraic framework for linear identification. ESAIM: Control Optim. Calc. Var. **9**, 151–168 (1996)
6. Juang, J.-N.: Applied System Identification. Prentice Hall, Englewood Cliffs (1994)
7. Golub, G., Van Loan, C.: An analysis of the total least squares problem. SIAM J. Numer. Anal. **17**, 883–893 (1980)
8. Wu, J-L., Chen, Ch-H.. Chen, Ch-F.: A unified derivation of operational matrices for integration in systems analysis. In: Proceedings of International Conference on Information Technology: Coding and Computing 2000, 436–442 2000
9. Beltrán-Carbajal, F., Silva-Navarro, G., Chávez-Conde, E.: Design of active vibration absorbers using on line estimation of parameters and signals. In: Beltrán Carbajal, F. (ed.) Vibration Analysis and Control – New Trends and Developments. InTech, Croatia (2011)
10. Tomlinson, G.R.: Developments in the use of the Hilbert transform for detecting and quantifying nonlinearity associated with frequency response functions. Mech. Syst. Sig. Process. **1**(2), 151–171 (1987)
11. Tomlinson, G.R., Ahmed, I.: Hilbert transform procedures for detecting and quantifying non-linearity in modal testing. Meccanica **22**(3), 123–132 (1987)

Chapter 33
Online State and Parameter Estimation of a Nonlinear Gear Transmission System

Dimitrios Giagopoulos, Vasilis Dertimanis, Eleni Chatzi, and Minas Spiridonakos

Abstract This study aims at modeling the nonlinear dynamic response of a gear transmission system, based on substructuring techniques. More specifically, a finite element (FE) model is introduced for the housing of the gearbox, while the essential effects of the gear-pair, the bearings and the shafts are described by a lumped parameter model. The latter is characterized by strongly nonlinear characteristics that account for gear backlash, meshing stiffness, transmission error properties and bearing stiffness nonlinearities. Accordingly, a joint state and parameter estimation (JS&PE) problem is formulated on the basis of the lumped model. The proposed framework uses vibration acceleration measurements from sensors attached on the housing and, through their propagation to the lumped nonlinear model via the FE substructure, an Unscented Kalman Filter (UKF) is activated for the solution of the JS&PE problem. In contrast to other alternatives (e.g., the Extended Kalman Filter), the UKF features a number of advantages in treating nonlinear systems, including a derivative free calculation and a capacity for higher order nonlinearities. The method's performance is examined using both numerical simulations and experimental tests.

Keywords Gear vibration • Finite elements • Nonlinear dynamics • Substructuring • Join state and parameter identification

33.1 Introduction

Geared rotor-bearing system is one of the most important mechanical system used for power and motion transmission in many engineering applications. The continuously rising technological needs for improved performance, compactness, longer life and reduced production costs, require new designs with higher operating speeds and lighter components. In order to satisfy these needs, research in the area of geared systems has been kept active, incorporating new technical advancements and theoretical developments in other related fields. These efforts are also greatly assisted by current rapid enhancements in the level of computing power, which in turn extends the range of applicability of involved numerical algorithms. In particular, dynamics of systems involving gear mechanisms has long been in the epicenter of intensive research efforts.

Previous studies on the subject have focused on developing mechanical models of geared systems, ranging from relatively low to high complexity levels, depending on the emphasis and the objectives of the investigation. Consequently, a large variety of important technical topics has already been examined, such as the effect of support and gear box flexibility, gyroscopics, internal and external damping, shaft shear deformation and coupled torsional-bending vibrations. The great majority of these studies assume constant average spin speed of the gear shafts. Both response and stability issues have been investigated by means of analytical, numerical and experimental techniques. Among all the technical parameters, those related to the gear backlash and the variable gear meshing stiffness were found to affect the system response in a significant manner. However, gear backlash introduces serious difficulties in the analysis because the equations of motion of such systems become strongly nonlinear [1, 2]. Moreover, these difficulties are further intensified by the variation in the number of gear teeth pairs which are in contact at a time, causing a variation of the equivalent gear meshing stiffness. On the other hand, some of the earlier studies shifted attention to more fundamental issues and have shown that these complications are responsible for the appearance of complicated and irregular dynamic response [3, 4].

D. Giagopoulos (✉)
Department of Mechanical Engineering, University of Western Macedonia, Kozani, Greece
e-mail: dgiagopoulos@uowm.gr

V. Dertimanis • E. Chatzi • M. Spiridonakos
ETH Zurich, Institute of Structural Engineering, Zurich, Switzerland

G. Kerschen (ed.), *Nonlinear Dynamics, Volume 1*, Conference Proceedings of the Society for Experimental Mechanics Series,
DOI 10.1007/978-3-319-29739-2_33

In this work first the emphasis is given in modeling and investigating the nonlinear dynamic response of a gear transmission system, based on substructuring techniques. A finite element (FE) model is introduced for the housing of the gearbox, while the essential effects of the gear-pair, the bearings and the shafts are described by a lumped parameter model. The system examined is characterized by strongly nonlinear characteristics that account for gear backlash, meshing stiffness, transmission error properties and bearing stiffness nonlinearities. The gear-pair model employed is presented in a way that can easily be adapted as a superelement in a general rotordynamic configuration. The goal is to build high fidelity model of the gear-pair in order to simulate the behaviour of the combined system. Due to a number of factors, the system may be characterized by uncertainties. To achieve this, the Unscented Kalman Filter (UKF), which comprises a nonlinear observer, is employed here for the joint state and parameter estimation (JS&PE) of the lumped substructure. The efficient performance of the UKF algorithm in real-time nonlinear system identification problems has been confirmed in several studies [10–12]. Due to its structured format, which calls for the utilization of a minimal number of sample points, the UKF is also preferable to Particle Filters where the required sample size may be significant. In order to identify the values of the parameters, accelerations time histories are used, obtained during various operating conditions of the gearbox. These measurements are recorded from a special experimental device, which was designed and set up for this purpose. Finally the experimental results was compared to those from the numerical model for verification of the numerical procedure and improvement of the numerical modeling of the gear transmission components.

33.2 Class of Mechanical Systems Examined: Equations of Motion

Many mechanical systems involve several structural components, which are deformable and possess linear characteristics, together with an appropriate set of interconnecting elements, possessing nonlinear properties. In such a case, the corresponding equations of motion can be cast in the following system of ordinary differential equations

$$\widehat{M}\ddot{\underline{x}} + \widehat{C}\dot{\underline{x}} + \widehat{K}\underline{x} + \widehat{\underline{h}}\left(\underline{x},\ \dot{\underline{x}}\right) = \widehat{\underline{f}}(t) \tag{33.1}$$

Vector $\underline{x}$ includes the set of the generalized coordinates, the terms $\widehat{M}$, $\widehat{C}$ and $\widehat{K}$ represent the classical mass, damping and stiffness matrix of the system, respectively, while the vector $\widehat{\underline{h}}\left(\underline{x}, \dot{\underline{x}}\right)$ includes the nonlinear smooth forces imposed by the interconnecting elements. Finally, the term $\widehat{\underline{f}}(t)$ includes the action of the externally applied forces. Prediction of the response of dynamical systems represented by Eq. (33.1) is a difficult task, since in most practical cases the number of the equations of motion is quite large and the nonlinearities are strong. As a result, such systems can only be studied by applying special numerical methodologies [5]. In many cases, the resulting computations are facilitated by first applying appropriate methodologies leading to a significant reduction of the original coordinates associated with the system deformability, without affecting considerably the accuracy of the results. The basic steps of this method are presented in the following paragraphs. In brief, neglecting temporarily the damping and the nonlinear forces and taking into account the sparsity pattern of the stiffness matrix, the equations of motion of the original system are first reordered and then split automatically in a number of mathematical substructures. As a consequence, the equations of motion for the i -th substructure alone appear in the following linear form

$$M_i\ddot{\underline{x}}_i + K_i\underline{x}_i = \underline{f}_i(t) \tag{33.2}$$

where M_i and K_i are the mass and stiffness matrix, respectively, while $\underline{f}_i(t)$ represents the terms arising from external forcing on the i -th component. Next, the displacement vector is split in the form $\underline{x}_i(t) = \begin{pmatrix} \underline{x}_I^i \\ \underline{x}_B^i \end{pmatrix}$ where $\underline{x}_I^i$ and $\underline{x}_B^i$ represent the internal and the boundary degrees of freedom of the i -th substructure, respectively. Next, through application of a Ritz coordinate transformation

$$\underline{x}_i(t) = T_i\ \underline{q}_i(t) \tag{33.3}$$

where the columns of matrix T_i include the fixed interface normal modes of the component up to a prespecified frequency plus a number of static correction modes. Then, the set of Eq. (33.2) is replaced by a considerably smaller set, which appears in the form

$$\widehat{M}_i \ddot{\underline{q}}_i + \widehat{K}_i \underline{q}_i = \widehat{\underline{f}}_i(t) \tag{33.4}$$

with $\widehat{M}_i = T_i^T M_i T_i$, $\widehat{K}_i = T_i^T K_i T_i$ and $\widehat{\underline{f}}_i(t) = T_i^T \underline{f}_i(t)$. After treating and connecting each component together, the linear undamped terms in the equations of motion of the composite system can eventually be cast in the vectorial form $\underline{\ell} \equiv M\ddot{\underline{q}} + K\underline{q} - \underline{f}(t)$, with

$$\underline{q} = \begin{pmatrix} \underline{\eta}_1 \\ \underline{\eta}_2 \\ \vdots \\ \underline{x}_B \end{pmatrix}, \quad M = \begin{bmatrix} I_1 & \mu_{1,2} & \cdots & \mu_{1,B} \\ & I_2 & \cdots & \mu_{2,B} \\ & & \ddots & \vdots \\ sym & & & M_{B,B} \end{bmatrix} \quad \text{and} \quad K = \begin{bmatrix} \Lambda_1 & 0 & \cdots & 0 \\ & \Lambda_2 & \cdots & 0 \\ & & \ddots & \vdots \\ sym & & & K_{B,B} \end{bmatrix}.$$

The vector $\underline{\eta}_i$ includes the generalized coordinates corresponding to the modes kept in the i -th component, while the matrix Λ_i is diagonal, with diagonal elements representing the squares of the related natural frequencies. The upper part of the transformed stiffness matrix, corresponding to the generalized sets of coordinates $\underline{\eta}_i$, is diagonal. Likewise, the corresponding diagonal blocks of the mass matrix are occupied with identity matrices, while from the off diagonal blocks only those involving coupling between the involved substructures are nonzero. Finally, the last part of vector $\underline{q}$, represented by $\underline{x}_B$, includes all the boundary degrees of freedom of the system. The corresponding parts of the mass and stiffness matrix, represented by $M_{B,B}$ and $K_{B,B}$, are full. However, the dimensions of these submatrices are usually much smaller than the dimensions of matrices M and K, which in turn are much smaller than the dimension of the mass and stiffness matrices of the original system. The set of the degrees of freedom is selected so that it includes all the points where nonlinear action is present. In this way, the exact nonlinear characteristics of the system are preserved.

33.3 Review of Unscented Kalman Filter Formulation for State and Parameter Estimation

The Kalman Filter is a Bayesian approximation technique which is widely used for estimating a linear system's response using noisy measurements from few of the degrees of freedom of a system with given governing equations, i.e., a given process mode [13]. In short, the mathematical setup of the time-discrete KF is explained in what follows by extending the discrete dynamical system of Eq. (33.1) through the addition of additive white Gaussian noise as follows,

$$\begin{aligned} \mathbf{x}_{n+1} &= \mathbf{A}\mathbf{x}_n + \mathbf{B}\mathbf{u}_n + \mathbf{w}_n \\ \mathbf{y}_n &= \mathbf{C}\mathbf{x}_n + \mathbf{D}\mathbf{u}_n + \mathbf{v}_n \end{aligned} \tag{33.5}$$

where $\mathbf{A} \in \mathbb{R}^{n\times n}$ is the system matrix, $\mathbf{B} \in \mathbb{R}^{n\times 1}$ is the input matrix, $\mathbf{C} \in \mathbb{R}^{m\times n}$ is the output matrix, $\mathbf{D} \in \mathbb{R}^{m\times 1}$ is the feed-through matrix, $\mathbf{u}_n \in \mathbb{R}$ is the control vector, $\mathbf{x}_n \in \mathbb{R}^n$ is the state vector at time step n comprising the system displacements $\mathbf{d}$ and velocities $\dot{\mathbf{d}}$, i.e., $\mathbf{x}_n = \left[\mathbf{d}_n,\ \dot{\mathbf{d}}_n\right]^T$, $\mathrm{y}_n \in \mathbb{R}^{m\times 1}$ is the observation vector and $n = 1,\ 2,\ 3,\ \ldots,\ T$ are the time discrete time steps. Also the stochastic nature of the system, reflected in the terms of $\mathbf{w}_n \in \mathbb{R}^{n\times 1}$, which is the process noise vector, assumed to be Gaussian distributed with $N(0, \mathbf{Q}_n)$, and $\mathbf{v}_n \in \mathbb{R}^{m\times 1}$, which is the Gaussian measurement noise vector distributed with $N(0, \mathbf{R}_n)$.

The linear KF is a recursive estimator whose optimality depends on (a) how accurately the process model can track the actual system, (b) the assumption of additive, independent white Gaussian noise and (c) the precision by which the process and measurement noise covariance matrices are known. Based on this, it becomes evident that for severe modeling uncertainties, and therefore significant modeling errors, the KF will have difficulties, or will be unable to deliver an accurate full state estimate based on noisy and incomplete measurements. To this end, the use of an alternate Bayesian filter is proposed herein, namely, the Unscented Kalman Filter (UKF), which is capable of joint parameter and state identification.

In handling linear systems of the type of Eq. (33.5), where the system properties, i.e., the elements of matrix $\mathbf{A}$, are considered as unknowns, a joint state and parameter formulation is adopted. This demands an augmentation of the regular state vector $\mathbf{x}$, in order to include those properties of the system that are considered as unknowns and which can be summarized in a parameter vector θ. The augmented state vector is defined as $\overline{\mathbf{x}} = [\mathbf{x},\ \theta]^T$. The resulting system is of nonlinear nature since it comprises bilinear products of the components $\mathbf{x}$ & θ of the state vector $\overline{\mathbf{x}}$.

The Unscented Kalman filter is chosen herein in place of the widely used nonlinear filter alternative, i.e., the *Extended Kalman Filter* (*EKF*) [7, 15], since it is able to overcome some significant shortcomings of the latter when dealing with higher order nonlinearities and noise contamination. The UKF models the state as a Gaussian random variable whose distribution can be approximated by a carefully chosen set of deterministic points, namely the sigma points. These points capture the prior mean and covariance of the state and when propagated through the nonlinear function, provide an improved posterior estimate of the transformed state. This process is known as the *Unscented Transformation* (*UT*) [9]. The process and observation equations are in this case reformulated for the general case of a nonlinear system as,

$$\begin{aligned} \overline{\mathbf{x}}_n &= \mathbf{f}\left(\overline{\mathbf{x}}_{n-1}, \mathbf{u}_{n-1}\right) + \mathbf{w}_{n-1} \\ \mathbf{y}_n &= \mathbf{h}\left(\overline{\mathbf{x}}_n\right) + \mathbf{v}_n \end{aligned} \tag{33.6}$$

where $\mathbf{f}(\cdot)$ &$\mathbf{h}(\cdot)$ can both be nonlinear functions, and $\mathbf{y}_n$, w_{n-1} and $\mathbf{v}_n$ are defined as previously. Note however that $\overline{\mathbf{x}}_n$ signifies here the joint state and parameter vector. Given the formulation provided above, the workings of the KF are summarized in Table 33.1.

Further information about the formulation of the UKF can be found in [6, 8, 9, 11, 15–17].

Table 33.1 The general scheme of the UKF algorithm for joint state and parameter estimation

- Initialization at time t_0:

$$\widehat{\overline{\mathbf{x}}}_0 = \mathbb{E}\left[\overline{\mathbf{x}}_0\right]$$

$$\mathbf{P}_0 = \mathbb{E}\left[\left(\overline{\mathbf{x}}_0 - \widehat{\overline{\mathbf{x}}}_0\right)\left(\overline{\mathbf{x}}_0 - \widehat{\overline{\mathbf{x}}}_0\right)^T\right]$$

- At time t_k, for n=1, ..., $\mathrm{N_t}$:

• The Unscented Transform

1. Augment the state vector to include the noise parameters

$$\overline{\mathbf{x}}^{\alpha}_{n-1} = \left[\overline{\mathbf{x}}^T_{n-1}, \mathbf{w}^T_{n-1}, \mathbf{v}^T_{n-1}\right]^T$$

2. Formulation of the Sigma Point vector:

$$\mathcal{X}_{n-1} = \left[\widehat{\overline{\mathbf{x}}}^{\alpha}_{n-1}, \quad \widehat{\overline{\mathbf{x}}}^{\alpha}_{n-1} + \sqrt{(L+\lambda)\,\mathbf{P}^{\alpha}_n}, \quad \widehat{\overline{\mathbf{x}}}^{\alpha}_{n-1} - \sqrt{(L+\lambda)\,\mathbf{P}^{\alpha}_n}\right]$$

where α, β, λ are the UKF parameters; L is the dimension of the augmented state vector.

• Prediction stage:

3. Propagation of the Sigma points through the system model:

$$\mathcal{X}^{x,i}_{n\left|n-1\right.} = \mathbf{f}\left(\mathcal{X}^{x,i}_{n-1}, \mathcal{X}^{w,i}_{n-1}\right), \quad i = 0, .., 2L$$

4. Calculation of the state and covariance priors:

$$\widehat{\overline{\mathbf{x}}}_{n\left|n-1\right.} = \sum_{i=0}^{2L} w^x_i \mathcal{X}^{x,i}_{n\left|n-1\right.} \quad ; \quad \mathbf{P}_{n\left|n-1\right.} = \sum_{i=0}^{2L} w^P_i \left[\mathcal{X}^{x,i}_{n\left|n-1\right.} - \widehat{\overline{\mathbf{x}}}_{n\left|n-1\right.}\right]\left[\mathcal{X}^{x,i}_{n\left|n-1\right.} - \widehat{\overline{\mathbf{x}}}_{n\left|n-1\right.}\right]^T$$

• Update stage:

5. Calculation of Kalman gain:

$$\mathbf{K}_n = \mathbf{P}^{xy}_n \left(\mathbf{P}^{yy}_n\right)^{-1}, \text{ where}$$

$$\mathbf{P}^{yy}_n = \sum_{i=0}^{2L} w^P_i \left[\mathbf{h}\left(\mathcal{X}^{x,i}_{n\left|n-1\right.}\right) - \widehat{\mathbf{y}}_{n\left|n-1\right.}\right]\left[\mathbf{h}\left(\mathcal{X}^{x,i}_{n\left|n-1\right.}\right) - \widehat{\mathbf{y}}_{n\left|n-1\right.}\right]^T, \mathbf{P}^{xy}_n = \sum_{i=0}^{2L} w^P_i \left[\mathcal{X}^{x,i}_{n\left|n-1\right.} - \widehat{\overline{\mathbf{x}}}_{n\left|n-1\right.}\right]\left[\mathbf{h}\left(\mathcal{X}^{x,i}_{n\left|n-1\right.}\right) - \widehat{\mathbf{y}}_{n\left|n-1\right.}\right]^T$$

6. Improve predictions of state (posterior estimates) using the latest observations:

$$\widehat{\mathbf{y}}_{n\left|n-1\right.} = \sum_{i=0}^{2L} w^x_i \mathbf{h}\left(\mathcal{X}^{x,i}_{n\left|n-1\right.}, \mathcal{X}^{v,i}_{n-1}\right)$$

$$\widehat{\overline{\mathbf{x}}}_n = \widehat{\overline{\mathbf{x}}}_{n\left|n-1\right.} + \mathbf{K}_n\left(\mathbf{y}_n - \widehat{\mathbf{y}}_{n\left|n-1\right.}\right)$$

$$\mathbf{P}_n = \mathbf{P}_{n\left|n-1\right.} - \mathbf{K}_n \mathbf{P}^{yy}_n \mathbf{K}^T_n$$

33.4 Application to Experimental Gearbox Simulator

For the purposes of the proposed work, a special experimental device will be designed and built, consisting of two power electric motors with adjustable rotational speed. One of them will cause the motion, while the second will resist this motion, acting as an electric generator. The mechanical system to be tested, including a gear-box with a single gear-pair connection, ball bearings supporting the rotating axes and couplings for the connection between the parts of the system. The device with the experimental setup and accelerometer locations is shown in Fig. 33.1a. Also a view of the spur gear pair are is depicted in Fig. 33.1b.

The pinion was connected to 0.75 HP electric motor driven through coupling and the gear was connected to a loading system. The gear and pinion has 24 and 16 teeth respectively. The diameter of the shafts that connects the gears with the motor and the loading system is 25 mm. The shafts are supported at its ends with SKF 6205 ball bearings. Between the motor drive and the gearbox placed a torque/tachometer sensor in order to measure the applied input torque and the shaft rotation speed. Also for the measurement of the shafts speed used and a portable optical tachometer. The vibration signals originating from the gearbox investigated at different loading conditions and shaft speeds (rotating frequencies).

In order to determine the dynamic response and provide the main effects due to the gear meshing action, an appropriate model was developed. In this model, the housing of the gearbox and the shafts are modeled by using finite elements, while the essential effects of the gear-pair and the bearings are taken into account via a lumped nonlinear mathematical model. A finite element model (FEM) of the specific gear-pair considered is shown in Fig. 33.2a. Moreover, the appropriate lumped mass model (LMM) of the same gear-pair is shown in Fig. 33.2b.

Upon satisfaction of certain conditions, the lumped mass model of the gear-pair can lead to sufficiently accurate results. The main reason for employing a LMM rather than a FEM of a gear-pair is that the former leads to a much faster and at least qualitatively correct picture of the dynamics. In particular, the LMM employs two rotating rigid disks, modeling the

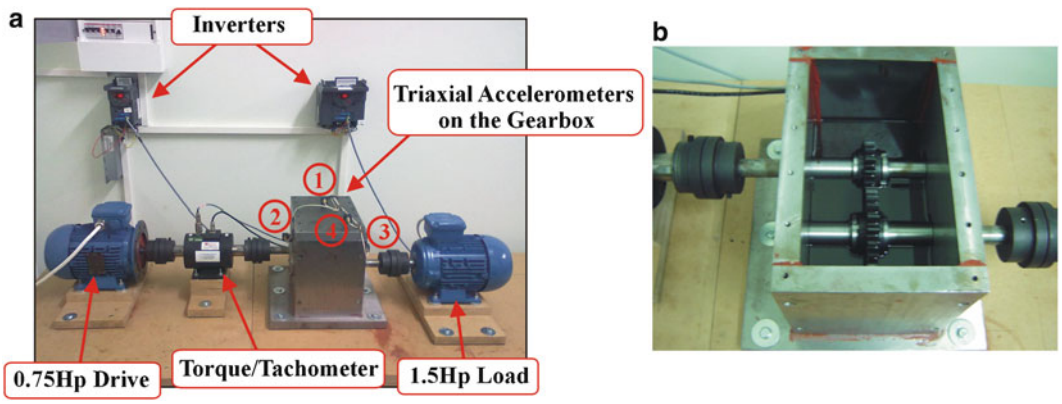

Fig. 33.1 (**a**) Experimental set up of the device with Acceleration measurement locations and, (**b**) view of the spur gear-pair

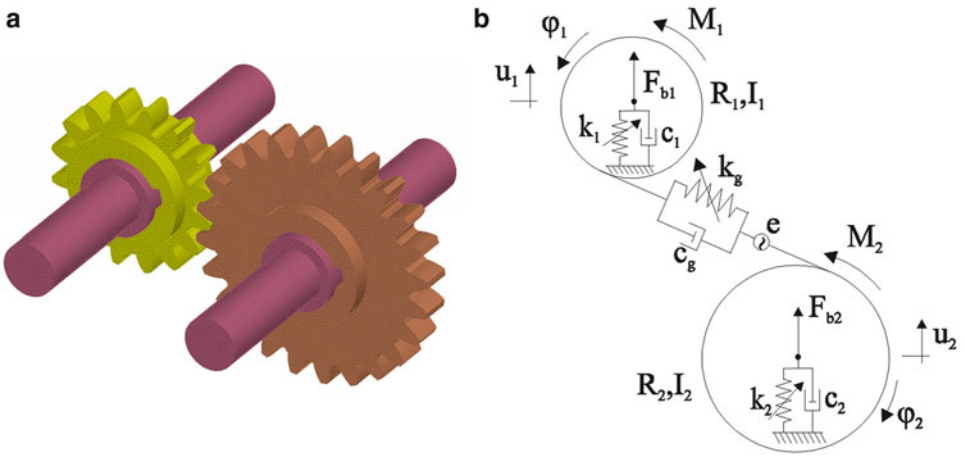

Fig. 33.2 (**a**) Finite element model (FEM) and, (**b**) lumped mass model (LMM) of a gear-pair system

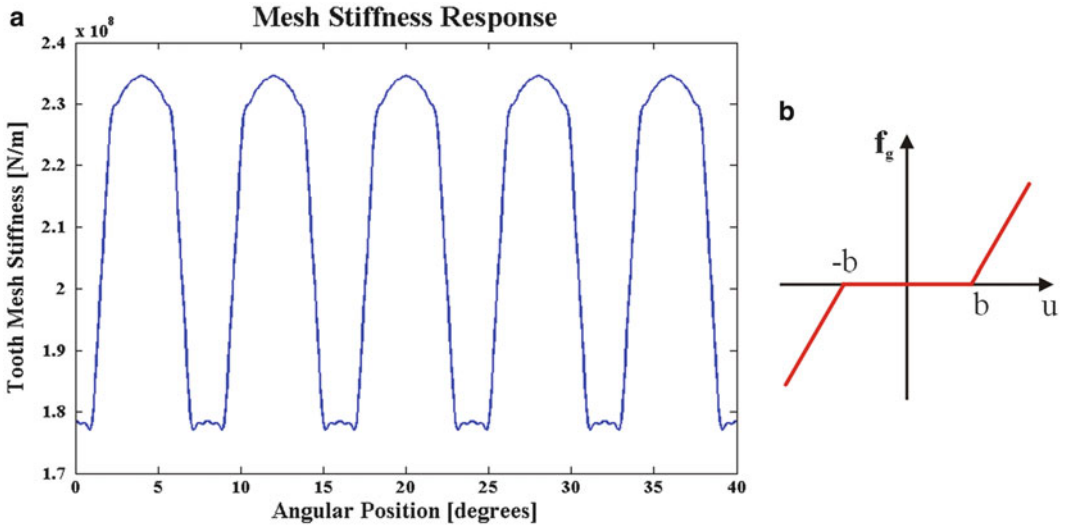

Fig. 33.3 (**a**) Effective value of the gear meshing stiffness. (**b**) Backlash modeling of the gear teeth

gear bodies, with masses m_n, mass moments of inertia I_n and base radii R_n ($n = 1, 2$), while both gears are supported on deformable bearings. Also the gear meshing force is reproduced by a set of a spring and a damper (k_g, c_g). The essential dynamics of the system is described by the coordinates ϕ_1, ϕ_2, u_1 and u_2. The action of the gear contact and meshing was modelled by an equivalent spring, whose stiffness coefficient $k_g(\phi)$ depends on the relative position of the two gears, where the damping mechanisms assumed to be linear. The form of gear mesh stiffness shown in Fig. 33.3a, and obtained from the finite element of the gear-pair system. The meshing stiffness creates a periodically varying forcing effect on the supporting structure, which produces periodic long term dynamics. In addition, the nonlinear backlash phenomenon, caused by the clearances between the mating gears, was also allowed to occur (Fig. 33.3b). The quantity *2b* represent the total gear backlash. Also the restoring force developed in the *n* -th rolling element bearing is expressed in this nonlinear form

$$f_n(u_n) = \begin{cases} \widehat{k}_n \sum_{r=1}^{N} (u_n \cos\alpha_{rn} - b_{bn})^{\nu} \cos\alpha_{rn}, & u_n \geq b_{bn} \\ 0, & |u_n| < b_{bn} \\ -\widehat{k}_n \sum_{r=1}^{N} (|u_n| \cos\alpha_{rn} - b_{bn})^{\nu} \cos\alpha_{rn}, & u_n \leq -b_{bn} \end{cases} \tag{33.8}$$

In this expression, $2b_{bn}$ represents the diametral clearance, α_{rn} is the angular position of the r -th rolling element (of the total N elements in contact), ν is a constant (equal to 3/2 for ball bearings), while the coefficient $\widehat{k}_n$ is determined from the bearing characteristics and loading conditions.

Final the coupling of the LMM gear-pair model with the gear shafts and the gearbox superstructure were performed. In particular, both the gear shafts and the gearbox were discretized by appropriate finite elements, as shown in Fig. 33.4, while the effect of the LLM were included in the system with the use of mass, damping, and nonlinear spring elements.

33.5 Results

In this section presented simulated numerical results for the complete gearbox system (gear-pair and housing), in an indicative input rotation speed at 2100RPM. First in Fig. 33.5a and b presented the "measured" acceleration time histories in the vertical direction, for the bearings locations 2 and 3 respectively. These accelerations time histories are used as input variables in the UKF. First, the UKF results are compared with the true system response in the case where all of the system parameters are considered to be known. These results summarized in Fig. 33.6a and b. In these figures presented the displacement time histories in the bearing locations for the UKF state estimation results with red dashed line and for the initial system response with black continuous line.

Next, in order to test the effectiveness of the UKF in state and parameter estimation, consider that the bearing stiffness parameters are unknown. A graphical representation of the true and identified values over the time provided in Fig. 33.7a

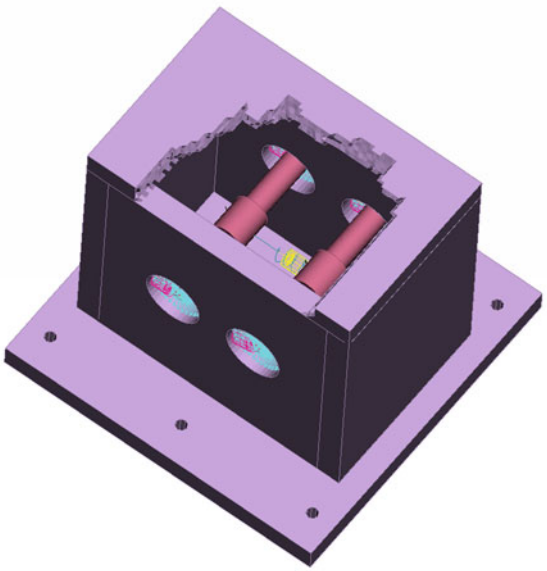

Fig. 33.4 Lumped mass of the gear-pair system, coupled with a finite element model of the flexible shafts and the gearbox

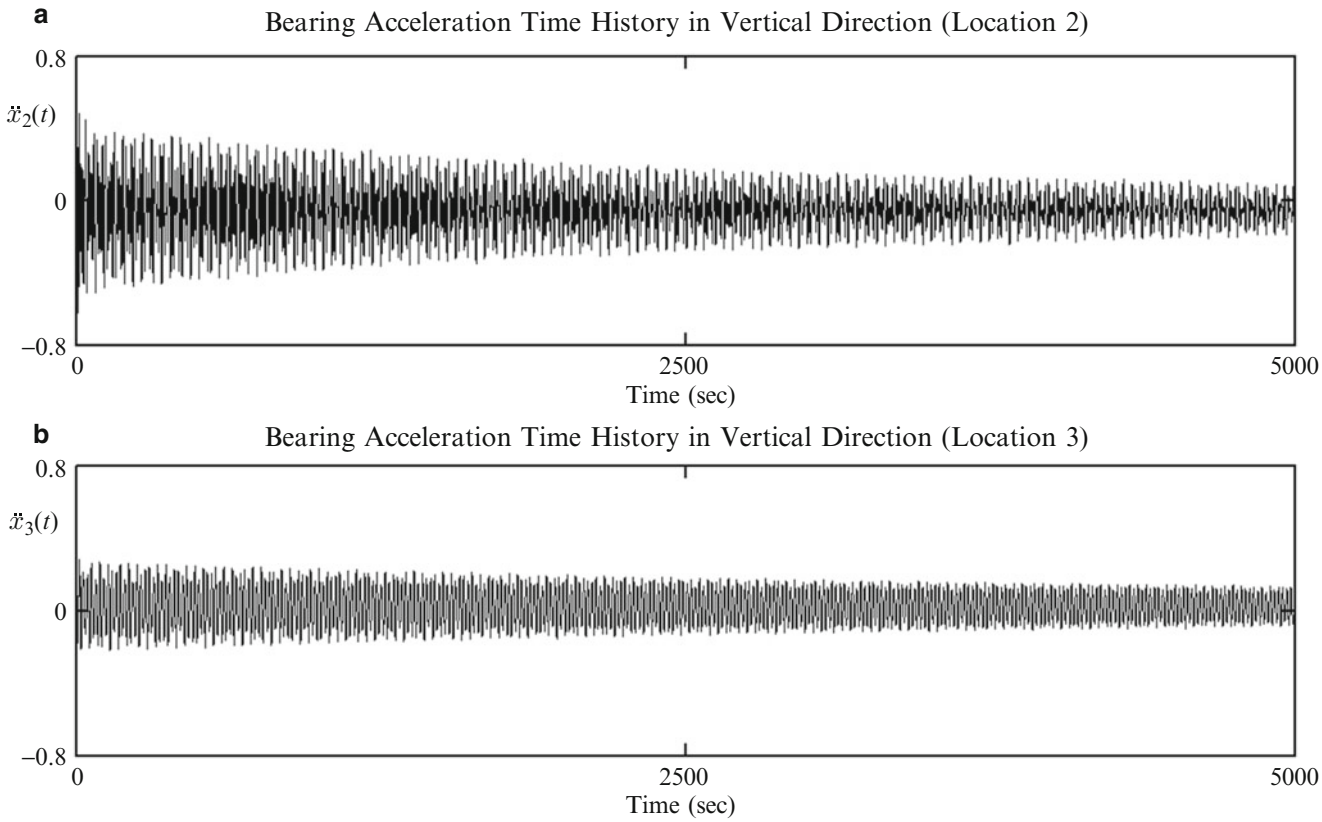

Fig. 33.5 "Measured" Acceleration time histories in vertical direction (**a**) Bearing Location 2 and, (**b**) Bearing Location 3

and b for the bearings stiffness parameters $\widehat{k}_n$. As is apparent in Fig. 33.7 after a very short initial convergence period, the parameter estimates remain stable throughout the entire simulation, which verifies the stability of the devised scheme. Also, the UKF results are compared with the true system response in this case with unknown the bearing stiffness parameters. The results summarized in Fig. 33.8a and b for the displacement time histories in the bearing locations. From these diagrams arising the efficiency of the UKF in the state and parameter estimation when applied in a system with highly nonlinear behavior.

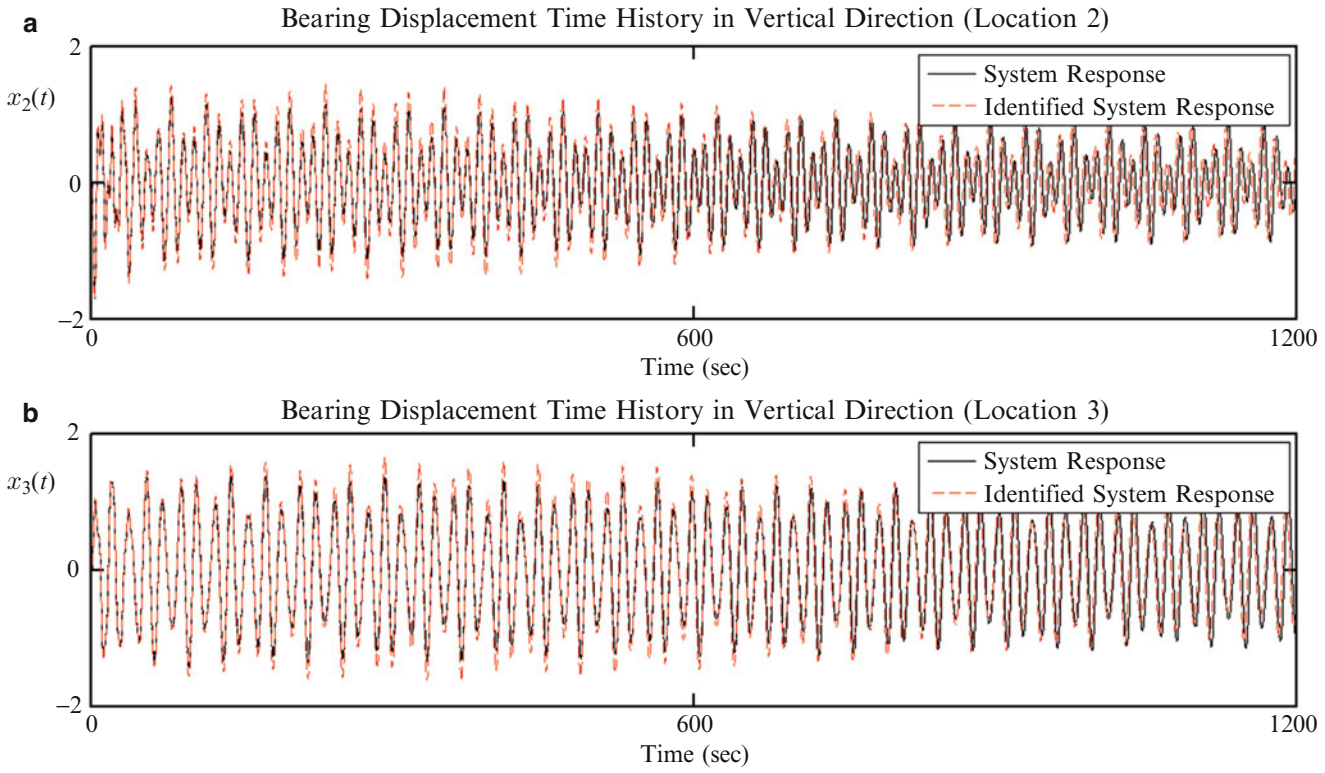

Fig. 33.6 UKF state estimation of displacement time histories in vertical direction (**a**) Bearing Location 2 and, (**b**) Bearing Location 3

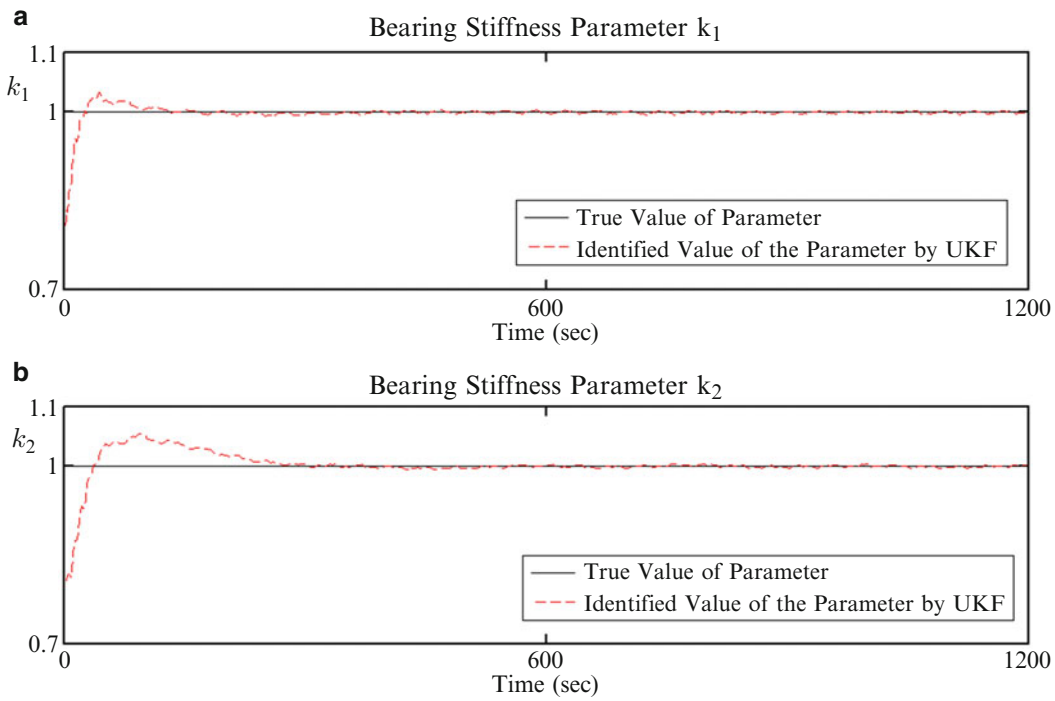

Fig. 33.7 Convergence of the bearing stiffness parameters (**a**) Bearing Location 2 and, (**b**) Bearing Location 3

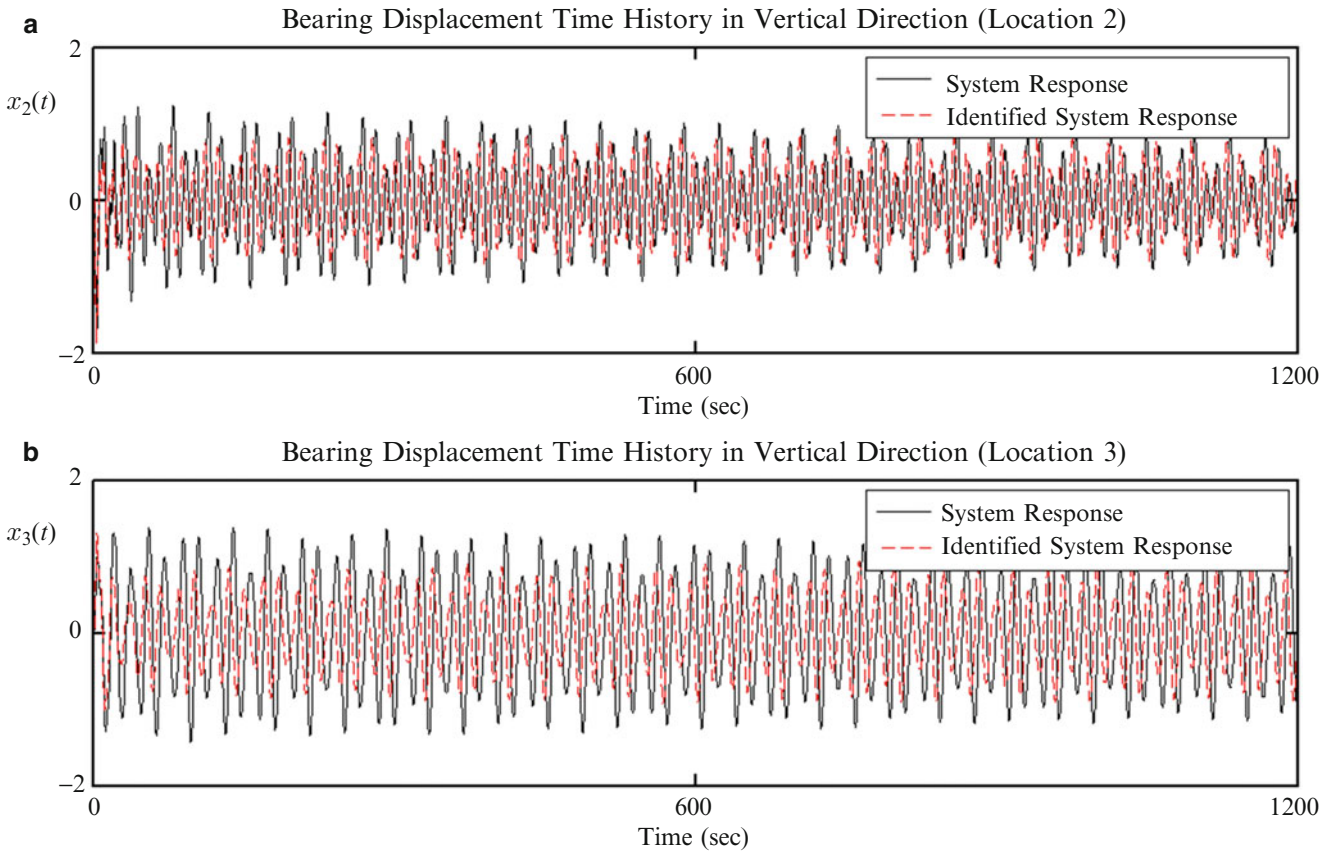

Fig. 33.8 UKF state and parameter estimation of displacement time histories in vertical direction (**a**) Bearing Location 2 and, (**b**) Bearing Location 3

33.6 Conclusions

This study includes the dynamic analysis of a nonlinear gear transmission system. The emphasis given in the build of high fidelity model of the gear-pair in order to simulate the behaviour of the combined system. To achieve this, the Unscented Kalman Filter (UKF), which comprises a nonlinear observer, is employed here for the joint state and parameter estimation (JS&PE) of the lumped substructure gear-pair and bearing model parameters. In order to identify the values of the parameters, accelerations time histories are used, obtained during various operating conditions of the gearbox. From the numerical analysis arising the efficiency of the UKF in the state and parameter estimation when applied in a system with highly nonlinear behavior.

References

1. Kahraman, A., Singh, R.: Interactions between time-varying mesh stiffness and clearance nonlinearities in a geared system. J. Sound Vib. **146**, 135–156 (1991)
2. Padmanabhan, C., Singh, R.: Analysis of periodically forced nonlinear Hill's oscillator with application to a geared system. J. Acoust. Soc. Am. **99**, 324–334 (1996)
3. Theodossiades, S., Natsiavas, S.: Nonlinear dynamics of gear-pair systems with periodic stiffness and backlash. J. Sound Vib. **229**, 287–310 (2000)
4. Giagopoulos, D., Salpistis, C., Natsiavas, S.: Effect of nonlinearities in the identification and fault detection of gear-pair systems. Int. J. Non-Linear Mech. **41**, 213–230 (2006)
5. Nayfeh, A.H., Balachandran, B.: Applied Nonlinear Dynamics. Wiley, New York (1995)
6. Chatzi, E., Smyth, A.: The unscented Kalman filter and particle filter methods for nonlinear structural system identification with non-collocated heterogeneous sensing. Struct. Control Health Monit. **16**(1), 99–123 (2009)

7. Corigliano, A., Mariani, S.: Parameter identification in explicit structural dynamics: performance of the extended Kalman filter. Comput. Meth. Appl. Mech. Eng. **193**(36–38), 3807–3835 (2004)
8. Chatzi, E.N., Smyth, A.W., Masri, S.F.: Experimental application of on-line parametric identification for nonlinear hysteretic systems with model uncertainty. Struct. Saf. **32**(5), 326–337 (2010)
9. Julier, S.J., Uhlmann, J.K.: New extension of the Kalman filter to nonlinear systems. In: Proceedings of SPIE 3068, Signal Processing, Sensor Fusion, and Target Recognition VI, 182–193 (1997)
10. Xie, Z., Feng, J.: Real-time nonlinear structural system identification via iterated unscented Kalman filter. Mech. Syst. Sig. Process. doi:10.1016/j.ymssp.2011.02.005 (2011)
11. Wu, M., Smyth, A.W.: Application of the unscented Kalman filter for real-time nonlinear structural system identification. Struct. Control Health Monit. **14**, 971–990 (2007). doi:10.1002/stc
12. Mariani, S., Ghisi, A.: Unscented Kalman filtering for nonlinear structural dynamics. Nonlinear Dyn. **49**(1–2), 131–150 (2007). doi:10.1007/s11071-006-9118-9
13. Kalman, R.: A new approach to linear filtering and prediction problems. J. Basic Eng. **82**(Series D), 35–45 (1960)
14. Mariani, S., Corigliano, A.: Impact induced composite delamination: state and parameter identification via joint and dual extended Kalman filters. Comput. Meth. Appl. Mech. Eng. **194**(50–52), 5242–5272 (2005)
15. Ristic, N.G.B., Arulampalam, S.: Beyond the Kalman Filter, Particle Filters for Tracking Applications. Artech House Publishers, Boston, London (2004)
16. Wan, E.A., van der Merwe, R.: The unscented Kalman filter. In: Haykin, S. (ed.) Kalman Filtering and Neural Networks. Wiley, New York (2002)
17. Miah, M.S., Chatzi, E.N., Weber, F.: Semi-active control for vibration mitigation of structural systems incorporating uncertainties. Smart Mater. Struct. **24**(5), 055016 (2015)
18. DYNAMIS 3.1.1, Solver Reference Guide, DTECH, Thessaloniki, Greece, 2013
19. ANSA and META-Post, BETA CAE Systems S.A., Thessaloniki, Greece

Chapter 34
Model Updating of a Nonlinear System: Gun Barrel of a Battle Tank

Güvenç Canbaloğlu and H. Nevzat Özgüven

Abstract Nonlinearities in a structural system make the use of model updating methods developed for linear systems difficult to apply nonlinear systems. If the FRFs of the underlying linear systems in a nonlinear system could be experimentally extracted, then the linear model updating methods could easily be applied to nonlinear systems as well. When there are complex nonlinearities in a structure together with frictional type of nonlinearity, linear FRFs cannot be accurately obtained by using low level forcing. In this present work, the model updating method—Pseudo Receptance Difference (PRD) method—recently developed by the authors for nonlinear systems, is applied to the gun barrel of a battle tank. The linear FRFs of the nonlinear gun barrel of the battle tank are obtained from measured nonlinear FRFs, and simultaneously the nonlinearities in the system are identified. Then the inverse eigensensitivity method is employed to update the linear finite element (FE) model of the gun barrel. Finally, in order to demonstrate the accuracy of the updated nonlinear model, the calculated and measured FRFs of the gun barrel at several different forcing levels are compared.

Keywords Nonlinear model updating • Nonlinear identification • Nonlinearity • Gun barrel • Nonlinear structures

34.1 Introduction

Integration of engineering systems to various platforms such as helicopters, aircrafts and battle tanks is a challenging problem in structural dynamics. Since integration of these systems may change the dynamic characteristics of the platforms, it is very important to understand the dynamic behavior of the platforms in order to increase the overall performance of the systems integrated to platforms. An example of that is to increase the shooting performance of a battle tank. The common problem encountered is to model the structural behaviors of the platforms or systems accurately. This modelling is commonly performed by using FE methods. However in all these types of integration applications there are nonlinear behaviors due to friction, joints or moving components in the integrated systems or platforms. Therefore the ultimate purpose is to have a mathematical model that simulates the nonlinear dynamic behavior of the system or the platform accurately. Since there are always discrepancies between predictions of the dynamic models and experimentally measured values, these models have to be updated.

Various model updating methods were developed in order to correct the mathematical models. However most of the model updating methods available in literature are for linear systems. Link and Zhang [1] investigated the effect of using different residual error vectors on the performance of the updating method. This study was demonstrated on a real test structure. Ibrahim et al. [2] used direct updating method for the model updating of FE models. For model updating, sensitivity based methods are used in different studies [3, 4]. A new model updating method is proposed by Lenoir et al. [5] which is based on the modal synthesis of experimental forced responses. In a later work, a new method was developed for structural model updating and identification of joint stiffness by Li [6]. In a more recent work Boulkaibet et al. [7] studied the use of the Shadow Hybrid Monte Carlo technique to determine the selection of updating parameters. Hemez [8] briefly overviewed the first 30 years of FE model updating development, from the mid-1960s to the mid-1990s and categorized FE model updating methods into broad categories that each offers their own benefits and limitations.

G. Canbaloğlu (✉)
Department of Mechanical Engineering, Middle East Technical University, 06800 Ankara, Turkey

MGEO Business Sector, ASELSAN Inc., 06750 Ankara, Turkey
e-mail: gcanbal@aselsan.com.tr

H.N. Özgüven
Department of Mechanical Engineering, Middle East Technical University, 06800 Ankara, Turkey
e-mail: ozguven@metu.edu.tr

G. Kerschen (ed.), *Nonlinear Dynamics, Volume 1*, Conference Proceedings of the Society for Experimental Mechanics Series,
DOI 10.1007/978-3-319-29739-2_34

In engineering problems there are usually nonlinearities in structures; therefore it is vital to have model updating techniques for nonlinear structures as well. In literature there are different studies performed to update directly the nonlinear model of a structure [9–11]. In a more recent work, Isasa et al. [12] presented an approach which is based on multi-harmonic balance method and extended constitutive relation error for the updating of nonlinear models.

For nonlinear structures, it is possible to employ the model updating techniques developed for the linear systems, provided that the dynamic characteristics of the linear part of the structure are extracted, which may require identification of nonlinearity in the system first. Kerschen et al. [13] presented a literature survey which is one of the most detailed nonlinear system identification literature surveys in which more than 400 papers were cited. Worden et al. [14] applied various time and frequency based nonlinear identification methods to a damper of an automobile. Eriten et al. [15] presented nonlinear system identification (NSI) approach in which experimental measurements are combined with slow-flow dynamic analysis and empirical mode decomposition. Very recently, Doranga and Wu studied [16] the Nonlinear Resonant Decay method for parameter identification of nonlinear dynamic systems. Canbaloglu and Özgüven, in another recent work, developed a method to identify nonlinearity and to obtain linear FRFs of nonlinear structures having multiple nonlinearities including friction type of nonlinearity, by using nonlinear FRF measurements [17], and used this method in the nonlinear model updating approach proposed [18]. The proposed method is experimentally validated by applying it to a real nonlinear T-beam test structure [19]. In this study, the method developed by the authors for nonlinear model updating [17, 18] is experimentally applied to the gun barrel of a battle tank. Dynamic modelling of the gun barrel of a battle tank is studied in different studies to improve the accuracy of the shooting and stabilization performance [20, 21] and it is shown that the fundamental mode of the gun barrel plays a key role in the response of the system. In this perspective, detailed model of the gun barrel at the fundamental mode is studied in this work. An equivalent single degree of freedom nonlinear model of the system is built for the fundamental mode of system. First, using the PRD method, both linear FRFs and the nonlinearities in the system are obtained from experimentally measured nonlinear FRFs. Afterwards, linear FE model of the test structure is built in ANSYS and it is updated by using the linear FRFs obtained through the PRD method. Thus, an updated nonlinear model of the test structure is constructed by using the identified nonlinearity and updated linear FE model of the system. Finally, predicted and measured FRFs of the test structure are compared at different forcing levels in order to demonstrate the accuracy of the updated nonlinear model of the system.

34.2 Theory

The model updating method developed by Canbaloglu and Özgüven [17, 18] is employed in this study for updating the FE model of a gun barrel. Only a very brief summary of the method is presented here. The theory of the method is given in detail in Refs. [17] and [18].

For a nonlinear system, it is possible to write the following equation.

$$[\Delta] = \left[\Delta_f\right] + [\Delta_{HF}] = \left[H^{NL}\right]^{-1} - \left[H^{L}\right]^{-1} \tag{34.1}$$

where $[\Delta]$, $[\Delta_f]$, $[\Delta_{HF}]$, $[H^{NL}]$, $[H^L]$ are the nonlinearity matrix, nonlinearity matrix due to friction, nonlinearity matrix due to remaining nonlinearities that are dominant at high forcing levels of excitation, response level dependent nonlinear and linear FRF matrices, respectively. Measuring FRFs experimentally several times at the same frequency but at different forcing levels the following set of equations can be written:

$$[\Delta_{HF}]_{i+1} - \left[\Delta_f\right]_1 = \left[H^{NL}\right]_{i+1}^{-1} - \left[H^{NL}\right]_1^{-1} \qquad i = 1, 2, \ldots, (n-1) \tag{34.2}$$

In Eq. (34.2), subscript 1 indicates low forcing case and subscripts 2, 3, … n indicate high forcing cases. The nonzero elements in the nonlinearity matrices at the left hand side which can be written as polynomial functions of response amplitudes with unknown coefficients are the describing functions of the corresponding nonlinearities. Applying polynomial fit to (*n-1*) data points in a least square sense, the equation of the corresponding regression curve can be obtained in order to find the unknown coefficients. By comparing the terms of the regression equation with the corresponding describing functions, nonlinearities can be identified and then linear FRFs can easily be calculated as [17]

$$\left[H^{L}\right]_1 = \left[\left[H^{NL}\right]_1^{-1} - \left[\Delta_f\right]_1\right]^{-1} \tag{34.3}$$

In order to avoid full matrix inversions given in Eq. (34.3), the formulation is improved for nonlinear structures where the nonlinearity is local [18]. For local nonlinearities it possible to partition the nonlinearity matrix as

$$[\Delta] = \begin{bmatrix} [\Delta_{aa}] & [0] \\ [0] & [0] \end{bmatrix} \tag{34.4}$$

where subscript a represents coordinates where nonlinear elements are connected (will be referred to as "nonlinear coordinates" in short). Pre-multiplying all the terms in Eq. (34.1) by $[H^L]$, post-multiplying by $[H^{NL}]$ and using Eq. (34.4) for the nonlinearity matrix, the following equation is obtained:

$$\begin{bmatrix} [H^L{}_{aa}] & [H^L{}_{ab}] \\ [H^L{}_{ba}] & [H^L{}_{bb}] \end{bmatrix} \begin{bmatrix} [\Delta_{aa}] & [0] \\ [0] & [0] \end{bmatrix} \begin{bmatrix} [H^{NL}{}_{aa}] & [H^{NL}{}_{ab}] \\ [H^{NL}{}_{ba}] & [H^{NL}{}_{bb}] \end{bmatrix} = \begin{bmatrix} [H^L{}_{aa}] & [H^L{}_{ab}] \\ [H^L{}_{ba}] & [H^L{}_{bb}] \end{bmatrix} - \begin{bmatrix} [H^{NL}{}_{aa}] & [H^{NL}{}_{ab}] \\ [H^{NL}{}_{ba}] & [H^{NL}{}_{bb}] \end{bmatrix} \tag{34.5}$$

Here subscript b corresponds to linear coordinates.

Considering the first submatrix of the resultant matrix and performing some matrix manipulations, the linear FRF matrix for the nonlinear coordinates can be written as [18]

$$\left[H^L{}_{aa}\right]_1 = \left[\left[H^{NL}{}_{aa}\right]_1{}^{-1} - \left[\Delta_f\right]_1\right]^{-1} \tag{34.6}$$

It is obvious that for locally nonlinear structures computational effort will be considerably reduced by using the above equation compared to Eq. (34.3). Once the linear FRFs are calculated by using Eq. (34.6), then they can be used in the model updating process of a FE model of the linear part of the system. Note that in several model updating methods having FRFs of limited number of coordinates is sufficient. Therefore, having FRF of even a single coordinate may be enough for model updating.

In this present work, the inverse eigensensitivity method [22] is used for the model updating. The method is based on the following equation:

$$\{\Delta r\} = [S]\{\Delta p\} \tag{34.7}$$

Here, $\{r\}$ is the response vector composed of mode shapes and natural frequencies, $\{p\}$ is the parameter vector composed of geometrical parameters or material properties used in the FE model, and $[S]$ is the modal sensitivity matrix. Modal sensitivity matrix $[S]$ can be written as

$$[S] = \begin{bmatrix} S_{r_1}{}^{p_1} & \cdots & S_{r_1}{}^{p_m} \\ \vdots & \ddots & \vdots \\ S_{r_n}{}^{p_1} & \cdots & S_{r_n}{}^{p_m} \end{bmatrix} \tag{34.8}$$

If the structure is complex, it is easier to calculate the sensitivities by numerical differentiation. After obtaining the sensitivity matrix $[S]$ and $\{\Delta r\}$ vector, $\{\Delta p\}$ which gives the changes required to be made in parameter vector, can be obtained from the following equation:

$$\{\Delta p\} = [S]^{-1}\{\Delta r\} \tag{34.9}$$

34.3 Experimental Study

In this section, PRD method developed recently [17] is applied to the gun barrel of a battle tank. Employing the PRD method, both linear FRFs and the nonlinearities in the system are obtained from experimentally measured nonlinear FRFs.

Fig. 34.1 Gun barrel test setup

34.3.1 Experimental Setup

The test set-up, which consists of the gun barrel of a battle tank, is shown in Fig. 34.1.

34.3.2 First Set of Experiments

In the first set of experiments, the structure is excited with a random force. In random excitation tests, 6 different force levels are used starting from a very low to high forcing levels. Since the accuracy of the PRD method proposed for obtaining linear FRFs and nonlinear identification depends on the excitation frequency and it is shown that when the structure is excited at around the linear resonance frequency of the structure the method gives more accurate results [17], in the first random excitation test low excitation signal level is selected.

In all the random excitation tests, a frequency resolution of 0.0625 Hz is used in measurements. In order to minimize the noise in measurements, 21 averages are taken. In all the random excitation tests, 6 accelerometers are used, and the gun barrel is excited with the shaker located at the tip of the gun barrel.

The accelerometer and the shaker locations and geometry constructed in the PULSE software are shown in Fig. 34.2.

The node numbering starts from the tip of gun barrel (node number 1) and continues till the root end of the gun barrel (node number 6) that is accessible from outside of the tank. The shaker is located at node 1 as shown in Fig. 34.3.

The force levels used in the random excitation tests are shown in Fig. 34.3, and their root mean square (rms) values are given in Table 34.1.

For the given excitation levels, FRFs are measured by using PULSE software, the FRFs at node 1 (tip of gun barrel) are shown in Fig. 34.4.

As the first observation from Fig. 34.4, it is seenthat FRFs are slightly different for different random excitation force levels. Therefore in order to see the differences more clearly, resonance regions are zoomed in and shown in Figs. 34.5, 34.6 and 34.7, respectively.

As can be seen from Figs. 34.5, 34.6 and 34.7, natural frequencies are shifted when the force level changes. Especially at the fundamental mode of the gun barrel this effect is much more pronounced. These observations give a clear indication of nonlinearity in the structure. In order to see the dynamical characteristic of the gun barrel in more detail, for each of the force levels, modal analysis is performed and the corresponding modal parameters are extracted by using ME'scope modal analysis software. Modal parameters extracted are compared to each other for all the random excitation force level cases. The

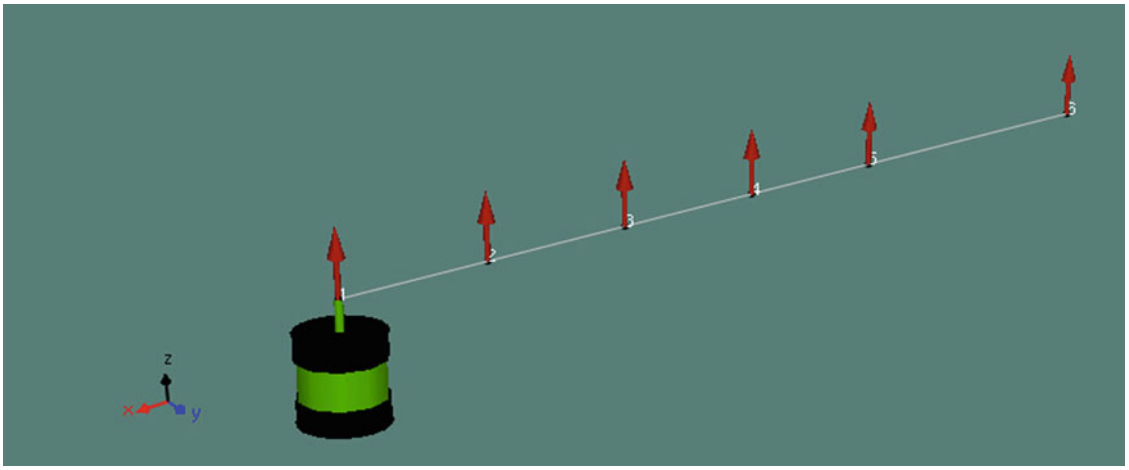

Fig. 34.2 Test geometry constructed in PULSE software

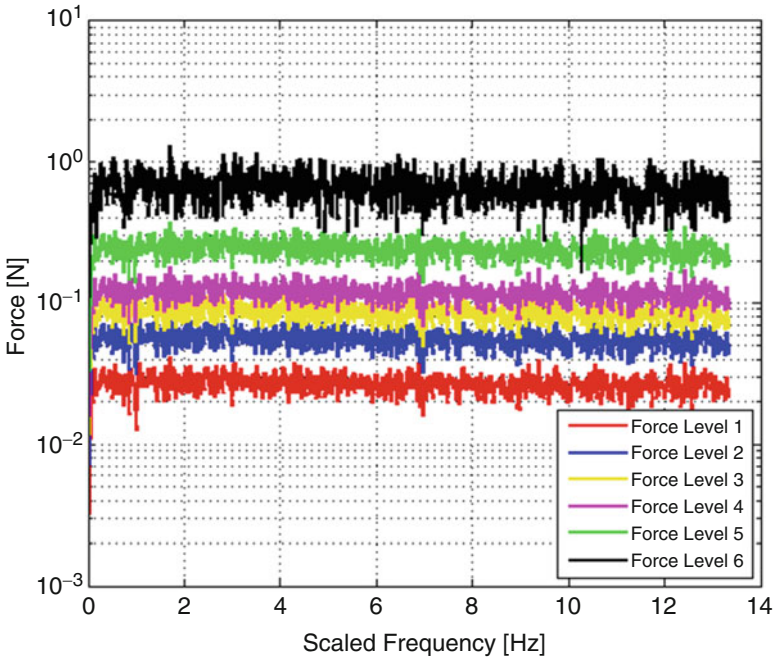

Fig. 34.3 Force levels used in random excitation tests

Table 34.1 Force levels used in random excitation tests

Force level	Rms (N)
1	0.88
2	1.829
3	2.809
4	3.859
5	7.888
6	21.851

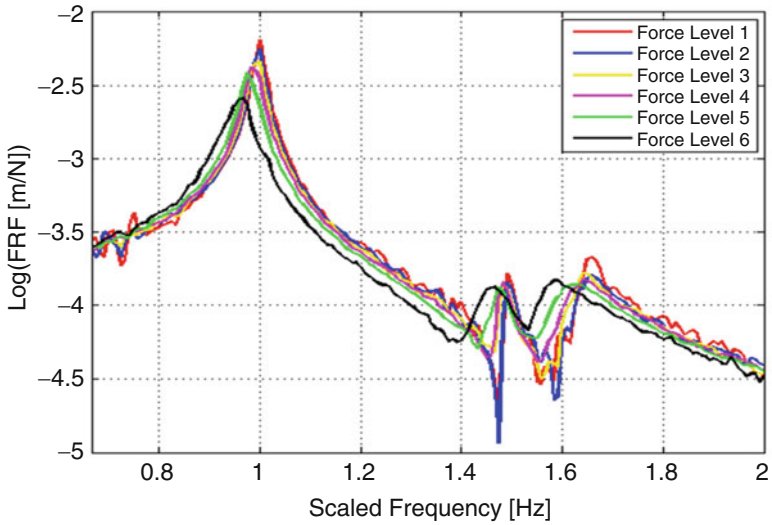

Fig. 34.4 Measured FRFs at node 1

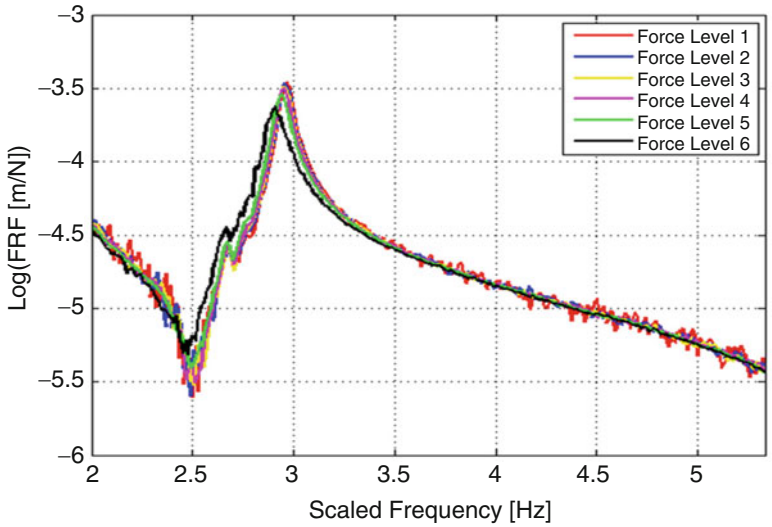

Fig. 34.5 Measured FRFs at node 1

natural frequencies are scaled such that the fundamental natural frequency of the gun barrel is 1 Hz for the lowest excitation force level. The natural frequency comparison is given in Table 34.2 and it is shown in Fig. 34.8.

As seen from Fig. 34.8 and Table 34.2, for the first three force levels, the second mode of the structure cannot be extracted from modal analysis. Also it is clearly seen that as the force level increases the natural frequencies tend to decrease for all the modes.

Similar comparison can be made for the damping values extracted from the analysis. The comparison of the damping values for each of the force levels is given in Table 34.3 and shown in Fig. 34.9.

As observed from Fig. 34.9 and Table 34.3, as the force level increases damping values of the modes tend to increase for all the modes except the third mode. Only in the third mode the damping value drops for force level 6.

From results of the random excitation tests, the existence of nonlinearity in the system is clearly seen. Since the fundamental mode of the gun barrel is under consideration, we can also conclude that, for the fundamental mode, as the force level increases in the random excitation tests, damping value of the fundamental mode increases and natural frequency decreases.

In order to apply the PRD method, the structure is excited at around 1 Hz (scaled frequency) with a pure sine excitation at different forcing levels. The structure is excited at a low forcing level and then at a number of high forcing levels. The

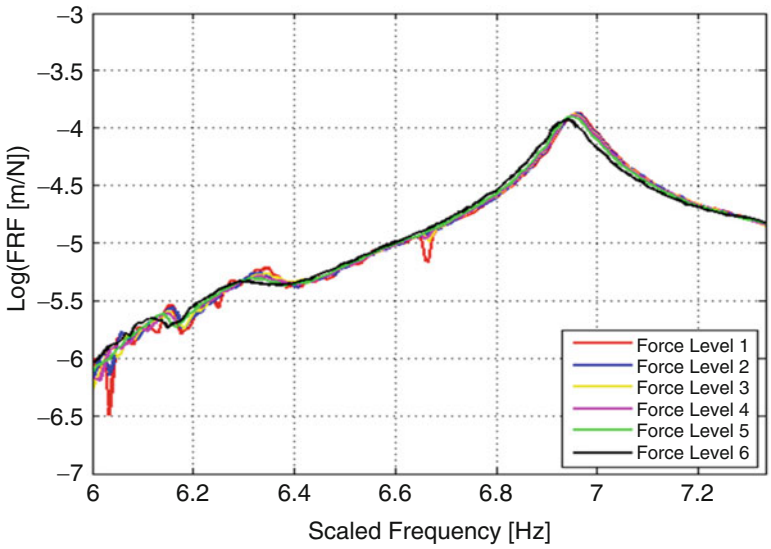

Fig. 34.6 Measured FRFs at node 1

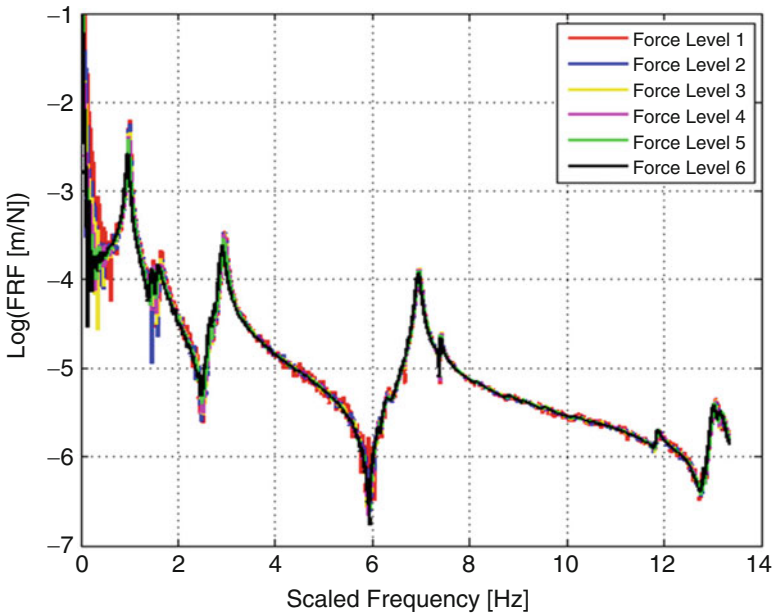

Fig. 34.7 Measured FRFs at node 1

advantage of this method is that, there is no need for any vibration controller as in the cases of constant forcing or constant amplitude testing over a certain frequency range.

In order to see the effect of choosing different frequencies of excitation on the performance of the method, five different excitation frequencies (1 Hz, 0.933 Hz, 0.95 Hz, 0.966 Hz, and 0.983 Hz) are used, and for each of these excitation frequencies, describing functions of the nonlinearities are obtained by using PRD method.

34.3.2.1 Application of PRD Method at Scaled Frequency 1 Hz for Identifying Nonlinearity

Real and imaginary parts of the describing function are obtained from experimental measurements at scaled frequency 1 Hz by applying PRD method. For the real and imaginary parts of the describing function, 3rd order polynomial functions are fit (Fig. 34.10). Corresponding coefficients of the polynomial functions are given in Table 34.4.

Table 34.2 Scaled natural frequency comparison for different force levels

	Force level 1	Force level 2	Force level 3	Force level 4	Force level 5	Force level 6
Mode number	Scaled natural frequency (Hz)					
1	1.0000	0.9964	0.9932	0.9888	0.9788	0.9595
2	***	***	***	1.4807	1.4737	1.4572
3	1.6491	1.6485	1.6305	1.6236	1.6059	1.5673
4	2.9604	2.9559	2.9525	2.9481	2.9357	2.9047
5	6.9588	6.9565	6.9548	6.9533	6.9483	6.9379

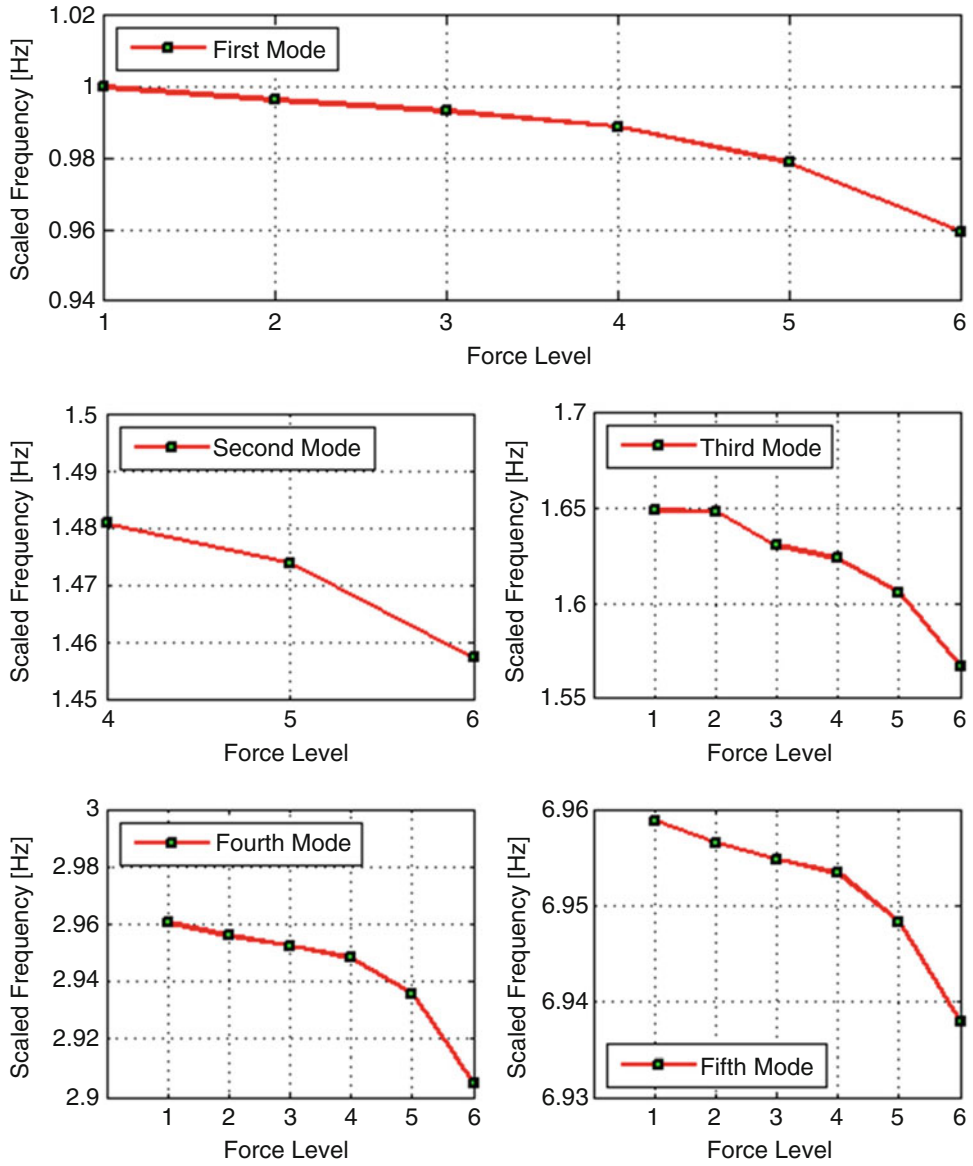

Fig. 34.8 Scaled natural frequency comparison for different force levels

Table 34.3 Modal damping comparison for different force levels

	Force level 1	Force level 2	Force level 3	Force level 4	Force level 5	Force level 6
Mode number	Modal damping (%)					
1	0.955	1.033	1.171	1.345	1.621	2.368
2	***	***	***	0.769	1.187	2.498
3	1.531	1.837	2.193	2.637	3.093	2.926
4	0.87	0.903	0.941	0.985	1.115	1.483
5	0.499	0.496	0.504	0.513	0.533	0.58

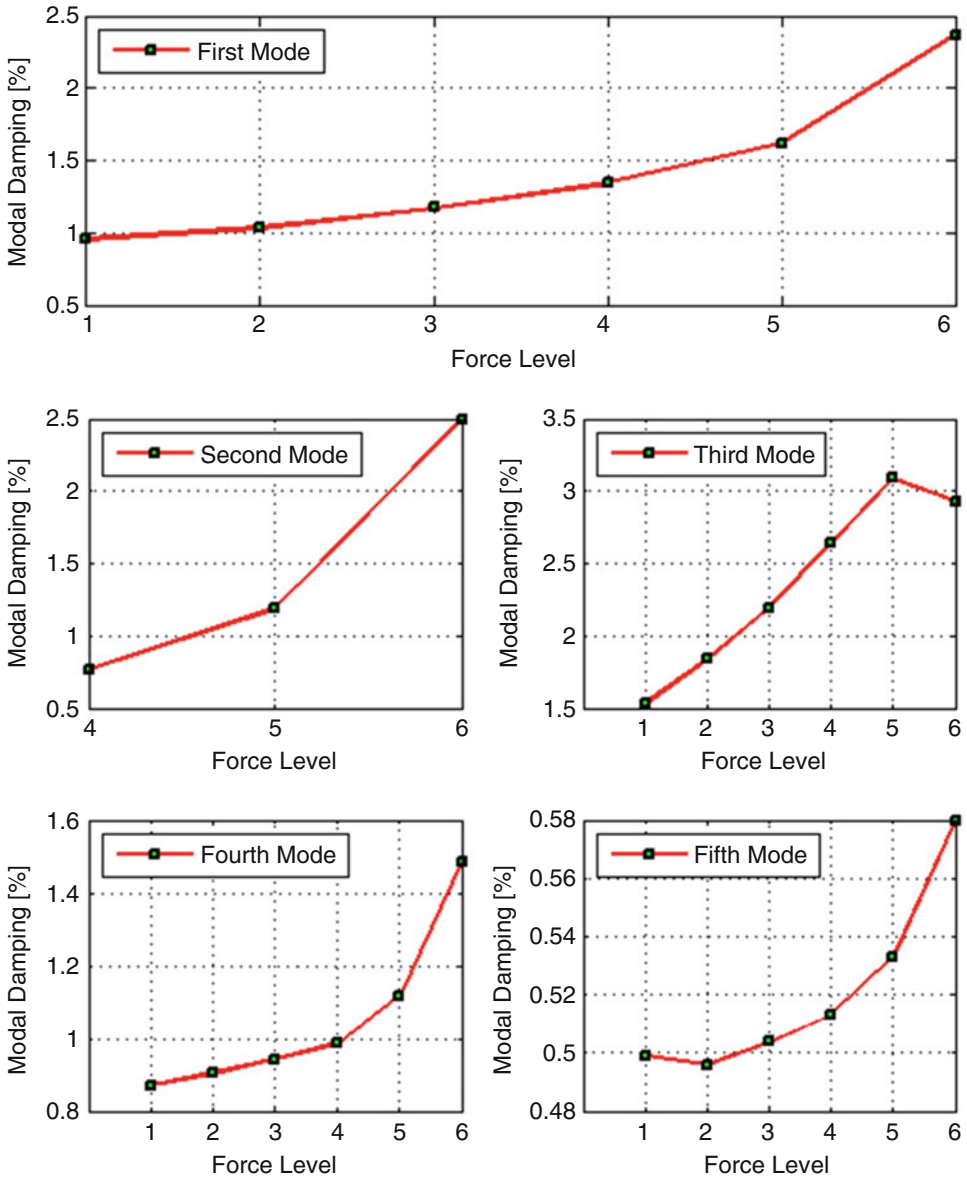

Fig. 34.9 Modal damping comparison for different force levels

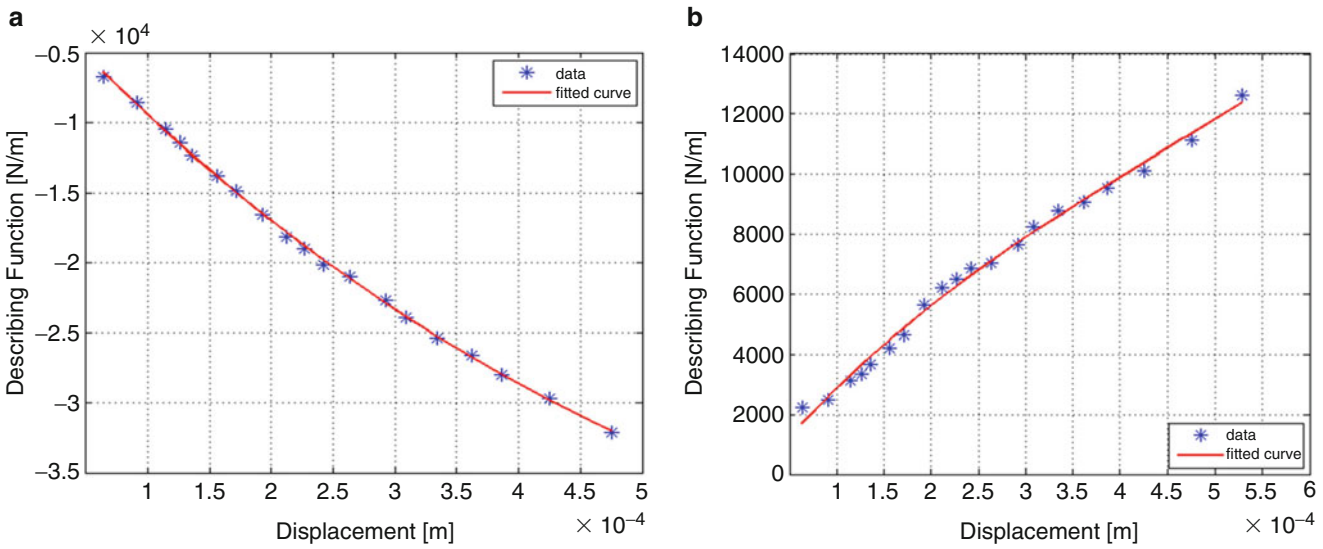

Fig. 34.10 Calculated describing function (**a**) Real part (**b**) Imaginary part

Table 34.4 Coefficients of the polynomials fit to the data for real and imaginary parts of the describing function

	p_3	p_2	p_1	p_0
Real part of describing function $p_3x^3 + p_2x^2 + p_1x + p_0$	-2.62×10^{13}	7.62×10^{10}	-9.64×10^{7}	-565
Imaginary part of describing function $p_3x^3 + p_2x^2 + p_1x + p_0$	3.12×10^{13}	-4.18×10^{10}	3.77×10^{7}	-518

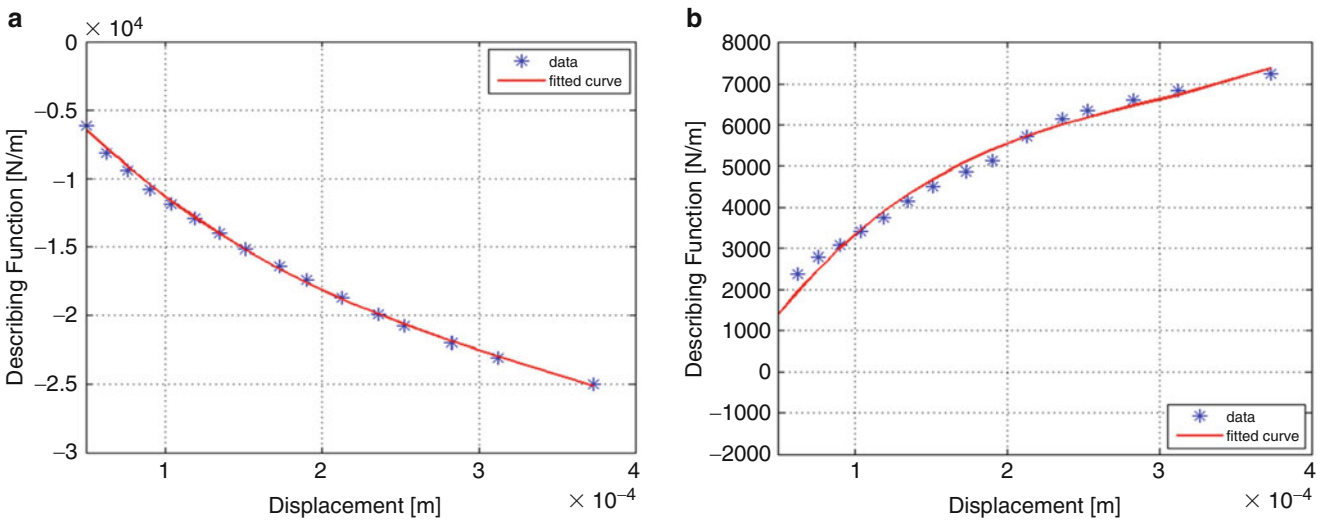

Fig. 34.11 Calculated describing function (**a**) Real part (**b**) Imaginary part

34.3.2.2 Application of PRD Method at Scaled Frequency 0.933 Hz for Identifying Nonlinearity

Real and imaginary parts of the describing function are obtained from experimental measurements at scaled frequency 0.933 Hz by applying PRD method. For the real and imaginary parts of the describing function, 3rd order polynomial functions are fit (Fig. 34.11). Corresponding coefficients of the polynomial functions are given in Table 34.5.

Table 34.5 Coefficients of the polynomials fit to the data for real and imaginary part of the describing function

	p_3	p_2	p_1	p_0
Real part of describing function $p_3x^3 + p_2x^2 + p_1x + p_0$	-2.52×10^{14}	2.72×10^{11}	-1.32×10^{8}	-579
Imaginary part of describing function $p_3x^3 + p_2x^2 + p_1x + p_0$	2.03×10^{14}	-1.79×10^{11}	6.17×10^{7}	-1260

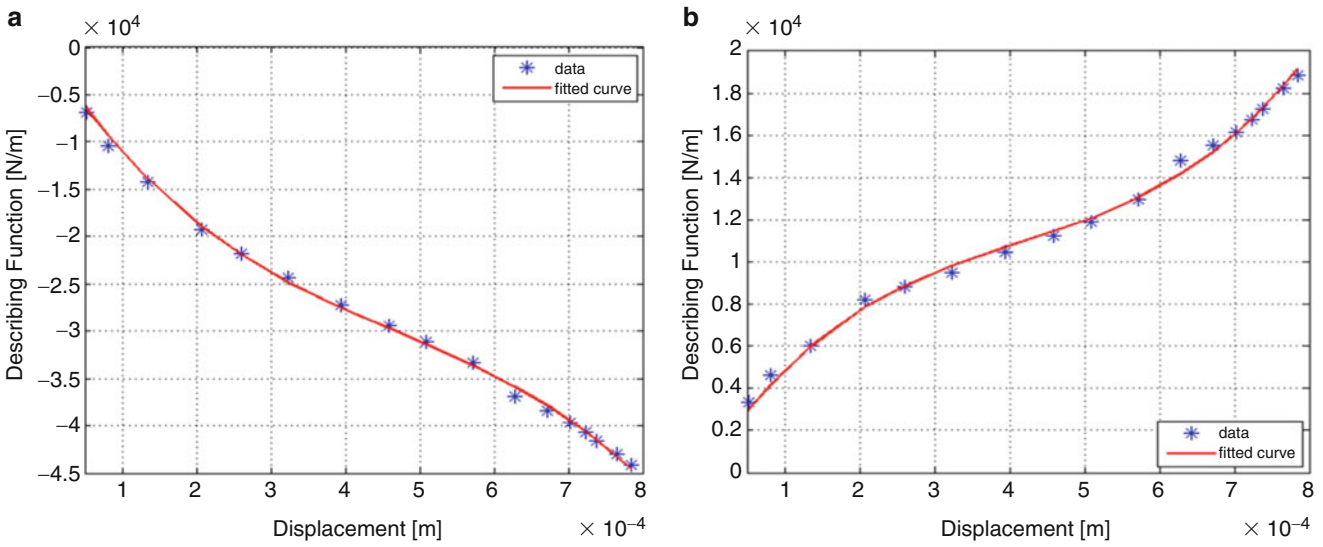

Fig. 34.12 Calculated describing function (**a**) Real part (**b**) Imaginary part

Table 34.6 Coefficients of the polynomials fit to the data for real and imaginary part of the describing function

	p_3	p_2	p_1	p_0
Real part of describing function $p_3x^3 + p_2x^2 + p_1x + p_0$	-1.33×10^{14}	1.88×10^{11}	-1.21×10^{8}	-608
Imaginary part of describing function $p_3x^3 + p_2x^2 + p_1x + p_0$	7.84×10^{13}	-9.78×10^{10}	5.21×10^{7}	523

34.3.2.3 Application of PRD Method at Scaled Frequency 0.95 Hz for Identifying Nonlinearity

Real and imaginary parts of the describing function are obtained from experimental measurements at scaled frequency 0.95 Hz by applying PRD method. For the real and imaginary parts of the describing function, 3rd order polynomial functions are fit (Fig. 34.12). Corresponding coefficients of the polynomial functions are given in Table 34.6.

34.3.2.4 Application of PRD Method at Scaled Frequency 0.966 Hz for Identifying Nonlinearity

Real and imaginary parts of the describing function are obtained from experimental measurements at scaled frequency 0.966 Hz by applying PRD method. For the real and imaginary parts of the describing function, 3rd order polynomial functions are fit (Fig. 34.13). Corresponding coefficients of the polynomial functions are given in Table 34.7.

34.3.2.5 Application of PRD Method at Scaled Frequency 0.983 Hz for Identifying Nonlinearity

Real and imaginary parts of the describing function are obtained from experimental measurements at scaled frequency 0.983 Hz by applying PRD method. For the real and imaginary parts of the describing function, 3rd order polynomial functions are fit (Fig. 34.14). Corresponding coefficients of the polynomial functions are given in Table 34.8.

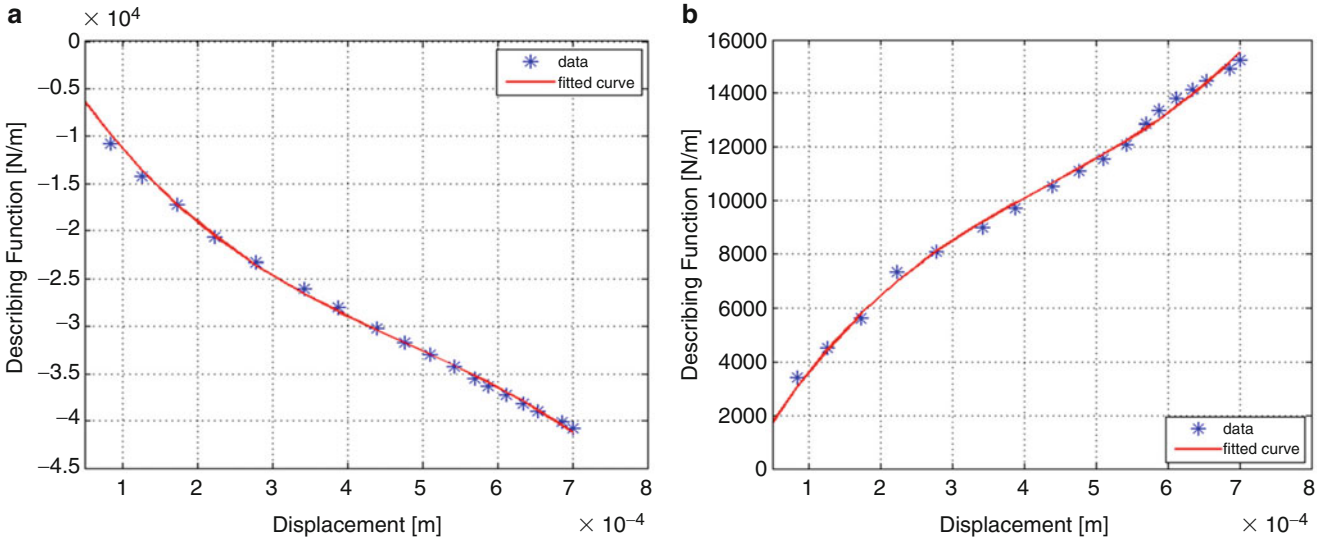

Fig. 34.13 Calculated describing function (**a**) Real part (**b**) Imaginary part

Table 34.7 Coefficients of the polynomials fit to the data for real and imaginary part of the describing function

	p_3	p_2	p_1	p_0
Real part of describing function $p_3x^3 + p_2x^2 + p_1x + p_0$	-1.30×10^{14}	1.85×10^{11}	-1.24×10^{8}	-618
Imaginary part of describing function $p_3x^3 + p_2x^2 + p_1x + p_0$	5.84×10^{13}	-7.62×10^{10}	4.75×10^{7}	-483

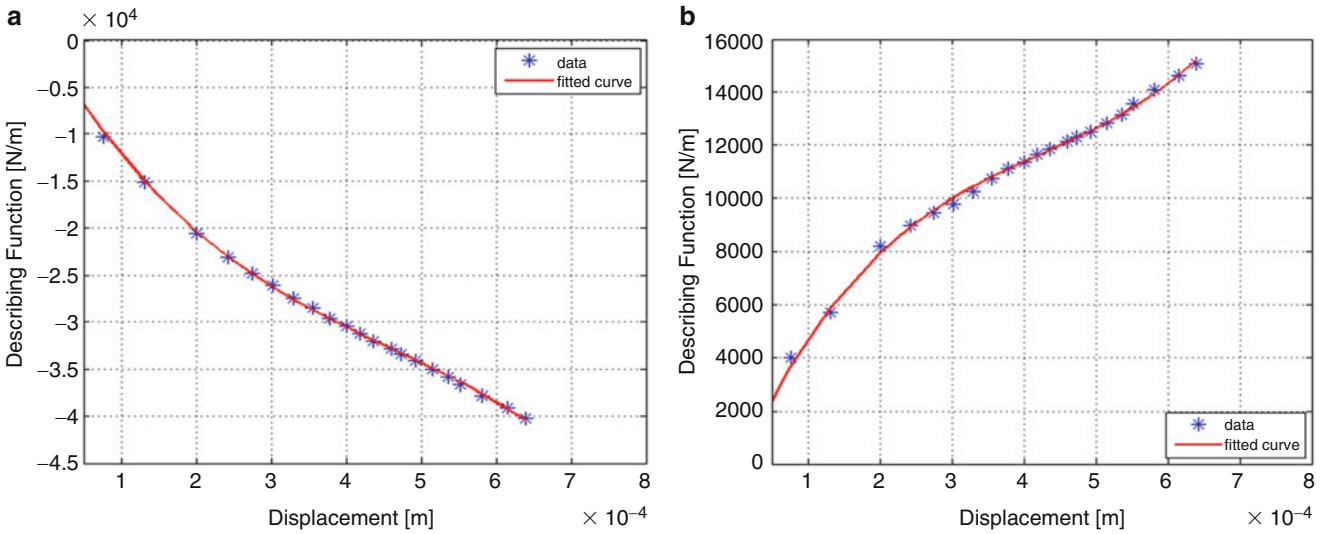

Fig. 34.14 Calculated describing function (**a**) Real part (**b**) Imaginary part

34.3.2.6 Comparison of Nonlinearities Identified by Using PRD Method at Different Frequencies

In this section, the real and imaginary parts of the describing function obtained from experimental measurements at scaled frequency 0.933 Hz, 0.95 Hz, 0.966 Hz, 0.983 Hz and 1 Hz by using PRD method are compared with each other. Comparisons of the real and imaginary parts of the describing functions are shown in Fig. 34.15.

When we compare the real part of describing functions obtained using the measurements at scaled frequency 0.933 Hz, 0.95 Hz, 0.966 Hz, 0.983 Hz and 1 Hz, it can be observed from Fig. 34.15 that identified functions are similar to each other.

Table 34.8 Coefficients of the polynomials fit to the data for real and imaginary part of the describing function

	p_3	p_2	p_1	p_0
Real part of describing function $p_3x^3 + p_2x^2 + p_1x + p_0$	-1.51×10^{14}	2.1×10^{11}	-1.34×10^{8}	-628
Imaginary part of describing function $p_3x^3 + p_2x^2 + p_1x + p_0$	1.05×10^{14}	-1.27×10^{11}	6.36×10^{7}	-498

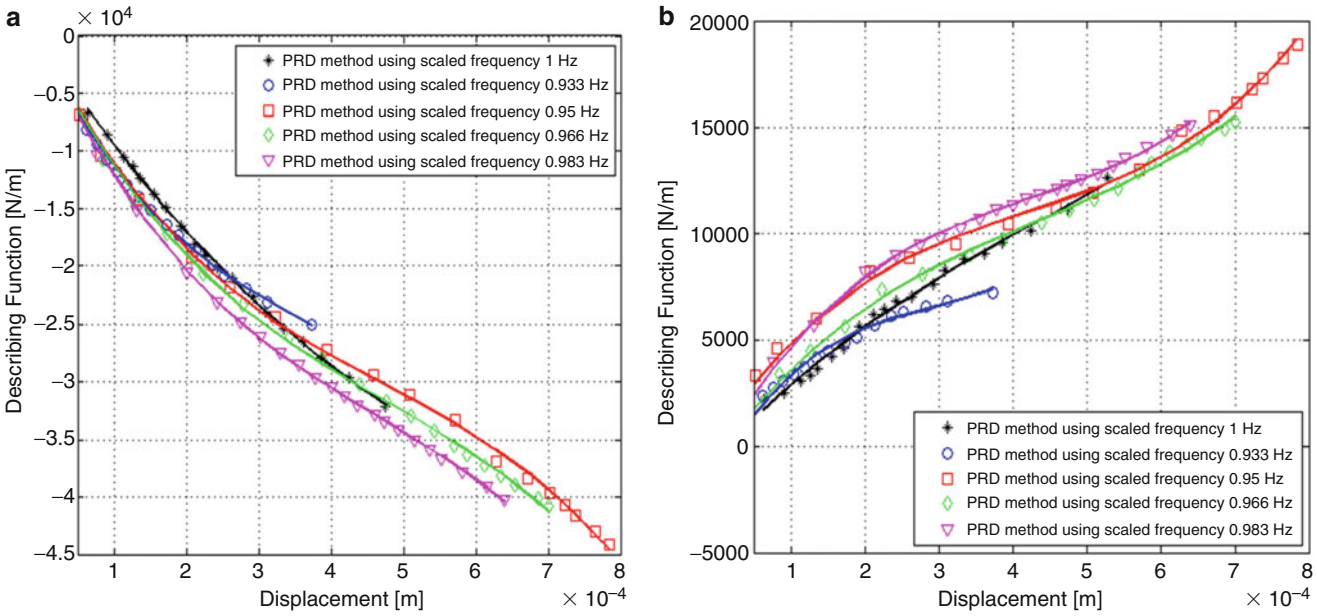

Fig. 34.15 Comparison of identified (**a**) real parts of the describing function (**b**) imaginary parts of the describing function

As seen from Fig. 34.15, the identified imaginary parts of describing functions are also similar to each other. Then we can conclude that the excitation frequency used in PRD method, does not have significant effect on the identified nonlinearity, if the excitation frequency is approximately in the 5 % range of the resonance of the underlying linear system.

As a final test in this set of experiments, frequency responses are measured for a constant low forcing level excitation. Stepped sine test is used as an excitation type by using the given test set-up. Excitation signal is a pure sinusoidal signal. In order to perform constant force vibration testing over the frequency range, a manual control strategy is used in the experiments. This control is maintained by checking the forcing level and changing the excitation voltage supplied to the shaker. In Fig. 34.16, measured FRFs for F = 0.5 N are shown.

It is observed from Fig. 34.16 that the FRF curve obtained for F = 0.5 N seems like a linear FRF curve, as expected. However, as it will be shown below, the measured FRF and the actual linear FRF curves of the system are different from each other even though a very low forcing is used in the experiment.

34.3.3 Second Set of Experiments

In the second set of experiments, the main purpose is to perform measurements which will be used to study the performance of the PRD method and the model updating approach proposed. A set of stepped sine constant force tests is used in the experiments. Similarly, the constant force excitation is maintained by manually checking the forcing level and changing the excitation voltage supplied to the shaker at each frequency point. The structure is excited at 3 different forcing levels (F = 5 N, F = 10.4 N, F = 15 N). The measured FRFs are shown in Fig. 34.17.

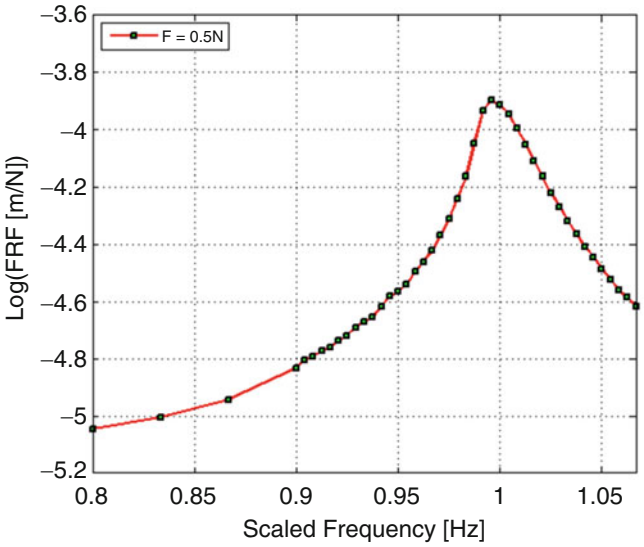

Fig. 34.16 Measured FRF at F = 0.5 N

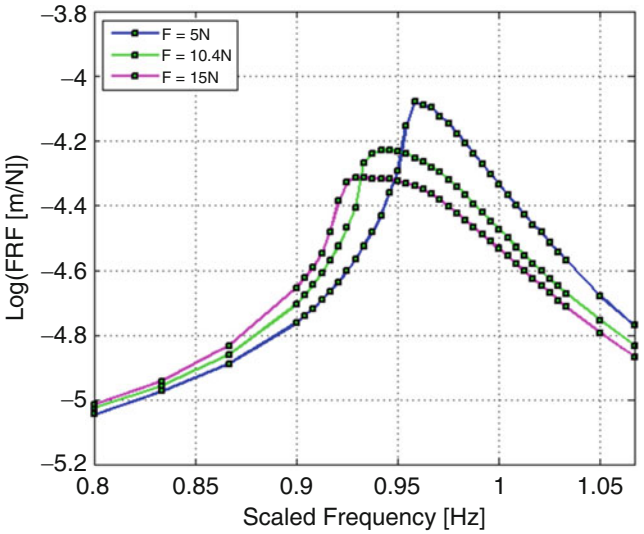

Fig. 34.17 Measured FRF at F = 5 N, F = 10.4 N, F = 15 N

34.3.4 Application of PRD Method for Obtaining Linear FRFs

Using the describing function values obtained by applying PRD method and the FRF values measured at F = 0.5 N in the first set of experiments, linear FRFs of the structure are predicted. Since, describing functions are obtained at 5 different excitation frequencies, in order to study the effects of test frequency on the performance of the method; five separate linear FRF curves are predicted. The linear FRF curves predicted by using the describing functions obtained from experiments made at scaled frequency 0.933 Hz, 0.95 Hz, 0.966 Hz, 0.983 Hz and 1 Hz are compared with the FRFs measured at F = 0.5 N in Figs. 34.18, 34.19 and 34.20 and with each other in Fig. 34.21.

As can be observed from Figs. 34.18, 34.19 and 34.20, FRFs measured at low forcing level (F = 0.5 N) do not accurately represent the linear FRFs of the system which can be obtained by using the PRD method proposed. FRFs measured at even a very low forcing level may not represent the linear FRF accurately. It is also observed from Fig. 34.21 that linear FRFs obtained using the describing functions identified from the tests made at scaled frequency 0.933 Hz, 0.95 Hz, 0.966 Hz, 0.983 Hz and 1 Hz may deviate from each other only around the resonance (deviation of the peak amplitude from the mean amplitude value is approximately less than 9 %). Based on these observations, if the excitation frequency used in PRD

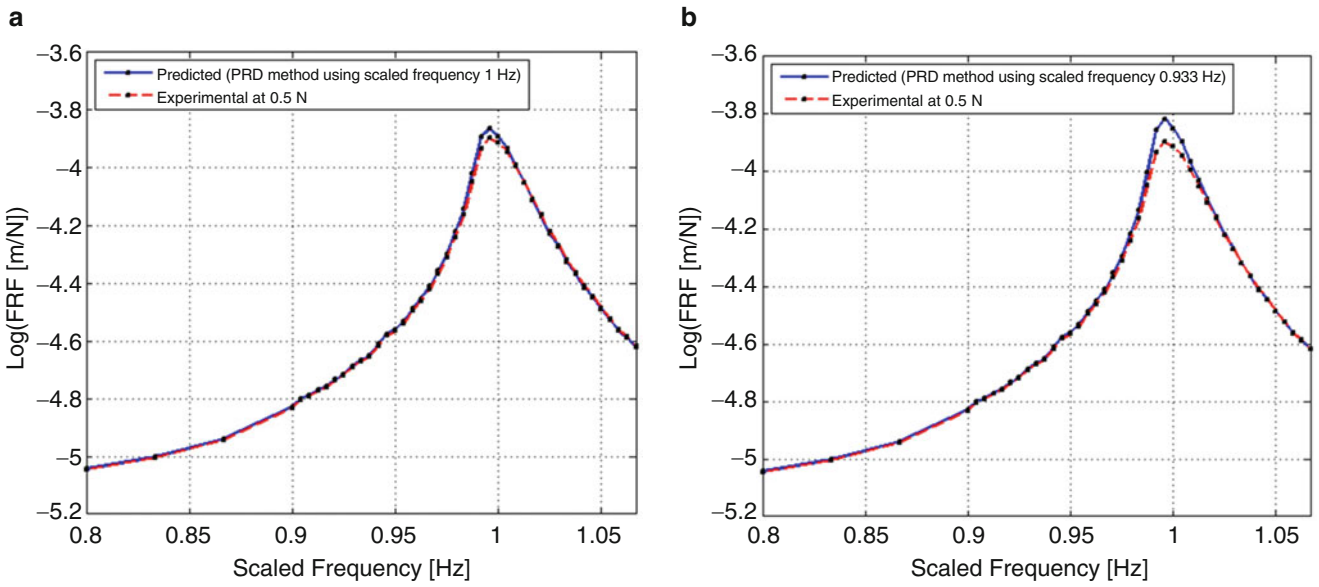

Fig. 34.18 Comparison of measured FRFs at F = 0.5 N with predicted linear FRFs by using PRD method at scaled frequency: (**a**) 1 Hz; (**b**) 0.933 Hz

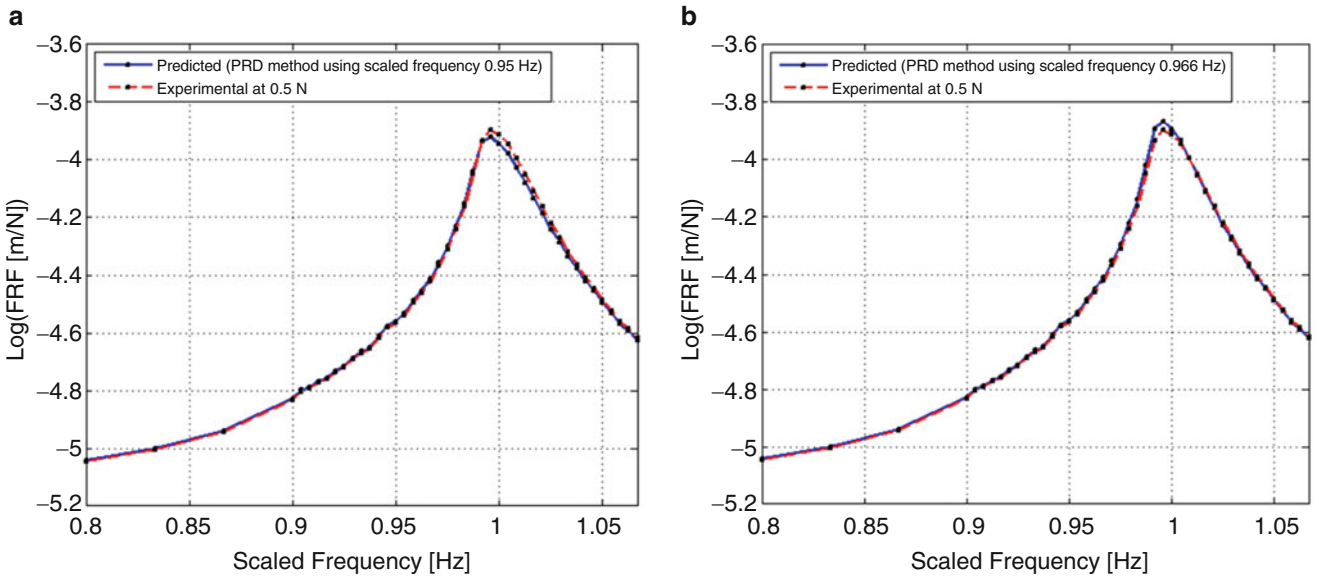

Fig. 34.19 Comparison of measured FRFs at F = 0.5 N with predicted linear FRFs by using PRD method at scaled frequency: (**a**) 0.95 Hz; (**b**) 0.966 Hz

method is approximately in the 5 % range of the resonance of the underlying linear system, there are no large discrepancies in the predicted linear FRFs.

34.4 Model Updating of the Test System and Verification of the Updated Model

In this section firstly linear FE model of the gun barrel is constructed and then it is updated by using the linear FRFs obtained through the PRD method and by applying inverse eigensensitivity method. The updated nonlinear model of the gun barrel is constructed by using the identified nonlinearity and updated linear FE model of the system. Then the nonlinear FRFs of the

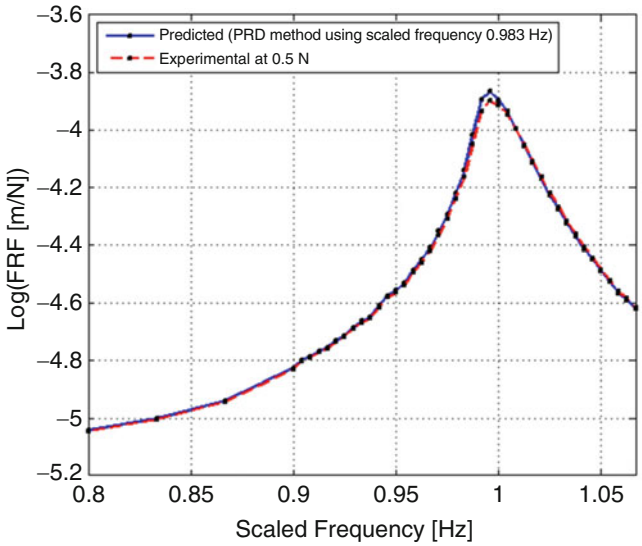

Fig. 34.20 Comparison of measured FRFs at F = 0.5 N with predicted linear FRFs by using PRD method at scaled frequency 0.983 Hz

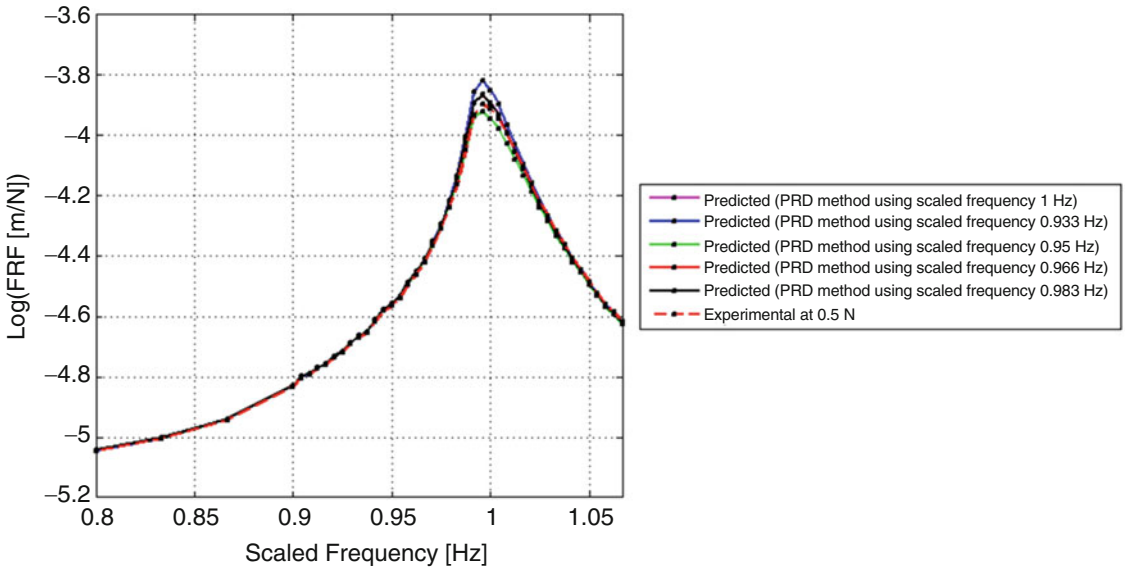

Fig. 34.21 Comparison of predicted linear FRFs by using PRD method

system are calculated at different forcing levels by using the updated model. Finally, predicted and measured FRFs of the system are compared and thus the accuracy of the updated nonlinear model of the system is studied.

34.4.1 FE Modeling of the Gun Barrel

In order to model the gun barrel in FE analysis software, firstly the components and the mechanism of the gun barrel should be understood. Typical gun barrel of a battle tank is shown in Fig. 34.22.

As seen from Fig. 34.22, gun barrel is mainly composed of gun tube, thermal shrouds, shielding-armor and rear components of the mechanism. The main part of the rear components is the elevation motor assembly which drives the gun barrel around the trunnion axis. The simplified model of the gun barrel system is shown in Fig. 34.23.

Simplified model of the gun barrel system is composed of turret, elevation motor assembly and gun tube. Elevation motor assembly is modelled by a linear stiffness which acts force along the gun tube axis.

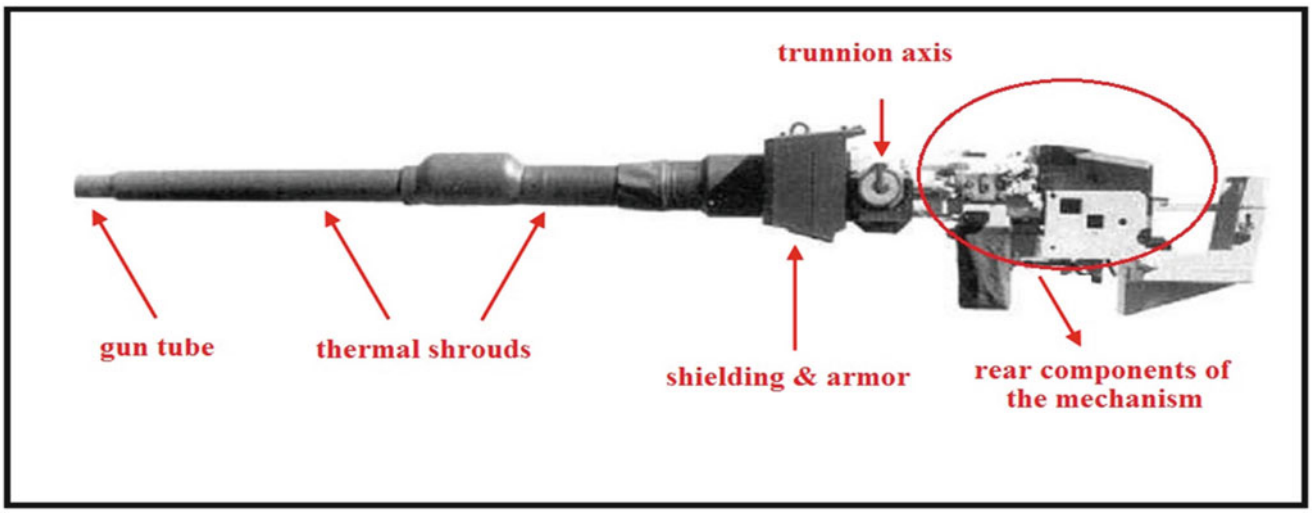

Fig. 34.22 Gun barrel of a battle tank

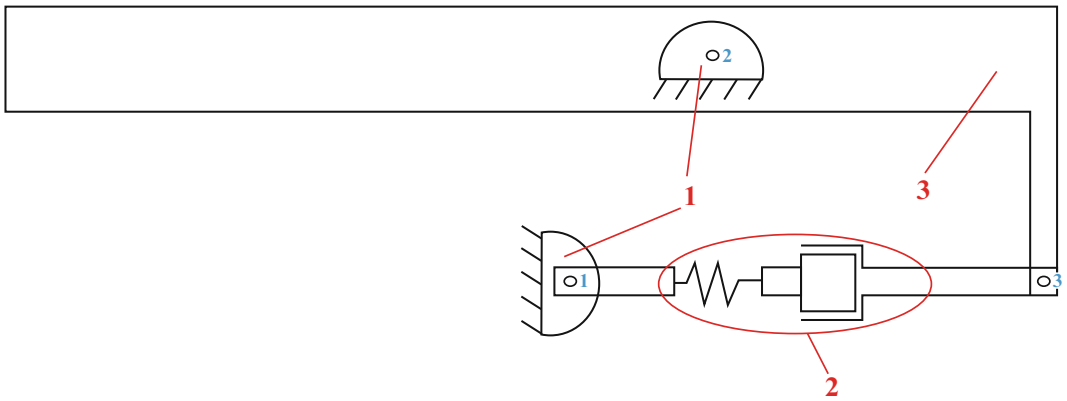

Fig. 34.23 Simplified model of gun barrel system

Table 34.9 Geometrical and material properties of the gun tube

Material	Carbon steel (0.4 % carbon)
Modulus of elasticity (GPa)	207
Length (m)	6.6
Inner diameter (mm)	120

The geometric and material properties of the gun tube of the gun barrel system are given in Table 34.9.

In the FE model constructed, mass of the thermal shrouds are neglected. The shielding-armor and the rear components of the system are modelled as lumped masses with mass and inertia properties.

The stiffness of the elevation motor is taken as 140×10^6 N/m which is a typical value for such gun barrel systems. However, there is an uncertainty in the value of stiffness of the elevation motor, therefore this parameter will be used as the updating parameter in FE model updating.

34.4.2 Mesh Sensitivity Analysis for the FE Model of Gun Barrel

In this section before the construction of the initial FE model of the gun barrel in ANSYS, mesh sensitivity analysis is performed in order to see the effect of mesh sizing on the estimation of the fundamental natural frequencies of the structure. FE model of the gun barrel used in the mesh sensitivity analysis is shown in Fig. 34.24.

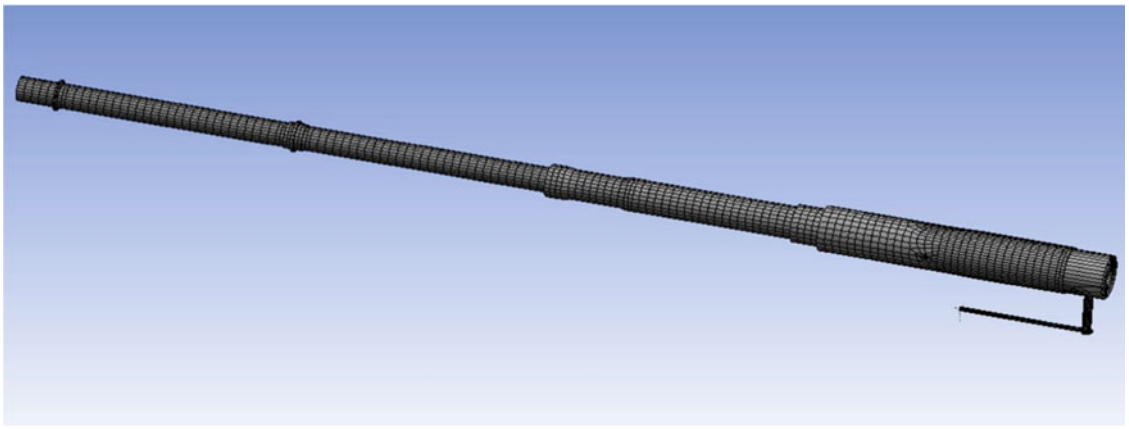

Fig. 34.24 FE model of the gun barrel

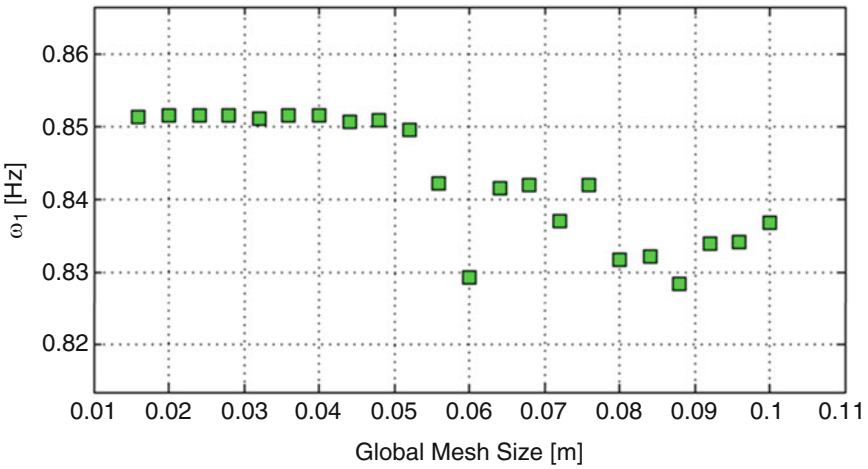

Fig. 34.25 Variation of the fundamental natural frequency of the gun barrel with respect to global mesh sizing

Global mesh size for the FE model is varied between 0.1 and 0.01 m, and for each of the global mesh size, modal analyses are performed in ANSYS. Fundamental natural frequency of the gun barrel is calculated for each case. In the analysis SOLID 186 element is used. The variation of the fundamental natural frequency with respect to global mesh sizing and the fundamental modeshape are shown in Figs. 34.25 and 34.26, respectively.

As seen from Fig. 34.25, scaled fundamental natural frequency is converged approximately to 0.85 Hz after global mesh size reaches to approximately 0.05 m. From the observations made for the mesh sensitivity analysis, mesh sizing of the initial FE model is selected as 0.05 m.

34.4.3 Model Updating of the FE Model of Gun Barrel System

In this section, by using the observations made from mesh sensitivity analysis, initial linear FE model of the gun barrel is built in ANSYS and then the linear FE model is updated by employing the approach proposed. The linear FE model of the gun barrel is updated by using the extracted linear FRFs employing the PRD method and then applying inverse eigensensitivity method. Using the identified nonlinearity and updated linear FE model, updated nonlinear mathematical model of the gun barrel system is built. Finally, in order to demonstrate the accuracy of the updated nonlinear model of the system, predicted and experimentally measured FRFs of the gun barrel are compared at different forcing levels.

In the initial FE model, the stiffness of the elevation motor is taken as 140×10^6 N/m. The fundamental natural frequency and the driving point FRF at the tip of gun barrel (node 1 in the experiments) in transverse direction are calculated in ANSYS

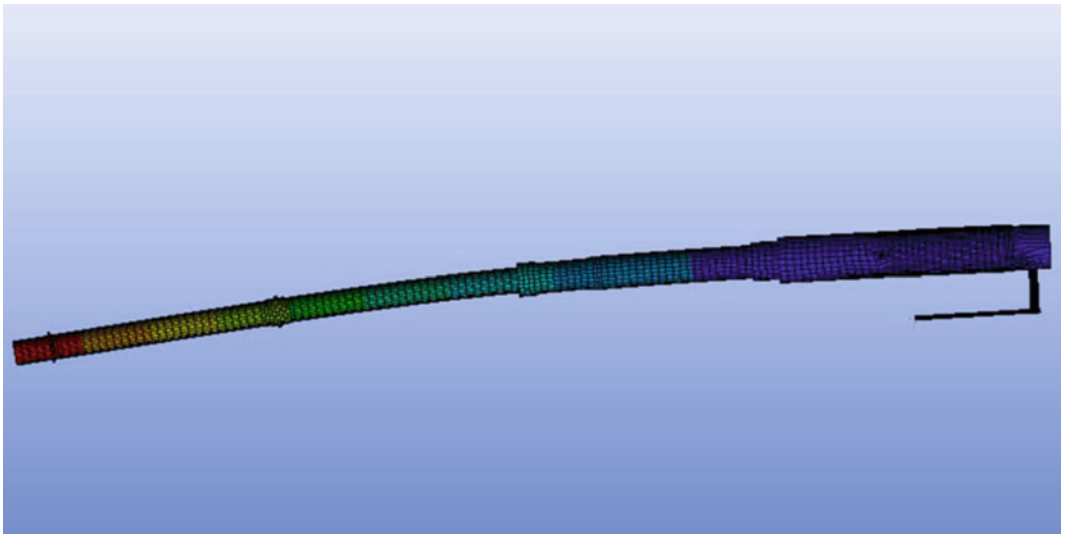

Fig. 34.26 Fundamental modeshape of the gun barrel

Table 34.10 Comparison of the fundamental natural frequency obtained from initial FE model with the one obtained from experimental FRFs by using PRD method

Mode number	Scaled natural frequency (PRD method) (Hz)	Scaled natural frequency (initial FE model) (Hz)	Error (%)
1	0.99583	0.85	−14.64

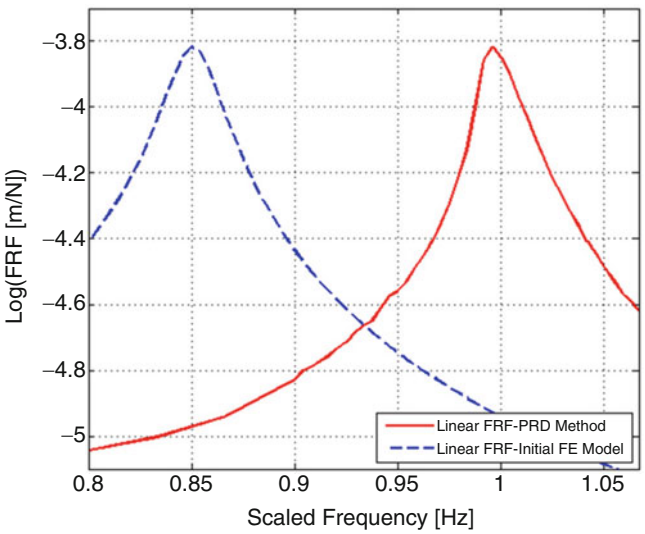

Fig. 34.27 Comparison of the linear FRFs obtained from initial FE model with those obtained from experimental FRFs by using PRD method

by using the FE model. Comparisons of the fundamental natural frequency and the linear FRFs obtained from FE analysis with those obtained from experiments by using PRD method are given in Table 34.10 and Fig. 34.27, respectively.

As can be seen in Table 34.10 and Fig. 34.27, there are considerable differences between two results; therefore the FE model of the gun barrel needs to be updated. As mentioned earlier there is a considerable uncertainty in the elevation motor stiffness, therefore elevation motor stiffness is selected as the updating parameter in the FE model. For the selected parameter, element of the sensitivity matrix is calculated by using the forward difference approximation with $O(h)$ which is given by Eq. (34.10) at each iteration step.

$$r'(p_i) = \frac{r(p_{i+1}) - r(p_i)}{\Delta h} \tag{34.10}$$

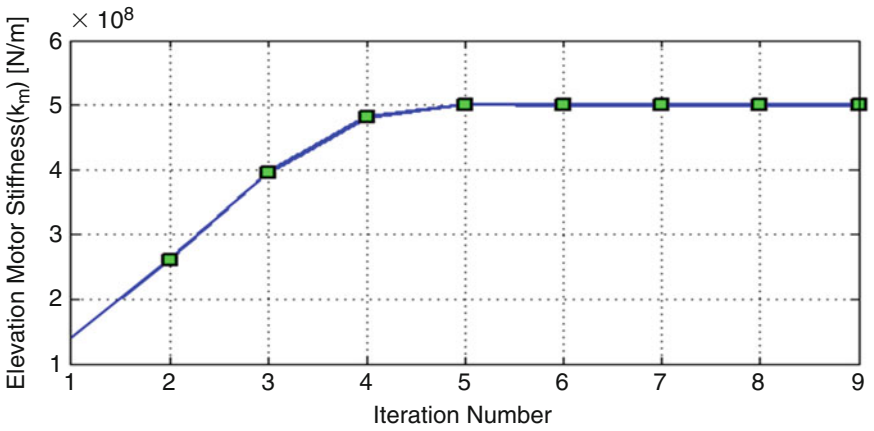

Fig. 34.28 Convergence of the stiffness of the elevation motor

Table 34.11 Comparison of the fundamental natural frequency obtained from initial and updated FE models with the value obtained from measurements by using PRD method

Mode number	Scaled natural frequency (PRD method) (Hz)	Scaled natural frequency (initial FE model) (Hz)	Error (%)	Scaled natural frequency (updated FE model) (Hz)	Error (%)
1	0.99583	0.85	−14.64	0.99583	0.00

Table 34.12 Comparison of the second and third natural frequency obtained from initial and updated FE models with experimental values

Mode number	Scaled natural frequency (experimental) (Hz)	Scaled natural frequency (initial FE model) (Hz)	Error (%)	Scaled natural frequency (updated FE model) (Hz)	Error (%)
2	2.9604	2.37	−19.94	2.9088	−1.74
3	6.9588	5.853	−15.89	6.0925	−12.45

After 9 iterations, stiffness of the elevation motor is converged to 499×10^6 N/m. The convergence graph of the stiffness of the elevation motor is given in Fig. 34.28.

Using the converged elevation motor stiffness value, the FE model is updated. Then, the fundamental natural frequency of the updated linear model of the gun barrel is calculated and compared with that of the initial FE model, as well as with the fundamental natural frequency obtained from experiments by using PRD method, in Table 34.11.

As can be seen in Table 34.11, the fundamental natural frequency of the gun barrel is perfectly estimated by using the updated FE model.

In order to see the performance of the updated FE model in the prediction of other natural frequencies which are not used in updating the FE model, the second and third natural frequency of the gun barrel in transverse direction are calculated by using the updated linear FE model and they are compared with those obtained from the initial FE model, as well as with the measured ones (Table 34.12).

As can be seen in Table 34.12, there is a considerable improvement in the calculated value of the second natural frequency, and only a slight improvement in the calculated value of the third natural frequency of the gun barrel.

In Fig. 34.29, the linear FRFs obtained from experimentally measured nonlinear FRFs by using PRD method are compared with those calculated from the initial and updated FE models of the gun barrel. As can be seen in Fig. 34.29 again a considerable improvement is obtained for the updated FE model.

Since the ultimate goal is to have accurate nonlinear response predictions from the updated FE model of the gun barrel, nonlinear FRFs experimentally measured at F = 5 N, F = 10.4 N and F = 15 N are compared with those obtained from the initial and FE updated models (composed of original and updated FE models, respectively, combined with the identified nonlinearity). The results are given in Fig. 34.30 for the forcing levels F = 5 N, F = 10.4 N and F = 15 N.

As can be observed in Fig. 34.30, considerable improvements are obtained with the updated FE model of the structure at all forcing levels. If the peak responses of the nonlinear FRF curves are observed, better match is obtained with the updated FE model at F = 15 N. From these results it can be concluded that, the developed model updating approach for nonlinear system is successfully applied to a complicated real engineering problem (gun barrel of a battle tank) and a much better nonlinear model of the gun barrel system is constructed for the fundamental mode of the system.

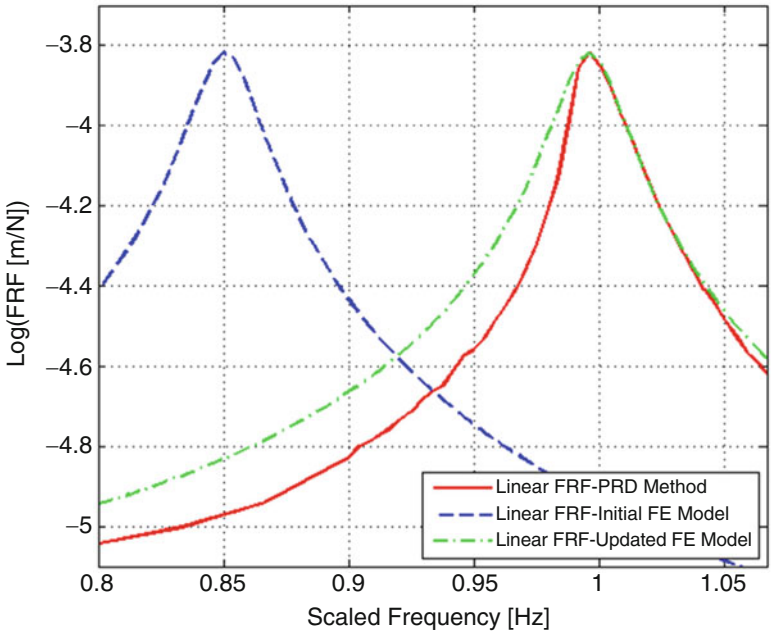

Fig. 34.29 Comparison of the linear FRF obtained by using PRD method from experimentally measured nonlinear FRFs, with those calculated from, initial and updated FE models

34.5 Summary and Conclusions

In this study, model updating approach proposed previously for a nonlinear system is applied to a real engineering structure, which is the gun barrel of a battle tank. In the first set of experiments, the structure is excited with random forcing. In the fundamental mode of the gun barrel, it is clearly shown that as the force level increases in the random excitation tests, damping value of the fundamental mode increases and natural frequency decreases. From the results of the random excitation tests, the nonlinearity in the system is clearly detected. In order to study the effect the excitation frequency used in the experiments on the performance of PRD method, the method is applied several times with different excitation frequencies. In each application, nonlinearities in the structure are parametrically identified in the form of describing functions, and also the linear FRFs are obtained. It is observed that FRFs measured at low forcing levels do not match with the linear FRFs of the system that are obtained by using the PRD method proposed. It is shown that the FRFs measured at even a very low forcing level may not represent the linear FRFs accurately. It is also observed that linear FRFs obtained through PRD method which use the describing functions identified from the tests made at different frequencies may deviate from each other only around the resonance (deviation of peak amplitude from the mean amplitude value is approximately less than 9 %). Based on these observations, it can be taken as a rule thumb that if the excitation frequency used in PRD method is approximately in the 5 % range of the resonance of the underlying linear system, there are no significant differences in the predicted linear FRFs.

After obtaining linear FRFs through the PRD method, linear FE model of the gun barrel constructed in ANSYS is updated by using the inverse eigensensitivity method. It is observed that the fundamental natural frequency of the gun barrel is perfectly estimated by using the updated FE model. Furthermore there is a considerable improvement in the calculated value of the second natural frequency, and a slight improvement in the calculated value of the third natural frequency of the gun barrel although these modes are not used in updating. Then the updated nonlinear model of the test structure is constructed by using the identified nonlinearity and updated linear FE model of the system. Finally, predicted and experimentally measured FRFs of the test structure are compared at different forcing levels and it is seen that considerable improvement is obtained for the updated FE model of the gun barrel at all forcing levels.

In conclusion, the model updating approach developed previously by the authors is successfully applied to a real complex engineering structure (gun barrel of a battle tank) and thus nonlinear mathematical model of the gun barrel system constructed initially for the fundamental mode of the system is substantially improved. The main advantage of PRD method is that, in the application of the method there is no need for any vibration controller as in the cases of constant forcing or constant amplitude testing over a certain frequency range. Furthermore, the method simultaneously identifies multiple nonlinearities in the system parametrically, and it has a feature of extracting the FRFs of the underlying linear system simultaneously. It

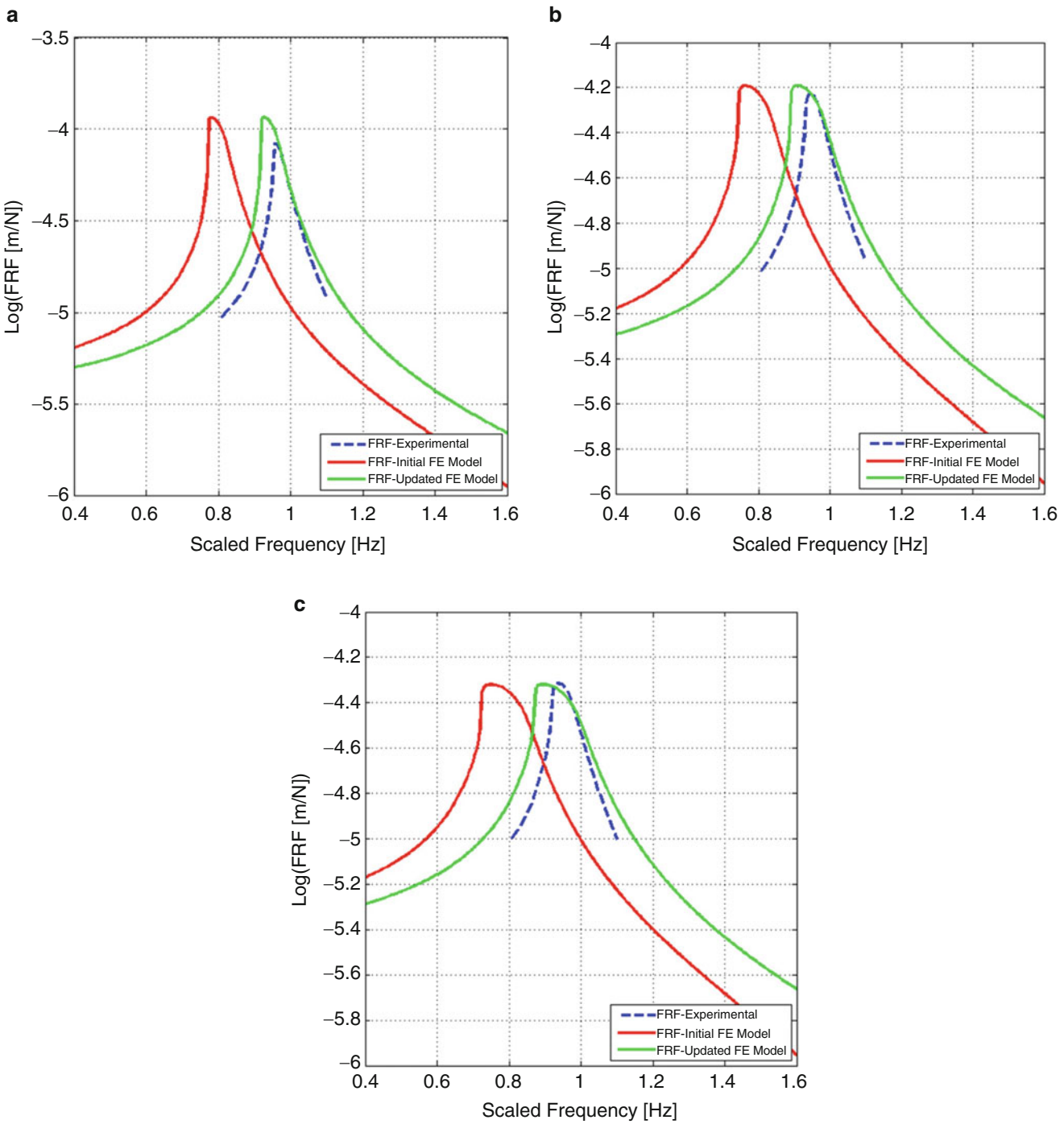

Fig. 34.30 Comparison of FRFs obtained from initial and updated models with the experimental ones for (**a**) F = 5 N, (**b**) F = 10.4 N, (**c**) F = 15 N

is thus concluded that the method previously proposed by the authors can successfully be applied to complex engineering problems for obtaining accurate nonlinear models.

Acknowledgements The authors would like to thank to the Scientific and Technological Research Council of Turkey (TÜBİTAK) for giving the financial support throughout this work.

References

1. Link, M., Zhang, L.: Experience with different procedures for updating structural parameters of analytical models using test data. In: Proceedings of the 10th International Modal Analysis Conference, San Diego, California, pp. 730–738, 1992
2. Ibrahim, S.R., D'Ambrogio, W., Salvani, P., Sestieri, A.J.: Direct updating of nonconservative finite element models measured input-output. In: Proceedings of the 10th International Modal Analysis Conference, San Diego, California, pp. 202–210, 1992
3. Miccoli, G., Agostoni, F.: Modal updating using sensitivity analysis. In: Proceedings of the 11th International Modal Analysis Conference, Kissimmee, Florida, pp. 683–689, 1993
4. Hemez, F.M.: Advanced tools for updating damped finite element models using static modal and flexibility data. In: Proceedings of the 14th International Modal Analysis Conference, Dearborn, Michigan, pp. 511–517, 1996
5. Lenoir, D., Cogan, S., Lallement, G., Bricout, J.N.: Model updating by modal synthesis of experimental forced responses. In: Proceedings of the 16th International Modal Analysis Conference, Santa Barbara, California, pp. 399–405, 1998
6. Li, W.L.: A new method for structural model updating and joint stiffness identification. Mech. Syst. Signal Process. **16**(1), 155–167 (2002)
7. Boulkaibet, I., Mthembu, L., Marwala, T., Friswell, M.I., Adhikari, S.: Finite element model updating using the shadow hybrid Monte Carlo technique. In: Proceedings of the 31st International Modal Analysis Conference, Orange County, California, USA, 2013
8. Hemez, F.M.: A brief history of 30 years of model updating in structural dynamics. In: Proceedings of the 32nd International Modal Analysis Conference, Orlando, Florida, USA, 2014
9. Hasselman, T.K., Anderson, M.C., Gan, W.: Principal components analysis for nonlinear model correlation, updating and uncertainty evaluation. In: Proceedings of the 16th International Modal Analysis Conference, Santa Barbara, California, pp. 644–651, 1998
10. Burton, T.D., Hemez, F.M., Rhee, W.: Combined model reduction/SVD approach to nonlinear model updating. In: Proceedings of the 18th International Modal Analysis Conference, San Antonio, Texas, pp. 116–123, 2000
11. Lenaerts, V., Kerschen, G., Golinval, J.C.: Proper orthogonal decomposition for model updating of non-linear mechanical systems. Mech. Syst. Signal Process. **15**(1), 31–43 (2001)
12. Isasa, I., Hot, A., Cogan, S., Sadoulet-Reboul, E.: Model updating of locally non-linear systems based on multi-harmonic extended constitutive relation error. Mech. Syst. Signal Process. **25**, 2413–2425 (2011)
13. Kerschen, G., Worden, K., Vakakis, A.F., Golinval, J.C.: Past, present and future of nonlinear system identification in structural dynamics. Mech. Syst. Signal Process. **20**, 505–592 (2006)
14. Worden, K., Hickey, D., Haroon, M., Adams, D.E.: Nonlinear system identification of automotive dampers: a time and frequency-domain analysis. Mech. Syst. Signal Process. **23**, 104–126 (2009)
15. Eriten, M., Kurt, M., Luo, G., McFarland, D.M., Bergman, L.A., Vakakis, A.F.: Nonlinear system identification of frictional effects in a beam with a bolted joint connection. Mech. Syst. Signal Process. **39**, 245–264 (2013)
16. Doranga, S., Wu, C.Q.: Parameter identification for nonlinear dynamic systems via multilinear least square estimation. In: Proceedings of the 32nd International Modal Analysis Conference, Orlando, Florida, USA, 2014
17. Canbaloglu, G., Özgüven, H.N.: Obtaining linear FRFs for model updating in structures with multiple nonlinearities including friction. In: Topics in Nonlinear Dynamics, Volume 1: Proceedings of the 31st IMAC, A Conference on Structural Dynamics, pp. 145–157, 2013
18. Canbaloglu, G., Özgüven, H.N.: Model updating of nonlinear structures, nonlinear dynamics. In: Volume 2: Proceedings of the 32nd IMAC, A Conference and Exposition on Structural Dynamics, pp. 69–81, 2014
19. Canbaloglu, G., Özgüven, H.N.: Experimental validation of Pseudo Receptance Difference (PRD) method for nonlinear model updating. In: Nonlinear Dynamics, Volume 1: Proceedings of the 33rd IMAC, A Conference and Exposition on Structural Dynamics, pp. 293–306, 2015
20. Bundy, M., Newill, J., Marcopoli, V., Ng, M., Wells, C.: A methodology for characterizing gun barrel flexure due to vehicle motion. Shock Vib. **8**, 223–228 (2001)
21. Ahmed, N., Brown, R.D., Hameed, A.: Finite Element Modelling and Simulation of Gun Dynamics using 'ANSYS'. Cranfield University, UK (2008)
22. Collins, J.D., Hart, G.C., Hasselman, T.K., Kennedy, B.: Statistical identification of structure. AIAA J. **12**(2), 185–190 (1974)

Chapter 35
Experimental Passive Flutter Mitigation Using a Linear Tuned Vibrations Absorber

E. Verstraelen, G. Habib, G. Kerschen, and G. Dimitriadis

Abstract The current drive for increased efficiency in aeronautic structures such as aircraft, wind turbine blades and helicopter blades often leads to weight reduction. A consequence of this tendency can be increased flexibility, which in turn can lead to unfavourable aeroelastic phenomena involving large amplitude oscillations and nonlinear effects such as geometric hardening and stall flutter. Vibration mitigation is one of the approaches currently under study for avoiding these phenomena.

In the present work, passive vibration mitigation is applied to an experimental aeroelastic system by means of a linear tuned vibration absorber. The aeroelastic apparatus is a pitch and flap wing that features a continuously hardening restoring torque in pitch and a linear one in flap. Extensive analysis of the system with and without absorber at subcritical and supercritical airspeeds showed an improvement in flutter speed around 34 %, a suppression of a jump due to stall flutter, and a reduction in LCO amplitude.

Mathematical modelling of the experimental system showed that optimal flutter delay can be obtained when two of the system modes flutter simultaneously. However, the absorber quickly loses effectiveness as it is detuned. The wind tunnel measurements showed that the tested absorbers were much slower to lose effectiveness than those of the mathematical predictions.

Keywords Wind tunnel testing • Nonlinear aeroelasticity • Stall flutter • Internal resonance • Bifurcations

35.1 Introduction

As aircraft become lighter and are pushed further in their flight envelope for performance reasons, they are more prone to undergo unfavourable aeroelastic oscillations due to flutter, a very dangerous mechanism occurring because of the coalescence of two vibration modes subjected to an airflow.

Common methods to avoid these oscillations include reducing the flight envelope, stiffening the structure, active control and increasing structural damping. The employment of a linear tuned vibration absorber (LTVA), also known as tuned mass damper (TMD), is an alternative vibration control approach that has not yet been fully explored in the aeroelastic literature.

The LTVA consists of a mass-spring-damper assembly attached to the primary system to be controlled. The natural frequency of the LTVA is tuned in accordance to the main resonant frequency of the host system, causing an effective transfer of energy between the two subsystems. The relatively high damping of the absorber reduces significantly the oscillation amplitude. LTVAs are widely used in civil engineering applications, such as tall buildings [1, 2] and long span bridges [3], to avoid vortex induced vibrations, galloping oscillations or human-induced vibrations [4]. However, in classical flutter, the loss of stability is due to two modes whose frequencies vary with the airspeed. The variation of the resonant frequencies undermines the 1:1 resonance, crucial for the correct operation of the LTVA. The design of an effective LTVA for increasing the flutter speed in aeroelastic system is thus more challenging. Analytical and numerical works showed that the LTVA can be successfully implemented for the suppression of flutter vibrations in long span bridges [5–8]. A few pioneering studies [9, 10] have illustrated that the same concept can be applied to aircraft wings. However, to the authors' knowledge, there is a lack of experimental work demonstrating the effectiveness of LTVAs for flutter suppression in the literature.

E. Verstraelen (✉) • G. Habib • G. Kerschen • G. Dimitriadis
Department of Aerospace and Mechanical Engineering, University of Liège, Liège, Belgium
e-mail: everstraelen@ulg.ac.be

G. Kerschen (ed.), *Nonlinear Dynamics, Volume 1*, Conference Proceedings of the Society for Experimental Mechanics Series,
DOI 10.1007/978-3-319-29739-2_35

In this study we attach a LTVA to a nonlinear pitch and flap wing (NLPFW) in order to delay the flutter onset speed. The study is conducted in three steps. Firstly, the aeroelastic system's behaviour is extensively investigated numerically and experimentally in the wind-tunnel. Secondly, numerical and experimental LTVAs are designed. Finally, the efficiency of these absorbers is assessed and tuning rules are derived.

35.2 Primary System

35.2.1 Experimental Setup

The experimental apparatus, installed in the large low-speed wind tunnel of the University of Liège, is designed to achieve very low linear damping (≈0.3 % at wind-off conditions) and flutter at an airspeed close to 12 m/s. To achieve such low structural damping, the apparatus does not use any bearings or rotational springs. The pitch and flap restoring torques are provided by a specially designed leaf spring and a nonlinear clamp assembly. The complete NLPFW is shown in Fig. 35.1. It is a stiff thin rectangular unswept flat plate with span $s = 800$ mm, chord $c = 200$ mm, thickness $t = 4$ mm and an aspect ratio of 4. It is hinged at its root at $0.3c$ from the leading edge. It features two rigid degrees of freedom (DOF): a pitch rotation θ and a flap rotation γ, as shown in Fig. 35.2. The pitch axis, e_s, is parallel to the leading edge and passes by the hinge while the flap axis, e_c is parallel to the root of the wing, at a distance s_1 above it.

The stiffness in both pitch and flap is provided by a thin C75S leaf spring. It is 100 mm long, 70 mm large and 0.7 mm thick. It is clamped linearly to the flat plate and nonlinearly to the roof of the test section of the wind tunnel. Figure 35.3a draws the geometry of the nonlinear root clamps and Fig. 35.3b plots the nonlinear restoring torque of the pitch DOF. The flap stiffness is linear in the displacement range considered. Finally, a 500 mm × 50 mm × 15 mm beam is bolted at the junction between the flat plate and the leaf spring (see Fig. 35.1a, b). It increases the rotational inertia of the system and consequently decreases its flutter speed to the target speed range: [10–15] m/s. Table 35.1 summarises all the wind-off characteristics of the system.

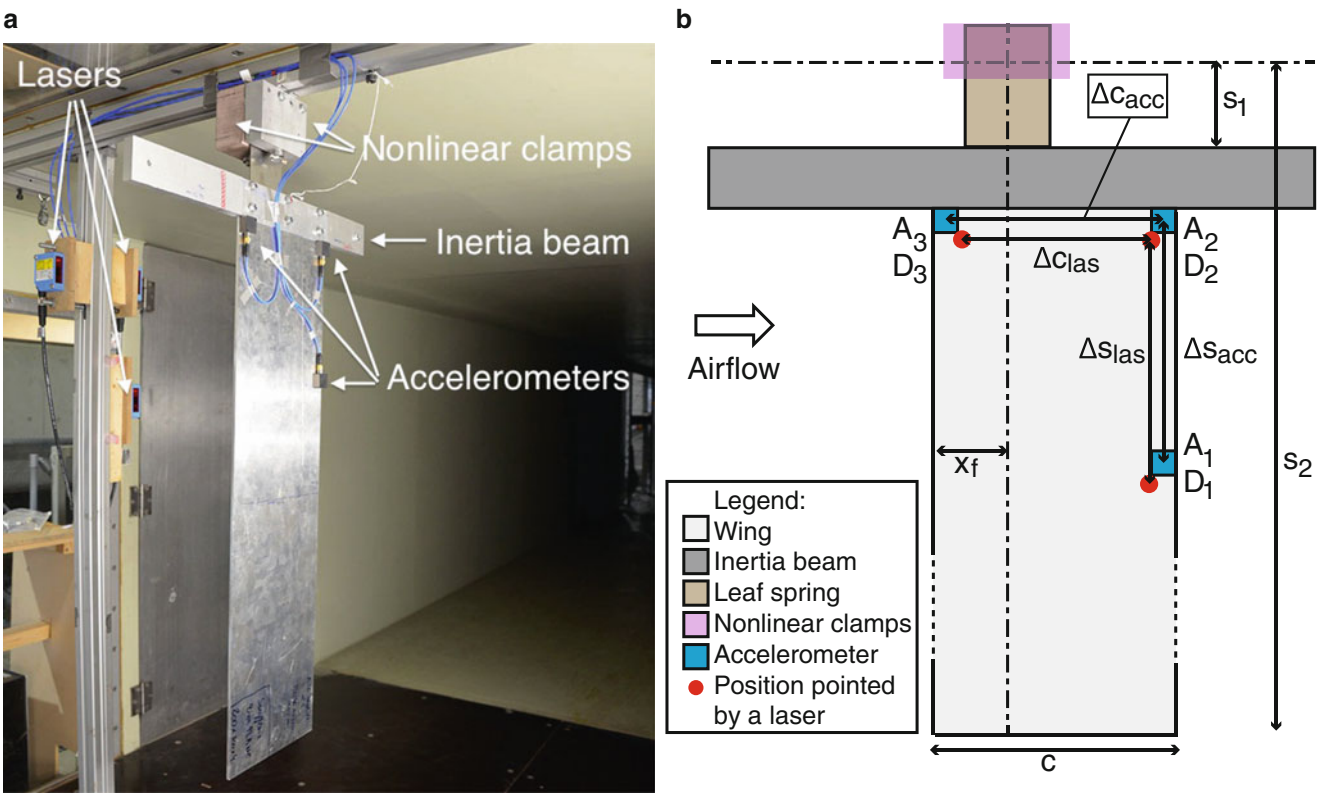

Fig. 35.1 Experimental setup showing wing, support and transducers. (**a**) Photo of the setup in the wind tunnel. (**b**) Diagram showing transducer locations and major components of the NLPFW

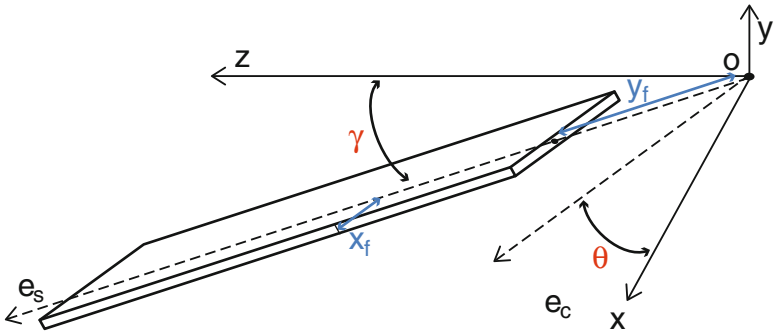

Fig. 35.2 Schematic of the Hancock Wing

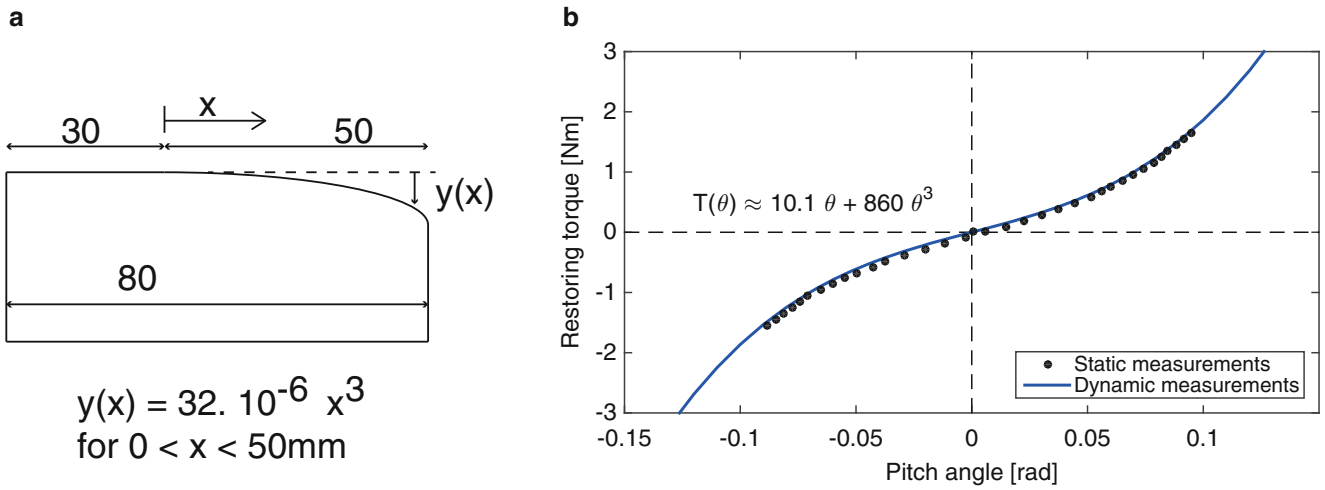

Fig. 35.3 Characteristics of the nonlinear clamps. (**a**) Sketch of the clamps. (**b**) Experimental restoring torque curve of the pitch DOF

The displacements are measured by means of three Sick OD2-P300W200I0 laser sensors with a sensitivity of 9.6 mV/mm, a range of 100–500 mm and a sampling frequency of 1000 Hz. The positions of all the sensors are shown in Fig. 35.1b and are denoted by D_1, D_2 and D_3. The measurements from sensors D_1 and D_2 are used to calculate the flap angle

$$\gamma = \arctan[(D_1 - D_2)(\Delta s_{las})^{-1}] \tag{35.1}$$

while those from sensors D_2 and D_3 are used to calculate the pitch angle

$$\theta = \arctan[(D_2 - D_3)(\Delta c_{las})^{-1}] \tag{35.2}$$

Figure 35.4 displays the system's relevant mode shapes and frequencies identified through a roving hammer test using a single accelerometer placed at the trailing edge of the wingtip and 24 impact locations. The flap mode features a frequency of 0.9 Hz and a damping of 1 % while the pitch mode features a linear frequency of 3.1 Hz and a damping ratio of 0.3 %. Finally the third mode, which could be considered as a superposition of flapping and plunging motion combined with very little flat plate deformation, was identified to make sure its frequency was high enough to have little impact on the flutter mechanics. This is in fact the case as it features a frequency of 9.6 Hz and a modal damping ratio of 0.5 %.

35.2.2 Reduced Order Model

The nonlinear pitch and flap wing is modelled as a two-DOF system, assuming that the flexible modes of the plate do not participate significantly in the observed aeroelastic phenomena. The structural nonlinear equations of motion are

Table 35.1 Wind-off characteristics of the NLPF

Characteristic	Symbol	Value	Unit
Dimensions of the wing			
Span	s	800	[mm]
Distance (flap axis−wing root)	s_1	65	[mm]
Distance (flap axis−wing tip)	s_2	865	[mm]
Chord	c	200	[mm]
Half chord	b	100	[mm]
Thickness	t	4	[mm]
Position of the center of mass	x_{cg}	$1/2c$	[mm]
Flap properties			
Linear stiffness	K_γ	≈ 5	[Nm/rad]
Inertia	I_γ	0.42	[kg m^2]
Damping	ζ_γ	≈ 1	[%]
Frequency	f_γ	0.85	[Hz]
Pitch properties			
Inertia	I_θ	0.029	[kg m^2]
Flexural axis position	x_f	$0.3c$	[mm]
Relative position of x_f and x_{cg}	a	$\frac{x_f - x_{cg}}{b}$	[–]
Linear stiffness coefficient	K_θ	10.1	[Nm/rad]
Quadratic stiffness coefficient	$K_{\theta,2}$	≈ 0	[Nm/rad^2]
Cubic stiffness coefficient	$K_{\theta,3}$	858	[Nm/rad^3]
Damping	ζ_θ	≈ 0.3	[%]
Frequency	f_θ	3.1	[Hz]
Position of the sensors			
Distance between A_1 and A_2	Δs_{acc}	200	[mm]
Distance between A_2 and A_3	Δc_{acc}	180	[mm]
Distance between D_1 and D_2	Δs_{las}	205.5	[mm]
Distance between D_2 and D_3	Δc_{acc}	168.5	[mm]

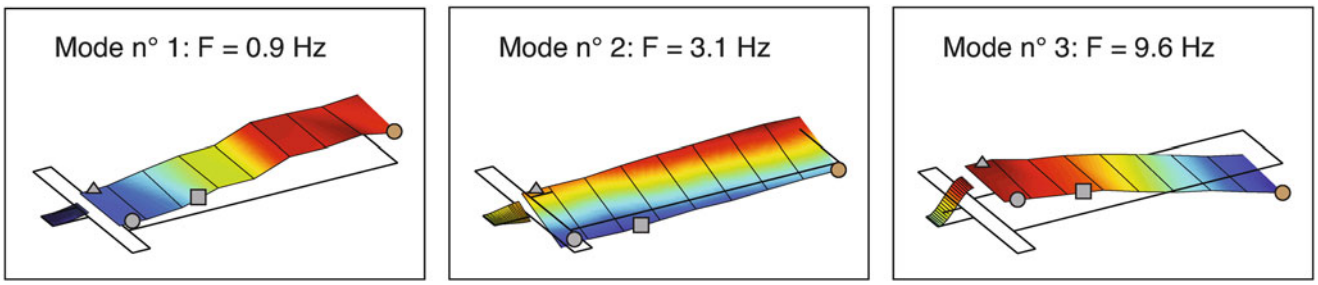

Fig. 35.4 Mode shapes of NLPFW

$$\begin{pmatrix} I_\gamma & S \\ S & I_\theta \end{pmatrix} \begin{pmatrix} \ddot{\gamma} \\ \ddot{\theta} \end{pmatrix} + \begin{pmatrix} c_\gamma & c_{\gamma\theta} \\ c_{\gamma\theta} & c_\theta \end{pmatrix} \begin{pmatrix} \dot{\gamma} \\ \dot{\theta} \end{pmatrix} + \begin{pmatrix} k_\gamma & k_{\gamma\theta} \\ k_{\gamma\theta} & k_\theta \end{pmatrix} \begin{pmatrix} \gamma \\ \theta \end{pmatrix} + \begin{pmatrix} M_{\gamma,NL}(\gamma) \\ M_{\theta,NL}(\theta) \end{pmatrix} = \begin{pmatrix} M_{\gamma,\mathrm{ext}}(t) \\ M_{\theta,\mathrm{ext}}(t) \end{pmatrix} \tag{35.3}$$

$$\begin{aligned} M_{\gamma,NL} &= 0 \\ M_{\theta,NL} &= k_{nl,3}\theta^3 \end{aligned} \tag{35.4}$$

where the inertia stiffness and damping parameters are given in Table 35.1. A nonlinear torque is applied only to the pitch DOF and it is a cubic function of θ.

The flap and pitch aerodynamic moments, M_γ and M_θ respectively, are computed using strip theory (see for instance Bisplinghoff et al. [11]), which calculates the total 3D aerodynamic loads as sums of 2D loads, dL and dM_θ, acting on small

spanwise strips of width dy. These infinitesimal forces and moments are computed assuming 2D aerodynamics. The strip theory assumption leads to the following formulation for the flap and pitch aerodynamic moments

$$M_\gamma = -\int_{s_1}^{s_2} y \, \mathrm{d}L(t) \tag{35.5}$$

$$M_\theta = \int_{s_1}^{s_2} \mathrm{d}M_\theta(t) \tag{35.6}$$

s_1 being the distance between the flap axis and the root of the wing and s_2 the distance between the flap axis and the tip of the wing. The lift force dL and pitch moment dM_θ of a strip can be computed using any 2D unsteady aerodynamic formulation. Unsteady aerodynamic modelling based on Wagner's function [12] was chosen here because the reduced frequency of oscillation $k = \frac{\omega b}{U} \approx 1.5 >> 0.02$ is too large to use quasi-steady aerodynamics while Theodorsen theory is defined in frequency domain, which makes it difficult to use on a nonlinear system. The growth of circulation around a flat uncambered airfoil after a step change of incidence is approximated by Wagner's function

$$\Phi(t) = 1 - \psi_1 e^{-\frac{\epsilon_1 U t}{b}} - \psi_2 e^{-\frac{\epsilon_2 U t}{b}} \tag{35.7}$$

Integrating Eqs. (35.5) and (35.6) with Fung's lift and moment expressions [12] and applying a transformation to replace the wake integrals by aerodynamic state variables [13] yields the complete equations of motion

$$\begin{aligned}
&\left[\begin{pmatrix} I_\gamma & S \\ S & I_\theta \end{pmatrix} + \rho\pi b^2 \begin{pmatrix} \Lambda_3/3 & -ab\Lambda_2/2 \\ -ab\Lambda_2/2 & b^2\Lambda_1(a^2+1/8) \end{pmatrix}\right]\begin{pmatrix} \ddot{\gamma} \\ \ddot{\theta} \end{pmatrix} \\
&+\left[\begin{pmatrix} c_\gamma & c_{\gamma\theta} \\ c_{\gamma\theta} & c_\theta \end{pmatrix} + \rho\pi Ub \begin{pmatrix} \frac{2}{3}\Phi(0)\Lambda_3 & b\Lambda_2[1/2-\Phi(0)(1-a/2)] \\ -b\Lambda_2\Phi(0)(a+1/2) & -\Lambda_1 b^2(a-1/2)[1+2\Phi(0)(a+1/2)] \end{pmatrix}\right]\begin{pmatrix} \dot{\gamma} \\ \dot{\theta} \end{pmatrix} \\
&+\left[\begin{pmatrix} k_\gamma & k_{\gamma\theta} \\ k_{\gamma\theta} & k_\theta \end{pmatrix} + \rho\pi U^2 \begin{pmatrix} \frac{2}{3}\Lambda_3[\frac{b\dot{\Phi}(0)}{U}] & b\Lambda_2[\Phi(0)+\frac{b\dot{\Phi}(0)}{U}(1/2-a)] \\ -b\Lambda_2[\frac{b\dot{\Phi}(0)}{U}(a+1/2)] & -2\Lambda_3(a+1/2)[\Phi(0)-\frac{b\dot{\Phi}(0)}{U}(a-1/2)] \end{pmatrix}\right]\begin{pmatrix} \gamma \\ \theta \end{pmatrix} \\
&+\left[\pi\rho U^3 \begin{pmatrix} -2\epsilon_1^2\psi_1\Lambda_3/3b & \epsilon_1^2\psi_1\Lambda_2(2a+1)/2 \\ -2\epsilon_2^2\psi_2\Lambda_3/3b & \epsilon_2^2\psi_2\Lambda_2(2a+1)/2 \\ \Lambda_2(\epsilon_1\psi_1-\epsilon_1^2\psi_1/2+a\epsilon_1^2\psi_1) & -2b\epsilon_1\psi_1\Lambda_1(a+1/2)(\epsilon_1(a-1/2)+1) \\ \Lambda_2(\epsilon_2\psi_2-\epsilon_2^2\psi_2/2+a\epsilon_2^2\psi_2) & -2b\epsilon_2\psi_2\Lambda_1(a+1/2)(\epsilon_2(a-1/2)+1) \end{pmatrix}^T\right]\begin{pmatrix} w_1 \\ w_2 \\ w_3 \\ w_4 \end{pmatrix} \\
&= \left[\begin{pmatrix} M_{\gamma,ext}(t) \\ M_{\theta,ext}(t) \end{pmatrix} + 2\pi\rho Ub\dot{\Phi}(t) \begin{pmatrix} \Lambda_3\gamma(0)/3 + (\frac{3b}{2}-x_f)\Lambda_2\theta(0)/2 \\ -(a+1/2)b[\Lambda_2\gamma(0)/2 + (\frac{3b}{2}-x_f)\Lambda_1\theta(0)] \end{pmatrix} - \begin{pmatrix} 0 \\ k_{nl,3}\theta^3 \end{pmatrix}\right]
\end{aligned} \tag{35.8}$$

with $\Lambda_j = s_2^j - s_1^j$. The left hand side of Eq. (35.8) includes inertia, damping, stiffness terms and the aerodynamic state proportionality matrix. The right hand side comprises three terms, the external loads (set to zero since self-excited oscillations are under investigation), a transient term, which is also set to zero since it quickly decays in time, and a term related to the structural nonlinearities. The nonlinear equations of motion are solved using a numerical continuation algorithm based on a finite difference formulation [14].

35.3 Aeroelastic Analysis

The system's aeroelastic behaviour is first studied at sub-critical airspeeds, where the average damping is positive and leads to decaying motions, as demonstrated by the pitch response time histories plotted in Fig. 35.5a for airspeeds of 0, 5.5 and 8.7 m/s. At higher airspeeds, the response is a self-excited limit cycle oscillation (LCO). This behaviour is demonstrated in Fig. 35.5b which plots pitch response time histories at airspeeds of 12.4, 13.3 and 14.8 m/s.

Figure 35.6 displays the variation of the modal parameters of the pitch and flap modes of the NLPFW with airspeed according to experimental measurements (black dots) and the analytical model (plain lines). The imaginary part of the response—identified using Fast Fourier Transform—is accurately reproduced by the model and shows the typical features

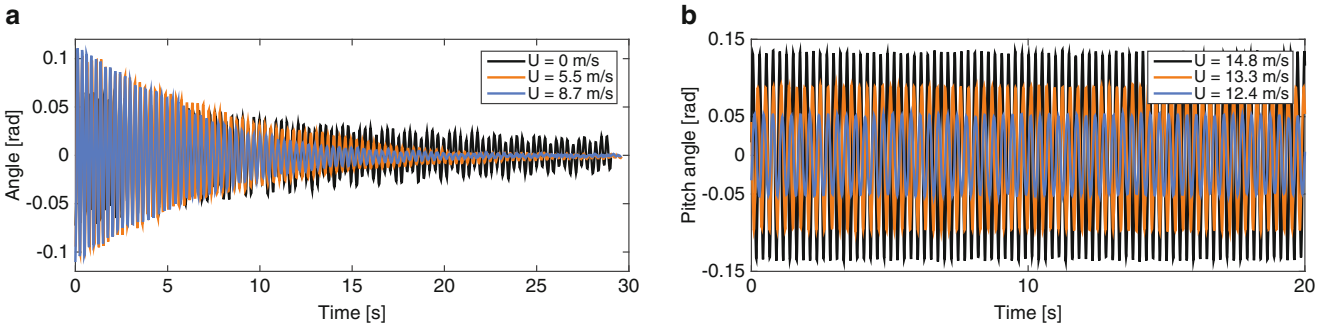

Fig. 35.5 Time series of the pitch response of the system at sub-critical and super-critical airspeeds. (**a**) Sub critical pitch response. (**b**) Super critical pitch response

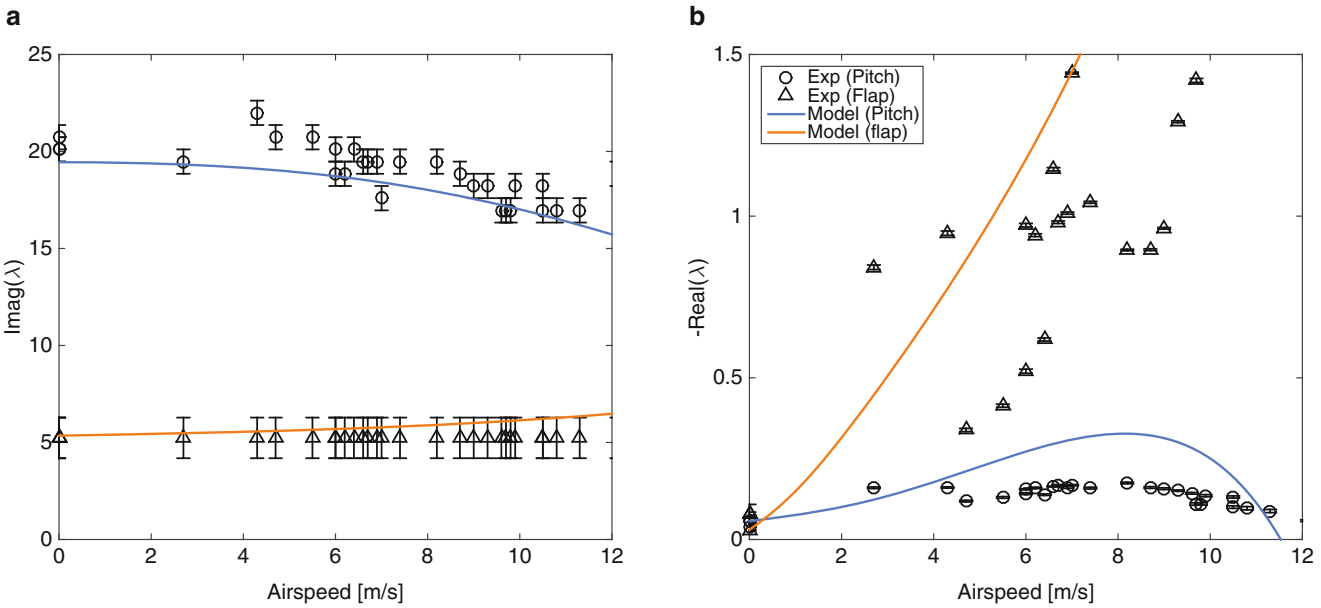

Fig. 35.6 Variation of the pitch and flap modal parameters with the airspeed. (**a**) Pulsation. (**b**) Decay rate

of an aeroelastic system undergoing flutter: the frequency gap between the two modes decreases as the airspeed is increased until the modes are close enough to interact and cause flutter. The real part—identified using an exponential fitting of the Hilbert transform of the response—is also typical of aeroelastic systems: the flap damping strongly increases while the pitch damping increases at first then decreases until it drops to zero and flutter occurs. In this case, the model seems to over-estimate the damping, however it must be noted that damping is very difficult to identify and even harder to model; considering the simplicity of the model, the estimate is satisfactory.

Once the flutter speed is reached, the average damping of the system drops to zero and limit cycle oscillations are observed. Figure 35.7a displays the bifurcation diagrams in pitch and flap angle of the system obtained from wind tunnel observations (triangles and dots) and from the numerical continuation analysis of Eq. (35.8). The airspeed was increased then decreased in the wind-tunnel to look for hysteresis effects but none were found. Both experimental and numerical results exhibit a supercritical Hopf bifurcation at 11.5 m/s, followed by increases in LCO amplitude and frequency, consistent with cubic hardening stiffness. At 13.5 m/s a discontinuity occurs in the experimental pitch measurements; both the amplitude and frequency increase sharply. This phenomenon is due to dynamic stall and is overlooked by the reduced order model, which uses linear aerodynamics. The flap displacement undergoes a gentle increase in amplitude that is predicted with reasonably accuracy by the model. Because of the coupling between the pitch and the flap modes, at 13.5 m/s a jump is observed also in the flap response. However, the increase in amplitude is not significant.

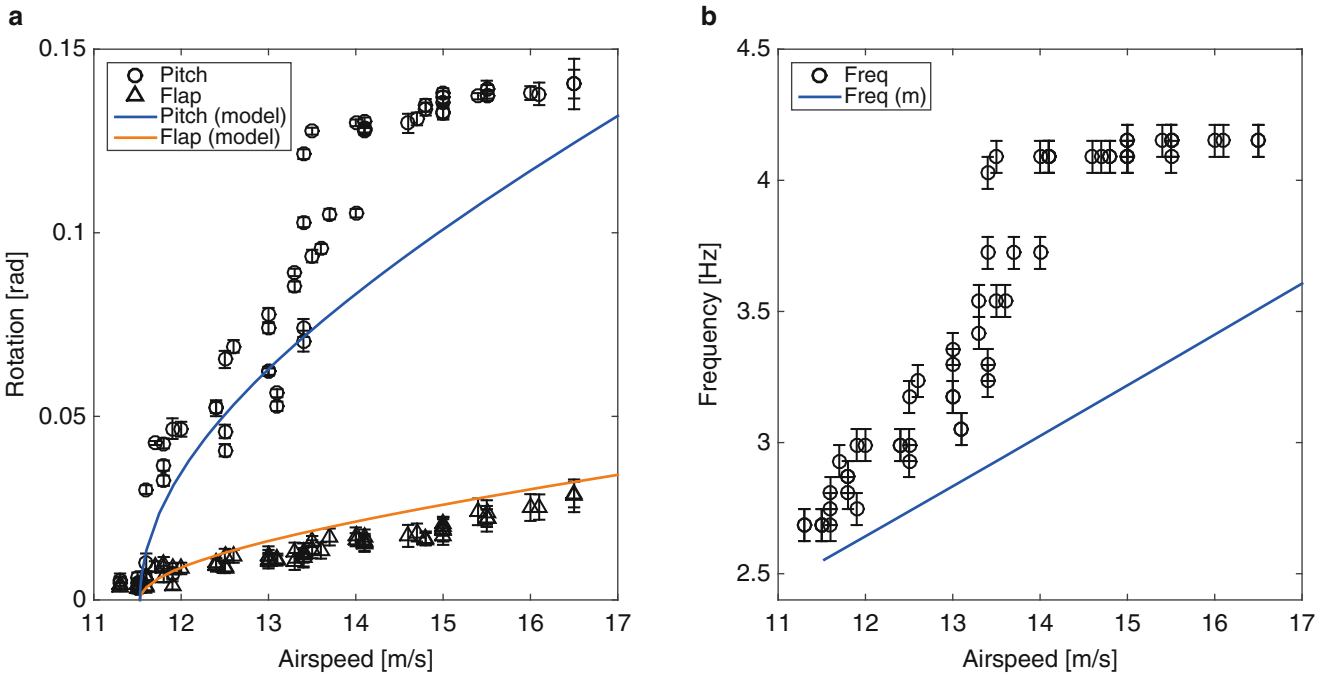

Fig. 35.7 Experimental and numerical bifurcation diagrams of the primary system. (**a**) Pitch and flap LCO amplitude. (**b**) LCO frequency

The variation of the LCO frequency with airspeed is shown in Fig. 35.7b. Flutter starts at 2.6 Hz in the wind tunnel, then the LCO frequency increases almost linearly with the airspeed until 13.5 m/s, where it jumps to 4.2 Hz. The model predicts a linear increase of the frequency with an absolute error around 0.3 Hz, until the jump where it fails because it cannot represent nonlinear aerodynamic effects.

Summarising, the NLFPW undergoes classical flutter at 11.5 m/s, followed by a gently increase in pitch amplitude until 13.5 m/s, where a jump is observed. These aeroelastic phenomena are predicted with reasonable accuracy by the model from 0 to 13.5 m/s. This speed range is used to assess the effect of a LTVA on the system.

35.4 LTVA Design

Figure 35.8a displays the experimental absorber configuration and Fig. 35.8b the numerical model. The LTVA consists of a flexible beam of length $r_{ltva} = 0.1$ m, clamped on one end at a distance $r_\theta = 0.125$ m from the pitch axis and $r_\gamma = 0.05$ m from the flap axis, and a mass m_{ltva} attached at the free end of the beam. The beam provides both stiffness, k_{ltva}, and damping, c_{ltva}.

The LTVA is modelled mathematically as a mass-spring-damper system with a rotational DOF, ξ, in the plane ϕ around the LTVA axis, which is parallel to the pitch axis. Assuming small displacements, the mathematical and experimental configurations are similar. The natural frequency and damping ratio of the LTVA are given by

$$\begin{aligned} f_{ltva} &= \frac{1}{2\pi}\sqrt{k_{ltva}/I_{ltva}} = \frac{1}{2\pi}\sqrt{k_{ltva}/(m_{ltva}r_{ltva}^2)} \\ \epsilon_{ltva} &= c_{ltva}/(2\sqrt{k_{ltva}I_{ltva}}) \end{aligned} \tag{35.9}$$

35.4.1 LTVA Equations of Motion

Adopting the Euler-Lagrange equation, the equations of motion of the coupled 3-DOFs are derived. The resulting inertia, damping and stiffness matrices are given by

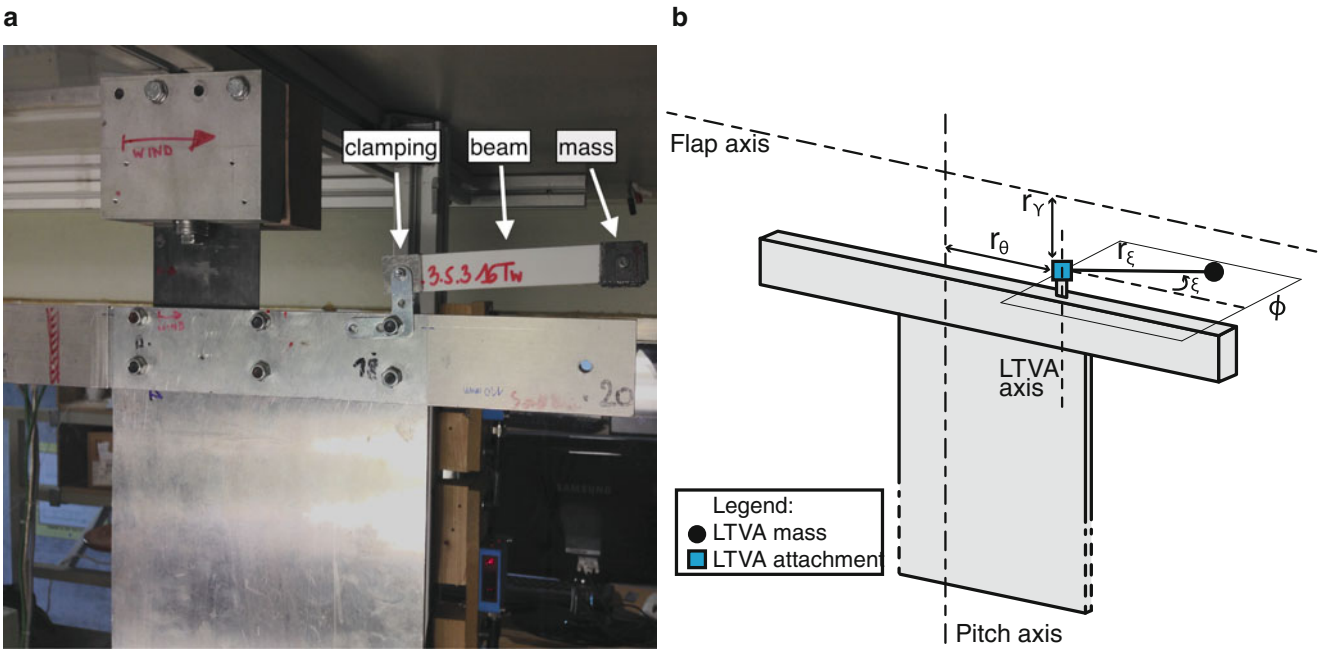

Fig. 35.8 Experimental and modelled LTVA configurations. (**a**) Picture of the experimental LTVA attached to the primary system. (**b**) Sketch of the model of the LTVA attached to the primary system

$$
\begin{aligned}
M_s &= \begin{pmatrix} I_\gamma & S & 0 \\ S & I_\theta & 0 \\ 0 & 0 & 0 \end{pmatrix} + m_{ltva} \begin{pmatrix} r_\gamma^2 & r_\gamma(r_\theta + r_{ltva}) & r_\gamma r_{ltva} \\ r_\gamma(r_\theta + r_{ltva}) & (r_\theta + r_{ltva})^2 & (r_\theta + r_{ltva}) r_{ltva} \\ r_\gamma r_{ltva} & (r_\theta + r_{ltva}) r_{ltva} & r_{ltva}^2 \end{pmatrix} \\
C_s &= \begin{pmatrix} c_\gamma & 0 & 0 \\ 0 & c_\theta & 0 \\ 0 & 0 & 0 \end{pmatrix} + c_{ltva} \begin{pmatrix} 0 & 0 & 0 \\ 0 & 0 & 0 \\ 0 & 0 & 1 \end{pmatrix} \\
K_s &= \begin{pmatrix} k_\gamma & 0 & 0 \\ 0 & k_\theta & 0 \\ 0 & 0 & 0 \end{pmatrix} + k_{ltva} \begin{pmatrix} 0 & 0 & 0 \\ 0 & 0 & 0 \\ 0 & 0 & 1 \end{pmatrix}
\end{aligned} \tag{35.10}
$$

where the contributions from the NLPFW and LTVA have been separated. The aerodynamic effects are assumed unchanged after the addition of the LTVA, i.e. the aerodynamic effects on the LTVA are neglected. Consequently, the full aeroelastic equations of motion, including the absorber, are still given by Eq. (35.8), after substituting the structural inertia, damping and stiffness matrices from those in Eq. (35.10).

35.4.2 Experimental LTVA Design and Identification

A number of different LTVAs were built. In order to achieve high damping ratios, the LTVA beams were made of a sandwich of three polymer sheets, with thicknesses varying from 0.3 to 0.5 mm, and 10 or 16 layers of viscoelastic tape wrapped around the central polymer sheet. The thickness of the polymer sheets and the number of layers of viscoelastic tape affected both the stiffness and the damping of the absorber.

The LTVAs were characterised by performing free response vibration tests such as the one displayed in Fig. 35.9a for the LTVA m54-30-50-30-16T. The amount of damping in the system and the shearing between the layers lead to asymmetric oscillations and drift so a special peak-picking routine was developed to measure the damping and the frequency. Instead of tracking the changes of sign to identify the successive periods, each cycle's period is computed from the extrema of the signal and the logarithmic decrement is computed from the average amplitude of each cycle defined as $(A_{max} - A_{min})/2$.

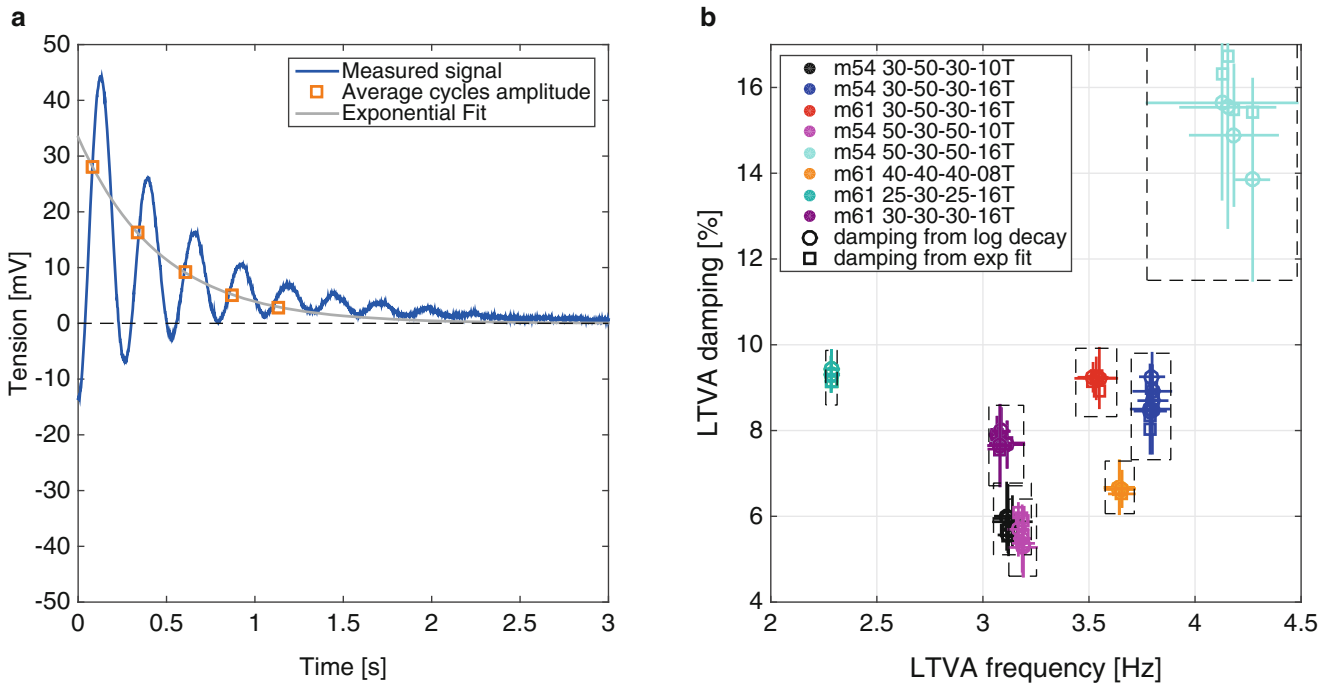

Fig. 35.9 Experimental identification of the LTVAs. (**a**) Free decay response of the LTVA 30-50-30-16T. (**b**) Identification results of all the experimental LTVAs

An exponential fitting of the amplitude at successive cycles was also carried out to identify the damping and the two methods gave similar damping estimates. To ensure that the drift of the response had little effect on the damping identification procedure, all the free response tests were repeated with both positive and negative initial displacements.

Figure 35.9b plots the frequencies and dampings obtained from of all the LTVA free response tests. The frequency varies from 2.3 to 4.5 Hz and the damping between 5 and 16 %. The names mxx – yy – yy – yy – zzT are related to the composition of the beam: mxx gives the mass in grams, yy denotes the thicknesses of the polymer sheets and zzT indicates the amount of viscoelastic tape layers placed in the sandwich. The errorbars indicate the standard deviation of the damping and frequencies measured from the free response tests. The LTVA with the higher frequency also featured the higher damping. It was found impossible to build an LTVA with low frequency and high damping, as increasing the number of viscoelastic tape layers increased both the damping and stiffness of the beams. Increasing the mass was not always possible because a high enough mass would cause buckling.

35.5 Numerical and Experimental Aeroelastic Analysis of the Primary System Coupled with the LTVA

35.5.1 Effect of the LTVA on the Flutter Speed

In the wind tunnel the critical flutter speed was defined as the first airspeed at which LCOs were clearly observed. Both increasing and decreasing airspeed tests were carried out to search for hysteresis effects. No such effects were observed, suggesting that all bifurcations were supercritical.

The flutter speed was also estimated from the mathematical model, for a very wide range of LTVA frequencies and damping ratios. The solid surface on Fig. 35.10 plots the results of this calculation; the flutter speed is plotted as a ratio of flutter speeds with and without LTVA. All the results in the figure were obtained for a LTVA mass of 64 g (≈2.3 % mass ratio). The experimental flutter speeds are plotted on the same axes. Figure 35.10b plots the same data seen from above, so that the effect of both frequency and damping ratio on the flutter speed is displayed.

The mathematical model predicts a maximum increase in flutter speed of 34 %. This optimum is obtained at 1.892 Hz and 14.47 % damping and quickly decreases as the LTVA gets detuned. The flutter speed is very sensitive to LTVA frequency;

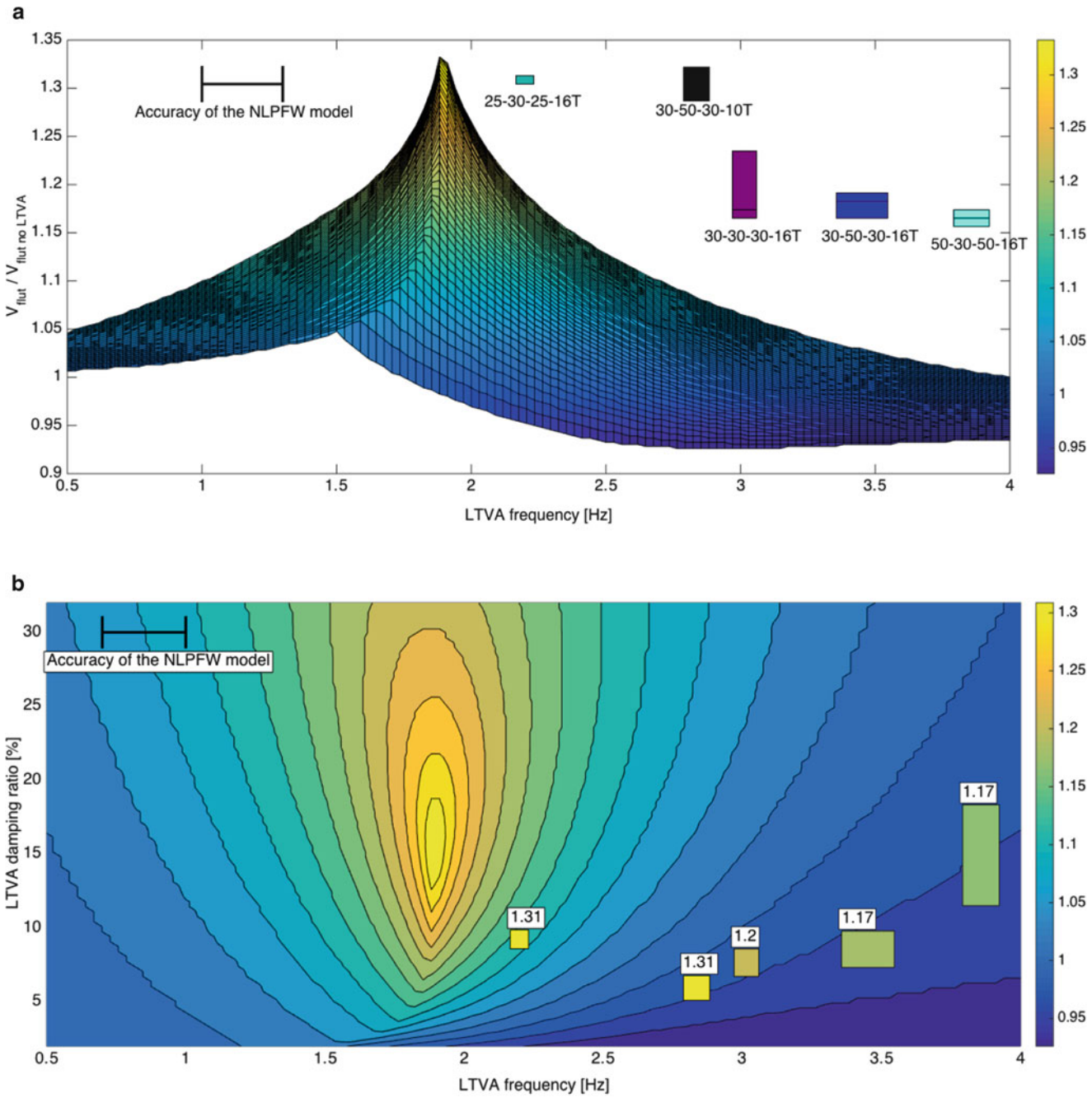

Fig. 35.10 Effect of the numerical and experimental LTVA on the flutter speed. (**a**) 3D plot of the flutter speed of the NLPFW as a function of the LTVA tuning. (**b**) 2D plot of the flutter speed of the NLPFW as a function of the LTVA tuning

a frequency change of 0.1 Hz can lead to a decrease in non-dimensional flutter speed from 1.34 to 1.24. The sensitivity to damping ratio is much lower. The LTVAs tested in the wind tunnel showed similar optimum flutter speeds, however the results appeared to be far less sensitive to detuning than in the case of the mathematical model. The cyan LTVA, for instance, was supposed to be completely detuned according to the model yet it yielded a commendable increase in flutter speed of 17 % in the wind-tunnel. There are several possible reasons for the difference between the detuning behaviour of the experiment and the mathematical model:

1. The LTVA structural damping may be nonlinear in practice but is modelled as linear.
2. The flow around the LTVA is not modelled but may have an affect on the absorber's effectiveness.

3. The difference between the modelled LTVA (rigid body rotation) and the experimental absorber (cantilever beam) may be too pronounced.

Finally it must be noted that the higher the damping the lower the sensitivity to frequency tuning. For a real life application it might be better to tune the LTVA to a damping higher than its optimum value.

35.5.2 *Effect of the LTVA on the Subcritical Response of the System*

The mechanism leading to an optimum tuning was investigated by studying numerically the effect of the LTVA on the variations of the modal frequencies and damping ratios with airspeed. These are variations are plotted in Fig. 35.11. The absorbers considered have mass $m_{ltva} = 64\,\text{g}$, damping $\zeta_{ltva} = 14.47\,\%$ and frequencies 1.892 Hz, 1.8 Hz and 2.0 Hz respectively from top to bottom.

Figure 35.11a, b display the results with an optimum LTVA. The system with absorber has three modes:

- Mode a: mostly flap motion (red).
- Mode b: in phase pitch and LTVA motion (blue).
- Mode c: out of phase pitch and LTVA motion (orange).

The absorber splits the uncontrolled system's pitch mode (black squares) into modes b and c (orange and blue) and has very low effect on the flap mode (black circles and red), because the flap inertia is larger than the pitch inertia and the LTVA is close to the flap axis and far from the pitch axis. Flutter occurs at 15.58 m/s on the system with LTVA. At flutter modes b and c have the same frequency and are essentially a single mode. The damping figure shows that again, modes b and c nearly merge at flutter.

Figure 35.11c, d plot the effect of a slightly undertuned LTVA (1.8 Hz). In this case mode c leads to flutter alone and does not merge with mode b at flutter. Figure 35.11e, f finally show the effect of a slightly overtuned LTVA (2.0 Hz). In this case, mode b leads to flutter alone and once again no frequency matching of modes b and c occurs.

The fact that, for optimal LTVA tuning, modes b and c undergo flutter simultaneously, resembles the classical Den Hartog's criterion for optimisation of LTVA for forced vibration, where the optimum corresponds to two equally high resonant peaks. This suggests that equating the flutter speed of the pitch modes could indeed be used to calculate the optimal tuning. Although up to now this conclusion is supported only by numerical calculations, in [15] a similar result was obtained for a LTVA applied to a van der Pol-Duffing oscillator.

35.5.3 *Effect of the LTVA on the Supercritical Response of the System*

Figure 35.12 displays experimental and numerical bifurcation diagrams in pitch LCO amplitude (Fig. 35.12a), flap LCO amplitude (Fig. 35.12b) and LCO frequency (Fig. 35.12c). The circles correspond to wind tunnel experiments with velocity sweeps up and down that did not show any hysteretic behaviour in any of the cases investigated. The thick lines show continuation computations from the model with three different LTVA frequencies, namely 1.8, 1.89 and 2.0 Hz, where 1.89 Hz corresponds to the optimal tuning.

The pitch bifurcation diagram plotted in Fig. 35.12a already provides most of the information. The model showed that the 1.8 Hz LTVA (dark blue) improves the flutter speed and barely changes the shape of the bifurcation. In this case the absorber is already detuned when flutter occurs. The 1.89 Hz LTVA (dark red) is the optimum case for increasing the flutter speed, however it features a narrow region of bi-stable solutions due to fold bifurcations occurring when the absorber is detuned. Finally the 2.0 Hz absorber (orange) leads to flutter at 14.3 m/s then decreases the amplitude of the ensuing LCOs until it gets detuned and the response jumps to a large amplitude limit cycle.

The experiments showed similar performance in flutter speed however no detuning was observed in the wind tunnel and the shape of the bifurcation branches is quite different because of the nonlinear damping, the effect of the airflow on the absorber and the difference in LTVA geometry. The light blue and orange curves correspond to the same LTVA beam with masses of 64 and 70 g respectively. They show that an increase in mass of just 10 % leads to a decrease in LCO amplitude of roughly 25 %. Moreover the heavier case leads to a smoother amplitude variation with airspeed close to the flutter speed. The purple line corresponds to the LTVA with the lowest frequency we could achieve, which should be the best one according to the model. In practice however it showed performance similar to the blue one. Furthermore, the maximum airspeed tested

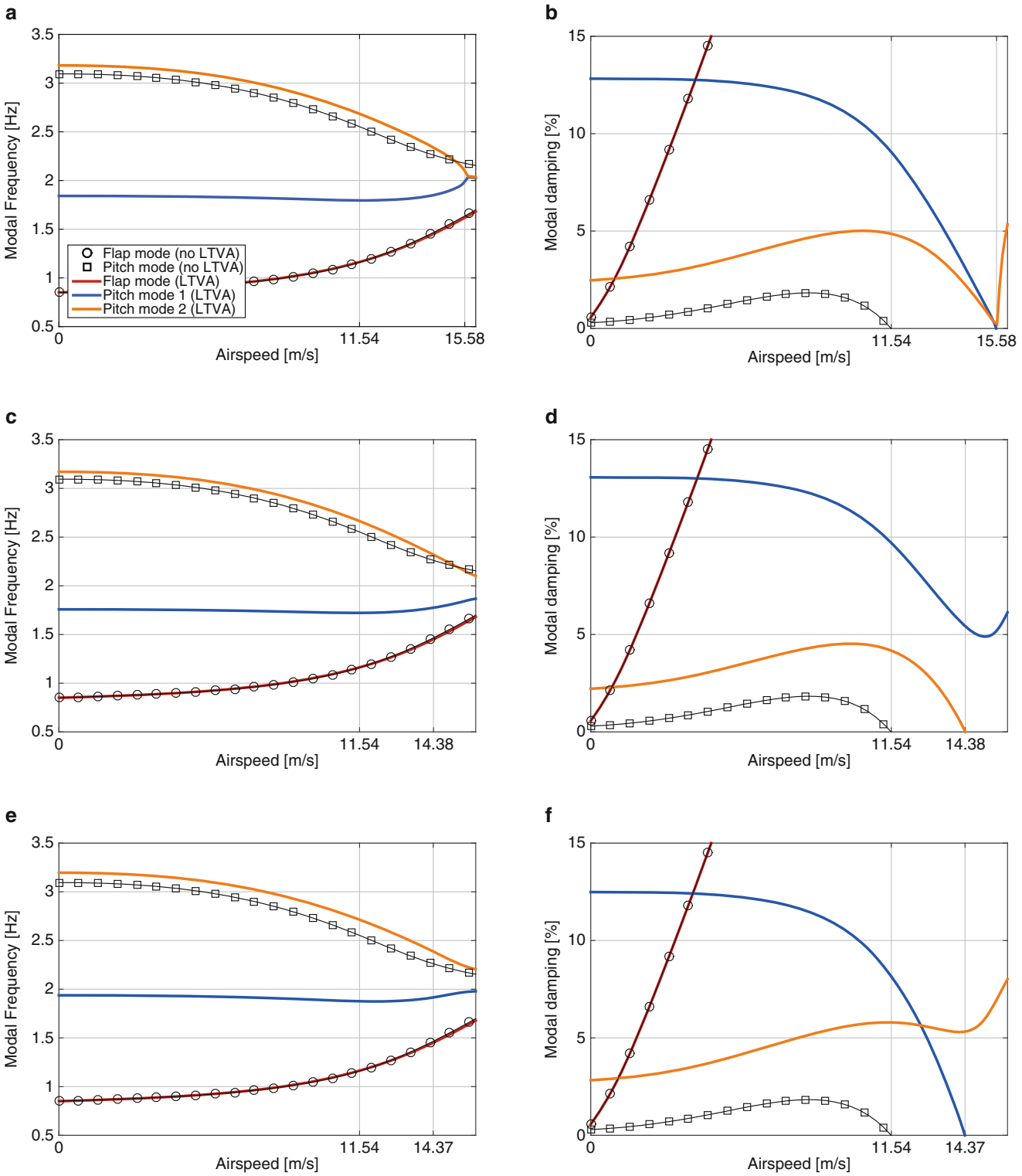

Fig. 35.11 Effect of the LTVA on the system modal damping and frequency variation with airspeed. (**a**) Modal frequency with $f_{ltva} = 1.89\,\text{Hz}, \zeta_{ltva} = 14.47\,\%$. (**b**) Modal damping with $f_{ltva} = 1.89\,\text{Hz}, \zeta_{ltva} = 14.47\,\%$. (**c**) Modal frequency with $f_{ltva} = 1.8\,\text{Hz}, \zeta_{ltva} = 14.47\,\%$. (**d**) Modal damping with $f_{ltva} = 1.8\,\text{Hz}, \zeta_{ltva} = 14.47\,\%$. (**e**) Modal frequency with $f_{ltva} = 2.0\,\text{Hz}, \zeta_{ltva} = 14.47\,\%$. (**f**) Modal damping with $f_{ltva} = 2.0\,\text{Hz}, \zeta_{ltva} = 14.47\,\%$

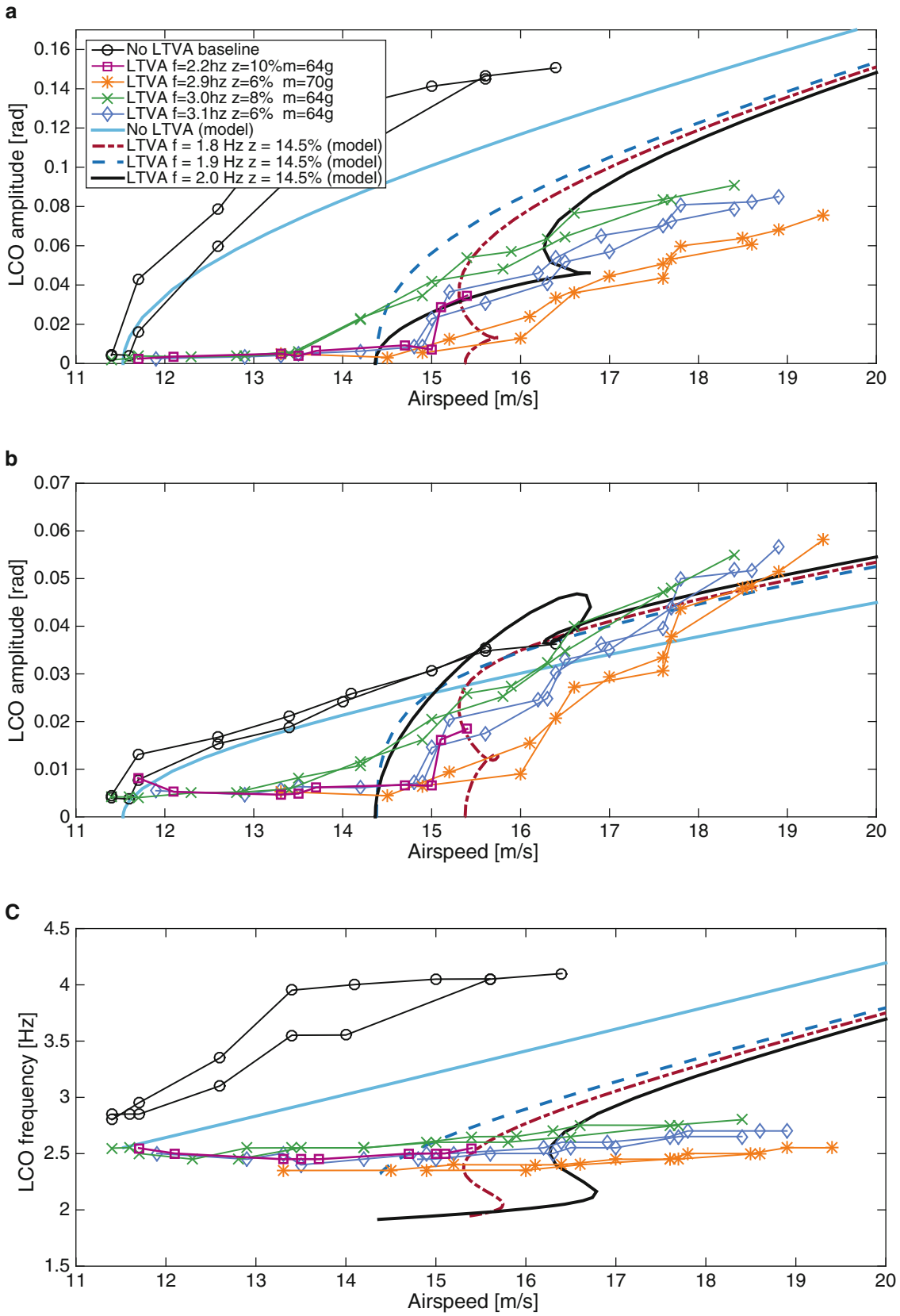

Fig. 35.12 Effect of the LTVA on the supercritical response of the system. (**a**) Pitch amplitude bifurcation diagram. (**b**) Flap amplitude bifurcation diagram. (**c**) LCO frequency bifurcation diagram

with this LTVA was lower than usual due to impacts phenomena between the absorber and the primary structure. Finally, the green curve corresponds to another intermediate LTVA that should have performed better than the blue one, according to the model, but which showed slightly worse performance.

Figure 35.12b displays the bifurcation diagrams of the system in flap amplitude. The model shows that the undertuned (dark blue) and optimum LTVAs (dark red) rapidly reach the amplitude of the system without absorber, and have a detrimental effect on the flap response. The overtuned LTVA (orange) leads to oscillations of larger amplitude until it is detuned, then it jumps down to the amplitude experienced by the system with the other absorbers. The experiments, on the other hand, featured a smooth increase in amplitude and a better performance than the system without absorber up to 16.5 m/s. Beyond this airspeed we did not take any measurements without absorber for safety reasons.

The variation of the LCO frequency plotted in Fig. 35.12c features significant differences after the addition of the LTVA. According to the experimental results, all the absorbers decreased the frequency of the oscillations. Furthermore, the limit cycle frequency varied very little with airspeed. The mathematical model showed that only the optimum and overtuned LTVAs decrease the frequency, for as long as they remain tuned (i.e. near the flutter speed and at low LCO amplitudes). The undertuned absorber has very little effect on the frequency. Once again, it appears that the experimental LTVAs remain tuned over a much wider airspeed range than the mathematical ones.

Considering the uncertainties in the LTVA identification and the complexity of the phenomena that occur in the wind tunnel, the predictions of the model are satisfactory. Finally, none of the experimental bifurcation diagrams performed with a LTVA attached to the system exhibited the jump due to stall-flutter. The increased damping and lower oscillation frequency is probably the reason.

35.6 Conclusions

The main purpose of this study was to demonstrate experimentally the effectiveness of the LTVA in delaying flutter and the appearance of limit cycle oscillations. Both the experiments and the mathematical model showed an improvement of about 30 % of the flutter speed with a damper mass of around 2.3 % of the mass of the full system.

The mathematical model demonstrated that optimal flutter delay occurs when the LTVA is tuned such that two of the system modes flutter simultaneously at the same airspeed. However, the effectiveness of the LTVA decreases steeply as the natural frequency of the absorber moves away from an optimum tuned value.

The major difference between the model and the experiments was the sensitivity of the LTVA to its tuning parameters. Absorbers that were totally detuned according to the model showed very good performance in the wind tunnel, which is encouraging for future experimental studies and applications. Furthermore, all the LTVAs suppressed the stall flutter phenomenon that occurs in the uncontrolled system.

Finally, it must be noted that this study considered a single LTVA position. The effects of the position of the LTVA on optimum tuning rules and effectiveness will be investigated in the future. Furthermore, the effect of the introduction of a nonlinear restoring force in the LTVA (leading to a nonlinear tuned vibration absorber [15–17]) will be assessed, with the objective of improving the supercritical response of the system.

Acknowledgement The authors would like to acknowledge the financial support of the European Union (ERC Starting Grant NoVib 307265).

References

1. Nagase, T., Hisatoku, T.: Tuned-pendulum mass damper installed in crystal tower. Struct. Des. Tall Build. **1**(1), 35–56 (1992)
2. Lu, X., Li, P., Guo, X., et al.: Vibration control using ATMD and site measurements on the Shanghai world financial center tower. Struct. Des. Tall Special Build. **23**(2), 105–123 (2014)
3. Gu, M., Chang, C., Wu, W., et al.: Increase of critical flutter wind speed of long-span bridges using tuned mass dampers. J. Wind Eng. Ind. Aerodyn. **73**(2), 111–123 (1998)
4. Dallard, P., Fitzpatrick, A., Flint, A., et al.: The London millennium footbridge. Struct. Eng. **79**(22), 17–21 (2001)
5. Gu, M., Chang, C., Wu, W., et al.: Increase of critical flutter wind speed of long-span bridges using tuned mass dampers. J. Wind Eng. Ind. Aerodyn. **73**(2), 111–123 (1998)
6. Lin, Y.-Y., Cheng, C.-M., Lee, C.-H.: A tuned mass damper for suppressing the coupled flexural and torsional buffeting response of long-span bridges. Eng. Struct. **22**(9), 1195–1204 (2000)
7. Chen, X., Kareem, A.: Efficacy of tuned mass dampers for bridge flutter control. J. Struct. Eng. **129**(10), 1291–1300 (2003)

8. Casalotti, A., Arena, A., Lacarbonara, W.: Mitigation of post-flutter oscillations in suspension bridges by hysteretic tuned mass dampers. Eng. Struct. **69**, 62–71 (2014)
9. Ingram, C., Szwarc, W.: Passive flutter suppression. J. Aircr. **13**(7), 542–543 (1976)
10. Karpel, M.: Design for Active and Passive Flutter Suppression and Gust Alleviation, vol. 3482. National Aeronautics and Space Administration, Scientific and Technical Information Branch (1981)
11. Bisplinghoff, R., Ashley, H., Halfman, R.: Aeroelasticity. Dover Publications, Mineola, NY (1996)
12. Fung, Y.: An Introduction to the Theory of Aeroelasticity. Dover Publications, Mineola, NY (1993)
13. Lee, B., Gong, L., Wong, Y.: Analysis and computation of nonlinear dynamic response of a two-degree-of-freedom system and its application in aeroelasticity. J. Fluids Struct. **11**, 225–246 (1997)
14. Dimitriadis, G.: Numerical continuation of aeroelastic systems: shooting vs finite difference approach. In: RTO-MP-AVT-152 Limit Cycle Oscillations and Other Amplitude-Limited Self-Excited Vibrations, AVT-152-025, Loen (2008)
15. Habib, G., Kerschen, G.: Suppression of limit cycle oscillations using the nonlinear tuned vibration absorber. In: Proceedings of the Royal Society of London A: Mathematical, Physical and Engineering Sciences, vol. 471, p. 20140976. The Royal Society, London
16. Habib, G., Detroux, T., Viguié, R., et al.: Nonlinear generalization of den Hartog's equal-peak method. Mech. Syst. Signal Process. **52**, 17–28 (2015)
17. Detroux, T., Habib, G., Masset, L., et al.: Performance, robustness and sensitivity analysis of the nonlinear tuned vibration absorber. Mech. Syst. Signal Process. **60**, 799–809 (2015)

Chapter 36
Adaptive Harmonic Balance Analysis of Dry Friction Damped Systems

Dominik Süß, Martin Jerschl, and Kai Willner

Abstract One of the most challenging tasks in structural dynamics is given by analyzing and predicting the behavior of jointed structures. In order to perform numerical investigations the Harmonic Balance Method (HBM) is a very mature and efficient technique for estimating the response behavior of such systems in the frequency domain. A better approximation can be obtained by accounting for more harmonic parts and introducing the Multiharmonic Balance Method (MHBM). This leads to a simultaneous reduction of efficiency due to a huge growth of the system dimensions.

The goal of this paper is to present an Adaptive Harmonic Balance Method joining together the advantages of both, HBM and MHBM. Therefore the number of harmonics accounted for is adaptively chosen as small as possible, in order to get an efficient procedure and as big as necessary, in order to obtain precise results. The selection is performed by various criteria estimating the most important harmonic parts from an user defined pool of harmonics.

Keywords Structural dynamics • Jointed structure • Harmonic balance • Adaptive procedure • FEM

36.1 Introduction

In this contribution, the focus is on investigating the behavior of a jointed structure over a broad range of excitation frequencies within the frequency domain corresponding to the stationary behavior in the time domain. Due to the nonlinear forces within the contact plane, it is not possible to perform an analytical transformation of the system equations into the frequency domain directly. Instead, a possible approach to approximate the nonlinear term is the usage of the HBM, e.g. [18], which was originally proposed by Kryloff and Bogoliuboff [10]. In the framework of the HBM it is assumed that a harmonic excitation of the system leads to a harmonic response. Dependant on the complexity of the contact law used, it might be necessary to adapt several further assumptions [6], in order to make it possible to analytically derive the fundamental harmonic Fourier coefficients of the nonlinear interface forces. The HBM is the most efficient method to calculate oscillations in the frequency domain. Nevertheless the negligence of higher harmonic parts might not always be a proper assumption for the underlying system dynamics.

Therefore a generalization or extension to periodic excitation $\boldsymbol{f}_e(t)$ and response functions $\boldsymbol{u}(t)$ can be achieved using the MHBM. They are approximated by the ansatz of a truncated Fourier series

$$\boldsymbol{f}_e(t) \approxeq \boldsymbol{F}_{e,(0)} + \sum_{k=1}^{n_h} \left(\widetilde{\boldsymbol{F}}_{e,(k)} e^{i \cdot k\omega t} + \widetilde{\boldsymbol{F}}^*_{e,(k)} e^{-i \cdot k\omega t} \right) \tag{36.1}$$

and

$$\boldsymbol{u}(t) \approx \boldsymbol{U}_{(0)} + \sum_{k=1}^{n_h} \left(\widetilde{\boldsymbol{U}}_{(k)} e^{i \cdot k\omega t} + \widetilde{\boldsymbol{U}}^*_{(k)} e^{-i \cdot k\omega t} \right) , \tag{36.2}$$

which resolves n_h harmonic parts and neglects all higher harmonics. In these formulae the subscript numbers in brackets show the respective harmonic part, the $\sim$ indicates that the corresponding values are complex and $*$ stands for the conjugate complex. By rearranging the Fourier coefficients,

$$\widetilde{\boldsymbol{U}} = \left[\boldsymbol{U}^T_{(0)} , \widetilde{\boldsymbol{U}}^T_{(1)} , \widetilde{\boldsymbol{U}}^T_{(2)} , \ldots , \widetilde{\boldsymbol{U}}^T_{(n_h)} \right]^T , \tag{36.3}$$

D. Süß (✉) • M. Jerschl • K. Willner
Chair of Applied Mechanics, University of Erlangen-Nuremberg, Egerlandstr. 5, 91058 Erlangen, Germany
e-mail: dominik.suess@ltm.uni-erlangen.de

G. Kerschen (ed.), *Nonlinear Dynamics, Volume 1*, Conference Proceedings of the Society for Experimental Mechanics Series,
DOI 10.1007/978-3-319-29739-2_36

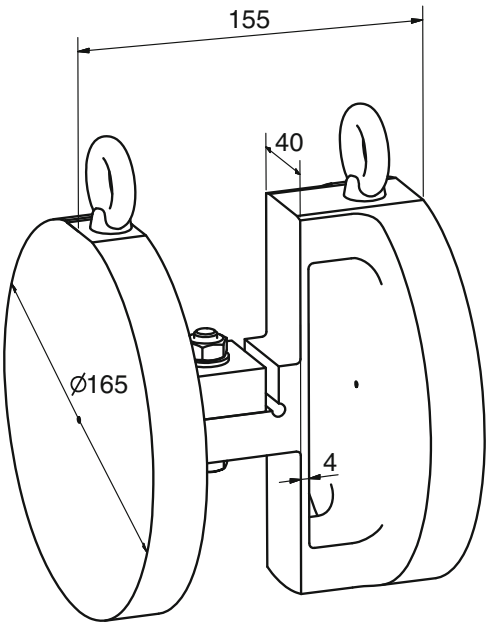

Fig. 36.1 Drawing of the friction resonator

the harmonic component representation of the system can be found as

$$\widetilde{\boldsymbol{S}}(\omega)\widetilde{\boldsymbol{U}}(\omega) + \widetilde{\boldsymbol{F}}_{nl}(\widetilde{\boldsymbol{U}}(\omega)) = \widetilde{\boldsymbol{F}}_{e}(\omega) \,, \tag{36.4}$$

where $\widetilde{\boldsymbol{S}}$ denotes the diagonal block matrix of harmonic dynamic stiffness matrices

$$\widetilde{\boldsymbol{S}}(\omega) = \mathrm{diag}(-k^2\omega^2\boldsymbol{M} + ik\omega\boldsymbol{D} + \boldsymbol{K}) \quad \text{with} \quad k \in \{1\,,\ 2\,,\ \ldots\,,\ n_h\}\,. \tag{36.5}$$

For the implementation of the MHBM there exist several strategies [3–5]. One of the most used techniques is the so called 'Alternating Frequency Time Domain Method' (AFT) [1, 2, 15]. Another alternative is used e.g. by [9, 11, 14] as a matrix transformation procedure with analytical integration of the Fourier integrals (here just abbreviated as SAI). The latter two algorithms are applied here in order to compute the frequency response of a jointed friction resonator, see Fig. 36.1.

Here the structure is represented by the FE model of Süß et al. [17] in combination with a three dimensional contact law based on Jenkin elements. Details about the integration of this law into the MHBM/AFT procedure can be found in [16]. The main advantage of the MHBM is, that it delivers quite precise results. However, the calculation times are much higher than using the classical HBM.

Figure 36.2 shows FRFs calculated with HBM and MHBM/AFT for a different number of harmonics accounted for.

The contact parameters for this investigation were fitted for the MHBM computation with 11 harmonics with respect to the measured FRF. This leads to a very good accordance of the calculation with the measurement. It can be seen that the HBM calculations results nearly do not differ from the MHBM results regarded for one harmonic. Both curves over-estimate the resonance peak. This is typical for calculations with only one harmonic, where the energy of the complete nonlinear system is pumped into this single harmonic. Nevertheless these two FRFs show a quite good accordance with the MHBM for 11 harmonics over a wide frequency range outside a certain region around the resonance.

The above mentioned facts led to the development of an Adaptive Harmonic Balance Method (AHBM) which combines the advantages of both HBM and MHBM in order to get an algorithm which is as precise and effective as possible. Since the HBM is the fastest way to calculate the stationary system response, this method should be used as often as possible whereas the MHBM for an adjustable number of harmonics should only be used if necessary. Therefore a good agreement of HBM and MHBM for one harmonic, like shown above, is important for the application of the AHBM. This directly depends on the assumptions made for the HBM.

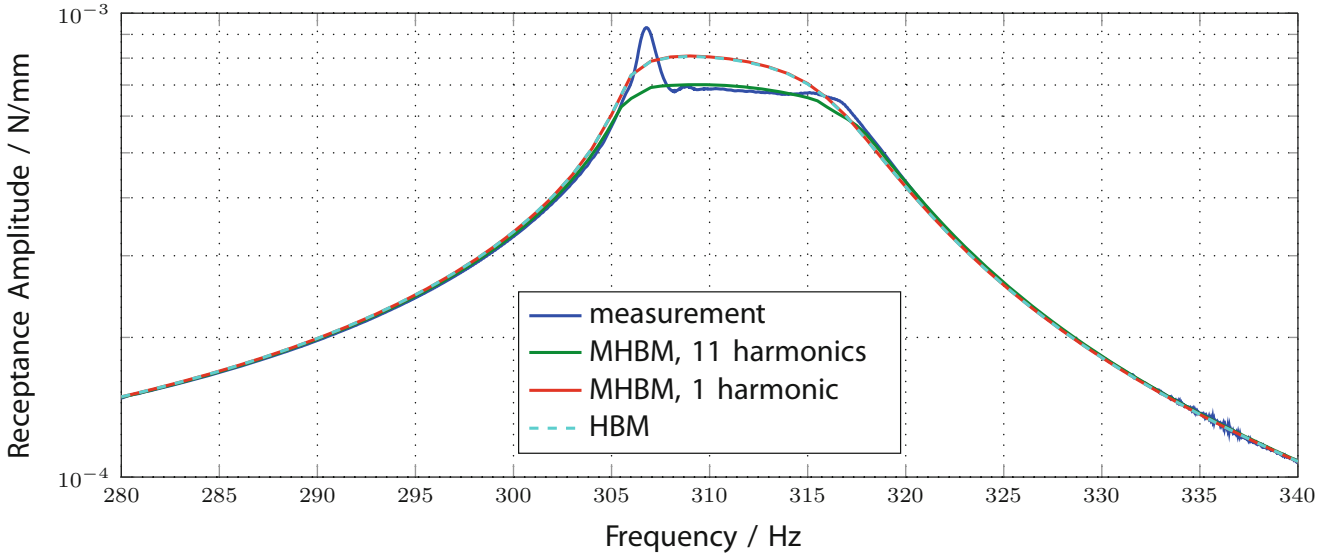

Fig. 36.2 Comparison of MHBM/AFT and HBM calculations with respect to a measured FRF of the friction resonator for an excitation force amplitude of 100 N and a bolting force of 1588 N

36.2 Adaptive Harmonic Balance Analysis

There already exists a variety of different approaches for the implementation of an Adaptive Harmonic Balance Method, see e.g. [12, 13] or [8]. However, most of these approaches seem not to be intended for an efficient performance. One problem comes through the repeated evaluation of one single frequency step in order to incrementally add harmonics. Another problem is the fixed addition of a user set number of harmonics without checking the relevance of these harmonics for the calculation.

A more convenient way is presented in [7] by utilizing an approximation of the Jacobian of all harmonics in order to derive a prediction of the harmonics needed for the next frequency increment. The approach presented in this paper has some similarities but was developed independently from the above citation. As already mentioned, the procedure shall be implemented as efficient as possible. Therefore the harmonics used for the calculation shall not be bound to an ascending sequence of natural numbers and shall be flexibly sorted in and out via a transformation procedure, see Sect. 36.2.1. Furthermore the additional effort for estimating harmonics shall be kept as low as possible and criteria for selecting harmonics shall be applied only once for each frequency increment, see Sect. 36.2.2.

36.2.1 Transformation of Harmonics

A transformation procedure is applied in order to flexibly put in and sort out harmonics. This transformation is applied each time the frequency iteration step (i) is incremented, see Fig. 36.3.

Regarding to that diagram this means that no separate iteration is used to stepwise de/activate harmonics since this is too time-consuming. Instead of that the last converged iteration (i) of the AHBM procedure is analyzed in order to get a guess for the harmonics needed for the next iteration ($i + 1$). The set of active harmonics does not have to be a continuous series, the harmonics can be chosen arbitrarily with only the first harmonic being set fixed. The transformation of the system equations is executed via a transformation matrix which is a zero matrix occupied with unit sub-matrices like sketched in Fig. 36.4.

Therefore harmonics which shall be neglected for the next iteration are just deleted and new harmonics are initialized with zeros.

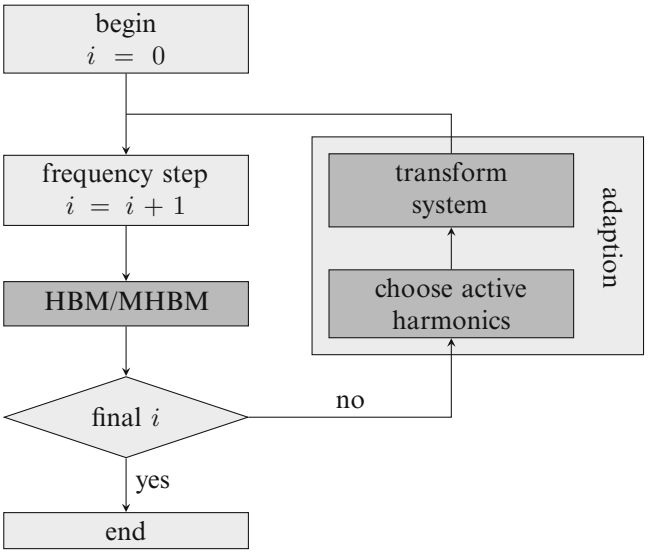

Fig. 36.3 Flow chart of the algorithm used for the AHBM

Fig. 36.4 Schematic assignment of transformation matrix in order to pick out harmonics 1 and 5 from the previous iteration and initialize harmonic 3 for the next iteration

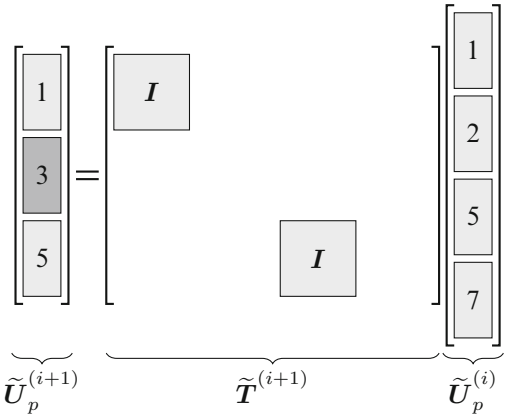

36.2.2 Criteria for Selecting Harmonics

For choosing the active harmonics (p) from the set of all possible harmonics (k) for the AHBM calculation, a proper criterion has to be found. Two possible approaches shall be presented here. The first one tries to estimate the appearing harmonics via the Fourier transform of the nonlinear contact forces. The second approach calculates the gradient of the nonlinear forces with respect to varying response displacements. For reasons of clarity subharmonics are neglected here although they can be integrated into the algorithm easily.

36.2.2.1 Approach 1: Estimation of Response Displacement Harmonics

During the (M)HBM procedure, only the active set of harmonics

$$\widetilde{\boldsymbol{U}}_{(p)}\,, \quad \text{with} \quad p \subset k\,, \tag{36.6}$$

is balanced. But for applying the selection criterion all harmonics

$$\widetilde{\boldsymbol{U}}_{(k)}\,, \quad \text{with} \quad k \in \{1\,,\ 2\,,\ \ldots\,,\ n_h\}\,, \tag{36.7}$$

have to be calculated/approximated. This can be achieved by first computing

$$\widetilde{\boldsymbol{F}}_{nl,\,(k\setminus p)}\left(\widetilde{\boldsymbol{U}}_{(p)}\right)\ , \tag{36.8}$$

which means the evaluation of the complete set of Fourier coefficients for all given harmonics of the response displacement. Afterwards the missing harmonics can be estimated by re-using Eq. (36.4),

$$\widetilde{\boldsymbol{U}}_{(k\setminus p)} = \left(\widetilde{\boldsymbol{S}}_{(k\setminus p)}\right)^{-1}\left(\widetilde{\boldsymbol{F}}_{e,\,(k\setminus p)} - \widetilde{\boldsymbol{F}}_{nl,\,(k\setminus p)}\right)\ . \tag{36.9}$$

For all coefficients now a filtering criterion can be set up. The following one checks if the distortion factor of harmonic (r) is greater than a user set tolerance:

$$c_{cor}\cdot\sqrt{\frac{\left\|\widetilde{\boldsymbol{U}}_{(r)}\right\|^2}{\sum_{q=1}^{n_h}\left\|\widetilde{\boldsymbol{U}}_{(q)}\right\|^2}} > tol\ . \tag{36.10}$$

Since all estimated/inactive harmonics $(k \setminus p)$ tend to be overestimated they are often put into the active set of harmonics although not really being important. If unimportant harmonics are activated, they are probably deactivated right after balancing them within the next frequency iteration step. This can lead to 'rattling' effects, where single harmonics are put in and out alternately. This effect can be reduced by firstly applying an adaptive correction coefficient c_{cor} for criterion (36.10), being a barrier for unimportant harmonics. Secondly, if harmonic (r) shall be rejected from the active set, a simple re-check is performed by setting it to zero,

$$\widetilde{\boldsymbol{U}}_{(p)} = \left[\widetilde{\boldsymbol{U}}_{(0)}\ ,\ \widetilde{\boldsymbol{U}}_{(1)}\ ,\ \ldots\ ,\ \boldsymbol{0}_{(r)}\ ,\ \ldots\right]^T\ , \tag{36.11}$$

and re-calculating

$$\widetilde{\boldsymbol{U}}_{(r)}\left(\widetilde{\boldsymbol{F}}_{nl,\,(r)}\left(\widetilde{\boldsymbol{U}}_{(p\setminus r)}\right)\right)\ . \tag{36.12}$$

Applying criterion (36.10) again, it can be evaluated, if harmonic (r) tends to be built up by the other harmonics. If this is the case, this harmonic should be kept active. Note that the importance of harmonics not only can be seen in high amplitudes but also in their influence on other harmonics and vice versa.

36.2.2.2 Approach 2: Estimation of Partial Derivatives

The second criterion presented here is not related to the response displacements themselves but to the influence of the variation of the displacements on the nonlinear forces. These partial derivatives are often already needed in order to apply a Newton-Raphson type solver and can be calculated analytically during the computation for all methods used here. Building the norm of the Jacobian

$$N_{(k,p)} = \left\|\frac{\partial\widetilde{\boldsymbol{F}}_{nl,\,(k)}}{\partial\widetilde{\boldsymbol{U}}_{(p)}}\right\| \quad \text{with} \quad k\in\{1\ ,\ 2\ ,\ \ldots\ ,\ n_h\} \quad \text{and} \quad p\subset k \tag{36.13}$$

the influence of one harmonic on all the other harmonics can be seen column wise. In order to get an objective result, the self-influence of the active harmonics is deleted by forcing the diagonal terms to equal zero,

$$N_{(p,p)} = 0\ . \tag{36.14}$$

Afterwards again a tolerance check can be set up to test the importance of harmonic (r):

$$N_{(r,p)} > tol\ . \tag{36.15}$$

On this way a single harmonic might be selected or deselected by other active harmonics. Therefore a 'majority decision' may be applied to un/select harmonics for the next frequency iteration.

The procedures explained above are now applied for calculations with a FEM model of a friction oscillator, see Fig. 36.1, with the results being limited to the approach 1 results. The chosen FE discretization is analogue to the one used in [17], which means a rather coarse mesh in order to get low computation times.

36.3 Numerical Results

Reference calculations using classical HBM and MHBM (AFT and SAI) are performed in order to validate the AHBM. In Fig. 36.5 all response displacement harmonics considered are shown as overlay for the MHBM/AFT calculation.

Besides the main resonance of the system around 313 Hz an interesting peak of the fourth harmonic can be found for an excitation frequency of 298 Hz. This corresponds to a modal interaction with the sixth eigenform of the system (a bending mode). The computational times needed for the reference calculations are summarized in Table 36.1.

As expected, the times are increased for MHBM calculations. Since the SAI delivers a much more efficient performance than the AFT, it shall be used for all following AHBM computations. For an excitation frequency of 311 Hz, friction hystereses are evaluated. These are plotted in Fig. 36.6 and show the 'viscous' elliptic hysteresis of the HBM calculation in comparison to the MHBM hysteresis, delivering the more likely form of a measurable friction hysteresis. An exact reproduction of measured hystereses cannot be established with the coarse mesh chosen here, but for a refined discretization the results are convincing, see [16]. The AHBM hystereses will lie somewhere in between these two reference curves.

In this contribution the AHBM shall be presented for the approach of estimating the response displacement harmonics. The distortion factor criterion is applied and three calculations for different tolerance values are performed. Figures 36.7, 36.8 and 36.9 show the corresponding spectra.

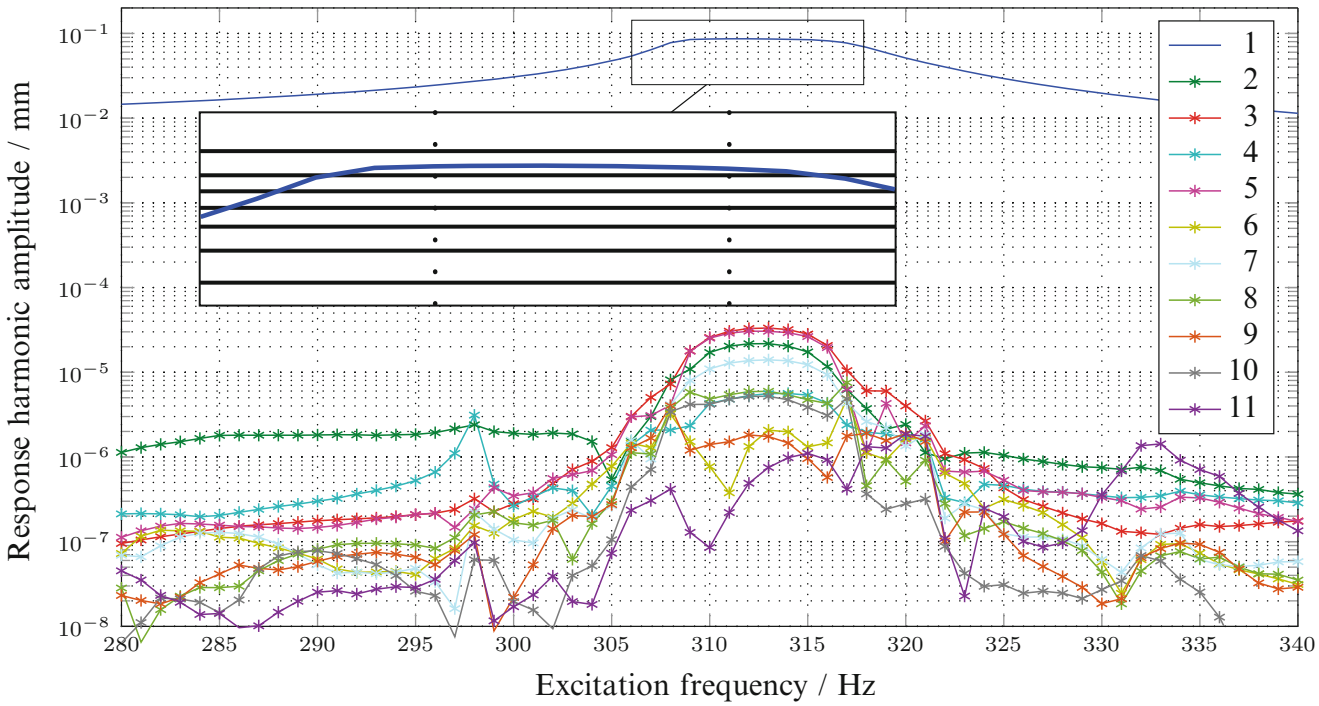

Fig. 36.5 Response displacement harmonics for a pure MHBM/AFT calculation considering 11 harmonics

Table 36.1 Comparison of calculation times for different (M)HBM methods

Method	Time (min)
HBM	1.8
MHBM/SAI	14.2
MHBM/AFT	253.5

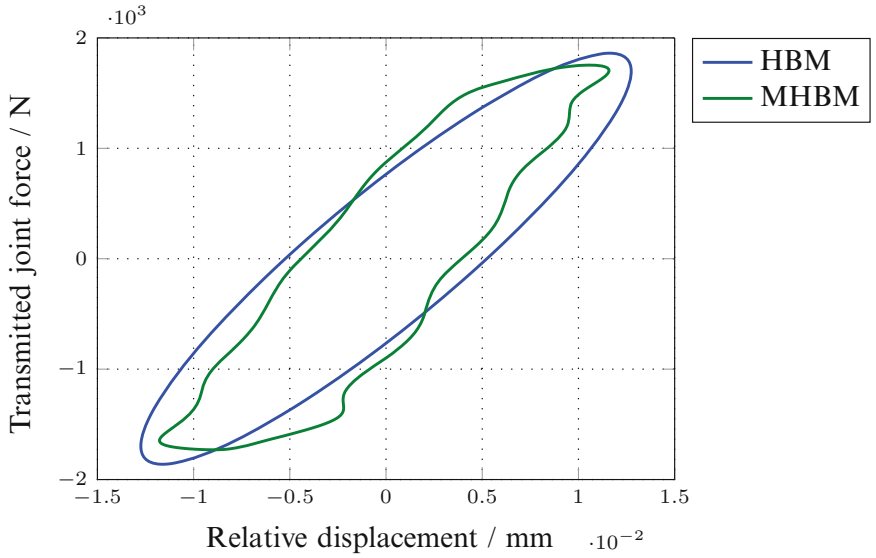

Fig. 36.6 Friction hystereses for a pure HBM and a MHBM/AFT calculation considering 11 harmonics

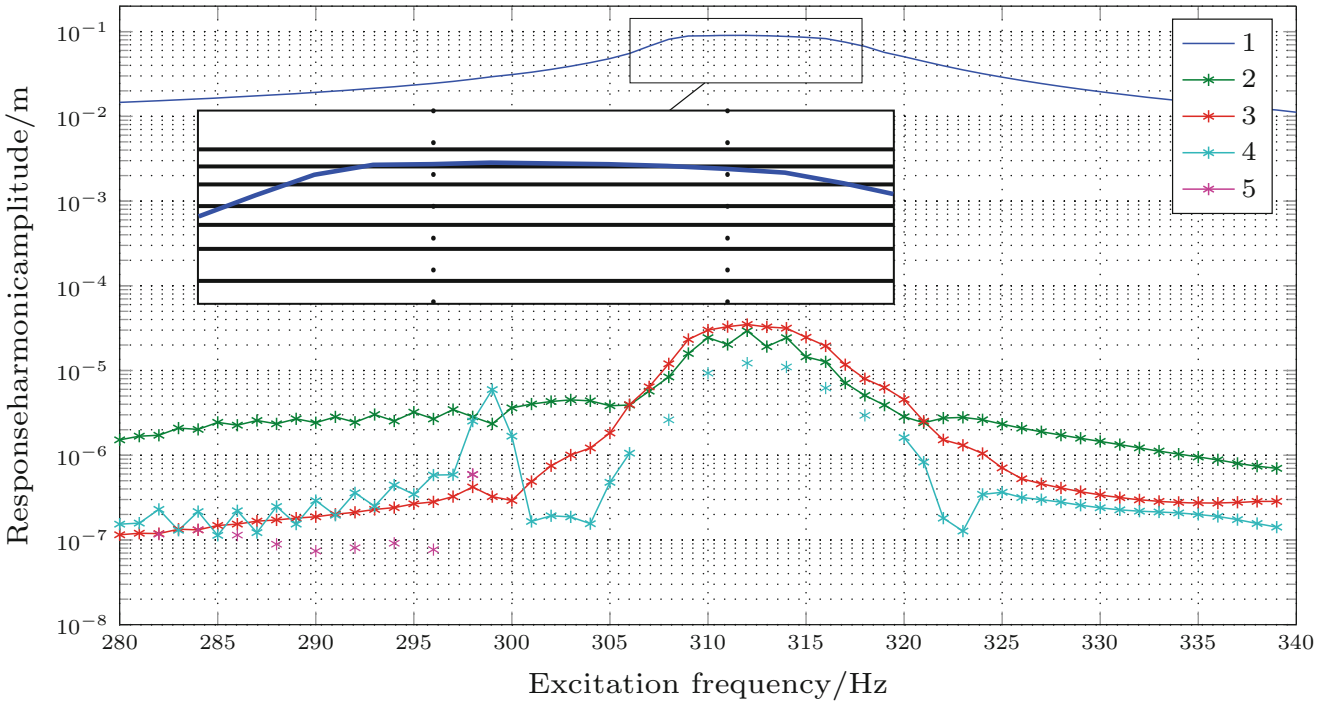

Fig. 36.7 Response displacement harmonics for an approach 1 AHBM/SAI calculation with a tolerance of $8 \cdot 10^{-2}$

It can be seen that for a decreasing tolerance the number of harmonics accounted for increases. A step-wise reduction of the first harmonic overestimation can be acknowledged. Although the algorithm was used analogue to Sect. 36.2.2 still some 'rattling' effects on the single harmonics can be recognized. Thus for example the fourth harmonic is de/activated alternately right within the resonance for the computation with a tolerance of $8 \cdot 10^{-2}$. In all three calculations the peak of the fourth harmonic at 298 Hz can be detected. The times of the respective calculations are summed up in Table 36.2.

The times rise parallel to the number of harmonics used for the computation and lie in the range of the reference times of HBM and MHBM. Having a look at the friction hystereses in Fig. 36.10 it can be seen that all three computations deliver a good compromise between the two reference calculations. Thus the AHBM with the best precision/efficiency ratio might be selected by the user.

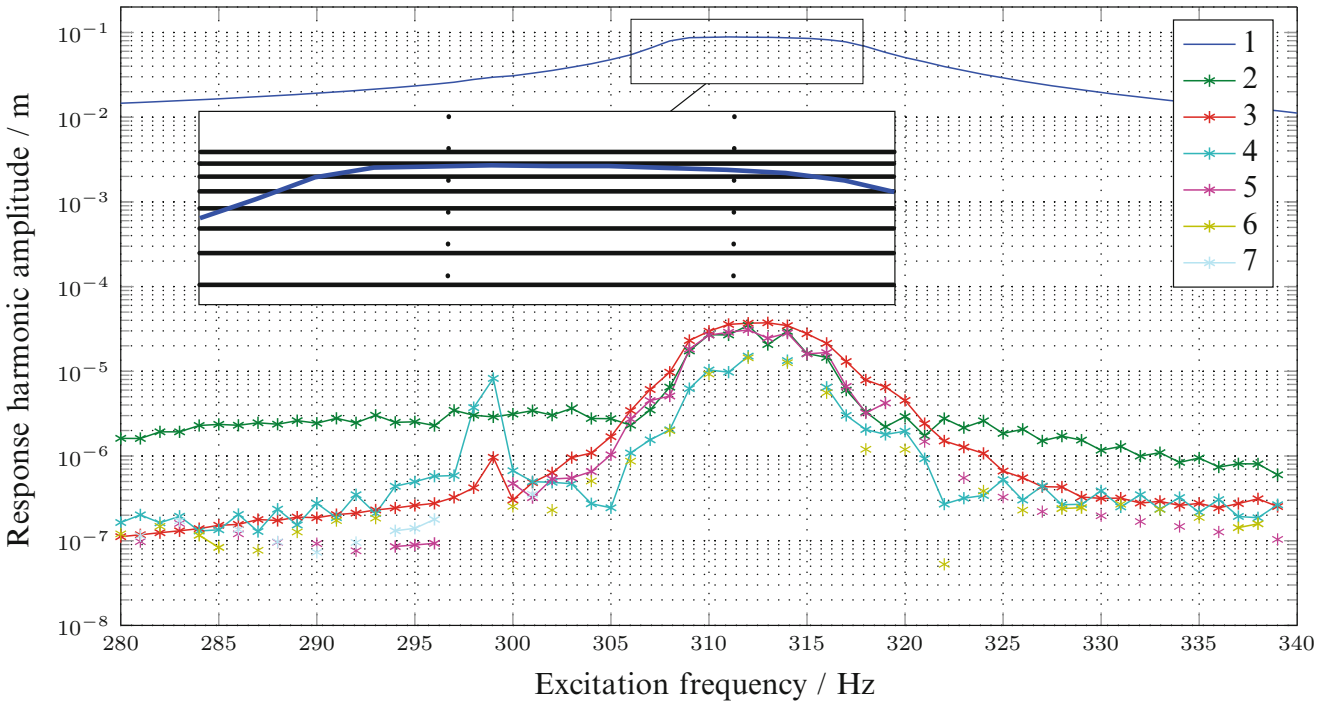

Fig. 36.8 Response displacement harmonics for an approach 1 AHBM/SAI calculation with a tolerance of $1 \cdot 10^{-2}$

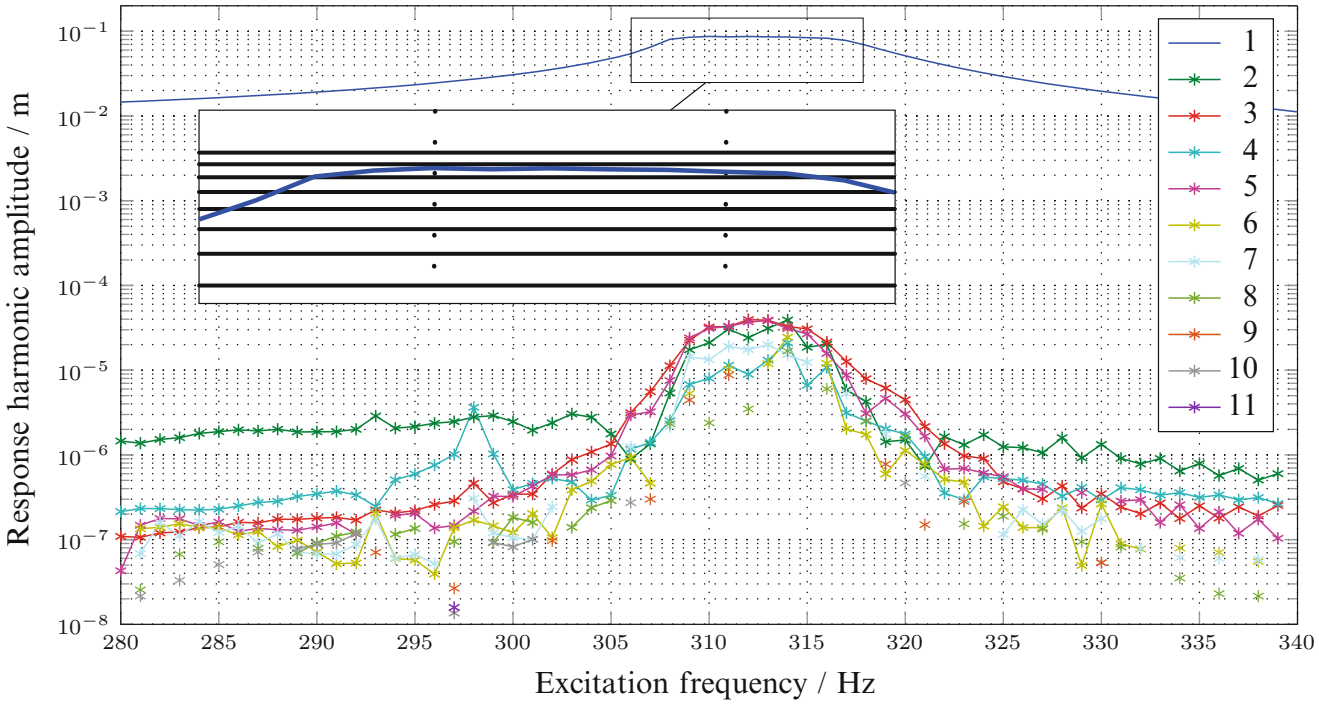

Fig. 36.9 Response displacement harmonics for an approach 1 AHBM/SAI calculation with a tolerance of $4 \cdot 10^{-3}$

Table 36.2 Comparison of calculation times for different approach 1 AHBM/SAI calculations

Tolerance	Time (min)
$8 \cdot 10^{-2}$	3.2
$1 \cdot 10^{-2}$	5.0
$4 \cdot 10^{-3}$	6.8

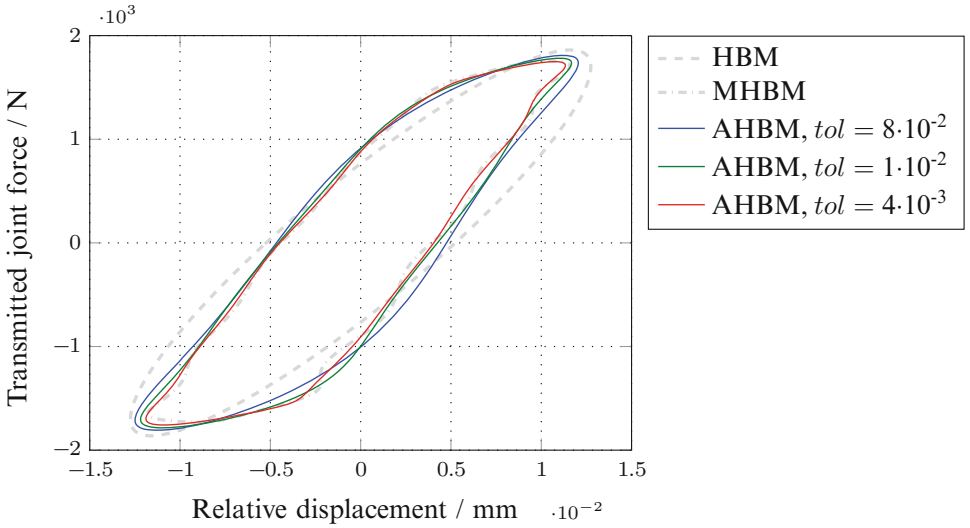

Fig. 36.10 Friction hystereses for approach 1 AHBM/SAI calculations with different tolerances

36.4 Conclusions

In this contribution an Adaptive Harmonics Balance Method is presented in order to perform calculations on a jointed structure in the frequency domain. The AHBM combines the advantages of classical HBM and MHBM. Two different approaches for the application of the AHBM are shown with both delivering different results. Approach 1 tends to bring out 'rattling', nervous behavior of single higher harmonics, but also manages to detect modal interactions for a wide range of tolerances. Approach 2 has smooth harmonic curves and a very good reproduction of the resonance peak. For both approaches the calculation times can be decreased compared to a full MHBM. The combination of both, the general modeling approach via ZT elements and the efficient computation using the AHBM brings out a powerful methodology for the calculation of the dynamics of jointed structures in the framework of the FEM.

References

1. Cameron, T.M., Griffin, J.H.: An alternating frequency/time domain method for calculating the steady-state response of nonlinear dynamic systems. J. Appl. Mech. **56**(1), 149–154 (1989)
2. Cardona, A., Lerusse, A., Géradin, M.: Fast Fourier nonlinear vibration analysis. Comput. Mech. **22**(2), 128–142 (1998)
3. Cochelin, B., Vergez, C.: A high order purely frequency-based harmonic balance formulation for continuation of periodic solutions. J. Sound Vib. **324**(1–2), 243–262 (2009)
4. Dunne, J.F., Hayward, P.: A split-frequency harmonic balance method for nonlinear oscillators with multi-harmonic forcing. J. Sound Vib. **295**(3–5), 939–963 (2006)
5. Ferri, A.A.: On the equivalence of the incremental harmonic balance method and the harmonic balance-Newton Raphson method. J. Appl. Mech. **53**(2), 455–457 (1986)
6. Geisler, J.: Numerische und experimentelle Untersuchungen zum dynamischen Verhalten von Strukturen mit Fügestellen. Ph.D. thesis, Friedrich-Alexander-Universität Erlangen (2010)
7. Grolet, A., Thouverez, F.: On a new harmonic selection technique for harmonic balance method. Mech. Syst. Signal Process. **30**, 43–60 (2012)
8. Jaumouillé, V., Sinou, J.-J., Petitjean, B.: An adaptive harmonic balance method for predicting the nonlinear dynamic responses of mechanical systems—application to bolted structures. J. Sound Vib. **329**(19), 4048–4067 (2010)
9. Krack, M., Panning-von Scheidt, L., Wallaschek, J.: A high-order harmonic balance method for systems with distinct states. J. Sound Vib. **332**(21), 5476–5488 (2013)

10. Kryloff, N.S., Bogoliuboff, N.N.: Introduction to Non-linear Mechanics. Annals of Mathematics Studies, vol. 11. Princeton University Press, Princeton (1947)
11. Lau, S.L., Zhang, W.-S.: Nonlinear vibrations of piecewise-linear systems by incremental harmonic balance method. J. Appl. Mech. Trans. ASME **59**(1), 153–160 (1992)
12. Laxalde, D.: Etude d'amortisseurs non-linéaires appliqués aux roues aubagées et aux systèmes multi-étages. Ph.D. thesis, Ecole Centrale de Lyon, Lyon (2007)
13. Maple, R.C., King, P.I., Oxley, M.E.: Adaptive harmonic balance solutions to Euler's equation. AIAA J. **41**(9), 1705–1714 (2003)
14. Petrov, E.P., Ewins, D.J.: State-of-the-art dynamic analysis for non-linear gas turbine structures. Proc. Inst. Mech. Eng. Part G: J. Aerosp. Eng. **218**(3), 199–211 (2004)
15. Poudou, O., Pierre, C.: Hybrid frequency-time domain methods for the analysis of complex structural systems with dry friction damping. In: 44th AIAA/ASME/ASCE/AHS/ASC Structures, Structural Dynamics, and Materials Conference. American Institute of Aeronautics and Astronautics, Norfolk, VA (2003)
16. Süß, D., Willner, K.: Investigation of a jointed friction oscillator using the multiharmonic balance method. Mech. Syst. Signal Process. **52–53**(1), 73–87 (2015)
17. Süß, D., Jerschl, M., Willner, K.: Investigation of jointed structures using the multiharmonic balance method. In: Kerschen, G., Adams, D., Carrella, A., (eds.) Topics in Nonlinear Dynamics, Volume 1. Conference Proceedings of the Society for Experimental Mechanics Series, vol. 35, pp. 223–228. Springer, New York, NY (2013)
18. Worden, K., Tomlinson, G.R.: Nonlinearity in Structural Dynamics: Detection, Identification and Modelling. Institute of Physics Publications, Bristol (2001)

Chapter 37
Dynamics of an MDOF Rotor Stator Contact System

Alexander D. Shaw, David A.W. Barton, Alan R. Champneys, and Michael I. Friswell

Abstract The vibrations of rotating machinery are an important issue in many engineered systems, from aircraft engines to drilling platforms. In many cases there is a possibility of rotor stator contact, which leads to non-smooth nonlinearities; this leads to complex multi period responses in a single rotor system, and poses a challenging problem when more degrees of freedom are considered. In this work we examine how interaction of the underlying modes of a two disc rotor, can lead to complex multi-period responses with intermittent contact. These motions can be excited at driving speeds that are well removed from the linear critical speeds of the rotor. However, it is demonstrated that the driving frequencies can be predicted and explained by synchronisation between two modal responses and the driving frequency.

Keywords Rotordynamics • Impact • Nonlinearity • Chaos • Whirl

37.1 Introduction

The vibrations of rotating machinery are an important issue in many engineered systems, from aircraft engines to drilling platforms[1]. Understanding of rotating machinery in linear operating regimes is well established, with classical matrix methods having been applied to deduce the whirl speeds of rotational systems with any number of degrees of freedom. However, there are many outstanding problems concerning nonlinearity in rotating systems, and these are leading to new approaches in a variety of industrial applications.

Patel and Darpe noted that cracks in rotors induce nonlinear effects and explored these effects with bifurcation analyses [2]. Ehrich has compiled a review of numerous nonlinear phenomena witnessed in tests on turbomachinery, including bifurcation routes to chaos, subharmonic resonance and other surprising effects such as bearing phenomenon that lead to a rotor slowly 'switching' between two amplitudes of vibration [3]. Contacts are a major source of nonlinearity in rotor systems; Jacquet-Richardet et al. published a comprehensive review on rotor-stator contact in turbomachinery [4].

Many studies are inspired by the complex needs of the drilling industry; a modern deep hole drilling assembly is a highly flexible rotor structure (relative to its length), subject to strong nonlinearity through contact forces. The complexity of this system is such that few studies describe it entirely; the majority of papers consist of far simpler studies on small aspects of the mechanics present. Richard et al. modelled the drill bit behaviour, demonstrating a stick-slip motion caused by the contact friction in combination with both axial and torsional modes of the shaft [5]. Germay et al. extended this work to consider the drill as a continuous structure, instead of as an equivalent discrete model [6]. Many of these phenomena are reported in on-site measurements reported by Leine et al. [7]. Liu et al. considered a model of the drill bit that allows non-smooth effects due to both friction and loss of contact when axial vibrations cause the drill bit to separate from the rock surface [8].

In other work, Karpenko et al. considered piecewise smooth models for rotors experiencing frictionless impacts with a snubber ring [9]. Karpenko et al. went on to compare these predictions with experiment in [10]. Edwards et al. considered a simple Jeffcott model with contact, and used time simulation to show that the bifurcation pattern changes significantly if torsional motion occurs.

The majority of studies in this field concern systems with relatively few degrees of freedom—typically they concern single disc systems, perhaps with the inclusion of torsional and flapping motions. There seems to be little literature aiming to handle nonlinearity in rotor systems with many more degrees of freedom. One exception to this is the experimental study by

A.D. Shaw (✉) • M.I. Friswell
College of Engineering, Swansea University, Bay Campus, Fabian Way, Swansea SA1 8EP, UK
e-mail: a.d.shaw@swansea.ac.uk

D.A.W. Barton • A.R. Champneys
University of Bristol, Queen's Building, University Walk, Clifton BS8 1TR, UK

G. Kerschen (ed.), *Nonlinear Dynamics, Volume 1*, Conference Proceedings of the Society for Experimental Mechanics Series,
DOI 10.1007/978-3-319-29739-2_37

Chu and Lu on a 2 disc system [11]. They showed some highly complex multi-period and quasiperiodic behaviour, although the authors comment that they could not directly trace the route into chaos due to experimental control issues. However, an alternative possible explanation for this is raised in a paper by Zilli et al. [12]. This showed how a synchronisation between the forward and backward whirl modes and the forcing of a single snubbed rotor system could cause a sudden onset of complex bouncing behaviour at certain drive speeds that are not near the linear critical speeds.

In this work we generalise the model in [12] to work with any two modes of a multi disk system, with any combination of forward and backward whirling. After developing the formulae, predictions are shown to compare well with simulations on a two disk shaft with a single snubber.

37.2 Synchronisation as the Cause of Bouncing Orbits

What follows is a generalisation of the analysis given in [12] to rotating systems with multiple whirling modes.

Consider a rotor consisting of a flexible shaft with N discs, located at the centre of a circular stator at one of the shaft sections. The shaft is slender, so that friction from impacts imparts negligible torque, hence friction and torsional degrees of freedom are neglected. The rotor is assumed to be driven at a constant angular speed Ω, and forced into vibration due to a small out of balance mass ε. This can be approximated as having $2N$ modes, a forward and a backward whirl for each disc. When no contact occurs, the system will achieve the largest amplitudes when Ω is near a forward whirl frequency; the out of balance forcing does not drive the backward whirl modes so they do not appear [1].

A necessary condition for a periodic motion with stator contacts is that at each contact there is an identical state of the rotor and the forcing, relative to the local surface angle of the stator. This state can be considered as a superposition of phasors, representing the whirling modes of the shaft and the forcing. If it is assumed (without loss of generality) that all phasors are in alignment at the start of a cycle, then it follows that they must be in alignment at the end of the cycle. The assumption of a perfectly centred circular stator then ensures that the above condition has been met.

In order to develop the reasoning above, we express this state in terms of three phasors; two whirling modes with angular speeds ω_{n1} and ω_{n2}, and the forcing phasor with angular speed Ω. The whirling speeds may be positive or negative, indicating forward or backward whirling respectively, whilst the forcing speed is always positive. A convention that $|\omega_{n2}| \geq |\omega_{n1}|$ is adopted. The two whirling phasors will align periodically, with period given by:

$$\tau = \frac{2\pi}{|\omega_{n2} - \omega_{n1}|} \tag{37.1}$$

Note that if the two speeds are opposite, this period will be shorter than either of the whirling periods. If the two speeds have the same sign, then this period is always greater than that of mode 2, and can be very large if the two speeds are similar. During this period, the first mode phasor will advance by an angle given by:

$$\gamma = \omega_{n1}\tau \tag{37.2}$$

At the same time, the forcing phasor will also advance by an angle

$$\alpha = \Omega\tau \tag{37.3}$$

A periodic alignment of all three phasors will occur if

$$\alpha = \gamma + 2\pi m \tag{37.4}$$

where m is an integer that will be positive if $\alpha > \gamma$, and negative for $\alpha < \gamma$. Substitution of Eqs. (37.1)–(37.3) into Eq. (37.4) gives a relationship for driving speeds that allow periodic contact motion:

$$\Omega = \omega_{n1} + m|\omega_{n2} - \omega_{n1}| \tag{37.5}$$

This equation shows that m cannot equal zero as this leads Eq. (37.5) to become $\Omega = \omega_{n1}$. If ω_{n1} is positive, a critical speed is present, in which case the resonant mode will dominate instead of the bouncing motion. Otherwise a negative ω_{n1} implies negative Ω which cannot occur. Finally, the requirement for $\Omega > 0$ defines a lower bound for m, and the maximum rotor speed of interest defines the upper bound.

37.3 Test System

The system under test is a simple two disc system shown in Fig. 37.1. The rotor is mounted on pinned bearings at each end of the shaft, with a stator with 1 mm clearance at the centre. The shaft is a steel tube with 5 mm outer diameter and thickness 1 mm. The discs are also made of steel with radii 0.15 and 0.2 m and thicknesses 0.01 and 0.02 m respectively. The shaft is 0.60 m long, with the smaller disc located 0.15 m from the left hand end, and the larger disc located 0.20 m from the right hand end. The stator is modelled as an additional stiffness of 100 kN/m always acting in the radial direction towards the centre. Forcing is provided by a small eccentricity ε on disc 1. The material definition includes a 1 % damping factor.

The system is mostly modelled using the free Matlab [13] scripts that accompany [1]. This was used to implement a simple finite element model of the structure, calculate critical speeds and provide a reduced order modal model for simulation, which was carried out in ODE45 with event detection used to locate changes between contacting and non-contacting motion, and restart the simulation with optimal properties accordingly.

The Campbell diagram for this system is shown in Fig. 37.2. Where forward whirl results cross the rotor speed line, we can expect to see classical whirling response when in the linear regime. Where the dot-dashed lines cross the rotor speed line, there is the possibility of bouncing contact oscillation involving the modes and value of m indicated.

37.4 Comparison with Simulation

In the following sections, a series of time simulations are performed in a similar process to that used in [12]. For each simulation, the rotor has an initial velocity of 750 rpm that is linearly ramped down to the target speed for the data point concerned in 0.5 s, creating initial transients with contacting motion. Then a period of 30 s is allowed for the response to settle, and then the system state at the stator is sampled once per forcing period for 250 periods. The radial displacement at each sample is then plotted on a graph against the forcing frequency. Whilst this is not a true bifurcation diagram, it gives a good indication of when complex non-periodic orbits have become stable.

37.4.1 Light Forcing

In this section, $\varepsilon = 0.50 \times 10^{-3}$, which is insufficient to cause significant nonlinearity as shown in Fig. 37.3. There is a strong peak in the response amplitude at approximately 80 rpm, and this agrees with the first crossing of a forward whirl frequency with the rotor speed in Fig. 37.2. A second weaker peak coincides with the second linear critical speed predicted by Fig. 37.2 at approximately 400 Hz. There is a small contact region at the top of the first peak.

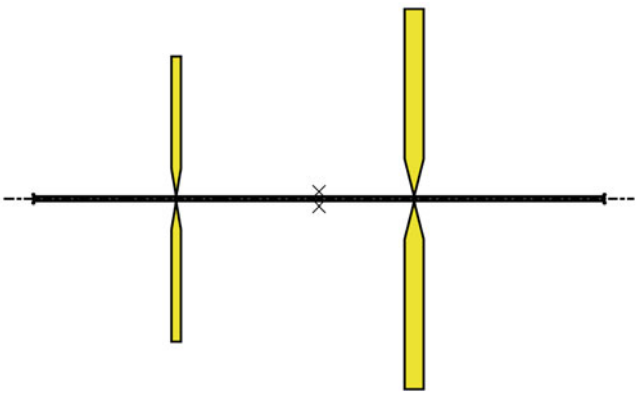

Fig. 37.1 Test system

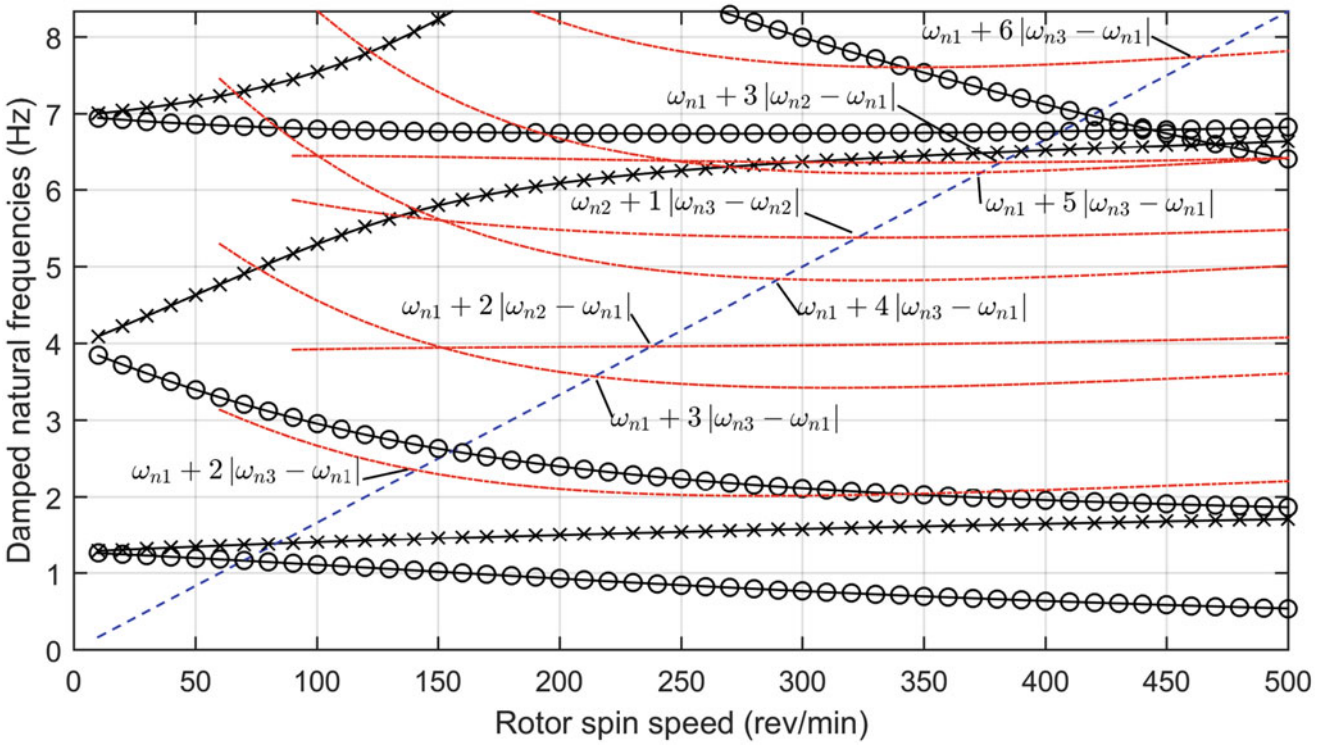

Fig. 37.2 Campbell diagram. *Crossed lines* indicate forward whirl modes, *circled lines* show backward whirl frequencies. The *blue dashed line* indicates the rotor speed, and the *dot-dashed lines* indicate the results of Eq. (37.5)

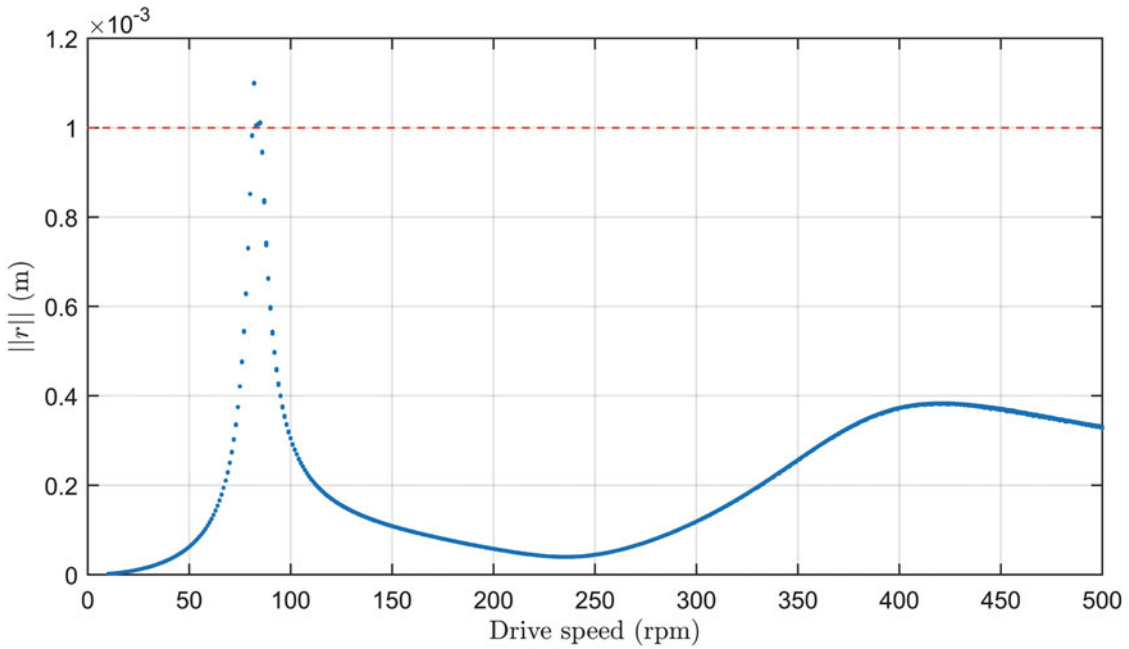

Fig. 37.3 Bifurcation plot at $\varepsilon = 0.50 \times 10^{-3}$

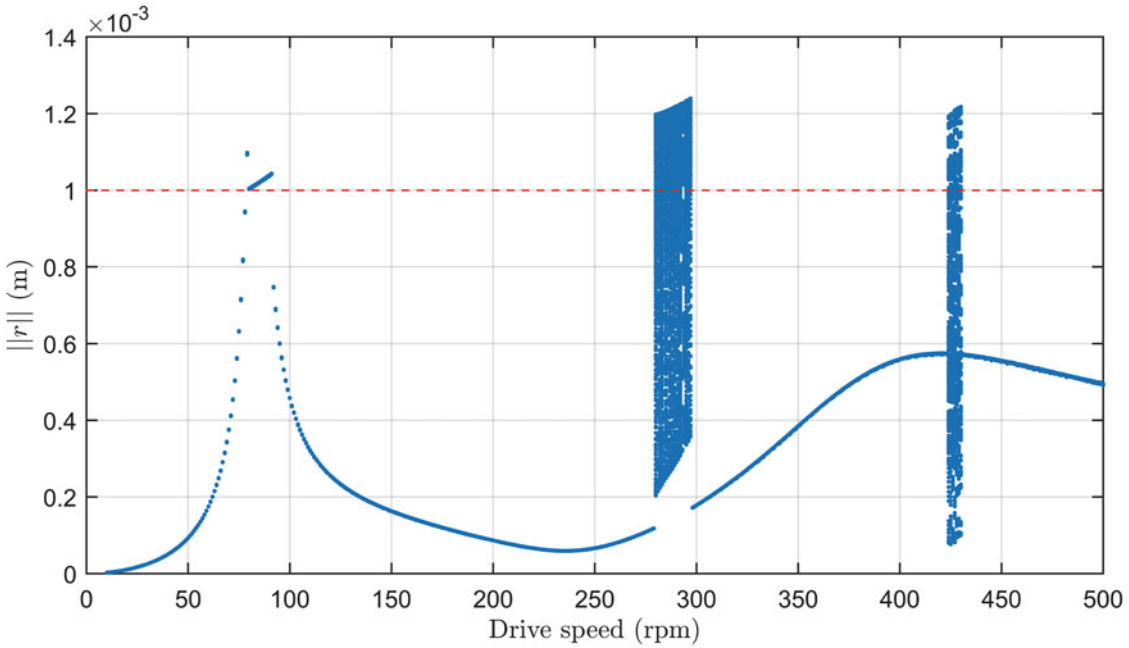

Fig. 37.4 Bifurcation plot at $\varepsilon = 0.75 \times 10^{-3}$

37.4.2 Moderate Forcing

With forcing increased to $\varepsilon = 0.75 \times 10^{-3}$, we see the introduction of abrupt transitions to high amplitude non-periodic response as shown in Fig. 37.4. It is clear however that not all the potential bouncing orbits indicated in Fig. 37.2 are activated at this forcing level. Furthermore, the onset of high amplitude motion at 280 rpm does not exactly match any of the crossing points shown in Fig. 37.2.

In order to gain further insight into the response at this region, we examine the response at 280 rpm and try to relate it to the known linear features of the system. From Fig. 37.5 we can instantly see that the motion is far from chaotic; the reason that it appears so on Fig. 37.4 must be that the period of motion is not an integer multiple of the forcing period used for sampling. If we consider the frequency content of this response, as shown in Fig. 37.6, again there is no exact match with the features shown in this graph and those in Fig. 37.2; the only clearly identifiable feature is the peak at 4.66 Hz, corresponding to the drive speed. However, it may be noted that the first two peaks (at 1.06 and 1.80 Hz) are just higher than the first forward and backward whirl modes at 280 rpm given in Fig. 37.2. These frequencies exactly satisfy Eq. (37.5) for $n = 1, m = 2$, confirming that this is an interaction between the first backward and forward whirling modes. The difference in frequencies is explained by the stiffening effect of the stator contact, as reported by Zilli et al. in [12].

A similar trend may be found for all the responses in this region up to 297 rpm. The fact that this region is relative broad, when the theory predicted isolated frequencies, shows that the amplitude dependence caused by nonlinearity is acting to broaden the region where this response is possible.

If we consider the second region between 424 and 430 rpm a similar analysis finds that this region is again an interaction between the first backward and forward modes, this time with $m = 3$. This motion has a highly complex orbit as shown in Fig. 37.7. Inspection of the time series of the magnitude of displacement in Fig. 37.8 shows that this motion features two contacts per cycle.

37.4.3 Harder Forcing

As the out of balance forcing is increased, we see a dramatic increase in the number of self sustaining impacting cycles that remain stable, as shown in Fig. 37.9. Furthermore, different combinations of whirling modes can become active. For example, at 387 rpm we see an orbit where the active modes are the first forward whirl and the second backward whirl as shown in

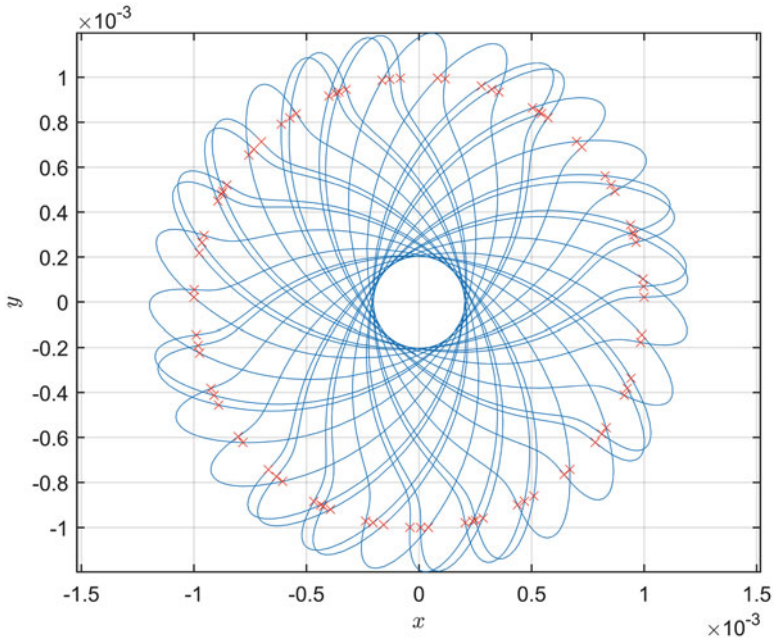

Fig. 37.5 Steady state orbits for $\varepsilon = 0.75 \times 10^{-3}$, drive speed 280 rpm. *Crosses* indicate transitions between contact and non-contact

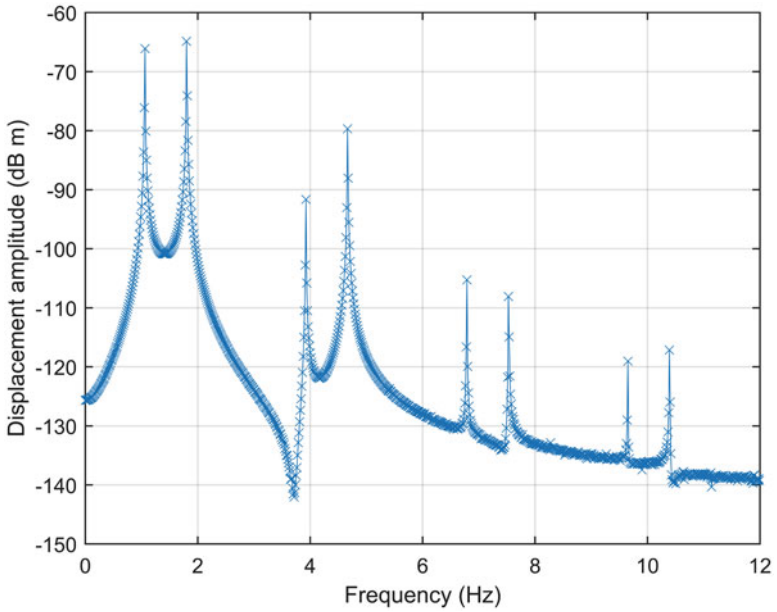

Fig. 37.6 Spectrum of x displacement response for $\varepsilon = 0.75 \times 10^{-3}$, drive speed 280 rpm

Fig. 37.10. In this figure, the first two peaks at 1.95 and 2.25 Hz are the first forward whirl and the second backward whirl respectively, while the peak at 6.65 Hz is the driving frequency. However, these values only approximately satisfy Eq. (37.5), an issue that requires further investigation.

At this amplitude, the use of Fig. 37.2 as a predictive tool is extremely limited, due to the distorting effect of nonlinearity on response frequencies. Furthermore, the majority of responses are now multi-period if not chaotic. For example, see the time signal of r for drive speed 240 rpm shown in Fig. 37.11.

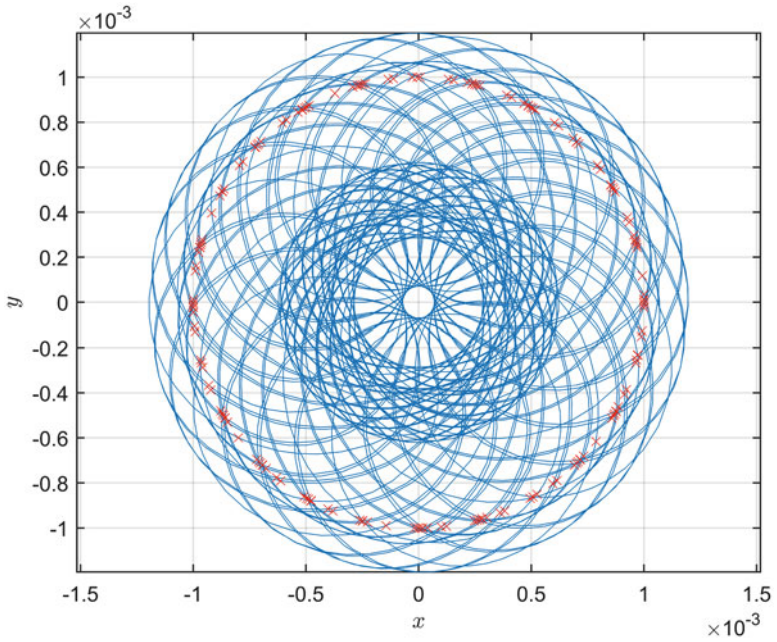

Fig. 37.7 Steady state orbits for $\varepsilon = 0.75 \times 10^{-3}$, drive speed 424 rpm. *Crosses* indicate transitions between contact and non-contact

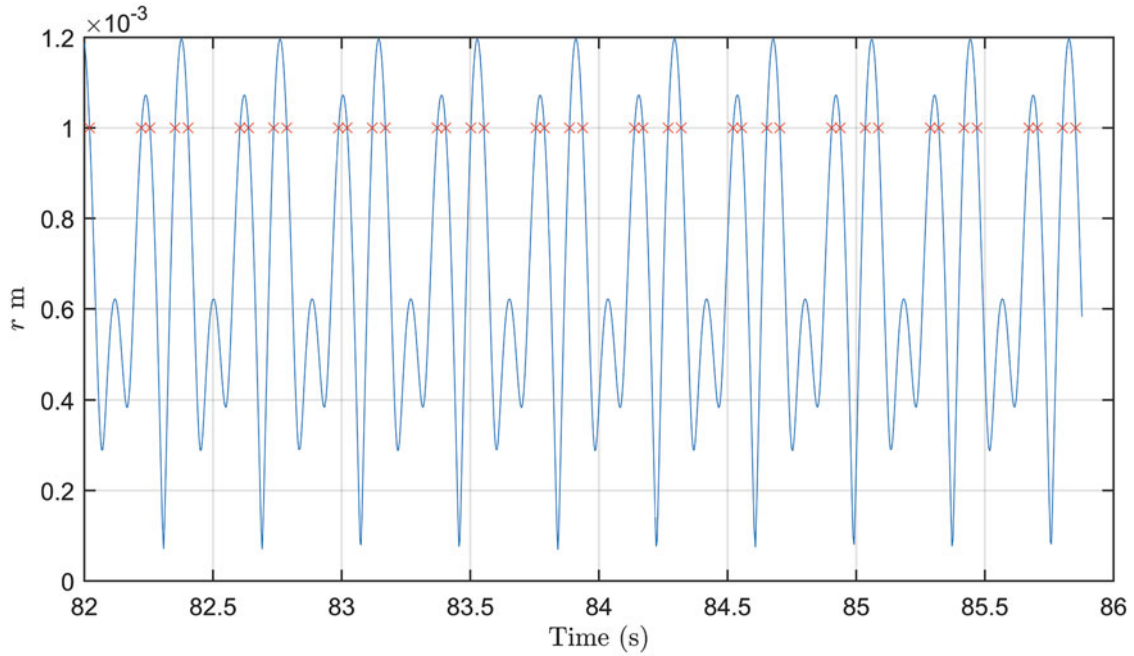

Fig. 37.8 Time series of radial displacement r, $\varepsilon = 0.75 \times 10^{-3}$, drive speed 424 rpm. *Crosses* indicate transitions between contact and non-contact

37.5 Conclusions and Future Work

A phasor analysis of when contacting oscillations of a snubbed rotor shaft may occur has been extended to shafts with higher numbers of degrees of freedom. Whilst there is a clear link between the underlying whirl modes and the onset of these oscillations, predictions are somewhat approximate, and the effect of nonlinearity on the whirling frequencies needs to be understood to improve accuracy. It has been seen that while these bouncing orbits are not in themselves chaotic, they can lead to chaotic or multiperiodic behaviour very rapidly.

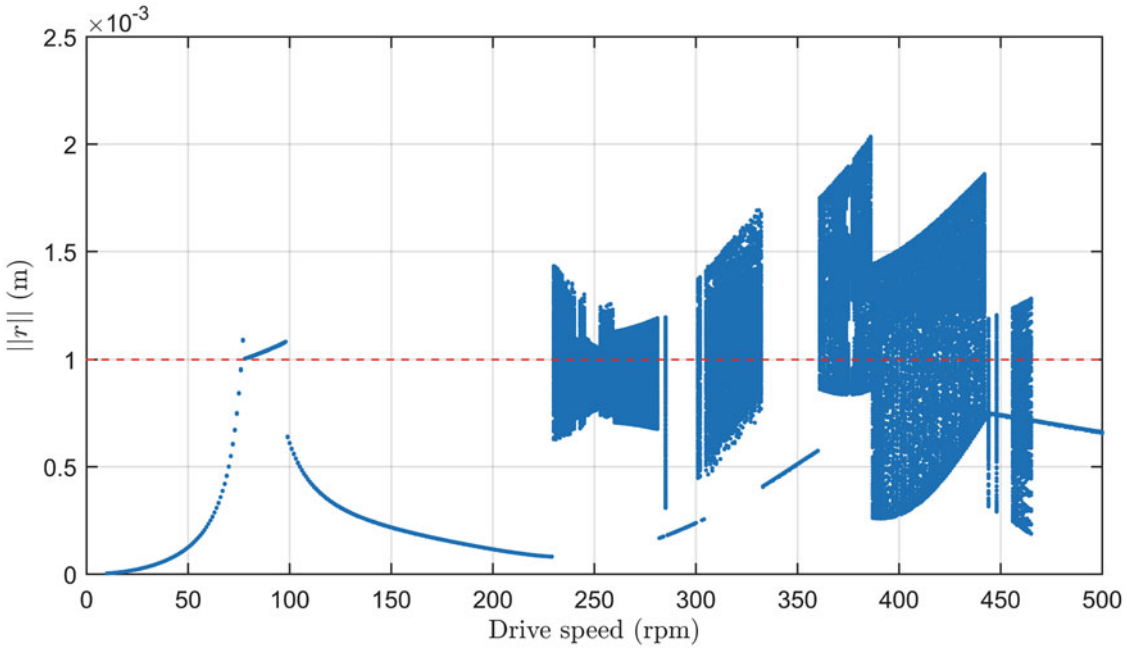

Fig. 37.9 Bifurcation plot at $\varepsilon = 1.00 \times 10^{-3}$

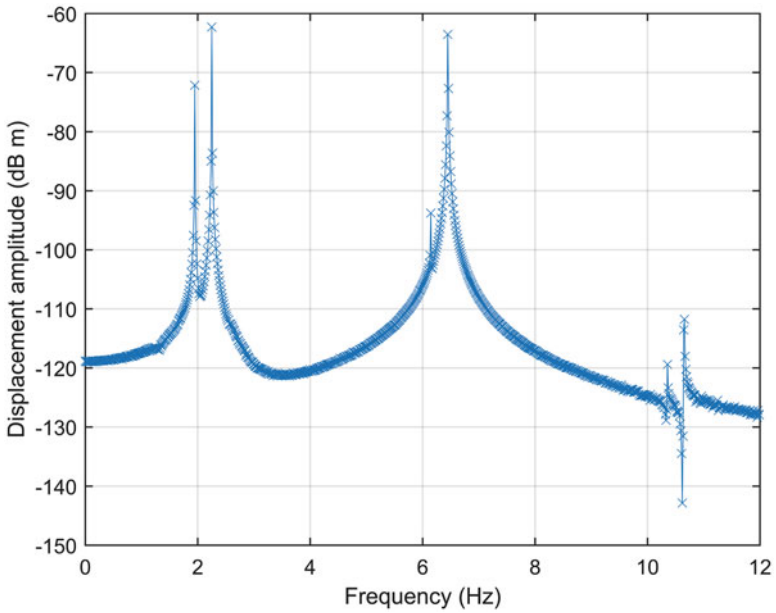

Fig. 37.10 Spectrum of x displacement response for $\varepsilon = 1.00 \times 10^{-3}$, drive speed 387 rpm

Acknowledgement The research leading to these results has received funding from the EPSRC grant 'Engineering Nonlinearity' EP/G036772/1.

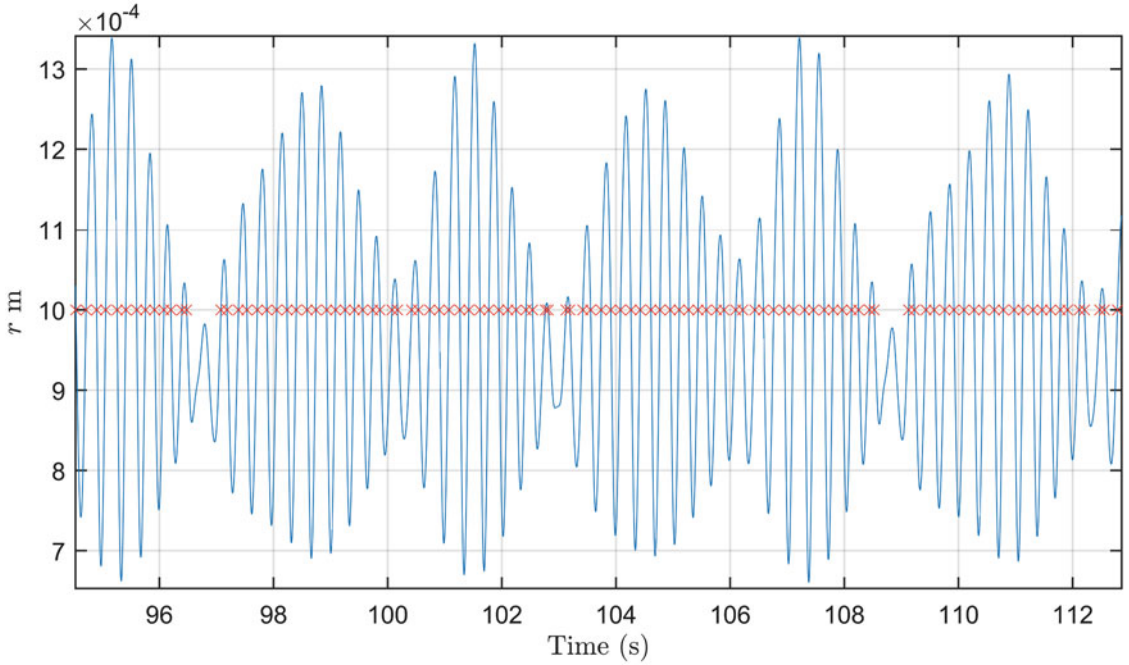

Fig. 37.11 Time series of radial displacement r, $\varepsilon = 1.00 \times 10^{-3}$, drive speed 240 rpm. *Crosses* indicate transitions between contact and non-contact

References

1. Friswell, M.I., Penny, J.E.T., Garvey, S.D., Lees, A.W.: Dynamics of Rotating Machines. Cambridge University Press, Cambridge (2010)
2. Patel, T.H., Darpe, A.K.: Influence of crack breathing model on nonlinear dynamics of a cracked rotor. J. Sound Vib. **311**(3), 953–972 (2008)
3. Ehrich, F.F.: Observations of nonlinear phenomena in rotordynamics. J. Syst. Des. Dyn. **2**(3), 641–651 (2008)
4. Jacquet-Richardet, G., Torkhani, M., Cartraud, P., Thouverez, F., Baranger, T.N., Herran, M., Gibert, C., Baguet, S., Almeida, P., Peletan, L.: Rotor to stator contacts in turbomachines. Review and application. Mech. Syst. Signal Process. **40**(2), 401–420 (2013)
5. Richard, T., Germay, C., Detournay, E.: Self-excited stick–slip oscillations of drill bits. C. R. Mec. **332**(8), 619–626 (2004)
6. Germay, C., Denoël, V., Detournay, E.: Multiple mode analysis of the self-excited vibrations of rotary drilling systems. J. Sound Vib. **325**(1), 362–381 (2009)
7. Leine, R., Van Campen, D., Keultjes, W.: Stick-slip whirl interaction in drillstring dynamics. J. Vib. Acoust. **124**(2), 209–220 (2002)
8. Liu, X., Vlajic, N., Long, X., Meng, G., Balachandran, B.: Nonlinear motions of a flexible rotor with a drill bit: stick-slip and delay effects. Nonlinear Dyn. **72**(1–2), 61–77 (2013)
9. Karpenko, E.V., Wiercigroch, M., Pavlovskaia, E.E., Cartmell, M.P.: Piecewise approximate analytical solutions for a Jeffcott rotor with a snubber ring. Int. J. Mech. Sci. **44**(3), 475–488 (2002)
10. Karpenko, E., Wiercigroch, M., Pavlovskaia, E., Neilson, R.: Experimental verification of Jeffcott rotor model with preloaded snubber ring. J. Sound Vib. **298**(4), 907–917 (2006)
11. Chu, F., Lu, W.: Experimental observation of nonlinear vibrations in a rub-impact rotor system. J. Sound Vib. **283**(3), 621–643 (2005)
12. Zilli, A., Williams, R.J., Ewins, D.J.: Nonlinear dynamics of a simplified model of an overhung rotor subjected to intermittent annular rubs. J. Eng. Gas Turbines Power **137**(6), 065001 (2015)
13. Matlab and Simulink for Technical Computing, July 2012